sustainability

Towards COP27

The Water-Food-Energy Nexus in a Changing Climate in the Middle East and North Africa

Edited by

Ahmed El Kenawy, Petra-Manuela Schuwerack, Zhongfeng Xu and Mohamed El-Alfy

MDPI

Towards COP27: The Water-Food-Energy Nexus in a Changing Climate in the Middle East and North Africa

Towards COP27: The Water-Food-Energy Nexus in a Changing Climate in the Middle East and North Africa

Editors

Ahmed El Kenawy
Petra-Manuela Schuwerack
Zhongfeng Xu
Mohamed El-Alfy

MDPI

Editors

Ahmed El Kenawy
Department of Geography
Mansoura University
Mansoura
Egypt

Petra-Manuela Schuwerack
School of Marine Science and
Engineering
Plymouth University
Plymouth
United Kingdom

Zhongfeng Xu
Institute of Atmospheric
Physics
Chinese Academy of Sciences
Beijing
China

Mohamed El-Alfy
Department of Geology
Faculty of Science
Mansoura University
Mansoura
Egypt

Contents

About the Editors

Ahmed El Kenawy

Dr. Kenawy is an assistant professor of Climatology at Mansour University, Egypt. He has authored or co-authored more than 100 peer-reviewed contributions, 3 books and 6 book chapters, with almost 4200 citations and a Hirsh index of 35 (Google Scholar). His research focuses on assessing, attributing and projecting climate extremes in arid and semi-arid regions and their socioeconomic and environmental implications. The research that Dr. Kenawy and his collaborators undertake has spanned the Arabian Peninsula, Syria, Iraq, and Jordan in the Middle East, North Africa (Libya and Egypt) and Ethiopia, throughout Spain and also South America: a testament to the global reach and application of his research activity. He has also acted as a reviewer for more than 45 leading SCI journals in the area of climatology, hydrology, and environmental sciences. He acts as a member of the editorial board for a range of SCI journals (e.g., *Hydrosphere*, *Journal of Water and Climate Change*, *Scientific African*, *PLOS Climate*).

Petra-Manuela Schuwerack

Petra-Manuela Schuwerack (B.Sc. Hons. M.Sc. Ph.D. PGCE) is an international scientist, based in Europe and the UK, is fluent in English, German, and has obtained good communication skills in Italian, French, and Spanish. Her multi-disciplinary approach builds links between man-made effects on a dynamic changing natural environment and the consequences for human resilience.

Zhongfeng Xu

Zhongfeng XU is a professor at the Institute of Atmospheric Physics (IAP), Chinese Academy of Sciences (CAS). He graduated from the school of atmospheric sciences, Nanjing University with bachelor's and Ph.D. degrees in 2001 and 2006, respectively. Dr. Xu was granted a postdoctoral fellowship from the University of Texas at Austin, USA in 2011. Dr. XU's research interests include: (1) land–atmosphere interaction with a special focus on the impacts of land use and land cover change on regional climate. (2) Dynamical downscaling of historical and future climate by using a high-resolution regional climate model driven by GCMs. He improved dynamical downscaling methods which can effectively constrain both GCM and RCM biases and lead to a more reliable projection of regional climate variability and extremes. (3) Developing novel statistical methods to quantitively assess model performance in simulating vector fields or model overall performance in simulating multiple fields.

As a climatologist, he has been involved in and led several research projects funded by National Natural Science Foundation of China or Ministry of Science and Technology of China. He published more than 50 peer-reviewed papers and served as reviewers for many international journals. He was awarded as excellent young researcher of Chinese meteorological society in 2014.

Mohamed El-Alfy

Professor Mohamed El Alfy is now employed in the Department of Geology at the University of Mansoura in Egypt. In arid areas, he conducts research in the areas of hydrogeology, hydrology, geostatistics, geographic information systems, and remote sensing. Groundwater and numerical modelling, saltwater intrusion in coastal aquifers, flash floods and rainwater harvesting, and water resource management in dry areas are among his research interests. He does research on integrated water management, aquifer recovery and restoration, and groundwater and surface water interaction. He collaborates with a number of national and international institutions.

Preface to "Towards COP27: The Water-Food-Energy Nexus in a Changing Climate in the Middle East and North Africa"

This MDPI journal of *Sustainability* provides a special contribution to its section Sustainable Water Management. The SI with its integrated approach to the dynamic interactions between water, food, and energy in a rapidly changing climate of the Middle East and North Africa (MENA) region is a compilation of 23 articles and contributions from more than 90 experts from multidisciplinary fields, such as hydrology, geography, meteorology, geology, pedology, engineering, etc.

Climate change has always existed throughout the 4.5 billion years of Earth's history. However, with the onset of the industrial revolution and an increasing global population, which reached 8 billion people on 14th November 2022, greenhouse gases through natural processes, such as the Sun's and volcanic activities, increased with human-induced activities, including the building of mega cities, so-called heat spots, with little to no plant life and aquatic systems, and enhanced CO2 levels due to the ever growing car and air traffic and industrial processes, to only name a few. Increased greenhouse gases (GHGs) in turn contributed vastly to a rise in atmospheric temperature leading to melting icecaps, accelerating heat transfer from air to water systems and erratic change of our global pressure systems and air–mass interactions.

High pressure arid regions with vast terrains of desert are first affected and include Africa and the Middle East. Little has been done to cultivate desert regions and integrate plant and tree life together with water sheds in mega cities. More than ever before it is vital for existing technologies and those introduced by authors of this SI to reach remote villages, as well as megacities, to eliminate water shortage and reduce heat output to support a balanced climate, guarantee the survival of global ecosystems and ultimately man, and the end of chaotic, unsustainable mass migration.

The past two decades have clearly shown a destabilization of the climate and its interaction and effects on nature and socio-economic activities which were magnified in 2022 with extreme atmospheric heating, leading to rapidly spreading, devastating forest and city fires, drying rivers, severe droughts in the MENA region and extending far into the European continent in the summer 2022.

It is therefore crucial that we focus on understanding the complex terrestrial and marine environments and their interactions with atmospheric dynamic processes. Added layers of human habitations and activities will then provide a better understanding of the effects these layers have on natural processes and, in turn, how human habitation and activities need to adapt and compensate. Investing present technology and changing habits and techniques in the MENA region for water and food production are absolutely vital not only for their own benefits but also to support a balanced global climate and socio-economic, as well as political stability.

Sharm el-Sheikh, Egypt, hosted to the 27th Conference of Parties (COP27) to the United Nations Framework Convention on Climate Change, from November 6 to 18, 2022. Discussions at the conference centered on what can be done to put plans into action, how to make good on financial promises, and how to compensate for loss and damage.

Thanks to Mansoura University and the MDPI, this SI was proposed and finalized. Explicit thanks to Mrs. Sally Li, the managing editor, and special gratitude to Mansoura University, Egypt, for covering publication fees, and for the MDPI for the guaranteed fee waivers of some accepted articles.

Ahmed El Kenawy, Petra-Manuela Schuwerack, Zhongfeng Xu, and Mohamed El-Alfy
Editors

Article

Evaluating the Impacts of Climate Change on Irrigation Water Requirements

Randa S. Makar [1,*], Sahar A. Shahin [1], Mostafa El-Nazer [2], Ali Wheida [2] and Mohamed Abd El-Hady [3]

1   Soils and Water Use Department, Agricultural and Biological Research Institute, National Research Centre, Dokki, Cairo 12622, Egypt
2   Theoretical Physics Department, Physics Research Institute, National Research Centre, Dokki, Cairo 12622, Egypt
3   Water Relations and Field Irrigation Department, Agricultural and Biological Research Institute, National Research Centre, Dokki, Cairo 12622, Egypt
*   Correspondence: randa_sgmm@yahoo.com or rs.georgy@nrc.sci.eg

Abstract: Climate change and its impact on agriculture and water resources have become a global concern. The implications of extreme weather events on food production and water resource availability are starting to have social and economic effects worldwide. The present research aims at integrating the analysis of the atmospheric parameters with remote sensing, geographic information systems, and CROPWAT 8 model to evaluate the impacts of climate change on the irrigation water requirements estimates in a selected area in El-Beheira governorate, Egypt. Remote sensing and GIS are incorporated to produce land-use/land-cover maps and soil properties maps. On the other hand, the atmospheric parameters were analyzed using python analytical coding. The study utilized the Land-use/Land-cover (LU/LC) map produced from Sentinel-2 data. The agricultural area covered about 89% of the studied area and was occupied by seven crops. Wheat and berseem were the major crops in the area and covered about 67% of the studied area; therefore, their irrigation water requirements were calculated utilizing the CROPWAT 8 model. Furthermore, citrus irrigation water requirements were also included in this research, even though it only covered 10% of the studied area because it had the highest amount of irrigation water requirements. Forecasting the potential climate changes under the best-case scenario for the next thirty years revealed that the studied area will have no rain and a slight decrease in the average temperature. Accordingly, the irrigation water requirements will increase by almost 4% under current practices, and the increase will reach about 13% under no-field loss practices.

Keywords: GIS; remote sensing; irrigation water requirements; CROPWAT model; climate change

1. Introduction

Climate change and global warming have become the main concern of studies in the field of water resources, agriculture, ecology, and other disciplines [1]. Global warming promoted shifts in the climatic zones of various parts of the world, causing expansion in arid zones and reduction of glacial areas—consequently resulting in changes in the abundance and seasonal activities of various plant and animal species. Climate change also caused changes in rainfall intensity, drought frequency and severity, wind speed, and rise in sea level [2]. An example of these changes was reported by [3]. They stated that the mean surface temperature in the Himachal Pradesh state of the Himalayan Mountains has increased by almost 0.5 °C from 2000 to 2014. These changes were directly related to global warming, caused a reduction in apple production in low altitudinal regions of the state, and created new opportunities for apple cultivation in higher regions where the growth conditions became more favorable for apples.

Irrigated agriculture depends on freshwater from rivers, lakes, and aquifers and it consumes about 70% of the total renewable water resources [4]. Agriculture is directly

affected by climatic conditions and changes, and it is essential to understand the impact of climate change on agricultural water resources for sustainable agriculture and to minimize the negative effects caused by such changes [1]. According to [5], lack of rainfall, soil moisture, and persistent above-normal temperatures are found to be the important factors in cases of severe loss in rice productivity in Bihar state, India. Furthermore, food security has been affected by climate change due to warming, changing precipitation patterns, and increasing frequency of extreme events [2]. Therefore, careful planning of water use by crops is of strategic importance from farm to the global level [6].

Remote sensing data have been excessively used in mapping the agriculture area and detecting their change as well as mapping water resources and their changes, which is vital for evaluating water availability and usability. Furthermore, the capability of GIS to analyze and visualize spatial information can be very important in water resources management. Considering their data collection and analysis capability, they are viewed as efficient and effective tools for irrigation water management. For example, remote sensing can be used in improving agricultural irrigation water accounting, both independently and in combination with in situ monitoring [7].

On the other hand, other studies utilized available models, such as CROPWAT, to develop sound water management strategies. The model was used to calculate the crop water requirements of selected crops under different environmental conditions, such as humid tropical areas [8] and Hungarian conditions [9]. The model was also utilized to study the crop water requirements when intercropping maize with rice, as well as intercropping maize with soybeans [10]. The model was also used to improve water management in selected on-farms in Egypt, and scenarios were suggested which could lead to saving irrigation water [11].

Moreover, remote sensing and GIS have been coupled with CROPWAT to simplify the water management process. CROPWAT was used to estimate the irrigation water requirements for selected crops and to compare the results with the farmer irrigation practices [12]. The author could verify that the irrigation practices exceeded the irrigation water requirement by 30%. The spatial distribution of irrigation water requirements in the study area derived by the GIS technique could be a good management tool for planners and decision-makers to minimize the overexploitation of the water recourses. An integrated approach of remote sensing, GIS, and CROPWAT model was used to determine the irrigation requirements of rice crops on different soils [13]. Satellite data were used to estimate the rice and fallow lands, and climate and soil data were integrated into the GIS platform. On the other hand, the CROPWAT model was used to determine crop evapotranspiration. Utilizing this approach, water deficiency and excess could be detected and could, thereafter, allow for better management in the studied area. The use of CROPWAT and GIS was studied to estimate crop water requirements in a selected area, and the results could be used for irrigation management of the different crops in the study area [14].

Moreover, CROPWAT was utilized in addition to climate models and under different scenarios to study the impact of climate change on crop water demand and irrigation requirements [6]. The results showed that under climatic changes in Serbia, irrigation water requirements will increase for sugar beet and potato to keep the actual quantity and quality of crop yield. A similar approach was followed, and the results revealed that there will be both rise and fall in crop water requirement for future scenarios when compared with baseline conditions depending on the crop [15].

The objective of the current work is to integrate the atmospheric data analysis remote sensing, GIS, and CROPWAT model to estimate the potential impacts of climate change on the irrigation water requirements of selected crops in a study area located in El-Beheira governorate, Egypt.

2. Materials and Methods

Figure 1 demonstrates the methodology and materials used in this study.
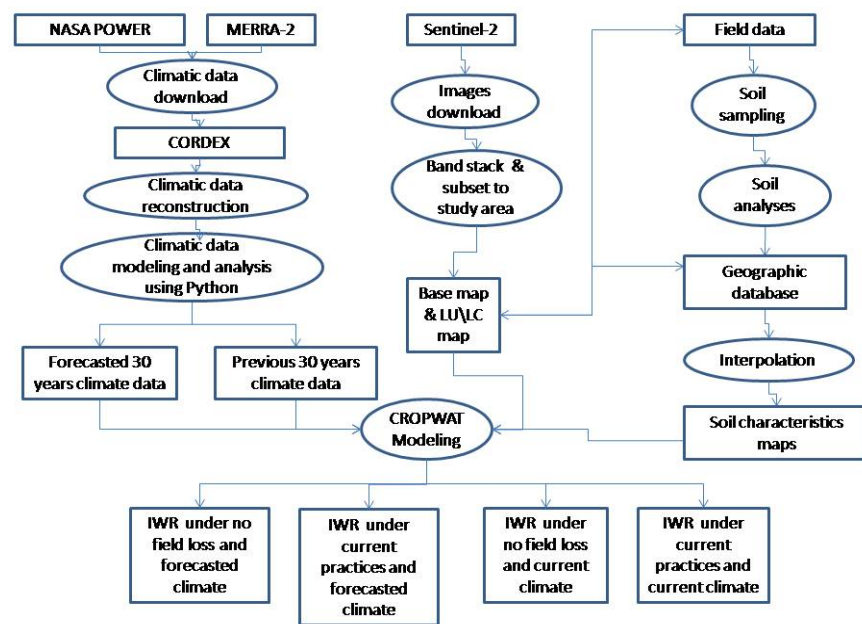
Figure 1. Methodology flowchart.

2.1. Study Area

The study area is located about 45 km south of Alexandria City and is considered part of El-Beheira governorate. The area is bounded by latitudes 30°41′55″ and 30°53′20″ N and longitudes 29°58′40″ and 30°11′20″ E. It extends to cover a total acreage of about 175 km². It is surrounded by three irrigation canals: Nubariyah Canal to the east, Al-Hidayah Canal to the north, and Al-Nasr Canal to the south, while Cairo–Alexandria Desert Road outlined its western boundary (Figure 2). The area is irrigated from An-Nasr canal via various small branches. Nevertheless, the area is characterized by shortage of irrigation water [16].

The land use/land cover map produced by [16] was used in this study. This map was produced from four Sentinel-2 (S2) images acquired on 18 October 2020, 27 December 2020, 17 March 2021, and 6 April 2021. The images used covered most of the winter growing season, which extended from October 2020 to May 2021. The overall classification accuracy was 86.8% (Figure 3). According to the same authors, wheat and berseem were the major crops in the study area and covered about 67% of the study area. Green beans, potato, and citrus covered about 21%, while guava and strawberry covered less than one percent each (Table 1).

Table 1. Acreage of the Land use/Land cover units.

Class	km²	%
Wheat	60.08	34.19
Berseem	57.27	32.59
Green beans	21.00	11.95
Potato	6.32	3.60
Citrus	10.00	5.69
Strawberry	0.87	0.50
Guava	0.80	0.46
Fish ponds	3.48	1.98
Settlements	15.89	9.04
Total	175.71	100.00
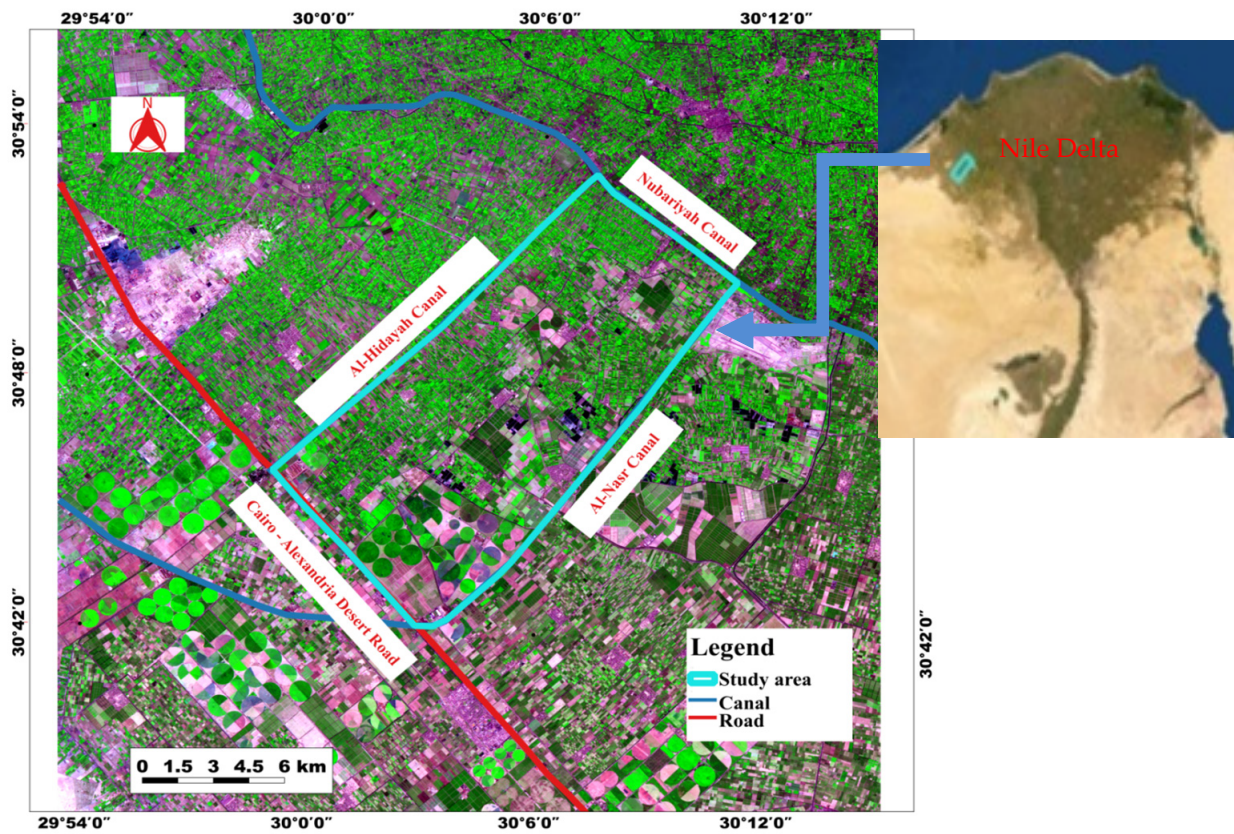
Figure 2. Location map of the study area (modified after [16]).
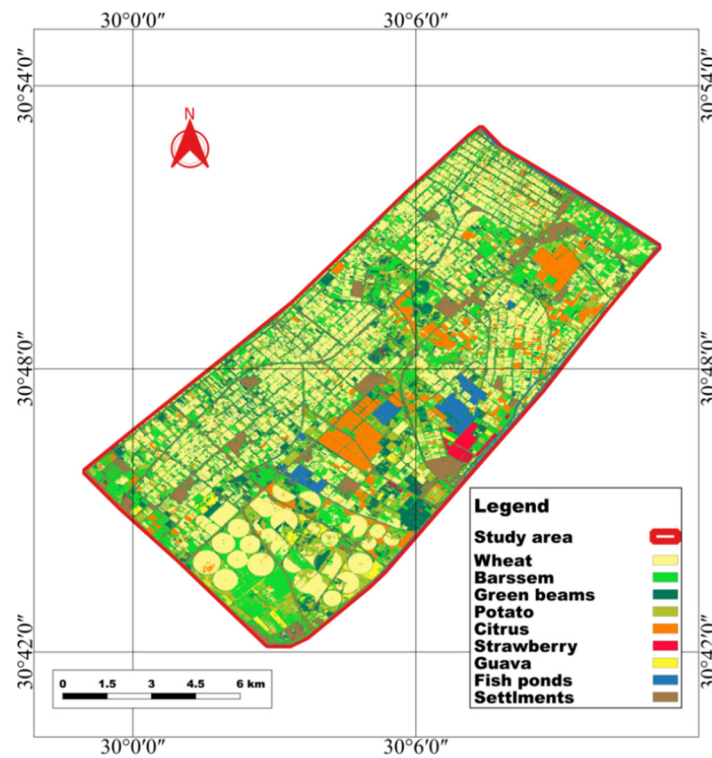
Figure 3. Land use/Land cover classification map of the study area (Modified after [16]).

2.2. Fieldwork

Fieldwork was carried out from December 2020 to March 2021. Soil sampling was designed along a grid system (1 observation per 1 km^2), and samples were collected using an auger. A total of 167 soil observations were planned for analyses, but only 149 samples were collected due to the inaccessibility of sample locations (Figure 4). Samples were geo-referenced using a GPS utility. For orchards, three soil samples were collected to 120 cm, while for other crops, two samples were collected to 75 cm depth. For each location, the weighted average of each measured soil characteristic was calculated [17].
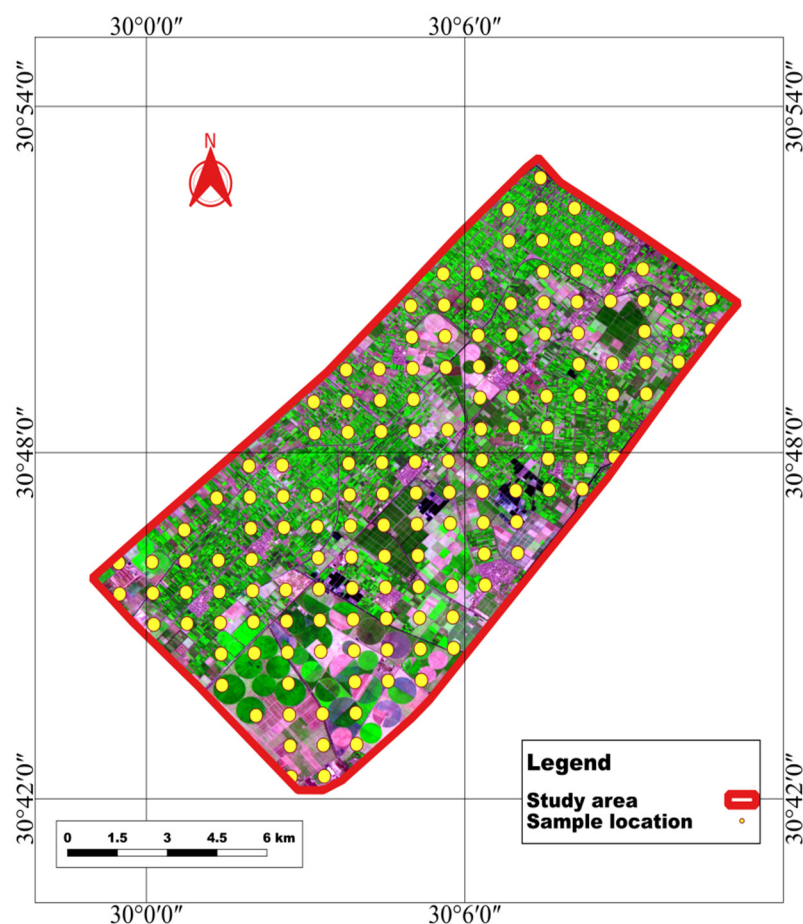
Figure 4. Location map of the soil samples.

2.3. Laboratory Analysis

The collected soil samples were air-dried, ground gently, and sieved through a 2 mm sieve. They were analyzed concerning the soil's physical properties. Determining the sample's particle size distribution was according to [18]. Other soil physical properties, including wilting point, field capacity, bulk density, hydraulic conductivity, and available water, were determined according to [19].

2.4. Geostatistical Analysis

After the average weight values calculated to the designated depths were calculated for each soil characteristic, these data were added to the QGIS software to produce a detailed soil database.

Spatial interpolation is the process of using a set of point data to create surface data [20]. Spatial interpolation has been widely and commonly used in many studies on a set of sampled points, such as soil properties, temperature, and precipitation, to produce a continuous representation of the phenomenon in question [21].

The inverse distance weighting (IDW) was developed by the U.S. National Weather Service in 1972. IDW is considered one of the most frequently used deterministic models in spatial interpolation. It is relatively fast and easy to compute, and straightforward to interpret. Its general idea is based on the assumption that the attribute value of an unsampled point is the weighted average of known values within the neighborhood, and the weights are inversely related to the distances between the prediction location and the sampled locations [22].

2.5. The CROPWAT Model

The crop water requirement refers to the total amount of water required by the crop from the time of cultivation to the time of harvest. On the other hand, the irrigation water requirement refers to the difference between the evapotranspiration of the crop under ideal conditions and the effective rainfall throughout the growing season. It is a measure of the excess quantity of water added through irrigation to guarantee optimum crop growth conditions [15].

The CROPWAT 8.0 is an empirical process-based crop model [23]. It provides an opportunity for automation of all the necessary calculations for evapotranspiration determination. The model uses the Penman–Monteith method as a base for calculations of evapotranspiration, crop water requirements, irrigation water requirements for separate crops and crop rotations, building of the irrigation schedules, etc. [24]. The Penman–Monteith methodology is recommended for estimating crop water requirements, especially for planning purposes [25]. The advantage of CROPWAT is its simplicity and easiness to use. Furthermore, the program requires less intense data. The model analyzes complex relationships of on-farm parameters, including crop, climate, and soil, for assisting in irrigation management and planning [9]. Its main functions are to calculate reference evapotranspiration, crop water requirements, and crop irrigation requirements to develop irrigation schedules under various management conditions, scheme water supply, and evaluate the efficiency of irrigation practices [26].

2.6. Climate Data Processing

2.6.1. Climate Data Download and Extraction

The climatic data used and analyzed in this study were obtained from NASA's POWER (Prediction Of Worldwide Energy Resource) and The Modern-Era Retrospective Analysis for Research and Applications, version 2 (MERRA-2). NASA POWER is available for download from https://power.larc.nasa.gov/data-access-viewer (accessed on 1 January 2021). The data available from this site are in grid resolution 0.5×0.5 degrees [27]. On the other hand, MERRA-2 is the latest atmospheric reanalysis of the modern satellite era produced by NASA's Global Modeling and Assimilation Office (GMAO), and has a spatial resolution of 0.5×0.67 degrees (latitude $\times$ longitude) [28]. MERRA-2 data are available at https://giovanni.gsfc.nasa.gov/giovanni (accessed on 1 January 2021).

The data collected and processed for the studied area included only: Day Length (sunshine hours), Precipitation (mm/month), Temperature at 2 m (°C), Maximum Temperature at 2 m (°C), Minimum Temperature at 2 m (°C), Wind Speed at 10 m (m/s), and Relative Humidity at 2 m (%).The temperature at 2 m, maximum and minimum temperatures were available at hourly time step and were used to deliver daily values, while the other variables were daily values already, and the data were continuous with no missing values. All the data were downloaded from MERRA-2, except the sunshine hours which were downloaded from NASA's POWER.

The Coordinated Regional Climate Downscaling Experiment (CORDEX), a framework sponsored by the World Climate Research Program, which is responsible for the global coordination of regional climate downscaling to improve regional climate change adaptation and impact assessment, was used in this study [29]. Both Weather Research and Forecasting model (WRF) and Regional Climate Model (RegCM) within the CORDEX were used to determine which could provide the necessary climate variables to reconstruct a

weather file that will be used as an input for at least one future scenario (temperature, solar radiation, relative humidity, atmospheric pressure, cloud cover, and wind speed) [30,31]. The reconstructed weather data were available in the popular NetCDF4 format.

2.6.2. Climate Data Analysis

The daily maximum and minimum temperature data were quality controlled for the period from 1991 to 2020 (i.e., outliers were checked and verified with metadata and corrected where applicable). Climate data analysis included checking and analyzing the temperatures over the historical period (1991–2020) as a reference period and carrying out a future run for the period 2021–2050; considering thirty years is standard in climatology to eliminate the uncertainty related to the internal climate variability. These historical periods are usually used in the literature and are the least referenced periods that are available on the platform. According to the literature, it is generally accepted that the 21st century can be divided into three equal future periods: The short-future (2011–2040), medium-future (2041–2070), and long-future (2071–2100) [30]. The data were processed using Python analytical coding.

3. Results and Discussion

3.1. Climatic Data Processing

The monthly meteorological data for the last thirty years (1991–2020) revealed that the maximum temperature ranged from 23.4 to 41.1 °C, while the minimum temperature ranged from 12.0 to 23.9 °C. The maximum temperature was recorded in June, whereas the minimum was recorded in January. The average minimum and maximum temperatures were 18.4 and 33.8 °C, respectively. The maximum relative humidity was 64.7%, while the minimum was 47.1%. The wind speed ranged from 229 to 286 km/day, with an average of 254 km/day. The average sunshine period was 10.5 h. There was no rain during August and almost no rain in May, June, July, and September. The highest amount of rain was in April and reached 7.6 mm/month. The total annual rain throughout the year was 39.4 mm (Table 2).

Table 2. Meteorological data of the studied area from 1991–2020.

Month	Temperature °C		Humidity (%)	Wind (km/Day)	Sunshine (Hours)	Precipitation (mm)	ET_o mm/Day
	Tmax	Tmin					
Jan.	23.4	12.0	64.7	240	10.4	6.1	3.01
Feb.	26.8	12.1	60.8	243	10.4	5.4	3.94
Mar.	31.9	14.8	55.8	256	10.5	6.9	5.51
Apr.	37.1	18.3	48.9	269	10.5	7.6	7.45
May	33.5	16.0	53.5	259	10.5	0.5	6.79
Jun.	41.1	22.4	47.1	286	10.5	0.5	8.74
Jul.	40.9	23.7	49.7	280	10.5	0.2	8.58
Aug.	39.8	23.9	52.1	259	10.6	0.0	7.80
Sep.	38.8	23.1	53.9	253	10.6	0.2	7.10
Oct.	36.1	21.4	57.6	237	10.6	2.4	5.71
Nov.	30.7	17.9	61.5	229	10.6	6.3	4.41
Dec.	25.4	14.5	64.5	237	10.7	3.3	3.14
Average/ Total	33.8	18.4	55.9	254	10.5	39.4	5.99

The monthly meteorological data for the next thirty years (2021–2050) are shown in Table 3. The data revealed that the maximum temperature ranged from 19.6 to 38.9 °C, while the minimum temperature ranged from 8.5 to 24.5 °C. The maximum temperature was recorded in August, whereas the minimum was recorded in January.The relative humidity ranged from 37.0% to 58.0%, with an average of 46.0%. The wind speed ranged from 250 to 379 km/day. The average sunshine hours were 12.2. There was no rain throughout the year.

Table 3. Meteorological forecasted data of the studied area from 2021 to 2050.

Month	Temperature °C		Humidity (%)	Wind (km/Day)	Sunshine Hours	Precipitation (mm)	ET$_o$ mm/Day
	Tmax	Tmin					
Jan.	19.6	8.5	54.6	279	10.4	0.00	3.14
Feb.	21.6	9.2	48.0	309	11.1	0.00	4.20
Mar.	25.5	12.0	41.8	350	12.0	0.00	5.94
Apr.	29.4	15.2	37.8	379	12.9	0.00	7.76
May	33.3	19.0	37.0	354	13.7	0.00	8.92
Jun.	36.8	22.8	37.2	364	14.1	0.00	10.05
Jul.	38.8	24.5	39.7	367	13.9	0.00	10.36
Aug.	38.9	24.4	41.2	344	13.2	0.00	9.71
Sep.	36.4	22.8	45.4	327	12.4	0.00	8.17
Oct.	30.8	19.4	51.8	275	11.4	0.00	5.67
Nov.	25.6	14.3	54.6	250	10.7	0.00	3.95
Dec.	20.7	9.9	58.0	252	10.2	0.00	2.94
Average/ Total	29.8	16.8	46.0	321	12.2	0.00	6.73

The data revealed that compared to the previous thirty years, there will be a noticeable decrease in the total amount of rain and an increase in the sunshine hours as well as wind speed. The ET$_o$ was calculated using the CROPWAT model and ranged from 3.01 to 8.74 mm/day, with an average of 5.99 mm/day in the previous thirty years. On the other hand, the ET$_o$ for the next thirty years ranged from 2.94 to 10.36 mm/day, averaging 6.73 mm/day. The observed difference between the monthly precipitation and ET$_o$ ensures that there is a need for efficient irrigation throughout the year, especially in the upcoming thirty years under such forecasted conditions.

3.2. Processing of the Soil Data for the CROPWAT Model

The results of the soil physical analyses were used to develop a geographic database of the studied area. Nevertheless, the data were in the form of a point database. To convert these point data into spatially continuous data, spatial interpolation using IDW was employed utilizing the QGIS software. The IDW was performed using the power of two, a minimum of four points, and a maximum of 16. The accuracy of results was obtained using the cross-validation procedure as described by [17] for all the studied soil properties.Twenty-two samples, representing about 15% of the samples, were used for validation, while the rest of the samples were used for IDW. The performance evaluation was applied using the root mean square error (RMSE) [17]. The results revealed that the RMSE was 9.77, 7.55, and 7.78 for sand, silt, and clay, respectively. On the other hand, the RMSE for available moisture content (AMC) and infiltration rate (IR) was 15.03 and 4.84, respectively.

Utilizing the raster calculator, a model was developed to classify the soils based on their content into different soil texture classes. The resulting data revealed that the study area could be classified into four texture classes; sandy loam, clay loam, silty loam, and loam (Figure 5). Most of the studied area was classified as loamy soils covering about 71.0% of the studied area. The sandy and silty loam covered almost similar areas of about 6% and 6.5%, respectively, while the clay loam soils covered about 16.5% of the studied area.

To determine the vegetation cover in each soil texture class, the cross-operation of the Integrated Land and Watershed Management Information System "ILWIS" software was used.Only the agriculture area, which covered about 89% of the studied area (156.34 km^2), was used in this operation, and the fish ponds and the settlements were excluded. The results of the cross-operation revealed that most berseem and wheat were cultivated in loamy soils, covering about 76.6 and 69.7% of the total area cultivated for each crop. For potatoes and citrus, about half of the crops were cultivated in loamy soils as well (Table 4).
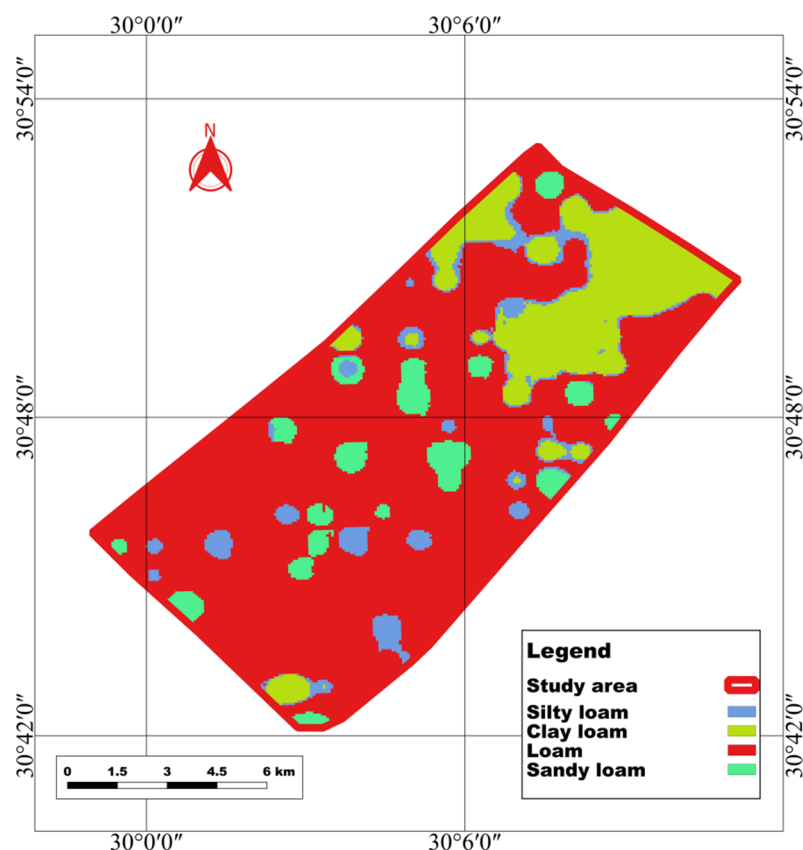
Figure 5. Soil texture class map of the studied area.

Table 4. Land cover classification within each soil texture class.

Class	Sandy Loam		Loam		Clay Loam		Silty Loam		Total	
	km^2	%	km^2	%	km^2	%	km^2	%	km^2	%
Wheat	2.11	3.51	45.99	76.55	9.05	15.06	2.93	4.88	60.08	10.00
Berseem	4.63	8.08	39.90	69.67	9.77	17.06	2.97	5.19	57.27	100.00
Green beans	1.43	6.81	14.75	70.24	2.46	11.71	2.36	11.24	21.00	100.00
Potato	0.89	14.08	3.21	50.79	1.15	18.20	1.07	16.93	6.32	100.00
Citrus	0.84	8.40	5.55	55.50	3.09	30.90	0.52	5.20	10.00	100.00
Strawberry	0.11	12.64	0.34	39.08	0.33	37.93	0.09	10.34	0.87	100.00
Guava	0.17	21.25	0.21	26.25	0.32	40.00	0.10	12.50	0.80	100.00

The interpolated AMC and IR are presented in Figure 6A,B, respectively. Utilizing the raster zonal statistics of the QGIS software, the average values of each soil texture class within the study area could be calculated. The silty loam soils had the highest average AMC within this study area, reaching 149.9 mm/m, while the lowest was the sandy loam soils, with an average of 124.7 mm/m. Concerning the infiltration rate, the lowest rate was for the clay loam soils, with an average of 7.8 mm/h, and the highest was for the sandy loam soils, with an average of 20.1 mm/h.

3.3. Crop Water Requirement (CWR)

As concluded from the LU/LC map, the agricultural area covered about 156 km^2. Citrus, wheat, and berseem were considered when determining the irrigation water requirements. While wheat and berseem were considered because they covered most of the agricultural area (about 75%), citrus was also considered because it is a permanent crop and is expected to consume the largest amount of irrigation water and covered about 6.4% of the agricultural area. The rooting depth, crop coefficient, critical depletion, and yield

response factor parameters were according to [32,33]. The crop growth stages and planting dates for seasonal crops were adapted according to the field conditions.

According to the CROPWAT model, the CWR was 746.2 and 587.5 mm/season for wheat and berseem, respectively. On the other hand, the highest amount of CWR was for citrus, reaching about 1653.5 mm per year. On the other hand, under the forecasted climate conditions, the CWR increased to 809.7 and 636.1 mm/season for wheat and berseem, respectively, while citrus reached about 1926 mm/year (Figure 7). Compared to the previous thirty years, there is an increase in the crop water requirements, which could be rendered to the lack of rain throughout the year, which decreased from about 40 mm/year to none, in addition to changes in the other climatic conditions. That increase ranged from 3 to 3.9% in the case of the field crops but reached about 14% in the case of citrus.
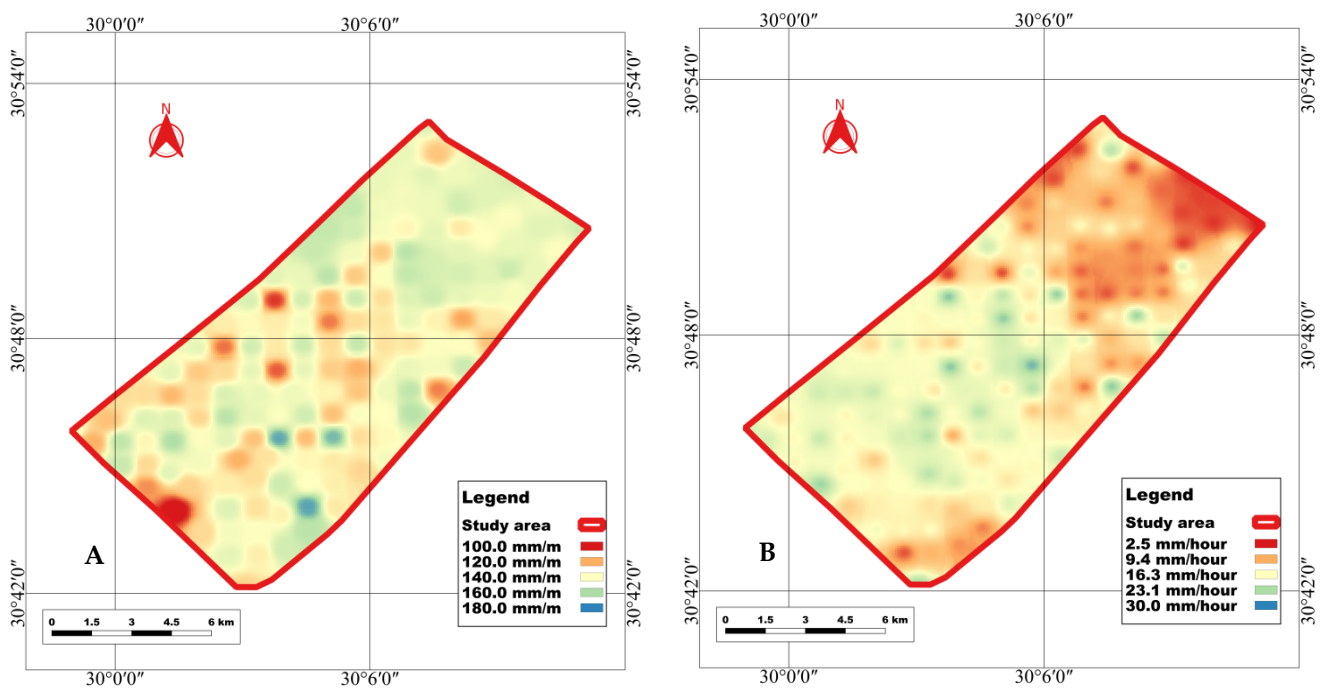
Figure 6. Interpolated soil properties maps, (**A**) available moisture content (AMC), (**B**) infiltration rate (IR).
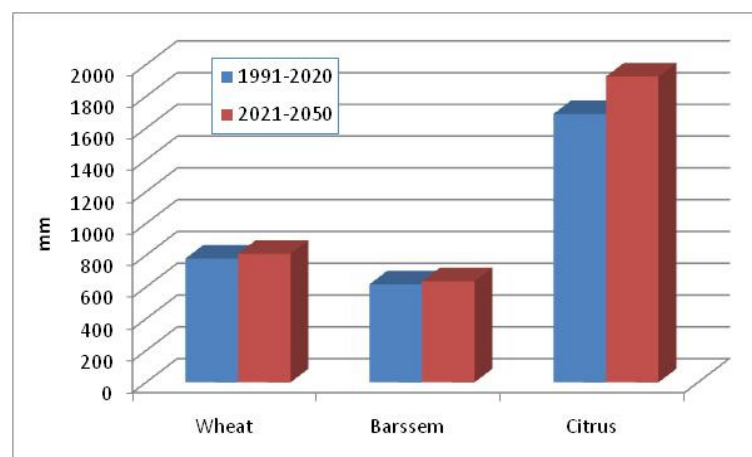
Figure 7. Crop water requirements under current and forecasted climate conditions.

3.4. Irrigation Water Requirements (IWR)

In the study area, the loamy soils were the dominant soils. Therefore, the loamy soils were considered when calculating the IWR. Furthermore, utilizing CROPWAT, the management practice that ensures no yield loss due to water deficiency was compared to current practices under current and forecasted climate conditions for the selected crops.

Wheat is mostly irrigated using sprinkle irrigation, whether fixed or movable. In loamy soils, the current irrigation practices include the application of irrigation water once almost every week, and adjustments are made when there is no irrigation water available in the irrigation canals. These practices should result in the reduction of the crop yield to 2.5%, according to CROPWAT.

Nevertheless, the decrease in crop yield reached about 10–20%, according to a field survey, which could be rendered to soil properties and/or management. Berseem is also irrigated using sprinkle irrigation and, in loamy soils, is irrigated almost once every two weeks, and adjustments are made when there is no irrigation water available in the irrigation canals. These practices should result in a reduction in crop yield reaching 10%, which matches the field survey. Under current practices, the amount of irrigation water required for wheat per feddan will increase by about 160 m^3/feddan under climate forecast conditions, while this increase will reach 288.6 m^3/feddan under the no-yield loss practices (Figure 8A).
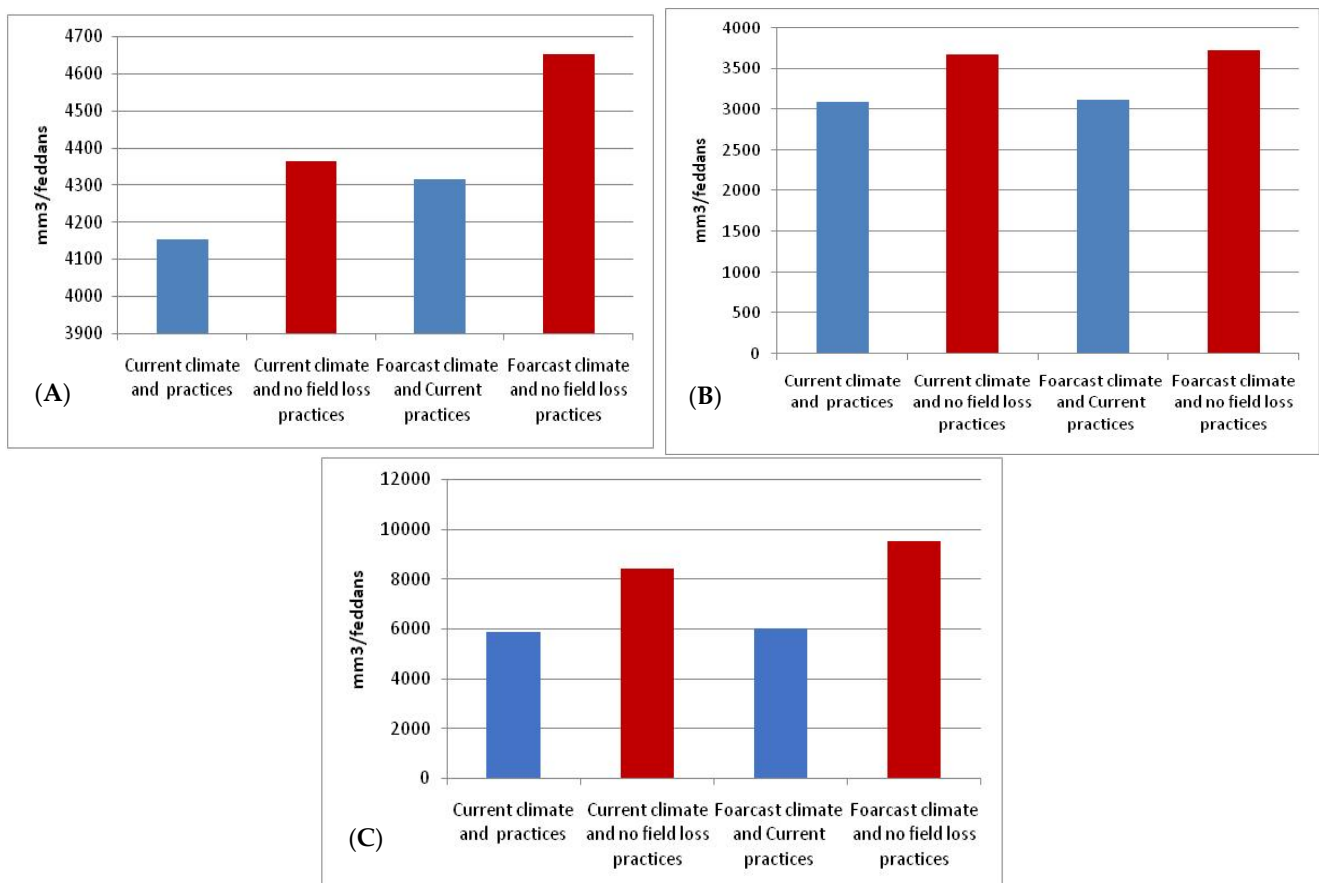
Figure 8. IWR of the studied crops under current and predicted climate, (**A**) wheat, (**B**) berseem, (**C**) citrus.

On the other hand, under the current practices, there will be an increase of the irrigation water for berseem by 22 m^3/feddan under forecast conditions, and under the no yield loss practices, there be an increase of about 50 m^3/feddan (Figure 8B).

Moreover, citrus is irrigated every day using drip irrigation. It is irrigated throughout the study area in almost a uniform application daily which accounts for about 125 m^3/feddan

per week of irrigation water from mid-May to mid-September and about 65 m³/feddan per week from December to January and the in the remaining months is irrigated using about 85 m³/feddan per week, which accounted for about 5871.2 m³/feddan/year irrigation water under field conditions.

Nevertheless, the expected crop yield loss reached about 25%, which matched the field survey. Citrus irrigation water requirements will increase by about 146 m³/feddans under current practices, while under no yield loss, the irrigation requirements increase will be about 1095 m³/feddans (Figure 8C).

4. Conclusions

The crop water requirements of major crops in a selected area in El-Beheira governorate were computed using CROPWAT 8.0 model and supported by remote sensing, GIS, and atmospheric data analysis. The major cultivated crops in the study area were wheat and berseem, while citrus was the major orchard. The study area is irrigated from El-Nasr Canal, and there is a problem with water availability in the study area, which is considered a major problem, especially in the initial growth stages.

The crop water requirements and irrigation requirements for the various crops grown in loamy soils have been computed using CROPWAT 8. Citrus had the largest amount of irrigation water requirements. The irrigation water requirements calculated according to the model based on the current practices showed an expected decrease in yield for the three studied crops.

The research results revealed that there will be an increase in CWR due to the expected climate change in the next thirty years under the best-case scenario. The IWR will increase to reach almost 3.9, 0.7, and 2.5% for wheat, berseem, and citrus, respectively, under the current irrigation practices. The increase will reach about 6.6, 1.4, and 13% for wheat, berseem, and citrus under no field loss practices.

The proposed approach took advantage of various sources of information, especially the freely available remote sensing data, whether related to LU\LC or climatic data, as well as various tools such as climatic models, CROPWAT, GIS, and remote sensing software. The application of such an approach will facilitate setting up an efficient irrigation management strategy by the decision makers and releasing the right amount of water in irrigation canals at the right time to avoid any wastage or shortage in the water supply. It also provides decision-makers with an insight into the expected changes in irrigation water requirements and, therefore, helps to change or adjust the forthcoming land use plans accordingly, especially since the climate models provide the forecasting conditions that may not be appropriate for the current land uses.

The proposed approach is applicable at any administrative level where enough soil and LU\LC data are available. Nevertheless, in Egypt, its application is recommended on the sub-administrative level, where updated soil and LU\LC data could be collected more easily. Furthermore, it is worth mentioning that unless such data are available, the approach will be somewhat time-consuming, and processing the climatic model is time-consuming as well.

Institutional Review Board Statement: Not applicable.

Informed Consent Statement: Not applicable.

Data Availability Statement: Not applicable.

References

1. Liu, Q.; Yan, C.; Yang, J.; Mei, X.; Hao, W.; Ju, H. Impacts of climate change on crop water requirements in Huang-Huai-Hai Plain, China. In *CABI Climate Change Series, Climate Change and Agricultural Water Management in Developing Countries*; CABI International: Wallingford, UK, 2016; pp. 48–62. Available online: https://www.researchgate.net/profile/Qin-Liu-4/publication/315729544_Climate_Change_and_Agricultural_Water_Management_in_Developing_Countries/links/58dfae024585153bfe97e008/Climate-Change-and-Agricultural-Water-Management-in-Developing-Countries.pdf (accessed on 1 May 2022).
2. Intergovernmental Panel on Climate Change (IPCC). Summary for policymakers. In *Climate Change and Land: An IPCC Special Report on Climate Change, Desertification, Land Degradation, Sustainable Land Management, Food Security, and Greenhouse Gas Fluxes Interrestrial Ecosystem*; Shukla, P.R., Skea, J., CalvoBuendia, E., Masson-Delmotte, V., Pörtner, H.O., Roberts, D.C., Zhai, P., Slade, R., Connors, S., van Diemen, R., et al., Eds.; IPCC: Geneva, Switzerland. Available online: https://www.ipcc.ch/site/assets/uploads/sites/4/2020/02/SPM_Updated-Jan20.pdf (accessed on 1 May 2022).
3. Sahu, N.; Saini, A.; Behera, S.K.; Sayama, T.; Sahu, L.; Nguyen, V.T.; Takara, K. Why apple orchards are shifting to the higher altitudes of the Himalayas? *PLoS ONE* **2020**, *15*, e0235041. [CrossRef] [PubMed]
4. FAO. *The State of Food and Agriculture. Overcoming Water Challenges in Agriculture*; FAO: Rome, Italy, 2020. [CrossRef]
5. Sahu, N.; Saini, A.; Behera, S.; Sayama, T.; Nayak, S.; Sahu, L.; Duan, W.; Avtar, R.; Yamada, M.; Singh, R.; et al. Impact of Indo-pacific climate variability on rice productivity in Bihar, India. *Sustainability* **2020**, *12*, 7023. [CrossRef]
6. Lalic, B.; Francia, M.; Jacimovic, G. Assessment of climate change impact on crop water requirements in Serbia in 2030 using CROPWAT model. In Proceedings of the International Scientific Conference on Environmental changes and adaptation strategies Skalica, Slovakia, 9–11 September 2013.
7. Foster, T.; Mieno, T.; Brozovic, N. Satellite-based monitoring of irrigation water use: Assessing measurement errors and their implications for agricultural water management policy. *Water Resour. Res.* **2020**, *56*, e2020WR028378. [CrossRef]
8. Surendran, U.; Sushanth, C.M.; Mammen, G.; Joseph, E.J. Modeling the crop water requirement using FAO-CROPWAT and assessment of water resources for sustainable water resource management: A case study in Palakkad district of humid tropical Kerala, India. *Aquat. Procedia* **2015**, *4*, 1211–1219. [CrossRef]
9. Halimi, A.H.; Tefera, A.H. Application of cropwat model for estimation of irrigation scheduling of tomato in changing climate of eastern Europe: The case study of Godollo, Hungary. *SSRG Int. J. Agric. Environ. Sci.* **2019**, *6*, 1–11. [CrossRef]
10. Suryadi, E.; Ruswandi, D.; Dwiratna, S.; Prawiranegara, B.M.P. Crop water requirements analysis using Cropwat 8.0 Software in maize intercropping with rice and soybean. *Int. J. Adv. Sci. Eng. Inf. Technol.* **2019**, *9*, 1364–1370. [CrossRef]
11. Swelam, A.; El-Marsafawy, S.; Elbana, M. Effective management of on-farm irrigation for some major crops in Egypt using CROPWAT model. *Misr J. Agric. Eng.* **2019**, *36*, 105–122. [CrossRef]
12. Al-Najar, H. The integration of FAO-CropWat Model and GIS techniques for estimating irrigation water requirement and its application in the Gaza strip. *Nat. Resour.* **2011**, *2*, 146–154. [CrossRef]
13. Naidu, C.; Giridhar, M. Irrigation demand vs supply-remote sensing and GIS approach. *J. Geosci. Environ. Prot.* **2016**, *4*, 43–49. [CrossRef]
14. Meena, S.K.; Punjabi, S.T.; Dadhich, P.N. Crop water estimation for Chaksu Tehsil of Jaipur using CROPWAT and GIS. *Int. J. Adv. Sci. Technol.* **2020**, *29*, 3540–3551. Available online: http://sersc.org/journals/index.php/IJAST/article/view/20887 (accessed on 1 May 2022).
15. Manasa, H.G.; Shivapur, A.V. Implications of climate change on crop water requirments in Hukkeri Taluk of Belagavi district, Karnataka, India. *Int. J. Res. Eng. Technol.* **2016**, *5*, 236–241. Available online: https://ijret.org/volumes/2016v05/i06/IJRET20160506044.pdf (accessed on 1 May 2022).
16. Makar, R.S.; Shahin, S.A.; El-Nazer, M.; Wheida, A. Development of a PCA-based land use/land cover classification utilizing Sentinel-2-time series. *Middle East J. Agric. Res.* **2022**, *11*, 630–637. [CrossRef]
17. Morgan, R.S.; Abd El-Hady, M.; Rahim, I.S.; Silva, J.; Ribeiro, S. Evaluation of various interpolation techniques for estimation of selected soil properties. *Int. J. GEOMATE* **2017**, *13*, 23–30. [CrossRef]
18. Gee, G.W.; Bauder, J.W. Particle size analysis. In *Methods of Soil Analysis, Part A*, 2nd ed.; Klute, A., Ed.; American Society of Agronomy/Soil Science Society of America: Madison, WI, USA, 1986; Volume 9, pp. 383–411.
19. Saxton, K.E.; Rawls, W.J.; Romberger, J.S.; Papendick, R.I. Estimating generalized soil-water characteristics from texture. *Soil Sci. Soc. Amer. J.* **1986**, *50*, 1031–1036. [CrossRef]
20. Longley, P.A.; Goodchild, M.F.; Maguire, D.J.; Rhind, D.W. *Geographic Information Systems and Sciences*, 2nd ed.; John Wiley & Sons Ltd.: West Sussex, UK, 2005.

21. Achilleos, G.A. The inverse distance weighted interpolation method and error propagation mechanism-creating a DEM from an analogue topographical map. *J. Spat. Sci.* **2011**, *56*, 283–304. [CrossRef]
22. Lu, G.Y.; Wong, D.W. An adaptive inverse-distance weighting spatial interpolation technique. *Comput. Geosci.* **2008**, *34*, 1044–1055. [CrossRef]
23. Food and Agriculture Organization (FAO). *CROPWAT 8.0*; Land and Water Development Division, Ed.; FAO: Rome, Italy, 2009.
24. Vozhehova, R.A.; Lavrynenko, Y.O.; Kokovikhin, S.V.; Lykhovyd, P.V.; Biliaieva, I.M.; Drobitko, A.V.; Nesterchuk, V.V. Assessment of the CROPWAT 8.0 software reliability for evapotranspiration and crop water requirements calculations. *J. Water Land Dev.* **2018**, *39*, 147–152. [CrossRef]
25. El-Magd, I.A.; Tanton, T. Remote sensing and GIS for estimation of irrigation crop water demand. *Int. J. Remote Sens.* **2005**, *26*, 2359–2370. [CrossRef]
26. Karuku, G.N.; Gachene, C.K.K.; Karanja, N.; Cornelis, W.; Verplancke, H. Use of CROPWAT model to predict water use in irrigated tomato production at Kabete, Kenya. *E. Afr. Agric. For. J.* **2014**, *80*, 175–183.
27. Sparks, A.H. NASAPOWER: A nasa power global meteorology, surface solar energy and climatology data client for R. *J. Open Source Softw.* **2018**, *3*, 1035. [CrossRef]
28. Gelaro, R.; McCarty, W.; Suárez, M.J.; Todling, R.; Molod, A.; Takacs, L.; Randles, C.A.; Darmenov, A.; Bosilovich, M.G.; Reichle, R.; et al. The modern-era retrospective analysis for research and applications, version 2 (MERRA-2). *J. Clim.* **2017**, *30*, 5419–5454. Available online: https://journals.ametsoc.org/view/journals/clim/30/14/jcli-d-16-0758.1.xml (accessed on 1 May 2022). [CrossRef] [PubMed]
29. Chen, W.; Castruccio, S.; Genton, M.G.; Crippa, P. Current and future estimates of wind energy potential over Saudi Arabia. *J. Geophys. Res. Atmos.* **2018**, *123*, 6443–6459. [CrossRef]
30. Mostafa, A.N.; Wheida, A.; El Nazer, M.; Adel, M.; El Leithy, L.; Siour, G.; Coman, A.; Borbon, A.; Magdy, A.; Omar, M.; et al. Past (1950–2017) and future –2100) temperature and precipitation trends in Egypt. *Weather. Clim. Extrem.* **2019**, *26*, 100225. [CrossRef]
31. Tyagi, N.; Jayal, T.; Singh, M.; Mandwal, V.; Saini, A.; Nirbhav; Sahu, N.; Nayak, S. Evaluation of observed and future climate change projection for Uttarakhand, India, using CORDEX-SA. *Atmosphere* **2022**, *13*, 947. [CrossRef]
32. Allen, R.G.; Pereira, L.S.; Raes, D.; Smith, M. Crop evapotranspiration-guidelines for computing crop water requirements. In *FAO Irrigation and Drainage Paper 56*; FAO: Rome, Italy, 1998.
33. Pereira, L.S.; Allen, R.G.; Smith, M.; Raes, D. Crop evapotranspiration estimation with FAO 56: Past and future. *Agric. Water Manag.* **2015**, *147*, 4–20. [CrossRef]

Review

An Overview of the Implication of Climate Change on Fish Farming in Egypt

Ahmed I. Mehrim * and Mohamed M. Refaey

Animal Production Department, Faculty of Agriculture, Mansoura University, Mansoura 35516, Egypt
* Correspondence: amehrim2002@yahoo.com; Tel.: +20-1002915069

Abstract: Aquaculture is an important component of the human diet, providing high-quality aquatic food for global or local consumption. Egypt is one of the countries most vulnerable to the potential impacts of climate change (CC), especially in the aquaculture sector. CC is one of the biggest challenges of our time and has negatively affected different water bodies. CC leads to the combination of changes in water availability, a decrease in water quality, the movement of salt water upstream due to rising sea levels, and the salinization of groundwater supplies will threaten inland freshwater aquaculture. Similarly, higher temperatures resulting from CC lead to reduce dissolved oxygen levels, increased fish metabolic rates, increased risk of disease spread, increased fish mortality, and consequently decreased fish production. CC may also indirectly affect aquaculture activities; for example, large areas of lowland aquaculture ponds can be highly vulnerable to flooding from rising sea levels. Thus, the current overview will briefly discuss the state of the aquaculture sector in Egypt, the meaning of CC, its causes, and its effects on the different elements of the aquaculture sector, and finally, we will review the appropriate ways to mitigate the adverse effects of CC on fish farming, especially in Egypt.

Keywords: climate change; aquaculture; sustainability; Egypt

1. Introduction

Fish is one of the most widely consumed foods in the world, and it is only becoming more popular over time, as fish is considered a healthy and nutritious food by many consumers and is expected to further grow in the next decade [1]. Millions of low-income women and men rely on the fishing and aquaculture sectors for income [2,3], which contribute both directly and indirectly to their food security. Since the 1990s, capture fisheries have plateaued at about 90 million tons. At the same time, the world's human population is growing rapidly. Thus, aquaculture is shaping up into a global venture, and it is considered the fastest-growing food-producing sector in the world to feed the ever-growing population. Moreover, the global aquaculture industry, in the current or future food systems, will become the most important source of high-quality aquatic food [1]. In 2020, global aquaculture's share was 49.2% of the world's fish production, compared to 25.7% in 2000. It is predicted that aquaculture will contribute 62% of the global food supply by 2030 [4]. Regionally, aquaculture accounted for 17.9% of total fish production in Africa, which is roughly 2.70% of world aquaculture production [1]. Compared to 57.7% in 2000, inland aquaculture produced the most farmed fish (51.3 million tons, or 62.5% of the global total), mostly in freshwater [1].

In Egypt, aquaculture has been practiced since ancient times. However, it still contributes significantly to a country's GDP, employment, and food security, as well as being important to nutritional well-being, the economy, and the lives of the population [5]. Egypt produces significantly more aquaculture than the rest of Africa combined. According to the most recent annual fish production statistics from GAFRD [6], Egypt's aquaculture industry supplied nearly 80.5% of the nation's fish needs in 2019 (Figure 1). Small- and

medium-sized privately owned farms produced more than 99% of this output, accounting for nearly all the output. The area being farmed increased from 42,000 ha in 1999 [7] to 123,327 ha in 2019 [6]. Egyptian aquaculture has played a critical role in increasing per capita fish consumption from 14.3 kg in 2002 to 25.4 kg per person by 2019, representing a 56.3% increase in per capita consumption over this period [6]. In addition, aquaculture plays an important role in the economy [8], where the total marketing value of the aquaculture industry in Egypt was USD 3.2 billion in 2019 [6]. In recent years, aquaculture has developed rapidly, creating many job opportunities for farm technicians and skilled laborers. Moreover, the development of new industries, financial services, and aquaculture-related activities has created employment opportunities [8,9]. Meanwhile, aquaculture expansion has reduced and stabilized the cost of fish in Egypt, making it more accessible to poorer rural populations and allowing them to consume healthy and affordable animal protein [9].
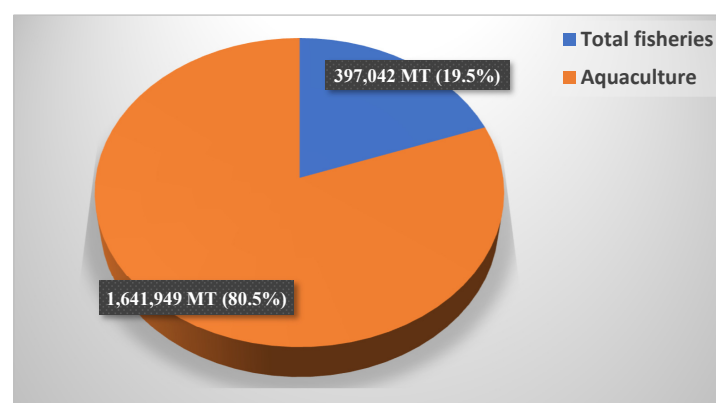
Figure 1. Annual total fisheries and aquaculture production in Egypt [6].

In Egypt, many fish culture systems include: (A) Extensive aquaculture that includes earthen pond culture, as well as restocking lakes with fry and fingerlings, adding to grass carp in the Nile River, its branches, and enclosures. (B) A semi-intensive culture system that accounts for 80% of Egypt's total output. (C) Intensive culture systems in concrete ponds, tank culture, greenhouse culture, and cage culture, all of which have grown in popularity in recent years [1]. Additionally, (D) integrated aquaculture production systems with plants (aquaponics) and animals (ducks) [10]. Fish farms are dispersed through the Nile Delta region and focused mainly on the Northern lakes (Manzala, Maruit, Boruls, and Edko; Figure 2). Historically, the extensive cultural system is the oldest system in Egypt. This system is characterized by a low input in fish density and a very poor output. Meanwhile, the semi-intensive system is more widely distributed and preferred by both small- and large-scale commercial farmers. This system plays the main role in increasingly contributing to the development of aquaculture in Egypt. The intensive culture systems depend on an increasing stocking density, which requires big capital investment and complete formulated feeds, representing 40–60% of the production costs. In the coming years, it is expected that intensive aquaculture will play a greater role in food security than semi-intensive systems in terms of production efficiency [11]. Additionally, El-Gayar [12] stated that there is a significant possibility for enhanced output in this system if the production process is intensified by increasing the stocking density of fish, aeration, the use of supplemental feeding, and improved pond management. Despite aquaculture being a significant industry, it is prohibited from using Nile water and is instead mostly reliant on groundwater and agricultural drainage systems [13], which are of poor quality. This water causes many problems, such as increased production costs for hatchers and fish farmers, declining fish production, and increases in disease outbreaks [14]. Moreover, drainage water negatively affects the quality of farmed fish due to the accumulation of pollutants and potential

contamination of fish [15], reducing opportunities for fish export. Therefore, fish farmers are demanding the use of fresh water in their fish production.
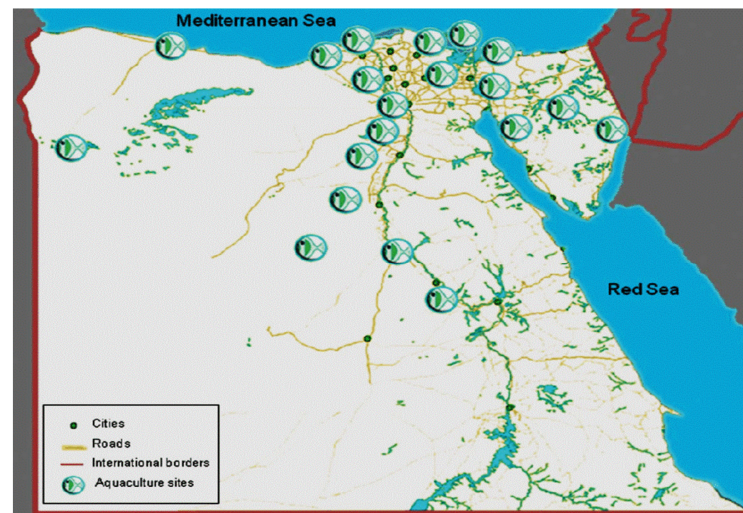
Figure 2. Distribution of the main aquaculture production sites in Egypt [9].

One of the most dynamic and defining environmental, legal, and political challenges of the twenty-first century is climate change. The production of agriculture is currently hampered by climate change worldwide, particularly in the Mediterranean region [16]. One of the most significant environmental issues that has an adverse impact on both the environment and human lives is global warming. Since 1950, the average global temperature has risen by 0.13 °C on average per decade [17]. It is expected to increase by between 0.3 and 0.7 °C in the global mean surface temperature during 2016–2035, which may be due to the emissions scenario [18]. In general, climate change has led to many environmental phenomena such as flooding, extreme heat, and water scarcity, which have had negative impacts on food security, the spread of infectious diseases, economic losses, and displacement. These impacts have led the World Health Organization to call climate change the greatest threat to global health in the 21st century. The problems of climate change are global, but Africa is likely to suffer to a greater degree compared with other regions. Scientists and policymakers in Africa need every available tool to help the continent adapt to the severity and scale of this problem [19]. For the aquaculture sector, climate change has had many negative impacts, resulting from direct or indirect impacts on the cultured organisms (fish—natural food) or the resources needed for aquaculture (water, land, seeds, feed, and energy) [20]. Changes in temperature and rainfall patterns affect water quality parameters such as pH, salinity, and oxygen, which are expected to impact reproduction, growth, survival, and pond productivity. Furthermore, climate change increases physiological stress, which leads to increased disease vulnerability, as well as higher risks and lower returns for farmers [21].

The threat of climate change is a major concern for food security, sustainability, and the resilience of the systems on which humans rely [22]. Similar with any food system, aquaculture is affected by climate change, effects that will differ depending on the cultivated taxa (e.g., finfish, shellfish, or seaweed), the farming ecosystem (e.g., freshwater, brackish, or marine), practices (open or closed systems), and the regions [23]. Climate change impacts on aquaculture are considered as direct, e.g., changes in either water availability, temperature, or damage by extreme climatic events, or indirect, such as in the case of increased fishmeal costs as well as for other aquaculture feeds [20]. Changes in climate-related factors, mainly temperature, directly affect the biochemical reaction rates that govern the rates of cellular processes, feeding, digestive, and metabolic performance of fish [24], which in turn, affect the growth performance [25,26], physiological status [27–29], immune responses [30–32], reproduction, behavior [33–35], and disease resistance [36,37] of different fish species in the

wild and in aquaculture. This, consequently, may have significant impacts on aquaculture productivity and thus may adversely affect food security in Egypt [38]. In addition, Egypt's precipitation may decrease due to climate change, with some modeling indicating an annual decline of up to 5.2% by 2030, 7.6% by 2050, and 13.2% by 2100 [39]. Therefore, it would be prudent for Egypt to identify adaptive strategies to manage climate risks in vulnerable areas [40]. Consequently, this overview classically represented the implications of climate change on the fish farming sector in Egypt.

2. The Meaning of Climate Change

Climate change is defined as significant, protracted changes in the world's climate. The world's climate is an interconnected system of the sun, earth, and oceans, as is the wind, rain, and snow, as well as forests, deserts, savannas, and human activity [41]. According to the Intergovernmental Panel on Climate Change (IPCC), climate change is defined scientifically as a change in the climate's state that can be determined by variations in the mean and/or variability of its properties that last for a considerable amount of time, typically decades or longer. The concepts given above define climate change as long-term changes in temperature and weather patterns. These changes could be caused by natural processes such as oscillations in the solar cycle. This quick increase is problematic because it is altering our climate too quickly for living things to adjust [42]. However, since the 1800s, human activity has been the primary cause of climate change, mostly as a result of the combustion of fossil fuels such as coal, oil, and gas. In addition to rising temperatures, other effects of climate change include rising sea levels, harsh weather, shifting wildlife populations and habitats, and a variety of other effects. The release of heat-trapping gases, often known as greenhouse gases (GHGs), to power our contemporary lives has clearly been the main driver of the last century's warming. We are achieving these using fossil fuels, land usage, agriculture, and other factors that contribute to climate change. Over the past 800,000 years, GHG levels have been at their highest point. This quick increase is problematic because it is altering our climate too quickly for living things to adjust [42].

3. The Cause Factors of Climate Change

The earth's climate changes as a result of a variety of human-made and natural forces. Thus, the two main causes of climate change are human and natural causes. The human causes relate to artificial factors and people's activities that change the climate on the Earth. The human (anthropogenic) factors that are causes of climate change (Figure 3), include the use of fossil fuels (transport, industries, and urbanization), air pollution, agriculture (animal digestion, manure, soil management), and land use changes (deforestation, upsetting grasslands and croplands) [17,41]; there are other human causes as well. Climate change includes both large-scale changes in weather patterns that come from human-caused global warming and shifts that result from these changes. Since the mid-20th century, people have had an unparalleled impact on the earth's climate system and have led to change on a global scale. Human actions are to blame for the current, rapid climate change, which is endangering humanity's basic existence. Global warming causes the emission of gases, of which more than 90% are carbon dioxide (CO_2) and methane (CH_4), which are the main causes of global warming. The primary source of these emissions is the burning of fossil fuels (coal, oil, and natural gas) for energy consumption, with smaller amounts coming from manufacturing, agriculture, and deforestation [43]. Most scientists accept that human causes refer to people's activities that change the atmosphere on the planet. People pollute the environment directly, which changes the climate; it is the human cause. Therefore, it is also known as the anthropogenic cause of climate change. Since the mid-1800s, scientists have known that CO_2 is one of the main GHGs of importance to Earth's energy balance. Direct measurements of CO_2 in the atmosphere and in air trapped in ice show that atmospheric CO_2 increased by more than 40% from 1800 to 2019. Measurements of different forms of carbon reveal that this increase is due to human activities. Other GHGs (notably CH_4 and nitrous oxide) are also increasing as a consequence of human

activities. The observed global surface temperature rise since 1900 is consistent with detailed calculations of the impacts of the observed increase in atmospheric GHGs (and other human-induced changes) on Earth's energy balance. Human activities—especially the burning of fossil fuels since the start of the Industrial Revolution—have increased atmospheric CO_2 concentrations by more than 40%, with over half the increase occurring since 1970. Since 1900, the global average surface temperature has increased by about 1 °C. CO_2 has also increased in the atmosphere due to deforestation. It is a primary human cause of rising GHGs and climate change. In 2019, deforestation was responsible for an increase of 11% of CO_2 [44].

The human (anthropogenic) factors causes of climate change

1. Fossil fuels
(transport, industries, and urbanization)

2. Air pollution

3. Agriculture
(animal digestion, manure, soil management)

4. Land use changes
(deforestation, upsetting grasslands and croplands)
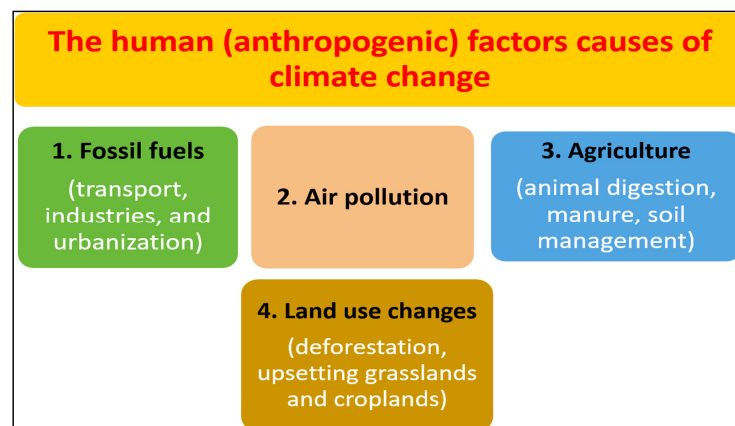
Figure 3. The human (anthropogenic) factors that are causes of climate change [17,41].

Livestock production is another primary human cause of climate change. It contributes to producing GHGs that trap heat in the atmosphere. Nowadays, people farm domestic animals for commercial purposes to produce meat, milk, leather, etc. The most common animals in livestock farms are cows and sheep. These animals generate CH_4 gas when they consume and digest foods. A report shows that cows generate around 150 billion gallons of methane gas daily. CH_4 is one of the GHGs that contributes to raising the temperature of the planet. Livestock production is responsible for producing 14.5% of GHGs. Domestic animal farming produces a large carbon footprint which causes climate change. The fluorinated and industrial gases are also human causes of climate change as people produce these gases for commercial purposes. Food waste is one of the silent human causes of climate change, which many people are unaware of. Food waste produces CH_4 gas when it decomposes in landfills. CH_4 is a powerful GHG that causes global warming and climate change on Earth. Around 6–8% of CH_4 gas is emitted from wasted food. Therefore, food waste is a significant factor of climate change [45].

The second factor of climate change is natural causes, which refer to the physical factors that contribute to the change of the atmosphere on earth. Over a period of thousands to millions of years, they have had an impact on the climate. Natural causes occur mostly automatically rather than through people's contributions [44]. These natural causes stimulate changes to the condition of the planet both instantly and slowly. For example, solar activities mean releasing various types of radiation from the sun from time to time. It includes sunspots, solar flares, and solar radiation. Sunspots emit many ultraviolet rays that hit the planet's surface and increase the temperature. In recent decades, the planet's temperature has risen by 0.1 °C due to the solar maximum. It makes the sun brighter and the planet warmer. Other natural causes, such as volcanic eruptions, axial tilt (obliquity), precession, eccentricity, continental drift, the ocean current, natural forest fires, and natural GHGs (Figure 4) also have different negative impacts on the climate of our planet: where they have led to the release of a massive amount of dust, magma, and gases that affect the environment, creating a dark ash cloud in the atmosphere; the planet consumes more solar radiation; it receives more heat from the sun, or it gets less heat when tilted away from the

sun due to the planet's orbital path variation; changing the atmosphere on the planet due to the slow movement of continental drifts of the planet's plates; the sea level increasing continuously due to the ocean current melting the ice on the northern part of the planet; the release of numerous GHGs, which trap the heat in space; increasing the temperature of the planet due to natural forest fires; and natural GHGs which additionally allow solar radiation to enter the planet easily [45].
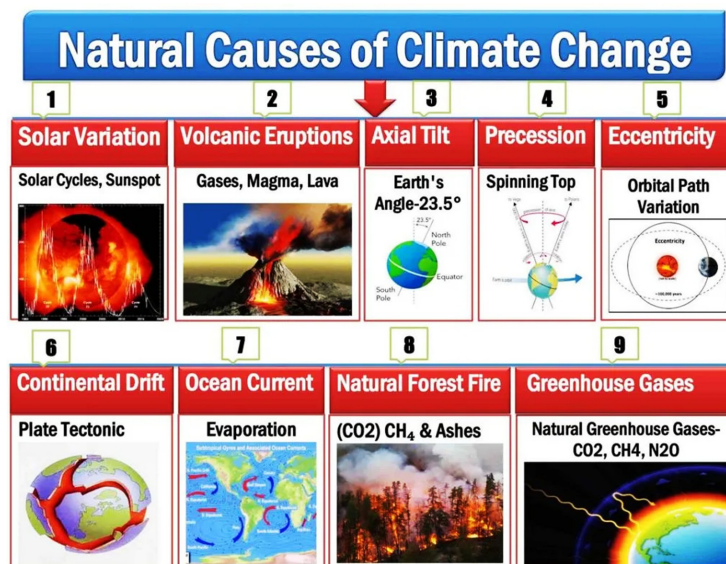
Figure 4. The natural factors that are causes of climate change [44].

4. Effects of Climate Change on the Fish Farming Sector in Egypt

In general, there are two effects of climate change on the planet, the direct and indirect impacts. The direct impacts include increasing the maximum temperature levels and reducing the minimum temperature levels. The prolonged maximum temperature melts the ice in the northern part of the earth and increases the sea level. Additionally, it raises the ocean's temperature and brings a humid atmosphere. The higher temperature of the ocean evaporates water into vapor and creates heavy rains. On the other side, the indirect impacts of climate change create a water crisis, and the groundwater level is decreasing daily. In many developing countries, people suffer from water crises. These countries experience droughts and floods every year, subsequently increasing hunger and diseases among poor people. Climate change is directly responsible for the loss of diversity and the ecosystem crisis. The contamination of CO_2 and HCO_3 concentrations in the water creates acid rain which is bad for people's health. Furthermore, climate change is also responsible for floods, erosion, landslides, and salinization. The sea level is increasing day by day due to global warming [41].The Egyptian fish farming industry uses several crucial inputs, including land, freshwater, feed, and energy, all of which have substantial environmental effects. At the same time, the supply of these inputs is constrained and is probably going to get even more so in the future [46]. Egypt is mostly reliant on the Nile River, which provides the nation with an annual water volume of about 55.5 km^3, accounting for 93% of its conventional water resources. There is a discrepancy between water demand and supply, which is filled by reusing drainage water, wastewater, and shallow groundwater. Additionally, the uncertainty of climate change implications is a difficulty for Egypt's water resources system. Climate change could have a direct impact on the quantity of water in Egypt, leading to indirect effects on Mediterranean saltwater intrusion into groundwater, exposing the agriculture to vulnerability [47]. Moreover, Chen et al. [48] reported that the Egyptian Nile Delta has been suffering from complex environmental hazards especially caused by climate change, which have led to adverse impacts on national food security. The development of aquaculture in Egypt during the next period will largely depend on finding

solutions to the key issues facing this industry, including conflicts over the use of resources (water and land), energy consumption, price changes for the primary raw materials used in the fish feed industry, and getting high-quality fish fry from a reliable source [49]. Egypt is one of the nations that are thought to be most susceptible to climate change impacts. These effects will have serious repercussions on all sectors of the country [50] including the aquaculture industry. Aquaculture could be impacted by climate change through adjustments to fish stocks, species, reduced aquaculture land, production volumes and efficiency, water quality, and fish pricing. The growth of sustainable aquaculture is likewise threatened by the effects of climate change, which require the implementation of mitigation and adaptation strategies. These measures will combine socioeconomic and technical strategies.

Due to Egypt's huge and expanding population and reliance on the Nile River, the effects of climate change on water resources is seen as a major concern. Egypt has already exceeded the threshold of water scarcity. Numerous international studies have been conducted in this area, including one by Hammond [51], who predicted that the management of water resources in the Nile River would grow more difficult as a result of socioeconomic and climatic changes. Schilling et al. [52] presented a comparison of the social impacts of climate change and their relation to the vulnerability of Algeria, Egypt, Libya, Morocco, and Tunisia. According to the findings, all nations are vulnerable to severe temperature increases and a high risk of drought due to climate change. Climate change and rapid population expansion in North Africa are very likely to exacerbate the region's already precarious water supply situation. Egypt is thus subject to several serious threats due to climate change. These concerns, which include a considerable decline in Nile River flow, sea level rise (SLR), and greater temperatures which result in decreased water supplies and loss of land, might have a negative impact on Egypt's economy, ecosystems, and people's health. Egypt already confronts significant water management issues due to the uncertain changes in availability brought on by climate change, as well as the more certain demographic trends and potential abstraction by upstream riparian countries. A decrease in the Nile's flow brought on by climate change might exacerbate the problem. Due to other urgent issues in Egypt, such as rising food and living expenses and decreased land productivity along the coast, climate change has recently risen to the top of the priority list for national decision-makers [53].

Egypt produces 93% of its fish needs from different sources [6]. Furthermore, a lot of social classes rely on freshwater fish as a primary source of animal protein. Increased temperatures will work on fish migrating to the north and to deeper waters, as well as fish farms, which will face competition over the redistribution of water usage and the productivity of some varieties of fish. Fish farms and small waterways are more vulnerable than fish in the sea and large water bodies. Thus, the rising air and water temperatures will affect an increased growth rate of fish and their vulnerability in fish farms. These changes will be related to a higher need for nutrition and increased competition between different fish species and other organisms in the fish pond, thus raising the biological oxygen demand (BOD). Additionally, in terms of the hydrological aspect, the Mediterranean Sea level rise—whether it is 50 cm or one meter—will have a significant impact on the rates and locations of egg hatching. Egypt is considered one of the top five countries expected to be vulnerable to the impacts of SLR [54], wherein in terms of aquaculture production, it is the largest African country and the tenth worldwide, with approximately 1.64 million tons/year [1]. In addition, the likelihood of increased water salinity in the northern Delta will negatively affect the productivity of freshwater fish and increase the productivity of saltwater fish [55]. The impacts of climate change on aquaculture are more complex than those on terrestrial agriculture due to the greater diversity of fish species produced and the systems used [56]. The extensive areas of aquaculture ponds that exist in the lowlands can be highly vulnerable to flooding from rising sea levels. Furthermore, the movement of saline water further upstream in rivers caused by rising sea levels, and the salinization of groundwater supplies, will threaten inland freshwater aquaculture [17]. Changes in

rainfall will cause a spectrum of changes in water availability and will reduce water quality. Similarly, rising temperatures from climate change events reduce dissolved oxygen levels and increase fish metabolic rates, consequently leading to an increase in the mortality rate of fish, decreased production of fish, and/or increased feed requirements, as well as increased risk and spread of disease [57].

Currently, the expanding aquaculture production hubs in Asia and Africa, particularly Egypt, are quite concerned about climate change. The dry and wet seasons have changed due to climate change. It is increasingly recognized that economic, social, and ecological systems are dynamic, interacting, and interdependent. In this way, the linkages between aquaculture and climate change are reciprocal—aquaculture influences and contributes to climate change. All areas of development, including aquaculture, will be significantly impacted by climate change in Egypt [50]. The Egyptian aquaculture may be impacted by climate change through changes in the amount of available land for fish farming, fish species, water quality, production volumes and efficiency, and fish pricing. Additionally, the growth of sustainable aquaculture is being threatened by the effects of climate change, necessitating the targeted application of mitigation measures. These initiatives will combine socioeconomic and technological strategies [58]. Aquaculture relies on resource inputs (water, land, seed, feed, and energy) that are connected to various feed, processing, transport, and other sectors of society. Aquaculture ecosystems produce products of economic value. In addition, uncontaminated wastewater and fish waste are produced from fish farms, which can be important inputs to environmentally designed aquaculture and terrestrial farming systems [58]. Thus, the following subsections will provide a quick overview of the main impacts of climate change on aquaculture inputs, including water, land, feed, seed, and energy.

4.1. Water

According to the FAO [57], Egypt is one of the African countries that is expected to be most vulnerable to the impacts of SLR [57]. Increased sea levels lead to coastal groundwater becoming more saline, especially in low-lying areas, which is reflected in the decrease in fresh water available for aquaculture [59]. Many studies have addressed the sensitivity of the Nile River waters to climate change. The sensitivity of different Nile basins to uniform changes in rainfall have been documented [60]. The sensitivity of Nile water flows and consequently species diversity are also affected by the change in temperature, which causes corresponding changes in evaporation and evapotranspiration [61,62]. An increase of 4% in evapotranspiration would result in a reduction of Blue Nile and Lake Victoria flows by 8% and 11%, respectively. In addition, Khordagui [63] expected that the Nile water would be reduced by 20% over the next 50 years. Meanwhile, the increasing temperatures will cause a rise in the evaporation process in natural ecosystems, which will lead to an increased water demand [17]. Recently, Radwan and Ellah [64] revealed that Egypt is one of the countries negatively affected by climate change within its borders, and, outside its borders, within the whole of the Nile River. The river is expected to be severely reduced. From the other side, aquaculture activities in desert areas depend on groundwater. Twenty commercial aquaculture farms operating in Egypt's desert regions total 893 hectares in size and produce roughly 13,000 tons annually [65]. According to El-Guindy [66], brackish and marine water may be very important for the development of aquaculture in the Egyptian desert in the long run.

Adaptation options for Egypt's water resources meanwhile are closely intertwined with Egypt's development choices and pathways. Any changes in water supply due to climate change over the medium term will occur alongside the certainty of increased demographic pressures (the national population is growing by one million every nine months) as well as the potential increases in Nile water abstractions by the upstream riparian countries. Adapting to climate change will have close resonance with adapting to water scarcity and is likely to require the implementation of water demand management strategies, which may require capacity building and awareness raising across institutions

and society. Adaptation measures on the supply-side include ways to improve rain harvesting techniques, increasing extraction of groundwater, water recycling, desalination, and improving water transportation [67]. Fish ponds can obtain water from various water sources depending on the availability, location, and law. In Egypt, the following water sources and percentages were identified: lake (13%), river (6%), agricultural drainage water (78%), and mixed drainage and Nile (45%). It was observed that most of the fish farmers relied on agricultural drainage water. The result is not far-fetched from the fact that aquaculture is the last user of water in Egypt because it makes use of reused water, according to the water policy in Egypt [68]. Apparently, Egypt represents a good example of a green aquaculture because 78% of the fish farmers depend solely on agricultural drainage water. In Egypt, recent research showed that the use of aquaculture drainage water for agriculture is preferred to the existing practice of agriculture drainage water for aquaculture. The use of aquaculture drainage water is best practice due to its numerous advantages. Aquaculture drainage water contains a lot more nutrients for the crops than the agricultural drainage water, which might at the same time not be good for the cultured fish. Efforts should be geared to convince the government in Egypt to pay more attention to the reuse of aquaculture drainage water for effective and maximum utilization of water in the country. Eighty percent (80%) of the fish farmers in Egypt state that the source/s of water to their farms/ponds is/are challenging, while only 20% believe the source/s of water is/are good and not challenging [68]. In Egypt, the problem that was highlighted and emphasized mainly on water sources was pollution. In Egypt, 57% of the respondents have taken precautionary measures with regards to reducing the effect of pollution on the water source that enters their farms by checking the water qualities, filtering the water when pumping, and treatment of the water and pond, but 43% are yet to take any precautionary measures. The reason might be due to the fact that they are constrained to the available water source to be used for aquaculture in the country [68].

4.2. Land

The Egyptian Nile Delta is considered an area vulnerable to SLR. The overturning of coastal defenses and increased flooding, harm to urban areas, the retreat of barrier dunes, increased coastal erosion, increased soil and lagoon water salinity, and lower agricultural and fishery products are all possible effects of SLR on the delta [69]. In addition, Yates and Strzepek [70] stated that a large portion of arable land located in the Nile Delta is particularly sensitive to increased sea levels and precipitation, and to temperature change in Egypt. Due to floods, SLR causes land to be lost, which reduces the area that can be used for aquaculture. It also affects estuary systems, species abundance, the distribution of fish stocks, and freshwater fisheries, as well as the availability of freshwater and aquaculture seeds. With rising sea levels, seawater intrusion into freshwater aquifers is becoming a bigger issue [71]. In many regions, salinization of the soil and groundwater due to SLR would result in optimal conditions for aquaculture [72]. Low-lying areas will be flooded. One hypothesis is that as freshwater supply declines, aquaculture will become more diverse due to a shift to species found in brackish waters. The expanded regions might be appropriate for the brackish water cultivation of valuable species such as shrimp and mud crab. A significant portion of the area used for current agricultural activities, primarily rice farming, has become unsustainable in these places as a result of SLR, which causes the salinization of the water to increase. These areas can still be used for aquaculture, thereby providing much-needed alternative livelihoods and food production [73]. Starting new culture systems in salinity-intense locations is thus aquaculture's largest challenge. Planning procedures must be implemented quickly in order to tackle this issue [73]. A greater significance of the integrated agricultural system is therefore assumed in these conditions of SLR, as well as its detrimental effects on agricultural activities and aquaculture for the adequate management of agricultural resources in order to reduce environmental degradation, improve agricultural productivity, improve the quality of life of poor farmers, and maintain sustainability [58]. Farmers are drawn to integrated systems in particular

because they produce three different crops thanks to the use of water sources enriched with organic fish waste from intensive aquaculture ponds as fertilizer for terrestrial crops and water for raising sheep and goats, which results in the production of three different crops from the same amount of water [65]. El-Keram (a trading investment company in Egypt) is an ideal model which has applied this integrated system since 1990 [66].

4.3. Feed

Aquaculture relies heavily on capture fisheries for fishmeal. Fish output could be dramatically impacted by climate change, which would limit the availability of fishmeal and fish oil. In 2003, the aquaculture industry consumed 2.94 million tons of fishmeal, equivalent to 14.95 to 18.69 million tons of trash fish, feed fish, and low-value fish [74]. Climate change has the potential to have a negative influence on world fishmeal output, as seen by periodic shortages related to weather oscillations such as the El Nino phenomenon. Aquaculture industry expansion is boosting the demand for global sources of wild fishmeal to provide protein and oil elements for aquafeeds. Approximately 30% of the world's fish harvest (29.5 million tons) is used to produce fishmeal and fish oil for use in agriculture, aquaculture, and industry. Depending on the species, they can account for more than 50% of the meal. As a result, there is an urgent need for plant-based alternatives to fishmeal [59]. Recently, Egypt is seeking to change from low-intensity fish farming systems such as extensive and semi-intensive cultures to an intensive system that relies mainly on manufactured feed. This strategy increases the demand for commercial fish feed [75]. Furthermore, between 50% and 99% of feed ingredients used in aquafeed production in Egypt are imported [76,77]. The prices of components and processed feeds have significantly increased as a result of rising feed raw material costs globally and the Egyptian pound's deteriorating exchange rate against major currencies [78]. Similarly, feed accounts for 70–95% (on average, 85%) of all farm operating expenses. Fishmeal's partial or entire replacement with alternative protein sources has become more important as a result of its growing price, decreasing availability, erratic supply, and poor quality [79]. As a result, there is ongoing interest in finding and developing ingredients as substitutes for the expensive fishmeal feed [80] as well as in reducing its usage. Furthermore, climate change could also reduce the agricultural production of soy, corn, and other ingredients that today's fish feeds rely upon; hence, the industry has to search for new and sustainable resources to produce cultured fish, such as algae, in the future. The industry is in need of innovative solutions to solve this urgent challenge. Thus, several attempts on the different types of protein sources that have the ability of partially and/or totally replacing fishmeal in aquaculture feeds without affecting the performance of growth rates of fish are being extensively studied [81]. Particularly, many studies have been conducted to assess the partial or complete substitution of fishmeal in feed diets for tilapia with less expensive, as well as locally available, plant and animal protein sources [82–85]. Technology may lower the risks of higher prices and overfishing. It can provide substitutes to the use of captured fish derived inputs. Fishmeal and fish oil substitution in aquafeeds with nutritionally equivalent feedstuffs will diminish the reliance of different kinds of aquaculture on wild stocks. This substitution may also minimize pressure on the prices of feed inputs that result from capture fisheries.

4.4. Seeds

The climate change-related effects of variations in water temperature can affect the neuroendocrine control of reproduction in fish by acting at multiple levels of the brain–pituitary–gonad axis [86]. Consequently, this climate change is likely affecting sexual maturation, reproductive behavior, gametogenesis, spawning, and reproductive output. All the cited climate change-related factors seem to affect steroidogenesis. It is also important to note that the effects of climate change are not limited to breeders and gametes, but they also have direct consequences on their progeny, in particular at the level of growth. For instance, thermal embryonic history, potentially impacted by global warming, will influence the growth and fitness of larvae and juveniles [87]. Mechanothermal nociceptors

responding to extreme heat (above 20 °C), but not to cold, have been found in the head trigeminal nerve of rainbow trout, and their properties are closely linked to the behavior of rainbow trout in natural and high-temperature stream pools [88,89]. Increased water temperature appears to represent the most detrimental factor of climate change, with the gonads as one the organs more damaged by high temperatures [90]. A high temperature regime also affects oocyte osmoregulation and causes a reduction in their phospholipids and free fatty acids content [91]. In fish, elevated temperatures may have irreversible effects during sensitive periods of early development, affecting larval growth, the incidence of malformations, and sex determination/differentiation, provoking functional masculinization [92,93]. Therefore, elevated temperatures might modulate the sex differentiation process and induce masculinization through its action on gonadal steroid synthesis and/or release during early developmental stages by acting at different levels of the developing reproductive axis (e.g., gonad and brain). Generally, temperature is the variable that influences fish seed production the most, followed by rainfall, humidity, and solar radiation intensity [94,95]. Unfavorable temperatures impair growth by changing the metabolic and developmental processes of fish [96,97], ultimately affecting seed production [20,98]. Rearing temperature considerably affects egg production, hatching rate, and larval growth rate [99,100]. Further climate change-related effects, such as hypoxia [101,102], acidification [103,104], and salinity [105,106] are likely to strongly affect the quality and amount of fish gamete and the viability of the offspring.

The Egyptian fish seed sector started in the 1980s when the General Fisheries Authority decided to establish 14 freshwater hatcheries to produce carp seed for stocking public and private fish farms, as well as to support the integration of aquaculture into rice fields and the stocking of natural reservoirs and lakes [107]. Private freshwater hatcheries started producing Nile tilapia fry in the early 1990s to satisfy growing demand from private fish farms, and to stock their own farms. The number of private hatcheries had increased from 7 by 1996 to some 86 licensed plus around 600 unlicensed hatcheries in 2020 [108]. According to the latest annual fish statistics in Egypt presented by GAFRD in 2020 [108], the annual production of fish fry from the fish hatcheries and wild fry collection centers developed from 538 million units in 2011 to 721 million unit in 2020. There are 15 governmental freshwater fish hatcheries; their total production of fingerlings are 55.9 l million units in 2020, while there were two governmental marine water fish hatcheries that produced 534.3 million units of fingerlings in 2020 [108]. Meanwhile, there were 86 licensed private hatcheries in 2020, which produced 64.8 million units of fry and fingerlings of tilapia fish in freshwater fish. In marine water, the private fish hatcheries produced 18.9 million units of fingerlings in 2020 [108]. Particularly, in Egypt, numerous tilapia hatcheries have sprouted up along with the development of the aquaculture sector, all of which produce fingerlings and male fingerlings with their sex reversed [109]. The seasonality of the climate is one of the major issues facing Egyptian aquaculture. The primary farmed species, Nile tilapia, develops and reproduces best in the summer (when temperatures range from 25 to 30 °C), whereas winter temperatures fall below the ideal range for growth and reproduction to satisfy the increased demand for seed by fish farmers at the beginning of the season [110]. A growing number of tilapia hatcheries in Egypt are bringing forward and prolonging their spawning season by heating the water in their systems [111]. The most popular method is solar heating, which involves enclosing breeding tanks or ponds in greenhouse tunnels. However, this can be supplemented by heating with a boiler or by utilizing groundwater that is warmer than surface water. As a result, the hatchery is able to satisfy the early-season high demand for seeds [109]. On the other hand, a major beneficial effect of the process is the generation of seeds and larvae for aquaculture for the creation of new or additional fishing resources for fisheries and livelihoods. Under the risks posed by climate change, restocking can offer significant potential to enhance fisheries or preserve and improve endangered species [49]. All the aforementioned climate change factors, in general, might have an immediate or long-term impact on aquaculture. As stated, these effects cannot

always be traced to just one aspect of climate change; in most situations, a variety of elements combine to cause the effects [112].

5. The Threats of Climate Change on Food Security in Egypt

The weather in Egypt is often dry, hot, and desert. The coastal region has winter rainfall, but summers are hot and dry [113]. Climate characteristics have changed during the past few decades, and this has been seen and documented. According to recent research by Yin et al. [114], the mean maximum and minimum air temperatures have risen by +0.34 °C; each decimate characteristic has changed during the past few decades, and this has been seen and documented. The average air temperature and atmospheric pressure are also rising, by 0.017 °C and 0.026 hectopascals (hPa), respectively, every decade and year. According to the IPCC in 2008, climate change would have a significant impact on industries that depend on water. Agriculture, forestry, and fisheries are the three primary industries that are impacted by climate change [115]. Climate change has an influence on each of their manufacturing processes, although the effects will differ depending on the location. Because of the decline in output in tropical regions and the potential for adaptation issues, emerging nations such as Egypt may have difficulty adapting because of their poor economic capabilities [57]. SLR is also a critical concern in the climate change discussion [115]. The study by Conway et al. [116] confirmed that SLR had an adverse impact on water security and an increase water scarcity in Egypt. Furthermore, Bizikova et al. [117] suggested that climate change would lead to high market prices for food and thus, food will not be available to the poorest people leading to a food utilization problem of getting insufficient nutrients from the food consumed. In addition, according to the FAO report in 2008, the effects of climate change are expected to have a high impact on global food systems and food security [57]. Climate change poses a serious threat to Egypt's agricultural sector, increasing desertification rates, increasing water scarcity, threatening biodiversity, and affecting crop productivity and leading to food deficits and low levels of investment agriculture.

Due to its low-cost, high-quality protein, micronutrients, and omega-3 polyunsaturated fatty acid content, fish plays a significant role in food security [118]. Food security, according to the World Food Summit (WFS), is the condition in which all individuals always have physical or financial access to an adequate supply of wholesome foods that satisfy their dietary requirements and food choices for an active and healthy life [119]. However, the FAO study has introduced a novel idea by explaining that socioeconomic conditions and food access, rather than agroclimatic variables and food availability, determine food security [57]. When all members of society have the natural, social, and economic ability to get enough food that is safe, nourishing, and satisfies their dietary needs and preferences in order to live an active and healthy life, then there is a state of food security. Food availability, food stability, food intake, and access to food are therefore the four key components of food security. The expected impacts of climate change are posing a growing danger to food security, particularly to the availability of dietary protein. Due to aquaculture's substantial contribution to global food security, nutrition, and livelihoods, its effects on the industry have been thoroughly investigated and assessed on both a regional and worldwide level [19]. Fresh fish consumption is a historic and important part of the Egyptian diet, particularly in coastal towns and the northern Delta, and is a significant source of animal protein for the majority of the population. Fish imports of certain varieties, such as mackerel, tuna, herring, sardines, salmon, and frozen shrimp, make up for the 325,000 MT yearly difference between local consumption and production of fish. The yearly growth of imports reflects the influence of growing affluence on the consumer demand for fish species that are not grown in Egypt. Population growth (102 million projected by 2021) and economic expansion are also factors contributing to an increase in fish consumption. Consumption of fish per person increased from 16.67 kg per year in 2012 to 20.26 kg per year in 2020 (imports excluded [1]). Due to the Mediterranean Sea's rising level, climate change directly affects food security in Egypt by posing several dangers to the Nile Delta.

As a result, agricultural regions will have more salt and groundwater. Additionally, the north's freshwater lakes will become more salinized, which will result in the loss of some of the region's most productive farmland and a decline in fish output and other plants and animals. Fish, which is Egypt's main supply of animal protein and a crucial and reasonably priced source of nourishment for the underprivileged, will vary in species and composition. Numerous residents of these areas have been forced to leave because of waterlogging, poor fertility, and a lack of other employment [120]. Egypt is currently putting into action a number of massive projects in the agricultural sector to address climate risks, including the construction of 100,000 greenhouses that can supply year-round vegetables at affordable prices to curb price increases and introduce high-quality agricultural products. Egypt has put in place a horizontal extension project for the reclamation and cultivation of 1.5 million acres, along with programs for agricultural industrialization [113].

Finally, because of the possibility of infrastructure damage or degradation, food systems, particularly those in poor nations, face a significant danger from the anticipated effects of climate change. Transporting food and supplies may be a challenge for local suppliers in this situation [121,122]. Therefore, all of these factors must be taken into account in all nations' adaptation efforts to climate change [122]. The hazards of climate change affect every element of the food system in Egypt. With the bulk of the population residing in the Delta and along the coast, agriculture is essential to Egypt's GDP and food production. Geographical distribution has a greater effect on the food chain since the delta and coastal regions are both at risk of drowning in the next decades. As a result, climate change has an impact on and is sensitive to Egypt's food system. Global food systems and food security are significantly and directly impacted by climate change as well. The FAO highlighted possible effects on the following elements: food system assets, activities, food availability and accessibility, livelihoods, and policies and regulations [57]. The anticipated consequences of climate change are posing a growing danger to food security, especially to the availability of dietary protein. Due to aquaculture's substantial contribution to global food security, nutrition, and livelihoods, its effects on the industry have been thoroughly investigated and assessed on both a regional and worldwide level [19].

6. Effect of Climate Change on the Sustainability of the Fish Farm Sector in Egypt

Sustainable development focuses on the management and conservation of natural resources and the orientation of technological and institutional changes in such a manner as to ensure the attainment and continued satisfaction of human needs for present and future generations [123]. As a concept, sustainable aquaculture is the practice of aquaculture that emphasizes environmental, economic, and social sustainability to enhance capacity building and utilize land for the aquaculture industry successfully. Similarly, sustainability can refer to the management of financial, technological, institutional, natural, and social resources to assure a consistent supply of human needs, not just for today but also for future generations [124], which refers to the management of institutional, environmental, financial, technological, and social resources to guarantee a steady supply of human needs for both the present and future generations [125]. Aquaculture may compete with other food-producing sectors for the same resources or be impacted by pollution from those sectors [46]. The sustainability of aquaculture has been debated for decades. Potential issues include habitat destruction, the use of marine ingredients in feeds, freshwater usage, using wild juveniles for farm stocking, influencing wild gene pools through farm escapees, and the excessive loss of stock through disease and associated overuse of antibiotics, which are environmentally non-degrading, technically appropriate, economically viable, and socially acceptable. Although the aquaculture industry is expanding in Egypt, the fish culture sector is also facing some problems, such as environmental degradation, water scarcity, limited availability of land for aquaculture, high input costs, etc. Thus, sustainability in the aquaculture sector is more needed nowadays. Concerns about nutrition and sustainability are significantly related; feed consumption, species choice, and the adaptability of production systems to climate change are crucial for both [126]. Environmental,

economic, and social sustainability indicators may be used to evaluate the sustainability of aquaculture systems. The effective use of natural resources and pollution are examples of environmental sustainability indicators, pollution prevention, and biodiversity conservation [125]. In Africa, Egypt is regarded as one of the top nations for aquaculture. Additionally, Egypt has a mixed economic system that combines a range of individual freedoms with centralized financial planning and governmental supervision [127]. Egypt is a classic example of a developing nation that is seriously at risk from climate change and has severe challenges to its capacity to maintain its economic, social, and environmental sustainability. As a result, the competitiveness of Egypt is under tremendous fundamental strain. Increasing dangers to national security can also be used to characterize these tensions. They are propelled by an expanding population, increasing demand, and the limitations imposed by a limited resource base. If not handled swiftly and forcefully, they could escalate into true crisis situations. The whole aquaculture value chain is sensitive to the effects of climate change, despite certain elements of this being unclear [128,129]. Aquaculture is not an exception to the fact that the viability of food production systems is progressively being threatened by climate change [1,42]. According to the IPCC [42], climate change consequences and solutions are directly related to sustainable development, which strikes a balance between environmental preservation, economic success, and social well-being. This implies that aquaculture output cannot be sustainable without addressing the consequences of climate change.

Although many constraints are facing fish farmers in Egypt, including climate change, there is a rapid expansion in aquaculture. Egypt has increased its aquaculture production significantly to become the first major producer in Africa, although the share of Africa is still low at about 2.7% of world aquaculture production [1]. Fish aquaculture farms are considered as the main source of Egyptian fish production, which represents about 79.2% [108]. Fish production represented 16.25% of the total Egyptian agricultural GDP [108]. Aquaculture is an effective solution to reduce the gap between fish production and demand in Egypt. Despite the economic importance of aquaculture, some fish farmers have abandoned it due to some challenges that make the project unprofitable. In Egypt, parts of the vast Nile Delta are dotted with man-made, open-air ponds stocked with tilapia, perch, and other fish. In Egypt, aquaculture has become increasingly popular in recent years, as breeding and technological improvements make each pond more productive and profitable. Fish farming produces more protein and revenue per acre than crop farming, and with a lower water and carbon emission footprint per kilo of product. One kilogram of farmed fish requires about 1000 L of water to produce, while the same weight of rice or wheat can require two to four times the volume of water [130]. Moreover, fish farmers are not really a consumer of water; they are a user of water. While in agriculture, water is only used once, fish farmers are able to use it several times. However, water scarcity and rising supply costs—the problems that loom over the Delta at large—are threatening to capsize the fish farming industry in Egypt. With a rapidly growing population, an unstable global supply chain for food imports, rising temperatures, and limited land and water resources, Egypt could still find a promising path to food security and economic growth in pisciculture, but only if it can be undertaken by a smarter sustainability process [131]. Aquaculture plays a crucial role in Egypt's economic development, contributing substantially to achieving the Sustainable Development Goals. However, contexts are increasingly changing and are characterized by shifts in dietary needs, more integrated value chains, globalization, population dynamics, and climate change. An enhanced understanding of aquaculture's performance under these rapidly changing contexts is necessary. Yet, the ability to generate the required knowledge is often constrained by a lack of accurate data about the integrated on-farm performance of aquaculture systems. In efforts to address this gap, in Egypt, farmers practicing tilapia monoculture stocked smaller fingerlings than their polyculture counterparts, reaching the same harvest weight and obtaining a 20% higher yield than under polyculture. Tilapia monoculture was 42% more profitable and 18% more cost-effective than polyculture systems. There were no significant differences in productivity, profitability,

and cost-effectiveness across different farm sizes. There is also a notable increase in the adoption of modern extruded feed. However, there is a growing trend in incidences of abnormal fish mortality. Farmers' perceptions of climate change and its impacts on tilapia aquaculture are very low. Similarly, farmers' awareness of fish food safety certification is very low and only a few are interested in participating in such schemes if established [130]. Thus, the need for continued efforts and investments to promote aquaculture in Egypt is necessary. Specifically, the results on the cost-effectiveness of tilapia culture present evidence about the scalability of tilapia in Egypt. At the same time, interventions to promote the wide-scale adoption of aquaculture and the best management practices might help to reverse the trends in abnormal fish mortality in the immediate and medium term. In the long term, breeding for resilience traits will be crucial. There is also a need for increased access to climate information services to improve farmers' perceptions of climate change and its impacts in order to facilitate timely adaptation.

7. The Mitigation of Negative Impacts of Climate Change on Fish Culture

The fastest-growing industry in Egypt is aquaculture, which is also the country's primary source of fish and animal protein. Fish farming in Egypt has gradually transitioned from extensive to semi-intensive to intensive, with rapid development in the use of modern technologies, such as the use of a recirculating aquaculture system (RAS), fish–plant integrated system (such as aquaponics), fish–animal integrated system, and biofloc technology (BFT), as well as enhanced farm management techniques. The demand for resources used in aquaculture, including fish food, seeds, water, energy, and land, has risen as a result of this strategy [108]. In addition, climate change is considered one such constraint as it may have negative implications on the productivity of aquaculture. For alleviating these severe effects of climate change on the fish farming sector not only in Egypt, but also all over the world, there are two ways: the first is mitigation action, and the second is adaptation action. Regarding mitigation action, we can mitigate climate change, which involves reducing the concentration of gases from the winter effect; there is a sea reduction in leaks or an increase in sinks. Aquaculture can produce wholesome food with a small carbon footprint by concentrating on herbivorous species. Growing aquatic plants aids in the removal of trash from contaminated waters, while raising shellfish such as oysters and mussels is not only profitable but also contributes to the cleaning of coastal waters. In contrast to the potential declines in agricultural yields in many parts of the world, the climatic environment provides new opportunities for aquaculture in the medium term; that is, farming more species [58]. In addition, Egypt has developed various policies and measures to internalize renewable energy, energy efficiency, and reduce GHG emissions, as endorsed by the UNFCCC. Technology transfer needs to mitigate the effects of climate change in the medium term to include environmentally friendly technologies to protect the Mediterranean coast in general and the low-lying coastal areas of the Nile Delta in particular. Technical and financial support is urgently needed to establish research programs with teams from existing universities and research institutes [132]. Consequently, the second strategy to cope with climate change is a possible adaptation option, to improve the resilience of Egyptian aquaculture to the impacts of climate change which is imperative for the future development and sustainability of the sector. Whilst Egypt considers all possible adaptation options and regards adaptation as a key part of its climate change policy [133], farmers need to adapt in order to protect their everyday operations, cope with harsh weather, and ensure their revenue [134]. As a result, adaptation measures are taken in Egypt to either mitigate or capitalize on the real and anticipated effects of climate change, either by raising or decreasing a system's resilience. To lessen the ecosystem's overall susceptibility to climate change, this may entail reprioritizing present activities and setting new goals and objectives. In addition, adaptation action can take place in legal, regulatory, institutional, or decision-making processes, as well as in on-site conservation activities. For example, measures to restore or protect wetlands and riparian zones can help to moderate or lower river temperatures, alleviate flooding and the erosive effects of extreme rainfall

or rapid snowmelt, improve habitat quality, and allow species to migrate. Thus, the early implementation of strategic adaptation measures can reduce severe impacts and avoid the need for more costly measures in the future. The actions aim to: eliminate other threats and reduce non-climate stressors that exacerbate the effects of climate change; establish, expand, or adapt protected areas, habitat buffer zones, and corridors; and improve monitoring and facilitate management under uncertainty, including scenario-based planning and adaptive management.

Role of Modern Aquaculture (Integrated) Systems to Mitigate the of Impacts of the Climate Change

Global food demand will increase by 70–100% by 2050 [135], and the key role of the agricultural sector in food security [136], one of the greatest issues of the 21st century, is to find a way to produce more food using fewer resources and minimizing environmental impacts [137]. Among the systems currently used by the agricultural sector, aquaculture seems to be the most suitable and convenient for counteracting shortages in food production [138]. In the integrated fish culture system, the main beneficiary is fish, which utilize animal and agricultural wastes directly or indirectly as food. As integrated farming involves the recycling of wastes, it has been considered an economic and efficient means of environmental management. Moreover, diversifying food systems and integrated agriculture production systems can be important climate change adaptation measures [139]. In this respect, modern aquaculture systems reuse the same volume of water [140,141], where the rate of water reuse ranges between 80 and 99%, therefore reducing water requirements and the environmental impact of aquaculture [142]. The unification of a RAS and aquaponics improves sustainability and ensures food sufficiency, providing various significant economic and social benefits [143].

A.   Recirculation aquaculture system (RAS)

The RAS is considered a promising intensive fish culture system. RAS is designed to raise large quantities of fish in relatively small volumes of water by treating the water to remove toxic waste products and then reusing it [144]. RAS is a technology where water is recycled and reused after mechanical and biological filtration and removal of suspended matter and metabolites. This method is used for the high-density culture of various species of fish, utilizing minimum land area and water. RASs have become more numerous and equally sophisticated as land-based aquaculture production has increased. The complexity of the system gives rise to a good deal of health management issues, whereby the water quality of the production system directly impacts the health of the fish. Additionally, the challenges of using RAS in a seawater environment pose unique issues of water chemistry, fish production biology, and health. Fish health management in RAS depends largely upon the quality of the intake water for controlling the known obligate fish pathogens [145]. RAS technology is based on the use of mechanical and biological filters and the method can be used for any species grown in aquaculture as shown in Figure 5. New water is added to the tanks only to make up for splash out, evaporation, and that used to flush out waste materials. The reconditioned water circulates through the system and not more than 10% of the total water volume of the system is replaced daily. In order to compete economically and to efficiently use the substantial capital investment in the recirculation system, the fish farmer needs to grow as many fish as possible in the inbuilt capacity [144]. The management of recirculating systems relies heavily on the quantity and quality of feed and the type of filtration. RASs have low direct land and water requirements and enable high stocking densities but do require large energy inputs and thus have high production costs and waste disposal challenges [146]. RAS technologies are typically beneficial when advantages in fish performance outweigh the increased costs. Grow-out operations in RAS are progressively focused on species with a high market value. In addition, RAS is an invaluable alternative for preventing water pollution by diminishing both the volume and the eutrophication potential of the effluents [147]. The development of a commercial-scale RAS has been stimulated primarily by an interest in producing high-value warm water fish and eels. RASs overcome the constraints imposed by temperate climates and other

environmental factors by providing a controlled, predictable, and biosecure environment for the cultured species [148]. Thus, RAS is an eco-friendly, water efficient, highly productive intensive farming system, which is not associated with adverse environmental impacts, such as habitat destruction, water pollution and eutrophication, biotic depletion, ecological effects on biodiversity due to captive fish and exotic species escape, disease outbreaks, or parasite transmission. Moreover, RASs operate in an indoor, controlled environment, and thus, are only minimally affected by climatic factors, including rainfall variation, flood, drought, global warming, cyclones, salinity fluctuation, ocean acidification, and sea level rise. However, energy consumption and GHG emissions are the two most stringent limiting factors for RASs. Despite these potentials and promises, RASs have not yet been widely practiced, particularly in developing countries, due to their complex and costly system designs. Further research with technological innovations is needed to establish low-cost, energy-efficient RASs for intensifying seafood production, reducing GHG emissions, and adaptation to climate change [149].
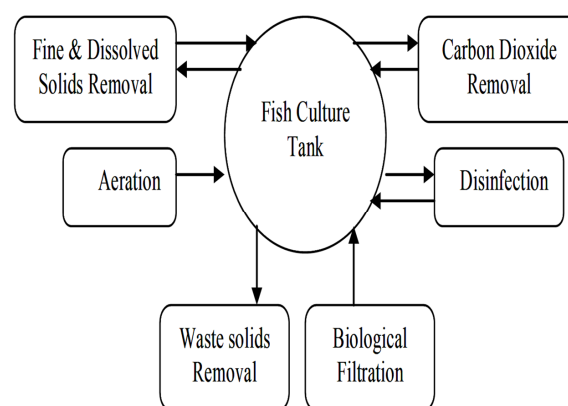
Figure 5. Recirculating aquaculture system components [144].

B.   Aquaponics system

The integrated fish–plant system is named an aquaponics system, where aquaponics is a symbiotic integration of two mature disciplines: aquaculture and hydroponics. It is a hybrid food technology system that helps mitigate climate change through the combination of fish tanks and crops. The name "aquaponics" derives from a mixture of two words; aqua from aquaculture, which is the farming of aquatic organisms, and ponics from hydroponics, which uses water instead of soil to grow plants [150,151]. Many different food products can be grown using a combination of plant and fish farming in an aquaponics system. Reusing water after mechanical and biological filtration and recirculation provides local healthy food that can support the local economy [152]. Plant roots and rhizobacteria take nutrients from fish manure in the water and absorb them as fertilizers to hydroponically grow plants. In return, hydroponics acts as a biofilter stripping off ammonia, nitrates, nitrites, and phosphorus. Then, the water can be recirculated, fresh and clean, into the fish tanks in a closed cycle as shown in Figure 6. Aquaponics is a sustainable production system with two methods of cultivation, plants and fish. It combines traditional aquaculture, which is the breeding of aquatic animals such as fish, crayfish, and shrimp, with hydroponics, where plants are grown in water in a symbiotic environment. It combines conventional aquaculture, or the tank-rearing of aquatic animals, with hydroponics, the growing of crops in nutrient-rich water [153]. Clearing land for crops, artificial fertilizers, insecticides, herbicides, and larger livestock herds accounts for almost one-quarter of anthropogenic GHG emissions. Meanwhile, the aquaponic technique produces crops and raises fish without relying on toxic chemical pesticides, synthetic fertilizers, genetically modified seeds, or practices that degrade soil, water, or other natural resources. More specifically, aquaponics is a hybrid food technology system that has the potential to remove the negative environmental impact of current farming techniques [154]. This system is a valuable

alternative to both traditional agriculture, fishing, and fish farming. Its advantages include water conservation, sustainability, and the eliminated need for soil [155]. In addition, aquaponics achieves the automatic and digital monitoring of aquaculture systems by controlling and mitigating abiotic factors. Generally, aquaponics systems achieve savings by requiring less water quality monitoring, less physical land, and the sharing of equipment such as pumps and heaters [151]. The operational cost savings for commercial use would also be evident through the elimination of insect and weed control. Moreover, aquaponics can be a strong alternative system to conventional agriculture and land reclamation in Egypt. Although the cost of aquaponics can be seen as expensive, especially for small farmers and startups, the profit per acre can reach 30 times more than the profit from land reclamation or conventional agriculture [156]. In developing countries or places that are frequently and heavily affected by climate change issues such as Egypt, the use of aquaponics delivers a source of food that is unaffected by climate change. Utilizing aquaponics systems could mitigate climate change and significantly add to increased food security to the benefit of people [157].
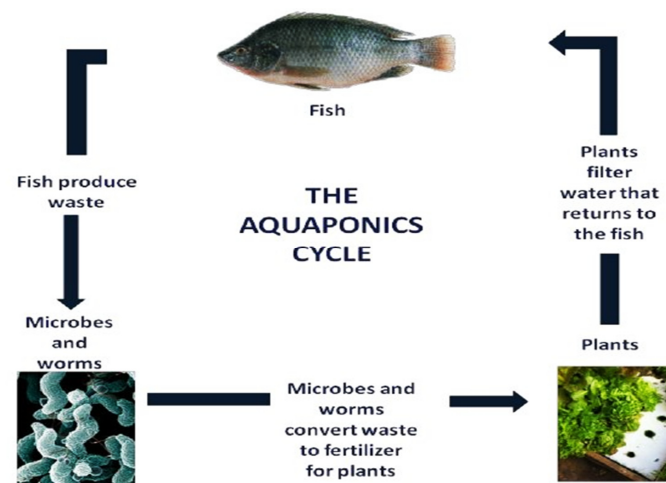
Figure 6. The aquaponics system cycle [158].

C. Biofloc technology (BFT)

Successful fish farming is entirely dependent on the physicochemical and biological qualities of water. Consequently, water quality control is required for optimum pond management [159]. Some studies suggest that the ratio between nitrogen (N) and carbon (C) in the water during the period of aquaculture should be controlled by implementing successful BFT [160]. Thus, BFT is an integrated system as shown in Figure 7, and the quality of this system, which depends on the biotic composition of biofloc and the quantity of suspended solids, is checked with Imhoff cones. For checking the biotic composition of biofloc, water collected from the system is reserved in Imhoff cones for precipitation. In this respect, BFT is a newly emerging frugal technology for fish cultivation in which nitrogenous wastes generated from fish/shellfish and unconsumed feed can be converted to protein-rich feed in the form of biofloc [161]. It was developed to improve ecological control over aquatic animal production or to treat wastewater, but now it has gained importance as an approach in aquaculture [162]. This operates the system on the principle of increasing carbon-to-nitrogen ratios, through the addition of an exogenous carbon source that consequently stimulates natural heterotrophic bacterial growth in the system, which converts them into microbial protein [163,164]. It is realized that fishmeal being used in aquaculture production systems as a protein source for the formulation of fish and shrimp feed can be significantly replaced by biofloc meal [165]. In addition, the sustainable approach of such a system is based on the growth of micro-organisms in the culture medium, the least amount or zero water exchange, high dissolved oxygen level, and a high C:N ratio; thus,

it can be considered an environmentally friendly strategy and an important tool against the drastic effects of climate change [166,167]. Therefore, BFT has been widely used to maximize tilapia production for its ability to support high-density cultivation, to improve water quality, and, simultaneously, recycle feed and protein production in the same culture unit [168,169]. Moreover, Kuhn et al. [170] reported that microbial floc meal in tilapia diets significantly increase weight gain. Biofloc consumption by fish could contribute about 50% of the dietary protein requirements of Nile tilapia [171].
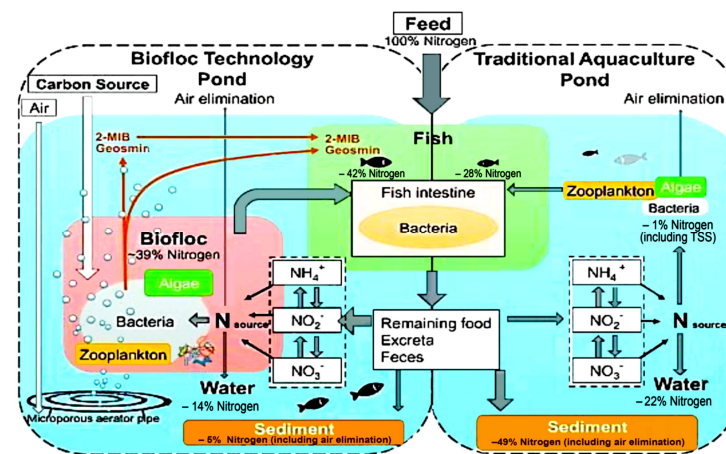
Figure 7. Role of microbial communities in biofloc technology (BFT) to improved water quality and fish yield in freshwater indoor and outdoor pond aquaculture [172].

D. Integrated multi-trophic aquaculture (IMTA)

To avoid or alleviate the negative effects posed by aquafarming, integrated multi-trophic aquaculture (IMTA) is proposed as a potential bio-mitigation approach. IMTA aims to achieve the sustainable development of aquaculture and improve the productivity of intensive monoculture through reusing waste as food resources. In this integrated system, the targeted species are co-cultivated with others that have dissimilar feeding habits in different trophic levels [173]. Various species of nutrient absorber, suspended feeder, deposit feeder, and other organic extractive organisms could be considered as the candidates to be co-cultured with targeted species (finfish, e.g., red sea bream *Pagrus major*, Atlantic salmon *Salmo salar*) in an IMTA system. Waste released from fish farms could offer food sources for inorganic and organic nutrient extractive species. For instance (Figure 8), as particulate organic waste (e.g., fish fecal matter, waste fish feed) mainly sinks down to the sea bottom, deposit feeders (e.g., Japanese sea cucumber *Apostichopus japonicus*, giant California sea cucumber *Parastichopus californicus*) will ingest it as food, consequently mitigating the problem of hypoxic bottom water due to increased oxygen consumption during the bacterial decomposition of excessive organic matter. As another form of aquaculture waste, dissolved nutrients (e.g., phosphorus, nitrogen) cause eutrophication, which increases the risk of harmful algal blooms. Planting nutrient absorbers (e.g., seaweeds *Gracilaria chilensis*, *Laminaria japonica*, *Ulva ohnoi*) could minimize this risk through their competition with phytoplankton for resources and harvesting macroalgae periodically will speed up the removal of dissolved nutrients [174]. Meanwhile, the supplement, suspension feeders, and other organic extractive species are capable of further filtering the phytoplankton, as well as the dispersed small particle organic materials from both fish food and feces in the water column. From an environmental point of view, these modern fish farming systems represent a novel technology that improves production efficiency, while mitigating environmental impacts (pollution load, including GHGs emissions), diversifying fish production, animal welfare in aquaculture systems, climate change studies, soil depletion, technologies that mitigate the emergence of animal diseases or parasites, and reducing the use of antibiotics, chemical fertilizers, new feed ingredients, and carbon footprint [175,176].

These systems also prevent the release of aquaculture waste that pollutes water bodies (eutrophication), allowing greater control of the water and production, which makes food safer against possible residues [151,177]. These integrated systems not only reduce waste but also increase productivity by using by-products from crops, livestock, fish systems, and other waste as inputs for different subsystems. This also reduces farmers' dependence on agro-industrial products such as commercial inorganic fertilizers and formulated pelleted feed.
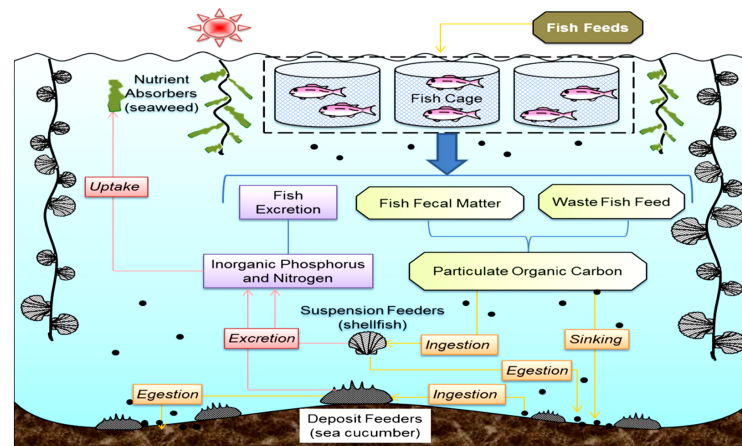
Figure 8. Conceptual diagram of the integrated multi-trophic aquaculture system (IMTA). Boxes represent state variables and/or interaction processes. Arrows denote the carbon cycle (brown color) and nutrient cycle (pink color), respectively [178].

By applying the concept of circularity, integrated agricultural systems can thus minimize energy and materials use, reduce environmental impacts, and create new business opportunities, as well as achieve more sustainability in the aquaculture sector [179]. Furthermore, traditional integrated agriculture–aquaculture (IAA) systems are semi-intensive, with limited feed and nutrient inputs and minimal use of electricity. This means that the GHG emissions from traditional IAA are negligible. Furthermore, in livestock–fish systems, where the manure of farm animals such as chickens is converted into nutrients for fish, methane and nitrous oxide emissions produced by decomposing animal waste are avoided. The Intergovernmental Panel on Climate Change (IPCC) has found that IAA systems can play an important role in making food systems more resilient while reducing GHG emissions [139]. By providing more protein for household diets, they may also reduce the demand for other kinds of meat production, including less sustainable forms of aquaculture. Ahmed et al. [180] estimated that converting 25% of the world's aquaculture area (4.5 million ha, of a total of 18 million) to agriculturally eutrophic impoundment and IAA would increase carbon storage by 95.4 million tons per year, which will consequently lead to mitigating the negative effects of climate change on this imperative sector. Particularly, in Egypt, IAA provides a proven method to increase production efficiency. An example is the tilapia farms, where integrated systems for horticulture and aquaculture focus on water use, especially in a region considered the most water-scarce in the world. With looming water wars if this crisis is not handled correctly, the efficient use of water such as these tilapia farms is much needed. One type of system is aquaponics, in which fish and plants are grown together and the nutrient-rich water resulting from fish waste is used as a fertilizer for the plants, instead of leaving the system. This is a perfect example of how interconnected interactions within an ecosystem, including humans, can serve to better address sustainability concerns. Adopting integrated aquaculture as a strategy not only increases output productivity and efficiency in a sustainable manner, it also plays a major role in reducing the sector's vulnerability and increasing its resilience to climate change, as well as offering a resilient solution to increased food security [181]. IMTA is a system that feeds species with species that remove organic substances and extractive

species that are inorganic, which use aquaculture waste for their development. Therefore, one of the key strategies currently being used is encouraging IMTA, a novel process of growing finfish alongside shellfish such as oysters and marine plants such as seaweeds. Interestingly, we are seeing more applications of this system in many forms, which are environmentally friendly [182]. Thus, IMTA is considered to be more sustainable than conventional monoculture systems because it may combine several species. A few examples include the recent announcement by the South Asian Association for Regional Cooperation (SAARC) countries of introducing IMTA as a means to reduce the impacts of climate change on the sector, trials in Europe focusing on culturing lobsters alongside salmon, a vision to have a rainforest in the ocean, or better yet, an effort to carbon capture more CO_2 than is produced by the Netherlands each year [183,184].

8. Conclusions

Climate change is the major global challenge today, and the world is becoming more vulnerable to this change. Climate change is expected to exacerbate in occurrence and intensity in the future, which results in negative impacts on social, economic, and environmental aspects. Specifically, Egypt's large population makes it one of the countries most affected by the negative effects of climate change. Egypt is particularly vulnerable to the impacts of climate variability and change, particularly with respect to water security, agriculture, fish culture and livestock, increasingly adverse conditions to public health, human settlements, and energy demand and supply. In addition, climate change could have significant adverse economic impacts in Egypt. The country is heavily dependent on the Nile River (which accounts for 96% of the water resources available), which may decrease in flow [185,186]. The negative effects of climate change adversely impact not only the agriculture sector in general, or the fish culture sector in particular, but also human health. Egypt has recently created a number of national programs in the fields of climate protection and adaptation to climate change. Out of a total budget of USD 324 billion, Egypt's mitigation and adaptation projects will cost around USD 211 and USD 113 billion, respectively, in addition to energy efficiency initiatives, wind energy initiatives, and environmentally friendly transportation initiatives. Other initiatives, such as biogas projects, landfills, and recycling facilities, try to use trash as fuel and promote complete waste management. As part of an integrated model for climate change mitigation and adaptation initiatives, they also include wastewater treatment facilities, sewer lining projects, seawater desalination, and water rationalization. This also includes the implementation of natural gas supply projects, waste management, sewage treatment plants, and afforestation.

Even though aquaculture plays an essential role in the Egyptian food system, accounting for approximately 80% of total fish production [108], climate change already affects aquaculture and the impacts are likely to increase in all aspects of this vital sector. In order to reduce the possible dangers of climate change on fish productivity, it is crucial that the Egyptian government and policymakers develop sound policies. Consequently, the Egyptian government is also investing in establishing huge sea aquaculture systems in coastal governorates to compensate for the lower yield from the open sea due to climate change. The Berka Ghalion aquaculture complex in Kafr El-Sheikh includes a fish hatchery, 454 fish ponds, 655 shrimps ponds, and 156 nursery ponds. The complex covers 4000 acres, including a fodder factory and fish packaging factory offering 5000 job opportunities. The government is also taking huge strides in the rehabilitation of Egyptian coastal lakes to protect fisheries, especially the production of fish seed and the maximization of the use of its natural lakes in the production of fish wealth. This also provides the restoration of ecosystem services, thus combating climate change and loss of biodiversity. In addition, the Ministry of Water Resources and Irrigation is introducing large investments through the Shore Protection Authority (SPA), in cooperation with the UNDP with funding from the Green Climate Fund (GCF) in upscaling an ecosystem-based approach, following an ecosystem-based approach for the protection of low-lying lands in the Nile Delta. Finally, we can summarize the possible solutions for adaptations against the negative effects of

climate change on aquaculture in Egypt to achieve the sustainability of this imperative sector in the following points:

a.   Greater public awareness, especially among all related stakeholders to the fish farming sector in Egypt, must be raised about the problems of climate change and its negative effects on the fish sector;

b.   Using environmentally friendly aquaculture techniques such as RAS, aquaponics, BFT, or cage farming systems;

c.   Using groundwater and effluent discharge in order to overcome the present and future anticipated limitations of fresh water and brackish water;

d.   Researchers should start to evaluate the economic feasibility and optimum usage of novel proteins as fishmeal substitutes. Furthermore, the improvement of local raw materials to be used in fish feed formulation is also highly recommended;

e.   The creation of new fish strains with increased salinity tolerance or increased temperature tolerance to cope with alterations by climate change;

f.   The easier solution is to diversify the production to a heat-tolerant fish species or gradually increase the production of fish species such as the African catfish, which is more resistant to higher temperatures, has a larger thermal window, and better responds to thermal stress;

g.   Increasing the production of fish seeds in hatcheries, as well as the genetic selection of seeds that adapt to new environmental conditions;

h.   Reducing energy use through energy conservation and introducing possible renewable energy approaches.

References

1.   FAO. *The State of World Fisheries and Aquaculture 2020. Sustainability in Action*; FAO: Rome, Italy, 2020. [CrossRef]
2.   Béné, C. *Small-Scale Fisheries: Assessing Their Contribution to Rural Livelihoods in Developing Countries*; FAO Fisheries Circular. No. 1008; Food and Agriculture Organization: Rome, Italy, 2006.
3.   Allison, E. *Aquaculture, Fisheries, Poverty and Food Security*; Working Paper 2011-65; The WorldFish Center: Penang, Malaysia, 2011.
4.   FAO. *The State of World Fisheries and Aquaculture 2016. Contributing to Food Security and Nutrition for All*; FAO: Rome, Italy, 2016.
5.   Ali, A.; ElSayed, M.; Radwan, R.; Hefny, R. An economic study of the fish production system in Egypt. *Sinai J. of Appl. Sci.* **2020**, *9*, 105–116. [CrossRef]
6.   GAFRD. *The General Authority for Fishery Resources Development: Fisheries Statistics Yearbook 2019*, 29th ed.; General Authority for Fish Resources Development, Ministry of Agriculture: Cairo, Egypt, 2019; 104p.
7.   El-Sayed, A.-F.M. *Aquaculture Feed and Fertilizer Resource Atlas of Egypt*; FAO, Regional Office of the Near East: Cairo, Egypt, 1999.
8.   Soliman, N.F.; Yacout, D.M.M. The prospects of analysing the environmental impacts of Egyptian aquaculture using life cycle assessment. *Int. J. Aquac.* **2015**, *5*, 1–9. [CrossRef]
9.   FAO. *Egypt—National Aquaculture Sector Overview*; FAO Fisheries Department, Fisheries Information, Data and Statistics Unit: Rome, Italy, 2010.
10. Wally, A. The state and development of aquaculture in Egypt. *Glob. Agric. Inf. Netw.* **2016**, 1–14. Available online: https://www.fas.usda.gov/data/egypt-state-and-development-aquaculture-egypt (accessed on 10 May 2022).
11. Suloma, A.; Ogata, H.Y. Future of rice-fish culture, desert aquaculture and feed development in Africa: The case of Egypt as the leading country in Africa. *Jpn. Agric. Res. Q.* **2006**, *40*, 351–360. Available online: https://www.jircas.affrc.go.jp (accessed on 22 March 2022). [CrossRef]
12. El-Gayar, O. Aquaculture in Egypt and Issue for Sustainable Development. *Aquac. Econ. Manag.* **2003**, *7*, 137–154. [CrossRef]
13. Naziri, D. Financial services for SME (small and medium-scale enterprise) aquaculture producers. *Marine Policy* **2003**, *37*, 106–114.

14. Mur, R. *Development of the Aquaculture Value Chain in Egypt: Report of the National Innovation Platform Workshop, 19–20 February 2014*; WorldFish: Cairo, Egypt, 2014.

15. FAO. *The State of World Fisheries and Aquaculture*; FAO Fisheries Department, Fisheries Information, Data and Statistics Unit: Rome, Italy, 2014.

16. Mansour, E.; Moustafa, E.D.; Qabil, N.; Abdelsalam, A.; Wafa, H.A.; Kenawy, A.E.; Casas, A.M.; Igartua, E. Assessing different barley growth habits under Egyptian conditions for enhancing resilience to climate change. *Field Crop. Res.* **2018**, *224*, 67–75. [CrossRef]

17. IPCC. *Climate Change 2007: The Physical Science Basis: Contribution of Working Group to the Fourth Assessment Report of the Intergovernmental Panel on Climate Change*; Solomon, S., Qin, D., Manning, M., Chen, Z., Marquis, M., Averyt, K.B., Tignor, M., Miller, H.L., Eds.; Cambridge University Press: Cambridge, UK, 2007.

18. IPCC. *Climate Change: Synthesis Report: Contribution of Working Groups I, II and III to the Fifth Assessment Report of the Intergovernmental Panel on Climate Change*; Core Writing Team, Pachauri, R.K., Meyer, L.A., Eds.; IPCC: Geneva, Switzerland, 2014.

19. Rutenberg, I.; Gwagwa, A.; Omino, M. *Use and Impact of Artificial Intelligence on Climate Change Adaptation in Africa*; Oguge, N., Ayal, D., Adeleke, L., da Silva, I., Eds.; African Handbook of Climate Change Adaptation; Springer: Cham, Switzerland, 2021. [CrossRef]

20. Maulu, S.; Hasimuna, O.J.; Haambiya, L.H.; Monde, C.; Musuka, C.G.; Makorwa, T.H.; Munganga, B.P.; Phiri, K.J.; Nsekanabo, J.D. Climate Change Effects on Aquaculture Production: Sustainability Implications, Mitigation, and Adaptations. *Front. Sustain. Food Syst.* **2021**, *5*, 609097. [CrossRef]

21. Cianconi, P.; Betrò, S.; Janiri, L. The Impact of Climate Change on Mental Health: A Systematic Descriptive Review. *Front. Psychiatry* **2020**, *11*, 74. [CrossRef]

22. Amoak, D.; Luginaah, I.; McBean, G. Climate Change, Food Security, and Health: Harnessing Agroecology to Build Climate Resilient Communities. *Sustainability* **2022**, *14*, 13954. [CrossRef]

23. Reid, G.; Gurney-Smith, H.; Marcogliese, D.; Knowler, D.; Benfey, T.; Garber, A.; Forster, I.; Chopin, T.; Brewer-Dalton, K.; Moccia, R.; et al. Climate change and aquaculture: Considering biological response and resources. *Aquacult. Environ. Interact.* **2019**, *11*, 569–602. [CrossRef]

24. Volkoff, H.; Rønnestad, I. Effects of temperature on feeding and digestive processes in fish. *Temperature* **2020**, *7*, 307–320. [CrossRef]

25. Huang, M.; Ding, L.; Wang, J.; Ding, C.; Tao, J. The impacts of climate change on fish growth: A summary of conducted studies and current knowledge. *Ecol. Indic.* **2021**, *121*, 106976. [CrossRef]

26. Magouz, F.I.; Amer, A.A.; Faisal, A.; Sewilam, H.; Aboelenine, S.M.; Dawood, M.A.O. The effects of dietary oregano essential oil on the growth performance, intestinal health, immune, and antioxidative responses of Nile tilapia under acute heat stress. *Aquaculture* **2022**, *548*, 737632. [CrossRef]

27. Skeeles, M.R.; Winkler, A.C.; Duncan, M.I.; James, N.C.; van der Walt, K.A.; Potts, W.M. The use of internalheart rate loggers in determining cardiac breakpoints of fish. *J. Therm. Biol.* **2020**, *89*, 102524. [CrossRef]

28. Haverinen, J.; Vornanen, M. Reduced ventricular excitability causes atrioventricular block and depression of heart rate in fish at critically high temperatures. *J. Exp. Biol.* **2020**, *223*, jeb225227. [CrossRef]

29. Yilmaz, S.; Ergün, S.; Çelik, E.Ş.; Banni, M.; Ahmadifar, E.; Dawood, M.A.O. The impact of acute cold water stress on blood parameters, mortality rate and stress-related genes in Oreochromis niloticus, Oreochromis mossambicus and their hybrids. *J. Therm. Biol.* **2021**, *100*, 103049. [CrossRef]

30. Kim, J.H.; Kim, S.-K.; Hur, Y.B. Temperature-mediated changes in stress responses, acetylcholinesterase, and immune responses of juvenile olive flounder Paralichthys olivaceusin a biofloc environment. *Aquaculture* **2019**, *506*, 453–458. [CrossRef]

31. Urbinati, E.C.; Zanuzzo, F.S.; Biller, J.D. *Stress and Immune System in Fish. InBiology and Physiology of Freshwater Neotropical Fish*; Academic Press: Cambridge, MA, USA; Elsevier: Amsterdam, The Netherlands, 2020; pp. 93–114. [CrossRef]

32. Feidantsis, K.; Pörtner, H.O.; Giantsis, I.A.; Michaelidis, B. Advances in understanding the impacts of globalwarming on marine fishes farmed offshore:Sparus aurataas a case study. *J. Fish Biol.* **2021**, *98*, 1509–1523. [CrossRef]

33. Cejko, B.I.; Krejszeff, S.; Judycka, S.; Targońska, K.; Kucharczyk, D. Effect of different treatment agents and post-treatment latency times on spermiation stimulation of northern pike (Esox lucius) under controlled conditions. *Theriogenology* **2019**, *142*, 260–267. [CrossRef]

34. Dadras, H.; Dzyuba, V.; Golpour, A.; Xin, M.; Dzyuba, B. In vitro antioxidant enzyme activity and sperm motility at different temperatures in starlet Acipenser ruthenus and rainbow trout Oncorhynchus mykiss. *Fish Physiol. Biochem.* **2019**, *45*, 1791–1800. [CrossRef] [PubMed]

35. Servili, A.; Canario, A.V.M.; Mouchel, O.; Muñoz-Cueto, J.A. Climate change impacts on fish reproduction aremediated at multiple levels of the brain-pituitary-gonad axis. *Gen. Comp. Endocrinol.* **2020**, *291*, 113439. [CrossRef] [PubMed]

36. Sun, J.L.; Zhao, L.L.; Liao, L.; Tang, X.H.; Cui, C.; Liu, Q.; Yang, S. Interactive effect of thermal and hypoxia on largemouth bass (Micropterus salmoides) gill and liver: Aggravation of oxidative stress, inhibition of immunity and promotion of cell apoptosis. *Fish Shellfish Immunol.* **2020**, *98*, 923–936. [CrossRef] [PubMed]

37. Cascarano, M.C.; Stavrakidis-Zachou, O.; Mladineo, I.; Thompson, K.D.; Papandroulakis, N.; Katharios, P. Mediterranean aquaculture in a changing climate: Temperature effects on pathogens and diseases of three farmed fish species. *Pathogens* **2021**, *10*, 1205. [CrossRef] [PubMed]

38. Islam, M.J.; Kunzmann, A.; Slater, J.M. Responses of aquaculture fish to climate change induced extreme temperatures: A review. *J. World Aquac. Soc.* **2022**, *53*, 314–366. [CrossRef]

39. Leach, K.; Zalat, S.; Gilbert, F. Egypt's protected area network under future climate change. *Biol. Conserv.* **2013**, *159*, 490–500. [CrossRef]

40. Ouda, S.; Ewise, M.; Noreldin, T. Projection of productivity of cultivated crops in rain-fed areas in Egypt under climate change. *Cogent Food Agric.* **2016**, *2*, 1136256. [CrossRef]

41. NRC National Research Council. *Climate Change: Evidence and Causes: Update 2020*; The National Academies Press: Washington, DC, USA, 2020. [CrossRef]

42. IPCC. Special Report on the Ocean and Cryosphere in a Changing Climate. 2019. Available online: https://www.ipcc.ch/srocc (accessed on 20 May 2022).

43. IPCC (Intergovernmental Panel on Climate Change). *Climate Change 2021: The Physical Science Basis*; Working Group I contribution to the IPCC Sixth Assessment Report; Cambridge University Press: Cambridge, UK, 2021. Available online: www.ipcc.ch/assessment-report/ar6 (accessed on 9 August 2022).

44. Kobiruzzaman, M.M. Cause of Climate Change-9 Natural Causes of Climate Change in 2022. Newsmoor- Educational Website For Online Learning. 2022. Available online: https://newsmoor.com/natural-causes-of-climate-change-9-natural-causes-of-climate-change/ (accessed on 15 July 2022).

45. Onoja, U.S.; Dibua, U.M.E.; Enete, A.A. Climate change: Causes, effects and mitigation measures-A Review. *GJPAS* **2011**, *17*, 469–479.

46. Waite, R.; Beveridge, M.; Brummet, R.; Castine, S.; Chaiyawannakarn, N.; Kaushik, S.; Mungkung, R.; Nawapakpilai, S.; Phillips, M. *Improving Productivity and Environmental Performance of Aquaculture*; Working Paper, Installment of Creating a Sustainable Food Future; World Resources Institute: Washington, DC, USA, 2014. Available online: http://www.worldresourcesreport.org (accessed on 23 January 2022).

47. Gado, T.A.; El-Agha, D.E. *Climate Change Impacts on Water Balance in Egypt and Opportunities for Adaptations*; Abu-hashim, M., Khebour Allouche, F., Negm, A., Eds.; Agro-Environmental Sustainability in MENA Regions. Springer Water; Springer: Cham, Switzerland, 2021. [CrossRef]

48. Chen, O.; Abdelhalim, A.; Liu, Y.; Rico-Ramirez, M.; Han, D. Climate change adaptations for food security in vulnerable areas of the Egyptian Nile—Or tackling the overlooked nexus hazards of hydrological extremes and waste pollutions. *Water* **2021**, *13*, 412. [CrossRef]

49. Soliman, N.F.; Yacout, D.M.M. Aquaculture in Egypt: Status, constraints and potentials. *Aquacult. Int.* **2016**, *24*, 1201–1227. [CrossRef]

50. El Raey, M. Impacts and implications of climate change for the coastal zones of Egypt. In *Coastal Zones and Climate Change*; Michel, D., Pandya, A., Eds.; The Henry L. Stimson Center: Washington DC, USA, 2010.

51. Hammond, M. *The Grand Ethiopian Renaissance Dam and the Blue Nile: Implications for Transboundary Water Governance*; Discussion Paper 1307; Global Water Forum: Canberra, Australia, 2013.

52. Schilling, J.; Hertig, E.; Tramblay, Y.; Scheffran, J. *Climate Change Vulnerability, Water Resources and Social Implications in North Africa*; Regional Environmental Change; Springer: Berlin/Heidelberg, Germany, 2020.

53. Smith, J.; McCarl, B.; Kirshen, P.; Jones, R.; Deck, L.; Abdrabo, M.; Borhan, M.; El-Ganzori, A.; El-Shamy, M.; Hassan, M.; et al. Egypt's economic vulnerability to climate change. *Clim. Res.* **2014**, *62*, 59–70. [CrossRef]

54. Dasgupta, S.; Laplante, B.; Murray, S.; Wheeler, D. *Sea-Level Rise and Storm Surges: A Comparative Analysis of Impacts in Developing Countries*; Policy Research working paper No. 4901; The World Bank-Development Research Group—Environment and Energy Team: Washington, DC, USA, 2009.

55. IUCN. *The National Strategy for Mainstreaming Gender in Climate Change in Egypt*; International Union for Conservation of Nature (IUCN): Grand, Swiss, 2011. Available online: https://genderandenvironment.org/resource/egypt-national-strategy-formainstreaming-gender-in-climate-change-in-egypt/ (accessed on 19 April 2021).

56. Brander, K.M. Global fish production and climate change. *Proc. Natl. Acad. Sci. USA* **2007**, *104*, 19704–19714. [CrossRef]

57. FAO. *Climate Change Implications for Fisheries and Aquaculture*; The State of Fisheries and Aquaculture 2008; FAO: Rome, Italy, 2008; pp. 87–91.

58. Soliman, N.F. *Aquaculture in Egypt under Changing Climate: Challenges and Opportunities*; Working Paper No. (4); Alexandria Research Center for Adaptation to Climate Change (ARCA): Alexandria, Egypt, 2017.

59. Swaminathan, M.S. Aquaculture and sustainable nutrition security in a warming planet, Keynote Address. In Proceedings of the Global Conference on Aquaculture—Farming the Waters for People and Food, Phuket, Thailand, 22–25 September 2010; Subasinghe, R.P., Arthur, J.R., Bartley, D.M., De Silva, S.S., Halwart, M., Hishamunda, N., Mohan, C.V., Sorgeloos, P., Eds.; pp. 3–19.

60. Sayed, M.A.-A. Impacts of Climate Change on the Nile Flows. Ph.D. Thesis, Faculty of Engineering, Ain Shams University, Cairo, Egypt, 2004.

61. Mohamed, Y.A.; van den Hurk, B.; Savenije, H.H.G.; Bastiaanssen, W.G.M. Hydroclimatology of the Nile: Results from a regional climate model. *Hydrol. Earth Syst. Sci.* **2005**, *9*, 263–278. [CrossRef]

62. Elshamy, M.E. Assessing the Hydrological Performance of the Nile Forecast System in Long Term Simulations. *Nile Basin Sci. Mag.* **2008**, *1*, 22–36.

63. Khordagui, H. Climate change in ESCWA region: Reasons for concern. In Proceedings of the Expert Group Meeting on Trade and Environment Priorities in the Arab Region, Cairo, Egypt, 11–13 November 2007.

64. Abd Ellah, R.G. Water resources in Egypt and their challenges, Lake Nasser case study. *Egypt. J. Aquat. Res.* **2020**, *46*, 1–12. [CrossRef]

65. Sadek, S. An overview on desert aquaculture in Egypt. In *Aquaculture in Desert and Arid Lands: Development Constraints and Opportunities: FAO Technical Workshop, 6–9 July 2010, Hermosillo, Mexico*; Crespi, V., Lovatelli, A., Eds.; FAO Fisheries and Aquaculture Proceedings No. 20; FAO: Rome, Italy, 2011; pp. 141–158.

66. El-Guindy, S. *The Use of Brackishwater in Agriculture and Aquaculture*; Panel Project on Water Management Workshop on brackish water use in agriculture and aquaculture. 2–5 December 2006; Ministry of Water Resources and Irrigation National Water Research Center Administration Building: Cairo, Egypt, 2006.

67. Mostafa, S.M.; Wahed, O.; El-Nashar, W.Y.; El-Marsafawy, S.M.; Zeleňáková, M.; Abd-Elhamid, H.F. Potential climate change impacts on water resources in Egypt. *Water* **2021**, *13*, 1715. [CrossRef]

68. Adeleke, M.L.; Al-Kenawy, D.; Nasr-Allah, A.M.; Dickson, M.; Ayal, D. Impacts of Environmental Change on Fish Production in Egypt and Nigeria: Technical Characteristics and Practice. In *African Handbook of Climate Change Adaptation*; Oguge, N., Ayal, D., Adeleke, L., da Silva, I., Eds.; Springer: Cham, Switzerland, 2021. [CrossRef]

69. MSEA. *National Environmental Action Plan (NEAP) 2002–2017*; Ministry of State for Environmental Affairs (MSEA): Cairo, Egypt, 2001.

70. Yates, D.N.; Strzepek, K.M. An assessment of integrated climate change impacts on the agricultural economy of Egypt. *Clim. Chang.* **1998**, *38*, 261–287. [CrossRef]

71. Moore, W.S. The subterranean estuary—A reaction zone of ground water and seawater. *Mar. Chem.* **1999**, *65*, 111–125. [CrossRef]

72. MAB. *Fisheries and Aquaculture in a Changing Climate*; FAO: Rome, Italy, 2009.

73. De Silva, S.S. Climate change impacts: Challenges for aquaculture. In Proceedings of the Farming the Waters for People and Food, Proceedings of the Global Conference on Aquaculture 2010, Phuket, Thailand, 22–25 September 2010; Subasinghe, R.P., Arthur, J.R., Bartley, D.M., De Silva, S.S., Halwart, M., Hishamunda, N., Mohan, C.V., Sorgeloos, P., Eds.; FAO: Rome, Italy; NACA: Bangkok, Thailand, 2012; pp. 75–110.

74. Tacon, A.D.J.; Hasan, M.R.; Subasinghe, R.P. *Use of Fishery Resources as Feed Inputs for Aquaculture Development: Trends and Policy Implications*; FAO Fisheries Circular No. 1018; FAO: Rome, Italy, 2006.

75. El-Sayed, A.-F.M. *Value chain Analysis of the Egyptian Aquaculture Feed Industry*; Project Report; WorldFish: Penang, Malaysia, 2014.

76. Tacon, A.G.; Hasan, M.R.; Metian, M. *Demand and Supply of Feed Ingredients for Farmed Fish and Crustaceans*; FAO: Rome, Italy, 2011.

77. FAO. FAOSTAT. 2013. Available online: http://faostat.fao.org/site/339/default.aspx (accessed on 20 May 2021).

78. El-Sayed, A.-F.M.; Dickson, M.W.; El-Naggar, G.O. Value chain analysis of the aquaculture feed sector in Egypt. *Aquaculture* **2015**, *437*, 92–101. [CrossRef]

79. Ramachandran, S.; Ray, A.K. Nutritional evaluation of fermented black gram (Phaseolus mungo) seed meal in compound diets for rohu, Labeo rohita (Hamilton), fingerlings. *J. Appl. Ichthyol.* **2007**, *23*, 74–79. [CrossRef]

80. Goda, A.M.A.-S.; Saad, A.; Wafa, M. Complete substitution of dietary wheat bran with Duckweed Lemna species supplemented with exogenous digestive enzymes for freshwater prawn, Macrobrachium rosenbergii (De Man 1879) post larvae. In Proceedings of the Oral Presentation at the International Conference and Exposition of Aquaculture Europe, San Sebastian, Spain, 14–17 October 2014.

81. Tacon, A.G.J. Use of fishmeal and fish oil in aquaculture: A global perspective. *Aquat. Resour. Cult. Dev.* **2004**, *1*, 3–14. [CrossRef]

82. Yones, A.M.M.; Metwalli, A.A. Effects of fishmeal substitution with poultry by-product meal on growth performance, nutrients utilization and blood contents of juvenile Nile tilapia (Oreochromis niloticus). *J. Aquac. Res. Dev.* **2015**, *7*, 1. [CrossRef]

83. Sharawya, Z.; Goda, A.M.A.; Hassaan, M.S. Partial or total replacement of fish meal by solid state fermented soybean meal with Saccharomyces cerevisiae in diets for Indian prawn shrimp, Fenneropenaeus indicus, Post larvae. *Anim. Feed Sci. Technol.* **2016**, *212*, 90–99. [CrossRef]

84. Al-Asgah, N.A.; Younis, E.M.; Abdel-Warith, A.A.; Shamlol, F.S. Evaluation of red seaweed, Gracilaria arcuata as dietary ingredient in African catfish, Clarias gariepinus. *Saudi J. Biol. Sci.* **2016**, *23*, 205–210. [CrossRef] [PubMed]

85. Abdel-Warith, A.A.; Younis, E.M.I.; Al-Asgah, N.A. Potential use of green macroalgae, Ulva lactuca as a feed supplement in diets on growth performance, feed utilization and body composition of the African catfish, Clarias gariepinus. *Saudi J. Biol. Sci.* **2016**, *23*, 404–409. [CrossRef]

86. Pankhurst, N.W.; Munday, P.L. Effects of climate change on fish reproduction and early life history stages. *Mar. Freshw. Res.* **2011**, *62*, 1015–1026. [CrossRef]

87. Alami-Durante, H.; Olive, N.; Rouel, M. Early thermal history significantly affects the seasonal hyperplastic process occurring in the myotomal white muscle of Dicentrarchus labrax juvenile. *Cell Tissue Res.* **2007**, *327*, 553–570. [CrossRef]

88. Sneddon, L.U. Trigeminal somatosensory innervation of the head of a teleost fish with particular reference to nociception. *Brain Res.* **2003**, *972*, 44–52. [CrossRef]

89. Ashley, P.J.; Sneddon, L.U.; Mccrohan, C.R. Nociception in fish: Stimulus–response properties of receptors on the head of trout Oncorhynchus mykiss. *Brain Res.* **2007**, *1166*, 47–54. [CrossRef]

90. Miranda, L.A.; Chalde, T.; Elisio, M.; Strussmann, C.A. Effects of global warming on fish reproductive endocrine axis, with special emphasis in pejerrey Odontesthes bonariensis. *Gen. Comp. Endocrinol.* **2013**, *192*, 45–54. [CrossRef]

91. Lahnsteiner, F.; Leitner, S. Effect of temperature on gametogenesis and gamete quality in brown trout, Salmo trutta. *J. Exp. Zool. A Ecol. Genet. Physiol.* **2013**, *319*, 138–148. [CrossRef]

92. Strussmann, C.A.; Patino, R. Sex determination, environmental. In *Encyclopedia of Reproduction*; Knobil, E., Neill, J.D., Eds.; Academic Press: New York, NY, USA, 1999; pp. 402–409.

93. Piferrer, F.; Blazquez, M.; Navarro, L.; Gonzalez, A. Genetic, endocrine, and environmental components of sex determination and differentiation in the European sea bass (*Dicentrarchus labrax* L.). *Gen. Comp. Endocrinol.* **2005**, *142*, 102–110. [CrossRef]

94. Usman, I.; Auta, J.; Abdullahi, S.A. Effect of monthly variation in water temperature on artificial breeding of common carp (*Cyprinus carpio* L.) in Zaria, Nigeria. *Int. J. Fish. Aquat. Stud.* **2015**, *3*, 353–356.

95. Khater, E.S.G.; Ali, S.A.; Mohamed, W.E. Effect of water temperature on masculinization and growth of Nile tilapia fish. *J. Aquac. Res. Dev.* **2017**, *8*, 8–12. [CrossRef]

96. Mazumder, S.K.; De, M.; Mazlan, A.G.; Zaidi, C.C.; Rahim, S.M.; Simon, K.D. Impact of global climate change on fish growth, digestion and physiological status: Developing a hypothesis for cause and effect relationships. *J. Water Clim. Chang.* **2015**, *6*, 200–226. [CrossRef]

97. O'Gorman, E.J.; Ólafsson, Ó.P.; Demars, B.O.L.; Friberg, N.; Guðbergsson, G.; Hannesdóttir, E.R.; Jackson, M.C.; Johansson, L.S.; McLaughlin, Ó.B.; Ólafsson, J.S.; et al. Temperature effects on fish production across a natural thermal gradient. *Glob. Chang. Biol.* **2016**, *22*, 3206–3220. [CrossRef]

98. Adhikari, S.; Chaudhury, A.K.; Gangadhar, B.; Ramesh, R.; Mandal, R.N.; Sarosh, I.; Saha, G.S.; De, H.K.; Sivaraman, I.; Mahapatra, A.S.; et al. Adaptation and mitigation strategies of climate change impact in freshwater aquaculture in some states of India. *J. FisheriesSciences.com* **2018**, *12*, 16–21.

99. Valeta, J.S.; Likongwe, J.S.; Kassam, D.; Maluwa, A.O. Temperature-dependent egg development rates, hatchability and fry survival rate of Lake Malawi Tilapia (Chambo), Oreochromis karongae (Pisces: Cichlidae). *Int. J. Fish. Aquac.* **2013**, *5*, 55–59. [CrossRef]

100. Okunsebor, S.; Ofojekwu, P.; Kakwi, D.; Audu, B. Effect of temperature on fertilization, hatching and survival rates of Heterobranchus bidorsalis eggs and hatchlings. *Br. J. Appl. Sci. Technol.* **2015**, *7*, 372–376. [CrossRef]

101. Marks, C.; Kaut, K.P.; Moore, F.B.; Bagatto, B. Ontogenetic oxygen changes alter zebra fish size, behavior, and blood glucose. *Physiol. Biochem. Zool.* **2012**, *85*, 635–644. [CrossRef]

102. Del Rio, A.M.; Davis, B.E.; Fangue, N.A.; Todgham, A.E. Combined effects of warming and hypoxia on early life stage Chinook salmon physiology and development. *Conserv. Physiol.* **2019**, *7*, coy078. [CrossRef] [PubMed]

103. Welch, M.J.; Munday, P.L. Contrasting effects of ocean acidification on reproduction in reef fishes. *Coral Reefs* **2016**, *35*, 485–493. [CrossRef]

104. Milazzo, M.; Cattano, C.; Alonzo, S.H.; Foggo, A.; Gristina, M.; Rodolfo-Metalpa, R.; Sinopoli, M.; Spatafora, D.; Stiver, K.A.; Hall-Spencer, J.M. Ocean acidification affects fish spawning but not paternity at CO2 seeps. *Proc. Biol. Sci.* **2016**, *283*, 20161021. [CrossRef] [PubMed]

105. Lehtonen, T.K.; Wong, B.B.; Kvarnemo, C. Effects of salinity on nest-building behaviour in a marine fish. *BMC Ecol.* **2016**, *16*, 7. [CrossRef] [PubMed]

106. Cruz Vieira, A.B.; Weber, A.A.; Ribeiro, Y.M.; Luz, R.K.; Bazzoli, N.; Rizzo, E. Influence of salinity on spermatogenesis in adult Nile tilapia (Oreochromis niloticus) testis. *Theriogenology* **2019**, *131*, 1–8. [CrossRef]

107. Saleh, M.A. Freshwater fish seed resources in Egypt. In *Assessment of Freshwater Fish Seed Resources for Sustainable Aquac*; BondadReantaso, M.G., Ed.; FAO Fisheries Technical Paper; FAO: Rome, Italy, 2007; pp. 241–255.

108. GAFRD. *The General Authority for Fishery Resources Development: Fisheries Statistics Yearbook 2020*, 30th ed.; General Authority for Fish Resources Development, Ministry of Agriculture: Cairo, Egypt, 2020; 102p.

109. Nasr-Allah, A.M.; Dickson, M.W.; Al-Kenawy, D.A.; Fathi, M.; El-Naggar, G.O.; Azazy, G.E.; Grana, Y.S.; Diab, A.M. Value chain analysis of Egyptian fish seed production. In Proceedings of the 4th Conference of Central Laboratory for Aquaculture Research, held in the International Agricultural Center, Doki, Egypt, 11–12 March 2014; pp. 351–372.

110. Macfadyen, G.; Nasr-Alla, A.M.; Al-Kenawy, D.; Fathi, M.; Hebicha, H.; Diab, A.M.; Hussein, S.M.; Abou-Zeid, R.M.; El-Naggar, G. Value-chain analysis—An assessment methodology to estimate Egyptian aquaculture sector performance. *Aquaculture* **2012**, *362*, 18–27. [CrossRef]

111. Naiel, R.A.; Aamer, M.G.; Ibrahim, A.A.; Azazy, G.E. Economics of fry production of fish hatcheries. *Zagazig J. Agric. Res.* **2011**, *38*, 1329–1341.

112. Abbass, K.; Qasim, M.Z.; Song, H.; Murshed, M.; Mahmood, H.; Younis, I. A review of the global climate change impacts, adaptation, and sustainable mitigation measures. *Environ. Sci. Pollut. Res.* **2022**, *29*, 42539–42559. [CrossRef]

113. Yassin, L. Climate Change and Food Security in Egypt. Master's Thesis, The American University, Cairo, Egypt, 2016.

114. Yin, Z.; Hu, Y.; Jenkins, K.; He, Y.; Forstenhäusler, N.; Warren, R.; Yang, L.; Jenkins, R.; Guan, D. Assessing the economic impacts of future fluvial flooding in six countries under climate change and socio-economic development. *Clim. Chang.* **2021**, *166*, 1–21. [CrossRef]

115. UNDP. *Adaptation to Climate Change in the Nile Delta through Integrated Coastal Zone Management. Climate Change Project Document*; United Nations Development Program: New York, NY, USA, 2016. Available online: https://iwlearn.net/iw-projects/3242 (accessed on 17 December 2021).

116. Conway, D.; Krol, M.; Alcamo, J.; Hulme, M. Future availability of water in Egypt: The interaction of global, regional and basin scale driving forces in the Nile Basin. *Ambio* **1996**, *25*, 336–342.

117. Bizikova, L.; Robinson, J.; Cohen, S. Linking climate change and sustainable development at the local level. *Clim. Policy* **2007**, *7*, 271–277. [CrossRef]

118. Li, D.; Hu, X. Fish and its multiple human health effects in times of threats to sustainability and affordability are there alternatives. *Asia Pac. J. Clin. Nutr.* **2009**, *18*, 553–563. [PubMed]

119. Shaw, D.J. World Food Summit, 1996. In *World Food Security*; Palgrave Macmillan: London, UK, 2007. [CrossRef]

120. Omar, M.E.M.; Moussa, A.M.A.; Hinkelmann, R. Impacts of climate change on water quantity, water salinity, food security, and socioeconomy in Egypt. *Water Sci. Eng.* **2021**, *14*, 17–27. [CrossRef]

121. Nelson, G.C.; Rosegrant, M.W.; Palazzo, A.; Gray, I.; Ingersoll, C.; Robertson, R.D.; Tokgoz, S.; Zhu, T.; Sulser, T.B.; Ringler, C.; et al. *Food Security, Farming, and Climate Change to 2050: Scenarios, Results, Policy Options*; International Food Policy Research Institute (IFPRI): Washington, DC, USA, 2010. [CrossRef]

122. Tielens, J.; Candel, J.J.L. Reducing Food Wastage, Improving Food Security? *Food and Business Knowledge Platform*. 2014. Available online: http://knowledge4food.net/wp-content/uploads/2014/07/140702_fbkp_report-foodwastage_DEF.pdf (accessed on 25 November 2021).

123. Tabthipwon, P. *Aquaculture Development toward the Sustainable and Current Situation of Aquaculture*; Food Fertil Technol Center: Taipei, China, 2008; pp. 45–55.

124. Johnston, P.; Everard, M.; Santillo, D.; Robert, K.H. Reclaiming the definition of sustainability. *Environ. Sci. Pollut. Res.* **2007**, *14*, 60–66. [CrossRef]

125. Valenti, W.C.; Kimpara, J.M.; Preto, B.L.; Moraes-Valenti, P. Indicators of sustainability to assess aquaculture systems. *Ecol. Indic.* **2018**, *88*, 402–413. [CrossRef]

126. Bogard, J.R.; Farmery, A.K.; Little, D.C.; Fulton, E.A.; Cook, M. Will fish be part of future healthy and sustainable diets? *Lancet Planet. Health* **2019**, *3*, e159–e160. [CrossRef]

127. Kaleem, O.; Singou Sabi, A.-F.B. Overview of aquaculture systems in Egypt and Nigeria, prospects, potentials, and constraints. *Aquac. Fish.* **2021**, *6*, 535–547. [CrossRef]

128. Bueno, P.B.; Soto, D. *Adaptation Strategies of the Aquaculture Sector to the Impacts of Climate Change*; FAO: Rome, Italy, 2017.

129. Barange, M.; Bahri, T.; Beveridge, M.C.M.; Cochrane, A.L.; Funge-Smith, S.; Paulain, F. *Impacts of Climate Change on Fisheries and Aquaculture, Synthesis of Current Knowledge, Adaptation and Mitigation Options*; FAO: Rome, Italy, 2018.

130. Shaalan, M.; El-Mahdy, M.; Saleh, M.; El-Matbouli, M. Aquaculture in Egypt: Insights on the current trends and future perspectives for sustainable development. *Rev. Fish. Sci. Aquac.* **2018**, *26*, 99–110. [CrossRef]

131. Yassien, S.A.; Abd El-Rahim, S.A.; Osman, M.F.; Hamouda, R.E.; Soliman, M.A.M.; Nageib, R.M. Factors affecting aquaculture farms' profitability and constraints facing fish farmers in Egypt. *Egypt. J. Aquat. Biol. Fish.* **2022**, *26*, 519–527. [CrossRef]

132. Khalil, M.T.; Fishar, M.R.; Emam, W.W.M.; Soliman, K.M.; El-Naggar, M.M. Impact of Climate Change on Aquatic Biodiversity of Egypt (A Concise Review). *Egypt. J. Aquat. Biol. Fish.* **2022**, *26*, 183–212. [CrossRef]

133. El-Ramady, H.R.; El-Marsafawy, S.M.; Lewis, L.N. Sustainable agriculture and climate changes in Egypt. In *Sustainable Agriculture Reviews*; Springer: Berlin/Heidelberg, Germany, 2013; pp. 41–95.

134. Kandlikar, M.; Risbey, J. Agricultural Impacts of Climate Change: If Adaptation is the Answer, What is the Question? *Clim. Chang.* **2000**, *45*, 529–539. [CrossRef]

135. Godfray, H.C.J.; Beddington, J.R.; Crute, I.R.; Haddad, L.; Lawrence, D.; Muir, J.F.; Pretty, J.; Robinson, S.; Thomas, S.M.; Toulmin, C. Food security: The challenge of feeding 9 billion people. *Science* **2010**, *327*, 812–818. [CrossRef] [PubMed]

136. Rivera-Ferre, M.; Ortega-Cerdà, M.; Baumgärtner, J. Rethinking. Study and Management of Agricultural Systems for Policy Design. *Sustainability* **2013**, *5*, 3858–3875. [CrossRef]

137. Velten, S.; Leventon, J.; Jager, N.; Newig, J. What Is Sustainable Agriculture: A Systematic Review. *Sustainability* **2015**, *7*, 7833–7865. [CrossRef]

138. Sae-Lim, P.; Kause, A.; Mulder, H.A.; Olesen, I. Breeding and genetics symposium: Climate change and selective breeding in aquaculture. *J. Anim. Sci.* **2017**, *95*, 1801–1812. [CrossRef]

139. Mbow, C.; Rosenzweig, C.; Barioni, L.G.; Benton, T.G.; Herrero, M.; Krishnapillai, M.; Liwenga, E.; Pradhan, P.; Rivera-Ferre, M.G.; Sapkota, T.; et al. Food Security. In *Climate Change and Land: An IPCC Special Report on Climate Change, Desertification, Land Degradation, Sustainable Land Management, Food Security and Greenhouse Gas Fluxes in Terrestrial Ecosystems*; IPCC: Geneva Switzerland, 2019. Available online: https://www.ipcc.ch/site/assets/uploads/sites/4/2020/02/SRCCLChapter-5.pdf (accessed on 28 December 2021).

140. Ebeling, J.M.; Timmons, M.B. Recirculating Aquaculture Systems. In *Aquaculture Production Systems*; Tidwell, J.H., Ed.; John Willey& Sons: Hoboken, NJ, USA, 2012.

141. Avnimelech, Y. *Biofloc Technology—A Practical Guidebook*, 3rd ed.; The World Aquaculture Society: Baton Rouge, LA, USA, 2014; 285p.

142. Kingler, D.; Naylor, R. Searching for Solutions in Aquaculture: Charting a Sustainable Course. *Annu. Rev. Environ. Resour.* **2012**, *37*, 247–276. [CrossRef]

143. Tyson, R.C.; Treadwell, D.D.; Simonne, E.H. Opportunities and Challenges to Sustainability in Aquaponic Systems. *HorTechnology* **2011**, *21*, 6–13. [CrossRef]

144. Farghally, H.M.; Atia, D.M.; El-madany, H.T.; Fahmy, F.H. Control methodologies based on geothermal recirculating aquaculture system. *Energy* **2014**, *78*, 826–833. [CrossRef]

145. Holan, A.B.; Good, C.; Powell, M.D. Health Management in Recirculating Aquaculture Systems (RAS). In *Aquaculture Health Management*; Kibenge, F.S.B., Powell, M.D., Eds.; Academic Press: Cambridge, MA, USA, 2020; pp. 281–318. [CrossRef]

146. Bregnballe, J. *A Guide to Recirculation Aquaculture: An Introduction to the New Environmentally Friendly and Highly Productive Closed Fish Farming Systems*; Food and Agriculture Organization of the United Nations (FAO): Rome, Italy; EUROFISH International Organisation: Rome, Italy, 2015; 100p.

147. Ramírez-Godínez, J.; Beltrán-Hernández, R.; Coronel-Olivares, C.; Contreras-López, E.; Quezada-Cruz, M.; Vázquez-Rodríguez, G. Recirculating systems for pollution prevention in aquaculture facilities. *J. Water Resour. Prot.* **2013**, *5*, 5–9. [CrossRef]

148. Piedrahita, R.H. Reducing the potential environmental impact of tank aquaculture effluents through intensification and recirculation. *Aquaculture* **2003**, *226*, 35–44. [CrossRef]

149. Ahmed, N.; Turchini, G.M. Recirculating aquaculture systems (RAS): Environmental solution and climate change adaptation. *J. Clean. Prod.* **2021**, *297*, 126604. [CrossRef]

150. Ako, H.; Baker, A. Small-Scale Lettuce Production with Hydroponics or Aquaponics. College of Tropical Agriculture and Human Resources, University of Hawaii at Mānoa. 2009. Available online: http://www.ctahr.hawaii.edu/oc/freepubs/pdf/SA-2.pdf (accessed on 24 December 2022).

151. Somerville, C.; Cohen, M.; Pantanella, E.; Stankus, A.; Lovatelli, A. Small-scale aquaponic food production. Integrated fish and plant farming. In *FAO Fisheries and Aquaculture*; Technical Paper. No. 589; FAO: Rome, Italy, 2014; 262p.

152. Wang, C.Y.; Chang, C.Y.; Chien, Y.H.; Lai, H.T. The performance of coupling membrane filtration in recirculating aquaponic system for tilapia culture. *Int. Biodeterior. Biodegrad.* **2016**, *107*, 21–30. [CrossRef]

153. Scott, J. Evolution of Aquaponics. *Aquaponics J.* **2002**, *6*, 14–17.

154. Rakocy, J.E.; Masser, M.P.; Losordo, M. *Recirculating Aquaculture Tank Production Systems: Aquaponics—Integrating Fish and Plant Culture*; Southern Regional Aquaculture Center (SRAC): Stoneville, MS, USA, 2006; SRAC Publication No. 454; pp. 1–15. Available online: http://www.aces.edu/dept/fisheries/aquaculture/documents/309884-SRAC454.pdf (accessed on 22 December 2022).

155. Goddek, S.; Delaide, B.; Mankasingh, U.; Ragnarsdottir, K.V.; Jijakli, H.; Thorarinsdottir, R. Challenges of sustainable and commercial aquaponics. *Sustainability* **2015**, *7*, 4199–4224. [CrossRef]

156. El Essawy, H. Aquaponics as a Sustainable Alternative to New Land Reclamation and Conventional Agriculture in Egypt. Master's Thesis, The American University, Cairo, Egypt, 2017. AUC Knowledge Fountain. Available online: https://fount.aucegypt.edu/etds/191 (accessed on 22 December 2022).

157. El Essawy, H.; Nasr, P.; Sewilam, H. Aquaponics: A sustainable alternative to conventional agriculture in Egypt—A pilot scale investigation. *Environ. Sci. Pollut. Res.* **2019**, *26*, 15872–15883. [CrossRef]

158. Goodman, E.R. Aquaponics: Community and Economic Development. Master's Thesis, Massachusetts Institute of Technology, Cambridge, MA, USA, 2011.

159. Sharma, A.; Bandhana, R.S.; Sangotra, R. Comparison of water quality and composition of bioflocs reared in indoor and outdoor conditions. *Int. Res. J. Biol. Sci.* **2018**, *7*, 1–9.

160. Avnimelech, Y. *Biofloc Technology: A Practical Guidebook*; World Aquaculture Society: Sorrento, FL, USA, 2009.

161. Crab, R.; Defoirdt, T.; Bossier, P.; Verstraete, W. Biofloc technology in aquaculture: Beneficial effects and future challenges. *Aquaculture* **2012**, *356–357*, 351–356. [CrossRef]

162. Anjalee, D.C.A.; Kurup, B.M. Biofloc Technology: An Overview and its application in animal food industry. *Int. J. Fish. Aquat. Sci.* **2015**, *5*, 1–20.

163. Hargreaves, J.A. Photosynthetic suspended-growth systems in aquaculture. *Aquac. Eng.* **2006**, *34*, 344–363–363. [CrossRef]

164. De-Schryver, P.; Crab, R.; Defoirdt, T.; Boon, N.; Verstraete, W. The basics of bioflocs technology: The added value for aquaculture. *Aquaculture* **2008**, *277*, 125–137. [CrossRef]

165. Khanjani, M.H.; Sharifinia, M. Biofloc technology as a promising tool to improve aquaculture production. *Rev. Aquac.* **2020**, *12*, 1836–1850. [CrossRef]

166. Bossier, P.; Ekasari, J. Biofloc technology application in aquaculture to support sustainable development goals. *Microb. Biotechnol.* **2017**, *10*, 1012–1016. [CrossRef] [PubMed]

167. Suneetha, K.; Kavitha, K.; Darwin, C.H. Biofloc Technology: An emerging tool for sustainable aquaculture. *Int. J. Zool. Stud.* **2018**, *3*, 87–90. [CrossRef]

168. Crab, R.; Avnimelech, Y.; Defoirdt, T.; Bossier, P.; Verstraete, W. Nitrogen removal techniques in aquaculture for a sustainable production. *Aquaculture* **2007**, *270*, 1–14. [CrossRef]

169. Azim, M.E.; Little, D.C. The biofloc technology (BFT) in indoor tanks: Water quality, biofloc composition, and growth and welfare of Nile tilapia (Oreochromis niloticus). *Aquaculture* **2008**, *283*, 29–35. [CrossRef]

170. Kuhn, D.D.; Boardman, G.D.; Lawrence, A.L.; Marsh, L.; Flick, J. Microbial floc meal as a replacement ingredient for fishmeal and soybean protein in shrimp feed. *Aquaculture* **2009**, *296*, 51–57. [CrossRef]

171. Avnimelech, Y. Feeding with microbial flocs by tilapia in minimal discharge bioflocs technology ponds. *Aquaculture* **2007**, *264*, 140–147. [CrossRef]

172. Liu, H.; Li, H.; Wei, H.; Zhu, X.; Han, D.; Jin, J.; Yang, Y.; Xie, S. Biofloc formation improves water quality and fish yield in a freshwater pond aquaculture system. *Aquaculture* **2019**, *506*, 256–269. [CrossRef]

173. Neori, A.; Chopin, T.; Troell, M.; Buschmann, A.H.; Kraemer, G.P.; Halling, C.; Shpigel, M.; Yarish, C. Integrated aquaculture: Rationale, evolution and state of the art emphasizing seaweed biofiltration in modern mariculture. *Aquaculture* **2004**, *231*, 361–391. [CrossRef]

174. Buschmann, A.H.; Varela, D.A.; Hernández-González, M.C.; Huovinen, P. Opportunities and challenges for the development of an integrated seaweed-based aquaculture activity in Chile: Determining the physiological capabilities of Macrocystis and Gracilaria as biofilters. *J Appl. Phycol.* **2008**, *20*, 571–577. [CrossRef]

175. Olesen, I.; Myhr, A.I.; Rosendal, G.K. Sustainable aquaculture: Are we getting there? Ethical perspectives on salmon farming. *J. Agric. Environ. Ethics* **2011**, *24*, 381–408. [CrossRef]

176. Vasdravanidis, C.; Alvanou, M.V.; Lattos, A.; Papadopoulos, D.K.; Chatzigeorgiou, I.; Ravani, M.; Liantas, G.; Georgoulis, I.; Feidantsis, K.; Ntinas, G.K.; et al. Aquaponics as a promising strategy to mitigate impacts of climate change on Rainbow trout culture. *Animals* **2022**, *12*, 2523. [CrossRef]

177. De Silva, S.S.; Soto, D. *Climate Change and Aquaculture: Potential Impacts, Adaptation and Mitigation, Climate Change Implications for Fisheries and Aquaculture: Overview of Current Scientific Knowledge*; FAO Fisheries and Aquaculture Technical Paper 2009, 530; FAO: Rome, Italy, 2009; pp. 151–212.

178. Zhang, J.; Kitazawa, D.; Yang, C. A numerical modeling approach to support decision-making on design of integrated multitrophic aquaculture for efficiently mitigating aquatic waste. *Mitig. Adapt. Strateg. Glob. Chang.* **2016**, *21*, 1247–1261. [CrossRef]

179. Padilla-Rivera, A.; Russo-Garrido, S.; Merveille, N. Addressing the social aspects of a circular economy: A systematic literature review. *Sustainability* **2020**, *12*, 7912. [CrossRef]

180. Ahmed, N.; Bunting, S.W.; Glaser, M.; Flaherty, M.S.; Diana, J.S. Can greening of aquaculture sequester blue carbon? *Ambio* **2017**, *46*, 468–477. [CrossRef]

181. Goda, A.M.A.-S.; Essa, M.A.; Hassaan, M.S.; Sharawy, Z. Bio economic features for aquaponic systems in Egypt. *Turk. J. Fish. Aquat. Sci.* **2015**, *15*, 525–532. [CrossRef]

182. Goda, A.M.A.-S.; Essa, M.A.; Hassaan, M.S.; Sharawy, Z. Bio–Economic Study of Freshwater Integrated Multi-Trophic Aquaculture (IMTA) Systems in Egypt. *World Appl. Sci. J.* **2014**, *32*, 1367.

183. OECD/Thierry Chopin. Integrated Multi-Trophic Aquaculture. In *Advancing the Aquaculture Agenda: Workshop Proceedings*; OECD Publishing: Paris, France, 2010. [CrossRef]

184. Islam, M.J.; Kieu, E. Tackling Regional Climate Change Impacts and Food Security Issues: A Critical Analysis across ASEAN, PIF, and SAARC. *Sustainability* **2020**, *12*, 883. [CrossRef]

185. Elshamy, M.E.; Seierstad, I.A.; Sorteberg, A. Impacts of climate change on Blue Nile flows using bias-corrected GCM scenarios. *Hydrol. Earth Syst. Sci.* **2009**, *13*, 551–565. [CrossRef]

186. Hassaan, M.A.; Abdrabo, M.A. Vulnerability of the Nile Delta coastal areas to inundation by sea level rise. *Environ. Monit. Assess* **2013**, *185*, 6607–6616. [CrossRef]

Article

Urban Water Management with a Full Cost Recovery Policy: The Impact of Externalities on Pricing

Sanju John Thomas [1,*], **Mukund Haribhau Bade** [2], **Sudhansu Sekhar Sahoo** [3], **Sheffy Thomas** [4], **Ajith Kumar** [1] **and Mohamed M. Awad** [5,*]

1   Department of Mechanical Engineering, Cochin University of Science and Technology (CUSAT), Cochin 682022, India
2   Department of Mechanical Engineering, Sardar Vallabhai National Institute of Technology (SVNIT), Surat 395007, India
3   Department of Mechanical Engineering, Odisha University of Technology and Research (OUTR), Bhubaneswar 751029, India
4   Department of Electronics and Instrumentation, Federal Institute of Science and Technology (FISAT), Angamaly 683577, India
5   Mechanical Power Engineering Department, Mansoura University, Mansoura 35516, Egypt
*   Correspondence: sanjujohnthomas@gmail.com (S.J.T.); m_m_awad@mans.edu.eg (M.M.A.)

Abstract: Water has complex cost dimensions and is considered a scarce commodity under a reduced-recycle-reuse system with a full cost recovery strategy. The impact of externalities from the social, economic, and ecological aspects of exploiting water resources are often not accounted into the pricing mechanism. We discuss the current work model as well as a pricing strategy for a water infrastructure program with a full cost recovery strategy. Single and multi-block pricing models are created, and their effect on water pricing is discussed. The impact of externalities is accounted for, and respective cost components, namely, environmental cost, opportunity cost, and ecological imbalance cost are included in the water pricing, to analyze the impact on the cost of produced water. A comparison under the normalized, single-block and multi-block pricing strategy are discussed and the payback period is found. It is seen that the unit cost of potable and non-potable water is brought down from 0.94 USD/m^3 and 0.51 USD/m^3 to 0.62 USD/m^3 and 0.29 USD/m^3, respectively using a multi-block pricing strategy. It is recommended that policy interventions in a full cost recovery water pricing strategy should consider the cost of externalities with a multi-block pricing system for breakeven in water infrastructural investments.

Keywords: water pricing; urban infrastructure; multi-block pricing; externality costing; single-block pricing

1. Introduction

Water scarcity is a huge challenge across the globe, especially in the region of the Middle East and North Africa (MENA), affecting cropping patterns and decisions on the import and export of cereals [1]. Over-consumption of water, non-metering, exploitation of new water resources, treatment cost of below-par quality water, and transformation of resources, demand a shift in egalitarian pricing strategy in water management programs [2]. It is found that addressing the energy, water, and food (WEF) nexus as a single entity shall address the water crisis in line with constraints, possible policy interventions, and meet sustainable development goals [3]. Analysis models to analyze the efficiency of water usage in the urban-peri-urban region in line with the WEF nexus to assess the importance of water usage optimally have proved successful [4]. Reformed price structures, direct benefit transfers, demand-side management, and the use of efficient technologies at the source are mechanisms that can compensate for the higher price demands. Water use and recycling for application in the WEF nexus is important to address the use of water efficiently

including agriculture which is found as the optimized way to address scarcity [5,6]. Two strategies that can address water scarcity are (i) providing incentives and taxation to meet the additional cost of water infrastructure and (ii) adopting pricing strategies with price discrimination [7]. Water pricing should focus on the socio-economics of the region and be aptly priced to keep the sustainable initiatives considering the naturally available resources and new technology [8]. Flat rate, uniform rate, block rate, and complex rate structures are the basic types of water pricing explored for urban-municipal corporations [9]. However, different pricing models were studied and experimented with to improve demand-supply management. Full cost recovery in water management programs with environmental cost components directly proportionated to respective impacts is an effective method of control [10]. The full cost with efficient use is the crucial strategy for optimal use of water resources in urban area water management programs [11]. The increasing block pricing is not idle for developing countries, considering the social justice for use of water. It is better to consider the old pricing strategy with rebates and discounts [12]. High uniform water pricing can be a direct intervention to curtail water use, while its impact on social rights for water to meet minimal needs can be questioned [13]. Increasing block pricing, which is a mix of efficient pricing strategy and egalitarian pricing philosophy, is an effective mechanism to curtail water waste, however, the sizing of blocks in a multi-tier social structure will be critical [10].

An exhaustive study on water management programs in a few cities across the globe shows that non-metered flat pricing privileges consumers to use water till the marginal benefit becomes zero resulting in aggregate consumption mismatches [2]. The study shows that pricing below the 'full cost' results in the ineffectiveness of water management, while the cities which used an increasing block pricing strategy have resulted in meeting social inequality and motivating the individual user to use water efficiently. The multi-block pricing system has shown effective results to bring a conscious effort to reduce the consumption of water [14]. The impact of block pricing, to improve water use efficiency, conclude that identifying the size of block and price slabs is difficult in a divergent socio-economic group [15].

The pricing structure for any naturally available resource should be based on the social parameters, environmental conditions, and cost recovery mechanism [7]. The water pricing should be done on three principles which are equality, efficiency, and environment [16,17]. Sustainable use of water is to use exhaustible renewable resources within their regeneration limits while having the rational judgment to use non-renewable resources or their availability for prolonged periods. Any impact whose reason can be traced back to human involvement and whose cost is not accounted for among the economic decision-makers can be considered an externality. The type of event, the scale of impact, system boundaries, and the social group determine the decision-making for reactive or pro-active decision-making and actions [16,17].

Water consumption and pricing strategy should consider water to be administratively priced to include the cost of externalities, as an incentive or subsidy [16]. There is a strong interlinking between energy, water, and food nexus, and sustainable initiatives should move immediately from concept to practice [18]. Along with block pricing, non-pricing interventions, such as raising social conscience for water use are proven as successful initiatives [13]. A range of options including pricing, restrictions, awareness, and efficient technologies can effectively control supply-demand management, for the benefit of suppliers and customers [16]. The full cost pricing and efficient use of water alone cannot control the sustainable use of water, but policy and instrumental changes to consider water as a limited natural resource are mandatory [19].

The literature survey concludes that earlier efforts for full cost recovery pricing have not taken the cost of externalities into the water pricing system for the water management scheme to be self-sustainable. In the current work, an urban water management program with water sources such as natural reservoirs, recycled water, and desalinated water are considered as water sources to meet the potable and non-potable requirements of the

city. The possibilities of levelized cost, single-block, and multi-block pricing systems are explored. Efforts are made to create a sustainable water pricing model, for different water quality levels for multiple water requirements. Considering the high capital cost of water infrastructural projects, the cost of externalities is included in the water pricing model, for a better cost breakeven. Social costs due to greenhouse gas emissions, opportunity costs due to depleting naturally available water resources, and ecological imbalance are costs accounted for impacts due to externalities. The structure of this paper adopted the following methodology: (1) Design the objective function to minimize the water infrastructural cost for efficient demand-supply management in a multi-resource variable demand environment; (2) Identify the unit cost of produced water under a single-block pricing strategy; (3) Identify the externalities and corresponding impacts whose costs can be accounted; (4) Structure an appropriate multi-block pricing slab to motivate efficient utilization of water; (5) Account the 'cost on externalities' into a multi-block pricing model to identify the impact on the cost of produced water. Identify policy interventions required for a full cost recovery pricing model in water infrastructure programs.

2. Design of the Water Infrastructure Model

The water infrastructure model for a greenfield industrial city with a full cost recovery strategy is modeled. Treated river water and desalinated seawater are considered potable water resources, while treated sewerage and industrial effluent are considered non-potable water resources. A water treatment plant (WTP) is considered for treating river water to potable standards. Since the river water is not a perennial source, water from a seawater reverse osmosis (SWRO) desalination plant is considered the second source of potable water. To promote sustainable activities, a renewable energy-based hybrid technology desalination plant, termed energy-efficient desalination (EED), is considered the third source of potable water. The produced water from WTP, SWRO, and EED is expected to provide potable water to total dissolved solvent (TDS) levels less than or equal to 200 ppm. The wastewater after human needs for washing and sanitation from residential and industrial establishments is recycled to reuse standards of 500 ppm and less by a sewerage treatment plant (STP). A common effluent treatment plant (CETP) recycles wastewater from industrial processes to TDS levels less than or equal to 500 ppm.

2.1. Assumptions Considered in the Water Management Program under Study

The assumptions considered for the design of the water management program are:

i. The water consumption per head is taken as 200 LPD (higher by 25% than normal standards) considering the future developments in a Greenfield project.

ii. The availability of the water in the river is seasonal and cannot meet the potable water requirement through all seasons. Hence the water treatment plant (WTP) is sized 40 MLD, half the size of the total potable water requirement for the city. The potable water network for the city is based on an 80 MLD design.

iii. To increase the reliability of potable water supply, seawater desalination is considered the second source of supply, with the size allotted at 50% of the total potable water requirement for the city. Out of 40 MLD, 35 MLD will be met by conventional seawater reverse osmosis (SWRO) technology, while 5 MLD will be met by a renewable energy powered, hybrid technology energy-efficient desalination (EED) plant.

iv. The recycled, treated water from the sewerage treatment plant will be the first source for the non-potable applications. The sizing of the STP is done based on the consumption of 80 MLD potable and 320 MLD non-potable by the city population. The non-potable water distribution network is designed based on STP sizing.

v. It is assumed that 80% of potable and non-potable water consumption can be recycled, which makes 320 MLD in total. However, to meet any uncertainty or shortfall, an additional 40 MLD of industrial effluent is treated by a common effluent treatment plant (CETP) to a quality of <500 TDS, for supply as a non-potable requirement.

vi. It is assumed that the water requirement for the process applications of industries is met by the federal administration on a chargeable basis. This water network is not considered in the current study.

vii. The cost of the potable and non-potable utility network lines, and sewerage/effluent collection network lines are not considered for the current analysis. It is assumed that this cost is borne by the urban administration.

The technology considered for the STP is a sequential batch reaction, automated to address variable parameters which are generally used by large municipalities. The common effluent treatment plant (CETP) is based on an activated sludge process (ASP), trickling filter (TF) technology and a tertiary treated reverse osmosis plant, which is an established combination for industrial effluent treatment. The water treatment plant is on the technology of settling, floatation, adsorption, ultrafiltration, and disinfection, ideal for surface water, including river water treatment. The seawater desalination plant considered in the analysis is multi-pass reverse osmosis technology, which is widely accepted [20–23]. The renewable energy-based, energy-efficient desalination plant will use combinations of technologies with reverse osmosis after the first pass to increase the recovery rate. The plant will operate on solar photovoltaic power, without battery backup, hence triple-sized, to operate on design size during sunlight hours [24]. The water infrastructure for a Greenfield city is modeled with the design conditions, costs, and assumptions from previous studies [20,25–30]. The parameters for design and modeling are described in Tables 1 and 2, respectively.

Table 1. Design parameters and assumptions are considered for problem modeling.

Population	2 Million Individuals
Potable water requirement (person/day), drinking and cooking	40 L
Water for sanitation (person/day)—Non-potable	80 L
Water for washing (person/day)—Non-potable	80 L
The efficiency of STP (BOD removal rate)	90%
The efficiency of CETP (BOD removal rate)	90%
Life of the plants	25 years
Interest on investment	4%
Discount rate/Return rate	4%
Acceptable total dissolved solids (TDS) for drinking	<200 ppm
Acceptable TDS for washing	<500 ppm
Acceptable TDS for sanitation	<500 ppm

Table 2. Cost parameters of various water infrastructures.

Source	Capital Expenses USD/MLD (Million)	Yearly Operational Expenses (%)	Operational Expenses USD/MLD (Million)
Water Treatment Plant (WTP)	0.4	8	0.03
Seawater Reverse Osmosis (SWRO) Plant	1.2	14	0.17
Energy-Efficient Desalination (EED)	5.14	6.5	0.33
Sewerage Treatment Plant (STP)	0.64	7	0.04
Common Effluent Treatment Plant (CETP)	1.36	12	0.16

[31–35].

While the capital cost of the EED is the highest, the operational cost of the SWRO and CETP is the highest. The operational cost and the trend of operational cost with a 5% annual increase are shown in Figures 1 and 2, respectively.
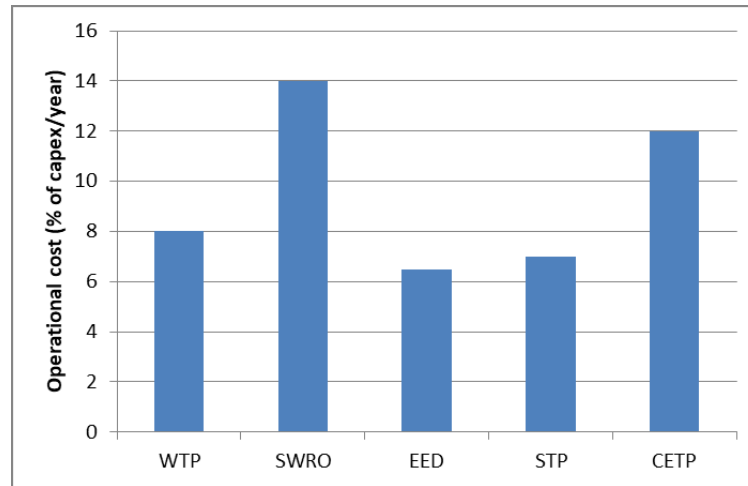
Figure 1. Operational cost percentage.
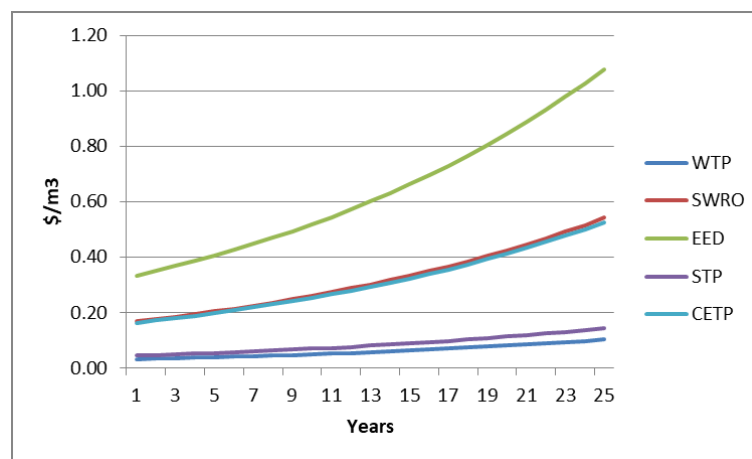
Figure 2. The trend with a 5% annual increase.

It is seen that there is a considerable difference between the components regarding capital cost and operational cost. This shows that there will be a considerable difference between various components concerning payback and the levelized cost of production.

2.2. Formation of the Objective Function for Multi-Resource and Variable Demand Allocation Model

The objective of the problem formation is to reduce the total cost of the water infrastructure program, by optimally allotting the capacities for each water source. The parameters and attributes used for modeling the problem statement are represented in Table 3, and the abbreviations used are as defined at the end of the paper.

Table 3. Parameters and attributes of the problem statement.

S N	Sources			ATC per Capacity of the Plant	Demands		
	Water Source Index	Total Water Available	TDS		Water Demand Index	Total Water Required	TDS
1	WS_1	Wa_1	Ws_{TDS1}	ATC_{S1}	WD_1	W_{r1}	Wd_{TDS1}
2	WS_2	Wa_2	Ws_{TDS2}	ATC_{S2}	WD_2	W_{r2}	Wd_{TDS2}
3	WS_3	Wa_3	Ws_{TDS3}	ATC_{S3}	WD_3	W_{r3}	Wd_{TDS3}
⋮	⋮	⋮	⋮	⋮	⋮	⋮	⋮
⋮	⋮	⋮	⋮	⋮	⋮	⋮	⋮
N	WS_n	Wa_n	Ws_{TDSn}	ATC_{Sn}	WD_m	Wr_m	Wd_{TDSm}

WS = Water source, WD = Water demand, W_r = Water required (MLD), TDS = Total dissolved solids (ppm), W_{STDS} = TDS of water at the source (ppm), W_{DTDS} = TDS of water required at the demand (ppm), ATC_i = Annualized total cost of source 'i', it includes annualized capital and operating cost for the ith source (USD).

The objective function of the problem is written as in Equation (1). The objective function is to minimize the overall cost meeting the demand with the optimized allocation of resources.

$$Minimize \sum_{i=1}^{n} \sum_{j=1}^{m} ATC_i * W_{i,j} \tag{1}$$

where,

i = index for number of water sources from 1, 2, 3 . . . . n

j = index for number of water demands from 1, 2, 3 . . . . m

$W_{i,j}$ = allocation of W resource from i^{th} source to j^{th} demand

The constraints for the objective function are expressed through Equations (2)–(5); Equation (2) states that each demand is satisfied completely by all the sources in TDS for the source is lower than or equal to the minimum limiting value of that demand:

$$\sum_{j=1}^{m} \sum_{i=1}^{n} W_{i,j} - WD_j = 0 \tag{2}$$

Each source is less than or equal to addition of all demands if TDS for source is lower than or equal to minimum limiting value of that demand, as indicated through Equation (3).

$$\sum_{i=1}^{n} \sum_{j=1}^{m} W_{i,j} - WS_i \leq 0 \tag{3}$$

Allocation of source and demand is feasible only when TDS for source is lower than or equal to a minimum limiting value of the demand TDS as explained through Equation (4), while the non-negativity constraint is expressed as in Equation (5):

$$For\ feasible\ W_{i,j}\ allocation,\ TDS_i \leq TDS_j \tag{4}$$

Non-negativity constrains:

$$\sum_{j=1}^{m} \sum_{i=1}^{n} W_{i,j} \geq 0 \tag{5}$$

The objective function is solved using a linear programming problem (LPP), simplex algorithm, and the tot of infrastructure cost is derived.

3. Water Pricing on Single-Block Theory

The following assumptions are made to determine the cost of potable and non-potable water under single-block pricing.

1. The cost of each source needs to be recovered completely so that economic feasibility will be established.
2. Water is considered a social commodity, and everyone has an equal right to water, irrespective of consumption quantity.

The unit cost of water under the single-block pricing strategy is found using Equation (6):

$$W_i C_{Bi} = ATC_i \tag{6}$$

The unit cost of water derived with a single-block price analysis is listed in Table 4. With the single-block approach pricing, it is found that the cost of water produced from SWRO and EED is multi-fold higher than the cost of water produced from WTP. Adopting a single-block pricing strategy will not be a viable option, considering breakeven in water infrastructure investments. Since the supply of a minimum quantity of water to meet social needs is a commitment, water cannot be higher priced to meet the infrastructural cost. Therefore a multi-block pricing strategy with increasing block tariff is investigated, considering the costs due to the impact of externalities.

Table 4. The unit cost of produced water from various resources in a single-block pricing strategy.

Source	Cost of Water (USD/m^3)
WTP	0.02
SWRO	0.79
EED	2.00
STP	0.26
CETP	0.75

4. Externality Components in Water Pricing

The environment cost, opportunity cost, and ecological system imbalance costs are the various externalities considered to account for the multi-block pricing strategy approach. The cost of emission of greenhouse gases (GHG), the opportunity cost of water from natural resources, and the cost incurred due to damage to ecological systems are taken as externalities in the current paper.

4.1. Environment Cost

Environment cost is defined as the cumulative monetary unit of the effects of environmental impacts through socio-economic activities to obtain water as a resource. The environmental impacts and their effect on cost structure are very complex to have a standard method of calculation [19].

For the current study, cost due to emission of greenhouse gases (C_{EGHG}) is accounted which is determined as units of electricity consumed from conventional energy sources for the generation of 1 L of water * cost of electricity produced by renewable energy source, which is mathematically given as in Equation (7):

$$C_{EGHG} = \left(\frac{\text{The total energy required for the process} - \text{Energy used from the renewable energy}}{\text{Quantity of water generated}} \right) \times \\ \text{Cost of energy generated per unit by renewable energy sources in India} \tag{7}$$

The cost of the impact of the emission of GHG per unit of electricity (1 kWh$_e$) generated from conventional sources is considered equivalent to the cost of green energy, which is USD 0.064/kWh [36]. The cost due to the emission of greenhouse gases by each water source is found using Equation (7) and is represented in Table 5.

Table 5. Cost per MLD on produced water considering emission through conventional electricity.

Source	Power Consumption (kWh/MLD)	Cost (USD/m^3)
Water treatment plant (WTP)	345	0.02
Seawater reverse osmosis plant (SWRO)	5000	0.32
Sewerage treatment plant (STP)	476	0.03
Common effluent treatment plant (CETP)	546	0.04

[37–39].

4.2. Opportunity Cost

Marginal opportunity cost is defined as the economic benefits lost in not allotting the additional unit of water for the second-best alternative for economically productive use. Hence estimation of opportunity cost is important in the process of efficient allocation of water while assessing the future infrastructure investments in water programs [40]. In the current work, the opportunity cost is considered as the cost of not allotting the freshwater (water from the river) for agricultural produce. The benefits that could have been recovered by using this water for the next better option, agriculture is 0.2 USD per m^3, considering the water requirement of 10 mm per square meter per day, with a yield of USD 2857 per acre per year [41–43]. The equation for opportunity cost is described in Equation (8):

$$C_O = \text{Income from yield per acre of land per year/Water requirement per year per acre of land} \tag{8}$$

4.3. Ecological System Imbalance Cost

Though seawater desalination is a reliable source of potable water, the brine rejection will have large environmental impacts, affecting the local ecology and marine life at the intake and reject locations. The ecological system imbalance cost due to desalination is defined as the change in gross domestic production (GDP) in the catchment area of the project due to the introduction of a technology derived per liter of desalinated water [44]. Advanced seawater reverse osmosis (SWRO) technologies have a 45–55% recovery ratio, with brine management costs accounting for 20–60%, of the produced water. Not much study is done on the direct impact on GDP due to brine rejection (Venkatesan, 2015), hence the ecological imbalance cost is taken as 20% of the cost of water produced by SWRO and EED, as indicated in Equation (9).

$$\begin{aligned} C_E = & \textit{ The cost to ecology due to brine} = \textit{cost for brine management} \\ = & \textit{ 20\% of the cost of produced water by SWRO and EED in single} \\ & \textit{--block pricing} \end{aligned} \tag{9}$$

5. Multi-Block Water Pricing Strategy

In a multiple block pricing system, water is considered a social and economic commodity. In this paper, two-block pricing is explored with quantity in block 1 taking care of minimum water requirement for potable requirements, considering water as a social commodity alone. To avoid the wastage and overuse of water, a second block is proposed setting only 10% of the total water quantity. The objective of the multi-block pricing strategy is to (i) Promote low-quality water for non-potable applications; (ii) Restrict usage of potable water beyond the social needs; (iii) Recover investments in water infrastructure; (iv) Self-sustainability of water infrastructure projects, to avoid incentives and subsidies. The quantities of water requirements allotted in each block for various applications are shown in Table 6.

Table 6. Allocation of water quantity in multi-block scenario.

Potable Water		Non-Potable	
Block 1	0 to 25 L	Block 1	0 to 125 L
Block 2	>25 L	Block 2	>125 L
Water consumption in Block 1	72 MLD	Water consumption in Block 1	288 MLD
Water consumption in Block 2	8 MLD	Water consumption in Block 2	32 MLD
Total water consumption	80 MLD	Total water consumption	320 MLD

The relation between the cost of potable water in block 1, to the cost of non-potable water in block 1 and the cost of water in block 2 is provided in Table 7. The multiplying factor is based on the quality of water, application to meet social causes, and measures for misuse or overuse of water.

Table 7. Relation of cost components in blocks 1 and 2 concerning potable water in block 1.

Cost Components	Relation with CPW_{B1}
Cost of potable water in block 1	CPW_{B1}
Cost of potable water in block 2 CPW_{B2}	$1.5 \times CPW_{B1}$
Cost of non-potable water in block 1 $CSWW_{B1}$	$0.6 \times CPW_{B1}$
Cost of non-potable water in block 2 $CSWW_{B2}$	$0.75 \times CPW_{B1}$

Considering the externalities in multi-block pricing, the cost balance of water is represented in Equation (10):

$$C_{B1} + C_{B2} + C_{EGHG} + C_O + C_E = ATC_{STP} + ATC_{CETP} + ATC_{WTP} + ATC_{SWRO} + ATC_{EED} \tag{10}$$

The socio-economic cost of potable water in Block 1 is found using Equation (10) and the cost of potable and non-potable water in block 1 and block 2 are found using the relation of potable water in block 1 concerning other water components as in Table 7. The calculated values of potable and non-potable water in different blocks are indicated in Table 8.

Table 8. Cost component due to various factors in block 1 and block 2 water pricing.

Cost of Water under Various Portfolios	Cost (USD/m^3)
The socio-economic cost of potable water in Block 1	0.41
The economic cost of potable water in Block 2	0.62
The socio-economic cost of non-potable water in Block 1	0.25
The economic cost of non-potable water in Block 2	0.31
The opportunity cost of water resources	0.04
Cost due to ecological imbalance due to brine	0.08

To obtain the cost competitiveness among various water sources and promote sustainable sources, while calculating the cost of produced water from each source, the cost of emission of greenhouse gases (C_{EGHG}), opportunity cost (C_O), and cost due to effect of brine discharge (C_E) are considered as an externality cost component.

The cost of producing unit water in multi-block pricing strategy from WTP, SWRO, and EED are given in Equations (11)–(13), respectively. The average cost of producing potable water is given in Equation (14). The cost of producing unit water for washing and

sanitation from the STP and CETP are given in Equations (15) and (16), respectively. The average cost of producing water for washing and sanitation is given in Equation (17).

Cost of unit water from Water Treatment Plant,

$$CW_{WTP} = \left(\frac{CPW_{B1} * W_{WTPB1} + CPW_{B2} * W_{WTPB2} + C_{EGHG} * W_{WTP} + C_O * W_{WTP}}{W_{WTP}} \right) \tag{11}$$

Cost of unit water from seawater reverse osmosis process,

$$CW_{SWRO} = \left(\frac{CPW_{B1} * W_{SWROB1} + CPW_{B2} * W_{SWROB2} + C_{EGHG} * W_{SWRO} + C_E * W_{SWRO}}{W_{SWRO}} \right) \tag{12}$$

Cost of unit water from seawater through energy-efficient desalination process,

$$CW_{EED} = \left(\frac{CPW_{B1} * W_{EEDB1} + CPW_{B2} * W_{EEDB2} + C_E * W_{EED}}{W_{EED}} \right) \tag{13}$$

Average Cost of potable water per unit liter,

$$CPW = \left(\frac{W_{WTP} * CW_{WTP} + W_{SWRO} * CW_{SWRO} + W_{EED} * CW_{EED}}{W_{WTP} + W_{SWRO} + W_{EED}} \right) \tag{14}$$

Cost of unit water produced through a sewerage treatment plant,

$$CSWW_{STP} = \left(\frac{CSWW_{B1} * W_{STPB1} + CSWW_{B2} * W_{STPB2} + C_{EGHG} * W_{STP}}{W_{STP}} \right) \tag{15}$$

Cost of unit water produced through a common effluent treatment plant,

$$CSWW_{CETP} = \left(\frac{CSWW_{B1} * W_{CETPB1} + CSWW_{B2} * W_{CETPB2} + C_{EGHG} * W_{CETP}}{W_{CETP}} \right) \tag{16}$$

The average cost of non-potable water,

$$CNPW = \left(\frac{W_{STP} * CSWW_{STP} + W_{CETP} * CSWW_{CETP}}{W_{STP} + W_{CETP}} \right) \tag{17}$$

Based on Equations (11)–(17), the cost of water from various resources under a multi-block pricing system considering the externalities is mentioned in Table 9.

Table 9. Cost of water under Multi-block pricing strategy.

Source	Capacity (MLD)	Cost of Water (USD/m^3)
Water Treatment Plant	40	0.57
Seawater Reverse Osmosis Plant (SWRO)	35	0.77
Seawater Energy-Efficient Desalination (EED)	5	0.51
The average cost of potable water		0.66
Non-potable water—Sewerage Treatment Plant (STP)	320	0.28
Non-potable water—Common Effluent Treatment Water (CETP)	40	0.29
The average cost of non-potable water		0.28

It is seen that the cost of producing water from the SWRO is brought close to the cost of water from WTP. Similarly, the cost of produced water from the EED has become cheaper than the water produced from the WTP. The average cost of produced water is brought to USD 0.66/m^3. Similarly, the cost of recycled water from the STP and CETP are brought to

almost the same, with the average at USD $0.29/m^3$. To improve cost competitiveness and to promote green energy sources, cross-subsidy may be given among various water resources.

6. Results, Discussions, and Policy Interventions

Water pricing is predominately based on a single-block strategy without considering the externalities of the system. However, the current study has compared the feasibility of multi-block pricing against single-block taking into consideration the externalities. The comparison of three scenarios, namely, levelized cost, and single-block and multi-block pricing strategies are shown in Figure 3. It is found that the levelized cost strategy cannot be considered a correct approach considering the high pricing for potable and non-potable components. The single-block pricing has brought down the price component considerably, but there is a huge disparity between the pricing of potable and non-potable components. The produced water from WTP is very much affordable, while the produced water from EED cannot be sold. Similarly, the water produced from STP is cheap, while the CETP-produced water is high-priced. The payback period for the single-block pricing strategy as shown in Figure 4, shows that few components in the potable and non-potable system may not be feasible with high payback periods. The multi-block pricing strategy has included the environment, opportunity, and cost towards the ecological imbalance thus making the unit cost of the produced water better than under the single-block and levelized cost pricing strategy. Large water infrastructure projects will have an impact on society, economy, and ecology, which are often not accounted into the cost economics.
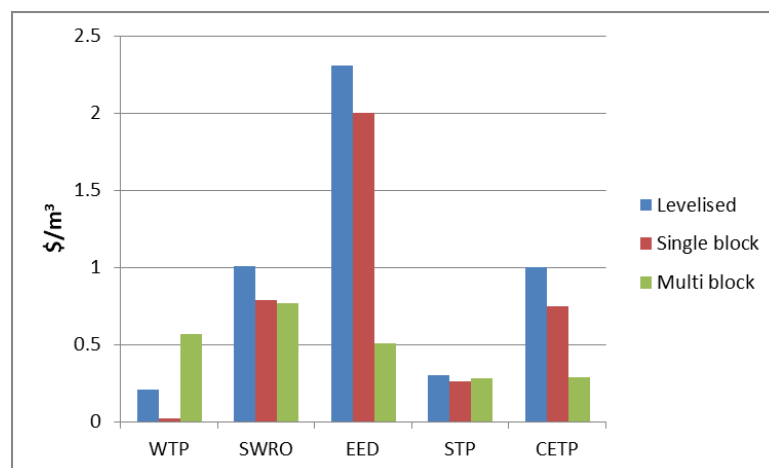
Figure 3. Unit cost under different scenarios.
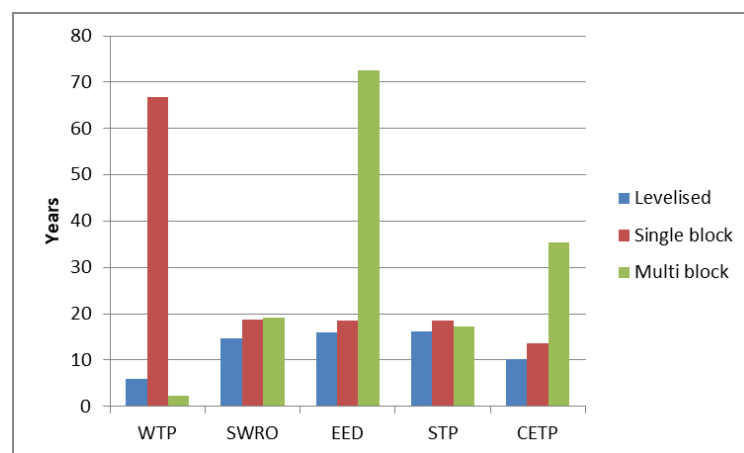
Figure 4. Payback under different scenarios.

The average cost of three potable and two non-potable sources under scenarios of levelized, and single-block, and multi-block pricing strategies are considered and depicted in Figure 5. It is seen that the multi-block pricing has shown a better sellable pricing strategy with potable and non-potable water sources at USD 0.62/m³ and USD 0.29/m³, respectively.
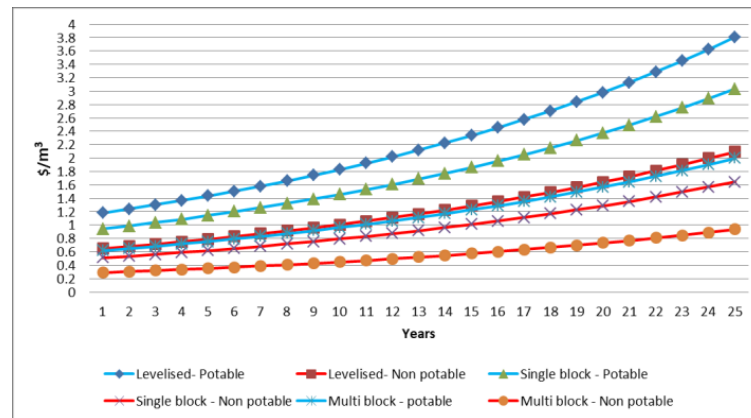
Figure 5. The unit cost of potable and non-potable water under different scenarios.

The payback period as indicated in Figure 6 shows that it is better to consider the potable and non-potable components as blocks than consider them individually. The multi-block pricing strategy has a higher payback, but the unit pricing can be normalized.
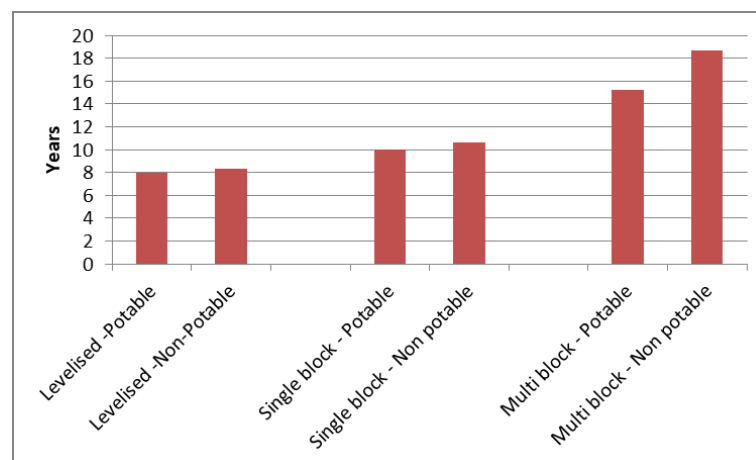
Figure 6. Payback period of potable and non-potable infrastructure under different scenarios.

Water is a social commitment to society and becomes the priority for urban administrations to native populations. Hence the financial impact of externalities often skips the cost assessment. However, a multi-block pricing strategy, factoring the impacts of externalities can normalize the cost of externalities and provide workable business models.

The following policy interventions are suggested:

(i) The outcome of the study indicates that multi-block pricing can be recommended with a full cost recovery objective. The full cost recovery requires considering the externalities due to the use of conventional power as a penalty or the use of renewables as an incentive.

(ii) The use of recycled water should be subsidized in a multi-block pricing philosophy which will extend the areas of use of recycled water. An accountable difference in the unit price of fresh and recycled water can make a difference in water consumption.

(iii) Incentivizing water from the high levelized cost of water (LCOW) resources and penalizing the use of low LCOW water resources in a multi-block water pricing system could normalize the unit cost of produced water. Cross subsidies should be considered from the cost breakeven perspective, effects of externalities, and depletion of naturally available resources.

7. Conclusions

In this research, single-block and multi-block pricing strategies were utilized to formulate a water infrastructure issue in a multi-resource variable demand context. The objective function is framed to minimize the overall cost, and the problem statement and constraints are specified. Demands are satisfied by the optimal distribution of resources. The issue statement was resolved using the linear programming problem approach. Investigated is the effect of single-block and multi-block pricing strategies. The goal of the single-block pricing method is to allocate the generated water's unit cost to completely recover the cost. While considering multi-block pricing, the impact of externalities of the project is considered. The impacts due to emission of greenhouse gases, the opportunity cost of naturally available water resources, and the cost due to ecological imbalance because of seawater intake and brine rejection are the externalities considered. While considering the size of the blocks, the following are given priority (i) water is considered more a social commodity than an economic one; (ii) encourage maximum use of recycled water; (iii) obtain breakeven on investments in water infrastructure projects. The single-block pricing strategy shows that the unit cost of water produced by SWRO and EED is many times higher than the unit cost of water produced by WTP. Hence the investments made on high CAPEX water infrastructure may not breakeven. The analysis of the multi-block pricing strategy shows that the high unit cost of produced water from SWRO and EED can be normalized. Similarly, the high unit cost of recycled water from CETP can be normalized to that of recycled water from STP.

Multi-block pricing blocks must be scaled to enforce optimal water usage and to maximize the use of recycled water, with water being considered a social commodity. Water infrastructure projects include externalities that the water price system does not take into account. The high manufacturing costs can be made more reasonable by including cost factors for externality implications. By including the impact of externalities into a multi-block pricing method, the high capital expenditure for integrating renewable energy into water infrastructure projects may be normalized. The significance of governmental action to require the inclusion of the cost of externalities in pricing models is stressed by the paper's conclusion. Future studies may examine the application of dynamic pricing in water management plans, taking into account the hours when renewable energy is available, the hours when water use is at its highest, and the amount of electricity used by dependable water sources.

Abbreviations

W_{WTPB1}	Quantity of potable water with block 1 pricing underwater treatment plant production
W_{WTPB2}	Quantity of potable water with block 2 pricing underwater treatment plant production
W_{WTP}	Quantity of water produced by the water treatment plant
W_{SWROB1}	Quantity of water with block 1 pricing under seawater reverse osmosis treatment produce
W_{SWROB2}	Quantity of water with block 2 pricing under seawater reverse osmosis treatment produce
W_{SWRO}	Quantity of water produced by seawater reverse osmosis method
$W_{SWEEDB1}$	Quantity of water with block 1 pricing under seawater energy-efficient desalination method
$W_{SWEEDB2}$	Quantity of water with block 2 pricing under seawater energy-efficient desalination method
W_{SWEED}	Quantity of water produced by seawater energy-efficient desalination method.
W_{STPB1}	Quantity of water with block 1 pricing under sewerage treatment plant produce
W_{STPB2}	Quantity of water with block 2 pricing under sewerage treatment plant produce
W_{STP}	Quantity of water produced by the sewerage treatment plant
W_{CETPB1}	Quantity of water with block 1 pricing under common effluent treatment plant produce
W_{CETPB2}	Quantity of water with block 2 pricing under common effluent treatment plant produce
W_{CETP}	Quantity of water produced by the common effluent treatment plant
CPW_{B1}	Cost of potable water in block 1
CPW_{B2}	Cost of potable water in block 2
CW_{WTP}	Cost of water from the water treatment plant
CW_{SWRO}	Cost of water from seawater reverse osmosis process
CW_{SWEED}	Cost of water from seawater energy-efficient desalination process
CW_{STP}	Cost of water from the sewerage treatment plant
CW_{CETP}	Cost of water from the common effluent treatment plant
CPW	The average cost of potable water
$CSWW$	The average cost of water for sanitation and washing
C_S	Sustainability cost
C_{EGHG}	Cost due to emission of greenhouse gases
C_{EE}	Cost due to environmental effects

References

1. Kashifi, M.T.; Al-Ismail, F.S.M.; Chowdhury, S.; Baaqeel, H.M.; Shafiullah, M.; Tiwari, S.P.; Rahman, S.M. Water-Energy-Food Nexus Approach to Assess Crop Trading in Saudi Arabia. *Sustainability* **2022**, *14*, 3494. [CrossRef]
2. Bithas, K. The sustainable residential water use: Sustainability, efficiency and social equity. *Eur. Exp. Ecol. Econ.* **2008**, *68*, 221–229. [CrossRef]
3. Papadopoulou, C.-A.; Papadopoulou, M.P.; Laspidou, C. Implementing Water-Energy-Land-Food-Climate Nexus Approach to Achieve the Sustainable Development Goals in Greece: Indicators and Policy Recommendations. *Sustainability* **2022**, *14*, 4100. [CrossRef]
4. Sani, Y.; Scholz, M. Interplay of Water-Energy Security and Food Consumption Patterns towards Achieving Nutrition Security in Katsina State, North-Western Nigeria. *Sustainability* **2022**, *14*, 4478. [CrossRef]
5. Gulati, A.; Banerjee, P. Emerging water crisis in India: Key issues and way forward. *Indian J. Econ.* **2016**, *96*, 681–704.
6. Alghassab, M.; Khan, Z.A.; Altamimi, A.; Imran, M.; Alruwaili, F.F. Prospects of Hybrid Energy in Saudi Arabia, Exploring Irrigation Application in Shaqra. *Sustainability* **2022**, *14*, 5397. [CrossRef]
7. Soto Rios, P.C.; Deen, A.T.; Nagabhatla, N.; Ayala, G. Explaining water pricing through a water security lens. *Water* **2018**, *10*, 1173. [CrossRef]
8. Sanabria, S.; Torres, J. Water Price: Environment Sustainability and Resource Cost. *Water* **2020**, *12*, 3176. [CrossRef]
9. Donnelly, K.; Christian-Smith, J. *An Overview of the New Normal and Water Rate Basics*; Pacific Institute: Oakland, CA, USA, 2011. Available online: http://pacinst.org/wp-content/uploads/2013/06/pacinst-newnormal-and-water-rate-basics.pdf (accessed on 1 September 2017).
10. Silvestre, J.G.; Tango, G.M.; Alonso, C.; Jalon, G. The environment costs of water flow regulation; An innovative approach based on 'Polluter Pays' principle. *Water Resour Manag.* **2018**, *31*, 2809–2822. [CrossRef]
11. Hewitt, J.A.; Hanemann, W.M. A discrete/continuous choice approach to residential water demand under block rate pricing. *Land Econ.* **1995**, *71*, 173–192. [CrossRef]
12. Al-Saidi, M. *Urban* Water Pricing in Yemen: A Comparison of Increasing Block Tariff to Other Pricing Schemes. *Water Int.* **2015**, *42*, 308–323. [CrossRef]
13. Lu, L.; Deller, D.; Hviid, M. Pure and behavioural signals to encourage household water conservations: Implications for UK. *Water Resour. Manag.* **2019**, *33*, 475–491. [CrossRef]

14. Sahin, O.; Bertone, E.; Beal, C.; Stewart, A.R. Managing water demand through dynamic pricing: A holistic system modelling approach. In Proceedings of the 12th Conference on Sustainable Development of Energy, Water and Environment Systems, Dubrovnik, Croatia, 18 October 2017.

15. Hoque, F.S.; Wichelns, D. State of art review; Designing urban water tariffs to recover costs and promote wise use. *Int. J. Water Resour. Dev.* **2013**, *29*, 472–491. [CrossRef]

16. Sjodin, J.; Zaeske, A.; Joyce, J. *Pricing Instruments for Sustainable Water Management*; Working Paper Nr. 28; SIWI: Stockholm, Sweden, 2016.

17. Frone, S. Issues on the role of efficient water pricing for sustainable water management, Romanian journal of economics. *Inst. Natl. Econ.* **2012**, *34*, 84–111.

18. Marinelli, E.; Radini, S.; Akyol, Ç.; Sgroi, M.; Eusebi, A.L.; Bischetti, G.B.; Mancini, A.; Fatone, F. Water-Energy-Food-Climate Nexus in an Integrated Peri-Urban Wastewater Treatment and Reuse System: From Theory to Practice. *Sustainability* **2021**, *13*, 10952. [CrossRef]

19. Bithas, K.; Kollimenakis, A.; Maroulis, G.; Stylianidou, Z. The water framework directive in Greece. Estimating the environmental and resource cost in the water districts of Western and Central Macedonia: Methods, results and proposals for water pricing. *Procedia Econ. Financ.* **2014**, *8*, 73–82. [CrossRef]

20. Shah, M. *Urban Water Systems in India: A Way Forward*; Working Paper, No. 323; Indian Council for Research on International Economic Relations (ICRIER): New Delhi, India, 2016.

21. Vincent, J.C.; Supate, R.A.; Desai, S.N. Efficient Wastewater Management for Sustainable Development: Challenges and Prospects in Indian Scenario. *Int. J. Health Serv. Res.* **2017**, *52*, 276–289.

22. Padelkar, A.; Kaur, S.; Kumar, R. Reliability analysis and removal efficiency relationship of common effluent treatment plant of industrial clusters. *Int. J. Environ. Sci. Technol.* **2019**, *16*, 1379–1394. [CrossRef]

23. Mohiyaden, A.H.; Sidek, M.L.; Ahmed Salih, H.G.; Birima, B.H.; MohdSabir, F.A.; NdNasir, N.M. Conventional methods and emerging technologies for urban river water purification plant: A short review. *ARPN J. Eng. Appl. Sci.* **2016**, *11*, 2547–2556.

24. Al-Jabr, H.A.; Rached, B.-M. Optimum Selection of Renewable Energy Powered Desalination Systems. *Proceedings* **2018**, *2*, 612.

25. Hingorani, P. *The Economics of Sewerage Water Recycling and Reuse in India*; Indian Infrastructural Report 2011, Water Policy and Performance for Sustainable Development, Indian Infrastructure Report; Oxford University Press: New Delhi, India, 2011; pp. 313–323.

26. Samuel, V.; Srinivas, T.G. Efficient treatment technologies ad cost research. *Int. J. Eng. Adv. Technol.* **2019**, *9*. [CrossRef]

27. Cox, W. World Urban Areas Population and Density: A 2012 Update. New Geography. 2012. Available online: http://www.newgeography.com/content/002808-world-urban-areas-population-and-density-a-2012-update (accessed on 8 April 2019).

28. Tumbe, C. *Urbanisation, Demographic Transition, and the Growth of Cities in India, 1870–2020*; Working paper; International Growth Centre: London, UK, 2016.

29. Howard, G. *Domestic Water Quantity: Service Level and Health*; WHO/SDE/WSH/03.02; World Health Organisation: Geneva, Switzerland, 2003.

30. World Health Organization (WHO); International Programme on Chemical Safety. *Guidelines for Drinking-Water Quality. Vol.2, Health Criteria and Other Supporting Information*, 2nd ed.; World Health Organization: Geneva, Switzerland, 1996. Available online: https://apps.who.int/iris/handle/10665/38551 (accessed on 5 June 2020).

31. Sankar, U. Common Effluent Treatment Plants: An Institutional Arrangement for Pollution Control in Small Scale Tanneries in India, World Bank Research Support. 2014. Available online: https://www.researchgate.net/publication/252196879 (accessed on 9 April 2022).

32. Tandel, M.A.; Shah, A.M. Performance Study of CETP (Common Effluent Treatment Plant)—A Case Study of Pandesara, Surat. *Int. J. Curr. Eng. Technol.* **2018**, *8*, 32–35. [CrossRef]

33. Heberling, T.M.; Nietch, T.C.; Price, I.J.; Thurston, W.H.; Elovitz, M. *Drinking Water Treatment Plant, Costs and Source Water Quality: An Updated Case Study*; US Environmental Protection Agency, Office of Research and Development: Cincinnati, OH, USA, 2017.

34. Bertone, E.; Rodney, A.; Stewart, I.; Zhang, H.; O'Halloran, K. Hybrid water treatment cost prediction model for raw water intake optimization. *Environ. Model. Softw.* **2016**, *75*, 230–242. [CrossRef]

35. Shouman, R.E.; Sorour, M.H.; Abulnour, A.G. Economics of Renewable Energy for Water Desalination in Developing Countries. *Int. J. Econ. Manag. Sci.* **2015**, *5*, 1. [CrossRef]

36. IRENA. *Renewable Power Generation Costs in 2017*; International Renewable Energy Agency: Abu Dhabi, United Arab Emirates, 2018.

37. Soares, B.R.; Memelli, S.M.; Roque, P.R.; Gonçalves, F.R. Comparative Analysis of the Energy Consumption of Different Wastewater Treatment Plants. *Int. J. Archit. Arts Appl.* **2017**, *3*, 79–86. [CrossRef]

38. Dabrowski, W.; Żyłka, R.; Rynkiewicz, M. Evaluation of energy consumption in Agro-industrial wastewater treatment plant. *J. Ecol. Eng.* **2016**, *17*, 73–78. [CrossRef]

39. Karabalas, J.A.; Koutssou, P.C.; Kostoglou, M.; Sioutoplulos, C.D. Analysis of Specific Energy Consumption in Reverse Osmosis Desalination Process. *Desalination* **2018**, *431*, 15–21. [CrossRef]

40. Rouge, C.; Harou, J.J.; Velazquez, P.M.; Matrosov, S.E. Estimating the Economic Opportunity Cost of Water Use with River Basin Simulators in a Computationally Efficient Way. In *Proceedings of the 19th EGU General Assembly, EGU2017-16348, Vienna, Austria, 23–28 April 2017*; Geophysical research abstracts; EGU General Assembly: Vienna, Austria; p. 16348. Volume 19. Available online: https://meetingorganizer.copernicus.org/EGU2017/EGU2017-16348.pdf (accessed on 4 July 2022).

41. Zomer, R.J.; Bossio, D.A.; Trabucco, A.; Yuanjie, L.; Gupta, D.C.; Singh, V.P. *Trees and Water: Smallholder Agroforestry on Irrigated Lands in Northern India*; IWMI Research Report 122; International Water Management Institute: Anand, India, 2007; 47p.

42. Chand, R. *Strategies for Doubling Farmers Income*; National Institute of Transforming India (Nitiaayog): New Delhi, India, 2017.

43. Economic Times. Farmers Earning as much as Rs 3 lakh per Acre by Cultivating Herbs. 2018. Available online: https://economictimes.indiatimes.com/news/economy/agriculture/farmers-earning-as-much-as-rs-3-lakh-per-acre-by-cultivating-herbs/articleshow/65802909.cms?utm_source=contentofinterest&utm_medium=text&utm_campaign=cppst (accessed on 4 July 2022).

44. Venkatesan, R.; Abraham, R. Costing and Evaluation of Desalination Technologies- Case Studies in India. In Proceedings of the Trombay Symposium on Desalination and Water Reuse, Mumbai, India, 22–23 January 2015.

Article

Delineation of Salinization and Recharge Sources Affecting Groundwater Quality Using Chemical and Isotopic Indices in the Northwest Coast, Egypt

Hesham A. Ezzeldin

Hydrogeochemistry Department, Desert Research Center, Cairo P.O. Box 11753, Egypt; h.ezzeldin@drc.gov.eg or h.ezzeldin@hotmail.com

Abstract: Salinization of coastal aquifers is a serious issue affected by climate change and enhanced by overexploitation of groundwater resources. This research aims to explore the hydrogeochemical processes that cause salinization of groundwater in coastal aquifers, such as the area located between Barrani and Baqbaq, on the northwestern coast of Egypt. Various techniques were applied, including Gibbs plots and hydrochemical facies diagrams (HFE-D), ion ratios and stable isotope bivariate plots, statistical analyses, a groundwater quality index for seawater intrusion (GQI_{SWI}), and a seawater mixing index (SMI). Based on the total dissolved solids (TDS), groundwater can be classified into four groups: slightly saline (9%), moderately saline (45%), highly saline (43%), and salty water (3%). The geochemical properties were further catergorized on the basis of other parameters and ion ratios, such as Ca_{excess}, $Na_{deficit}$, Na/Cl, Cl/HCO_3, and Br/Cl, which suggest the influence of cation exchange, seawater, and marine sediment dissolution. Additionally, stable isotopes indicated two groups. One of these has relatively high salinity and low isotopic content and is affected by the leaching and dissolution of marine deposits. The other group is enriched in $\delta^{18}O$ and δD content, with much higher salinity due to mixing with seawater and evaporation. The GQI_{SWI} categorizes groundwater as saline and mixed (55 and 41%, respectively), followed by saltwater (4%), whereas the SMI calculations indicate that about 10% of the groundwater samples are impacted by seawater. Finally, the areal distribution of GQI_{SWI} and SMI identified some patches along the coastline as well as other inland places located about 12.5 km away from the sea that have undergone saltwater intrusion. In conclusion, overexploitation of groundwater should be avoided because the amount of annual rainfall is very limited.

Keywords: groundwater salinization; ion ratios; stable isotopes; seawater mixing index (SMI); northwest coast

1. Introduction

Water demand has increased, especially in coastal areas, with the rapid growth of residential, agricultural, industrial, and tourism activities. Coastal aquifers are considered one of the main sources of freshwater supplies in many countries worldwide, especially in the Mediterranean [1]. The geological heterogeneity as well as spatial and temporal variability in flow patterns play a critical role in governing the distribution of fresh and saline waters in the coastal aquifers [2]. Salinization of groundwater takes place in many coastal aquifers [3–5]. It has been found through previous studies that sources and causes of groundwater salinization in coastal aquifers are due to several processes. Among these are water–rock interactions, cation exchange, redox reactions, carbonate and evaporate mineral dissolution, wastewater disposal, and intrusion of fossil seawater and modern seawater induced by groundwater overexploitation [6–9]. All of these are linked to climate change's effects on precipitation and patterns of recharge as well as to evapotranspiration, which in turn puts pressure on the coastal aquifer systems. This likely speeds up the quantitative and qualitative degradation of groundwater. Therefore, in order to support

the sustainable management of coastal resources in the near future, it is urgent that we enhance our understanding of the spatial distribution of groundwater salinity and the factors controlling changes [10].

The most important process that degrades groundwater quality in coastal areas is the excessive abstraction of groundwater, which reduces freshwater discharge to the sea and creates a local water table depression, causing seawater upwelling [11–13]. This phenomenon is known as seawater intrusion, and it is considered one of the main reasons limiting the use of groundwater in coastal areas. When reviewing the literature around the world, it was found that the phenomenon of seawater intrusion has been documented in North America [14,15], Australia [16], Europe [17], South America [18], and Africa [19]. Recently, developing countries along the Mediterranean Sea in North Africa are facing environmental pressures resulting from high population growth, rapid urbanization, and insufficient water sector services, which necessitate identifying effective solutions to address these problems [20,21].

Many authors have conducted regional geomorphological studies on the Northwestern coast of Egypt, [22–24]. The geology and subsurface geology were also studied by others [25–27]. AbdelMogheeth [28] and Atwa [29] studied the hydrogeology and water resources of the Northwestern coastal zone, focusing on hydrogeology and hydrochemistry. Additionally, the hydrogeology of the El-Salloum area, located to the west of the study area, was investigated by Salem and Mohamed [30], who concluded that the main water bearing formation is of Middle Miocene age. Other studies in the Mediterranean basin concluded that water resources are primarily found in alluvial Pleistocene aquifers connected with stream deltas and within karst aquifers scattered across elevated coastline ridge zones [31]. Groundwater extraction from the Pleistocene oolitic and Miocene fractured limestone aquifers is the primary source of freshwater supply in the study area. Such aquifers receive significant recharge during the winter, where depressions extending between elongated coastal ridges serve as sites for groundwater replenishment [32]. Two types of factors primarily affect the chemical evolution of groundwater during flow: natural and anthropogenic activities. Natural factors include aquifer lithology, geological structures, and recharge conditions. Anthropogenic activities primarily relate to agricultural intensity, industrial and/or sewage water discharge, and groundwater overexploitation, which in turn take part in groundwater salinization, especially in coastal aquifers [33,34].

The sources and mechanisms of the groundwater salinization must be evaluated for the effective management of groundwater resources, especially in arid and semi-arid regions. However, various sources of salinity make determining the origin and mechanism of groundwater salinization extremely complex [35]. There are many factors that cause seawater intrusion, namely aquifer properties, anthropogenic activities, recharge rates, variable density flow, and effects relating to global climate change, such as higher surface air temperature, lower annual precipitation, and sea level rise. The multiplicity of such effects makes seawater intrusion a complicated hydrogeological process [36–39]. Therefore, the use of groundwater chemistry and stable isotopes (such as $\delta^{18}O$ and δ^2H) along with the previous geophysical and hydrogeological studies is very useful to identify groundwater recharge sources as well as to assess the geochemical processes that lead to groundwater quality deterioration in arid regions [40–42]. Additionally, stable oxygen-18 and deuterium isotopes can be considered among the tools used in water management, as they are used to identify factors affecting groundwater quality such as evaporation, precipitation, and mixing processes [43,44]. A basic assumption in the use of isotopic and chemical techniques in tracking sources of salinization is that the fingerprint of the original source is preserved during the salinization process [45]. However, the original isotopic composition, as well as the chemical composition of the salinity source, could change as a result of evaporation, dilution, mixing, or rock–water interactions. For this reason, chemical and isotopic signatures of reference waters as end members (such as seawater, rainwater or paleo-groundwater) should be monitored in the studied groundwater. To achieve the main objective of this study, multiple approaches, such as hydrochemical facies

evaluation, ion ratio relationships, statistical techniques, and salinity mixing indexes are applied for a realistic interpretation of the results. This work aims to shed light on the causes of groundwater salinization and propose some solutions to mitigate or limit the aggravation of such problems. The overarching goal of this work is to help better predict, manage, and respond to environmental contaminants that threaten human health. In light of this, a clearer picture will be provided to decision-makers and/or water authorities that enables them to take the necessary measures and precautions to confront such problems.

2. Study Area

The study area extends from Sidi Barani in the east to Baqbaq in the west, for a distance of about 35 km. It extends also for about 9 km south of the Mediterranean shore line, as shown in (Figure 1). It lies between Latitudes 31°15′00″ and 31°40′00″ N and Longitudes 25°25′00″ and 26°25′00″ E, with an area of about 32 km^2.
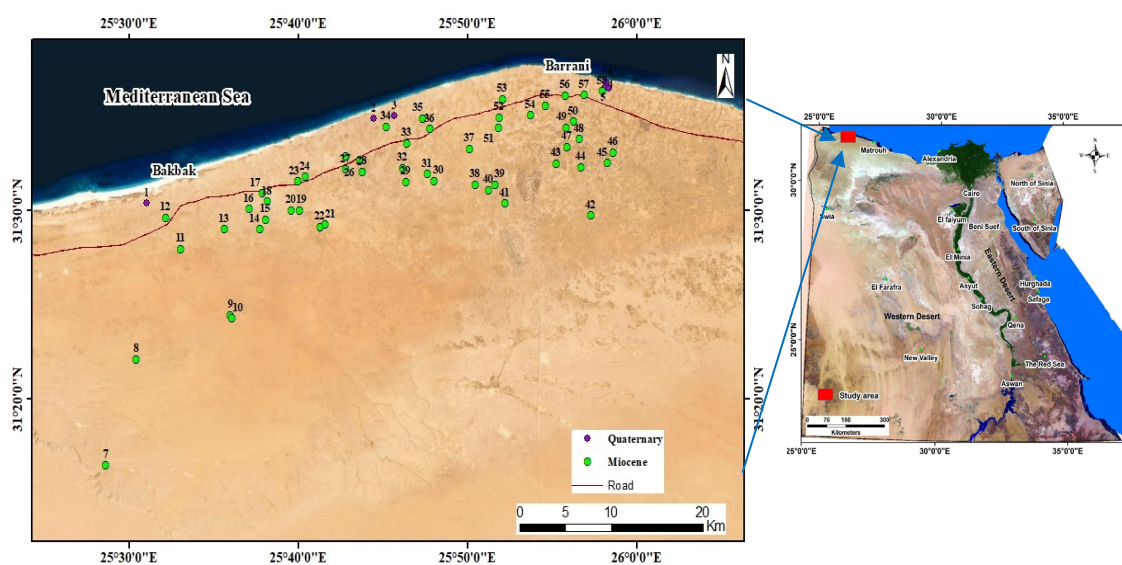
Figure 1. Study area showing the geographic location of the sampled groundwater wells (the sampling points are shaded purple for the Quaternary aquifer, while those related to the Miocene aquifer are shaded green).

3. Geomorphological and Geological Aspects

Geomorphologically, the landforms within the study area reflect the influences of endo-genetic factors (e.g., faulting, folding, lithologic features, etc.) and exo-genetic factors (e.g., climatic conditions, weathering, deposition, erosion, etc.) [46,47]. These factors result in the emergence of various landforms, such as tablelands, ridges, depressions, and dunes as well as drainage lines, all of which are affected by the distribution of surface runoff in addition to the accumulation and storage of groundwater. Three main geomorphologic units were identified: the southern tableland, the piedmont plain, and the coastal plain [27] (Figure 2). The southern tableland extends southwards to the Qattara Depression, with a maximum elevation of 250 m above sea level. The northern bounding slopes of this tableland are usually dissected by the drainage lines that discharge to the coastal plain. The piedmont plain, with low land and hills, is a transitional zone between the tableland to the south and the coastal plain to the north. Its elevation ranges from 30 to 90 m above sea level, while it varies between 2 and 25 kilometers wide. The inland depressions can be seen within this plain in between the ridges [48]. The coastal plain occupies a narrow strip of land that extends parallel to the Mediterranean Sea, with elevations ranging from 0 to 50 meters above sea level. The existence of alternating low-lying ridges separated by narrow depressions along the coast reflects the influence of lithologic and structural conditions as well as the fluctuation of sea level [23].
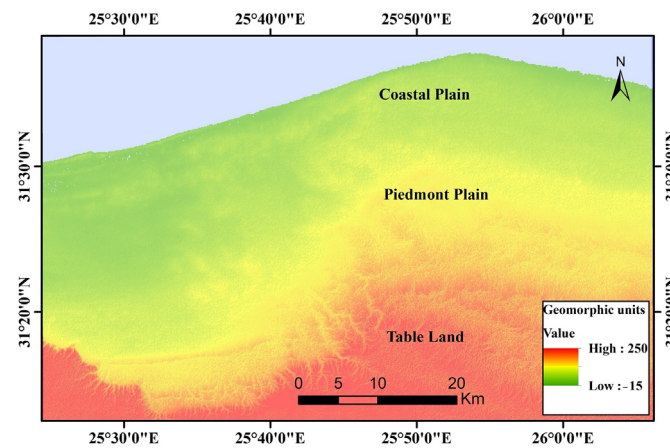
Figure 2. Geomorphological units.

Geologically, the study area, which is a part of the northwestern Mediterranean coast, is mainly underlain by sedimentary rocks ranging in age from Tertiary to Quaternary [23]. The Miocene deposits are represented by Moghra and Marmarica Formations. The Moghra Formation is composed of argillaceous limestone intercalated with sand and shale related to fluviatile to fluviomarine deposits, while the overlying shallow marine rocks belong to the Marmarica Formation. It is formed of fracture white limestone and a lower grey calcarenite interbedded with clay lenses. The overlaying Quaternary deposits are exposed in the study area. They are formed by a thin cover of drift sands and loamy deposits covering mainly low-lying areas and the floors of narrow valleys dissecting the tableland (Figure 3). The study area's climatic conditions are typically arid, with a long, hot, dry summer, a mild winter with little rainfall, high evaporation, and moderate to high relative humidity, with a mean annual rainfall of 155 mm [49].
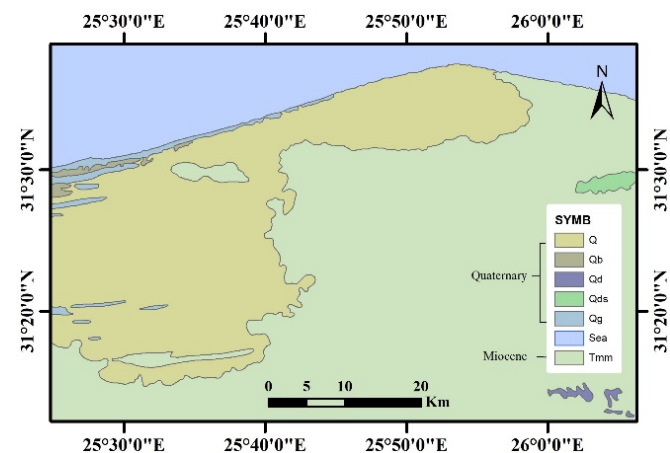
Figure 3. Surface geology map.

Hydrologically, the Quaternary and Miocene aquifers are considered as the two main water-bearing formations in the area under consideration. The Quaternary carbonate aquifer comprises wadi fill and oolitic limestone deposits, with a thickness ranging from 10 m to about 40 m [50,51]. It is mainly recharged from the infiltration of the precipitation over its outcropping rocks [50]. The Quaternary aquifer is directly connected to the Mediterranean Sea, which has a significant impact on groundwater salinity [51]. Groundwater, in this aquifer, exists under unconfined conditions and is represented by six groundwater samples. The depth to water ranges from 3.15 m (well 6) to 9.30 m (well 2), while the water level ranges between 2 m below sea level (well 1) and +4.7 m (well 3). The Miocene limestone aquifer of middle Miocene age (Marmarica Formation) is the main water-bearing formation

in the study area. It is mainly composed of successions of chalky, marly, argillaceous, and dolomitic limestones interbedded with clay lenses. The groundwater in this aquifer exists under two conditions: perched groundwater, where the water level is above mean sea level, and main water table, where the water is free or semi-confined. The perched water table is recharged indirectly by the overlying fractured rocks, while the fractured free to semi-confined aquifer is indirectly recharged by natural groundwater movement from south to north [51]. The degree of recharge depends on the nature of the fault from which this aquifer derives its water. The depth to water ranges from 16 m (well 11) to 72 m (well 41), whereas the water level ranges between 5.3 m below sea level (well 12) and +8 m (well 33). Despite the fact that there is a general relationship between water level and salinity because salinity frequently rises with the direction of water flow, Figure 4 shows that the relationship between the two variables is not clearly defined in each of the Quaternary and Miocene aquifers. This characteristic could mean that other hydrological factors, rather than the absolute water level, have a significant impact on the salinity of the water, as is the case in some localities within the study area, which showed perched aquifer conditions. In general, the figure shows a general direction of groundwater flow from southeast to northwest.
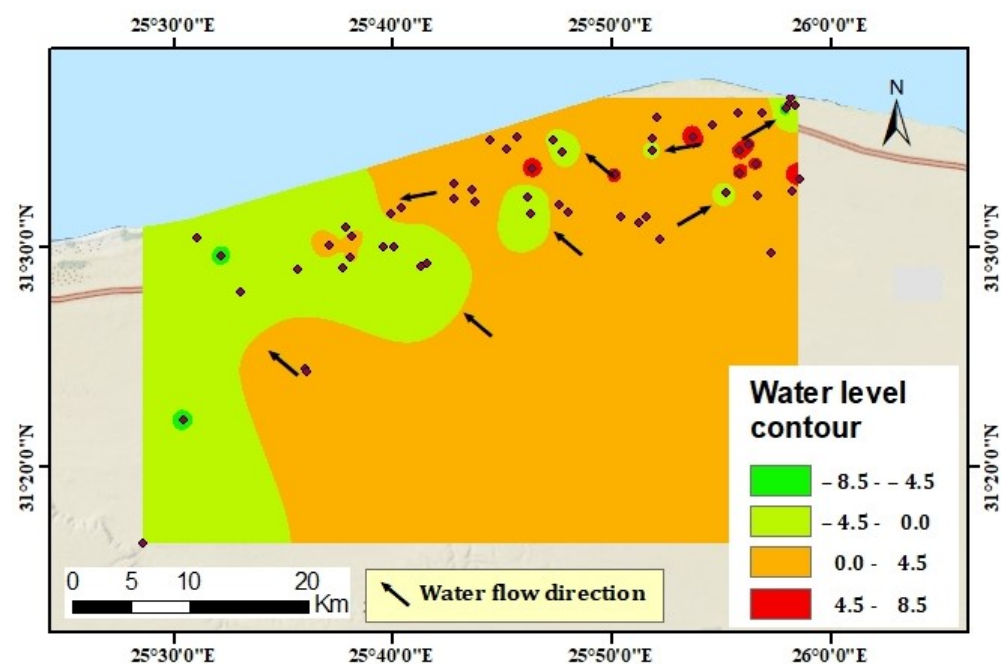
Figure 4. Water flow contour map. Points indicate sampling sites, while circles indicate areas with different water levels. The red circles represent the areas with the highest water level, while the green circles represent the areas with a low level of groundwater.

According to Morad et al. [51], the maximum discharge from the Quaternary and Miocene aquifers in the Barrani area is 52,200 m^3/day and 135,000 m^3/day, respectively. A hydrogeological cross-section extending from the southeast to the northwest towards the city of Baqbaq, with a distance of about 50 km (Figure 5), indicates that groundwater recharge is possible, with precipitation on the tablelands to the south and flowing to the Mediterranean Sea to the north. Because the karst aquifer's rocks are mostly fractured, recharge is possible and increasing along the drainage lines, where these drainage lines act as water collectors [52].
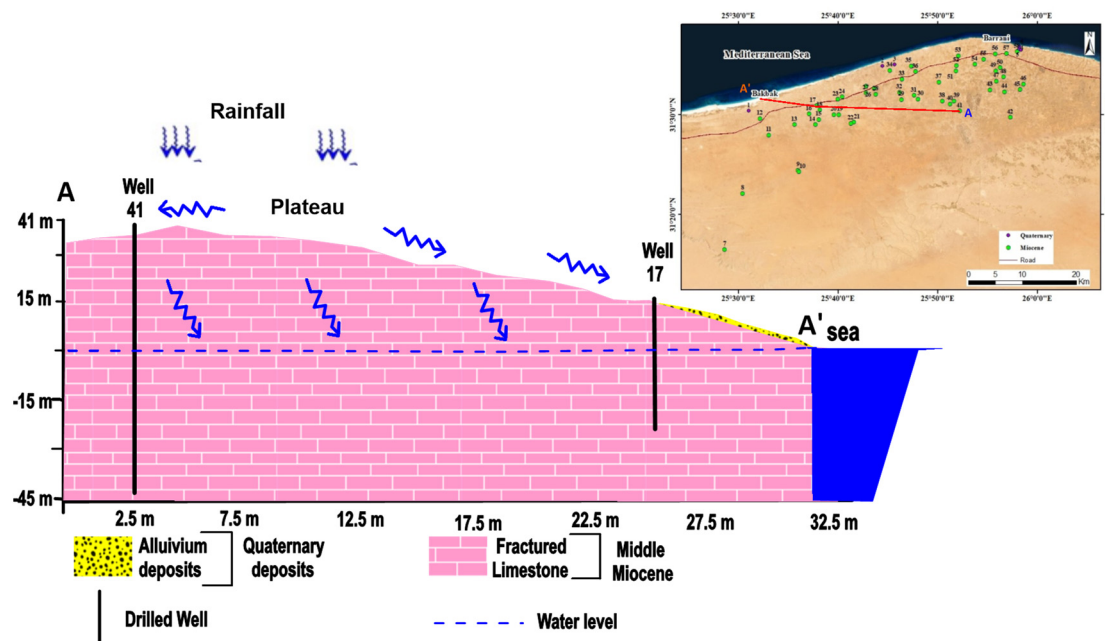
Figure 5. Hydrogeological cross section (A-A'), illustrating the karst aquifer subsurface succession and rainfall recharge opportunities.

4. Methodology

Fifty-eight groundwater samples were collected, throughout 2021, from all the available water points. These water points represent shallow hand dug and deep wells. The Quaternary aquifer was represented mostly by hand dug wells (6 samples), while the Miocene aquifer was primarily represented by drilled wells (52 samples). All the studied groundwater wells are private, with the exception of three governmental wells (12, 23, 44), which have desalination plants installed. Additionally, two water samples representing the local rainfall and the Mediterranean Sea were collected during the winter of 2020 to be used as reference waters. The rainwater sample (59) was collected from the rain gauge station located in the support center of the Desert Research Center in the Sidi Barani area, while the seawater sample (60) was collected from the Mediterranean Sea. The field activities included depth to water measurements and geographic locations of the wells, in addition to measuring the hydrogen ion activity (pH) and electrical conductivity (EC). During the field trip, only one water sample was collected from each well in order to perform the necessary chemical analyses. Another set of water samples was collected from selected wells for the purpose of conducting stable isotope analyses. The collected water samples were analyzed for major and minor ion concentrations (such as Ca, Mg, Na, CO_3, HCO_3, SO_4, Cl, SiO_2, and Br), in addition to environmental stable isotopes including $\delta^{18}O$ and δ^2H. The concentrations of both CO_3 and HCO_3 were measured by the titration method using 0.01 normal H_2SO_4. The concentrations of the other major and minor ions were detected using ion chromatography (Dionex, ICS-1100, Thermo Fisher Scientific Inc., Waltham, MA, USA). All of the aforementioned analyses were conducted according to the methods adopted by Rainwater and Thatcher, Fishman and Friedman, and the American Society for Testing and Materials [53–55] at the Laboratory of the Desert Research Center, Egypt. The results of all of the analyzed water samples were within the acceptable error limit (± 5).

The concentration of stable isotopes for some selected water samples were estimated according to the method described by Coplen et al. and Coplen [56,57] at the Center for Stable Isotopes at the University of New Mexico, USA. The results were reported in delta per mille (‰) notation for O-18 and deuterium (^2H) to identify the recharge sources as well as the factors affecting groundwater quality change. The assessment of the different hydrogeochemical and mixing processes were studied using multiple techniques, including the groundwater quality index for seawater intrusion (GQI$_{SWI}$), hydrochemical

facies evaluation diagram (HFE-D), ionic ratios and stable isotopes relationships, principle component analysis (PCA), and salinity mixing index (SMI) model. The software program Aquachem version 10 was used to identify the chemical water types, while ArcGIS desktop version 10.2 software, (Environmental Systems Research Institute, Inc. "ESRI", Redlands, CA, USA, was used to construct maps.

4.1. Gibbs Diagram

This diagram, a simple plot of the total dissolved solids (TDS) versus the weight ratio of Na/(Na + Ca) or Cl/(Cl + HCO$_3$), is used to identify the relationships between the chemical water composition and the types of the rocks in which the water circulates [58]. Three distinct fields, including precipitation dominance, evaporation dominance, and rock weathering dominance, constitute the segments in the Gibbs diagram.

4.2. Hydrochemical Facies Evolution Diagram (HFE-D)

This diagram was suggested by Gimenez Forcada [59] as an alternative to other hydrochemical diagrams such as the piper diagram, to clearly identify the hydrogeochemical changes in groundwater during recharge and saltwater intrusion processes. The importance of this diagram is that it helps in the identification of the salinization–freshening phases in coastal aquifers. In addition, it contributes to a clearer identification of possible groups of samples and their evolution trends in the aquifer [60,61]. In this diagram, four main facies are defined, namely NaCl, CaCl$_2$, NaHCO$_3$, and CaHCO$_3$. Each group is divided in turn into four other subfacies, resulting in sixteen subdivisions. These subdivisions are the following: 1. Na–HCO$_3$/SO$_4$, 2. Na–MixHCO$_3$/MixSO$_4$, 3. Na–MixCl, 4. Na–Cl, 5. MixNa–HCO$_3$/SO$_4$, 6. MixNa–MixHCO$_3$/MixSO$_4$, 7. MixNa–MixCl, 8. MixNa– Cl, 9. MixCa–HCO$_3$/SO$_4$, 10. MixCa–MixHCO$_3$/MixSO$_4$, 11. MixCa–MixCl, 12. MixCa–Cl, 13. Ca–HCO$_3$/SO$_4$, 14. Ca–MixHCO$_3$/MixSO$_4$, 15. Ca–MixCl, 16. Ca–Cl [62]. The facies in this diagram are determined by the percentage of Ca and Na cations, as well as by HCO$_3$ (or SO$_4$) and Cl$^-$ anions, in relation to the sum of cations and anions. The term Mix is used for the facies names to indicate that the percentage of the cations or anions is less than 50% but greater than the percentage of any of the other cations and anions considered. For example, if a sample is plotted in subdivision 6, it belongs to MixNa–MixHCO$_3$/MixSO$_4$, which means none of the Na, HCO$_3$, and SO$_4$ ions reached 50%, yet Na% remains greater than Ca and Mg, and similarly, HCO$_3$ and SO$_4$ will be greater than Cl. In addition to the mixing processes, the diagram also explains both the direct and reverse exchange reactions.

4.3. Correlation Coefficients (Ion–Ion Relationships)

Changes in the chemical composition of groundwater are affected by many factors, such as rock–water interaction, mixing, and ion-exchange processes. Some parameters and ion ratios calculated in meq/L (such as Ca$_{excess}$, Na$_{deficit}$, Na/Cl, Mg/Ca, SO$_4$/Cl, and Br/Cl) are addressed. They were correlated with each other as well as with the TDS in bivariate diagrams in order to distinguish between the mixing mechanisms of fresh water and saline water from other chemical reactions, such as rock weathering and ion exchange.

4.4. Principal Component Analysis (PCA)

Principal component analysis (PCA) is a data transformation technique that attempts to visualize a simple underlying structure that is assumed to exist within a multivariate data set [63]. It quantifies the relationship between different variables by computing the correlation matrix for the entire data set. As a result, the data set is easily summarized without losing much information [64]. When using this technique, data sets are first standardized, and then the correlation matrix is created. The eigenvalues and factor loadings for the correlation matrix are determined and a scree plot is drawn. The extraction factors are based on the variances and co-variances of the variables. The eigenvalues and eigenvectors are evaluated, which represent the amount of variance explained by each factor. An eigenvalue greater than 1 is set as a criterion to extract factors [65]. Finally, by the

process of rotation, the loading of each variable on one of the extracted factors is maximized, and the loadings of all the other factors are minimized. These factor loadings are useful in grouping the water quality parameters and providing information for interpreting the data. This study considered pH, EC, Na, K Ca, Mg, Cl, CO_3, HCO_3, and SO_4 as water quality parameters. Statistical Package for the Social Sciences (SPSS) version 16 was used for the statistical analysis.

4.5. Groundwater Quality Index for Seawater Intrusion (GQI_{SWI})

The GQI_{SWI} index was developed by Tomaszkiewicz et al. [66] as another tool, calculated according to Piper [67], to interpret groundwater quality change (in terms of seawater salinization). Equation (1) is developed from Equations (2)–(4):

$$GQI_{SWI} = \frac{GQI_{Piper\ (mix)} + GQI_{fsea}}{2} \tag{1}$$

$$GQI_{Piper\ (mix)} = \left(Ca^{2+} + Mg^{2+} + HCO_3^-\right) \times 50\ (in\ \%\ meq/l) \tag{2}$$

$$GQI_{fsea} = (1 - f_{sea}) \times 100 \tag{3}$$

where

$GQI_{Piper\ (mix)}$ is the freshwater seawater mixing index of the piper diagram;
GQI_{fsea} is seawater fraction index.
The seawater fraction (f_{sea}) is calculated according to the following equation:

$$f_{sea} = \frac{m_{Cl\ sample} - m_{Cl\ fresh}}{m_{Cl\ sea} - m_{Cl\ fresh}} \tag{4}$$

Chloride ion is used as a conservative parameter, where $m_{Cl\ sea} - m_{Cl\ fresh}$ is equal to about 35‰ (grams of salt per kilogram) seawater, based on the concentration of Cl^- in mmol/L [66,68]. GQISW is a numerical indicator used to interpret data from the Piper diagram as well as seawater intrusion. It ranges from 0 to 100, with 100 representing freshwater and 0 representing seawater.

4.6. Seawater Mixing Index (SMI)

The seawater mixing index (*SMI*) is applied to calculate the degree of seawater mixing [69]. Major ion compositions, including (Cl, SO_4, Na and Mg), are used to calculate this index according to the following equation:

$$SMI = a \times \frac{C_{Na}}{T_{Na}} + b \times \frac{C_{Mg}}{T_{Mg}} + c \times \frac{C_{Cl}}{T_{Cl}} + d \times \frac{C_{SO_4}}{T_{SO_4}} \tag{5}$$

The constants *a*, *b*, *c*, and *d* are estimated based on the relative concentration proportion of Na^+, Cl^-, Mg^{2+}, and SO_4^{2-} in seawater and recorded as 0.31, 0.04, 0.57, and 0.08, respectively. *C* is the measured ion concentration in mg/L. *T* represents the values of threshold of the selected ions, which can be estimated from the cumulative probability curves by determining the inflection points for each ion. The water is said to be impacted by seawater mixing if the *SMI* is more than 1 [70].

5. Results and Discussion

Groundwater characterization mainly depends on its chemical constituents. The concentrations of these constituents are mostly a result of the interaction between groundwater and its host rocks. In this part, different aspects are addressed, including hydrochemical characterization, salinization process identification, and mixing ratio quantification.

5.1. Hydrochemistry and Its Prevailing Factors

The physical, chemical, and isotopic characteristics of groundwater samples from the shallow Quaternary (samples 1 to 6) and deeper Miocene (samples 7 to 58) wells are presented in Table 1 and Figure 6. The total dissolved solids (TDS) displayed high variance, ranging from 1113 mg/L to 51,975 mg/L (Avg. 10,290 mg/L). The high values and extreme outliers in TDS values are probably due to salt water. The major cations followed the order Na (260–15,000 mg/L, Avg., 2738 mg/L) > Mg (46–2292 mg/L, Avg., 500 mg/L), or Ca (47–1887 mg/L, Avg. 423 mg/L), while the major anions are of the order Cl (406–29,200 mg/L, Avg., 4786 mg/L) > SO$_4$ (200–4300 mg/L, Avg., 1778 mg/L) > HCO$_3$ (49–460 mg/L, Avg., 174), indicating that groundwater is dominated by two hydrochemical types: Na-Cl and Na-SO$_4$. Groundwater samples collected from the Quaternary and Miocene aquifers were classified into four groups according to USGS [71]. Group A, which is classified as slightly saline water (5 samples, and its percentage is 9%), ranged from 1000 to less than 3000 mg/L. Group B (26 samples, about 45%), with salinity ranging from 3000 to 10,000 mg/L, is classified as moderately saline water. Group C (25 samples of about 43%), whose salinity ranged from 10,000 to 35,000 mg/L, is classified as highly saline water. Finally, group D, with a very high salinity (more than 35,000 mg/L), is represented by two samples of about 3%. The majority of the studied groundwater samples, which mainly belong to the Miocene aquifer, are represented by Group B and C, while almost all the Quaternary samples belong to Group D. The hydrogen ion activity (pH) values reveal that groundwaters are neutral to slightly alkaline, with a mean pH value of 7.18. The water type shown in Table 1 is mainly characterized as a Cl–Na type, except two samples are of Cl-SO$_4$-Na type, indicating advanced evolutionary stages of groundwater.
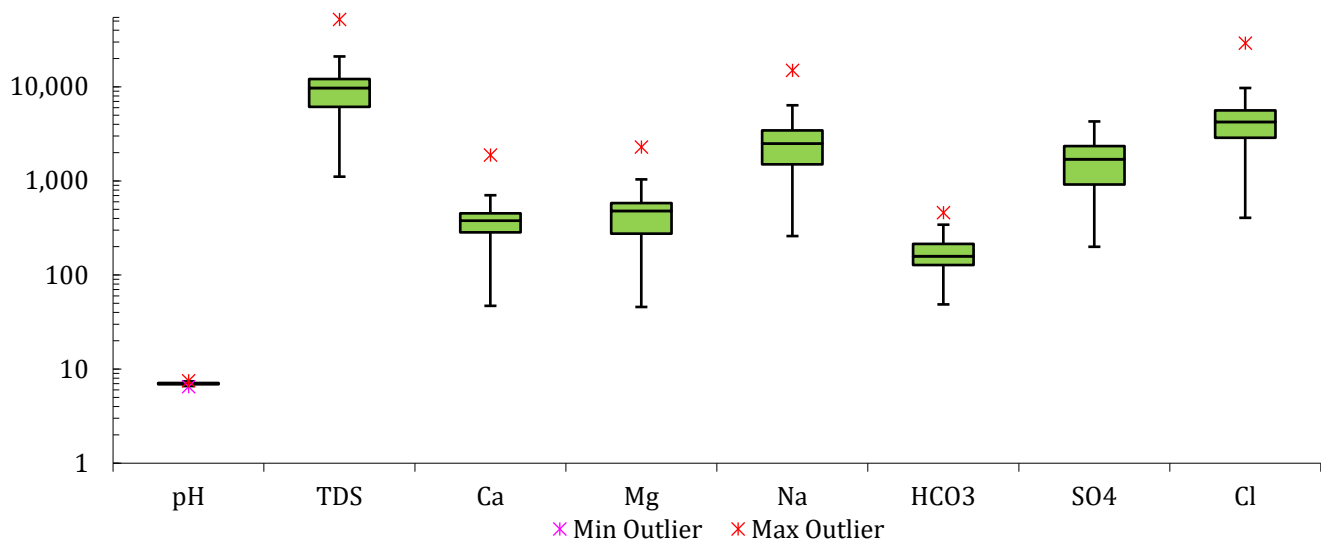
Figure 6. Box plot showing the distribution of the major cations and anions for the studied groundwater samples.

Table 1. Chemical and isotopic data of the sampled wells.

Aquifer	Well	EC (µs/cm)	pH	TDS mg/L	Water Level	Water Type	Cations (mg/L)				Anions (mg/L)				SiO$_2$ mg/L	Br mg/L	δ^{18}O‰	δD‰
							Ca	Mg	Na	K	CO$_3$	HCO$_3$	SO$_4$	Cl				
Quaternary	1	95,400	6.8	51,975	−2	Na-Cl	1886.79	2292.45	15,000	35	18	85.4	3500	29,200.00	20.33	29.50	0.26	1.40
	2	25,380	17	13,589	0.7	Na-Cl	603.77	550.19	3700	67	6	115.9	2000	6603.77	12.98	6.60	−3.82	−21.80
	3	12,420	7.1	5315	4.7	Na-Cl	226.42	412.64	1100	60	6	359.9	500	2830.19	17.11	3.66	−4.39	−19.50
	4	21,820	6.9	11,178	−1	Na-Cl	127.7	239.8	3500	87	12	286.7	3200	3867.92	13.40	7.55	−	−
	5	28,450	7	16,854	0	Na-Cl	371.3	412.6	5000	90	12	128.1	4300	6603.77	19.80	9.45	−	−
6	30,600	7	17,420	−2.15	Na-Cl	220.7	339.0	5500	200	21	128.1	4000	7075.47	11.32	10.70	−	−		
Miocene	**7**	2711	7.3	1217	−2	Na-Cl	75.47	74.50	260	10	6	237.9	200	471.70	33.44	0.63	−6.38	−33.25
	8	10,920	7.1	5306	−4.75	Na-Cl	207.55	171.93	1350	148	0	140.3	1330	2028.30	33.74	2.77	−5.34	−31.20
	9	6750	7.3	3696	3.5	Na-Cl	188.68	91.70	980	22	12	256.2	1000	1273.05	42.36	2.25	−5.56	−28.70
	10	5170	7.4	3013	3.5	Na-Cl	113.21	126.08	740	43	6	134.2	880	1037.30	19.77	1.63	−	−
	11	68,500	6.7	37,548	−1	Na-Cl	1886.79	1833.96	10,000	24	24	158.6	2900	20,800.00	13.94	22.40	−	−
	12	30,400	6.9	16,249	−5.3	Na-Cl	377.36	550.19	5000	100	6	48.8	1700	8490.57	4.97	8.52	0.62	5.10
	13	8670	7.2	5148	−2	Na-Cl	230.00	320.00	1050	40	6	219.6	1600	1792.45	14.30	2.41	−5.17	−28.36
	14	21,290	7	10,006	−4	Na-Cl	374.40	581.26	2600	77	31.2	126.88	700	5578.70	28.20	1.68	−	−
	15	23,250	7	12,042	0.75	Na-Cl	264.15	550.19	3300	82	9	140.3	2200	5566.04	15.51	6.63	−4.62	−27.40
	16	29,340	7	14,509	2	Na-Cl	452.83	550.19	4000	110	9	195.2	2120	7169.81	25.85	10.20	−	−
	17	25,880	7	14,131	−4	Na-Cl	377.36	596.04	3700	91	30	103.7	3200	6084.91	18.15	8.69	−4.19	−25.50
	18	31,300	6.9	14,585	2	Na-Cl	450.00	800.00	3600	106	6	146.4	2050	7500.00	14.04	8.91	−	−
	19	9800	7.1	55.80	−2.3	Na-Cl	301.89	183.40	1500	33	18	158.6	540	2924.53	23.06	3.22	−6.30	−35.30
	20	4590	7.4	2126	−23	Na-Cl	108.16	111.20	500	29	23.4	261.69	220	1003.19	13.23	3.24	−	−
	21	4460	7.4	2044	−2.3	Na-Cl	47.17	85.97	560	26	6	225.7	440	766.51	18.04	1.33	−6.65	−33.61
	22	2388	7.5	1395	0.4	Na-Cl	96.00	75.00	280	14	6	195.2	390	436.32	16.16	0.72	−4.31	−24.60
	23	31,400	6.8	16,793	−	Na-Cl	452.83	916.98	4200	67	18	128.1	3150	7924.53	22.81	9.37	−	−
	24	16,720	7.3	9389	1.5	Na-Cl	452.83	275.09	2600	50	12	146.4	1020	4905.66	29.57	5.28	−	−
	25	15,180	7.1	8553	1.25	Na-Cl	452.83	366.79	2000	46	18	91.5	1850	3773.58	14.40	4.64	−	−
	26	14,730	7.1	7836	2	Na-Cl	377.36	275.09	2150	38	12	115.9	680	4245.28	37.34	4.41	−	−
	27	16,630	7	8999	0.5	Na-Cl	603.77	320.94	2200	35	18	158.6	2440	3301.89	25.72	3.60	−	−
	28	13,170	7.1	6870	1	Na-Cl	452.83	275.09	1600	35	18	140.3	1400	3018.87	17.22	3.83	−4.62	−27.00
	29	20,410	7	10,436	−5	Na-Cl	332.80	833.98	2300	53	7.8	222.04	2100	4697.86	38.60	5.26	−4.28	−24.30
	30	20,870	7	10,582	3	Na-Cl	624.00	505.44	2500	51	7.8	459.94	2260	4404.24	38.71	5.86	−	−
	31	28,400	6.8	14,015	0.5	Na-Cl	665.60	808.70	3400	61	7.8	237.9	2200	6753.17	23.04	8.00	−4.19	−24.50
	32	19,310	6.8	11,140	−4	Na-Cl	374.40	581.26	2600	57	15.6	166.53	3220	4208.50	38.79	5.06	−	−
	33	19,540	6.6	9470	8	Na-Cl	332.80	505.44	2300	61	7.8	222.04	1650	4502.11	17.37	5.55	−	−
	34	17,820	6.9	9722	0.8	Na-Cl	377.36	366.79	2700	30	0	170.8	2200	3962.26	15.15	4.92	−	−
	35	17,030	6.9	10,565	−0.5	Na-Cl	301.89	504.34	2800	60	12	427	2900	3773.58	16.39	4.56	−	−
	36	10,740	7.1	5879	−3	Na-SO4	264.15	298.02	1300	37	12	176.9	2700	1179.25	13.88	3.05	−4.95	−25.50
	37	26,060	6.9	14,136	5.2	Na-Cl	540.80	808.70	3500	74	7.8	182.39	2850	6263.81	21.36	−	−4.38	−23.40
	38	18,740	7.1	10,445	4	Na-Cl	332.80	606.53	2600	33	7.8	214.11	2060	4697.86	20.30	4.82	−4.60	−26.20
	39	13,170	7	8144	3.1	Na-Cl	478.40	694.98	1470	54	15.6	111.02	1950	3425.52	27.39	5.88	−	−
	40	11,940	7.1	6569	4	Na-Cl	291.20	454.90	1500	33	7.8	214.11	750	3425.52	18.21	3.82	−	−
	41	15,550	7.1	7507	2	Na-Cl	395.20	518.08	1700	22	7.8	142.74	780	4012.75	14.26	4.22	−5.17	−31.00
	42	12,350	7.1	6396	2	Na-Cl	452.83	412.64	1300	33	6	122	1300	2830.19	15.00	3.45	−5.31	−32.20
	43	19,980	7.1	9958	−3	Na-Cl	374.40	505.44	2500	31	7.8	150.67	2060	4404.24	14.60	5.10	−1.42	−9.20
	44	20,150	7	12,520	2	Na-Cl	452.83	458.49	3400	62	0	103.7	3000	5094.34	13.02	5.50	−	−
	45	1872	7.1	1113	1	Na-Cl	60.38	45.85	270	7	6	115.9	260	405.66	10.52	0.75	−	−
	46	11,460	7	6884	9	Na-Cl	301.89	137.55	2000	35	6	146.4	1500	2830.19	13.02	3.27	−	−
	47	19,580	6.9	8197	5.4	Na-Cl	224.0	231.7	2600	61	12	91.5	400	4622.64	13.00	4.49	−4.57	−23.30

Table 1. *Cont.*

Aquifer	Well	EC (µs/cm)	pH	TDS mg/L	Water Level	Water Type	Cations (mg/L)				Anions (mg/L)				SiO₂ mg/L	Br mg/L	δ¹⁸O‰	δD‰
							Ca	Mg	Na	K	CO₃	HCO₃	SO₄	Cl				
	48	15,070	6.5	6905	4.8	Na-Cl	206.2	212.5	2000	55	6	158.6	950	3396.23	15.58	4.09	–	–
	49	20,850	6.9	11,705	5	Na-Cl	247.3	319.5	3600	61	6	131.15	2500	4905.66	14.31	6.26	–	–
	50	20,850	6.9	11,160	5	Na-Cl	240.4	331.2	3300	70	12	91.5	1500	5660.38	13.42	4.47	–	–
	51	25,210	6.8	14,890	−1	Na-Cl	452.83	687.74	3900	50	6	122	3600	6132.08	19.29	6.94	–	–
	52	23,230	6.9	10,649	0	Na-Cl	377.36	504.34	2900	75	6	183	1600	5094.34	18.28	6.86	–	–
	53	22,520	6.7	10,617	1	Na-Cl	528.30	458.49	2800	51	0	158.6	1700	5000.00	13.18	6.21	−4.35	−22.10
	54	20,220	6.9	12,178	7	Na-Cl	528.30	412.64	3500	36	0	115.9	1700	5943.40	14.08	5.41	–	–
	55	11,430	7.2	6564	1	Na-Cl	250.1	157.0	1900	50	15	146.4	1100	3018.87	14.05	3.06	–	–
	56	15,060	6.9	5631	4	Na-Cl	231.4	226.9	1500	60	6	210.45	200	3301.89	16.08	4.68	–	–
	57	8790	7.1	5319	3.8	Na-Cl-SO4	106.1	145.6	1500	42	18	213.5	1750	1650.94	12.90	2.63	–	–
	58	8240	7.1	4148	1	Na-Cl	126.0	111.7	1200	37	6	237.9	850	1698.11	16.26	2.95	–	–
Rain	59	120	8.73	74	–	Na-HCO3	8.00	3.50	15.1	2	2.6	47.45	13	6.40	0.00	0.45	−3.85	−13.98
Sea	60	59,300	7.71	36,226	–	Na-Cl	518.00	1441.00	10,210	371	24	148	3129	20,459.00	0.62	298.00	1.34	9.58

(−) not measured.

5.2. Groundwater Salinization and Mixing Processes

Different geochemical mechanisms, including rock–water interaction, evaporation, and precipitation, were identified when water samples were plotted on Gibbs diagrams (Figure 7). It is clearly shown on these diagrams that the water chemistry of almost all the Quaternary and Miocene groundwater samples is mainly controlled by evaporation-precipitation processes and seawater intrusion, plotted in the upper right corner of the diagram. It is also apparent that most of the samples with Na/(Na + Ca) or Cl/(Cl + HCO$_3$) ratios greater than 0.6 and TDS values greater than 5000 mg/L were mainly affected by saline water mixing or evaporation. This plot showed also that few samples were located in the rock dominance region, indicating that rock–water interaction has little impact on groundwater chemistry.
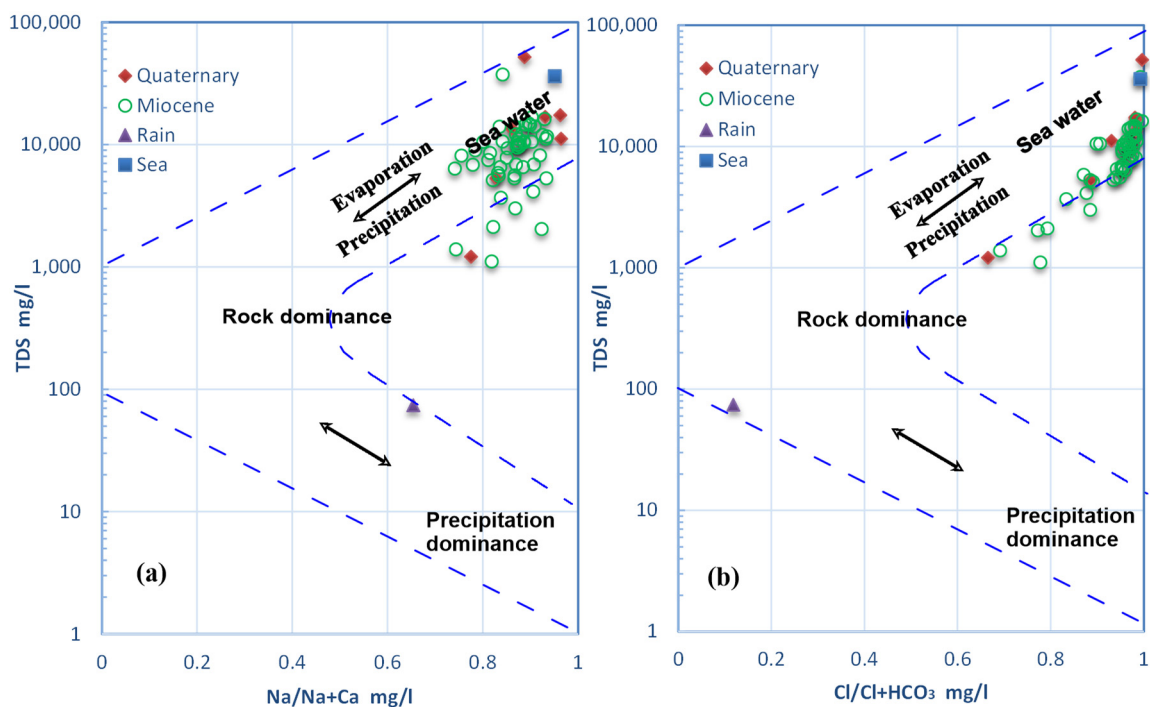
Figure 7. Gibbs diagrams showing TDS versus (**a**) Na/(Na + Ca) and (**b**) Cl/(Cl + HCO$_3$).

Groundwater samples were plotted in the Hydrochemical Facies Evolution Diagram (HFE-D); seawater and freshwater were connected through a mixing line (Figure 8). It is shown that the dominant water facies type is Na-Cl, where almost all samples were plotted in subdivision 4, and only two samples are of Mix/Na-Cl, located in subdivision 8. This means that Na ions exceed 50% of the total percent of cations as is also the case with respect to Cl ions. Samples can be divided into two groups. The first group is located below and to the right of the seawater/freshwater mixing line, indicating seawater/saltwater intrusion. The other group is situated down to the left of the line. While it still has the same facies, it is somewhat affected by recharge from fresh water. This diagram also indicates that a group of samples were subjected to direct cation exchange, with Na ions being released to the solution, while other samples were affected by an inverse cation exchange reaction. Delineation of the salinization processes in the study area will be more clearly elucidated in the following sections.
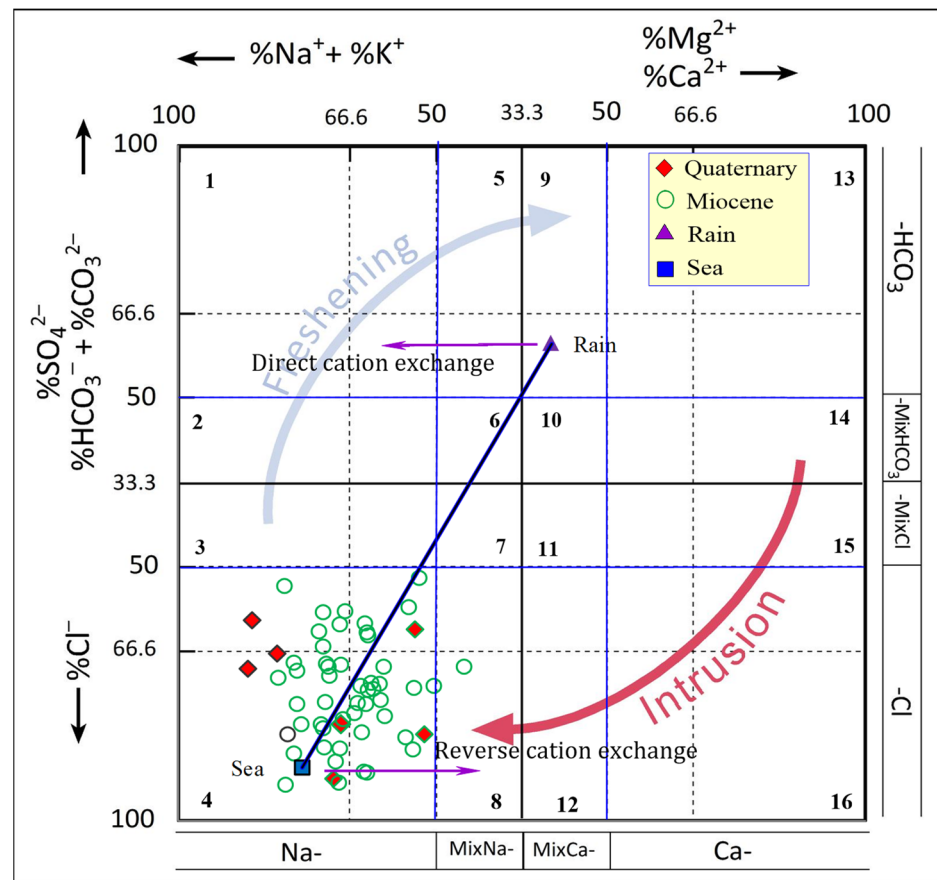
Figure 8. Hydrochemical facies evaluation diagram (HEF-D).

5.2.1. Ion Ratios and Correlation Coefficients

Ionic chemical ratios are useful for the identification of different hydrochemical processes affecting water quality as well as the impact of seawater intrusion on groundwater chemistry [72,73]. The ion ratios selected are summarized in Table 2.

Table 2. Ranges and average values of some ratios of the studied groundwater samples.

Ratio	Na/Cl	Mg/Ca	SO$_4$/Cl	Br/Cl
Quaternary aquifer				
Range	0.60–1.4	1.5–3.1	0.09–0.61	0.0044–0.0087
Average	1.00	2.33	0.33	0.0061
Miocene aquifer				
Range	0.65–1.7	0.75–4.13	0.04–1.69	0.0013–0.0143
Average	0.92	1.95	0.36	0.0058
Rain	3.64	0.72	1.5	0.0312
Sea	0.77	4.59	0.11	0.0065

The Na/Cl ratio is less than unity in the majority of the Miocene samples and in half of the Quaternary samples, while the rest of the samples showed values greater than unity. The relationship between Cl and Na/Cl (Figure 9A) showed that many samples plot on the 1:1 line, indicating the role of halite dissolution as a major process contributing to groundwater salinization [68]. A few samples showed slight increases in sodium relative to chloride, reflecting the effect of recharge from rainwater and/or ion exchange. The majority of samples plot slightly below that line, with a higher chloride content compared to sodium, indicating the probability of seawater intrusion.
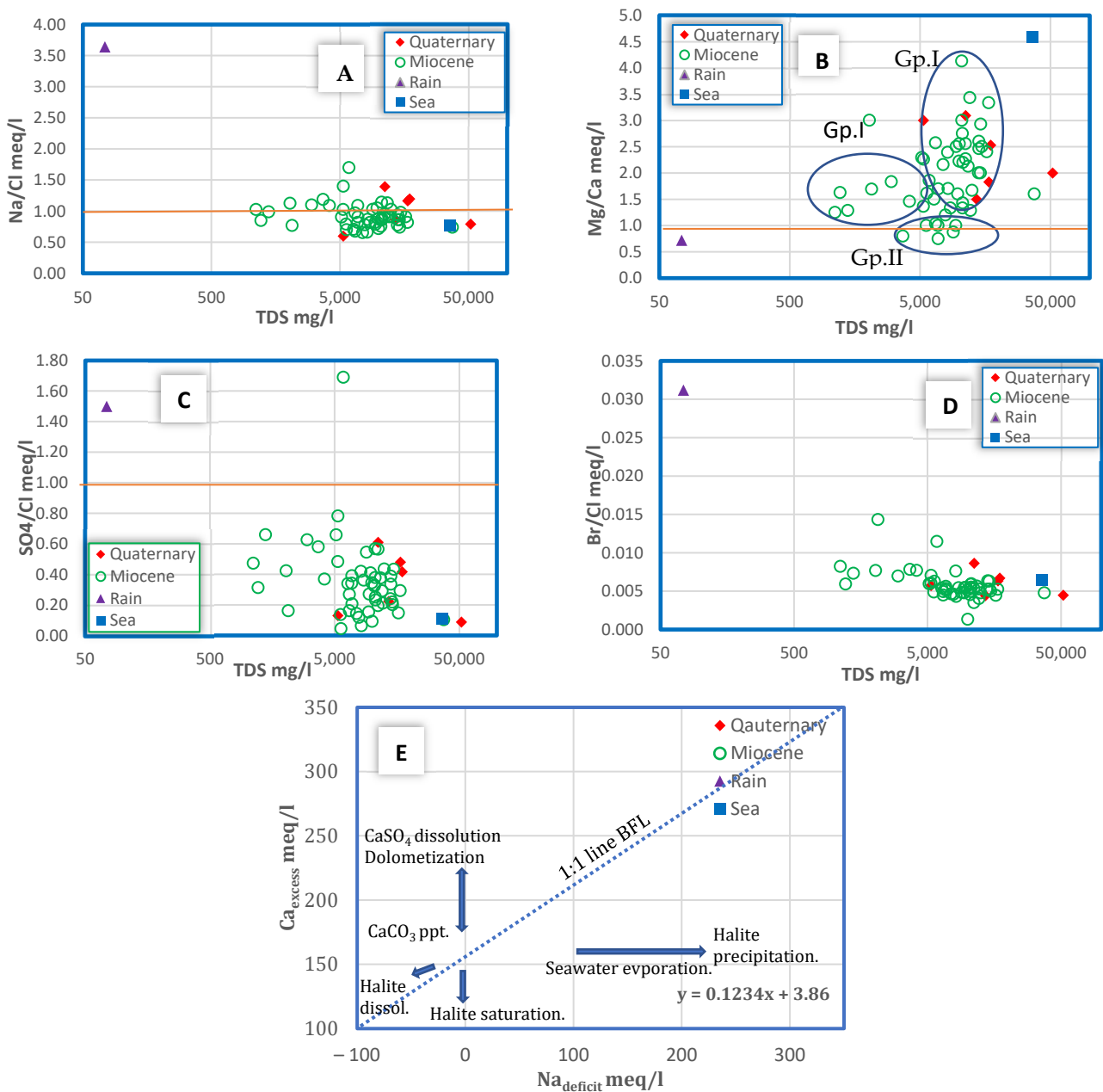
Figure 9. (**A**–**D**) Bivariate plots of some ion ratios vs. TDS; (**E**) $Na_{deficit}$ meq/L vs. Ca_{excess} meq/L plot.

The Mg/Ca ratio is used to interpret the impact of the aquifer matrix dominated by carbonate rocks as well as the effect of seawater on groundwater; it tends to be 1 in freshwater and approaches 5 in seawater [74,75]. In Figure 9B, there are three groups. The first is a group with slightly lower salinity (less than or equal 5000 mg/L) and a higher value of Mg/Ca, reflecting cation exchange and recharge from freshwater. The second group, which represents the majority of samples, has higher values of TDS as well as Mg/Ca. This group is mainly affected by marine rock–water interaction and seawater intrusion processes. The third group, with lower Mg/Ca and relatively higher Cl content, indicates a long residence time in carbonate rocks and recharge from fresh water. The SO_4/Cl ratio is considered as evidence of the influence of marine deposits as well as seawater on groundwater, with values below unity in almost all samples (Figure 9C). As Br and Cl are relatively conservative in hydrological systems, the Br/Cl ratio is used to distinguish whether groundwater salinity is of marine or non-marine origins [76]. As shown in both Table 2 and Figure 9D, the Br/Cl ratios of most of the studied groundwater samples are

within the normal seawater range (0.0040–0.0070) as salinity increases, with a mean value of about 0.006, indicating that the salinization of these groundwaters resulted from dissolution of marine sediments and mixing with seawater.

The slight decrease of the Br/Cl ratio with higher salinity is likely due to interaction with rocks rich in evaporites. On the other hand, samples with relatively low salinity but with a higher Br/Cl ratio suggest the impact of anthropogenic activities on groundwaters [77]. This could be explained as a result of the impact of the on-site wastewater disposal on groundwater, as some residents resort to using abandoned wells for sewage in the area under consideration. The relationship between $Na_{deficit}$ and Ca_{excess} in basinal fluids is presented according to Davisson et al. and Davisson and Criss [78,79] using two parameters:

$$Ca_{excess} = 2[Ca_{meas} - (Ca/Cl)_{SW} \times Cl_{meas}]/40.08 \qquad (6)$$

$$Na_{deficit} = [(Na/Cl)_{SW} \times Cl_{meas} - Na_{meas}]/22.99 \qquad (7)$$

A straight $Na_{deficit}$ Ca_{excess} regression line with a 1:1 slope, known as the Basinal Fluid Line (BFL; [79]), is plotted for the majority of basinal brines in the world, showing water–rock interaction with a net cation exchange ratio of 1 Ca for 2 Na (Figure 9E). This diagram shows the various chemical processes that the groundwater has undergone. Such processes include (i) halite dissolution with a trend that extends from the origin (0,0 point) towards the negative quadrant of the plot; (ii) cation exchange for the samples plotted on the 1:1 line; and (iii) seawater evaporation after calcite precipitation following a nearly horizontal trend, with a slope of 0.123. Further evaporation with a decrease in Na concentration will result in the precipitation of halite, as indicated by the samples plotted slightly above the seawater sample.

5.2.2. Saturation Indices

PHREEQC version 3 [80] calculated saturation indices by comparing the chemical activities of the mineral's dissolved ions (ion activity product, IAP) with their solubility product (Ksp). The saturation indices (SI) for selected minerals, including anhydrite, calcite, dolomite, gypsum, and halite, were calculated to confirm the precipitation and dissolution of these minerals. They have negative values when the minerals tend to dissolve, positive values when the minerals tend to precipitate, and zero values when the water and minerals are in chemical equilibrium. The minerals chosen were based on the major ions encountered in the study area's groundwater. Figure 10 depicts a bivariate diagram of SI values for anhydrite, calcite, dolomite, gypsum, and halite against the chloride concentration of the studied groundwater samples. It shows a positive correlation between Cl concentration and SI values. The plot shows that groundwater samples are undersaturated with respect to calcite and dolomite, with 78% and 40%, respectively. All samples exhibited undersaturation in relation to anhydrite, gypsum, and halite. The positive values of the calculated SI with respect to calcite and dolomite were about 22% and 60%, respectively, and the negative values of SI for all groundwater samples with respect to anhydrite and gypsum suggest that these salts have a major role in the enrichment of groundwater with calcium and sulphate.

This figure also shows that there are three groups; group I, with intermediate Cl concentration; group II, with a higher Cl concentration; group III, with much higher Cl concentration, which reached or exceeded the seawater values (as in samples 1 and 11). Group I is plotted near the midway between the recharge water (rainwater) and the seawater, indicating the leaching and dissolution of marine sediments. gp II is closely plotted next to seawater, reflecting mixing with seawater as a result of groundwater overexploitation and scarcity of recharge from precipitation. Finally, gp III includes seawater and samples subjected to the dissolution of salt marches rich in evaporates.
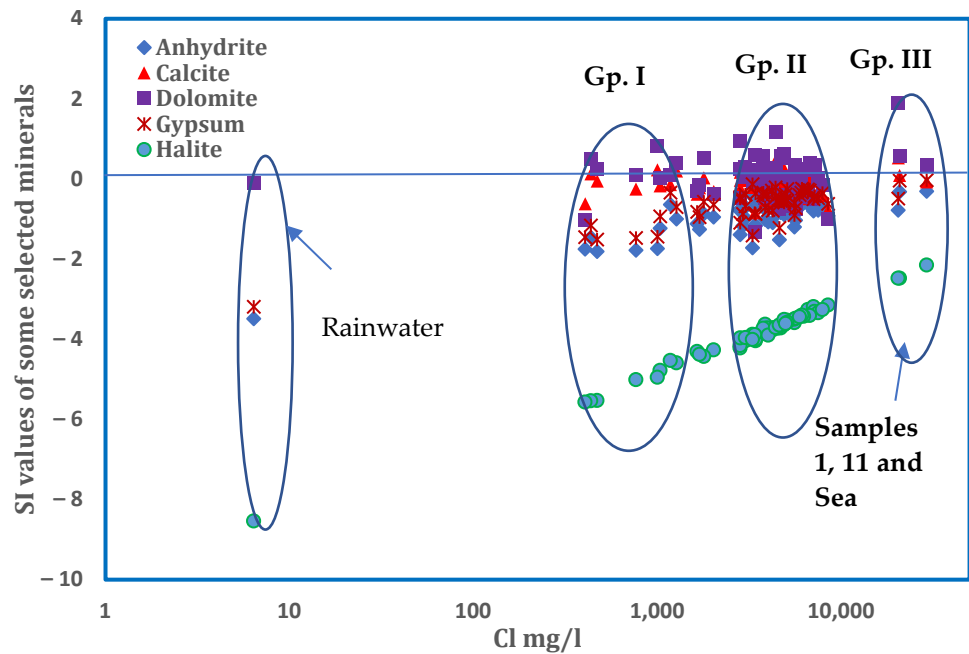
Figure 10. Relationship between Cl in mg/L and saturation indices for selected minerals.

5.2.3. Stable Isotopes

Environmental stable isotopes such as Oxygen-18 and deuterium are good indicators for tracing the recharge sources and the origin of groundwaters, as they do not participate in geochemical reactions except in geothermal systems. Isotope exchange usually takes place within geothermal water systems only at elevated temperatures (>250 °C) [81]. The stable isotopic compositions of the collected water samples are listed in Table 1. The isotopic content of the Quaternary samples ranged from −4.39 to 0.26‰ (Avg. −2.65) for $\delta^{18}O$; from −21.80‰ to 1.40‰ (Avg. −13.30) for deuterium. For the Middle Miocene aquifer, $\delta^{18}O$ values ranged from −6.65‰ to 2.60‰ (Avg. −4.56‰) and ranged between −35.30‰ and 5.10‰ (Avg. −25.31‰) for deuterium. The plot of $\delta^{18}O$ versus δD for the studied groundwater samples is shown in Figure 11a. The global meteoric water line GMWL [82], described by the equation $\delta D = 8 \, \delta^{18}O +10‰$, and the corresponding line for Mediterranean precipitation MMWL [83], described by the equation $\delta D = 8 \, \delta^{18}O +22‰$, are shown as references. It is shown that most of the groundwater samples plot very close to the Mediterranean meteoric water line (MMWL), indicating recharge from Mediterranean precipitation. According to Olive [84], if there is mixing between the coastal groundwater and seawater, the water samples will plot on a mixing line (ML) with the equation $\delta D = 5.5 \, \delta^{18}O + 0.0‰$.
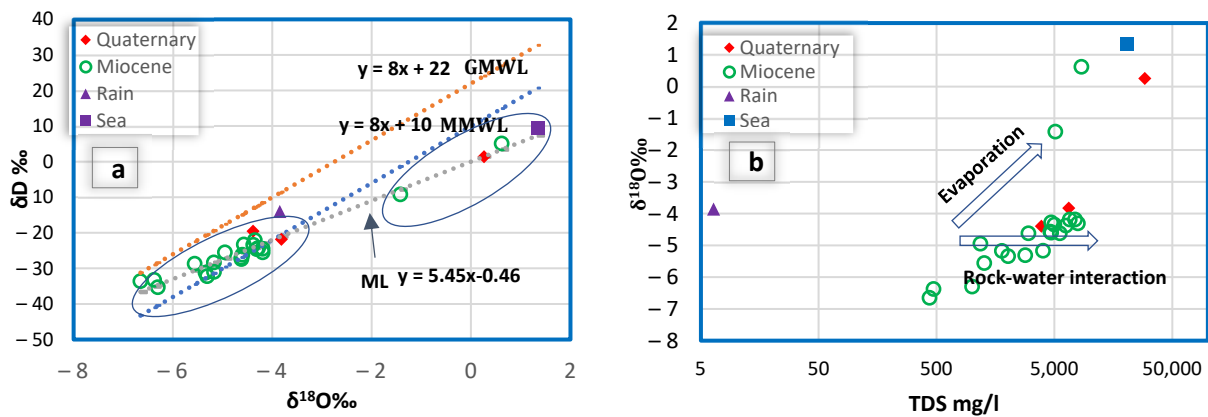
Figure 11. (**a**) $\delta^{18}O‰$ vs. δD; (**b**) TDS vs. $\delta^{18}O‰$.

The distinctive trend expressing the mixing of groundwater with more evaporated water (seawater) is represented by the mixing line (ML) (Figure 11a). This line is described by the equation $\delta D = 5.45\ \delta^{18}O - 0.46‰$, which is similar to the equation proposed by Olive [84]. It is shown that almost all groundwater samples were situated on that line and can be divided into two groups. First is the group with depleted isotope values, indicating that it is of meteoric origin. The other group, with more enriched in $\delta^{18}O$ and δD values, is assumed to have been exposed to mixing with seawater and/or the fractionation during evaporation from the shallow groundwater aquifers. The purpose of using the relationship between TDS and $\delta^{18}O$ is to distinguish between samples that were exposed to evaporation from those that were subjected to leaching and dissolution. It is noted from Figure 11b that the majority of groundwater samples, characterized by relatively high salinity, were mainly subjected to leaching and dissolution of marine deposits. The remaining group of samples, of much higher salinity, was affected by dissolution of evaporites (such as halite, anhydrite, and/or gypsum).

5.2.4. Principle Component Analysis (PCA)

Principle component analysis was applied to identify relationships between different variables, including pH, TDS, Ca, Mg, Na, K, CO_3, HCO_3, SO_4, Cl, $\delta^{18}O$, δD, SMI, and GQI_{SWI}, and to extract different factors affecting groundwater quality (Tables 3 and 4). The correlations established between the selected parameters (Table 3) show that there is a strong correlation between TDS and the concentrations of the variables Ca, Mg, Na, SO_4, Cl, Br, $\delta^{18}O$, δD, and SMI ($r^2 \geq 0.7$), indicating that such variables are enriched due to mineralization processes. The high correlation between TDS and both $\delta^{18}O$ and δD is evidence of the exposure of groundwater to evapoconcentration processes. Although the aquifer matrix is dominated by carbonate rocks, bicarbonates are not correlated with calcium, indicating a source other than calcite dissolution. Meanwhile, calcium is well correlated with SO_4 ($r^2 \geq 0.53$), suggesting gypsum dissolution. The factor loadings of the correlation matrix were defined based on eigenvalues that exceeded unity [65].

Table 3. Correlation matrix for selected parameters.

| Variable	pH	TDS	Ca	Mg	Na	K	CO_3	HCO_3	SO_4	Cl	Br	SiO_2	$\delta^{18}O$	δD	SMI	GQI_{SWI}
pH	1.00															
TDS	0.00	1.00														
Ca	0.07	0.94	1.00													
Mg	−0.04	0.95	0.93	1.00												
Na	0.01	1.00	0.92	0.92	1.00											
K	0.04	0.14	−0.03	0.06	0.15	1.00										
CO_3	−0.10	0.23	0.19	0.22	0.24	−0.32	1.00									
HCO_3	−0.14	−0.45	−0.45	−0.38	−0.46	−0.32	0.17	1.00								
SO_4	−0.01	0.65	0.53	0.63	0.63	0.33	0.05	−0.19	1.00							
Cl	0.00	0.99	0.94	0.95	0.99	0.10	0.25	−0.47	0.57	1.00						
Br	−0.03	0.99	0.93	0.94	0.99	0.13	0.30	−0.39	0.63	0.99	1.00					
SiO_2	−0.12	−0.12	−0.08	−0.02	−0.14	−0.10	−0.01	0.43	−0.12	−0.11	−0.12	1.00				
$\delta^{18}O$	0.00	0.77	0.66	0.66	0.79	0.32	−0.04	−0.63	0.60	0.75	0.73	−0.32	1.00			
δD	−0.01	0.74	0.61	0.60	0.77	0.28	−0.03	−0.56	0.58	0.72	0.70	−0.32	0.98	1.00		
SMI	−0.01	1.00	0.94	0.95	1.00	0.12	0.24	−0.48	0.60	1.00	0.99	−0.12	0.77	0.74	1.00	
GQI_{SWI}	−0.03	−0.97	−0.87	−0.90	−0.98	−0.29	−0.19	0.53	−0.64	−0.96	−0.96	0.18	−0.82	−0.79	−0.97	1.00

Three factors, with a total cumulative variance of about 80%, were assigned to explain changes made to groundwater (Table 4). Such factors are presented in two biplots to clearly illustrate their correlation with the different variables (Figure 12). The first factor f_1 (Figure 12a), with about 60% of the total variance, has high positive loading with the variables TDS, Ca, Mg, Na, Cl, and SO_4, $\delta^{18}O$, δD, and SMI and also has strong negative loading with GQI_{SWI}. This strong correlation can be interpreted as a result of different mechanisms. Among these are (1) rock–water interaction, (2) cation exchange, and (3) seawater intrusion. The second factor f_2 (Figure 12a) accounts for 11% of the total variance, which has a moderate positive loading with SO_4, $\delta^{18}O$, and δD as well as high positive loading with K. This suggests evaporation and dissolution of evaporites occurred in the shallower aquifers. The third factor f_3 (Figure 12b), with about 9% of the total variance, is

positively correlated with HCO_3 and SiO_2. This factor represents the freshening and the impact of the weathered silicate minerals on groundwater.

Table 4. Factor analysis from rotated component matrix.

Variable	Factor 1	Factor 2	Factor 3
pH	−0.059	−0.076	−0.524
TDS	**0.995**	−0.016	−0.056
Ca	**0.926**	−0.15	−0.096
Mg	**0.954**	−0.082	0.051
Na	**0.988**	−0.007	−0.084
K	0.143	**0.822**	0.002
CO_3	0.253	**−0.713**	0.061
HCO_3	−0.428	−0.339	**0.626**
SO_4	**0.676**	0.318	0.111
Cl	**0.985**	−0.064	−0.075
Br	**0.987**	−0.068	−0.025
SiO_2	−0.078	−0.07	**0.806**
$\delta^{18}O$	**0.787**	**0.371**	−0.313
δD	**0.756**	**0.353**	−0.299
SMI	**0.99**	−0.035	−0.079
GQI_{SWI}	**−0.968**	−0.11	0.13
Eigenvalue	9.74	1.93	1.15
Total variance %	60%	11%	9%
Cumulative %	60%	70%	80%

(**a**)

(**b**)
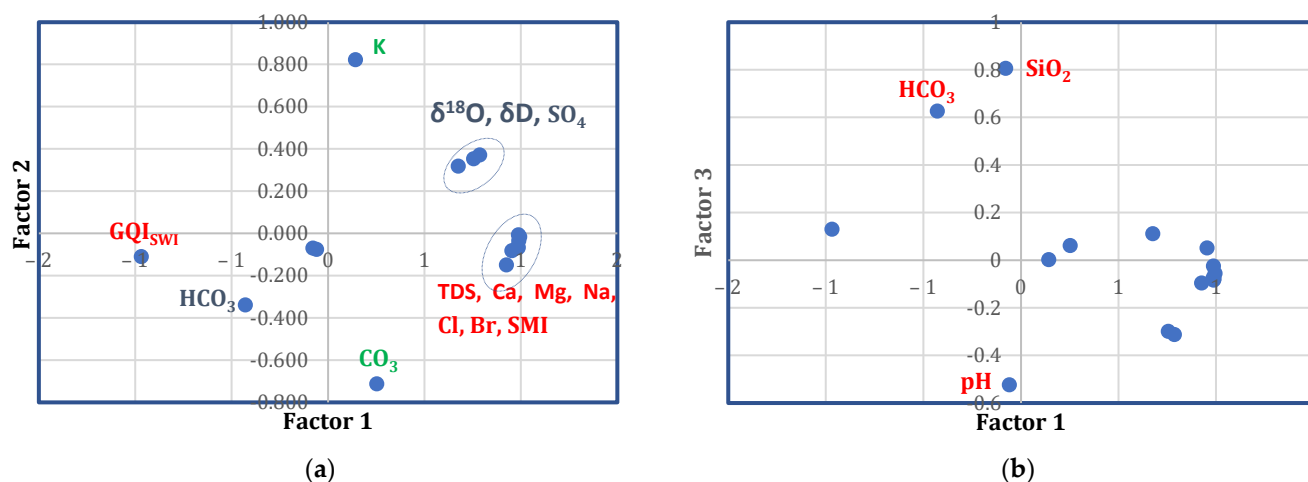
Figure 12. (**a**) Variable representation with F1 and F2 (high loading with F1 in red; high loading with F2 in green; medium loading with both in grey); (**b**) variable representation with F1 and F3 (high loading with F3 in red).

5.2.5. Groundwater Quality Index (GQI_{SWI}) and Seawater Mixing Index (SMI)

The GQI_{SWI} varies from 0 to 100, and the values above 75 can be considered as freshwater, while when below 50, groundwater is classified as saline or seawater. If groundwater has GQI_{SWI} values ranging between 50 and 75, it will be deemed as mixed water. The calculated GQI_{SWI} values presented in Table 5 reveal that the study area is dominated by saline and mixed groundwater (55 and 41%, respectively), followed by saltwater (4%).

Table 5. Classification of groundwater based on GQI$_{SWI}$ and SMI.

Classification According to GQI$_{SWI}$	GQI$_{SWI}$		Classification According to SMI	SMI	
	Range	Sample%		Range	Sample%
Freshwater	75–100	0%	Freshwater	less than 1	90%
Mixed groundwater	50–75	41%	Moderately polluted	1–6	10%
Saline groundwater	10–50	55%	Seriously polluted	6–10	0%
Saltwater	0–10	4%	Seawater	10–150	0%

The SMI was calculated when the cumulative probability percentages of Cl, SO$_4$, Na, and Mg ions were plotted against their concentration in mg/L (Figure 13). The inflection points of each plot characterize the threshold values (T) of each ion that were substituted in Equation (5) to calculate the SMI values for each groundwater sample. If the SMI value was more than 1, the water may have been influenced by seawater mixing [69,70]. The results of the calculated SMI show that about 90% (52 samples) of the groundwater samples are of meteoric origin, and the remaining 10% (6 samples) are related to saline groundwater. This hypothesis is compatible with the results obtained from the ion ratios and stable isotopes analyses. It should be noted that the variation in SMI and GQI$_{SWI}$ calculated values is due to how each method characterizes groundwater. In other words, the SMI considers seawater as a pollutant, and its percentage in groundwater is calculated, so that if the index value exceeds unity, this indicates seawater intrusion. The GQI index, on the other hand, classifies groundwater based on its origin and takes into account the changes that occurred as a result of various geochemical processes, including intrusion of sea water.
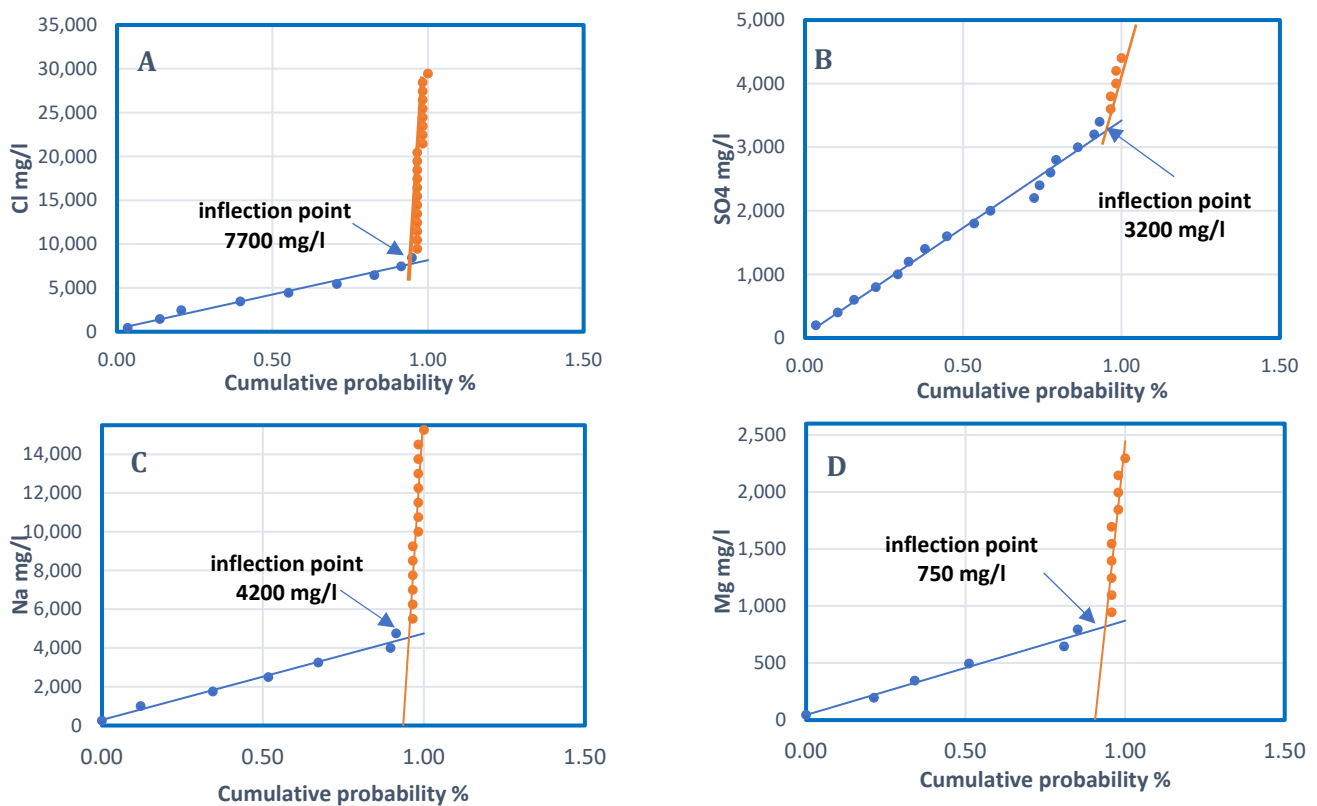
Figure 13. Threshold values (T) of (**A**) Cl, (**B**) SO$_4$, (**C**) Na, and (**D**) Mg in the studied groundwater samples. The intersection of the background concentration (highlighted in blue) and the trend line representing the anomalous concentrations (highlighted in orange) indicates the regional threshold of relevant element.

The spatial distribution of the groundwater quality index (GQI$_{SWI}$) as well as the seawater mixing index (SMI) were used as complementary tools to delineate the salinization zones in accordance with the extent to which groundwater was affected either by freshwater mixing with seawater or rock–water interaction. According to the spatial distribution maps for GQI$_{SWI}$ and SMI (Figure 14A,B), it was revealed that almost all the groundwater in the study area is mainly of meteoric origin, which in turn reaches a progressive evolutionary stage due to the interaction with marine sediments and mixing with salt water. Patches that have undergone saltwater intrusion were identified in some locations along the shoreline of the Mediterranean Sea. However, saline water was also identified in some other inland locations west of the study area, about 12.5 km away from the sea.
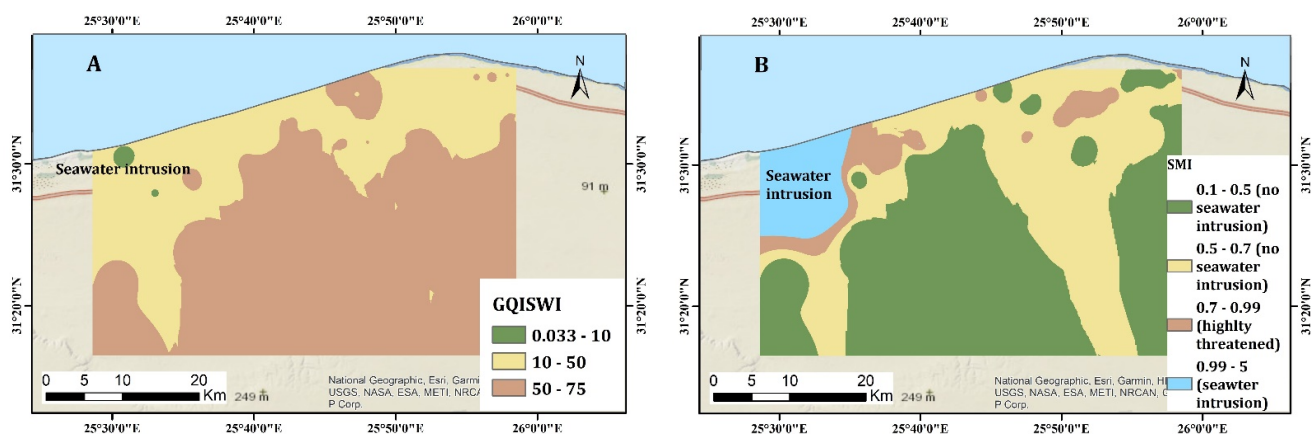
Figure 14. Iso-contour map of GQI$_{SWI}$ and SMI. Figures (**A**,**B**) indicated the areas, which are thought to be affected by seawater intrusion based on GQI$_{SWI}$, and SMI calculations, respectively.

6. Conclusions

This paper highlighted the different processes and mechanisms impacting groundwater salinization using multi-hydrochemical parameters and stable isotopes. The groundwater in the study area is classified as brackish, saline, and highly saline water. Different methods, including ion ratio relationships, isotope bivariate plots, evolution diagrams, and statistical analyses, were applied to recognize the main geochemical processes controlling the salinization processes. According to Gibbs classifications, groundwaters are dominated by evaporation followed by rock–water interaction. The HFE-D indicated mixing with saline water and the occurrence of both reverse and direct cation exchange. The correlation of the ion ratios Na/Cl, Mg/Ca, SO$_4$/Cl, and Br/Cl with TDS indicates the effect of marine sediments and seawater as well as the anthropogenic activities on some of the studied groundwater samples. Furthermore, the Na$_{deficit}$ and Ca$_{excess}$ bi-plot revealed different processes, including halite dissolution, cation exchange, and seawater evaporation after calcite precipitation. The δ^{18}O vs. δD and TDS vs. δ^{18}O relationships revealed that some samples were exposed to mixing with seawater and/or fractionation during the evaporation from shallow groundwater aquifers. The factors extracted by PCA suggest the aforementioned processes, in addition to the impact of freshening and silicate weathering on groundwater. The mixing with seawater was confirmed in some locations along the coastline and extended to about 12.5 km away from shore in the Bqabaq area. Additionally, statistical analyses as well as hydrogen and oxygen-18 stable isotope relationships identified the effect of recharge by rainwater in few locations. The findings from this study can be used to enhance our understanding of the different hydrogeochemical processes that led to the deterioration in the groundwater quality. Moreover, it sheds light on the locations that have experienced groundwater quality deterioration as well as other areas that are not or are little affected by seawater intrusion. This will enable the decision makers to take the necessary measures to use groundwater in those areas in a way that ensures its sustainability and does not lead to any further deterioration.

References

1. Gaaloul, N.; Pliakas, F.; Kallioras, A.; Schuth, C.; Marinos, P. Simulation of Seawater Intrusion in Coastal Aquifers: Forty Five'Years exploitation in an Eastern Coast Aquifer in NE Tunisia. *Open Hydrolgeol. J.* **2012**, *6*, 31–44. [CrossRef]
2. McInnis, D.; Silliman, S.E. Geoelectrical investigation of the freshwater–saltwater interface in coastal Benin, West Africa. In Proceedings of the American Geophysical Union, Fall Meeting, San Francisco, CA, USA, 13–17 December 2010.
3. Edmunds, W.M.; Milne, C.J. *Palaeowaters in Coastal Europe: Evolution of Groundwater since the Late Pleistocene*; Geological Society of London: London, UK, 2001.
4. De Montety, V.; Radakovitch, O.; Vallet-Coulomb, C.; Blavoux, B.; Hermitte, D.; Valles, V. Origin of groundwater salinity and hydrogeochemical processes in a confined coastal aquifer: Case of the Rhone delta (Southern France). *Appl. Geochem.* **2008**, *23*, 2337–2349. [CrossRef]
5. Somay, M.A.; Gemici, U. Assessment of the salinization process at the coastalarea with hydrogeochemical tools and geographical information systems (GIS): Selcuk Plain, Izmir, Turkey. *Water Air Soil Pollut.* **2009**, *201*, 55–74. [CrossRef]
6. Kim, Y.; Lee, K.S.; Koh, D.C.; Lee, D.H.; Lee, S.G.; Park, W.B.; Koh, G.W.; Woo, N.C. Hydrogeochemical and isotopic evidence of groundwater salinization in a coastal aquifer: A case study in Jeju volcanic island, Korea. *J. Hydrol.* **2003**, *270*, 282–294. [CrossRef]
7. Tijani, M.N. Evolution of saline waters and brines in the Benue-Trough. Nigeria. *Appl. Geochem.* **2004**, *19*, 1355–1365. [CrossRef]
8. Ghabayen, S.M.S.; McKee, M.; Kemblowski, M. Ionic and isotopic ratios for identification of salinity sources and missing data in the Gaza aquifer. *J. Hydrol.* **2006**, *318*, 360–373. [CrossRef]
9. Mirzavand, M.; Ghasemieh, H.; Sadatinejad, S.J.; Bagheri, R.; Clark, I.D. Saltwater intrusion vulnerability assessment using AHPGALDIT Model in Kashan plain aquifer as critical aquifer in a semi-arid region. *Desert* **2018**, *32*, 255–264.
10. Pérez-Martín, M.A.; Estrela, T.; Andreu, J.; Ferrer, J. Modeling water resources and river-aquifer interaction in the Júcar River Basin, Spain. *Water Resour. Manag.* **2014**, *28*, 4337–4358. [CrossRef]
11. Masciopinto, C. Simulation of coastal groundwater remediation: The case of Nardò fractured aquifer in Southern Italy. *Environ. Model. Softw.* **2006**, *21*, 85–97. [CrossRef]
12. Mjemah, I.C.; Van Camp, M.; Walraevens, K. Groundwater exploitation and hydraulic parameter estimation for a Quaternary aquifer in Dar-es-Salaam, Tanzania. *J. Afr. Earth Sci.* **2009**, *55*, 134–146. [CrossRef]
13. Van Camp, M.; Mtoni, Y.E.; Mjemah, I.C.; Bakundukize, C.; Walraevens, K. Investigating seawater intrusion due to groundwater pumping with schematic model simulations: The example of the Dar Es Salaam coastal aquifer in Tanzania. *J. Afr. Earth Sci.* **2014**, *96*, 71–78. [CrossRef]
14. Bear, J.; Cheng, A.; Sorek, S.; Ouazar, D.; Herrera, I. *Seawater Intrusion in Coastal Aquifers Concepts, Methods and Practices*; Springer: Berlin/Heidelberg, Germany, 1999.
15. Barlow, P.M.; Reichard, E.G. Saltwater intrusion in coastal regions of North America. *Hydrogeol. J.* **2010**, *18*, 247–260. [CrossRef]
16. Werner, A.D. A review of seawater intrusion and its management in Australia. *Hydrogeol. J.* **2010**, *18*, 281–285. [CrossRef]
17. Custodio, E. Coastal aquifers of Europe: An overview. *Hydrogeol. J.* **2010**, *18*, 269–280. [CrossRef]
18. Bocanegra, E.; Da Silva, G.C.; Custodio, E.; Manzano, M.; Montenegro, S. State of knowledge of coastal aquifer management in South America. *Hydrogeol. J.* **2010**, *18*, 261. [CrossRef]
19. Steyl, G.; Dennis, I. Review of coastal-area aquifers in Africa. *Hydrogeol. J.* **2010**, *18*, 217–225. [CrossRef]
20. UN—United Nations. *Water for People, Water for Life*; UN World Development Report (WWDR); UN: New York, NY, USA, 2003.
21. WHO—World Health Organization. *Guidelines for Drinking-Water Quality: First Addendum to Third Edition*; WHO: Geneva, Switzerland, 2006; Volume 1 Recommendations.
22. El Shamy, I. The Geology of Soil and Water Resources in El Daba'a Area. Master's Thesis, Faculty of Science, Cairo University, Giza, Egypt, 1968.
23. Selim, A.A. Geology of El-Salum Area. Ph.D. Thesis, Faculty of Science, Alexandria University, Alexandria, Egypt, 1969.
24. Rizk, Z.E. Geological and Hydrogeological Studies on the North Wetern Coast of Egypt. Master's Thesis, Faculty of Science, Menofia University, Shibin el Kom, Egypt, 1982. Unpublished.
25. Hammad, F.A. The Geology of Soils and Water Resources in the Area between Ras El Hekma and Ras El Rum (Western Mediterranean Littoral Zone, Egypt). Ph.D. Thesis, Faculty of Science, Cairo University, Giza, Egypt, 1972.

26. Misak, R. Geomorphology and Geology of the Area between El Daba'a and Ras El Hekma, Western Mediterranean Coastal Zone, Egypt. Master's Thesis, Ain Shamas University, Cairo, Egypt, 1974.
27. Mousa, B.M. Geomorphology and Subsurface Geology of the Area between El Alamein and Qattara Depression, Northern Western Desert, Egypt. Master's Thesis, Faculty of Science, Ain Shams University, Cairo, Egypt, 1976.
28. AbdelMogheeth, S. Sedimentology, Geochemistry and Evaluations of the Marmarica Limestone, Western Desert, Egypt. Ph.D. Thesis, Faculty of Science, Al Azhar University, Cairo, Egypt, 1968.
29. Atwa, S.M. Hydrology and Hydrogeochemistry of the Northwestern Coast of Egypt. Ph.D. Thesis, Faculty of Science, Alexandria University, Alexandria, Egypt, 1979.
30. Salem, A.A.; Mohamed, A.H. Hydrogeological studies of the groundwater aquifers in El Sallum depression, Northwestern coast, Egypt. *Sedimentol. Egypt.* **2011**, *19*, 97–112.
31. Aureli, A.; Ganoulis, J.; Margat, J. *Groundwater Resources in the Mediterranean Region: Importance, Uses and Sharing*; UNESCO International Hydrological Programme (IHP): Paris, France, 2008; pp. 96–105.
32. Hammad, F.A. The Geology of Water Supplies in Ras El Hekma Area, Western Mediterranean Coastal Zone, Egypt. Master's Thesis, Cairo University, Giza, Egypt, 1966.
33. Guo, X.; Feng, Q.; Liu, W.; Li, Z.; Wen, X.; Si, J.; Jia, B. Stable isotopic and geochemical identification of groundwater evolution and recharge sources in the arid Shule River Basin of Northwestern China. *Hydrol. Process.* **2015**, *29*, 4703–4718. [CrossRef]
34. Budiyanto, E.; Muzayanah; Prasetyo, K. Karst Groundwater Vulnerability and Risk to Pollution Hazard in the Eastern Part of Gunungsewu Karst Area. *IOP Conf. Ser. Earth Environ. Sci.* **2020**, *412*, 012020. [CrossRef]
35. Richter, B.C.; Kreitler, C.W. *Geochemical Techniques for Identifying Sources of Ground-Water Salinization*; CRC Press: Boca Raton, FL, USA, 1993.
36. Smith, A.J.; Turner, J.V. Density-dependent surface water-groundwater interaction and nutrient discharge in the Swan-Canning Estuary. *Hydrol. Process.* **2001**, *15*, 2595–2616. [CrossRef]
37. Simpson, M.J.; Clement, T.P. Improving the worthiness of the Henry problem as a benchmark for density-dependent groundwater flow models. *Water Resour. Res.* **2004**, *40*, W01504. [CrossRef]
38. Narayan, K.A.; Schleeberger, C.; Bristow, K.L. Modelling seawater intrusion in the Burdekin Delta Irrigation Area, North Queensland, Australia. *Agr. Water Manag.* **2007**, *89*, 217–228. [CrossRef]
39. Werner, A.D.; Simmons, C.T. Impact of sea-level rise on seawater intrusion in coastal aquifers. *Groundwater* **2009**, *47*, 197–204. [CrossRef] [PubMed]
40. Edmunds, W.M.; Walton, N.R.G. A geochemical and isotopic approach torecharge evaluation in semi-arid zones, past and present. In *Arid-Zone Hydrology, Investigations with Isotope Techniques*; International Atomic Energy Agency: Vienna, Austrian, 1980; pp. 47–68.
41. Simmers, I. Natural Groundwater Recharge Estimation in (Semi-)Arid Zones; Some State-of-the-art Observations. In *Sahel Forum on the State-of the-Art of Hydrology and Hydrogeology in the Arid and Semi-Arid Areas of Aji-Ica*; Stout, G.E., Demissie, M., Eds.; UNESCO: New York, NY, USA, 1990; pp. 373–386.
42. Edmunds, W.M.; Gaye, C.B. Estimating the spatial variability of groundwater recharge in the Sahel using chloride. *J. Hydrol.* **1994**, *156*, 47–59. [CrossRef]
43. Clark, I.D.; Fritz, P. *Environmental Isotopes in Hydrogeology*; Lewis Publishers: Boca Raton, FL, USA, 1997.
44. Mook, G.W. *Environmental Isotopes in the Hydrological Cycle*; IHP-V Technical Document in Hydrology No. 39 VI; UNESCO: Paris, France, 2001.
45. Vengosh, A. *Salinization and Saline Environments, Treatise on Geochemistry*, 2nd ed.; Elsevier Ltd.: Amsterdam, The Netherlands, 2013; 333p. [CrossRef]
46. Raslan, S.M. Geomorpholiogical and Hydrogeological Studies on Some Localities Along the Northwestern Coast of Egypt. Master's Thesis, Faculty of Science, Menoufia University, Shibin el Kom, Egypt, 1995; p. 172.
47. Khalil, M.M. Origin, Genesis, Formation and classification of Sidi Barrani Soils, Northwestern Coastal Zone. Master's Thesis, Faculty of Agriculture, Zagazig University, Cairo, Egypt, 2008.
48. El Shazly, M.M. Geology, Pedology and Hydrogeology of Mersa Matruh Area, Western Mediterranean Littoral, U.A.R. Ph.D. Thesis, Faculty of Science, Cairo University, Cairo, Egypt, 1964.
49. Ali, A.O.; Rashid, M.; El Naggar, S.; Abdul Al, A. Water harvesting options in the drylands at different spatial scales. *Land Use Water Resour. Res.* **2007**, *7*, 1–13.
50. El Sabri, M.A.; Salem, W.M. Management of groundwater resources in El Saloum depression, Western Desert, Egypt. *Ann. Geol. Surv. Egypt* **2016**, *XXXIII*, 193–210. Available online: https://www.researchgate.net/profile/Mohamed-El-Sabri/publication/333208963_Annalas_Geol_Surv_Egypt_V_XXXIII_2016_pp_197-213 (accessed on 3 November 2022).
51. Morad, N.; Masoud, M.; Abdel Moghith, S. Hydrologic factors controlling groundwater salinity in northwestern coastal zone. *Egypt. J. Earth Syst. Sci.* **2014**, *123*, 1567–1578. [CrossRef]
52. Yousif, M.; Oguchi, T.; Anazawa, K.; Ohba, T. Framework for Investigation of Karst Aquifer in an Arid Zone, Using Isotopes, Remote Sensing and GIS Applications: The Northwestern Coast of Egypt. *Environ. Process.* **2015**, *2*, 37–60. [CrossRef]
53. Rainwater, F.H.; Thatcher, L.L. *Methods for Collection and Analysis of Water Samples*; Paper No. 1454; U.S. Geological Survey: Washington, DC, USA, 1960; p. 301.

54. Fishman, M.J.; Friedman, L.C. *Methods for Determination of Inorganic Substances in Water and Fluvial Sediments*; Open-File Report, 85–495; U.S. Geological Survey: Denver, CO, USA, 1985; Volume 5, Chapter A1.

55. ASTM (American Society for Testing and Materials). *Annual Book of ASTM Standards*; ASTM: Baltimore, MD, USA, 2002; Volume 11, 939p.

56. Coplen, T.B.; Wildman, J.D.; Chen, J. Improvements in the gaseous hydrogen-water equilibrium technique for hydrogen isotope ratio analysis. *Anal. Chem.* **1991**, *63*, 910–912. [CrossRef]

57. Coplen, T.B. Reporting of stable hydrogen carbon and oxygen isotopic abundances. *Pure Appl. Chem.* **1994**, *66*, 273–276. [CrossRef]

58. Gibbs, R.J. Mechanisms controlling world water chemistry. *Science* **1970**, *170*, 1088–1090. [CrossRef] [PubMed]

59. Gimenez Forcada, E. Dynamic of seawater interface using hydro chemical facies evolution diagram. *Groundwater* **2010**, *48*, 212–216. [CrossRef]

60. Najib, S.; Fadili, A.; Mehdi, K.; Riss, J.; Makan, A. Contribution of hydrochemical and geoelectrical approaches to investigate salinization process and seawater intrusion in the coastal aquifers of Chaouia, Morocco. J. *Contam. Hydrol.* **2017**, *198*, 24–36. [CrossRef] [PubMed]

61. Naseem, S.; Bashir, E.; Ahmed, P.; Rafique, T.; Hamza, S.; Kaleem, M. Impact of Seawater Intrusion on the Geochemistry of Groundwater of Gwadar District, Balochistan and Its Appraisal for Drinking Water Quality. *Arab. J. Sci. Eng.* **2018**, *43*, 281–293. [CrossRef]

62. Gimenez-Forcada, E.; Roman, F.J.S.S. An Excel Macro to Plot the HFE-Diagram to Identify Seawater Intrusion Phases. *Groundwater* **2014**, *53*, 819–824. [CrossRef] [PubMed]

63. Davis, J.C. *Statistics and Data Analysis in Geology*; John Wiley & Sons, Inc.: New York, NY, USA, 2002.

64. Rao, N.S.; Devadas, D.J.; Rao, K.V.S. Interpretation of groundwater quality using principal component analysis from Anantapur district, Andhra Pradesh, India. *Environ. Geosci.* **2006**, *13*, 239–259.

65. Kaiser, H.F. The varimax criteria for analytical rotation in factor analysis. *Psychometrika* **1958**, *23*, 187–200. [CrossRef]

66. Tomaszkiewicz, M.; Najm, M.A.; El-Fadel, M. Development of a groundwater quality index for seawater intrusion in coastal aquifers. *Environ. Model. Softw.* **2014**, *57*, 13–26. [CrossRef]

67. Piper, A.M. A graphic procedure in the geochemical interpretation of water-analyses. *Eos Trans. Am. Geophys. Union.* **1944**, *25*, 914–928. [CrossRef]

68. Appelo, C.A.J.; Postma, D. *Geochemistry, Groundwater and Pollution*, 2nd ed.; CRC Press: London, UK, 2005; 683p.

69. Park, S.-C.; Yun, S.-T.; Chae, G.-T.; Yoo, I.-S.; Shin, K.-S.; Heo, C.-H.; Lee, S.-K. Regional hydrochemical study on salinization of coastal aquifers, western coastal area of South Korea. *J. Hydrol.* **2005**, *313*, 182–194. [CrossRef]

70. Sinclair, A. Selection of threshold values in geochemical data using probability graphs. *J. Geochem. Explor.* **1974**, *3*, 129–149. [CrossRef]

71. USGS (United States Geological Survey). Water Science School, Saline Water and Salinity. 2018. Available online: https://www.usgs.gov/special-topics/water-science-school/science/saline-water-and-salinity (accessed on 3 November 2022).

72. Sukhija, B.S.; Varma, V.N.; Nagabhushanam, P.; Reddy, D.V. Differentiation of paleomarine and modern seawater intruded salinities in coastal groundwaters (of Karaikal and Tanjavur, India) based on inorganic chemistry, organic biomarker fingerprintsand radiocarbon dating. *J. Hydrol.* **1996**, *174*, 173–201. [CrossRef]

73. El Moujabber, M.; BouSamra, B.; Darwish, T.; Atallah, T. Comparison of different indicators for groundwater contamination by seawater intrusion on the Lebanese coast. *Water Resour. Manag.* **2006**, *20*, 161–180. [CrossRef]

74. Jacobson, R.L.; Langmuir, D. The chemical history of some spring waters in carbonate rocks. *Groundwater* **1970**, *8*, 5–9. [CrossRef]

75. Jones, B.F.; Vengosh, A.; Rosenthal, E.; Yechieli, Y. Chapter 3: Geochemical Investigations. In *Seawater Intrusion in Coastal Aquifers–Concepts, Methods and Practices*; Bear, J., Cheng, A.H.D., Sorek, S., Ouazar, D., Herrera, I., Eds.; Kluwer Academic Publishers: Dordrecht, The Netherlands, 1999; pp. 51–72.

76. Andreasen, D.C.; Fleck, W.B. Use of bromide: Chloride ratios to differentiate potential sources of chloride in a shallow, unconfined aquifer affected by brackish-water intrusion. *Hydrogeol. J.* **1997**, *5*, 17–26. [CrossRef]

77. Hem, J.D. *Study and Interpretation of the Chemical Characteristics of Natural Wate*; USGS Water-Supply Paper; USGS: Reston, VA, USA, 1992; Volume 2254, 263p.

78. Davisson, M.L.; Presser, T.S.; Criss, R.E. Geochemistry of tectonically expelled fluids from the northern coast ranges, rumsey hills, california, USA. *Geochim. Cosmochim. Acta* **1994**, *58*, 1687–1699. [CrossRef]

79. Davisson, M.L.; Criss, R.E. Na-Ca-Cl relations in basinal fluids. *Geochim. Cosmochim. Acta* **1996**, *60*, 2743–2752. [CrossRef]

80. Parkhurst, D.L.; Appelo, C. Description of input and examples for PHREEQC version 3—A computer program for speciation, batch-reaction, one-dimensional transport, and inverse geochemical calculations. *US Geol. Surv. Tech. Methods* **2013**, *6*, A43–497.

81. Geyh, M. Environmental Isotopes in the Hydrological Cycle Principles and Applications, Principales and Applications, IAEA/UNESCO; Volume 4, 424p. 2000. Available online: https://www.naweb.iaea.org/napc/ih/documents/global_cycle/Environmental%20Isotopes%20n%20the%20Hyrological%20Cycle%20Vol%204.pdf (accessed on 9 September 2022).

82. Craig, H. Isotopic variations in meteoric waters. *Science* **1961**, *133*, 1702–1703. [CrossRef]

83. Gat, J.R.; Carmi, I. Evolution of the isotopic composition of atmospheric waters in the Mediterranean Sea area. *J. Geophys. Res.* **1970**, *75*, 3039–3048. [CrossRef]

84. Olive, P. *Introduction to Isotope Hydrology, Geodynamic Research Center*; Didactic and Pedagogical Publishing House: Bucharest, Romania, 1996; 126p. (in French)

Article

Evaluation of Groundwater Sensitivity to Pollution Using GIS-Based Modified DRASTIC-LU Model for Sustainable Development in the Nile Delta Region

Nesma A. Arafa [1,2,*], Zenhom El-Said Salem [2], Mahmoud A. Ghorab [1], Shokry A. Soliman [1], Abdelaziz L. Abdeldayem [2], Yasser M. Moustafa [3] and Hosni H. Ghazala [4]

[1] Exploration Department, Egyptian Petroleum Research Institute (EPRI), 1 Ahmed El-Zomer St., Nasr City, Cairo 11727, Egypt
[2] Geology Department, Faculty of Science, Tanta University, Tanta 31527, Egypt
[3] Analysis and Evaluation Department, Egyptian Petroleum Research Institute (EPRI), 1 Ahmed El-Zomer St., Nasr City, Cairo 11727, Egypt
[4] Geology Department, Faculty of Science, Mansoura University, Mansoura 35516, Egypt
[*] Correspondence: nesma_arafa90@yahoo.com

Abstract: The groundwater resources in the Nile Delta region are an important resource for freshwater because of rising water demand due to anthropogenic activities. The goal of this study is to quantify groundwater sensitivity to pollution in the Nile Delta by a modified GIS-based DRASTIC-LU model. In this study, we utilized two types of modified DRASTIC-LU models, generic and pesticide, to determine the groundwater vulnerability rates to contamination. The results of the generic DRASTIC-LU model showed that the research region, except for the northwestern part with moderate vulnerability of 3.38%, is highly and very highly vulnerable to pollution with 42.69 and 53.91%, respectively. Results from the pesticide DRASTIC-LU model, on the other hand, also confirmed that, except for the northwestern and southern parts with a moderate vulnerability of 9.78%, most the Nile Delta is highly and very highly vulnerable with 50.68 and 39.53%, respectively. A validation of the model generated was conducted based on nitrate concentrations in the groundwater and a sensitivity analysis. Based on the nitrate analysis, the final output map showed a strong association with the pesticide vulnerability model. Examining the model sensitivity revealed that the influence of depth to water and net recharge were the most important factors to consider.

Keywords: GIS; Nile Delta region; modified DRASTIC-LU; groundwater vulnerability; geospatial technique

1. Introduction

Groundwater is the lifeblood for plenty of rural people around the world, as well as a critical component of worldwide food production. Approximately half of the world's drinking water and a large portion of the world's irrigation water supply is derived from groundwater. In Egypt, the depletion of groundwater for farming, industry, and residential purposes has increased. Thus, reliance on groundwater and its quality are progressively increasing day after day and became a huge issue of considerable environmental and social concern. Particularly, there are numerous reasons that can seriously disturb the groundwater quality, for example, rapid population growth, random planning, different land-use–land-class patterns, and invalid drainage systems, including dumping waste from industrial, agricultural, and rural regions. All these factors have made groundwater pollution a hugely challenging problem [1,2]. Consequently, several techniques have been established to assess the groundwater pollution potential, with the groundwater vulnerability techniques being the most popular. Principally, groundwater vulnerability describes the sensitivity of an aquifer system to deterioration because of an outside action.

In the last few decades, a variety of models based on diverse techniques and procedures have been utilized around the world. The modified DRASTIC-LU model based on a geographic information system (GIS) is one of the most popular techniques applied to monitor groundwater susceptibility to pollution depending on the aquifer's hydrogeological conditions. The DRASTIC evaluation was developed by [3], and it is an abbreviation for seven hydrological elements: depth to water, net recharge, aquifer media, soil media, topography, impact of the vadose zone, and aquifer hydraulic conductivity. This model was later modified to improve the evaluation of groundwater vulnerability for a specific aquifer system by adding new model elements that is the land-use layer [4–6]. The modified DRASTIC-LU model consists of eight factors; each is given a relative weight between one and five, and then separated into subclasses based on a grading scale of one to ten. Based on its impact on the aquifer's susceptibility to pollution, the most critical factor is given a weight of five and the least significant is given a weight of one. Similarly, subclasses are given ratings based on the kind of data, the range of data, and the rate of contamination risk. Static ratings and weights are allocated to the parameters as a result. GIS has been found useful when utilized in studies applying the DRASTIC model [7–17].

The modified DRASTIC model is distinguished by its ability to use a simple and flexible criteria structure. The biggest disadvantage of this model is that the weights and rates are originally assumed or based on the experiences of evaluation specialists. Some researchers have offered various strategies to address this problem, including modifying the structure's weights and/or rates, deleting or adding other components, employing sensitivity analyses and calibration procedures, and combination with the analytic hierarchy process [4,18]. Shirazi and his coworkers used DRASTIC and GIS methodologies to assess groundwater susceptibility in the Malaysian state of Melaka, and generated a risk map to quantify the impact of land use on groundwater susceptibility [19]. Some other researchers utilized the land-use factor in a modified DRASTIC model, including [4,8]. Many researchers have suggested using nitrate as a sign of groundwater contamination to estimate the accuracy of the susceptibility method and its relevance to the study region [18,20].

The major goals of this research are to (1) compute the modified DRASTIC vulnerability value to acquire a groundwater susceptibility map for the research region, (2) use the single parameter sensitivity analysis to detect the influence of each modified DRASTIC input layer on the model, and (3) use map removal sensitivity analysis to detect the most sensitive model factors. It is hoped that the yield of this work can be utilized as a helpful guide for groundwater management and protection decision-making at both planning and operational levels. It can also be applied to other portions of the world with similar hydrogeologic and socio-economic settings.

The Study Area

The Nile Delta lies between longitudes 29°30′ and 32°00′ East and latitudes 30°00′ and 31°30′ North. It is surrounded by the Mediterranean Sea from the north, its apex is Cairo from the south, the Suez Canal from the east, and Nubariya Canal from the west (see Figure 1). It is situated in an arid climatic zone along the Mediterranean coast, with an average annual precipitation of 150 mm/y. Although the Nile Delta only accounts for roughly 2% of Egypt's total area, it is home to almost 41% of the country's people and over 63% of its agricultural land [21]. It is characterized by low relief.

The Nile Delta is comprised of Quaternary and Tertiary deposits. The Quaternary is represented by Holocene and Pleistocene sediments. The Holocene consists of sand dunes, coastal deposits, sabkha deposits and silty clay sediments capping the flood plain (Bilqas Formation). The Pleistocene comprises desert crusts and graded sand and gravel that contain the main water-bearing formation (Mit Ghamr Formation) (see Figure 2) [22,23]. The Tertiary, on the other hand, comprises sediments of Pliocene, Miocene, Oligocene, Eocene, and Paleocene ages. The Pliocene sediments represent the lower limit of the major water-bearing formation on top of the Miocene sediments [22,24,25]. In the study area, the most significant regional aquifer is the Quaternary aquifer that is made up of Pleistocene

sand and gravel interbedded with clay. It extends over the entire Nile Delta flood plain. The Nile aquifer's clay cap is a semi-confining layer that ranges in thickness from 5 to 20 m in the south and the central parts of the Delta and reaches 60 m in the north [22,26]. The Nile Delta has long been exposed to many geological, hydrogeological and geophysical studies [21,23,27–32].

Figure 1. Location map of the study area.

Figure 2. Three north (A', B' and C')–south (A, B and C) lithological cross-sections in the Nile Delta region [22,23].

2. Materials and Methods

The DRASTIC model is a numerical rating system created by Aller et al. (1987) [3] for assessing the tendency of groundwater to contaminate. It depends on seven hydrogeologic factors, namely, depth to water, net recharge, aquifer media, soil media, topography, impact of vadose zone and hydraulic conductivity. Based on a range of values and interpretation of obtainable data, each of these parameters is evaluated from 1 to 10. The ratings are then multiplied by a relative weight ranging from one to five (Table 1). The most important factor will have a weight of five, while the least important will have a weight of one. The DRASTIC index (DI) is computed by multiplying and summing the rates and weights of each factor as shown in Equation (1). Groundwater becomes more vulnerable as the DI value increases [3].

$$DI = D_rD_w + R_rR_w + A_rA_w + S_rS_w + T_rT_w + I_rI_w + C_rC_w \tag{1}$$

where D, R, A, S, T, I, and C are the seven factors of the DRASTIC method and subscripts *R* and *W* represent the rating and weight of the factors.

Table 1. Weights of modified DRASTIC-LU factors.

	Modified Generic DRASTIC	Modified Pesticide DRASTIC
Depth to water (D)	5	5
Net recharge (R)	4	4
Aquifer media (A)	3	3
Soil media (S)	2	5
Topography (T)	1	3
Impact of vadose zone (I)	5	4
Hydraulic conductivity (C)	3	2
Land use (LU)	5	5

Modified DRASTIC-LU model: by adding a new parameter to the generic and pesticide DRASTIC model, a new DRASTIC-LU model was developed by Secunda et al. (1998), Brindha and Elango (2015), and Allouche et al. (2017) [4–6]. The LU factor has been assigned a weight of five ($LU_w = 5$) as shown in Table 1. By adding the LU factor to Equation (2), the DRASTIC-LU index model is calculated as follows:

$$\text{The DRASTIC-LU index (Vulnerability Index)} = D_rD_w + R_rR_w + A_rA_w + S_rS_w + T_rT_w + I_rI_w + C_rC_w + LU_rLU_w \tag{2}$$

where D = depth to water table, R = aquifer recharge, A = aquifer media, S = soil media, T = topography, I = impact of vadose zone, C = hydraulic conductivity, LU = land use and subscripts r and w represent, respectively, the rating and weight of these factors.

There are two types of modified DRASTIC-LU model, generic and pesticide to evaluate the groundwater vulnerability to contamination. Each of these two types includes eight parameters.

We used the nitrate concentrations in groundwater to validate the model, where it is considered as an effective indicator of pollutant migration from the surface to the groundwater, predominantly in farming areas. We collected 121 representative groundwater samples from the eastern side of Nile Delta where the sensitivity analysis method was also applied to validate the model's final output map.

3. Application of Modified DRASTIC-LU Model Using GIS

The GIS technique was used in this research to execute the modified DRASTIC-LU model as shown in the flowchart of Figure 3 and described in the following steps:
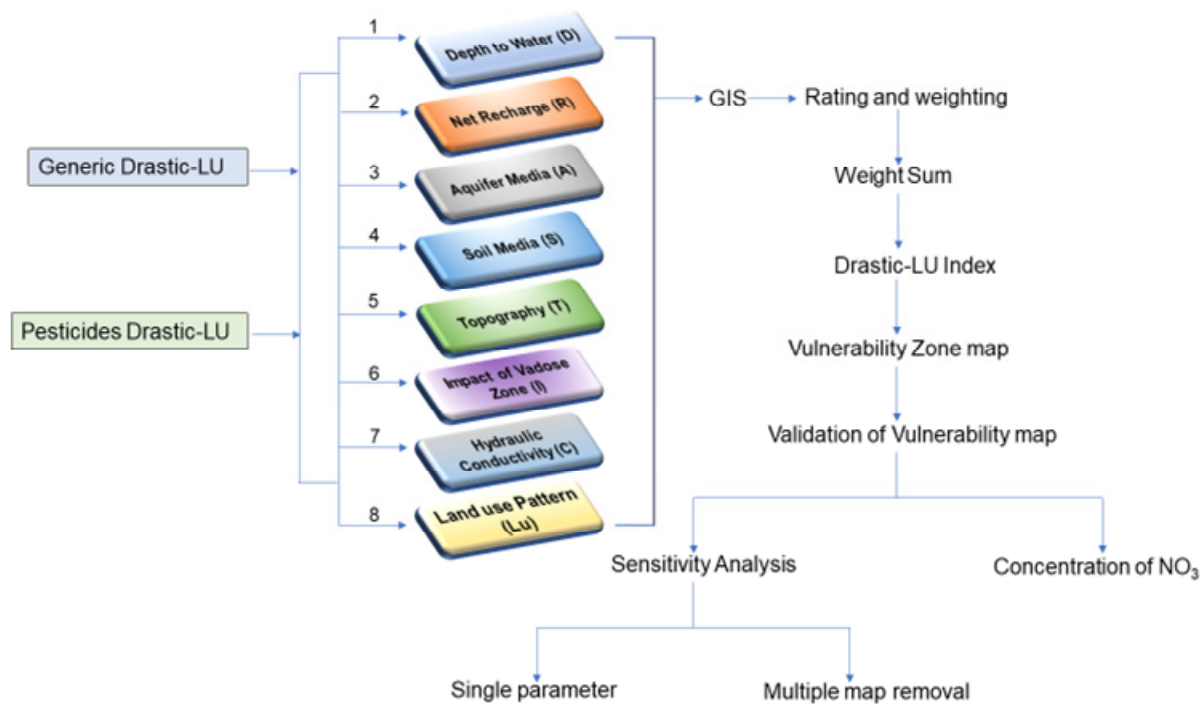
Figure 3. Flow diagram of the methodology implemented for groundwater vulnerability analysis.

3.1. Data Layers Collection

Here, the modified DRASTIC-LU model was used to create a map of the groundwater's susceptibility to contamination in the Nile Delta area. The weights and ratings of the modified generic DRASTIC model and modified pesticide DRASTIC model, were used. This model consisted of eight factors and each factor was derived from different maps as follows: depth to water (D) was produced from [33–35], the topography (T) was generated using a digital elevation model (DEM) derived from SRTM global elevation data (1 Arc second resolution, SRTM plus v3), and the aquifer media (A) were derived from [36]. Recharge (R) of the Pleistocene aquifer was created from [37], the hydraulic conductivity (C) was from [38], the soil (S) was derived from [39], the vadose zone (I) was derived from [40,41] and land use (LU) was from Sentinel-2 imagery at 10 m resolution by ESRI.

3.2. Management of Data Layers

Each of the data layers exploited to determine groundwater vulnerability was adjusted using the following procedures:

1. The first phase entails that every data layer that has an impact on groundwater vulnerability was digitized through turning of visible features on a map image into editable features that can be given extra spatial and non-spatial properties. The digitizing process began with the creation of new layers in ArcCatalog, followed by the addition of features such as points, lines, or polygons to them in ArcMap.
2. The data was converted from vector features such as points, lines, or polygons to raster data.
3. Interpolation by inverse distance weighting (IDW) was applied to convert the data layers in the point feature to a raster surface [42,43], while rasterization was used to convert the data layers in the polygon feature to a raster structure.
4. Reclassification of layers was defined as the replacing of input cell values with new output cell values [42,44]. Every data layer was classed in this research according to a general scale that illustrates its impact on groundwater contamination. For each data layer, there were ten classes varying from ten to one, with ten representing the largest pollution risk and one representing the least contamination risk. All data layers were

reclassified using the spatial analyzer provided in ArcGIS program, as illustrated in Table 2.

5. As a result of these steps, a relative weight ranging from 1 to 5 was given to the reclassified layers, and all cell values in each layer were multiplied by their weight. The most critical component was assigned a weight of 5, while the least important was assigned a weight of 1, based on their influence on the aquifer's susceptibility to pollution [3].

6. The final step was analyzing data by overlapping all layers. The overlap method is defined as "the spatial process of placing a thematic layer above another to form a new layer". All data layers were overlaid during this process to create a modified DRASTIC-LU model for groundwater susceptibility to contamination as shown in Equation (2).

Table 2. Ranges and ratings for modified DRASTIC-LU factors be according [3].

Parameter	Range	Rating
Depth to water	0.27–3.5	10
	3.6–6.7	9
	6.8–9.8	7
	9.9–13	5
	14–16	3
	17–19	3
	20–23	3
	24–26	2
	27–29	2
	30–32	1
Net recharge (mm/day)	0.03–0.35	6
	0.36–0.66	8
	0.67–0.98	9
	0.99–1.3	9
	1.4–1.6	9
	1.7–1.9	9
	2–2.2	9
	2.3–2.6	9
	2.7–2.9	9
	3–3.2	9
Aquifer media	Gravel and Gravelly sand	9
	Sand dunes	7
	Sand and Clay loams	5
	Sabkha deposits	3
	Nile alluvium	1
Soil	Dissected Limestone	10
	Gravelly sand and Sand dunes	10
	Sand and sand loam	9
	Mixed sandy and Carbonate	9
	Sand and clay loam	8
	Urban	5
	Clay loam	3
	Silty Clay	1
Topography (slope) (%)	0–0.17	10
	0.18–0.55	10
	0.56–1.5	10
	1.6–4.9	9

Table 2. *Cont.*

Parameter	Range	Rating
Impact of vadose zone	Sand dunes	7
	Sandy clay	5
	Clayed sand	5
	Sabkha Deposits	3
	Silty clay	1
Hydraulic conductivity (m/day)	15–32	1
	33–50	2
	51–67	3
	68–85	4
	86–100	5
	110–120	6
	130–140	7
	150–150	8
	160–170	9
	180–190	10
Land use	Water	7
	Agriculture	6
	Urban	5
	Desert	3
	Limestone	1

4. Results and Discussion

4.1. Depth to Water Table (D)

The depth to groundwater parameter has a major influence on determining groundwater contamination risk. Groundwater tables that are deep have adequate residence time to detoxify water as it flows within soil layers, making them less sensitive to contaminants [45]. The raster layer was divided into 10 classes by the spatial analyst (reclassify tool) in the GIS environment, and ratings were assigned to the classes depending on their risk of contamination as shown in Table 2. The depth to water map shows that the majority of the Nile Delta region, especially eastern parts, are within a range from 0.27 to 9.8 m, where this area has rates of 7, 9 and 10, indicating strong contamination capability as shown in Figure 4a,b. The northwestern parts of the Nile Delta reflected high sensitivity to pollution with rates from five to nine, while the southwestern parts of the area are distinguished by low susceptibility to contamination with rates one to three due to the very high depth to water. The central parts of the region around Tanta and Kafr El-shiekh Cities have rates of five, seven, and nine, indicating strong contamination. These results are in agreement with other published work reported from the northwestern and central portions of the Nile Delta by Salem et al. (2019) and Metwally et al. (2022) [16,46], respectively.

4.2. Net Recharge (R)

The recharge rate varied between 0.03 and 3.2 mm per day (Figure 5a). As indicated in Figure 5b, the research area's net recharge was classified into three classes, with ratings of six, eight, and nine, compatible with the DRASTIC rating regulation. The more recharge, the more pollution is likely to be directed to the groundwater table. Most parts of the study region show very high susceptibility to contamination with a rate of nine, probably due to the presence of a large percentage of drainage and irrigation canals which leads to an increase in the amount of recharge, while the northeastern and southwestern parts showed rates varying from six to eight [35].
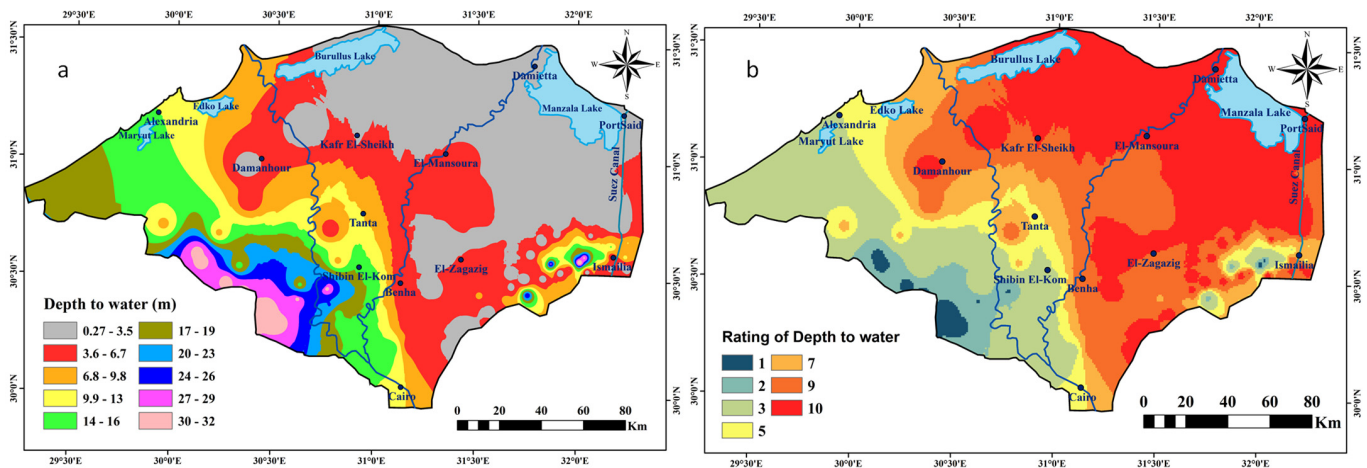
Figure 4. The map indicates to the spatial distribution of (**a**) depth to water and (**b**) depth to groundwater rating map.
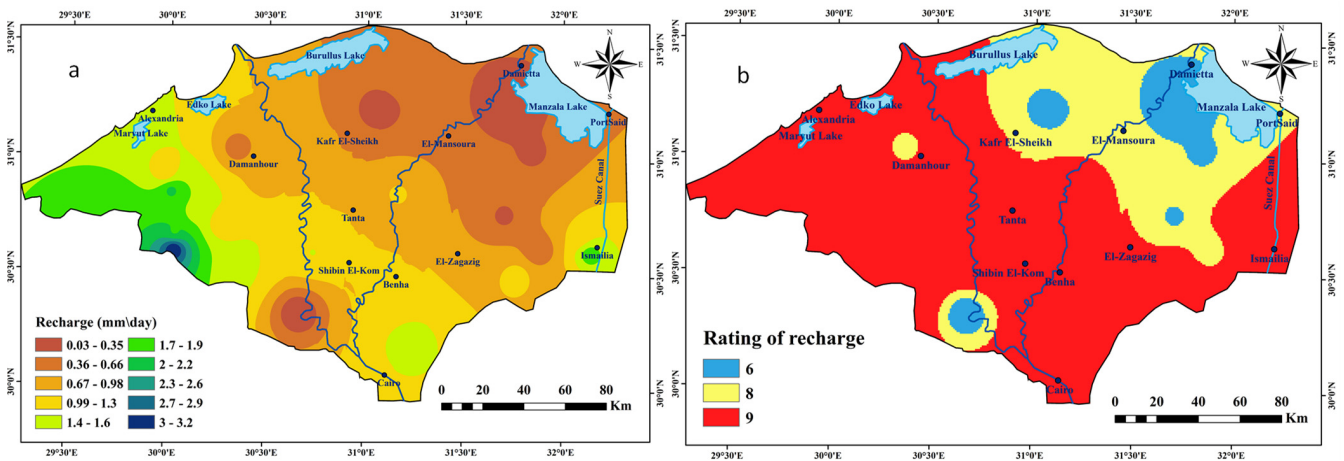
Figure 5. (**a**) Groundwater recharge map of the study area and (**b**) recharge rating map.

4.3. Aquifer Media (A)

The state of the rock, whether consolidated or unconsolidated, acts as an aquifer. The contaminant's mobility through the aquifer is determined by the aquifer's material [47]. The coarser media receive a higher rating than the finer media (Table 2). Overall, the larger the grain and the more fractures, the greater the permeability of the rock medium and the greater the risk of contamination to the aquifer [48]. The generated aquifer media map in the research region shows that the region of the Nile Delta has a rate of one to nine as shown in Figure 6a,b. A huge part of the study region has silty clay and sand with clay loam as the Nile Delta region is completely covered by Quaternary deposits [49].

4.4. Soil (S)

USDA (2010) divided the Nile Delta soil into taxonomic groupings and the soil texture of these units that cover the Nile Delta region is divided into silty clay, clay loam, mixed sandy and carbonates, gravelly sand, gravel sand and sand dunes, and dissected limestone as indicated in Figure 7a [50]. The type of clay present in a soil, in addition to the grain size of the soil, have a significant influence on its contamination risk [3]. The soil medium has six classes, as shown in Figure 7b. The silty clay type dominates the soil texture in the eastern and middle regions. The northern section of the affected area is distinguished by clay loamy soil. Sandy soil dominates the southwestern portion and the northeastern part of the research region.
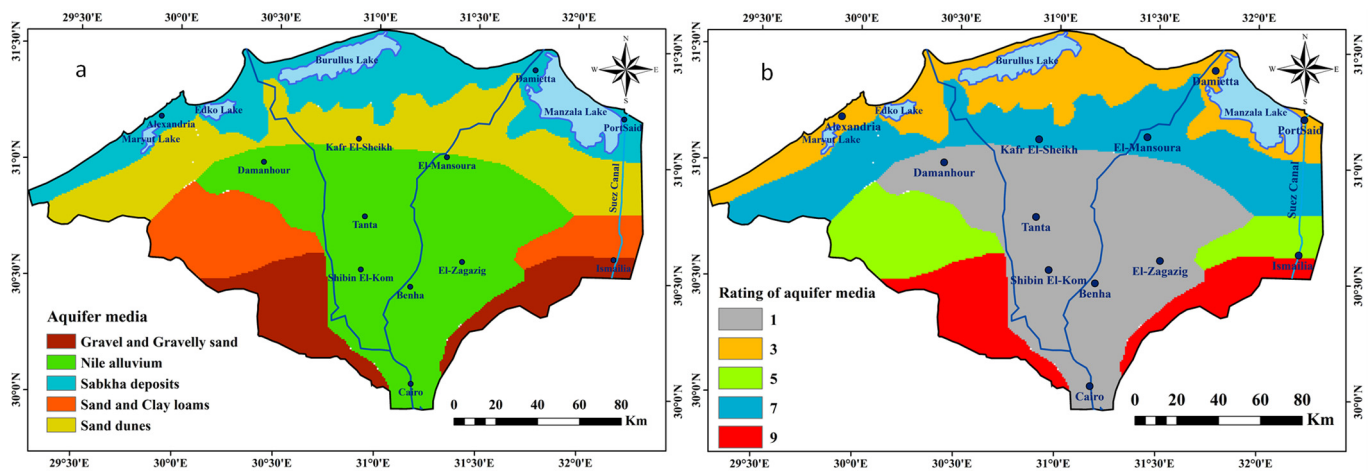
Figure 6. (**a**) Aquifer media layer and (**b**) rating map of aquifer media.
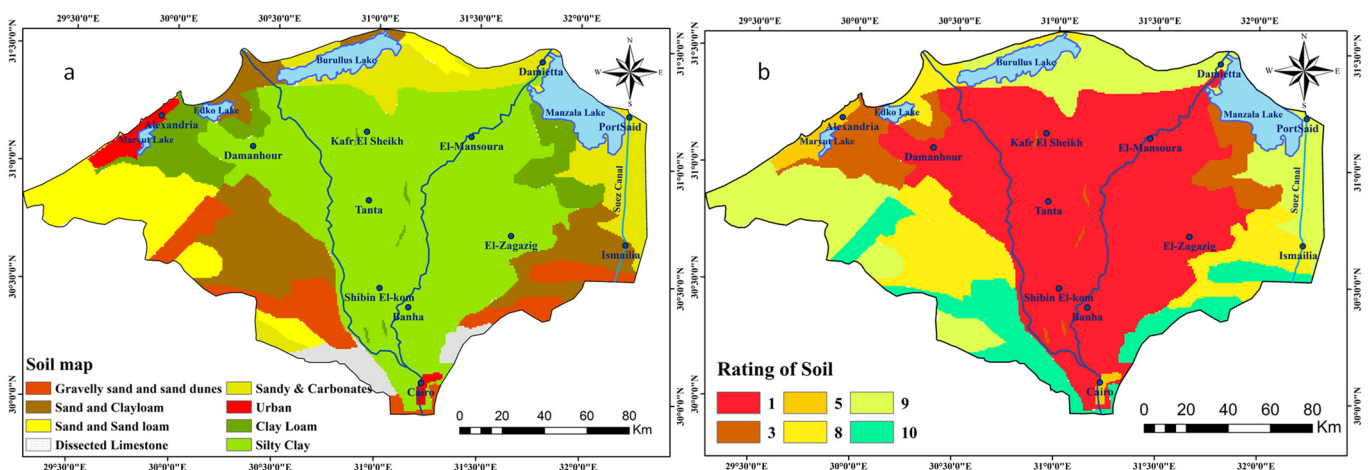
Figure 7. (**a**) Soil media map of the study area and (**b**) rating of soil media.

4.5. Topography (T)

The slope map of the study region was calculated as a percentage from a digital elevation model (DEM) (see Figure 8a). The research region was divided into four classes, which reflected a relatively flat slope in keeping with the DRASTIC rating. The area was given a 9 and 10 rating (see Figure 8b). The majority of the area is highly susceptible to pollution, probably as a result of its low relief [16].

4.6. Impact of Vadose Zone (I)

The unsaturated zone (vadose zone) is defined as the soil zone above the water table that is unsaturated or discontinuously saturated. Sorption, biodegradation, mechanical infiltration and dispersion are all controlled by the soil type in the vadose zone [3]. The vadose zone is assigned to the study area by the Bilqas Formation. As shown in Figure 9a, the lithology of the formation varies from clayey sand in the south to sandy clay in the centre to sandy facies in the north [40]. Figure 9b describes the effect of vadose zone rating in the research region. The northern parts were given a rate of seven because they demonstrated a high susceptibility to contamination due to their sandy facies. Because the middle and southern regions have clayey vadose zones, they were assigned ratings of one and five, respectively.
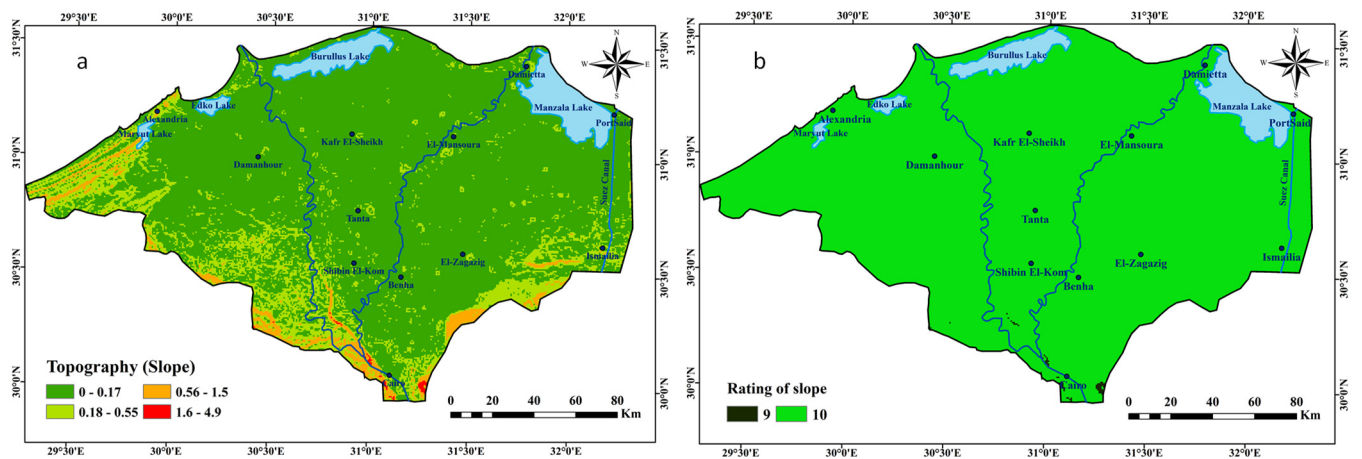
Figure 8. (**a**) Slope map ranges of the study area and (**b**) rating of slope layer.
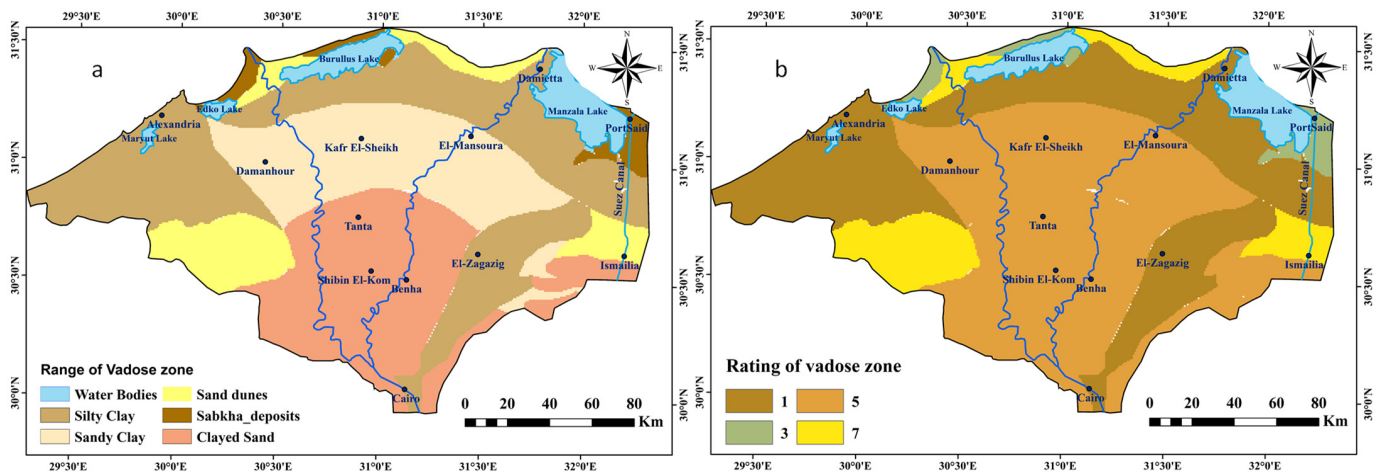
Figure 9. (**a**) Impact of the vadose zone layer and (**b**) vadose zone rating map.

4.7. Hydraulic Conductivity (C)

The pollutant movement is greatly influenced by hydraulic conductivity: the greater the hydraulic conductivity, the higher the potential for contamination [3]. As demonstrated in Figure 10a,b, hydraulic conductivity in the study region was classed into ten classes that range from 15 to 190 m/day, with ratings of 1 to 10. The eastern parts of the Nile Delta reflected high sensitivity to pollution with rates from 6 to 10 due to their high values of hydraulic conductivity, while the western parts of the region revealed low sensitivity with rates from 1 to 3 and the central parts showed moderate sensitivity with rates of 5 and 6.

4.8. Landuse (LU)

The land-use (LU) pattern has a substantial effect on the quality of the groundwater [4]. When the research region is primarily covered by farming fields, using LU as an input may be a suitable way to analyze the susceptibility of aquifers. Contaminants infiltrate groundwater in different ways depending on land usage. Most parts of the study region are used for agricultural, according to the land-use classification. The second significant section of the area is made up of urban areas. The remainder of the region is divided into three categories: desert, water body, and limestone as shown in Figure 11a. Land-use classification revealed that agricultural and urban activities had a huge influence on groundwater contamination in the research region, where they represent 69.26 and 16.45% with rates of six and five, respectively. Limestone and desert have less effect on groundwater pollution with 3.04 and 2.92% with rates of one and three, respectively (Figure 11b). All these results are compatible with published outcomes of [35,51].
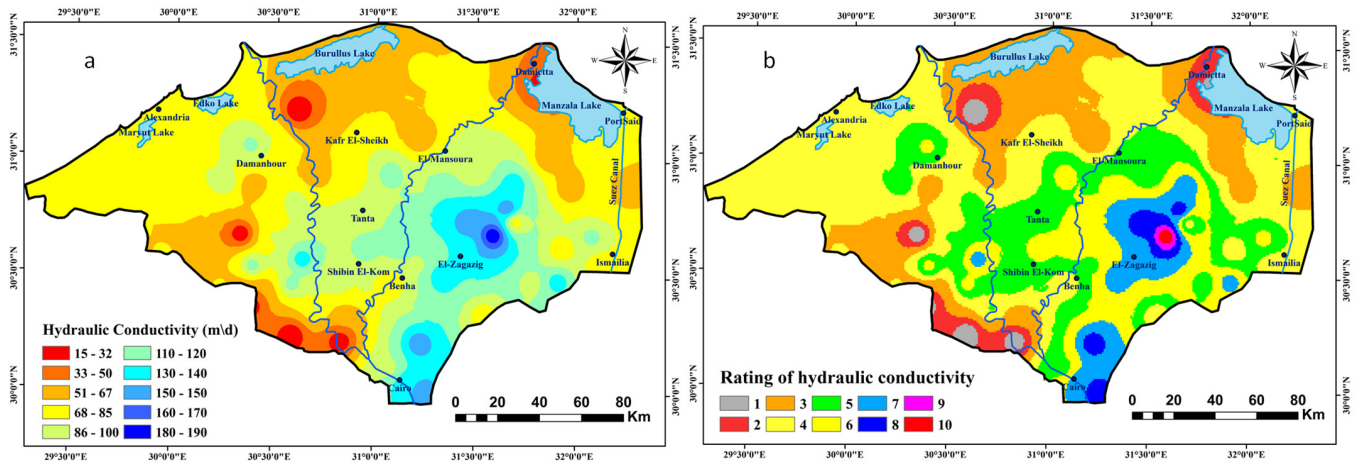
Figure 10. (**a**) Spatial distribution of hydraulic conductivity and (**b**) rating of hydraulic conductivity.
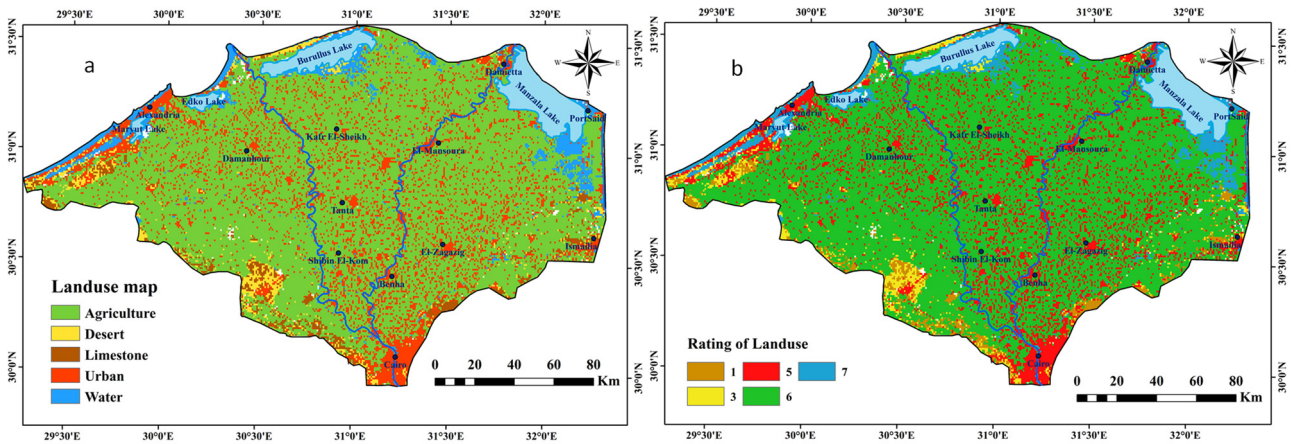
Figure 11. (**a**) Land-use map of study area and (**b**) rating of land use.

5. Creation of Vulnerability Map

The adjusted DRASTIC-LU Index [DI] was computed to build a vulnerability map by adding the products of each factor's ratings and weights using Equation (2) and the results are shown in Figure 12a,b. When the value of DI increases, the relative pollution risk or aquifer vulnerability rises with it [3]. The weights and ratings from the generic DRASTIC model and the pesticide DRASTIC model were used to create two susceptibility maps.
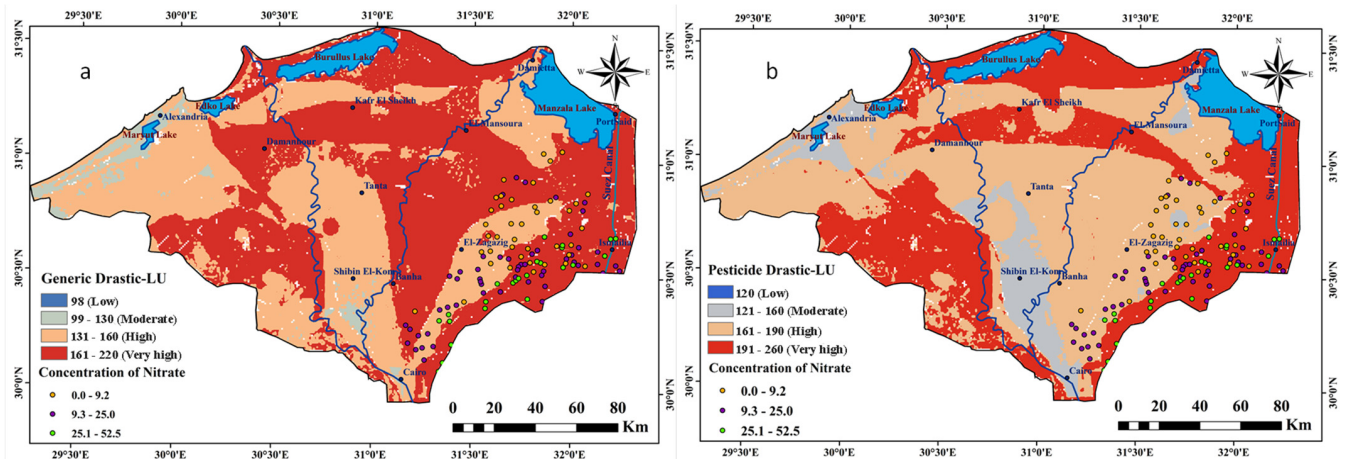
Figure 12. Vulnerability map generated by (**a**) generic DRASTIC-LU and (**b**) pesticide DRASTIC-LU model.

Figure 12a shows the susceptibility map formed by the generic DRASTIC-LU model, while Table 3 shows the brief of susceptibility levels and percentage of each class. It is shown that 53.91% of the study region has an extreme vulnerability to pollution, 42.69% has high susceptibility to pollution, 3.38% has a moderate vulnerability and about 0.01% has a low vulnerability.

Table 3. Generic DRASTIC-LU vulnerability classes.

Generic DRASTIC-LU	Vulnerability Level	Area %
Legend		
98	Low	0.01
99–130	Moderate	3.38
131–160	High	42.69
161–220	Very High	53.91

The vulnerability map of the pesticide DRASTIC-LU model illustrated in Figure 12b and Table 4 shows that 39.53% of the research region has a very high susceptibility to pollution around the eastern and western parts of the region, 50.68% has a high vulnerability, 9.78% covering the northeast and south parts of the study region has a moderate susceptibility and 0.01% has a low susceptibility.

Table 4. Pesticide DRASTIC-LU vulnerability classes.

Pesticide DRASTIC-LU	Vulnerability Level	Area %
Legend		
120	Low	0.01
121–160	Moderate	9.78
161–190	High	50.68
191–260	Very High	39.53

5.1. Validation of the Vulnerability Map

5.1.1. Assessment the Status of Nitrate Pollution

Nitrate values were evaluated for 121 groundwater samples obtained from the eastern parts of the research region to validate the vulnerability evaluation. NO_3 values ranged from 0.08 to 52.5 mg/L. Fertilizers, animal waste, and sewage all contribute to nitrate levels in the water [52]. The nitrate data show a strong association with the pesticide vulnerability DRASTIC-LU model (Figure 12b). This result shows that models that use the land-use parameter are better at assessing an aquifer's contamination vulnerability. All recorded nitrate polluted wells were located in moderate to very high-hazard areas, according to the confirmation test, and the dispersion of wells in moderate, high, and very high-risk areas is revealed in Figure 12a,b. This is probably because most parts of the study region are covered by farm areas, and thus the "agricultural runoff flow" significantly added to the higher NO_3 levels reported in the groundwater of the region. This is accompanied by the effect of urban expansion, industrial discharges, and other sources.

5.1.2. Sensitivity Analysis of Modified DRASTIC-LU Model

A sensitivity analysis evaluates the level of doubt or variety in the final outcomes of a model [53]. It may be useful to determine the most effective vulnerability indicators, and then investigate how to deal with pollution and aquifer crisis management correctly. Single component sensitivity analysis and map removal sensitivity analysis were performed in this analysis.

Single-Parameter Sensitivity Analysis Method (SPSA)

The theoretical and effective weights of the elements utilized to create the modified DRASTIC-LU index were compared. The effective weight was calculated using Equation (3) below [54]:

$$W = ((Pr \times Pw) \div V) \times 100 \tag{3}$$

where W refers to the effective weight of every factor, Pr and Pw represent the rating value and weight of each factor, and V indicates the total vulnerability index.

Results from the single component sensitivity method for the modified DRASTIC-LU model are summarized in Table 5a,b. As shown in the table, the effective and theoretical weights of the modified DRASTIC-LU elements did not match completely, and in some cases were notably different.

Table 5. Statistics of sensitivity analysis according to a single parameter for:

(a) Generic DRASTIC-LU.								
Index		**The Single Parameter Sensitivity Analysis**						
Generic DRASTIC-LU		**Theoretical Weight**	**Theoretical Weight %**	**Effective Weight**				**Effective wt**	**Effective wt %**
	Parameter			**Min.**	**Max.**	**Mean**	**Standard Deviation**		
	D	5	17.8	2.94	35.9	21.9	8.93	6.15	21.9
	R	4	14.2	14.04	30.0	21.5	3.10	6.02	21.5
	A	3	10.7	1.69	20.1	7.51	5.34	2.10	7.51
	S	2	7.14	1.05	15.0	5.26	4.58	1.47	5.26
	T	1	3.57	4.74	8.33	6.22	0.71	1.74	6.22
	I	5	17.8	2.65	22.1	11.2	6.54	3.16	11.2
	C	3	10.7	1.88	18.7	8.62	2.97	2.41	8.62
	LU	5	17.8	2.62	23.08	17.6	3.15	4.94	17.6

(b) Pesticide DRASTIC-LU.								
Index		**The single Parameter Sensitivity Analysis**						
Pesticide DRASTIC-LU		**Theoretical Weight**	**Theoretical Weight %**	**Effective Weight**				**Effective wt**	**Effective wt %**
	Parameter			**Min.**	**Max.**	**Mean**	**Standard Deviation**		
	D	5	16.1	2.42	31.8	19.3	8.24	6.01	19.3
	R	4	12.9	12.6	25.5	18.7	2.82	5.80	18.7
	A	3	9.68	1.38	15.3	6.38	4.42	1.98	6.38
	S	5	16.1	2.48	28.2	10.8	9.00	3.37	10.8
	T	3	9.68	11.9	21.1	16.2	2.02	5.04	16.2
	I	4	12.9	1.72	15.3	7.93	4.63	2.46	7.93
	C	2	6.45	1.02	11.6	5.05	1.92	1.57	5.05
	LU	5	16.1	2.17	20.6	15.4	2.91	4.77	15.4

The most impactful factors in vulnerability evaluation by the generic DRASTIC-LU model were depth to water and net recharge, with average effective weights of 21.96 and 21.51%, respectively. The depth to water and net recharge further exposed a high impact on susceptibility evaluation in the pesticide DRASTIC-LU model, with average effective weights of 19.39 and 18.72%, respectively. To optimize the DRASTIC-LU index's factor selection, the obtained modified DRASTIC-LU index values needed to be revised by applying the SPSA and weights evaluation. The new effective weight of the eight parameters had to be applied to obtain SPSA DRASTIC-LU index as shown in Figure 13a,b. A contrast of the SPSA DRASTIC-LU map with the nitrate concentration values reveals that the SPSA-DRASTIC-LU model is more valid than the DRASTIC-LU model.
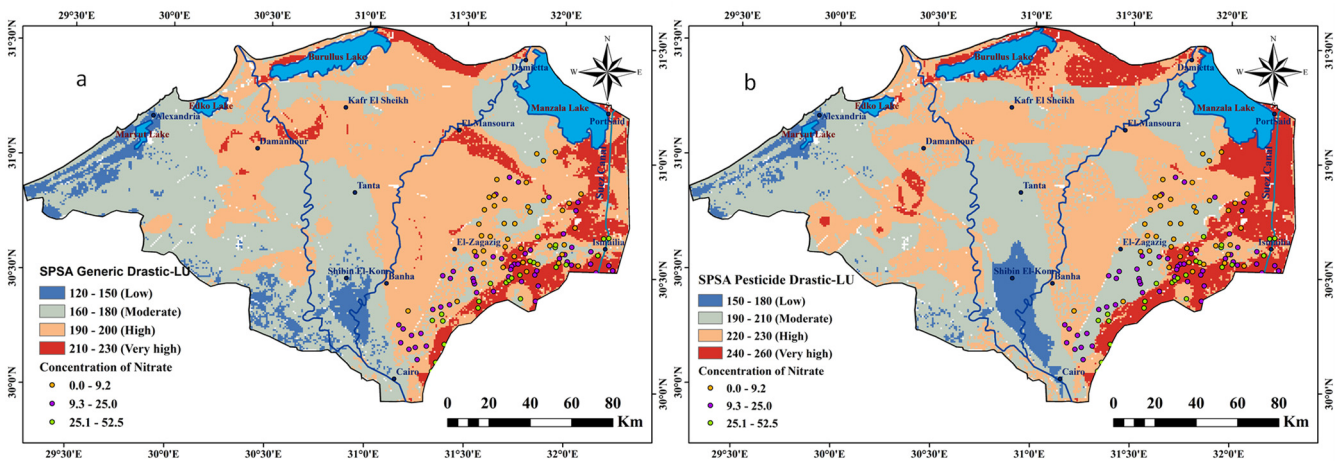
Figure 13. Validation of vulnerability map generated by (**a**) SPSA Generic DRASTIC-LU and (**b**) SPSA pesticide DRASTIC-LU model.

Map Removal Sensitivity Analysis Method (MRSA)

The map removal process, as published via Lodwick et al. (1990) [55] evaluates the susceptibility of the modified DRASTIC-LU index by eliminating one or more components at a time. This is achieved using Equation (4):

$$S = \left\{ \left(\frac{V}{N} - \frac{V'}{n} \right) / V \right\} \times 100 \tag{4}$$

where
S = sensitivity evaluation
V = disturbed susceptibility index (actual index resulting from the application of all eight factors);
V' = disturbed vulnerability index (a lower number of factors were used to estimate the susceptibility index.) N and n = sum of data layers applied to compute V and V'.

Table 6a displays the outcomes of the sensitivity analysis of the MRSA method and the variation of the susceptibility index for the modified DRASTIC-LU model. The factor of depth to water showed a higher mean variation than the other factors, due to the strong sensitivity of the susceptibility index in the generic DRASTIC-LU model to the absence of these factors. Furthermore, hydraulic conductivity was the least effective factor in the generic DRASTIC-LU model (a mean variation index of 0.61 percent).

Moreover, the depth to water was the highest vulnerable factor of all eight elements applied in the pesticide DRASTIC-LU model, as the factor's removal result was 1.37%. After depth to water, the removal of soil and the influence of hydraulic conductivity factors were significantly less sensitive to the vulnerability index, because the weights and mean variation of these two factors were lower (1.26 and 1.06). Moreover, land use was the least effective factor in the pesticide DRASTIC-LU model (a mean variation index of 0.50%). Table 6b displays the conclusions of the multiple map removal sensitivity analysis method after eliminating several DRASTIC-LU factor layers at a time.

Table 6. Statistics of sensitivity analysis upon:

(a) One Map Removal.									
	Variation Index %					**Variation Index %**			
Generic DRASTIC-LU	**Min**	**Max**	**Mean**	**Standard Deviation**	**Pesticide DRASTIC-LU**	**Min**	**Max**	**Mean**	**Standard Deviation**
D	0.00	3.35	1.62	0.8992	D	0.00	2.76	1.37	0.69
R	0.22	2.50	1.29	0.4429	R	0.02	1.86	0.89	0.40

Table 6. *Cont.*

(a) One Map Removal.								
	Variation Index %					**Variation Index %**		
Generic DRASTIC-LU	**Min**	**Max**	**Mean**	**Standard Deviation**	**Pesticide DRASTIC-LU**	**Min**	**Max**	**Mean**	**Standard Deviation**
A	0.02	1.54	0.87	0.5703	A	0.01	1.59	0.90	0.59
S	0.04	1.64	1.05	0.6242	S	0.44	2.25	1.26	0.34
T	0.60	1.11	0.90	0.1008	T	0.00	1.23	0.54	0.28
I	0.00	1.41	0.82	0.4692	I	0.01	1.54	0.70	0.61
C	0.00	1.52	0.61	0.3338	C	0.12	1.64	1.06	0.27
LU	0.00	1.51	0.80	0.3212	LU	0.00	1.48	0.50	0.30
(b) Multiple map removal sensitivity analysis								
Generic DRASTIC-LU	**Variation Index %**				**Pesticide DRASTIC-LU**	**Variation Index %**			
Removed Maps	**Min.**	**Max.**	**Mean**	**Standard Deviation**	**Removed Maps**	**Min.**	**Max.**	**Mean**	**Standard Deviation**
DR	0.00	5.48	3.08	1.35	DR	0.00	4.52	2.28	1.23
DRA	0.17	5.62	2.72	1.36	DRA	0.00	4.27	1.69	1.05
DRAS	0.00	5.87	1.87	1.41	DRAS	0.00	5.26	1.76	1.29
DRAST	0.02	5.92	1.95	1.20	DRAST	0.06	8.11	3.09	1.85
DRASTI	0.00	8.40	1.77	1.44	DRASTI	0.00	9.96	2.42	1.74
DRASTIC	0.00	10.58	5.59	2.25	DRASTIC	0.00	10.33	3.53	2.09

6. Conclusions

The groundwater sensitivity to widespread pollution in the Nile Delta region was evaluated by a GIS-based modified DRASTIC-LU method. The groundwater susceptibility map was found to be the most cost-effective method for the detection zones of probable groundwater pollution, especially given the disorganized and unconstrained expansion of land and undesirable activities harming groundwater conditions. Here, two types of modified DRASTIC-LU models, generic and pesticide, were utilized to evaluate the levels of groundwater pollution vulnerability. Based on the results of the susceptibility map developed by the generic DRASTIC-LU model, we divided the study region into four susceptibility groupings for groundwater pollution: very high, high, moderate, and low susceptibility. The ratio of vulnerability to pollution was found to be very high for 53.91% of the area, high for 42.69%, moderate for 3.38%, and low for only 0.01%. The susceptibility map formed by the pesticide DRASTIC-LU model, on the other hand, showed that around 39.53% of the study region seemed to have a very high susceptibility to pollution, 50.68% had a high susceptibility, and 9.78% had a moderate susceptibility, and about 0.01% of the research region had a low susceptibility.

The concentration levels of nitrates measured from the 121 groundwater samples gathered from the eastern part of the study region varied from 0.08 to 52.5 mg/L.

The nitrate data show a strong association with the pesticide vulnerability model DRASTIC-LU. The results of SPSA using the generic DRASTIC-LU model proved that depth to water and net recharge had the greatest effect on the susceptibility evaluation, with a mean of 21.96 and 21.51, while they represented 19.39 and 18.72 using the pesticide DRASTIC-LU. Moreover, the results of the MRSA method by the generic and pesticide DRASTIC-LU models showed that depth to water and soil had the largest influence on susceptibility, with mean values of 1.62 and 1.05 (generic) and 1.37 and 1.26 (pesticide), respectively.

In light of the obtained results, it is recommended that there should be measures put in place to: (1) establish effective environmental policies to preserve groundwater from pollution; (2) improve the ecological integrity through the application of land-use planning; (3) avoid the extra use of fertilizers in agricultural activities as they can quickly penetrate groundwater.

References

1.   Singh, R.; Syed, T.H.; Kumar, S.; Kumar, M. Hydrogeochemical assessment of surface and groundwater resources of Korba coalfield, Central India: Environmental implications. *Arab. J. Geosci.* **2017**, *10*, 318. [CrossRef]
2.   Singh, R.; Tajdarul, A.S.V.; Surinaidu, H.S.L.; Pasupuleti, S.; Manoj, S.P.R. Stable isotope systematics and geochemical signatures constraining groundwater hydraulics in the mining environment of the Korba Coalfield, Central India. *Environ. Earth Sci.* **2018**, *77*, 548. [CrossRef]
3.   Aller, L.; Lehr, J.; Petty, R. *DRASTIC: A Standardized System to Evaluate Groundwater Pollution Potential Using Hydrogeologic Settings*; Bennett, T., Ed.; National Water Well Association: Worthington, OH, USA; Bennett and Williams, Inc.: Columbus, OH, USA, 1987; p. 43229.
4.   Secunda, S.; Collin, M.L.; Melloul, A.J. Groundwater vulnerability assessment using a composite model combining DRASTIC with extensive agricultural land use in Israel's Sharon region. *J. Environ. Manag.* **1998**, *54*, 39–57. [CrossRef]
5.   Brindha, K.; Elango, L. Cross Comparison of Five Popular Groundwater Pollution Vulnerability Index Approaches. *J. Hydrol.* **2015**, *524*, 597–613. [CrossRef]
6.   Allouche, N.; Maanan, M.; Gontara, M.; Rollo, N.; Jmal, I.; Bouri, S. Environmental Modelling & Software A global risk approach to assessing groundwater vulnerability. *Environ. Model. Softw.* **2017**, *88*, 168–182. [CrossRef]
7.   Zhang, R.; Hamerlinck, J.D.; Gloss, S.P.; Munn, L. Determination of Nonpoint-Source Pollution Using GIS and Numerical Models. *J. Environ. Qual.* **1996**, *3*, 411–418. [CrossRef]
8.   Al-Adamat, R.A.; Foster, I.D.; Baban, S.M. Groundwater Vulnerability and Risk mapping for the Basaltic aquifer of the Azraq basin of Jordan using GIS, Remote Sensing and DRASTIC. *Appl. Geogr.* **2003**, *23*, 303–324. [CrossRef]
9.   Rahman, A.A. GIS Based DRASTIC Model for Assessing Groundwater Vulnerability in Shallow Aquifer in Aligarh, India. *Appl. Geogr.* **2008**, *28*, 32–53. [CrossRef]
10. Ahmed, A.A. Using Generic and Pesticide DRASTIC GIS-based models for vulnerability assessment of the Quaternary aquifer at Sohag, Egypt. *Hydrogeol. J.* **2009**, *17*, 1203–1217. [CrossRef]
11. Javadi, S.; Kavehkar, N.; Mohammadi, K.; Khodadadi, A.; Kahawita, R. Calibrating DRASTIC using field measurements, sensitivity analysis and statistical methods to assess groundwater vulnerability. *Water Int.* **2011**, *36*, 719–732. [CrossRef]
12. Kazakis, N.; Voudouris, K.S. Groundwater vulnerability and pollution risk assessment of porous aquifers to nitrate: Modifying the DRASTIC method using quantitative parameters. *J. Hydrol.* **2015**, *525*, 13–25. [CrossRef]
13. Tiwari, A.K.; Singh, P.K.; De Maio, M. Evaluation of aquifer vulnerability in a coal mining of India by using GIS-based DRASTIC model. *Arab. J. Geosci.* **2016**, *9*, 438. [CrossRef]
14. Wu, H.; Chen, J.; Qian, H. Amodified DRASTIC model for assessing contamination risk of groundwater in the northern suburb of Yinchuan, China. *Environ. Earth Sci.* **2016**, *75*, 483. [CrossRef]
15. Saida, S.; Tarik, H.; Abdellah, A.; Farid, H.; Hakim, B. Assessment of Groundwater Vulnerability to Nitrate Based on the Optimised DRASTIC Models in the GIS Environment (Case of Sidi Rached Basin, Algeria). *Geosciences* **2017**, *7*, 20. [CrossRef]
16. Salem, Z.E.; Sefelnasr, A.M.; Hasan, S.S. Assessment of groundwater vulnerability for pollution using DRASTIC Index, young alluvial plain, Western Nile Delta, Egypt. *Arab. J. Geosci.* **2019**, *12*, 1–13. [CrossRef]
17. Kozłowski, M.; Sojka, M. Applying a Modified DRASTIC Model to Assess Groundwater Vulnerability to Pollution: A Case Study in Central Poland. *Pol. J. Environ. Stud.* **2019**, *28*, 1223–1231. [CrossRef]
18. Huan, H.; Wang, J.; Teng, Y. Science of the Total Environment Assessment and Validation of Groundwater Vulnerability to Nitrate based on A modified DRASTIC model: A case study in Jilin City of northeast China. *Sci. Total Environ.* **2012**, *440*, 14–23. [CrossRef]
19. Shirazi, S.M.; Imran, H.M.; Akib, S.; Yusop, Z.; Harun, Z.B. Groundwater vulnerability assessment in the Melaka State of Malaysia using DRASTIC and GIS techniques. *Environ. Earth Sci.* **2013**, *70*, 2293–2304. [CrossRef]

20. Saadeh, M.; Assaf, H. Geostatistical Assessment of Groundwater Nitrate Contamination with Reflection on DRASTIC Vulnerability Assessment: The Case of the Upper Litani Basin, Lebanon. *Water Resour. Manage.* **2009**, *23*, 775–796. [CrossRef]

21. Sharaky, A.M.; El Hasanein, A.S.; Atta, S.A.; Khallaf, K.M. Nile and groundwater interaction in the western Nile Delta, Egypt. *Handb. Environ. Chem.* **2017**, *55*, 33–62. [CrossRef]

22. Serag EI-Din, H. Geological, Hydrogeological and Hydrological Studies on the Quaternary Aquifer, Egypt. Ph.D. Thesis, Mansoura University, Mansoura, Egypt, 1989.

23. Salem, Z.E.; Al Temamy, A.M.; Salah, M.K.; Kassab, M. Origin and characteristics of brackish groundwater in Abu Madi coastal area, Northern Nile Delta, Egypt. *Estuar. Coast. Shelf Sci.* **2016**, *178*, 21–35. [CrossRef]

24. Coutellier, V.; Stanley, D.J. Late Quaternary Stratigraphy and Paleogeography of the Eastern Nile Delta, Egypt. *Mar. Geol.* **1987**, *77*, 257–275. [CrossRef]

25. Said, R. *The Nile River: Geology, Hydrology, and Utilization*; Pergamon: New York, NY, USA, 1993; p. 320.

26. Diab, M.S.; Dahab, K.; El Fakharany, M. Impacts of the Paleohydrological Conditions on the Groundwater Quality in the Northern Part of Nile Delta. *Geol. Soc. Egypt. J. Geol.* **1997**, *41*, 779–796.

27. Geirnaert, W.; Laeven, M.P. Composition and history of ground water in the western Nile Delta. *J. Hydrol.* **1992**, *138*, 169–189. [CrossRef]

28. Wahaab, R.A.; Badawy, M.I. Water quality assessment of the River Nile system: An overview. *Biomed. Environ. Sci.* **2004**, *17*, 87–100.

29. Sefelnasr, A.; Sherif, M. Impacts of Seawater Rise on Seawater Intrusion in the Nile Delta Aquifer, Egypt. *Groundwater* **2014**, *52*, 264–276. [CrossRef]

30. Al-Agha, D.E.; Closas, A.; Molle, F. *Survey of Groundwater Use in the Central Part of the Nile Delta. Water and Salt Management in the Nile Delta: Report No. 6*; International Water Management Institute (IWMI): Colombo, Sri Lanka, 2015; pp. 1–49.

31. Wassef, R.; Schüttrumpf, H. Impact of sea-level rise on groundwater salinity at the development area western delta, Egypt. *Groundw. Sustain. Dev.* **2016**, *2–3*, 85–103. [CrossRef]

32. Salem, Z.E.; Osman, O.M. Use of major ions to evaluate the hydrogeochemistry of groundwater influenced by reclamation and seawater intrusion, West Nile Delta, Egypt. *Environ. Sci. Pollut. Res.* **2017**, *24*, 3675–3704. [CrossRef]

33. RIGW. *Safe Use Studies for Groundwater Reservoirs in the Nile Delta and Upper Egypt*; Research Institute for Groundwater, Ministry of Water Resources and Irrigation MWRI: Cairo, Egypt, 1980.

34. Ismael, A.M.A. Application of Remote Sensing, GIS, and Groundwater Flow Modelling in Evaluating Groundwater Resources: Two case studies—East Nile Delta, Egypt and Gold Valley, California. Ph.D. Thesis, University of Texas at El Paso, El Paso, TX, USA, 2007.

35. Armanuos, A.M.; Allam, A.; Negm, A.M. Assesment of Groundwater Vulnerability to Pollution in Western Nile Delta Aquifer. *Int. Water Technol. J.* **2020**, *10*, 18–40.

36. Fergany, E.A.; Sylvette, B.C. Microtremor Measurements in the Nile Delta Basin, Egypt: Response of the topmost sedimentary layer. *Seismol. Res. Lett.* **2009**, *80*, 591–598. [CrossRef]

37. Morsy, W.S. Environmental Management to Groundwater Resources for Nile Delta Region. Ph.D. Thesis, Faculty of Engineering, Cairo University, Cairo, Egypt, 2009.

38. Mabrouk, M.; Jonoski, A.; Essink, G.H.P.O.; Uhlenbrook, S. Assessing the fresh-saline groundwater distribution in the Nile delta aquifer using a 3D variable-density groundwater flow model. *Water* **2019**, *11*, 1946. [CrossRef]

39. Gad, A.A.; Ali, R. Creation of GIS digital Land Resources database of the Nile delta, Egypt, for optimal soil management. *Procedia Soc. Behav. Sci.* **2011**, *19*, 641–650. [CrossRef]

40. El-Fayoumi, I.F. *Geology of the Quaternary Succession and Its Impact on the Groundwater Reservoir in the Nile Delta Region*; Bull Faculty of Science, Mansoura University: Mansoura, Egypt, 1987.

41. El Bastawesy, M.; Cherif, O.H.; Sultan, M. The Geomorphological Evidences of Subsidence in the Nile Delta: Analysis of high resolution topographic DEM and multi-temporal satellite images. *J. Afr. Earth Sci.* **2017**, *136*, 252–261. [CrossRef]

42. McCoy, J.; Johnston, K. *Using Arcgis Spatial Analyst*; Environmental Systems Research Institute, Inc.: Redlands, CA, USA, 2001; p. 230.

43. ElTahlawi, M.R.; Abo-El Kassem, M.; Baghdadi, G.Y.; Saleem, H.A. Assessment of Groundwater Vulnerability—A Case Study. *Int. J. Adv. Remote Sens. GIS* **2016**, *5*, 1561–1579. [CrossRef]

44. Salem, Z.E.; Hasan, S.S. Use of GALDIT model and HFE-Diagram to assess seawater intrusion vulnerability in West Nile Delta, Egypt. *Arab. J. Geosci.* **2021**, *14*, 1318. [CrossRef]

45. Saidi, S.; Bouri, S.; Dhia, H.B. Groundwater management based on GIS techniques, chemical indicators and vulnerability to seawater intrusion modelling: Application to the Mahdia-Ksour Essaf aquifer, Tunisia. *Environ. Earth Sci.* **2013**, *70*, 1551–1568. [CrossRef]

46. Metwally, M.I.; Armanuos, A.M.; Zeidan, B.A. Comparative study for assessment of groundwater vulnerability to pollution using DRASTIC methods applied to central Nile Delta, Egypt. *Int. J. Energy Water Resour.* **2022**. [CrossRef]

47. Singh, A.; Srivastav, S.K.; Kumar, S.; Chakrapani, G.J. A modified-DRASTIC model (DRASTICA) for assessment of groundwater vulnerability to pollution in an urbanized environment in Lucknow, India. *Environ. Earth Sci.* **2015**, *74*, 5475–5490. [CrossRef]

48. Umar, R.; Ahmed, I.; Alam, F. Mapping groundwater vulnerable zones using modified DRASTIC approach of an alluvial aquifer in parts of central Ganga plain, western Uttar Pradesh. *J. Geol. Soc. India.* **2009**, *73*, 193–201. [CrossRef]

49. Elewa, H.H.; El Nahry, A.H. Hydro-environmental Status and Soil Management of the River Nile Delta, Egypt. *Environ. Geol.* **2009**, *57*, 759–774. [CrossRef]

50. USDA. *Keys to Soil Taxonomy*, 11th ed.; United State Department of Agriculture, Natural Resources, Conservation Service: Washington, DC, USA, 2010.

51. Metwally, M.I.; Armanuos, A.M.; Zeidan, B.A. Mapping of Groundwater Vulnerability to Pollution by Nitrates Using Pesticide DRASTIC Model in the Central Nile Delta, Egypt. In Proceedings of the 2nd International Conference on Civil Engineering: Recent Applications and Future Challenges, ICCE, Hurghada, Egypt, 30 October–2 November 2021; pp. 282–290.

52. Glibert, P.M.; Harrison, J.; Heil, C.; Seitzinger, S. Escalating Worldwide Use of Urea–A global Change Contributing to Coastal Eutrophication. *Biogeochemistry* **2006**, *77*, 441–463. [CrossRef]

53. Saltelli, A.; Ratto, M.; Andres, T.; Campolongo, F.; Cariboni, J.; Gatelli, D.; Saisana, M.; Tarantola, S. *Global Sensitivity Analysis. The Primer*; John Wiley & Sons, Ltd.: Hoboken, NJ, USA, 2008. [CrossRef]

54. Napolitano, P.; Fabbri, A.G. Single-parameter sensitivity analysis for aquifer vulnerability assessment using DRASTIC and SINTACS. In Proceedings of the Vienna Conference on Hydrology GIS 96, Vienna, Austria, 16–19 April 1996.

55. Lodwick, W.A.; Monson, W.; Svoboda, L. Attribute error and sensitivity analysis of map operations in geographical informations systems: Suitability analysis. *Int. J. Geogr. Inf. Syst.* **1990**, *4*, 413–428. [CrossRef]

Article

Delineating Groundwater Potential Zones in Hyper-Arid Regions Using the Applications of Remote Sensing and GIS Modeling in the Eastern Desert, Egypt

Hesham Morgan [1,*] **, Hussien M. Hussien** [2] **, Ahmed Madani** [1] **and Tamer Nassar** [1]

[1] Department of Geology, Faculty of Science, Cairo University, Giza 12613, Egypt
[2] Geology Department, Desert Research Center, El Mataryia, Cairo 11753, Egypt
* Correspondence: hesham.hashem.geo@cu.edu.eg; Tel.: +20-1023994752

Abstract: The increasing demand for freshwater supplies and the effects of climate change in arid and hyper-arid regions are pushing governments to explore new water resources for food security assurance. Groundwater is one of the most valuable water resources in these regions, which are facing water scarcity due to climatic conditions and limited rainfall. In this manuscript, we provide an integrated approach of remote sensing, geographic information systems, and analytical hierarchical process (AHP) to identify the groundwater potential zone in the central Eastern Desert, Egypt. A knowledge-driven GIS-technique-based method for distinguishing groundwater potential zones used multi-criteria decision analysis and AHP. Ten factors influencing groundwater were considered in this study, including elevation, slope steepness, rainfall, drainage density, lineament density, the distance from major fractures, land use/land cover, lithology, soil type, and the distance from the channel network. Three classes of groundwater prospective zones were identified, namely good potential (3.5%), moderate potential (7.8%), and poor potential (88.6%) zones. Well data from the study area were used to cross-validate the results with 82.5% accuracy. During the last 8 years, the static water level of the Quaternary alluvium aquifer greatly decreased (14 m) due to excessive over pumping in the El-Dir area, with no recorded recharges reaching this site. Since 1997, there has been a noticeable decline in major rainfall storms as a result of climate change. The current study introduces a cost-effective multidisciplinary approach to exploring groundwater resources, especially in arid environments. Moreover, a significant modern recharge for shallow groundwater aquifers is taking place, even in hyper-arid conditions.

Keywords: remote sensing; weighted overlay model; analytical hierarchical process (ahp); thematic layers; climate change

1. Introduction

Groundwater is an important and vital source of freshwater supplies and sometimes a key issue in a country's socio-economic development, especially in places that fall within arid/hyper-arid belts [1,2]. About 2.5 billion people worldwide depend completely on groundwater to fulfill their basic water needs [3]. The demand for freshwater resources is expected to rise, with global water deficiency expected to reach 40 % by 2030 [4]. Because of the increased demand for freshwater in arid and hyper-arid regions, governments are looking for alternate water resources. Egypt is dependent on the Nile for 98.26% of its annual water demand [5]. The Grand Ethiopian Renaissance Dam has complicated the problem, and it may result in a major water shortage for the Nile River's downstream countries, whose populations are heavily reliant on the river's water [6]. Furthermore, Water resource demand has risen in recent decades as a result of population, economic, and agricultural growth.

Traditional methods for identifying, delineating, and mapping groundwater potential zones depend on expensive and time-consuming ground surveys using geological, geo-

physical, and hydrogeological tools [7–10]. Geospatial tools, on the other hand, are quick and inexpensive for producing and modeling useful data from a wide variety of geoscience fields [11–14]. The geographic information system (GIS) and remote sensing have proven to be extremely effective tools in groundwater exploration on their own. For groundwater potential zone identification, several GIS techniques have been used. They are beneficial in fuzzy logic analysis [15], analytical hierarchical processes (AHPs) [16], multi-influence factor analysis [7], etc. Satellite data with moderate and high spatial resolutions provide indirect information on groundwater storage. A small to great amount of information about indirect parameters can be gained from these satellites [17,18].

Several writers have published articles about employing remote sensing and GIS approaches to produce groundwater potential zones (Table 1). According to [19], the significant factors influencing groundwater accumulation are classified into three categories, including (a) major water supplies, including the water source and the possible contribution to the groundwater (e.g., rainfall and the distance from the channel network); (b) possible infiltration pathways (e.g., lithology (geology), lineament density, the distance from a major fracture, soil type, and land use/land cover); and (c) opportunity, which refers to the amount of time available to infiltrate the water supply; (e.g., elevation, slope steepness, and drainage density).

The main problems in the study area are the arid condition and water scarcity, which require a good plan for groundwater exploration and the sustainable management of water resources. The mapping of groundwater potentiality is highlighted in the early planning. This study uses the AHP model in a GIS environment to identify groundwater potential zones. The results of this study will have a significant influence on the early planning of groundwater exploration since it could provide preliminarily accurate information on the best location to target to drill good potential groundwater wells. After that, the use of geophysical techniques is a later step to confirm the results of the model before starting the drilling process, especially in an arid location which has no groundwater information.

In this paper, a cost-effective multidisciplinary research approach comprises the integration of the geographic information system, satellite and well log datasets as well as thematic layers produced from ArcGIS and field data to identify groundwater potential zones (potentiality mapping) in dry wadies in arid environments. This approach was achieved through the following: (1) extracting suitable thematic layers; (2) integrating all thematic layers using the analytical hierarchical process (AHP) and initiating a groundwater potential map for the study area based on the extracted thematic layers; (3) validating the applied model using the measured static water level during field trips to estimate the accuracy of obtained results; and (4) carrying out a frequency analysis for the historical rainfall data over 39 years to understand the rainfall behavior and identify the return period of the average annual precipitation, which could affect the groundwater recharging of the shallow aquifers in the study area. Finally, this manuscript provides a cost-efficient research approach for potential aquifer mapping in arid and hyper-arid environments, which could be a replicable model used in similar places that have the same conditions as our study area.

Table 1. Summary of the literature review of the different features that are used to identify groundwater potential zones (GWPZ).

N	Literature Review	NGWR	GWQ	ED	RI	M	D	Aspect	AR	SWB	WTD	WTF	SPS	ASPR	SPI	R	STh	ST	MF	ND	TWI	TPI	Vg	LU/LC	Gm	G	LD	DD	Rf	Sl	El
1	[20]									×	×														×	×	×	×		×	
2	[21]								×															×	×	×	×	×	×	×	
3	[22]										×														×	×	×	×		×	
4	[23]																							×	×	×	×	×		×	×
5	[24]																							×		×	×	×	×	×	
6	[25]										×							×						×	×		×	×		×	
7	[26]																	×					×	×	×	×					
8	[11]																	×			×		×				×			×	×
9	[27]	×	×								×															×	×	×	×	×	
10	[28]																								×	×	×	×		×	
11	[29]																	×						×		×	×	×	×	×	
12	[30]																									×	×	×		×	×
13	[31]					×												×							×	×	×	×		×	
14	[32]																								×		×			×	
15	[33]														×			×			×		×	×		×	×	×	×	×	×
16	[18]																							×		×	×	×	×	×	
17	[34]											×						×						×	×	×			×		
18	[35]																×	×						×	×		×	×		×	
19	[36]																	×						×	×	×	×	×		×	
20	[37]																	×						×	×	×	×	×	×	×	
21	[38]																	×						×	×	×	×	×	×	×	×
22	[39]																	×						×	×	×	×				×
23	[40]																							×	×	×				×	
24	[41]										×							×					×	×	×	×	×	×	×	×	×
25	[42]																	×								×	×	×		×	×
26	[43]										×													×	×						×
27	[16]															×		×			×	×	×	×		×	×	×	×	×	
28	[44]																	×						×	×	×	×	×	×	×	
29	[45]																	×						×	×	×	×	×	×	×	
30	[46]								×	×								×			×		×	×		×	×	×	×	×	×

Table 1. *Cont.*

N	Literature Review	El	Sl	Rf	DD	LD	G	Gm	LU/LC	Vg	TPI	TWI	ND	MF	ST	STh	R	SPI	ASPR	SPS	WTF	WTD	SWB	AR	Aspect	D	M	RI	ED	GWQ	NGWR
31	[47]		×	×	×	×	×		×	×		×	×	×																	
32	[48]		×	×	×	×	×	×							×				×	×											
33	[4]		×	×	×	×	×	×							×																
34	[49]	×	×	×	×	×	×	×	×																						
35	[50]		×	×	×	×	×								×	×															
36	[19]		×	×		×	×					×													×						
37	[51]		×		×	×	×	×	×																						
38	[52]	×		×	×	×	×	×	×						×					×		×									
39	[53]		×	×	×	×	×	×	×							×															
40	[54]	×	×	×	×	×	×	×																		×	×	×	×		
41	[55]		×		×	×	×	×							×												×	×	×		
42	[56]		×	×	×	×	×	×	×						×							×									
43	[57]	×	×	×	×	×	×	×	×	×		×			×																
44	[58]		×		×	×	×	×							×						×										
45	[59]	×	×		×	×	×		×					×	×																

El = Elevation, Sl = Slope, Rf = Rainfall, DD = Drainage Density, LD = Lineament Density, G = Geology, Gm = Geomorphology, LU/LC = Land Use/Land Cover, Vg = Vegetation (NDVI), TPI = Topographic Position Index, TWI = Topographic Wetness Index, ND = Node Density, MF = Major Faults, ST = Soil Type, STh = Soil Thickness, R = Roughness, SPI = Stream Power Index, ASPR = Available Space for Recharge, SPS = Sand Percentage in the Soil, WTF = Water Table Fluctuation, WTD = Water Table Depth, SWB = Surface Water Body, AR = Apparent Resistivity, D = Depressions, M = Morphometry, RI = Radar Intensity, ED = Earthquake Density, GWQ: Groundwater quality, NGWR: Net Groundwater Recharge potentiality.

2. Site Description

The study area is located in the Nile valley, east of the cities of Idfu and Esna (Figure 1a). It crosses through the center of the Eastern Desert in a NE–SW direction. Geographically, it is bounded by the longitudes 32°33′ and 34°15′ E and the latitudes 24°52′ and 25°37′ N. It has a wide surface area that reaches around 8000 Km². The area's relief ranges from + 1043 m at the upstream portion to +74 m in the downstream parts. The central Eastern Desert is classified as an arid to hyper-arid region with an annual mean precipitation of about 8 mm/year, while the maximum air temperature was 43.7 °C and the minimum air temperature recorded during the period from 1981 to 2019 was 3 °C [60]. Geomorphologically, the Eastern Desert is separated into four major morphologic units, including the Red Sea crystalline mountains, the southern Sandstone plateau, the northern dissected limestone plateaus, and the narrow coastal plain. According to [61], the study area is mostly located on the Nubia Sandstone's southern sandstone plateau (Figure 1a). On the regional scale, the study area can be divided into two distinct topographic zones. The first is rugged, with high relief, and is made up of basement rocks. The second zone has low relief and is made up of sedimentary rocks. This zone slopes gently westward towards the Nile River and rises further east more steeply towards the basement range. Wadi Abadi and its subbasins, (e.g., El Baramya, Um Tanduba, El Shaghab, and El Myah) are located to the south of the study area. Among the studied catchments, Wadi Abadi has the largest drainage network, which covers about 6700 km². It extends 200 Km to the east until reaches the Red Sea mountainous terrains. To the north of the Abadi basin, many Wadies dissect the area from the east to the west, including Nuzul, El-Shikh Ali, Domi, Salah Nasr, Al-Mafallis, Hilal, Abu-Almahamid, El-Shaykh Nagar, Salim Judah, El-sharwna El-keblya, El-sharwna El-baharya, Kelabya, El-sabil, El-Dir, and El-Foley (Figure 1b). These Wadies are mostly cut in the sandstone plateau and do not reach the basement terrains.
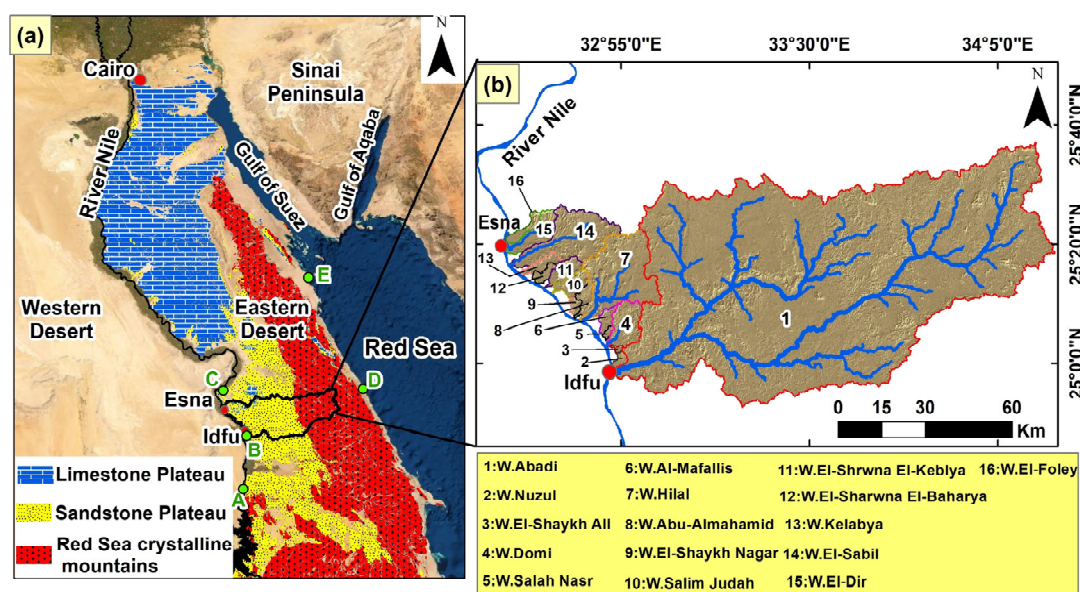

Figure 1. (**a**) General map of Egypt illustrating the geographic location of the study area associated with the nearest meteorological rain gauge stations (A: Aswan, B: Idfu, C: Luxor, D: Marsa Alam, and E: Hurghada); (**b**) close-up view of the different wadies dissecting the study area trending in an east–west direction.

3. Geological Setting

The East Esna–Idfu region is dominated by sedimentary succession ranging in age from Precambrian to recent. The exposed rock units are represented by a sedimentary succession underlain by Precambrian basement rocks. Taref Sandstone is a member of the Nubia Formation that overlies Precambrian rocks. Upper Cretaceous rocks lie non-

conformably on top of Precambrian basement rocks and are divided into four formations, including (from bottom to top) Nubia Sandstone, Quseir variegated shale, then Duwi and Dakhla formations [62]. The exposed sedimentary successions in the area are mainly marked by Upper Cretaceous rocks, and they mainly consist of Nubia Sandstone Fm. and Quseir Fm., covering the majority of the investigated area. The geological map shows the distribution of the rock units along Wadi Abadi (Figure 2).
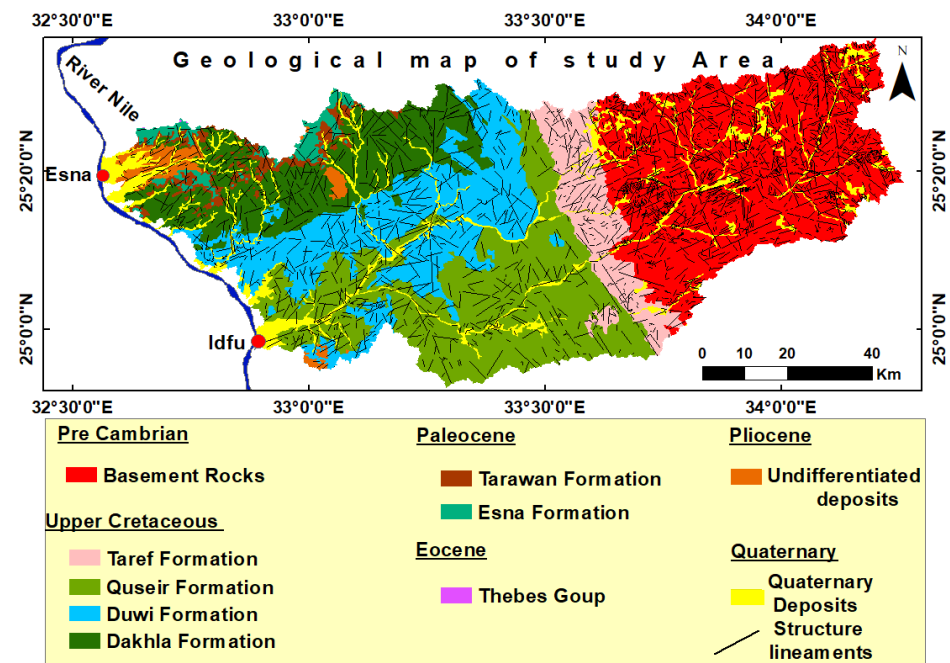

Figure 2. The distribution of various lithological units associated with extracted lineaments is shown on a geological map of the study area.

4. Methodology and Data

The current manuscript used several types of data to define the groundwater potential zones in the study area. In Figure 3, a flow chart illustrates the integrated approaches that were used to create the final map of groundwater potential zones during the current study. Four types of satellite remote sensing data were prepared for digital image processing, along with geologic maps [62] and fieldwork data, to create the groundwater characteristic layers needed to generate the potential groundwater map. The remote sensing data sources, included (1) a Landsat-8 Operational Land Imager (OLI) satellite image acquired on 1 July 2021 with a 30 m spatial resolution as well as a panchromatic band with a 15 m spatial resolution; (2) sentinel-2A satellite image data with a 10 m spatial resolution acquired on 29 June 2021; (3) Shuttle Radar Topography Mission (SRTM)s' Digital Elevation Model (DEM) of 1 arc-sec data with a 30 m resolution downloaded from [63]; and (4) The Modern-Era Retrospective Analysis for Research and Applications, version 2 (MERRA-2) Rainfall data of the last four decades over 39 years between January 1981 and December 2019 downloaded from [60]. MERRA-2 precipitation values were calibrated by the nearest meteorological rain gauge stations (Idfu, Aswan, Luxor, Hurghada, and Marsa Alam) and were obtained from the Egyptian meteorological authority. Principal component analyses (PCA), band ratio, and false color composite techniques were all used in this study to analyze spatial data. Lithology, lineament, major fractures, and soil type layers were all generated using these techniques. SRTM-DEM, sentinel-2A (verified by Google Earth), and MERRA-2 data were used to create elevation, slope steepness, drainage density, land use/land cover, distance from the channel network, and rainfall layers. To create these thematic layers, remote sensing and GIS techniques were used in different software environments, including ArcGIS 10.8 and Envi 5.1.
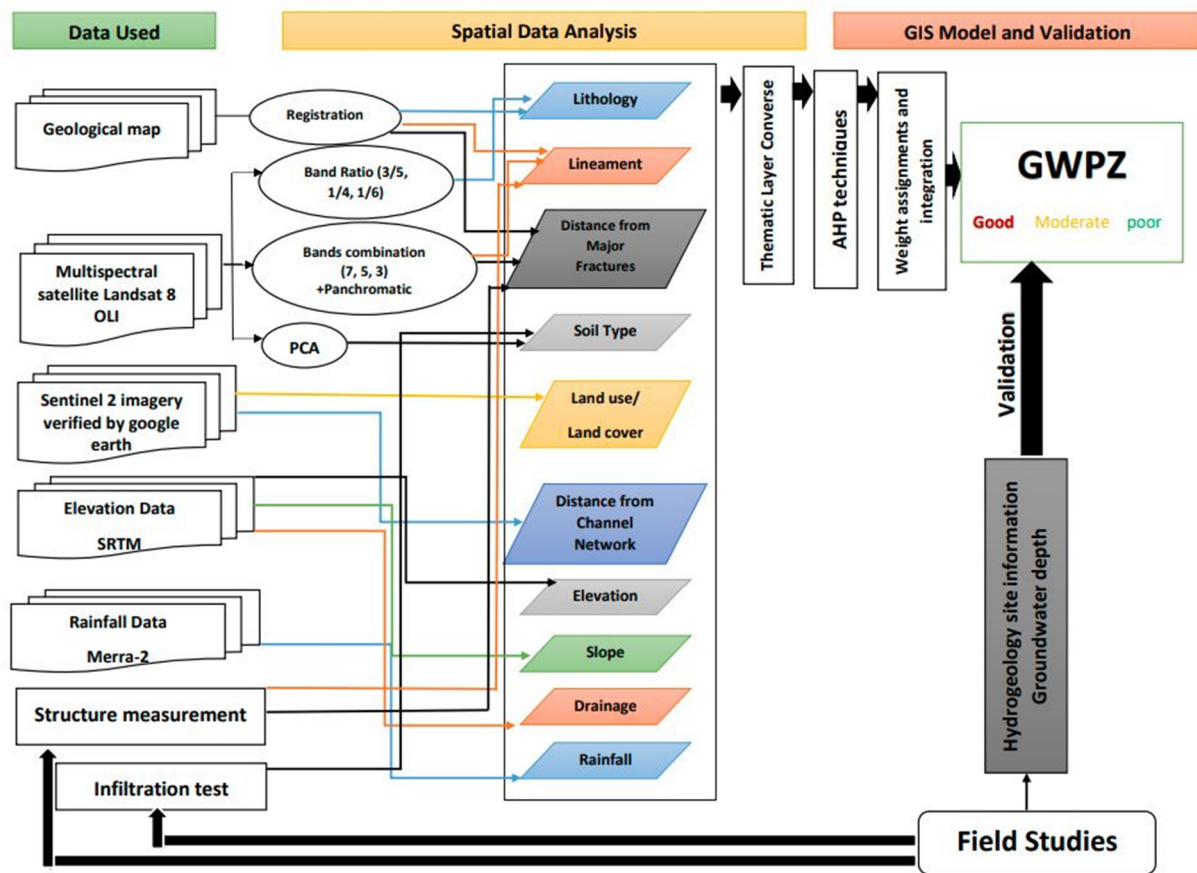
Figure 3. The flowchart illustrates the procedures involved in creating a groundwater potential zone map.

The most popular and well-known knowledge-driven GIS-technique-based method for distinguishing groundwater potential zones is a multi-criteria decision analysis using the analytical hierarchical process (AHP) [16,54]. This method helps in the integration of all thematic layers. This study included a total of ten different thematic layers. The ArcGIS 10.8 software was used to convert each continuous layer into a thematic layer with about five classes. Some guidelines were taken in the GIS model, including (1) based on their respective contributions to the occurrence of groundwater, assigning the following weight values (5, 4, 3, 2, or 1) to each class within the layer, with the greatest value going to high-potential areas; (2) ten groundwater parameters were integrated using an index overlay model; and (3) model validation using the static water level in the field. The weighting of these influencing factors was based on their reaction to the occurrence of groundwater and an expert viewpoint. A high weight parameter represents a layer with a large impact on groundwater potential, whereas a low weight parameter represents a layer with a minimal impact. The relative importance values of each parameter were assigned according to Saaty's scale (1–9). In addition, the weights were assigned based on a review of previous studies and field experience. According to Saaty's relative importance scale, a value of 9 indicates extreme importance, 8 indicates very strong importance, 7 indicates very strong to extreme importance, 6 indicates more than strong importance, 5 indicates strong importance, 4 indicates more than moderate importance, 3 indicates moderate importance, 2 indicates weak importance, and 1 indicates equal importance.

All of the thematic layers were compared to one another in a pair-wise comparison matrix (Table 2). The classes of each thematic layer ranking were awarded a score from 1 to 5 based on their proportionate effect on groundwater potentiality. Table 3 illustrates the criteria weight percent of the thematic layers associated with the rank and area of each class within every thematic layer. The following steps were used to calculate the consistency

ratio (CR): (1) the Eigen vector technique was used to calculate the principal Eigen value (Λ) (Table 4), and (2) Equation (1) was used to obtain the consistency index (CI):

$$\Lambda\text{max} = 100/10 = 10$$

$$CI = \frac{L\text{max} - n}{n - 1} \tag{1}$$

where, n denotes the number of analyzed parameters.

$$Cl = (10 - 10)/(10 - 1) = 0$$

Table 2. Pair-wise comparison matrix of the ten thematic layers used in the current study.

Them	Assigned Weight	Elevation	Slope	Rainfall	Drainage Density	Lineament Density	Major Fractures	LULC	Lithology	Soil Type	Channel Network	Criteria Weight	Criteria Weight (Percent)
Elevation	3	3/3	3/3	3/5	3/4	3/6	3/3	3/2	3/7	3/8	3/3	0.068	6.8%
Slope	3	3/3	3/3	3/5	3/4	3/6	3/3	3/2	3/7	3/8	3/3	0.068	6.8%
Rainfall	5	5/3	5/3	5/5	5/4	5/6	5/3	5/2	5/7	5/8	5/3	0.113	11.4%
Drainage Density	4	4/3	4/3	4/5	4/4	4/6	4/3	4/2	4/7	4/8	4/3	0.091	9.1%
Lineament Density	6	6/3	6/3	6/5	6/4	6/6	6/3	6/2	6/7	6/8	6/3	0.136	13.6%
Major Fractures	3	3/3	3/3	3/5	3/4	3/6	3/3	3/2	3/7	3/8	3/3	0.068	6.8%
LULC	2	2/3	2/3	2/5	2/4	2/6	2/3	2/2	2/7	2/8	2/3	0.045	4.5%
Lithology	7	7/3	7/3	7/5	7/4	7/6	7/3	7/2	7/7	7/8	7/3	0.159	15.9%
Soil Type	8	8/3	8/3	8/5	8/4	8/6	8/3	8/2	8/7	8/8	8/3	0.181	18.2%
Channel Network	3	3/3	3/3	3/5	3/4	3/6	3/3	3/2	3/7	3/8	3/3	0.068	6.8%

Table 3. Factors influencing groundwater potential zones were classified associated with the area of each class.

Thematic Layer	Criteria Weight (%)	Class		Rank	Area km^2	Area (%)
(1) Elevation (DEM)	6.8	74–208 (ma.s.l)	(Very Low)	5	1122.4	14.1
		208–302 (ma.s.l)	(Low)	4	2903.2	36.4
		302–407 (ma.s.l)	(Moderate)	3	1768.6	22.1
		407–534 (ma.s.l)	(High)	2	1324.8	16.6
		534–1043 (ma.s.l)	(Very High)	1	866.5	10.9
(2) Slope Steepness (Degree)	6.8	0–3.6°	(Flat)	5	3299.9	41.3
		3.6–7.6°	(Gentle)	4	2601.6	32.6
		7.6–12.9°	(Moderate)	3	1308.9	16.4
		12.9–20°	(Steep)	2	598.1	7.5
		20–67.1°	(Very Steep)	1	177.1	2.2
(3) Drainage Density	9.1	1.112–1.171 (km/km^2)	(Very Low)	1	2586	32.4
		1.171–1.215 (km/km^2)	(Low)	2	2213.2	27.7
		1.215–1.259 (km/km^2)	(Moderate)	3	1840.6	23.1
		1.259–1.326 (km/km^2)	(High)	4	1200	15
		1.325–1.434 (km/km^2)	(Very High)	5	145.7	1.8

Table 3. *Cont.*

Thematic Layer	Criteria Weight (%)	Class		Rank	Area km²	Area (%)
(4) Rainfall	11.4	2.33–3.46 (mm)	(Very Low)	1	4608.3	57.7
		3.46–4.15 (mm)	(Low)	2	1706.5	21.4
		4.15–5.08 (mm)	(Moderate)	3	912.8	11.4
		5.08–6.21 (mm)	(High)	4	415.3	5.2
		6.21–7.67 (mm)	(Very High)	5	342.6	4.3
(5) Lineament Density	13.6	0.27–0.47 (km/km²)	(Very Low)	1	1784.7	22.3
		0.47–0.67 (km/km²)	(Low)	2	3531.7	44.2
		0.67–0.87 (km/km²)	(Moderate)	3	885	11.1
		0.87–1.08 (km/km²)	(High)	4	1114.7	14
		1.08–1.28 (km/km²)	(Very High)	5	669.3	8.4
(6) Distance from Major Fractures	6.8	<200 (m)	(Very Near)	5	212.2	2.7
		200–400 (m)	(Near)	4	231.5	2.9
		400–600 (m)	(Intermediate)	3	242	3
		600–800 (m)	(Far)	2	245.7	3
		800–1000 (m)	(Very Far)	1	148.7	3.1
(7) Lithology	15.9	Wadi Deposits (Quaternary) Different types of soil		5	810.3	10.1
		Taref Fm. (Paleozoic–Cret. "Turonian") Sandstone, fine to medium grained		4	526.1	6.6
		Issawia Fm. (Pliocene) Sandy clays, marls, shales, siliceous brecciated limestone, and conglomerates		3	114.6	1.4
		Duwi Fm. (Upper Cret. "Maastrichtian") Phosphate beds with black shale, marl, and oyster bed sandstone.		3	1339.6	16.8
		Tarwan Fm. (Paleocene) White Chalk and chalky limestone		3	164.4	2.1
		Thebes Group (Eocene) Chalk and chalky limestone bed rich in chert beds		3	3.6	0.1
		Quseir Fm. (Upper Cret. "Campanian") Varicolored shale, siltstone, and flaggy sandstone		2	1535.1	19.2
		Dakhla Fm. (Upper Cret. "Maastrichtian") Dark grey shallow marine marl and shale with intercalated limestone		2	1004.3	12.6
		Esna Fm. (Paleocene) Green to grey shales with gypsum veinlets altered with a marl bed		2	142.8	1.8
		Precambrian Basement rocks Igneous, metamorphic, and metasediments		1	2344.7	29.4
(8) Land Use/Land Cover	4.5	Wadi Deposit		5	685.7	8.6
		Natural desert grassland		5	29.7	0.4
		Cultivated Land		4	104	1.3
		Mining Area		2	106.7	1.3
		Barren Land		1	7059	88.4

Table 3. *Cont.*

Thematic Layer	Criteria Weight (%)	Class		Rank	Area km^2	Area (%)
(9) Soil Type (according to in-filtration rate)	18.2	Index 1 Infiltration capacity equilibrium = 13.8mm/min	(Very high)	5	218.8	2.7
		Index 2 Infiltration capacity equilibrium = 4.5mm/min	(High)	4	271.3	3.4
		Index 3 Infiltration capacity equilibrium = 2mm/min	(Moderate)	3	122.9	1.5
		Index 4 Infiltration capacity equilibrium = 0.53mm/min	(Low)	2	213.4	2.7
		Index 5 Not Soil "Rock"	(Very low)	1	7158.9	89.7
(10) Distance from Channel Network	6.8	0–600 (m)	(Very Near)	5	63.2	0.8
		601–1200 (m)	(Near)	4	38.6	0.5
		1201–1800 (m)	(Intermediate)	3	35.4	0.4
		1801–2400 (m)	(Far)	2	39	0.5
		2401–3000 (m)	(Very Far)	1	43.4	0.5

Table 4. The results of the consistency ratio.

Theme	Elevation	Slope	Rainfall	Drainage Density	Lineament Density	Major Fractures	LULC	Lithology	Soil Type	Channel Network	Weight Sum (Value)	λ
Elevation	0.068	0.068	0.068	0.068	0.068	0.068	0.068	0.068	0.068	0.068	0.682	10
Slope	0.068	0.068	0.068	0.068	0.068	0.068	0.068	0.068	0.068	0.068	0.682	10
Rainfall	0.114	0.114	0.114	0.114	0.114	0.114	0.114	0.114	0.114	0.114	1.136	10
Drainage Density	0.091	0.091	0.091	0.091	0.091	0.091	0.091	0.091	0.091	0.091	0.909	10
Lineament Density	0.136	0.136	0.136	0.136	0.136	0.136	0.136	0.136	0.136	0.136	1.364	10
Major Fractures	0.068	0.068	0.068	0.068	0.068	0.068	0.068	0.068	0.068	0.068	0.682	10
LULC	0.045	0.045	0.045	0.045	0.045	0.045	0.045	0.045	0.045	0.045	0.455	10
Lithology	0.159	0.159	0.159	0.159	0.159	0.159	0.159	0.159	0.159	0.159	1.591	10
Soil Type	0.182	0.182	0.182	0.182	0.182	0.182	0.182	0.182	0.182	0.182	1.818	10
Channel Network	0.068	0.068	0.068	0.068	0.068	0.068	0.068	0.068	0.068	0.068	0.682	10

The consistency ratio was defined using Equation (2), as follows:

$$CR = CI/RC \qquad (2)$$

where RCI is the value of the random consistency index, whose values were taken from Saaty's standard (Table 5).

$$CR = 0/1.49 = 0$$

According to [64], a CR of 0.10 or less is appropriate for the analysis to continue. If the consistency value is larger than 0.10, the judgement should be revised to identify the sources of inconsistency and correct them. If the CR value is 0, it means that the pair-wise comparison has a perfect level of consistency. All ten thematic layers were combined in ArcGIS software using the weighted overlay analysis approach of Equation (3) to build a groundwater potential zone map for the research region [16,65].

Table 5. Saaty's ratio index for various N values.

	The Indices of Consistency of Randomly Generated Reciprocal Matrices [64]									
	The Matrix's Order									
N	1	2	3	4	5	6	7	8	9	10
RCI value *	0.00	0.00	0.58	0.90	1.12	1.24	1.32	1.41	1.45	1.49

* Random Consistency Index.

$$GWPZ = \sum_{i}^{n}(XA \times YB) \tag{3}$$

where, GWPZ refers to the groundwater potential zone, X denotes the weight of the thematic layers, and Y denotes the rank of the thematic layer class. The thematic map is represented by the A term (A = 1, 2, 3, ... , X), and the thematic map classes are represented by the B term (B = 1, 2, 3, ... , Y). The final groundwater potential zone map was divided into three groups: poor, moderate, and good.

Soil infiltration tests and sieve analyses were carried out in locations with different soil types that were selected based on the discrimination created by PCA technique to measure the infiltration capacity and calculate the hydraulic conductivity and specific yield using the Hazen method [66]. Sampling cores were made in Nubia Sandstone water-bearing rock at two different hand-dug wells located within Wadi Abadi to measure the actual porosity and permeability using a KA-210 gas permeameter and porosimeter and to identify the homogeneity of the major aquifer in the study area related to groundwater potentiality. A prediction of the rainfall return period for the future was made using the hydrologic engineering center (HEC) software to understand the behavior of rainfall and its impact on the aquifer potentiality in the study area. In order to undertake a frequency analysis and other statistical calculations, the HEC software supported a number of statistical software packages, such as HEC-DSSVUE and HEC-SSP2.2. HEC-DSSVUE allows users to edit and manipulate data in an HEC_DSS database file. HEC-SSP performs statistical analyses of hydrologic data.

5. Results and Discussion

5.1. Hydrogeological Condition

In the study area, three major aquifers have been identified; (a) an unconfined Quaternary alluvium aquifer; (b) a semi-confined Nubia Sandstone aquifer, which was detected in the middle and downstream of the Abadi basin; and (c) a Precambrian fractured basement aquifer. The inspection of well log data for three drilled wells illustrated that the Nubia Sandstone aquifer is the main water-bearing formation in the Abadi basin. This aquifer was tapped by 16 water points located at the main course of the wadi. Moreover, the fractured basement was tapped by six water points at the upstream portion of Wadi Abadi. Based on new drilling activity in the study area, two well log data points (well 8 and well 9) were obtained to illustrate the subsurface succession of the Nubia Sandstone aquifer, which is represented by the Taref Sandstone Formation. The cross-section (Figure 4) shows that the total penetrated thickness is about 360 m of fine to medium Sandstone with sandy shale and/or shale lenses. The two drilled wells fully penetrate the total thickness of the sandstone to the basement rocks at 425 m and 416 m at well 8 and well 9, respectively. The flow of groundwater generally runs from east to west. The depth to water ranges from 55 m to 44 m. The total dissolved salts in the three aquifers range from 1241 to 5826 mg/L. On the other hand, the Quaternary aquifer was detected in the Wadi El Dir area and was tapped by 11 water points. The depth to water ranged from 20 m to 63 m. The water level data of the three aquifers were used to validate the result of the tested model.
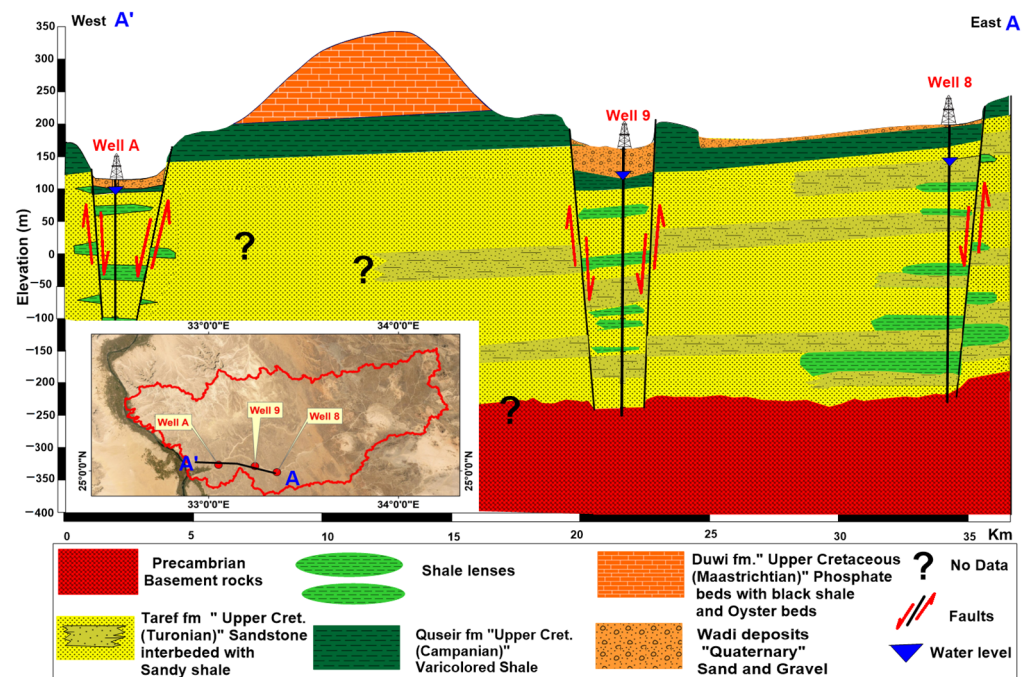
Figure 4. Schematic hydrogeological cross section (A–A') illustrates the subsurface lithological composition of the Nubia Sandstone aquifer at Wadi Abadi.

5.2. Preparation of Thematic Layers Influencing Groundwater Recharge

Remote sensing satellite data were utilized in this work to construct ten thematic factors (features) that govern groundwater potentiality. These features are elevation, slope steepness, drainage density, rainfall, lineament density, the distance from major fractures, lithology, land use/land cover, soil type, and the distance from the channel network. The paragraphs that follow explain in detail how each factor was generated from satellite data as well as the link to groundwater potentiality.

5.2.1. Elevation

Elevation has an indirect and inverse proportion to groundwater potentiality. As a result, greater elevations promote more recharge and assure groundwater supplies in a watershed's lowland parts. Mountainous areas typically contribute to recharging low-lying confined aquifers. [67,68]. Water tends to accumulate more at lower elevations than at higher elevations.

The digital elevation model (DEM) (Figure 5a) of the study area and SRTM-DEM data were used. The DEM is classified into five zones (Figure 5b) in the study area. The elevation ranges from 74 to 1043 m a.s.l. Very high elevations and the highest elevations are located in the eastern part, where basement rocks exist. Low-elevation zones encourage water accumulation and infiltration. The altitudes were reclassified into five groups depending on their ability to store and collect surface water. These classes included the following: very low (74–208), low (208–302), moderate (302–407), high (407–534), and very high (534–1043) elevations, covering around 14, 36, 22, 16.6, and 10.8 percent of the surface area, respectively. Very low and low elevations were given high weights. High and very high elevations were awarded low weights according to their relation to groundwater recharge.
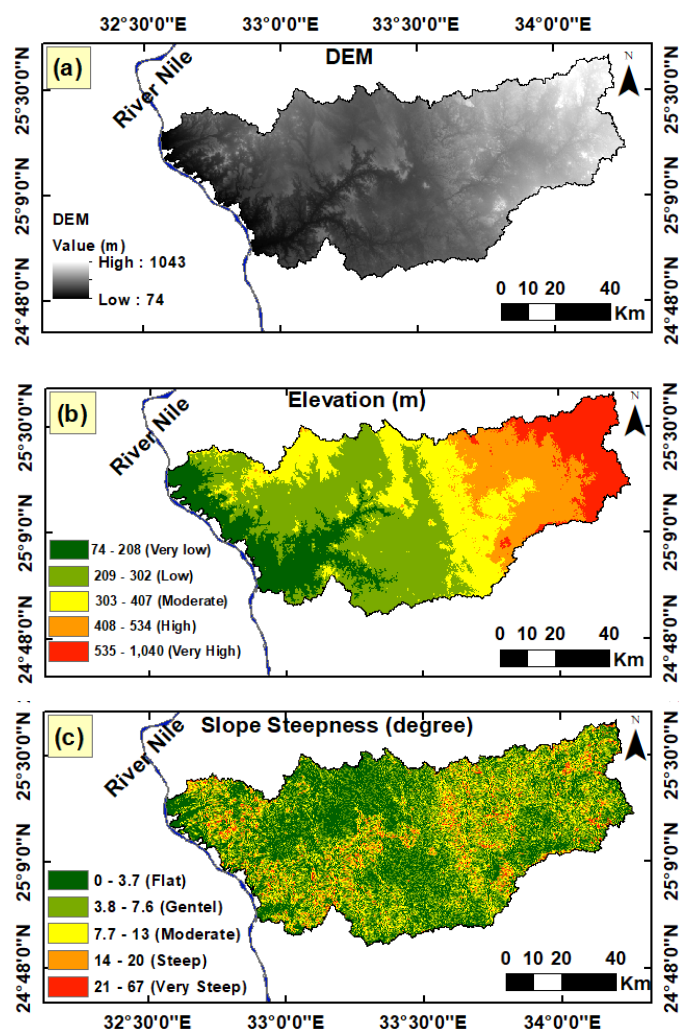
Figure 5. Digital elevation model and its derivatives. (**a**) SRTM-DEM data of the study area; (**b**) Elevation class map for the study area; (**c**) slope steepness map in degrees extracted from the digital elevation model.

5.2.2. Slope Steepness

Slope has a significant impact on the occurrence and movement of surface water and groundwater. Therefore, the slope can be a significant factor in runoff and infiltration. Groundwater prospecting areas were determined using the slope layer as an important feature [23]. Because the surface runoff resulting from precipitation flows quickly down to low-lying areas during rainfall storms, high slopes make a non-significant contribution to groundwater recharge.

The slope ranges from 0° to 67.14° (Figure 5c). From the slope map, the high slope steepness that ranges from 20.1 to 67.144 degrees is located around the main streams of the Abadi watershed, in the basement rocks, and in the northern area close to the limestone plateau. On the other hand, low-slope zones are preferable places for water accumulation and infiltration. The slope steepness values were classified into five categories based on their ability to store water. The slope steepness classes included the following: very gentle (0–3.6), gentle (3.6–7.6), moderate (7.6–12.9), steep (12.9–20), and very steep (20–67.1), covering approximately 41, 32.5, 16, 7, and 2 percent of the area, respectively. Very gentle and gentle slopes were given high weights. The steep and very steep slopes were awarded low weights since they do not give enough time for surface runoff to infiltrate and reach the shallow aquifer.

5.2.3. Density of Drainage Network

The drainage pattern and density provide excellent indicators of the hydrogeological properties of the land. Several factors influence the shape of the drainage pattern in a drainage basin, including the structure, climate, topography, soil type, geology, and vegetation [69,70]. The main patterns that characterize the study area are parallel and dendritic drainage patterns. In the upper and middle parts of the wadies, especially the largest one (Wadi Abadi), a dendritic drainage pattern can be seen, whereas a parallel drainage pattern characterizes the lower part near the outlets on the Nile River. The drainage networks in the investigated area (Figure 6a) were derived from SRTM-DEM data and processed in ArcGIS software using spatial analyst tools. The drainage density is the total length of streams per unit of area [71].
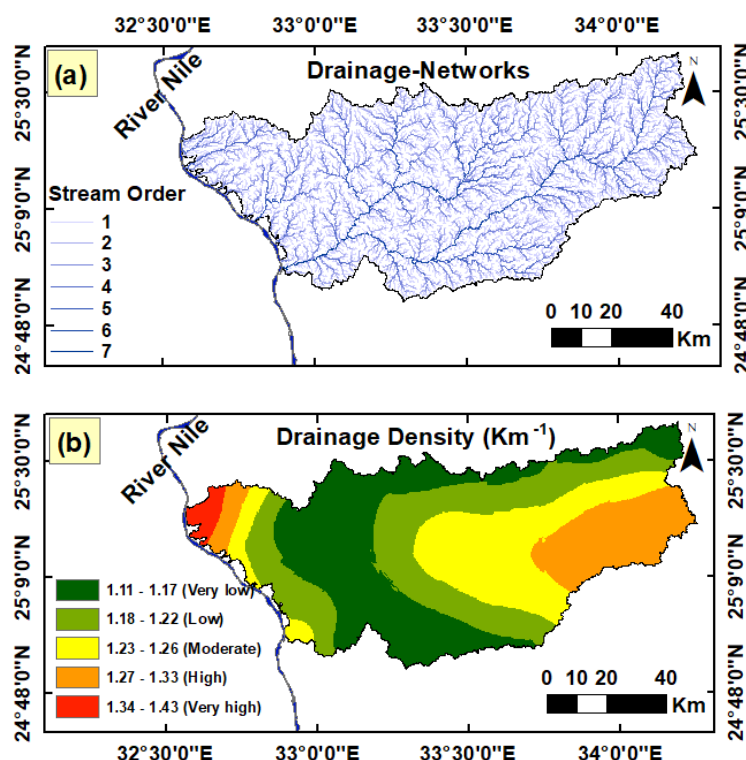
Figure 6. (**a**) Thematic layer of drainage networks of the study area extracted from DEM in the ArcGIS environment; (**b**) Drainage density map of the study area to illustrate the density distribution of the streams.

Several studies have found that the density of stream networks is inversely related to the rate of recharge processes [29,51], but other researchers have stated that the high drainage density reveals a high infiltration capability due to the highly dissected land surface [28,43,50]. In this research, we linked high-density locations to increased suitability for recharging and infiltration capacity. The average drainage density of the study area was 1097 km/km^2. The investigation and analysis of the drainage density map (Figure 6b) showed that high-drainage-density zone is located in the northwestern and eastern parts of the study area. Based on the availability of recharging and the infiltration capacity, the generated drainage density map was classified into five categories: very low (1.11–1.17 km/km^2), low (1.17–1.21 km/km^2), moderate (1.21–1.25 km/km^2), high (1.25–1.32 km/km^2), and very high (1.32–1.43 km/km^2), covering around 32, 27.7, 23, 15, and 1.8 percent of the studied surface area, respectively. Very high drainage density areas and high-drainage-density areas were given high weights. Low-drainage-density areas and very low drainage density areas were awarded low weights.

5.2.4. Precipitation (Rainfall Distribution)

In this study, The Modern-Era Retrospective Analysis for Research and Applications, version 2 (MERRA-2) for precipitation data were used to evaluate the amount of precipitation in the study area and to generate the rainfall layer used in the GIS model. Following the introduction of NOAA-18 in 2005, MERRA had no new satellite observation sources. MERRA-2, on the other hand, includes a slew of extra satellite observations both before and after this period. MERRA-2 is the latest atmospheric reanalysis of the modern satellite era produced by NASA's Global Modeling and Assimilation Office (GMAO) [72]. It is made available on a worldwide grid with a spatial resolution of 0.5° of latitude by 0.5° of longitude. MERRA-2 provides data beginning in 1981, so it is better than TRMM, which provides data beginning in 1997 because MERRA-2 has more historical data, and the MERRA-2 dataset produces more accuracy than the TRMM dataset [73,74].

To validate the MERRA-2 precipitation in the study area, two different methods were used in this research. First, the calibration of MERRA-2 with values from the nearest metrological rain gauge stations (Idfu, Aswan, Luxor, Hurghada, and Marsa Alam) using 10 values in different years with associated rainfall events. This validation was carried out using the following method: (a) drawing a scatter plot between MERRA-2 and the data of the metrological rain gauge stations, which showed a high R2 value (R2 = 0.98) (Figure 7a); (b) for land stations close to the study area, by validating the nearest rain gauge station (Idfu) on 14 January 1997 (rain gauge = 4.7, while MERRA-2 = 4.29) and in May-2020 (rain gauge = 5.4, while MERRA-2 = 5.27), MERRA-2 gave high accuracy; and (c) calibration of Hurghada station in October-2016 (rain gauge = 51.6, while MERRA-2 = 36.9) and Aswan station in May-1993 (rain gauge = 0.5, while MERRA-2 = 0), which showed that MERRA-2 is a conservative (underestimating) value. For the second method, we used daily soil moisture index (SMI) data available from [75], but unfortunately the lack of data before 2007 prevented the confirmation of all storms. Therefore, we are focused on the storm of 26–27 October 2016 by measuring the SMI during and after the effects of the storms (Figure 7b,c).

Figure 7d illustrates the rainfall accumulation comparison between the upstream and downstream regions of the study area during a 39-year period (1981–2019). The topographic effects were strongly reflected in the rainfall distribution. The upstream parts of the basin (1043 m a.s.l.) received significantly more rainfall than the lower parts of the basin, which received <20 mm near the Nile River. Despite the paucity of rainfall in the study area, occasional flash flood events are recorded in the study area once every 3 to 4 years, especially in the Eastern Desert. These flash floods are very important for recharging groundwater aquifers. Many storms occurred in the last four decades. The investigation of the obtained rainfall data showed that the biggest rainfall storms that led to flash floods occurred in 1986, 1993, 1997, and 2016. Climate change has had a significant impact on the reduction in large rainfall storms since 1997.

The rainfall thematic layer (Figure 7e) was constructed using monthly MERRA-2 average annual rainfall data for 39 years (from January 1981 to December 2019) for gridded points and interpolated a raster surface from points using kriging ArcGIS software. The rainfall map was then classified into five zones based on the amount of rainfall. The very low (2.33–3.46 mm), low (3.46–4.15 mm), moderate (4.15–5.08 mm), high (5.08–6.21 mm), and very high (6.21–7.67 mm) rainfall classes covered around 57.7, 21, 11, 5, and 4 percent of the land, respectively. The very high rainfall class and the high-rainfall class were given high weights. The low-rainfall class and very low rainfall class were awarded low weight.
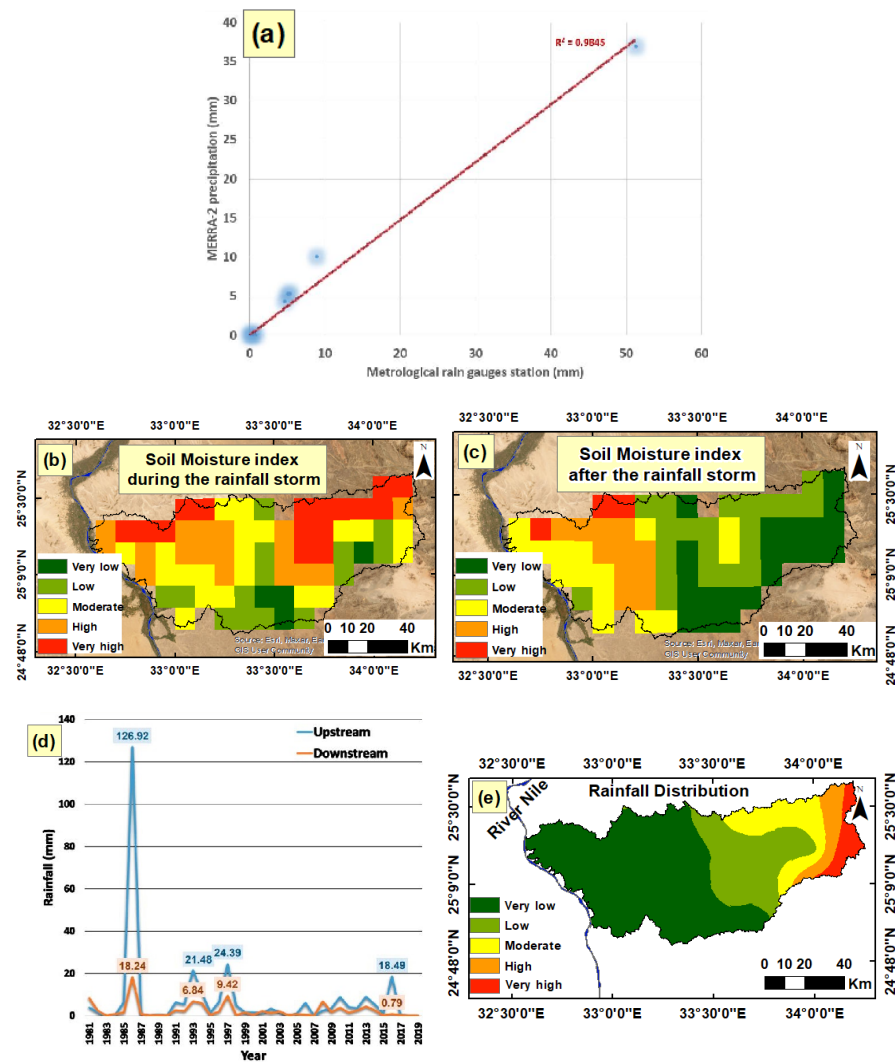
Figure 7. (**a**) Scatter plot of ten values in some rainfall events for validation of MERRA-2 precipitation by meteorological rain gauge stations near the study area (Idfu, Aswan, Luxor, Hurghada, and Marsa Alam) associated with R2; (**b**) Daily soil moisture index (SMI) during the major storm on 26 October 2016; (**c**) Daily soil moisture index (SMI) after the major storm on 28 October 2016; (**d**) A comparison of accumulated annual rainfall between the upstream and downstream parts of the study area during the 39 years from 1981 to 2019; (**e**) Average annual rainfall map of the last four decades (1981–2019).

5.2.5. Structure Lineament Density

Lineament is a significant feature to be considered when investigating groundwater potentiality. Cracks, fissures, faults, shear zones, and joints are formed as a result of the tectonic stress/strain. These linear features, which are considered secondary porosities, are responsible for infiltrating surface runoff and recharging shallow groundwater aquifers. High lineament density correlates strongly to high groundwater potentiality [76–78]. In the eastern part of the study area, basement complex rocks have undergone significant polyphase deformation. Joints, faults, folds, foliations, shear zones, and rock cleavages are all caused by these deformations. Remote sensing data, such as the panchromatic band of Landsat 8 as well the Landsat 8 band combination (7,5,3) were associated with a published geological map [62] to visually extract structure lineaments.

The analysis and investigation of Figure 8a display the spatial distribution of the structure lineaments in the study area. Moreover, the associated rose diagram for these linear features in basement rocks and soft rocks illustrates the major trends of the lineaments. Three significant major trends emerged from the rose diagrams. The NW–SE trend formed

as a result of Red Sea tectonic activity. Furthermore, the NE–SW direction is considered the major structural trend controlling the formation of Wadi Abadi. Moreover, the inspection of a hand-dug well in the Nubian sandstone aquifer (well no. 11) showed the subsurface continuity of that trend in the subsurface succession (Figure 8d). The creation of the porous and permeable zone for probable recharging processes and managing groundwater flow is structurally related, which creates a conduit acting as pipes transferring both groundwater and surface water. Moreover, the NW–SE and NNE–SSW trends that characterize the Arabian-Nubian Shield across the Eastern Desert of Egypt have been detected in the study area (Figure 8e). The lineament density was computed using Equation (4) of [79].

$$Ld = \frac{\sum_{i=1}^{i=n} L}{A} \ (km^{-1}) \tag{4}$$
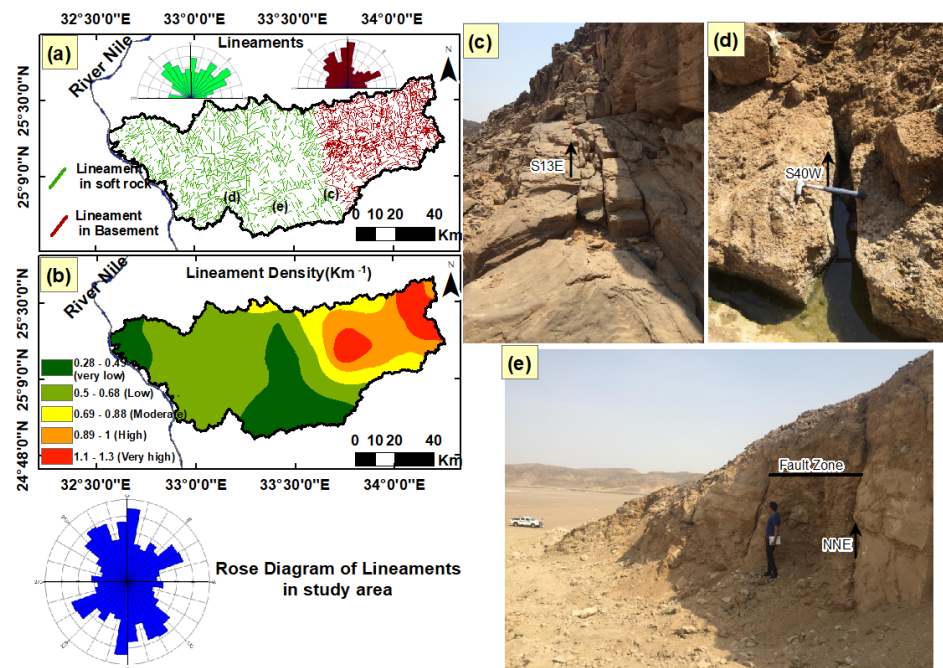
Figure 8. (**a**) Structure lineament network extracted from Landsat image and geologic maps. Rose diagrams for lineaments in basement and sedimentary rocks are also shown to illustrate the major trends controlling the groundwater recharge and flow; (**b**) Thematic layer of structure the lineament density map; (**c**) The NW–SE trend of fracture set in Nubia Sandstone exposures in Wadi Abadi; (**d**) The NE–SW trend of fracture was detected at the Nubia aquifer at the bottom of hand-dug well 11 in Wadi Abadi; (**e**) The trends of dominated fractures are NW–SE and NNE–SSW, which cross Wadi Abadi.

The estimated average lineament density was 0.67 km^{-1} for the whole study area, while the recorded values of the lineament density for the basement and soft rocks were 1 km^{-1} and 0.51 km^1, respectively. The higher values of lineament density in basement rocks positively affect the creation of porous and permeable zones favorable for probable recharging processes from precipitation and surface runoff. While the formation of the Nubia Sandstone aquifer was mainly based on its primary porosity between the classic sediments of the aquifer matrix, it was also affected by structural lineaments, raising its potentiality for aquifer recharging. According to these results, the lineament density is one of the most important factors affecting groundwater potentiality in the study area. A lineament density map (Figure 8b) was created by grading the study area by 10 min and splitting it into polygons, then calculating the lineament density for each polygon using the kriging method to interpolate a raster surface from points. The lineament density map was classified into five numerical groups. These classes were very low (0.27–0.49 km^{-1}), low (0.49–0.67 km^{-1}), moderate (0.67–0.87 km^{-1}), high (0.87–1.03 km^{-1}), and very high

$(1.03–1.28 \text{ km}^{-1})$. The percentage values of each lineament density class area were around 22, 44, 11, 13.9, and 8 percent of the total surface area of the studied locations, respectively. The very high and high lineament densities were given high weights. The low and very low lineament densities were awarded low weights.

5.2.6. Distance from Major Fractures

In hydrogeological studies, the distance from major fractures is also an important criterion because significant hydrogeological zones must be mainly located close to major linear structures [47]. The extracted map of major faults (Figure 9a) shows the major linear fractures affecting the basement and sedimentary rocks in the study area. The investigation of the rose diagram for these major fractures illustrated that the NNW–SSE trend is the dominant trend in soft rocks. This trend is mainly related to the effect of tectonic activity as a result of Red Sea opening. Moreover, the investigation of Landsat images with the extracted major faults in the arcGIS environment showed that the NNW–SSW trend formed a major graben in the southern part of the study area, especially at Wadi Abadi (Figure 9c,d). This graben was formed along the extension of the red sea trend, where two major faults running through the sandstone plateau were mapped. As a subsided block, the two faults bound the Quseir formation, which is composed of shales and siltstone of the Upper Cretaceous between two main blocks of the Nubian Sandstone (Taref Formation). This structural feature reflects the degree of deformation and tectonic reactivation in the study area, which have positive impacts on enhancing the recharging process for the shallow aquifer from surface runoff and the precipitated rainfall during a major event. Furthermore, the WNW–ESE trend is the dominant trend in the basement rocks in the Arabian-Nubian Shield's extension. In this study, the areas closest to major fractures (400 m) were the most promising for effective infiltration, but as distances increased further than 1000 m, the effect of this parameter vanished (Figure 9b). The area affected by this factor covers about 15% of the study area.
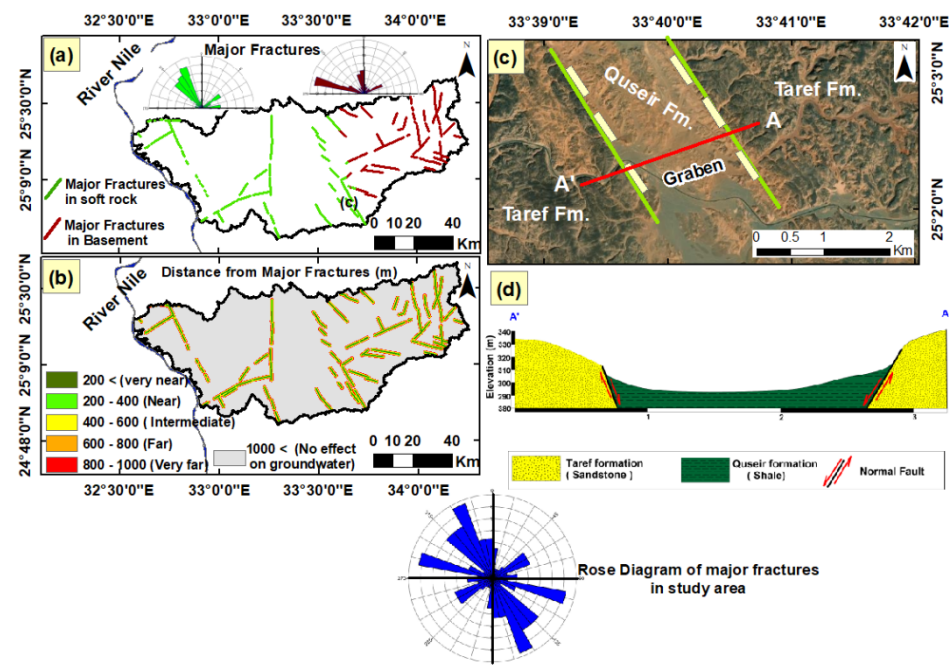
Figure 9. (**a**) Major fractures in basement and sedimentary rocks. Rose diagrams are also shown for major fractures, illustrating the main trends; (**b**) Thematic layer illustrate the distance from major fractures classes and values; (**c**) Close-up view from a satellite image illustrating the faulting processes, which controls both groundwater movement and aquifer recharge; (**d**) Cross section of the exposed rock, illustrating a graben structure formed as a result of two major faults trending NNW–SSE.

5.2.7. Lithology

The thematic layer of lithology is essential in groundwater potential mapping because the porosity and permeability of the surface layer mainly control the infiltration of the precipitated water into the shallow groundwater aquifers [56,57]. The interpretation of the false color composite (FCC) of the Landsat 8 band ratios (3/5, 1/4, and 1/6) associated with a published geological map [62] were used in the lithological discrimination of various rock units (Figure 10a,b). The eastern part of study area is dominated by massive crystalline basement rocks, while the western part is occupied by the Cretaceous/Tertiary succession. The basement rocks, Nubia Sandstone, Upper Cretaceous/Tertiary succession, and Quaternary deposits cover about 29.36, 6.59, 53.9, and 10.15% of the total area, respectively. The porosity and permeability of the Nubia Sandstone Formation and Wadi deposits, which are composed of friable sand and gravel, are great aspects for groundwater recharge. On the other hand, shale and basement rocks have very low permeability characteristics. The Taref Sandstone Formation, which is exposed at the surface in some areas (Figure 10c), dips to the east under the other sedimentary succession to form the Nubia aquifer.
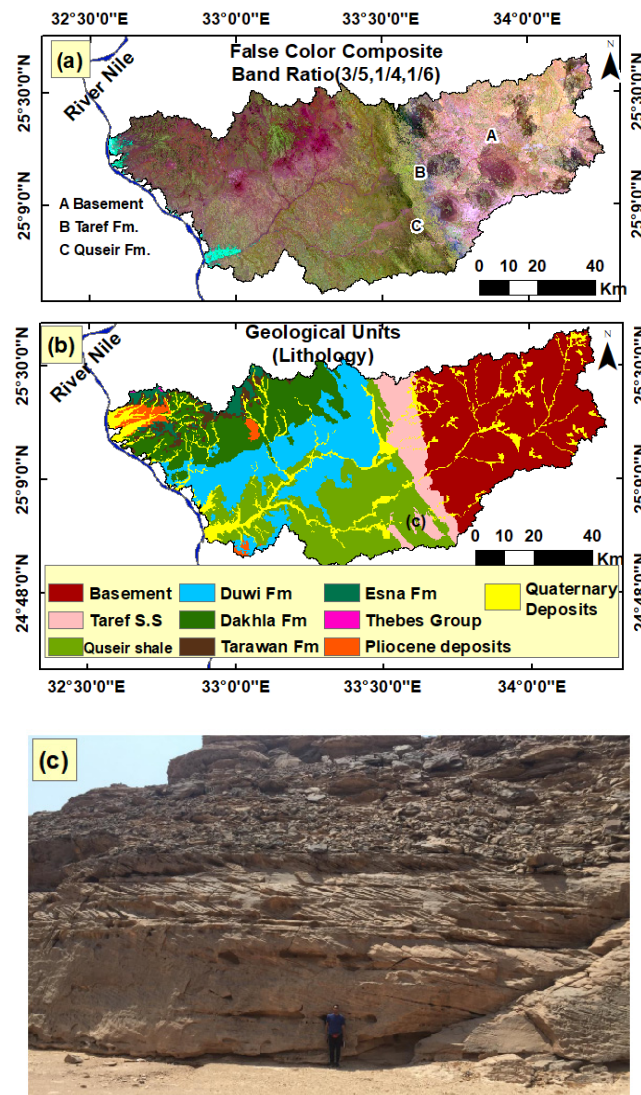
Figure 10. (**a**) False color composite (FCC) of Landsat 8 band ratios (3/5, 1/4, and 1/6); (**b**) Modified geological map (Figure 2) based on band ratios describing the lithology in Table 3; (**c**) Field photo illustrating primary sedimentary structure cross-bedding in Nubia Sandstone in Wadi Abadi.

The porosity and permeability were measured in a core sample from the Nubia Sandstone aquifer at well no. 11 and well no. 18. The measured porosity ranged from 31.02% to 38.36%, while the permeability ranged between 21 millidarcy and 2000 millidarcy. This result illustrates that the Nubia Sandstone aquifer has a different character, with small changes in porosity and extreme changes in permeability from site to site through the study area. The examination of microfacies associations that influence the porosity and permeability in Nubian Sandstone rocks is illustrated in the Supplementary Material.

5.2.8. Land Use/land Cover (LULC)

Groundwater recharging is influenced by the land use/land cover types [52,80–83]. It affects various hydrologic components (surface runoff, infiltration, evapotranspiration, and interception). An LULC map (Figure 11a) was created using a visual interpretation technique that was based on sentinel-2A and verified by Google Earth satellite imagery. Wadi deposits and natural desert grassland are examples of LULC classes that hold significantly higher proportions of water than barren land, rocky surfaces, and mining areas [18,40]. There are five main classes in the study area: barren land, Wadi deposits, mining areas, cultivated land, and natural desert grassland, which cover 88.4, 8.6, 1.3, 1.3, and 0.4 percent of the total area of the studied locations, respectively.
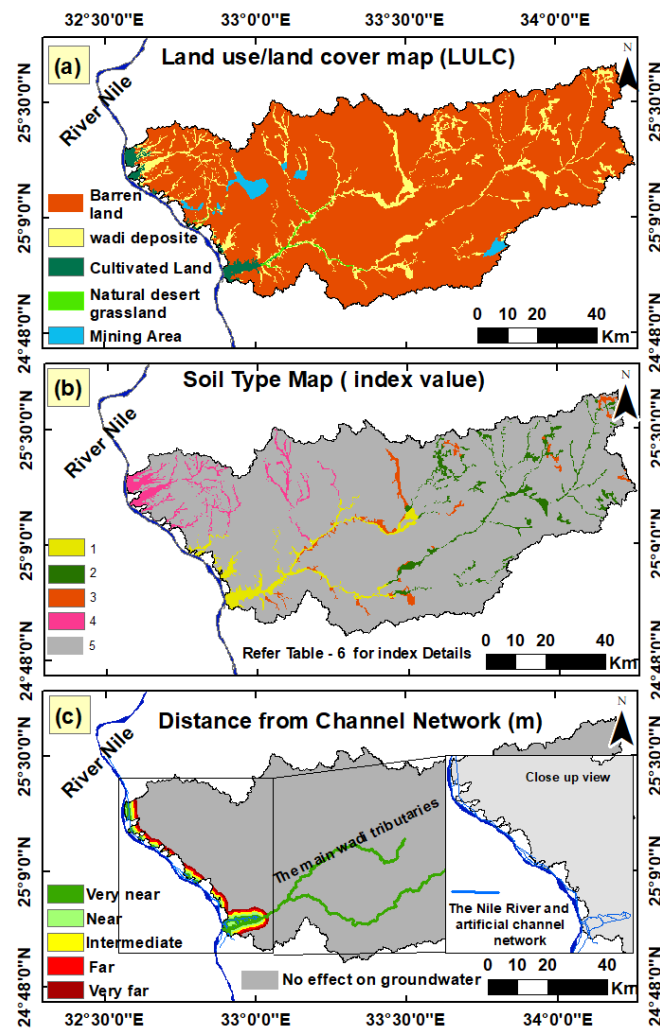
Figure 11. (**a**) The created land use/land cover map (LULC); (**b**) Thematic layer of soil type classes; (**c**) Distance from the channel network, with a close-up view of the Nile river associated with the artificial channel network and the main wadi tributaries crossing the study area.

5.2.9. Soil Type

Soil types determine the amount of water that may percolate into subsurface formations and hence influence groundwater recharge [35,39]. A PCA was created from a Landsat 8 satellite image to distinguish between the different soil types in the Quaternary deposits in the study area. A simplified soil type map was created for the study area based on the field investigation and infiltration test (Figure 11b). The details of the soil types identified in the investigated areas are summarized in Table 6. Sandy gravelly soil infiltrates more rapidly than loamy fine sand soil.

Table 6. The soil types of the study area and their properties, which describe the colors in Figure 11b.

Index	Soil Type
1	• Sandy gravelly soil. • Infiltration capacity equilibrium is about 13.8 mm/min. • Calculated hydraulic conductivity is 7.144×10^{-3} cm/s (very high permeability). • Calculated specific yield (effective porosity) = 31.4%.
2	• Sand to loamy sand soil. • Infiltration capacity equilibrium is about 4.5 mm/min. • Calculated hydraulic conductivity is 4.84×10^{-3} cm/s (high permeability). • Calculated specific yield (effective porosity) = 26%.
3	• Loamy sand soil. • Infiltration capacity equilibrium is about 2 mm/min. • Calculated hydraulic conductivity is 4.84×10^{-3} cm/s (moderately permeability). • Calculated specific yield (effective porosity) = 30%.
4	• Loamy fine sand soil associated with pebbly coarse sand in some parts. • Infiltration capacity equilibrium is about 0.53 mm/min. • Calculated hydraulic conductivity is 1.01×10^{-3} cm/s (low permeability). • Calculated specific yield (effective porosity) = 22%.
5	• Rock land

5.2.10. Distance from Channel Network (DCN)

Groundwater recharge is also influenced by the distance from the surface channel network and water bodies [46,84,85]. In the study area, this factor has a low weight because there is a small contribution of recent Nile water recharge to the Quaternary aquifer but no recent Nile water recharge to the Nubia aquifer [86]. A visual interpretation technique that was based on sentinel-2A and verified by Google Earth satellite imagery was used to extract the channel network. The prepared map (Figure 11c) was divided into five classes, considering acceptable buffer distances from the channel network or water bodies. There was no effect from this factor above 3000 m in distance from a channel network or water body. The main tributaries of Wadi Abadi were considered in this thematic layer, where the main course of the wadi was affected the groundwater recharge, but the locations outside the main channel were less affected.

5.3. The Rainfall Pattern and Return Period in Light of Climatic Change

In light of climatic changes, which have a related impact on water resources, it is necessary to use historical rainfall data in a return period method to identify the rates of rainfall in the future. The repeated maximum precipitation events have a direct relation to the recharging process of the shallow aquifer. A return period analysis for the historical rainfall data during the last four decades was carried out. The calculated results, along with the SWAT model, are useful for estimating the runoff as well as the transmission losses (recharge) for future maximum precipitation events [14,87]. Equation (5) was used to calculate the recurrence interval for precipitation events:

$$R_P = \frac{N+1}{M} \tag{5}$$

where R_p is the return period, M is the rank of the data corresponding to the event, and N is the number of years of data.

The HEC-DSSVue and HEC-SSP 2.2 programs were used to identify the return period using various statistical distributions. Kolmogorov–Smirnov and chi-square tests were used to evaluate the degree of fitness of probability distribution models with the observed data. Acceptable distributions were graded using two statistics: the mean relative deviation (MRD) and the mean square relative deviation (MSRD), as described in Equations (6) and (7). On the observed data, the distribution with the smallest MRD and MSRD fits the best.

$$\text{M.R.D} = \frac{\sum_{i=1}^{n} |x - \hat{x}|}{(N - m)} \tag{6}$$

$$\text{M.S.R.D} = \frac{\sum_{i=1}^{n} (x - \hat{x})^2}{(N - m)} \tag{7}$$

where x represents the observed data, $\hat{x}$ represents the estimated value, N represents the number of data points, and (m) denotes the number of parameters of the distribution [88]. From an analysis of the average annual accumulation of the study area, an exponential function (Figure 12a) fit the rainfall dataset (1981–2019) best, depending on the MRD and MSRD. The exceedance probability versus the rainfall is illustrated in Figure 12b. The calculated return period rainfall values in Wadi Abadi each 2, 5, 10, 20, and 50 years were 2.95, 6.89, 10.07, 13.25, and 17.39 mm, respectively (Table 7). The lithologic nature of Wadi Abadi is composed of nearly 40% massive rocks (carbonate and basement), which promotes surface runoff from the smallest amount of precipitation. Consequently, the aforementioned amounts of precipitation will participate in creating surface runoff and recharging the shallow aquifer through the transmission losses.

(a) (b)
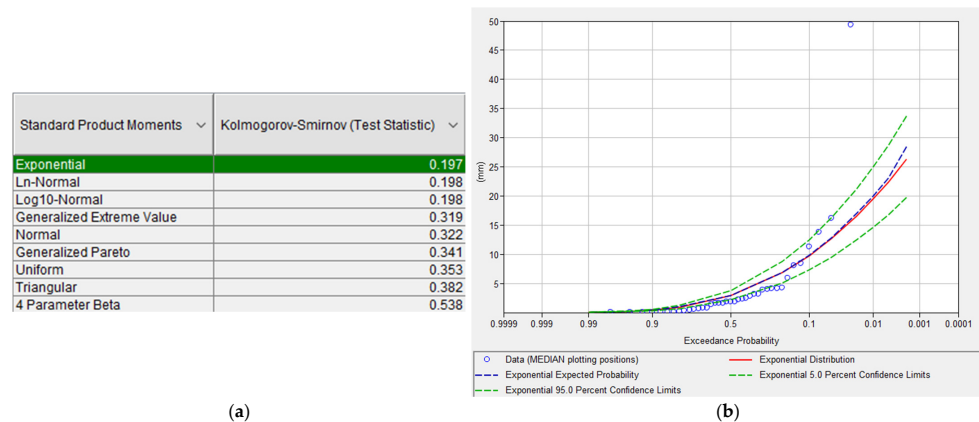
Figure 12. (**a**) Different types of statistical distributions of rainfall data using HEC-SSP2.2 software illustrate that an exponential function had the lowest error in fitting the rainfall dataset for the study area; (**b**) The exceedance probability versus the rainfall using HEC-SSP2.2 software.

Table 7. The HEC-SSP2.2 software was used to calculate the 100-year return period.

Return Period (Years)	Percent Chance Exceedance	Median (mm)	Expected Probability (mm)	Confidence Limits Probability 5% (mm)	Confidence Limits Probability 95% (mm)
2	50	2.934	2.952	3.759	2.196
5	20	6.812	6.894	8.728	5.099
10	10	9.746	10.074	12.487	7.295
20	5	12.679	13.245	16.246	9.492
50	2	16.557	17.393	21.215	12.395
100	1	19.491	20.477	24.974	14.591

The Impact of Climate Change on Groundwater Recharge

Globally, water resources such as groundwater will be impacted directly and indirectly by climate change [89,90]. The results can be used to evaluate the effects of global warming and climate change at a local scale. They offer the effects of the climate change information with a higher resolution. By analyzing the biggest precipitation events in the last four decades in the Abadi basin, the largest precipitation was about 48 mm in 1986, and this has not been repeated (Figure 13). Since 1997, this area has lacked high precipitation for about 20 years (Figure 7d). The recent major precipitation in 2016 was only 7.25 mm. It is expected that a detected major storm (maximum precipitation in one day) could enhance the groundwater recharge to the shallow aquifer in the Abadi basin. On the other hand, the decrease in the precipitation amount could cause the aquifer to deteriorate over time due and reduce the groundwater recharge. The amount of precipitation based on the return period for the next 50 years is only 17.4 mm. The predicted low recharges due to the effects of climate change need more groundwater management for sustainable development. The other wadies, especially in the Esna area, suffer from the reduction in the amount of precipitation for the last four decades.
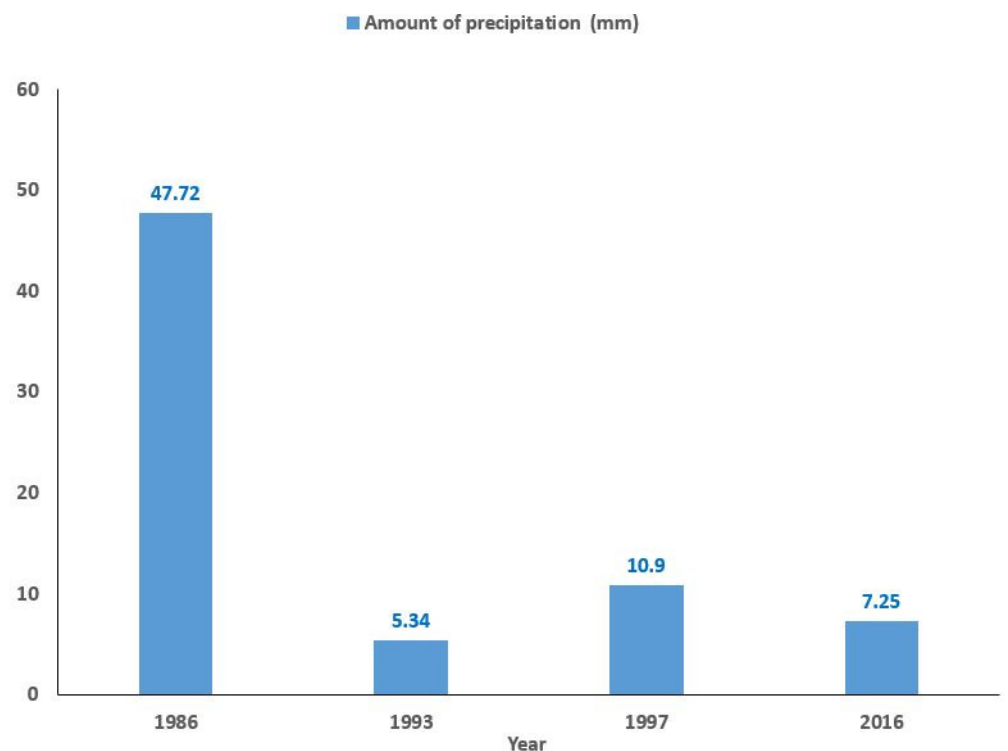
Figure 13. The precipitation and related recharge to the main aquifer in the Abadi basin in major rainfall events in the last four decades.

5.4. Groundwater Potential Zone (GWPZ)

The groundwater potential zone (GWPZ) map was created using a weighted overlay model that divided the study area into three classes: poor, moderate, and good potential recharge zones occupying 7073.47 km^2 (88.6%), 625.08 km^2 (7.8%), and 281.23 km^2 (3.52%) of the total surface area of the studied locations (Figure 14). The downstream portion of the studied wadies in the northwestern part of the study area near Esna has moderate potentiality (Figure 14a). Good potential zones are concentrated in the southwestern part (Figure 14b) and basement area (Figure 14c). The lineament density and major fractures play a major role in the groundwater potential recharge in the basement area. The result of the petrographic analysis illustrates that the Nubia Sandstone aquifer changes its character throughout the study area and that major fractures play a significant role in groundwater

movement and recharging processes. Based on a pumping test downstream of Wadi Abadi, the values of transmissivity were calculated, and they ranged between 78 m^2/day (well 19) and 346.3 m^2/day (well 13). The return period and rainfall analyses were used to predict the precipitation in the future for 100 years, illustrating that precipitation is limited and groundwater potentiality should be managed. On the other hand, the analysis and examination of the rainfall data over the study area for the last four decades using satellite-based spatial and temporal precipitation (MERRA-2) data were carried out. Our analysis showed that the largest precipitation events occurred in the Wadi Abadi basin, which experienced average annual precipitation through the last four decades of 7.67 mm, while the northwestern part of the study area in the El-Dir basin received only 91 mm. Moreover, the applied weighted overlay model of potential recharging zones illustrated that the good potential recharge areas are located in Wadi Abadi, especially in the upstream portion and some sites in the downstream area (Figure 14b,c). However, the result of the weighted overlay model of Wadi El-Dir showed that it falls within the moderate zone of potential recharge for groundwater, but no recharging from groundwater reaching the aquifer was observed, and a remarkable drop in the water level for the Quaternary aquifer was detected from 2014, ranging from 2 m proximal to the Nile River to 14 m distal from the river Nile (Figure 15). This drawdown could be related to two reasons: (a) low rainfall, which leads to a low recharge rate, and (b) overpumping, where the locals use flood irrigation to farm their lands. Therefore, more hydrological studies are required in order to determine the hydraulic properties of the Quaternary aquifer and to identify the safe discharge from the wells to protect the aquifer from deterioration.
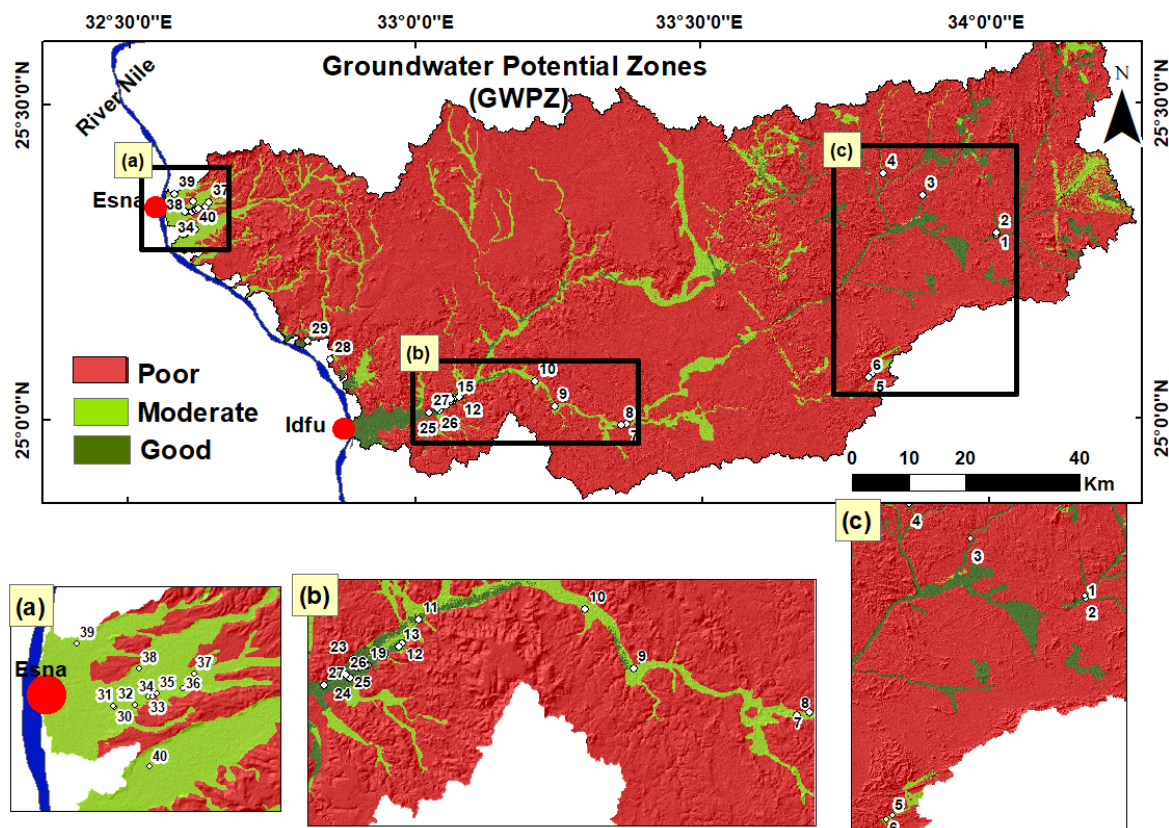
Figure 14. Groundwater potential zone map (GWPZ) associated with observation wells draped over a hill-shaded relief map illustrating the classes of potential recharge zoning; (**a**) observation wells in the Esna area; (**b**) observation wells in the Idfu area; (**c**) observation wells in the basement area at Wadi Abadi.
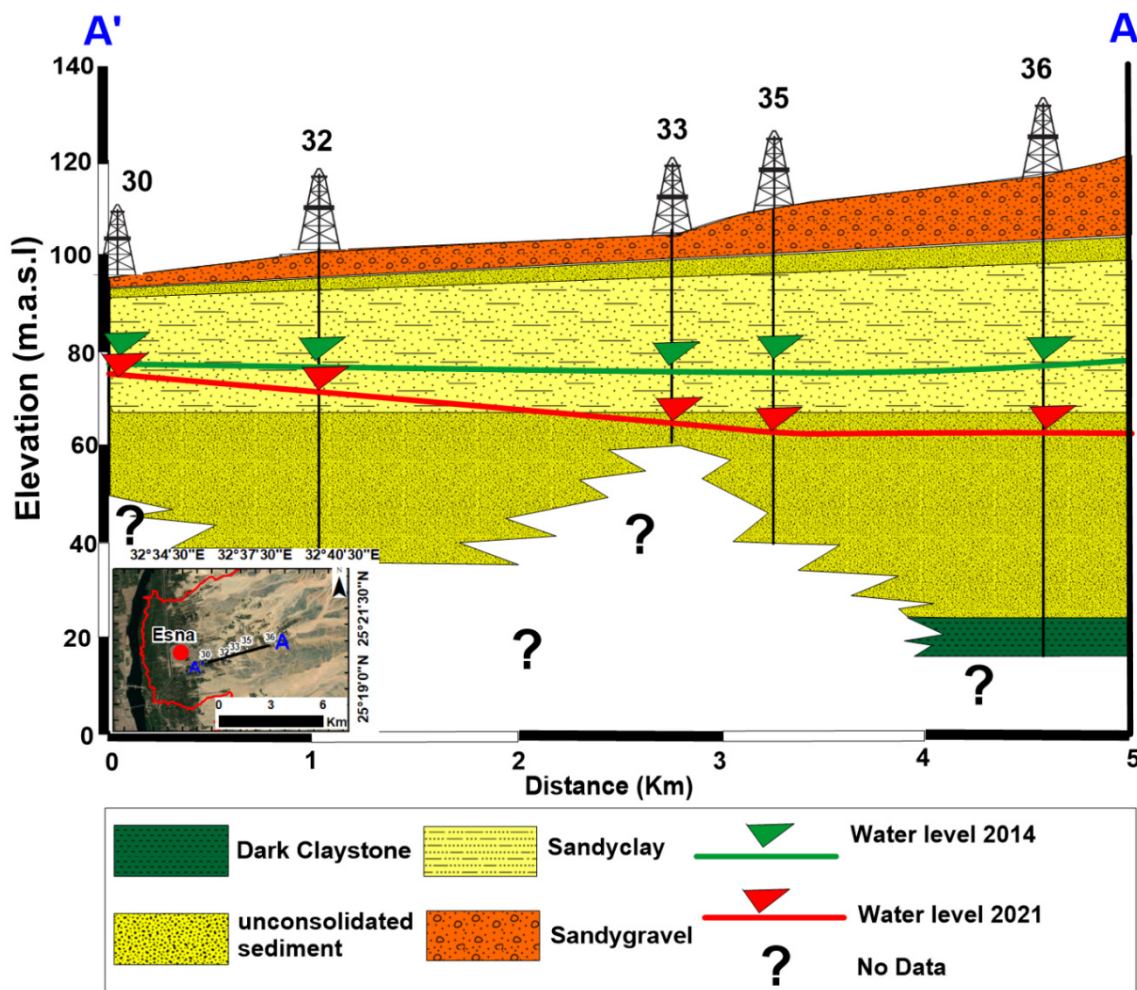
Figure 15. Subsurface hydrogeological cross section (A'-A) showing the drop in the static water level during the period from 2014 to 2021 at 5 wells in the Quaternary aquifer at Wadi El-Dir.

5.5. Model Validation

The water level data (depth to water) were detected at 40 observed wells (Figure 14a–c) of the study area. The validation was based on (a) the depth to water and (b) the drawdown in the water level through 7 years (2015–2021), which illustrates that the Wadi El-Dir area suffers from a drop in the water level (2–14 m), so it shows moderate potential recharge. On the other hand, the recorded drawdown in Wadi Abadi ranged from 0.5 m to 1.5 m within the same period, taking into consideration that they had nearly the same discharge for irrigation activity. (c) The high values of transmissivity in some wells downstream of Wadi Abadi ranged from 78 m^2/day (well 19) to 346.3 m^2/day (well 13), reflecting the high potentiality of the aquifer in this area. The poor zone mainly falls within the highly mountainous and/or hilly areas that are not prospected locations for groundwater exploration or development. The values used to validate the groundwater potential zone map reflect the actual recharge condition and the groundwater potential in certain locations. A comparison study was performed between the groundwater level in each well and the groundwater potential zones. (Table 8). The validation conclusions show that about 82.5 percent of the wells correctly fit the zonation of the groundwater potential map.

$$\text{Overall accuracy} = \frac{\text{Number of correct Observation well location}}{\text{Total number of Observation well location}} = \frac{33}{40} = 82 \tag{8}$$

Table 8. Groundwater level accuracy assessment of the GWPZ map.

S No.	Aquifer type	Basin	Well Type	Latitude	Longitude	Depth to Water (2015–2021)			Groundwater Level	Well Location on GWPZ Map	Validation Remarks
						2015	2021	Drawdown			
1				25.29305	34.01715	21	-	-	Medium	Poor	Disagree
2	Basement	Abadi	Hand-dug	25.2962	34.01673	13.5	-	-	Shallow	Good	
3				25.35523	33.8881	11.22	-	-	Shallow	Good	Agree
4				25.39138	33.8192	3.31	-	-	Very Shallow		Agree
5				25.07295	33.79751	-	36.3	-	Medium	Moderate	
6				25.06789	33.79088	-	32.8	-	Medium	Moderate	
7			Drilled	24.99508	33.36889	-	60	-	Medium/Deep		Partially agree
8				24.99331	33.35946	-	55	-	Medium/Deep	Moderate	
9				25.02363	33.24399	-	44	-	Medium		Agree
10				25.06227	33.20951	-	32.3	-	Medium		Agree
11			Hand-dug	25.05524	33.09096	8.5	10	1.5	Shallow	Good	Agree
12	Nubia	Abadi		25.03958	33.07906	-	10.2	-	Shallow	Good	Agree
13				25.03756	33.07654	8.7	10	1.3	Shallow	Good	Agree
14				25.03233	33.06653	7.5	8	0.5	Very Shallow	Good	Agree
15			Drilled	25.03411	33.06639	10	11	1	Shallow	Moderate	Partially agree
16				25.03237	33.06243	-	15.8	-	Shallow		
17				25.03537	33.062	-	4.2	-	Very Shallow		
18				25.02555	33.05486	8.6	10	1.4	Shallow	Good	Agree
19				25.02591	33.05341	-	12	-	Shallow		
20				25.02426	33.04908	5	6	1	Very Shallow		
21	Quaternary		Hand-dug	25.02464	33.04648	4	5.2	1.2	Very Shallow	Good	Agree
22	Nubia			25.02999	33.04420	-	6.7	-	Very Shallow	Good	Agree
23		Abadi	Drilled	25.0296	33.04430	-	7.8	-	Very Shallow	Good	Agree
24				25.0177	33.04155	3	4	1			Agree
25	Quaternary		Hand-dug	25.01735	33.04177	2.9	4.2	1.3	Very Shallow	Good	Agree
26				25.01964	33.03901	-	4.1	-			Agree
27				25.0128	33.02373	-	3	-			Agree
28		Al-Mafallis	Drilled	25.09834	32.85235	-	2.9	-		Moderate	Disagree
29	Nubia	Hilal	Spring	25.12756	32.81267	Flowing			Very Shallow	Good	Agree
30				25.33117	32.59856	18	20	2			
31				25.33142	32.59790	18	20	2			
32				25.33219	32.60896	25	30	5	Medium		Agree
33		El-Dir	Drilled	25.33567	32.61537	30	40	10			
34				25.33562	32.61775	-	44.6	-		Moderate	
35	Quaternary			25.33738	32.61988	35	47	12			
36				25.33968	32.63270	40	54	14	Medium/Deep		Partially agree
37				25.34631	32.6385	-	63	-	Medium/Deep		
38				25.34867	32.611	-	32	-			
39		El-Foley		25.35972	32.57956	-	20	-	Medium		Agree
40		El-Sabil		25.30405	32.61621	-	36	-			

6. Conclusions

An integrated approach using remote sensing datasets, including Landsat, sentinel images, and a digital elevation model, along with field investigation and GIS modeling was conducted to delineate groundwater potential zones in arid environments. The spatial analysis gained from the remote sensing datasets with geologic maps and field investigations revealed that the study area is highly affected by the structure discontinuity appearing in the extensive lineament network and major fractures. This fracture system, which is considered a main factor in the applied GIS model, has a directly impact on groundwater recharge and identifying potential zones. The major findings are (1) remote sensing and GIS in conjunction with the AHP method are effective techniques for delineating a groundwater potential map with accuracy (82.5%); (2) the analysis of historical rainfall data for last 39 years revealed that the study area had not received any significant precipitation since 1997, which was nearly 20 years, due to the effects of climatic changes; (3) by comparing the static water levels in 2014 and 2021 at five wells in Wadi El-Dir, there were drawdowns in the water levels ranging from 2 to 14 m due to the excessive discharge and the lack of rainfall in this area; and (4) the estimated porosity of the Nubia Sandstone aquifer in the

middle and downstream parts of Wadi Abadi revealed that the porosity ranged from 31 to 38% and the permeability ranged from 21 to 2000 millidarcy.

The integration of remote sensing datasets with field investigations and GIS technologies is very effective for improving the results of preliminarily examinations for groundwater exploration in areas where well data are scarce. The application of this approach is cost-effective in arid environments and developing countries and could be applicable for similar regions worldwide.

References

1. Yousif, M. A new theory to enhance the groundwater-related decisions based on deciphering the palaeohydrologic regime under climate change in the Sahara. *Model. Earth Syst. Environ.* **2021**, *8*, 3885–3895. [CrossRef]
2. Yousif, M.; Hussien, H.M.; Abotalib, A.Z. The Respective roles of modern and paleo recharge to alluvium aquifers in continental rift basins: A case study from El Qaa Plain, Sinai, Egypt. *Sci. Total Environ.* **2020**, *739*, 139927. [CrossRef] [PubMed]
3. UNESCO. *The United Nations World Water Development Report 2015*; Water for a Sustainable World; UNESCO: Paris, France, 2015.
4. Ghosh, D.; Mandal, M.; Karmakar, M.; Banerjee, M.; Mandal, D. Application of geospatial technology for delineating groundwater potential zones in the Gandheswari Watershed, West Bengal. *Sustain. Water Resour. Manag.* **2020**, *6*, 1–14. [CrossRef]
5. Global Information System on Water and Agriculture. Available online: https://www.fao.org/aquastat/en/databases/ (accessed on 4 December 2021).
6. Heggy, E.; Sharkawy, Z.; Abotalib, A.Z. Egypt's water budget deficit and suggested mitigation policies for the grand ethiopian renaissance dam filling scenarios. *Environ. Res. Lett.* **2021**, *16*, 074022. [CrossRef]
7. Senanayake, I.P.; Dissanayake, D.M.D.O.K.; Mayadunna, B.B.; Weerasekera, W.L. An approach to delineate groundwater recharge potential sites in Ambalantota, Sri Lanka using GIS techniques. *Geosci. Front.* **2016**, *7*, 115–124. [CrossRef]
8. Jha, M.K.; Chowdary, V.M.; Chowdhury, A. Groundwater assessment in Salboni Block, West Bengal (India) using remote sensing, geographical information system and multi-criteria decision analysis techniques. *Hydrogeol. J.* **2010**, *18*, 1713–1728. [CrossRef]
9. Jha, M.K.; Chowdhury, A.; Chowdary, V.M.; Peiffer, S. Groundwater management and development by integrated remote sensing and geographic information systems: Prospects and constraints. *Water Resour. Manag.* **2007**, *21*, 427–467. [CrossRef]
10. Israil, M.; Al-hadithi, M.; Singhal, D.C. Application of a resistivity survey and geographical information system (GIS) analysis for hydrogeological zoning of a Piedmont Area, Himalayan Foothill Region, India. *Hydrogeol. J.* **2006**, *14*, 753–759. [CrossRef]
11. Oh, H.J.; Kim, Y.S.; Choi, J.K.; Park, E.; Lee, S. GIS mapping of regional probabilistic groundwater potential in the area of Pohang City, Korea. *J. Hydrol.* **2011**, *399*, 158–172. [CrossRef]
12. Adiat, K.A.N.; Nawawi, M.N.M.; Abdullah, K. Assessing the accuracy of GIS-based elementary multi criteria decision analysis as a spatial prediction tool—A case of predicting potential zones of sustainable groundwater resources. *J. Hydrol.* **2012**, *440–441*, 75–89. [CrossRef]

13. Russo, T.A.; Fisher, A.T.; Lockwood, B.S. Assessment of managed aquifer recharge site suitability using a GIS and modeling. *Groundwater* **2015**, *53*, 389–400. [CrossRef] [PubMed]

14. Hussien, H.M.; Kehew, A.E.; Aggour, T.; Korany, E.; Abotalib, A.Z.; Hassanein, A.; Morsy, S. An integrated approach for identification of potential aquifer zones in structurally controlled terrain: Wadi Qena Basin, Egypt. *Catena* **2017**, *149*, 73–85. [CrossRef]

15. Tiwari, K.; Goyal, R.; Sarkar, A. GIS-based spatial distribution of groundwater quality and regional suitability evaluation for drinking water. *Environ. Process.* **2017**, *4*, 645–662. [CrossRef]

16. Arulbalaji, P.; Padmalal, D.; Sreelash, K. GIS and AHP techniques based delineation of groundwater potential zones: A case study from Southern Western Ghats, India. *Sci. Rep.* **2019**, *9*, 1–17. [CrossRef]

17. Hussien, H.M.; Yousif, M.; El Sheikh, A. Investigation of groundwater occurrences in structurally controlled terrain, based on geological studies and remote sensing data: Wadi El Morra, South Sinai, Egypt. *NRIAG J. Astron. Geophys.* **2020**, *9*, 512–531. [CrossRef]

18. Madani, A.; Niyazi, B. Groundwater potential mapping using remote sensing techniques and weights of evidence GIS model: A case study from Wadi Yalamlam Basin, Makkah Province, Western Saudi Arabia. *Environ. Earth Sci.* **2015**, *74*, 5129–5142. [CrossRef]

19. Fildes, S.G.; Clark, I.F.; Somaratne, N.M.; Ashman, G. Mapping Groundwater potential zones using remote sensing and geographical information systems in a fractured rock setting, southern flinders ranges, South Australia. *J. Earth Syst. Sci.* **2020**, *129*, 1–25. [CrossRef]

20. Srinivasa Rao, Y.; Jugran, D.K. Delineation of Groundwater potential zones and zones of groundwater quality suitable for domestic purposes using remote sensing and GIS. *Hydrol. Sci. J.* **2003**, *48*, 821–833. [CrossRef]

21. Kumar, P.K.D.; Gopinath, G.; Seralathan, P. International journal of remote application of remote sensing and GIS for the demarcation of groundwater potential zones of a River Basin in Kerala, Southwest Coast of India. *Int. J. Remote Sens.* **2007**, *28*, 5583–5601. [CrossRef]

22. Prasad, R.K.; Monda, N.C.; Banerjee, P.; Nandakumar, M.V.; Singh, V.S. Deciphering Potential Groundwater Zone in Hard Rock Through The Application of GIS. *Environ. Geol.* **2008**, *55*, 467–475. [CrossRef]

23. Ganapuram, S.; Kumar, G.T.V.; Krishna, I.V.M.; Kahya, E.; Demirel, M.C. Mapping of groundwater potential zones in the Musi Basin using remote sensing data and GIS. *Adv. Eng. Softw.* **2009**, *40*, 506–518. [CrossRef]

24. Al Saud, M. Mapping potential areas for groundwater storage in Wadi Aurnah Basin, Western Arabian Peninsula, using remote sensing and geographic information system techniques. *Hydrogeol. J.* **2010**, *18*, 1481–1495. [CrossRef]

25. Avtar, R.; Singh, C.K.; Shashtri, S.; Singh, A.; Mukherjee, S. Identification and analysis of groundwater potential zones in Ken-Betwa River linking area using remote sensing and geographic information system. *Geocarto Int.* **2010**, *25*, 379–396. [CrossRef]

26. Dar, I.A.; Sankar, K.; Dar, M.A. Remote sensing technology and geographic information system modeling: An integrated approach towards the mapping of groundwater potential zones in Hardrock Terrain, Mamundiyar Basin. *J. Hydrol.* **2010**, *394*, 285–295. [CrossRef]

27. Elewa, H.H.; Qaddah, A.A. Groundwater potentiality mapping in the Sinai Peninsula, Egypt, using remote sensing and GIS-watershed-based modeling. *Hydrogeol. J.* **2011**, *19*, 613–628. [CrossRef]

28. Abdelkareem, M.; El-Baz, F.; Askalany, M.; Akawy, A.; Ghoneim, E. Groundwater prospect map of Egypt's Qena Valley Using data fusion. *Int. J. Image Data Fusion* **2012**, *3*, 169–189. [CrossRef]

29. Magesh, N.S.; Chandrasekar, N.; Soundranayagam, J.P. Delineation of groundwater potential zones in Theni District, Tamil Nadu, using remote sensing, GIS and MIF techniques. *Geosci. Front.* **2012**, *3*, 189–196. [CrossRef]

30. Abdalla, F. Mapping of groundwater prospective zones using remote sensing and GIS techniques: A case study from the Central Eastern Desert, Egypt. *J. African Earth Sci.* **2012**, *70*, 8–17. [CrossRef]

31. Deepika, B.; Avinash, K.; Jayappa, K.S. Integration of hydrological factors and demarcation of groundwater prospect zones: Insights from remote sensing and GIS techniques. *Environ. Earth Sci.* **2013**, *70*, 1319–1338. [CrossRef]

32. Nag, S.K.; Ghosh, P. Delineation of groundwater potential zone in Chhatna Block, Bankura District, West Bengal, India using remote sensing and GIS techniques. *Environ. Earth Sci.* **2013**, *70*, 2115–2127. [CrossRef]

33. Nampak, H.; Pradhan, B.; Manap, M.A. Application of GIS based data driven evidential belief function model to predict groundwater potential zonation. *J. Hydrol.* **2014**, *513*, 283–300. [CrossRef]

34. Agarwal, R.; Garg, P.K. Remote sensing and GIS based groundwater potential & recharge zones mapping using multi-criteria decision making technique. *Water Resour. Manag.* **2016**, *30*, 243–260. [CrossRef]

35. Ibrahim-Bathis, K.; Ahmed, S.A. Geospatial technology for delineating groundwater potential zones in Doddahalla Watershed of Chitradurga District, India. *Egypt. J. Remote Sens. Sp. Sci.* **2016**, *19*, 223–234. [CrossRef]

36. Selvarani, A.G.; Maheswaran, G.; Elangovan, K. Identification of artificial recharge sites for Noyyal River Basin using GIS and remote sensing. *J. Indian Soc. Remote Sens.* **2017**, *45*, 67–77. [CrossRef]

37. Hussein, A.-A.; Govindu, V.; Nigusse, A.G.M. Evaluation of groundwater potential using geospatial techniques. *Appl. Water Sci.* **2017**, *7*, 2447–2461. [CrossRef]

38. Thapa, R.; Gupta, S.; Guin, S.; Kaur, H. Assessment of groundwater potential zones using multi-influencing factor (MIF) and GIS: A case study from Birbhum District, West Bengal. *Appl. Water Sci.* **2017**, *7*, 4117–4131. [CrossRef]

39. Das, S. Delineation of groundwater potential zone in hard rock terrain in Gangajalghati Block, Bankura District, India using remote sensing and GIS techniques. *Model. Earth Syst. Environ.* **2017**, *3*, 1589–1599. [CrossRef]

40. Rajaveni, S.P.; Brindha, K.; Elango, L. Geological and geomorphological controls on groundwater occurrence in a hard rock region. *Appl. Water Sci.* **2017**, *7*, 1377–1389. [CrossRef]

41. Patra, S.; Mishra, P.; Mahapatra, S.C. Delineation of groundwater potential zone for sustainable development: A case study from Ganga Alluvial plain covering Hooghly District of India using remote sensing, geographic information system and analytic hierarchy process. *J. Clean. Prod.* **2018**, *172*, 2485–2502. [CrossRef]

42. Adeyeye, O.A.; Ikpokonte, A.E.; Arabi, A.S. The dual use of drainage characteristics in groundwater potential modelling using remote sensing and GIS: An example from Dengi Area, Northcentral Nigeria. *Sustain. Water Resour. Manag.* **2018**, *4*, 1105–1115. [CrossRef]

43. Pande, C.B.; Khadri, S.F.R.; Moharir, K.N.; Patode, R.S. Assessment of groundwater potential zonation of Mahesh River Basin Akola and Buldhana Districts, Maharashtra, India using remote sensing and GIS techniques. *Sustain. Water Resour. Manag.* **2018**, *4*, 965–979. [CrossRef]

44. Murmu, P.; Kumar, M.; Lal, D.; Sonker, I.; Singh, S.K. Delineation of groundwater potential zones using geospatial techniques and analytical hierarchy process in Dumka District, Jharkhand, India. *Groundw. Sustain. Dev.* **2019**, *9*, 100239. [CrossRef]

45. Çelik, R. Evaluation of groundwater potential by GIS-Based multicriteria decision making as a spatial prediction tool: Case study in the Tigris River Batman-Hasankeyf Sub-Basin, Turkey. *Water* **2019**, *11*, 2630. [CrossRef]

46. Mallick, J.; Khan, R.A.; Ahmed, M.; Alqadhi, S.D.; Alsubih, M.; Falqi, I.; Hasan, M.A. Modeling groundwater potential zone in a Semi-Arid Region of Aseer using Fuzzy-AHP and geoinformation techniques. *Water* **2019**, *11*, 2656. [CrossRef]

47. Benjmel, K.; Amraoui, F.; Boutaleb, S.; Ouchchen, M.; Tahiri, A.; Touab, A. Mapping of groundwater potential zones in techniques, and multicriteria data analysis (Case of the Ighrem Region, Western Anti-Atlas, Morocco). *Water* **2020**, *12*, 471. [CrossRef]

48. Achu, A.L.; Reghunath, R.; Thomas, J. Mapping of groundwater recharge potential zones and identification of suitable site-specific recharge mechanisms in a tropical river basin. *Earth Syst. Environ.* **2020**, *4*, 131–145. [CrossRef]

49. Berhanu, K.G.; Hatiye, S.D. Identification of groundwater potential zones using proxy data: Case study of Megech Watershed, Ethiopia. *J. Hydrol. Reg. Stud.* **2020**, *28*, 100676. [CrossRef]

50. Lentswe, G.B.; Molwalefhe, L. Delineation of potential groundwater recharge zones using analytic hierarchy process-guided GIS in the semi-arid Motloutse Watershed, Eastern Botswana. *J. Hydrol. Reg. Stud.* **2020**, *28*, 100674. [CrossRef]

51. Mukherjee, I.; Singh, U.K. Delineation of groundwater potential zones in a drought-prone semi-arid region of East India using GIS and analytical hierarchical process techniques. *Catena* **2020**, *194*, 104681. [CrossRef]

52. Kaur, L.; Rishi, M.S.; Singh, G.; Nath Thakur, S. Groundwater potential assessment of an alluvial aquifer in Yamuna Sub-Basin (Panipat Region) using remote sensing and GIS techniques in conjunction with Analytical Hierarchy Process (AHP) and Catastrophe Theory (CT). *Ecol. Indic.* **2020**, *110*, 105850. [CrossRef]

53. Ahmadi, H.; Kaya, O.A.; Babadagi, E.; Savas, T.; Pekkan, E. GIS-based groundwater potentiality mapping using AHP and FR models in Central Antalya, Turkey. *Environ. Sci. Proc.* **2021**, *5*, 11. [CrossRef]

54. Zhu, Q.; Abdelkareem, M. Mapping groundwater potential zones using a knowledge-driven approach and GIS analysis. *Water* **2021**, *13*, 579. [CrossRef]

55. Ranganathan, M.; Murugesan, B.; Mukesh, M.; Islam, Z.; Gebremedhin, D.T.; Brhane, G.K. Groundwater potentiality mapping in Viruthachalam Taluk, Tamil Nadu, India: AHP and GIS approaches. *Hydrospatial Anal.* **2021**, *5*, 24–33. [CrossRef]

56. Anteneh, Z.L.; Alemu, M.M.; Bawoke, G.T.; Kehali, A.T.; Fenta, M.C.; Desta, M.T. Appraising groundwater potential zones using geospatial and Multi-Criteria Decision Analysis (MCDA) techniques in Andasa-Tul Watershed, Upper Blue Nile Basin, Ethiopia. *Environ. Earth Sci.* **2022**, *81*, 1–20. [CrossRef]

57. Melese, T.; Belay, T. Groundwater potential zone mapping using analytical hierarchy process and GIS in Muga Watershed, Abay Basin, Ethiopia. *Glob. Chall.* **2022**, *6*, 2100068. [CrossRef]

58. Ramachandra, M.; Babu, K.R.; Kumar, B.P.; Rajasekhar, M. Deciphering groundwater potential zones using AHP and geospatial modelling approaches: A case study from YSR District, Andhra Pradesh, India. *Int. J. Energy Water Resour.* **2022**, 1–11. [CrossRef]

59. Ogungbade, O.; Ariyo, S.O.; Alimi, S.A.; Alepa, V.C.; Aromoye, S.A.; Akinlabi, O.J. A combined GIS, remote sensing and geophysical methods for groundwater potential assessment of Ilora, Oyo Central, Nigeria. *Environ. Earth Sci.* **2022**, *81*, 1–13. [CrossRef]

60. NASA Prediction of Worldwide Energy Resources Data Access Documentation Resources about Contact. Available online: https://power.larc.nasa.gov/data-access-viewer/ (accessed on 14 October 2021).

61. Izz, A.A. *Landforms of Egypt*; American University Press: Cairo, Egypt, 1971.

62. Conco, C. *Geological Map of Egypt, Scale 1: 500,000*; Egyptian General Petroleum Corporation: Cairo, Egypt, 1987.

63. USGS Earth Explorer. Available online: https://earthexplorer.usgs.gov/ (accessed on 14 October 2021).

64. Saaty, T.L. *Decision Making for Leaders: The Analytic Hierarchy Process for Decisions in a Complex World*; RWS Publications: Bangalore, India, 1990.

65. Singh, L.K.; Jha, M.K.; Chowdary, V.M. Assessing the accuracy of GIS-based multi-criteria decision analysis approaches for mapping groundwater potential. *Ecol. Indic.* **2018**, *91*, 24–37. [CrossRef]

66. Hazen, A. Discussion: Dams on sand foundations. *Trans. Am. Soc. Civ. Eng.* **1911**, *73*, 190–208.

67. Todd, D.K.; Mays, L.W. *Groundwater Hydrology*, 3rd ed.; John Wiley & Sons, Inc.: New York, NY, USA, 2005; ISBN 978-0-471-05937-0.

68. Duffy, C.J.; Al-Hassan, S. Groundwater circulation in a closed desert basin: Topographic scaling and climatic forcing. *Water Resour. Res.* **1988**, *24*, 1675–1688. [CrossRef]

69. Twidale, C.R. River patterns and their meaning. *Earth Science Rev.* **2004**, *67*, 159–218. [CrossRef]

70. Charlton, R. *Fundamentals of Fluvial Geomorphology*; Routledge: New York, NY, USA, 2008; ISBN 0203371089.

71. Horton, R.E. Drainage-basin characteristics. *Eos Trans. Am. Geophys. Union* **1932**, *13*, 350–361. [CrossRef]

72. Gelaro, R.; McCarty, W.; Suárez, M.J.; Todling, R.; Molod, A.; Takacs, L.; Randles, C.A.; Darmenov, A.; Bosilovich, M.G.; Reichle, R.; et al. The modern-era retrospective analysis for research and applications, version 2 (MERRA-2). *J. Clim.* **2017**, *30*, 5419–5454. [CrossRef]

73. Kuswanto, H.; Naufal, A. Evaluation of performance of drought prediction in Indonesia based on TRMM and MERRA-2 using machine learning methods. *MethodsX* **2019**, *6*, 1238–1251. [CrossRef]

74. Reichle, R.H.; Liu, Q.; Koster, R.D.; Draper, C.S.; Mahanama, S.P.P.; Partyka, G.S. Land surface precipitation in MERRA-2. *J. Clim.* **2017**, *30*, 1643–1664. [CrossRef]

75. Europe's eyes on Earth. The Copernicus Global Land Service (CGLS). Available online: https://land.copernicus.eu/global/ (accessed on 19 September 2022).

76. Hung, L.Q.; Batelaan, O.; De Smedt, F. Lineament extraction and analysis, comparison of LANDSAT ETM and ASTER imagery. Case study: Suoimuoi Tropical Karst Catchment, Vietnam. *Remote Sens. Environ. Monit. GIS Appl. Geol. V* **2005**, *5983*, 59830T. [CrossRef]

77. Magowe, M.; Carr, J.R. Relationship between lineaments and ground water occurrence in Western Botswana. *Groundwater* **1999**, *37*, 282–286. [CrossRef]

78. Al-Ruzouq, R.; Shanableh, A.; Yilmaz, A.G.; Idris, A.E.; Mukherjee, S.; Khalil, M.A.; Gibril, M.B.A. Dam site suitability mapping and analysis using an integrated GIS and machine learning approach. *Water* **2019**, *11*, 1880. [CrossRef]

79. Edet, A.E.; Okereke, C.S.; Teme, S.C.; Esu, E.O. Application of remote-sensing data to groundwater exploration: A case study of the Cross River State, Southeastern Nigeria. *Hydrogeol. J.* **1998**, *6*, 394–404. [CrossRef]

80. Jasrotia, A.S.; Kumar, A.; Singh, R. Integrated remote sensing and GIS approach for delineation of groundwater potential zones using aquifer parameters in Devak and Rui Watershed of Jammu and Kashmir, India. *Arab. J. Geosci.* **2016**, *9*, 1–15. [CrossRef]

81. Martin, S.L.; Hayes, D.B.; Kendall, A.D.; Hyndman, D.W. The land-use legacy effect: Towards a mechanistic understanding of time-lagged water quality responses to land use/cover. *Sci. Total Environ.* **2017**, *579*, 1794–1803. [CrossRef] [PubMed]

82. Lerner, D.N.; Harris, B. The relationship between land use and groundwater resources and quality. *Land Use Policy* **2009**, *26*, 265–273. [CrossRef]

83. Collin, M.L.; Melloul, A.J. Combined land-use and environmental factors for sustainable groundwater management. *Urban Water* **2001**, *3*, 229–237. [CrossRef]

84. Machiwal, D.; Jha, M.K.; Mal, B.C. Assessment of groundwater potential in a semi-arid region of India using remote sensing, GIS and MCDM techniques. *Water Resour. Manag.* **2011**, *25*, 1359–1386. [CrossRef]

85. Adeyeye, O.A.; Ikpokonte, E.A.; Arabi, S.A. GIS-based groundwater potential mapping within Dengi Area, North Central Nigeria. *Egypt. J. Remote Sens. Sp. Sci.* **2019**, *22*, 175–181. [CrossRef]

86. Mohallel, S.A.; Abdella, H.F.; Habibah, A.Z. Hydrogeochemical assessment of groundwater quality at Wadi Abbadi, Southern Part of Eastern Desert, Egypt. *Curr. Sci. Int.* **2019**, *8*, 422–438.

87. Ezz, H.; Gomaah, M.; Abdelwares, M. Watershed delineation and estimation of groundwater recharge for Ras Gharib Region, Egypt. *J. Geosci. Environ. Prot.* **2019**, *07*, 202–213. [CrossRef]

88. Adeyemo, J.; Olofintoye, O.O. Optimized Fourier approximation models for estimating monthly streamflow in the Vanderkloof Dam, South Africa. In *Advances in Intelligent Systems and Computing*; Springer International Publishing: Cham, Switzerland, 2014; Volume 288, pp. 293–306. ISBN 978-3-319-07493-1.

89. Swain, S.; Taloor, A.K.; Dhal, L.; Sahoo, S.; Al-Ansari, N. Impact of climate change on groundwater hydrology: A comprehensive review and current status of the Indian hydrogeology. *Appl. Water Sci.* **2022**, *12*, 1–25. [CrossRef]

90. Hassan, W.H.; Hussein, H.H.; Nile, B.K. The effect of climate change on groundwater recharge in unconfined aquifers in the western desert of Iraq. *Groundw. Sustain. Dev.* **2022**, *16*, 100700. [CrossRef]

91. Folk, R.L. *Petrologie of Sedimentary Rocks*; Hemphill Publishing Co.: Austin, TX, USA, 1974; ISBN 0-914696-14-9.

Article

Morphometric, Meteorological, and Hydrologic Characteristics Integration for Rainwater Harvesting Potential Assessment in Southeast Beni Suef (Egypt)

Hakeem Musaed [1,2,*], Ahmed El-Kenawy [3] and Mohamed El Alfy [1]

1   Geology Department, Faculty of Science, Mansoura University, Mansoura 35516, Egypt
2   Department of Engineering Geology, Faculty of Oil and Minerals, University of Shabwah, Shabwah, Yemen
3   Department of Geography, Mansoura University, Mansoura 35516, Egypt
*   Correspondence: hakeem21112@gmail.com; Tel.: +0020-1119101981

Abstract: In arid areas, the forecast of runoff is problematic for ungauged basins. The peak discharge of flashfloods and rainwater harvesting (RWH) was assessed by the integration of GIS, the RS tool and hydrologic modeling. This approach is still under further improvement to fully understand flashflood and rainwater harvesting potentialities. Different morphometric parameters are extracted and evaluated; they show the most hazardous sub-basins. Vulnerability potential to flooding is high relative to steep slopes, high drainage density, and low stream sinuosity. Using hydrologic modeling, lag time, concentration time, peak discharge rates, runoff volume, rainfall, and total losses are calculated for different return periods. The hydrologic model shows high rainfall rates, and steep slopes are present in the southeastern part of the study area. Low rainfall rates, moderate–high runoff, and gentle slopes are found in the central and downstream parts, which are suitable sites for rainwater harvesting. An analytic hierarchy process is utilized for mapping the best sites to RWH. These criteria use land-cover, average annual max 24 h rainfall, slope, stream order, and lineaments density. About 4% of the basin area has very high potentialities for RWH, while 59% of the basin area has high suitability for RWH. Ten low dam sites are proposed to impact flooding vulnerability and increase rainwater-harvesting potentialities.

Keywords: climate change; rainwater harvesting; arid areas; metrologic analysis; hydrologic modeling; AHP

1. Introduction

Flashflood evaluation is an important issue for creating suitable development plans in arid regions. Arid or semiarid areas may experience more floods than moist regions with higher rainfall intensity [1]. They are one of the major natural hazards that cause loss of life and economy [2]. In comparison to other natural hazards, flashfloods are the most overwhelming and the highest of the natural tragedies that damage houses, irrigation systems, streets, crops, and tapwater networks, besides causing economic damage in many regions throughout the world. It is reported that nearly 44% of deaths caused by natural hazards worldwide, especially in arid regions, are related to flooding events [3–6].

Although this natural hazard is mainly driven by unexceptional atmospheric conditions, it is largely impacted by other non-climatic variables like topography, urban and vegetation cover, and high-velocity water movements [7–9].

In arid regions, flashfloods are driven by a high variability of rainfall over space and time. Rainfall in arid and semi-arid regions is sporadic and less frequent but more intense when it occurs. Flashfloods commonly occur in valleys that are distinguished by their dry state [10]. In arid regions, monitoring flashfloods is a challenge due to inadequate observational data, absence of monitoring systems, and lack of infrastructure, especially in

remote sites. Flashfloods represent a significant source of water in arid regions, and a small part is infiltrated for groundwater [10,11].

The idea of rainwater harvesting (RWH) was used in various portions of the world 3000 years ago. Nevertheless, the utilization of RWH systems declined with the development of technology in the twentieth century. The increasing usage of RWH methods through the last two decades can be attributed to an increasing gap between rising water demands attributable to population growth and declining water supplies due to prospective climatic changes [12–14]. This has resulted in increases in the focus of researchers on the scientific parts and environmental influences of RWH methods [15]. Several methods for RWH and artificial recharge have been proposed, involving the creation of surface basins, the creation of deep channels, and the drilling of recharge wells [16–18].

In arid regions, climate change and the rising water demands for drinking and agricultural and industrial purposes can increase the pressure on limited water resources and clearly represent the water scarcity problems [19,20]. The overexploitation of groundwater in arid areas can cause a decline in water levels [21,22]. Because of the spatial and temporal variability of rainfall in arid areas, normal groundwater recharge is not stable, which constitutes a challenge to proper aquifer sustainability. RWH suggests a good method for improving groundwater resources in these arid areas, which can assist in the depletion of groundwater [14]. Several studies have been carried out related to RWH. Mahmoud et al. (2014) [23] used the analytical hierarchy process (AHP) with five thematic layers to identify RWH-suitable areas in Egypt. Alataway and El Alfy (2019) [14] assessed rainwater harvesting in central Saudi Arabia and determined artificial groundwater recharge potentialities in four dam reservoirs; they correlated the surface water level in these reservoirs and water table measurements in five recharge wells. The AHP technique was also used by Balkhair and Ur Rahman (2021) [24] to create a suitable map for RWH sites in the basin of wadi Al-Lith, Saudi Arabia, where eight appropriate criteria were applied. Ouali et al. (2022) [25] assessed the RWH in the Toudgha basin of southeastern Morocco by using the APH method, wherein the RWH map provides good information to decision-makers on water supply planning.

In the Eastern Desert, Egypt, groundwater is the main source for agriculture and drinking. Drought, climatic change, overpumping and low annual rainfall rates are foremost challenges to farmers. To increase the availability of water resources, harvesting techniques can be used through the construction of low–high dams. Numerous studies were carried out using geographic information system (GIS) and remote sensing (RS) for the assessment of flashfloods [26–29]. Therefore, an assessment of the flashfloods and their drivers are extremely important. The aim of this study is to build a framework for evaluating flashflood risk and rainwater-harvesting potentialities in the east Bani Suef area, Egypt. The main innovative aspects of the current study are to assess rainwater-harvesting potentialities. Specifically, this study proposes an integrated approach, based on a geographic information system (GIS), remote sensing techniques, and morphometric and rainfall–runoff modeling. This study correlates the risk of flashfloods using a morphometric ranking method, as well as the AHP method for the determination of suitable areas of rainwater harvesting in low-terrain arid areas.

2. Study Area

The study area is located in the southeastern part of the Beni Suef Governorate between latitudes 27°10′ N and 28°40′ N and longitudes 30°85′ E and 32°35′ E (Figure 1). It has an area of approximately 10,646 km^2, length of 178 km, and average width of 60 km. The elevation varies between 26 m (asl) at the low-lying zone near the Nile River (western part) and 1266 m in the northeastern part close to the Red Sea Mountains (Figure 1).
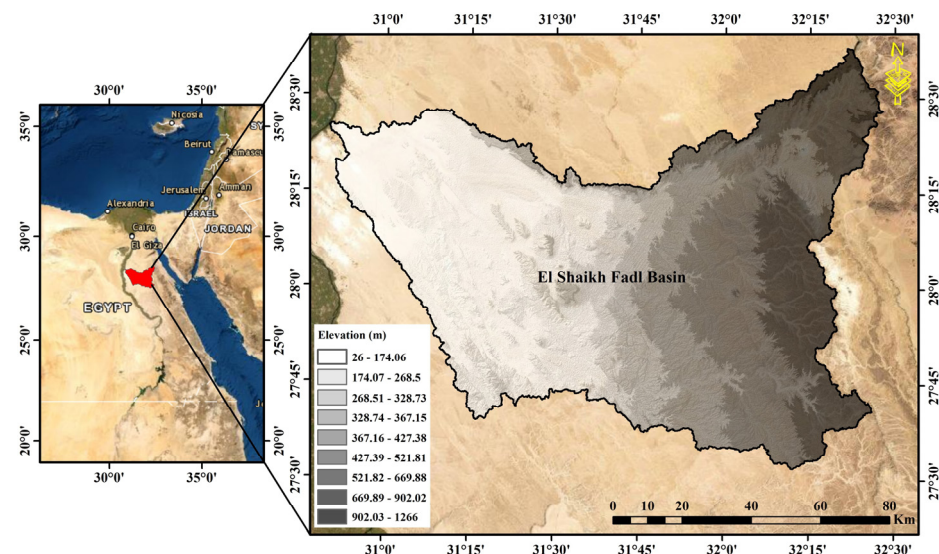
Figure 1. Location map of the study area.

The studied area is situated in the arid zone in the Eastern Desert, with hot summers reaching 40 °C, and cold winters with a minimum temperature near zero °C. Evaporation rates range between 4.8 mm/day in winter to 12.4 mm/day in summer [30,31]. The average annual rainfall ranges between 2.75 mm and >50 mm at the extreme southeastern part. In the last 50 years, floods were recorded in 1969, 1980, 1984, 1985, 1994 and 2020. Nevertheless, the volume of precipitation is quite low, and floods are the foremost natural risk in the Eastern Desert [32,33].

3. Materials and Methods

The used methodology uses three consequent steps. The first one described the morphometric parameters to evaluate the flashflood risk assessment. The second one provided processes of rainfall–runoff modeling. A spatio-temporal lumped model is used to evaluate the runoff volumes for each sub-basin. The third step determined the good locations for rainwater harvesting (Figure 2). These steps were executed through processing spatial data, counting digital elevation model DEM, RS, soil, and rainfall–runoff data. Several software packages were used: ArcGIS 10.2 [34], ERDAS Imagine 2015 [35], HyfranPlus [36], WMS 11.1 [37], HEC-HMS 4.5 [38], PCI-Geomatics 2015 [39], ENVI 4.5 [40] and RockWorks 16 [41].

3.1. Rainfall Processing

Daily rainfall data were provided by the Directorate General of Meteorology (DGM) in Egypt for the period 1979–2014. Data were provided for the Beni-Suef meteorological station (29.04° N, 31.09° E). Given the lack of metadata for these observed data, it was crucial to guarantee the accuracy and reliability of the data. The goal was to make weather and climate variability the primary drivers of climate variability, rather than other non-climatic variables (e.g., relocations of observatories, changes in instruments, observers and observation practices, urbanization, etc.) [42]. Therefore, the data went through a rigid quality assurance process. The process was designed to get rid of anomalies and outlier values in the data. In order to test the homogeneity of the data, we applied relative homogeneity tests (which consider data from neighboring stations) in order to identify potential break points in the series. This procedure is recommended when there is a lack of a convincing history and metadata for the meteorological records. In particular, we used a semi-automated protocol by way of the R package HOMER, which is designed for detecting and fixing inhomogeneities in monthly climatic data by means of relative homogeneity techniques [43].
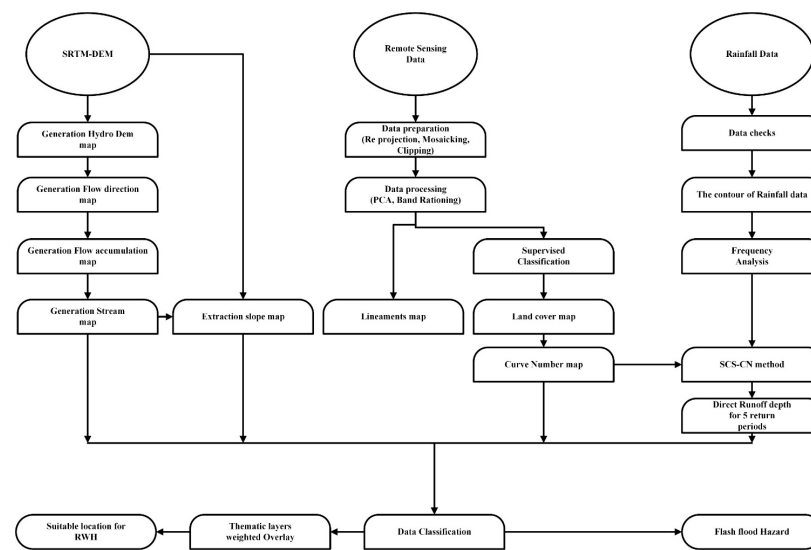
Figure 2. Flow chart of the methodology used for assessing the flashflood hazard and RWH sites.

In light of recent developments in numerical weather prediction modeling and data assimilation, a growing number of reanalysis datasets are available, providing information on a wide range of climate variables with enhanced spatial continuity and long and continuous temporal coverage. Given the scarcity of local meteorological records in the study domain, a decision was made to employ the National Center for Environmental Prediction's (NCEP) Climate Forecast System Reanalysis (CFSR) [44]. Based on a fully coupled ocean–land–atmosphere model, the NCEP-CFSR reanalysis dataset (https://www.ncdc.noaa.gov/data-access/model-data/model-datasets (accessed on 14 February 2022)) is used to assimilate and predict atmospheric states through the application of numerical weather prediction techniques [44]. NCEP-CFSR (hereinafter CFSR) has been widely used in hydroclimatic analysis and simulation, especially in regions with sparsely distributed weather stations, due to its improved spatial resolution (0.5°) and relatively long time series (1979 onwards) [45] Herein, it is noteworthy that several reanalysis datasets are available for research community, such as the National Centers for Environmental Prediction reanalysis II (NCEP-2), the European Centre for Medium-Range Weather Forecasts (ECMWF) Interim Reanalysis (ERA-Interim), the Japanese 55-year Reanalysis Project (JRA-55), and the National Aeronautics and Space Administration (NASA) Modern Era Reanalysis for Research and Applications Version-2 (MERRA-2). However, in our study, the preference was made to employ the CFSR dataset for characterizing flashfloods because of its uniform spatial and temporal resolutions across a wide range of hydrometeorological variables that contribute significantly to rainfall-harvesting assessment, including maximum and minimum air temperatures, precipitation, etc. In this work, the spatiotemporal distribution of precipitation in each sub-basin within the study domain was analyzed by selecting the adjacent gridded data. The events were assigned one of five fictitious proposal storms with return periods of 5, 10, 25, 50, and 100 years. Then, we used statistical frequency analysis to determine the maximum 24 h precipitation values for 5-, 10-, 25-, 50-, and 100-year return periods. Curves for five return periods were fitted using the Log-Pearson type 3, method of moments (BOB), which provides the best-fit curve for the used rainfall data with the smallest root-mean-square error (RMSE). Precipitation spatial analysis for the five previous return periods was performed using the Kriging method.

In order to look at the possible impacts of climate change on rainfall-harvesting capabilities, we assessed long-term changes (1979–2014) in a range of selected climatic variables (e.g., maximum and minimum air temperatures, rainfall totals, relative humidity, etc) (Appendix A, Tables A1–A3). Trends were assessed using the linear least squares regression technique. For each variable and time series under study, we calculated the slope to indicate the rate of change over the period of interest. To determine whether

or not the observed changes were statistically significant at the 95% confidence interval ($p < 0.05$), the modified Mann–Kendall statistic was used [44]. This is an example of a non-parametric test, which does not presume anything about the data's distribution in advance. This metric's positive values indicate an increasing trend, while its negative values point to a declining trend. The impact of serial autocorrelation presented in the data on trend detection is limited when using the modified Mann–Kendall test, as opposed to the standard Mann–Kendall test. This is simply due to the fact that the sample size is taken into account, and a correction factor is applied to the original variance formulation when serial autocorrelation is present in the data [43,44].

3.2. Morphometric Analysis [45,46]

The ASTER Digital Elevation Model with 30 m resolution was obtained from the United States Geological Survey (USGS, ASTER). The study area was covered by four USGS DEM quadrangles. Analyses of the ASTER DEM was used to determine watershed delineations, flow directions, flow accumulations, stream orders, morphometric parameters, and ground surface slope.

The morphometric parameters were extracted for the main basin and its sub-basins. These parameters were classified into three types: linear [47–50], areal [47,49,51], and relief [47,49,51–53] (Appendix A, Tables A4–A6). Some morphometric parameters were utilized to evaluate the flashflood hazard using the morphometric ranking method. The morphometric ranking method was used to calculate the degree of the vulnerability to flashflood for each sub-basin [10,54,55]. Fourteen morphometric parameters sensitive to the flooding process were selected. All of these parameters were positively correlated to the hazard degree of flood, while the length of overland flow (Lg), weighed mean bifurcation ratios (WMRb), and mean bifurcation ratio (MRb) were inversely correlated. The morphometric ranking score for each parameter was determined by the following equations:

$$Y = \frac{(Ymax - Ymin)(X - Xmin)}{(Xmax - Xmin)} + Ymin \tag{1}$$

For Lg, MRb, and WMRb showing an inverse correlation [56], the degree of hazard was determined by utilizing the following equation;

$$Y = \frac{(Ymax - Ymin)(X - Xmax)}{(Xmin - Xmax)} + Ymin \tag{2}$$

where Y is the relative degree of hazard, and Ymax and Ymin are the highest and the lowest limits of the projected scale. Xmax and Xmin are the maximum and minimum assessed values of any parameter. X is the value of any parameter located between the maximum and minimum values [56]. The score for flashflood hazard for each basin ranged from 1 to 5, which was dependent on the parameter relative to the susceptibility of flooding.

3.3. Image Analysis

Multi-spectral satellite images from September 2021 of the Landsat-8 was used (USGS, https://earthexplorer.usgs.gov/ (accessed on 1 September 2021)). It was obtained from USGS with a spatial resolution of 30 m (multi-spectral) and 15 m (panchromatic) and land cloud cover of 0.06%. The mosaicking and clipping bands were made using spatial analyst tools in ArcMap10.2. Resampling the multi-spectral bands with panchromatic band was carried out to increase the spatial and spectral range resolution. Composites bands, band rations, and principle component analyses were completed to determine the soil types, curve number (CN), and land-use classes. Supervised classification was done after the initial unsupervised classification [57,58].

The final output of the image analysis categorized the study area into different classes with different curve numbers. This curve number is an experiential parameter applied as a portion of the hydrology calculation. It predicts the direct runoff and infiltration from

surplus rainfall. Areas of low CN point to absorption, evaporation, surface storage, and transpiration processes [59]. The higher values of CN point to impervious areas leading to high runoff potentials. This variation based on slope, soil type, land-cover units, vegetation potency, and moisture content [60].

3.4. Rainfall–Runoff Modeling

Rainfall–runoff modeling was done using the package HEC-HMS (Hydrologic Engineering Center-Hydrologic Modeling Systems); it was established to simulate the processes of rainfall–runoff into watershed systems [61]. It has flexible options for assessing the penetration losses and hydrograph parameterizations [62].

Rainfall–runoff modeling uses various datasets such as DEM, land-use, soil type, and meteorological data. The soil conservation service curve number (SCS-CN) method was utilized. It calculates stream volume flow and create the hydrographs at the outlet of the main basin and sub-basins. This technique uses Equations (3)–(6) as follows:

$$CNw = \frac{\Sigma CNi * Ai}{At} \tag{3}$$

$$S = \left(\frac{100}{CNw}\right) - 10 \tag{4}$$

$$Q = \frac{(p - 0.25)^2}{(p + 0.8S)} \, for \, Q > 0.2S : else \, Q = 0 \tag{5}$$

$$Ia = 0.2S \tag{6}$$

where CN_w is the weight of CN, CN_i is the CN of the same value in a sub-basin, A_i the area of CN_i in a sub-basin (km^2), and A_t the total area of the sub-basin (km^2). While S is the potential maximum soil moisture retention depth, I_a is the initial abstraction loss depth. Q is the direct runoff depth over the entire sub-basin for any return period, and P is the precipitation depth for 24 h duration storm for any return period at the same sub-basin. Moreover, the time of concentration, lag time, time to peak, and the maximum of the discharge parameters are assessed by using Equations (7) [63] and (8) [64] as follows:

$$T_c = \frac{5}{3} + TL \tag{7}$$

where T_c is the time of concentration (h) of any sub-basin, and TL is the lag time (h) for the same sub-basin.

$$T_p = \frac{\Delta D}{2} + TL \tag{8}$$

where T_p is the time to peak, and ΔD is the duration time for excess rainfall (h).

3.5. Mapping of the Suitable Potential Sites for RWH

The used methods for determine the suitable locations of RWH are based on GIS, RS, and variables techniques. The analytical hierarchical process (AHP) technique was used, and the professional knowledge of six experts was utilized (Table 1) and Appendix B, Figure A1. It is one of the best-known and most commonly used multicriteria decision analysis (MCDA) methods [65–67]. Although this method needs a lot of metrological, morphometric, and land-use information, and it has a difficult validation process, it is a significant method, since a different construction may lead to a diverse final ranking [68–70]. It chooses the required criteria by ranking the factors and the qualitative and quantitative parameters [71]. It gives a framework, that can handle diverse opinions on determining the elements of a decision and arrange the elements into a hierarchical construction [72]. AHP has the advantage of permitting a hierarchical structure of the criteria, which provides users with a better focus on specific criteria and sub-criteria when allocating the weights. Furthermore, it aids decision-makers in finding the one that best suits their needs and their

understanding of the problem, whereas it decreases bias in the decision-making procedure and provides group decision creation through agreement, utilizing the symmetrical mean of the separate decisions. The integration of AHP with GIS gives an efficient and user-friendly way of solving complex problems [60].

Table 1. Profiles of the experts.

Stakeholder Group	ID	Role	Division	Experience (Year)
Universities (UN)	E1	Assistant Lecturer	Hydrogeology	11
	E2	Professor	Hydrogeology	31
	E3	Professor	Meteorology	28
	E4	Professor	Environment	30
Water Research Center	E5	Associate Professor	Structural Engineering	25
Universities (UN)	E6	Professor	Soil	29

The land-cover, average of annual max 24 h rainfall, slope, stream order, and lineaments density were selected to determine suitable locations for RWH. The different data categories were reclassified into classes, and each class was given a definite rank that will impact RWH. The relative significance of different criteria are defined [69,73,74].

The rating rank is assigned to each layer based on the strength of significance [75] (Appendix A, Table A7) for each criteria. The pairwise comparison diagonal matrix was constructed. Then the relative weights were computed by standardizing any rows and columns for pairwise comparison diagonal matrices. However, a division of each component in each column is calculated by the summation of that column. The eigenvectors of these matrices are calculated by obtaining the mean of the normalizing matrix. Furthermore, the eigenvector of the normalizing matrices is equal to the weight values of every criterion. The pairwise comparison matrix is utilized in the description of weights for each criterion. The principal eigenvector of the pairwise comparison matrix is determined to give a good fit to the weight set. However, values of weight are absolute numbers ranging from zero to one. Utilizing a weighted linear combination shows that the sum of weights is equal to one.

The final mapping of suitable locations for RWH was delineated by establishing the AHP-GIS multi-criteria model, wherein the overlaying of the reclassified weighted raster was done. This criterion divided the raster into five classes; excellent, very good, moderate, poor, and unsuitable for RWH.

4. Results and Discussion

4.1. Morphometric Analysis

The study area was distinguished by composite and intertwining patterns that indicate the morphotectonic growth of the drainage basins. It was divided into fifteen sub-basins (Figure 3A). The morphometric analysis was classified into three morphometric attributes: linear, areal, and relief characteristics.

4.1.1. Linear Characteristics

The stream orders (U) are the 9th and 7th of the main basin and its sub-basins, respectively (Figure 3B). The high stream orders are related to the large areas and high discharge of stream flow. The stream number (Nu) for the main basin is 162,577, while the values for the 7th order sub-basins ranged from 2517 to 12,072 (sub-basins No. 4 and 10, respectively), with an average of 6294 and a standard deviation of 3041 (Table 2 and Appendix C, Table A8). The Nu of each order forms an inverse geometric sequence with order number and a direct relation with the basin size (Appendix C, Table A8). The high stream number value of sub-basin No. 10 referred to the small permeability and infiltration of the ground surface. Moreover, the different geological structures in each sub-basin are the main reason for the unequal stream number in each order.
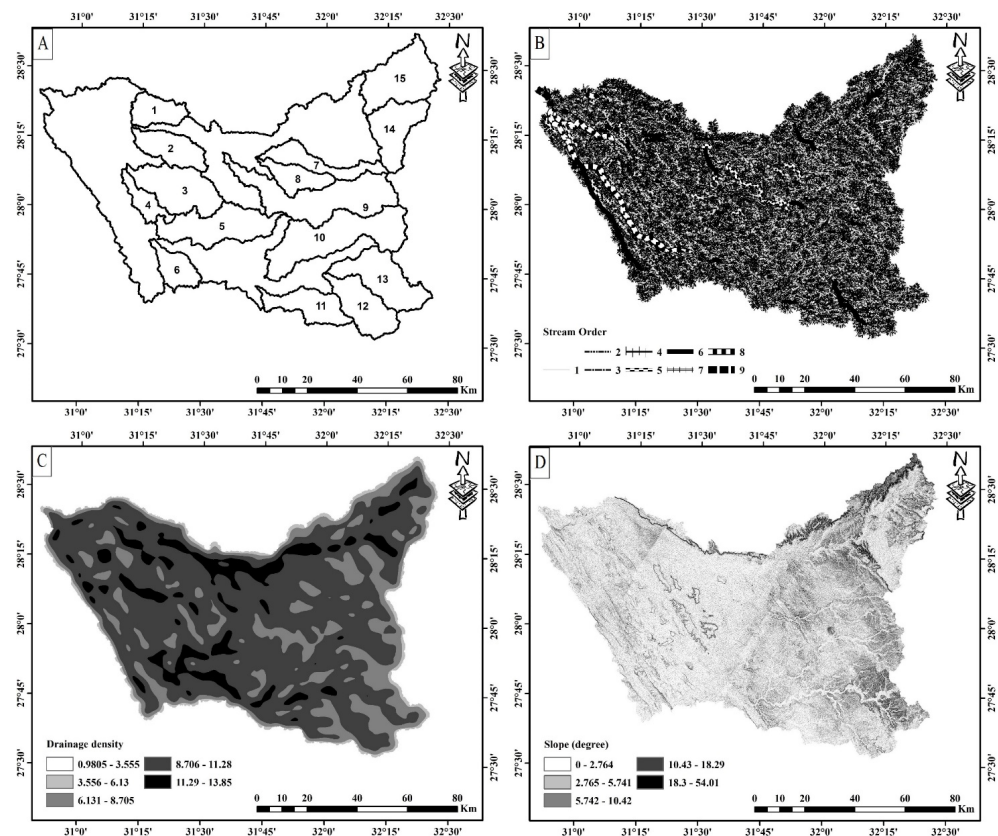
Figure 3. (**A**) Sub-basin number l; (**B**) stream order; (**C**) drainage density; (**D**) slope (degree).

Table 2. Descriptive statistics of the linear characteristics for 15 sub-basins in study area.

Parameters	Minimum	Maximum	Mean	Std. Deviation
Stream number (Nu)	2517	12,072	6294.53	3041.13
Stream length (Lu) in km	836.82	3818.30	2029.51	952.60
Mean bifurcation ratio (MRb)	3.70	8.98	4.50	1.27
Weighted mean bifurcation ratio (WMRb)	3.55	5.72	4.50	0.64
Basin length (Lb) in km	23.80	73.56	41.87	13.82
Length of overland flow (Lg) in km	2.30	2.66	2.49	0.10

The stream total length (Lu) for the main basin is 52,577 km, whereas, the values for the 7th order sub-basins ranged from 837 to 3818 km (sub-basins No. 4 and 10, respectively), with an average of 2029 km and standard deviation 952 (Table 2 and Appendix C, Table A8). The differences in the wadi length in these sub-basins are due to the variation of topography and geological structures that exist in these areas.

The value of the weighed mean bifurcation ratios (WMRb) for the main basin was 4.35 while the values for the 7th order sub-basin ranged from 3.55 to 5.72 (sub-basins No. 5 and 13, respectively), with a mean of 4.50 and a standard deviation of 0.64. Both the MRb (mean bifurcation ratio) and WMRb for the main basin and its sub-basins are >3 (Table 2 and Appendix C, Table A9). The high values of Rb indicate high mountainous areas and an elongated basin shape with low flooding potentialities. The small Rb value of the 7th order sub-basins indicate a circular basin shape with rapid hydrographic high peak flooding. These results can be explained by the sub-basins No. 12, 13, 14, and 15, which are more vulnerable to flooding (Appendix C, Table A9). The length of the main basin was 178 km, and the 7th order sub-basins length ranged from 24 to 74 km (sub-basins No. 1 and 9, respectively), with an

average value of 42 km and a standard deviation of 13.82 (Table 2 and Appendix C, Table A9). The travel time of flood in sub-basin No. 9 is greater than in sub-basin No. 1, where the sub-basin No. 9 has good priorities for groundwater recharge (Appendix C, Table A9). The length of overland flow (Lg) indicates the flow length of the surface water before it reaches the specified channel of the main basin; it is 2.47 km for the mean basin, whereas, for the 7th order sub-basins, it ranged from 2.30 to 2.66 km (Sub-basins No. 13 and 6, respectively), with a mean value of 2.49 and a standard deviation of 0.10 (Table 2 and Appendix C, Table A9). The low values of Lg refer to a gentle slope with a longer flow path and more vulnerability to flash flooding (Appendix C, Table A9).

4.1.2. Areal Characteristics

The main basin area is 10,646 km^2, while the areas of the 7th order sub-basins range from 159 to 789 km^2 (sub-basins No. 4 and 10, respectively), with an average of 411 km^2 and a standard deviation of 198 (Table 3 and Appendix C, Table A10). The sub-basins are classified according to Horton (1945) into the category of large basins with an area >100 km^2, indicating the accumulation of a large amount of surface water.

Table 3. Descriptive statistics of the areal and relief characteristics of the main basin and its sub-basins.

Parameters	Minimum	Maximum	Mean	Std. Deviation
Basin area (A) in km^2	159.01	789.01	411.32	198.15
Basin perimeter (P) in km	90.08	258.93	144.00	48.81
Drainage density (Dd) in (km/km^2)	4.60	5.30	4.97	0.21
Stream frequency (Fs)	13.95	16.65	15.35	0.75
Texture ratio (T) in (km^{-1})	24.35	55.72	42.32	9.61
Relief ratio (Rh)	0.0046	0.0171	0.0084	0.0033
Basin slope (BS)	0.0406	0.1145	0.0620	0.0220

The basin perimeter (P) of the main basin is 808 km, whereas, the values for the 7th order sub-basin ranges from 90 to 259 km (sub-basin No. 6 and 9, respectively), with an average of 144 km and a standard deviation 49 (Table 3 and Appendix C, Table A10).

The drainage density (Dd) value of the main basin is 4.94 km/km^2, while the values of the 7th order sub-basins ranged from 4.60 to 5.30 km/km^2 (sub-basins No. 13 and 6, respectively), with a mean of 4.97 and a standard deviation of 0.21 (Table 3 and Appendix C, Table A10). The geological structure controls the areal distribution of drainage density in these sub-basins (Figure 3c). The high values of drainage density indicated high runoff potentialities, whereas, the low values indicate fractured rocks cover the ground surface. The high values of Dd for sub-basins No. 1–6 and 14 refer to impermeable rocks and, in some localities, sporadic vegetation (Appendix C, Table A10), while the low values of Dd refers to permeable rocks and soils with a low relief. Therefore, sub-basins with low Dd values could be good sites for groundwater recharge, while sub-basins with high values can form larger surface runoff.

The stream frequency (Fs) for the main basin is 15.27 km^{-2}, while the values for the 7th order sub-basins ranged from 13.95 to 16.65 km (sub-basins 13 and 5, respectively), with an average of 15.35 and a standard deviation of 0.75 (Table 3 and Appendix C, Table A10). The stream frequency is directly associated with lithological features; the basins with structural hills have high values of Fs and low values with alluvial deposits. Most of these sub-basins are distinguished by impermeable rocky areas with a low penetration capacity and a high vulnerability to flashflood.

The texture ratio (Rt) value of the main basin is 201 km^{-1}, while the values for the 7th order sub-basins range from 24 to 55 km^{-1} (sub-basin No. 4 and 10, respectively), with a mean of 43 km^{-1} and a standard deviation of 9.61 (Table 3 and Appendix C, Table A10). Sub-basins

with lower values of Rt refer to plain basins with slight slopes [76,77], and these sub-basins have proper locations for groundwater recharge, such as sub-basin No. 4 (Figure 3a).

4.1.3. Relief Characteristics

The relief ratio (Rh) of the main basin is 0.007, whereas, the values for the 7th order sub-basins range from 0.005 to 0.017 (sub-basins No. 4 and 15, respectively), with an average value of 0.008 and a standard deviation of 0.003 (Table 3 and Appendix C, Table A10). The sub-basin No. 15 is like to experience large-scale flooding, and its high Rh value is directly related to flooding and contrary to the time of concentration. This can be explained by the presence of large areas of high-relief impervious limestone with a steep ground surface.

The slope value of the ground surface for the main basin is 0.056, while the values for the 7th order sub-basins range from 0.041 to 0.115 (sub-basins No. 5 and 15, respectively), with a mean of 0.062 and a standard deviation of 0.022 (Table 3, Appendix C, Table A10, and Figure 3d). The basins with gentle slopes are characterized by a long concentration time, little runoff, and small hydrograph peaks, such as sub-basins No. 2, 3, 4, 5, 6, and 11 (Figure 3d), whereas sub-basin 15 had a high slope value with a high amount of runoff and a shorter concentration time to the hydrograph peak. Therefore, sub-basin No. 15 could be more vulnerable to flooding events compared to other sub-basins.

Most of the sub-basins have a dendritic drainage pattern, reflecting little infiltration and extreme runoff events, particularly in the highly terrain areas. The main trend of the extracted liniments from Landsat image analysis is NW–SE, which is comparable with the Red Sea trend (Figure 4A,B).
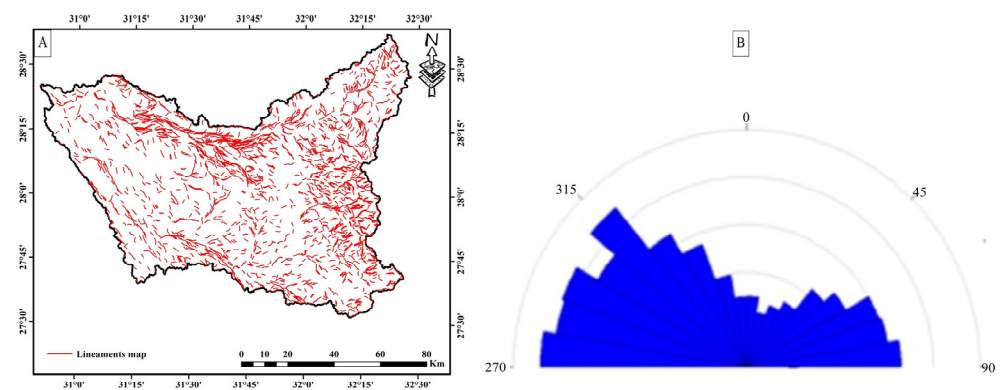
Figure 4. (**A**) Lineament map; (**B**) Rose diagram for lineaments.

4.2. Flashflood Hazard Assessment

The morphometric ranking method was used to define the degree of flashflood hazards. It was carried out by an analysis of different scores of morphometric variables (Table 4). The 7th order sub-basins were categorized according to flooding vulnerability by different relative hazard degrees, which are divided into five classes: extremely high, high, moderate, low, and very low (Figure 5). The low-flooding-susceptibility area is in sub-basin No. 4. On the other hand, sub-basins No. 15, 14, 10, 9, and 3 show extremely high scores, representing the most dangerous sub-basins.

The most hazardous and threatening sub-basins are located in the upper part of the basin. The potential for vulnerability to flooding is high due to high slopes and a lack of stream meanders. Several solutions must be carried out to protect the area. Three and six sub-basins have a moderate and low-flooding-susceptibility degree, respectively.

Table 4. Hazard degrees of the effective parameters.

Basin No	Relative Hazard Degrees of the Effective Parameters														Basin Hazard Degree
	A	Dd	Fs	Rr	SI	Rn	Rt	Ish	BS	ΣN	ΣL	Lg	WMRb	MRb	
1	1.41	3.85	3.22	3.74	3.02	5.00	2.88	1.90	2.60	2.13	1.39	1.41	2.26	4.92	3
2	1.91	3.77	2.88	3.89	1.57	3.10	1.47	1.58	3.09	1.03	1.88	1.96	2.11	4.71	2
3	3.24	4.77	4.80	4.29	1.33	3.61	1.54	2.04	5.00	1.36	3.49	3.44	1.71	4.51	4
4	1.00	4.58	3.78	4.68	1.00	2.23	1.00	1.01	1.00	1.04	1.00	1.00	1.32	5.00	1
5	3.44	5.00	5.00	3.98	1.37	2.30	1.42	2.40	3.75	1.00	3.73	3.62	2.02	1.00	3
6	1.30	3.97	3.57	5.00	1.25	3.49	1.07	1.00	2.48	1.07	1.30	1.35	1.00	4.93	2
7	1.77	2.85	2.80	2.39	1.81	1.00	2.68	3.90	1.33	2.50	1.73	1.70	3.61	4.67	2
8	1.41	4.02	4.01	2.21	1.79	2.38	2.42	2.18	2.27	2.61	1.44	1.32	3.79	4.73	2
9	4.97	3.25	2.97	2.38	1.55	1.64	2.21	4.54	3.79	2.40	4.96	4.98	3.62	4.20	4
10	5.00	3.01	3.00	2.31	1.74	2.35	2.22	3.89	4.84	2.21	5.00	5.00	3.69	4.29	4
11	2.02	2.66	3.32	2.66	1.53	2.17	1.64	2.01	2.66	1.28	2.02	1.98	3.34	4.67	2
12	2.46	1.93	2.31	1.73	1.54	3.48	1.90	1.94	4.02	2.04	2.36	2.35	4.27	4.56	2
13	3.10	1.00	1.00	1.00	1.68	3.05	2.35	2.71	3.69	4.37	2.81	2.91	5.00	4.54	3
14	2.49	2.37	1.80	3.25	5.00	4.70	3.55	3.10	4.07	2.33	2.34	2.52	2.75	4.68	4
15	3.50	1.63	1.60	2.25	3.60	4.42	5.00	5.00	4.77	5.00	3.27	3.46	3.75	4.50	5

Sub-basin area (A), drainage density (Dd), stream frequency (Fs), relief ratio (Rr), slope index (SI), ruggedness number (Rn), texture ratio (Rt), shape index (Ish), basin slope (BS), total stream number (ΣN), total stream length (ΣL), length of overland flow (Lg), weighed mean bifurcation ratios (WMRb), mean bifurcation ratio (MRb).
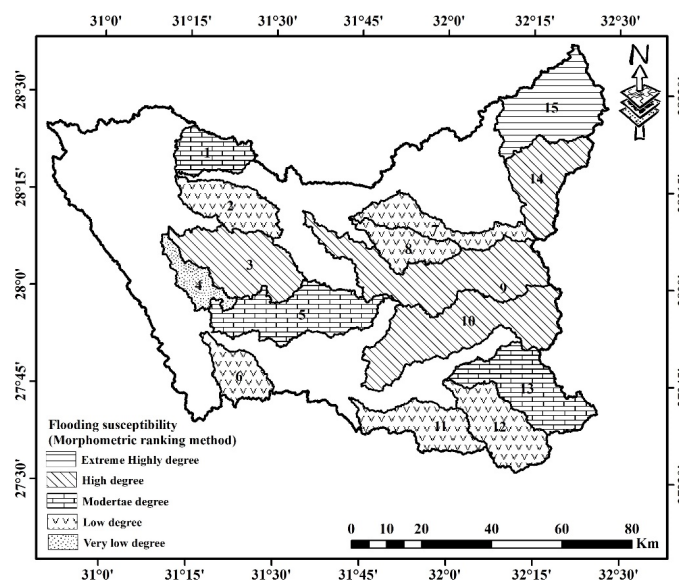
Figure 5. Flooding susceptibility: morphometric ranking method.

4.3. Rainfall–Runoff Modeling

Five hypothetical proposed storms were established for rainfall events with 5-, 10-, 25-, 50-, and 100-year return periods. The maximum 24 h rainfall data of the five return periods ranges from 1 to 55 mm/year (Appendix B, Figure A2). The appropriate curves between the return period and the historic 24 h rainfall depth was calculated with a confidence level of about 95% (Figure 6). The southeastern part of the study area is characterized by high rates of rainfall. Due to the prevalence of steep slopes in this area, rainwater harvesting is unfavorable. The central part of this basin is characterized by low rainfall rates, moderate runoff, and gentle slopes; therefore, potential sites for rainwater harvesting can be delineated (Figure 3d).
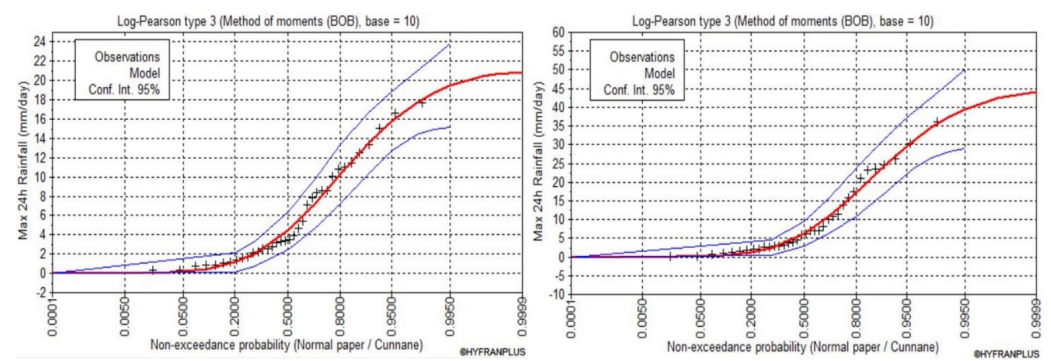
Figure 6. The maximum 24 h rainfall data for the temporal analysis of rainfall data.

The CN values of the different land-use classes vary between 55 and 89 (Appendix C, Table A11); they indicate vegetation, quarries, recent alluvium, weathered limestone, old alluvium, and massive limestone (Figure 7A). The CN values were validated using field observations and geological map. Also, band ratio (7/5, 3/2, 4/5), principal component analysis (1, 4, 3), and composite bands (7, 6, 2) were used in confirming this validation (Figure 7B–F).
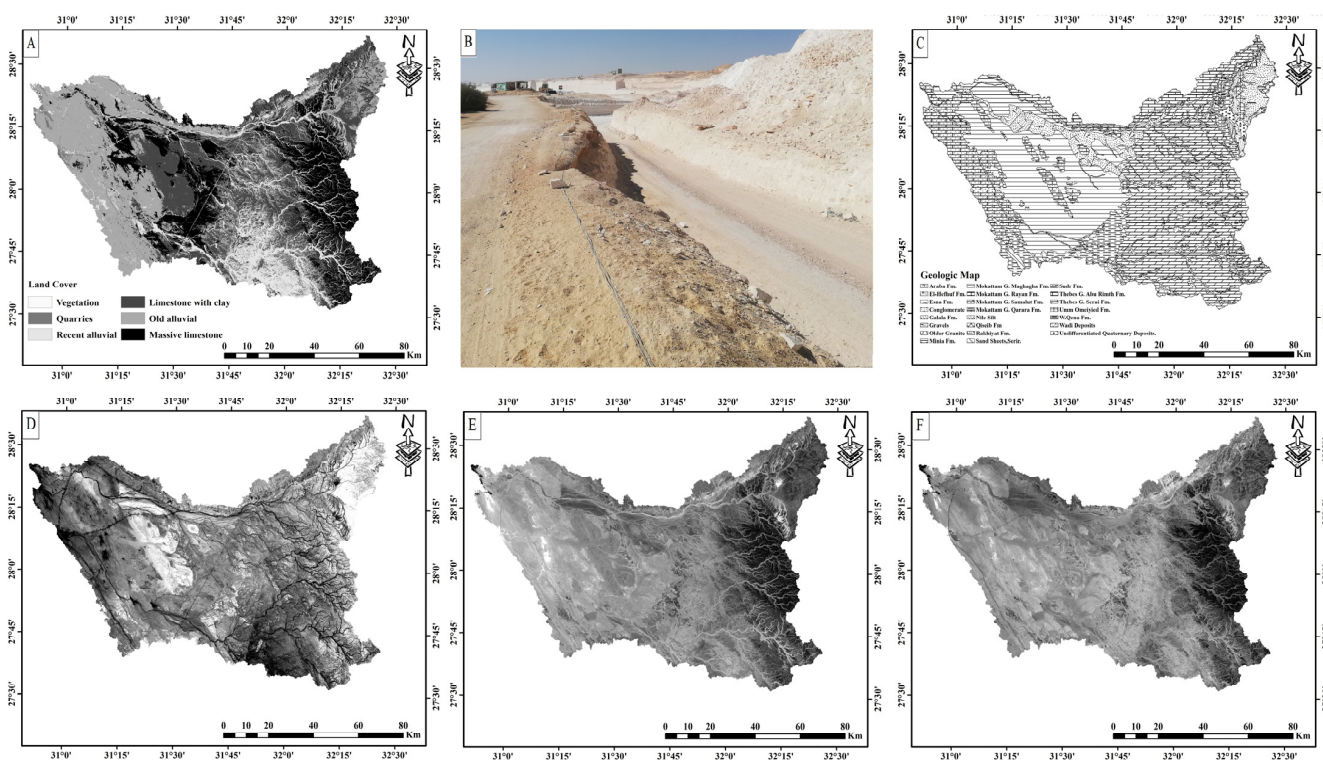
Figure 7. (**A**) Curve number map; (**B**) field plot; (**C**) geologic map; (**D**) band ratio (7/5, 3/2, 4/5); (**E**) principle component (1, 4, 3); (**F**) composite bands (7, 6, 2).

The different input factors of the constructed hydrological model were investigated. To simulate the hydrological probability, the SCS-CN method was utilized (Appendix C, Table A12). The hydrograph and peak discharge of each return period were calculated and assessed at the outlet of each sub-basin (Table 5 and Figure 8). The values of the flood peak increase with the increasing of return periods. The values of the peak discharge of sub-basin No. 15 are the greatest compared to the other sub-basins. It ranged from 40.5 to 201.5 m^3/s (5- and 100-year return periods, respectively). Sub-basin No. 4 presented the lowest values of peak discharge; it ranged from 1.8 to 4.3 m^3/s (5- and 100-year return periods, respectively).

Sub-basin No. 15 showed high vulnerability to flooding, as illustrated by morphometric ranking (Table 4). For the main basin, the value of peak runoff discharge ranged between 60.3 and 358.3 m^3/s, with a total volume of 102,478 m^3 and 60826.4 m^3 (5-year and 100-year periods, respectively), (Figure 9).

Table 5. Peak discharge of runoff values (m^3/s) for each sub-basin and each return period.

Basin No	Return Period (Year)				
	5	**10**	**25**	**50**	**100**
1	3.6	4.7	6	6.7	7.6
2	7.6	11.9	20	25.8	31.9
3	35	49.9	67.2	83.7	99.1
4	1.8	2.5	3.1	3.4	4.3
5	9.1	14.3	24.9	35.8	46.5
6	4.1	6.1	9.3	13.7	18.7
7	8.5	15.4	27.1	36.2	44.9
8	2.8	4.2	7.8	11.4	14.7
9	16.5	29.7	52	68.2	80.4
10	11.2	18.1	32.7	44.4	54.7
11	2.7	4.2	6.2	7.4	9.2
12	5.5	10.1	26.5	43.7	61.3
13	8.8	22.6	55.1	82.7	109.4
14	21.6	39.2	70.1	93.8	115
15	40.5	72.5	127.2	167.3	201.5
Main basin	60.3	95.9	188.4	273.7	358.3

The outcropped massive limestone rocks are highly affecting the hydrological setting. They decrease the rate of infiltration and increase runoff, therefore leading to high flooding events. Consequently, intensive rainfall storms can form high peak floods in short times, which can threaten urban areas and agricultural areas (Appendix A, Figure A3). Therefore, low dams are proposed at proper sites for protection. In areas covered with alluvium deposits and gentle slopes, water can be harvested to recharge groundwater or is used directly for domestic and agriculture purposes.

4.4. Multi-Criteria Decision Analysis for the Study Area

Five layers of information were used to assess flooding potentialities and in particular propose suitable locations for RWH. Six units of land-cover were extracted using a supervised analysis of Landsat-8 images (Figure 10A). These six units were classified into six classes; the hard massive and impervious unit took the high rate. The different land-cover units had different scores, which were relative to rock type, permeability, and vegetation cover: massive limestone, limestone with clay, quarries, old alluvial, recent alluvial, and vegetation (6, 5, 4, 3, 2, and 1, respectively), (Figure 10B and Appendix C, Table A12). The intensity of importance for land-cover ranged from 1 to 3, with a total value of 5.53 and an eigenvector of 0.21 (Tables 6 and 7). The average annual max 24 h rainfall was extracted from a historical data log (1979 to 2014). The max 24 h rainfall distribution was reclassified into five classes, wherein the high-intensity rainfall was taken as a high rate (Figure 10C,D and Appendix C Table A12). The intensity of importance for rainfall criteria with other criteria ranged from one to three, with a total of 5.67 and an eigenvector of 0.19 (Tables 6 and 7). Figure 10c shows the rainfall distribution in the study area, where the higher values are recorded in the upstream area to the east, where it is characterized

by steep slopes with high run-off events, therefore making it unsuitable for RWH. DEM processing and analysis was used to extract the different slope classes (Figure 10E). The rating criteria reclassifies the slope into five classes, wherein the low-slope areas result in a high rate value (Figure 10F and Appendix C Table A12). The slope importance criteria relative to other variables ranged from 0.14 to 1, with a total of 2.01 and a high value of the eigenvector at 0.47 (Tables 6 and 7). Runoff flows very fast in steep areas in the upstream basin, whereas a slow flow was recorded in the gentle-slope areas in the downstream basin. The main stream order (U) is ninth (Figure 10G), and the order criteria rates and reclassified basin into nine classes, wherein the ninth class has a high rate (Figure 10H and Appendix C Table A12). The intensity of the importance value for stream order ranged from one to seven, with a total value of 17 and an eigenvector of 0.06 (Tables 6 and 7). The nominated best sites for RWH are close to the main stream; this has adequate economic feasibility because it reduces the cost of construction (dam No. 1 and 2), and it can also collect a large amount of rainwater. Lineament density was extracted from Landsat-8 image analysis (Figure 10I). The lineament density map was reclassified into five classes, wherein the high-density class has a high rate (Figure 10J and Appendix C Table A12). The lineaments importance criteria in relation to other variables ranged from 1 to 5, with a total of 13 and an eigenvector of 0.07 (Tables 6 and 7). The density of lineaments is an important factor in locating RWH sites; areas with high lineaments density are suitable for RWH, as it assists with rainwater infiltration to the groundwater.
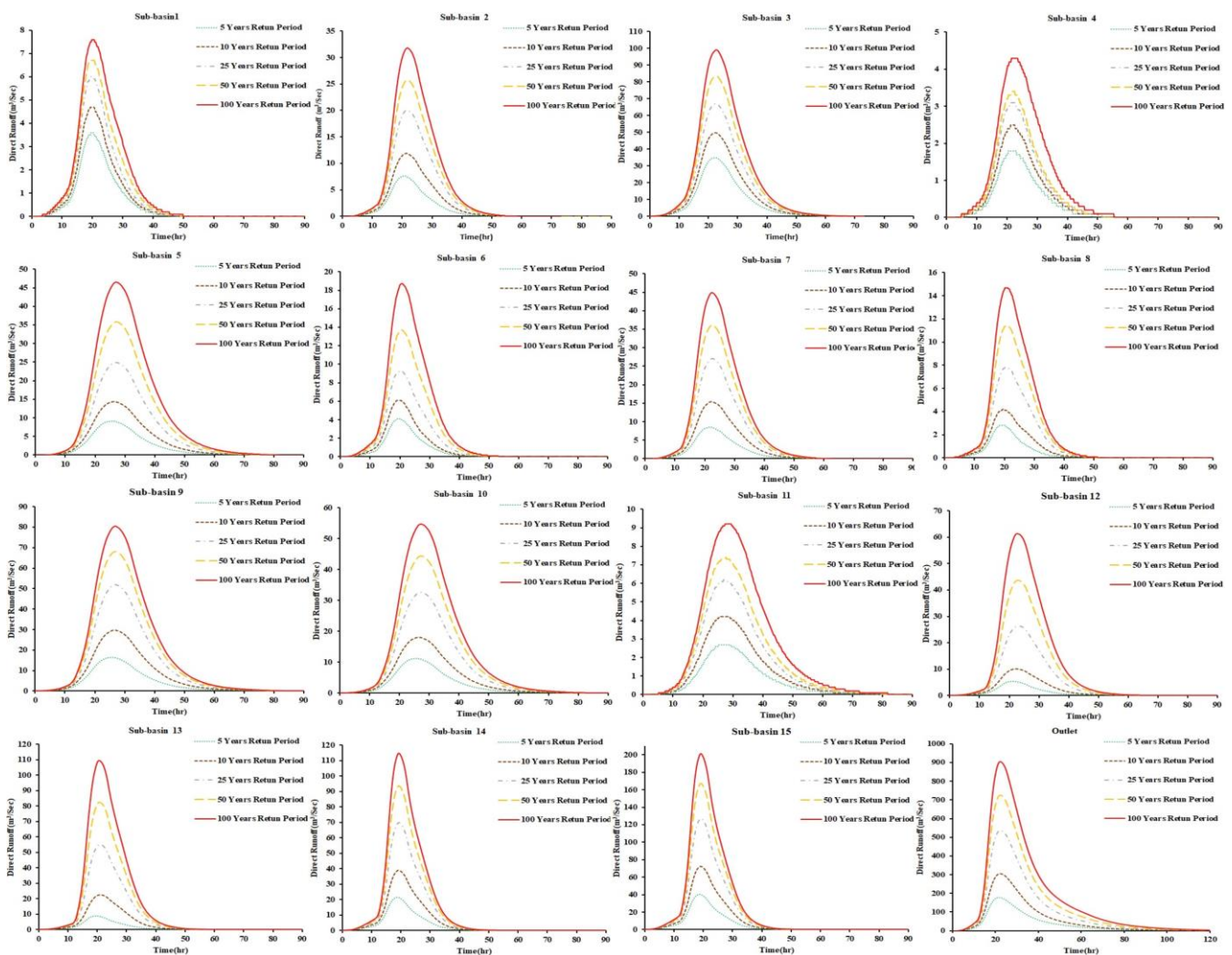
Figure 8. Hydrograph curves for each sub-basin and each return period.
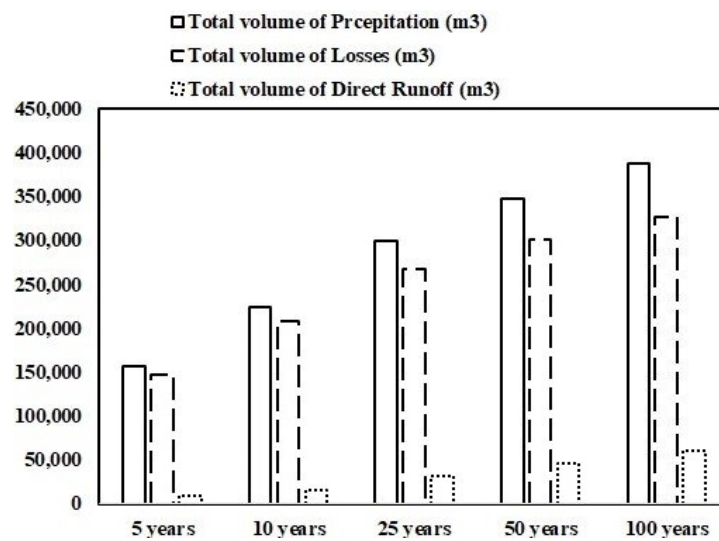
Figure 9. Histogram showing rainfall, runoff, and return period for the main basin.

Table 6. Comparison matrix for the criteria for suitable locations for RWH.

Criteria	Rainfall	Land Cover	Slope	Stream Order	Lineaments
Land cover	1	1	0.33	5	3
Rainfall	1	1	0.33	3	3
Slope	3	3	1	7	5
Stream order	0.33	0.2	0.14	1	1
Lineaments	0.33	0.33	0.2	1	1
Total	5.67	5.53	2.01	17	13

Table 7. Normalizing the columns of the RWH criteria to obtain the normalized matrix.

Criteria	Rainfall	Land Cover	Slope	Stream Order	Lineaments	Egin Vector
Land cover	0.18	0.18	0.16	0.29	0.23	0.21
Rainfall	0.18	0.18	0.16	0.18	0.23	0.19
Slope	0.53	0.54	0.50	0.41	0.38	0.47
Stream order	0.059	0.04	0.07	0.06	0.08	0.06
Lineaments	0.059	0.06	0.10	0.06	0.08	0.07
Total	1	1	1	1	1	1

Rainfall-Harvesting Map

The AHP multi-criteria method was used to determine the appropriate locations for rainwater harvesting. The RWH map was constructed by overlaying reclassified maps, which were selected by different criteria: land cover, average annual max 24 h rainfall, slope, stream order, and lineaments density (Figure 10). Each of these parameters had its relative weight according to the normalized matrix (Table 7).
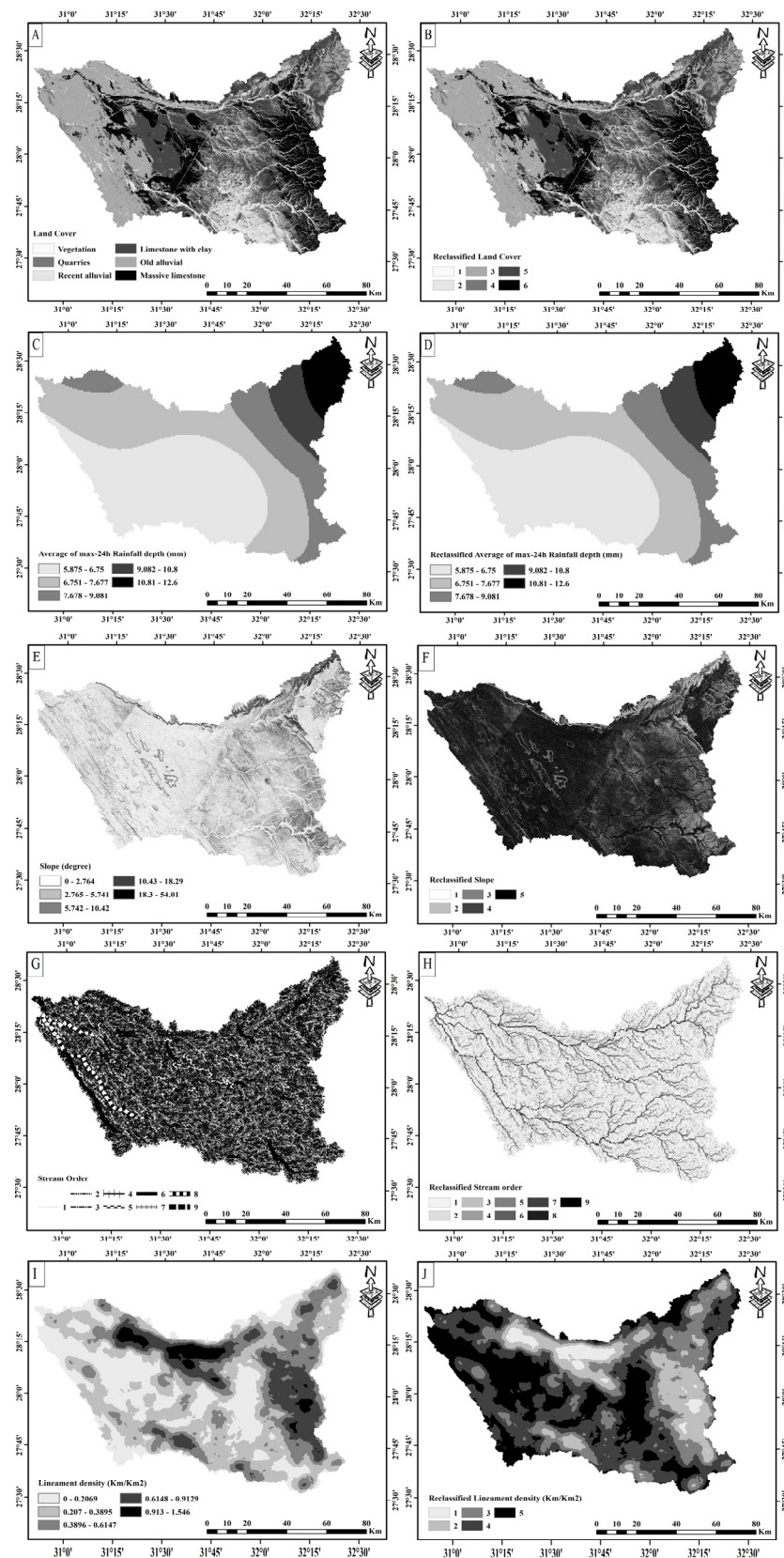
Figure 10. Criteria maps for the AHP of rainwater harvesting in the study area. (**A**) land cover; (**B**) reclassified land cover; (**C**) average of max 24 h rainfall depth (mm); (**D**) reclassified average of max 24 h rainfall depth (mm); (**E**) slope; (**F**) reclassified slope; (**G**) stream order; (**H**) reclassified stream order; (**I**) lineament density; (**J**) reclassified lineament density.

Most parts of the northeast and southeast region have a high value of rainfall; slopes and fine hydrological network. While the steep central parts of the basin are characterized by gentle slopes with little rainfall. However, there low rates of rainfall in this area, where the main stream passes through the central part of the basin. Therefore, these areas are suitable sites for rainwater harvesting (Figure 11). Low-potential sites for rainwater harvesting are distributed in different parts of the basin. They are affected by steep slopes with little rainfall compared with other criteria. The ground surface slope has great impact, more than other variables for delineating areas suitable for rainwater harvesting (Figure 3D). The highly suitable sites for rainfall harvesting cover 6708 km^2, while the moderate- and low-suitability zones cover 3620 km^2 and 319 km^2, respectively (Figure 11B). Ten sites have been proposed for dam construction to locate suitable dam reservoirs (Figure 11A); they are dependent mainly on topography, average rainfall rates, and the economic importance of the site. The values of peak discharge at dam No. 2 ranged from 44.0 to 288.5 m^3/s (5- and 100-year return periods, respectively). Dam No. 1 presents the minimum values of peak discharge; it ranged from 0.9 to 2.0 m^3/s (5- and 100-year return periods, respectively), (Table 8, Figure 12 and Appendix C, Tables A13 and A14).
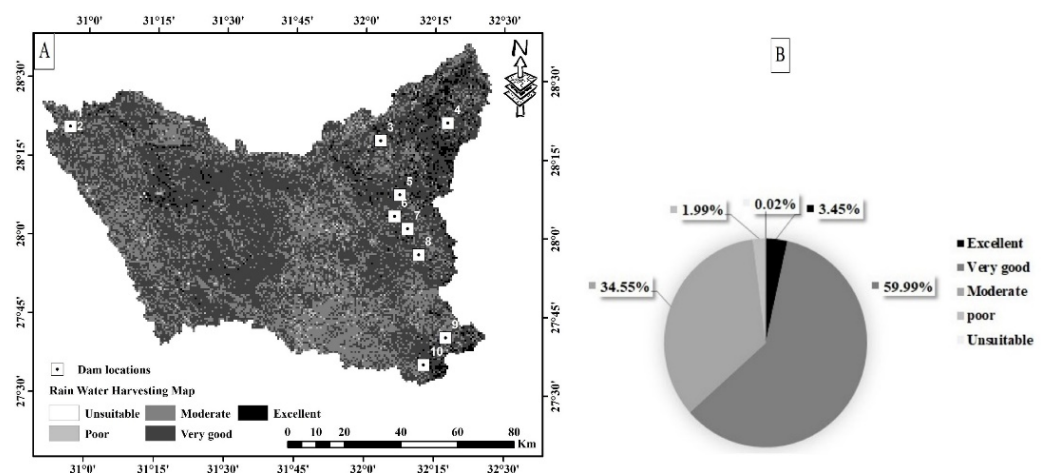
Figure 11. (**A**) Rainwater-harvesting map for the study area; (**B**) percentage of the area covered by different rainwater-harvesting suitability.

Table 8. Peak discharge of runoff values (m^3/s) for each dam and each return period.

Dam No	Return Period (Year)				
	5	10	25	50	100
1	0.90	1.20	1.60	1.80	2.00
2	44.00	84.60	164.70	229.00	288.50
3	4.00	6.20	9.50	11.90	14.10
4	5.70	8.80	14.80	19.70	23.80
5	1.60	2.30	3.10	3.50	3.90
6	17.30	24.70	32.80	37.90	41.90
7	5.20	7.50	9.80	11.40	12.60
8	3.10	4.70	6.00	6.90	7.60
9	2.30	4.00	6.90	9.00	11.00
10	11.40	18.90	29.00	36.40	43.20
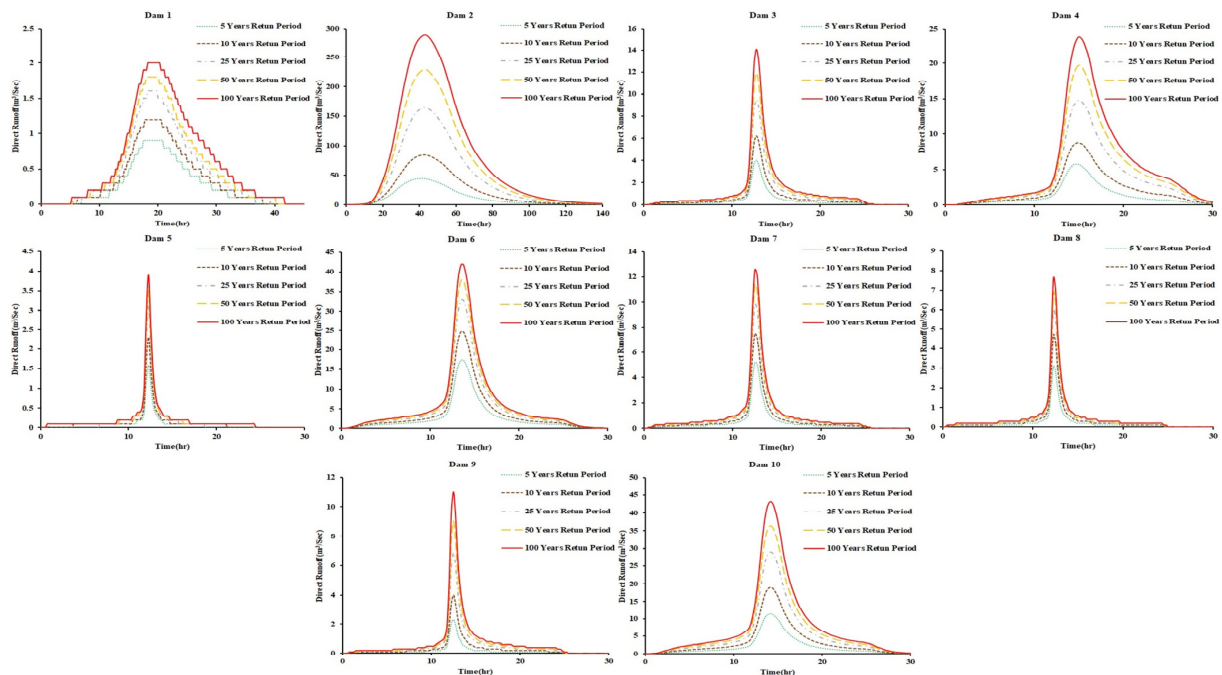
Figure 12. Hydrograph curves for each dam and each return period.

5. Conclusions

Predicting runoff events is a prodigious problem in ungauged arid areas, where the monitoring of flashfloods is a big challenge due to inadequate observational data, the absence of monitoring systems, and a lack of infrastructure. The peak discharge of flashfloods and RWH could be assessed by the integration of GIS, RS techniques, and hydrologic modeling. Dlimate change and the rising of water demands for drinking and agricultural and industrial purposes can increase the pressure on limited water resources. The study area was divided into fifteen sub-basins. Most of the sub-basins have a dendritic drainage pattern. The different morphometric parameters (linear, areal, and relief characteristics) were extracted. They show that the most hazardous and threatening sub-basins were located in the upstream zone of the basin (sub-basins No. 15, 14, 10, and 9). The vulnerability potential for flooding is high in upstream areas. The steep slopes, high drainage density and frequency, and the low degree of stream sinuosity are high relative to the possibility of flooding.

The hydrologic model shows that high rates of rainfall and steep slopes are present in the southeastern part of the study area. The high discharge peak is recorded in sub-basin No. 15 (40.5–201.5 m^3/s for 5- and 100-year return periods, respectively), while the low peak is in sub-basin No. 4 (1.8–4.3 m^3/s for 5- and 100-year return periods, respectively). For the main basin, the value of peak runoff discharge ranged between 60.3 and 358.3 m^3/s, with a total volume of 102,478 m^3 and 60,826.4 m^3 (5-year and 100-year periods, respectively). Low rainfall rates, moderate–high runoff, and gentle slopes were found in the central and downstream parts. Therefore, these areas are appropriate sites for rainwater harvesting. In central and downstream areas covered with alluvium deposits and having gentle slopes, water can be harvested to replenish groundwater or used directly for domestic and agriculture purposes. An analytic hierarchy process (AHP) was applied for mapping the best sites to RWH. This criterion used land-cover, average annual max 24 h rainfall, slope, stream order, and lineaments density. The ground surface slope had a great impact, more than other variables for delineating suitable areas for rainwater harvesting. About 4% of the basin area had a very high potentialities for RWH, while 59% of the basin area had high RWH suitability. Several solutions are recommended to be carried out to protect the area against flashflood hazards. In the study area, ten low dam sites were proposed to impact flooding vulnerability and rainwater-harvesting potentialities. This approach can be used successfully to delineate

suitable sites for rainwater harvesting for proper adaptation practice against climate change in similar arid conditions.

Appendix A

Table A1. Maximum and minimum temperature trend.

ID	Lon(x)	Lat(y)	Begin	End	Max-Trend		Min-Trend	
					LinTrend/Decade	*p*-Value of *t*-Test	LinTrend/Decade	*p*-Value of *t*-Test
N276313	31.25	27.632	1979	2014	0.270	0.018	0.210	0.037
N276322	32.188	27.632	1979	2014	0.280	0.024	0.120	0.255
N276325	32.5	27.632	1979	2014	0.370	0.002	0.160	0.075
N279309	30.938	27.945	1979	2014	0.300	0.005	0.250	0.010
N279313	31.25	27.945	1979	2014	0.270	0.015	0.180	0.075
N279316	31.563	27.945	1979	2014	0.320	0.007	0.130	0.217
N279319	31.875	27.945	1979	2014	0.370	0.002	0.130	0.212
N279322	32.188	27.945	1979	2014	0.390	0.001	0.150	0.112
N283309	30.938	28.257	1979	2014	0.340	0.001	0.420	0.001
N283313	31.25	28.257	1979	2014	0.290	0.010	0.150	0.129
N283316	31.563	28.257	1979	2014	0.310	0.008	0.040	0.735
N283319	31.875	28.257	1979	2014	0.390	0.001	0.080	0.442
N283322	32.188	28.257	1979	2014	0.430	0.000	0.040	0.686
N286309	30.938	28.569	1979	2014	0.380	0.000	0.450	0.001
N286313	31.25	28.569	1979	2014	0.280	0.010	0.100	0.317
N286316	31.563	28.569	1979	2014	0.300	0.010	−0.050	0.660
N286319	31.875	28.569	1979	2014	0.420	0.001	0.040	0.723
N286322	32.188	28.569	1979	2014	0.310	0.011	−0.170	0.156
N289309	30.94	28.88	1979	2014	0.340	0.001	0.360	0.002
N289313	31.25	28.88	1979	2014	0.310	0.004	−0.030	0.788
N289316	31.56	28.88	1979	2014	0.410	0.000	−0.010	0.923
N289319	31.88	28.88	1979	2014	0.630	0.000	0.150	0.139
N292313	31.250	29.193	1979	2014	0.390	0.000	0.050	0.566
N292316	31.563	29.193	1979	2014	0.360	0.001	0.190	0.028
N292319	31.875	29.193	1979	2014	0.400	0.000	0.190	0.026
N295313	31.250	29.506	1979	2014	0.460	0.000	0.180	0.022
N295316	31.563	29.506	1979	2014	0.440	0.000	0.280	0.002
N295319	31.875	29.506	1979	2014	0.340	0.002	0.170	0.041

Table A2. Precipitation and relative humidity trend.

ID	Lon(x)	Lat(y)	Begin	End	Precipitation Trend		Relative Humidity Trend	
					LinTrend/Decade	*p*-Value of *t*-Test	LinTrend/Decade	*p*-Value of *t*-Test
N276313	31.25	27.632	1979	2014	−8.520	0.015	0.000	0.000
N276322	32.188	27.632	1979	2014	−8.080	0.023	−0.010	0.018
N276325	32.5	27.632	1979	2014	−7.110	0.025	0.000	0.092
N279309	30.938	27.945	1979	2014	−6.880	0.039	0.000	0.000
N279313	31.25	27.945	1979	2014	−5.730	0.068	0.000	0.000
N279316	31.563	27.945	1979	2014	−5.270	0.079	0.000	0.198
N279319	31.875	27.945	1979	2014	−5.100	0.085	−0.010	0.054
N279322	32.188	27.945	1979	2014	−5.100	0.090	0.000	0.000
N283309	30.938	28.257	1979	2014	−5.080	0.107	0.000	0.000
N283313	31.25	28.257	1979	2014	−4.790	0.117	0.000	0.166
N283316	31.563	28.257	1979	2014	−4.690	0.158	0.000	0.000
N283319	31.875	28.257	1979	2014	−4.590	0.191	0.000	0.000
N283322	32.188	28.257	1979	2014	−3.990	0.205	−0.010	0.295
N286309	30.938	28.569	1979	2014	−3.900	0.209	−0.010	0.213
N286313	31.25	28.569	1979	2014	−3.900	0.215	0.010	0.147
N286316	31.563	28.569	1979	2014	−3.620	0.216	0.000	0.166
N286319	31.875	28.569	1979	2014	−3.530	0.239	0.000	0.638
N286322	32.188	28.569	1979	2014	−3.450	0.266	−0.010	0.175
N289309	30.94	28.88	1979	2014	−3.300	0.269	−0.010	0.444
N289313	31.25	28.88	1979	2014	−3.210	0.308	0.010	0.063
N289316	31.56	28.88	1979	2014	−2.500	0.360	0.000	0.498
N289319	31.88	28.88	1979	2014	−2.410	0.361	−0.010	0.291
N292313	31.250	29.193	1979	2014	−2.230	0.384	0.000	0.166
N292316	31.563	29.193	1979	2014	−2.220	0.387	0.000	0.166
N292319	31.875	29.193	1979	2014	−2.180	0.473	−0.010	0.152
N295313	31.250	29.506	1979	2014	−1.740	0.519	−0.010	0.161
N295316	31.563	29.506	1979	2014	−1.510	0.574	−0.020	0.059
N295319	31.875	29.506	1979	2014	−0.740	0.773	−0.010	0.072

Table A3. Sunshine and wind trend.

ID	Lon(x)	Lat(y)	Begin	End	Sunshine Trend		Wind Trend	
					LinTrend/Decade	*p*-Value of *t*-Test	Amount/Decade	Sig. Level
N276313	31.25	27.632	1979	2014	0.180	0.005	−0.030	0.084
N276322	32.188	27.632	1979	2014	0.190	0.004	−0.060	0.005
N276325	32.5	27.632	1979	2014	0.200	0.003	−0.090	0.002
N279309	30.938	27.945	1979	2014	0.230	0.001	−0.020	0.088
N279313	31.25	27.945	1979	2014	0.180	0.004	−0.020	0.048
N279316	31.563	27.945	1979	2014	0.150	0.013	−0.050	0.004
N279319	31.875	27.945	1979	2014	0.150	0.014	−0.070	0.000
N279322	32.188	27.945	1979	2014	0.210	0.003	−0.070	0.002
N283309	30.938	28.257	1979	2014	0.240	0.001	−0.010	0.387
N283313	31.25	28.257	1979	2014	0.200	0.004	−0.010	0.323
N283316	31.563	28.257	1979	2014	0.170	0.009	−0.040	0.006
N283319	31.875	28.257	1979	2014	0.170	0.008	−0.060	0.002
N283322	32.188	28.257	1979	2014	0.220	0.003	−0.070	0.001
N286309	30.938	28.569	1979	2014	0.240	0.001	0.010	0.528
N286313	31.25	28.569	1979	2014	0.180	0.005	−0.010	0.213
N286316	31.563	28.569	1979	2014	0.160	0.009	−0.050	0.001

Table A3. *Cont.*

ID	Lon(x)	Lat(y)	Begin	End	Sunshine Trend		Wind Trend	
					LinTrend/Decade	*p*-Value of *t*-Test	Amount/Decade	Sig. Level
N286319	31.875	28.569	1979	2014	0.190	0.005	−0.050	0.001
N286322	32.188	28.569	1979	2014	0.240	0.002	−0.080	0.000
N289309	30.94	28.88	1979	2014	0.240	0.001	0.000	0.883
N289313	31.25	28.88	1979	2014	0.170	0.007	−0.020	0.063
N289316	31.56	28.88	1979	2014	0.170	0.011	−0.060	0.001
N289319	31.88	28.88	1979	2014	0.210	0.003	−0.060	0.000
N292313	31.250	29.193	1979	2014	0.200	0.003	−0.020	0.095
N292316	31.563	29.193	1979	2014	0.210	0.002	−0.040	0.005
N292319	31.875	29.193	1979	2014	0.240	0.002	−0.060	0.000
N295313	31.250	29.506	1979	2014	0.250	0.001	−0.010	0.281
N295316	31.563	29.506	1979	2014	0.250	0.001	−0.030	0.004
N295319	31.875	29.506	1979	2014	0.260	0.001	−0.040	0.004

Table A4. Linear aspects of the drainage watershed.

Morphometric Parameters	Formula	Reference
Stream order (U)	Hierarchical order	[1]
Stream Length (LU) km	The total length of the stream of order (u)	[2]
Bifurcation Ratio (Rb)	Rb = Nu/Nu + 1, where Nu = number of stream segments in order (u), Nu + 1 = number of segments of the next higher order	[3]
Mean bifurcation ratio (MRb)	The average of bifurcation ratios of all orders	[1]
Weighted Mean bifurcation ratio (WMRb)	$\text{WMRb} = \dfrac{\Sigma\,(\text{Nu/Nu} + 1)/ \times (\text{Nu} + \text{Nu} + 1)}{\text{N}}$ Where Nu = number of stream segments in order (u), Nu+1 = number of segments of the next higher order, N = total number of streams involved	[4]
Basin length (Lb) km	Extracted by the spatial analyst tool in ArcMap	[3]
Length of overland flow (Lg) km	Lg = 1/2 Dd, where Dd = drainage density	[2]

Table A5. Areal aspects of the drainage watershed.

Morphometric Parameters	Formula	Reference
Basin area (A) km^2	Extracted by the spatial analyst tool in ArcMap	[3]
Basin perimeter (P) km	Extracted by the spatial analyst tool in ArcMap	[3]
Drainage density (Dd) km/km^2	Dd = L/A, where L = total length of the stream, A = area of the basin	[5]
Stream frequency (Fs) km^{-2}	Fs = ΣN/A, where ΣN = total number of stream segments in all orders, A = area of the basin	[5]
Texture ratio (T)	T = ΣN/P, where ΣN = Total number of stream segments in all orders, P = perimeter of the basin	[2]
Shape index (Ish)	Ish = 1.27 × R$_f$ (R$_f$ form factor)	[2,3]

Table A6. Relief aspects of the drainage watershed.

Morphometric Parameters	Formula	Reference
Relief ratio (Rh)	Rh = Bh/Lb, where Bh = basin relief, Lb = basin length	[3]
Basin slope (BS)	Extracted by (WMS software)	[2]
Drainage patterns (Dp)	Stream network using GIS software analysis	[5]
Ruggedness Number (Rn)	Rn = Bh × Dd, where Bh = basin relief, Dd = drainage density	[6]
Slope index (SI)	SI = Bh/Lms, where Bh = basin relief, Lms = length of main stream	[7]

Table A7. Scale for pair-wise comparisons [8].

Intensity of Importance	Definition	Description
1	Equally important	Two factors contribute equally to the objective.
3	Moderately more important	Experience and judgment slightly favor one over the other.
5	Strongly more important	Experience and judgment strongly favor one over the other.
7	Very strongly more important	Experience and judgment very strongly favor one over the other. Its importance is demonstrated in practice.
9	Extremely more important	The evidence favoring one over the other is of the highest possible validity.
2, 4, 6, 8	Intermediate values	When compromise was needed

Appendix B
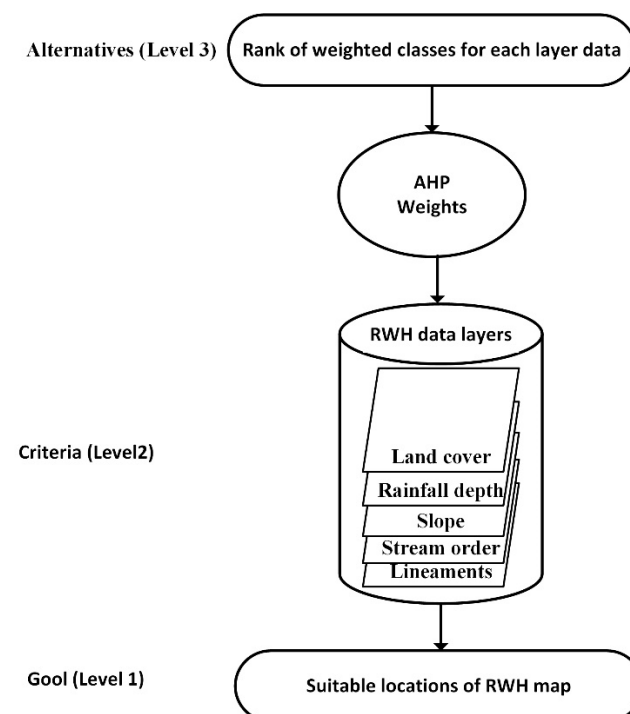
Figure A1. Flow chart of the AHP method for suitable locations for RWH mapping.
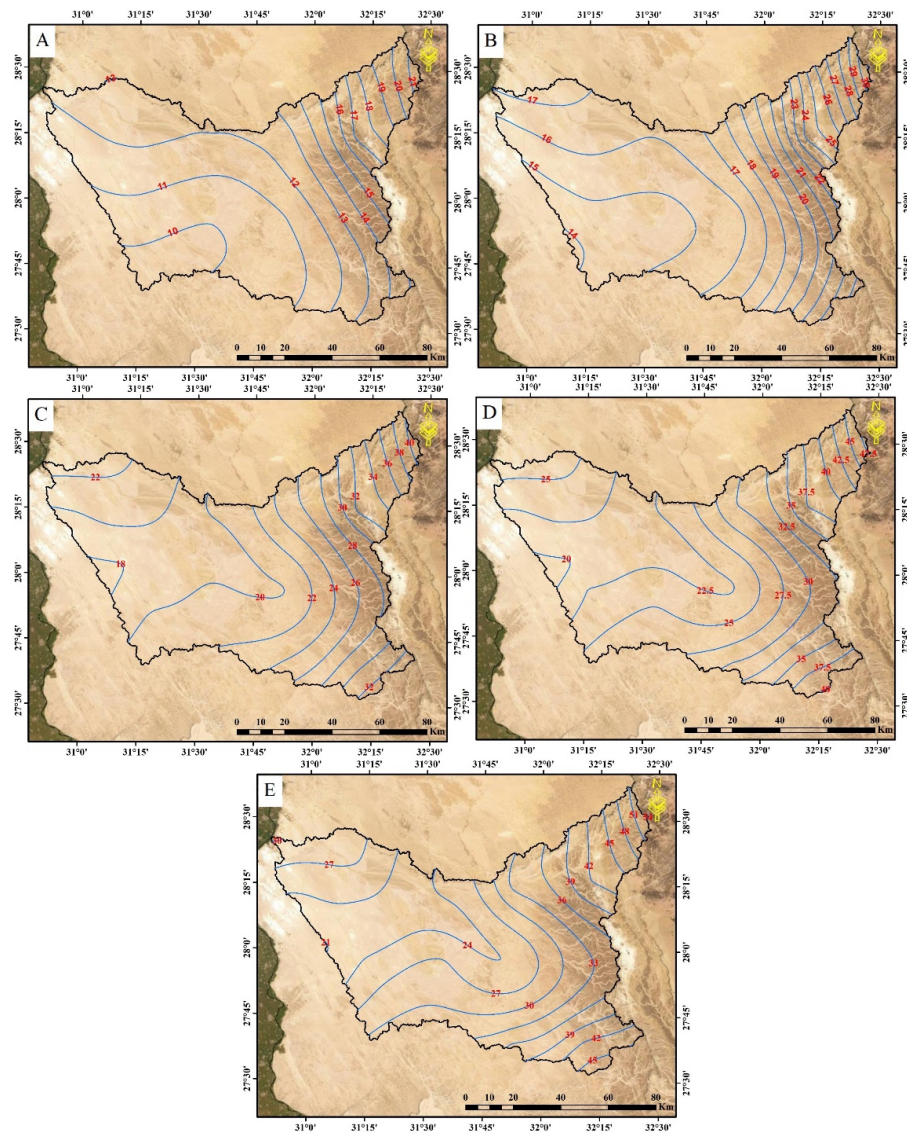
Figure A2. Spatial distribution of maximum 24 h rainfall mm; (**A**) 5-year return period; (**B**) 10-year return period; (**C**) 25-year return period; (**D**) 50-year return periods; (**E**) 100-year return period.
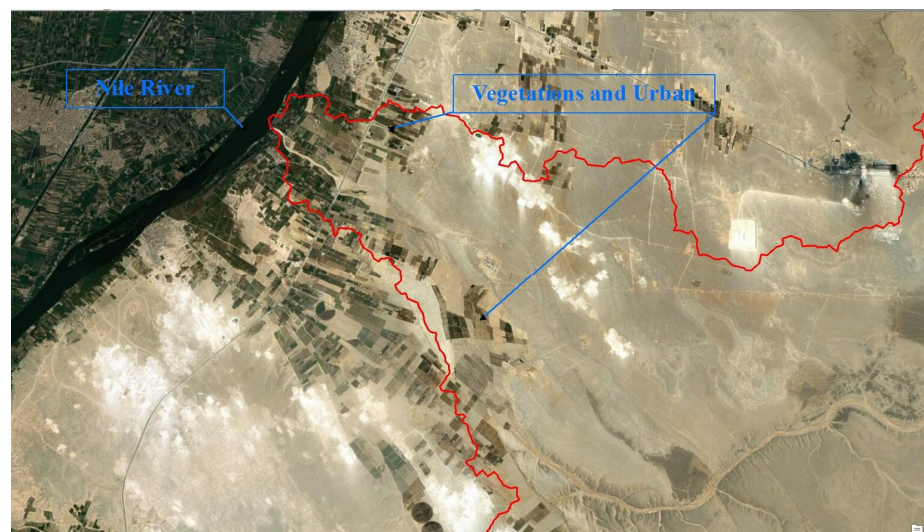
Figure A3. Vegetation and urban area in the study area.

Appendix C

Table A8. Result of linear characteristics of the main basin and its sub-basins.

Basin No	U	1	2	3	4	5	6	7	8	9
1	Nu	2625	652	140	29	8	3	1		
	Lu (km)	556.29	275.67	149.07	82.28	56.47	13.16	7.12		
2	Nu	3505	877	172	41	11	2	1		
	Lu (km)	776.29	382.13	194.00	110.30	51.87	27.41	8.80		
3	Nu	5993	1997	362	80	16	6	1		
	Lu (km)	1348.86	669.64	318.08	168.54	81.74	37.71	33.26		
4	Nu	1843	519	123	24	5	2	1		
	Lu (km)	434.04	222.36	85.16	42.72	28.17	11.98	12.39		
5	Nu	6376	2034	543	73	15	4	1		
	Lu (km)	1430.07	669.93	348.81	182.92	89.67	30.04	39.11		
6	Nu	2447	604	138	36	8	2	1		
	Lu (km)	577.43	257.21	144.54	65.79	18.14	22.07	12.21		
7	Nu	3344	733	143	22	7	2	1		
	Lu (km)	699.06	326.43	163.55	62.02	56.98	42.07	10.49		
8	Nu	2676	676	178	26	5	2	1		
	Lu (km)	549.64	244.73	155.16	54.20	53.85	5.80	11.42		
9	Nu	9213	2300	354	93	15	5	1		
	Lu (km)	1994.32	894.01	437.24	211.35	125.83	65.09	75.56		
10	Nu	9446	2123	386	90	22	4	1		
	Lu (km)	2023.56	901.20	401.82	242.77	140.58	48.76	59.62		
11	Nu	3934	813	168	38	9	2	1		
	Lu (km)	833.14	359.14	178.75	102.65	51.98	23.56	19.43		
12	Nu	4663	871	191	38	9	2	1		
	Lu (km)	972.49	440.32	206.93	114.37	66.52	34.78	7.63		
13	Nu	5612	921	236	55	12	3	1		
	Lu (km)	1176.75	540.18	269.20	137.82	87.75	16.95	29.10		
14	Nu	4553	881	204	54	12	3	1		
	Lu (km)	996.85	490.41	250.82	121.25	68.16	33.02	11.84		
15	Nu	6427	1121	299	72	16	4	1		
	Lu (km)	1379.75	650.98	302.15	170.50	104.58	22.70	39.71		
Main basin	Nu	125,068	29,081	6835	1225	279	70	15	3	1
	Lu (km)	27,120.47	12,688.2	6344	3193	1672.78	772.08	382.19	393	11.08

Stream order (U), stream number (Nu), stream length km (Lu).

Table A9. Result of the linear characteristics of the main basin and its sub-basins.

Basin No	U	MRb	WMRb	Lb	Lg
1	7	3.80	4.17	23.80	2.55
2	7	4.09	4.21	34.57	2.56
3	7	4.35	3.67	41.87	2.60
4	7	3.70	3.77	28.99	2.63
5	7	8.98	3.55	52.91	2.57
6	7	3.79	4.11	27.02	2.66
7	7	4.14	4.71	53.65	2.43
8	7	4.05	4.08	33.39	2.41
9	7	4.75	4.49	73.56	2.43
10	7	4.64	4.63	63.09	2.42
11	7	4.14	4.82	41.63	2.45
12	7	4.28	5.21	37.16	2.37
13	7	4.31	5.72	44.26	2.30
14	7	4.13	4.98	32.49	2.50
15	7	4.36	5.38	39.63	2.41
Main basin	9	4.40	4.35	177.72	2.47

Stream order (U), mean bifurcation ratio (MRb), weighted mean bifurcation ratio (WMRb), basin length km (Lb), length of overland flow km (Lg).

Table A10. Results of areal characteristics and relief characteristics of the main basin and its sub-basins.

Basin No	A	P	Dd	Fs	T	Rh	BS	Dp
1	223.79	93.66	5.09	15.45	36.92	0.0105	0.0615	Dendritic
2	302.86	113.17	5.12	15.22	40.72	0.0060	0.0411	Dendritic
3	511.88	151.73	5.19	16.52	54.17	0.0063	0.0473	Dendritic
4	159.01	103.37	5.26	15.83	24.35	0.0046	0.0413	Dendritic
5	543.16	196.98	5.14	16.65	45.92	0.0059	0.0406	Dendritic
6	206.29	90.08	5.32	15.69	35.93	0.0048	0.0419	Dendritic
7	280.38	157.98	4.85	15.17	26.91	0.0098	0.0684	Dendritic
8	222.95	103.91	4.82	15.99	34.30	0.0090	0.0703	Dendritic
9	783.91	258.93	4.85	15.28	46.27	0.0083	0.0664	Dendritic
10	789.01	221.50	4.84	15.30	54.50	0.0084	0.0629	Dendritic
11	320.00	132.89	4.90	15.52	37.36	0.0066	0.0457	Dendritic
12	389.19	120.16	4.74	14.84	48.06	0.0074	0.0599	Dendritic
13	490.33	150.54	4.60	13.95	45.44	0.0088	0.1028	Dendritic
14	393.99	117.86	5.01	14.49	48.43	0.0126	0.0652	Dendritic
15	553.10	147.26	4.83	14.36	53.92	0.0171	0.1145	Dendritic
Main basin	10646.40	807.59	4.94	15.27	201.31	0.0070	0.0556	Dendritic

Basin area km^2 (A), basin perimeter km (P), drainage density km/km^2 (Dd), stream frequency km^{-2} (Fs), texture ratio (T), relief ratio (Rh), basin slope degree (BS), drainage patterns (Dp).

Table A11. Calculation of the input parameters of the HEC-HMS model for the basin.

Basin No	A (km²)	ΣA × CN	CNw	S (in)	Ia (in)	BS%	FL (ft)	TL (h)	TC (h)
1	223	15,933.44	71.22	4.04	0.81	6.15	72,377.15	5.08	8.47
2	302	25,157.41	83.07	2.04	0.41	4.11	119,060.67	6.50	10.83
3	511	42,278.18	82.59	2.11	0.42	4.73	178,378.32	8.50	14.17
4	159	11,413.72	71.77	3.93	0.79	4.13	121,821.39	9.27	15.45
5	543	44,544.76	82.01	2.19	0.44	4.06	204,723.68	10.44	17.41
6	206	15,924.80	77.19	2.96	0.59	4.19	94,069.65	6.41	10.68
7	280	23,276.96	83.01	2.05	0.41	6.84	260,557.45	9.44	15.74
8	222	17,573.92	78.83	2.69	0.54	7.03	150,120.48	6.85	11.41
9	783	64,419.36	82.18	2.17	0.43	6.64	356,437.61	12.66	21.10
10	789	62,472.33	79.18	2.63	0.53	6.29	271,505.66	11.50	19.17
11	319	20,926.63	65.40	5.29	1.06	4.57	160,659.67	13.03	21.72
12	389	30,302.01	77.87	2.84	0.57	5.99	160,031.35	8.04	13.40
13	490	40,018.41	81.63	2.25	0.45	10.28	206,709.81	6.70	11.16
14	393	31,334.85	79.54	2.57	0.51	6.52	71,064.32	3.82	6.37
15	553	43,916.03	79.40	2.59	0.52	11.45	164,929.31	5.68	9.47
Mainbasin	10,646	829,384.58	77.90	2.84	0.57	5.56	765,364.20	29.14	48.57

Area (A), curve number (CN), soil moisture (s), initial abstraction (Ia), basin slope (BS), flow length (FL), lag time (TL), time concentration (TC).

Table A12. Weighted RWH-suitable locations ranking in basin.

Decision Factors at Level 2 (i)	Relative Weight at Level 2 of Decision Factor i = RIW2 i	Decision Sub-Factors (j) at Level 3 (Cell Attribute)	Ranking Decision
Land-cover units	0.2085	Vegetation Recent Alluvial Old Alluvial Quarries Limestone with clay Massive limestone	1 2 3 4 5 6
Average of max 24 h rainfall depth (mm)	0.1852	5.875200748–6.75068903 6.750689031–7.658358574 7.658358575–9.030816078 9.030816079–10.76387215 10.76387216–12.63123417	1 2 3 4 5
Slope (degrees)	0.477	0–2.764199904 2.764199905–5.74103057 5.741030571–10.41890733 10.41890734–18.28624552 18.28624553–54.00821351	5 4 3 2 1
Stream order	0.0592	1 2 3 4 5 6 7 8 9	1 2 3 4 5 6 7 8 9
Lineaments density (km/km²)	0.0701	0–0.206917985 0.206917985–0.389492678 0.389492678–0.614668133 0.614668133–0.912873465 0.912873465–1.55188489	5 4 3 2 1

Table A13. Calculation of the input parameters of the HEC-HMS model for dams.

Basin No	A (km^2)	ΣA × CN	CNw	S (in)	Ia (in)	BS%	FL (ft)	TL (h)	TC (h)
1	52.98	3670.83	69.29	4.43	0.89	3.80	63,692.77	6.15	10.26
2	4747.77	37,9441.81	79.92	2.51	0.50	5.91	729,000.85	25.56	42.60
3	7.53	642.97	85.44	1.70	0.34	10.72	18,217.73	0.83	1.38
4	39.07	3002.85	76.85	3.01	0.60	9.40	52,865.40	2.73	4.54
5	0.85	75.43	88.41	1.31	0.26	7.40	3026.79	0.21	0.35
6	22.17	1935.19	87.29	1.46	0.29	7.11	30,812.99	1.44	2.41
7	4.27	367.02	85.98	1.63	0.33	10.67	15,192.13	0.70	1.17
8	2.12	182.83	86.37	1.58	0.32	8.45	6726.45	0.41	0.68
9	3.99	335.43	84.15	1.88	0.38	15.91	12,422.02	0.52	0.87
10	23.01	1936.89	84.16	1.88	0.38	6.21	37,567.51	2.02	3.37

Area (A), curve number (CN), soil moisture (s), initial abstraction (Ia), basin slope (BS), flow length (FL), lag time (TL), time concentration (TC).

Table A14. Characteristics of proposed dams.

Dam No	Max Elevation (m)	Max Height (m)	Max Storage capacity (m^3)	Max surface area (m^2)
1	107	24	2,653,602.08	291,793.19
2	103	23	10,720,852.86	1,489,698.49
3	565	20	1,629,981.86	296,494.06
4	693	18	1,189,841.62	154,441.31
5	705	17	1,107,544.42	157,873.34
6	660	18	3,421,759.67	501,554.30
7	711	19	2,716,737.12	295,154.51
8	740	22	4,905,677.69	581,781.67
9	710	22	2,277,794.88	261,692.23
10	650	20	2,411,787.02	284,858.42

References

1. Costa, J.E. Hydraulics and Basin Morphometry of the Largest Flash Floods in the Conterminous United States. *J Hydrol.* **1987**, *93*, 313–338. [CrossRef]
2. He, B.; Huang, X.; Ma, M.; Chang, Q.; Tu, Y.; Li, Q.; Zhang, K.; Hong, Y. Analysis of Flash Flood Disaster Characteristics in China from 2011 to 2015. *Nat. Hazards* **2018**, *90*, 407–420. [CrossRef]
3. Abdalla, F.; Shamy, I.E.; Bamousa, A.O.; Mansour, A.; Mohamed, A.; Tahoon, M. Flash Floods and Groundwater Recharge Potentials in Arid Land Alluvial Basins, Southern Red Sea Coast, Egypt. *Int. J. Geosci.* **2014**, *5*, 971–982. [CrossRef]
4. Davies, R. World Disasters Report—Most Deaths Caused by Floods. 2014. Available online: https://floodlist.com/dealing-with-floods/world-disasters-report-100-million-affected-2013 (accessed on 15 October 2022).
5. Dano, U.L. Flash Flood Impact Assessment in Jeddah City: An Analytic Hierarchy Process Approach. *Hydrology* **2020**, *7*, 10. [CrossRef]
6. Prama, M.; Omran, A.; Schröder, D.; Abouelmagd, A. Vulnerability Assessment of Flash Floods in Wadi Dahab Basin, Egypt. *Env. Earth Sci.* **2020**, *79*, 1–17. [CrossRef]
7. Lin, X. Flash Floods in Arid and Semi-Arid Zones. *Tech. Doc. Hydrol.* **1999**. Available online: https://unesdoc.unesco.org/ark:/48223/pf0000118882 (accessed on 15 October 2022).
8. Youssef, A.M.; Pradhan, B.; Hassan, A.M. Flash Flood Risk Estimation along the St. Katherine Road, Southern Sinai, Egypt Using GIS Based Morphometry and Satellite Imagery. *Environ. Earth Sci.* **2011**, *62*, 611–623. [CrossRef]
9. Moawad, M.B.; Aziz, A.O.A.; Mamtimin, B. Flash Floods in the Sahara: A Case Study for the 28 January 2013 Flood in Qena, Egypt. *Geomat. Nat. Hazards Risk* **2016**, *7*, 215–236. [CrossRef]

10. Abdelkader, M.M.; Al-Amoud, A.I.; El-Alfy, M.; El-Feky, A.; Saber, M. Assessment of Flash Flood Hazard Based on Morphometric Aspects and Rainfall-Runoff Modeling in Wadi Nisah, Central Saudi Arabia. *Remote Sens. Appl.* **2021**, *23*, 100562. [CrossRef]

11. Elsebaie, I.H.; el Alfy, M.; Kawara, A.Q. Spatiotemporal Variability of Intensity–Duration–Frequency (IDF) Curves in Arid Areas: Wadi AL-Lith, Saudi Arabia as a Case Study. *Hydrology* **2021**, *9*, 6. [CrossRef]

12. Tizro, A.T.; Voudouris, K.S.; Akbari, K. Simulation of a Groundwater Artificial Recharge in a Semi-Arid Region of Iran. *Irrig. Drain.* **2011**, *60*, 393–403. [CrossRef]

13. Sarma, D.; Xu, Y. The Recharge Process in Alluvial Strip Aquifers in Arid Namibia and Implication for Artificial Recharge. *Hydrogeology* **2017**, *25*, 123–134. [CrossRef]

14. Alataway, A.; El-Alfy, M. Rainwater Harvesting and Artificial Groundwater Recharge in Arid Areas: Case Study in Wadi Al-Alb, Saudi Arabia. *J. Water Resour. Plan. Manag.* **2019**, *145*, 05018017. [CrossRef]

15. Sturm, M.; Zimmermann, M.; Schütz, K.; Urban, W.; Hartung, H. Rainwater Harvesting as an Alternative Water Resource in Rural Sites in Central Northern Namibia. *Phys. Chem. Earth Parts A/B/C* **2009**, *34*, 776–785. [CrossRef]

16. El-Alfy, M. Applications of Engineering Geology on the Geomorphological and Hydrogeological Situations of the Area between Rafah and Ras El-Naqab. Master's Thesis, Mansoura University, Mansoura, Egypt, 1998.

17. Escalante, E.F.; Gil, R.C.; Fraile, M.Á.S.M.; Serrano, F.S. Economic Assessment of Opportunities for Managed Aquifer Recharge Techniques in Spain Using an Advanced Geographic Information System (GIS). *Water* **2014**, *6*, 2021–2040. [CrossRef]

18. Qi, Q.; Marwa, J.; Mwamila, T.B.; Gwenzi, W.; Noubactep, C. Making Rainwater Harvesting a Key Solution for Water Management: The Universality of the Kilimanjaro Concept. *Sustainability* **2019**, *11*, 5606. [CrossRef]

19. Ammar, A.; Riksen, M.; Ouessar, M.; Ritsema, C. Identification of Suitable Sites for Rainwater Harvesting Structures in Arid and Semi-Arid Regions: A Review. *Int. Soil Water Conserv. Res.* **2016**, *4*, 108–120. [CrossRef]

20. Musaed, H.A.H.; Al-Bassam, A.M.; Zaidi, F.K.; Alfaifi, H.J.; Ibrahim, E. Hydrochemical Assessment of Groundwater in Mesozoic Sedimentary Aquifers in an Arid Region: A Case Study from Wadi Nisah in Central Saudi Arabia. *Environ. Earth Sci.* **2020**, *79*, 1–12. [CrossRef]

21. El-Alfy, M.; Merkel, B. Hydrochemical Relationships and Geochemical Modeling of Ground Water in Al Arish Area, North Sinai, Egypt. *Hydrol. Sci. Technol.* **2006**, *22*, 47–62.

22. El-Alfy, M. Hydrochemical Modeling and Assessment of Groundwater Contamination in Northwest Sinai, Egypt. *Water Environ. Res.* **2013**, *85*, 211–223. [CrossRef]

23. Mahmoud, S.H.; Alazba, A.A.; Adamowski, J.; El-Gindy, A.M. GIS Methods for Sustainable Stormwater Harvesting and Storage Using Remote Sensing for Land Cover Data—Location Assessment. *Environ. Monit. Assess.* **2015**, *187*, 1–19. [CrossRef]

24. Balkhair, K.S.; Ur Rahman, K. Development and Assessment of Rainwater Harvesting Suitability Map Using Analytical Hierarchy Process, GIS and RS Techniques. *Geocarto. Int.* **2021**, *36*, 421–448. [CrossRef]

25. Ouali, L.; Hssaisoune, M.; Kabiri, L.; Slimani, M.M.; el Mouquaddam, K.; Namous, M.; Arioua, A.; ben Moussa, A.; Benqlilou, H.; Bouchaou, L. Mapping of Potential Sites for Rainwater Harvesting Structures Using GIS and MCDM Approaches: Case Study of the Toudgha Watershed, Morocco. *EuroMediterr. J. Env. Integr.* **2022**, *7*, 49–64. [CrossRef]

26. El-Magd, S.A.A.; Pradhan, B.; Alamri, A. Machine Learning Algorithm for Flash Flood Prediction Mapping in Wadi El-Laqeita and Surroundings, Central Eastern Desert, Egypt. *Arab. J. Geosci.* **2021**, *14*, 1–14. [CrossRef]

27. Taha, M.M.N.; Elbarbary, S.M.; Naguib, D.M.; El-Shamy, I.Z. Flash Flood Hazard Zonation Based on Basin Morphometry Using Remote Sensing and GIS Techniques: A Case Study of Wadi Qena Basin, Eastern Desert, Egypt. *Remote Sens. Appl.* **2017**, *8*, 157–167. [CrossRef]

28. El-Bastawesy, M.; Abu El Ella, E.M. Quantitative Estimates of Flash Flood Discharge into Waste Water Disposal Sites in Wadi Al Saaf, the Eastern Desert of Egypt. *J. Afr. Earth Sci.* **2017**, *136*, 312–318. [CrossRef]

29. Abbas, M.; Carling, P.A.; Jansen, J.D.; Al-Saqarat, B.S. Flash-Flood Hydrology and Aquifer-Recharge in Wadi Umm Sidr, Eastern Desert, Egypt. *J. Arid Environ.* **2020**, *178*, 104170. [CrossRef]

30. Harmsen, J. A New and Scalable Approach for Rural Sanitation in Egypt: The Deir Gabal El-Tair Pilot. The Environmental Technology for Impact Conference (ETEI2015). 2016. Available online: https://scholar.google.com/scholar?hl=en&as_sdt=0%2C5&q=A+New+and+Scalable+Approach+for+Rural+Sanitation+in+Egypt%3A+The+Deir+Gabal+El-Tair+Pilot&btnG= (accessed on 15 October 2022).

31. Khalil, M.; Abotalib, A.; Farag, M.; Rabei, M.; Abdelhady, A.A.; Pichler, T. Poor Drainage-Induced Waterlogging in Saharan Groundwater-Irrigated Lands: Integration of Geospatial, Geophysical, and Hydrogeological Techniques. *Catena* **2021**, *207*, 105615. [CrossRef]

32. Moneim, A.A.A. Overview of the Geomorphological and Hydrogeological Characteristics of the Eastern Desert of Egypt. *Hydrogeol. J.* **2005**, *13*, 416–425. [CrossRef]

33. El-Saadawy, O.; Gaber, A.; Othman, A.; Abotalib, A.Z.; Bastawesy, M.E.; Attwa, M. Modeling Flash Floods and Induced Recharge into Alluvial Aquifers Using Multi-Temporal Remote Sensing and Electrical Resistivity Imaging. *Sustainability* **2020**, *12*, 10204. [CrossRef]

34. Mapping Products | GIS Software Products—Esri. Available online: https://www.esri.com/en-us/arcgis/products/index (accessed on 15 October 2022).

35. ERDAS IMAGINE 2015 (64-Bit). Available online: https://download.hexagongeospatial.com/en/downloads/imagine/erdas-imagine-2015-64-bit (accessed on 15 October 2022).

36. HYFRAN 1.2 Download (Free Trial)—Hyfran.Exe. Available online: https://hyfran.software.informer.com/1.2/ (accessed on 15 October 2022).

37. WMS Downloads | Aquaveo.Com. Available online: https://www.aquaveo.com/downloads-wms?s=WMS&v=11.0 (accessed on 15 October 2022).

38. HEC-HMS Downloads. Available online: https://www.hec.usace.army.mil/software/hec-hms/downloads.aspx (accessed on 15 October 2022).

39. About Us—CATALYST.Earth. Available online: https://catalyst.earth/about/ (accessed on 15 October 2022).

40. ITT Visual Information Solutions | Make Informed Decisions. Available online: https://www.ittvis.com/ (accessed on 15 October 2022).

41. RockWorks16—RockWare. Available online: https://www.rockware.com/demo_downloads/rockworks16/ (accessed on 15 October 2022).

42. el Kenawy, A.M.; Lopez-Moreno, J.I.; McCabe, M.F.; Robaa, S.M.; Domínguez-Castro, F.; Peña-Gallardo, M.; Trigo, R.M.; Hereher, M.E.; Al-Awadhi, T.; Vicente-Serrano, S.M. Daily Temperature Extremes over Egypt: Spatial Patterns, Temporal Trends, and Driving Forces. *Atmos. Res.* **2019**, *226*, 219–239. [CrossRef]

43. Mestre, O.; Domonkos, P.; Picard, F.; Auer, I.; Robin, S. HOMER: A Homogenization Software–Methods and Applications. 2013. Available online: https://scholar.google.com/scholar?hl=en&as_sdt=0%2C5&q=HOMER%3A+A+Homogenization+Software%E2%80%93Methods+and+Applications&btnG= (accessed on 15 October 2022).

44. Saha, S.; Moorthi, S.; Pan, H.; Wu, X.; Wang, J.; Nadiga, S.; Goldberg, M. The NCEP Climate Forecast System Reanalysis. *Bull. Am. Meteorol. Soc.* **2010**, *91*, 1015–1058. [CrossRef]

45. El-Kenawy, A.M.; al Buloshi, A.; al Awadhi, T.; al Nasiri, N.; Navarro-Serrano, F.; Alhatrushi, S.; Robaa, S.M.; Domínguez-Castro, F.; McCabe, M.F.; Schuwerack, P.M.; et al. Evidence for Intensification of Meteorological Droughts in Oman over the Past Four Decades. *Atmos. Res.* **2020**, *246*, 105126. [CrossRef]

46. El-Kenawy, A.; López-Moreno, J.I.; Stepanek, P.; Vicente-Serrano, S.M. An Assessment of the Role of Homogenization Protocol in the Performance of Daily Temperature Series and Trends: Application to Northeastern Spain. *Int. J. Climatol.* **2013**, *33*, 87–108. [CrossRef]

47. Horton, R.E. Erosional Development of Streams and Their Drainage Basins; Hydrophysical Approach to Quantitative Morphology. *Geol. Soc. Am. Bull.* **1945**, *56*, 275–370. [CrossRef]

48. Strahler, A.N. Revisions of Horton's Quantitative Factors in Erosional Terrain. *Trans. Am. Geophys. Union* **1953**, *34*, 345.

49. Schumm, S.A. Evolution of Drainage Systems and Slopes in Badlands at Perth Amboy, New Jersey. *Geol. Soc. Am. Bull.* **1956**, *67*, 597–646. [CrossRef]

50. Strahler, A.N. Quantitative Geomorphology of Drainage Basin and Channel Networks. *Handb. Appl. Hydrol.* **1964**. Available online: https://scholar.google.com/scholar?hl=en&as_sdt=0%2C5&q=Quantitative+Geomorphology+of+Drainage+Basin+and+Channel+Networks&btnG= (accessed on 15 October 2022).

51. Horton, R.E. Drainage-Basin Characteristics. *Trans. Am. Geophys. Union* **1932**, *13*, 350–361. [CrossRef]

52. Taylor, A.B.; Schwarz, H.E. Unit-hydrograph Lag and Peak Flow Related to Basin Characteristics. *Eos Trans. Am. Geophys. Union* **1952**, *33*, 235–246. [CrossRef]

53. Melton, M.A. An Analysis of the Relations among Elements of Climate, Surface Properties, and Geomorphology. *Columbia Univ. N. Y.* **1957**. Available online: https://apps.dtic.mil/sti/pdfs/AD0148373.pdf (accessed on 15 October 2022).

54. Farhan, Y.; Anbar, A.; Enaba, O.; Al-Shaikh, N. Quantitative Analysis of Geomorphometric Parameters of Wadi Kerak, Jordan, Using Remote Sensing and GIS. *J. Water Resour. Prot.* **2015**, *07*, 456–475. [CrossRef]

55. Mahmood, S.; Rahman, A. Flash Flood Susceptibility Modeling Using Geo-Morphometric and Hydrological Approaches in Panjkora Basin, Eastern Hindu Kush, Pakistan. *Environ. Earth Sci.* **2019**, *78*, 1–16. [CrossRef]

56. Davis, J.; Sampson, R. Statistics and Data Analysis in Geology. 1986. Available online: https://www.kgs.ku.edu/Mathgeo/Books/Stat/ClarifyEq4-81.pdf (accessed on 15 October 2022).

57. Hasmadi, M.; Pakhriazad, H.Z.; Shahrin, M.F. Evaluating Supervised and Unsupervised Techniques for Land Mapping Using Remote Sensing Data. *Geogr. Malays. J. Soc. Space* **2009**, *5*, 1–10.

58. Abburu, S.; Golla, S.B. Satellite Image Classification Methods and Techniques: A Review. *Int. J. Comput. Appl.* **2015**, *119*, 1–6. [CrossRef]

59. Cronshey, R.; Roberts, R.; Miller, N. Urban Hydrology for Small Watersheds (TR-55 Rev.). *Hydraul. Hydrol. Small Comput. Age* **1985**, 1268–1273. Available online: https://cedb.asce.org/CEDBsearch/record.jsp?dockey=0045976 (accessed on 15 October 2022).

60. Gheith, H.; Sultan, M. Construction of a Hydrologic Model for Estimating Wadi Runoff and Groundwater Recharge in the Eastern Desert, Egypt. *J. Hydrol.* **2002**, *263*, 36–55. [CrossRef]

61. Kamali, B.; Mousavi, S.J.; Abbaspour, K.C. Automatic Calibration of HEC-HMS Using Single-Objective and Multi-Objective PSO Algorithms. *Hydrol. Process.* **2013**, *27*, 4028–4042. [CrossRef]

62. Fleming, M. Description of the Hydrologic Engineering Center's Hydrologic Modeling System (HEC-HMS) and Application to Watershed Studies. *Eng. Res. Dev. Cent. Vicksbg. Ms.* **2004**. Available online: https://scholar.google.com/scholar?hl=en&as_sdt=0%2C5&q=Description+of+the+Hydrologic+Engineering+Center%E2%80%99s+Hydrologic+Modeling+System+%28HEC-HMS%29+and+Application+to+Watershed+Studies&btnG= (accessed on 15 October 2022).

63. De-Simas, M.J.C. Lag-Time Characteristics in Small Watersheds in the United States. *Univ. Ariz.* **1996**. Available online: https://scholar.google.com/scholar?hl=en&as_sdt=0%2C5&q=Lag-Time+Characteristics+in+Small+Watersheds+in+the+United+States&btnG= (accessed on 15 October 2022).

64. Cronshey, R. Urban Hydrology for Small Watersheds. *US Dept. Agric. Soil Conserv. Serv. Eng. Div.* **1986**. Available online: https://tamug-ir.tdl.org/handle/1969.3/24438 (accessed on 15 October 2022).

65. Orencio, P.M.; Fujii, M. A Localized Disaster-Resilience Index to Assess Coastal Communities Based on an Analytic Hierarchy Process (AHP). *Int. J. Disaster Risk Reduct.* **2013**, *3*, 62–75. [CrossRef]

66. Ekmekcioğlu, Ö.; Koc, K.; Özger, M. Stakeholder Perceptions in Flood Risk Assessment: A Hybrid Fuzzy AHP-TOPSIS Approach for Istanbul, Turkey. *Int. J. Disaster Risk Reduct.* **2021**, *60*, 102327. [CrossRef]

67. Ekmekcioğlu, Ö.; Koc, K.; Özger, M. Towards Flood Risk Mapping Based on Multi-Tiered Decision Making in a Densely Urbanized Metropolitan City of Istanbul. *Sustain. Cities Soc.* **2022**, *80*, 103759. [CrossRef]

68. Estoque, R.C.; Murayama, Y. Suitability Analysis for Beekeeping Sites in La Union, Philippines, Using GIS and Multi-Criteria Evaluation Techniques. *Res. J. Appl. Sci.* **2010**, *5*, 242–253. [CrossRef]

69. Ouma, Y.O.; Tateishi, R. Urban Flood Vulnerability and Risk Mapping Using Integrated Multi-Parametric AHP and GIS: Methodological Overview and Case Study Assessment. *Water* **2014**, *6*, 1515–1545. [CrossRef]

70. Xiao, Y.; Yi, S.; Tang, Z. Integrated Flood Hazard Assessment Based on Spatial Ordered Weighted Averaging Method Considering Spatial Heterogeneity of Risk Preference. *Sci. Total Environ.* **2017**, *599*, 1034–1046. [CrossRef]

71. Saaty, R.W. The Analytic Hierarchy Process—What It Is and How It Is Used. *Math. Model.* **1987**, *9*, 161–176. [CrossRef]

72. Zavadskas, E.K.; Vilutienė, T.; Turskis, Z.; Šaparauskas, J. Multi-Criteria Analysis of Projects' Performance in Construction. *Arch. Civ. Mech. Eng.* **2014**, *14*, 114–121. [CrossRef]

73. Kazakis, N.; Kougias, I.; Patsialis, T. Assessment of Flood Hazard Areas at a Regional Scale Using an Index-Based Approach and Analytical Hierarchy Process: Application in Rhodope-Evros Region, Greece. *Sci. Total Environ.* **2015**, *538*, 555–563. [CrossRef]

74. Papaioannou, G.; Vasiliades, L.; Loukas, A. Multi-Criteria Analysis Framework for Potential Flood Prone Areas Mapping. *Water Resour. Manag.* **2015**, *29*, 399–418. [CrossRef]

75. Hajeeh, M. Application of the Analytical Hierarchy Process in the Selection of Desalination Plants. *Desalination* **2005**, *174*, 97–108. [CrossRef]

76. Gajbhiye, S.; Mishra, S.K.; Pandey, A. Prioritizing Erosion-Prone Area through Morphometric Analysis: An RS and GIS Perspective. *Appl. Water Sci.* **2014**, *4*, 51–61. [CrossRef]

77. Pareta, K.; Pareta, U. Quantitative Morphometric Analysis of a Watershed of Yamuna Basin, India Using ASTER (DEM) Data and GIS. *Int. J. Geomat. Geosci.* **2011**, *2*, 248.

Article

Assessment of Hydrological Extremes for Arid Catchments: A Case Study in Wadi Al Jizzi, North-West Oman

Eyad Abushandi [1,]* and Manar Al Ajmi [2]

1   School of Natural Science, University of Dublin, 2 D02 PN40 Dublin, Ireland
2   Civil Engineering Stream, Faculty of Engineering, Sohar University, Sohar 311, Oman
*   Correspondence: eabushandi@gmail.com

Abstract: The objective of this research was to analyse hydrological variability by conducting an intensive analysis of extreme events, under dry and wet conditions. Drought conditions were assessed using the Standard Precipitation Index (SPI) and Rainfall Anomaly Index (RAI), while the Soil Conservation Service (SCS) method was used to simulate flooding at four stations. The SPI results indicated that the amount of rainfall within the catchment area is near to normal, ranging from 64% to 75%, with some extremely wet exceptions which may cause flash floods. The RAI results also indicated that the amount of rainfall within the catchment area is near to normal, but the extremely wet category obtained the largest percentage (ranging from 36% to 50%) and the very wet category had the lowest percentage (ranging from 9% to 36%). The simulated flooding, using SCS, tended to slightly underestimate the observed streamflow, while the performance showed some weaknesses when the observed flooding was less than $1 \text{ m}^3/\text{s}$. The Nash–Sutcliffe Efficiency showed higher performance at closer rainfall stations to the outlet, with values of 0.92 and 0.94. Distant stations simulated floods that showed a lower level of efficiency, with values of 0.77 and 0.81. Given the fact that hydrological extremes (dry and wet conditions) are connected, the findings of the two indices and the SCS method are consistent and suitable for monitoring drought and flood events under climate change.

Keywords: drought; flood; standard precipitation index; rainfall anomaly index; soil conservation service-curve number

1. Introduction

Extreme hydrological conditions can lead to major natural disasters at global, regional, and catchment scales, resulting in the loss of property, infrastructure, and life, as well as causing poverty. The Sultanate of Oman suffers annual flood events, particularly along coastal areas where the main cities and buildings are located. On the other hand, the country is also suffering a significant regional drought [1]. It is important to provide policy-makers with drought estimates, in terms of severity and duration [2].

Unlike flood frequency, drought only becomes obvious when it causes significant damage [3–5]. However, droughts may have long-term adverse effects on the environment, including social and economic aspects [6]. Undoubtedly, the recognition of hydrological extremes in arid climate catchments, as a part of the integrated water resources system, is not well understood and will depend on the level of research, development, and national awareness of the problem's significance. Furthermore, drought phenomena can be seen in some other indicators, such as rainfall, streamflow, soil moisture content, and ground water level [7].

Based on Kleist (1993), the time scale, duration, frequency, and intensity of droughts become important themes in any drought analysis [7]. Many researchers have studied extreme hydrological conditions in arid regions, particularly during drought events. Recently, a regional study was conducted by El Kenawy et al. (2020), to assess drought in Oman

using the Standard Precipitation Index (SPI) and Standardized Precipitation Evapotranspiration Index (SPEI) [1]. The results showed a significant increase of drought severity for the last four decades, at the country level. Ali et al. (2019) achieved accurate drought forecasts at a small scale on three agricultural plots, using a new multi-stage separation model for estimating Standard Precipitation Index (SPI), at 1, 3, 6, and 12 monthly intervals [8]. Similarly, Zhao et al. (2021) indicated that the SPI could better reflect annual and seasonal dry weather and flood changes in the field of study based on long-term grade measurements [9]. Tsesmelis et al. (2022) implemented the SPI to provide accurate results of drought, at a spatiotemporal regional scale, for Greece [10]. To better perceive and characterise agricultural droughts, Łabędzki (2007) used the 1–3 month SPI which greatly assists the drought detection achieved by the 6-month SPI [11]. He recommended the use of more than one index to evaluate drought risk levels. Kourgialas (2021) assessed hydrological events in the north-western part of Crete (Greece) based on the SPI method, between 1960 and 2019 [5]. Interesting correlations were found between groundwater capacity levels and several interrelated factors, such as rainfall, evapotranspiration, soil, available water capacity, and runoff accumulation. Zhai et al. (2010) used the Rainfall Anomaly Index (RAI), Bhalme–Mooley Index (BMI), the Standard Anomaly Index (SAI), and the Palmer Drought Index (PDSI) to highlight local variations in climatic drought and wet conditions in ten catchments, during the period 1961–2005 [12]. Tufaner and Özbeyaz (2020) applied Machine Learning Algorithms to evaluate the Z index of drought phenomena in Palmer, based on observed rainfall and soil moisture data [13].

The Soil Conservation Service (SCS) was used to effectively assess flooding for arid catchments. Abushandi and Merkel (2011) and Abushandi (2016) applied the SCS method to different arid regions in the Middle East [14,15]. However, there are always problems with assessing hydrological behaviour in arid catchments due to hydrological complexities or data acquisition accuracy. In addition, Shadeed and Almasri (2010) applied a GIS-based SCS-CN approach to develop an estimate of four storm surface runoff events in Palestine [16]. The analysis by Alzghoul and Al-husban (2021) indicated that there is a strong correlation between the curve number used in the SCS method and the values obtained from measured runoff and the rainfall depth [17]. El-Hames (2012) applied an empirical method for runoff prediction in arid and semi-arid catchments based on morphological data and SCS-curve number [18]. The results were validated and calibrated from six different countries using a significant number of rainfall events. Al-Ghobari et al. (2020) studied spatial runoff behaviour due to different land cover types, slopes, and maximum retention, as they are the major parameters for SCS [19]. Braud et al. (2016) tried to explain these phenomena by presenting European and international flood warning systems [20]. The rainfall depth is calculated by the reverse implementation of the hydrological model, based on iterative rainfall inputs to obtain flood peaks. Furthermore, anthropogenic influences were studied by Karagiorgos et al. (2016). They analysed the vulnerability components, including physical and social factors, due to unexpected flooding [21]. The analysis was based on a review of the disability assessment and focused on weaknesses as a framework for outlining and evaluating the negative impact. Mahmood et al. (2017) used daily hydrological data for the years 2013 and 2014, to understand the characteristic distribution of storm rainfall [22].

An estimation of flash flooding in the Wadi Al Jizzi catchment by Abushandi and Al Sarihi (2022), using two different lumped models, showed that a statistical readjustment was needed to avoid underestimation of the small flood values [23]. On the other side of Oman, Al Ruheili et al. (2019) estimated flood damage in the floodplain in the southern part of Oman under current and future conditions [24]. They also determined the flood extent and amount of flood damage using the 3Di model for the year 2002 cyclone (ARB01). While the study gives an overview of the political decisions contributing to the sustainable development of resources, future assessment of the flood damage at catchment scales was also performed.

Further research was based on the integrated implementation of lumped and distributed hydrologic models. Recently, Niyazi et al. (2020) evaluated the runoff compensa-

tion equivalent using two models dealing with morphological parameters and hydrological properties [25]. In addition, these models include the Watershed Modelling System (WMS) and the Hydrological Modelling System (HEC-HMS). In addition, Saber et al. (2015) developed physics-based hydrological models adapted to flash floods, to help understand hydrological processes and cope with water-related issues, such as the scarcity of water and data [26]. An ecological assessment for a suggested distributed model of a river basin, in which the wadi system (Hydro-BEAM-WaS) is coupled with remote sensing data, performed well in the absence of high-quality ground observations. However, El Alfy (2016) used a comprehensive approach to assess the effects of floods in urban areas, integrating distributed models and forecast precipitation [27]. The flow model was developed as an activity for capturing objects with daily precipitation measurements. The study showed that rapid urbanisation has a negative impact on the hydrological process, as the sprawl of alluvial channels is important. Jodar-Abellan et al. (2019) evaluated hydrological responses using geographic information system tools (SWAT) in five basins of the Mediterranean (south-eastern Spain) with pixel units from 10.2 to 200.9 km^2 [28]. Furthermore, Aghabeigi et al. (2020) compared the IHACRES model (Identification of unit Hydrographs And Component flows from Rainfall, Evaporation, and Streamflow data) to the Complex SWAT model for three watersheds: one dry and two semi-dry [29]. The SWAT model performed better than the IHACRES model for some climate zones. Moreover, Abushandi and Merkel (2013) simulated a single flood event in the northern part of Jordan, that occurred in the year 2008, using two models: HEC-HMS and IHACRES, at an hourly scale [30]. An integrating satellite reconnaissance to generate rainfall data (GSMaP_MVK +) was used. The performance of the IHACRES lumped model had some errors, while the calibrated runoff results had a good level of performance in the distributed HEC-HMS.

The Wadi Al Jizzi arid catchment in the northern part of Oman experiences extreme rainfall storms and irregular flash floods due to topographical, climatological, and hydrological complexities. This, however, destroys the infrastructure of the city at the outlet of the catchment, arousing the need for an improved understanding of flood behaviour at a catchment scale. Although the water is limited, the Wadi Al Jizzi catchment is particularly sensitive to flash flooding due to the following field survey findings:

i.   A series of basaltic mountains surrounding the catchment from the western part, known as Al Hajar Al Gharbi.

ii.   Hyper arid catchment characteristics, including a limited number of high-intensity, annual storm rainfall events in a short time.

iii. The catchment is dominated by bare soil and very limited vegetation cover.

For the better planning, operation, and development of water, energy, and food production, an understanding of extreme hydrologic conditions at a regional scale is an important step. The shortage of both surface and ground water resources controls the difficulties of present and future agricultural activities. Changing the negative impact of flash floods into a fruitful source of water has not been achieved in many areas of Oman. In fact, the main portion of flood water flows into the sea, after destroying the infrastructure. The SPI and RAI methods were successfully applied to arid areas where the observed hydrologic dataset is limited. While both methods are characterised by uncomplicated generic structures, the SCS-CN requires more inputs to simulate wet seasons. Substantial storm rainfall occurred in the upper part of Wadi Al Jizzi, causing serious damage to the infrastructure of Sohar City, located at the catchment outlet. Furthermore, the frequency of flash flooding has dramatically increased over the last 20 years and requires urgent action. However, only a few studies have been conducted to investigate hydrologic wet and drought severities in Oman. The aim of this research is to assess the behaviour of the extreme drought and wet conditions in Wadi Al Jizzi, using the SPI and RAI for drought evaluation and the SCS-CN model for wet seasons.

2. Study Area

The catchment considered in this study is the Wadi Al Jizzi in the North Al Batina Governorate in Oman, alongside the Sohar–Al Buraimi city highway and with a length of 77.8 km. Wadi Al Jizzi represents a major valley in the region and ends in the Sohar coastal outlet. The catchment area is around 870.5 km^2, with an average slope of 0.56%. The highest mountain around the catchment is more than 1000 m above sea level (Figure 1).
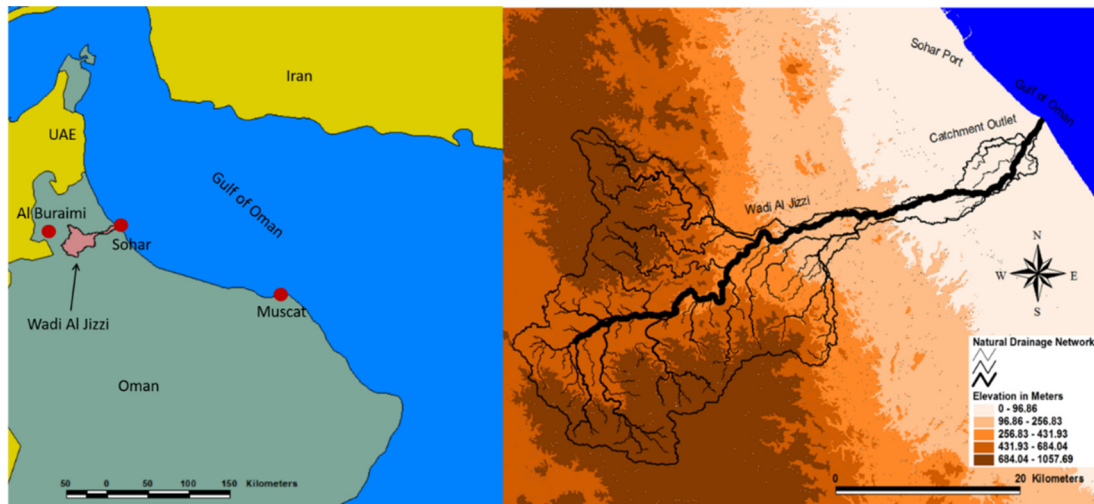
Figure 1. Location and natural drainage network of the Wadi Al Jizzi catchment.

Sohar is the major city located at the outlet of the Wadi Al Jizzi catchment, an area of important crop production. Since the introduction of mechanical pumps, the development of agricultural land has increased since the early 1970s.

There are many villages near Wadi Al Jizzi: some of them belong to Sohar City, and some to Al Buraimi City. The villages belonging to Sohar are Al-Jahili, Al-Huwailat, Sahban, Al-Farfar, Al-Khan, Al-Suhaila, Dhahran, Al-Arja, and others. The state of Buraimi includes the villages of Al-Swadif, Al-Hail, Al-Rabi, Al-Wasit, Katana, Al-Daqiq, and others. The major activity in these villages is agriculture and the water resource is groundwater [31].

The Wadi Al Jizzi catchment is characterised by the presence of many types of impermeable basaltic rocks (Figure 2), the most important of which are igneous rocks, which were formed between 800 million years ago until the present [32]. Sedimentary and metamorphic rocks are present in the region, as sediments of different ages were deposited and then experienced several folding and cracking periods [33]. The soil type is mainly loamy soil with small portions of sandy soil and clay, based on the physical tests conducted. The catchment has only one dam, with an area of 2.7 km^2, a length of 1350 m, a height of 14 m, and a maximum volume of 5.4×106 m^3 [34]. There were two purposes for constructing this dam:

i.   To recharge the ground water which has a water table level of 172 m underground, and
ii.   To protect Sohar City from flash floods during wet seasons.

Generally, the area is considered as being a hyper arid, coastal area: hot and humid during the summer, with an average temperature of 37 °C, and moderate in winter, with an average temperature of 18.5 °C, except for highly elevated land, where the climate remains mild throughout the entire year [35].

Localised thunderstorms occur high over the Al Hajar Al Gharbi Mountain range, in the north of Oman, during the summer months and irregular droughts sweep across the Arabian Peninsula. Rain occurs inland and on the coastal regions in the winter. Rainfall is highly variable from one location to another and from one year to another. Orographic impacts are sometimes affected by local patterns. The amount of surface runoff depends on rainfall intensity and frequency. Apart from some short periods of data loss, records of the

wadi runoff since 1984 are both efficient and complete. The runoff of surface water mostly happens between January and April, which are the wet months. Such records are relevant and could be used in statistical predictions. The catchment under study is classified as an ephemeral stream where any water flow within the major wadi catchment is considered as being in flood. The magnitudes of the flooding have been categorised as low, medium, and high.

Figure 2. The volcanic stones in Wadi Al-Jizzi.

3. Methodology

3.1. Rainfall and Runoff Data

Rainfall data are very limited within the catchment area. To conduct any accurate hydrological analysis, continuous long-term rainfall data are required. In this research, four meteorological stations were selected to provide daily rainfall rates collected from the Ministry of Regional Municipal and Water Resource in Oman (Table 1). The average annual rainfall varies from 98.4 mm (in Al Khan station) to 110 mm (in Al Farfar station), while the average annual rainfall for the entire catchment is approximately 101 mm. The recorded data periods of rainfall range from 24 years to 70 years. Figure 3 shows the monthly rainfall distribution for the selected stations.

Table 1. Summary of selected meteorological stations.

Elevation Above Sea Level (m)	Annual Rainfall	Acquisition Period	Station Name
524	99.0	1947–2017	Hayl Al Adhah
364	98.4	1982–2017	Al Khan
534	110.0	1974–2016	Al Farfar
459	98.6	1993–2017	Al Jizzi (Near the Dam)

The maximum daily rainfall of 248 mm was recorded in Hayl Al Adhah station in the year 1988. The next highest daily value (242 mm) occurred in Al Khan station in the year 1996. However, there seems to be no clear influence on which month the maximum rainfall may occur. The highest twenty daily rainfall rates (greater than 110 mm) were recorded in all the stations at no specified months. A Pearson correlation was conducted to test the relationship between maximum daily rainfall rates and showed a moderate relationship between the stations, with an average of 0.66 indicating localised storm events in space and time. The average standard deviation of daily rainfall was about 16.5. The area also commonly experiences several years with very limited or no rainfall. Approximately 12% of the stations' records are affected by missing rainfall intervals. To bridge the gaps in data acquisition periods between the four locations, a similarity analysis using cross-correlation was implemented.

Furthermore, 26 observed ephemeral runoff events from the Sallan monitoring station were used for validation purposes (Figure 4), using differential pressure flowmeters located at the outlet areas, between the years 1987 and 2007. The number of runoff records ranges from one to four events per year, with an average of 1.3 per year. The individual runoff is characterised by a sharp rise, to generate a narrow hydrograph and short time lags, depending on soil antecedent conditions and rainfall intensity, in addition to the topographic features.
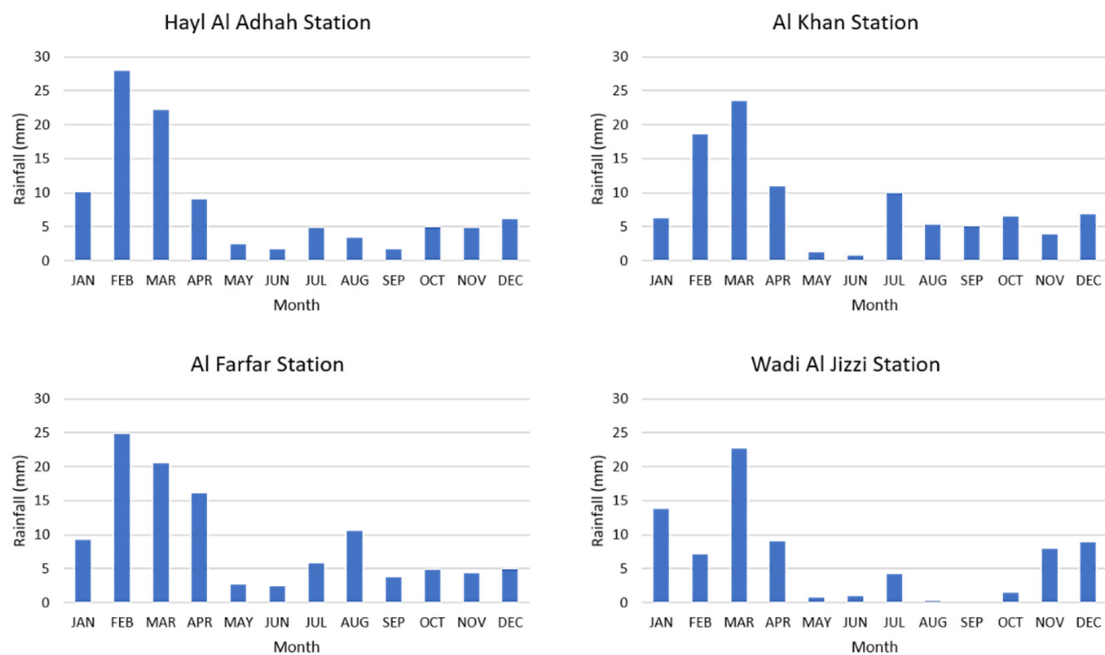
Figure 3. The mean of monthly climatological rainfall distribution for the selected stations.
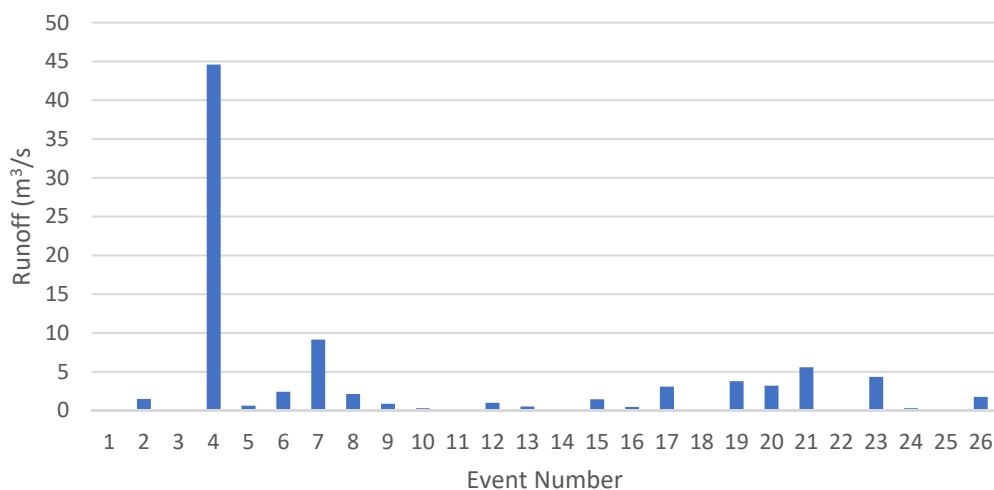
Figure 4. Runoff records from Sallan station for the period between 1987 and 2007.

Additionally, soil types were determined using double ring infiltration tests, conducted at eight points within the catchment area, as shown in Figure 5.

In this research, a comparative analysis was conducted to understand drought conditions. The SPI and RAI were used as they are the most extensively used drought indices for hydrologic monitoring, water resource management, and drought prediction. Using two well-reviewed indices should ensure the results' accuracy.
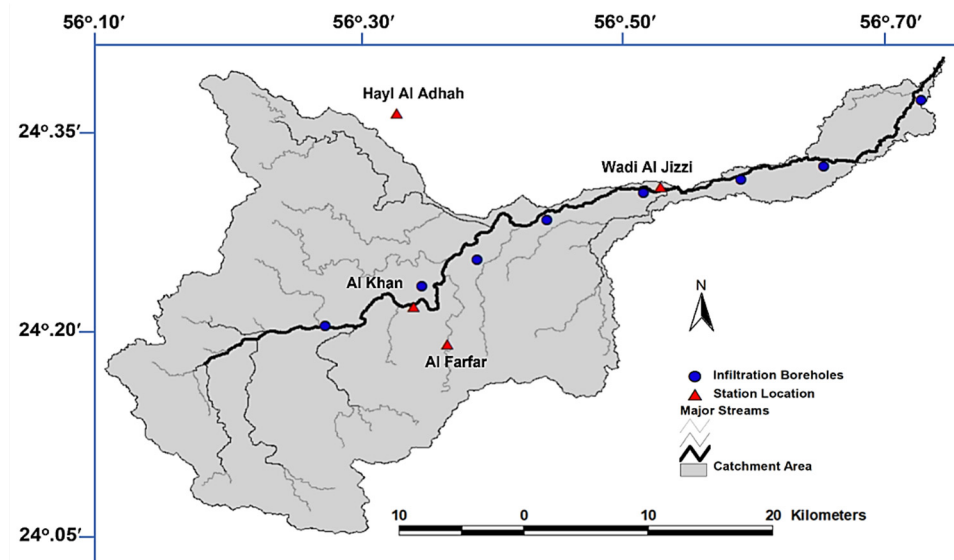
Figure 5. Infiltration boreholes and station locations within the catchment area.

3.2. Standard Precipitation Index (SPI)

The Standard Precipitation Index (SPI) has been used by many meteorologists and climatologists all over the world for many years. Simple indices such as 'percentage of normal precipitation' and 'precipitation percentage' were used, as well as more complicated indices such as the Palmer Drought Severity Index. The American scientists McKee, Doesken, and Kleist developed the Standard Precipitation Index (SPI) in 1993, after realising that a lack of precipitation has different effects on underground water, groundwater storage, moisture levels, precipitation, and streamflow. However, all methods performed in this field have a single target, which is to identify the extreme scarcity of rainfall in a particular area. For the purpose of analysing extreme hydrological changes, the Standard Precipitation Index (*SPI*) was utilised. The equation for determining *SPI* is:

$$SPI = \frac{x_i - \overline{x}}{S} \tag{1}$$

where x_i is the monthly precipitation, $\overline{x}$ is the average precipitation, and S is the standard deviation, while:

$$S = \frac{x_i - \overline{x}}{\overline{x}}. \tag{2}$$

Based on *SPI* values, the climate can be classified into one of seven classes, as in Table 2. The classification is based on monthly rainfall values per year, over four selected station periods.

Table 2. Climatic classification according to the SPI values [7].

SPI Value	Category
SPI $\geq$ 2.00	Extremely wet
1.50 $\leq$ SPI $\leq$ 1.99	Severely wet
1.00 $\leq$ SPI $\leq$ 1.49	Moderately wet
$-0.99 \leq$ SPI $\leq$ 0.99	Near normal
$-1.49 \leq$ SPI ≤ -1.00	Moderately dry
$-1.99 \leq$ SPI ≤ -1.50	Severely dry
SPI ≤ -2.00	Extremely dry

3.3. Rainfall Anomaly Index (RAI)

According to Costa and Rodrigues (2017), the Rainfall Anomaly Index (*RAI*) was developed by Rooy in the year 1965 and it uses a classification procedure to assign measures for positive and negative precipitation classes [36]. The *RAI* considers two types of anomalies: positive and negative. The equations for *RAI* are:

$$RAI = 3 \left[\frac{N - \overline{N}}{\overline{M} - \overline{N}} \right] \; for \; positive \; anomalies \tag{3}$$

$$RAI = -3 \left[\frac{N - \overline{N}}{\overline{x} - \overline{N}} \right] \; for \; negative \; anomalies \tag{4}$$

where:

N = Current monthly/yearly rainfall (mm),
$\overline{N}$ = Monthly/yearly average rainfall of the historical series (mm),
$\overline{M}$ = Average of the ten highest monthly/yearly precipitations of the historical series (mm), and
$\overline{x}$ = Average of the ten lowest monthly/yearly precipitations of the historical series (mm).

Based on the *RAI* values, the climate will be classified into one of six classes, as in Table 3. The classification is based on monthly rainfall values per year, over four selected station periods.

Table 3. Climatic classification according to the RAI values [37].

Criterion	Classifications of RAI Intensity
Above 4	Extremely wet
2 to 4	Very wet
0 to 2	Wet
−2 to 0	Dry
−2 to −4	Very dry
Below −4	Extremely dry

3.4. Soil Conservation Service-Curve Number (SCS-CN) Method

The method of the SCS-curve number is simple, commonly used, and an efficient way of determining the estimated amount of runoff from rainfall in a specific area. Although the method is intended for individual storm events [30,38,39], the average annual runoff values can be downscaled [40]. For this method, the input datasets are very small (i.e., precipitation quantity and curve number). Moreover, the SCS method depends on the treatment, hydrological conditions, the soil hydrological group, and land use of the area, as follows:

$$Q = \frac{(P - I_a)^2}{(P - I_a) + S} \tag{5}$$

$$I_a = 0.2 \, S \tag{6}$$

$$Q = \frac{(P - 0.2 \, S)^2}{(P - 0.8 \, S)} \tag{7}$$

$$S = \frac{1000}{CN} - 10 \tag{8}$$

where:

Q = Runoff depth (mm),
P = Rainfall (mm),
I_a = Initial abstraction (mm),
S = Maximum retention after runoff begins (mm × 25.4 to convert from inches),

CN = Curve number, and

Basic descriptive inputs must be efficiently converted into numeric values of CN, reflecting the catchment runoff potential in the empirical SCS-CN model of hydrological abstraction. The method considers the major characteristics of runoff-producing catchments, such as soil type, land cover type, surface condition, and antecedent soil moisture conditions, in order to determine CN values.

The Nash–Sutcliffe Efficiency was used to evaluate the good fit of simulated runoff using the SCS method, in comparison to the observed runoff:

$$\text{NSE} = 1 - \frac{\sum_{t-1}^{T}(Q_m - Q_o)^2}{\left(Q_o - \overline{Q_o}\right)^2} \tag{9}$$

Q_m = Simulated runoff using SCS method (m^3/s),
Q_o = Observed runoff records (m^3/s), and
$\overline{Q_o}$ = Average observed runoff (m^3/s).

Pearson correlation was used to find the relationships between several data types, such as observed runoff in comparison with simulated runoff, and different drought classes of *RAI* and *SPI*. In addition, the impact of the station's elevation above sea level on average rainfall was also tested using the Pearson correlation.

4. Results and Discussion

4.1. Drought Indices Analysis

All rainfall data were classified into categories ranging from extremely wet to extremely dry. The maximum SPI at a monthly basis (*SPI*1) value for Hayl Al Adhah Station was 5.46 in May 1977, while the minimum SPI1 value was −0.65 in March and April (for 18 times in 39 years). However, the maximum *SPI*1 value for Al Khan Station was 5.27 in July 1995, while the minimum *SPI*1 value was −0.87 in March (for 12 times in 36 years). Furthermore, the maximum *SPI*1 value for Al Farfar Station was 5.85 in July 1995, while the minimum *SPI*1 value was −0.66 in April (for 21 times in 43 years). The maximum *SPI*1 value for Wadi Al Jizzi Station was 4.1 in July 1995, while the minimum *SPI*1 value was −0.82 in March (3 times in 25 years). It is worth mentioning that the average maximum *SPI*1 value was 4.04, while the average minimum *SPI*1 was −0.69. Table 4 summarises the maximum and minimum values of the four meteorological stations used in this study.

Table 4. Maximum and minimum SPI monthly interval values for each meteorological station.

Station Name	SPI Boundary	January	February	March	April	May	June
Hayl Al Adhah	Maximum	4.55	4.32	2.83	3.18	5.46	5.22
	Minimum	−0.59	−0.55	−0.65	−0.65	−0.29	−0.29
Al Khan	Maximum	4.51	4.51	2.82	4.19	2.77	5.27
	Minimum	−0.44	−0.35	−0.57	−0.45	−0.58	−0.36
Al Farfar	Maximum	4.99	3.14	4.11	3.12	5.11	5.08
	Minimum	−0.52	−0.60	−0.57	−0.66	−0.31	−0.39
Al Jizzi (Near the Dam)	Maximum	4.55	4.32	2.83	3.18	5.46	5.22
	Minimum	−0.59	−0.55	−0.65	−0.65	−0.29	−0.29

Station Name	SPI Boundary	July	August	September	October	November	December
Hayl Al Adhah	Maximum	4.81	4.95	4.29	4.05	2.92	4.32
	Minimum	−0.33	−0.39	−0.38	−0.51	−0.49	−0.38
Al Khan	Maximum	3.81	4.81	3.33	2.79	4.93	3.84
	Minimum	−0.47	−0.30	−0.58	−0.87	−0.41	−0.58
Al Farfar	Maximum	5.85	4.04	3.96	3.33	5.15	4.87
	Minimum	−0.29	−0.47	−0.41	−0.46	−0.35	−0.33
Al Jizzi (Near the Dam)	Maximum	4.81	4.95	4.29	4.05	2.92	4.32
	Minimum	−0.33	−0.39	−0.38	−0.51	−0.49	−0.38

The SPI1 values were classified into several categories (Table 2), where the near-normal category obtained the largest percentage, ranging from 64% to 75%, while the extremely wet category obtained the lowest percentage, ranging between 2% and 9% (Figure 6). The SPI1 results indicated that the amount of rainfall within the catchment area is in a near to normal condition, with some extremely wet exceptions that may cause runoff. It is worth mentioning that none of the stations showed dry or extremely dry categories of SPI1 values. In another words, the hydrometeorological aspect of the catchment is characterised by a limited number of extreme storms. However, there is high correlation between extremely and severely wet classifications and runoff.
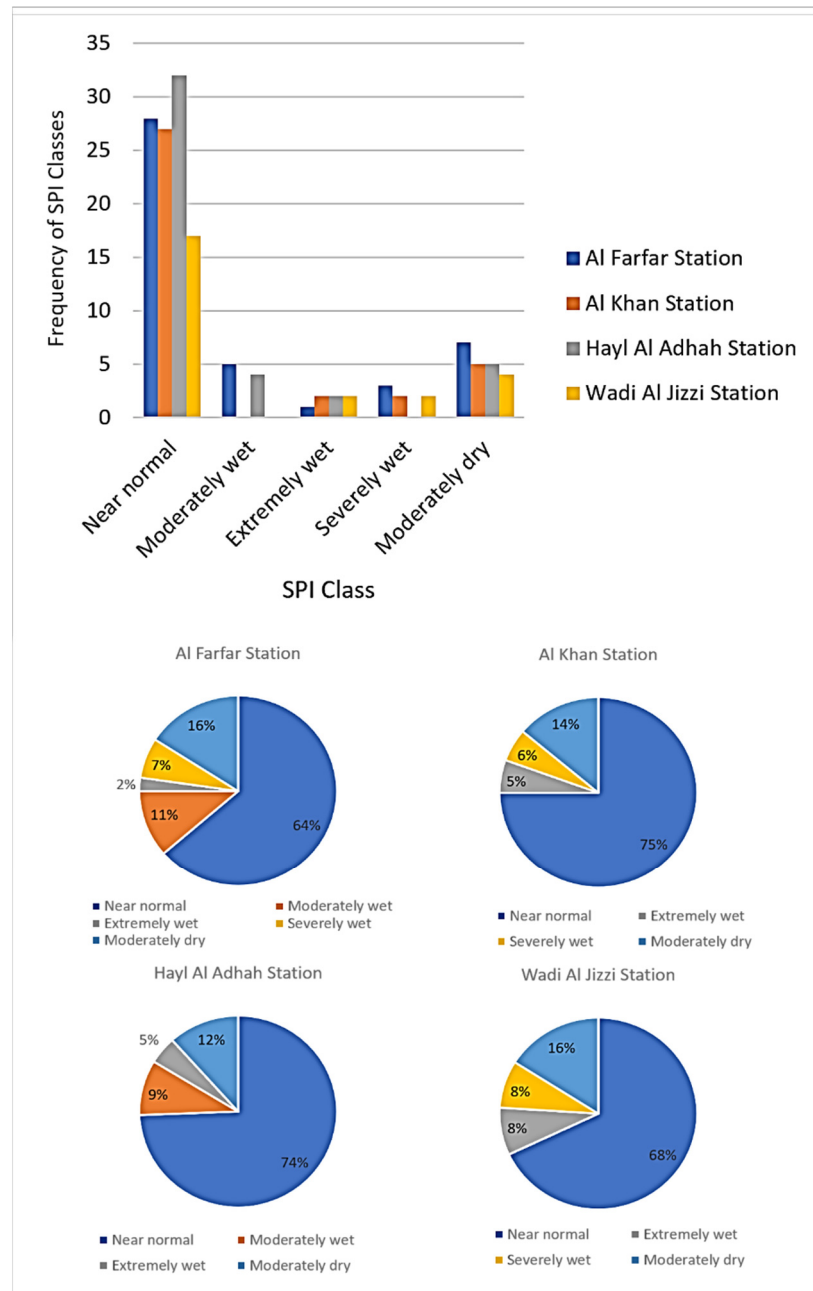
Figure 6. The SPI1 classification frequencies and percentages at the four selected rainfall stations.

Similarly, the Annual Rainfall Anomaly Index (*RAI*) was calculated for the four stations, to obtain the frequency and intensity of dry and wet seasons, between extremely wet and extremely dry. Furthermore, the monthly *RAI* was determined to examine the

distribution of rainfall in the years of highest anomaly. The *RAI* values were classified into several categories (see Table 3); the extremely wet category obtained the largest percentage, ranging from 36% to 50%, while the very wet category obtained the lowest percentage, ranging between 9% and 36% (Figure 7). The *RAI* results indicated that the amount of rainfall within the catchment area is in a near to normal condition. Unlike the SPI1 method, RAI showed many extreme wet cases. However, not all extreme wet cases caused flash floods. In addition, contrasting rainfall analysis using *RAI* recommends the use of SPI1 rather than the *RAI* method.
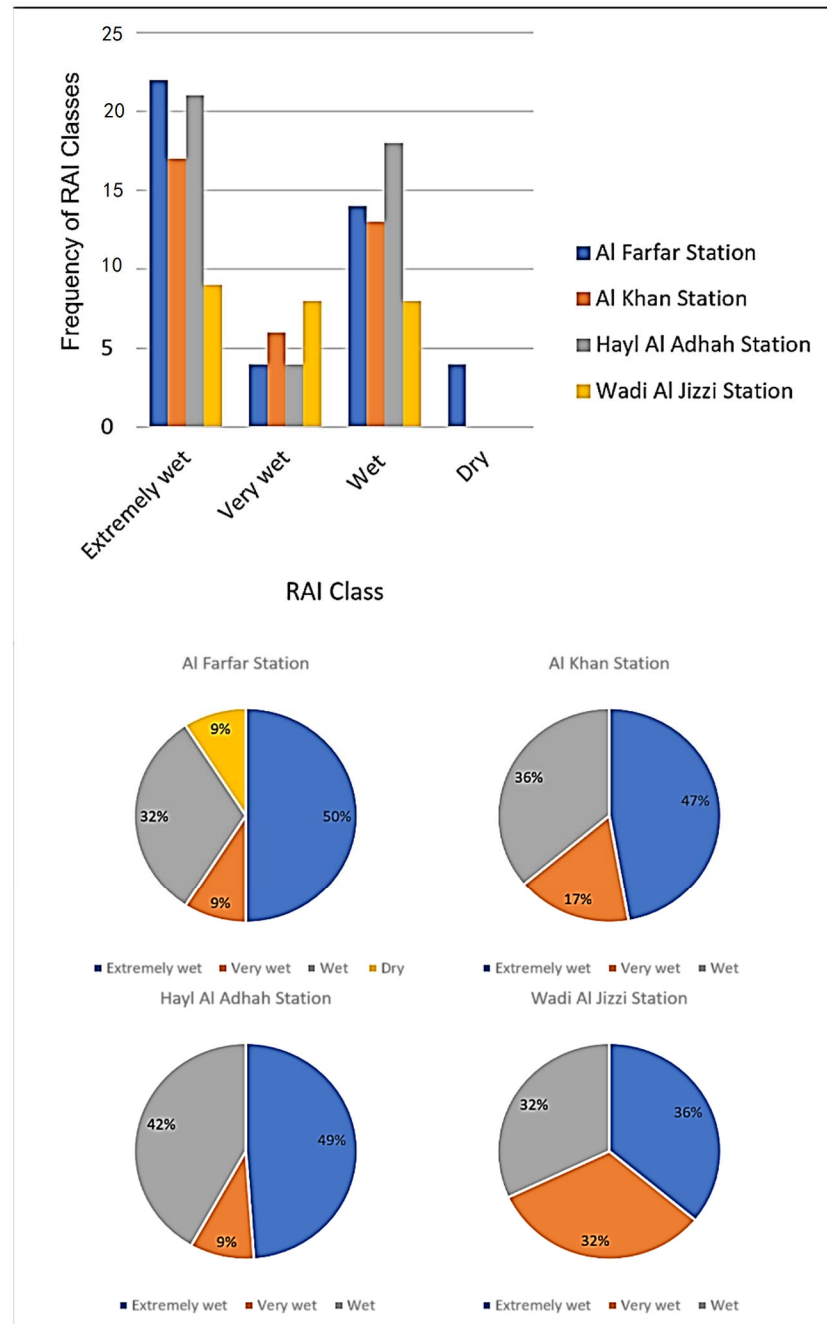
Figure 7. The *RAI* classification frequencies and percentages at the four selected rainfall stations.

In fact, whilst it is important to find the relationships between the wet condition of drought indices and flood probabilities, it is a challenging task to identify and predict severe droughts and flood phenomena in arid catchments.

Similar to the SPI1, none of the stations showed extreme dry categories of RAI values, while only one station (Al Farfar) showed a dry class. The maximum RAI value was 17.79 for Hayl Al Adhah station in the year 2009, whereas the minimum RAI value was 0.07 for Wadi Al Jizzi station for the same year. This, in fact, shows how the rainfall storms are localised.

There is an agreement that both drought indices, *SPI*1 and *RAI*, showed almost the same hydrometeorological aspects of the catchment, which is characterised by low rainfall rates and a limited number of extreme storms. *SPI*1 and *RAI* were also compared for selected hydrologic events which caused flash floods. However, the *SPI*1 showed a high Pearson correlation between extremely and severely wet categories and observed runoff (0.83), while the *RAI* was not able to detect the connection between runoff and extremely and severely wet categories, with a Pearson correlation of around 0.52.

Similar findings introduced by Shadeed (2013) and Sienz et al. (2012) showed that 67.0% and 68.2% of drought occurrences are near normal class for arid catchments, respectively [41,42]. However, the four stations under study showed almost similar trends of drought severity. Several previously related studies have revealed that there is no evidence supporting the suggestion that extreme droughts will always occur because of topographic complexity for the same arid catchment. Although the droughts have been much more obvious in recent years, Conradie et al. (2022) classified the topography at each station according to its altitude. They concluded that the altitude was not an important determinant of overall drought severity [43] and catchment areas of more than 2000 km^2 showed more hydrologic variability [44]. Furthermore, the high number of zero precipitations for periods of 1 to 6 months is one important challenge when using drought indices for arid catchments [45], referring to non-normal distributions. The non-normal distribution of the SPI is caused by a high probability of no-rain cases [46].

The monitoring station density will improve the results and decrease the uncertainty level. In comparison, Musonda et al. (2020) monitored the long-term global and drought conditions in Zambia from 1981 to 2017 using the SPI method and showed that the number of monitoring stations plays a major role in identifying drought [47]. Mehr and Vaheddoost (2020) highlighted that longer monthly rainfall and adjusted temperature can provide accurate drought rates using SPI and standardised precipitation evapotranspiration indices (*SPEI*) at 3, 6, and 12 month intervals [48]. Drought was examined at a 3-month time scale, covering the rainy season. The results (Figure 8) showed that 1996 presented the highest value for all stations.
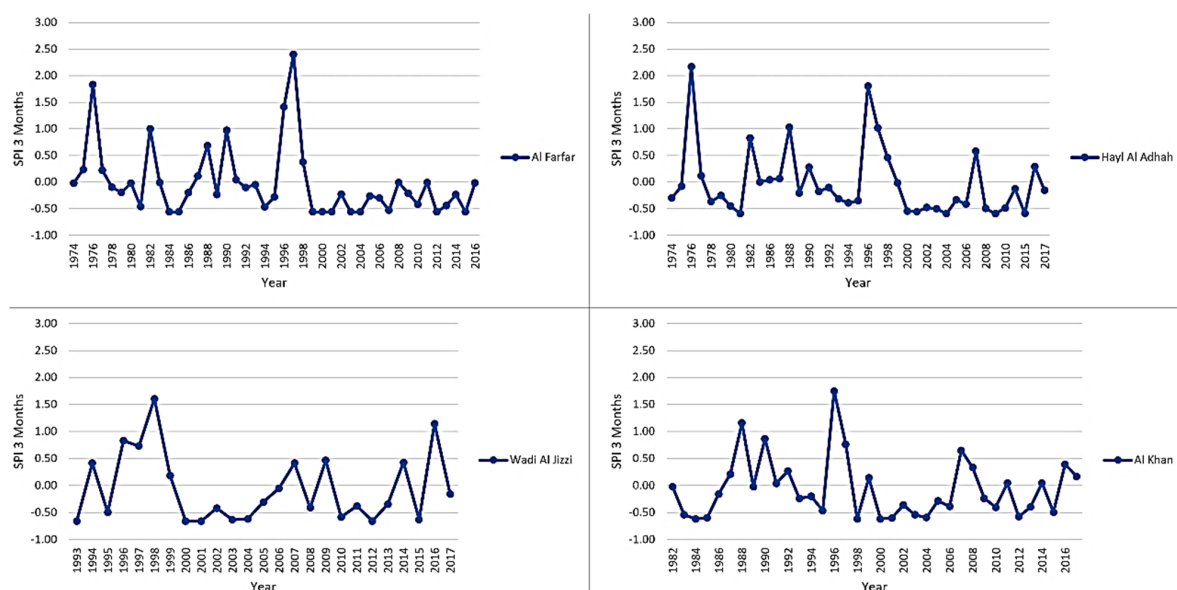
Figure 8. SPI 3-month drought records for the wet season.

4.2. Rainfall-Runoff Modelling

Soil Conservation Service-Curve Number (SCS-CN) Method

The soil type within the catchment area was classified as Sand and Loamy Sand soil, based on the 8-point double ring infiltration field tests (Table 5).

Table 5. Double ring infiltration in situ tests conducted to identify soil types.

Location ID	IR (mm/h)	Soil Type
A1	176.69	Sand
A2	59.48	Loamy sand
A3	157.50	Sand
A4	244.29	Sand
A5	124.68	Loamy sand
A6	379.49	Sand
A7	123.54	Loamy sand
A8	157.70	Sand

Soils are classified into four Hydrologic Soil Groups (HSGs): A, B, C, and D, based on soil infiltration rates (which is important for CN calculations). In accordance with the U.S. Department of Agriculture, Soil Group A is characterised by high infiltration rates, while the Soil Group B has moderate infiltration rates [49]. In addition, Groups C and D are characterised by low to very low infiltration rates, respectively. This classification was mainly based on the empirical experiments conducted by Cronshey (1986) of soil particle sizes. Consequently, the classification of the infiltration rate was identified as Group B, which is moderately low runoff potential. While the land use was described as an open space, the CN for Group B soil is 69 [50].

In addition, the impact of the station's elevation above sea level on average rainfall was tested using the Pearson correlation, which gave a slightly significant value of around 0.59. However, the maximum retention after runoff begins at 4.49 mm, while initial abstraction is 0.90 mm. In addition, the antecedent soil moisture condition in the catchment fluctuates, based on several factors:

i. Rainfall intensity and storm duration.
ii. Soil type and retention time.
iii. Temperature and other weather parameters.

As per Abushandi and Merkel (2013), there are three conditions of the Antecedent Moisture Condition (AMC) [30]:

i. The soil moisture content is at welting point (soil profile is practically dry).
ii. Below saturation level: average condition occurred by some short rainfall storms but not long enough to create a runoff.
iii. The soil profile is practically saturated or super saturated from antecedent rainfall storms.

Generally, the behaviour of simulated runoff follows the observed runoff in the SCS method (Figure 9), while the performance showed some weaknesses when the observed runoff was less than 1 m^3/s. In most cases, the simulated runoff using SCS tends to slightly underestimate the observed flood.

To simulate runoff using the SCS-CN method, the rainfall storms causing 26 runoff events were selected on a storm basis. The Nash–Sutcliffe Efficiency (NSE) was used to assess how perfectly the modelled SCS values compared with observed values. The NSE showed high performance at Hayl Al Adhah and Al Khan stations, with values of 0.92 and 0.94, respectively. The SCS results at Wadi Al Jizzi and Al Farfar stations showed a lower level of NSE, with values of 0.77 and 0.81, respectively. In reference to the station's distance from the outlet, it is obvious that Wadi Al Jizzi and Al Farfar stations lie at greater distances from the outlet, which offers a chance for more water penetration and a higher level of uncertainty.
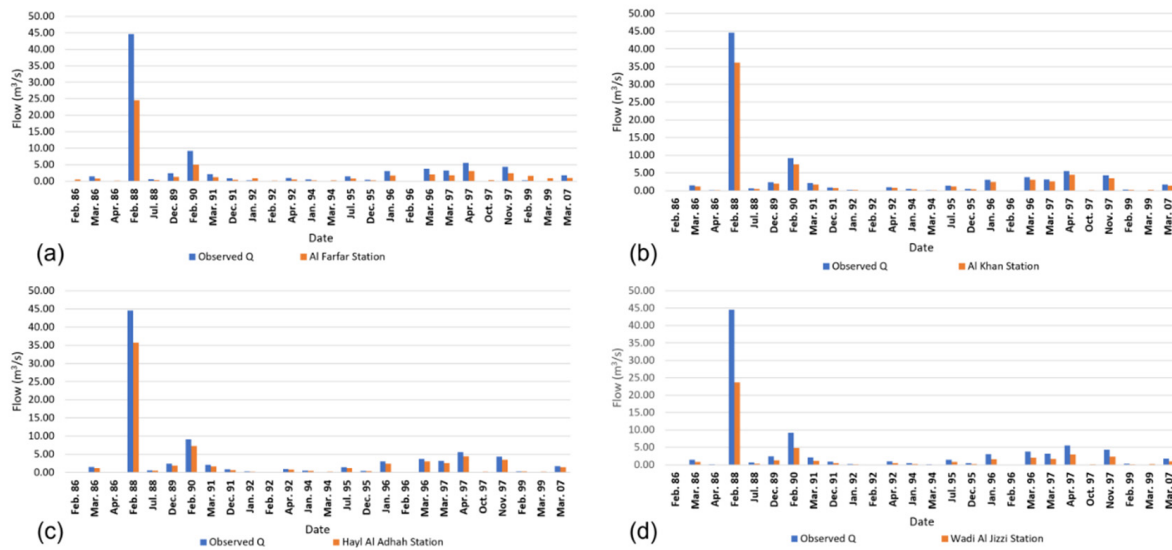
Figure 9. Wadi Al Jizzi catchment observed vs. SCS simulated runoff (26 runoff records), where: (**a**) is Al Farfar Station; (**b**) is Al Khan Station; (**c**) is Hayl Al Adhah Station; and (**d**) is Wadi Al Jizzi Station.

Based on the results, the Pearson correlation between the observed and simulated floods, using individual stations, was conducted. As expected, Wadi Al Jizzi and Al Farfar stations have lower values (Table 6).

Table 6. Pearson correlation coefficient of simulated versus observed runoff rates for the four meteorological stations.

Simulated Runoff Using SCS	Observed Runoff at Sallan Station
Hayl Al Adhah	0.80
Al Khan	0.81
Al Farfar	0.59
Wadi Al Jizzi	0.56

The most sensitive parameter which may impact the values of SCS is the rainfall and its intensity. In addition, stream length influences the modelled values, coupled with curve number values. Approximately 50% of runoff occurs mainly in the months of February and March. The wet season starts in January to April with limited runoff in the summertime, due to tropical cyclonic storms from the Indian Ocean. The runoff event durations take place from a few minutes up to a couple of hours only. Nowadays, there are big efforts to produce raw data for further extreme hydrologic identification. Satellite-based precipitation products might be an alternative source of data to feed the Standard Precipitation Index (*SPI*) or any other drought indices. This will bridge the gap of data scarcity in arid areas (feeding lumped and distributed models) and allow possible drought and runoff risk analyses. Of course, some satellite data may produce misleading results, as the hydrologic algorithm simply does not reflect the variability of arid regions.

5. Conclusions

The application of the *SPI* and *RAI* showed the ability of both indices to identify extreme wet or dry levels. The *SPI*1 had a clear identification of dry or wet season, in connection to observed runoff records for the same periods. However, there was a consistent hydrologic distribution among the four stations, in terms of drought classification. In other words, distant stations from the outlet (closer to the mountains) have more extremely wet cases than the ones closer to the outlet. This phenomenon has been reflected by the higher performance of the Nash–Sutcliffe Efficiency for distant stations. Hence, rainfall intensity, catchment topography, and storm duration are important parameters in forming wet events.

The SCS runoff simulation method could assess runoff events in arid catchments, taking into consideration that most of the simulated runoff is underestimated for all stations. However, this issue can be solved by re-adjusting the value using a simple linear regression model. The vital advantage of using the SCS runoff simulation method is the use of a different curve number value, based on the stations distributed in the catchment area, especially in regions with complex land cover types, and different stream lengths and soil types. In general, this research method can be utilised to estimate extreme events in arid areas if hydrological data are available. The performance of any model or indices on a different storm event could be different based on the recording interval and, therefore, the results will change accordingly. Sustainable development of the water sector during this difficult time is complicated, with a growing demand for using non-renewable water resources. Oman, as with many countries in the Middle East, is struggling to provide enough quality water for its domestic and agricultural needs. Therefore, this study is important for the understanding of hydrologic behaviour in arid catchments.

References

1. El Kenawy, A.M.; Al Buloshi, A.; Al-Awadhi, T.; Al Nasiri, N.; Navarro-Serrano, F.; Alhatrushi, S.; Robaa, S.M.; Domínguez-Castro, F.; McCabe, M.F.; Schuwerack, P.-M.; et al. Evidence for intensification of meteorological droughts in Oman over the past four decades. *Atmos. Res.* **2020**, *246*, 105126. [CrossRef]
2. Szalai, S.; Szinell, C.S. Comparison of two drought indices for drought monitoring in Hungary—A case study. In *Drought and Drought Mitigation in Europe*; Springer: Berlin/Heidelberg, Germany, 2000; pp. 161–166.
3. Conway, D. Extreme Hydrological Events: Precipitation, Floods and Droughts. *J. Arid Environ.* **1995**, *29*, 124–125. [CrossRef]
4. Dutta, R.; Maity, R. Time-varying network-based approach for capturing hydrological extremes under climate change with application on drought. *J. Hydrol.* **2021**, *603*, 126958. [CrossRef]
5. Kourgialas, N.N. Hydroclimatic impact on mediterranean tree crops area–Mapping hydrological extremes (drought/flood) prone parcels. *J. Hydrol.* **2021**, *596*, 125684. [CrossRef]
6. Adikari, K.E.; Shrestha, S.; Ratnayake, D.T.; Budhathoki, A.; Mohanasundaram, S.; Dailey, M.N. Evaluation of artificial intelligence models for flood and drought forecasting in arid and tropical regions. *Environ. Model. Softw.* **2021**, *144*, 105136. [CrossRef]
7. McKee, T.B.; Doesken, N.J.; Kleist, J. The relationship of drought frequency and duration to time scales. In Proceedings of the Proceedings of the 8th Conference on Applied Climatology, Anaheim, CA, USA, 17–22 January 1993; pp. 179–183.
8. Ali, M.; Deo, R.C.; Maraseni, T.; Downs, N.J. Improving SPI-derived drought forecasts incorporating synoptic-scale climate indices in multi-phase multivariate empirical mode decomposition model hybridized with simulated annealing and kernel ridge regression algorithms. *J. Hydrol.* **2019**, *576*, 164–184. [CrossRef]
9. Zhao, W.; Yan, T.; Peng, S.; Ding, M.; Lai, X. Drought and flood characteristics evolution in peninsular region of Shandong Province based on standardized precipitation index. In *IOP Conference Series: Earth and Environmental Science*; IOP Publishing: Bristol, UK, 2020; Volume 601, p. 12021.
10. Tsesmelis, D.E.; Vasilakou, C.G.; Kalogeropoulos, K.; Stathopoulos, N.; Alexandris, S.G.; Zervas, E.; Oikonomou, P.D.; Karavitis, C.A. Chapter 46—Drought assessment using the standardized precipitation index (SPI) in GIS environment in Greece. In *Computers in Earth and Environmental Sciences*; Pourghasemi, E.S., Ed.; Elsevier: Amsterdam, The Netherlands, 2022; pp. 619–633. ISBN 978-0-323-89861-4.

11. Łabędzki, L. Estimation of local drought frequency in central Poland using the standardized precipitation index SPI. *Irrig. Drain. J. Int. Comm. Irrig. Drain.* **2007**, *56*, 67–77. [CrossRef]

12. Zhai, J.; Su, B.; Krysanova, V.; Vetter, T.; Gao, C.; Jiang, T. Spatial variation and trends in PDSI and SPI indices and their relation to streamflow in 10 large regions of China. *J. Clim.* **2010**, *23*, 649–663. [CrossRef]

13. Tufaner, F.; Özbeyaz, A. Estimation and easy calculation of the Palmer Drought Severity Index from the meteorological data by using the advanced machine learning algorithms. *Environ. Monit. Assess.* **2020**, *192*, 1–14. [CrossRef]

14. Abushandi, E.; Merkel, B. Rainfall estimation over the Wadi Dhuliel arid catchment, Jordan from GSMaP_MVK+. *Hydrol. Earth Syst. Sci. Discuss.* **2011**, *8*, 1665–1704.

15. Abushandi, E. Flash flood simulation for Tabuk City catchment, Saudi Arabia. *Arab. J. Geosci.* **2016**, *9*, 1–10. [CrossRef]

16. Shadeed, S.; Almasri, M. Application of GIS-based SCS-CN method in West Bank catchments, Palestine. *Water Sci. Eng.* **2010**, *3*, 1–13.

17. Alzghoul, M.; Al-husban, Y. Estimation of Runoff by applying SCS Curve Number Method, in a complex arid area; Wadi Al-Mujib watershed; Study case. *Dirasat Hum. Soc. Sci.* **2021**, *48*. Available online: https://archives.ju.edu.jo/index.php/hum/article/view/104919 (accessed on 22 May 2022).

18. El-Hames, A.S. An empirical method for peak discharge prediction in ungauged arid and semi-arid region catchments based on morphological parameters and SCS curve number. *J. Hydrol.* **2012**, *456*, 94–100. [CrossRef]

19. Al-Ghobari, H.; Dewidar, A.; Alataway, A. Estimation of Surface Water Runoff for a Semi-Arid Area Using RS and GIS-Based SCS-CN Method. *Water* **2020**, *12*, 1924. [CrossRef]

20. Braud, I.; Borga, M.; Gourley, J.; Hurlimann, M.; Zappa, M.; Gallart, F. Flash floods, hydro-geomorphic response and risk management. *J. Hydrol.* **2016**, *541*, 1–5. [CrossRef]

21. Karagiorgos, K.; Thaler, T.; Heiser, M.; Hübl, J.; Fuchs, S. Integrated flash flood vulnerability assessment: Insights from East Attica, Greece. *J. Hydrol.* **2016**, *541*, 553–562. [CrossRef]

22. Mahmood, M.I.; Elagib, N.A.; Horn, F.; Saad, S.A.G. Lessons learned from Khartoum flash flood impacts: An integrated assessment. *Sci. Total Environ.* **2017**, *601–602*, 1031–1045. [CrossRef]

23. Abushandi, E.; Al Sarihi, M. Flash flood inundation assessment for an arid catchment, case study at Wadi Al Jizzi, Oman. *Water Pract. Technol.* **2022**, *17*, 1155–1168. [CrossRef]

24. Al Ruheili, A.; Dahm, R.; Radke, J. Wadi flood impact assessment of the 2002 cyclonic storm in Dhofar, Oman under present and future sea level conditions. *J. Arid Environ.* **2019**, *165*, 73–80. [CrossRef]

25. Niyazi, B.A.; Masoud, M.H.; Ahmed, M.; Basahi, J.M.; Rashed, M.A. Runoff assessment and modeling in arid regions by integration of watershed and hydrologic models with GIS techniques. *J. Afr. Earth Sci.* **2020**, *172*, 103966. [CrossRef]

26. Saber, M.; Hamaguchi, T.; Kojiri, T.; Tanaka, K.; Sumi, T. A physically based distributed hydrological model of wadi system to simulate flash floods in arid regions. *Arab. J. Geosci.* **2015**, *8*, 143–160. [CrossRef]

27. El Alfy, M. Assessing the impact of arid area urbanization on flash floods using GIS, remote sensing, and HEC-HMS rainfall–runoff modeling. *Hydrol. Res.* **2016**, *47*, 1142–1160. [CrossRef]

28. Jodar-Abellan, A.; Valdes-Abellan, J.; Pla, C.; Gomariz-Castillo, F. Impact of land use changes on flash flood prediction using a sub-daily SWAT model in five Mediterranean ungauged watersheds (SE Spain). *Sci. Total Environ.* **2019**, *657*, 1578–1591. [CrossRef] [PubMed]

29. Aghabeigi, N.; Esmali, O.A.; Mostafazadeh, R.; Golshan, M. The Effects of Climate Change on Runoff Using IHACRES Hydrologic Model in Some of Watersheds, Ardabil Province. *Irrig. Water Eng.* **2020**, *10*, 178–189.

30. Abushandi, E.; Merkel, B. Modelling rainfall runoff relations using HEC-HMS and IHACRES for a single rain event in an arid region of Jordan. *Water Resour. Manag.* **2013**, *27*, 2391–2409. [CrossRef]

31. Siebert, S.; Nagieb, M.; Buerkert, A. Climate and irrigation water use of a mountain oasis in northern Oman. *Agric. Water Manag.* **2007**, *89*, 1–14. [CrossRef]

32. Searle, M.P. Preserving Oman's geological heritage: Proposal for establishment of World Heritage Sites, National GeoParks and Sites of Special Scientific Interest (SSSI). *Geol. Soc. London, Spec. Publ.* **2014**, *392*, 9–44. [CrossRef]

33. Al-Kindi, R.S. *Assessment of Groundwater Recharge from the Dam of Wadi Al-Jizzi, Sultanate of Oman*; United Arab Emirates University: Al Ain, United Arab Emirates, 2014.

34. Al Maqbali, N. *Risk Assessment of Dams*; University of Adelaide: Adelaide, Australia, 1999.

35. Abushandi, E. Flood Water Management in Arid Regions, Case Studies: Wadi Al Jizzi, Oman, Wadi Abu Nsheifah, Saudi Arabia, and Wadi Dhuleil, Jordan. In *Recent Advances in Environmental Science from the Euro-Mediterranean and Surrounding Regions*; Kallel, A., Ksibi, M., Ben Dhia, H., Khélifi, N., Eds.; Springer International Publishing: Cham, Switzerland, 2018; pp. 1813–1814.

36. Costa, J.A.; Rodrigues, G.P. Space-time distribution of rainfall anomaly index (RAI) for the Salgado Basin, Ceará State-Brazil. *Ciência e Nat.* **2017**, *39*, 627–634. [CrossRef]

37. Zhao, H.; Gao, G.; An, W.; Zou, X.; Li, H.; Hou, M. Timescale differences between SC-PDSI and SPEI for drought monitoring in China. *Phys. Chem. Earth Parts A/B/C* **2017**, *102*, 48–58. [CrossRef]

38. Wang, S.; Najafi, M.R.; Cannon, A.J.; Khan, A.A. Uncertainties in Riverine and Coastal Flood Impacts under Climate Change. *Water* **2021**, *13*, 1774. [CrossRef]

39. Verma, S.; Singh, P.K.; Mishra, S.K.; Singh, V.P.; Singh, V.; Singh, A. Activation soil moisture accounting (ASMA) for runoff estimation using soil conservation service curve number (SCS-CN) method. *J. Hydrol.* **2020**, *589*, 125114. [CrossRef]

40. Liu, J.; Yuan, D.; Zhang, L.; Zou, X.; Song, X. Comparison of Three Statistical Downscaling Methods and Ensemble Downscaling Method Based on Bayesian Model Averaging in Upper Hanjiang River Basin, China. *Adv. Meteorol.* **2016**, *2016*, 7463963. [CrossRef]

41. Shadeed, S. Spatio-temporal drought analysis in arid and semi-arid regions: A case study from Palestine. *Arab. J. Sci. Eng.* **2013**, *38*, 2303–2313. [CrossRef]

42. Sienz, F.; Bothe, O.; Fraedrich, K. Monitoring and quantifying future climate projections of dryness and wetness extremes: SPI bias. *Hydrol. Earth Syst. Sci.* **2012**, *16*, 2143–2157. [CrossRef]

43. Conradie, W.S.; Wolski, P.; Hewitson, B.C. Spatial heterogeneity of 2015–2017 drought intensity in South Africa's winter rainfall zone. *Adv. Stat. Clim. Meteorol. Oceanogr.* **2022**, *8*, 63–81. [CrossRef]

44. Glad, P.A. Meteorological and Hydrological Conditions Leading to Severe Regional Drought in Malawi. Master's Thesis, University of Oslo, Oslo, Norway, 2010.

45. Mahmoudi, P.; Ghaemi, A.; Rigi, A.; Amir Jahanshahi, S.M. Recommendations for modifying the Standardized Precipitation Index (SPI) for drought monitoring in arid and semi-arid regions. *Water Resour. Manag.* **2021**, *35*, 3253–3275. [CrossRef]

46. Wu, H.; Svoboda, M.D.; Hayes, M.J.; Wilhite, D.A.; Wen, F. Appropriate application of the standardized precipitation index in arid locations and dry seasons. *Int. J. Climatol. A J. R. Meteorol. Soc.* **2007**, *27*, 65–79. [CrossRef]

47. Musonda, B.; Jing, Y.; Iyakaremye, V.; Ojara, M. Analysis of Long-Term Variations of Drought Characteristics Using Standardized Precipitation Index over Zambia. *Atmosphere* **2020**, *11*, 1268. [CrossRef]

48. Mehr, A.D.; Vaheddoost, B. Identification of the trends associated with the SPI and SPEI indices across Ankara, Turkey. *Theor. Appl. Climatol.* **2020**, *139*, 1531–1542. [CrossRef]

49. U.S. Department of Agriculture. Hydrologic Soil Groups. In *National Engineering Handbook. Part 630 Hydrology, Chapter 7*; U.S. Department of Agriculture: Washington, DC, USA, 2009; pp. 1–13.

50. Cronshey, R. *Urban Hydrology for Small Watersheds*; No. 55; US Department of Agriculture, Soil Conservation Service, Engineering Division: Washington, DC, USA, 1986.

Article

Satellite-Based Discrimination of Urban Dynamics-Induced Local Bias from Day/Night Temperature Trends across the Nile Delta, Egypt: A Basis for Climate Change Impacts Assessment

Waleed Abbas [1,*] and **Islam Hamdi** [2]

1   Department of Geography & GIS, Ain Shams University, Cairo 11566, Egypt
2   Department of Geography & GIS, Beni-Suef University, Beni-Suef 62521, Egypt
*   Correspondence: walid.abbas@art.asu.edu.eg; Tel.: +20-01-1467-59223

Abstract: The Nile Delta is the most vital region of the desert-dominated country of Egypt. Due to its prominent level of vulnerability to climate change's negative impacts and its low capacity for adaptation and mitigation, the current study aims to provide accurate quantification of temperature change across the Nile Delta as an integral basis for sustainability and climate change impacts assessment studies. This was achieved through monitoring urban dynamics and detecting LST trends in 91 cities and their rural surroundings. The relevant local urban bias was discriminated from regional/background changes present in diurnal/nocturnal temperature records. The temperature records were then corrected/adjusted by removing this urban bias. Owing to the insufficiency of ground-based meteorological observatories, the investigation utilized moderate resolution imaging spectroradiometer (MODIS) land surface temperatures (LSTs) and Landsat-based datasets (2000–2021). The widely used Mann–Kendall test (MKT) and Theil–Sen estimator (TSE) were employed to assess trends in urban sprawl, LST time series, and the implied association. The analysis revealed that the region has experienced dramatic urbanization, where the total urban expansion was greater than two-thirds (69.1%) of the original urban area in 2000. This was accompanied by a notable warming trend in the day/night and urban/rural LST records. The nocturnal LST exhibited a warming tendency (0.072 °C year^{-1}) larger than the diurnal equivalent (0.065 °C year^{-1}). The urban dynamics were positively correlated with LST trends, whereas the Mediterranean Sea appeared as a significant anti-urbanization moderator, in addition to the Nile River and the prevailing northerly/northwesterly winds. The urban–rural comparison approach disclosed that the urbanization process caused a warming bias in the nighttime LST trend by 0.017 °C year^{-1} (21.8%) and a cooling bias in the daytime by −0.002 °C year^{-1} (4.4%). All results were statistically significant at a confidence level of 99%. It is recommended that studies of climate-related sustainability and climate change impact assessment in the Nile Delta should apply a distinction of urban-induced local effect when quantifying the actual regional temperature change.

Keywords: urban warming; urban bias; land surface temperature; MODIS; GAIA dataset; Mann–Kendall test; Theil–Sen estimator

1. Introduction

It is incontrovertible that there is no other country in the world that is as reliant on a mono-fluvial system, i.e., the Nile River, as Egypt. With a sizable population of more than 100 million people and about 96% of desert lands, Egypt is one of the most densely populated countries throughout the globe [1]. Although it constitutes just 2.4%, the Nile Delta is the most vital region in Egypt. It supports 63% of the country's arable land, yields most crop production, and offers residence for nearly 50% of the population [2]. Under these circumstances, the region's resources are invaluable but, at the same time, scarce and insufficient. Therefore, the studies concerning the environmental impact assessment and

sustainable development are crucial to evaluate the overall region's sensitivity to possible hazards, notably impactful climate change.

Recent studies have been appraising possible impacts of past climate change and future scenarios on the world environment [3–13]. Owing to their paramount importance, the low-lying deltaic systems have broadly attracted special attention as land/sea interfaces and as hotspots of climate change-related threats [8,9,14–17]. The Nile Delta was identified as one of the most vulnerable regions to adverse influences related to climate change, including sea-level rise and seawater intrusion [2,18,19], and accelerated coastal erosion [1], threatening the agricultural and rural communities [20,21]. At the same time, the region's adaptive capacity and mitigative/adjustable capability with these implications are weak since its marginal ecosystem can be described as fragile or highly susceptible to climate change.

Urban dynamics, on the other hand, are the most significant anthropogenic influence on the atmospheric system after human-made climate change [22]. Realizing the long-term dynamics of urbanization is increasingly significant for addressing the relevant environmental implications and sustainable development goals [23,24]. This issue has manifold critical consequences on the environmental biophysical systems and the national socio-economic sectors. In Egypt, the uncontrolled urban dynamics with high rates are complicated because of the rapid population growth, accelerated national development, and scanty resources of the arable lands [25,26]. So, the conversion of the Nile Delta's cultivated lands to urban LULC is one of the most irreversible negative human impacts. These urban dynamics over the old deltaic lands severely damage the richest natural reservoir containing invaluable agriculture-supporting resources and food-producing systems. In the current context, the atmospheric system is not an exception, where diversified micro-scale modifications were observed as a result of the urbanization process, including the conspicuous urban heat island (UHI) [27,28]. It is a phenomenon that occurs when urban land uses/land covers (LULC) replace the natural vegetation lands, causing a strong micro-scale overheating within three layers of the cities, i.e., surface, canopy, and boundary layers, compared to the surrounding environment [29]. The local effect of UHI can exacerbate the temperature trend observed in the urban areas relative to that detected in the rural surroundings [30–32].

Considering the above-mentioned arguments, as accurate as possible quantification of temporal temperature change can be counted as a fundamental ground for assessing the expected environmental impacts of potential climate change on the Nile Delta's water–food–energy systems and the relevant concerns of sustainability. The accurate estimation of temporal temperature changes requires unbiased temperature records. Many triggers are well-recognized as contaminants that can introduce biases into the systematically observed records of temperature [33–36], primarily the unavoidable processes of urban dynamics.

Early research works embarked on eliminating the systematic urban effect existing in temperature records (e.g., [30,37–39]), where the city has been recognized long ago as a serious contamination source of the climate signals [40]. This was originally triggered and encouraged as an integral part of the wider scientific interest in the global climate change issue. Correcting the urbanization effect should be conducted to provide bias-free temperature records necessary for monitoring the actual long-term climate change, namely "Macro and/or Large-scale and/or Background and/or Regional Component" of climate change [41,42]. Advancements in the methodologies of urban bias removal can be divided into the urban–rural comparison approach and the urban-based approach.

Kukla et al., (1986) demonstrated the early urban bias estimations by comparing trends of air temperature datasets collected in urban environments and countryside sites worldwide [37]. This technique was then mostly adopted in North America [37], the United States [38], the Northern Hemisphere [39], Prague [43], and South Korea [44]. Jones et al., (1989) used linear regression between urban–rural temperature differences and population growth to discover the urban effect in the United States and the Northern Hemisphere temperature records [39]. The urban–rural distinction was initially based on population size, population density, and census area categorization [45]. Later, satellite night-light metadata was used for this purpose [46,47]. A new machine learning-based method was proposed

by [48] to classify weather stations into rural/urban based on a satellite-based global LULC product. They then estimated the urbanization contribution to the global/regional time series of annual land mean/extreme temperature indices.

In case the reference rural stations are inadequate, another methodological approach was invented based solely on the urban conditions. Some papers estimated urban bias by utilizing the upper-air temperature records collected through atmospheric vertical soundings, which are not sensitive to urbanization [22,49,50]. An innovative analysis drew an analogy between air temperature trends in windy and calm weathers to extract the net urban effect [51]. Yuan and Guo-Yu [52] developed a new method to adjust urban bias in Beijing using linear correction between the accumulated urbanization effect and surface air temperature. A similar work [53] connected trends of urban fraction around weather stations to quantify the nexus between urban sprawl and urban warming in China. Integration between remote sensing and weather observations was employed to assess Brussels' UHI effect on the summertime air temperature series of Uccle [54]. Bassett et al., created a statistical model to estimate the daily urban warming across Great Britain based on the relationships between UHI intensity, urban fraction, and wind speed [55]. Recently, Shi et al., (2021) corrected the urbanization bias at a typical station in the Yangtze River Delta. The discussion suggested that the new satellite-based technology can be more effective in correcting the urbanization effect around the station [32].

It has long been acknowledged that remote sensing is a robust system for monitoring the Earth's environmental conditions and ecological problems [56–60]. It consistently provides a long historical record of imagery acquired in diverse spatial/temporal resolutions, which is essentially advantageous in the assessment of urban dynamics [61–63] and LULC changes [64–66] over time. Satellites operating in thermal infrared (TIR) imaging have an extraordinary prominence in terms of LSTs calculation and investigation [67,68], including Landsat missions 4/5/7/8, the advanced space-borne thermal emission and reflection radiometer (Terra ASTER), and Aqua/Terra MODIS. TIR satellites were designated to supply thermal data in a high spatial sampling rather than any other data source. They are specifically optimal for exploring and analyzing local-to-site thermal characteristics and UHI effects [28,69–72]. Consequently, those systems overcome the rooted shortages that devalue the ground-based observatory network of the atmospheric system, particularly in developing countries' regions, such as the Nile Delta, whose meteorological service contains very few weather stations with limited capacity for micro-scale applications of urban climate.

In addition, the localized nature of per-pixel LSTs makes TIR products remarkably valid in separating the urban warming component from the regional atmospheric change. On the contrary, in the case of ambient air temperature data measured systematically by sparse, inadequate weather stations, the achievement of that local–regional thermal separation is largely defective because of the well-mixed urban–rural air masses. This air mixing prompts the urbanized contamination effect in meteorological stations located within peri-urban and rural surroundings. This urban-induced corruption is mainly caused by the horizontal outgrowth of the UHI effect beyond the city's built-up zone, namely the well-known phenomenon of the UHI footprint [73–77].

In this paper, we monitor the dynamics of the urban centers across the Nile Delta, explore diurnal/nocturnal LST trends in both urban areas and rural surroundings, and analyze the urbanization–warming nexus. Finally, the local-to-regional temperature changes are discriminated using quantification of the urban bias. We utilized LST data products acquired by Aqua/Terra MODIS sensors (2000–2021) and Landsat-based annual coverage of urban settlements, namely the "Global Artificial Impervious Areas (GAIA)" dataset.

2. Materials and Methods

2.1. Study Area

The Nile Delta is a major physiographic division of Egypt. It is an inverted triangle-like region situated in the northern territory of Egypt, as shown in Figure 1. Its southernmost

tip is formed by the divergence of the Nile River's main course into the eastern (namely Damietta) and the western (namely Rosetta) distributaries. The northern arc-shaped edge of the region stretched along the middle part of the Egyptian Mediterranean coastline. The region spans latitudes between 30°10′25.9″–31°36′11.6″ north and longitudes between 29°22′35.7″–32°33′15.8″ east. Hence, it is located within the African subtropical zone, fully influenced by Köppen's hot desert climate BWh [78].
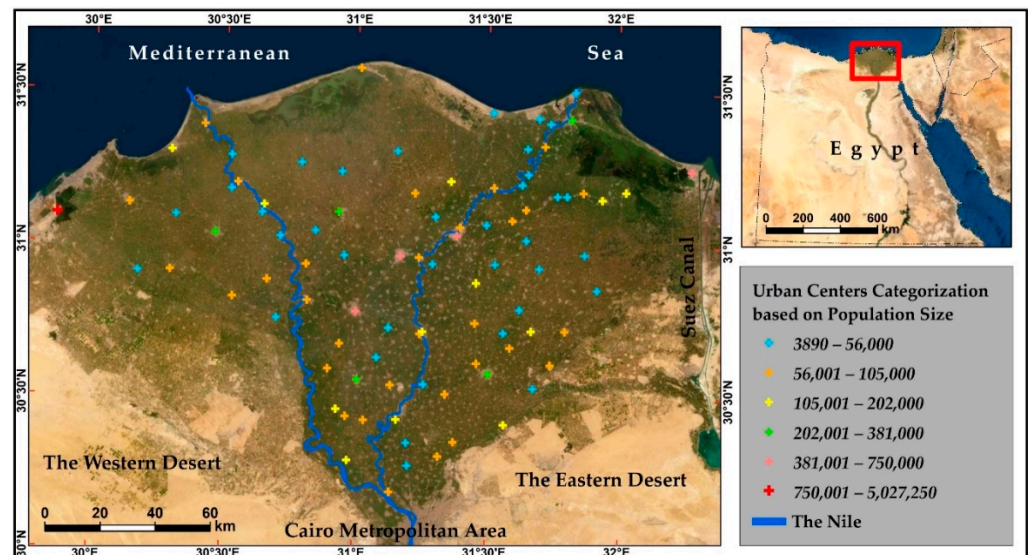
Figure 1. Location map and geographical setting of the study area (the red box) using ESRI true-color satellite images. The Nile Delta (the dark greenish cultivated surface) extends between the Western and Eastern Desert surfaces (the yellowish surfaces). The urban system under consideration includes 91 urban centers symbolized using the natural breaks (Jenks) method into six categories according to population size: small towns (37 centers), large towns (32 centers), small cities (12 centers), medium cities (5 centers), large cities (4 centers), and megacities (single center). This method of classification groups the original population data into similar natural classes of urban centers to maximize the differences between classes. The limits of each population class were rounded for generalization purposes.

The key aspect of the climatic conditions is the enormous evapotranspiration that exceeds the rainfall amount, forming a vast arid zone as a part of the Northern African Sahara, which is interrupted by the Nile River and its own Delta intrusion. Broadly speaking, the region experiences warm-to-hot summers with mild winters. The westerlies dominate the general wind system, acting as a temperature-moderating agent. Based on the spatial average of climate data observed for the period 1976–2005 in 10 meteorological stations within the Nile Delta, the annual maximum, minimum, and daily temperature normals were 25.9 °C, 15.4 °C, and 20.4 °C, respectively. The summer maximum temperatures frequently exceed 30 °C, while minimum temperatures in winters are usually above 5 °C. The absolute maximum (highest) and minimum (lowest) temperature values observed were 44.4 °C and 0.1 °C, respectively.

The region covers an onshore area of about 21,427.1 sq km, only 2.4% of Egypt's mainland [2]. The Nile Delta's alluvial formation within a desert-dominated country makes it the richest agricultural environment that offers a habitat for about 50% of the country's population. Considering the above-mentioned socio-economic impetus, the region has been undergoing considerably intensified urban dynamics. The cultivated surface of the Nile Delta plain is speckled with a wide variety of urban/non-urban settlements. The urban system occupying the Nile Delta's old lands includes 91 municipalities out of the total 241 Egyptian urban settlements. Figure 1 illustrates their spatial distribution and categories with respect to population size. The total population of the urban centers of

interest is 14.2 million, with a considerable domain ranging between the smallest town of Gamasa (3890 inhabitants) and the largest megacity of Alexandria (5,027,250 inhabitants).

2.2. Datasets Description and Analysis Procedure

2.2.1. Urban Dynamics Data and Mapping

Monitoring large-scale urban dynamics is crucial for numerous environmental applications on a changing globe. The practicality of big imagery data archives collected by satellite remote sensing systems was frequently expanded to produce ready-to-use long-term urban impervious surfaces and LULC products for mapping urban dynamics worldwide [24,79–81]. The current study exploited the so-called GAIA dataset generated by [81] to map and explore the urban dynamics across the Nile Delta in terms of urban sprawl. It is a web-based repository that offers high-resolution (30 meters) raster layers of the human urban/rural settlements' footprints. The dataset has a planetary-scale spatial extension, with temporal coverage spanning more than 30 years (1985–2018) at annual intervals. Human settlements were extracted and mapped annually based on the full image archive of Landsat satellite missions on the Google Earth engine platform. The developers of GAIA reported that they evaluated the dataset using a five-year interval sample, namely 1985, 1990, 1995, 2000, 2005, 2010, and 2015, and the overall accuracy was +90%. The cross-comparison and temporal trend in GAIA agreed well with the similar local, regional, and global datasets. The full dataset is freely downloadable and sharable from http://data.ess.tsinghua.edu.cn (accessed on 5 January 2022).

After downloading, the preprocessing procedures involved clipping the dataset spatial coverage by the Nile Delta's boundary and transforming the layers from the geographic coordinate system (GCS) of WGS 1984 to the commonly used projected coordinate system (PCS) of Universal Transverse Mercator (UTM) Zone 36 N. Owing to its inclusion of all settlement types, we masked GAIA raster layers to eliminate rural settlements. The final outputs contained only the annual built-up footprints of the 91 urban centers under investigation within the Nile Delta region. Because the GAIA dataset ends in 2018, the yearly urban expansions up to 2021 were derived from 30-meter Landsat images using on-screen digitizing. The area (sq km) of each urban settlement was computed on a year-to-year basis during the study timeframe (2000–2021).

2.2.2. Vegetation Indices and Urban–Rural Distinction

The most straightforward approach of quantifying the urbanization effect is to compare the urban areas with the neighboring rural environment that is considered free of the urban influence. The current study adopted an urban–rural comparison approach for measuring the local contribution of urbanization in the LST time series. So, it was necessary to accurately distinguish the urbanized built-up zones and the rural vegetated surroundings. Simply put, the Nile Delta's urban built-up zones were extracted based on the GAIA dataset [81] described before in Section 2.2.1.

As for the rural areas, since the standard height of the thermometer shelter is 1.5 m, the maximum possible impact of the urbanized built-up area on the temperature data under advection and turbulence conditions does not exceed 5 km [32,82,83]. Therefore, the reference rural surroundings were delineated as well by creating a GIS Euclidean distance analysis to determine the areas extending +5 km around each urban center. The rural environments occupying the immediate vicinity (0–5 km) of the urban areas were neglected so as to eliminate the well-recognized UHI footprint effect. Figure 2 shows an example of the conceptual framework used to identify the urban center, the ignored ring buffer, and the reference rural surroundings required for removing urban bias from the LST records.

(**a**)   (**b**)
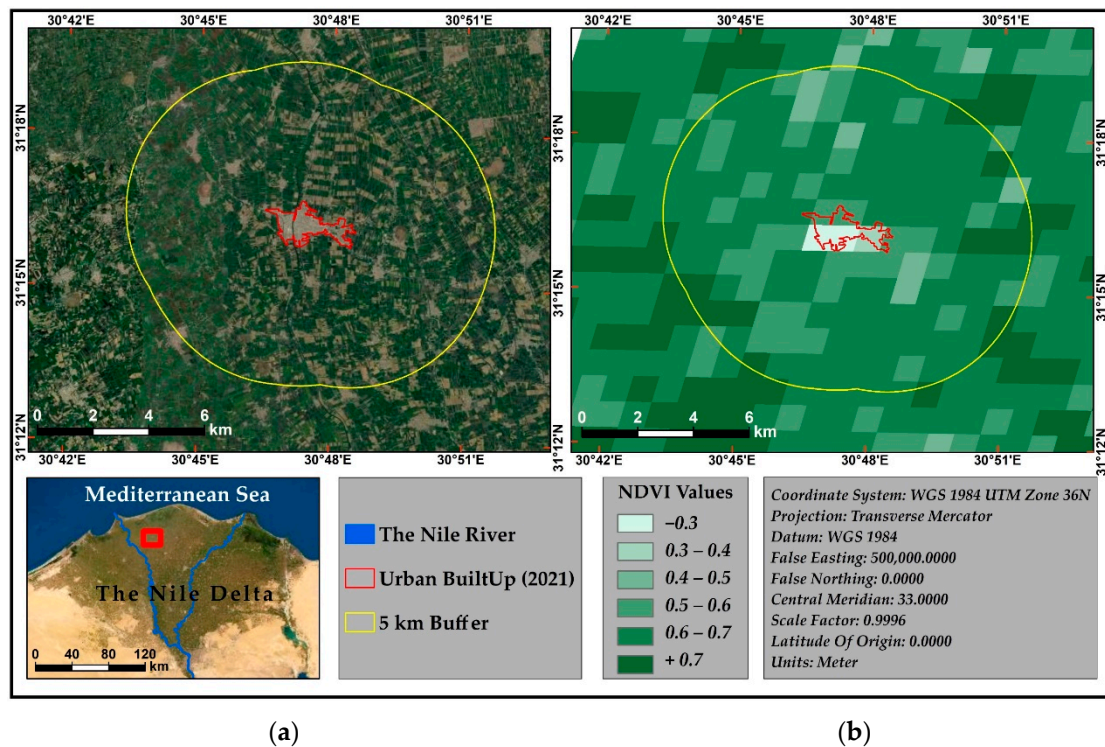
Figure 2. (**a**) The conceptual framework adopted in the study to identify (1) the urban area whose temperature record endures the UHI signals and needs to be corrected (the red border), (2) the ignored 0–5 km rural surrounding which is affected by the UHI footprint (inside the yellow border), and (3) the reference +5 km rural surroundings utilized for urban bias removal (outside the yellow border). (**b**) The reference +5 km rural surroundings were selected based on Terra MODIS NDVI values. As indicated by the left panel (**a**), the region is highly urbanized and numerous villages spread across its surface. We used GIS-based processing to exclude these unfavorable built-up areas from the rural benchmark zone to avoid introducing uncertainty to the analysis results. The illustrative mapped example is for the small town of Sidi Salem.

As a matter of fact, the LST values in rural areas are expected to be largely affected by the interannual variations of vegetation greenery/extent expressed in NDVI values. This situation can introduce much uncertainty when comparing urban/rural environments to measure the effect of urban expansion on LST. We neutralized the vegetation-induced LST variations in the reference rural locations by exclusively utilizing the highly vegetated pixels in which NDVI $\geq$ 0.65 and no significant trend was observed in the 22-year time series of the NDVI dataset. It should be noted that the web-based accessible (https://earthexplorer.usgs.gov/ (accessed on 14 January 2022)) Terra MODIS product of MOD13A3 V6.1 was manipulated to identify vegetated areas in the reference rural zone located +5 km from each city. The product involves the vegetation indices of the normalized difference vegetation index (NDVI) and the enhanced vegetation index (EVI) provided monthly at 1 km spatial resolution. More improvements were applied to the reference rural surroundings by eliminating the pixels containing high water content or small built-up settlements, which may elevate the errors in the analysis results.

2.2.3. LST Time-Series Construction

In determining the local response of temperature to urban dynamics, nine LST time series were imperative for analysis, i.e., diurnal, nocturnal, and daily collections for urban, rural, and area averaged LST values. Moreover, per-city LST records were crucial to analyze the dependency of temperature bias on the city size and rates of urban dynamics. The work relied entirely on satellite data acquired by Aqua/Terra MODIS sensors available for use at

https://earthexplorer.usgs.gov (accessed on 9 January 2022). The imagery datasets cover a continuous, relatively prolonged period of about 22 years (2000–2021). The Aqua/Terra MODIS sensors detect four scenes a day for the study area, both in diurnal ($\approx$10:00 AM and 02:00 PM) and nocturnal ($\approx$10:00 PM and 02:00 AM) times. We drew Terra MODIS-derived MOD11A2 and Aqua MODIS-derived MYD11A2 version 6.1 products, which provide an average 8-day per-pixel LST and emissivity at 1 km spatial resolution.

Preprocessing for each imagery collection included sub-setting the study area, projecting the scene to PCS UTM Zone 36 N coordinate system, transforming the scene's digital numbers (DNs) to LSTs by the provided scale factor (0.02), and conducting emissivity correction of LST using the supplied per-pixel emissivity values. Temporal and spatial missing LST values were estimated using the inverse distance weight (IDW) interpolator and forecasting function. Subsequently, the annual LST averages of daytime, nighttime, and day imagery records were computed. Ultimately, the above-mentioned temporal daytime, nighttime, and day LST records were spatially segmented using GIS zonal analysis to more homogeneous urban, rural, and area-averaged composites.

2.2.4. Trend Analysis

Upward and downward trends are detectable in hydrometeorological time series using different statistical parametric and nonparametric tests [84–88]. We applied the widely used MKT [89,90] and TSE [91,92] to assess trends in urban sprawl and LST time series, and the relevant intercorrelation. MKT is a rank-based, nonparametric test developed to detect positive/negative monotonic trends in environmental impact assessments [93,94]. Unlike the parametric methods, MKT is a distribution-independent test, i.e., it does not require the data to be normally distributed, a presumption that is statistically rare in atmospheric data. However, the dataset should have no serial correlation [95]. All LST trends were evaluated at a statistical significance of 0.01 (confidence level of 99%).

The MKT statistic S is given by [94]:

$$S = \sum_{i=1}^{n-1} \sum_{j=i+1}^{n} sgn(X_j - X_i) \tag{1}$$

where X_i and X_j are the values of sequence i, j; n is the length of the time series, and:

$$sgn\,(\theta) = \begin{cases} +1 & if\ \theta > 0 \\ 0 & if\ \theta = \theta \\ -1 & if\ \theta < 0 \end{cases} \tag{2}$$

The statistic S is approximately normally distributed when $n \geq 8$, with mean and variance as follows:

$$E(S) = 0 \tag{3}$$

$$V\,(S) = \frac{n\,(n-1)(2n-5) - \sum_{i=1}^{m} T_i i\,(i-1)(2i+5)}{18} \tag{4}$$

where T_i is the number of data points in the tied group and m is the number of groups of tied ranks. The standardized test statistic Z is computed by:

$$Z = \begin{cases} \frac{S-1}{\sqrt{V(S)}} & S > 0 \\ 0 & S = \theta \\ \frac{S+1}{\sqrt{V(S)}} & S < 0 \end{cases} \tag{5}$$

Although the MKT is robust, it does not provide a quantitative estimation of the trend line's slope, i.e., the magnitude of a positive or negative trend. For this purpose, trend analysis utilized the TSE to compute the trend magnitude. The TSE was first outlined by Theil (1950) and later expanded by Sen (1968). It is a nonparametric estimator and resistant

to outlier data points. It uses medians to fit the trend line as an alternative to the parametric mean-based method of least squares [96].

The TSE model for trend magnitude is conducted by calculating the slopes of all possible combinations of data pairs as follows [97]:

$$\begin{pmatrix} n \\ V \\ 2 \end{pmatrix} = \frac{n(n-1)}{2} \tag{6}$$

The final slope $\hat{\beta}_1$ is then defined as the median of all slopes:

$$\hat{\beta}_1 = median\ \{\widetilde{B}\},\ \widetilde{B} = \{b_{ij}|b_{ij}\} = \frac{y_j - y_i}{x_j - x_i}\ ,\ x_i \neq x_j,\ 1 \leq i < j < n \tag{7}$$

Because the TSE computes the trend line's slope alone, the model "intercept $\hat{\beta}_0$" can be given by:

$$\hat{\beta}_0 = Y_{median} - \hat{\beta}_1 \times X_{median} \tag{8}$$

where X_{median} and Y_{median} are the medians of the measurements and of the response variables, respectively.

2.2.5. Local–Regional Warmings Separation

The annual average of micro-scale urban bias expected to exist in the city's LST record was computed by comparing trends of LST datasets collected in both urban environments against countryside locations. This was achieved based on the following simple formula:

$$LST\ Bias_{urban} = LST_{urban} - LST_{rural} \tag{9}$$

where LST_{urban} and LST_{rural} are the average LST values in both urban and rural environments, respectively. The urban bias trend was then obtained by conducting trend analysis on the 22-year record of the annual average LST biases. Ultimately, this urban-induced bias trend was utilized to correct the original LST time series. Adjustment of the annual LST average for the annual average of UHI intensity/bias was derived from [45]:

$$LST_{corr-i} = LST_i - (LST_{urban} - LST_{rural}) \tag{10}$$

where LST_{corr-i} is the corrected annual LST average of the year *i* and LST_i is the observed annual average of LST of the year *i*. Correction of the annual LST average for the trend of UHI intensity/bias was calculated from [45]:

$$LST_{corr-i} = LST_i - \left(UHI_{slope} \times i - i_{start} \right) \tag{11}$$

where UHI_{slope} is the trend TSE slope of the annual UHI intensity record and i_{start} is the start year of the time series under investigation, i.e., 2000. Equations (10) and (11) can be aggregated in the following one:

$$LST_{corr-i} = LST_i - \left\{ LST_{urban} - LST_{rural} + \left[UHI_{slope} \times i - i_{start} \right] \right. \tag{12}$$

The urban-induced bias of LST time series was then linked to the urban dynamics time series to disclose the possible nexus between urbanization and local urban warming.

3. Results and Discussion

3.1. Urban Dynamics in the Overall Nile Delta

This section is intended to provide a holistic view of the observed temporal tendency in urban dynamics across the overall Nile Delta and per-city time series on a yearly basis. Figure 3 shows a mapping of the 22-year period (2000–2021) of urban dynamics across the

Nile Delta, basically in terms of urban ground coverage. The temporal growth and trend line of the total urban area and built-up increments (sq km) using MKT and TSE analysis are also visualized. Analysis revealed that the total urban footprint in the Nile Delta consistently grew from 455.47 sq km in 2000 to 770.23 sq km in 2021, at an average growth rate of 14.99 sq km year^{-1} and a standard deviation of 22.85 sq km. Figure 3 indicates that there was a perfect positive monotonous linear trend in the total urban area as calculated from MKT analysis, where Kendall's tau value was 1. According to TSE, the magnitude of the trend line slope was 9.8 with a confidence interval of 9.74–9.9. This means that the annual increment of urban expansion was 9.8 sq km year^{-1}. The results were statistically significant at a confidence level of 99%, where the computed *p*-value of MKT was < 0.0001, or less than the alpha threshold (α = 0.01). It was observed, as well, that the largest annual growth rates in the urban built-up were 106.6, 42.2, 22.1, 18.8, and 16.9 sq km, which were detected in the years 2020, 2015, 2001, 2021, and 2014, respectively. The measured annual expansions during the remaining years were mostly less than 10 sq km.
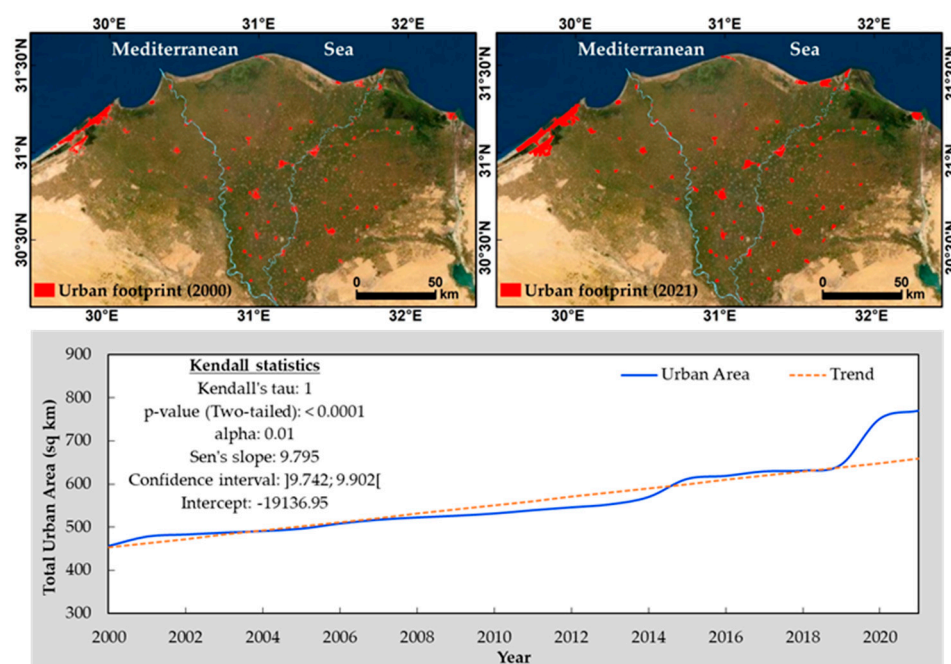
Figure 3. Mapping urban area footprints across the Nile Delta 2000–2021 (upper panels) and trend analysis of the total urban area (sq km) using MKT and TSE (lower panel).

These findings suggested that the Nile Delta has experienced a dramatic urbanization process, in terms of urban sprawl, during the period 2000–2021. The total built-up zone of about 314.8 sq km was appended as an urbanized extension to the base-year urban area, i.e., 455.5 sq km in 2000. This expansion was estimated to be greater than two-thirds (69.1%) of the original urban area during a relatively short time span (22 years). The main motives behind the rapid urbanization were the natural population growth at an annual rate of 2–3%, the immense rural-to-urban people migration, and the fast national development through modernization, industrialization, and diversification of the economic structure [25]. The exponential pattern of the population growth in the region implied sharper increases over time [26]. In addition, the urban dynamics in the Nile Delta were tremendously complicated and usually exceeded the expected rates because the urban development was mostly informal, unplanned, and uncontrolled [98]. Considering its alluvial formation within the desert-dominated surfaces, the Nile Delta's richest agricultural environment supports 63% of the country's farmland and offers habitat for about 50% of the country's population. So, the region has undergone a considerable intensified human-induced pressure, predominately the urban dynamics.

It should be noted that those dynamic expansions in urban built-up zones implicitly involved LULC alterations across the Nile Delta, specifically the urban encroachment over the old rural lands fully enveloping the cities, as shown in Figure 3. This pattern of urban expansion should be accompanied by exacerbated urban warming and prompting urban bias in the temperature records. Similar studies have been investigating the observed LULC changes and the relevant urban sprawl over rural farmlands. Throughout the Nile Delta, urban settlements have expanded mostly at the expense of the fluvial lands dedicated to cultivation rather than the barren lands or desert fringes.

Analysis of Landsat MSS and TM datasets (1972–1990) showed that urban expansion of about 58% in 18 years was endangering the region's agricultural lands [99]. In the period from 1984–2006, the change detection technique applied to Landsat TM and ETM+ images disclosed that the total urban expansion amounted to 689.2 sq km [100]. The expansion was mostly at the expense of the vegetated lands, while the urban encroachment over the nonarable soils was very limited. Landsat-derived estimation of urban expansion in the middle Nile Delta between 1997 and 2017 was approximately 21.19% (from 1192.56 sq km to 1445.33 sq km). This expansion implicitly referred to a decrease in rural environments enveloping the cities by about the same size [25]. Radwan et al. [26] monitored changes in the Nile Delta's LULC during a 24-year period (1992–2015) using a multi-sensor dataset. A dramatic urban expansion of about 746 sq km was detected in the region, leading to a loss of the old, cultivated land at a rate of 31.08 sq km year^{-1}. In the same period, 2061 sq km of bare desert surfaces were reclaimed to be new farmlands at a rate of 85.88 sq km year^{-1}. Landsat 5/7/8 data were used to assess modifications of LULC classes for the Nile Delta from 1987 to 2015 [101]. There was a continuous increase in urban, agricultural, fish farms, and natural vegetation classes, while continuous decreases were detected in both water bodies and barren sandy areas. The urban area had the highest increase during 2000–2015 (979.408 sq km with a rate of 34.8%) compared to the period 1987–2000 (531.126 sq km with a rate of 47.6%). Overall, the total growing rates of LULC classes during the period 1987–2015 were 99% in urban areas and 25.8% in cultivated lands. By the 1990s, the total area of lagoons and wetlands occupying the northern Nile Delta has declined by about 45% of its observed size in the 1950s [2].

Figure 4 shows the urban classes according to the total growth in the built-up area of each urban center (2000–2021) and the total number of urban areas per class. It is notable that the vast majority of the urban centers (66 urban settlements) are located in the first category, in which the total per-city expansion was 2 sq km or less. The smallest urban expansion of about 0.21 sq km was recorded by the town of Kafr Saad in the Damietta Governorate. On the other hand, the megacity of Alexandria occupied a unique and prominent stature regarding the urban growth, where it was enormously expanded by approximately 129.7 sq km. The second largest urban growth within the period 2000–2021 was 15 sq km, which was observed in the city of New Damietta located along the Mediterranean coast in the Damietta Governorate.

3.2. Day/Night and Urban/Rural LST Trends and the Nexus with Urban Dynamics

For this section of the study, the analysis aims at examining the inter-annual trends of LST time series within the urban area, rural surroundings, and across the overall Nile Delta on three timescales, i.e., the daytime, nighttime, and daily datasets. Figure 5 exhibits the inter-annual variability and Kendall trend analysis for these time series. The LST data were calculated based on Terra and Aqua MODIS imagery acquired during the period 2000–2021. The descriptive statistics and MKT and TSE outputs for the 22-year LST time series are displayed in Table 1. As illustrated in Figure 5, the LST series have consistently risen since 2000 and their inter-annual variability had a general increasing tendency through time with different magnitudes for all the series. The descriptive statistics provided in Table 1 indicate that the lowest LST values throughout the time series were always measured in the first quarter of the period, i.e., the years 2000 and 2005, whereas the highest readings in LSTs were observed in the last quarter of the period, specifically in the years 2018 and 2021.

This is a strong indicator of the warming phenomenon in the Nile Delta region, including its urban and rural environments, in the daytime and nighttime hours. Furthermore, the LST values in all datasets were homogeneous in terms of the statistical dispersion, where the standard deviation ranged in a noticeably short domain between 0.4 °C and 0.6 °C.
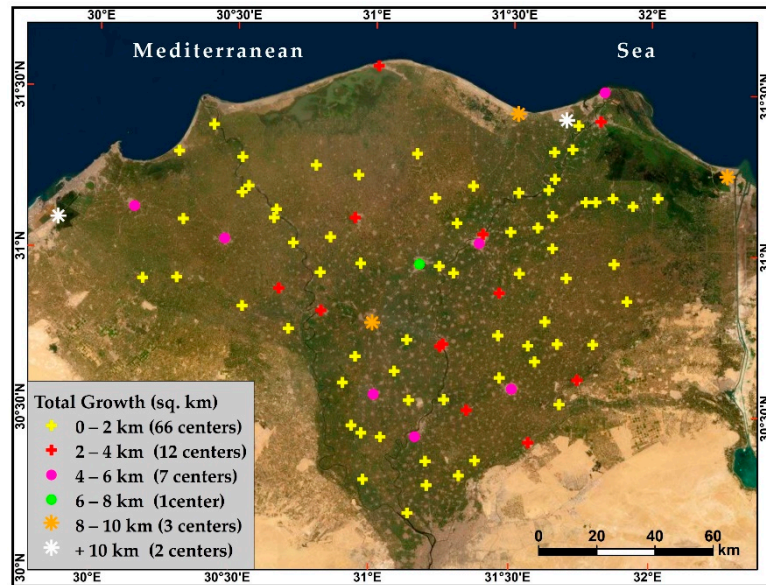
Figure 4. Categories of the urban centers in the Nile Delta based on the total built-up expansion from 2000 to 2021. The number of urban centers within each category is written between brackets.
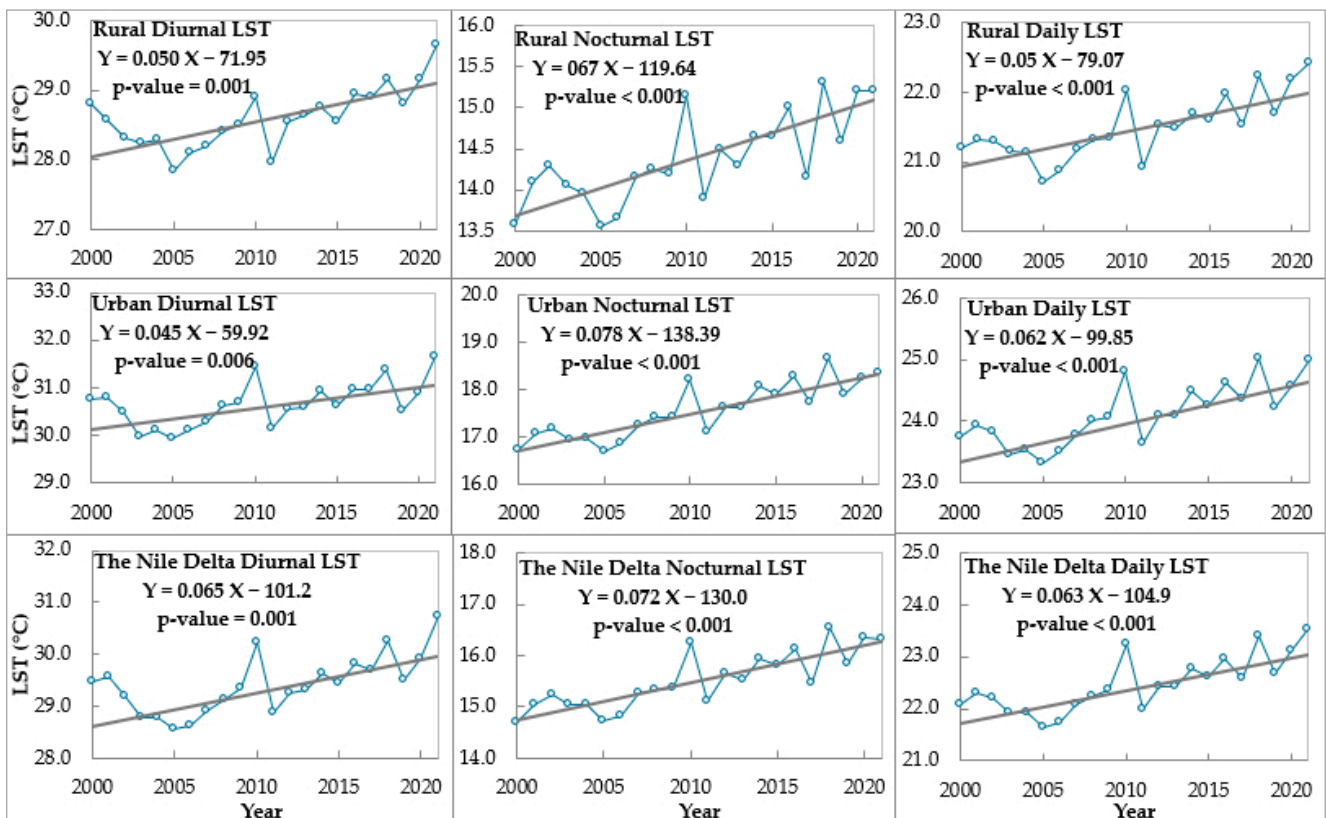
Figure 5. Year-to-year variations and Kendall trend analysis for the rural, urban, and overall Nile Delta's diurnal, nocturnal, and daily LST records (°C) derived from Terra/Aqua MODIS imagery detected during the period 2000–2021.

Table 1. Basic analysis outputs of descriptive and Kendall trend statistics for the rural, urban, and overall Nile Delta's diurnal, nocturnal, and daily LST time series (°C) calculated based on Terra and Aqua MODIS imagery acquired during the period 2000–2021.

Statistics	Item	Rural LST (°C)			Urban LST (°C)			The Nile Delta LST (°C)		
		Day	Night	Daily	Day	Night	Daily	Day	Night	Daily
Descriptive	Obs.	22	22	22	22	22	22	22	22	22
	Min.	27.9 (2005)	13.5 (2000/5)	20.7 (2005)	29.9 (2005)	16.7 (2000/5)	23.3 (2005)	28.6 (2005)	14.7 (2000/5)	21.6 (2005)
	Max.	29.7 (2021)	15.3 (2018)	22.4 (2021)	31.6 (2021)	18.6 (2018)	25.0 (2018/21)	30.7 (2021)	16.5 (2018)	23.5 (2021)
	Mean	28.6	14.4	21.5	30.7	17.6	24.1	29.4	15.5	22.5
	Std. dev.	0.4	0.5	0.5	0.5	0.6	0.5	0.6	0.6	0.5
Trend	K. tau	0.51	0.57	0.60	0.43	0.70	0.62	0.51	0.68	0.62
	S	116.0	131.0	139.0	99.0	161.0	143.0	117.0	157.0	143.0
	Var(S)	1254.7	1255.7	1255.7	1257.7	1257.7	1257.7	1257.7	1257.7	1257.7
	p-value	0.001	<0.001	<0.001	0.006	<0.001	<0.001	0.001	<0.001	<0.001
	alpha	0.01	0.01	0.01	0.01	0.01	0.01	0.01	0.01	0.01
	Sen Slope	0.050	0.067	0.050	0.045	0.078	0.062	0.065	0.072	0.063
	Intercept	−71.95	−119.64	−79.07	−59.92	−138.39	−99.85	−101.2	−130.0	−104.9

Regarding the overall Nile Delta's LST datasets, the lowest and highest annual averages of LST were 21.6 °C (2005) and 23.5 °C (2021), respectively, with a period average of 22.5 °C and a standard deviation of 0.5 °C. It is clear that the Nile Delta's daily record of LST experienced substantial warming during the study period. Statistical analysis using MKT discovered that daily LST had an upward trend, where Kendall's tau value was 0.62, which indicates the elevation of LSTs throughout the time, as shown in Table 1. TSE suggested that the observed elevation rate in daily LSTs was 0.063 °C year^{-1}, with a total warming magnitude of 1.32 °C for the whole period. For the diurnal and nocturnal records, there was an obvious tendency of LST amplification in both measures. The lowest LST values were 28.6 °C in 2005 and 14.7 °C in 2000 for daytime and nighttime datasets, respectively, whereas the highest readings in the daytime and nighttime LSTs were 30.7 °C in 2021 and 16.5 °C in 2018, respectively. The overall period means of diurnal and nocturnal LST were 29.4 °C and 15.5 °C, respectively, with a standard deviation of 0.6 °C for both measures. According to TSE Analysis, Table 1 reports that diurnal and nocturnal datasets warmed throughout the study period at rates of 0.065 °C year^{-1} and 0.072 °C year^{-1}, respectively. The total warming magnitudes in both measures were 1.36 °C and 1.51 °C, respectively. The statistical analysis outputs were significant at a confidence level of more than 99%. Table 1 specifies that *p*-values were <0.001 for all statistics.

It has become apparent that LST records collected during nighttime for the whole Nile Delta exhibited a warming tendency slightly larger than the equivalent records derived for the daytime. This aspect of the day/night LST trends was far greater observed in both urban and rural environments, where the day/night warming rates in the urban areas were 0.045 °C year^{-1} and 0.078 °C year^{-1}, respectively, and in the rural areas were 0.050 °C year^{-1} and 0.067 °C year^{-1}, respectively, as shown in Table 1. It is well-known that a more apparent increasing trend can appear in the minimum temperature time series than in the maximum temperature records. Similar studies in neighboring regions have shown comparable findings with these results. In Kuwait [102], an investigation of 23-year air temperature data indicated that the minimum temperatures were rising at a significant rate, while the maximum temperatures showed a decreasing trend. This contrast supports a strong signal of the urban effect on temperature trends. Across the eastern Middle East during the period 1983–2012, trends in temperature-related indices were examined [103]. The results showed warming trends throughout the region. The nighttime high-temperature extremes have risen at more than twice their corresponding daytime

extremes. The minimum temperature indices exhibited a higher rate of warming than the maximum ones in terms of intensity and frequency. However, unlike the previous studies, Almazroui et al., (2013) [104] conducted a national-scale correlation analysis between urbanization and atmospheric warming in Saudi Arabia by utilizing air temperature data (1981–2010) for 24 weather stations and population census data. They reported that the observed warming is not likely due to the urbanization process. The population increase did not necessarily equate with the rising temperature trend. The largest population growth was observed in two cities whose trends were not the highest. Large warming trends were noticed in sites located near small cities with low population growth. In addition, in the 17 largest Mediterranean cities [105], the comparison between temporal trends of LST and UHI, and urban population changes resulted in poor correlation (R = 0.28). The authors reported that this result was expected because of differences in climatic conditions, city structures, and human activities. We think that changes in population size are not a reasonable indicator of urbanization in most cases.

On the urban/rural comparison basis, the Nile Delta's urban areas constituted a conspicuous positive UHI over the course of the day. The average annual nocturnal UHI intensity was stronger (3.2 °C) than the diurnal one (2.1 °C), where the average annual LSTs were 17.6 °C and 14.4 °C during the nighttime, and 30.7 °C and 28.6 °C during the daytime for the urban and rural areas, respectively. In general, we found statistically significant (at a +99% confidence level) positive trends in the inter-annual averages of daytime, nighttime, and daily LST records within both urban environments and rural surroundings across the Nile Delta. Based on the TSE, the LST upward trend was greater in the urban areas than in the rural embracing outskirts of the nocturnal (0.078 °C year^{-1} and 0.067 °C year^{-1}, respectively) and the daily (0.062 °C year^{-1} and 0.05 °C year^{-1}, respectively) scales. This effect supports the role of urbanization in exacerbating the atmospheric warming in the Nile Delta region, where it is more compatible with the fact that the UHI effect is a nocturnal phenomenon. It is worth mentioning that the consistent LST pattern of the monotonous upward trends within the diversified urban/rural environments emphasized the large-scale nature of the regional atmospheric warming in the Nile Delta. However, the different trend magnitudes for urban and rural LST series pointed out the local contribution of the urban dynamics. So, the total detectable changes in the temperature records are a result of both the background atmospheric factors and the microscale anthropogenic drivers, chiefly the urbanization process.

Our findings concerning the nocturnal UHI and LST trend seem to be geographically dominated in the wider near regions. For example, a unique work [105] analyzed MODIS nighttime data (2001–2012) to investigate the characteristics and trends of the nighttime LST and surface UHI in the 17 largest Mediterranean cities. In general, urban areas exhibited higher LST values compared to non-urban surroundings, forming a UHI effect with an average intensity of 1 °C. The strongest UHI intensities were 3.9 °C, 3.5 °C, and 2.8 °C in Damascus, Alexandria, and Cairo, respectively. A warming trend was found for 82% of the urban areas, while mixed positive and negative trends were detected in non-urban surroundings. An overall increasing rate of a 0.1 °C decade^{-1} was detected in urban LST. The higher positive trends appeared in the eastern Mediterranean cities, where the Nile Delta extended.

On the other hand, the increasing trend of the diurnal LST records was slightly larger in the rural fringes (0.05 °C year^{-1}) than that found in the urban areas (0.045 °C year^{-1}). This unexpected urban-rural pattern in the diurnal LST trends was noticed in China [53] during the period 1980–2009 using different datasets and methodology. The research used ERA-interim reanalysis datasets of the average air maximum and minimum temperatures and relied on an urban-derived approach to correlate the urban warming to the urban fraction in 10 × 10 km around 753 weather stations. The urban growth enhanced the average minimum temperature by +1.7 ± 0.3 °C, whereas the average maximum temperature trend was slightly declined due to urbanization by −0.4 ± 0.2 °C. However, the study provides no explanation for this situation. A recent study [106] discovered close results

when employing similar datasets and procedures to the current study. It utilized two decades (2001–2018) of Aqua/Terra MODIS imagery to investigate the day/night temporal trends in LST and surface UHI for three diverse Indian cities (Lucknow, Kolkata, and Pune). Positive trends of daytime (0.003 to 0.059 °C year^{-1}) and nighttime (0.03 to 0.078 °C year^{-1}) LST records were observed in the cities, except in Pune City where urban cooling was detected during the daytime. The increase in the aerosol concentration, the consequent decrease in surface insolation and air temperature, and expanding the vegetative areas over time were considered the primary reasons for the urban daytime cooling effect in Pune.

Despite the greater nighttime LST trend than the daytime opposite being a well-documented feature of the urban centers, the same daytime/nighttime pattern of LST trend was disclosed in the Nile Delta's rural area as well. Table 1 shows that the detected trends in the rural LST records were 0.05 °C and 0.067 °C during the day and night, respectively (daily trend 0.059 °C). In fact, this discovery may be substantial proof indicating the contamination of rural environments by the horizontal advection of the urban footprint effect. This was noteworthy enough to make us skeptically reconsider the criteria by which the rural surroundings were chosen as a reference thermal environment to which the urban LST will be compared. For the purpose of verifying and validating our findings, we decided to reiterate the analysis using remoter reference surroundings that are distant enough from the potential contamination that may be caused by the Nile Delta's urban system. An idealized remote, human-activity-free barren area in the Western Desert was selected, as shown in Figure 1. Interestingly, we almost found the same results where the day/night trends of the desert LST records were 0.048 °C and 0.07 °C (daily average 0.059 °C), so close to the rural reference trend magnitudes formerly reported. This referred to the high trustworthiness of the methodology our research followed and the results we obtained. Furthermore, this discovery distinctly indicated the fact that the greater nocturnal LST trend than the diurnal one is not a rule confined to the urban areas.

Figure 6 presents a per-city assessment of the trend pattern observed in both day/night LST records. It is clear that the first class, in which the nocturnal LST trend is greater than the diurnal LST trend (Figure 6a), is the most common, where it included 68 urban centers or three-quarters of the urban areas. The remaining quarter (23 urban centers) was characterized by a nocturnal LST trend that is less than the diurnal one. All the per-city LST series showed an increasing trend during the day and night. However, just four urban centers had a decreasing trend in the diurnal LST series, including the coastal cities of Gamasa (−0.042 °C), New Damietta (−0.041 °C), Idku (−0.026 °C), and El-Borollos (−0.013 °C) (Figure 6a). It was noted that the results of the four cities were statistically nonsignificant.

This finding demonstrates the significant role of the Mediterranean Sea in modulating urban warming during the daytime. This role during the daytime can be proved as well by the megacity of Alexandria. Among the 91 urban centers under investigation, Alexandria City has the largest built-up area (roughly 285.1 sq. km), population size (more than 5 million inhabitants), and the greatest annual rate of urban growth (6.2 sq km year^{-1}), as shown in Figures 1 and 4. However, its annual trend slope of the diurnal LST was just 0.021 °C, making it one of the modest urban centers with an upward LST trend, as shown in Figure 6a. This can be chiefly explained by its coastal location in the northwesternmost point of the study area, where it immediately overlooks the sea. In the nighttime, Figure 6b stressed the same effect of the Mediterranean Sea. It is clear that there was a remarkable spatial pattern, in which the per-city annual magnitude (in terms of TSE slope) of the nocturnal LST trend decreased in a generally south–north direction. This distribution largely agrees with the maritime influence blowing from the north. Furthermore, this role of the Mediterranean Sea is expected to be maximized because of the function of the prevailing northwesterly and northerly winds in transferring the maritime effect into the coastal urban areas.
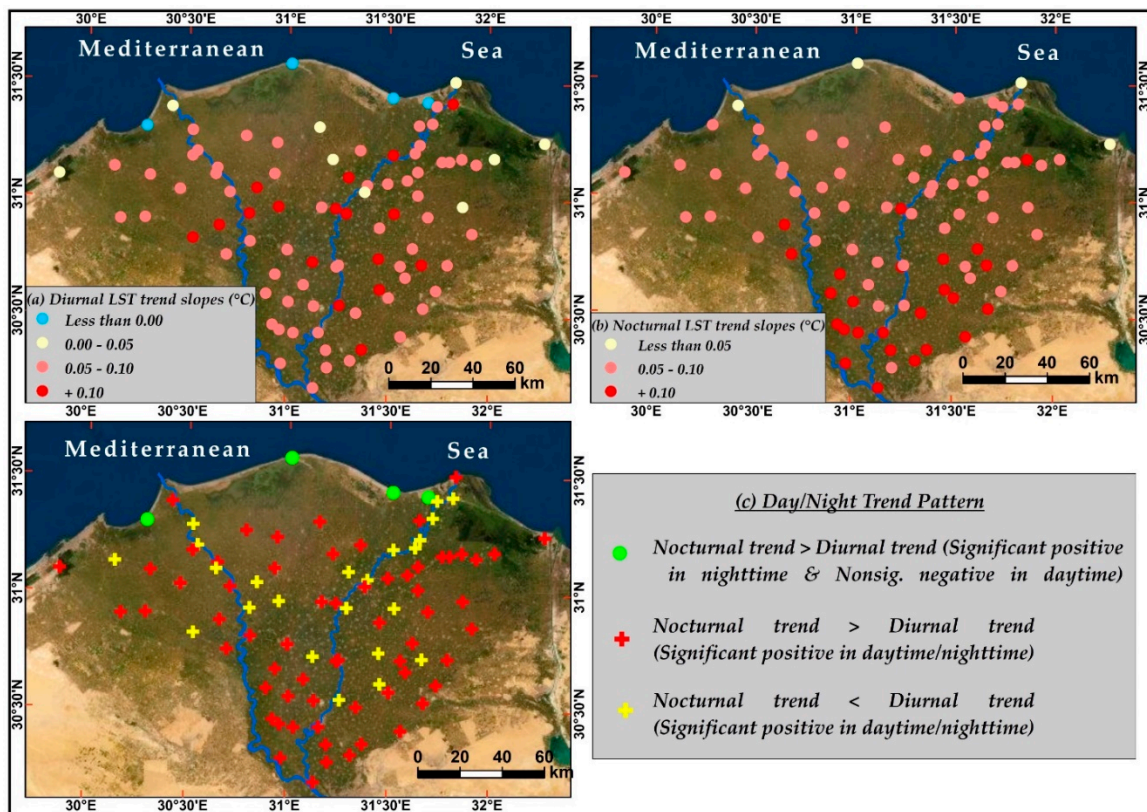
Figure 6. Per-city assessment of LST trends across Nile Delta (2000–2021), including (**a**) the annual trend slopes of the diurnal LST, (**b**) the annual trend slopes of the nocturnal LST, and (**c**) day/night trend pattern and the relevant statistical significance.

Evaluating the association between the maritime effects, in terms of the distance between each city and the Mediterranean Sea coast, and the magnitudes of LST trends using the Kendall correlation, unveiled a stronger positive connection between the two variables during the nighttime (R = 0.67) than the daytime (R = 0.33). These significant correlations (*p*-values < 0.0001) pointed out that the proximity to the maritime influences of the Mediterranean Sea can explain 45% of the nighttime LST trend and 11% of the daytime LST trend, as suggested by the coefficient of determination. Linear regression analysis of the cities' proximities to the Mediterranean Sea (independent variable) against their LST trends (dependent variable) showed that the magnitude of the diurnal LST trends increased more rapidly than the nocturnal LST trends with increasing the distance by which the city is far from the sea. The increasing rates of LST trends were 0.005 °C per 10 km and 0.004 °C per 10 km in diurnal and nocturnal LST trends, respectively. Consequently, the Mediterranean Sea and the related maritime leverage can be considered an anti-urbanization moderator for the urban warming across the Nile Delta.

From the same perspective, the warming–limiting influence is expected to be found in the urban centers located immediately beside or around the water surfaces of the Nile Delta branches, i.e., the Rosetta and Damietta distributaries. It is worth noting that most of the urban areas (16 out of 23) with a nocturnal LST trend less than the diurnal one are located along the Rosetta and Damietta distributaries, as shown in Figure 6c. The concentrated distribution pattern of such urban centers along the Nile River's channels is consistent with the above-mentioned discovery indicating that the water moderating effect is greater in the nighttime than in the daytime. Since the riverine urban centers are subjected to double water influence by the Mediterranean Sea and the Nile River, this is probably the reason for reducing the nocturnal warming trend than the diurnal one in these centers. It should be confirmed that the water influence of the Nile River is less noticeable than that produced

by the Mediterranean Sea as suggested by the water body characteristics, e.g., surface area, water depth, and salinity.

Regarding the urbanization–warming nexus, measuring the bivariate linear relationship using the nonparametric Kendall rank correlation analysis, as shown in Figure 7, unveiled a direct positive relationship between the annual urban expansion and urban LST records. It was remarkable that the strength of association is stronger (the correlation coefficient R = 0.7) in the case of nighttime LST values, and weaker (R = 0.43) during the daytime, with an average R of 0.62 in the daily LST dataset. The relevant coefficients of determination (R^2) were 0.49, 0.18, and 0.38 in the nighttime, daytime, and daily relationships, respectively. All results were dependable in terms of the statistical significance at a confidence level of 99%, where the supplied *p*-values were <0.001 for all variables. This discovery emphasized that the urbanization effect on temperature change throughout the region is a substantial phenomenon. Interpretation of the coefficients of determination (R^2) suggested that urban dynamics have weak-to-moderate effects on the urban LST datasets, where these dynamics can explain just 18%, 49%, and 38% of the inter-annual variations observed in the urban LST records collected throughout the daytime, nighttime, and daily, respectively. This non-strong relationship between annual urban sprawl and urban LST time series was expected, where temporal changes in LST are caused not only by such urban expansion but also by various biophysical and anthropogenic forcing factors. However, the stronger connection between urbanization rates and nighttime LSTs than that in daytime ones can be considered as hard evidence of the urbanization signals in the Nile Delta's LST records. The preponderance of evidence refers that man-made agents, particularly urban dynamics, are mostly responsible for this warming. This is because the urbanization effect on temperature and the relevant UHI pattern is fundamentally a nocturnal phenomenon [107–111] that is attributable to the differential urban/rural cooling (rather than heating) rates, the high thermal inertia of concrete and asphalt materials used in urban constructions, and the anthropogenic heat emissions from transportation, residential and commercial buildings, power plants, and industrial zones.

3.3. Urban Bias Estimation and Removal

The discovered findings in Sections 3.1 and 3.2 explicitly indicated that urban dynamics have had a profound impact on the Nile Delta temperature records over time. The urbanization signals in the LST time series included a greater upward trend in the nighttime than daytime LST records, larger urban warming than what existed in the surrounding rural environments, and finally the statistically inferred urbanization–warming nexus. Consequently, it is critical for studies concerning sustainability and climate change impact assessment in the region to accurately provide basic quantification of the background temperature change over time through estimating and removing the local urban bias contaminating the temperature time series. This removal has the ability of refining temperature records from the possible overestimations of trend analysis resulting from the urban influence.

Table 2 provides the observed day/night annual LST averages for the Nile Delta's urban/rural areas, the calculated year-to-year averages of UHI intensities, and the bias-free LST record of the urban areas. Screening the annual averages of the observed LST values suggested that urban LSTs were always greater than the rural ones, whether during the day or night hours. Diurnally, the urban/rural LST averages ranged between 29/27.9 °C and 31.6/29.7 °C, respectively. At nighttime, the lowest urban/rural LST averages were 16.7/13.6 °C, and the highest values were 18.6/15.3 °C, respectively. Accordingly, the Nile Delta's urban areas formed a positive UHI with average annual intensities between 1.7 °C and 2.5 °C during the day, and 2.9 °C and 3.6 °C at night. This implicitly denoted that there were annual urban-induced biases in the Nile Delta urban thermal environment by about the same magnitudes of the above-mentioned UHI intensity. The average annual nocturnal bias was stronger (3.2 °C) than the diurnal one (2.1 °C), where the average annual LSTs

were 17.6 °C and 14.4 °C during the nighttime, and 30.7 °C and 28.6 °C during the daytime for the urban and rural areas, respectively.
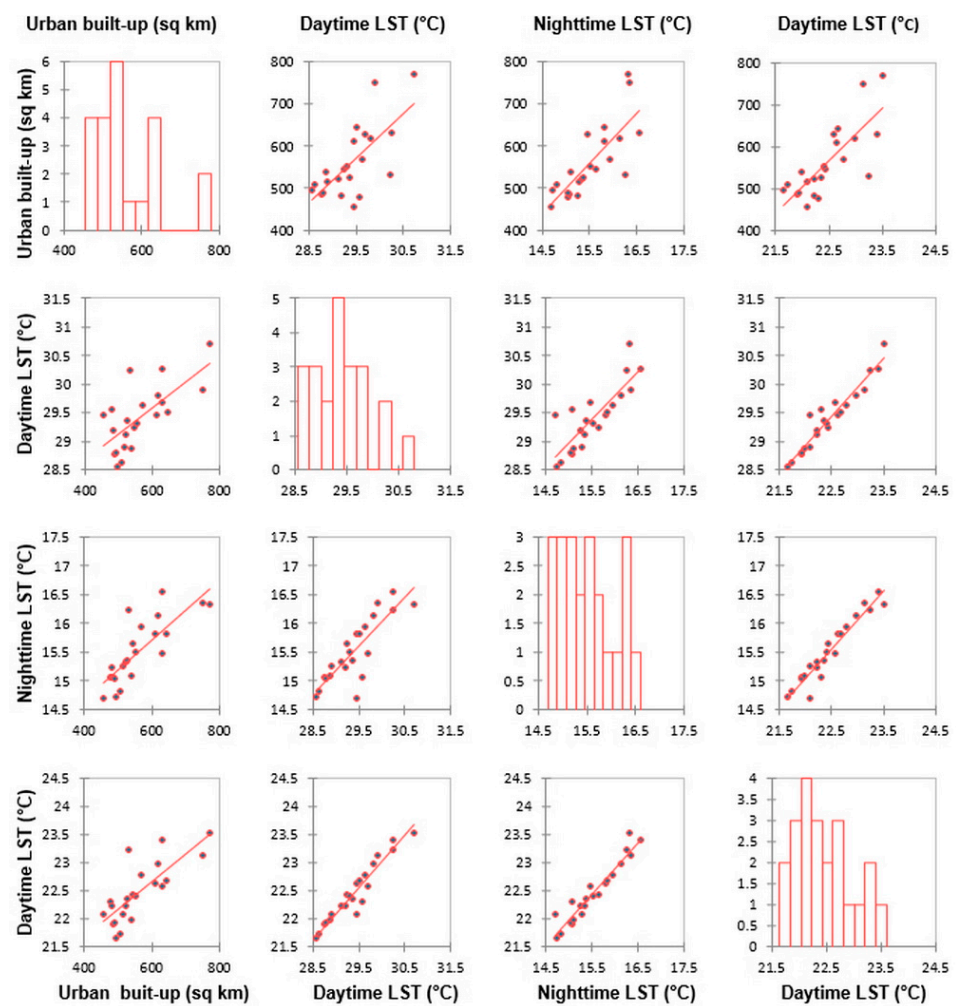
Figure 7. Scatter plots and best-fit trend lines depicting the bivariate association of the annual urban expansions against the Nile Delta's diurnal, nocturnal, and daily LST time series (2000–2021).

With regard to the urban-derived bias observed in the temporal trend, the analysis revealed that there have been significantly increasing trends in LST records measured across the Nile Delta's urban/rural areas during the study period (2000–2021). The greater slope of the urban LST trend (0.078 °C year^{-1}) than the rural LST trend (0.067 °C year^{-1}) throughout the nighttime indicated that there was a micro-scale bias in urban LST records across the Nile Delta by about 0.011 °C year^{-1}, which caused total additional warming in the urban environment (overall warming 1.638 °C) compared to the rural surroundings (overall warming 1.407 °C) by about 0.231 °C during the period 2000–2021. This spurious urban-made warming trend constituted about 14.1% of the overall detectable warming in the Nile Delta's urban system. The urbanization influence on the nocturnal LST trend can also be noticed from the increasing trend of the nocturnal UHI intensity (bias), estimated by 0.017 °C year^{-1} (the total trend was 0.357 °C), as shown in Table 2 and Figure 8. Based on the UHI intensity trend of 0.017 °C year^{-1}, the urban bias in the nocturnal LST record can be estimated to be 21.8% of the total observed warming in the Nile Delta.

Table 2. The observed annual averages of the Terra/Aqua LST collected for the Nile Delta's urban/rural areas during the daytime and nighttime. The table also contains the calculated year-to-year averages of UHI intensities, and the bias-free LST record of the urban areas.

Year	Observed Urban LST (°C)		Observed Rural LST (°C)		Calculated UHI Intensity/Bias (°C)		Corrected LST (°C) for Trend		Corrected LST (°C) for Trend/UHI	
	Day	**Night**	**Day**	**Night**	**Day**	**Night**	**Day**	**Night**	**Day**	**Night**
2000	30.77	16.71	28.81	13.59	1.96	3.13	30.77	16.71	28.81	13.59
2001	30.78	17.07	28.56	14.09	2.22	2.99	30.78	17.06	28.56	14.07
2002	30.47	17.18	28.31	14.28	2.16	2.90	30.48	17.15	28.32	14.25
2003	29.96	16.93	28.25	14.05	1.71	2.88	29.97	16.88	28.26	14.00
2004	30.10	16.97	28.30	13.95	1.80	3.02	30.11	16.90	28.31	13.88
2005	29.94	16.69	27.85	13.55	2.09	3.14	29.95	16.61	27.86	13.47
2006	30.11	16.88	28.10	13.65	2.01	3.23	30.13	16.78	28.11	13.55
2007	30.29	17.25	28.20	14.15	2.09	3.10	30.31	17.13	28.22	14.03
2008	30.61	17.41	28.40	14.25	2.21	3.16	30.63	17.27	28.42	14.11
2009	30.70	17.42	28.50	14.20	2.20	3.22	30.72	17.27	28.52	14.05
2010	31.44	18.19	28.90	15.15	2.54	3.04	31.47	18.02	28.92	14.98
2011	30.15	17.11	27.95	13.90	2.20	3.21	30.17	16.93	27.98	13.71
2012	30.55	17.61	28.55	14.50	2.00	3.11	30.58	17.41	28.58	14.30
2013	30.60	17.61	28.65	14.30	1.95	3.31	30.63	17.39	28.68	14.08
2014	30.93	18.07	28.75	14.65	2.18	3.42	30.96	17.83	28.78	14.41
2015	30.62	17.88	28.55	14.65	2.07	3.23	30.65	17.63	28.59	14.40
2016	30.96	18.28	28.95	15.00	2.01	3.28	31.00	18.01	28.99	14.73
2017	30.98	17.74	28.90	14.15	2.08	3.59	31.02	17.45	28.94	13.86
2018	31.38	18.64	29.15	15.30	2.23	3.34	31.42	18.34	29.19	15.00
2019	30.53	17.91	28.80	14.60	1.73	3.31	30.58	17.59	28.85	14.28
2020	30.91	18.23	29.15	15.20	1.76	3.03	30.96	17.89	29.20	14.86
2021	31.65	18.34	29.65	15.20	2.00	3.14	31.70	17.99	29.70	14.85
Yearly Trend	0.045	0.078	0.05	0.067	−0.002	0.017	—	—	—	—
Total Trend	0.945	1.638	1.05	1.407	−0.042	0.357	—	—	—	—
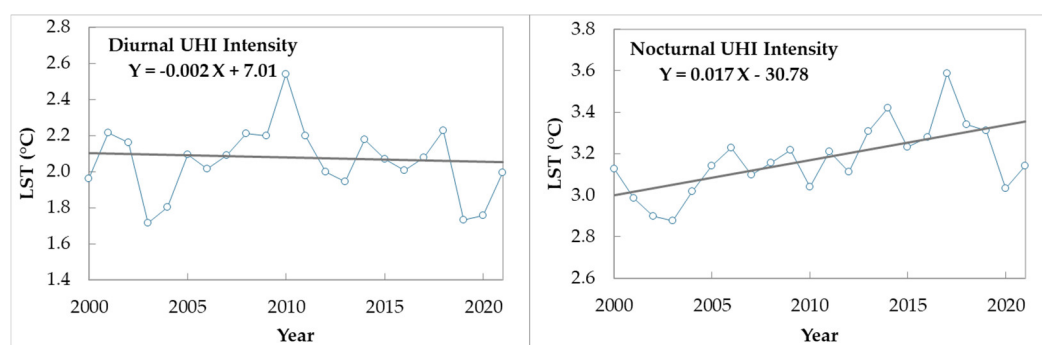
Figure 8. Trend analysis using MKT of the diurnal and nocturnal UHI intensity/bias across the Nile Delta (2000–2021).

Contrary to the nighttime record, the investigation discovered an unexpected cooling bias in the daytime LST record of the Nile Delta, where the observed diurnal trends were 0.045 °C year^{-1} and 0.05 °C year^{-1} in the urban areas and rural outskirts, respectively. This means that the urbanization process was responsible for diminishing the diurnal LST trend in the urban areas by about −0.005 °C less than in the rural areas. Hence, the overall warming trend in the urban areas of 0.945 °C throughout the study period was underestimated by about 0.105 °C (11.1%) compared to the overall increasing trend of 1.05 °C in the rural surroundings. This was emphasized by the decreasing trend of the

diurnal UHI intensity/bias by −0.002 °C year⁻¹ (the total trend was −0.042 °C), Table 2 and Figure 8. Considering the UHI intensity trend of −0.002 °C year⁻¹, the urban bias in the diurnal LST record can be calculated to be just 4.4% of the total observed warming in the Nile Delta.

In Table 2, estimations of the urban biases caused by both annual UHI intensity and inter-annual UHI trend were calculated for each year, 2000–2021, using Equations (9)–(12). The observed diurnal/nocturnal LSTs were then corrected with the aid of a bias-removal adjustment process for each annual LST average. As mentioned earlier, all the yearly bias estimates were always greater than zero and have grown since the year 2000. This process of correcting the temperature records across the Nile Delta is highly recommended as an initial preprocessing for studies of climate-related sustainability and climate change impact assessment. After the correction procedure, the diurnal LST record of the urban areas has increased to reverse the cooling urban effect during the daytime, whilst the nocturnal LST record has decreased to remove the local urban warming.

Although the urban cooling effect in the daytime LST trend was tiny, it was also completely unexpected. This was fundamentally because of the strong positive heat island the urban areas formed in the Nile Delta region, as illustrated in Table 2. Within the diurnal division of the day, it was clear that the urban settlements were always warmer than their rural envelopes throughout the study period, in which the UHI intensity oscillated between its minimum strength of 1.7 °C in 2003, and the maximum strength of 2.5 °C in 2010. This conflict in urban effects among the positive intensities of annual UHI and the negative trend of inter-annual UHI needs further research to be diagnosed and clarified. As a tentative attribution of the diurnal urban cooling effect through time, we suggest the increasing shading effect within the urban environment by buildings. Another possible cause is the thermal inertia, i.e., the ability of urban material to absorb heat and store it subsurface during the daytime, then release it later in the nighttime. This effect delays thermal sensation and prevents overheating during daytime hours. In addition, the elevated levels of the man-made pollutants and aerosols in the urban canopy and boundary layers can increase the atmospheric albedo in the city rather than in the rural areas.

The same phenomenon was noticed in China [53] during the period 1980–2009 using different datasets and methodology. The research used ERA-interim reanalysis datasets of the average air maximum and minimum temperatures and relied on an urban-derived approach to correlate the urban warming to the urban fraction in 10 × 10 km around 753 weather stations. The urban growth enhanced the average minimum temperature by +1.7 °C ±0.3 °C, whereas the average maximum temperature trend declined slightly because of urbanization by −0.4 °C ±0.2 °C. Based on this estimation, the local urban warming represented about 9% of the overall regional warming trend in minimum temperature and reduced the maximum temperature trend by 4%. However, the study provides no explanation for this. A promising study [106] utilized two decades (2001–2018) of Aqua/Terra MODIS imagery to investigate the day/night temporal trends in LST and surface UHI for three diverse Indian cities (Lucknow, Kolkata, and Pune). Positive trends in the inter-annual averages of daytime (0.003 to 0.059 °C/year) and nighttime (0.030 to 0.078 °C/year) LST records were observed in the cities, except in Pune City where urban cooling was detected during the daytime. The increase in the aerosol concentration, the consequent decrease in surface insolation and air temperature, and expanding the vegetative areas over time were considered as the primary reasons for the urban daytime cooling effect in Pune. Nighttime UHI was positive for all cities (mean annual intensities ranged from 1.34 °C to 2.07 °C). Statistically significant upward trends were observed in mean annual UHI intensity (0.009 °C/year to 0.022 °C/year) for Kolkata and Pune. A downward trend was observed over Lucknow.

The discoveries of this study were found to partially support the numerous investigations adopting the significance of the urbanization process and the UHI effect on the temperature records. For example, early studies assessed the significance of warming produced by the local urbanization effect on large-scale mean temperature time series. The

urban bias was identified by about just 0.1 °C in the Northern Hemispheric landmass's temperature datasets during 1904–1984 [39] and ranged between 0.15–0.26 °C/30 years in China's northern plains (1954–1983) using a statistical methodology of the rank-score procedure [45]. In South Korea [44], estimations of urban trends were positive, indicating an increasing trend in the urban bias over time. Warming trends oscillated from 0.039 °C/year to 0.042 °C/year in the urban stations, while the rural areas had the minimum trend magnitude (0.028 °C/year). Lately, in Great Britain, urbanization's contribution to atmospheric warming in the daily mean temperature was computed to be 0.02–0.06 °C (1961–2015) by utilizing a statistical model linking the UHI intensity with urban fraction and wind speed. More recently, 42 weather stations (2009–2018) in the western Yangtze River Delta were selected to analyze the environmental factors dominating within a 5 km buffer around the old and new station locations based on remote sensing technology [32]. The multiple linear regression models between temperature data and the 17 environmental conditions were efficient to correct the urbanization effect with an error range of 3.66–18.21%, and an average error of 10.09%.

However, the upward LST trend of the Nile Delta's urban areas at a smaller magnitude than the nearby countryside in the daytime datasets minifies the urban contribution to the climate change issue. The underestimation of the urban role in changing the temperature record over time is a scientific thought that was suggested by some previous studies to the degree that the urban effect can be fully neglected. This premise was reinforced by analysis over the globe [51,112], world lands [113–116], global rural areas [117], and the contiguous United States [46].

4. Conclusions

Under the circumstances of the paramount importance of the Nile Delta and its high vulnerability to climate change and the relevant negative environmental impacts, and the sharp insufficiency of the ground meteorological network, the main objectives of the study were to employ the available satellite-based products of Aqua/Terra LSTs and Landsat GAIA settlement coverage to detect and monitor urban dynamics across the Nile Delta, explore the relevant changes in day/night and urban/rural temperature records, and assess the possible local urban bias in those records. It was found that the region has been subjected to an intensified LULC change because of the rapid urbanization resulting from accelerated population growth. A dramatic increase in urban areas has taken place at the expense of the rural fringes throughout the Nile Delta. The total urban expansion was greater than two-thirds (69.1%) of the original urban area in 2000. This was accompanied by a notable warming trend in the day/night and urban/rural LST records. The nocturnal LST exhibited a warming tendency (0.072 °C year^{-1}) larger than the diurnal equivalent (0.065 °C year^{-1}). The urban–rural comparison approach disclosed that the urbanization process caused a warming bias in the nighttime LST trend by 0.017 °C year^{-1} (21.8%) and a cooling bias in the daytime by −0.002 °C year^{-1} (4.4%). Correlation analysis detected a positive nexus between the urban dynamics and LST trends. All the results were statistically significant at a confidence level of 99%, where the *p*-value was always equal to 0.01 or less.

Based on these findings, the key research contribution was to provide accurate quantification of the temperature change across the region. Identifying the local urban warming/cooling effect enables applying corrections to temperature records to estimate the actual regional climate change. This separation of local and regional components of the temperature change is of critical importance in the subsequent investigations concerning the climate change impact assessment and sustainable development in the region. Conducting the analysis in both daytime and nighttime scales enriched the research results and widened its applicability. It should be noted that urban sprawl is a substantial factor causing temperature change over time and space. There are other driving factors controlling such changes, such as sea–land interaction, the water body of the Nile River, micro-scale aspects of climate, LULC types, building geometry, and anthropogenic heat emissions. The current study's scope focused on urban sprawl as a reliable measure of urban dynamics,

in addition to some other mechanisms, including the maritime role, the Nile River effect, and the prevailing winds. However, the concentrated domain of the study has no effect on introducing uncertainty in the key research findings, i.e., the temperature trend analysis and temperature record adjustments. The other driving factors of temporal temperature change could be a topic for future research, particularly the LULC change. Promising research works can integrate all measures of urban dynamics, e.g., intra-urban surface configuration [118], population growth [104], and built-up sprawl, to provide a holistic assessment of the urbanization–warming nexus.

The study concluded that the urban dynamic process, in terms of city sprawl, is a dominant, substantial degradation mechanism of the urban thermal environments. It can prompt a significant micro-scale bias in the temperature records of the Nile Delta cities. Therefore, discriminating the local-to-regional components of these records is an indispensable prior requirement to provide accurate quantification of the macro-scale climate change acting as an integral basis for studies of sustainability and climate change impacts assessment.

References

1. Stanley, D.J.; Warne, A.G. Nile Delta in its Destruction Phase. *J. Coast. Res.* **1998**, *14*, 794–825. Available online: https://www.jstor.org/stable/4298835 (accessed on 28 March 2022).
2. Fishar, M.R. Nile Delta (Egypt). In *The Wetland Book: II: Distribution, Description, and Conservation*; Finlayson, C.M., Milton, G.R., Prentice, R.C., Davidson, N.C., Eds.; Springer: Dordrecht, The Netherlands, 2018; pp. 1251–1260.
3. IPCC. Climate Change: The IPCC Impacts Assessment. Canberra. 1990. Available online: https://www.ipcc.ch/site/assets/uploads/2018/03/ipcc_far_wg_II_full_report.pdf (accessed on 2 April 2022).
4. IPCC. Climate Change 1995: Impacts, Adaptations and Mitigation of Climate Change: Scientific-Technical Analyses. Cambridge. 1995. Available online: https://www.ipcc.ch/site/assets/uploads/2018/03/ipcc_sar_wg_II_full_report.pdf (accessed on 2 April 2022).
5. IPCC. Climate Change 2022: Impacts, Adaptation, and Vulnerability. Cambridge. 2022. Available online: https://www.ipcc.ch/report/ar6/wg2/downloads/report/IPCC_AR6_WGII_FinalDraft_FullReport.pdf. (accessed on 2 April 2022).
6. IPCC. The Regional Impact of Climate Change: An Assessment of Vulnerability. Cambridge. 1997. Available online: https://www.ipcc.ch/site/assets/uploads/2020/11/The-Regional-Impact.pdf (accessed on 2 April 2022).
7. IPCC. Climate Change 2001: Impacts, Adaptation, and Vulnerability. Cambridge. 2001. Available online: https://www.ipcc.ch/site/assets/uploads/2018/03/WGII_TAR_full_report-2.pdf (accessed on 2 April 2022).
8. IPCC. Climate Change 2007: Impacts, Adaptation and Vulnerability. Cambridge. 2007. Available online: https://www.ipcc.ch/site/assets/uploads/2018/03/ar4_wg2_full_report.pdf (accessed on 2 April 2022).
9. IPCC. Climate Change 2014: Impacts, Adaptation, and Vulnerability. Part A: Global and Sectoral Aspects. Contribution of Working Group II to the Fifth Assessment Report of the Intergovernmental Panel on Climate Change. Cambridge. 2014. Available online: https://www.ipcc.ch/site/assets/uploads/2018/02/WGIIAR5-PartA_FINAL.pdf (accessed on 2 April 2022).
10. IPCC. Climate Change 2014: Impacts, Adaptation, and Vulnerability. Part B: Regional Aspects. Contribution of Working Group II to the Fifth Assessment Report of the Intergovernmental Panel on Climate Change. Cambridge. 2014. Available online: https://www.ipcc.ch/site/assets/uploads/2018/02/WGIIAR5-Chap21_FINAL.pdf (accessed on 2 April 2022).
11. FAO. Climate Change and Food Security: Risks and Responses. Rome. 2015. Available online: https://www.fao.org/3/i5188e/I5188E.pdf (accessed on 4 April 2022).
12. Ammann, P.; Dietler, D.; Winkler, M.S. Health impact assessment and climate change: A scoping review. *J. Clim. Chang Health* **2021**, *3*, 100045. [CrossRef]
13. Maldonado-Erazo, C.P.; Álvarez-García, J.; Río-Rama, M.D.L.C.D.; Durán-Sánchez, A. Scientific Mapping on the Impact of Climate Change on Cultural and Natural Heritage: A Systematic Scientometric Analysis. *Land* **2021**, *10*, 76. [CrossRef]

14. Chapman, A.; Darby, S. Evaluating sustainable adaptation strategies for vulnerable mega-deltas using system dynamics modelling: Rice agriculture in the Mekong Delta's An Giang Province, Vietnam. *Sci. Total Environ.* **2016**, *559*, 326–338. [CrossRef] [PubMed]

15. Szabo, S.; Brondizio, E.; Renaud, F.G.; Hetrick, S.; Nicholls, R.J.; Matthews, Z.; Tessler, Z.; Tejedor, A.; Sebesvari, Z.; Foufoula-Georgiou, E.; et al. Population dynamics, delta vulnerability and environmental change: Comparison of the Mekong, Ganges–Brahmaputra and Amazon delta regions. *Sustain. Sci.* **2016**, *11*, 539–554. [CrossRef]

16. Cazcarro, I.; Arto, I.; Hazra, S.; Bhattacharya, R.N.; Adjei, P.O.-W.; Ofori-Danson, P.K.; Asenso, J.K.; Amponsah, S.K.; Khondker, B.; Raihan, S.; et al. Biophysical and Socioeconomic State and Links of Deltaic Areas Vulnerable to Climate Change: Volta (Ghana), Mahanadi (India) and Ganges-Brahmaputra-Meghna (India and Bangladesh). *Sustainability* **2018**, *10*, 893. [CrossRef]

17. Arto, I.; García-Muros, X.; Cazcarro, I.; González-Eguino, M.; Markandya, A.; Hazra, S. The socioeconomic future of deltas in a changing environment. *Sci. Total Environ.* **2018**, *648*, 1284–1296. [CrossRef]

18. El-Nahry, A.H.; Doluschitz, R. Climate change and its impacts on the coastal zone of the Nile Delta, Egypt. *Environ. Earth Sci.* **2009**, *59*, 1497–1506. [CrossRef]

19. Abutaleb, K.A.A.; Mohammed, A.H.E.-S.; Ahmed, M.H.M. Climate Change Impacts, Vulnerabilities and Adaption Measures for Egypt's Nile Delta. *Earth Syst. Environ.* **2018**, *2*, 183–192. [CrossRef]

20. Kassem, H.S.; Bello, A.R.S.; Alotaibi, B.M.; Aldosri, F.O.; Straquadine, G.S. Climate Change Adaptation in the Delta Nile Region of Egypt: Implications for Agricultural Extension. *Sustainability* **2019**, *11*, 685. [CrossRef]

21. Gouda, D.M. *Climate Change, Agriculture and Rural Communities' Vulnerability in the Nile Delta BT—Climate Change Impacts on Agriculture and Food Security in Egypt: Land and Water Resources—Smart Farming—Livestock, Fishery, and Aquaculture*; Omran, E.-S.E., Negm, A.M., Eds.; Springer International Publishing: Cham, Switzerland, 2020; pp. 525–576.

22. Kalnay, E.; Cai, M. Impact of urbanization and land-use change on climate. *Nature* **2003**, *423*, 528–531. [CrossRef] [PubMed]

23. Zhao, M.; Zhou, Y.; Li, X.; Cheng, W.; Zhou, C.; Ma, T.; Li, M.; Huang, K. Mapping urban dynamics (1992–2018) in Southeast Asia using consistent nighttime light data from DMSP and VIIRS. *Remote Sens. Environ.* **2020**, *248*, 111980. [CrossRef]

24. Zhao, M.; Cheng, C.; Zhou, Y.; Li, X.; Shen, S.; Song, C. A global dataset of annual urban extents (1992–2020) from harmonized nighttime lights. *Earth Syst. Sci. Data* **2022**, *14*, 517–534. [CrossRef]

25. Vasisith, S. *Detecting Urban Sprawl in the Middle Nile Delta Region to Assess the Effects on Egypt's Agriculture*; Central European University: Budapest, Hungary, 2018.

26. Radwan, T.M.; Blackburn, G.A.; Whyatt, J.D.; Atkinson, P.M. Dramatic Loss of Agricultural Land Due to Urban Expansion Threatens Food Security in the Nile Delta, Egypt. *Remote Sens.* **2019**, *11*, 332. [CrossRef]

27. Yang, L.; Qian, F.; Song, D.-X.; Zheng, K.-J. Research on Urban Heat-Island Effect. *Procedia Eng.* **2016**, *169*, 11–18. [CrossRef]

28. De Almeida, C.R.; Teodoro, A.C.; Gonçalves, A. Study of the Urban Heat Island (UHI) Using Remote Sensing Data/Techniques: A Systematic Review. *Environments* **2021**, *8*, 105. [CrossRef]

29. Rossi, F.; Cardinali, M.; Gambelli, A.M.; Filipponi, M.; Castellani, B.; Nicolini, A. Outdoor thermal comfort improvements due to innovative solar awning solutions: An experimental campaign. *Energy Build.* **2020**, *225*, 110341. [CrossRef]

30. Karl, T.R.; Jones, P.D. Urban Bias in Area-averaged Surface Air Temperature Trends. *Bull. Am. Meteorol. Soc.* **1989**, *70*, 265–270. [CrossRef]

31. Ya, Z. Identifying and Correcting Urban Bias for Regional Surface Air Temperature Series of North China over Period of 196Q_2000. *Clim. Environ. Res.* **2005**, *10*, 743–753.

32. Shi, T.; Huang, Y.; Sun, D.; Lu, G.; Yang, Y. A New Method for Correcting Urbanization-Induced Bias in Surface Air Temperature Observations: Insights From Comparative Site-Relocation Data. *Front. Environ. Sci.* **2021**, *9*, 625418. [CrossRef]

33. Janis, M.J. Observation-Time-Dependent Biases and Departures for Daily Minimum and Maximum Air Temperatures. *J. Appl. Meteorol.* **2002**, *41*, 588–603. Available online: http://www.jstor.org/stable/26184999 (accessed on 20 March 2022). [CrossRef]

34. Vose, R.S.; Williams, C.N.; Peterson, T.C.; Karl, T.R.; Easterling, D.R. An evaluation of the time of observation bias adjustment in the U.S. Historical Climatology Network. *Geophys. Res. Lett.* **2003**, *30*, 2046. [CrossRef]

35. Böhm, R.; Jones, P.D.; Hiebl, J.; Frank, D.; Brunetti, M.; Maugeri, M. The early instrumental warm-bias: A solution for long central European temperature series 1760–2007. *Clim. Chang.* **2010**, *101*, 41–67. [CrossRef]

36. Dienst, M.; Lindén, J.; Engström, E.; Esper, J. Removing the relocation bias from the 155-year Haparanda temperature record in Northern Europe: Removing the relocation bias from a 155-year temperature record. *Int. J. Climatol.* **2017**, *37*, 4015–4026. [CrossRef]

37. Kukla, G.; Gavin, J.; Karl, T.R. Urban Warming. *J. Clim. Appl. Meteorol.* **1986**, *25*, 1265–1270. [CrossRef]

38. Karl, T.R.; Diaz, H.F.; Kukla, G. Urbanization: Its Detection and Effect in the United States Climate Record. *J. Clim.* **1988**, *1*, 1099–1123. [CrossRef]

39. Jones, P.D.; Kelly, P.M.; Goodess, C.M.; Karl, T. The Effect of Urban Warming on the Northern Hemisphere Temperature Average. *J. Clim.* **1989**, *2*, 285–290. Available online: http://www.jstor.org/stable/26195817 (accessed on 1 March 2022). [CrossRef]

40. Landsberg, H.E. *The Climate of Towns. Man's Role in Changing the Face of the Earth*; Hutchinson: London, UK, 1956; pp. 584–603.

41. Ren, G.; Zhou, Y.; Chu, Z.; Zhou, J.; Zhang, A.; Guo, J.; Liu, X. Urbanization Effects on Observed Surface Air Temperature Trends in North China. *J. Clim.* **2008**, *21*, 1333–1348. [CrossRef]

42. Wang, J.; Yan, Z.-W. Urbanization-related warming in local temperature records: A review. *Atmos. Ocean. Sci. Lett.* **2015**, *9*, 129–138. [CrossRef]

43. Brázdil, R.; Budíková, M. An urban bias in air temperature fluctuations at the Klementinum, Prague, The Czech Republic. *Atmos. Environ.* **1999**, *33*, 4211–4217. [CrossRef]

44. Choi, Y.; Jung, H.-S.; Nam, K.-Y.; Kwon, W.-T. Adjusting urban bias in the regional mean surface temperature series of South Korea, 1968–1999. *Int. J. Clim.* **2003**, *23*, 577–591. [CrossRef]

45. Portman, D.A. Identifying and Correcting Urban Bias in Regional Time Series: Surface Temperature in China's Northern Plains. *J. Clim.* **1993**, *6*, 2298–2308. [CrossRef]

46. Peterson, T.C. Assessment of Urban Versus Rural In Situ Surface Temperatures in the Contiguous United States: No Difference Found. *J. Clim.* **2003**, *16*, 2941–2959. [CrossRef]

47. Manalo, J.A.; Matsumoto, J.; Takahashi, H.G.; Ii, M.Q.V.; Olaguera, L.M.P.; Ren, G.; Cinco, T.A. The effect of urbanization on temperature indices in the Philippines. *Int. J. Clim.* **2021**, *42*, 850–867. [CrossRef]

48. Zhang, P.; Ren, G.; Qin, Y.; Zhai, Y.; Zhai, T.; Tysa, S.K.; Xue, X.; Yang, G.; Sun, X. Urbanization Effects on Estimates of Global Trends in Mean and Extreme Air Temperature. *J. Clim.* **2021**, *34*, 1923–1945. [CrossRef]

49. Epperson, D.L.; Davis, J.M.; Bloomfield, P.; Karl, T.R.; McNab, A.L.; Gallo, K.P. Estimating the Urban Bias of Surface Shelter Temperatures Using Upper-Air and Satellite Data. Part I: Development of Models Predicting Surface Shelter Temperatures. *J. Appl. Meteorol.* **1995**, *34*, 340–357. [CrossRef]

50. Epperson, D.L.; Davis, J.M.; Bloomfield, P.; Karl, T.R.; McNab, A.L.; Gallo, K.P. Estimating the Urban Bias of Surface Shelter Temperatures Using Upper-Air and Satellite Data. Part II: Estimation of the Urban Bias. *J. Appl. Meteorol.* **1995**, *34*, 358–370. [CrossRef]

51. Parker, D.E. Urban heat island effects on estimates of observed climate change. *WIREs Clim. Chang.* **2009**, *1*, 123–133. [CrossRef]

52. Yuan, Z.; Guo-Yu, R.E.N. Correcting urban bias for surface air temperature series of Beijing Station over time period 1915–2012. *Chin. J. Geophys.* **2014**, *57*, 2197–2207. (In Chinese) [CrossRef]

53. Wang, J.; Tett, S.F.B.; Yan, Z. Correcting urban bias in large-scale temperature records in China, 1980-2009. *Geophys. Res. Lett.* **2017**, *44*, 401–408. [CrossRef]

54. Hamdi, R.; Van De Vyver, H. Estimating urban heat island effects on near-surface air temperature records of Uccle (Brussels, Belgium): An observational and modeling study. *Adv. Sci. Res.* **2011**, *6*, 27–34. [CrossRef]

55. Bassett, R.; Young, P.J.; Blair, G.S.; Cai, X.-M.; Chapman, L. Urbanisation's contribution to climate warming in Great Britain. *Environ. Res. Lett.* **2020**, *15*, 114014. [CrossRef]

56. National Research Council; Division on Earth and Life Studies; Board on Atmospheric Sciences and Climate; Committee on Scientific Accomplishments of Earth Observations from Space. *Earth Observations from Space: The First 50 Years of Scientific Achievements*; National Academies Press: Washington, DC, USA, 2008.

57. Li, G.; Cao, C. Development of environmental monitoring satellite systems in China. *Sci. China Earth Sci.* **2010**, *53*, 1–7. [CrossRef]

58. Guo, H.-D.; Zhang, L.; Zhu, L.-W. Earth observation big data for climate change research. *Adv. Clim. Chang. Res.* **2015**, *6*, 108–117. [CrossRef]

59. Young, R.; Onoda, M. *Satellite Earth Observations in Environmental Problem-Solving BT—Satellite Earth Observations and Their Impact on Society and Policy*; Springer: Singapore, 2017; pp. 3–27.

60. Andries, A.; Murphy, R.J.; Morse, S.; Lynch, J. Earth Observation for Monitoring, Reporting, and Verification within Environmental Land Management Policy. *Sustainability* **2021**, *13*, 9105. [CrossRef]

61. Huzui, A.E.; Abdelkader, A.; Pătru-Stupariu, I. Analysing urban dynamics using multi-temporal satellite images in the case of a mountain area, Sinaia (Romania). *Int. J. Digit. Earth* **2013**, *6*, 563–579. [CrossRef]

62. Cao, W.; Zhou, Y. Remote Sensing of Urban Dynamics. In *Landscape and Land Capacity*; Taylor & Francis Group: Abingdon, UK, 2020; pp. 387–391.

63. Chaudhuri, G.; Mainali, K.P.; Mishra, N.B. Analyzing the dynamics of urbanization in Delhi National Capital Region in India using satellite image time-series analysis. *Environ. Plan. B Urban Anal. City Sci.* **2021**, *49*, 368–384. [CrossRef]

64. Lin, X.; Xu, M.; Cao, C.; Singh, R.P.; Chen, W.; Ju, H. Land-Use/Land-Cover Changes and Their Influence on the Ecosystem in Chengdu City, China during the Period of 1992–2018. *Sustainability* **2018**, *10*, 3580. [CrossRef]

65. Twisa, S.; Buchroithner, M.F. Land-Use and Land-Cover (LULC) Change Detection in Wami River Basin, Tanzania. *Land* **2019**, *8*, 136. [CrossRef]

66. Inalpulat, M.; Genc, L. Quantification of LULC Changes and Urbanization Effects on Agriculture Using Historical Landsat Data in North-West Anatolia, Turkey. *Pol. J. Environ. Stud.* **2021**, *30*, 3999–4007. [CrossRef]

67. Kuenzer, C.; Dech, S. (Eds.) *Thermal Infrared Remote Sensing: Sensors, Methods, Applications*, 1st ed.; Springer: Dordrecht, The Netherlands, 2013.

68. Tang, H.; Li, Z.-L. *Quantitative Remote Sensing in Thermal Infrared: Theory and Applications*; Springer: Berlin/Heidelberg, Germany, 2014.

69. Weng, Q.; Larson, R.C. *Satellite Remote Sensing of Urban Heat Islands: Current Practice and Prospects BT—Geo-Spatial Technologies in Urban Environments*; Jensen, R.R., Gatrell, J.D., McLean, D.D., Eds.; Springer: Berlin/Heidelberg, Germany, 2005; pp. 91–111.

70. Imhoff, M.L.; Zhang, P.; Wolfe, R.E.; Bounoua, L. Remote sensing of the urban heat island effect across biomes in the continental USA. *Remote Sens. Environ.* **2010**, *114*, 504–513. [CrossRef]

71. Zhou, D.; Xiao, J.; Bonafoni, S.; Berger, C.; Deilami, K.; Zhou, Y.; Frolking, S.; Yao, R.; Qiao, Z.; Sobrino, J.A. Satellite Remote Sensing of Surface Urban Heat Islands: Progress, Challenges, and Perspectives. *Remote Sens.* **2019**, *11*, 48. [CrossRef]

72. Abulibdeh, A. Analysis of urban heat island characteristics and mitigation strategies for eight arid and semi-arid gulf region cities. *Environ. Earth Sci.* **2021**, *80*, 259. [CrossRef]

73. Hung, T.; Uchihama, D.; Ochi, S.; Yasuoka, Y. Assessment with satellite data of the urban heat island effects in Asian mega cities. *Int. J. Appl. Earth Obs. Geoinf.* **2006**, *8*, 34–48. [CrossRef]

74. Zhou, D.; Zhao, S.; Zhang, L.; Sun, G.; Liu, Y. The footprint of urban heat island effect in China. *Sci. Rep.* **2015**, *5*, 11160. [CrossRef]

75. Sfîcă, L.; Ichim, P.; Apostol, L.; Ursu, A. The extent and intensity of the urban heat island in Iași city, Romania. *Arch. Meteorol. Geophys. Bioclimatol. Ser. B* **2017**, *134*, 777–791. [CrossRef]

76. Qiao, Z.; Wu, C.; Zhao, D.; Xu, X.; Yang, J.; Feng, L.; Sun, Z.; Liu, L. Determining the Boundary and Probability of Surface Urban Heat Island Footprint Based on a Logistic Model. *Remote Sens.* **2019**, *11*, 1368. [CrossRef]

77. Yang, Q.; Huang, X.; Tang, Q. The footprint of urban heat island effect in 302 Chinese cities: Temporal trends and associated factors. *Sci. Total Environ.* **2018**, *655*, 652–662. [CrossRef] [PubMed]

78. Kottek, M.; Grieser, J.; Beck, C.; Rudolf, B.; Rubel, F. World map of the Köppen-Geiger climate classification updated. *Meteorol. Z.* **2006**, *15*, 259–263. [CrossRef]

79. Gong, P.; Wang, J.; Yu, L.; Zhao, Y.; Zhao, Y.; Liang, L.; Niu, Z.; Huang, X.; Fu, H.; Liu, S.; et al. Finer resolution observation and monitoring of global land cover: First mapping results with Landsat TM and ETM+ data. *Int. J. Remote Sens.* **2013**, *34*, 2607–2654. [CrossRef]

80. Chen, J.; Chen, J.; Liao, A.; Cao, X.; Chen, L.; Chen, X.; He, C.; Han, G.; Peng, S.; Lu, M.; et al. Global land cover mapping at 30 m resolution: A POK-based operational approach. *ISPRS J. Photogramm. Remote Sens.* **2015**, *103*, 7–27. [CrossRef]

81. Gong, P.; Li, X.; Wang, J.; Bai, Y.; Chen, B.; Hu, T.; Liu, X.; Xu, B.; Yang, J.; Zhang, W.; et al. Annual maps of global artificial impervious area (GAIA) between 1985 and 2018. *Remote Sens. Environ.* **2019**, *236*, 111510. [CrossRef]

82. Shi, T.; Huang, Y.; Wang, H.; Shi, C.-E.; Yang, Y.-J. Influence of urbanization on the thermal environment of meteorological station: Satellite-observed evidence. *Adv. Clim. Chang. Res.* **2015**, *6*, 7–15. [CrossRef]

83. Yang, Y.; Zhang, M.; Li, Q.; Chen, B.; Gao, Z.; Ning, G.; Liu, C.; Li, Y.; Luo, M. Modulations of surface thermal environment and agricultural activity on intraseasonal variations of summer diurnal temperature range in the Yangtze River Delta of China. *Sci. Total Environ.* **2020**, *736*, 139445. [CrossRef]

84. Mudelsee, M. Trend analysis of climate time series: A review of methods. *Earth-Sci. Rev.* **2018**, *190*, 310–322. [CrossRef]

85. Song, Z.; Chen, L.; Wang, Y.; Liu, X.; Lin, L.; Luo, M. Effects of urbanization on the decrease in sunshine duration over eastern China. *Urban Clim.* **2019**, *28*, 100471. [CrossRef]

86. Kim, S.W.; Jung, D.; Choung, Y.-J. Development of a Multiple Linear Regression Model for Meteorological Drought Index Estimation Based on Landsat Satellite Imagery. *Water* **2020**, *12*, 3393. [CrossRef]

87. Malik, S.; Pal, S.C.; Sattar, A.; Singh, S.K.; Das, B.; Chakrabortty, R.; Mohammad, P. Trend of extreme rainfall events using suitable Global Circulation Model to combat the water logging condition in Kolkata Metropolitan Area. *Urban Clim.* **2020**, *32*, 100599. [CrossRef]

88. Tong, X.; Wang, P.; Wu, S.; Luo, M. Urbanization effects on high-frequency temperature variability over South China. *Urban Clim.* **2022**, *42*, 101092. [CrossRef]

89. Mann, H.B. Nonparametric tests against trend. *Econometrica* **1945**, *13*, 245–259. [CrossRef]

90. Kendall, M.G. *Rank Correlation Methods*, 4th ed.; Charles Griffin: London, UK, 1975.

91. Theil, H. A Rank-Invariant Method of Linear and Polynomial Regression Analysis. In Proceedings of the Koninklijke Nederlandse Akademie Wetenschappen, Series A Mathematical Sciences, Amsterdam, The Netherlands; 1950; pp. 386–392.

92. Sen, P.K. Estimates of the regression coefficient based on Kendall's tau. *J. Am. Stat. Assoc.* **1968**, *63*, 1379–1389. [CrossRef]

93. Hipel, K.W.; McLeod, A.I. (Eds.) Chapter 23 Nonparametric Tests for Trend Detection. In *Time Series Modelling of Water Resources and Environmental Systems*; Elsevier: Amsterdam, The Netherlands, 1994; Volume 45, pp. 853–938.

94. Wang, F.; Shao, W.; Yu, H.; Kan, G.; He, X.; Zhang, D.; Ren, M.; Wang, G. Re-evaluation of the Power of the Mann-Kendall Test for Detecting Monotonic Trends in Hydrometeorological Time Series. *Front. Earth Sci.* **2020**, *8*, 14. [CrossRef]

95. Ahmad, I.; Tang, D.; Wang, T.; Wang, M.; Wagan, B. Precipitation Trends over Time Using Mann-Kendall and Spearman's rho Tests in Swat River Basin, Pakistan. *Adv. Meteorol.* **2015**, *2015*, 1–15. [CrossRef]

96. Mohsin, T.; Gough, W.A. Characterization and estimation of urban heat island at Toronto: Impact of the choice of rural sites. *Arch. Meteorol. Geophys. Bioclimatol. Ser. B* **2011**, *108*, 105–117. [CrossRef]

97. Chervenkov, H.; Slavov, K. Theil–Sen estimator vs. Ordinary least squares—Trend analysis for selected ETCCDI climate indices. *Comptes Rendus Acad. Bulg. Sci.* **2019**, *72*, 47–54. [CrossRef]

98. Redeker, C.; Kantoush, S.A. The Nile Delta: Urbanizing on Diminishing Resources. *Built Environ.* **2014**, *40*, 201–212. Available online: http://www.jstor.org/stable/43296887 (accessed on 25 February 2022). [CrossRef]

99. Sultan, M.; Fiske, M.; Stein, T.; Gamal, M.; El Araby, H.; Madani, A.; Mehanee, S.; Becker, R. Monitoring the urbanization of the Nile Delta, Egypt. *Ambio* **1999**, *28*. Available online: https://www.ostgov/biblio/942608 (accessed on 5 March 2022).

100. Shalaby, A.; Moghanm, F.S. Assessment of urban sprawl on agricultural soil of northern Nile Delta of Egypt using RS and GIS. *Chin. Geogr. Sci.* **2015**, *25*, 274–282. [CrossRef]

101. Elagouz, M.; Abou-Shleel, S.; Belal, A.; El-Mohandes, M. Detection of land use/cover change in Egyptian Nile Delta using remote sensing. *Egypt. J. Remote Sens. Space Sci.* **2019**, *23*, 57–62. [CrossRef]

102. Nasrallah, H.A.; Brazel, A.J.; Balling, R.C. Analysis of the Kuwait city urban heat island. *Int. J. Clim.* **1990**, *10*, 401–405. [CrossRef]

103. Cheng, W.L.; Saleem, A.; Sadr, R. Recent warming trend in the coastal region of Qatar. *Theor. Appl. Climatol.* **2017**, *128*, 193–205. [CrossRef]

104. Almazroui, M.; Islam, M.N.; Jones, P.D. Urbanization effects on the air temperature rise in Saudi Arabia. *Clim. Chang.* **2013**, *120*, 109–122. [CrossRef]

105. Benas, N.; Chrysoulakis, N.; Cartalis, C. Trends of urban surface temperature and heat island characteristics in the Mediterranean. *Arch. Meteorol. Geophys. Bioclimatol. Ser. B* **2016**, *130*, 807–816. [CrossRef]

106. Siddiqui, A.; Kushwaha, G.; Nikam, B.; Srivastav, S.; Shelar, A.; Kumar, P. Analysing the day/night seasonal and annual changes and trends in land surface temperature and surface urban heat island intensity (SUHII) for Indian cities. *Sustain. Cities Soc.* **2021**, *75*, 103374. [CrossRef]

107. Oke, T.R. The energetic basis of the urban heat island. *Q. J. R. Meteorol. Soc.* **1982**, *108*, 1–24. [CrossRef]

108. Van Hove, L.W.A.; Jacobs, C.M.J.; Heusinkveld, B.G.; Elbers, J.A.; van Driel, B.L.; Holtslag, A.A.M. Temporal and spatial variability of urban heat island and thermal comfort within the Rotterdam agglomeration. *Build. Environ.* **2015**, *83*, 91–103. [CrossRef]

109. Chen, X.; Jeong, S.-J. Shifting the urban heat island clock in a megacity: A case study of Hong Kong. *Environ. Res. Lett.* **2017**, *13*, 014014. [CrossRef]

110. Abbas, W.; Ismael, H. Assessment of constructing canopy urban heat island temperatures from thermal images: An integrated multi-scale approach. *Sci. Afr.* **2020**, *10*, e00607. [CrossRef]

111. Parlow, E. Regarding Some Pitfalls in Urban Heat Island Studies Using Remote Sensing Technology. *Remote Sens.* **2021**, *13*, 3598. [CrossRef]

112. Easterling, D.R.; Horton, B.; Jones, P.D.; Peterson, T.C.; Karl, T.R.; Parker, D.E.; Salinger, M.J.; Razuvayev, V.; Plummer, N.; Jamason, P.; et al. Maximum and minimum temperature trends for the globe. *Science* **1997**, *277*, 364–367. [CrossRef]

113. Jones, P.D.; Groisman, P.Y.; Coughlan, M.; Plummer, N.; Wang, W.-C.; Karl, T.R. Assessment of urbanization effects in time series of surface air temperature over land. *Nature* **1990**, *347*, 169–172. [CrossRef]

114. Parker, D.E. Large-scale warming is not urban. *Nature* **2004**, *432*, 290. [CrossRef] [PubMed]

115. Parker, D.E. A Demonstration That Large-Scale Warming Is Not Urban. *J. Clim.* **2006**, *19*, 2882–2895. [CrossRef]

116. Wickham, C.; Rohde, R.; Muller, R.A.; Wurtele, J.; Curry, J.; Groom, D.; Jacobsen, R.; Perlmutter, S.; Rosenfeld, A.; Mosher, S. SInfluence of Urban Heating on the Global Temperature Land Average using Rural Sites Identified from MODIS Classifications. *Geoinform. Geostat. Overv.* **2013**, *1*. [CrossRef]

117. Peterson, T.C.; Gallo, K.P.; Lawrimore, J.; Owen, T.W.; Huang, A.; McKittrick, D.A. Global rural temperature trends. *Geophys. Res. Lett.* **1999**, *26*, 329–332. [CrossRef]

118. Zhang, Q.; Wu, Z.; Singh, V.P.; Liu, C. Impacts of Spatial Configuration of Land Surface Features on Land Surface Temperature across Urban Agglomerations, China. *Remote Sens.* **2021**, *13*, 4008. [CrossRef]

Article

Monitoring Coastal Changes and Assessing Protection Structures at the Damietta Promontory, Nile Delta, Egypt, to Secure Sustainability in the Context of Climate Changes

Hesham M. El-Asmar [1,*] **and Maysa M. N. Taha** [2]

1   Department of Geology, Damietta University, Damietta 34517, Egypt
2   Department of Geology, Helwan University, Helwan 11795, Egypt
*   Correspondence: hmelasmar@yahoo.com

Abstract: The Damietta Promontory is a distinct coastal region in the Nile Delta Egypt, which comprises several communities with strategic economic projects. The promontory has experienced numerous inundation crises due to anthropogenic intervention and/or sea level rise (SLR). The recorded rate of erosion detected is from -18 to -53 m/yr., and -28 to -210 m/yr. along the promontory's western and eastern coasts, respectively, with a total loss of about 3 km during the past century. It is critical to ensure sustainability of this coastal region in case of future climate changes and expected SLR; accordingly, the state has implemented a long-term plan of coastal protection. The current study updates the coastal changes and assesses the efficiency of the protection structures. For such study, Ikonos satellite images of 1 m high-resolution were acquired on 30 July 2014 and 10 August 2022, respectively. These were compared to multitemporal Landsat images dated 30 June 2015, 29 September 1987, 15 October 1984, and the Landsat 4 MSS images dated 20 October 1972. The results confirm the presence of accretion along the western jetty of the Damietta Harbor with an average of $+10.91$ m/yr., while erosion of -4.7 m/yr. was detected at the east of the eastern harbor jetty. At the detached breakwaters along Ras El-Bar, an accretion of $+4$ m/yr. was detected, and then erosion was measured westward to the tip of the detached breakwaters with an average of -1.77 m/yr. At the eastern coast of the promontory, eastward erosion was recorded with rates of -44.16, -34.33, and -20.33 m/yr., respectively, then the erosion stopped after the construction of the seawall. The current study confirms the efficiency of the detached breakwaters and seawalls as coastal protection structures. However, the seawalls lack swimming-friendly long, wide beaches like those found on the detached breakwaters. The groins seem ineffective with rips and reversed currents like those at Ras El -Bar. To develop a fishing community at the Manzala triangle similar in nature to Venice, it is recommended to extend the seawall to 12 km and then construct detached breakwaters eastward to the El-Diba inlet. To secure sustainability of the coast, a continuous maintenance of the protection structures to keep their elevations between 4–6 m above sea level (a.s.l.) is a critical task, in order to reduce the potential risks that could arise from a tsunami, with sand nourishment as a preferred strategy.

Keywords: assessment; protection structures; inundation; hazards; shoreline changes; Nile Delta

1. Introduction

The Nile Delta is a classical globally studied river mouth, formed from the interplay of the River Nile and the Mediterranean Sea across the geologic time scale. The Nile Delta has seen significant development in recent years as part of the national strategy for sustainable development 2030 [1]. The Nile Delta coast is a subaerial part of the fluvio-marine Bilqas Formation of the Holocene age [2]. The Holocene is composed of fluvial sediments of prodelta clays and delta-front sands and silts, with marine and subaerial coastal sediments such as beach ridges and coastal sand dunes [2]. The structural sequence

shows a continuous prograding delta with a coarsening upward sequence [2,3]. Study of the coastal geomorphology reflects that the delta beaches are described as having fine to extremely fine sands and being fully dissipative, divergent, smooth, wide, gently sloped beach faces [4]. Due to SLR and anthropogenic intervention, the Nile Delta coast is currently neither dissipative nor divergent [3,4], and new wave and current patterns have resulted in new coastal segmentations related to the direction of the shoreline, the relationship to induced waves and currents, and the implemented protection structures. The studies of LC/LU of the coastal Nile Delta reveals the presence of geomorphic units including the beach ridges, coastal dunes, and interdune depressions with sabkhas [5,6]. Most of these features were obliterated through the coastal development [5,6]. The beaches show cuspate features, steep berm gradients, and shell distribution [4], and these features, supported with the results of satellite images, help in reliable interpretation of coastal dynamics and understanding the role of the interplay of different factors along the coast [4].

The Damietta Promontory (31°27′55.15″ N and 31°2′13.51″ E to 31°22′22.8″ N and 32°2′32.66″ E) was selected for the current study a number of reasons, including the fact that it supports the economy through industries such as tourism and fishing and is expected to attract additional investment. This area is prone to seasonal inundation, which may threaten ongoing development. The Damietta branch of the Nile is like an artery that runs through the body of the Damietta Promontory, and meets the Mediterranean Sea at the Damietta mouth (Figure 1a), dividing the promontory into two coastal segments (Figure 1). The western one is oriented NE–SW, comprising Ras El-Bar Resort and Damietta Harbor. The eastern one is oriented NW–SE, and comprises Ezbet El-Borg City and the Manzala Lagoon (Figure 1a,c), [7]. The Damietta branch, along with the historical branches, discharges more than 150 million m^3 of sediment into the Mediterranean annually [3]. Such huge discharge has led to accretion, with the coast protruding into the sea for 2–3 km [4,5]. Of these sediments, 0.6 to 1.8 million m^3/yr. moves along the coast, forming the promontory [5]. The extension of the promontory into the sea reflects the quantity of discharge reaching the coast from the Damietta branch relative to the drift by longshore transport [5].

The wave propagations at Ras El-Bar come principally from the NW (78%), NE (21%), and SW (1%) directions [8]. The resultant longshore currents have SW and NE directions, and are produced from N, NNW, and NW (50°) and WWN (40°) waves, respectively. On the other hand, wave propagations at Ezbet El-Borg come from the N, NNW, and NE (90°), resulting in a unidirectional NE longshore current without reversals (Figure 1a) [7,8]. Additionally, ground subsidence of up to 5 mm/yr. [9,10] and SLR of 5–6.9 mm/yr [11] both have contributed to coastline retreat [12,13] and a generally termed relative sea level rise [14].

Ras El-Bar and Ezbet El-Borg cities (Figure 1a,b) comprise 10% of the Damietta province's total population of about 1,600,000, of whom 25,000 live at Ras El Bar, and make their livelihood by serving from 250,000 to one million tourists and visitors a year at resort facilities and by providing summer entertainment. On the other hand, Ezbet El-Burg City is inhabited by 100,000 people, of whom 10,000 are anglers (1% of Egypt's total). It is one of the world's most famous cities in the fields of fishing and shipping [15]. It is the base of Egypt's largest fishing boat fleet, including boats of the traditional felucca type. The city itself hosts 65% of the Egyptian naval fleet, approximately 926 fishing boats, and receives a number of other ships, bringing the number of boats operating along the Damietta coast to 1350 boats. The city is also home to a sardine-canning factory operated by the Edfina Company [15].
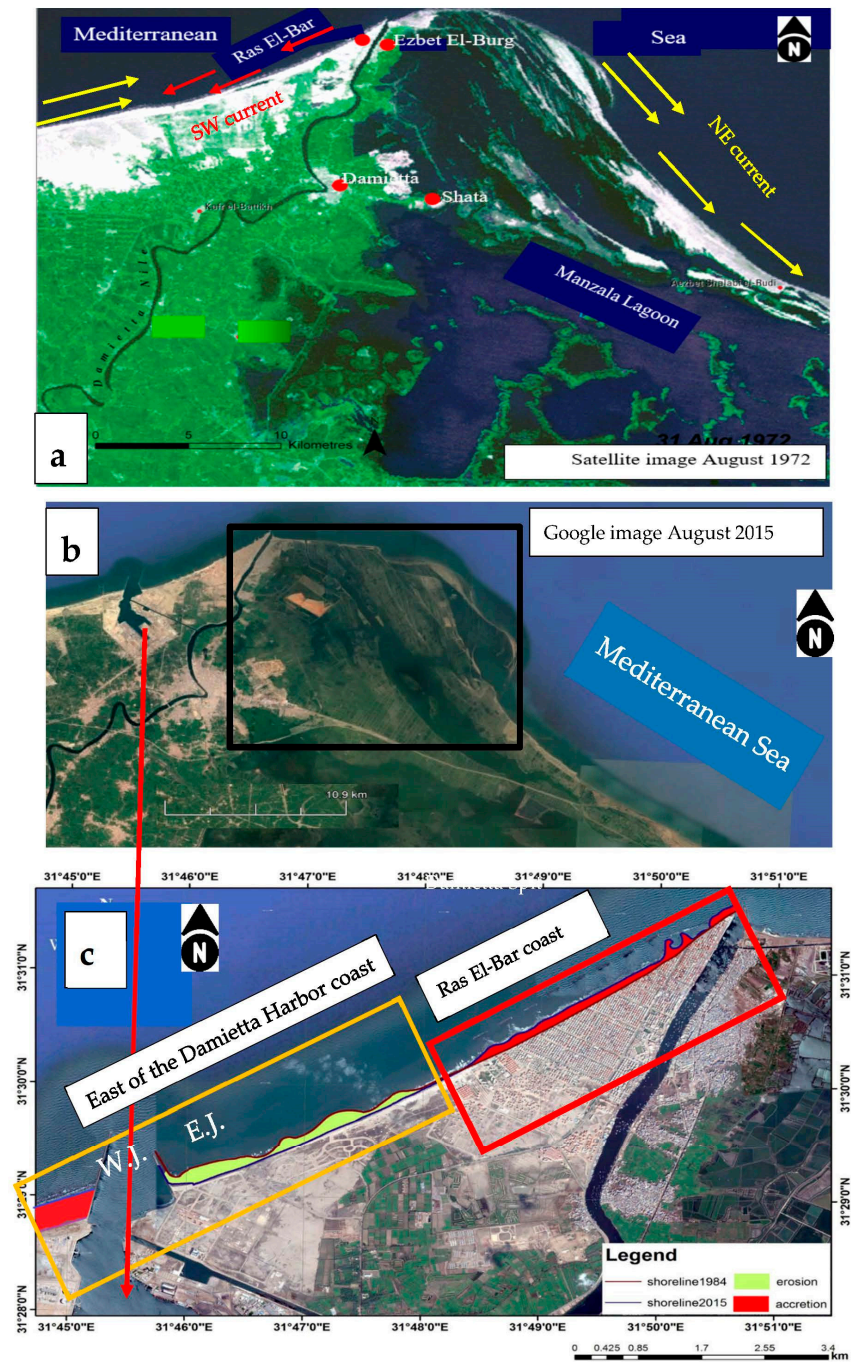
Figure 1. Satellite image from 1972 of the Damietta Promontory with the western coast including Ras El-Bar resort and Damietta Harbor, with the eastern coast comprising the Ezbet El-Borg fishing city and the Manzala lagoon triangle (**a**,**b**). The black rectangle refers to the location of Figure 4c. The situation at 2015 and comparison with 1984 satellite image showing segments of accretion in red color and erosion in yellow (**c**) W.J. and E.J. are the western and eastern jetties of the Damietta Harbor. The yellow rectangle refers to the location of Figure 5f–h, while the red rectangle refers to the location of Figure 5a–e (**c**).

The fishing sector provides the main source of income for the locals. Many of the fishing boats venture far into the Eastern Mediterranean and the Red Sea [15]. In addition, the city has interesting historical values with several archaeology sites and possible underwater antiquities. The annual inundation of these cities by winter storms represents a critical crisis for these benefited people and influences their way of life. A possible SLR

through climate changes may represent a catastrophic episode for these vulnerable areas and residences [12,13,16].

In 1981, construction of the Damietta Harbor (Figure 1c) began in order to meet the needs of increasing international trade in the Eastern Mediterranean [17]. It was also planned to build the harbor inland to minimize the effects of waves and currents and to avoid storm conditions [18]. The location of the harbor was selected along an embayment with minimum wave energy and shoreline changes [19,20]. The navigation channel of the harbor was protected by construction of two jetties, the western (WJ) and the eastern (EJ), later extended to 1300 m and 600 m, respectively (Figure 1c) [21]. The annual net rate of littoral drift on the western side of the harbor is about 1.43×10^5 m^3 (accretion with an average 2.13 m/yr.) while the annual net rate of littoral drift on the eastern side is about 2.54×10^5 m^3 (-92 m erosion on average over the past 45 years) (Figure 1c) [20,22]. Therefore, the harbor is threatened by problems of erosion along its eastern jetty and sedimentation along its navigation channel. The orientation of the navigation channel and its depth represent a sinking area receiving more west-to-east drifted sediments, reducing the channel depth form 14 m to10 m, which impedes the navigation of ships along the channel [23]. It is intended to construct a new section of harbor to increase its capacity to accommodate the greater cargo trade and to ensure a depth of 18 m in the navigation channel to allow passage of giant ships, required for transferring the products of the liquid natural gas (LNG) plant, the methane and formaldehyde industry, and for a free industrial zone [24].

In order to assess the coastal dynamic and shoreline changes, the current study's main novelty is the use of high-resolution Geo-Eye (Ikonos) satellite images that compare to other Landsat images, and a real field investigation including identification of beach and nearshore geo-features expressing the coastal dynamic and shoreline changes. Such high-resolution results will offer $\pm$ 1 m accuracy of shoreline measurements, and allow an excellent opportunity to assess the current situation and the efficiency of the protection works. It will be a prototype for sustainable development of relevant fragile coasts suffering erosion problems. Among the current study's objectives are to: (1) update rates of shoreline changes; (2) assess the implemented protection structures based on a comparison of shoreline changes; (3) demonstrate their efficiency to protect the coast from inundation; (4) determine the role of SLR, land subsidence, and the anthropogenic intervention in creating the problem of coastal inundation; (5) propose a role model of investment of the islands of the Manzala triangle; (6) confirm the role of Integrated Coastal Zone Management (ICZM) as a sustainable approach in dealing with coastal areas.

2. Data and Methods

The resolution of satellite images is increasing: observations are becoming more frequent, and this trend is expected to continue in the near future [25]. However, images always contain some uncertainty, which is one of the most common challenges [25]. Thus, quantitative uncertainty information associated with the data is required. It is also a critical scientific effort for both data producers and end users, as the process will reveal error characteristics that will guide further improvements in data production and rational data use [26]. To avoid uncertainty of remote sensing results, the selected images should not include more than 10% cloud. Geometric correction is used to correct the variation between the actual location coordinates and the raw image data on the ground or target image [27]. Geometric correction was performed through image-to-image geo-referencing in the Universal Transverse Mercator Projection (UTM/zone 36 WGS 84). In the current study, at least 10 prominent well-distributed ground control points (GCP) were selected in the master images, located in the other images, and then a nearest-neighbor resampling method was applied in addition to ground verification of several well-known points that were easily identified and observed in the field. In the current study, three points were detected and verified; one at the eastern jetty of the Damietta Harbor, the second at the tip of the eighth breakwaters, and the third at the lighthouse of the western jetty of the

Damietta branch of the Nile. It was considered for remote sensing applications to use images taken at various dates prior to and after the construction of the protection structures to demonstrate the efficiency of the structures in protecting the coast concerned. We needed data from at least two dates to track changes in coastline locations. The impact of shifting shorelines is not as obvious, and a large set of data is required to track changes in coastline locations [27,28]. Atmospheric correction was applied using Fast Line-of-sight Atmospheric Analysis of Spectral Hypercubes (FLAASH) as a method in ENVI for retrieving spectral reflectance from hyperspectral radiance images. FLAASH incorporates the MODTRAN radiation transfer model to compensate for atmospheric effects [27,29].

Multitemporal Landsat images were used in the current study (Table 1) to identify environmental changes: (1) the Multispectral Landsat 8-OLI (dated 30 June 2015, path 176, row 38), (2) the Landsat 5 TM (dated 29 September 1987 and 15 October 1984, path 176, row 38), and (3) the Landsat 4 MSS (dated 20 October 1972, path 189, row 38). The data were obtained from the USGS's GLOVIS and EARTH EXPLORER websites [30]. All image scenes were processed using ENVI 5.1 and arc GIS 10.4 software. These were compared with the results deduced from the high-resolution 1 m ground IKONOS satellite images acquired on 30 July 2014 and 10 August 2022, respectively. The image data were acquired from the World Imagery Wayback—ArcGIS Living Atlas sites [31]. Images of the two shorelines at different dates were extracted using photo-interpretation techniques covering 8 years (2014 and 2022, respectively).

Table 1. Satellite data acquired and utilized in the present study in a chronological order from 1972 to 2022.

Satellite	Sensors	Resolution (m)	Date	Spectral Bands
Landsat 4	MSS	60	20 October 1972	0.5–0.6 μm visible green 0.6–0.7 μm visible red 0.7–0.8 μm near infrared 0.8–1.1 μm infrared
Landsat 5	TM	30	15 October 1984 29 September 1987	0.45–0.52 μm visible blue 0.52–0.60 μm visible green 0.63–0.69 μm visible red 0.76–0.90 μm near infrared 1.55–1.75 μm infrared 10.4–12.5 μm thermal
Landsat 8	OLI	30	30 June 2015	0.43–0.45 μm coastal 0.45–0.51 μm visible blue 0.53–0.59 μm visible green 0.63–0.67 μm visible red 0.85–0.87 μm near infrared 1.56–1.65 μm infrared 10.6–11.1 μm thermal 11.5–12.5 μm thermal 2.10–2.294 μm infrared 0.503–0.676 μm panchromatic 1.363–1.384μm cirrus
IKONOS	IKONOS	1–4	30 July 2014 10 August 2022	450–520 nm Blue 510–600 nm Green 630–700 nm Red 760–850 nm Near-IR 530–930 nm Panchromatic

The DSAS tool was used to determine the rate of shoreline displacement (Figure 2). DSAS is an add-on for Esri ArcGIS that enables users to compute shoreline change rate data from numerous coastlines with various dates [32,33]. This feature enables the creation of transects along the shore that are positioned perpendicular to the baseline at the desired user

spacing [34]. A new transect layer was made using the Digital Shoreline Analysis System (DSAS) tool, with a transect spacing of 100 m. DSAS extracted the required data from the input baseline, shoreline, and transect files covering a 5 km long section of shoreline.
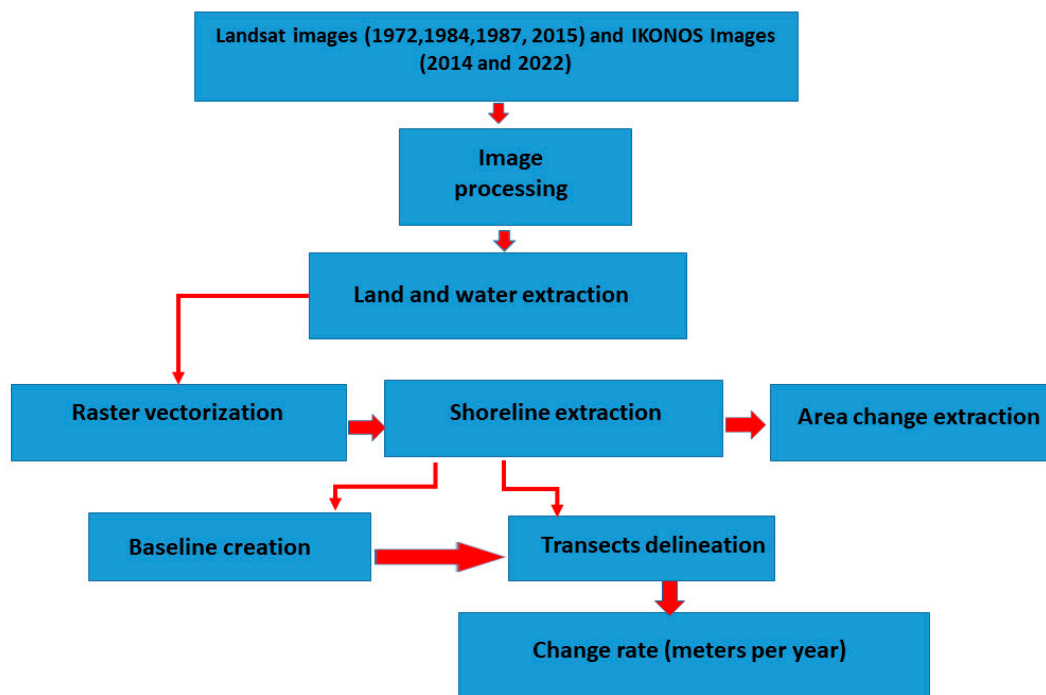
Figure 2. Flow chart showing the procedures applied on the selected satellite images used in the current study.

The methodology for calculating rates was based on observing how shorelines changed over time. A quick and effective way for estimating the rate of shoreline changes is the end point rate (EPR) (Figure 2). The mean annual rate of shoreline change (meters per year) for the oldest and most recent coastlines is calculated by dividing the distance of shoreline movement by the amount of elapsed time [35]. EPR is one of six methods used by DSAS to calculate rate-of-change statistics for a time series of shoreline vector data [36]. EPR is used to assess the annual rate of shoreline alterations for periods between 2014 and 2022. Similar assessments and predictions of shoreline change using EPR and linear LRR tools in DSAS have been utilized on the Andhra Pradesh coastline in India [37].

3. Results and Discussion

The global SLR in most of the world's oceans and seas, including the Mediterranean, may have serious consequences on the low-lying land of fragile coasts, including the Nile Delta. The studies of coastal changes along these vulnerable coasts are usually of global interest. Such studies update our understanding of SLR in the context of climate change, land subsidence, and other anthropogenic interventions. This section is dedicated to disclosing the current high-resolution Geo-Eye (Ikonos) satellite images compared with the historical results in order to update the records, determine the changes, understand the situations that led to the implementation of several protection structures, and then to recommend the preferred model for coastal stability. The recorded results are listed in Figure 3 and compared with the current study's results.

Name	Period	Western Jetty Average m/yr.			Eastern Jetty Average m/yr.			Ras El-Bar Average m/yr.			Ezbet El-Borg Average m/yr.		Other related works
The current study	1984-1987	+391	+13.00	+10.91	+304	+10.13		-80	-2.70		-1325	-44.16	
	1987-2015	+372	+12.40		-124	-4.13	-4.7	+106	+3.55	+4.00	-1030	-34.33	
	1984-2015	+217	+7.32		-120	-5.27		+134	+4.47		-610	-20.33	
	2014-2022				-2405 / -2626/-3076 m² +391 /+432/+1253/+1765 m²			+3.17m/yr. +106692 m²		-1.77m/yr. -2359 m²	No Changes -340444m²		
El-Asmar et al. (2016)	1973-1984				-590	-53.6		-915	-83.20				
	1984-1998				-7.43	-7.15		+4.73	+3.45				
	1998-2003				-10.90			+5.00					
	2003-2015				-3.11			+0.89					
El-Asmar et al. (2014)	1973-2003	+66.00			+20.00			-48.00			-45.00		
	1984-1987	+24.00	+19.02		+67.66	+67.66		-39.00	-34.50		-51.67		
	1987-1991	+24.00			-18.00	-10.46		-30.00			-47.50		
	1991-2003	+18.08			-10.33			+20.00	+21.0		-24.19		
	2003-2006	+10.00			-20.00			+22.00			-56.66		
	2000-2005							+11.53			-51.41		Moawad (2021)
	2005-2010							+3.56			-46.67		
	2010-2015							+12.17			-51.73		
	1984-2018		+15.20								- 47.99		Abu Samra and Ali (2021)
	1978-1994	+ 5.00	+4.37		+2.19	-1.05		+2.46					Ezzeldin et al. (2020)
	1995-2018	+ 3.73			-4.28								
	1985-2000										-75.11	296.14	Elnabwy et al. (2020)
	1985-2018										-65.16	314.75	
	1971-2013	+9-16	+0.244 km²		-1.5-15	-1.13 km²		+2-8	0.23 km²		-4.5	1.4 km²	Deabes (2017)
	1990-2014										-1330	-53.30	Ali and Abu El-Magd (2016)
	1972-2007	+10.00			-5.00			-5.35/-10.26 +5-15			-1500	-43.00	Dewidar and Frihy (2010)
	1993-2000				-9.00			+12.00			-39 to -11		Aly et al. (2012)
	1990-2002		+15.00		-12.00			+12-14					El-Banna (2007)
	1909-1972										-23.00		Frihy and Lawrence (2004)
	1972-2000										-52.00		
	1909-1991							-18.00			-28.00		Frihy (1992), Frihy and Khafagy (1991). Frihy and Komar (1993)
	1971-1990							-24.00			-42.00		
	Before 1902							-53.00			-210.00		El-Fishawi and badr (1989) Fanos et al. (2001).

Figure 3. Summary of the recorded data base of shoreline changes along the Damietta Promontory (references are listed in the last column) compared with the current results (first raw). The erosion is given in negative values while accretion rates expressed in positive values [1,4,5,8,16,22,38–48].

3.1. The Coastal Dynamics and Protection Structures

To measure the coastal dynamics and shoreline changes we must take into consideration some aspects of interest, among which are the physical conditions and the nature of coastal materials and whether these are rocks or soft sediments, and the orientation of the coastline in relation to waves and currents [4]. While the western side of the promontory is oriented NE–SW, and most waves come from NW propagation, these have resulted in two opposing SW and NE longshore currents. The eastern one is oriented NW–SE and the waves oriented N, NNW, and NE have resulted in a unidirectional NE longshore current (Figure 1a) [7,8]. The presence of bidirectional currents may little impede the drifting of sediment, which does not apply in the unidirectional current [4]. This may explain why erosion along both sides of the promontory appears different: while the recorded rate of erosion on the promontory's western coast was between −18 and −53 m/yr., at the same time, rates of −28 to −210 m/yr. were detected on the promontory's eastern coast [5,7,8].

Since 1902, coastal changes have been attributed to the development of numerous barrages and dams to regulate water flow, which altered the river system. The promontory then underwent erosion and shoreline retreat (Figures 1a, 3 and 4a), with rates of −53 m/yr. and −210 m/yr., on the promontory's western and eastern coasts, respectively [38,39].
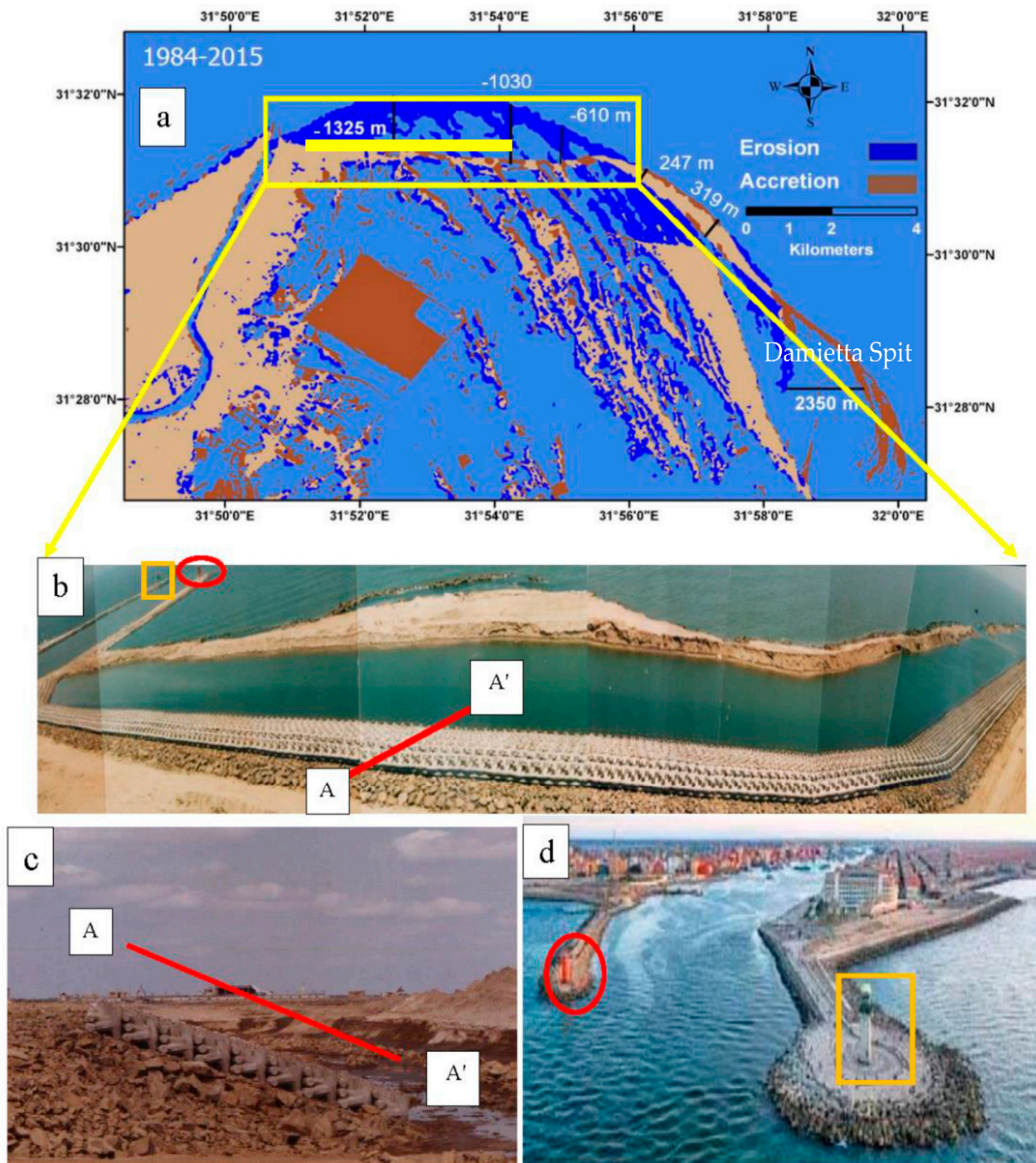
Figure 4. Comparison of satellite images of 1984 and 2015 showing the values of eroded and accreted coast in meters. The yellow bar shows the location of the seawall at "b" (**a**). The seawall constructed in 2000; A–A′ is a location of cross section along the seawall (**b**) illustrated section at (**c**) [14], with basalt, dolomite and tetrapod dolos of 3 tons (**c**). The two jetties at the Damietta branch river mouth (**d**). The red circle and yellow rectangle at (**b**,**d**) refer to the eastern and western jetties at the Damietta branch, respectively.

From 1909 to 1980, these rates changed to −18 m/yr. and −28 m/yr., respectively [5,7]. Beginning in 1972, the promontory's erosion rates increased to −23 m/yr. and −52 m/yr. on the west and east promontory coasts, respectively [7]. This was strongly linked to the entrapment of sediment discharges after the construction of the Aswan High Dam [40,46,49,50].

This confirms that the problem of erosion along the Nile Delta coast is old and started as early as the start of the 20th century, which enforced the state to react to the problem and build several protection structures. Some of these structures were damaging to the coast due to several physical and geological conditions.

The history of protection structures began around 1929, when the Damietta estuary was constantly subjected to sedimentation and shifting of the river mouth because of longshore drift, causing shoaling in the estuary and preventing fishing boats from entering across the river mouth to the sea and vice versa [46,51]. This prompted the construction of two jetties of 240 m and 290 m in length (Figure 4d), to keep the river mouth open [7,8,51], which were later renewed in 2007. Between 1984 and 1991, the promontory retreated by an average of −196 m (e.g., −28 m/yr.), and total erosion of the promontory from 1984 to 2015 was calculated as −1631 m (Figure 4a), with an average erosion rate of −20.61 m/yr. [7,8]. Other results detected between 1971 and 1990 were that the shoreline retreated −24 m/yr. to the west, and −41 m/yr. to the east of the promontory [5,43], and the lengths decreased by −1.9 km to the west, and −3.3 km to the east [5,43]. Rates of erosion were recorded at −15 m/yr., −39 to −11 m/yr. [16,51], and at −47.99 m/yr., −43 m/yr. and −53.30 m/yr. near the promontory's tip [41,42,51] (Figure 3), which led to the building of a seawall at the eastern promontory.

A 6 km long and 4 m a.s.l. seawall was constructed along the eastern side of the Damietta Promontory in 2000 [42,43,52] (Figure 4a,b). It is made up of prefabricated 4 to 7 tons dolos alternated with carbonate and basaltic rocks to protect the promontory from erosion (Figure 4c) [47,49]. However, severe erosion was detected at the down-drift of the seawall [53] (Figures 4a and 7c for comparison), which led the state to add 6 km in length to the wall to cover the erosional coast at the tip of the Manzala lagoon (the Manzala triangle, Figure 1b). The erosion then transferred eastward, eroding a considerable part of the Damietta Spit (Figures 1b and 2a). Rates of erosion between −24 m/yr. to −65 m/yr. were detected at the sand spit from 1972 to 2018 (Figure 3), [44,45,48].

In 1963, a concrete seawall was constructed (Figure 5a) along the western side of the promontory at the Ras El-Bar resort to reduce erosion along the southern edge of the western jetty of the Damietta Promontory. This seawall was subjected to sediment undermining, which caused a partial collapse (Figure 5a). The seawall was later rebuilt as a rip-rap structure that stands around 3.5 m a.s.l. (Figure 5b) [48,53]. To the west of this seawall, three 120 m long concrete groins were built in 1971. These were constructed as prefabricated blocks that were protected by concrete dolos (Figure 5c), but when erosion persisted, the groin's blocks broke and fell. Two of these groins were replaced in 2010, and they were extended to form a small bay with a tiny exit (Figure 5d) [4,49]. Some of the drifting sands ended up in this bay, forming a new sandy beach with a highly safe swimming location.

Until 1990 Ras El-Bar coast was still eroded, with rates up to −83.20 m/yr. recorded prior to the construction of the detached breakwaters [4,49] (Figure 3). Four detached breakwaters were built between 1991 and 1994. By the year 2000, four more breakwaters were added, bringing the total number to eight (about 400 m from the shoreline and a depth of 4 m b.s.l.). Each breakwater is 200 m long, with a 200 m space, and 3 m elevation a.s.l. (Figure 5e). Beyond these breakwaters, a shadow area was created with reduced (only 25%) wave energy (Figure 5e), ensuring coastal accretion of +4 m/yr. (Figures 6 and 7b), and a total area of 0.46 km ^{2} (Figure 1d).

Figure 5. The coast west of the promontory at Ras El-Bar showing the concrete seawall. (**a**) The yellow rectangle refers to the lighthouse; the modified 1200 m seawall extends westward of the Damietta Nile branch. (**b**) One of the three 120 m long concrete groins that were constructed to the west of the seawall at "b" and (**c**) later renewed. (**d**) The successful detached breakwaters that create shadow zones of 25% of the waves' energy. (**e**) Eastward evidence of erosion including shell accumulation, cuspate beach "red arrows" (**f**) at the coast east of the harbor eastern jetty (see Figure 1c yellow area), with developed rip currents (yellow arrows) (**g**) and waves rolled mud balls along the eroded coast (pink arrows) (**g**), [4]. The new Y groins east of the harbor jetty (blue arrows) (**h**) with accretion along the groins and erosion along the spaces in between.
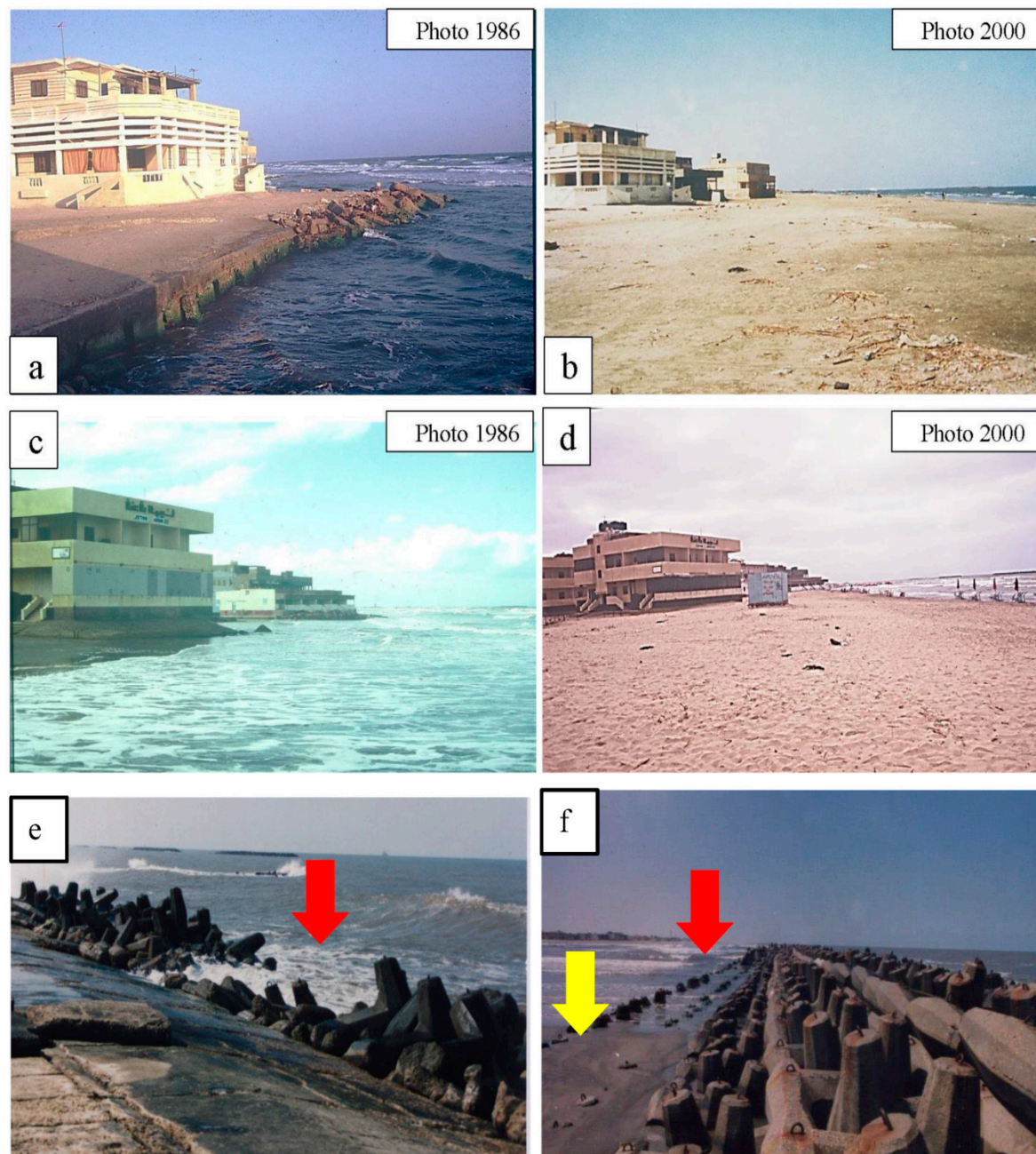
Figure 6. Comparison of summer houses at Ras El-Bar during inundation in 1986 where water sea water attacks the houses and they lose the swimming beaches, and later in 2000 after the construction of the detached breakwaters the same house have regained a wide sandy beach (**a–d**). Partial collapse "red arrows" and sedimentation "yellow arrow" at the protection structures, such collapse lowered the elevation of the breakwaters to less than 1 m a.s.l. (**e,f**).

The beach in front of the summer residences inundated during 1986 was restored as a wide flat beach during 2000 (Figure 6a–d). The detached breakwater structures showed rates of accretion of +12–14 m/yr. [16,53], and up to 21 m/yr. [49] (Figure 3). According to El-Asmar [49] a new reversing eddy current formed westward of the detached breakwaters resulted in erosion on the coast with an annual rate of −4.7 m/yr., and a total erosional area of 0.57 km^2 (Figure 1d). The development of a cuspate beach with shell accumulations and rip currents (Figure 5f,g) confirm the evidence of such erosion [4].
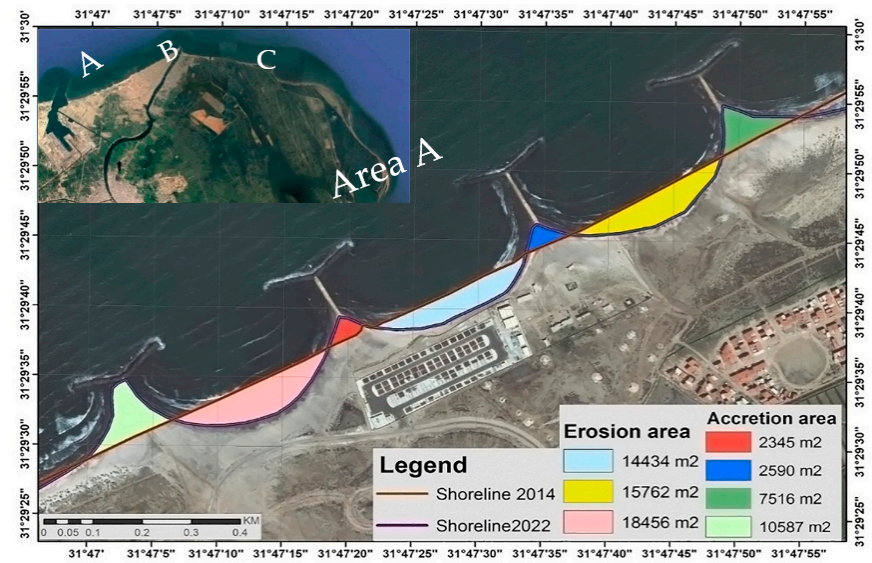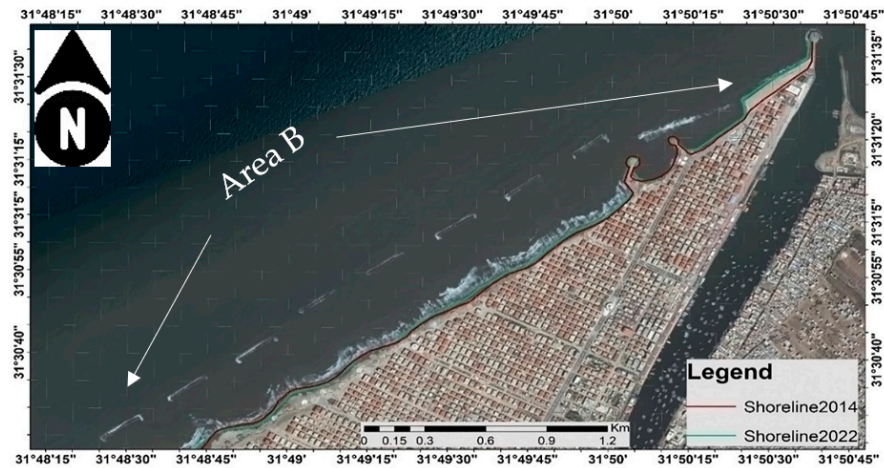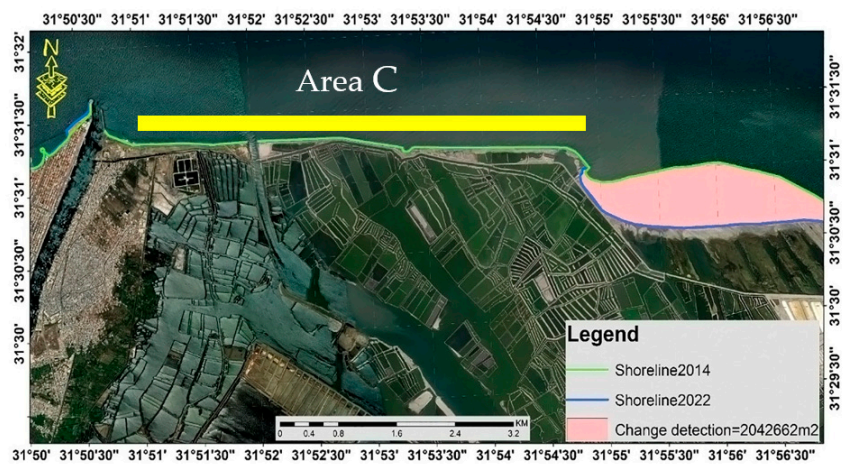
Figure 7. GeoEye (Ikonos) satellite images captured 30 July 2014 and 10 August 2022 showing the changes in three coastal zones A, B, and C (**a**) the erosion and accretion around the Y-groins (**a**) and at the detached breakwaters Area B (**b**). The changes after the construction of the seawall "the yellow bar location" and erosion to the down drift "pink shadow" and at the sand spit (**c**).

Inspection of this area of the coast shows evidences of sediments undermining sands, resulting in local subsidence (Figure 6e) of the detached breakwater with considerable sedimentation around the breakers' body (Figure 6f). At the present time, the elevation of these breakers reached in some places less than 1 m (Figure 6e–f). Annual sand nourishment, as well as maintenance and support of the breakwaters with replenishment materials to secure their elevation at not less than 6 m, are critical tasks.

To protect the Damietta Harbor from physical conditions (waves, currents, and littoral drift), two jetties were built in 1981; these jetties are the western (WJ) and the eastern jetties (EJ). From 1984 to 1987, the shoreline west of the western jetty accreted at an average rate of +13.00 m/yr. (Figure 3). From 1987 to 2015, it displayed continuous accretion of +12.4 m/yr. (Figure 3). Later, the accretion continued at a rate of +15 m/yr. at the west of the harbor's western jetty [16,53]. Other rates were reported as +9–16 m/yr. and an area of +0.244 km^2 up to 2018 [8,16,22,44,47,51]. During the years 1984 to 1987, the coastline at the eastern jetty increased by an average of +10.13 m/yr. (Figure 1c EJ; Figure 7a Area A). A few years later, the erosion along this coast reached an average of −4.7 m/yr. (Figure 3), which threat the inland body of the eastern harbor's jetty. This prompted the 2014 announcement of construction of a new project by Egyptian General Authority of Coastal Protection.

3.2. High Resolution Geo-Eye (Ikonos) Satellite Images

More than 20 years of monitoring this coastal area has been supported by research, ICZM, and coastal geomorphology, and supplemented with data from Geo-Eye (Ikonos) satellite images taken on 30 July 2014, and 2 August 2022, with a ground resolution of 1 m. In addition, a massive database was compiled through long-term research along the Nile Delta's coast. These enabled a more accurate assessment of the current coastal situation at the Damietta Promontory, as well as an evaluation of the protection structures put in place to ensure sustainability in the face of climate change and sea-level rise. The data collected from the Geo-Eye (Ikonos) satellite images of the western and eastern coasts of the Damietta Promontory from 2014 to 2022 are listed in Figure 3, and satellite images are illustrated in Figure 7. It is worth mentioning that no results have been detected for the area west of the harbor's western jetty (Figure 1c WJ), due to the ongoing construction of the harbor extension.

During 2014, four Y groins were built, three of the groins designed to be 170 m in length and the fourth 120 m, with 400 m space in between (area A, Figure 7a). The satellite images ensure the actual lengths at 188, 177, 149, and 125 m from east to west, respectively (Figures 5h and 7a), whereas the gaps set at 430 m. Erosion areas between groins east of the eastern jetty are −14,434m^2, −15,762m^2, and −18,456m^2 with an average of −2405, −2626, −3076 m^2/yr. (Figures 3 and 7a). While areas of accretion were observed at the groin bodies (Figure 7a) with areas of +2345 m^2, 2590 m^2, 7517 m^2 and 10,587 m^2 (Figure 7a, Area A) and an average of +391, +432, +1253, +1765 m^2/yr. (Figure 3). These are about to create tombolos. It was the first time the Y groins have been used as a protection structure along this coastal region. It is too early to evaluate their performance, with new figures on erosion/accretion. However, sand nourishment for the groin's gaps is important [54,55]. The favored solutions include ideas that combines both hard and soft structures, such as detachable breakwaters with sand nourishment to secure beaches safe for swimming [54–56].

The current study has proven that the groins cannot protect the beach when rip currents are present (Figure 5g) or from two opposing currents. Sand undermining has caused fracture and collapse (Figure 5c) and groins have failed to maintain the shoreline against erosion. A similar conclusion emerged when 15 groins were constructed along the Rosetta Promontory, which negatively affected the coastal morphology of the Rosetta Promontory [57,58], with an average of −30.8 m/yr. lost [50]. There are 47 traditional groins covering a total length of 3652 m and another 31 groins covering a coastal length of 4421 m at R. Morto Nuovo, Italy. Most of these groins are either completely or partially submerged, and the coast lost resort and tourism facilities [59].

The detached breakwaters seem to be relatively effective in protecting the coast [54,56,60] and freeing up more beaches for swimming. Both the submerged and emerging detached breakwaters are successful protective measures that keep beaches safe, which is a requirement of the tourism industry and recreational beaches [56,60]. The constraint of the detached breakwater is the adjustment of the shadow area beyond the breakers' body to prevent tombolo formation, as seen in Tunisia [59] or at Baltim and Port Said (Figure 8a,b). If they comply with environmental regulations and address drowning issues, detached breakwaters meet communities' preferences for long-term coastal protection [61] while also providing recreational facilities needed by the tourism industry.
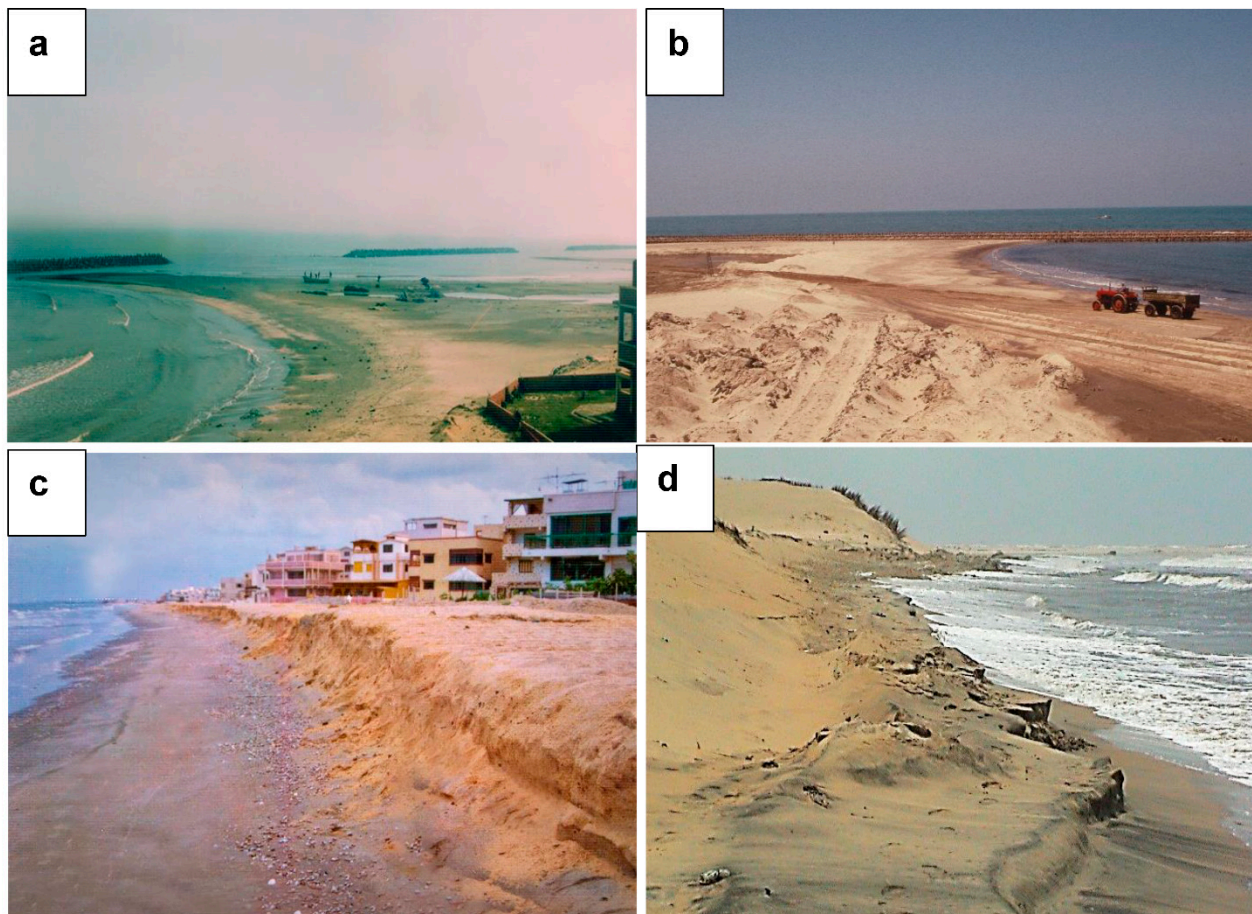
Figure 8. Two photos showing the unsuccessful detached breakwaters at Pot Said (**a**), and at Baltim (**b**) due to short length of the shadow area. Field photos showing unsuccessful sand nourishment along El-Gamiel tourist village at Port Said the waves attacked the coast and obliterated all sands due to the non-efficient quantities of sands m^3/m and the grain size (**c**). Finally, the coastal dunes natural defense measure subjected to erosion (**d**) at Baltim, threats the International coastal road and the Burullus coast.

While sand nourishment has been unsuccessful along the Port Said coast (Figure 8c), the current study recommends the use of sand nourishment, which is the least expensive method of coastal protection [45,54]. The success of sand nourishment depends on the coastal nature (coastal extension and beach gradient), the presence of plenty of sand (unit sand volume m^3/m, per meter of the beach length) and a critical point is the size of the sand used compared with the native sediments. Unsuccessful sand nourishment cases were mentioned in Israel [62], and explained as a result of the presence of wide coasts with strong waves that dredge most sands, and the use of small-grain sand—the size should be 1.5–2 times that of the native beach sands [62]—insufficient sand sources due to environmental restrictions of quarrying, and the lack of maintenance and replenishment [62]. On

the Dutch coast, sand nourishment is considered a strategic approach and a state trend for coastal protection. By 2000, the area of sand was increased from 6.4 to 12 million m^3/yr., adding to the coastline 432 km, which enabled the coastal zone to stay in equilibrium with sea level rise [63].

It is interesting to shed some light on the problem of coastal sand dune quarrying. Natural sand dunes and backshores along the coast of the Mediterranean region act as natural defense measures, reducing erosion and shoreline retreat [64]. Removal of these dunes is a risky course [28]. Most of the dunes along the Nile Delta, between Baltim and Damietta, have been removed for urbanization [65], including the construction of recreational resorts and new communities [66,67]. Such anthropogenic intervention, while claiming to be sustainable development and investment in the tourism industry, is actually a major threat to the environment and the stability of the coast. Due to the lack of awareness of ICZM, several strategic projects were built in inconvenient coastal areas. Focusing on human demands for entertainment and investments such as tourism-accommodating beaches and recreational facilities in face of strategic industries imply risks and pollution. Such imbalance causes deterioration of highly vulnerable systems, compromising both ecosystem integrity and health, as well as tourism itself [68].

Finally, a discussion about the possible inundation scenarios of the northern Nile Delta coast seems very interesting. Recent research has postulated two scenarios of 0.5 m and 1 m SLR of future inundated land areas and the affected populations. The extreme scenario of SLR to 1 m will affect about 3900 km^2 of cropland, 1280 km^2 of vegetation, 205 km^2 of wetland, 146 km^2 of urban areas at the northern borders, and cause more than 6 million people to lose their houses [69]. However, a more optimistic scenario is based on the measurements of a SLR gauge and referred to a value ranges between 6.7–6.9 mm/yr. [70]. An interpolation process has been performed for the SLR rates up to year 2050 (a time period of 35 yeas) has been calculated at 0.24 m. In addition to the average subsidence rate (calculated at Damietta Promontory to be 2.6 mm/yr., which appears consistent with the global positioning system rate of 3.5 mm/yrm. Accordingly, the areas vulnerable to inundation by year 2050 will be 38.40 km^2, 3.80 km^2, 5.20 km^2, and 2.60 km^2 for the urban, agricultural lands, fishing farms, and bare areas, respectively [70].

Tenths of papers have been devoted to the effect of SLR and land subsidence since 1988, when Stanley and his colleagues [9–11] published their pioneering studies on the Nile Delta subsidence scenarios, with suggested inundated areas. Since then several scenarios have been published, estimating future inundation of hundreds of kilometres and the migration of millions of people from their first homes to other areas to the south [11–13]. A 35 years period has passed (1988 to 2022) during which a SLR equal to 0.33 m. is supposed to inundate 1/3 of the suggested areas, a case that has not yet occurred. The present situation undoubtfully forced us to conclude that such a gradual increase in SLR is a secondary player and the predicted 2050 [70] scenario will be similar to that of Stanley [9–11] unless a new strong and rapid player, such as Tsunami [71], enters the game. Therefore, the anthropogenic factors are strongly involved. Such as compaction of the Holocene sediments (8000 to 2500) [13], and urban-induced loading at major cities (12 to 20 mm/yr.). The major cities such as Cairo, Tanta, Mahala, Mansoura, Damietta, and Port Said, show estimated subsidence are around 6.4 ± 0.4 mm/year, 4.0 ± 0.6 mm/year, 4.8 ± 1.0 mm/year, 10.0 ± 1.2 mm/yr., 10.3 ± 1.6 mm/yr., and 4.9 ± 1.6 mm/yr. respectively [72,73]. In addition, the role of groundwater overexploitation (16 to 20 mm/yr.) that recorded at newly reclaimed lands and most agricultural lands (like Menoufia governorate) [74], and high subsidence rates (up to 0.7 mm/year) over onshore gas fields, particularly the Abu Madi [74]. The localization of subsidence signals on InSAR and GPS imited at the big cities [75], and about 15.56% of the coastal cities are affected by subsidence [76], the subsidences related to anthropogenic activities seem to be more effective rather than SLR [76].

4. Conclusions

Owing to its historical values, economic resources of oil and gas and dense population, the Nile Delta is a traditional global model for delta research. Several scenarios of inundation due to SLR are emerging, however; inspection of several areas of the coast confirms the role of anthropogenic interventions in coastal erosion problems rather than SLR and land subsidence. In unawareness with the ICZM several economic projects, resorts, and profession communities were constructed in inconvenient coastal areas, which were later subjected to erosion. These led the state to implement a plan for coastal protection. The current study used high-resolution satellite images to detect the shoreline changes at the Damietta Promontory and to assess the efficiency of the implemented protection structures in securing sustainability of the coast against SLR and climate changes.

- The current study confirms the efficiency of detached breakwaters in protecting the coast, with annual sand nourishment preferred in order to secure wide and gently sloped beaches convenient for swimming. However, the dimensions of the breaker bodies, gaps, and shadow areas must be taken into considerations.
- Seawalls, on the other hand, are effective in protecting the coast-facing non-available beaches. The case presented was at the promontory facing the Manzala triangle, where the seawall may offer stability of the coast against most storms, which allows better investments for the islands along the Manzala triangle in a model similar in nature to that of Venice, Italy.
- The seawall at the Damietta Promontory should be extended to the El-Diba Inlet, the ancient mouth of the Nile's Mendisian branch. Additionally, we encourage the presence of detached breakwaters to offer water circulation within the Manzala triangle and restore beaches for the new resort communities.
- Sand nourishment is the preferred way for protection; this depends on the presence of a suitable source of sand of the right grain size.
- Due to the absence of continuous maintenance, several areas of collapses are observed and parts of the breaker body reached an elevation of less than 1 m a.s.l. Such a situation represents a great risk and continuous maintenance is a critical task to keep the elevation of the breakers not less than 6 m a.s.l. in order to impede tsunamic waves.
- The groins failed in protecting the coast in cases where there are multidirectional currents or rip currents perpendicular to the coast due to the resultant sand undermining, resulting in collapse as seen at Ras El-Bar.
- It is still too early for the Y groins to be evaluated; however, these create a new pattern of erosion between groins and accretion along the groins' bodies that will transform the groins to tombolos.
- The protection structures must be built to cover an entire cell or sector, not just a small segment. A segment of coast between two bodies of water or outlying headlands is referred to as a segment in this definition.
- Building the protection structures in an opposite direction to currents is not recommended. Such a situation creates unusual waves and currents that may threaten the works.
- The current study confirms the role of anthropogenic intervention rather than SLR by comparing the 35 year time period from 1988 postulated by Stanley and another 35 year period of a new scenario for SLR through to 2050. In fact, nothing has changed along the coast since 1988, except the construction of protecting structures. The historical changes are linked to the entrapment of the discharge rather than action of SLR in addition to some anthropogenic activities along the coast near big cities. However, a sudden tsunami is not ruled out.

References

1. Moawad, M.B. Recent landscape changes at Damietta Promontory, Nile Delta-Egypt. *Egypt. J. Remote Sens. Space Sci.* **2021**, *24*, 525–535. [CrossRef]
2. Coutellier, V.; Stanley, D.J. Late Quaternary Stratigraphy and Paleogeography of the Eastern Nile Delta Shelf. *Mar. Geol.* **1987**, *77*, 257–275. [CrossRef]
3. Sestini, G. Nile Delta: A Review of Depositional Environments and Geological History. *Geol. Soc.* **1989**, *41*, 99–127. [CrossRef]
4. El-Asmar, H.M.; Taha, M.M.N.; El-Sorogy, A.S. Morphodynamic Changes as an Impact of Human Intervention at the Ras El-Bar-Damietta Harbor Coast, NW Damietta Promontory, Nile Delta, Egypt. *J. Afr. Earth Sci.* **2016**, *124*, 323–339. [CrossRef]
5. Frihy, O.E.; Khafagy, A.A. Climate and Human Induced Changes in Relation to Shoreline Migration Trends at the Nile Delta Promontories, Egypt. *CATENA* **1991**, *18*, 197–211. [CrossRef]
6. Masria, A.; Nadaoka, K.; Negm, A.; Iskender, M. Detection of Shoreline and Land Cover Changes around Rosetta Promontory, Egypt, Based on Remote Sensing Analysis. *Land* **2015**, *4*, 216–230. [CrossRef]
7. Frihy, O.E.; Debes, E.A.; El Sayed, W.R. Processes Reshaping the Nile delta Promontories of Egypt: Pre- and Post-Protection. *Geomorphology* **2003**, *53*, 263–279. [CrossRef]
8. Frihy, O.E.; Lawrence, D. Evolution of the Modern Nile Delta Promontories: Development of Accretional Features during Shoreline Retreat. *Environ. Geol.* **2004**, *46*, 914–931. [CrossRef]
9. Stanley, D.J. Recent Subsidence and Northeast Tilting of the Nile Delta, Egypt. *Mar. Geol.* **1990**, *94*, 147–154. [CrossRef]
10. Stanley, D.J.; Warne, A.G. Nile Delta: Recent Geological Evolution and Human Impact. *Science* **1993**, *260*, 628–634. [CrossRef]
11. Stanley, J.D.; Clemente, P.L. Increased land Subsidence and Sea-Level Rise are Submerging Egypt's Nile Delta Coastal Margin. *GSA Today* **2016**, *27*, 4–11. [CrossRef]
12. Marriner, N.; Flaux, C.; Morhangem, C.; Kaniewski, D. Nile Delta's sinking past: Quantifiable Links with Holocene Compaction and Climate-Driven Changes in Sediment Supply. *Geology* **2012**, *40*, 1083–1086. [CrossRef]
13. Becker, R.H.; Sultan, M. Land Subsidence in the Nile Delta: Inferences from Radar Interferometry. *Holocene* **2009**, *19*, 949–954. [CrossRef]
14. El-Asmar, H.M. Short term coastal changes along Damietta-Port Said coast Northeast of the Nile Delta. *Egypt. J. Coast. Res.* **2002**, *18*, 433–441.
15. Abaza, J.; Mostafa, M.; El-Fekki, A. The Forgotten Fishermen of Ezbet El-Borg. *Daily News*, 14 April 2015; 1/9–9/9.
16. Aly, M.H.; Giardino, J.R.; Klein, A.G.; Zebker, H.A. InSAR study of shoreline change along the Damietta Promontory, Egypt. *J. Coast. Res.* **2012**, *28*, 1263–1269. [CrossRef]
17. ASRT. *Sedimentation in Damietta Harbor*; Academy of Scientific Research and Technology Final Report; ASRT: Cairo, Egypt, 1988.
18. Tetra Tech. Shoreline Master Plan for the Nile Delta Coast. *Prog. Rep.* **1984**, *1*, 143.
19. Sogreah, M. Effects on the construction of the Port of Damietta on the evolution of the littoral drift. *Consult. Rep.* **1982**, *9*, 35/1202.
20. AboZed, B.I. Effects of Waves and Currents on the Siltation Problem of Damietta harbor, Nile Delta coast, Egypt. *Mediterr. Mar. Sci.* **2007**, *8*, 33–47. [CrossRef]
21. El-Asmar, H.M. Impact of protection structures on Physical and Sedimentary Parameters along the Damietta coastal area, Nile Delta, Egypt. *J. Sedimentol. Egypt.* **1995**, *3*, 111–124.
22. Ezzeldin, M.M.; Rageh, O.S.; Saad, M.E. Assessment impact of the Damietta Harbor (Egypt) and its deep navigation channel on adjacent shorelines. *J. Integr. Coast. Zone Manag.* **2020**, *20*, 265–281. [CrossRef]
23. El-Asmar, H.M.; White, K. Changes in coastal sediment transport processes due to construction of New Damietta Harbor, Nile Delta, Egypt. *Coast. Eng.* **2002**, *46*, 127–138. [CrossRef]
24. Deabes, E.A. Sedimentation Processes at the Navigation Channel of the Liquefied Natural Gas (LNG) Port, Nile Delta, Egypt. *Int. J. Geosci.* **2010**, *1*, 14–20. [CrossRef]

25. Stein, A.; Ge, Y.; Fabris-Rotelli, I. Introduction to the Special Issue "Uncertainty in Remote Sensing Image Analysis". *Remote Sens.* **2018**, *10*, 1975. [CrossRef]

26. Wang, W.; Hall-Beyer, M.; Wu, C.; Fang, W.; Nsengiyumva, W. Uncertainty Problems in Image Change Detection. *Sustainability* **2020**, *12*, 274. [CrossRef]

27. Wu, W.; Mhaimeed, A.S.; Al-Shafie, W.M.; Ziadat, F.; Dhehibi, B.; Nangia, V.; De Pauw, E. Mapping soil salinity changes using remote sensing in Central Iraq. *Geoderma Reg.* **2014**, *2*, 21–31. [CrossRef]

28. Taha, M.M.N. Monitorig Changing Position of the Shoreline along Burullus–Baltim, Nile Delta, Egypt, and the Role of Coastal Sand dunes as a Natural Defense Against Erosion in a Geoheritage Site: Remote sensing application. *Egypt. J. Geol.* **2020**, *64*, 111–121.

29. Do, A.T.; Vries, S.D.; Stive, M.J. The Estimation and Evaluation of Shoreline Locations, Shoreline-Change Rates, and Coastal Volume Changes Derived from Landsat Images. *J. Coast. Res.* **2019**, *35*, 56–71. [CrossRef]

30. Available online: http://earthexplorer.usgs.gov/ (accessed on 21 August 2022).

31. Available online: https://livingatlas.arcgis.com/wayback/#active=47471&ext=-115.34940,36.03763,-115.24760,36.09036 (accessed on 21 August 2022).

32. Thieler, E.R.; Himmelstoss, E.A.; Zichichi, J.L.; Ergul, A. *The Digital Shoreline Analysis System (DSAS) Version 4.0—An ArcGIS Extension for Calculating Shoreline Change*; Open-File Report, 2008-1278; U.S. Geological Survey: Reston, VA, USA, 2009. [CrossRef]

33. Dewidar, K.; Bayoumi, S. Forecasting Shoreline Changes along the Egyptian Nile Delta Coast using Landsat Image Series and Geographic Information System. *Environ. Monit. Assess.* **2021**, *193*, 429. [CrossRef]

34. Fountoulis, I.; Vassilakis, E.; Mavroulis, S.; Alexopoulos, J.; Dilalos, S.; Erkeki, A. Synergy of Tectonic Geomorphology, Applied Geophysics and Remote Sensing Techniques Reveals New Data for Active Extensional Tectonism in NW Peloponnese (Greece). *Geomorphology* **2015**, *237*, 52–64. [CrossRef]

35. Thieler, E.R.; Hammar-Klose, E.S. *National Assessment of Coastal Vulnerability to Sea-Level Rise, U.S. Atlantic Coast*; U.S. Geological Survey: Reston, VA, USA, 1999; Volume 1, pp. 99–593.

36. Elkafrawy, S.B.; Basheer, M.A.; Mohamed, H.M.; Naguib, D.M. Applications of remote sensing and GIS techniques to evaluate the effectiveness of coastal structures along Burullus headland-Eastern Nile Delta, Egypt. *Egypt. J. Remote Sens. Space Sci.* **2021**, *24*, 247–254. [CrossRef]

37. Basheer, A.K.K.; Chandra, A.P. Assessment and Prediction of Shoreline Change using Multi-temporal Satellite Data and Geo-statistics: A Case Study on the Eastern Coast of India. *J. Water Clim. Chang.* **2022**, *13*, 147. [CrossRef]

38. E1-Fishawi, N.M.; Badr, A.A. Volumetric changes of nearshore sediments between Rosettaand Damietta, Egypt. *INQUA Comm. Quat. Shorel. Newsl.* **1989**, *11*, 39–42.

39. Fanos, A.M.; Khafagy, A.A.; El Kady, M.M. Variations of the Nile River discharge and sediment regime during the periodfrom 1800 to 2000 and its effects on the Nile Delta coast. In Proceedings of the 8th International Symposium on River Sedimentation, Cairo, Egypt, 3–5 November 2001.

40. Frihy, O.E. Sea-level rise and shoreline retreat of the Nile Delta Promontories, Egypt. *Nat. Hazards* **1992**, *5*, 65–81. [CrossRef]

41. El-Asmar, H.M.; El-Kafrawy, S.; Taha, M.M.N. Monitoring coastal changes along Damietta promontory and the barrier beach toward Port Said east of the Nile Delta. Egypt. *J. Coast. Res.* **2014**, *30*, 993–1005. [CrossRef]

42. Ali, E.; El-Magd, I.A. Impact of Human Interventions and Coastal Processes along the Nile Delta Coast, Egypt during the Past Twenty-Five Years. *Egypt. J. Aquat. Res.* **2016**, *42*, 1–10. [CrossRef]

43. Dewidar, K.; Frihy, O.E. Automated Techniques for Quantification of Beach Change Rates using Landsat Series along the North-Eastern Nile Delta, Egypt. *J. Oceanog. Mar. Sci.* **2010**, *1*, 28–39.

44. Abou Samra, R.M.; Ali, R.R. Applying DSAS Tool to Detect Coastal Changes along the Nile Delta Egypt. *Egypt. J. Remote Sesing Space Sci.* **2021**, *24*, 463–470. [CrossRef]

45. Frihy, O.E.; Komar, P.D. Long-term Shoreline Changes and the Concentration of Heavy Minerals in Beach Sands of the Nile Delta, Egypt. *Mar. Geol.* **1993**, *115*, 253–261. [CrossRef]

46. El-Banna, M. Erosion and Accretion Rates and their Associated Sediment Characters along Ras El Bar Coast, Northeast Nile Delta, Egypt. *Environ. Geol.* **2007**, *52*, 41–49. [CrossRef]

47. Fanos, A.M.; Khafagy. A.A.; Dean, R.G. Protective Works on the Nile Delta Coast. *J. Coast. Res.* **1995**, *11*, 516–528.

48. Elnabwy, M.T.; Emad Elbeltagi, E.; El Banna, M.M.; Elshikh, M.M.Y.; Motawa, I.; Kaloop, M. An Approach Based on Landsat Images for Shoreline Monitoring to Support Integrated Coastal Management—A Case Study, Ezbet Elborg, Nile Delta, Egypt. *ISPRS Int. J. Geo-Inf.* **2020**, *9*, 199. [CrossRef]

49. Ghoneim, E.; Mashaly, J.; Gamble, D.; Halls, J.; Abu Bakr, M. Nile Delta exhibited a spatial reversal in the rates of shoreline retreat on the Rosetta promontory comparing pre- and post-beach protection. *Geomorphology* **2015**, *228*, 1–14. [CrossRef]

50. White, K.; El-Asmar, H.M. Monitoring Changing Position of Coastlines using Thematic Mapper Imagery, an example from the Nile Delta. *Geomorphology* **1999**, *29*, 93–105. [CrossRef]

51. Masria, A.; Negm, A.; Iskender, M.; Savedra, O.C. Numircal Modeling of Rosetta River Mouth, Egypt. *Int. Water Technol. J. IWTJ* **2014**, *4*, 190.

52. Deabes, E.A.M. Applying ArcGIS to Estimate the Rates of Shoreline and Back-Shore Area Changes along the Nile Delta Coast, Egypt. *Int. J. Geosci.* **2017**, *8*, 332–348. [CrossRef]

53. El-Gamal, A.; Balbaa, S.H.; Rashed, M.A.; Mansour, A.S. Three Decades Monitoring of Shoreline Change Pattern of Damietta Promontory, Nile Delta, Egypt. *Aquat. Sci. Technol.* **2020**, *8*, 1–14. [CrossRef]

54. Khalifa, A.M.; Soliman, M.R.; Yassin, A.A. Assessment of a combination between hard structures and sand nourishment eastern of Damietta harbor using numerical modeling. *Alex. Eng. J.* **2017**, *56*, 545–555. [CrossRef]

55. Masria, A.; Nadaoka, K.; Kuriyama, Y.; Negm, A.; Iskender, M.; Savedra, O.C. Neashore and Beach nourishments Effects on the Stability of the Rosette Promontory, Egypt. In Proceedings of the Eighteenth International Water Technology Conference, IWTC18 2015, Sharm El-Sheikh, Egypt, 12–14 March 2015.

56. Masria, A.; Iskender, M.; Negm, A.; Savedra, O.C. The Effect of potential Discharges on the Stability of the Rosetta Promontory, Egypt. *J. Geogr. Tech.* **2014**, *2*, 6976.

57. Negm, A.; Masria, A.; Iskender, M.; Savedra, O.C. Towards a Sustainable Stability of Coastal Zone at Rosetta Promontory/Mouth, Egypt. *Oceanography* **2015**, *3*, 132. [CrossRef]

58. Pranzini, E.; Anfuso, G.; Cinelli, I.; Marco Piccardi, M.; Vitale, G. Shore Protection Structures Increase and Evolution on the Northern Tuscany Coast (Italy): Influence of Tourism Industry. *Water* **2018**, *10*, 1647. [CrossRef]

59. Saı¨di, H.; Souissi, R.; Zargouni, F. Environmental Impact of Detached Breakwaters on the Mediterranean Coastline of Soliman (NE of Tunisia) end. *Fis. Acc. Lincei* **2012**, *23*, 339–347. [CrossRef]

60. Zidan, A.R.; Rageh, O.S.; Sarhan, T.E.; Esmail, M. Effect of Breakwaters on Wave Energy Dissipation: Case Study, Ras El-Bar beach, Egypt. *Int. Water Technol. J.* **2012**, *2*, 268–283.

61. Saengsupavanich, C. Detached Breakwaters: Communities' Preferences for Sustainable Coastal Protection. *J. Environ. Manag.* **2013**, *115*, 106–113. [CrossRef] [PubMed]

62. Bitan, M.; Zviely, D. Sand Beach nourishment: Experience from the Mediterranean Coast of Israel. *J. Mar. Sci. Eng.* **2020**, *8*, 273. [CrossRef]

63. Brand, E.; Ramaeker, G.; Lodder, Q. Dutch Experience with Sand Nourishments for Dynamic Coastline Conservation- An Operational Overview. *Ocean Coast. Manag.* **2022**, *217*, 106008. [CrossRef]

64. Enríquez, A.R.; Marcos, M.; Falqués, A.; Roelvink, D. Assessing Beach and Dune Erosion and Vulnerability under Sea Level Rise: A case Study in the Mediterranean Sea. *Front. Mar. Sci.* **2019**, *6*, 4. [CrossRef]

65. Iskader, M. Stability of the Northern coast of Egypt under the effect of urbanization and climate change. *Water Sci.* **2021**, *35*, 1–10. [CrossRef]

66. El-Banna, M. Nature and human impact on Nile Delta coastal sand dunes, Egypt. *Environ. Geol.* **2004**, *45*, 690–695. [CrossRef]

67. El-Banna, M. Vulnerability and Fate of a Coastal Sand Dune Complex, Rosetta-Idku, northwestern Nile Delta, Egypt. *Environ. Geol.* **2008**, *54*, 1291–1299. [CrossRef]

68. Della Bella, A.; Fantinato, E.; Scarton, F.; Buffa, G. Mediterranean Developed Coasts: What Future for the Foredune Restoration? *J. Coast. Conserv.* **2021**, *25*, 49. [CrossRef]

69. Hasan, E.; Khan, S.I.; Yang, H. Investigation of Potential Sea Lvel Rise Impact on the Nile Delta, Egypt using Digital Elevation Models. *Environ. Monit. Assess.* **2015**, *187*, 649. [CrossRef] [PubMed]

70. El-Quilish, M.; El-Ashquer, M.; Dawod, G.; El Fiky, G. Development of an Inundation Model for the Northern Coastal Zone of the Nile Delta Region, Egypt Using High-Resolution DEM. *Arab. J. Sci. Eng.* **2022**. [CrossRef]

71. Polonia, A.; Vaiani, S.C.; Lange, G.J. Did the A.D. 365 Crete Earthquake/Tsunami Trigger Synchronous Giant Turbidity Currents in the Mediterranean Sea? *Geology* **2016**, *44*, 191–194. [CrossRef]

72. Rateb, A.; Abotalib, A.Z. Inferencing the Land Subsidence in the Nile Delta using Sentinel-1 Satellites and GPS between 2015 and 2019. *Sci. Total Environ.* **2020**, *729*, 138868. [CrossRef] [PubMed]

73. El-Bastawesy, M.; Cherif, O.H.; Sultan, M. The Geomorphological Evidences of Subsidence in the Nile Delta: Analysis of High Resolution Topographic DEM and Multi-temporal Satellite Images. *J. Afr. Earth Sci.* **2017**, *136*, 252–261. [CrossRef]

74. Gebremichael, E.; Sultan, M.; Becker, R.; El-Bastawesy, M.; Cherif, O.H.; Emil, M. Assessing Land Deformation and Sea Encroachment in the Nile Delta: A Radar Interferometric and Inundation Modeling Approach. *J. Geophys. Res. Solid Earth* **2018**, *123*, 3208–3224. [CrossRef]

75. Saleh, M.; Becker, M. New estimation of Nile Delta Subsidence Rates from InSAR and GPS Analysis. *Environ. Earth Sci.* **2019**, *78*, 6. [CrossRef]

76. Hassaan, M.A.; Abdrabo, M.A. Vulnerability of the Nile Delta Coastal Areas to Inundation by Sea Level Rise. *Environ. Monit. Assess.* **2013**, *185*, 6607–6616. [CrossRef]

Article

Characterization of Hydrologic Sand and Dust Storm Sources in the Middle East

Ramin Papi [1,2], Sara Attarchi [1,*], Ali Darvishi Boloorani [1,*] and Najmeh Neysani Samany [1]

1   Department of Remote Sensing and GIS, Faculty of Geography, University of Tehran, Azin Alley. 50, Vesal Str, Tehran 11369, Iran
2   National Cartographic Center (NCC), Meraj Alley, Azadi Square, Tehran 11369, Iran
*   Correspondence: satarchi@ut.ac.ir (S.A.); ali.darvishi@ut.ac.ir (A.D.B.)

Abstract: Due to diverse hydroclimatic conditions and human interventions, the Middle East hosts a variety of active sources of sand and dust storms (SDS). Discrimination of different types of SDS sources is the most important factor for adopting optimal mitigation measures to combat SDS. This study employed a binary mask-based modeling framework to identify Middle East SDS sources. Accordingly, using time series of remotely sensed data of land surface and atmospheric aerosol parameters, SDS sources covering an area of 1 million Km^2 were identified with an overall accuracy of 82.6%. Considering the type of land use and spatial-temporal changes in water bodies, SDS sources were categorized into seven types in terms of origin. Desert sources have the largest share (>79%), whereas hydrologic sources accounted for about 8.4%. The results showed that water bodies had a declining trend after 2000. The occurrence of two severe drought periods in 2000–2001 and 2007–2012 led to a 52% decrease in water bodies and a 14–37% increase in SDS emission compared to the pre-2000 period. The latter drought period also led to a sharp decrease in groundwater resources across the region. Our results revealed that natural circumstances and drought actively contribute to the depletion of water resources that led to the formation of SDS sources in the Middle East, while the role of anthropogenic factors is predominant in the case of hydrologic SDS sources.

Keywords: sand and dust storms; hydrology; surface and ground water changes; spatial-temporal analysis; remote sensing; Middle East

1. Introduction

Middle East (ME) is the most affected region by climate change with a significant contribution (15–20%) to global SDS emission [1]. Accordingly, as a prominent feature of this region, SDS has affected climatic parameters [2,3], human health [4,5], socio-economic factors [6], and terrestrial and marine ecosystems [7]. ME is the second most SDS-affected region in the world after North Africa. Considering its location within the subtropical high-pressure belt of the Northern Hemisphere and its expansive deserts [8], ME is experiencing SDS events in hot and dry seasons. However, the maximum activity period varies in different regions of ME. SDS events generally occur in the northwestern parts of the region in winter and spring. In addition, the most intense events form in the southwestern parts of the region in the summer [9].

SDS events are driven by a mixture of natural and anthropogenic factors [10]. Natural factors such as topographic diversity, climatic variability, and several seasonal effective air masses have created a highly complex situation in this region [11]. With mean annual precipitation of less than 200 mm, most parts of the Middle East suffer from dry and semi-arid climates. Therefore, water scarcity has been a lasting problem in the region with serious consequences for the stability and development of the region's economy [12]. The spatial-temporal patterns of precipitation and temperature vary to a great extent across the region with over 1800 mm along the Caspian Sea in Northern Iran and zero annual precipitation in

some desert areas in Central Iran and Saudi Arabia [11]. In addition to climatic conditions, global warming, climate change, and drought occurrence have intensified the spatial-temporal frequency of SDS events in the region [13,14]. Mismanagement of water, soil, and vegetation resources in different parts of the ME, especially in Iran, Iraq, Syria, and Turkey are recounted as anthropogenic factors affecting the SDS occurrence and intensity over the past few decades [13,15].

Numerous studies have explored the identification of the ME SDS sources, mostly identifying local scale sources in, e.g., Khuzestan [16] and Razavi Khorasan [17] provinces in Southwestern and Northeastern Iran, respectively. Other studies have been conducted on the catchment scale, for instance, the Euphrates River Basin [18], the Central Iran Basin [15], and the Tigris and Euphrates Rivers Basin [19,20]. Rashki et al. 2021 [21] identified and characterized the SDS sources in Iran on a national scale. Some studies such as [22–25] investigated ME SDS sources on a regional scale. As reported in the literature and by [10], the highest density of SDS sources is in the northern and northwestern parts of Iraq between the Tigris and Euphrates rivers and along the Syrian–Iraqi border. Considering the location of the mountains and the direction of the dominant regional wind (Shamal wind) [26], these sources affect Iraq as well as Iran and Kuwait, in the spring and summer. These sources are generally located in lands with extensive desert cover, low population density, and sparse agriculture along rivers. Iraq, Saudi Arabia, and the Persian Gulf margins, respectively, experience the greatest number of SDS events [10].

SDS occurrence is essentially a function of geographic and hydroclimatic conditions. Therefore, SDS sources located in different geographical regions may have different origins and types. Furthermore, various environmental parameters such as wind speed, evapotranspiration, precipitation, soil physicochemical properties (e.g., soil moisture, texture, and organic matter), vegetation cover, and topography are known as effective SDS drivers [19]. These drivers are interactively involved in the formation of SDS. For instance, water resources affect vegetation cover and are recognized as an essential factor in SDS emission [27]. Water bodies (e.g., rivers, wetlands, and permanent and seasonal lakes) accumulate fine-grained sediments, which are highly susceptible to wind erosion. These erodible lands are so-called "hydrological SDS sources". As confirmed by the literature, changes in water resources (e.g., Urmia Lake [28,29], Hamoun Lakes [30,31], and Iraq's lakes and wetlands [13]) have played a key role in the Middle East SDS emission. Therefore, it can be argued that the hydrological cycle parameters (e.g., precipitation, surface runoff, evapotranspiration, soil moisture, river flows, and surface water and groundwater resources [32]) have a determining role in the formation of SDS sources, which calls for further investigations.

A wide range of natural and anthropogenic factors contribute to the formation of SDS sources in the ME [22]. In addition to the identification of SDS sources, discriminating between types of sources is an essential way to adopt mitigation measures. Discrimination and characterization of SDS sources can provide useful information for better understanding and management of this environmental hazard. In this regard, at the basin scale, recently [15] identified SDS sources in Central Iran using remote sensing data and characterized them in terms of their origin. SDS is naturally a highly dynamic phenomenon driven by the large-scale interactions of environmental parameters of Earth's ecosystems, which highlights the importance of identifying SDS sources at the regional scale. In [22], the authors identified the ME SDS sources and categorized them by their origin on a regional scale using atmospheric aerosol indices. This approach relied on the thresholding of atmospheric aerosol indices, which is not accurate enough and so the location of the identified sources is not entirely reliable.

Remote sensing methods are equipped with special capabilities for spatial-temporal modeling of SDS from the local [15] to global scales [33,34]. Previous studies have developed different approaches for SDS source identification using remote sensing data. They can be in three categories, namely aerosol loading-based [35], spectral indices-based [36], and susceptibility mapping [19]. Some innovative approaches have recently been devel-

oped, including the multi-step binary masking approach proposed by [15]. This approach benefits from not only simplicity but also provides more acceptable results considering the inclusion of the main SDS drivers and atmospheric aerosol indices in the modeling process.

Considering the effects of water resources on SDS activity in the Middle East, the main goal of this study is to identify hydrologic SDS sources. To achieve this goal, SDS sources are identified and then categorized based on their origin. Then, the long-term changes in surface and ground water in the hydrologic SDS sources are analyzed.

2. Materials and Methods

Methodology

As illustrated in Figure 1, the developed methodology to characterize hydrological SDS sources of the Middle East using remote sensing data can be summarized in three main steps. In the first step, SDS sources were identified by using a combination of atmospheric aerosol indices and land surface parameters (e.g., vegetation cover, wind speed, soil moisture, and soil sediment thickness) based on a multi-step masking approach. The second step involved categorizing the identified SDS sources in terms of their origin and type based on different land cover classes. In the final step, focusing on hydrologic SDS sources, spatial-temporal patterns of changes in surface and ground water resources were analyzed.
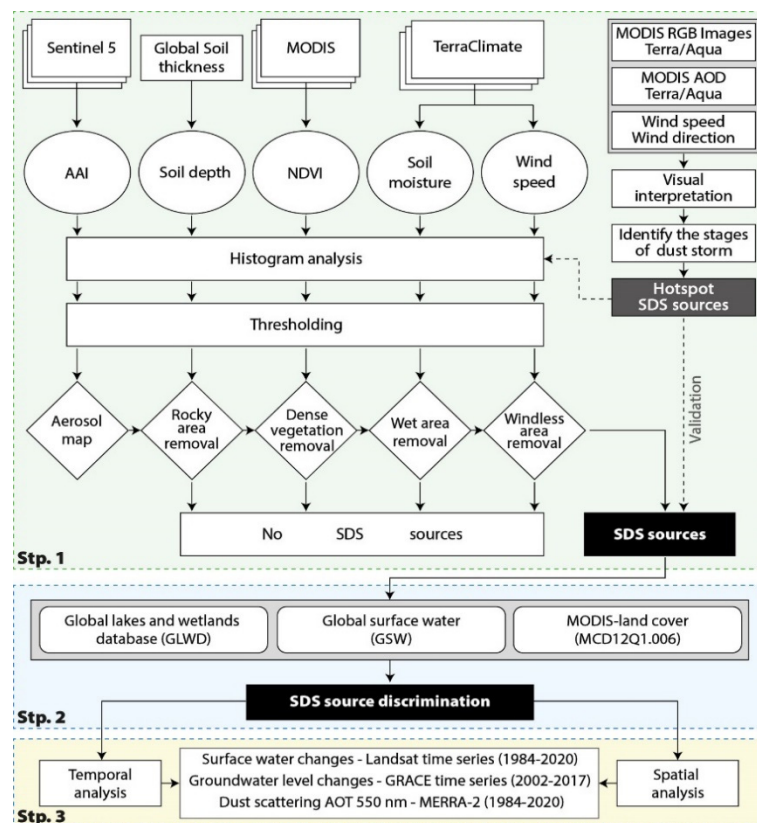
Figure 1. Stepwise approach to characterize hydrologic SDS sources of the Middle East.

- *Identifying SDS sources (Stp. 1)*

This study used a multi-step binary masking procedure [15] to identify SDS sources in the Middle East. In general, SDS sources are associated with long-term dense atmospheric aerosol content. However, a high aerosol content does not necessarily correspond to an SDS source. As [15] acknowledged, taking advantage of the spatial-temporal patterns of effective environmental parameters (i.e., SDS drivers) in combination with satellite atmospheric aerosol indices in a modeling framework can be useful to improve the accuracy

of identified SDS sources. Because in this way, the long-term conditions of the atmosphere and the Earth's surface are simultaneously considered to identify SDS emission sources. Accordingly, the preliminary SDS sources map was produced using atmospheric aerosol indices. Then, the accurate SDS sources map was generated by accounting for other effective SDS drivers through binary masks.

Sentinel 5 satellite was launched on 13 October 2017, by ESA to perform atmospheric measurements to be used for air quality, ozone, and UV radiation, and climate monitoring and forecasting. By thresholding, the mean absorbing aerosol index (AAI) of the Sentinel 5 (OFFL/L3_AER_AI) in the period from 11 July 2018 to 1 June 2022, the preliminary SDS sources map was generated. AAI is an aerosol index based on wavelength-dependent changes in the UV radiation for a specific wavelength pair (354 and 388 nm) during Rayleigh scattering. It is calculated from the difference between the observed top of the atmosphere reflectance and the modeled reflectance (the theoretical reflectance calculated from an atmosphere with only Rayleigh scattering). Positive values of AAI indicate the existence of UV-absorbing aerosols such as dust and smoke in the atmosphere. Moreover, ozone absorption is extremely low in the wavelengths used to produce the AAI product. Unlike aerosol optical depth (AOD) measurements that are highly affected by cloud cover [37], the AAI can be calculated even in cloudy conditions [38]. The mean AAI map shows the overall spatial patterns of atmospheric aerosol over a four-year period in the study area. An appropriate threshold must be defined to separate SDS from other aerosols when attempting to identify SDS sources using atmospheric aerosol indices [39], since only high atmosphere aerosol content in a region could not be an accurate indicator for identifying the emission sources. Therefore, surface SDS drivers must be considered to identify accurate SDS sources.

To identify SDS sources, it could be assumed that future sources will be created by the same past drivers and conditions [17]. Various environmental parameters play a role in the formation of SDS sources [40]. There is no specific rule for choosing these drivers [17]. In this study, the most important drivers including vegetation status, wind speed, soil moisture, and soil sediment thickness, which are mainly employed in the literature, were considered. Accordingly, MODIS 16-day normalized difference vegetation index (NDVI) (1 km spatial resolution) (MOD13A2.v006), TerraClimate monthly average 10 m wind speed and monthly soil moisture (4 km) [41], and global 1 km gridded thickness of soil [42] were used as SDS drivers. The 4-years mean maps (11 July 2018 to 1 June 2022) were obtained for all parameters except for soil thickness. There are four main stages in SDS formation from an emission source: start, maximum lifting, cutoff, and dispersion. Satellite imagery can be used to identify SDS sources with high accuracy in the initial stages (start and maximum lifting) via visual interpretation. By creating a color composite image (RGB), SDS events and their emission sources can be discriminated from other phenomena in the satellite image through image interpretation keys, including shape, size, pattern, tone, texture, etc. Based on the approach proposed by [19], a total of 1014 SDS hotspots were identified via visual interpretation of MODIS-Terra/Aqua sub-daily true-color composite images (RGB$_{143}$) from 2018 to 2022 (Figure 2). Here, 70% of SDS hotspots were used as training samples for histogram analysis and determining appropriate thresholds for generating preliminary SDS sources maps and binary masks from SDS drivers. Histogram slicing and thresholding were performed based on the histograms of SDS drivers in hotspots. The appropriate thresholds were determined at the 99% confidence interval, and values outside this interval were assumed to be errors or outliers. Accordingly, the maps of SDS drivers were separated into two binary classes 0 (no SDS) and 1 (SDS). In the next step, the bitmaps were masked from the preliminary SDS sources to obtain the accurate SDS sources map, which was validated using the remaining 30% of SDS hotspots.
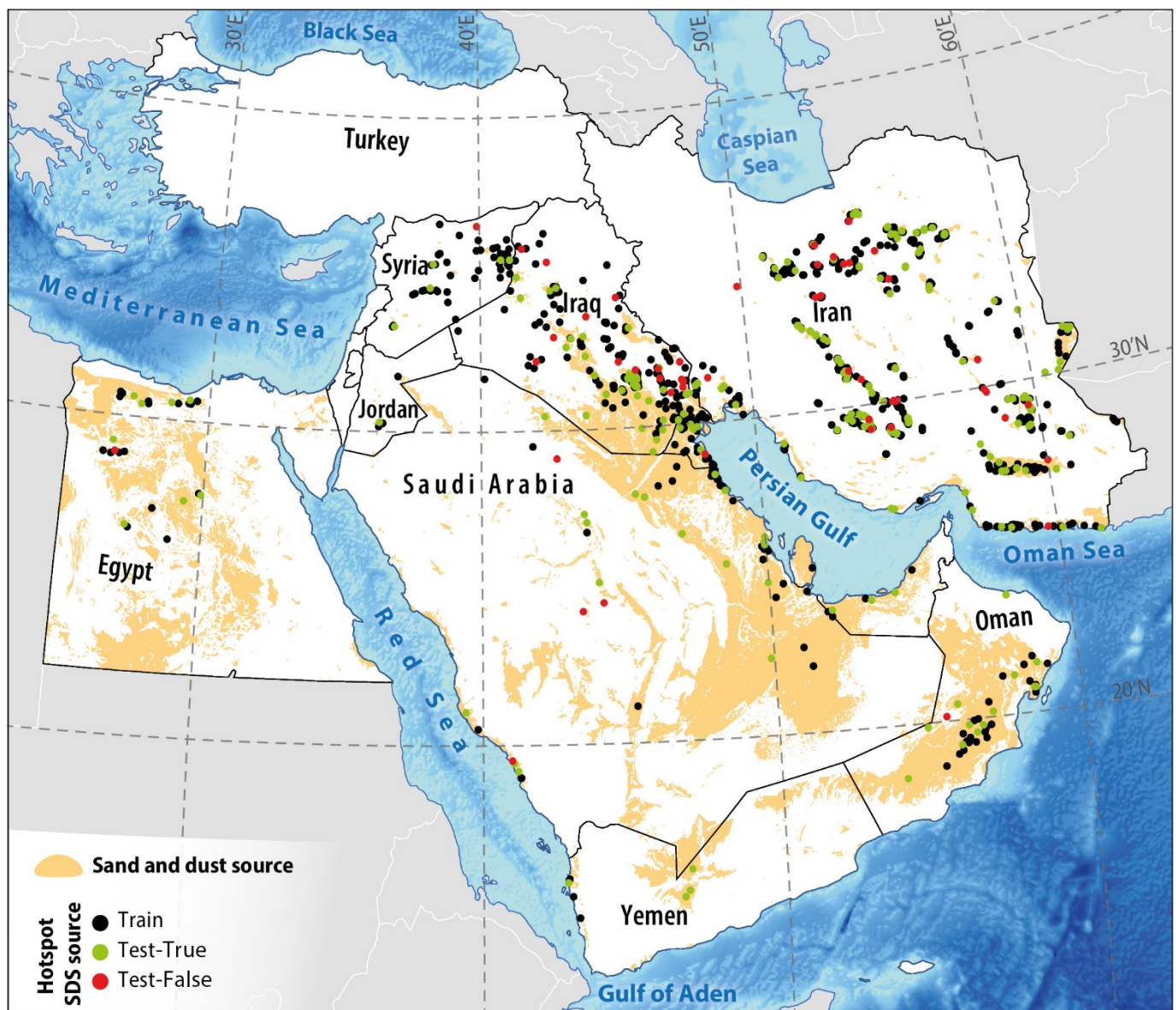
Figure 2. SDS sources of Middle East. The colored solid dots are SDS hotspots identified using visual interpretation of MODIS-RGB images used for histogram analysis (70%: black dots) and accuracy assessment (30%: green and red dots).

- *SDS Source Discrimination (Stp. 2)*

The global lakes and wetlands database (GLWD), global surface water (GSW), and MODIS-land cover 2020 map (MCD12Q1.006) were used to attribute the identified SDS sources to the land cover type and surface conditions. GLWD is obtained from an aggregation of the best maps, data, and information available for global-scale lakes and wetlands using GIS functions [43]. GSW was produced using the time series of Landsat 5, 7, and 8 images from 16 March 1984 to 31 December 2020. Each pixel is classified into water and no-water classes using an expert system. The monthly GSW data available from 1984–2020 are applicable to change detection purposes [44]. The change detection map demonstrates the spatial-temporal pattern of changes in surface water. This makes it possible to identify intermittent lakes and wetlands and discriminate the corresponding SDS sources.

The identified sources were discriminated in terms of origin by overlaying the SDS sources map on different land cover classes. Ephemeral water bodies (wetlands, lakes, and rivers) contribute to SDS emissions [13]. Therefore, GLWD and GSW products were used

to discriminate hydrologic SDS sources. Here, hydrologic SDS sources correspond to the margins and beds of permanent, seasonal, and dried lakes, wetlands, and rivers. Coastal SDS sources were discriminated by proximity analysis based on shorelines.

- *Surface and ground water changes (Stp. 3)*

Surface and ground water resources in hydrologic SDS sources were analyzed through Landsat and Gravity Recovery and Climate Experiment (GRACE) satellite data. The normalized difference water index (NDWI) [45] based on Landsat 5, 7, and 8 data from 1984 to 2022 was used to extract surface water and assess their spatial-temporal changes. In this index, values greater than zero are assumed as water [45].

Monitoring of the groundwater changes based on GRACE data was performed through three products from different data processing centers, namely CSR (UT Center for Space Research), GFZ (GeoForschungsZentrum Potsdam), and JPL (NASA Jet Propulsion Laboratory) [46]. These centers are part of the GRACE Ground System and produce the level 2 data used in this dataset. The values of these three products are slightly different. Therefore, the average of these products from April 2002 to July 2017 was used to detect the spatial-temporal changes in the underground water level.

3. Results

3.1. Identification and Attribution of SDS Sources

Histogram analysis based on reference SDS hotspots (Figure 2) was performed and the thresholds of 0, 0.15, 2.7 m/s, 5 mm, and 3 m at a 95% confidence level were determined for AAI, NDVI, wind speed, soil moisture, and soil thickness, respectively. Based on the thresholding of the average AAI map, a preliminary SDS sources map was produced for the Middle East. The binary masks of SDS drivers were then multiplied in the preliminary SDS sources map to obtain the accurate SDS sources (Figure 2). By using the reference SDS hotspots, the overall accuracy of the SDS sources map was obtained at 82.6%, which shows the reliability of the results. The green dots (Figure 2) are SDS hotspots that correspond correctly to the identified SDS sources. In contrast, the red dots are incorrectly identified as SDS sources. Despite the acceptable accuracy, it is worth noting that uncertainty is an inevitable part of modeling process. However, the precise amount for each independent parameter is unknown. Nevertheless, the accuracy assessment shows the overall uncertainty (17.4%) imposed on the model by the input parameters. Finally, the SDS sources were categorized into seven groups in terms of origin and type (Figure 3).

Table 1 shows the area of identified SDS sources by type and country. The largest and smallest sources corresponded to the desert (~79.1%) and coastal wetland (~0.9%), respectively. Saudi Arabia hosted the largest SDS sources (~41%) in the Middle East.

According to Figure 3, hydrologic SDS sources include permanent lake, intermittent lake/wetland, and freshwater marsh & floodplain classes. Coastal wetlands are also considered SDS sources with a hydrological origin. They are not highly affected by human activities and climatic events (e.g., drought) since they can benefit from seawater, unlike other hydrologic sources. Therefore, coastal wetlands were considered independently in this study. In terms of area, in total, hydrologic SDS sources cover 8.4% of the ME, of which the largest area (~5.9%) is corresponding to intermittent lake/wetland (Table 1). Intermittent lake/wetland SDS sources were identified in all countries listed in Table 1 with the largest area belonging to Iran (~41%). Meanwhile, permanent lake SDS sources were observed only in Iran (~68%), Iraq (~26%), and Syria (~6%). Freshwater marsh & floodplain sources were observed only in Iraq (~77%) and Iran (~23%). Overall, Iran (41%), Iraq (21%), Oman (14%), and Saudi Arabia (13%) have the largest area of hydrologic SDS sources (Table 1). Sources in Oman and Saudi Arabia correspond to only the intermittent lake/wetland class.
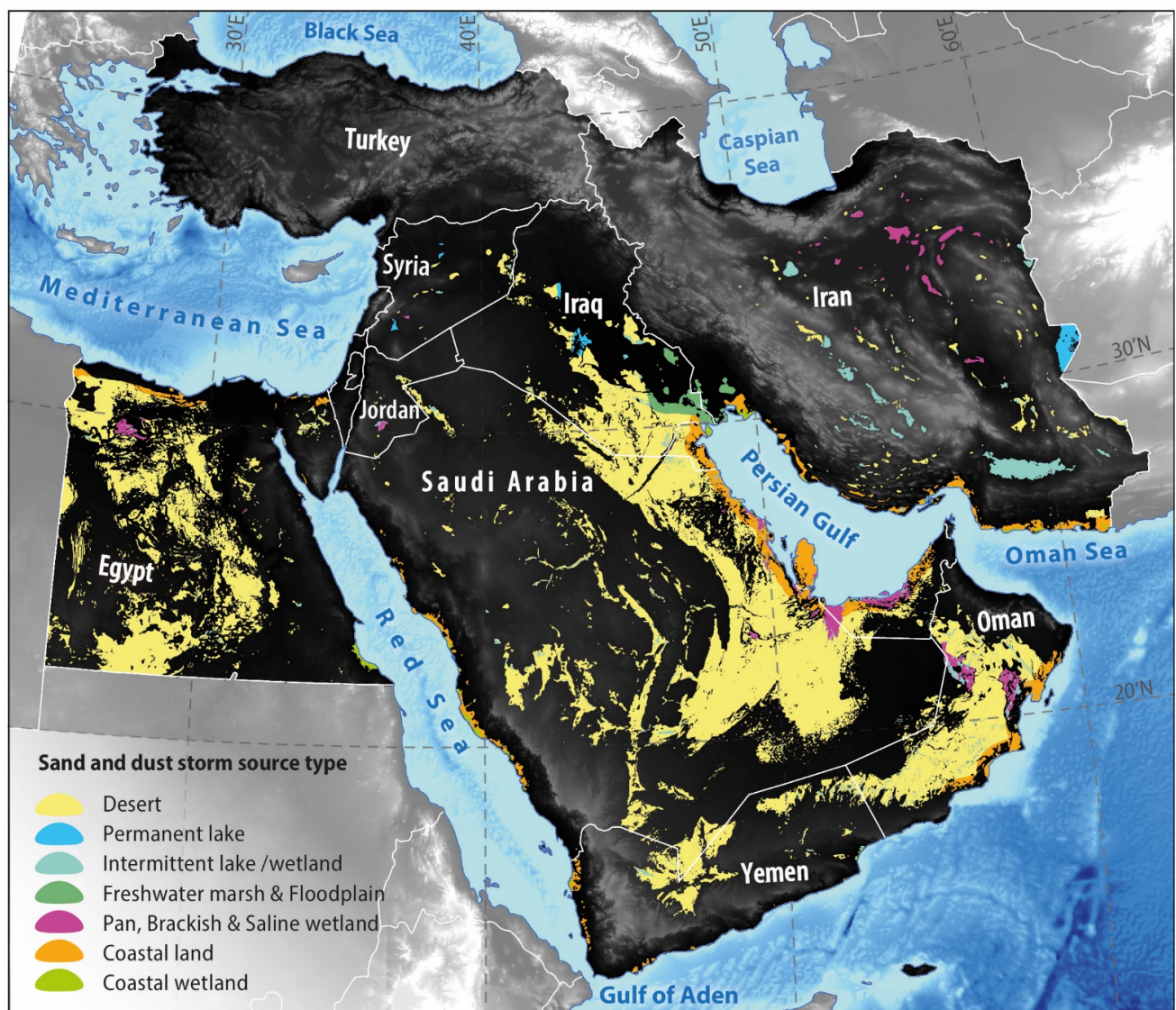
Figure 3. SDS source discrimination in the Middle East in terms of origin.

Table 1. The area (km²) of different types of SDS sources in the Middle Eastern countries.

Country	Desert	Permanent Lake	Freshwater Marsh & Floodplain	Coastal Wetland	Pan, Brackish & Saline Wetland	Intermittent Lake/Wetland	Coastal Land	Total	%
Bahrain	-	-	-	12	-	31	43	86	<0.1
Egypt	201,503	-	-	1938	3068	2755	6476	215,739	19.9
Iran	14,934	7362	3685	2972	9555	26,392	16,000	80,899	7.5
Iraq	74,858	2834	12,282	-	-	3974	695	94,643	8.8
Jordan	936	-	-	-	999	440	30	2406	0.2
Kuwait	5972	-	-	743	-	395	6042	13,152	1.2
Oman	108,898	-	-	415	10,977	13,192	12,572	146,053	13.5
Qatar	-	-	-	148	372	241	8417	9179	0.9
Saudi Arabia	396,711	-	-	2720	7528	12,117	24,562	443,639	41
Syria	3039	698	-	-	157	522	-	4416	0.4
UAE	10,980	-	-	-	7137	805	6843	25,765	2.4
Yemen	38,386	-	-	448	-	3531	3434	45,800	4.2
Total	856,215	10,894	15,966	9397	39,793	64,397	85,114	1,081,776	100
%	79.1	1.0	1.5	0.9	3.7	5.9	7.9	100	

3.2. Temporal Analysis of Surface and Ground Water Changes in Hydrologic SDS Sources

The temporal pattern of water area changes in the ME lakes and wetlands was extracted using the long-term data archive (1984–2022) of Landsat 5, 7, and 8 satellites (Figure 4). The temporal pattern of SDS in the same period was obtained using the reanalysis MERRA-2 dust scattering AOT 550 nm, monthly 0.5 × 0.625 deg product (Figure 4).
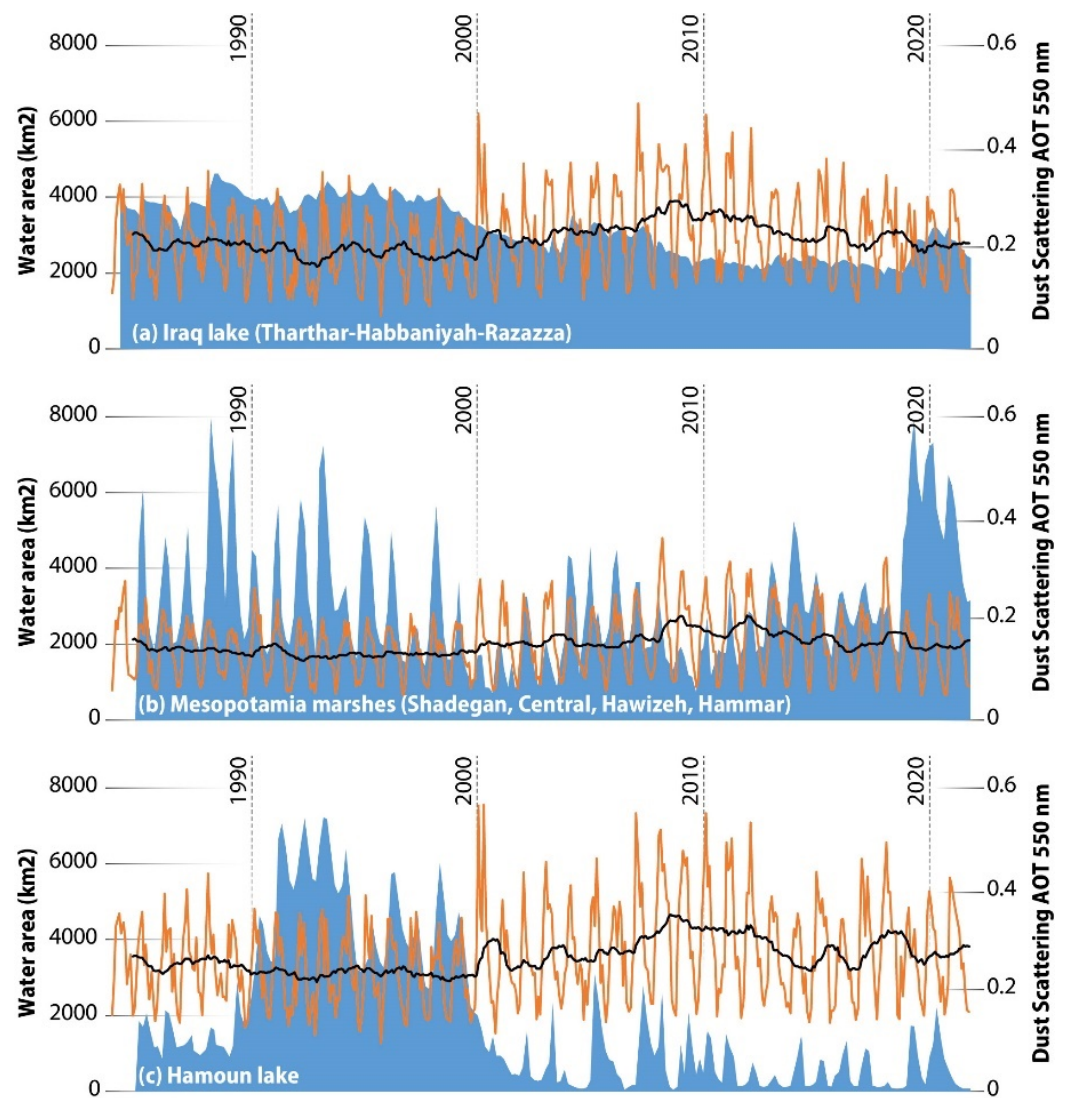
Figure 4. The temporal pattern of changes in water bodies and SDS levels in the Middle East. Blue graph shows the surface water area changes and the brown and black graphs are dust scattering and its moving average, respectively.

As shown in Figure 4a,c, the lakes generally had an increasing trend before 2000 and a decreasing trend after 2000. The first drop in the lakes area occurred in the 2000–2001 period. The second drop can be seen from 2007 onwards, which continued nearly until 2012. Disregarding the seasonal changes, Mesopotamian wetlands exhibited an almost steady trend in the pre-2000 period (Figure 4b). Still, a decreasing trend can be seen since the 1990s, with the highest reduction observed in 2001. From 2003 to 2007, there has been a moderate increasing trend, which again reversed after this period. The second sharp drop occurred in 2008–2009 period and continued until 2012. A sharp and sudden increase can be seen after 2019 in Iran and Iraq due to the increase in rainfall and floods [47].

Dust scattering AOT temporal pattern shows a smaller change in the pre-2000 compared to the post-2000 period. In terms of seasonal patterns, extreme peaks can be seen after

2000, especially in spring and summer (brown graph in Figure 4). Regardless of seasonal changes, as indicated by the dust-scattering AOT moving average (black graph in Figure 4), SDS has increased by an average of 18.4% since 2000.

The correlation between changes in water bodies and SDS was calculated at −0.72, −0.64, and −0.39 for Iraqi lakes, Mesopotamian wetlands, and Hamoun Lake, respectively. Negative values indicate an inverse correlation between water body changes and SDS. The correlation is high for Iraqi lakes and Mesopotamian wetlands while it is low for Hamoun Lake. The correlation analysis showed an inverse but not very strong relationship between the area of water bodies and SDS emission.

Figure 5 shows the Mann–Kendall test for trend analysis of surface water area and dust scattering AOT. Where the z-value equal to −3.15 indicates that surface water has experienced a decreasing trend, while 3.18 for dust scattering AOT shows an increasing trend. These findings are approved by the Sen's estimate lines of both graphs.
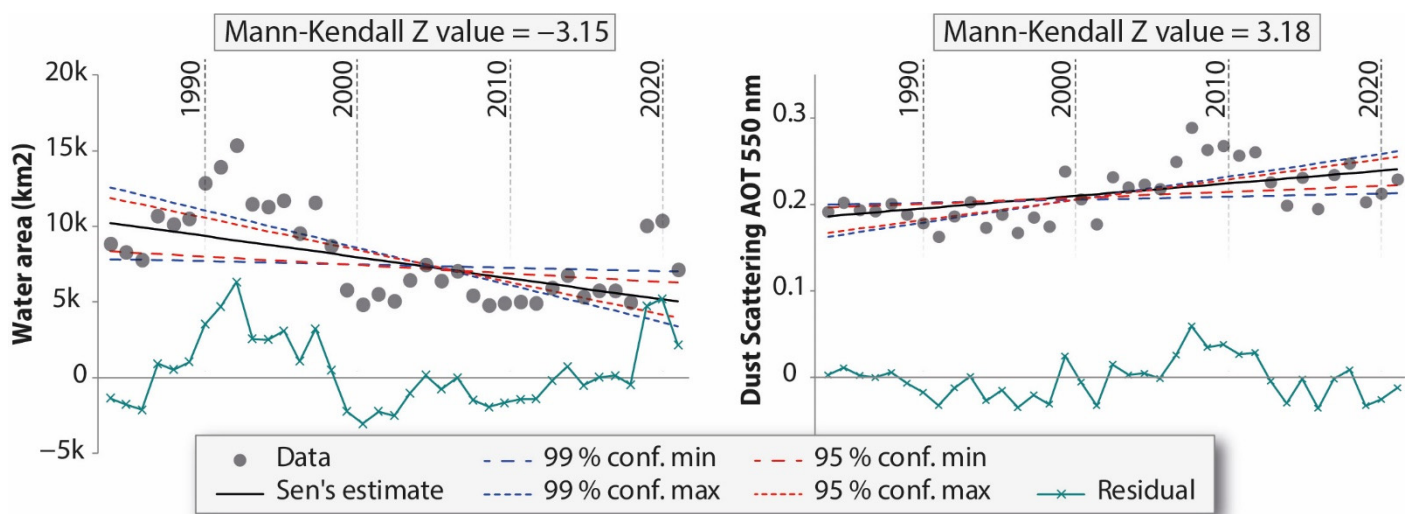
Figure 5. Mann–Kendall test for trend analysis of surface water area and dust emission AOT.

Figure 6 shows the temporal pattern of monthly changes in the groundwater level using GRACE data for SDS sources. The temporal signals of groundwater level changes in SDS sources indicate a high correlation. Accordingly, all SDS sources, except for freshwater marsh & floodplain, had an almost identical temporal change pattern, but their levels of change are different. Overall, a clear decreasing trend can be seen in the groundwater level of the ME SDS sources since 2008. The highest negative changes occurred in hydrologic SDS sources, particularly in freshwater marsh & floodplains. The least changes were observed in desert sources.
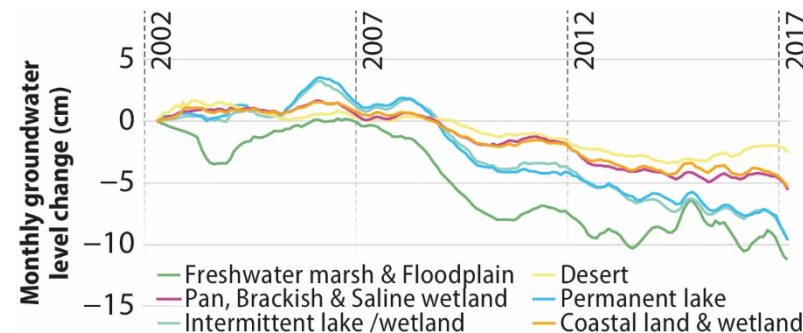
Figure 6. Temporal pattern of groundwater level changes in the Middle East SDS sources obtained from GRACE monthly data.

3.3. Spatial Analysis of Surface and Ground Water Changes in Hydrologic SDS Sources

The spatial pattern of changes in the surface water area (including lakes, wetlands, and rivers) was acquired for two periods before 2000 (1984–1999) and after 2000 (2000–2020) using GSW data (Figure 7a). The increasing and decreasing changes are illustrated in blue and red, respectively. As shown in Figure 7b, the highest changes in surface water occurred in Iran, Iraq, Turkey, and Egypt, respectively. In Iran, negative changes were roughly three times more than positive changes. For Iraq, negative changes were almost twice the positive changes. For all countries except Egypt, the decrease in surface water was greater than the increase. Negative changes in surface water in Iran were about 30% more than in Iraq, twice as much as in Turkey, and three times as much as in Egypt. The highest density of surface water changes was detected in the hydrologic SDS sources of Iraq, especially the southwestern areas and Mesopotamian wetlands (Figure 7a).
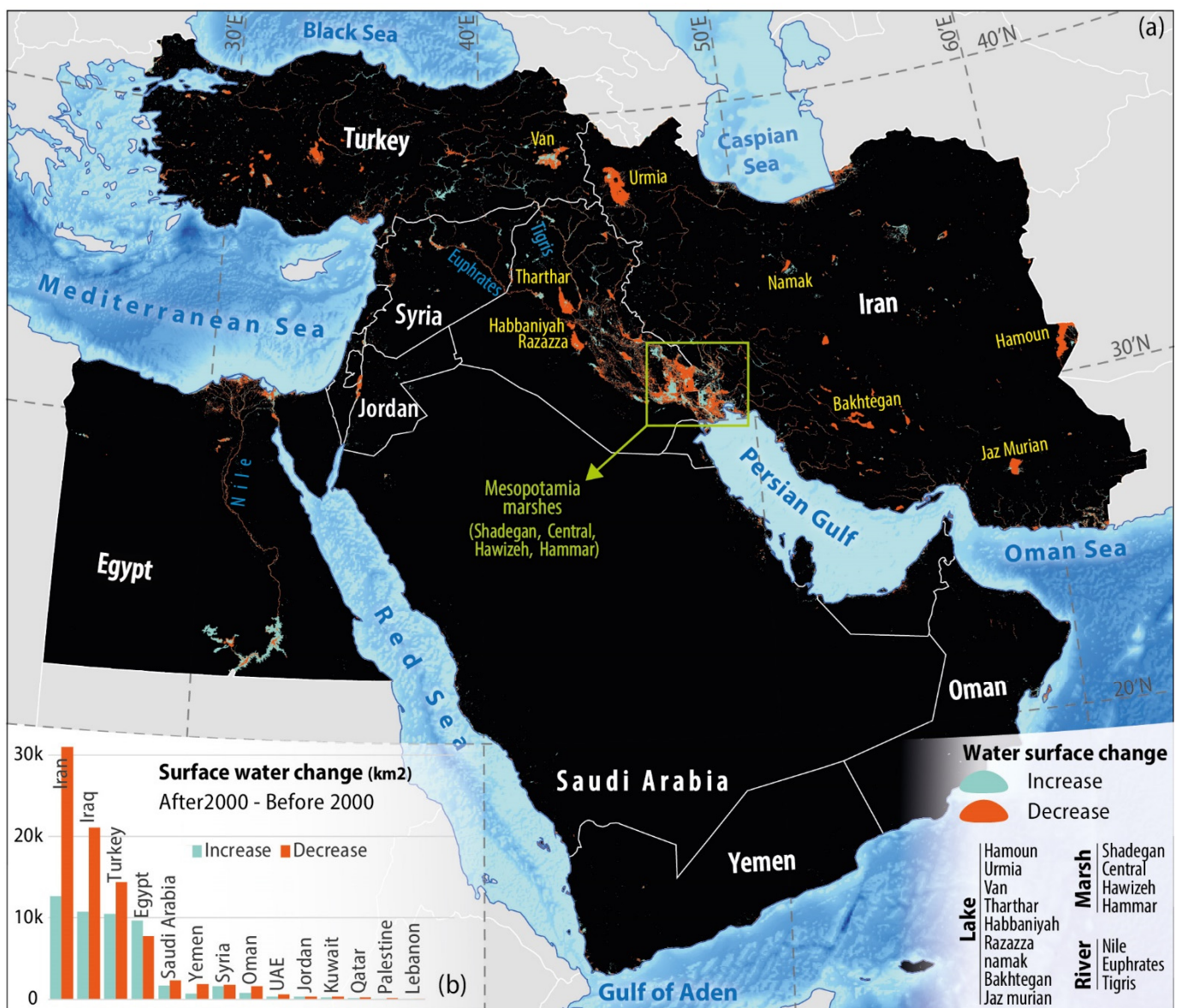
Figure 7. Changes in the surface water area of the Middle Eastern hydrologic SDS sources based on GSW data (**a**) and surface water area changes by country (**b**).

The spatial pattern of total groundwater level changes in the Middle East was extracted from April 2002 to July 2017 (Figure 8a). The variation of groundwater level in this

period is between −10 and +3 m. The highest decrease and increase in groundwater level were observed for the northwestern regions of Iran and the western regions of Turkey, respectively. In hydrologic SDS sources, the groundwater level has mainly decreased. On the other hand, the spatial pattern of the groundwater level shows far fewer changes in desert SDS sources. Groundwater level changes by country are presented in Figure 8b. On average, the highest drop in the groundwater level occurred in Iraq, Iran, and Syria, respectively. Additionally, the largest area of hydrologic SDS sources can be found in Iraq and Iran. In addition, permanent lakes and freshwater marsh & floodplain SDS sources are located only in these three countries. The lowest decrease in groundwater level occurred in Oman. Oman has the largest area of hydrologic SDS sources after Iran and Iraq (Table 1).
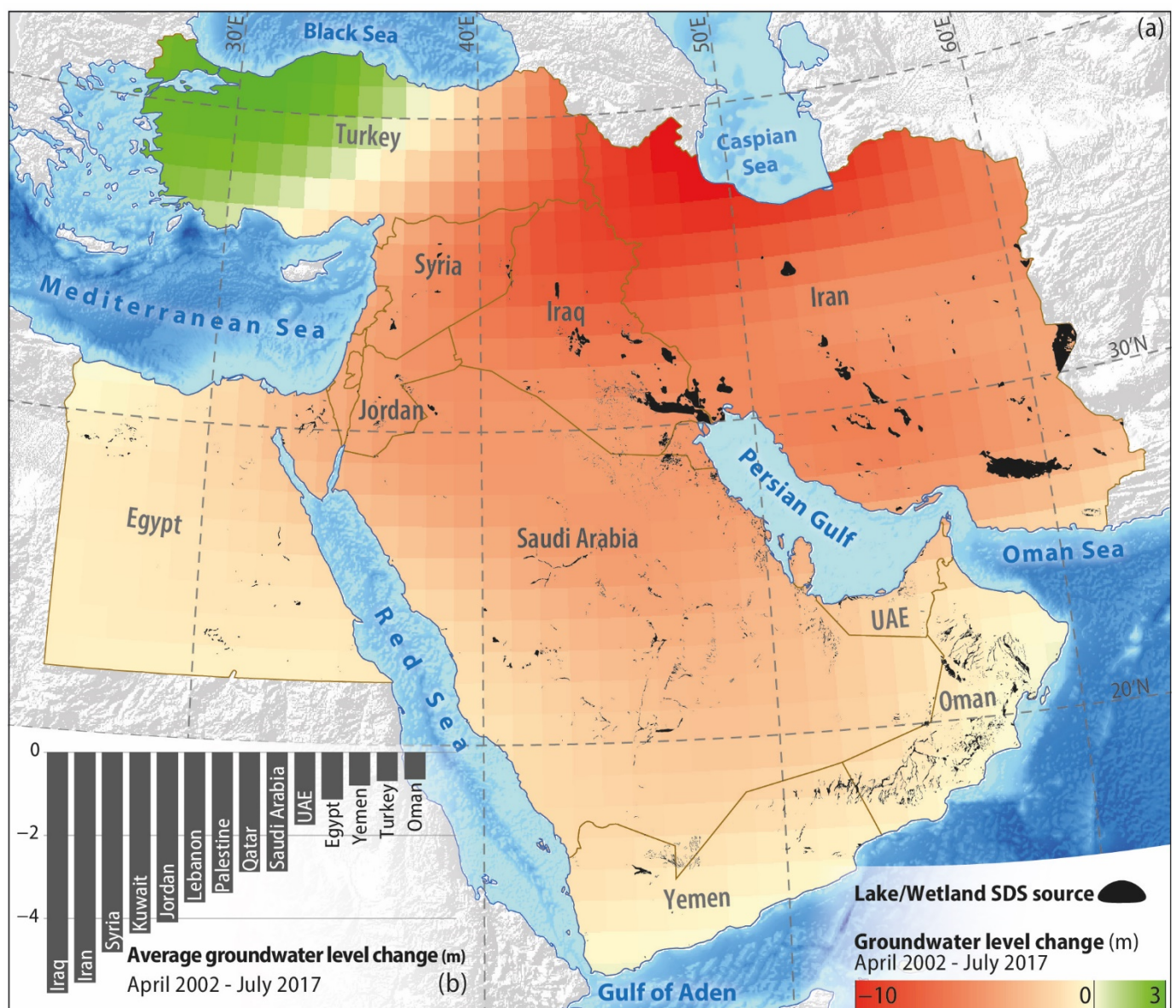
Figure 8. Groundwater level changes in the Middle East from April 2002 to July 2017, obtained from GRACE monthly data (**a**) and average changes by country (**b**).

4. Discussion

4.1. Characterization of Middle Eastern SDS Sources

The occurrence of SDS in different regions and from different emission sources exerts various impacts on the environment. Therefore, combating SDS in different sources requires specific mitigation measures [48]. Accordingly, an essential step for the proper management

of SDS sources is identifying the source type. In desert sources, for example, common mitigation measures include stabilizing soil surface by mulching, planting climate-compatible shrubs and trees, using windbreaks, creating mechanical and biological barriers (e.g., dead vegetation), and employing other soil and plant resource management methods [48]. On the other hand, hydrologic SDS sources, including lakes, wetlands, and rivers, demand water resource management [27,49]. Water resource management in countries with shared basins such as Iran, Iraq, Turkey, and Syria could be undertaken through joint efforts.

The accurate identification of SDS sources is considered a challenging task. In the last few decades, various approaches have been used to identify and discriminate the SDS sources in ME. Most of these approaches fall under the atmospheric aerosol loading-based category (e.g., [21,22,35]). In these approaches, a region with a high concentration of atmospheric aerosols is generally considered an SDS source. The aerosol loading-based approaches often detect SDS events regardless where they are emitted from. Due to the highly dynamic nature of SDS, detected events may originate from more distant regions. Accordingly, using only atmospheric aerosol indices such as AOD and AAI may lead to errors in modeling and significantly reduce the accuracy of identifying SDS sources. To tackle this problem, by considering the multi-year average of thresholded atmospheric aerosol indices and SDS drivers through a supervised approach (by taking advantage of the SDS hotspots identified by visual interpretation), it is possible to identify SDS sources with satisfactory accuracy. However, compared to previous studies that have identified SDS sources only based on aerosol indices, the present approach gives more reliable results.

Most of the Middle East is located within the global desert belt given its low annual precipitation [50]. Here, as the results showed, over 79% of the identified SDS sources are in the desert class. SDS sources of Saudi Arabia, Egypt, Oman, and Yemen are mainly sandy deserts. Those in Iran, Iraq (especially Mesopotamian wetlands), and Syria are generally composed of fine-grained alluvial sediments. The larger size of the sources does not essentially mean greater activity and SDS emission. Accordingly, despite the high area, desert SDS sources in Saudi Arabia, Egypt, Oman, and Yemen they have low activity in terms of SDS frequency and intensity. Previous studies indicate that the highest SDS activity occurs in the northern and northwestern parts of Iraq and along the Syrian–Iraqi border [25]. This issue is dependent on the source type, particle diameter, time, duration, and intensity of erosive winds. Fine-grained particles (e.g., SDS sources in the alluvial plains of Iran, Iraq, and Syria) are lightweight and are easily detached from the Earth's surface and lifted into the upper layers of the atmosphere, so they can travel over long distances [51]. These fine-grained SDS particles are easier to detect in satellite images due to their durability and the longer movement of the plume in the atmosphere.

The spatial-temporal analysis of water bodies showed that that both surface water (Figures 4 and 6) and groundwater (Figures 5 and 8) have decreased in the Middle East, which reveals the instability of the water balance conditions in the region. The results show that the water balance in hydrologic SDS sources is more negative than in other sources. In this regard, both surface water and groundwater resources have experienced severe reductions. Regarding coastal SDS sources, it is worth mentioning that these sources are influenced by the sea and its physicochemical reactions. Although they are considered hydrologic sources, reduction in their groundwater levels is not evident since they are recharged by the sea. Desert SDS sources have experienced much less groundwater depletion than other sources, which may be attributed to limited agricultural and low groundwater exploitation in these areas.

4.2. Influence of Drought on SDS Sources in Middle East

The long-term analysis of surface water changes in hydrologic SDS sources showed a relatively sharp decrease in the 2000–2001 and 2007–2012 periods compared to pre-2000. Further examination revealed that these two periods correspond almost to two very severe drought periods hitting the ME in the last 50 years [47,52]. As shown in Table 2, surface water resources in the first and second drought periods have decreased by 51% and 52.9%,

respectively, compared to the pre-2000. Hamoun Lakes have experienced a very severe decrease (over 72%) in both drought periods compared to other water bodies. Iraqi lakes and Hamoun Lake experienced a sharper decrease in the second period compared to the first. In contrast, the Mesopotamia wetlands show a lower decline in the second period.

Table 2. Surface water changes and dust scattering AOT from hydrologic SDS sources during drought periods.

	Name	Pre-2000	First Drought	Change in First Drought Compared to Post-2000 (%)	Second Drought	Change in Second Drought Compared to Pre-2000 (%)
Water area (km^2)	Iraq lake	3942	3037	−23.0	2496	−36.7
	Marshes	3343	1275	−61.9	1699	−49.2
	Hamoun	3535	990	−72.0	899	−74.6
	Total	10821	5301	−51.0	5094	−52.9
AOT	Iraq lake	0.19	0.22	12.0	0.26	33.3
	Marshes	0.13	0.15	18.1	0.18	40.6
	Hamoun	0.24	0.27	13.5	0.33	37.9
	Mean	0.19	0.21	14.5	0.26	37.3

In the first and second periods, dust scattering AOT in water bodies increased by 14.5% and 37.3%, respectively, compared to the pre-2000 (Table 2), which the greatest increase occurred in Mesopotamian wetlands in both episodes. This increase in SDS from hydrological sources mainly occurred in spring and summer. This can be attributed to the predominance of seasonal wet conditions and regional wind regimes (e.g., Shamal Winds). Interestingly, SDS occurrence is a response to drought-induced climatic conditions (Figure 6), since the increase in SDS does not exactly coincide with the decrease in water bodies, and, generally, a rather irregular time lag is observed between the two. This is essentially because there is a delay between the reduction of water bodies and their complete desiccation and the erodibility of their substrate sediments. The duration of this time lag is a function of the hydroclimatic conditions and the soil's physicochemical properties. Therefore, based on correlation analysis, there is no straightforward statistical relationship between water area changes and SDS activity. It can be argued that, in general, the reduction of surface water in most cases (especially during drought episodes) has been accompanied by an increase in SDS activity and vice versa. Another possible reason for the lack of a high correlation between surface water changes and SDS activity is the effect of human activities.

There was no information available about groundwater changes before 2002. Still, the effect of the second drought period on the reduction of ground water levels is clearly visible in Figure 8. The continuation of the decreasing groundwater trends after 2012 is likely due to insufficient aquifer recharge resulting from low precipitation and overexploitation. It can be argued that periodic droughts have directly affected the water balance and hydrological resources of the Middle East, leading to increased SDS activity.

A severe flood occurred in 2019 in the central and eastern regions of the Middle East, including Iran and Iraq [53], which caused the temporary restoration of wetlands and lakes in these regions (Figure 6). However, after that, the area of water bodies has been decreasing. The connection between surface water reduction and SDS occurrence means that the continuation of these conditions will intensify SDS activity in the Middle East in the future.

4.3. Influence of Human Interventions on Middle Eastern SDS Sources

Human intervention and exploitive intentions have always been artificial agents manipulating the environment. The population of the ME countries is estimated at 460 million in 2022, which is a significant growth compared to the previous decades. The rapid population growth in the past few decades has intensified the demand for water, food, and

energy [12,54]. This has in turn increased and intensified water diversion projects (e.g., the construction of dams, pumping stations, irrigation canals, or other man-made structures that modifies the natural flow of a waterway) in the region to provide drinking water, expand agricultural lands, meet industrial uses, and hydropower energy [13]. In addition, the non-cooperation of countries, war, and insecurity in Iraq, Syria, and Yemen [55,56] have also contributed to the mismanagement of water resources and SDS in the Middle East.

Turkey's GAP projects on the Tigris and Euphrates Rivers and Egypt's dam construction on the Nile River are among the most intrusive anthropogenic activities affecting water resources in the Middle East. However, SDS sources in Egypt are mostly non-hydrologic (Figure 3) and this project has not so far affected SDS activity to a great extent. Still, the formation of new hydrologic SDS sources, particularly on the margins of the Nile in the future is not far-fetched. However, GAP dam construction projects have already reduced the environmental water right of wetlands and led to the drying of some lakes downstream. The same has happened in Iran due to the mismanagement of water resources in basins located in Central Iran [15]. Accordingly, as shown in Figure 3, some SDS sources in Southern and Central Iraq and Central and Eastern Iran have hydrologic origins. It can be concluded that human intervention has played a key role in the formation of hydrologic SDS sources and a limited role in coastal and desert sources.

Despite the occurrence of severe drought episodes in the region, there have been cases of increase in surface water resources in countries such as Egypt and Turkey (Figure 4). The analysis of the past 40-year trends does not show a significant increase in their precipitation. Therefore, this increase has been mainly due to human activities such as water diversion projects on the Nile River in Egypt and the Tigris and Euphrates Rivers in Turkey. Nevertheless, these projects have reduced the amount of downstream water flow and have disrupted the natural hydrological balance of their respective basins and sub-basins. On the other hand, the creation of artificial surface water resources may trigger the formation of new SDS sources in the future, as happened in the case of the artificial lakes of Tharthar, Habbaniyah, and Razzaza in Iraq. Therefore, the increase in surface water resources does not necessarily ensure SDS control in long term. Streams and rivers carry and deposit fine-grained sediments in lakes, wetlands, and floodplains. The permanent or seasonal desiccation of these water bodies accompanied by erosive winds prompts the formation of new SDS sources. This accentuates the critical importance of protecting natural and artificial surface water sources from instabilities caused by hydroclimatic conditions and human intervention to combat SDS.

5. Conclusions

This study investigated the Middle East as one of the global sand and dust storms (SDS) sources focusing on hydrological parameters. First, the SDS sources were identified using remote sensing data and a multi-step binary mask approach with an overall accuracy of 82.6%. The sources were categorized into seven classes based on land cover type, which included desert, permanent lake, freshwater marsh & floodplain, coastal wetland, pan, brackish & saline wetland, intermittent lake/wetland, and coastal land.

According to the findings, desert sources (over 79%) have the highest area of SDS sources. Hydrologic SDS sources including the permanent lake, intermittent lake/wetland, and freshwater marsh & floodplain accounted for 8.4% of SDS sources in the Middle East. The largest area of hydrologic SDS sources belonged to Iran (41%), Iraq (21%), Oman (14%), and Saudi Arabia (13%).

Our results revealed that Iran, Iraq, Turkey, and Egypt showed the highest amount of decreasing and increasing surface water changes, respectively. The highest density of surface water change was observed in those of the Mesopotamian wetlands in Southern Iraq. The highest decrease in groundwater was observed in Iran and Iraq, which includes the highest areas of hydrologic SDS sources.

The correlation analysis showed an inverse but not very strong relationship between surface water changes and SDS activities. The temporal pattern of changes in surface waters,

including wetlands and lakes, showed a declining trend in the post-2000 compared to the pre-2000 period. Similarly, SDS activities have increased by an average of 18.4% since 2000. In the 2000–2001 and 2007–2012 periods, severe droughts corresponded to the shrinking of surface water up to 51% and 52.9%, respectively. SDS activities in surface water in the first and second periods increased by an average of 14.5% and 37.3%, respectively. Overall, it can be argued that periodic droughts have negatively affected the water resources in the Middle East, leading to an increase in SDS activity, especially from hydrologic SDS sources.

Despite the occurrence of severe drought episodes in the region, human interventions such as water diversion projects have reduced the water flow to downstream regions, which caused the SDS activities. For instance, the Mesopotamian wetlands of Iraq have experienced the highest density of hydrologic SDS sources, which is the consequence of anthropogenic activities upstream.

In general, it can be concluded that the main causes of SDS sources formation in the Middle East consist of natural factors such as the predominance of drought. Specifically, the hydrologic SDS sources are suffering from mismanagement of water resources, which greatly contributes to SDS activities.

The most important challenge of this approach was the identifying SDS hotspots using visual interpretation. Because these hotspots, as a training dataset, strongly affect the accuracy of the binary mask-based model. To perform this task, the interpreter must have sufficient knowledge about SDS and the study area. In addition, in general, visual interpretation is a time-consuming and expensive process, especially on a large scale. However, this approach can be extended to other areas, and in this way, global SDS sources can be discriminated.

References

1. Zittis, G.; Almazroui, M.; Alpert, P.; Ciais, P.; Cramer, W.; Dahdal, Y.; Fnais, M.; Francis, D.; Hadjinicolaou, P.; Howari, F.; et al. Climate Change and Weather Extremes in the Eastern Mediterranean and Middle East. *Rev. Geophys.* **2022**, *60*, e2021RG000762. [CrossRef]
2. Booloorani, A.D.; Najafi, M.S.; Soleimani, M.; Papi, R.; Torabi, O. Influence of Hamoun Lakes' dry conditions on dust emission and radiative forcing over Sistan plain, Iran. *Atmospheric Res.* **2022**, *272*, 106152. [CrossRef]
3. Francis, D.; Chaboureau, J.P.; Nelli, N.; Cuesta, J.; Alshamsi, N.; Temimi, M.; Pauluis, O.; Xue, L. Summertime dust storms over the Arabian Peninsula and impacts on radiation, circulation, cloud devel-opment and rain. *Atmos. Res.* **2021**, *250*, 105364. [CrossRef]
4. Khaniabadi, Y.O.; Daryanoosh, S.M.; Amrane, A.; Polosa, R.; Hopke, P.K.; Goudarzi, G.; Mohammadi, M.J.; Sicard, P.; Armin, H. Impact of Middle Eastern Dust storms on human health. *Atmos. Pollut. Res.* **2017**, *8*, 606–613. [CrossRef]
5. Soleimani, Z.; Teymouri, P.; Booloorani, A.D.; Mesdaghinia, A.; Middleton, N.; Griffin, D.W. An overview of bioaerosol load and health impacts associated with dust storms: A focus on the Middle East. *Atmos. Environ.* **2020**, *223*, 117187. [CrossRef]
6. Middleton, N.; Kashani, S.S.; Attarchi, S.; Rahnama, M.; Mosalman, S.T. Synoptic Causes and Socio-Economic Consequences of a Severe Dust Storm in the Middle East. *Atmosphere* **2021**, *12*, 1435. [CrossRef]
7. Jish Prakash, P.; Stenchikov, G.; Kalenderski, S.; Osipov, S.; Bangalath, H. The impact of dust storms on the Arabian Pen-insula and the Red Sea. *Atmos. Chem. Phys.* **2015**, *15*, 199–222. [CrossRef]

8. Rezazadeh, M.; Irannejad, P.; Shao, Y. Climatology of the Middle East dust events. *Aeolian Res.* **2013**, *10*, 103–109. [CrossRef]

9. Kutiel, H.; Furman, H.K.H. Dust Storms in the Middle East: Sources of Origin and Their Temporal Characteristics. *Indoor Built Environ.* **2003**, *12*, 419–426. [CrossRef]

10. World Bank. *Sand and Dust Storms in the Middle East and North Africa Region: Sources, Costs, and Solutions*; World Bank: Washington, DC, USA, 2019.

11. Heydarizad, M.; Minaei, M.; Ichiyanagi, K.; Sorí, R. The effects of local and regional parameters on the δ18O and δ2H values of precipitation and surface water resources in the Middle East. *J. Hydrol.* **2021**, *600*, 126485. [CrossRef]

12. Bozorg-Haddad, O.; Zolghadr-Asli, B.; Sarzaeim, P.; Aboutalebi, M.; Chu, X.; Loáiciga, H.A. Evaluation of water shortage crisis in the Middle East and possible remedies. *J. Water Supply: Res. Technol.* **2020**, *69*, 85–98. [CrossRef]

13. Boloorani, A.D.; Papi, R.; Soleimani, M.; Karami, L.; Amiri, F.; Samany, N.N. Water bodies changes in Tigris and Euphrates basin has impacted dust storms phenomena. *Aeolian Res.* **2021**, *50*, 100698. [CrossRef]

14. Hamzeh, N.H.; Karami, S.; Opp, C.; Fattahi, E.; Jean-François, V. Spatial and temporal variability in dust storms in the Middle East, 2002–2018: Three case studies in July 2009. *Arab. J. Geosci.* **2021**, *14*, 538. [CrossRef]

15. Papi, R.; Kakroodi, A.; Soleimani, M.; Karami, L.; Amiri, F.; Alavipanah, S.K. Identifying sand and dust storm sources using spatial-temporal analysis of remote sensing data in Central Iran. *Ecol. Inform.* **2022**, *70*, 101724. [CrossRef]

16. Gholami, H.; Mohamadifar, A.; Collins, A.L. Spatial mapping of the provenance of storm dust: Application of data mining and ensemble modelling. *Atmos. Res.* **2020**, *233*, 104716. [CrossRef]

17. Boroughani, M.; Pourhashemi, S.; Hashemi, H.; Salehi, M.; Amirahmadi, A.; Asadi, M.A.Z.; Berndtsson, R. Application of remote sensing techniques and machine learning algorithms in dust source detection and dust source susceptibility mapping. *Ecol. Inform.* **2020**, *56*, 101059. [CrossRef]

18. Papi, R.; Argany, M.; Moradipour, S.; Soleimani, M. Modeling the potential of Sand and Dust Storm sources formation using time series of remote sensing data, fuzzy logic and artificial neural network (A Case study of Euphrates basin). *Eng. J. Geo-spatial Inf. Technol.* **2021**, *8*, 61–82. [CrossRef]

19. Boloorani, A.D.; Samany, N.N.; Papi, R.; Soleimani, M. Dust source susceptibility mapping in Tigris and Euphrates basin using remotely sensed imagery. *Catena* **2022**, *209*, 105795. [CrossRef]

20. Boloorani, A.D.; Kazemi, Y.; Sadeghi, A.; Shorabeh, S.N.; Argany, M. Identification of dust sources using long term satellite and climatic data: A case study of Tigris and Euphrates basin. *Atmos. Environ.* **2020**, *224*, 117299. [CrossRef]

21. Rashki, A.; Middleton, N.J.; Goudie, A.S. Dust storms in Iran–Distribution, causes, frequencies and impacts. *Aeolian Res.* **2021**, *48*, 100655. [CrossRef]

22. Ginoux, P.; Prospero, J.M.; Gill, T.E.; Hsu, N.C.; Zhao, M. Global-scale attribution of anthropogenic and natural dust sources and their emission rates based on MODIS Deep Blue aerosol products. *Rev. Geophys.* **2012**, *50*. [CrossRef]

23. Cao, H.; Amiraslani, F.; Liu, J.; Zhou, N. Identification of dust storm source areas in West Asia using multiple environmental datasets. *Sci. Total Environ.* **2015**, *502*, 224–235. [CrossRef] [PubMed]

24. Moridnejad, A.; Karimi, N.; Ariya, P.A. A new inventory for middle east dust source points. *Environ. Monit. Assess.* **2015**, *187*, 1–11. [CrossRef]

25. Moridnejad, A.; Karimi, N.; Ariya, P.A. Newly desertified regions in Iraq and its surrounding areas: Significant novel sources of global dust particles. *J. Arid Environ.* **2015**, *116*, 1–10. [CrossRef]

26. Parajuli, S.P.; Yang, Z.; Kocurek, G. Mapping erodibility in dust source regions based on geomorphology, meteorology, and remote sensing. *J. Geophys. Res. Earth Surf.* **2014**, *119*, 1977–1994. [CrossRef]

27. Hamidi, M. The key role of water resources management in the Middle East dust events. *Catena* **2020**, *187*, 104337. [CrossRef]

28. Boroughani, M.; Hashemi, H.; Hosseini, S.H.; Pourhashemi, S.; Berndtsson, R. Desiccating Lake Urmia: A New Dust Source of Regional Importance. *IEEE Geosci. Remote Sens. Lett.* **2019**, *17*, 1483–1487. [CrossRef]

29. Ghale, Y.A.G.; Tayanc, M.; Unal, A. Dried bottom of Urmia Lake as a new source of dust in the northwestern Iran: Understanding the impacts on local and regional air quality. *Atmospheric Environ.* **2021**, *262*, 118635. [CrossRef]

30. Rashki, A.; Kaskaoutis, D.; Goudie, A.; Kahn, R. Dryness of ephemeral lakes and consequences for dust activity: The case of the Hamoun drainage basin, southeastern Iran. *Sci. Total Environ.* **2013**, *463–464*, 552–564. [CrossRef]

31. Miri, A.; Maleki, S.; Middleton, N. An investigation into climatic and terrestrial drivers of dust storms in the Sistan region of Iran in the early twenty-first century. *Sci. Total Environ.* **2021**, *757*, 143952. [CrossRef]

32. Thakur, P.K.; Nikam, B.R.; Garg, V.; Aggarwal, S.P.; Chouksey, A.; Dhote, P.R.; Ghosh, S. Hydrological Parameters Estimation Using Remote Sensing and GIS for Indian Region: A Review. *Proc. Natl. Acad. Sci. India Sect. A Phys. Sci.* **2017**, *87*, 641–659. [CrossRef]

33. O'Loingsigh, T.; Mitchell, R.; Campbell, S.; Drake, N.; McTainsh, G.; Tapper, N.; Dunkerley, D. Correction of dust event frequency from MODIS Quick-Look imagery using in-situ aerosol measurements over the Lake Eyre Basin, Australia. *Remote Sens. Environ.* **2015**, *169*, 222–231. [CrossRef]

34. Baddock, M.C.; Bryant, R.G.; Acosta, M.D.; Gill, T.E. Understanding dust sources through remote sensing: Making a case for CubeSats. *J. Arid Environ.* **2021**, *184*, 104335. [CrossRef]

35. Prospero, J.M.; Ginoux, P.; Torres, O.; Nicholson, S.E.; Gill, T.E. Environmental characterization of global sources of at-mospheric soil dust identified with the Nimbus 7 Total Ozone Mapping Spectrometer (TOMS) absorbing aerosol product. *Rev. Geophys.* **2002**, *40*, 1–2. [CrossRef]

36. Karimi, N.; Moridnejad, A.; Golian, S.; Samani, J.M.V.; Karimi, D.; Javadi, S. Comparison of dust source identification techniques over land in the Middle East region using MODIS data. *Can. J. Remote Sens.* **2012**, *38*, 586–599. [CrossRef]

37. Soleimani, M.; Argany, M.; Papi, R.; Amiri, F. Satellite aerosol optical depth prediction using data mining of climate parameters. *Phys. Geogr. Res. Q.* **2021**, *53*, 319–333. [CrossRef]

38. Stein Zweers, D.C. TROPOMI ATBD of the UV aerosol index. S5P-KNMI-L2-0008-RP. 1.0. Available online: http://www.tropomi.eu/sites/default/files/files (accessed on 1 August 2022).

39. Nabavi, S.O.; Haimberger, L.; Samimi, C. Climatology of dust distribution over West Asia from homogenized remote sensing data. *Aeolian Res.* **2016**, *21*, 93–107. [CrossRef]

40. Shepherd, G.; Terradellas, E.; Baklanov, A.; Kang, U.; Sprigg, W.; Nickovic, S.; Joowan, C. *Global Assessment of Sand and Dust Storms*; WMO: Geneva, Switzerland, 2016.

41. Abatzoglou, J.T.; Dobrowski, S.Z.; Parks, S.A.; Hegewisch, K.C. TerraClimate, a high-resolution global dataset of monthly climate and climatic water balance from 1958–2015. *Sci. Data* **2018**, *5*, 170191. [CrossRef]

42. Pelletier, J.D.; Broxton, P.D.; Hazenberg, P.; Zeng, X.; Troch, P.A.; Niu, G.; Williams, Z.C.; Brunke, M.A.; Gochis, D. *Global 1-km Gridded Thickness of Soil, Regolith, and Sedimentary Deposit Layers*; ORNL DAAC: Oak Ridge, TN, USA, 2016.

43. Lehner, B.; Döll, P. Development and validation of a global database of lakes, reservoirs and wetlands. *J. Hydrol.* **2004**, *296*, 1–22. [CrossRef]

44. Pekel, J.-F.; Cottam, A.; Gorelick, N.; Belward, A.S. High-resolution mapping of global surface water and its long-term changes. *Nature* **2016**, *540*, 418–422. [CrossRef]

45. Gao, B.-C. Normalized Difference Water Index for Remote Sensing of Vegetation Liquid Water from Space. In Proceedings of the SPIE'S 1995 Symposium on OE/Aerospace Sensing and Dual Use Photonics, Orlando, FL, USA, 17–21 April 1995; pp. 225–236. [CrossRef]

46. Darvishi Boloorani, A.; Soleimani, M.; Papi, R.; Alavipanah, S.K.; Al-Quraishi, A.M.F. Zoning Areas Susceptible to Land Subsidence in Tigris and Euphrates Basins. *Eng. Technol. J.* **2019**, *37*, 265–272. [CrossRef]

47. Barlow, M.; Zaitchik, B.; Paz, S.; Black, E.; Evans, J.; Hoell, A. A Review of Drought in the Middle East and Southwest Asia. *J. Clim.* **2016**, *29*, 8547–8574. [CrossRef]

48. Middleton, N.; Kang, U. Sand and Dust Storms: Impact Mitigation. *Sustainability* **2017**, *9*, 1053. [CrossRef]

49. Al-Ansari, N.; Adamo, N.; Sissakian, V. Water shortages and its environmental consequences within Tigris and Euphrates Rivers. *J. Earth Sci. Geotech. Eng.* **2019**, *9*, 27–56.

50. Batanouny, K.H. Climatic Aridity in the Deserts of the Middle East. In *Plants in the Deserts of the Middle East*; Springer: Berlin/Heidelberg, Germany, 2001; pp. 11–24. [CrossRef]

51. Bolin, B.; Aspling, G.; Persson, C. Residence time of atmospheric pollutants as dependent on source characteristics, at-mospheric diffussion processes and sink mechanisms. *Tellus* **1974**, *26*, 185–195. [CrossRef]

52. Trigo, R.M.; Gouveia, C.; Barriopedro, D. The intense 2007–2009 drought in the Fertile Crescent: Impacts and associated atmospheric circulation. *Agric. For. Meteorol.* **2010**, *150*, 1245–1257. [CrossRef]

53. Yadollahie, M. The Flood in Iran: A Consequence of the Global Warming? *Int. J. Occup. Environ. Med.* **2019**, *10*, 54–56. [CrossRef]

54. Roudi-Fahimi, F.; Creel, L.; De Souza, R.-M. *Finding the Balance: Population and Water Scarcity in the Middle East and North Africa*; Population Reference Bureau: Washington, DC, USA, 2002.

55. Allan, J.A. Hydro-Peace in the Middle East. *SAIS Rev.* **2002**, *22*, 255–272. [CrossRef]

56. Amery, H.A. Water wars in the Middle East: A looming threat. *Geogr. J.* **2002**, *168*, 313–323. [CrossRef]

Article

Climate Change during the Third Millennium—The Gulf Cooperation Council Countries

Mohamed E. Hereher [1,2] (ORCID)

1 Department of Environmental Sciences, Faculty of Science, Damietta University, New Damietta 34517, Egypt; mhereher@gmail.com
2 Geography Department, College of Arts and Social Sciences, Sultan Qaboos University, Muscat 123, Oman

Abstract: The Gulf Cooperation Council (GCC) is a union occurring in the arid subtropical belt of the world. Contemporary climate change is a serious environmental issue at the regional and global levels. The main purpose of this study was to investigate the changes and trends in the regional climate in the GCC countries in terms of the land surface temperatures and surface anomalies, precipitation, and sea surface temperatures over the first two decades of this millennium. Research data exclusively relied on satellite remote sensing. Spatial, statistical, and cartographic analyses were performed to extract, manipulate, and display thematic maps reflecting the changes and trends of the regional climate. The results showed that notable climate changes were obvious and frequent throughout the GCC countries, with symptoms influencing the atmosphere, lithosphere, and the hydrosphere of the region. However, a prominent gradient in the severity of climate change occurred from north to south. Remarkably, serious impacts were observed in Kuwait and eastern Saudi Arabia, while the least effects were recorded in Oman. The study denotes the competence of remote sensing for monitoring regional climate change.

Keywords: greenhouse gases; geospatial analysis; remote sensing; Arabian Peninsula

1. Introduction

The global CO_2 emissions increased from 6 billion tons in 1950 to 22 billion tons in 1990 and eventually approached 34 billion tons in 2020 [1]. As it contains more than 60% of the world's population, Asia is the largest contributor of CO_2 in the world, with about 53% of global emissions. There is a direct correlation between the high rates of greenhouse gas (GHG) emissions (mostly CO_2 and methane) from burning fossil fuels (oil, gas, and coal) and global warming [2]. This issue of climate change has received universal interest in the last decades. International endeavors pursue the goal of keeping global warming from approaching 2 °C by encouraging the countries that emit the most GHGs to restrict the increase in global temperatures below 1.5 °C [3]. However, the rates of GHG emission could increase the global temperatures by 6 °C by the end of this century [4]. Recently, the United Nations Climate Change Conference (COP26), which was held in November 2021 in Glasgow, Scotland, emphasized again the responsibility of all countries to limit the world temperature increase by 1.5 °C above the pre-industrial revolution levels. The world witnesses not only enormous emissions of GHGs but many other air pollutants as well. Hence, global warming is just one facet of the problem. Air pollution is considered the most significant environmental health issue in the world. It ranks among the top five risks for attributable deaths globally [5] and causes about 4.2 million premature deaths every year [6]. Air pollution consists of particulate matter and gaseous constituents, e.g., sulfur dioxide (SO_2), nitrogen dioxide (NO_2), ozone, particulates, and carbon monoxide (CO).

The Gulf Cooperation Council (GCC) is a regional geographical union established in 1981 between six Arab countries (Kuwait, Saudi Arabia, Bahrain, Qatar, United Arab Emirates, and Oman) (Figure 1). These oil-producing countries are all experiencing remarkable socio-economic developments depending on their tremendous fossil fuel production

(Table 1). They hold approximately 40% of the world's known oil and about 24% of the world's known gas reserves [7]. These states have also experienced accelerated population growth accompanied by extensive energy utilization. Energy consumption in the GCC countries is the highest in the world and is as much as 2.5 times the consumption of the European Union [8]. There is a direct relationship between energy consumption and CO_2 emissions as well as between economic growth and energy consumption in the GCC countries [9]. All the GCC countries are listed as being among the largest per capita CO_2 emitters in the world, as they emit 3.08% of global CO_2, with the maximum being from Saudi Arabia (1.8%) in 2020. Major sources of GHGs and air pollutants in the GCC countries are numerous. However, the burning of fossil fuels for energy, transportation, petrochemical industries, and oil refineries are at the top. Unfortunately, regional studies on GHGs and air pollution studies are generally few. However, there are some local investigations that demonstrate the rates of GHG emissions and their projections for the near future. For example, CO_2 emissions have tripled in Oman between 2000 and 2014 due to the expansion of the industrial sector [10]. Ref. [11] showed that the CO_2 emissions from the transportation sector of Saudi Arabia increased from 2000 through 2010 to 2020 to a total of 56 million tons, 98 million tons, and 163 million tons, respectively. In the United Arab Emirates (UAE), the major emissions (90%) of GHGs are produced from the energy sector [12].

The GCC region is under a hot desert climate (BWh), according to the Koppen climate classification. Summers are generally hot to extremely hot, and air temperatures usually approach 40 °C during the summer months. However, winters are generally mild with temperatures seldom falling below 10 °C, particularly in coastal regions. Rainfall in the area is generally scant, except for in Oman, where Al-Hajar Mountain receives up to 300 mm/year. The relative humidity is high (up to 85%) along the coastal zones. The GCC countries are usually exposed to frequent dust storms accompanying the *Al-Shamal* (northern in Arabic) winds, and these storms can significantly reduce visibility and cause problems regarding the air and traffic [13]. The region is experiencing fast population growth. The majority of the region's population resides in Saudi Arabia, UAE, Kuwait, and Oman. The total population of the GCC countries exceeds 50 million [14].

The impacts of climate change on the GCC region were also addressed in some previous studies, with a particular focus on air temperatures, precipitation, and the Arabian Gulf environment. For example, Ref. [15] observed a tendency toward increasing drought intensity and frequency between 1981 and 2000 over the Arabian Peninsula due to climate change. Ref. [13] reported a significant increase in air temperatures between 1996 and 2010. Ref. [16] observed that between 2003 and 2018, the annual increase in the gulf water surface temperatures exceeded the global ocean warming that occurred since 1900. In addition, Ref. [17] reported a correlation between the warming of seawater and the locations of bleached coral reefs in the Arabian Gulf. Moreover, Ref. [18] observed significant nighttime warming caused by the urban heat islands of the major cities in the region, particularly in Dubai (1.9 °C/decade). The warming of the climate is generally associated with drought, an increase in the frequency of heatwaves, the deterioration of terrestrial biodiversity and marine ecosystems, and sea-level rise [19–21]. To the best of the author's knowledge, there has been little major research on regional climate change, and most of the published work was at the country level. In addition, the majority of the previous studies relied on data from existing ground meteorological stations, which are relatively little in space compared to the huge area of the region. The present study entirely depends on remotely sensed data, which covers all the spatial gaps and boundaries of the region. In addition, there is a necessity for regional climate change studies in order to determine appropriate management procedures and to prioritize the available natural resources in the region with particular focus upon the renewable resources [22–26]. Therefore, the present study attempts to fill the gap in the literature and provides a comprehensive regional and synoptic overview on the status of climate change over the past two decades using remotely sensed data. The goal is to focus on the decadal changes in the land surface temperatures, precipitation, and

sea surface temperatures, as revealed by satellite images. Therefore, the current research aims to answer the following questions: 1—what are the temporal regional changes in the emission of GHGs and air pollution? 2—are there any changes in land surface temperatures, precipitation, and sea surface temperatures? And 3—what are the decadal rates of these changes? The time frame of most studied parameters extends to two decades, while some others extend to 40 years.
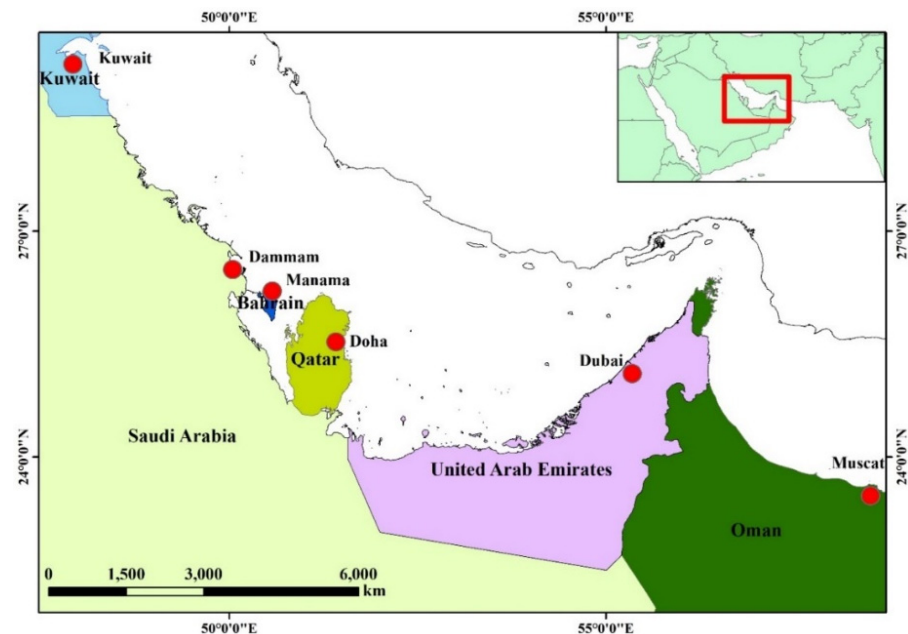
Figure 1. The study region of the GCC countries (the red square in the upper map) and the major cities along the coast of the Arabian Gulf and the Sea of Oman.

Table 1. Synopsis of the GCC countries (Source: https://www.gccstat.org/en; accessed on 18 February 2022).

Country	Area (km^2)	Population in 2017 (Million)	Oil Production in 2017 (Million Barresls/Day)	Natural Gas-Marketed Production in 2019 (Million m^3)	Electricity Production in 2019 (GWH)
Kuwait	17,818	4.2	2.70	13,952	75,082
KSA	2,149,690	32.6	9.96	117,000	342,622
Bahrain	778	1.5	0.19	17,149	17,854
Qatar	11,600	2.7	0.60	176,000	49,873
UAE	83,600	9.3	2.96	55,097	138,454
Oman	309,500	4.5	0.97	36,462	37,513

2. Materials and Methods

2.1. Atmospheric Data

In this investigation, the goal was to probe into the geographical changes of atmospheric constituents, considering those that are the most related to global warming and climate change in this important fossil fuel stock region. The atmospheric data include two GHGs: carbon dioxide (CO_2) and methane (CH_4), as well as three air pollutants: sulfur dioxide (SO_2), nitrogen dioxide (NO_2), and black carbon (BC). The data utilized are gridded (monthly/daily records) time series raster images covering the entirety of the GCC countries along the Arabian Gulf (Table 2). All these data were acquired by means of remote sensing. The CO_2 and CH_4 datasets cover the periods 2003–2016 and 2003–2020, respectively. On the other hand, the dataset of BC and SO_2 extends to 40 years (1980–2020), while NO_2 data cover the period 2005–2020. The data were acquired for a window covering the entirety of the GCC countries overlooking the Arabian Gulf. All the data were downloaded from the Geospatial Interactive Online Visualization and Analysis Infrastructure (Giovanni)

(https://giovanni.gsfc.nasa.gov/giovanni/, (accessed on 11 November 2021)) portal; Version (V.4.36). Giovanni is a web-based platform developed by the Goddard Earth Sciences Data and Information Services Center (GES DISC) that provides a simple and instinctive way to visualize, analyze, and access the earth science remotely sensed data acquired from many sources and satellites, such as TRMM, TOMS, OMI, AIRS, MERRA, MLS, MODIS, etc. [27]. These data were provided as daily or monthly records shown as timely averaged maps in different spatial resolutions ranging from 0.25 × 0.25 to 2 × 2.5 degrees in GeoTiff format and at the Geographical Coordinate System (GCS).

Table 2. Characteristics of the analyzed data (Source: https://giovanni.gsfc.nasa.gov/giovanni/; accessed on 18 February 2022).

Parameter	Source	Spatial Resolution (Degree)	Temporal Resolution	Temporal Coverage	Units of Measurements
CO_2	AIRS *	2 × 2.5	Monthly	2003–2016	Parts per million (ppm)
CH_4	AIRS	1	Monthly	2003–2020	Parts per billion per volume (ppbv)
SO_2	MERRA-2 **	0.5 × 0.6	Monthly	1980–2020	Kg/m^3
NO_2	OM I ***	0.25	Daily	2005–2020	$Molecules/cm^2$
Black carbon	MERRA-2	0.5 × 0.6	Monthly	1980–2020	Kg/m^3
Nighttime Temp. anomaly	AIRS	1	Monthly	2003–2016	Degrees Celsius

* Atmospheric Infrared Sounder. ** The Modern-Era Retrospective analysis for Research and Applications. *** Ozone Monitoring Instrument.

2.2. Land Surface Temperatures and Precipitation Data

The Land Surface Temperature (LST) data were acquired from the Moderate Resolution Imaging Spectroradiometer (MODIS) instrument onboard the *Aqua* satellite. In this study, LST data were selected from the MYD11B3.V6 product, which provides average monthly land surface temperature in a pixel size of 0.05° × 0.05° (5600 m × 5600 m) within a 1200 by 1200 km (km) tile. This product provides both daytime (at 13:30) and nighttime (01:30) land surface temperatures. MODIS data were found to well agree with ground LSTs, as they were validated in different environments, including lakes, vegetation, and soil sites in clear sky conditions by the radiance-based approach to have a mean bias within 1 K [28]. The LST data were obtained from the NASA's Land Processes Distributed Active Archive Center (LP DAAC) (https://lpdaac.usgs.gov, (accessed on 1 December 2021)) from the tiles H22V06 and H23V06 for the period from January 2003–December 2020. In this investigation, the daytime LST images were extracted from the MYD11B3 product on a monthly basis, and the digital numbers were converted to degrees Celsius at the pixel level. The two tiles were mosaicked together in order to compile one continuous image, and a subset covering the study area was then produced. In addition, the nighttime anomalies of surface air temperatures were also investigated. Surface nighttime temperature anomalies data were also acquired from the Giovanni web portal for the period from 2003–2016. The data were acquired from the Atmospheric Infrared Sounder (AIRS) satellite for the main cities along the Arabian Gulf. Regarding precipitation, gridded data were acquired from the World Climate (https://www.worldclim.org, (accessed on 19 February 2022)) web portal. This platform provides a monthly raster database of the global monthly precipitation obtained via the reanalysis of 9000 to 60,000 ground weather stations worldwide for the period from 1960–2018 via interpolation techniques. The global cross-validation correlations were 0.86 for precipitation, revealing high confidence estimations. Details on acquiring, processing, and validating these climate data are shown in Ref. [29]. In the present study, the monthly precipitation dataset acquired between 2000 and 2018 was downloaded at 2.5° × 2.5° (~20 km^2) for the GCC region in GeoTiff format. The precipitation profile for the study area was generated, from which the mean annual precipitation and the decadal trend were statistically determined.

2.3. Sea Surface Temperatures Data

The GCC countries overlook the western side of the Arabian Gulf. The oceanographic characteristics of this semi-enclosed inland sea are affected by the regional climate. Therefore, climate change should influence not only the lithosphere but the hydrosphere as well. The sea surface temperatures (SST) of the gulf water were extracted by thermal remote sensing satellites. In this context, MODIS data are highly beneficial for mapping SST gradients and have high confidence results, as they significantly correlate to the in situ SST measurements [30]. They have been processed and calibrated by the NASA technical laboratories using the most recent updates and algorithms. In this study, level-3 (9 km) global monthly SST data for the period of 2003–2018 were downloaded from the NASA Ocean Color web portal (http://oceancolor.gsfc.nasa.gov, (accessed on 19 May 2019)). The monthly images were stacked together, the entire time series profile was produced, and the geographical subset of the gulf was extracted.

2.4. Data Analysis and Visualization

In the beginning, all the acquired data were re-projected to the Geographical Coordinate System. However, the pixel size of all images in each parameter was kept without resampling, as each element was independently treated. For each parameter, images of the individual monthly records were stacked together, forming one file of multi-date profiles (from the first to the last date) for this parameter. This raster dataset was then converted to vector data in a tabular format (the American Standard Code for Information Interchange, ASCII) for consequent analysis. For each parameter, the converted ASCII table shows the coordinates and the record of each point for every date in the time series. This table was eventually used for statistical analysis. The monthly and annual average values for each point for each parameter were computed from the monthly records to yield a mean layer for that parameter. In addition, the rate of change at every point of that parameter was obtained from the slope of the linear regression relationship of the time series records. For example, the LST for a given pixel at a given date is calculated as follows:

$$Y = \alpha X + \beta \tag{1}$$

where X, Y, α, and β are the time, LST, slope, and intercept, respectively. The modeled slope of the regression (α) was defined as the temperature rate of change (°C/decade). In the same manner, the decadal trend for every studied parameter was determined at the pixel level. The tables of the mean and trend for each parameter were displayed in ArcMap for interpolation analysis. The Inverse Distance Weighted (IDW) algorithm is the interpolator used to produce the surface of distribution maps of the mean and rate of change throughout the study region. This technique, which considers the spatial density of data points when producing the continuous surface, is widely used in environmental and climatic studies [31,32]. Thematic maps for the mean and decadal trends of each parameter, including the atmospheric, terrestrial, and sea surface temperature changes, were prepared and visualized. In addition to the regional mean and trend maps, all the GHGs and air pollutants were investigated to reveal the monthly profile during the study period of each parameter. Then the monthly distribution pattern was analyzed for the main cities overlooking the Arabian Gulf (Kuwait City, Dammam, Manama, Doha, Dubai, and Muscat), and a window of 50 × 50 km was selected for each city. The monthly profiles for GHG/air pollutant parameters for these cities were displayed in order to visualize the temporal variations of these inputs to the atmosphere.

3. Results

3.1. Greenhouse Gases and Air Pollution

All the GCC countries are experiencing notable high emissions of greenhouse gases [33]. There has been a significant increase in the CO_2 gas concentration throughout the entire region, which increased from 375 ppm in 2003 to 402 ppm in 2016. Figure 2a shows that

the mean CO_2 emissions were remarkably high in Kuwait, KSA, Bahrain, Qatar, and UAE. This high concentration reflects the dependence of these countries upon crude oil for their energy, industry, and transport sectors. Globally, two-thirds of carbon dioxide (CO_2) originated from the energy sector [26]. The decadal trend of CO_2 gas emissions (Figure 2b) revealed maxim emission rates in Kuwait, KSA, and UAE (up to 21.6 ppm/decade). Saudi Arabia alone contributed 1.8% of the global CO_2 emissions in 2020 [26]. The lower rates of emissions were clearly observed in areas that were farther away from the gulf in the Arabian desert. At the monthly level, it was observed that the concentrations of CO_2 are higher during spring and summer, with the maximum values occurring during May and June. The lowest concentrations were recorded in January and October (Figure 2c). The highest monthly CO_2 record ever was observed in Dubai in June.
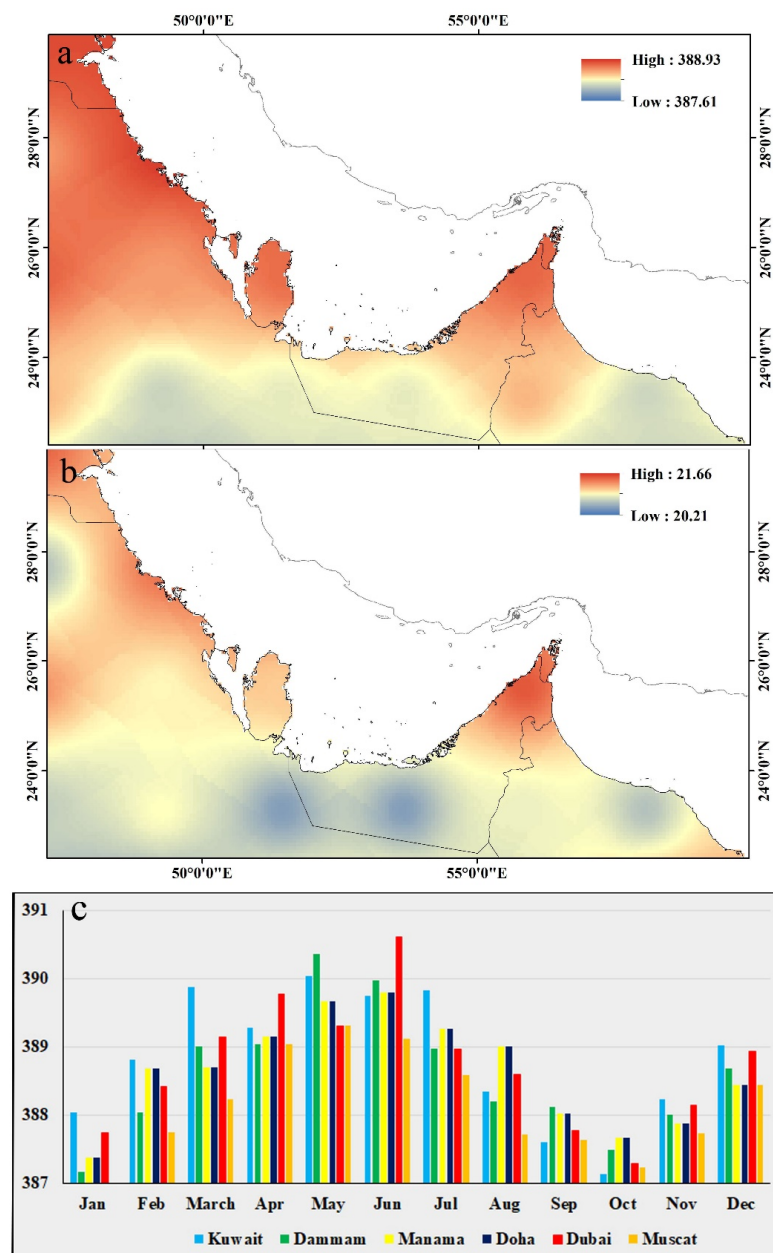
Figure 2. (**a**) is the distribution of the mean CO_2 gas emissions in ppm over the GCC countries between 2003 and 2016, (**b**) represents the trend (ppm/decade), which are maximal in Kuwait, KSA, and UAE, and (**c**) shows the average monthly concentration of CO_2 in the six main cities. The source of the raw data is: https://giovanni.gsfc.nasa.gov/giovanni/; accessed on 18 February 2022.

Methane (CH_4) is considered a major greenhouse gas that is responsible for global warming. In contrast to CO_2 gas, methane has a short lifetime (~12 years); however, it absorbs much energy in the troposphere compared to CO_2 [34]. The energy sector, which depends on oil and gas reserves, is the primary source of atmospheric methane. The distribution of the mean monthly concentration of CH_4 emissions between 2003 and 2020 (Figure 3a) revealed that many emissions were clear in UAE (1862 ppbv), Kuwait (1860 ppbv), and Saudi Arabia (1854 ppbv). In addition, there has been a notable increase in the decadal rate of emissions in the GCC countries, with maximal rates in Oman (456 ppbv/decade) and UAE (437 ppbv/decade). This is evident in the increase in CH_4 emissions in Oman (mainly from the energy sector), which increased from 288 Gg in 2000 to 825 Gg in 2015 [35]. The peak emission was observed during August, whereas the lowest record was observed during February (Figure 3c).
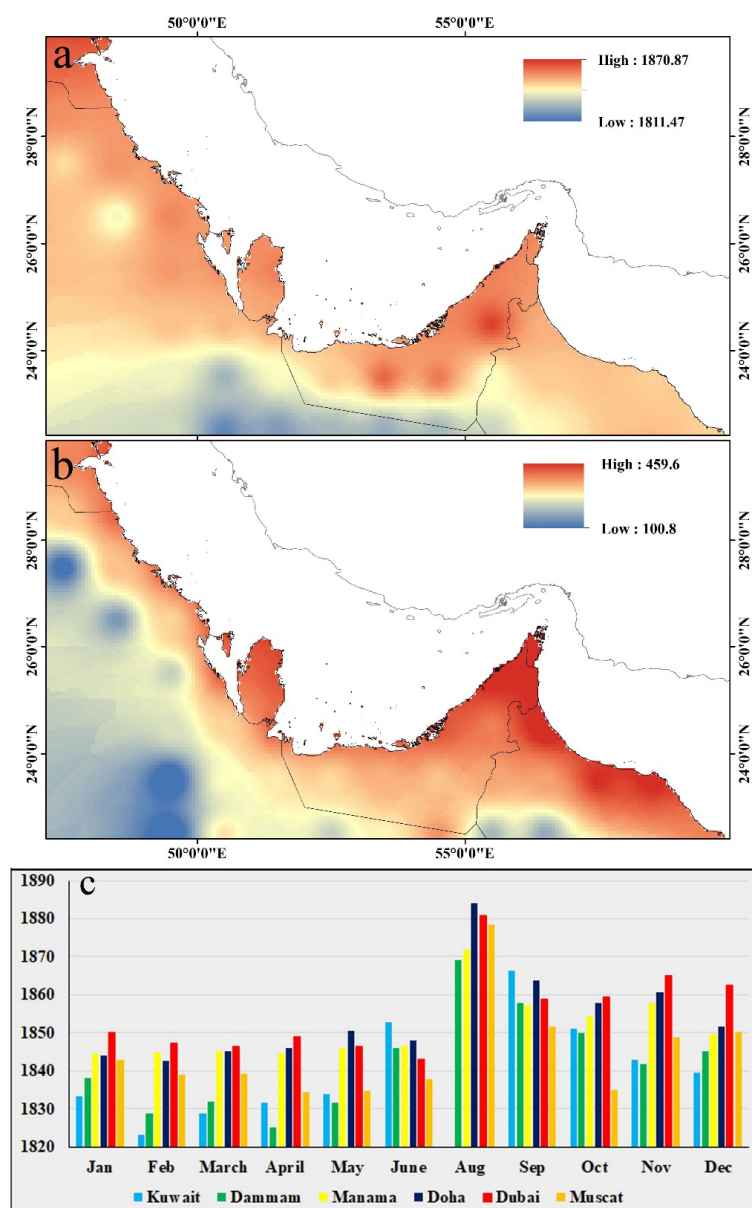
Figure 3. (**a**) is the distribution of the mean monthly CH_4 gas emissions in ppbv over the GCC countries between 2003 and 2020, (**b**) represents the trend (ppbv/decade), which are maximal in Oman and UAE, and (**c**) shows the average monthly concentration of CH_4 in the six main cities. The source of the raw data is: https://giovanni.gsfc.nasa.gov/giovanni/; accessed on 18 February 2022.

The three air pollutants analyzed in this study are SO_2, NO_2, and black carbon. SO_2 concentrations and trends are shown in Figure 4. The primary sources of SO_2 are oil refineries, desalination, and power plants using diesel [14,36]. The mean monthly concentrations of SO_2 for the period from 1980–2020 revealed maximum values in both the Dammam region of Saudi Arabia (15 μg/m^3) and Kuwait (13 μg/m^3). The decadal trends concurred with the monthly averages, where maximal trends occurred in these two locations. Specifically, KSA and Kuwait are among the top 25 countries producing SO_2 in the world in 2018 [37]. In addition, Ref. [38] reported that SO_2 emissions from power plants in Kuwait are greatly exceeding the annual national standards (80 μg/m^3). At the monthly level (Figure 4c) and in contrast to the CO_2 emissions, winter and fall witnessed maximum SO_2 emissions, while the minimum was recorded during June and July.
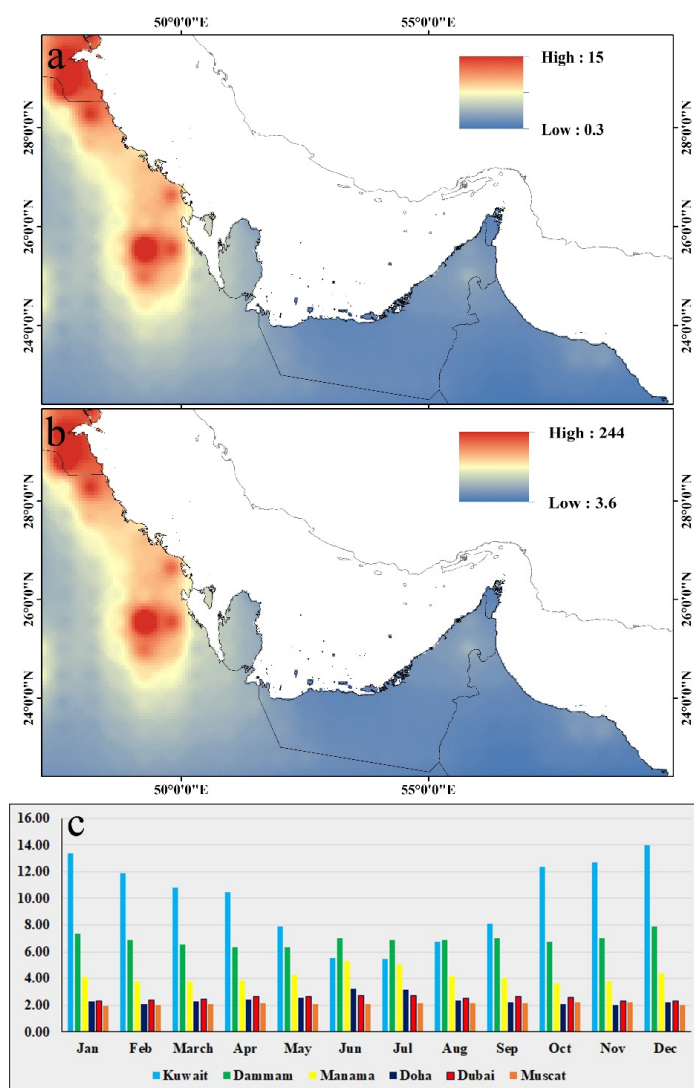
Figure 4. (**a**) is the distribution of the mean monthly SO_2 emissions in μgm/m^3 over the GCC countries between 1980 and 2020, (**b**) represents the trend (μgm/m^3 per decade), which are maximal in Dammam and Kuwait, and (**c**) shows the average monthly concentration of SO_2 in the six main cities. The source of the raw data is: https://giovanni.gsfc.nasa.gov/giovanni/; accessed on 18 February 2022.

The distribution of NO_2 is correlated mainly to the road traffic and to the indoor use of stoves, heaters, and fossil-fuel-burning appliances [39]. Therefore, it is obvious that the high mean concentrations of this pollutant are apparent in all the metropolitan agglomerations of the GCC countries, such as Kuwait City, Dammam, Manama, Doha, and Dubai (Figure 5a)

during the period from 2005–2020. The maximum monthly concentrations were observed in Abu Dhabi (9.2 Molecules/cm^2) and Kuwait cities (8.9 Molecules/cm^2). Interestingly, Ref. [40] reported that the GCC countries with high NO_2 emissions are UAE, KSA, and Kuwait. In addition, higher NO_2 from traffic was also reported in Kuwait City [41] and Abu Dhabi, UAE [40]. However, the decadal rate of NO_2 revealed recent inputs from other regions, such as Sohar in northern Oman (Figure 5b). This is confirmed by Ref. [42], who reported that the traffic near Sohar City in Oman yields double the average concentration of NO_2. In contrast, some cities, such as Dammam, experienced a decrease in the decadal trend. It is also clear that all the GCC cities have comparable monthly emissions, with relatively high emissions during the winter months (Figure 5c).
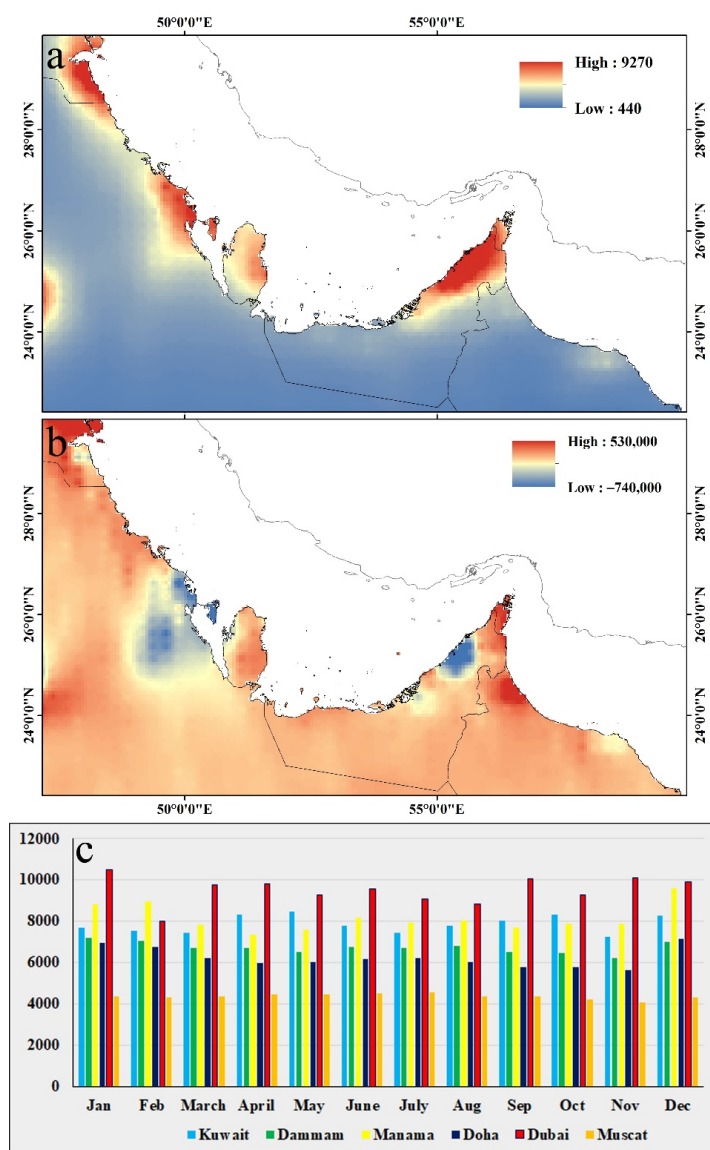
Figure 5. (**a**) is the distribution of the mean monthly NO_2 gas emissions in trillion molecules/cm^2 throughout the GCC countries between 2005 and 2020, (**b**) represents the trend (trillion molecules/cm^2 per decade), which is maximal in Sohar (Oman), and (**c**) shows the average monthly concentration of NO_2 in the six main cities. The source of the raw data is: https://giovanni.gsfc.nasa.gov/giovanni/; accessed on 18 February 2022.

Black carbon (BC) is considered to be a fine carbonaceous particulate matter (PM2.5) and occurs in the exhaust of the diesel-engine vehicles due to the incomplete combustion of fossil fuel. It is also produced from non-fossil fuels, such as biomass combustion [43]. It is a

significant source of climate change. Specifically, BC is the second largest anthropogenic contributor to global warming after CO_2 [44]. This pollutant was clearly observed in the GCC countries between 1980 and 2020, particularly in UAE and Kuwait. The maximum monthly averages were observed in Dubai (0.73 μg/m^3) and Kuwait (0.57 μg/m^3). The decadal trends were also remarkably the highest in both Kuwait and UAE (Figure 6a,b). The monthly distribution pattern was shown to be high during the late spring and early summer months, while the minimum values were recorded in January (Figure 6c). The peak occurrence of BC was encountered in Dubai, either at the monthly level, the annual mean, or the decadal trend.
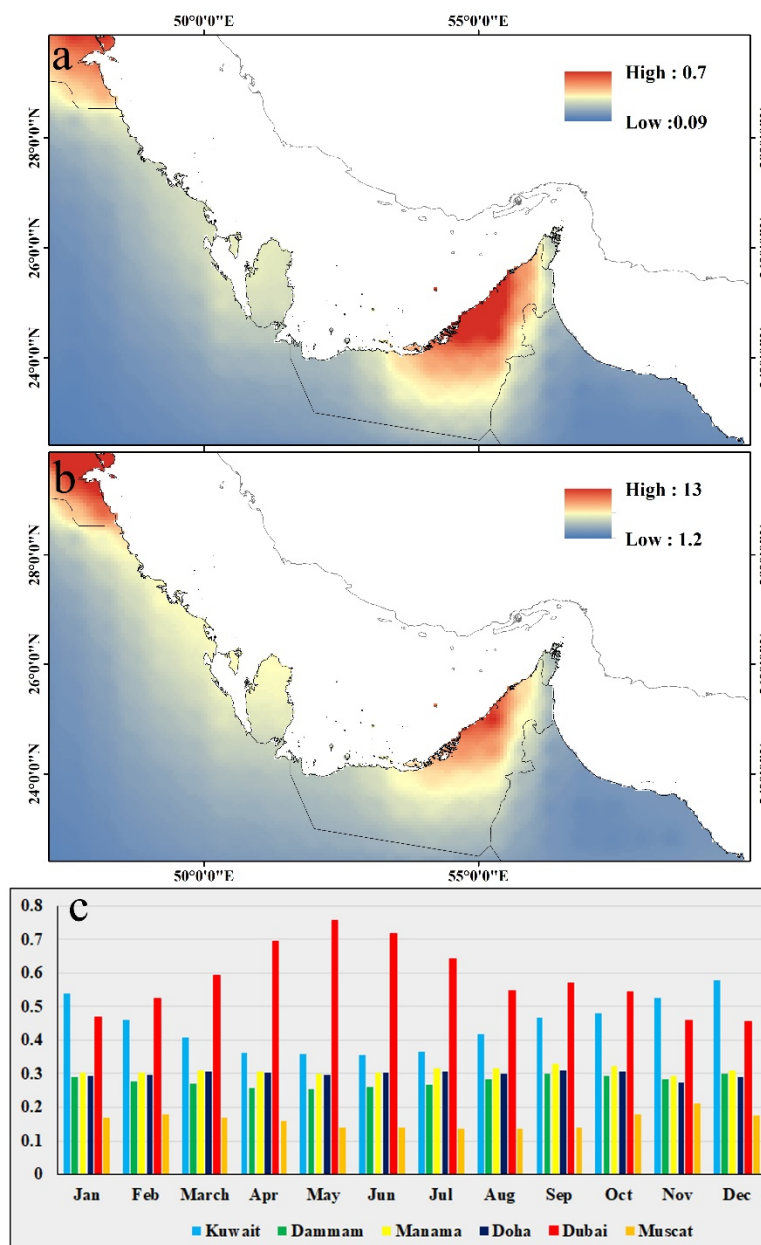
Figure 6. (**a**) is the distribution of the mean monthly BC emissions in μgm/m^3 throughout the GCC countries between 1980 and 2020, (**b**) represents the trend (μgm/m^3 per decade), which is maximal in Kuwait and Dubai, and (**c**) shows the average monthly concentration of BC in the six main cities. The source of the raw data is: https://giovanni.gsfc.nasa.gov/giovanni/; accessed on 18 February 2022.

3.2. Precipitation, Land Surface Temperatures and Anomalies of Surface Temperatures

The annual rainfall along the GCC countries for the period 2000–2018 significantly varies from one country to another. It is discernable that the mountainous ranges in Oman and UAE receive the maximum rainfall (>300 mm/year) by the orographic and monsoonal rains from the Indian Ocean [13]. The remaining parts receive less precipitation (~50 mm/year), except for northeastern Saudi Arabia, which receives relatively higher annual rainfall (up to 150 mm) (Figure 7a). The majority of rainfall occurs during winter; however, heavy torrential rainstorms may hit the region during fall and spring. The statistical analysis of the precipitation trends for this period (2000–2018) indicated a clear decrease (9.7 mm/decade) in precipitation, mostly over Kuwait and some parts of the KSA. On the other hand, Al-Hajar Mountain in northern Oman and the northern part of UAE are witnessing a rise in precipitation rates (up to 12.6 mm/decade). This is obvious due to the recent increase in the frequency of torrential rainstorms over Al-Hajar Mountain in Oman.
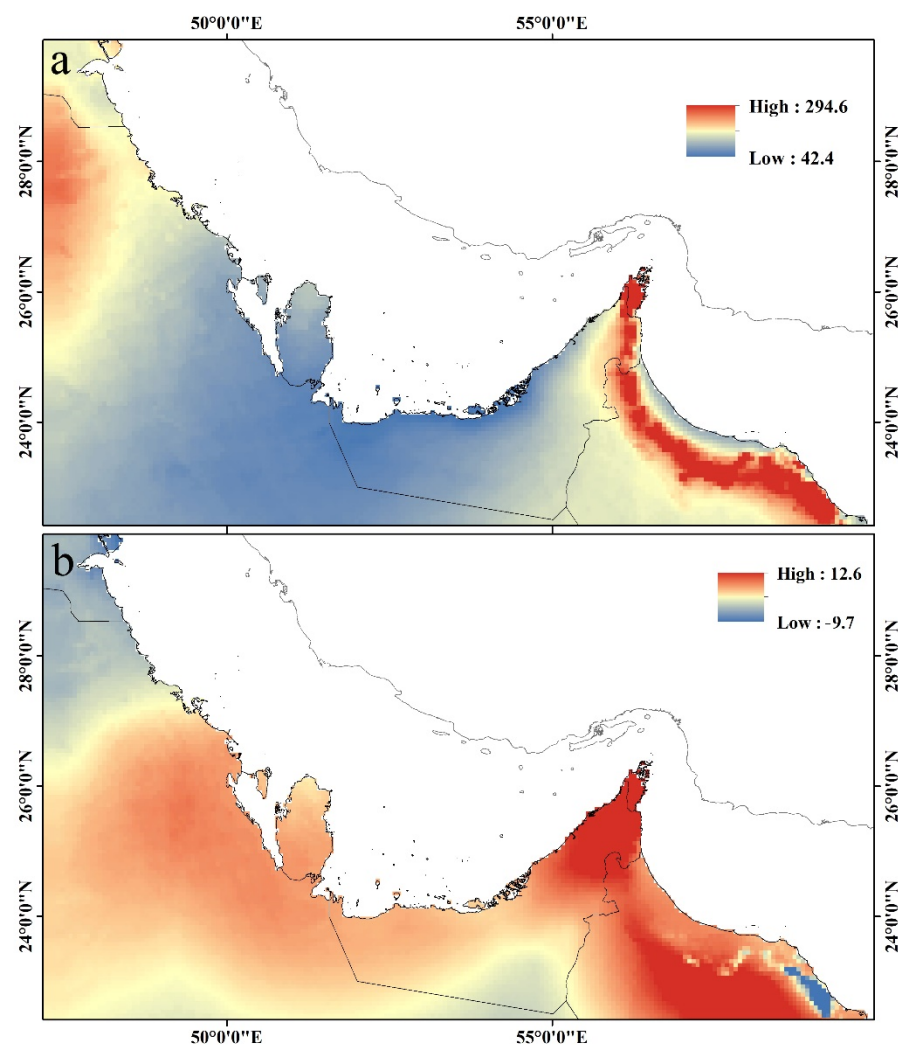
Figure 7. (**a**) is the distribution of the mean annual precipitation in mm throughout the GCC countries between 2000 and 2018, and (**b**) is the trend (mm/decade), which is positive (wetting) over Oman and negative (drying) over Kuwait. The source of the raw data is: https://www.worldclim.org; accessed on 18 February 2022.

The mean values of the land surface temperatures (LST) for the period from 2003–2020 showed higher records for the southern GCC countries, e.g., UAU and Oman, where the mean LSTs approached 50 °C for the plains and sandy terrains of these countries. The highlands in Oman and UAE have conspicuously lower LST than surrounding plateaus

(Figure 8a). The northern section of the GCC courtiers, including Kuwait, KSA, Bahrain, and Qatar, exhibited relatively lower mean LST, with a difference approaching 10–15 °C, as this region experiences colder winters than UAE and Oman due to the continental and latitudinal effects. The statistical LST trend for the study period (2003–2020) revealed a contradictory pattern to the mean values. Certainly, it is very clear that Kuwait, Bahrain, Qatar, the eastern province of KSA, and the middle part of the UAE have been exposed to a decadal LST warming (Figure 8b). Specifically, this warming has reached up to 2.0 °C/decade in Kuwait, 1.7 °C in Bahrain, and 1.5 in Dammam and Abu Dhabi (UAE). On the other hand, the inland desert of KSA and the highlands of Oman have experienced a decadal cooling in LST by about 0.1 to 0.8 °C/decade. The regional change of the LST for the entire region was toward warming by 0.62 °C/decade.
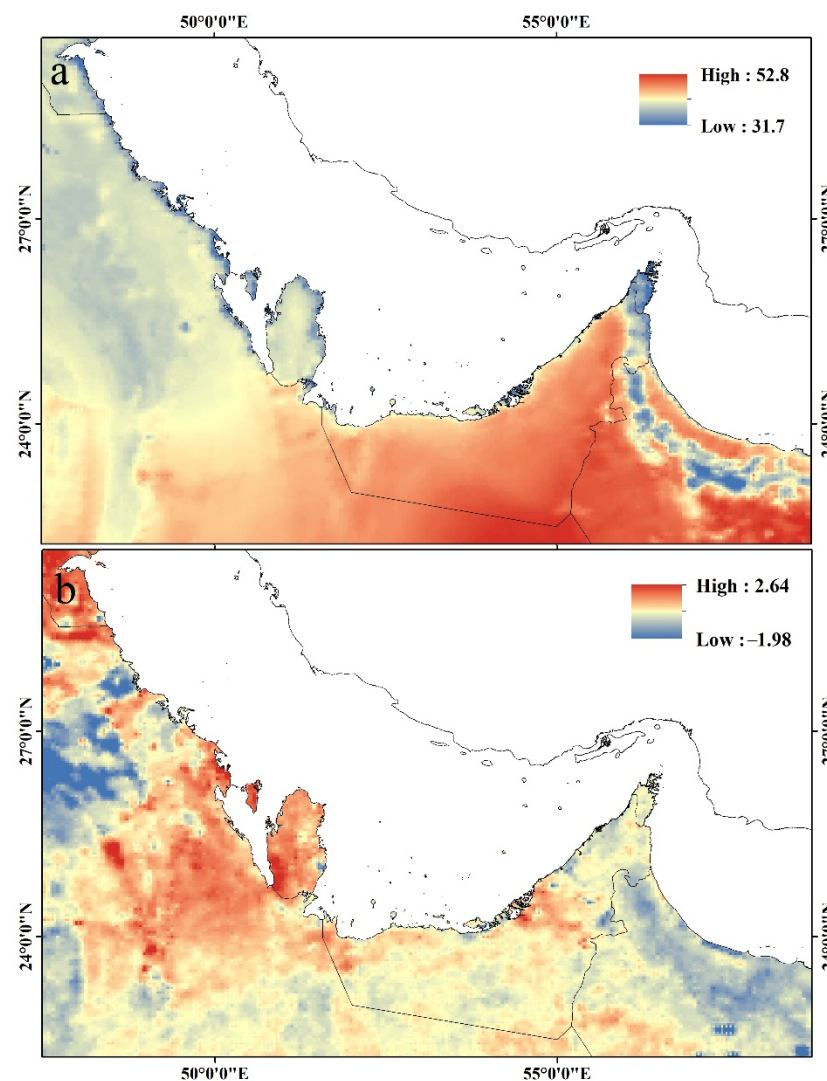
Figure 8. (**a**) is the distribution of the mean annual LST in degree Celsius over the GCC countries (2003–2020), and (**b**) is the trend (°C/decade), which reveals warming over Kuwait, Dammam, Bahrain, and Qatar and cooling over Oman and parts of KSA. The source of the data is: https://lpdaac.usgs.gov; accessed on 18 February 2022.

The average anomaly of nighttime surface temperature, as acquired from the AIRS satellite, showed that there has been an increase in the anomalies of extraordinary temperatures, particularly toward the warming of nights. However, it was observed that some of the GCC countries were exposed to several colder nights during the period from 2003–2016. Minimal nighttime anomalies occurred in 2005, 2008, and 2011, mostly in Kuwait and

Dubai, and reached 0.6 °C below average. Nevertheless, during the years 2010, 2015, and 2016, all the GCC countries experienced extreme warmer nights that were above the annual average. This is conspicuous, with maximal anomalies approaching 0.99 °C in Kuwait, Doha, and Manama (Figure 9a). Ref. [45] attributes the anomalous increase in temperatures during 2015/2016 to the El Niño/La Niña Southern Oscillation (ENSO) event. At the monthly level, it was observed that surface temperature anomalies are frequent during summer and early fall (from July to October), and the maximal values occurred in Kuwait and Muscat. However, during March, there was a decrease in temperatures that went below the average, with a minimum value in Manama. The remaining months exhibited values close to the average records. Generally, extraordinary nighttime heatwaves were frequent in Kuwait, Manama, Doha, and Dammam between 2003 and 2016, with minimal occurrences in Muscat.
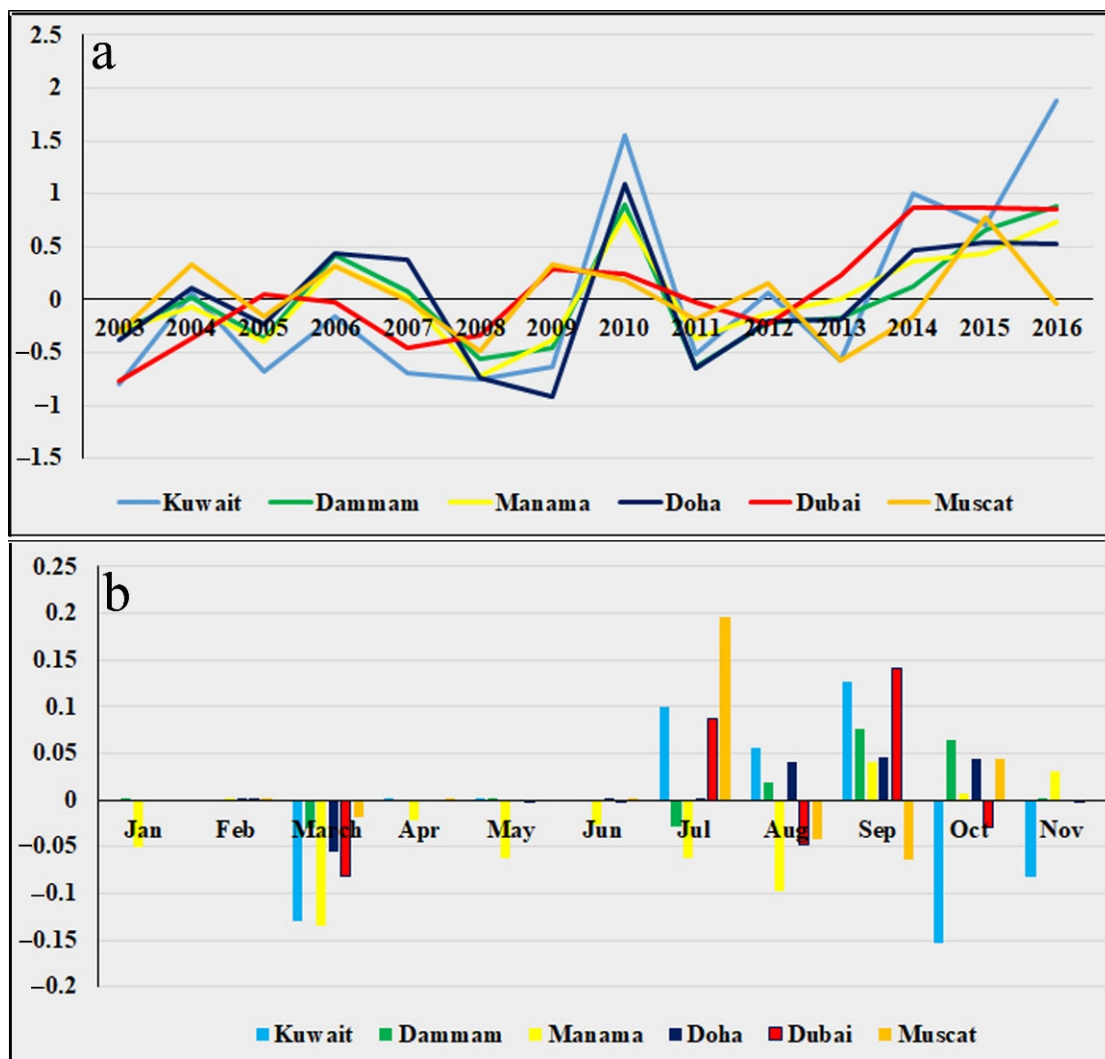
Figure 9. (**a**) is the average nighttime surface temperature anomalies in degree Celsius for the main cities along the gulf between 2003 and 2016, and (**b**) is the monthly distribution of nighttime surface temperature anomalies. The source of the raw data is: https://giovanni.gsfc.nasa.gov/giovanni/; accessed on 18 February 2022.

3.3. Sea Surface Temperatures

The Arabian Gulf, which is a shallow inland sea with a mean depth of about 40 m, reveals considerable variations in its sea surface temperatures. This is attributed mainly to the latitudinal location of this semi-enclosed, inland water body. In addition, the gulf

environment is significantly influenced by evaporation, circulation, and lateral exchange with the Arabian Sea [46]. There is a thermal gradient in the mean LST of the gulf from south to north. The mean annual SST for the period from 2003–2018 was maximal along the coasts of UAE and Oman (~28 °C) in the south, while the coldest waters occurred near the offshores of Kuwait (~24 °C) in the north (Figure 10a). The decadal trends of SST agree with the regional LST decadal trend, where the northern section is warming up at maximal rates. This is obvious in areas where there has been a warming of 1.64 °C/decade, such as the coasts of Kuwait and KSA. The least warming was recorded near the entrance of the gulf at the Strait of Hurmuz (~0.2 °C/decade). Considerable warming (0.6–1.0 °C/decade) was also observed near the offshores of Qatar, Bahrain, and UEA (Figure 10b). The overall decadal rate of the entire gulf is 0.7 °C/decade. The low warming trend in the southern part of the gulf might be attributed to the connection with the Indian Ocean and the exchange of energy with the deep, colder water body along the Sea of Oman.
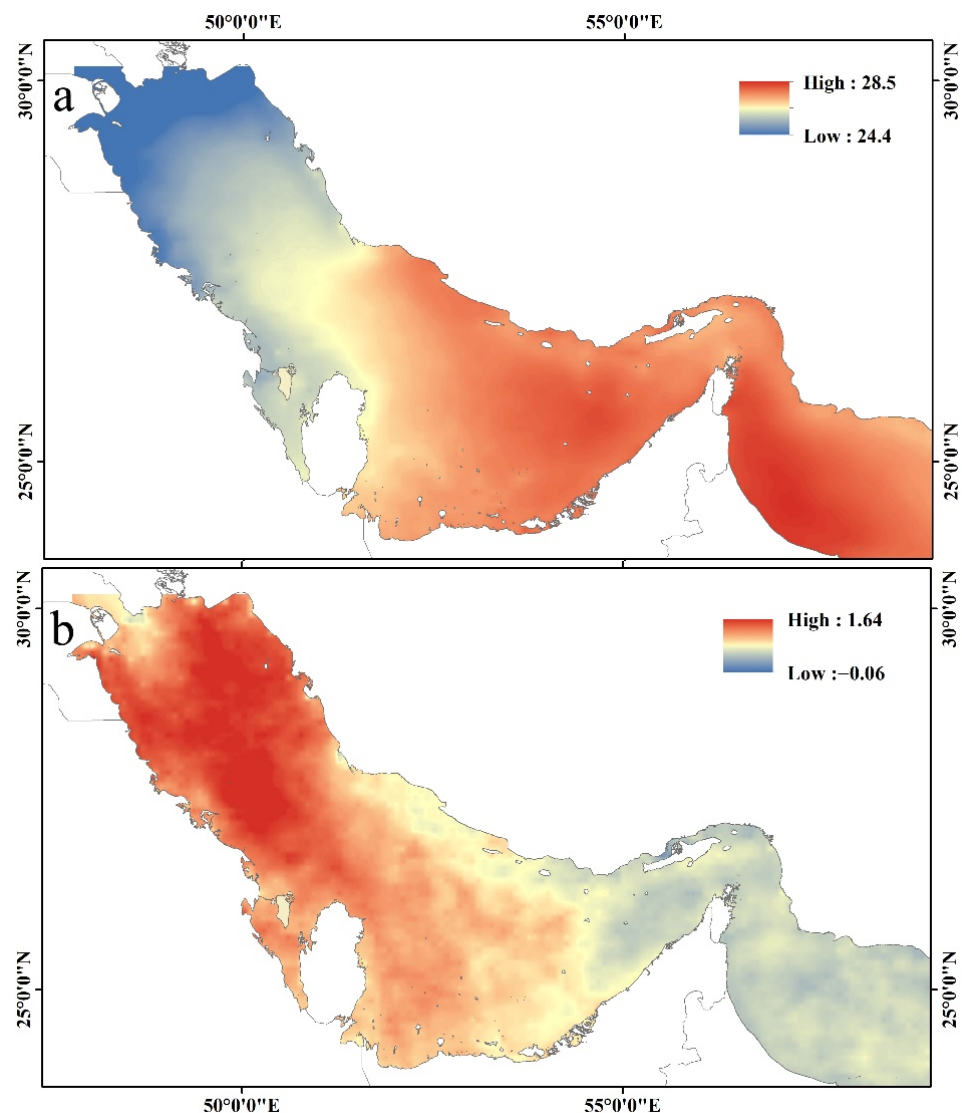
Figure 10. (**a**) is the distribution of the mean annual SST degree Celsius over the Arabian Gulf (2003–2018), and (**b**) is the trend (°C/decade), which reveals high warming near Kuwait, Dammam, Bahrain, and Qatar. The source of the raw data is: http://oceancolor.gsfc.nasa.gov; accessed on 18 February 2022.

4. Discussion and Conclusions

The GCC union includes some of the countries with the most excessive energy consumption and is considered a global hub for oil and gas reserves. Lately, fossil-fuel related activities have bloomed in the region, resulting in substantial and immense emissions of greenhouse gases and air pollutants. The GCC countries have a unique socio-economic setting that relies on huge oil reserves. These countries account for about a quarter of the world's crude oil production, mostly stemming from Saudi Arabia, the UAE, and Kuwait, and these three countries were among the ten largest producers of crude oil in the world in 2018 [47]. In addition, the majority of the GCC countries can be found in the top ten worldwide ranks of energy consumption per capita [48]. Moreover, the low energy prices have attracted foreign companies to establish investments, which has not only influenced the economy but also increased the energy demand [49]. In addition, the number of motor vehicles in GCC countries was 221% more than the average value in Asia, Oceania, and the Middle East in 2015 [50]. The excessive use of energy, specifically fossil fuels, imposes considerable pressure upon these non-renewable resources. As such, the current study proves that there are considerable emissions of GHGs and air pollution. Looking at the emissions of the two greenhouse gases (CO_2 and CH_4), it is clear that there has been a substantial increase in both gases during the past two decades. CO_2 increased from 375 ppm to more than 400 ppm. In this context, Ref. [13] mentioned that the CO_2 emissions in 2012 alone were four times the average per capita in the world. However, this increase in CO_2 emission has been documented to be ubiquitous and remarkable worldwide. The present study indicates that the highest rates of emissions were encountered in KSA, UAE, and Kuwait, where energy sources rely mainly on fossil fuels [51]. In Saudi Arabia, for example, the demand for crude oil for the energy sector increased by 340% between 2006 and 2011 [52]. Simultaneously, CH_4 emissions also showed increased rates in the third millennium. For a country like Oman, where the decadal rate of emission is the highest of the GCC countries, CH_4 emissions from the oil and gas sectors are the primary contributor to the country's total GHG emissions [35]. It is also remarkable that GHGs were at a maximum during the summer months and at a minimum during winter. Regionally, the GCC countries contributed 2.4% of GHG emissions during a time when only 0.6% of the world's population was alive [53]. In addition to these GHGs, significant air pollutants also showed higher outputs into the atmosphere in GCC countries, particularly Kuwait, UAE, and KSA. In contrary to GHGs, SO_2 and NO_2 emissions are maximal during winter, while BC emissions are maximal during summer. The present study demonstrates that GCC countries reveal higher emissions of SO_2, NO_2, and BC. Many concentrations of these air pollutants are quite observable in the industrial regions of GCC countries. Consequent impacts involve the deterioration of air quality and the blooming of air-borne diseases. The health impacts of air pollution are noteworthy in GCC countries due to the higher relative humidity in the region [54]. Some studies attribute the high health risk and mortality in Kuwait to the increased levels of air pollution [55,56], while Ref. [57] claims that air pollution is responsible for 9% of mortality in Saudi Arabia. The lowest emissions of the studied air pollutants were observed in Oman.

Decadal changes in regional precipitation, land surface temperatures, and sea surface temperatures were apparent from the remotely sensed data. Statistical analysis revealed a decline in precipitation in the northern part, including the entire State of Kuwait and some parts of Saudi Arabia. This observation is confirmed by Ref. [58], who reported declining rates of rainfall in this region of the Arabian Peninsula. These results also agree with the projected climate change scenarios in terms of the aridity and drought of the Arabian Peninsula, where wetter conditions will prevail south of 25 °N and drier conditions will occur north of 25 °N [59]. Interestingly, the present study showed a relative wetting in some parts of Oman (south of 25 °N). It is worth noting that there was a substantial increase in the surface temperature anomalies during summer nights. This concept was previously established in Saudi Arabia by Ref. [60], who observed that the number of abnormal warm nights increased by 21 days during the decades between 1979 and 2019.

Concurrently, remotely sensed land surface temperature analysis showed considerable warming, particularly along the northern section. The present study demonstrates that GCC countries revealed a net warming of the land by 0.6 °C/decade over the past twenty years, with maximal warming (2 °C/decade) in Kuwait. It is important to note that the rate of global temperatures increased globally by 1.1 °C in the last 150 years, with higher rates after 1970 [61]. Remarkably, Ref. [58], in their analysis regarding the changes in the regional air temperatures using data acquired from 25 meteorological stations for the period from 1980–2010, reported an increase in the air temperatures of the Arabian Peninsula by 0.63 °C/decade. In addition, Ref. [62], using data from 44 stations, reported that the Arabian Peninsula witnessed a warming trend of 0.55/decade for the period from 1980–2008. Climate change has been also observed to influence the Arabian Gulf's surface water temperatures. Although the northern section of the gulf is the coldest, it experiences the most warming of the entire water body. The study indicates that the warming of this part of the gulf approaches 0.7 °C/decade. This was also confirmed by Ref. [63], who reported the comparable warming (0.6/decade) of the Kuwait Bay for the period from 1985–2002. The southern section of the Gulf witnessed the least warming during the study period due to the connection with the Indian Ocean through the Sea of Oman. Overall, it was observed that there is a dipole pattern in the severity of climate change elements (LST, precipitation, and SST) in the GCC countries. The northern section of the GCC countries, particularly Kuwait and northern KSA, revealed the highest degree of climate change in terms of decreasing rates of precipitation, increasing LST, warm nighttime anomalies, and a warming of the sea surface temperatures of the gulf water. On the other hand, the southern side of the GCC countries, mostly Oman and parts of UAE, exhibited lower degrees of climate change, mostly a localized warming in LST.

The present study could help to prioritize the management of the natural resources of the GCC region. However, the truthfulness of the results is definitely related to the quality of the data used. Limitations of this research include the coarse resolution of the data, the short period of coverage for some parameters, and the absence of ground-based measurements for validation. The launch of the recent atmosphere-monitoring satellites, such as the Sentinel-5 Precursor in 2017, will provide detailed information about the atmosphere and its constituents via fine spatial resolution data. Also, as the study period in the current investigation is still limited to draw a solid trend of climate change and there should be longer time-series data to yield reliable results, observations of temperature and precipitation changes agree with localized previous studies, which utilized a longer time span. Furthermore, future research will focus on the integration between space-based and ground-based measurements for more trustworthy outcomes.

References

1. Ritchie, H.; Roser, M. CO$_2$ and Greenhouse Gas Emissions. 2020. Available online: https://ourworldindata.org/co2-and-other-greenhouse-gas-emissions (accessed on 4 April 2022).
2. Intergovernmental Panel on Climate Change (IPCC). *Climate Change 2013: The Physical Science Basis*; Working Group I Contribution to the IPCC Fifth Assessment Report; Cambridge University Press: Cambridge, UK, 2013.
3. Nyambuu, U.; Semmler, W. Climate change and the transition to a low carbon economy—Carbon targets and the carbon budget. *Econ. Model.* **2020**, *84*, 367–376. [CrossRef]
4. Department of Energy and Climate Change (DECC). *The UK Low Carbon Transition Plan: National Strategy for Climate and Energy*; Department of Energy and Climate Change: London, UK, 2009.
5. Borroni, E.; Pesatori, A.; Bollati, V.; Buoli, M.; Carugno, M. Air pollution exposure and depression: A comprehensive updated systematic review and meta-analysis. *Environ. Pollut.* **2022**, *292*, 118245. [CrossRef]

6.   WHO. *Ambient Air Pollution: A Global Assessment of Exposure and Burden of Disease*; World Health Organization: Geneva, Switzerland, 2016.

7.   *Statistical Review of World Energy, June 2008*; BP: London, UK, 2008. Available online: https://www.bp.com/en/global/corporate/energy-economics/statistical-review-of-world-energy.html (accessed on 15 January 2022).

8.   Asif, M. Growth and sustainability trends in the buildings sector in the GCC region with particular reference to the KSA and UAE. *Renew. Sustain. Energy Rev.* **2016**, *55*, 1267–1273. [CrossRef]

9.   Salahuddin, M.; Gow, J. Economic growth, energy consumption and CO_2 emissions in Gulf Cooperation Council countries. *Energy* **2014**, *73*, 44–58. [CrossRef]

10. Charabi, Y.; Al Nasiri, N.; Al Awadhi, T.; Choudri, B.; Al Bimani, A. GHG emissions from the transport sector in Oman: Trends and potential decarbonization pathways. *Energy Strategy Rev.* **2020**, *32*, 100548. [CrossRef]

11. Rahman, S.; Khondaker, A.; Hasan, M.; Reza, I. Greenhouse gas emissions from road transportation in Saudi Arabia—A challenging frontier. *Renew. Sustain. Energy Rev.* **2017**, *69*, 812–821. [CrossRef]

12. Khondaker, A.N.; Hassan, M.; Rahman, S.; Malik, K.; Shafiullah, M.; Muhyedeen, M. Greenhouse gas emissions from energy sector in the United Arab Emirates—An overview. *Renew. Sustain. Energy Rev.* **2016**, *59*, 1317–1325. [CrossRef]

13. Al-Maamary, H.M.; Kazem, H.A.; Chaichan, M.T. Climate change: The game changer in the Gulf Cooperation Council Region. *Renew. Sustain. Energy Rev.* **2017**, *76*, 555–576. [CrossRef]

14. Omidvarborna, H.; Baawain, M.; Al-Mamun, A. Ambient air quality and exposure assessment study of the Gulf Cooperation Council countries: A critical review. *Sci. Total Environ.* **2018**, *636*, 437–448. [CrossRef] [PubMed]

15. Kim, D.-W.; Byun, H.-R. Future pattern of Asian drought under global warming scenario. *Arch. Meteorol. Geophys. Bioclimatol. Ser. B* **2009**, *98*, 137–150. [CrossRef]

16. Scafetta, N. Climate change and its causes, a discussion about some key issues. *arXiv* **2010**, arXiv:1003.1554.

17. Hereher, M. Assessment of climate change impacts on sea surface temperatures and sea level rise—The Arabian Gulf. *Climate* **2020**, *8*, 50. [CrossRef]

18. Al-Fazari, A.; El-Kenawy, A.; Al-Nasiri, N.; Hereher, M. *Monitoring Urban Heat Islands in Selected Cities of the Gulf Region Based on Nighttime MODIS LST Data (2003–2018). Urban Heat Island (UHI) Mitigation: Hot and Humid Regions*; Springer: Berlin/Heidelberg, Germany, 2020; Chapter 12; pp. 249–276.

19. IPCC. *Global Warming of 1.5 °C*; IPCC Special Report on the impacts of global warming of 1.5 °C above pre-industrial levels and related global greenhouse gas emission pathways, in the context of strengthening the global response to the threat of climate change, sustainable development, and efforts to eradicate poverty; Masson-Delmotte, V., Zhai, P., Pörtner, H.-O., Roberts, D., Skea, J., Shukla, P.R., Pirani, A., Moufouma-Okia, W.C., Péan, R., Pidcock, S., et al., Eds.; The Intergovermnetal Panel on Climate Change: Geneva, Switzerland, 2018; Available online: https://www.ipcc.ch/sr15 (accessed on 20 February 2022).

20. Martins, F.; Benassi, R.; Torres, R.; Neto, F. Impacts of 1.5 °C and 2 °C global warming on Eucalyptus plantations in South America. *Sci. Total Environ.* **2022**, *825*, 153820. [CrossRef] [PubMed]

21. Fotso-Nguemo, T.; Vondou, D.; Diallo, I.; Diedhiou, A.; Weber, T.; Tanessong, R.; Nghonda, J.; Yepdo, Z. Potential impact of 1.5, 2 and 3 °C global warming levels on heat and discomfort indices changes over Central Africa. *Sci. Total Environ.* **2021**, *804*, 150099. [CrossRef]

22. Hereher, M.; El Kenawy, A. Exploring the potential of solar, tidal, and wind energy resources in Oman using an integrated climatic-socioeconomic approach. *Renew. Energy* **2020**, *161*, 662–675. [CrossRef]

23. Elrahmani, A.; Hannun, J.; Eljack, F.; Kazi, M.-K. Status of renewable energy in the GCC region and future opportunities. *Curr. Opin. Chem. Eng.* **2020**, *31*, 100664. [CrossRef]

24. Ünal, F.; Temir, G.; Köten, H. Energy, exergy and exergoeconomic analysis of solar-assisted vertical ground source heat pump system for heating season. *J. Mech. Sci. Technol.* **2018**, *32*, 3929–3942. [CrossRef]

25. Cura, D.; Yilmaz, M.; Koten, H.; Senthilraja, S.; Awad, M.M. Evaluation of the technical and economic aspects of solar photovoltaic plants under different climate conditions and feed-in tariff. *Sustain. Cities Soc.* **2022**, *80*, 103804. [CrossRef]

26. Alharbi, F.; Csala, D. Gulf Cooperation Council Countries' Climate Change Mitigation Challenges and Exploration of Solar and Wind Energy Resource Potential. *Appl. Sci.* **2021**, *11*, 2648. [CrossRef]

27. Flores, R.; Kaya, N.; Eser, O.; Saltan, S. The effect of mineral dust transport on PM 10 concentrations and physical properties in Istanbul during 2007–2014. *Atmos. Res.* **2017**, *197*, 342–355. [CrossRef]

28. Wan, Z. New refinements and validation of the MODIS Land-Surface Temperature/Emissivity products. *Remote Sens. Environ.* **2008**, *112*, 59–74. [CrossRef]

29. Fick, S.E.; Hijmans, R.J. WorldClim 2: New 1-km spatial resolution climate surfaces for global land areas. *Int. J. Climatol.* **2017**, *37*, 4302–4315. [CrossRef]

30. Carlson, D.F.; Yarbro, L.A.; Scolaro, S.; Poniatowski, M.; McGee-Absten, V.; Carlson, P.R., Jr. Sea surface temperatures and seagrass mortality in Florida Bay: Spatial and temporal patterns discerned from MODIS and AVHRR data. *Remote. Sens. Environ.* **2018**, *208*, 171–188. [CrossRef]

31. Apaydin, H.; Sonmez, F.; Yildirim, Y. Spatial interpolation techniques for climate data in the GAP region in Turkey. *Clim. Chang.* **2004**, *28*, 31–40. [CrossRef]

32. Ozelkan, E.; Bagis, S.; Ozelkan, E.; Ustundag, B.; Yucel, M.; Ormeci, C. Spatial interpolation of climatic variables using land surface temperature and modified inverse distance weighting. *Int. J. Remote Sens.* **2015**, *36*, 1000–1025. [CrossRef]

33. Mahmood, H. The effects of natural gas and oil consumption on CO2 emissions in GCC countries: Asymmetry analysis. *Environ. Sci. Pollut. Res.* **2022**, 1–17. Available online: https://pubmed.ncbi.nlm.nih.gov/35359204/ (accessed on 15 January 2022). [CrossRef]

34. Farahat, A. The Impact of the 2020 Oil Production Fluctuations on Methane Emissions over the Gulf Cooperation Council (GCC) Countries: A Satellite Approach. *Atmosphere* **2022**, *13*, 11. [CrossRef]

35. Charabi, Y. Digging deeper into cutting methane emissions from the oil and gas industry in the era of volatile prices. *Mitig. Adapt. Strateg. Glob. Chang.* **2021**, *26*, 6. [CrossRef]

36. Al-Jahdali, M.O.; Bin Bisher, A.S. Sulfur Dioxide (SO$_2$) Accumulation in Soil and Plant's Leaves around an Oil Refinery: A Case Study from Saudi Arabia. *Am. J. Environ. Sci.* **2008**, *4*, 84–88. [CrossRef]

37. Dahiya, S.; Myllyvirta, L.; Global SO2 Emission Hotspot Database. Greenpeace Environment Trust. 2019. Available online: https://www.greenpeace.org (accessed on 29 March 2022).

38. Al-Rashidi, M.; Nassehi, V.; Wakeman, R. Investigation of the efficiency of existing air pollution monitoring sites in the state of Kuwait. *Environ. Pollut.* **2005**, *138*, 219–229. [CrossRef]

39. Hereher, M.; Eissa, R.; Alqasemi, A.; El Kenawy, A.M. Assessment of air pollution at Greater Cairo in relation to the spatial variability of surface urban heat island. *Environ. Sci. Pollut. Res.* **2021**, *29*, 21412–21425. [CrossRef]

40. Lelieveld, J.; Hoor, P.; Jöckel, P.; Pozzer, A.; Hadjinicolaou, P.; Cammas, J.P.; Beirle, S. Severe ozone air pollution in the Persian Gulf region. *Atmos. Chem. Phys.* **2009**, *9*, 1393–1406. [CrossRef]

41. Khan, A.; Al-Salem, S. Seasonal variation effect on airborne pollutants in an urban area of the state of Kuwait. *J. Environ. Res. Dev.* **2007**, *1*, 215–218.

42. Chaichan, M.T.; Al-Asadi, K.A. Environmental impact assessment of some vehicles pollutants in Sohar, Oman. *Int. J. Sci. Eng. Res.* **2015**, *6*, 493–496.

43. Wyche, K.P.; Cordell, R.L.; Smallbone, K.L.; Lyons, P.; Hama, S.M.L.; Monks, P.S.; Staelens, J.; Hofman, J.; Stroobants, C.; Roekens, E.; et al. The spatio-temporal evolution of black carbon in the North-West European 'air pollution hotspot'. *Atmos. Environ.* **2020**, *243*, 117874. [CrossRef]

44. Comer, B. Including Estimates of Black Carbon Emissions in the Fourth IMO GHG Study. The International Council of Clean Transportation (ICCT). 2019. Available online: https://wwwcdn.imo.org/localresources/en/OurWork/Environment/Documents/CSC-Bryan%20Comer.pdf (accessed on 31 March 2021).

45. Varotsos, C.A.; Cracknell, A.P.; Efstathiou, M.N. The global signature of the El Niño/La Niña Southern Oscillation. *Int. J. Remote Sens.* **2018**, *39*, 5965–5977. [CrossRef]

46. Xue, P.; Eltahir, E. Estimation of the Heat and Water Budgets of the Persian (Arabian) Gulf Using a Regional Climate Model. *J. Clim.* **2015**, *28*, 5041–5062. [CrossRef]

47. BP. Statistical Review of World Energy. 2019. Available online: https://www.bp.com/en/global/corporate/news-and-insights/press-releases/bp-statistical-review-of-world-energy-2019.html (accessed on 5 April 2022).

48. Iriani, M.; Trabelsi, M. The economic impact of phasing out energy consumption subsidies in GCC countries. *J. Bus. Econ. Manag.* **2016**, *87*, 35–49. [CrossRef]

49. Bhutto, A.W.; Bazmi, A.A.; Zahedi, G.; Klemeš, J.J. A review of progress in renewable energy implementation in the Gulf Cooperation Council countries. *J. Clean. Prod.* **2014**, *71*, 168–180. [CrossRef]

50. OICA. International Organization of Motor Vehicle Manufacturers, Vehicle in Use by Country and Type 2005–2015. Available online: https://www.oica.net/wp-content/uploads//Total_in-use-All-Vehicles.pdf (accessed on 9 April 2022).

51. Statistica Research Department. Volume of Greenhouse Gas Emissions in the Gulf Cooperation Council in 2014, by Country. 2017. Available online: https://www.statista.com/statistics/814843/gcc-volume-of-ghg-emissions-by-country/ (accessed on 5 April 2022).

52. IEA. World Energy Outlook 2010, Paris Cedex, France. 2011. Available online: https://www.iea.org/reports/world-energy-outlook-2010 (accessed on 1 March 2022).

53. Reiche, D. Energy Policies of Gulf Cooperation Council (GCC) Countries—Possibilities and Limitations of Ecological Modernization in Rentier States. *Energ. Policy* **2010**, *38*, 2395–2403. [CrossRef]

54. Amoatey, P.; Omidvarborna, H.; Baawain, S.; Al-Mamun, A. Indoor air pollution and exposure assessment of the gulf cooperation council countries: A critical review. *Enviro. Int.* **2018**, *121*, 491–506. [CrossRef]

55. Achilleos, S.; Al-Ozairi, E.; Alahmad, B.; Garshick, E.; Eophytou, A.; Bouhamra, W.; Yassin, M.; Koutrakis, P. Acute effects of air pollution on mortality: A 17-year analysis in Kuwait. *Environ. Int.* **2019**, *126*, 476–483. [CrossRef]

56. Al-Hemoud, A.; Gasana, J.; Al-Dabbous, A.; Alajeel, A.; Al-Shatti, A.; Behbehani, W.; Malak, M. Exposure levels of air pollution (PM2.5) and associated health risk in Kuwait. *Environ. Res.* **2019**, *179*, 108730. [CrossRef] [PubMed]

57. Rojas-Rueda, D.; Alsufyani, W.; Herbst, C.; AlBalawi, S.; Alsukait, R.; Alomran, M. Ambient particulate matter burden of disease in the Kingdom of Saudi Arabia. *Environ. Res.* **2021**, *197*, 111036. [CrossRef]

58. Almazroui, M.; Islam, N.; Saeed, S.; Saeed, F.; Ismail, M. Future Changes in Climate over the Arabian Peninsula based on CMIP6 Multimodel Simulations. *Earth Syst. Environ.* **2020**, *4*, 611–630. [CrossRef]

59. Waha, K.; Krummenauer, L.; Adams, S.; Aich, V.; Baarsch, F.; Coumou, D.; Schleussner, C.F. Climate change impacts in the Middle East and Northern Africa (MENA) region and their implications for vulnerable population groups. *Reg. Environ. Change* **2017**, *17*, 1623–1638. [CrossRef]

60. Almazroui, M. Changes in Temperature Trends and Extremes over Saudi Arabia for the Period 1978–2019. *Adv. Meteorol.* **2020**, *2020*, 1–21. [CrossRef]

61. Intergovernmental Panel on Climate Change (IPCC). Summary for Policymakers. In *Climate Change 2021: The Physical Science Basis*; Contribution of Working Group I to the Sixth Assessment Report of the Intergovernmental Panel on Climate Change; Masson-Delmotte, V., Zhai, P., Pirani, A., Connors, S.L., Péan, C., Berger, S., Caud, N., Chen, Y., Goldfarb, L., Gomis, M., et al., Eds.; Cambridge University Press: Cambridge, UK, 2021; *in press*.

62. AlSarmi, S.; Washington, R. Recent observed climate change over the Arabian Peninsula. *J. Geophys. Res. Atmos.* **2011**, *116*, 1–15. [CrossRef]

63. Al-Rashidi, T.B.; El-Gamily, H.I.; Amos, C.L.; Rakha, K.A. Sea surface temperature trends in Kuwait bay, Arabian Gulf. *Nat. Hazards* **2009**, *50*, 73–82. [CrossRef]

Article

Mathematical Modelling of Biogas Production in a Controlled Landfill: Characterization, Valorization Study and Energy Potential

Mabrouki Jamal (ID)

Laboratory of Spectroscopy, Molecular Modeling, Materials, Nanomaterial, Water and Environment, CERNE2D, Faculty of Science, Mohammed V University in Rabat, Avenue Ibn Battouta, Agdal, Rabat BP1014, Morocco; jamal.mabrouki@um5r.ac.ma

Abstract: Methane potential is the volume of methane gas produced during anaerobic degradation in the presence of the bacteria of an initially inserted sample. This paper presents a degradation study of the green and industrial fermentable waste sheltered by the landfill of Mohammedia in which the biogas deposit and the associated recoverable energy at the end of exploitation is estimated and the power of the gas engine of the proposed cogeneration unit is calculated. The Total potential biogas production value of the household waste of the city of Mohammedia is much higher than that of the American and French household waste recommended by the US EPA and French ADEME. This calls into question the adaptability of the modeling tools for biogas production to Moroccan waste. The four modeling equations for landfill will be evaluated. The results show that the ADEME model proved to be more descriptive and better adapted to this case.

Keywords: modeling; biogas; methane; landfill of Mohammedia; upgrading

1. Statement of Novelty

The recuperation of biogas from the Mohammedia site landfill was calculated utilizing four demonstrating conditions, and the present models included only family waste, with methanogenic potential estimations of 100 m^3 to 170 m^3 of CH_4/ton of waste for the American models and 50 out of 100 for the French ADEME model. To adjust to the Moroccan setting, and especially to the instance of Mohammedia, we extrapolated a lot of information on waste from various regions and enterprises so as to get values depicting the methanogenic potential specific to the various substrates. This permitted us to gauge the biogas deposit indicated by the given operating horizon.

2. Introduction

Landfill is an easy to implement and relatively inexpensive waste disposal technique. Without proper management, however, it can lead to a variety of hygienic, health and environmental problems. Only a landfill that has been stabilized, and is therefore without further development, can be defined as no longer being harmful to the environment. When it comes to renewable energies, wind turbines, solar collectors and hydropower are most often mentioned. However, there are other solutions, such as energy production from biomass: wood, biofuels or biogas [1]. The population of developing countries is growing, leading to an increase in the needs of the poor and the production of waste and effluents. Waste recycling contributes to poverty alleviation and environmental sanitation [2].

Mechanization is an anaerobic digestion process that generally achieves double the energy yield of the original process. The objective of energy recovery by methane (CH_4) is the recovery and stabilisation of organic waste with a view to material recovery by its partial restitution to the ground [3,4]. With ever-increasing and more diversified consumption all over the world, waste production is constantly increasing in quantity and quality, thus creating enormous risks to the environment and both the safety and health of local

265

populations [3]. Landfilling remains the predominant method of disposal of household and similar waste in Africa, particularly in Morocco, in part because of its simplicity, but also because of its lower cost compared with other methods, such as incineration.

The Mohammedia control landfill receives a significant amount of waste with high methanogenic potential every day, such as household waste (61% organic matter), green waste, poultry droppings and tannery waste. By anaerobic decomposition, this mixture generates a good quality biogas (CH_4 55.6%, CO_2 32%, H_2S 600 ppm, O_2 1%) which reminds us of its value in other applications [3]. This study was carried out in order to quantify the biogas deposit at the Mohammedia site using four modelling equations, these models using only household waste, with methanogenic potential values in the order of 100 m^3 to 170 m^3 of CH_4/tonne of waste for the American models [5] and 50 of 100 for the French ADEME model [6], corresponding to the specificities of the waste and the regions where these tools were developed [7]. In order to adapt them to the Moroccan context, in particular to the case of Mohammedia, we extrapolated a heap of data on waste from different municipalities and industries in order to obtain values describing the methanogen potential specific to the different substrates. This allowed us to estimate the biogas deposit according to the given operating horizon.

3. Description of the Studied Zone

The Mohammedia interprovincial control landfill is located in the municipality of Ben Yakhlef, on the shoreline. It is west of Chaaba el Hamra, a tributary of the west bank of the Nfifikh river, about 270 m south of the Dayat Al Hila security perimeter (X = 32440, Y = 338979) and occupies an area of 47 hectares.

The zone is moderately hilly and ends at the edge of the west bank of a talweg (Chaaba El Hamra) perpendicular to the west bank of Oued Nfifikh. From upstream to downstream, the site has a height difference of 27 m. Its proximity to the ocean gives this region a temperate and humid climate (80% humidity) with a mild winter and a summer cooled by the ocean breezes. The average temperature is 23 °C and the annual precipitation level is 400 mm, in addition to a daily evapotranspiration potential of 5–6 mm/12 h. Eleven rural and urban municipalities (including Mohammedia, Ain Harrouda, Bouznika, Ben Sliman, El Mansouria, Ech-Challalat, Ben Yakhlaf, Sidi Mousa ben ali and Sidi Mousa El Majdoub) are served by the so-called landfill centre, which started in 2012 and is scheduled to close in 2032. The project area is divided between the landfill area and other landfill accessories, as described in the plan below, which shows the biogas collection network of crates 1 and 2, already in operation [8].

4. Materials and Methods

4.1. Experimental Design

In order to measure the amount of biogas produced by the waste studied, an anaerobic digestion device and a device for determining the volume of biogas generated by water displacement were established in the laboratory. A mass of 20 g of each sample was crushed and mixed with 100 mL of water and incubated for 40 days in a bioreactor placed in a water bath at a constant temperature (35 °C), promoting bio-mechanisation (Figure 1) [9].

4.2. Modeling Equations

4.2.1. EPA Model

The US EPA (Environmental Protection Agency) has also carried out a study; this led to a model based on data collected on site. This Model is based on a first-order Equation (1) with a decreasing generation rate of biogas over time [10,11]:

$$\mathbf{Qt} = \mathbf{2} \times \mathbf{L_0} \times \mathbf{R}\left(\ \mathbf{e}^{(-\mathbf{KC})} - \mathbf{e}^{(-\mathbf{Kt})}\right) \tag{1}$$

Qt: quantity of biogas generated over time t (m^3/year);
L₀: total potential biogas production (m^3 CH_4/t of waste);

K: kinetic constant for biogas generation (year^{-1});
T: time elapsed since storage began (year);
R: average rate of waste accepted during the site's operating period (t/year);
C: time since site closure (C = 0 year for active sites) (year).

$$L_0 = FCM. \ COD. \ CODF.A.\frac{16}{12} . \ 1000 \tag{2}$$

FCM: correction factor of the CH$_4$, expressed as a percentage;
COD: degradable organic carbon, expressed as t of C/t of waste;
CODF: concealed COD fraction;
A: fraction of CH$_4$ in biogas;
16/12: stoichiometry coefficient.

$$COD = 0.4E + 0.17F + 0.15G + 0.3H \tag{3}$$

E: fraction of waste consisting of paper and textiles;
F: fraction of waste consisting of garden and/or park waste;
G: fraction of waste consisting of food waste;
H: fraction of waste consisting of wood and/or straw.
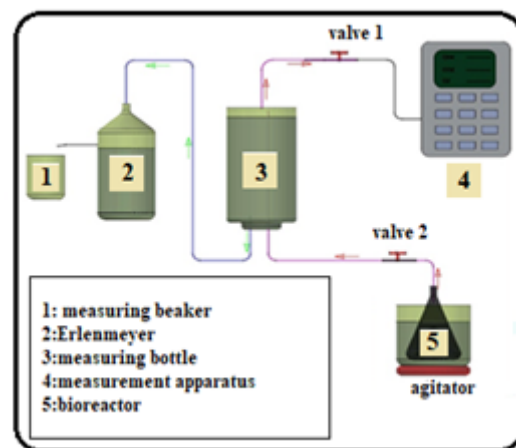
Figure 1. Device for measuring methanogenic potential by the displacement of water [9].

4.2.2. LANDGEM Model

The LANDGEM model is based on a first-order degradation equation that is estimated over several years. Indeed, for a mass of waste accepted in year i (Mi), methane production follows a decreasing exponential law. For several years, production is evaluated every tenth of a year. The equation used to estimate the total amount of methane produced in a TEC is [12,13]:

$$Q(CH_4) = \sum_{i=1}^{n} \sum_{j=0.1} K \ L_0 \ \frac{M_i}{10} \ e^{(-Kt_{ij})} \tag{4}$$

i: time increment of 1 year;
j: cutting the year into tenths.

4.2.3. ADEME Model

ADEME estimates the methane emissions from the TECs by calculating the quantity of methane produced (uncaptured methane and captured methane) using this expressions [14,15]

$$Q(CH4) = \sum L_0 \sum_{i=1}^{3} A_i P_i K_i e^{(-K_i(t-x))} \tag{5}$$

$$L_0 = 0.934.C_0(0.014.T + 0.28) \text{ en} \frac{\mathbf{m^3}}{\mathbf{t}} \tag{6}$$

i: the subdivision into three categories of waste;

P_i: the fraction of waste with degradation constant i;

C_0: biodegradable organic carbon;

T: degradation temperature 30 °C;

A_i: factor of the mass of waste accepted in year i;

x: year of landfilling of waste.

The three degradation constants K depend on the biodegradability of the waste:

K_1 = 0.5 in order to degrade 15% of waste (easily biodegradable);

K_2 = 0.10 in order to degrade 55% of waste (moderately biodegradable);

K_3 = 0.04 in order to degrade 30% of waste (poorly biodegradable);

The degradation kinetics are assumed to be the same regardless of the composition of the waste [16].

4.2.4. Scholl Canyon Model

The Scholl Canyon Model is a first-order decomposition model. It allows the calculation of CH_4 resulting from the decomposition of waste, taking into account the fact that this waste decomposes over many years. It is expressed in Equation (6) [17]:

$$\mathbf{Qt} = \sum (\mathbf{K\ L_0\ M_x} (\mathbf{e^{(-K(\ t-x))}})) \tag{7}$$

Qt: quantity of methane produced during the year in question (T) (kg of CH_4/year);

x: year of entry of the waste;

M_x: amount of waste landfilled during the year $\times$ (Mt);

L_0: methane production potential (kg of CH_4/t of waste);

T: considered year.

4.3. Sampling and Analysis

The samplings were made in Tedlar bags and glass ampules. The H_2 and N_2 were analyzed by chromatography on a molecular sieve using a detector with thermal conductivity. The CH_4 and CO_2 were measured by porous polymer analysis with a thermal conductivity detector (TCD). The C_2 to C_5 were analyzed by chromatography on a porous polymer with a flame ionization detector (FID). The CO was analyzed using the non-dispersive infrared technique.

5. Results and Discussion

5.1. Tonnage of Waste

The Mohammedia controlled landfill receives on average 500 t/d of DMA that constitutes 74% of the total tonnage of various types (Table 1): household waste (OM); green waste; mixtures of household waste, soil and gravel; and common industrial waste considered to be AMD.

Table 1. Percentage by type of waste.

Designation	Value (t/d)	%
Household garbage	387	70%
Green waste	5	1%
Household garbage, soil and rubble	100	18%
Non-hazardous industrial waste	64	11%

Among the wastes with high methanogenic potential destined for landfill are DM, green waste and two types of industrial waste, namely: waste from the Mohammedia tannery and poultry droppings brought in by the Delicate-meat company. The two graphs that follow show the tonnage of this waste since the landfill opened (Figures 2 and 3).
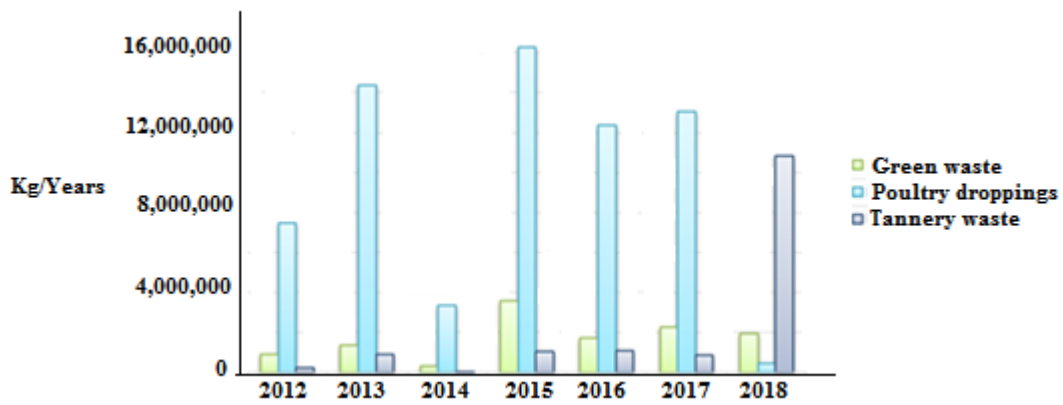
Figure 2. Tonnage of green waste, poultry droppings and tannery waste.
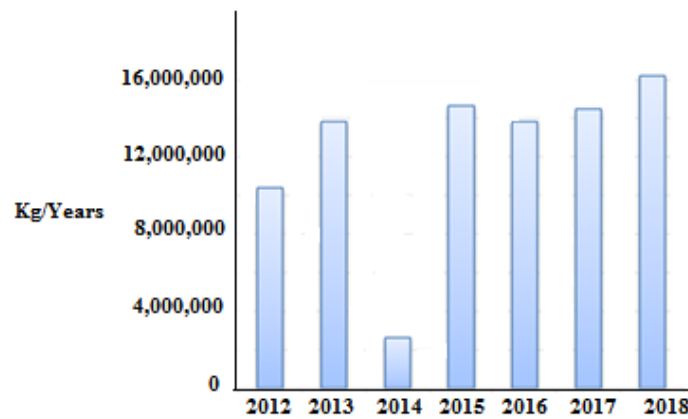
Figure 3. Annual tonnage of household waste.

5.2. Waste Characterization

The studies on the characterization of household and similar waste in the city of Mohammedia conducted by A. Ouatmane in 2018 and A. El Maguiri et al. in 2016 [7–9] report that the fraction is <80 mm, which represents fermentable organic matter in the order of 61%. However, the >80 mm fraction can be divided into categories and sub-categories, as shown in Figure 4.
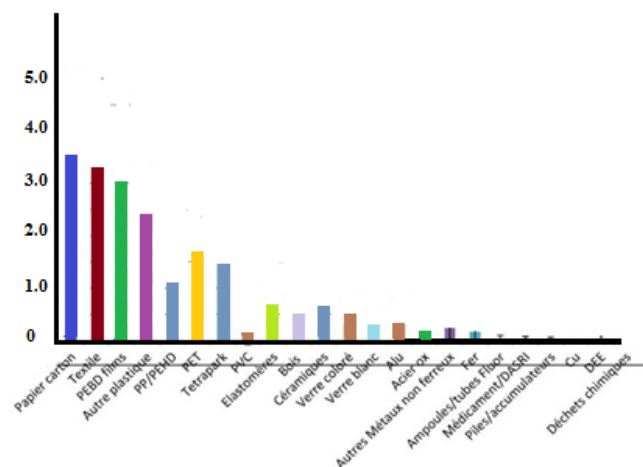
Figure 4. Average of the mass percentages of the fractions from the household and similar waste in the city of Mohammedia.

Bi-monthly sampling of the same landfill waste pile showed (Table 2) a clear evolution in the physical and chemical parameters during the landfilling of the waste, in particular a significant decrease in the organic carbon content due to mineralisation. The total nitrogen content showed a significant increase during fermentation. This variation corresponds in fact to a relative enrichment in nitrogen of the residual dry matter of the compost, the total amount of nitrogen actually decreasing as illustrated. The mineral nitrogen contents are always low, and their evolution is typical of what is found in compost heaps with a low level of ammoniac nitrogen and traces of nitrate, which then forms nitrate at the end of maturation. This maturation results in a lowering of the C/N ratio from 32, indicating a stabilisation of the organic compounds. Similarly, the equivalent humidity of the product falls, this last point being related to the concomitant rise in pH. Table 2 shows the results of the physicochemical analyses carried out during the DMA characterization.

Table 2. Results of physicochemical analyses of the waste fraction <80 mm.

Description	Unit	Value
Density: fraction < 80 mm	t/m^3	1.09
Humidity	%	38.02
Organic matter	g/100 g MS	69.93
Total organic carbon	g/100 g MS	40.26
Nitrogen	g/100 g MS	1.25
Report C/N	-	32.21
PCI fraction < 80 mm	Kcal/Kg	1002
PCI fraction > 80 mm	Kcal/Kg	2071

All the results are presented in Table 2. Total organic carbon corresponds to approximately 40% of the dry matter of the composts analyzed. Given the very heterogeneous composition of these materials and the diversity of their origins, we can assume that the variations observed were moderate (Table 3).

Table 3. TOC value in g/100 g [3,4].

Type of Waste	TOC (g/100 g)	C/N
Household waste	40.26 [2]	32.21
Green waste	27 [3]	55
Poultry droppings	13.59 [4]	3.68
Tannery waste	14 [4]	3

The C/N ratio is around 32.21 at the beginning of the first phase of the process. Subsequently, a decrease in this ratio is noted, which becomes equal to 28 at the end of the first phase. This reduction is explained by the active transformation of the carbon into carbon dioxide, accompanied by a decrease in the content of organic acids in the waste mass. The purpose of this input is to amplify the microbial activity to prepare for the start of the next stage.

5.3. Methanogenic Potential

The potential for biogas generation by anaerobic decomposition of the various fermentable wastes sheltered by the TEC is a critical parameter for modelling biogas production. The US EPA recommends L0 values ranging from 170 m^3 of CH_4 per tonne of waste for arid areas to 96 m^3 for wetlands [17,18], though these values take into consideration the composition and physicochemical properties of household waste in the United States, which are certainly different from those in Morocco (Table 4).

Table 4. Table of COD and L0 calculation results.

	COT (g/100 g)	COD	FCM	CS	F (%)	L0 M³/t
Household waste	40.26	0.099	1	1.333	55.6	563.77
Green waste	27	0.37	1	1.333	65 [18]	1649.77
Poultry droppings	13.59	0.542	1	1.333	60 [18]	1124.23
Tannery waste	14	0.3	1	1.333	60 [18]	640.24

Equation (2) includes in its expression three key elements (TOC, COD and F) that define the methanogenic potential of waste. The first expresses the carbon content, an essential element in the formation of methane. The term COD (3) relates the composition of waste, and knowing the composition and physical and chemical properties of its waste enables the calculation of L0 specific to a region.

The estimate of L0 using Equation (6) of the ADEME model gives a value of 26.3 m³/t. Compared with the values recommended by the EPA and LANDGEM, this is extremely small and does not reflect the methanogenic potential of Mohammedia household waste (Figure 5), whose fermentable organic matter fraction is around 61% [6], which is probably significant compared with the % MO of waste in France and the US.
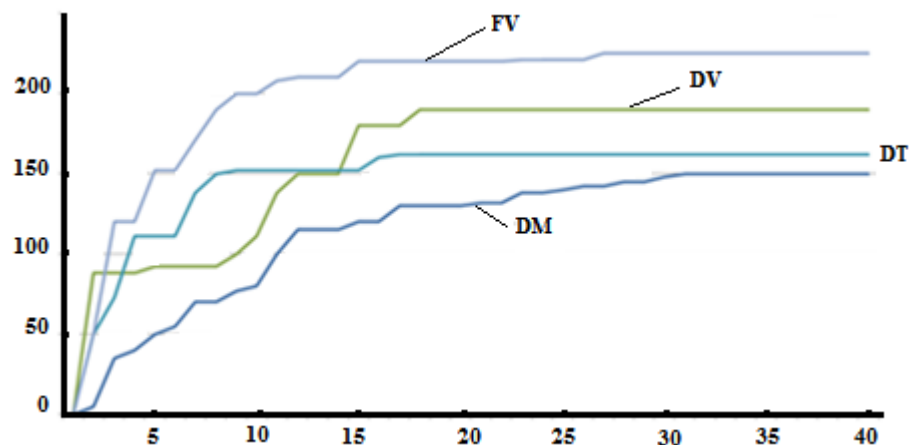
Figure 5. Biogas production kinetics for the four types of waste in ml.

After 40 days of fermentation of the different substrates at a temperature of 35 °C, the graph of the biogas production kinetics, which is strongly related to temperature and C/N ratio [7], shows that poultry droppings produce the largest volume of biogas (266 mL), which is certainly due to the abundance of lipids in the substrate. Then come in decreasing order green waste, tannery waste and household waste, with respective volumes of 189 mL, 160 mL and 150 mL.

These experimental results do not coincide at all with the empirically calculated values of L0 since this series of experiments is limited in time to 40 days, while the methanogenic potential calculation equation given by the US EPA takes into account the total consumption of the substrate.

In addition, the monitoring of the quality of biogas generated for all samples shows that the oxygen content increases from 19%/V to 7%/V during the first week, with carbon dioxide production averaging 5%/V. However, methane only appeared during the last week in insignificant quantities ranging from 1% to 2% by volume.

5.4. Biogas Production Modelling via the Four Models

The different modelling equations mentioned in this work utilize three terms (tonnage, K and L0) that define the volume of biogas/methane generated in a time interval.

The methane generation constant (K) represents the decomposition rate. This depends mainly on waste and precipitation on site. High levels of K indicate a higher level of

gas production over time [7]. As with L0, the US EPA has set values of K ranging from 0.02 year^{-1} to 0.7 year^{-1} for arid and humid areas respectively, as well as a conventional value of 0.05 year^{-1} [19].

The French model developed by ADEME, on the other hand, uses three degradation constants K according to the biodegradability of the waste:

K$_1$ = 0.5 (easily biodegradable);
K$_2$ = 0.10 (moderately biodegradable);
K$_3$ = 0.04 (poorly biodegradable).

The values of the methane generation constant adopted by ADEME are somewhat higher than those of the American models. However, due to the high humidity content of the waste and the climatological conditions characterizing the study area, the ADEME model is the most suitable for modelling biogas production for waste from the city of Mohammedia (Figure 6). In addition, it offers the possibility of modelling methane production for waste of a different nature, which is the case in this study, by summing the L0i and Ki for n substrates (Equation (5)).
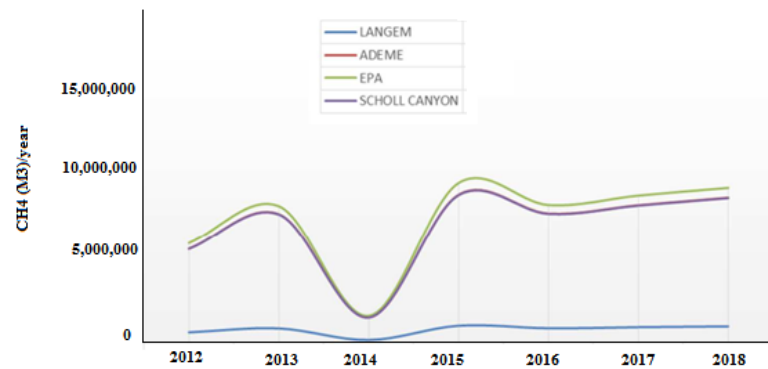
Figure 6. Modeling results of CH$_4$ production via the four models.

In this study, we assigned values of K to the different types of waste studied (0.1 for household waste, 0.5 for green waste and 0.04 for poultry droppings and tannery waste) according to their degree of biodegradability by comparing the carbon/nitrogen ratios.

The modelling results show only a slight variation between three of the models, the EPA, SCHOLL CANYON and ADEME, but the LANDGEM model showed a significant difference compared with the others, which is why production is evaluated on a tenth of a year basis [20].

Details of the calculations are provided in Appendix A.

5.5. Estimate of the Biogas Field

The estimation of the tonnage of household waste from the different urban and rural municipalities between 2018 and 2032, according to their respective waste production ratios of 0.76 and 0.3 Kg/inhab/d [19], begins with the calculation of the population evolution and the ratio using Equations (8)–(10) (Appendix B).

$$\textbf{EP} = \textbf{Ai} \times \left(1 - \frac{\textbf{rate of increase}}{\textbf{100}} \right)^{\textbf{Ai} - \textbf{A0}} \tag{8}$$

$$\textbf{ER} = \textbf{0.76}(\textbf{ou 0.3}) \times (1 + 1.36/100)^{\textbf{Ai} - \textbf{A0}} \tag{9}$$

$$\textbf{T} = (\textbf{population} \times \textbf{ratio} \times \textbf{365}/\textbf{1000}) \tag{10}$$

EP: population evolution;
ER: ratio evolution;
T: annual tonnage;
Ai: population i.

In view of the difficulty of estimating the tonnage of green and industrial waste, the average percentages of the apparent tonnage recorded between 2012 and 2018 of each substrate and their percentages of contribution to methane production were used to predict the tonnage of fermentable waste until the end of operation, including the volume of biogas related to it (Figure 7).
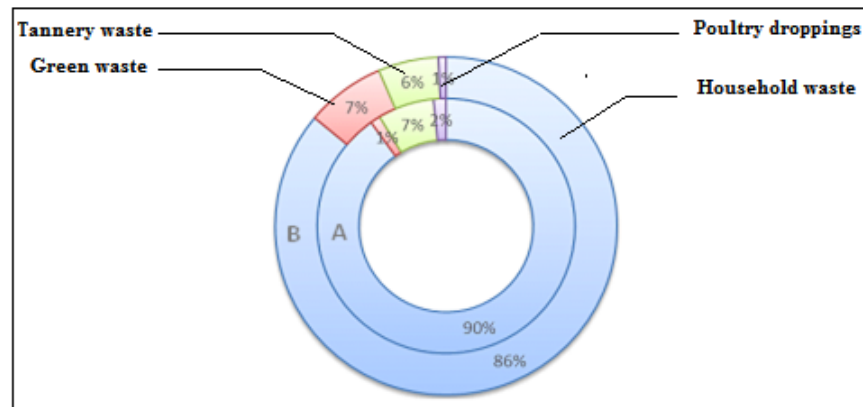
Figure 7. (A) % tonnage; (B) % contribution to CH_4 production of the four substrates.

The calculation of greenhouse gas emissions is performed using Equation (11) below:

$$\text{GH G}_p = 21 \left(0.016 \times \frac{Q_p}{22.4} \right) \tag{11}$$

GHG$_p$: equivalent CO_2 emissions (t CO_2/year);
Q$_p$: quantity of methane produced (m^3/year);
21: ratio of CH_4 to 1 CO_2.

Table 5 below shows the modelling results of biogas production from anaerobic decomposition for four types of waste studied using the ADEME model.

Table 5. Calculation results for the annual production of biogas, CH_4 and CO_2 equivalent.

Year	Tonnage DM	Tonnage (DM, DV, FV, DT)	Biogas	CH4	GHGp
Unit	MKg/Years	MKg/Years	MM³/Years	MM³/Years	KT CO₂/Year
2012	103.88	114.27	10.64	5.92	88.75
2013	138.26	152.09	14.60	8.12	121.81
2014	26.35	28.99	2.863	1.59	23.88
2015	146.72	161.40	16.81	9.34	140.19
2016	138.23	152.05	14.68	8.16	122.44
2017	144.72	159.19	15.62	8.67	130.34
2018	161.96	178.15	16.48	9.16	137.47
2019	101.27	111.40	9.29	5.17	77.49
2020	101.60	111.76	9.32	5.18	77.74
2021	101.93	112.12	9.35	5.20	78.00
2022	102.26	112.49	9.38	5.21	78.25
2023	102.59	112.85	9.41	5.23	78.50
2024	102.93	113.22	9.44	5.25	78.76
2025	103.26	113.59	9.47	5.27	79.01
2026	103.60	113.96	9.50	5.28	79.27
2027	103.93	114.33	9.53	5.32	79.53
2028	103.93	114.33	9.54	5.31	79.53
2029	104.61	115.07	9.60	5.34	80.05
2030	104.95	115.45	9.63	5.35	80.31
2031	105.29	115.82	9.66	5.37	80.57
Total	**230.79**	**253.87**	**224.55**	**124.85**	**1872.73**

5.6. Potential for Energy Recovery by Cogeneration

The cogeneration unit consists of a gas engine or turbine, an alternator and optional heat recovery circuits. The gas is burned in the engine and then the mechanical energy of the engine is transformed into electricity via the alternator (Figure 8).
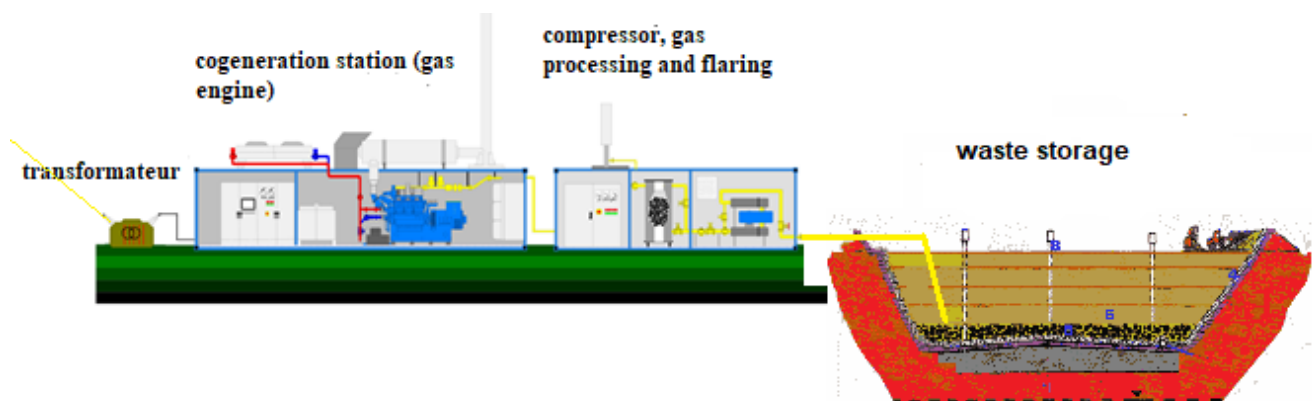
Figure 8. Overview of the cogeneration station [20].

Well before cogeneration, the biogas purification step is necessary. This requires the presence of hydrogen sulphide at levels exceeding 900 ppm, which is the case for the controlled landfill in Fez, where the H_2S content in the biogas is around 1200 ppm compared with 600 ppm for the Mohammedia landfill (Table 6).

Table 6. Biogas energy balance.

Year	MCH$_4$ m^3/Year	Total Energy GWh	Recoverable Energy GWh	Energy MWh
2012	5.91	58.81	55.87	6.38
2013	8.12	80.72	76.68	8.75
2014	1.60	15.82	15.03	1.77
2015	9.34	92.90	88.25	10.07
2016	8.16	81.13	77.08	8.79
2017	8.69	86.37	82.05	9.37
2018	9.16	91.09	86.54	9.88
2019	5.17	51.35	48.78	5.57
2020	5.19	51.51	48.94	5.59
2021	5.20	51.68	49.10	5.60
2022	5.22	51.85	49.26	5.62
2023	5.23	52.02	49.42	5.64
2024	5.25	52.19	49.58	5.66
2025	5.28	52.36	49.74	5.68
2026	5.28	52.53	49.90	5.70
2027	5.30	52.70	50.07	5.71
2028	5.30	52.70	50.07	5.71
2029	5.34	53.04	50.39	5.75
2030	5.35	53.21	50.56	5.771
2031	5.37	53.39	50.72	5.79
2032	5.39	53.56	50.88	5.80
totaux	124.85	1240.99	1178.94	134.58

The total annual energy produced from biogas is the product of the volume of methane multiplied by its lower calorific value, which is 9.94 kWh/m^3 under normal temperature and pressure conditions [21–28].

$$\mathbf{E_{totale} = PCI_{CH4} \times V_{CH4} \ [KWh]} \tag{12}$$

We allow for 5% energy loss in order to be sure that the engine is more supercharged than underfuelled [22]. The energy recoverable by the motor is therefore as follows:

$$\mathbf{E_{Valorisable} = 0.95 \times E_{totale}} \quad [\mathbf{KWh}] \tag{13}$$

$$\mathbf{E_{t=1h} = \frac{E_{Valorisable}}{365 \times 24}} \quad [\mathbf{KW}] \tag{14}$$

Taking into account an Et = 1 h average of 7288 KW, the gas engine would need to be designed to operate between 50% and 100% of its rated load, with an optimal efficiency around 75%. We are therefore looking for an engine with a power of about 9715 kW to be close to this optimum [12,21–28].

6. Conclusions

The projected depletion of fossil energy resources associated with the environmental issue of global warming has intensified the interest in renewable energies and the possible options they can offer. In this research study, it was possible to determine the value of the methanogenic potential of household waste and other substrates of the landfill of the city Mohammedia, which were significantly higher than the values usually used in modelling efforts due to the high proportion of organic waste. From an analysis of the total stability of the mathematical model of the process equilibrium, we constructed a criterion that, based on the inputs of the process and the parameters of the model, determines whether the mode of operation represents a risk to the sustainability of the process. The volume of methane that would be generated after twenty years of operation is of the order of 124,848,407 m^3, thus producing 1,178,943,512 KWh of recoverable energy, a very large deposit that justifies investment.

Data Availability Statement: No data are available.

Conflicts of Interest: The authors declare no conflict of interest regarding the publication of this manuscript.

Abbreviations

DMA	household and similar waste
CET	Technical Landfill Centre
DM	household waste
DV	green waste
FV	poultry droppings
DT	tannery waste
MO	organic matter
K	methane generation constant
L_0	methane production potential

Appendix A

Table A1. Results the Calculations of Modeling By LANDGEM.

Modeling By LANDGEM (KM^3 of CH4 per T of Waste)				
	DM	**DV**	**FV**	**DT**
2012	579.84	45.13	33.54	0.59
2013	771.72	66.62	64.39	2.25
2014	147.083	16.13	14.97	0.058
2015	818.96	17.76	72.91	26.26
2016	771.53	86.42	55.36	27.21
2017	807.76	11.328	58.50	21.24
2018	903.98	96.65	20.52	27.67

Table A2. Results the Calculations of Modeling By SCHOLL CANION.

Modeling By SCHOLL CANION (MM^3 of CH$_4$ per T of Waste)				
	DM	**DV**	**FV**	**DT**
2012	5.28	0.29	0.32	0.005
2013	7.03	0.42	0.62	0.0216
2014	1.34	0.10	0.14	0.0005
2015	7.46	0.11	0.70	0.0252
2016	7.03	0.55	0.53	0.0261
2017	7.37	0.72	0.56	0.0204
2018	8.24	0.61	0.02	0.2661

Table A3. Results the Calculations of Modeling By EPA.

Modeling By EPA (MM3 of CH4 per T of Waste)				
	DM	**DV**	**FV**	**DT**
2012	5.57	0.37	0.330	0.0058
2013	7.41	0.55	0.633	0.0221
2014	1.41	0.13	0.147	0.0006
2015	7.87	0.15	0.718	0.0258
2016	7.41	0.71	0.544	0.0269
2017	7.76	0.94	0.576	00209
2018	8.69	0.79	0.020	0.2723

Table A4. Results the Calculations of Modelling by ADEME.

Modelling by ADEME (MM^3 of CH4 per T of Waste)				
	DM	**DV**	**FV**	**DT**
2012	5.30	0.29	0.32	0.0060
2013	7.05	0.42	0.62	0.0220
2014	1.34	0.10	0.14	0.0005
2015	7.48	0.11	0.70	0.0253
2016	7.05	0.55	0.53	0.0262
2017	7.38	0.72	0.56	0.0205
2018	8.261	0.62	0.20	0.2669

Appendix B

Table A5. Population evolution.

| | Urban Communes | | | | | | Rural Communities | | |
Communes	Mohammedia	Ain Harouda	Bouznika	Bensliman	El Mansouria	Ech-Challalat	Ben yakhlef	Sidi Moussa Ben Ali	Sidi Moussa El Majdoub
Initial population	187,708	41,853	27,028	46,478	12,955	40,311	18,233	9,368	12412
Rate of increase	1.01	1.04	1.03	1.02	1.04	1.03	1.1	1.02	1.05
2005	185,812.149	41,417.7288	26,749.6116	46,003.9244	12,820.268	39,895.7967	18,032.437	9272.4464	12,281.674
2006	183,935.446	40,986.9844	26,474.0906	45,534.6844	12,686.9372	39,429.0356	17,862.9438	9172.30482	12,412
2007	182,077.698	40,560.7198	26,201.4075	45,070.2306	12,554.9931	39,078.1758	17,637.9053	9084.2532	12,025.1129
2008	180,238.714	40,138.8883	25,931.533	44,610.5142	12,424.4211	38,675.6706	17,443.8884	8991.59382	11,898.84922
2009	178,418.303	39,721.4439	25,664.4382	44,155.487	12,295.2072	38,277.3112	17,252.0056	8899.87956	11,773.9113
2010	176,616.278	39,308.3408	25,400.0945	43,705.101	12,167.337	37,883.0549	17,062.2335	8809.10079	11,650.28523
2011	174,832.453	38,899.5341	25,138.4735	43,259.309	12,040.7967	37,492.8594	16,874.549	8719.24796	11,527.95723
2012	173,066.646	38,494.9789	24,879.5472	42,818.064	11,915.5724	37,106.683	16,688.9289	8630.31163	11,406.91368
2013	171,318.673	38,094.6312	24,623.2879	42,381.3198	11,791.6505	36,724.4842	16,505.3507	8542.28245	11,287.14109
2014	169,588.354	37,698.447	24,369.668	41,949.303	11,669.173	36,346.222	16,323.7918	8455.15117	11,168.62611
2015	167,875.512	37,306.3831	24,118.6604	41,521.1502	11,547.6595	35,971.8559	16,144.2301	8368.90863	11,051.35553
2016	166,179.969	36,918.3968	23,870.2382	41,097.6345	11,427.5639	35,601.3458	15,966.6436	8283.54576	10,935.3163
2017	164,501.551	36,534.4454	23,624.3748	40,678.4386	11,308.7172	35,234.6519	15,791.0105	8199.05359	10,820.49548
2018	162,840.086	36,154.4872	23,381.0437	40,263.5185	11,191.1065	34,871.735	15,617.3094	8115.42325	10,706.88028
2019	161,195.401	35,778.4805	23,140.219	39,852.8307	11,074.719	34,512.5561	15,445.519	8032.64593	10,594.45803
2020	159,567.327	35,406.3843	22,901.8747	39,446.3318	10,959.5419	34,157.0768	15,275.6183	7950.71294	10,483.21623
2021	157,955.697	35,038.1579	22,665.9854	39,043.9792	10,845.5627	33,805.2589	15,107.5865	7869.61567	10,373.14246
2022	156,360.345	34,673.7611	22,432.5258	38,645.7306	10,732.7689	33,457.0647	14,941.403	7789.34559	10,264.22446
2023	154,781.105	34,313.154	22,201.4707	38,251.5442	10,621.1481	33,112.457	14,777.0476	7709.89426	10,156.4501
2024	153,217.816	33,956.2972	21,972.7956	37,861.3784	10,510.6881	32,771.3987	14,614.5001	7631.25334	10,049.80738
2025	151,670.316	33,603.1517	21,746.4758	37,475.1923	10,401.377	32,433.8533	14,453.7406	7553.41456	9944.284399
2026	150,138.446	33,253.6789	21,522.4871	37,092.9454	10,293.2026	32,099.7846	14,294.7494	7476.36913	9839.869413
2027	148,622.048	32,907.8407	21,300.8055	36,714.5973	10,186.1533	31,769.1568	14,137.5072	7400.11076	9736.550784
2028	147,120.965	32,565.5991	21,081.4072	36,340.1084	10,080.2173	31,441.9345	13,981.9946	7324.62963	9634.317001
2029	145,635.04	32,226.917	20,864.269	35,969.469	9975.3831	31,118.083	13,828.193	7249.9184	9533.156672
2030	144,164.13	31,891.757	20,649.367	35,602.551	9871.6391	30,797.566	13,676.083	7175.9692	9433.058527
2031	142,708.071	31,560.0827	20,436.6782	35,239.405	9768.97405	30,480.3514	13,525.6456	7102.77435	9334.011413
2032	141,266.72	31,231.8578	20,226.1805	34,879.9631	9667.37672	30,166.4037	13,376.8635	7030.32606	9236.004293

Table A6. Evolution of the Ratio.

| | Urban Communes | | | | | | Rural Communities | | |
Communes	Mohammedia	Ain Harouda	Bouznika	Bensliman	El Mansouria	Ech-Challalat	Ben yakhlef	Sidi Moussa Ben Ali	Sidi Moussa El Majdoub
2005	0.770336	0.770336	0.770336	0.770336	0.770336	0.30408	0.30408	0.30408	0.30408
2006	0.78081257	0.78081257	0.78081257	0.78081257	0.78081257	0.30821549	0.30821549	0.30821549	0.30821549
2007	0.79143162	0.79143162	0.79143162	0.79143162	0.79143162	0.31240722	0.31240722	0.31240722	0.31240722
2008	0.80219509	0.80219509	0.80219509	0.80219509	0.80219509	0.31665596	0.31665596	0.31665596	0.31665596
2009	0.81310494	0.81310494	0.81310494	0.81310494	0.81310494	0.32096248	0.32096248	0.32096248	0.32096248
2010	0.82416317	0.82416317	0.82416317	0.82416317	0.82416317	0.82416317	0.82416317	0.82416317	0.82416317
2011	0.83537179	0.83537179	0.83537179	0.83537179	0.83537179	0.83537179	0.83537179	0.83537179	0.83537179
2012	0.84673285	0.84673285	0.84673285	0.84673285	0.84673285	0.33423665	0.33423665	0.33423665	0.33423665
2013	0.85824841	0.85824841	0.85824841	0.85824841	0.85824841	0.33878227	0.33878227	0.33878227	0.33878227
2014	0.86992059	0.86992059	0.86992059	0.86992059	0.86992059	0.34338971	0.34338971	0.34338971	0.34338971
2015	0.88175151	0.88175151	0.88175151	0.88175151	0.88175151	0.34805981	0.34805981	0.34805981	0.34805981
2016	0.89374333	0.89374333	0.89374333	0.89374333	0.89374333	0.35279342	0.35279342	0.35279342	0.35279342
2017	0.90589824	0.90589824	0.90589824	0.90589824	0.90589824	0.35759141	0.35759141	0.35759141	0.35759141
2018	0.91821846	0.91821846	0.91821846	0.91821846	0.91821846	0.36245465	0.36245465	0.36245465	0.36245465
2019	0.93070623	0.93070623	0.93070623	0.93070623	0.93070623	0.36738404	0.36738404	0.36738404	0.36738404
2020	0.94336383	0.94336383	0.94336383	0.94336383	0.94336383	0.37238046	0.37238046	0.37238046	0.37238046
2021	0.95619358	0.95619358	0.95619358	0.95619358	0.95619358	0.37744483	0.37744483	0.37744483	0.37744483
2022	0.96919781	0.96919781	0.96919781	0.96919781	0.96919781	0.38257808	0.38257808	0.38257808	0.38257808
2023	0.9823789	0.9823789	0.9823789	0.9823789	0.9823789	0.38778115	0.38778115	0.38778115	0.38778115
2024	0.99573926	0.99573926	0.99573926	0.99573926	0.99573926	0.39305497	0.39305497	0.39305497	0.39305497
2025	1.00928131	1.00928131	1.00928131	1.00928131	1.00928131	1.00928131	1.00928131	1.00928131	1.00928131
2026	1.02300754	1.02300754	1.02300754	1.02300754	1.02300754	0.40381876	0.40381876	0.40381876	0.40381876
2027	1.03692044	1.03692044	1.03692044	1.03692044	1.03692044	0.4093107	0.4093107	0.4093107	0.4093107
2028	1.05102256	1.05102256	1.05102256	1.05102256	1.05102256	0.41487733	0.41487733	0.41487733	0.41487733
2029	1.06531646	1.06531646	1.06531646	1.06531646	1.06531646	0.42051966	0.42051966	0.42051966	0.42051966
2030	1.07980477	1.07980477	1.07980477	1.07980477	1.07980477	0.42623872	0.42623872	0.42623872	0.42623872
2031	1.09449011	1.09449011	1.09449011	1.09449011	1.09449011	0.43203557	0.43203557	0.43203557	0.43203557
2032	1.10937518	1.10937518	1.10937518	1.10937518	1.10937518	0.43791125	0.43791125	0.43791125	0.43791125

References

1. Bouhadiba, B.; Mezouri, F.; Kehila, Y.; Matejka, G. For an integrated Management for Municipal solid wast in Algeria.Systemic and Methodological Approaches. *Int. Rev. Chem. Eng. Rapid Commun.* **2010**, *2*, 426–429.
2. Gu, Y.; Zhou, G.; Wu, Y.; Xu, M.; Chang, T.; Gong, Y.; Zuo, T. Environmental performance analysis on resource multiple-life-cycle recycling system: Evidence from waste pet bottles in China. *Resour. Conserv. Recycl.* **2020**, *158*, 104821. [CrossRef]
3. Gautam, P.; Kumar, S.; Lokhandwala, S. Energy-aware intelligence in megacities. In *Current Developments in Biotechnology and Bioengineering*; Elsevier: Amsterdam, The Netherlands, 2019; pp. 211–238.

4. Joseph, O.; Rouez, M.; Métivier-Pignon, H.; Bayard, R.; Emmanuel, E.; Gourdon, R. Adsorption of heavy metals on to sugar cane bagasse: Improvement of adsorption capacities due to anaerobic degradation of the biosorbent. *Environ. Technol.* **2009**, *30*, 1371–1379. [CrossRef] [PubMed]

5. Mabrouki, J.; Moufti, A.; Bencheikh, I.; Azoulay, K.; El Hamdouni, Y.; El Hajjaji, S. Optimization of the Coagulant Flocculation Process for Treatment of Leachate of the Controlled Discharge of the City Mohammedia (Morocco). In Proceedings of the International Conference on Advanced Intelligent Systems for Sustainable Development, Tangier, Morocco, 8–11 July 2019; Springer: Cham, Switzerland, 200; pp. 200–212.

6. Finon, D. La pénétration à grande échelle des ENR dans les marchés électriques. La perte de repère des évaluations économiques. *Rev. De L'energie* **2016**, *633*, 366–390. (In French)

7. Mabrouki, J.; Moufti, A.; Bencheikh, I.; Azoulay, K.; El Hamdouni, Y.; El Hajjaji, S. Optimization of the Coagulant Flocculation Process for Treatment of Leachate of the Controlled Discharge of the City Mohammedia (Morocco). In *Advances in Intelligent Systems and Computing, Proceedings of the International Conference on Advanced Intelligent Systems for Sustainable Development (AI2SD-2018), Tangier, Morocco, 12–14 July 2018*; Ezziyyani, M., Ed.; Springer: Berlin/Heidelberg, Germany, 2018; pp. 200–212.

8. Andriani, D.; Atmaja, T.D. The potentials of landfill gas production: A review on municipal solid waste management in Indonesia. *J. Mater. Cycles Waste Manag.* **2019**, *21*, 1572–1586. [CrossRef]

9. Mabrouki, J.; El Yadini, A.; Bencheikh, I.; Azoulay, K.; Moufti, A.; El Hajjaji, S. Hydrogeological and hydrochemical study of underground waters of the tablecloth in the vicinity of the controlled city dump Mohammedia (Morocco). In *Advances in Intelligent Systems and Computing, Proceedings of the International Conference on Advanced Intelligent Systems for Sustainable Development (AI2SD-2018), Tangier, Morocco, 12–14 July 2018*; Ezziyyani, M., Ed.; Springer: Berlin/Heidelberg, Germany, 2018; pp. 22–33.

10. El Maguiri, A.; Fawaz, N.; Abouri, M.; Idrissi, L.; Taleb, A.; Souabi, S.; Vincent, R. Caractérisation physique et valorisation des déchets ménagers produits par la ville de Mohammedia, Maroc. *Rev. Nat. Technol. C. Sci. L'environ.* **2016**, *14*, 16–25.

11. Elkadi, A.; Maatouk, M.; Raissouni, M.; Chafik, T.; Mouhssine, A. Caractérisation des déchets ménagers et assimilés de la ville de Tanger/Characterization of household and assimilated waste in the city of Tangier. *Int. J. Innov. Appl. Stud.* **2016**, *18*, 512.

12. Mabrouki, J.; Bencheikh, I.; Azoulay, K.; Es-soufy, M.; el Hajjaji, S. Smart Monitoring System for the Long-Term Control of Aerobic Leachate Treatment: Dumping Case Mohammedia (Morocco). In *Big Data and Networks Technologies, Proceedings of the 3rd International Conference on Big Data and Networks Technologies (BDNT 2019), Leuven, Belgium, 29 April–2 May 2019*; Springer: Berlin/Heidelberg, Germany, 2019; pp. 220–230.

13. El Asri, O.; Afilal, M.E.; Laiche, H.; Elfarh, A. Evaluation of physicochemical, microbiological, and energetic characteristics of four agricultural wastes for use in the production of green energy in Moroccan farms. *Chem. Biol. Technol. Agric.* **2020**, *7*, 1–11.

14. Mabrouki, J.; Benbouzid, M.; Dhiba, D.; El Hajjaji, S. Simulation of wastewater treatment processes with Bioreactor Membrane Reactor (MBR) treatment versus conventional the adsorbent layer-based filtration system (LAFS). *Int. J. Environ. Anal. Chem.* **2020**, 1–11. [CrossRef]

15. Porowska, D. Review of Research Methods for Assessing the Activity of a Municipal Landfill Based on the Landfill Gas Analysis. *Period. Polytech. Chem. Eng.* **2021**, *65*, 167–176. [CrossRef]

16. Mabrouki, J.; Fattah, G.; Al-Jadabi, N.; Abrouki, Y.; Dhiba, D.; Azrour, M.; Hajjaji, S.E. Study, simulation and modulation of solar thermal domestic hot water production systems. *Model. Earth Syst. Environ.* **2022**, *8*, 2853–2862. [CrossRef]

17. Ortiz-Oliveros, H.B.; Flores-Espinosa, R.M. Design of a mobile dissolved air flotation system with high rate for the treatment of liquid radioactive waste. *Process. Saf. Environ. Prot.* **2020**, *144*, 23–31. [CrossRef]

18. Spokas, K.; Bogner, J.; Chanton, J.P.; Morcet, M.; Aran, C.; Graff, C.; Hebe, I. Methane mass balance at three landfill sites: What is the efficiency of capture by gas collection systems? *Waste Manag.* **2006**, *26*, 516–525. [CrossRef] [PubMed]

19. Hijazi, O.; Munro, S.; Zerhusen, B.; Effenberger, M. Review of life cycle assessment for biogas production in Europe. *Renew. Sustain. Energy Rev.* **2016**, *54*, 1291–1300. [CrossRef]

20. Scharff, H.; Jacobs, J. Applying guidance for methane emission estimation for landfills. *Waste Manag.* **2006**, *26*, 417–429. [CrossRef]

21. Mouhssine, A.; Brigui, J. Organic waste characterization in Tangier City and evaluation of its potential biogas. *Int. J. Innov. Appl. Stud.* **2017**, *20*, 1042–1052.

22. Mabrouki, J.; Azrour, M.; Hajjaji, S.E. Use of internet of things for monitoring and evaluating water's quality: A comparative study. *Int. J. Cloud Comput.* **2021**, *10*, 633–644. [CrossRef]

23. El Baz, F.; Arjdal, S.; Bakrim, M.; Mediouni, T.; Faska, N. Methanisation of Agadir urban solid waste: Theoretical evaluation of the energy production potential. In *Materials Today, Proceedings of the International Congress: Applied Materials for the Environment (CIMAE-2018), Agadir, Morocco, 5–7 December 2018*; Dahham, O.S., Zulkepli, N.N., Eds.; Elsevier: Amsterdam, The Netherlands, 2019; pp. 97–99.

24. Wu, Z.L.; Lin, Z.; Sun, Z.Y.; Gou, M.; Xia, Z.Y.; Tang, Y.Q. A comparative study of mesophilic and thermophilic anaerobic digestion of municipal sludge with high-solids content: Reactor performance and microbial community. *Bioresour. Technol.* **2020**, *302*, 122851. [CrossRef]

25. Trianni, A.; Cagno, E.; Accordini, D. Energy efficiency measures in electric motors systems: A novel classification highlighting specific implications in their adoption. *Appl. Energy* **2019**, *252*, 113481. [CrossRef]

26. Blewitt, J. Deschooling society? A lifelong learning network for sustainable communities, urban regeneration and environmental technologies. *Sustainability* **2010**, *2*, 3465–3478. [CrossRef]

27. Suther, T.; Fung, A.; Koksal, M.; Zabihian, F. Macro level modeling of a tubular solid oxide fuel cell. *Sustainability* **2010**, *2*, 3549–3560. [CrossRef]
28. Richardson, R.B. Ecosystem services and food security: Economic perspectives on environmental sustainability. *Sustainability* **2010**, *2*, 3520–3548. [CrossRef]

Review

Biochar as a Soil Amendment for Restraining Greenhouse Gases Emission and Improving Soil Carbon Sink: Current Situation and Ways Forward

Ahmed Mosa [1,*] **, Mostafa M. Mansour** [1] **, Enas Soliman** [1] **, Ayman El-Ghamry** [1] **, Mohamed El Alfy** [2] **and Ahmed M. El Kenawy** [3]

1   Department of Soils, Faculty of Agriculture, Mansoura University, Mansoura 35516, Egypt
2   Department of Geology, Faculty of Science, Mansoura University, Mansoura 35516, Egypt
3   Department of Geography, Mansoura University, Mansoura 35516, Egypt
*   Correspondence: ahmedmosa@mans.edu.eg

Abstract: The global exponential rise in greenhouse gas (GHG) emissions over the last few decades has triggered an urgent need to contextualize low-cost and evergreen technologies for restraining GHG production and enhancing soil carbon sink. GHGs can be mitigated via incorporating biochar into soil matrix to sequestrate the mineralized carbon in a stable form upon organic matter decomposition in soil. However, the efficiency of using biochar to offset GHG emissions from soil and terrestrial ecosystems is still debatable. Moreover, in the literature, biochar shows high functionality in restraining GHG emissions in short-term laboratory studies, but it shows minimal or negative impacts in field-scale experiments, leading to conflicting results. This paper synthesizes information on the ability of biochar to mitigate carbon dioxide (CO_2), nitrous oxide (N_2O), and methane (CH_4) emissions from soil and organic biomass, with an emphasis on cropland soils. The feedstock type, pyrolysis temperature, and application rate factors showed significant effects on controlling the effectiveness of biochar in restraining GHG emissions. Our study demonstrates that biochar, taken as a whole, can be seen as a powerful and easy-to-use tool for halting the rising tide of greenhouse gas emissions. Nonetheless, future research should focus on (i) identifying other indirect factors related to soil physicochemical characters (such as soil pH/EH and $CaCO_3$ contents) that may control the functionality of biochar, (ii) fabricating aged biochars with low carbon and nitrogen footprints, and (iii) functionalizing biologically activated biochars to suppress CO_2, CH_4, and N_2O emissions. Overall, our paradoxical findings highlight the urgent need to functionalize modern biochars with a high capacity to abate GHG emissions via locking up their release from soil into the carbonaceous lattice of biochar.

Keywords: biochar; croplands and rangelands; carbon sequestration; organic manures

1. Introduction

The exponential increase in greenhouse gas (GHG) emissions following anthropogenic activities in the last few decades has caused a pronounced rise in climatic changes with consequent environmental crises in global warming, drought, salinity, biodiversity, and diseases [1]. Human agricultural practices account for about 13.5% of global GHG emissions, including 80.4 petagrams of CO_2 per year (11 times the current rate of fossil fuel combustion), and about 63% of the world's non–CO_2 GHG emissions, including 84% of global N_2O and 54% of global CH_4 emissions [2]. Other indirect emissions, such as those from machinery and transportation, are also produced by common agricultural practices. The greenhouse effect, which raises the earth's temperature, is caused when the produced GHGs trap infrared (IR) radiation that is emitted from the earth's surface [3]. It was reported that seven countries (China, USA, India, Australia, Brazil, Canada, and Chile) contribute to producing more than 50% of the world's total soil emissions, and about

49% of the agricultural–related emissions [4]. Since irrigated agriculture is the dominant cultivation system in arid and semi-arid regions, large amounts of GHGs are emitted due to different agricultural practices including manure application, rice cultivation, enteric fermentation, burning crop residues, manure storage in the open air, and using energy for operating irrigated pumps [5]. Egypt's GHG emissions (as an example for arid countries) increased rapidly to more than 133% between 1990 and 2012, with a total emission of around 318 million tonnes eq. CO_2 [6].

Although agriculture led to substantial increases in GHGs, some agricultural practices could have significant impacts on reducing these emissions. Agriculture can make considerable contributions to mitigating GHG emissions in the atmosphere by (i) increasing soil organic carbon sinks, (ii) reducing the carbon and nitrogen footprint of soil organic amendments, (iii) recycling crop residues into value-added products instead of burning, and (iv) reducing GHG emissions generated during organic matter decomposition [7–9]. Pyrolysis has received attention recently as an effective method of treating organic waste and agricultural byproducts. Thermal processing of agricultural crop residues lowers waste volume and transportation costs while producing value-added products. Biochar has become a focal point of multidisciplinary study over the last decade as a solution to various worldwide challenges due to its high functionality, non-sophisticated processing, and renewability potential. Biochar is a charcoal-like substance made from pyrolyzed biomass intended for utilization as a soil improver. It has been credited with multiple benefits, including its abilities to improve the fertility and water-holding capacity of soil, protect water quality, capture greenhouse gases, generate carbon neutral energy, and increase agricultural output, as well as its contributions to carbon sequestration and the removal of pathogens [10–13]. The appropriate pyrolysis technology for biochar production should be considered based on the targeted field of application. Slow pyrolysis is the most common technique for biochar production, with a pyrolysis temperature ranging between 300 and 700 °C at a long residence time (300 to 7200 s) and low heating rate (0.1 to 1 °C/s) [14]. Fast pyrolysis is operated at high pyrolysis temperature within the range of 500–1200 °C at a high heating rate (10–200 °C/s) [15]. Flash pyrolysis, however, features a higher pyrolysis temperature (>900 °C) and heating rate (>1000 °C/s) [16]. Vacuum pyrolysis is another technique, in which biomass is converted under sub-atmospheric pressure (pyrolysis temperature, heating rate, and pressure are within the ranges of 300–700 °C, 0.1–1 °C/s, and 0.01–0.20 MPa, respectively) [17]. Hydro-pyrolysis is another technology, which involves using a high-pressure hydrogen atmospheric condition inside the pyrolysis reactor (pyrolysis temperature = 350–600 °C, heating rate = 10–300 °C/s, pressure = 10–17 MPa, and residence time > 60 s) [18]. Unlike other pyrolysis techniques, the heating energy in microwave pyrolysis penetrates the carbonaceous biomass and causes a vibration in their internal molecules [19].

The high functionality of biochar, including its physical properties (porosity, large surface area, and high water-holding capacity) as well as its chemical properties (abundance of oxygen-containing functional groups, surface charge, and pH-modulating effect), suggests its potential utilization in reducing GHG emissions [20]. However, a great deal of uncertainty remains surrounding the competitiveness of biochar with traditional soil amendments (e.g., compost and farmyard manures) given its low nutrient content and high pH value [21]. Additionally, the efficacy of pristine biochar for restraining GHG emissions under field-scale applications is still questionable. The wide range of variation between biochars depends upon the multiplicity of factors that underlie thermochemical conversion of organic biomass [22–24]. The novelty of this review relies on assessing the key factors that might impede the functionality of biochar in restraining GHG emissions. In addition, this review highlights the urgent need to develop fit-for-purpose forms of functionalized biochars tailored to improving soil carbon sink and restraining GHG emissions from soil matrix.

Several key factors control the properties of biochar and its effectiveness in reducing GHG emissions, including (i) feedstock type (e.g., agricultural wastes, sludge and manures,

algal biomass, and crustacean shell wastes), (ii) pyrolysis type (slow/fast pyrolysis, flash pyrolysis, microwave pyrolysis, vacuum pyrolysis, and hydro-pyrolysis), (iii) thermal processing protocol (e.g., heating rate, pressure and carries gas, residence time, and reactor design), and (iv) soil application rates and methods (e.g., broadcasting, in-furrow, or mixture with soil amendments) [25]. Consequently, biochar functionalization has emerged as a new trend, providing a roadmap for enhancing the competitiveness of biochar and its sustainable soil application for reducing GHG emissions.

In this review, we aimed to (i) summarize the recent research undertaken to remove CO_2, N_2O, and CH_4 emissions from soil and terrestrial ecosystems; (ii) review the anomalies and similarities among several investigations of factors affecting the efficiency of biochar in restraining GHG emissions; (iii) examine research done to lessen greenhouse gas emissions from the composting process; and (iv) highlight recent attempts undertaken to functionalize modern biochars with high capacity to achieve neutrality of carbon/nitrogen and net zero emissions. This review will help the academic/research community, as well as decision-making entities and environmental agencies, in establishing a decision-making framework for the large-scale application of biochar to mitigate GHG emissions. Overall, this review synthesizes data from different dimensions of biochar utilization for achieving carbon neutrality and reducing GHG emissions from agricultural ecosystems.

2. Bibliographic Data Collection

Books, book chapters, research articles, review articles, and proceedings were all scoured for this review. All selected sources were written in English and published within the last decade (2010 onwards). All of these articles came straight from reputable sources (e.g., Scopus, Web of Science, ProQuest, EBSCO, and JSTOR). Figure 1 shows a sample of the growing body of literature in the Scopus database on the topic of using biochar to mitigate agricultural GHG emissions. In our review, the International Biochar Initiative (IBI), the United States Department of Agriculture (USDA), and the European Environment Agency all contributed to the credibility of our review by providing official reports, statistics, and proceedings. Use of Get-Data Graph Digitizer (ver. 2.22, Russian Federation) allowed us to convert the data visualizations into corresponding numerical values. In this review, biochar + carbon dioxide emissions, biochar + nitrogen oxide emissions, biochar + chlorofluorocarbon emissions, biochar + soil + carbon dioxide emissions, biochar + soil + nitrogen oxide emissions, and biochar + soil + chlorofluorocarbon emissions were the initial search keywords. In addition, a number of meta-analyses were reported from a variety of published articles to establish a solid assessment of the current state of the potential use of biochar for limiting GHG emissions and the prospects for this direction.
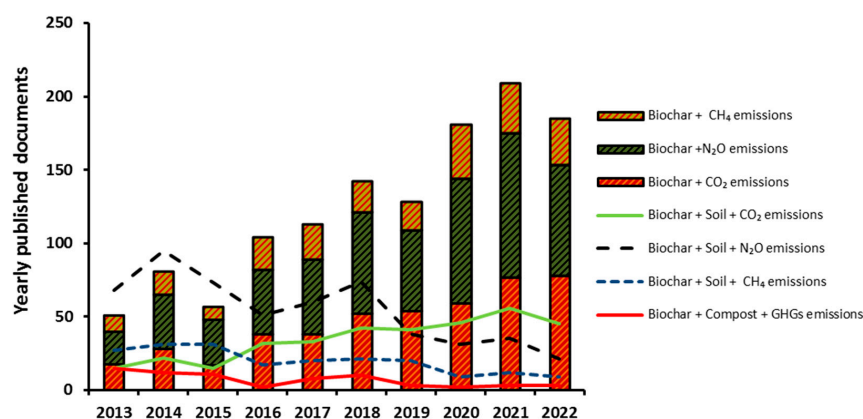
Figure 1. Number of documents published yearly in the Scopus database based on a query that employed the following keywords: biochar + CO_2 emissions, biochar + N_2O emissions, biochar + CH_4 emissions, biochar + soil + CO_2 emissions, biochar + soil + N_2O emissions, and biochar + soil + CH_4 emissions.

3. Effect of Biochar Application on Reducing GHG Emissions from Soil and Terrestrial Ecosystems

The research on biochar has attained significant momentum over the last decade. However, research related to field-scale applications has rarely been approached, highlighting the need for systematic efforts to fabricate end-use-appropriate biochars. The efficiency of biochar in reducing GHG emissions as compared with other soil amendments is summarized in Table 1. Endowed with unique functionality, biochar has been introduced as a promising adsorbent able to abate GHG emissions. Attempts have been undertaken to deploy biochar and its derivatives for mitigating CO_2, N_2O, and CH_4 emissions (Table 2). A comprehensive discussion of the mechanisms involved in CO_2, N_2O, and CH_4 emissions by biochar is provided below based on recent published results.

3.1. Effect of Biochar Application on Reducing CO2 Emissions

Biochar exhibits a high potential for soil carbon sequestration given its high and resistant carbon content (particularly when its oxygen:carbon ratio is less than 0.2), prevalence of aromatic structures, and abundance of active functional groups, which improves its recalcitrant nature against decomposition in soil [33]. The carbon footprint of biochar ranges between 0.04 tCO_2eq (net emissions) and 1.67 tCO_2eq per t of biomass (net reduction) based on the feedstock type, system boundaries, and modalities of life cycle assessment studies [34]. Upon its soil application, biochar tends to change soil physical characteristics (e.g., water-holding capacity and bulk density) given its low skeletal density and higher surface area compared with particles of soil matrix [35,36]. The key role of biochar in modulating the pore structure parameters of soil (porosity, pore size distribution, connectivity, anisotropy, and fractal dimension) was a significant mechanism involved in restraining CO_2 emissions [37]. According to literature data, the overall average ability of biochar to reduce CO_2 emissions is −0.43%. This poor efficiency highlights the critical need to functionalize contemporary biochars with greater sorption capacity (Figure 2).
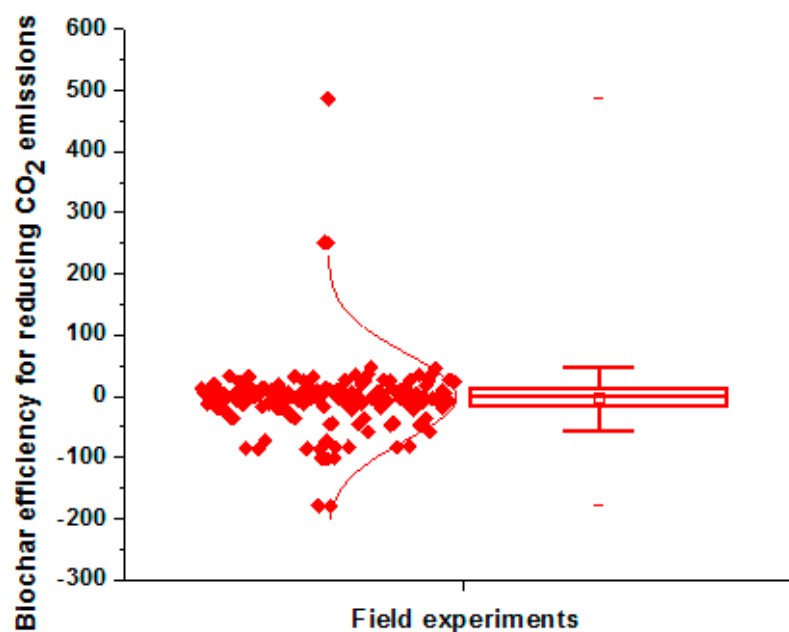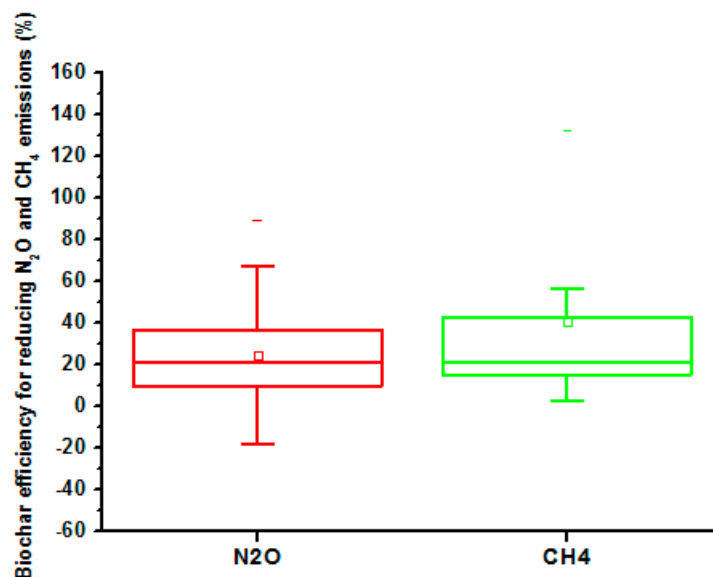

Figure 2. Biochar efficiency in reducing CO_2 emissions (%). Data are extracted from 38 field investigations comprising 165 individual observations. Box chart is illustrated by the mean (dot), median (centerline), lower and upper quartiles (the lower and upper borders of the box, respectively), and whiskers-error bars (the minimum and maximum observations).

Table 1. A comparision between biochar and other soil amendments in reducing GHG emissions.

Country	Climatic Conditions	Soil Properties			Soil Amendments	Application Rate (Mg ha⁻¹)	Cultivated Crop	Years of Study	Yield (%) Compared with Control	GHGs Emission Rate Compared with Control (%)			Reference
		Texture	pH	OC (g kg⁻¹)						CO₂	N₂O	CH₄	
South Korea	-	Clay loam	5.8	22.98	Fly ash	2.0	Rice	1	7.33	-	3.53	-3.68	[26]
					Silicate slag				21.75	-	5.74	33.74	
					Phosphogypsum				17.02	-	12.58	31.90	
					Revolving furnace slag				20.57	-	7.73	26.99	
					Blast furnace slag				13.00	-	8.83	9.82	
Japan	-	Sandy loam	6.1	21.32	Biochar	2.0	Rice	1	10.47	-	31.83	-13.99	
					Silicate slag				25.58	-	17.65	14.68	
					Phosphogypsum				23.26	-	14.88	20.14	
					Biochar + azolla-cyanobacteria				27.91		26.30	7.85	
					Silicate slag + azolla-cyanobacteria	2.0 + 5.0			37.21		15.22	22.39	
					Phosphogypsum + azolla-cyanobacteria				30.23	-	11.07	25.60	
Bangladesh	-	Clay loam	5.9	10.35	Biochar	2.0	Rice	1	15.85	-	20.00	-9.49	
					Silicate slag				28.05		14.18	18.35	
					Phosphogypsum				24.39		9.87	27.22	
					Biochar + azolla-cyanobacteria				25.61		25.06	9.49	
					Silicate slag + azolla-cyanobacteria	2.0 + 5.0			40.24		12.15	26.58	
					Phosphogypsum + azolla-cyanobacteria				34.15		7.34	29.11	
China	Warm temperate and semi-humid monsoon	Clay	7.4	5.79	Wheat straw	7.5	Soybean	1	32.79	-	-37.37	-	[27]
					Pig manure	15			24.59	-	-49.49	-	
					Cattle manure	30			52.46	-	-61.61	-	
					Wheat straw	7.5		2	11.57	-	-20.55	-	
					Pig manure	15			34.77	-	-31.51	-	
					Cattle manure	30			64.81	-	-31.51	-	
					Wheat straw	7.5	Wheat	1	7.25	-	-5.74	-	
					Pig manure	15			3.63	-	-30.33	-	
					Cattle manure	30			8.69	-	-62.30	-	
					Wheat straw	7.5		2	10.32	-	-44.21	-	
					Pig manure	15			12.20	-	-52.63	-	
					Cattle manure	30			16.87	-	-67.37	-	
Southeastern China	-	Silt loam	6.5	18.10	Steel slag	8.0	Early rice	1	0.86	4.08	27.56	10.45	[28]
					Biochar rice straw				6.05	9.87	15.75	-7.37	
					Steel slag + biochar	8.0 + 8.0			9.29	18.71	20.47	34.10	
					Steel slag	8.0	Late rice	1	1.49	12.25	27.40	14.89	
					Biochar rice straw				3.57	25.36	15.07	43.60	
					Steel slag + biochar	8.0 + 8.0			6.98	21.32	20.55	33.43	

Table 1. *Cont.*

Country	Climatic Conditions	Texture	pH	OC (g kg⁻¹)	Soil Amendments	Application Rate (Mg ha⁻¹)	Cultivated Crop	Years of Study	Yield (%) Compared with Control	CO₂	N₂O	CH₄	Reference
India	Sub-tropical, semi-arid	Loam	8.1	5.90	Azolla	-	Rice	2	14.33	-	8.73	9.62	[29]
					Blue-green algae (BGA)	-			6.39	-	12.04	7.07	
					Azolla + BGA	-			9.97	-	40.74	13.27	
					Hyphomicrobium facile (A)	-			4.86	-	1.85	4.95	
					Burkholderia sp. (B)	-			−0.84	-	−1.59	4.10	
					Methylobacterium oryzae (C)	-			1.71	-	−3.83	19.91	
					A + B + C	-			4.60	-	1.06	−10.41	
China	Sub-tropical monsoon	Clay	8.6	11.77	Humic acid	0.6	Rice	1	18.37	-	−3.77	−6.20	[30]
					Gypsum	0.6			2.30	-	9.43	19.36	
					Humic acid + gypsum	0.6 + 0.6			10.45	-	−26.42	27.25	
China	Temperate continental monsoon	Loam	6.8	8.81	Humic acid + controlled-release fertilizer	-	Maize	1	4.72	−2.47	−40.94	-	[31]
								2	11.10	−2.94	−40.40	-	
Australia	Humid sub-tropical	Clay	7.8	15.00	Chicken manure + conventional N application rate	-	Green beans + sorghum + broccoli + lettuce	1	−4.55	14.16	−23.53	-	[32]
					Composted chicken manure +conventional N application rate				0.00	11.80	8.82	-	
					Chicken manure + reduced N application rate				−6.82	11.98	−41.18	-	
					Composted chicken manure + reduced N application rate				2.27	−1.81	23.53	-	

Table 2. Effect of biochar application on mitigating GHG emissions under field conditions.

Country	Texture	pH	EC ds m⁻¹	OC g kg⁻¹	Biochar Feedstock	Pyrolysis temp. (°C)	Application Rate (Mg ha⁻¹)	Cultivated Crop	Years of Study	Yield (%) Compared with Control	CO₂	N₂O	CH₄	Reference
Australia	Clay loam	4.6	-	4.5	Cattle feedlot waste	550	10.0	Ryegrass	3	-	0.27	−13.67	-	[38]
China	loam	-	-	-	Wheat	550	20	Corn-wheat	2	-	0.13	20.79	-	[26]
							40			-	−5.40	31.54	-	
USA	Silt loam	7.7	0.4	18	Wood	500	22.4	Corn Silage	1	28.1	6.25	25.67	13.61	[39]
									2	32.37				
									3	41.62				

Table 2. *Cont.*

Country	Soil Properties				Biochar Feedstock	Pyrolysis temp. (°C)	Application Rate (Mg ha⁻¹)	Cultivated Crop	Years of Study	Yield (%) Compared with Control	GHG emissions Rate (%) Compared with Control			Reference
	Texture	pH	EC ds m⁻¹	OC g kg⁻¹							CO₂	N₂O	CH₄	
China	-	-	-	-	Wheat straw	450	20.0 / 40.0	Corn	1 / 2	-	−4.17 / −7.99	34.34 / 33.62	-	[40]
Japan	- / -	8.45 / 8.30	- / -	6.3 / 14.1	Bamboo	700–800	20.0	Kabocha squash / Bok choy / Kabocha squash / Bok choy	1 / 1 / 1 / 1	- / −173.68 / 3.76 / −38.02	−346.4 / −347.0 / −108.45 / −146.83	−42.85 / −29.50 / −163.59 / −0.56	- / - / - / -	[41]
Australia	Loamy sand / Sandy loam	7.1 / 6.4	0.11 / 0.04	2.6 / 1.8	Wood	500	10.0 / 20.0 / 10.0 / 20.0	Grass	2	-	6.25 / −9.38 / −18.24 / 17.57	19.50 / 1.58 / 9.18 / 19.77	- / - / - / 40.00	[42]
China	-	6.04	-	20.1	Wheat straw	350–550	10 / 20 / 40	Rice	1	10.0 / 25.1 / 26.3	−1.05 / 15.81 / 23.91	7.14 / 30.71 / 48.57	−14.00 / −11.33 / −30.67	[43]
China	-	8.1	-	49.6	Corn straw	550	26.0 / 64.0 / 128.0	Cabbage + carrot	1	-	−20.12 / −59.98 / −87.21	11.19 / −18.33 / 5.48	-	[44]
Germany	-	7.1	-	-	Beech wood	400	60.0	Corn	3	-	42.86	62.96	-	[45]
USA	Clay loam	6.1	0.17	20.1	Pinewood	-	10.0	Corn + soybean	1 / 2 / 3	-	−13.04 / 9.16 / 1.33	20.72 / 7.58 / 32.41	- / 20.76 / -	[46]
					Corn stover	-	10.0	Corn + soybean	1 / 2 / 3	-	−6.60 / 11.90 / −13.65	19.55 / 9.41 / 11.11	- / 20.13 / -	
					Switchgrass	-	10.0	Corn + soybean	1 / 2 / 3	-	−19.90 / 5.64 / −17.94	15.67 / 5.84 / 28.93	- / 2.39 / -	
South korea	Silt loam	5.18	0.50	17.8	South korea	Barley straw	400	Chinese cabbage	1	-	-	60.60	-	[47]
China	Sandy loam	6.5	-	18.1	China	Rice Straw	600	Rice	Early paddy / Late paddy	5.7 / 3.6	9.87 / 25.36	15.75 / 43.60	−7.37 / 15.07	[28]
China	-	7.4	-	12.7	Rice straw	600	20.0 / 40.0	Rice	1 / 2	9.4 / 15.9 / 24.0 / 36.3	- / - / -	−65.46 / 11.64 / 58.01 / 43.12	29.67 / 6.35 / 29.87 / 15.58	[48]
China	Sandy loam	8.5	0.32	14.5	Corn straw	400	15.0 / 30.0 / 45.0 / 15.0 / 30.0 / 45.0	Corn	1 / 2	6.29 / 7.34 / 1.77 / 1.45 / 7.57 / 3.15	24.66 / 17.57 / 22.13 / 19.27 / 25.85 / 40.60	71.13 / - / - / 43.71 / 46.69 / 38.74	-	[49]
Canada	silty clay loam	5.6	-	60.9	Wheat straw	450	20	Barley	1 / 2	20.37	6.22 / 3.56	33.18 / 34.32	-	[50]
China	-	4.5	-	21.4	-	-	20.0	Tea	1 / 2	0.0 / 0.0	- / -	14.36 / 7.10	-	[51]

In temperate forests, proper management strategies (including biochar application) should be undertaken since about 70% of the global carbon fluxes are generated from respiration [52]. This modulating effect on the respiration of temperate forests might maximize the carbon pool of the soil matrix. In this regard, bamboo leaf biochar application at rates of 5 and 10 Mg ha^{-1} increased carbon stock in moso bamboo forest by about 486 and 253%, respectively [53]. In the same regard, Ge et al. [54] recommended the combined application of biochar and nitrogen fertilizers for maintaining soil fertility and reducing CO_2 emissions from moso bamboo forest. The recalcitrant nature of biochar, its high water holding capacity, and its high potential to form soil aggregates with labile organic components may support its impact on maximizing soil carbon sequestration [53]. It is suggested that the safeguard effect of biochar against CO_2 emissions is associated with the predominance of soil bacterial species dealing with the tricarboxylic acid cycle [55]. Moreover, the key role of biochar in stimulating soil catalase, sucrose, urease, and β–glucosidase activities might support the protective effect of biochar against CO_2 emission from soil [56]. The stimulation of CO_2-fixing bacteria (e.g., *Chloroflexi*) following soil addition of biochar was also reported as a mechanism responsible for reducing CO_2 emissions [57].

On the other hand, cultivated land has almost lost 30–75% of its antecedent organic carbon pool as a result of soil respiration [58]. Therefore, effective soil management is highly recommended to maintain its soil carbon pool and offset the CO_2 emissions from cultivated land. To sustain the soil carbon pool in soil, organic additives application (e.g., farmyard manures) has been widely used as a common technique to sustain the productivity of soil. However, the high mineralization rate of organic carbon in soil (particularly under arid conditions) increases the potential of high CO_2 emissions from soil. Therefore, scientists recommend the application of organic manure in its pyrolyzed form given its carbon-negative nature. For instance, pig manure biochar application to sandy loam soil (northeast Toledo, Spain) decreased carbon mineralization compared to the original pig manure form [59]. In Zheng et al.'s work, biochar application over four years in sandy loam soil located in a semi-arid region (Henan Province, China) led to an increase in soil organic carbon (up to 22.1%), as well as the recalcitrant organic carbon fraction (up to 32.3%) [60]. Moreover, biochar application altered the bacterial community structure by motivating the abundance of *Chloroflexi* phylum (a bacterial community with low carbon mineralization and high carbon fixation potential).

In addition, biochar application was effective in reducing CO_2 emissions from saline soils in arid regions. Specifically, 400 °C corn stalks biochar application to coastal saline soil increased grain yield by about 28% without a significant effect on GHGs (CO_2, CH_4, and N_2O); however, the raw corn stalks increased N_2O emission by 18% [61]. Conversely, other reports point to a neutral or stimulating effect of biochar in increasing CO_2 emission. For instance, the contribution of biochar additives (*Conocarpus erectus* L. at 400 °C) in mitigating CO_2 emissions from sandy–calcareous soil in Saudi Arabia was negligible relative to the original biomass form [62]. The stimulating effect of biochar application increasing CO_2 emissions could be due to the enhancement of dissolved organic carbon content, as well as the enrichment of *Proteobacteria* (copiotrophic bacteria) and inhibition of *Acidobacteriota* (oligotrophic bacteria) [63]. Besides, the role of biochar in reducing soil bulk density might provide a hospitable environment for microorganism respiration [56].

3.2. Effect of Biochar Application on Reducing N_2O Emissions

Nitrous oxide (N_2O) is an atmospheric GHG derived mainly from agricultural practices (60%) that has greater global warming potential (300 folds) relative to CO_2 [64]. Scientists have noted a steady increase of N_2O emissions of about 12% over the last 75 years (290 vs. 330 ppbv) [65]. Due to the progressive transition toward intensive agriculture, the excessive utilization of mineral fertilizers has led to the increase of N_2O emissions by about 80% over the past century [66]. It is estimated that nearly 70% of global N_2O emissions are generated from soil nitrogen transformation processes, which are associated with synthetic nitrogen inputs and soil tillage, including nitrification (conversion of NH_4

to NO_3^-) and denitrification (conversion of NO_3^- to N_2) [67]. Interestingly, compost has been recognized as an important source for generating both of CO_2 and N_2O. The high CO_2 and N_2O footprints of compost and other organic fertilizers cause substantial losses from the inherent carbon (0.1–10%) and nitrogen (2.0–3.0%) [68]. For example, livestock manure compost is produced annually by about 1.2×10^6 metric tons of N_2O [69].

Biochar has been suggested as a non-sophisticated solution for maximizing the stability of organic fertilizers and reducing N_2O emissions given its high porosity and high number of active functional groups. Data extracted from the literature point to a relatively low efficiency of biochar (24.64%) in mitigating N_2O emissions (Figure 3).

Figure 3. Biochar efficiency in reducing N_2O and CH_4 emissions (%). Data are extracted from 19 investigations comprising 66 individual observations. Box chart is illustrated by the mean (dot), median (centerline), lower and upper quartiles (the lower and upper borders of the box, respectively), and whiskers-error bars (the minimum and maximum observations).

Authors have introduced numerous mechanisms that are responsible for alleviating N_2O emissions. Song et al. suggested that biochar reduced N_2O emissions directly by reducing the gross nitrification/denitrification rates of soil, and indirectly by reducing the content of soil-available N (ammonium, nitrate, and soluble organic nitrogen) and the activities of urease and protease [70]. Ji et al. [71] demonstrated that the application of biochar as a soil amendment was responsible for minimizing fungal abundance, thereby reducing N_2O emissions by about 28%. The promotion of nitrifying bacteria and the inhibition of denitrifying bacteria by biochar application were also highlighted as mechanisms responsible for mitigating N_2O emissions [72]. In addition, the inhibitory effect of biochar on bacterial-related nitrification/denitrification and N-cycle bacterial genes was further recorded in the rhizospheric layer of soil [73]. Another investigation pointed to the modulating effect of soil bulk density, nitrate reductase, nitrite reductase, and hydroxylamine reductase activities related to the denitrification process [74].

The ability of biochar to suppress N_2O emissions has a long-lasting effect, even seven years following its soil application [75]. In a ^{15}N-tracer incubation experiment, the protective effect of raw wood biochar (600 °C) on an alkaline soil (pH = 8.57) was due to the inhibition of the mineralization rate (gross autotrophic/heterotrophic nitrification and mineralization) and increasing the gross immobilization rates in soil [76]. The ability of biochar to modulate soil properties (e.g., aeration, pH/E_H, and organic carbon) has a subsequent effect on regulating soil nitrogen transformations and reducing N_2O emissions [77].

Biochar soil application along with mineral nitrogen fertilizers might have a protective effect in reducing cumulative N_2O emissions. In a microplot experiment, biochar appli-

cation (12 Mg ha^{-1} of maize straw @ 450 °C) with ^{15}N-labeled urea to sandy loam soil for three years maintained the retention of mineral nitrogen in the rhizosphere through reducing N$_2$O emissions and NO$_3^-$ leaching [78]. Moreover, the combined application of biochar with nitrification inhibitors shows a high potential to reduce N$_2$O emissions. In this regard, the application of manure biochar and nitrification inhibitor (nitrapyrin) reduced N$_2$O emissions from urea by about 45.2% in a 60-day laboratory incubation experiment [79].

In contrast, other reports have suggested an adverse effect of biochar on increasing N$_2$O emissions. For example, application of peanut shell biochar (pyrolyzed at 550 °C) along with nitrogen fertilizers to a grazing grassland (sandy loam in texture) in Queensland, Australia, increased N$_2$O emissions compared to the unamended treatment (without biochar). This is mainly due to the increment of soil pH, which caused an abundance of narG, nirS, and AOB genes in the soil [80]. In this regard, the volatile matter of biochar has a key role in controlling the capacity of biochar for reducing N$_2$O emissions since volatile matter content acts as a decomposable source of organic carbon for the denitrifying organisms [81]. Fresh biochar application was also responsible for increasing N$_2$O emissions given the stimulation of the AOB-*amoA* gene abundance through autotrophic nitrification and denitrification [82].

3.3. Effect of Biochar Application on Reducing CH$_4$ Emissions from Rice Basins

Rice is the second largest cereal crop grown worldwide, representing the staple diet of two-thirds of the human population. A large amount (about 95%) of the world's rice yield is produced in developing countries, since it is considered an important source of employment and high income in rural areas. Among all agricultural ecosystems, paddy rice basins are one of the major sources of CH$_4$ emissions. The annual CH$_4$ emissions from paddy rice basins range between 31 and 112 Tg per year, which contributes about 5–19% of total greenhouse gas emissions [83]. Due to intensive wet rice farming all over the world, a tremendous increase in CH$_4$ emissions have been recorded by about 1.2 Tg/decade between 1961 and 2016 [84]. CH$_4$ is generated during the decomposition of organic matter by the aid of methanogenic archaea (methanogens) [85]. Although the contribution of CH$_4$ to total GHG emissions is not significant, it has a 25-fold higher global warming potential than CO$_2$ [86]. In addition, under waterlogging paddy ecosystems, the denitrification process is always very active and tends to convert nitrate to nitrous oxide [87].

The contribution of biochar to the reduction of CH$_4$ emissions has been highlighted in the literature. Analysis of recent literature showed moderate removal efficiency (40.49%) of CH$_4$ by biochar application to rice basins (Figure 3). The motivating effect of biochar application on activities of Acetyl-CoA synthase and β-glucosidase involved in carbon fixation reduced coenzyme activities related to methanogens [88]. Sriphirom et al. illustrated that 500 °C *Rhizophora apiculata* biochar application up to 4% led to a reduction in CH$_4$ emissions (9–21%) due to the abundance of electron donors (organic acids) and acceptors (NO$_3^-$, SO$_4^{2-}$, and Fe^{3+}), which accelerate redumethanogenesis reduction [89]. The beneficial effect of biochar in improving soil aeration and the readiness of O$_2$ supplies may inhibit methanogenesis [90]. In Wang et al.'s study, application of straw-derived biochar at 24 and 48 Mg ha^{-1} mitigated CH$_4$ emissions by 20–51% through inhibiting the abundances of some methanogen populations (e.g., *Methanosaeta* and *Methanoregula*) [84]. Further study demonstrated that amending paddy soil with 550 °C biochar derived from *Rosa anemoniflora* branches inhibited the emission of CH$_4$ by motivating an abundance of mcrA and a high ratio of pmoA/mcrA [91]. The large surface area of biochar might also favor the electron transfer between bacteria and Fe minerals, thereby motivating the domination of Fe-reducing bacteria that discourage methanogens and inhibit CH$_4$ emissions [92]. The porous nature of biochar might promote CH$_4$ oxidation after adsorption into the abundant pores [93]. The biochar aging process might also facilitate the interaction with soil organic matter, Fe/Al oxides, and silicon, thereby forming coating layers on the internal and external surfaces of biochar [94].

The long-lasting effect of biochar application showed a high effectiveness for reducing CH_4 emissions. In the study of Nan et al., biochar derived from rice straw reduced the emissions of CH_4 over three successive years by about 43, 31, and 30%, and increased rice productivity by 8.0%, 1.6%, and 7.3%, respectively [95]. This long–term retardation of CH_4 emissions highlights the safeguarding effect of biochar as a stable and suitable microenvironment for carbon sequestration in rice basins. According to Wang et al., biochar application (24–48 Mg ha^{-1}) into rice paddies inhibited CH_4 emissions by 20–51% over four years of rice cropping due to the aerating effect of biochar, which enhanced the abundance of methanotrophic bacteria and decreased the abundance ratio of methanogens to methanotrophs [96].

In contrast, some reports have pointed to an increment of cumulative CH_4 emissions due to the abundance of methanogenic and methanotrophic genes in soil following biochar application [97]. The safeguarding effect of biochar against CH_4 emissions depends upon the pyrolysis technique and its temperature. Biochar showed higher efficacy for methane oxidation as compared with hydrochar, with higher pyrolysis temperature being superior. According to Liu et al., hydrochar application suppressed the growth of *Bacillus*, *Methylocystis,* and *Methylobacter*; however, biochar motivated an abundance of methane-oxidizing bacteria (methanotrophs) such as *Methylobacter* and *Methylocystis* [98].

4. Factors Affecting the Efficiency of Biochar in Mitigating GHG Emissions

4.1. Effect of Feedstock Type

The efficiency of biochar in reducing GHGs from soil depends mainly upon the inherent components of the feedstock. From recent published data (147 observations comprising 34 investigations), it is found that the average values of biochar efficiency in mitigating GHGs were 9.81, 6.68, and 20.37% with feedstocks of agricultural residuals, woody materials, and manures, respectively (Figure 4).
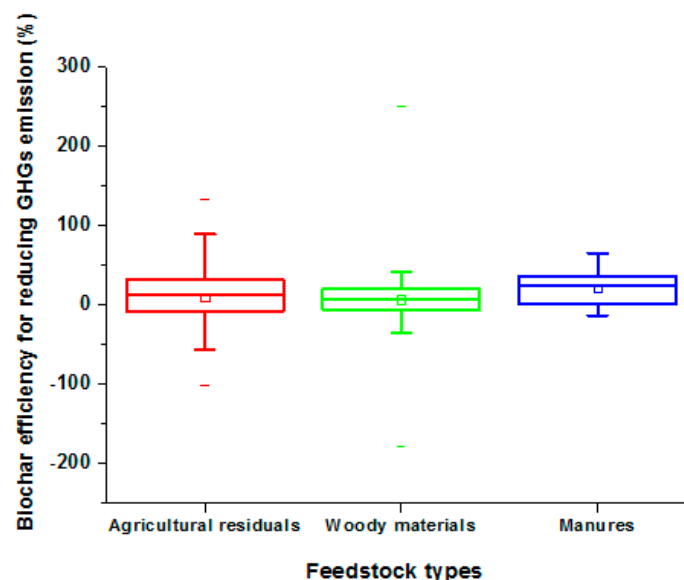
Figure 4. Effect of feedstock type on biochar efficiency in reducing GHG emissions from soil. Data are extracted from 34 investigations comprising 147 individual observations. Box chart is illustrated by the mean (dot), median (centerline), lower and upper quartiles (the lower and upper borders of the box, respectively), and whiskers-error bars (the minimum and maximum observations).

In other global meta-analyses, the magnitudes of N_2O reduction index of biochars were feedstock-dependent: bamboo (31.9%) > field crop straw (27.1%) > manures (27.0%) > hardwood (18.1%) > field crop husks (0.47%) [99]. Contradictory results, however, were reported by other investigations since the high nitrogen content in manure-derived biochars favors its higher N_2O emission footprint relative to other woody/herbaceous-derived

biochars [100]. Another study showed that plant-derived biochars showed higher values of aromatic carbon with high stability and resistance against microbial decay than other manure-derived biochars [101]. In a further study, there were no significant differences between manure and sawdust biochar (2.4 kg m^{-2}) for inhibiting emissions of N_2O and CH_4 from soil [102]. It was also noticed that soils amended with biochars with a small C:N ratio exhibited higher CO_2 efflux than those amended with other biochars with a large C:N ratio [103].

4.2. Effect of Pyrolysis Temperature

Pyrolysis temperature plays a pivotal role in regulating GHG emissions following biochar soil application. The slow pyrolysis technique involves using low temperature, low heating rates, and high residence times to generate a high yield of high-quality biochar [104]. However, other pyrolysis types (fast and flash pyrolysis) generate low biochar yield with low surface functionality [105]. Specifically, the low rate of heating (24 °C min^{-1}) can form biochars with high aromaticity relative to the heating rate (62 °C min^{-1}) [106]. In terms of biochar stability, a higher mineralization rate was noticed with biochars produced under shorter residence time of pyrolysis compared to slow-pyrolyzed biochars, which exhibit less mobile organic matter and high resistance against microbial degradation [107]. The carrier gas (e.g., N_2, CO_2, or Ar) pointedly impact the yield, active functional groups, and volatile organic carbon content of biochar [108]. Moreover, the reactor design significantly affects the physicochemical properties of biochar. In this regard, a microwave pyrolysis reactor produces highly stable biochar relative to fixed/fluidized bed, rotating cone, screw feeder/auger, and vacuum pyrolizers [109]

Data extracted from recent literature illustrated that pyrolysis temperature was crucial for the performance of biochar in mitigating GHG emissions (Figure 5). Average values of inhibition efficiency of biochar-amended soils relative to the unamended ones are–60.71, 2.82, 25.42, and 7.86% with pyrolysis temperatures of 300–399, 400–499, 500–599, and 600–699 °C, respectively. Therefore, the utilization of low-pyrolyzed biochar in mitigating GHG emissions is not recommended given its high carbon footprint.
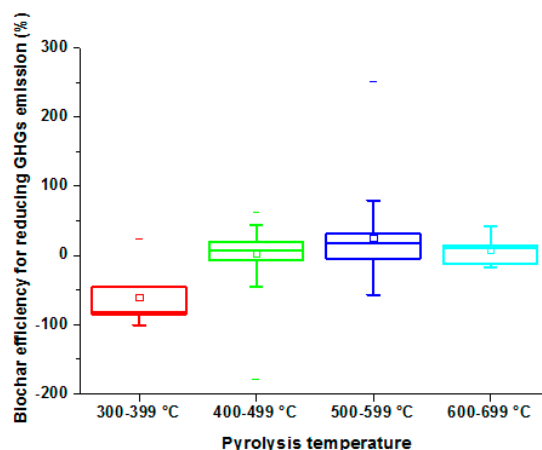
Figure 5. Effect of pyrolysis temperature on biochar efficiency in reducing GHG emissions from soil. Data are extracted from 26 investigations comprising 82 individual observations. Box chart is illustrated by the mean (dot), median (centerline), lower and upper quartiles (the lower and upper borders of the box, respectively), and whiskers-error bars (the minimum and maximum observations).

Based on a global meta-analysis, biochars produced at higher pyrolysis temperatures (>500 °C) exhibited higher potentials in reducing GHG emissions due to: (i) higher values of specific surface area, ash content, and polycondensed moieties; (ii) lower values of dissolved organic carbon, aliphatic compounds, and total surface charge; and (iii) suppressing the activity of soil microorganisms [110]. To summarize, low pyrolysis temperatures generate biochars with high volatile matter contents, low aromaticity, and high O:C ratio that are

less stable than those generated at high pyrolysis temperatures [111,112]. In the study of Yang et al., 300 °C maize straw biochar increased CO_2 emissions over the control treatment by about 46% owing to the increment of dissolved organic matter following the stimulation of copiotrophic bacteria (*Proteobacteria*) and the inhibition of oligotrophic bacteria (*Acidobacteriota*) [84]. In their study, they also reported that increasing pyrolysis temperature up to 450 and 600 °C reduced CO_2 emissions by about 10.5 and 14.0%, respectively, due to a subsequent decline in dissolved organic matter following biochar application. In Spain, biochar application (pig manure at 300 °C) to sandy loam soil resulted in a positive impact on dehydrogenase enzyme activity; however, the pyrolysis temperature of 500 °C did not show positive impacts on the activities of soil enzymes [59]. This modulating effect of biochar on soil enzymes was significantly correlated with CO_2 emissions by soil. According to Al-Rabaiai et al., high amounts of water-soluble organic compounds in biochars derived at low pyrolysis temperature might have a priming effect on stimulating microbial activities and soil respiration [85]. In contrast, spent-mushroom-substrate-derived biochar applied to moso bamboo forest soil at the rate of 50 g kg^{-1} caused a considerable increase in CO_2 emissions by about 73, 43, and 16.6% with pyrolysis temperatures of 300, 450, and 600 °C, respectively [113].

Likewise, the performance of biochar in mitigating N_2O emissions declined sharply at low pyrolysis temperatures owing to the smaller surface area and the low aromaticity of the produced biochar [114]. In addition, the extremely high pyrolysis temperature (900 °C) led to an increase in N_2O emissions from soil amended with walnut shell biochar due to favoring the denitrification process [115]. It was also reported that a high pyrolysis temperature of biochar (700–900 °C) can increase the cumulative emission of CH_4 fluxes, given the formation of biochars with highly condensed aromatic graphite structures, motivating electronic transfer ability of methanogens and the inherent salts in biochar additives [116,117]. In an incubation experiment, CH_4 generation from a paddy soil following straw biochar application was ranked as follows: biochar at 300 °C > biochar at 500 °C > biochar at 700 °C [118].

4.3. Effect of Application Rate

Restraining GHG emissions by biochar is an application-dependent strategy. Biochar often applied through broadcasting and mixing with soil matrix by tillage methods [58]. However, this application method is responsible for wind loss of biochar by about 25% of the applied amount [119]. In addition, biochar is frequently applied to a trench as furrow application after crop planting with a lower amount of application and minimal soil disturbance [120]. On the other hand, biochar could be indirectly applied to the soil by mixing with several soil amendments (e.g., lime, compost, and manure) [121,122].

A subsequent initial flush of CO_2 is emitted from soil following biochar application, which declines sharply with the recalcitrant aged biochar [123]. The inhibitory effect of biochar application to CO_2 emissions can be associated with the sorption of rhizodeposits and enzymes onto biochar, which lead to a reduction in carbon-degrading microbial activity in soil [124]. Numerous attempts have been made to specify the optimum rate of biochar soil application; however, a great deal of uncertainty remains surrounding the appropriate rate for each soil type. The extracted data from 31 investigations comprising 146 individual observations illustrate the average removal efficiency values of GHGs from biochar-amended soils relative to the unamended ones. Biochar efficiency in reducing GHG emissions was, on average, 15.91, 6.13, −2.13, and −4.45% with application rates of 1–10, 11–20, 21–40, and >40 Mg ha^{-1} (Figure 6). According to the obtained results, there seems to be a consensus that the low rate of biochar (up to 10 Mg ha^{-1}) is more preferable to achieve net carbon neutrality. However, a high application rate of biochar might increase the cumulative GHG emissions.
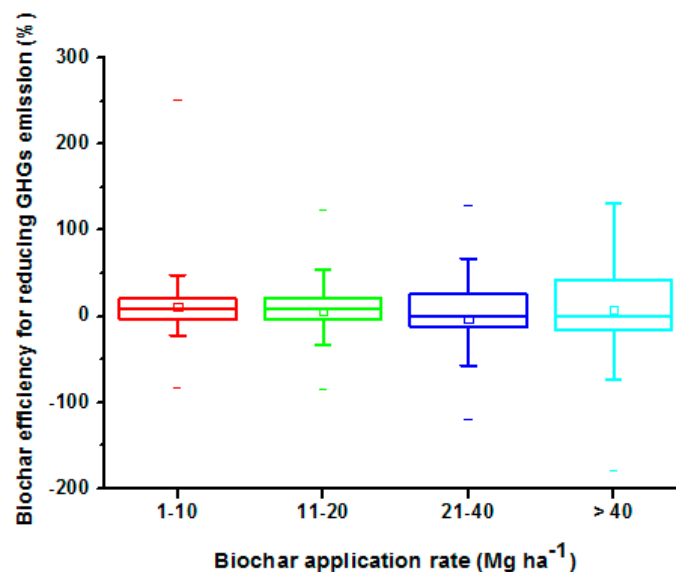
Figure 6. Effect of biochar application rate on efficiency in reducing GHG emissions. Data are extracted from 26 investigations comprising 82 individual observations. Box chart is illustrated by the mean (dot), median (centerline), lower and upper quartiles (the lower and upper borders of the box, respectively), and whiskers-error bars (the minimum and maximum observations).

Former studies have monitored the effect of the biochar application rate on the efficacy of regulating GHG emissions. Under upland rice production, the highest application rate of 350 °C rice-husk-derived biochar (25 Mg ha^{-1}) showed the highest CO_2 emissions (3.06 CO_2–C g/m^2) relative to the one-fifth application rate (2.78 CO_2–C g/m^2) [125]. Similarly, a low level of biochar (5 Mg ha^{-1} of 500 °C bamboo branches) could be more effective than the high application dosage (20 Mg ha^{-1}) in reducing CO_2 emissions and improving soil carbon sequestration in forest soils [126]. Another investigation revealed that increasing the application rate of bamboo leaf biochar did not show substantial alterations in CO_2 emission [127].

As mentioned earlier, the optimum application rate of biochar might change according to the soil type. For instance, soil biochar application (20 Mg ha^{-1} 650 °C) to deciduous mixed forest led to a substantial decline in CO_2 emissions; however, this emission rate was not significantly changed in a long-term fertilized apple orchard [128]. Other reports suggested raising the application rate of biochar to offset the cumulative GHG emissions. In the study of Shen et al., increasing the application rate of 450 °C maize straw biochar from 10 up to 30 Mg ha^{-1} was associated with a progressive reduction in cumulative CO_2 emissions (from 3.9 to 11.8%) due to the sorption of labile carbon onto internal and external surfaces of biochar, thus suppressing the rate of soil respiration [129].

The application rate also affects the performance of biochar in regulating GHG emissions from different soil layers. For instance, cumulative N_2O emissions from the topsoil (0–5 cm) following the application of pruning waste biochar (@ 600 °C) at rates of 2 and 10% declined N_2O emissions by 12.5% and 26.3%, respectively. However, the safeguard effect of pruning waste biochar in reducing N_2O emissions from a soil layer of 0–10 and the rhizospheric layer was only observed with the rate of 10% (15.1 and 13.8%, respectively) [130]. Biochar application as film-mulching has recently been investigated on cropping systems grown under drip irrigation. In view of that, corn-residue-derived biochar (produced under pyrolysis at 400–500 °C) was applied as a film mulch to drip-irrigated corn grown in sandy loam soil in Inner Mongolia, China. Results showed that increasing the application rate from 15 up to 45 Mg ha^{-1} as a film mulch system was associated with significant reductions in GHGs over two growing seasons: CO_2 (19 –33%), CH_4 (124–132%), and N_2O (55–79%) [49].

5. Effect of Biochar on Reducing GHG Emissions during Composting

Composting is a process in which organic wastes are transformed via complicated biochemical reactions into recalcitrant organic products (humic substances in particular) that can serve as fertilizers to sustain soil fertility and productivity [131]. However, the composting process is responsible for emitting substantial amounts of GHGs that raised concerns from ecological point of view. In particular, CH_4 accounts for about 6% of the total carbon loss during the composting process, and the emission of N_2O accounts for approximately 3.8% of the total nitrogen losses [132]. Furthermore, the release of ammonia (NH_3) during composting not only harms the ecosphere but also declines the agricultural revenues from compost additives. Related research investigations revealed that animal husbandry is the main source of agricultural non-CO_2 emissions, accounting for about 37 and 65% of CH_4 and N_2O, respectively (12% of the anthropogenic GHG emissions globally) [133]. The emission of GHGs is more pronounced in the initial phase of the composting process (the thermophilic phase), in which the temperature reaches about 70 °C; however, this emission declines dramatically in the ultimate maturation phase (the mesophilic phase), when the temperature drops to 40–50 °C [134].

The applicability of biochar additives to reducing GHG emissions during composting is illustrated in Table 3. The high functionality of biochar has attracted research attention for utilization as a supplemental additive during the composting process to accelerate the startup of decomposition, shorten the period of composting, and reduce the amounts of GHG emissions [135]. Furthermore, biochar might reduce the mobility of water-soluble organic substances and avoid their losses during the composting process [136]. In view of this, biochar application during composting might inhibit the abundance of the nirK gene in denitrifying bacteria, which causes a significant reduction of N_2O emissions during composting [137]. In the study of Guo et al., bamboo charcoal application during composting led to minimizing NH_3 emissions following the active nitrification by *Nitromonas* [138]. In another study to evaluate the effect of 5% biochar application during pig manure composting, it was reported that biochar could shorten the composting period and reduce emissions of CO_2, CH_4, N_2O, and NH_3 by about 35.9, 15.4, 19.9, and 18.8%, respectively [139]. However, in another study, chicken manure biochar application (up to 10%) during chicken manure composting declined the release of GHGs: N_2O (19.0–27.4%), CH_4 (9.3–55.9%), and NH_3 (24.2–56.9%) [132]. Likewise, the co-application of bamboo biochar with poultry manure during composting (up to 10% w:w) reduced CO_2 and NH_3 losses by about 542–149% and 48–11%, respectively [140].

The composting of sewage sludge is a green technology for reducing the negative impacts associated with its ecological hazards [141]. However, a great deal of uncertainty arises surrounding its high GHG footprint [142]. To address this environmental constraint, Awasthi et al. [143] added rice straw biochar at a high rate (8–18%) during sewage sludge composting and recorded remarkable declines in GHG emissions: CH_4 (93–95%), NH_3 (58–65%), and N_2O (95–97%). In yet another investigation, bamboo biochar application along with bacterial agents during sewage sludge composting mitigated CH_4 and N_2O emissions (45.7% and 3.7%, respectively) due to the beneficial effect of biochar on filling the space between compost particles, thereby minimizing the potential heat losses and motivating microbial activity and consequent heat production [144]. Vermicomposting is a benign and modern eco-friendly technique for addressing the vast accumulation of organic wastes, although the incorporation of earthworms in these organic fertilizers showed higher emissions of N_2O relative to other traditional composts [145]. According to Wu et al., the incorporation of 500 °C rice straw biochar with vermicompost significantly reduced cumulative N_2O emissions (~19%) [146].

The application of biochar as a ruminant diet showed a significant impact on improving the digestion performance of animals, reducing enteric CH_4 and increasing the value of post-excretion biochar–manure mixture. In a recent study, the effect of pine-based biochar application on cattle diet increased stockpile/compost aromaticity with a high content of more humic-like organic matter precursors [147].

Table 3. Effect of biochar application on mitigating GHG emissions during composting.

Feedstock	Biochar Characteristics			Composting Materials	Compost Characteristics		GHG Emissions Reduction Effect (% Compared with Control)				References
	Pyrolysis Temperature (°C)	Biochar Application (% *w/w*)	Particle Size (mm)		Bulk Density (g cm^{-3})	C/N Ratio	CO_2	CH_4	N_2O	NH_3	
Hardwood+ softwood	500–700	27.4	≤16	Hen manure + barley straw	0.49	17.4–13.7	21.5–22.9	77.9–83.6	35.3–43.0	35.3–43.0	[148]
Woody material	-	4	-	Sewage sludge + woodchips	-	22–25	-	-	-	8.5–9.2	[149]
Holm oak	650	10	-	Green waste + municipal solid waste	-	27.5–16.2	52.9	95.1	14.2	-	[150]
Green waste + poultry litter	550	10	-	Poultry litter + sugarcane straw	-	-	-	77.8–83.3	68.2–74.9	54.9 –60.2	[151]
Wheat straw	500–600	2–18	2–5	Sewage sludge + wheat straw	0.50	25.0	-	92.8–95.3	95.1–97.3	58.0–65.2	[143]
Bamboo	-	5	2–3	Pig manure + sawdust	0.50	-	-	54.4	36.1	12.4	[152]
Chicken manure + wheat straw	550–600	2–10	-	Chicken manure	0.50	16.8–14.2	-	24.4–63.4	6.8–16.9	22.9–50.5	[132]
Bamboo	-	2–10	-	Poultry manure + wheat straw	0.50	24.3–18.9	5.5–72.6	12.5–72.9	12.4–81.6	19.0–77.4	[140]
Cornstalk	450–500	10.0	≤2.0	Hen manure, sawdust	0.42	-	-	-	-	12.4	[153]
Waste wood pellets	520	10 15	-	Chicken mortalities	-	20.3 20.0	-	-	- -	40.0 56.8	[154]

6. Designer/Functionalized Biochar for Efficient Retardation of GHG Emissions from Soil and Terrestrial Ecosystems

The scientific community is interested in maximizing the functionality of biochar so that it can be tailored to a variety of agro-environmental applications [11–13,155]. In a meta-analysis study, acidic oxidation was the most efficient method for enhancing the physicochemical properties of biochar (specific surface area, micro-pores, oxygen-containing functional groups, and cation exchange capacity) relative to other oxidation methods (physical, alkaline, metal oxide, and natural oxidation methods) [156]. Recently, designer biochar functionalization (specialization) has attracted increasing attention in recent research to lessen GHG emissions from agricultural ecosystems. Several reports highlighted the activation of pristine biochar (raw biochar) via physical and chemical modification methods to improve the functionality of biochar (increase its surface area and porous structure) for the sorption of GHGs. However, most of these reports are still under lab-scale experimentations. In addition, most of these reports are focused on capturing CO_2 emissions. Data extracted from published reports (97 values) showed that the average values of CO_2 sorption with pristine, physically activated, and chemically activated biochars were 37.8, 56.5, and 59.4 mg g^{-1}, respectively (Figure 7).
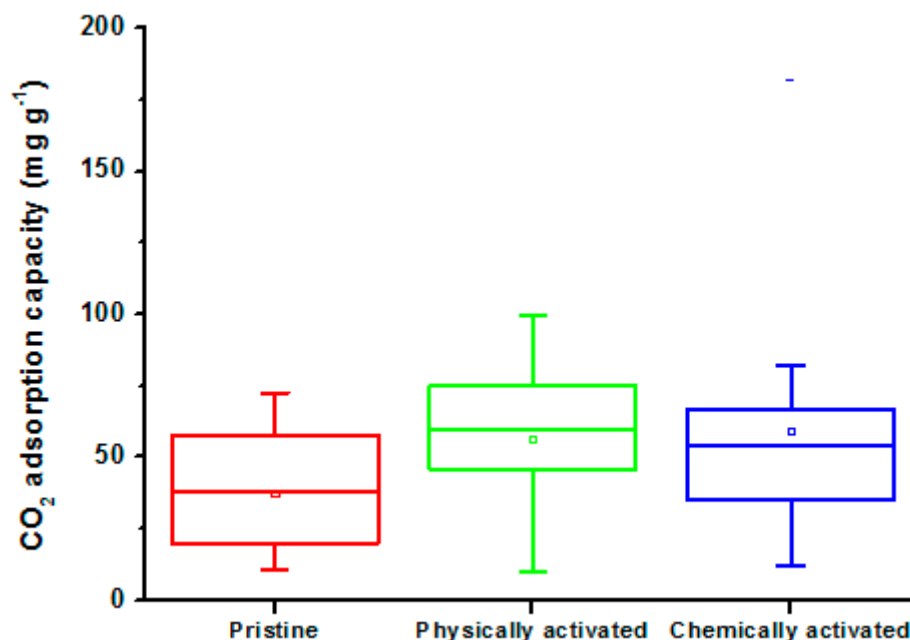
Figure 7. Effect of activation methods on sorption capacity of CO_2 (mg g^{-1}) with pristine and designer biochars. Data are extracted from 97 individual observations. Box chart is illustrated by the mean (dot), median (centerline), lower and upper quartiles (the lower and upper borders of the box, respectively), and whiskers-error bars (the minimum and maximum observations).

A wide range of researchers have highlighted physical modification as the preferable activation method to maximize the functionality of biochar relative to chemical modifications methods [157,158]. Proponents of physical modification point to the high risk of deteriorating the carbonaceous lattice following chemical modifications and the potential to block the pore structures of the biochar matrix, which might reduce gases sorptivity [159]. Steam and high-temperature gas activation have been attempted to improve the porosity of biochar; however, the NH_3 activation not only improved the pore structure of activated biochar, but also introduced active functional groups onto the carbonaceous lattice [160]. Physical treatment with NH_3 can also increase the alkaline nature of biochar and the base–acid interaction between CO_2 and the originated nitrogen-containing functional groups [161]. Furthermore, NH_3 treatment grafted pyrrolic–N groups onto the biochar

matrix, which facilitated the H–bonding interaction between CO_2 molecules, and the proton of pyrrolic–N [162].

Opponents of physical activation methods, however, point toward the higher energy consumption, longer activation time, and higher activation temperature. Several chemical activation methods have been reviewed for the functionalization of biochar for capturing GHGs. Among them, alkali and acid-modified biochars have shown high sorptivity with low cost and simple processing. Alkali treatment of wood pellet biochar maximized the capture capacity of CO_2 by about five folds relative to untreated biochar (50.73 vs. 10.45 mg g^{-1}) due to improving surface area, porosity, and abundance of active functional groups on the biochar matrix [163]. High CO_2 capture (160 mg g^{-1}) was further recorded by 350 °C pine cone biochar activated with KOH [164]. In yet another study, high capacities of CO_2 retardation (136.7–182.0 mg g^{-1}) were recorded by KOH-activated biochars derived from pine sawdust and sewage sludge mixture as compared with plain biochar (35.5–42.9 mg g^{-1}) given the formation of tunable porous features in biochar matrix [165].

In their studies on rice plant, Shin and coworkers [166] reported that activated biochar (alkali-treated rice hull pellets)-doped mineral fertilizer (40% N) reduced cumulative CO_2 and N_2O emissions by about 10 and 0.003 kg ha^{-1}, respectively, compared to the control treatment, with a negligible effect on the emission of CH_4. In another experiment, 700 °C rice husk biochar was acid modified with H_3PO_4 and further combined with nano-zero-valent iron (nZVI) to enhance its sorption capacity for GHGs. The functionalized biochar form reduced CO_2 and N_2O emissions; however, CH_4 emission showed a noticeable increase [167].

The doping of heteroatoms (e.g., Mg, N, S, and Ni) into the carbonaceous lattice of biochar exhibited promising values for capturing GHGs due to the electron-withdrawal effect. In view of this, Mg-doped rice straw biochar application (at 9%) to a dryland soil in Hunan Province, China, showed a minimal effect on CH_4 emission but reduced cumulative emissions of CO_2 (9%) and N_2O (32%) as compared to the control treatment [168]. Nitrogen-doped biochar (mixture of rice straw and waste wood pyrolyzed at 600 °C and applied at 0–8 Mg ha^{-1}) was further studied in rice cropping soils under a short-term study [169]. Compared with the control treatment, nitrogen-doped biochar application increased CO_2 emissions and reduced emissions of CH_4 with the application rate of 8 Mg ha^{-1}.

Iron species receive high attention for biochar specialization in several agro-environmental applications. As a result of its effect on denitrification functional genes (nirk, narG, nirS, and nosZ), methanogenesis (mcrA), and methanotrophs (pmoA), modified biochar (derived from reed, walnut, saw dust, and sludge) supported by nano-zero-valent iron (nZVI) was able to reduce N_2O, CO_2, and CH_4 emissions [170]. Biochar (600 °C *Camellia oleifera* fruit shell) modified with $Fe(NO_3)_3$/KOH showed a high efficacy in N_2O retardation with an increment of about 8.6% over pristine biochar [171]. Developing enriched biochar derivatives with higher functionality (organo-mineral complexes, surface area, exchanging capacity of ions and dissolved organic carbons) has been proposed to enhance the sequestration of GHGs. The carbon footprint of either conventional rice straw biochar or enriched biochar with lime, clay, ash, and manure was compared under paddy field conditions [172]. They indicated that the difference in the carbon footprint between biochar types is mainly associated with variations in CH_4 emissions among plain and functionalized biochars.

7. Conclusions and Future Prospects

In recent years, lowering the rise in emissions of greenhouse gases has become one of the issues that requires global attention. In this work, we performed a review of the recent literature on biochar, as a tool to lessen the impact of emissions and mitigate their negative consequences. Overall, this review assesses the different methods of biochar production and their effectiveness. This review primarily summarizes the biochemical processes occurring in the charosphere. In addition, recent developments in our understanding of how to activate biochar for maximum effectiveness in achieving carbon neutrality goals are covered. To conclude:

- Biochar and its derivatives have been shown to reduce emissions of CO_2, N_2O, and CH_4 from soil and organic manures. Recent field-scale studies have found that biochar has the potential to reduce emissions of CO_2, N_2O, and CH_4 on the order of -0.430, 24.681, and 40.486%, respectively.
- While biochar showed promising results in reducing greenhouse gas emissions when tested in controlled laboratory settings, studies conducted on a larger scale have shown either no effect or even a negative one on efforts to lower GHG emissions.
- Notably, biochar's effectiveness in cutting greenhouse gas emissions is proportional to its application rate, pyrolysis temperature, and the type of feedstock used to make it.
- To produce effective amendments with a high capacity for restraining GHG production and enhancing soil carbon sink, it is recommended that manure-derived biochars be pyrolyzed between 500 and 600 °C, and applied at a rate of less than 10 Mg ha^{-1}.
- Overall, biochar can be seen as a highly effective and relatively simple tool for reversing the upward trend in greenhouse gas emissions.
- Since carbon and nitrogen transformation processes are microbially dependent, future research should be directed toward (i) investigating other indirect factors related to soil physicochemical characters (such as soil pH/Eh, colloidal and $CaCO_3$ contents) that may control the functionality of biochar, (ii) fabricating aged biochars with low carbon and nitrogen footprints, and (iii) functionalizing biologically activated biochars to suppress CO_2, CH_4, and N_2O emissions.

Author Contributions: Conceptualization, A.M. and M.M.M.; methodology, A.M. and E.S.; software, A.E.-G. and M.E.A.; validation, A.M., M.M.M. and A.M.E.K.; formal analysis, A.M. and E.S.; investigation, A.M. and M.M.M.; resources, M.E.A. and A.M.E.K.; data curation, A.M. and E.S.; writing—original draft preparation, A.M., M.M.M. and E.S.; writing—review and editing, A.M., M.E.A. and A.M.E.K.; visualization, A.E.-G. and E.S.; supervision, A.M. and A.E.-G.; project administration, A.M. and A.M.E.K.; funding acquisition, A.M.E.K. and M.E.A. All authors have read and agreed to the published version of the manuscript.

Institutional Review Board Statement: We choose to exclude this statement because our study did not involve humans or animals.

Informed Consent Statement: We choose to exclude this statement because our study did not involve humans or animals.

Data Availability Statement: Not applicable.

Conflicts of Interest: The authors declare no conflict of interest.

References

1. Thakur, I.S.; Kumar, M.; Varjani, S.J.; Wu, Y.; Gnansounou, E.; Ravindran, S. Sequestration and utilization of carbon dioxide by chemical and biological methods for biofuels and biomaterials by chemoautotrophs: Opportunities and challenges. *Bioresour. Technol.* **2018**, *256*, 478–490. [CrossRef] [PubMed]
2. Chen, M.; Cui, Y.; Jiang, S.; Forsell, N. Toward carbon neutrality before 2060: Trajectory and technical mitigation potential of non-CO_2 greenhouse gas emissions from Chinese agriculture. *J. Clean. Prod.* **2022**, *368*, 133186. [CrossRef]
3. IPCC. *Climate Change 2013: The Physical Science Basis. Contribution of Working Group I to the Fifth Assessment Report of the Intergovernmental Panel on Climate Change*; Cambridge University Press: Cambridge, UK, 2013; p. 1535.
4. Maraseni, T.N.; Qu, J. An international comparison of agricultural nitrous oxide emissions. *J. Clean. Prod.* **2016**, *135*, 1256–1266. [CrossRef]
5. Filho, W.L.; Setti, A.F.F.; Azeiteiro, U.M.; Lokupitiya, E.; Donkor, F.K.; Etim, N.N.; Matandirotya, N.; Olooto, F.M.; Sharifi, A.; Nagy, G.J.; et al. An overview of the interactions between food production and climate change. *Sci. Total Environ.* **2022**, *838*, 156438. [CrossRef] [PubMed]
6. Moussa, R.R. Reducing carbon emissions in Egyptian roads through improving the streets quality. *Environ. Dev. Sustain.* **2022**, 1–22. [CrossRef]

7. Alshaal, T.; El-Ramady, H.; Al-Saeedi, A.H.; Shalaby, T.; Elsakhawy, T.; Omara, A.E.D.; Gad, A.; Hamad, E.; El-Ghamry, A.; Mosa, A. The rhizosphere and plant nutrition under climate change. In *Essential Plant Nutrients*; Springer: Berlin/Heidelberg, Germany, 2017; pp. 275–308.

8. Mosa, A.; Taha, A.A.; Elsaeid, M. In-situ and ex-situ remediation of potentially toxic elements by humic acid extracted from different feedstocks: Experimental observations on a contaminated soil subjected to long-term irrigation with sewage effluents. *Environ. Technol. Innov.* **2021**, *23*, 101599. [CrossRef]

9. Frank, S.; Havlík, P.; Soussana, J.-F.; Levesque, A.; Valin, H.; Wollenberg, E.; Kleinwechter, U.; Fricko, O.; Gusti, M.; Herrero, M. Reducing greenhouse gas emissions in agriculture without compromising food security? *Environ. Res. Lett.* **2017**, *12*, 105004. [CrossRef]

10. Laird, D.A.; Brown, R.C.; Amonette, J.E.; Lehmann, J. Review of the pyrolysis platform for coproducing bio-oil and biochar. *Biofuels Bioprod. Biorefining* **2009**, *3*, 547–562. [CrossRef]

11. El-Naggar, A.; Mosa, A.; Ahmed, N.; Niazi, N.K.; Yousaf, B.; Sarkar, B.; Rinklebe, J.; Cai, Y.; Chang, S.X. Modified and pristine biochars for remediation of chromium contamination in soil and aquatic systems. *Chemosphere* **2022**, *303*, 134942. [CrossRef]

12. Shaheen, S.M.; Mosa, A.; El-Naggar, A.; Faysal Hossain, M.; Abdelrahman, H.; Khan Niazi, N.; Shahid, M.; Zhang, T.; Tsang, Y.F.; Trakal, L.; et al. Manganese oxide-modified biochar: Production, characterization and applications for the removal of pollutants from aqueous environments—A review. *Bioresour. Technol.* **2022**, *346*, 126581. [CrossRef]

13. El-Naggar, A.; Mosa, A.; Amin, A.E.-E.; Yang, X.; Yousaf, B.; El-Naggar, A.H.; Cai, Y.; Chang, S.X. Chapter 18—Biochar for remediation of alkaline soils contaminated with toxic elements. In *Biochar in Agriculture for Achieving Sustainable Development Goals*; Tsang, D.C.W., Ok, Y.S., Eds.; Academic Press: Cambridge, MA, USA, 2022; pp. 223–240. [CrossRef]

14. Tsang, D.C.W.; Ok, Y.S. *Biochar in Agriculture for Achieving Sustainable Development Goals*; Elsevier: Amsterdam, The Netherlands, 2022.

15. Danesh, P.; Niaparast, P.; Ghorbannezhad, P.; Ali, I. Biochar Production: Recent Developments, Applications, and Challenges. *Fuel* **2022**. [CrossRef]

16. Li, Y.; Gupta, R.; Zhang, Q.; You, S. Review of biochar production via crop residue pyrolysis: Development and perspectives. *Bioresour. Technol.* **2023**, *369*, 128423. [CrossRef] [PubMed]

17. Gabhane, J.W.; Bhange, V.P.; Patil, P.D.; Bankar, S.T.; Kumar, S. Recent trends in biochar production methods and its application as a soil health conditioner: A review. *SN Appl. Sci.* **2020**, *2*, 1–21. [CrossRef]

18. Oh, S.; Lee, J.; Lam, S.S.; Kwon, E.E.; Ha, J.-M.; Tsang, D.C.W.; Ok, Y.S.; Chen, W.-H.; Park, Y.-K. Fast hydropyrolysis of biomass Conversion: A comparative review. *Bioresour. Technol.* **2021**, *342*, 126067. [CrossRef] [PubMed]

19. Ethaib, S.; Omar, R.; Kamal, S.M.M.; Awang Biak, D.R.; Zubaidi, S.L. Microwave-assisted pyrolysis of biomass waste: A mini review. *Processes* **2020**, *8*, 1190. [CrossRef]

20. Wang, L.; Ok, Y.S.; Tsang, D.C.W.; Alessi, D.S.; Rinklebe, J.; Mašek, O.; Bolan, N.S.; Hou, D. Biochar composites: Emerging trends, field successes and sustainability implications. *Soil Use Manag.* **2022**, *38*, 14–38. [CrossRef]

21. Shaheen, S.M.; Mosa, A.; Jeyasundar, A.; Soundari, P.G.; Hassan, N.E.E.; Yang, X.; Antoniadis, V.; Li, R.; Wang, J.; Zhang, T. Pros and Cons of Biochar to Soil Potentially Toxic Element Mobilization and Phytoavailability: Environmental Implications. *Earth Syst. Environ.* **2022**, 1–25. [CrossRef]

22. Mosa, A.; El-Ghamry, A.; Tolba, M. Functionalized biochar derived from heavy metal rich feedstock: Phosphate recovery and reusing the exhausted biochar as an enriched soil amendment. *Chemosphere* **2018**, *198*, 351–363. [CrossRef]

23. Zou, R.; Qian, M.; Wang, C.; Mateo, W.; Wang, Y.; Dai, L.; Lin, X.; Zhao, Y.; Huo, E.; Wang, L. Biochar: From by-products of agro-industrial lignocellulosic waste to tailored carbon-based catalysts for biomass thermochemical conversions. *Chem. Eng. J.* **2022**, *441*, 135972. [CrossRef]

24. Lin, J.-C.; Mariuzza, D.; Volpe, M.; Fiori, L.; Ceylan, S.; Goldfarb, J.L. Integrated thermochemical conversion process for valorizing mixed agricultural and dairy waste to nutrient-enriched biochars and biofuels. *Bioresour. Technol.* **2021**, *328*, 124765. [CrossRef]

25. Abhishek, K.; Srivastava, A.; Vimal, V.; Gupta, A.K.; Bhujbal, S.K.; Biswas, J.K.; Singh, L.; Ghosh, P.; Pandey, A.; Sharma, P. Biochar application for greenhouse gas mitigation, contaminants immobilization and soil fertility enhancement: A state-of-the-art review. *Sci. Total Environ.* **2022**, *853*, 158562. [CrossRef] [PubMed]

26. Liu, W.-J.; Zeng, F.-X.; Jiang, H.; Zhang, X.-S. Preparation of high adsorption capacity bio-chars from waste biomass. *Bioresour. Technol.* **2011**, *102*, 8247–8252. [CrossRef] [PubMed]

27. Zhang, X.; Qian, H.; Hua, K.; Chen, H.; Deng, A.; Song, Z.; Zhang, J.; Raheem, A.; Danso, F.; Wang, D. Organic amendments increase crop yield while mitigating greenhouse gas emissions from the perspective of carbon fees in a soybean-wheat system. *Agric. Ecosyst. Environ.* **2022**, *325*, 107736. [CrossRef]

28. Wang, C.; Wang, W.; Sardans, J.; Singla, A.; Zeng, C.; Lai, D.Y.F.; Peñuelas, J. Effects of steel slag and biochar amendments on CO_2, CH_4, and N_2O flux, and rice productivity in a subtropical Chinese paddy field. *Environ. Geochem. Health* **2019**, *41*, 1419–1431. [CrossRef]

29. Malyan, S.K.; Bhatia, A.; Tomer, R.; Harit, R.C.; Jain, N.; Bhowmik, A.; Kaushik, R. Mitigation of yield-scaled greenhouse gas emissions from irrigated rice through Azolla, Blue-green algae, and plant growth–promoting bacteria. *Environ. Sci. Pollut. Res.* **2021**, *28*, 51425–51439. [CrossRef]

30. Sun, L.; Ma, Y.; Liu, Y.; Li, J.; Deng, J.; Rao, X.; Zhang, Y. The combined effects of nitrogen fertilizer, humic acid, and gypsum on yield-scaled greenhouse gas emissions from a coastal saline rice field. *Environ. Sci. Pollut. Res.* **2019**, *26*, 19502–19511. [CrossRef]

31. Guo, Y.; Ma, Z.; Ren, B.; Zhao, B.; Liu, P.; Zhang, J. Effects of Humic Acid Added to Controlled-Release Fertilizer on Summer Maize Yield, Nitrogen Use Efficiency and Greenhouse Gas Emission. *Agriculture* **2022**, *12*, 448. [CrossRef]

32. De Rosa, D.; Rowlings, D.W.; Biala, J.; Scheer, C.; Basso, B.; Grace, P.R. N_2O and CO_2 emissions following repeated application of organic and mineral N fertiliser from a vegetable crop rotation. *Sci. Total Environ.* **2018**, *637*, 813–824. [CrossRef]

33. Sohi, S.P.; Krull, E.; Lopez-Capel, E.; Bol, R. A review of biochar and its use and function in soil. *Adv. Agron.* **2010**, *105*, 47–82.

34. Leppäkoski, L.; Marttila, M.P.; Uusitalo, V.; Levänen, J.; Halonen, V.; Mikkilä, M.H. Assessing the carbon footprint of biochar from willow grown on marginal lands in Finland. *Sustainability* **2021**, *13*, 10097. [CrossRef]

35. Brewer, C.E.; Chuang, V.J.; Masiello, C.A.; Gonnermann, H.; Gao, X.; Dugan, B.; Driver, L.E.; Panzacchi, P.; Zygourakis, K.; Davies, C.A. New approaches to measuring biochar density and porosity. *Biomass Bioenergy* **2014**, *66*, 176–185. [CrossRef]

36. Lim, T.J.; Spokas, K.A.; Feyereisen, G.; Novak, J.M. Predicting the impact of biochar additions on soil hydraulic properties. *Chemosphere* **2016**, *142*, 136–144. [CrossRef]

37. Fan, R.; Zhang, B.; Li, J.; Zhang, Z.; Liang, A. Straw-derived biochar mitigates CO_2 emission through changes in soil pore structure in a wheat-rice rotation system. *Chemosphere* **2020**, *243*, 125329. [CrossRef] [PubMed]

38. Scheer, C.; Grace, P.R.; Rowlings, D.W.; Kimber, S.; van Zwieten, L. Effect of biochar amendment on the soil-atmosphere exchange of greenhouse gases from an intensive subtropical pasture in northern New South Wales, Australia. *Plant Soil* **2011**, *345*, 47–58. [CrossRef]

39. Lentz, R.D.; Ippolito, J.A.; Spokas, K.A. Biochar and manure effects on net nitrogen mineralization and greenhouse gas emissions from calcareous soil under corn. *Soil Sci. Soc. Am. J.* **2014**, *78*, 1641–1655. [CrossRef]

40. Zheng, M.; Chen, H.; Li, D.; Zhu, X.; Zhang, W.; Fu, S.; Mo, J. Biological nitrogen fixation and its response to nitrogen input in two mature tropical plantations with and without legume trees. *Biol. Fertil. Soils* **2016**, *52*, 665–674. [CrossRef]

41. Watanabe, A.; Ikeya, K.; Kanazaki, N.; Makabe, S.; Sugiura, Y.; Shibata, A. Five crop seasons' records of greenhouse gas fluxes from upland fields with repetitive applications of biochar and cattle manure. *J. Environ. Manag.* **2014**, *144*, 168–175. [CrossRef]

42. Keith, A.; Singh, B.; Dijkstra, F.A.; van Ogtrop, F. Biochar field study: Greenhouse gas emissions, productivity, and nutrients in two soils. *Agron. J.* **2016**, *108*, 1805–1815. [CrossRef]

43. Zhang, A.; Bian, R.; Li, L.; Wang, X.; Zhao, Y.; Hussain, Q.; Pan, G. Enhanced rice production but greatly reduced carbon emission following biochar amendment in a metal-polluted rice paddy. *Environ. Sci. Pollut. Res.* **2015**, *22*, 18977–18986. [CrossRef]

44. Fang, B.; Lee, X.; Zhang, J.; Li, Y.; Zhang, L.; Cheng, J.; Wang, B.; Cheng, H. Impacts of straw biochar additions on agricultural soil quality and greenhouse gas fluxes in karst area, Southwest China. *Soil Sci. Plant Nutr.* **2016**, *62*, 526–533. [CrossRef]

45. Hagemann, N.; Harter, J.; Kaldamukova, R.; Guzman-Bustamante, I.; Ruser, R.; Graeff, S.; Kappler, A.; Behrens, S. Does soil aging affect the N_2O mitigation potential of biochar? A combined microcosm and field study. *GCB Bioenergy* **2017**, *9*, 953–964. [CrossRef]

46. Abagandura, G.O.; Chintala, R.; Sandhu, S.S.; Kumar, S.; Schumacher, T.E. Effects of biochar and manure applications on soil carbon dioxide, methane, and nitrous oxide fluxes from two different soils. *J. Environ. Qual.* **2019**, *48*, 1664–1674. [CrossRef]

47. Kang, S.-W.; Kim, S.-H.; Park, J.-H.; Seo, D.-C.; Ok, Y.S.; Cho, J.-S. Effect of biochar derived from barley straw on soil physico-chemical properties, crop growth, and nitrous oxide emission in an upland field in South Korea. *Environ. Sci. Pollut. Res.* **2018**, *25*, 25813–25821. [CrossRef]

48. Yang, S.; Xiao, Y.n.; Sun, X.; Ding, J.; Jiang, Z.; Xu, J. Biochar improved rice yield and mitigated CH_4 and N_2O emissions from paddy field under controlled irrigation in the Taihu Lake Region of China. *Atmos. Environ.* **2019**, *200*, 69–77. [CrossRef]

49. Yang, W.; Feng, G.; Miles, D.; Gao, L.; Jia, Y.; Li, C.; Qu, Z. Impact of biochar on greenhouse gas emissions and soil carbon sequestration in corn grown under drip irrigation with mulching. *Sci. Total Environ.* **2020**, *729*, 138752. [CrossRef]

50. Duan, M.; Wu, F.; Jia, Z.; Wang, S.; Cai, Y.; Chang, S.X. Wheat straw and its biochar differently affect soil properties and field-based greenhouse gas emission in a Chernozemic soil. *Biol. Fertil. Soils* **2020**, *56*, 1023–1036. [CrossRef]

51. Han, Z.; Lin, H.; Xu, P.; Li, Z.; Wang, J.; Zou, J. Impact of organic fertilizer substitution and biochar amendment on net greenhouse gas budget in a tea plantation. *Agric. Ecosyst. Environ.* **2022**, *326*, 107779. [CrossRef]

52. Hawthorne, I.; Johnson, M.S.; Jassal, R.S.; Black, T.A.; Grant, N.J.; Smukler, S.M. Application of biochar and nitrogen influences fluxes of CO_2, CH_4 and N_2O in a forest soil. *J. Environ. Manag.* **2017**, *192*, 203–214. [CrossRef]

53. Xu, L.; Fang, H.; Deng, X.; Ying, J.; Lv, W.; Shi, Y.; Zhou, G.; Zhou, Y. Biochar application increased ecosystem carbon sequestration capacity in a Moso bamboo forest. *For. Ecol. Manag.* **2020**, *475*, 118447. [CrossRef]

54. Ge, X.; Cao, Y.; Zhou, B.; Xiao, W.; Tian, X.; Li, M.-H. Combined application of biochar and N increased temperature sensitivity of soil respiration but still decreased the soil CO_2 emissions in moso bamboo plantations. *Sci. Total Environ.* **2020**, *730*, 139003. [CrossRef]

55. Li, X.; Yao, S.; Wang, Z.; Jiang, X.; Song, Y.; Chang, S.X. Polyethylene microplastic and biochar interactively affect the global warming potential of soil greenhouse gas emissions. *Environ. Pollut.* **2022**, 120433. [CrossRef] [PubMed]

56. Wang, Q.; Yuan, J.; Yang, X.; Han, X.; Lan, Y.; Cao, D.; Sun, Q.; Cui, X.; Meng, J.; Chen, W. Responses of soil respiration and C sequestration efficiency to biochar amendment in maize field of Northeast China. *Soil Tillage Res.* **2022**, *223*, 105442. [CrossRef]

57. Wang, L.; Gao, C.; Yang, K.; Sheng, Y.; Xu, J.; Zhao, Y.; Lou, J.; Sun, R.; Zhu, L. Effects of biochar aging in the soil on its mechanical property and performance for soil CO_2 and N_2O emissions. *Sci. Total Environ.* **2021**, *782*, 146824. [CrossRef]

58. Song, B.; Almatrafi, E.; Tan, X.; Luo, S.; Xiong, W.; Zhou, C.; Qin, M.; Liu, Y.; Cheng, M.; Zeng, G.; et al. Biochar-based agricultural soil management: An application-dependent strategy for contributing to carbon neutrality. *Renew. Sustain. Energy Rev.* **2022**, *164*, 112529. [CrossRef]

59. Gascó, G.; Paz-Ferreiro, J.; Cely, P.; Plaza, C.; Méndez, A. Influence of pig manure and its biochar on soil CO_2 emissions and soil enzymes. *Ecol. Eng.* **2016**, *95*, 19–24. [CrossRef]

60. Zheng, H.; Liu, D.; Liao, X.; Miao, Y.; Li, Y.; Li, J.; Yuan, J.; Chen, Z.; Ding, W. Field-aged biochar enhances soil organic carbon by increasing recalcitrant organic carbon fractions and making microbial communities more conducive to carbon sequestration. *Agric. Ecosyst. Environ.* **2022**, *340*, 108177. [CrossRef]

61. Lin, X.W.; Xie, Z.B.; Zheng, J.Y.; Liu, Q.; Bei, Q.C.; Zhu, J.G. Effects of biochar application on greenhouse gas emissions, carbon sequestration and crop growth in coastal saline soil. *Eur. J. Soil Sci.* **2015**, *66*, 329–338. [CrossRef]

62. El-Mahrouky, M.; El-Naggar, A.H.; Usman, A.R.; Al-Wabel, M. Dynamics of CO_2 Emission and Biochemical Properties of a Sandy Calcareous Soil Amended with Conocarpus Waste and Biochar. *Pedosphere* **2015**, *25*, 46–56. [CrossRef]

63. Yang, Y.; Sun, K.; Liu, J.; Chen, Y.; Han, L. Changes in soil properties and CO_2 emissions after biochar addition: Role of pyrolysis temperature and aging. *Sci. Total Environ.* **2022**, *839*, 156333. [CrossRef]

64. Van Kessel, C.; Venterea, R.; Six, J.; Adviento-Borbe, M.A.; Linquist, B.; van Groenigen, K.J. Climate, duration, and N placement determine N_2O emissions in reduced tillage systems: A meta-analysis. *Glob. Chang. Biol.* **2013**, *19*, 33–44. [CrossRef]

65. Thompson, R.L.; Lassaletta, L.; Patra, P.K.; Wilson, C.; Wells, K.C.; Gressent, A.; Koffi, E.N.; Chipperfield, M.P.; Winiwarter, W.; Davidson, E.A. Acceleration of global N_2O emissions seen from two decades of atmospheric inversion. *Nat. Clim. Chang.* **2019**, *9*, 993–998. [CrossRef]

66. Tian, H.; Yang, J.; Xu, R.; Lu, C.; Canadell, J.G.; Davidson, E.A.; Jackson, R.B.; Arneth, A.; Chang, J.; Ciais, P. Global soil nitrous oxide emissions since the preindustrial era estimated by an ensemble of terrestrial biosphere models: Magnitude, attribution, and uncertainty. *Glob. Chang. Biol.* **2019**, *25*, 640–659. [CrossRef] [PubMed]

67. Mateo-Marín, N.; Quílez, D.; Guillén, M.; Isla, R. Feasibility of stabilised nitrogen fertilisers decreasing greenhouse gas emissions under optimal management in sprinkler irrigated conditions. *Agric. Ecosyst. Environ.* **2020**, *290*, 106725. [CrossRef]

68. Ge, J.; Huang, G.; Huang, J.; Zeng, J.; Han, L. Particle-scale modeling of methane emission during pig manure/wheat straw aerobic composting. *Environ. Sci. Technol.* **2016**, *50*, 4374–4383. [CrossRef] [PubMed]

69. Wang, C.; Lu, H.; Dong, D.; Deng, H.; Strong, P.J.; Wang, H.; Wu, W. Insight into the effects of biochar on manure composting: Evidence supporting the relationship between N_2O emission and denitrifying community. *Environ. Sci. Technol.* **2013**, *47*, 7341–7349. [CrossRef]

70. Song, Y.; Li, Y.; Cai, Y.; Fu, S.; Luo, Y.; Wang, H.; Liang, C.; Lin, Z.; Hu, S.; Li, Y.; et al. Biochar decreases soil N_2O emissions in Moso bamboo plantations through decreasing labile N concentrations, N-cycling enzyme activities and nitrification/denitrification rates. *Geoderma* **2019**, *348*, 135–145. [CrossRef]

71. Ji, C.; Han, Z.; Zheng, F.; Wu, S.; Wang, J.; Wang, J.; Zhang, H.; Zhang, Y.; Liu, S.; Li, S.; et al. Biochar reduced soil nitrous oxide emissions through suppressing fungal denitrification and affecting fungal community assembly in a subtropical tea plantation. *Agric. Ecosyst. Environ.* **2022**, *326*, 107784. [CrossRef]

72. Tang, Z.; Liu, X.; Li, G.; Liu, X. Mechanism of biochar on nitrification and denitrification to N_2O emissions based on isotope characteristic values. *Environ. Res.* **2022**, *212*, 113219. [CrossRef]

73. Zhong, L.; Li, G.; Qing, J.; Li, J.; Xue, J.; Yan, B.; Chen, G.; Kang, X.; Rui, Y. Biochar can reduce N_2O production potential from rhizosphere of fertilized agricultural soils by suppressing bacterial denitrification. *Eur. J. Soil Biol.* **2022**, *109*, 103391. [CrossRef]

74. Yang, X.; Sun, Q.; Yuan, J.; Fu, S.; Lan, Y.; Jiang, X.; Meng, J.; Han, X.; Chen, W. Successive corn stover and biochar applications mitigate N_2O emissions by altering soil physicochemical properties and N-cycling-related enzyme activities: A five-year field study in Northeast China. *Agric. Ecosyst. Environ.* **2022**, *340*, 108183. [CrossRef]

75. Kalu, S.; Simojoki, A.; Karhu, K.; Tammeorg, P. Long-term effects of softwood biochar on soil physical properties, greenhouse gas emissions and crop nutrient uptake in two contrasting boreal soils. *Agric. Ecosyst. Environ.* **2021**, *316*, 107454. [CrossRef]

76. Liao, X.; Mao, S.; Chen, Y.; Zhang, J.; Müller, C.; Malghani, S. Combined effects of biochar and biogas slurry on soil nitrogen transformation rates and N_2O emission in a subtropical poplar plantation. *Sci. Total Environ.* **2022**, *848*, 157766. [CrossRef] [PubMed]

77. Pokharel, P.; Qi, L.; Chang, S.X. Manure-based biochar decreases heterotrophic respiration and increases gross nitrification rates in rhizosphere soil. *Soil Biol. Biochem.* **2021**, *154*, 108147. [CrossRef]

78. Liao, X.; Liu, D.; Niu, Y.; Chen, Z.; He, T.; Ding, W. Effect of field-aged biochar on fertilizer N retention and N_2O emissions: A field microplot experiment with 15N-labeled urea. *Sci. Total Environ.* **2021**, *773*, 145645. [CrossRef] [PubMed]

79. Cai, Y.; Akiyama, H. Effects of inhibitors and biochar on nitrous oxide emissions, nitrate leaching, and plant nitrogen uptake from urine patches of grazing animals on grasslands: A meta-analysis. *Soil Sci. Plant Nutr.* **2017**, *63*, 405–414. [CrossRef]

80. Lan, Z.M.; Chen, C.R.; Rezaei Rashti, M.; Yang, H.; Zhang, D.K. Linking feedstock and application rate of biochars to N_2O emission in a sandy loam soil: Potential mechanisms. *Geoderma* **2019**, *337*, 880–892. [CrossRef]

81. Ameloot, N.; De Neve, S.; Jegajeevagan, K.; Yildiz, G.; Buchan, D.; Funkuin, Y.N.; Prins, W.; Bouckaert, L.; Sleutel, S. Short-term CO_2 and N_2O emissions and microbial properties of biochar amended sandy loam soils. *Soil Biol. Biochem.* **2013**, *57*, 401–410. [CrossRef]

82. Zhang, X.; Zhang, J.; Song, M.; Dong, Y.; Xiong, Z. N_2O and NO production and functional microbes responding to biochar aging process in an intensified vegetable soil. *Environ. Pollut.* **2022**, *307*, 119491. [CrossRef]

83. Bernstein, L.; Bosch, P.; Canziani, O.; Chen, Z.; Christ, R.; Riahi, K. *IPCC, 2007: Climate Change 2007: Synthesis Report*; IPCC: Geneva, Switzerland, 2008.

84. Wang, C.; Shen, J.; Liu, J.; Qin, H.; Yuan, Q.; Fan, F.; Hu, Y.; Wang, J.; Wei, W.; Li, Y.; et al. Microbial mechanisms in the reduction of CH_4 emission from double rice cropping system amended by biochar: A four-year study. *Soil Biol. Biochem.* **2019**, *135*, 251–263. [CrossRef]

85. Sun, B.; Bai, Z.; Li, Y.; Li, R.; Song, M.; Xu, S.; Zhang, H.; Zhuang, X. Emission mitigation of CH_4 and N_2O during semi-permeable membrane covered hyperthermophilic aerobic composting of livestock manure. *J. Clean. Prod.* **2022**, *379*, 134850. [CrossRef]

86. Solomon, S.; Qin, D.; Manning, M.; Averyt, K.; Marquis, M. *Climate Change 2007-the Physical Science Basis: Working Group I Contribution to the Fourth Assessment Report of the IPCC*; Cambridge University Press: Cambridge, UK, 2007; Volume 4.

87. Zhang, A.; Bian, R.; Pan, G.; Cui, L.; Hussain, Q.; Li, L.; Zheng, J.; Zheng, J.; Zhang, X.; Han, X. Effects of biochar amendment on soil quality, crop yield and greenhouse gas emission in a Chinese rice paddy: A field study of 2 consecutive rice growing cycles. *Field Crops Res.* **2012**, *127*, 153–160. [CrossRef]

88. Lin, X.; Wang, N.; Li, F.; Yan, B.; Pan, J.; Jiang, S.; Peng, H.; Chen, A.; Wu, G.; Zhang, J.; et al. Evaluation of the synergistic effects of biochar and biogas residue on CO_2 and CH_4 emission, functional genes, and enzyme activity during straw composting. *Bioresour. Technol.* **2022**, *360*, 127608. [CrossRef] [PubMed]

89. Sriphirom, P.; Towprayoon, S.; Yagi, K.; Rossopa, B.; Chidthaisong, A. Changes in methane production and oxidation in rice paddy soils induced by biochar addition. *Appl. Soil Ecol.* **2022**, *179*, 104585. [CrossRef]

90. Kim, J.; Yoo, G.; Kim, D.; Ding, W.; Kang, H. Combined application of biochar and slow-release fertilizer reduces methane emission but enhances rice yield by different mechanisms. *Appl. Soil Ecol.* **2017**, *117–118*, 57–62. [CrossRef]

91. Ji, B.; Chen, J.; Li, W.; Mei, J.; Yang, Y.; Chang, J. Greenhouse gas emissions from constructed wetlands are mitigated by biochar substrates and distinctly affected by tidal flow and intermittent aeration modes. *Environ. Pollut.* **2021**, *271*, 116328. [CrossRef]

92. Wang, N.; Chang, Z.-Z.; Xue, X.-M.; Yu, J.-G.; Shi, X.-X.; Ma, L.Q.; Li, H.-B. Biochar decreases nitrogen oxide and enhances methane emissions via altering microbial community composition of anaerobic paddy soil. *Sci. Total Environ.* **2017**, *581*, 689–696. [CrossRef]

93. Liu, Y.; Yang, M.; Wu, Y.; Wang, H.; Chen, Y.; Wu, W. Reducing CH_4 and CO_2 emissions from waterlogged paddy soil with biochar. *J. Soils Sediments* **2011**, *11*, 930–939. [CrossRef]

94. Joseph, S.; Graber, E.R.; Chia, C.; Munroe, P.; Donne, S.; Thomas, T.; Nielsen, S.; Marjo, C.; Rutlidge, H.; Pan, G.-X. Shifting paradigms: Development of high-efficiency biochar fertilizers based on nano-structures and soluble components. *Carbon Manag.* **2013**, *4*, 323–343. [CrossRef]

95. Nan, Q.; Wang, C.; Yi, Q.; Zhang, L.; Ping, F.; Thies, J.E.; Wu, W. Biochar amendment pyrolysed with rice straw increases rice production and mitigates methane emission over successive three years. *Waste Manag.* **2020**, *118*, 1–8. [CrossRef]

96. Wang, C.; Liu, J.; Shen, J.; Chen, D.; Li, Y.; Jiang, B.; Wu, J. Effects of biochar amendment on net greenhouse gas emissions and soil fertility in a double rice cropping system: A 4-year field experiment. *Agric. Ecosyst. Environ.* **2018**, *262*, 83–96. [CrossRef]

97. Qi, L.; Pokharel, P.; Chang, S.X.; Zhou, P.; Niu, H.; He, X.; Wang, Z.; Gao, M. Biochar application increased methane emission, soil carbon storage and net ecosystem carbon budget in a 2-year vegetable–rice rotation. *Agric. Ecosyst. Environ.* **2020**, *292*, 106831. [CrossRef]

98. Liu, F.; Ji, M.; Xiao, L.; Wang, X.; Diao, Y.; Dan, Y.; Wang, H.; Sang, W.; Zhang, Y. Organics composition and microbial analysis reveal the different roles of biochar and hydrochar in affecting methane oxidation from paddy soil. *Sci. Total Environ.* **2022**, *843*, 157036. [CrossRef] [PubMed]

99. Lee, S.-I.; Park, H.-J.; Jeong, Y.-J.; Seo, B.-S.; Kwak, J.-H.; Yang, H.I.; Xu, X.; Tang, S.; Cheng, W.; Lim, S.-S.; et al. Biochar-induced reduction of N_2O emission from East Asian soils under aerobic conditions: Review and data analysis. *Environ. Pollut.* **2021**, *291*, 118154. [CrossRef] [PubMed]

100. Nguyen, T.T.N.; Xu, C.-Y.; Tahmasbian, I.; Che, R.; Xu, Z.; Zhou, X.; Wallace, H.M.; Bai, S.H. Effects of biochar on soil available inorganic nitrogen: A review and meta-analysis. *Geoderma* **2017**, *288*, 79–96. [CrossRef]

101. Domingues, R.R.; Trugilho, P.F.; Silva, C.A.; Melo, I.C.N.A.d.; Melo, L.C.A.; Magriotis, Z.M.; Sanchez-Monedero, M.A. Properties of biochar derived from wood and high-nutrient biomasses with the aim of agronomic and environmental benefits. *PLoS ONE* **2017**, *12*, e0176884. [CrossRef]

102. Lin, Z.; Liu, Q.; Liu, G.; Cowie, A.L.; Bei, Q.; Liu, B.; Wang, X.; Ma, J.; Zhu, J.; Xie, Z. Effects of Different Biochars on Pinus elliottii Growth, N Use Efficiency, Soil N_2O and CH_4 Emissions and C Storage in a Subtropical Area of China. *Pedosphere* **2017**, *27*, 248–261. [CrossRef]

103. Rittl, T.F.; Butterbach-Bahl, K.; Basile, C.M.; Pereira, L.A.; Alms, V.; Dannenmann, M.; Couto, E.G.; Cerri, C.E.P. Greenhouse gas emissions from soil amended with agricultural residue biochars: Effects of feedstock type, production temperature and soil moisture. *Biomass Bioenergy* **2018**, *117*, 1–9. [CrossRef]

104. Al-Rumaihi, A.; Shahbaz, M.; McKay, G.; Mackey, H.; Al-Ansari, T. A review of pyrolysis technologies and feedstock: A blending approach for plastic and biomass towards optimum biochar yield. *Renew. Sustain. Energy Rev.* **2022**, *167*, 112715. [CrossRef]

105. Amenaghawon, A.N.; Anyalewechi, C.L.; Okieimen, C.O.; Kusuma, H.S. Biomass pyrolysis technologies for value-added products: A state-of-the-art review. *Environ. Dev. Sustain.* **2021**, *23*, 14324–14378. [CrossRef]

106. Yang, W.; Shang, J.; Sharma, P.; Li, B.; Liu, K.; Flury, M. Colloidal stability and aggregation kinetics of biochar colloids: Effects of pyrolysis temperature, cation type, and humic acid concentrations. *Sci. Total Environ.* **2019**, *658*, 1306–1315. [CrossRef] [PubMed]

107. Nguyen, D.H.; Scheer, C.; Rowlings, D.W.; Grace, P.R. Rice husk biochar and crop residue amendment in subtropical cropping soils: Effect on biomass production, nitrogen use efficiency and greenhouse gas emissions. *Biol. Fertil. Soils* **2016**, *52*, 261–270. [CrossRef]

108. Zhao, T.; Yao, Y.; Li, D.; Wu, F.; Zhang, C.; Gao, B. Facile low-temperature one-step synthesis of pomelo peel biochar under air atmosphere and its adsorption behaviors for Ag (I) and Pb (II). *Sci. Total Environ.* **2018**, *640*, 73–79. [CrossRef] [PubMed]

109. Lewandowski, W.M.; Januszewicz, K.; Kosakowski, W. Efficiency and proportions of waste tyre pyrolysis products depending on the reactor type—A review. *J. Anal. Appl. Pyrolysis* **2019**, *140*, 25–53. [CrossRef]

110. Zhang, Q.; Xiao, J.; Xue, J.; Zhang, L. Quantifying the effects of biochar application on greenhouse gas emissions from agricultural soils: A global meta-analysis. *Sustainability* **2020**, *12*, 3436. [CrossRef]

111. McBeath, A.V.; Smernik, R.J.; Krull, E.S.; Lehmann, J. The influence of feedstock and production temperature on biochar carbon chemistry: A solid-state 13C NMR study. *Biomass Bioenergy* **2014**, *60*, 121–129. [CrossRef]

112. Shaheen, S.M.; Mosa, A.; Abdelrahman, H.; Niazi, N.K.; Antoniadis, V.; Shahid, M.; Song, H.; Kwon, E.E.; Rinklebe, J. Removal of toxic elements from aqueous environments using nano zero-valent iron-and iron oxide-modified biochar: A review. *Biochar* **2022**, *4*, 1–21. [CrossRef]

113. Deng, B.; Shi, Y.; Zhang, L.; Fang, H.; Gao, Y.; Luo, L.; Feng, W.; Hu, X.; Wan, S.; Huang, W.; et al. Effects of spent mushroom substrate-derived biochar on soil CO_2 and N_2O emissions depend on pyrolysis temperature. *Chemosphere* **2020**, *246*, 125608. [CrossRef]

114. Wang, Z.; Zheng, H.; Luo, Y.; Deng, X.; Herbert, S.; Xing, B. Characterization and influence of biochars on nitrous oxide emission from agricultural soil. *Environ. Pollut.* **2013**, *174*, 289–296. [CrossRef]

115. Mukome, F.N.D.; Six, J.; Parikh, S.J. The effects of walnut shell and wood feedstock biochar amendments on greenhouse gas emissions from a fertile soil. *Geoderma* **2013**, *200–201*, 90–98. [CrossRef]

116. Nan, Q.; Xin, L.; Qin, Y.; Waqas, M.; Wu, W. Exploring long-term effects of biochar on mitigating methane emissions from paddy soil: A review. *Biochar* **2021**, *3*, 125–134. [CrossRef]

117. Chiappero, M.; Norouzi, O.; Hu, M.; Demichelis, F.; Berruti, F.; di Maria, F.; Mašek, O.; Fiore, S. Review of biochar role as additive in anaerobic digestion processes. *Renew. Sustain. Energy Rev.* **2020**, *131*, 110037. [CrossRef]

118. Cai, F.; Feng, Z.; Zhu, L. Effects of biochar on CH_4 emission with straw application on paddy soil. *J. Soils Sediments* **2018**, *18*, 599–609. [CrossRef]

119. Husk, B.; Major, J. Commercial Scale Agricultural Biochar Field Trial in Québec, Canada over Two Years: Effects of Biochar on Soil Fertility, Biology and Crop Productivity and Quality. 2010. Available online: http://www.blue-leaf.ca/main-en/report_a3.php (accessed on 3 March 2011).

120. Rahman, M.A.; Jahiruddin, M.; Kader, M.A.; Islam, M.R.; Solaiman, Z.M. Sugarcane bagasse biochar increases soil carbon sequestration and yields of maize and groundnut in charland ecosystem. *Arch. Agron. Soil Sci.* **2022**, *68*, 1338–1351. [CrossRef]

121. Novak, J.M.; Ippolito, J.A.; Watts, D.W.; Sigua, G.C.; Ducey, T.F.; Johnson, M.G. Biochar compost blends facilitate switchgrass growth in mine soils by reducing Cd and Zn bioavailability. *Biochar* **2019**, *1*, 97–114. [CrossRef] [PubMed]

122. An, X.; Wu, Z.; Shi, W.; Qi, H.; Zhang, L.; Xu, X.; Yu, B. Biochar for simultaneously enhancing the slow-release performance of fertilizers and minimizing the pollution of pesticides. *J. Hazard. Mater.* **2021**, *407*, 124865. [CrossRef] [PubMed]

123. Zimmerman, A.R.; Gao, B.; Ahn, M.-Y. Positive and negative carbon mineralization priming effects among a variety of biochar-amended soils. *Soil Biol. Biochem.* **2011**, *43*, 1169–1179. [CrossRef]

124. Van Zwieten, L.; Singh, B.P.; Tavakkoli, E.; Joseph, S.; Macdonald, L.M.; Rose, T.J.; Rose, M.T.; Kimber, S.W.L.; Morris, S.; Cozzolino, D. Biochar built soil carbon over a decade by stabilizing rhizodeposits. *Nat. Clim. Chang.* **2017**, *7*, 371–376.

125. Olaniyan, J.O.; Isimikalu, T.O.; Raji, B.A.; Affinnih, K.O.; Alasinrin, S.Y.; Ajala, O.N. An investigation of the effect of biochar application rates on CO_2 emissions in soils under upland rice production in southern Guinea Savannah of Nigeria. *Heliyon* **2020**, *6*, e05578. [CrossRef]

126. Ge, X.; Cao, Y.; Zhou, B.; Wang, X.; Yang, Z.; Li, M.-H. Biochar addition increases subsurface soil microbial biomass but has limited effects on soil CO_2 emissions in subtropical moso bamboo plantations. *Appl. Soil Ecol.* **2019**, *142*, 155–165. [CrossRef]

127. Lu, X.; Li, Y.; Wang, H.; Singh, B.P.; Hu, S.; Luo, Y.; Li, J.; Xiao, Y.; Cai, X.; Li, Y. Responses of soil greenhouse gas emissions to different application rates of biochar in a subtropical Chinese chestnut plantation. *Agric. For. Meteorol.* **2019**, *271*, 168–179. [CrossRef]

128. Walkiewicz, A.; Kalinichenko, K.; Kubaczyński, A.; Brzezińska, M.; Bieganowski, A. Usage of biochar for mitigation of CO_2 emission and enhancement of CH_4 consumption in forest and orchard Haplic Luvisol (Siltic) soils. *Appl. Soil Ecol.* **2020**, *156*, 103711. [CrossRef]

129. Shen, Y.; Zhu, L.; Cheng, H.; Yue, S.; Li, S. Effects of biochar application on CO_2 emissions from a cultivated soil under semiarid climate conditions in Northwest China. *Sustainability* **2017**, *9*, 1482. [CrossRef]

130. Oo, A.Z.; Sudo, S.; Win, K.T.; Shibata, A.; Gonai, T. Influence of pruning waste biochar and oyster shell on N_2O and CO_2 emissions from Japanese pear orchard soil. *Heliyon* **2018**, *4*, e00568. [CrossRef] [PubMed]

131. Mosa, A.A.; Taha, A.; Elsaeid, M. Agro-environmental applications of humic substances: A critical review. *Egypt. J. Soil Sci.* **2020**, *60*, 211–229. [CrossRef]

132. Chen, H.; Awasthi, S.K.; Liu, T.; Duan, Y.; Ren, X.; Zhang, Z.; Pandey, A.; Awasthi, M.K. Effects of microbial culture and chicken manure biochar on compost maturity and greenhouse gas emissions during chicken manure composting. *J. Hazard. Mater.* **2020**, *389*, 121908. [CrossRef]

133. Millennium Ecosystem Assessment. *Synthesis Report*; Millennium Ecosystem Assessment: Washington, DC, USA, 2005.

134. Mahapatra, S.; Ali, M.H.; Samal, K. Assessment of compost maturity-stability indices and recent development of composting bin. *Energy Nexus* **2022**, *6*, 100062. [CrossRef]

135. Chung, W.J.; Chang, S.W.; Chaudhary, D.K.; Shin, J.; Kim, H.; Karmegam, N.; Govarthanan, M.; Chandrasekaran, M.; Ravindran, B. Effect of biochar amendment on compost quality, gaseous emissions and pathogen reduction during in-vessel composting of chicken manure. *Chemosphere* **2021**, *283*, 131129. [CrossRef]

136. Zhang, L.; Sun, X. Changes in physical, chemical, and microbiological properties during the two-stage co-composting of green waste with spent mushroom compost and biochar. *Bioresour. Technol.* **2014**, *171*, 274–284. [CrossRef]

137. Li, S.; Song, L.; Jin, Y.; Liu, S.; Shen, Q.; Zou, J. Linking N_2O emission from biochar-amended composting process to the abundance of denitrify (nirK and nosZ) bacteria community. *AMB Express* **2016**, *6*, 1–9. [CrossRef]

138. Guo, H.; Gu, J.; Wang, X.; Yu, J.; Nasir, M.; Zhang, K.; Sun, W. Microbial driven reduction of N_2O and NH_3 emissions during composting: Effects of bamboo charcoal and bamboo vinegar. *J. Hazard. Mater.* **2020**, *390*, 121292. [CrossRef]

139. Wang, X.; Liu, X.; Wang, Z.; Sun, G.; Li, J. Greenhouse gas reduction and nitrogen conservation during manure composting by combining biochar with wood vinegar. *J. Environ. Manag.* **2022**, *324*, 116349. [CrossRef] [PubMed]

140. Awasthi, M.K.; Duan, Y.; Awasthi, S.K.; Liu, T.; Zhang, Z. Influence of bamboo biochar on mitigating greenhouse gas emissions and nitrogen loss during poultry manure composting. *Bioresour. Technol.* **2020**, *303*, 122952. [CrossRef] [PubMed]

141. Ghorbani, M.; Konvalina, P.; Walkiewicz, A.; Neugschwandtner, R.W.; Kopecký, M.; Zamanian, K.; Chen, W.-H.; Bucur, D. Feasibility of Biochar Derived from Sewage Sludge to Promote Sustainable Agriculture and Mitigate GHG Emissions—A Review. *Int. J. Environ. Res. Public Health* **2022**, *19*, 12983. [CrossRef] [PubMed]

142. Jiang, J.; Kang, K.; Wang, C.; Sun, X.; Dang, S.; Wang, N.; Wang, Y.; Zhang, C.; Yan, G.; Li, Y. Evaluation of total greenhouse gas emissions during sewage sludge composting by the different dicyandiamide added forms: Mixing, surface broadcasting, and their combination. *Waste Manag.* **2018**, *81*, 94–103. [CrossRef]

143. Awasthi, M.K.; Wang, M.; Chen, H.; Wang, Q.; Zhao, J.; Ren, X.; Li, D.-s.; Awasthi, S.K.; Shen, F.; Li, R. Heterogeneity of biochar amendment to improve the carbon and nitrogen sequestration through reduce the greenhouse gases emissions during sewage sludge composting. *Bioresour. Technol.* **2017**, *224*, 428–438. [CrossRef] [PubMed]

144. Xue, S.; Zhou, L.; Zhong, M.; Kumar Awasthi, M.; Mao, H. Bacterial agents affected bacterial community structure to mitigate greenhouse gas emissions during sewage sludge composting. *Bioresour. Technol.* **2021**, *337*, 125397. [CrossRef] [PubMed]

145. Lv, B.; Cui, Y.; Wei, H.; Chen, Q.; Zhang, D. Elucidating the role of earthworms in N_2O emission and production pathway during vermicomposting of sewage sludge and rice straw. *J. Hazard. Mater.* **2020**, *400*, 123215. [CrossRef]

146. Wu, D.; Feng, Y.; Xue, L.; Liu, M.; Yang, B.; Hu, F.; Yang, L. Biochar Combined with Vermicompost Increases Crop Production While Reducing Ammonia and Nitrous Oxide Emissions from a Paddy Soil. *Pedosphere* **2019**, *29*, 82–94. [CrossRef]

147. Romero, C.M.; Redman, A.-A.P.H.; Owens, J.; Terry, S.A.; Ribeiro, G.O.; Gorzelak, M.A.; Oldenburg, T.B.P.; Hazendonk, P.; Larney, F.J.; Hao, X.; et al. Effects of feeding a pine-based biochar to beef cattle on subsequent manure nutrients, organic matter composition and greenhouse gas emissions. *Sci. Total Environ.* **2022**, *812*, 152267. [CrossRef]

148. Chowdhury, M.A.; de Neergaard, A.; Jensen, L.S. Potential of aeration flow rate and bio-char addition to reduce greenhouse gas and ammonia emissions during manure composting. *Chemosphere* **2014**, *97*, 16–25. [CrossRef]

149. Malińska, K.; Zabochnicka-Świątek, M.; Dach, J. Effects of biochar amendment on ammonia emission during composting of sewage sludge. *Ecol. Eng.* **2014**, *71*, 474–478. [CrossRef]

150. Vandecasteele, B.; Sinicco, T.; D'Hose, T.; Nest, T.V.; Mondini, C. Biochar amendment before or after composting affects compost quality and N losses, but not P plant uptake. *J. Environ. Manag.* **2016**, *168*, 200–209. [CrossRef] [PubMed]

151. Agyarko-Mintah, E.; Cowie, A.; Singh, B.P.; Joseph, S.; van Zwieten, L.; Cowie, A.; Harden, S.; Smillie, R. Biochar increases nitrogen retention and lowers greenhouse gas emissions when added to composting poultry litter. *Waste Manag.* **2017**, *61*, 138–149. [CrossRef] [PubMed]

152. Mao, H.; Lv, Z.; Sun, H.; Li, R.; Zhai, B.; Wang, Z.; Awasthi, M.K.; Wang, Q.; Zhou, L. Improvement of biochar and bacterial powder addition on gaseous emission and bacterial community in pig manure compost. *Bioresour. Technol.* **2018**, *258*, 195–202. [CrossRef] [PubMed]

153. Zhang, H.; Marchant-Forde, J.N.; Zhang, X.; Wang, Y. Effect of cornstalk biochar immobilized bacteria on ammonia reduction in laying hen manure composting. *Molecules* **2020**, *25*, 1560. [CrossRef]

154. Wang, Y.; Akdeniz, N.; Yi, S. Biochar-amended poultry mortality composting to increase compost temperatures, reduce ammonia emissions, and decrease leachate's chemical oxygen demand. *Agric. Ecosyst. Environ.* **2021**, *315*, 107451. [CrossRef]

155. El-Naggar, A.; Ahmed, N.; Mosa, A.; Niazi, N.K.; Yousaf, B.; Sharma, A.; Sarkar, B.; Cai, Y.; Chang, S.X. Nickel in soil and water: Sources, biogeochemistry, and remediation using biochar. *J. Hazard. Mater.* **2021**, *419*, 126421. [CrossRef]

156. Ghorbani, M.; Konvalina, P.; Kopecký, M.; Kolář, L. A meta-analysis on the impacts of different oxidation methods on the surface area properties of biochar. *Land Degrad. Dev.* **2022**. [CrossRef]

157. Liu, W.-J.; Jiang, H.; Yu, H.-Q. Development of biochar-based functional materials: Toward a sustainable platform carbon material. *Chem. Rev.* **2015**, *115*, 12251–12285. [CrossRef]

158. Zhang, X.; Zhang, S.; Yang, H.; Feng, Y.; Chen, Y.; Wang, X.; Chen, H. Nitrogen enriched biochar modified by high temperature CO_2–ammonia treatment: Characterization and adsorption of CO_2. *Chem. Eng. J.* **2014**, *257*, 20–27. [CrossRef]

159. Lian, F.; Cui, G.; Liu, Z.; Duo, L.; Zhang, G.; Xing, B. One-step synthesis of a novel N-doped microporous biochar derived from crop straws with high dye adsorption capacity. *J. Environ. Manag.* **2016**, *176*, 61–68. [CrossRef] [PubMed]

160. Zhang, X.; Wu, J.; Yang, H.; Shao, J.; Wang, X.; Chen, Y.; Zhang, S.; Chen, H. Preparation of nitrogen-doped microporous modified biochar by high temperature CO_2–NH_3 treatment for CO_2 adsorption: Effects of temperature. *RSC Adv.* **2016**, *6*, 98157–98166. [CrossRef]

161. Xing, W.; Liu, C.; Zhou, Z.; Zhang, L.; Zhou, J.; Zhuo, S.; Yan, Z.; Gao, H.; Wang, G.; Qiao, S.Z. Superior CO_2 uptake of N-doped activated carbon through hydrogen-bonding interaction. *Energy Environ. Sci.* **2012**, *5*, 7323–7327. [CrossRef]

162. Ma, X.; Li, L.; Wang, S.; Lu, M.; Li, H.; Ma, W.; Keener, T.C. Ammonia-treated porous carbon derived from ZIF-8 for enhanced CO_2 adsorption. *Appl. Surf. Sci.* **2016**, *369*, 390–397. [CrossRef]

163. Zhang, C.; Sun, S.; Xu, S.; Wu, C. CO_2 capture over steam and KOH activated biochar: Effect of relative humidity. *Biomass Bioenergy* **2022**, *166*, 106608. [CrossRef]

164. Kaya, N.; Uzun, Z.Y. Investigation of effectiveness of pine cone biochar activated with KOH for methyl orange adsorption and CO_2 capture. *Biomass Convers. Biorefinery* **2021**, *11*, 1067–1083. [CrossRef]

165. Li, K.; Zhang, D.; Niu, X.; Guo, H.; Yu, Y.; Tang, Z.; Lin, Z.; Fu, M. Insights into CO_2 adsorption on KOH-activated biochars derived from the mixed sewage sludge and pine sawdust. *Sci. Total Environ.* **2022**, *826*, 154133. [CrossRef]

166. Shin, J.; Park, D.; Hong, S.; Jeong, C.; Kim, H.; Chung, W. Influence of activated biochar pellet fertilizer application on greenhouse gas emissions and carbon sequestration in rice (*Oryza sativa* L.) production. *Environ. Pollut.* **2021**, *285*, 117457. [CrossRef]

167. Liu, Z.; Tang, J.; Ren, X.; Schaeffer, S.M. Effects of phosphorus modified nZVI-biochar composite on emission of greenhouse gases and changes of microbial community in soil. *Environ. Pollut.* **2021**, *274*, 116483. [CrossRef]

168. Khan, M.N.; Li, D.; Shah, A.; Huang, J.; Zhang, L.; Núñez-Delgado, A.; Han, T.; Du, J.; Ali, S.; Sial, T.A.; et al. The impact of pristine and modified rice straw biochar on the emission of greenhouse gases from a red acidic soil. *Environ. Res.* **2022**, *208*, 112676. [CrossRef]

169. Yang, X.; Wang, W.; Chen, X.; Sardans, J.; Wang, C.; Vancov, T.; Fang, Y.; Wang, S.; Yuan, X.; Llusià, J.; et al. Effects of N-enriched biochar on ecosystem greenhouse gas emissions, rice yield, and bacterial community diversity in subtropical rice paddy soils. *Eur. J. Soil Biol.* **2022**, *113*, 103440. [CrossRef]

170. Kong, F.; Wang, J.; Hou, W.; Cui, Y.; Yu, L.; Zhang, Y.; Wang, S. Influence of modified biochar supported sulfidation of nano-zero-valent-iron (S-nZVI/BC) on nitrate removal and greenhouse gas emission in constructed wetland. *J. Environ. Sci.* **2023**, *125*, 568–581. [CrossRef] [PubMed]

171. Gao, Y.; Wang, B.; Luo, L.; Deng, B.; Shad, N.; Hu, D.; Aly, H.M.; Zhang, L. Effects of hydroxyapatite and modified biochar derived from Camellia oleifera fruit shell on soil Cd contamination and N_2O emissions. *Ind. Crops Prod.* **2022**, *177*, 114476. [CrossRef]

172. Mohammadi, A.; Cowie, A.; Mai, T.L.A.; de la Rosa, R.A.; Brandao, M.; Kristiansen, P.; Joseph, S. Quantifying the greenhouse gas reduction benefits of utilising straw biochar and enriched biochar. *Energy Procedia* **2016**, *97*, 254–261. [CrossRef]

Article

Cogeneration Systems Performance Analysis as a Sustainable Clean Energy and Water Source Based on Energy Hubs Using the Archimedes Optimization Algorithm

Magda I. El-Afifi [1,2], **Magdi M. Saadawi** [1] and **Abdelfattah A. Eladl** [1,*]

1   Electrical Engineering Department, Faculty of Engineering, Mansoura University, Mansoura 35516, Egypt
2   Nile Higher Institute of Engineering and Technology, Mansoura 35511, Egypt
*   Correspondence: eladle7@mans.edu.eg

Abstract: Different energy requirements of the residential sector are varied, such as electricity, heating, cooling, water, etc., and these necessities are met by multi-energy systems using various energy sources and converters. In this paper, an optimal day-ahead operation of a large residential demand sector is presented based on the energy hub (EH) model with combined heat and power (CHP) as a cogeneration system. The purpose of the optimization is to maximize social welfare (SW) and minimize environmental emissions subjected to numerous technical constraints. To explore the effectiveness of the proposed model, real cases were studied and results were analyzed. Moreover, to evaluate the efficiency of the proposed methodology, the Archimedes optimization algorithm (AOA) is implemented for optimizing the EH system. The performance of the AOA is compared with the genetic algorithm, and the results depict that the AOA is better in terms of convergence speed and global search ability. Implementation of the proposed framework shows that the total SW is increased by 27.44% and environmental emissions are reduced by 18.36% compared to the base case without the EH. Additionally, there is 512.26 MWh and 149.4 m^3 as a surplus in the electricity and water that are sold to every network, respectively.

Keywords: energy hub; cogeneration systems; Archimedes optimization algorithm; sustainable; emissions; water management

1. Introduction

Currently, urban areas comprise more than half of the world's population, and this number is expected to increase to nearly 5 billion by 2030 [1]. The increase in the world population has prompted researchers to conduct more studies on energy. To achieve this conclusion, researchers face serious economic and public issues that include the development of low carbon, pollution reduction, energy efficiency, shared energy supply, fresh water supply, and more. Figure 1 summarizes the percentage increase in world water withdrawals and consumption, population, and carbon dioxide emissions from 1900 to 2040 [2]. It can be seen that carbon dioxide emissions are predicted to reach a significant amount by 2040. Moreover, water withdrawal and consumption have also increased by more than 1000% [2]. On the other hand, the world was shocked in late December 2019 by the sudden outbreak of COVID-19, which impeded progress toward sustainable energy [3] and caused many major damages to the global economy [4]. As these circumstances persist, post-COVID-19 energy planning should be factored into an appropriate level of investment cost as the global economy continues to recover.
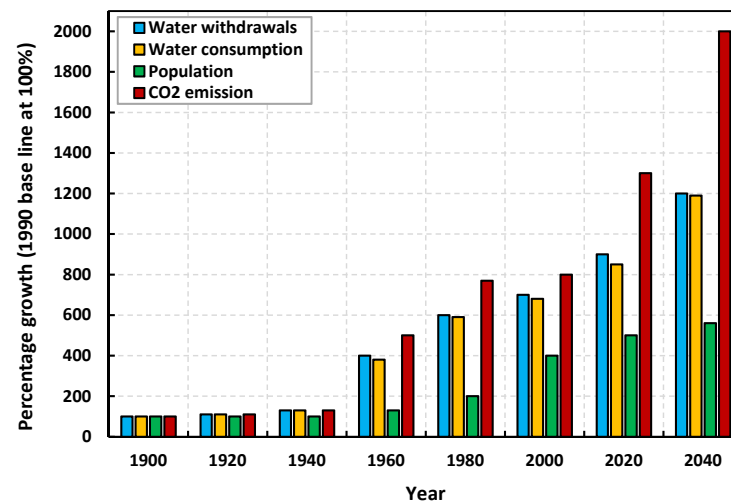
Figure 1. Water, population and CO_2 emission percentage growth rate from 1900 to 2040 (1900 baseline at 100%) [2].

One such suitable candidate is a cogeneration or combined heat and power (CHP) system. The operation mechanism of the CHP units depends on the generation of electricity and heat simultaneously, which increases its efficiency by 80–90%, compared to the traditional stand-alone generation, which has a typical efficiency of 35–55% [5]. Approximately 10–15% of the power transmission losses in the network can be eliminated by using CHP generators [6]. Applying the CHP units reduces overall energy production costs and greenhouse gas emissions because they use less fuel. Many energy systems are integrated through the CHP units such as electricity, gas, and heating systems, which are known as multi-energy systems. An energy hub (EH) concept is introduced for multi-energy systems modeling.

Nowadays, several works of literature have been presented investigating the scheduling of EH. Some different work has been carried out recently on EH planning in the stochastic situation. A new energy management technique for sustainable urban energy systems through EH is presented in [7]. This technique consists of two levels of integrated system modeling based mainly on CHP and renewable energy sources (RESs) but without taking into account these resources' uncertainty. Residential, commercial, and industrial hubs with similar internal configurations and equipment are proposed in [8]. CHP is a major component of these hubs to feed both electrical and thermal requirements. Work in [9] investigated the optimal scheduling of an EH integrated with CHP and solar energy for two days considering uncertainties via various scenarios. In [10], a technical economic evaluation of EH based on CHP for a medical complex was presented. In this work, an improvement of EH model efficiency and the economic benefits of using CHP were discussed. The risk-constrained probabilistic schedule of an integrated EH with a CHP module has been optimized considering the demand-side resources of a multi-objective model in [11]. Additionally, a multi-objective scheduling model for a small network based on CHP with the integration of an energy storage system (ESS) was presented in [12]. In [13], the optimum size of the EH system was presented using a mid-size CHP unit, where the reliability of supply was evaluated. A robust operating model for an EH with multicarrier including electric vehicles and CHP was presented in [14]. An EH model with CHP was designed for a residential building in [15].

On the other hand, some studies investigated the role of electrical heat pumps (EHPs) in hub schemes. In [16], the performance of residential EH integrated with EHP was discussed. The optimal model of bidding strategy for EH to participate in the target energy market which includes the EHP system was proposed in [17]. The authors investigated the flexibility of an EH operation including CHP and EHP in [18]. A day-ahead optimized scheduling model for an EH including EHP was presented and discussed [19]. Mixed

integer linear programming (MILP) was implemented to model the optimization problem in the general algebraic modeling language (GAMS) program for an EH with CHP and ESS to reduce annual costs and emissions without considering RESs [20]. The effect of CHP units feeding many loads to achieve less fuel consumption and less pollution was studied [21]. In [22], an optimal operating strategy for CHP was proposed to reduce the total cost while also satisfying the thermoelectric coupling reduction. An optimal operation technique has been proposed in buildings supplied with CHP units integrated with RESs [23]. The particle swarm algorithm (PSO) algorithm was applied for the optimum planning of multi-source EH systems including RES to feed electrical and thermal loads [24]. An optimal multi-objective method was proposed to optimize a hybrid combined cooling, heating, and power system in order to reduce the total cost, and carbon dioxide emissions and increase the system flexibility [25]. A multi-objective technique based on a genetic algorithm (GA) was proposed in [26] to optimize the performance of an integrated natural gas combined, cooling, heating, and power unit and a ground source heat pump from the energy, economy, and emission perspectives without considering uncertainties of RESs.

Providing clean and reliable fresh water sources for various uses of human societies has always been a major global problem, especially in water-deficient regions. Recently, water desalination (WD) based on reverse osmosis technology has received more attention compared to other technologies because of its economic performance [27]. An optimal day-ahead operation of a microgrid based on coastal EH to minimize operational and environmental costs was presented [2]. Authors in [1] proposed a new model of a smart island in the power system composed of different energy resources including smart EH equipped with a desalination unit to supply electricity, thermal, and water demand. Authors in [28] studied the operation of multi-carrier energy systems integrated with CHP, wind turbines (WTs), gas-fired power plants, heat buffer tanks, pumped-storage systems, and gas storage technologies to meet daily electric power, gas, heating, and water loads. In [29], the optimal management of a water grid constructed for a pilot agro-industrial district, based on greenhouse cultivation, was analyzed. The proposed algorithm was based on the EHs approach and took into account economic terms and the optimal use of the available resources. EH scheduling for day-ahead has been studied in the presence of WT and electrical, thermal, and pico-hydel energy storage [30]. In [31], a proposed EH consisting of electricity, heat, and WD production equipment was optimized based on the GA to reduce costs and pollutants and increase the exergy efficiency.

In light of the previous studies, the current study contributes to presenting an optimization-based model to address the planning and operation of the EH system. Different loads, unpredictable wind power, photovoltaic (PV) power, and ESSs are taken into account. The optimal integration among various types of resources, environmental requirements, and economic criteria will be explored. In addition, the optimization problem will be solved based on the Archimedes optimization algorithm (AOA) to maximize total social welfare (SW) by reducing the total system operation cost and carbon dioxide emissions. A comparison between the most recent applied research and the proposed method is shown in Table 1.

Table 1. Comparison between the proposed system and some related literature.

Ref.	Year	PV	WT	CHP	EHP	GB	WD	ES	HS	WS	Demand	CO [#]	EA [&]	UA [¥]	Grid-Connected	SA [□]
[1]	2020	✗	✗	✓	✗	✓	✓	✓	✗	✓	E-H-W [*]	✓	✗	✓	✓	GA
[2]	2021	✓	✓	✗	✗	✗	✓	✗	✓	✓	E-H-W	✓	✓	✓	✓	GAMS
[12]	2017	✗	✗	✓	✗	✓	✗	✓	✓	✗	E-H [+]	✓	✗	✓	✓	MILP
[16]	2018	✗	✓	✓	✓	✓	✗	✓	✗	✗	E-H	✓	✗	✓	✓	MILP
[19]	2021	✗	✓	✓	✓	✓	✗	✗	✗	✗	E-H	✓	✓	✓	✓	MINLP
[20]	2021	✗	✗	✓	✗	✓	✗	✓	✓	✗	E-H	✓	✗	✗	✓	MILP-GAMS
[21]	2020	✓	✓	✓	✗	✓	✗	✓	✓	✗	E-H-C [↓]	✓	✓	✓	✓	QPSO
[22]	2019	✗	✓	✓	✗	✗	✗	✗	✓	✗	E-H	✓	✗	✓	✓	-
[23]	2020	✓	✓	✗	✗	✗	✗	✓	✗	✗	E-H-C	✗	✗	✗	✓	-
[24]	2020	✗	✗	✓	✗	✗	✗	✗	✗	✗	E-H	✓	✓	✗	✓	PSO

Table 1. *Cont.*

Ref.	Year	PV	WT	CHP	EHP	GB	WD	ES	HS	WS	Demand	CO [#]	EA [&]	UA [¥]	Grid-Connected	SA [□]
[25]	2020	✓	✗	✗	✓	✗	✗	✓	✗	✓	E-H-C	✓	✓	✗	✓	NSGA
[26]	2019	✓	✗	✗	✓	✗	✗	✓	✗	✗	E-H-C	✓	✓	✗	✓	NSGA-II
Proposed		✓	✓	✓	✓	✓	✓	✓	✓	✓	E-H-W	✓	✓	✓	✓	AOA

GB: Gas boiler, ES: Electrical storage, HS: Heating storage, WS: Water storage, E-H-W *: Electrical-Heating-Water, E-H [+]: Electrical-Heating, E-H-C [⁺]: Electrical-Heating-Cooling, CO [#]: Cost analysis, EA [&]: Environmental analysis, UA [¥]: Uncertainty analysis, SA [□]: Solution algorithm MINLP: Mixed integer nonlinear programming, QPSO: Quantum Particle Swarm Optimization, NSGA: Non-dominated sorting genetic algorithm.

The major contributions of this paper can be briefed as:

- Proposing a methodology to address integrations among EH components and energy networks, while satisfying different system constraints. Economic and environmental objective functions are considered to address the configuration and optimal operation of the EH system. Moreover, seeking to address reliability enhancement for electrical, thermal, and drinking water as vital requirements.
- Applying the AOA and GA to optimally solve the optimization problem to maximize the total SW and minimize emissions. Moreover, analyzing the performance of CHP units and verifying their effectiveness with EHs.
- Verifying the effectiveness of the proposed method in a short-term situation; a day is examined within one hour.

2. Energy Hub (EH) Modelling

Figure 2 shows an architecture of a proposed EH. The proposed EH consists of three integrated networks. The main energy sources of the hub are electricity, natural gas, and water whereas the output side supplies electricity, heat, and freshwater loads. The integration among these networks occurs through the EH components, such as CHP, EHP, boiler, and WD. Additionally, electrical, thermal, and water storage units were used to maximize utilization during periods of low load and to fill the deficit at peak loads. RESs (PV and WT) are also used in the EH to minimize total operating costs and emissions. The EH input and output are coupled by mathematical relationships which are defined in (1) and (2) as follows [32]:

$$[L] = [C][P] \tag{1}$$

$$[L] = \begin{bmatrix} L_1 \\ L_2 \\ \vdots \\ L_M \end{bmatrix}_{m \times 1}, \quad [C] = \begin{bmatrix} C_{11} & \dots & C_{1n} \\ \vdots & \ddots & \vdots \\ C_{m1} & \dots & C_{mn} \end{bmatrix}_{m \times n}, \quad [P] = \begin{bmatrix} P_1 \\ P_2 \\ \vdots \\ P_n \end{bmatrix}_{n \times 1} \tag{2}$$

where L, C, and P are output loads, coupling matrix, and input energy carriers, respectively, which are illustrated in detail in the following subsections.

Nowadays, many companies all over the world apply the EH concept and distribute water, gas, electric power, and RES. The first real EH was presented in Switzerland by the Regionalwerke AG Baden company [33]. The hub was composed of wood chips, a cogeneration plant, and methane gasification. The objective was to obtain natural gas and heat from burning wood chips available in the company's supply area. Natural gas was pumped either directly into the natural gas system or converted into electricity through the cogeneration unit and integrated into the electrical grid. In either case, the wasted heat was injected into the local heating network. Nitrogen and steam were used for the gasification process which was also provided at the hub entrance in addition to the above-mentioned energy carriers.
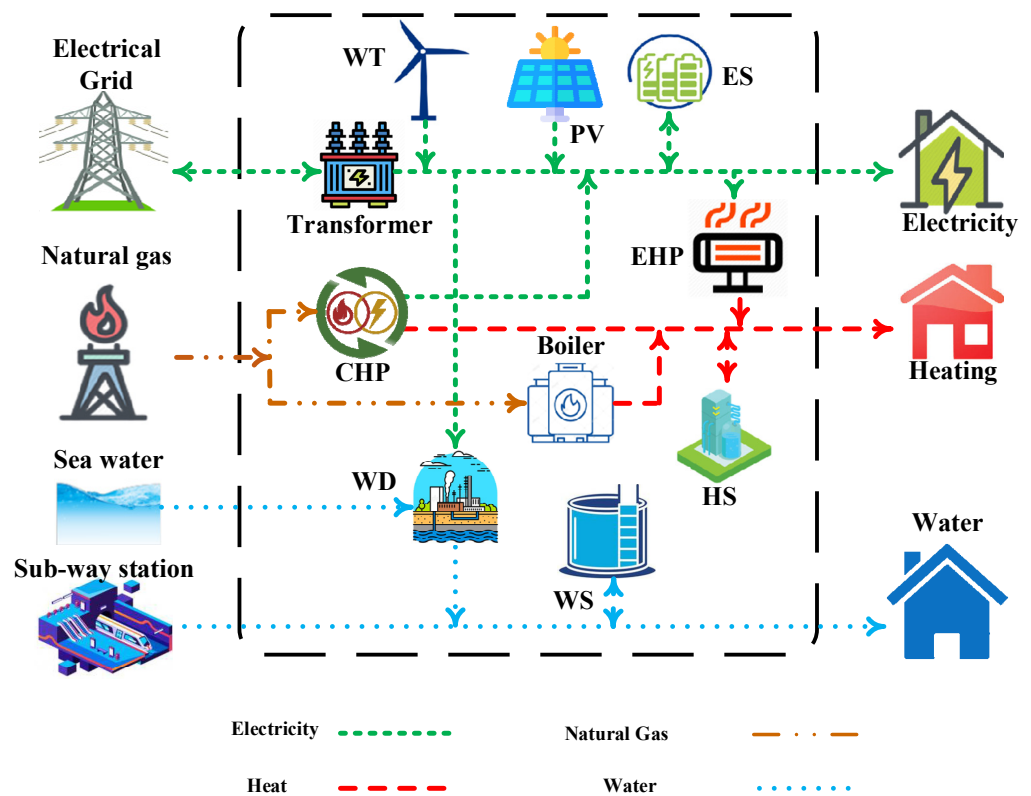
Figure 2. The architecture of studied EH.

2.1. PV Unit Output Power Modelling

Integrating PV modules into the electrical grid is a great solution to meet electrical demand and reduce carbon dioxide emissions. On the other hand, the development of PV modules faces a major challenge which is their unpredictable nature [34]. The power produced from PV arrays $(P_{PV}(t))$ is calculated by:

$$P_{PV}(t) = \frac{G(t)}{1000} \, P_{PVr} \, \eta_{PV} \tag{3}$$

where $G(t)$ is the solar radiation at time t (kW/m^2), P_{PVr} is the PV cell rated power (MW), and η_{PV} is PV cell efficiency.

2.2. WT Output Power Modelling

The generation of electrical energy from wind is one of the most promising types of generation in the world. The flow of air is converted into electrical energy without a negative impact on the environment [34]. Despite the different geographical conditions, seasonal changes, and other factors, the proposed model in this work of wind power is applicable under any operating conditions. Additionally, the power generation of WTs is highly uncertain and is formulated as a function of wind speed as represented in this work. The power generated $(P_W(t))$ of a WT is calculated by (4):

$$P_W(t) = \begin{cases} 0 & 0 \leq v(t) \leq v_i \ \& \ v_o \leq v(t) \\ P_{Wr} \times \frac{(v(t)-v_i)}{(v_r-v_i)} & v_i \leq v(t) \leq v_r \\ P_{Wr} & v_r \leq v(t) \leq v_o \end{cases} \tag{4}$$

where $v(t)$, v_i, v_o, and v_r are the actual wind speed at time t, cut-in speed, cut-out speed, and rated speed (m/s), respectively. P_{Wr} is the rated value of wind power (MW).

2.3. ESSs Model

ESSs are used to feed loads in case of low power generation. ESSs were modeled similarly to the authors presented in [35].

2.4. CHP Model

Both heat and power are generated from the CHP units. Each CHP unit has a thermal-electrical characteristic. One of the most used and feasible thermoelectric operation regions is shown in Figure 3. The complete model of CHP is illustrated in [11,36].
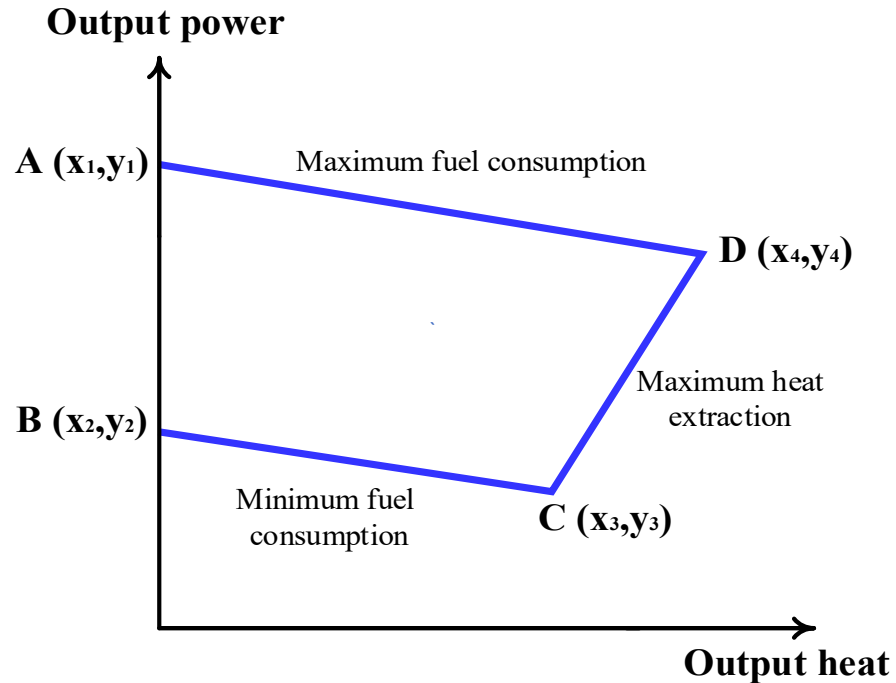
Figure 3. The thermal-electrical characteristic of the CHP unit.

2.5. EHP Model

EHP is powered by electric energy and extracted the heat from the cold ambient air and transfers it to heat the water in the heating system. The electrical power ($P_{EHP}(t)$) taken from EH by EHP is [37]:

$$P_{EHP}(t) = \frac{Q_{EHP}(t)}{COP} \tag{5}$$

where COP is the EHP coefficient of performance, and $Q_{EHP}(t)$ is EHP thermal energy produced (MWth) at time t.

2.6. GB Model

In the proposed EH system, GB is a standby unit for supplying thermal demand requirements when the heat produced by the CHP and EHP, and the available ESS capacity, is insufficient. The heat produced by the GB unit is given as [21].

$$Q_{GB}(t) = \gamma_{GB} \, P_{GB}(t) \tag{6}$$

where $Q_{GB}(t)$ is EHP thermal energy produced (MWth) at time t, γ_{GB} is the GB coefficient of performance, and $P_{GB}(t)$ is the quantity of natural gas absorbed by GB at time t (MW).

2.7. WD Unit Modelling

In this paper, one of the components of a water supply system is a WD unit, which can be established anywhere in the system (near the sea or groundwater). This paper focused on reducing costs and emissions without addressing the optimal location of the WD units (which can be considered in future work). Additionally, the WD unit is considered an aggregate device that imports electrical energy from EH and exports fresh water. Therefore, the detailed thermodynamic formula for the water grid is not taken into account. The WD unit is supplied with electric power to produce fresh water from seawater. The relationship between the produced water ($W_{WD}(t)$) and the consumed electricity ($P_{WD}(t)$) can be calculated as [2]:

$$P_{WD}(t) = \frac{W_{WD}(t)}{\eta_{WD}} \tag{7}$$

where η_{WD} is the performance coefficient of WD (m^3/MW).

3. Uncertainty Analysis of RESs

The high uncertainty in the energy produced from RESs makes it important to model the stochastic behavior of these resources. So, the planning and operation of an EH are managed, taking into account the unpredictable nature of these units. In this section, the uncertainties in RESs power generation are addressed. In order to account for differences in wind speed data, the Weibull distribution is used to continuously track changes in wind speed through a scale factor k and a form factor c. The Weibull distribution probability density function (pdf) is defined as [32]:

$$f_W(P_{W_{av}}) = \begin{cases} \left(\frac{klv_i}{c}\right)\left(\frac{(1+\rho l)v_i}{c}\right)^{k-1} exp\left(\left(\frac{(1+\rho l)v_i}{c}\right)^k\right) & 0 \leq P_{W_{av}} \leq P_{W_r} \\ 1 - exp\left[-\left(\frac{v_i}{c}\right)^k\right] + exp\left[-\left(\frac{v_o}{c}\right)^k\right] & P_{W_{av}} = 0 \\ exp\left[-\left(\frac{v_r}{c}\right)^k\right] - exp\left[-\left(\frac{v_o}{c}\right)^k\right] & P_{W_{av}} = P_{W_r} \end{cases} \tag{8}$$

where $P_{W_{av}}$ is the total available wind power (MW), $\rho = \frac{P_{W_{av}}}{P_{W_r}}$ and $l = \frac{v_r - v_i}{v_i}$.

To model the uncertainties in the *PV* modules' generated power, the beta distribution function is used [32]:

$$f_{PV}(P_{PV_{av}}) = \begin{cases} G^{\alpha-1}(1-G)^{\beta-1}\frac{\Gamma(\alpha+\beta)}{\Gamma(\alpha)+\Gamma(\beta)} & 0 \leq G \leq 1, \alpha, \beta \geq 0 \\ 0 & otherwise \end{cases} \tag{9}$$

where $P_{PV_{av}}$ is the total available PV power (MW), α and β are beta pdf parameters.

4. Thermal Generation Emissions

In most electric power grids, the bulk of the electric power generated is by thermal power plants which produce high carbon dioxide emissions. Hence, the number of emissions (E_G) can be expressed as [38]:

$$E_G = a_E P_G^2 + b_E P_G + d_E + \gamma_E exp(\delta_E P_G) \tag{10}$$

where a_E, b_E, d_E, γ_E, and δ_E are emission coefficients of the thermal generators and P_G is the power of the thermal generator (MW).

5. Problem Formulation and Methodology

The primary objective of this paper is to provide the electricity, heating, and water requirements of EH at the highest SW by minimizing total system operating costs and lowering CO$_2$ emissions while taking into account various system constraints.

5.1. Objective Function

This work aims to obtain the optimum values of power, heat, and water output from available generators subject to coordinated constraints. The total operating cost can be expressed as a summation of individual operating costs.

This paper deals with a system that includes a conventional power unit, a CHP unit, and an HOU. Reliable models describing the off-design process (partial load relationships between power production and fuel consumption) per unit as well as reliable optimization methods are required in order to improve the optimization problem. Depending on the nature of these relationships, the appropriate method should be applied to solve the optimization problem. However, in practice, second-order or linear convex input/output relationships are applied. The cost function per unit is obtained when the input/output curve is multiplied by the cost of fuel burned per unit. Assuming convex input/output curves for conventional power, CHP and HOU, their cost functions will also be convex [39] as follows:

- Conventional power generators' operating cost can be represented by a quadratic form as [36]:

$$C_G(P_G) = a_G P_G^2 + b_G P_G + c_G \tag{11}$$

where C_G is the conventional generator-produced power cost ($), and $a_G, b_G,$ and c_G are the conventional generator cost coefficients.

- CHP generator operation cost can be represented by a quadratic form as [32]:

$$C_{CHP}(P_{CHP}, Q_{CHP}) = a_{Co} + b_{Co} P_{CHP} + c_{Co} P_{CHP}^2 + d_{Co} Q_{CHP} + e_{Co} Q_{CHP}^2 + f_{Co} P_{CHP} Q_{CHP} \tag{12}$$

where C_{CHP} is the CHP generator produced energy cost ($), $a_{Co}, b_{Co}, c_{Co}, d_{Co}, e_{Co},$ and f_{Co} are the CHP generation cost coefficients, and P_{CHP}, Q_{CHP} are the electrical and heating outputs of the CHP unit.

- The operating cost of a heat-only unit (HOU) can be represented by a quadratic form as [36]:

$$C_{HOU}(Q_{HOU}) = V_{HOU} Q_{HOU}^2 + M_{HOU} Q_{HOU} + R_{HOU} \tag{13}$$

where C_{HOU} is the produced heat cost ($), and $V_{HOU}, M_{HOU},$ and R_{HOU} are the heat generation cost coefficients of an HOU.

- Because of the uncertainty of the available RESs at any given time, the factors for overestimating and underestimating the available RESs must be included in the model. The overestimation factor can be easily explained in that if a certain amount of RES power is assumed and that power is not available at the assumed time, then the power must be purchased from an alternative source or the loads must be disposed of. In the case of an underestimation penalty, if the available RES power is more than was assumed, then that power will be wasted, and it is reasonable for the system operator to pay a cost to the RES power product for the wastage of available capacity. Surplus RES power is usually sold to neighboring utilities, or by rapid redistribution. The output of non-RES generators is correspondingly reduced. Only if this cannot be achieved should the phantom load resistors be connected to "waste" the excess power. Obviously, these actions can be modeled by a simple minimization penalty cost function as [36]:

$$C_W(P_W) = d_W f_W(P_{W_{av}}) P_W + c_{p.W}(P_{W_{av}} - P_W) + c_{r.W}(P_W - P_{W_{av}}) \tag{14}$$

$$C_{PV}(P_{PV}) = h_{PV} f_{PV}(P_{PV_{av}})(P_{PV}) + c_{p.PV}(P_{PV_{av}} - P_{PV}) + c_{r.PV}(P_{PV} - P_{PV_{av}}) \tag{15}$$

where C_W and C_{PV} are the total cost of WT and PV generators ($), d_W and h_{PV} are the cost coefficient of WT and PV generators ($/MW), respectively, $f_W(P_W)$ and $f_{PV}(P_{PV})$ are the Weibull *pdf* and beta *pdf* of WT and PV generator, respectively, $c_{p.W}$ and $c_{p.PV}$ are the cost coefficient of WT and PV generators because of over-generation ($/MW), P_W and P_{PV} are the scheduled output of WT and PV generators, and $c_{r.W}$ and $c_{r.PV}$ are

the cost coefficient of WT and PV generators because of under-generation (\$/MW). The cost coefficients of WT and PV generation are calculated as follows [36]:

$$c_{p.W}(P_{W_{av}} - P_W) = c_{p.W} \int_{P_W}^{P_{W_r}} (P_{W_{av}} - P_W) f_W(P_{W_{av}}) dP_W \tag{16}$$

$$c_{r.W}(P_W - P_{W_{av}}) = c_{r.W} \int_0^{P_W} (P_W - P_{W_{av}}) f_W(P_{W_{av}}) dP_W \tag{17}$$

$$c_{p.PV}(P_{PV_{av}} - P_{PV}) = c_{p.PV} \int_{P_{PV}}^{P_{PV_r}} (P_{PV_{av}} - P_{PV}) f_{PV}(P_{PV_{av}}) dP_{PV} \tag{18}$$

$$c_{r.PV}(P_{PV} - P_{PV_{av}}) = c_{r.PV} \int_0^{P_{PV}} (P_{PV} - P_{PV_{av}}) f_{PV}(P_{PV_{av}}) dP_{PV} \tag{19}$$

- The operating cost of charge/discharge of ESSs can be represented by different models but this paper deals with a simple linear function, as the ESSs should be considered as a load when being charged and be considered as a generation source when discharging to the network [40]:

$$C_{ESSi}(P_{ESSi}) = C_{dsi} P_{dsi} - C_{chi} P_{chi} \tag{20}$$

where C_{ESSi} is the ESS power cost (\$), C_{dsi} and C_{chi} are the discharging and charging cost of the ith ESSs (\$/MW), respectively, and P_{dsi} and P_{chi} are the discharging and charging power of the ith ESSs (MW), respectively.

The operation cost of GB, EHP, WD, and WG is supposed to be linear. Where the output energy of each unit is linearly related to the quantity of fuel entering the unit and the cost coefficients.

- The operating cost of EHP can be represented by a linear function as [37]:

$$C_{EHP}(Q_{EHP}) = a_{EHP} P_{EHP} \tag{21}$$

where C_{EHP} is the power absorbed cost (\$) and a_{EHP} is the EHP unit cost coefficient (\$/MW).

- The operating cost of GB can be represented by a linear function as [41]:

$$C_{GB}(P_{GB}) = a_{GB} P_{GB} \tag{22}$$

where C_{GB} is the natural gas absorbed cost (\$) and a_{GB} is GB unit cost coefficient (\$/MW).

- The operating cost of a WD unit can be represented by a linear function as [42]:

$$C_{WD}(P_{WD}) = K_{WD} P_{WD} \tag{23}$$

where C_{WD} is the power absorbed cost (\$) and K_{WD} is the WD unit cost coefficient (\$/MW).

- The operating cost of the water grid (WG) can be represented in a linear form as [35]:

$$C_{WG}(W_{WG}) = K_{WG} W_{WG} \tag{24}$$

where C_{WG} is the total cost of water produced from WG (\$), K_{WG} is the cost coefficient of the WG (\$/m^3), and W_{WG} is the volume of the water produced from the WG (m^3).

To calculate the total system operation cost during period T, (10)–(24) are integrated into one formula as follows:

$$Cost = \sum_{t=1}^{T} C_G(P_G) \quad + \sum_{t=1}^{T} C_{CHP}(P_{CHP}, H_{CHP}) + \sum_{t=1}^{T} C_W(P_W) + \sum_{t=1}^{T} C_{PV}(P_{PV}) + \sum_{t=1}^{T} \sum_{i=1}^{N_{ESSs}} C_{ESSi}(P_{ESSi}) + \sum_{t=1}^{T} C_{EHP}(Q_{EHP})$$
$$+ \sum_{t=1}^{T} C_{HOU}(Q_{HOU}) + \sum_{t=1}^{T} C_{GB}(P_{GB}) + \sum_{t=1}^{T} C_{WD}(P_{WD}) + \sum_{t=1}^{T} C_{WG}(W_{WG}) \tag{25}$$

In this work, a single objective optimization problem is solved to find the minimum cost. So, a penalty factor h ($/kg) is used to convert emissions value into cost [38]. The optimum solutions are then achieved while minimizing operation cost, minimizing emission cost, and meeting the load requirements and system operation constraints. The maximum penalty rate factor is defined as the ratio between the highest predictable value of operating cost ($cost^{max}$) and the highest estimated value for emissions (E_G^{max}), which is given by:

$$h = cost^{max} / E_G^{max} \tag{26}$$

Then, the corresponding cost of emissions (C_E) can be calculated by total emissions (E_G) as follows [38]:

$$C_E = h \ E_G \tag{27}$$

The revenue (R_D) achieved from selling the energy to end users can be expressed as:

$$R_D = \lambda_e \ P_{ED} + \lambda_h \ Q_{HD} + \lambda_W \ W_{WR} \tag{28}$$

where λ_e is electrical energy consumed cost ($/MW), λ_h is heat energy consumed cost ($/MWth), λ_w is water consumed cost ($/m^3), and P_{ED}, Q_{HD}, and W_{WR} are the electrical, heat, and water demand, respectively.

Social welfare is given by:

$$SW = R_D - Cost - C_E \tag{29}$$

The overall objective function (F) is defined as:

$$Max \ \rightarrow F = SW \tag{30}$$

This objective is constrained by the following:

1. Electrical power balance

The sum of power generated by the EH components in addition to electricity supplied by the electrical grid should be equal to the total electrical requirements, EHP, WD, and electrical losses of the system. So, the electric power balance constraint is defined as:

$$P_G + P_W + P_{PV} + P_{CHP} \pm P_{ES} = P_{EHP} + P_{WD} + P_{ED} + P_{loss} \tag{31}$$

where P_{ES} is the ES power (MW) and P_{loss} is the value of total power losses (MW) which is illustrated in [32].

2. Heating power balance

The sum of heat produced by CHP, GB, and EHP should be enough to supply heating demand in the EH. Therefore, the heat power balance can be met as follows:

$$Q_{HOU} + Q_{CHP} + Q_{GB} + Q_{EHP} \pm Q_{HS} = Q_{HD} + Q_{loss} \tag{32}$$

where Q_{HS} is the power of HS (MWth) and Q_{loss} is the heat loss (MWth) which is illustrated in detail in [32].

3. Water balance

The total generated water from the WD unit, WS, and WG should supply water demand in the EH. This constraint can be met by water balance as follows:

$$W_{WD} + W_{WG} \pm W_{WS} = W_{WR} \tag{33}$$

where W_{WS} is the volume of water storage (m^3).

4. Line flow and bus voltage limits:

$$\left. \begin{array}{c} \lfloor S_{flow,i} \rfloor \leq S_{flow,i}^{max} \\ V_i^{min} \leq V_i \leq V_i^{max} \end{array} \right\} \tag{34}$$

where $S_{flow,i}$ is the flow of apparent power in the *i*th line (MVA), $S_{flow,i}^{max}$ is the maximum apparent power flow limit in the ith line (MVA), and V_i^{max}, V_i^{min} are the maximum and minimum voltage limits of the ith bus (p.u).

5. Ramp rate limits for thermal generator, CHP, EHP, GB, WD, WG, and HOU:

$$\left. \begin{array}{c} P_{i,t-1} - P_{i,t} < DR_i \\ P_{i,t} - P_{i,t-1} < UR_i \end{array} \right\} \tag{35}$$

where DR_i, UR_i are the down-ramp rate and up-ramp rate limit of the ith unit, $P_{i,t-1}$ is the power of the *i*th unit at time $t - 1$, and $P_{i,t}$ is the power of the ith unit at time *t*.

6. Real operating power limits for wind, PV, CHPs, EHP, and WD units:

$$\left. \begin{array}{c} 0 \leq P_W \leq P_{W_r} \\ 0 \leq P_{PV} \leq P_{PV(K_{t\,max})} \\ P_{CHP}^{min} \leq P_{CHP} \leq P_{CHP}^{max} \\ 0 \leq P_{EHP} \leq P_{EHP}^{max} \\ 0 \leq P_{WD} \leq P_{WD}^{max} \end{array} \right\} \tag{36}$$

where $P_{PV(K_{t\,max})}$ is PV output power at maximum solar radiation (MW), P_{CHP}^{max}, P_{CHP}^{min} are the maximum and minimum power outputs of a cogeneration generator (MW), P_{EHP}^{max} is the maximum installed capacity of the EHP unit (MW), and P_{WD}^{max} is the maximum installed capacity of the WD unit (MW).

7. Heat limits for CHPs, HOUs, EHP, and GB:

$$\left. \begin{array}{c} Q_{CHP}^{min} \leq Q_{CHP} \leq Q_{CHP}^{max} \\ Q_{HOU}^{min} \leq Q_{HOU} \leq Q_{HOU}^{max} \\ 0 \leq Q_{EHP} \leq Q_{EHP}^{max} \\ 0 \leq Q_{GB} \leq Q_{GB}^{max} \end{array} \right\} \tag{37}$$

where Q_{CHP}^{max}, Q_{CHP}^{min} are the maximum and minimum heat outputs of the CHP generator (MWth), Q_{HOU}^{max}, Q_{HOU}^{min} are the maximum and minimum heat outputs of HOU (MWth), Q_{EHP}^{max} is the maximum installed capacity of the EHP unit (MWth), and Q_{GB}^{max} is the maximum installed capacity of a GB unit (MWth).

8. Charging/discharging limits of ESSs:

$$P_{ESS_i}^{min} \leq P_{ESSC_i}, \qquad P_{ESSD_i} \leq P_{ESS_i}^{max} \tag{38}$$

where $P_{ESS_i}^{max}$, $P_{ESS_i}^{min}$ are the maximum and minimum power limits of ESSs (MW).

9. Initial and final energy in ESSs:

$$E_{ESS_i}^{min} \leq E_{ESS_i}^{ini} + P_{ESSC_i}\Delta t - P_{ESSD_i}\Delta t \leq E_{ESS_i}^{max} \tag{39}$$

where $E_{ESS_i}^{max}$, $E_{ESS_i}^{min}$ are the maximum and minimum limit energy of ESSs (MWh), and $E_{ESS_i}^{ini}$ is the initial energy of the ith ESSs (MWh).

5.2. Optimization Algorithm

The AOA is a novel optimization algorithm that has been proposed to address real-world problems [43]. This optimizer derives the idea of his work from Archimedes' principles states, and it depends on the behavior of the force exerted when an object is partially or completely immersed in a liquid. Similar to most swarm optimizers and metaheuristic algorithms, the AOA proposes population-based solutions. In this case, the proposed solutions are represented by immersed objects. The optimization process starts with proposing an initial set of random particles (objects/locations/solutions). Each particle has its size, density, and acceleration which are updated in an iterative process. Theoretically, the AOA includes many explorations and exploitations processes because it is a global optimization algorithm. Figure 4 introduces the pseudo-code of the AOA; including population initialization, population assessment, and parameter updating [44].

Archimedes Optimization Algorithm (AOA) : Pseudo code

- **Inputs:**
  $N, T_{max}, C_1, C_2, C_3,$ and C_4
- **Output:**
  Object with best fitness value
- **Steps:**
  1. **Initialize objects population with random positions, densities and volumes using:**
     $O_i = lb_i + rand \times (ub_i - lb_i); i = 1, 2, \dots, N$
     $den_i = rand$
     $vol_i = rand$
     $acc_i = lb_i + rand \times (ub_i - lb_i)$
  2. **Evaluate initial population and select the one with the best fitness value**
  3. **Set iteration counter $t = 1$**
  4. **While $t \leq t_{max}$ do**
     For each object i do
  5. **Update density and volume of each object by**
     $den_i^{t+1} = den_i^t + rand \times (den_{best} - den_i^t)$
     $vol_i^{t+1} = vol_i^t + rand \times (vol_{best} - vol_i^t)$
  6. **Update transfer and density decreasing factors by**
     $$= exp\left(\frac{t - t_{max}}{t_{max}}\right)$$
     $$d^{t+1} = exp\left(\frac{t - t_{max}}{t_{max}}\right) - \left(\frac{t}{t_{max}}\right)$$
     if $TF \leq 0.5$ then ▶**Exploration phase**
  7. **Update acceleration and normalization acceleration by**
     $$den_i^{t+1} = \frac{den_{mr} + vol_{mr} \times acc_{mr}}{den_i^{t+1} \times vol_i^{t+1}}$$
     $$acc_{i-norm}^{t+1} = u \times \frac{acc_i^{t+1} - min(acc)}{max(acc) - min(acc)} - 1$$
  8. **Update position by**
     $x_i^{t+1} = x_i^t + C_1 \times rand \times acc_{i-norm}^{t+1} \times d \times (x_{rand} - x_i^t)$
     else ▶**Exploration phase**
  9. **Update acceleration and normalization acceleration by**
     $$den_i^{t+1} = \frac{den_{best} + vol_{best} \times acc_{best}}{den_i^{t+1} \times vol_i^{t+1}}$$
     $$acc_{i-norm}^{t+1} = u \times \frac{acc_i^{t+1} - min(acc)}{max(acc) - min(acc)} - 1$$

  10. **Update direction flag F by**
      $$F = \begin{cases} +1 \; if \; P \leq 0.5 \\ -1 \; if \; P > 0.5 \end{cases}$$
      $$P = 2 \times rand - C_4$$
      $$x_i^{t+1} = x_{best}^t + F \times C_2 \times rand \times acc_{i-norm}^{t+1} \times d \\ \times (T \times x_{best} - x_i^t)$$
      end if
      end for
  11. **Evaluate each object and select the one with the best fitness value**
  12. **Set $t = t + 1$**
      end while
      return object with the best fitness value

Algorithm parameters	
N	Population size
T_{max}	Maximum iterations
C_1, C_2, C_3, C_4	Control variables
O_i	i^{th} object in a population
lb_i, ub_i	Lower and upper bounds of the search-space
vol_i, den_i, acc_i	Volume, density and acceleration for each ith object
$rand$	**D** dimensional vector randomly generates number between [0, 1]
$vol_{best}, den_{best} \; acc_{best}$	Volume, density and acceleration associated with the best object found
$T \; F$	Transfer operator
t	Iteration number
d	Density decreasing factor
$vol_{mr}, den_{mr}, acc_{mr}$	Volume, density and acceleration of random material
x_i	Position for each ith object

Figure 4. AOA Pseudo code.

5.3. Proposed Stochastic Planning Structure

The primary objective of stochastic planning is the total SW and emissions reduction since all demand requirements are satisfied. In this paper, the AOA algorithm was used to improve the EH system performance. The suggested methodology for EH planning taking into account electrical, thermal, and water energy balancing is illustrated in Figure 5. Heat network, electrical grid, water network specifications, economic data, weather data, power generation of RESs, and various types of demands are the inputs to the proposed system. Further, the electrical, thermal, and water energy balances are analyzed in the planning procedure.
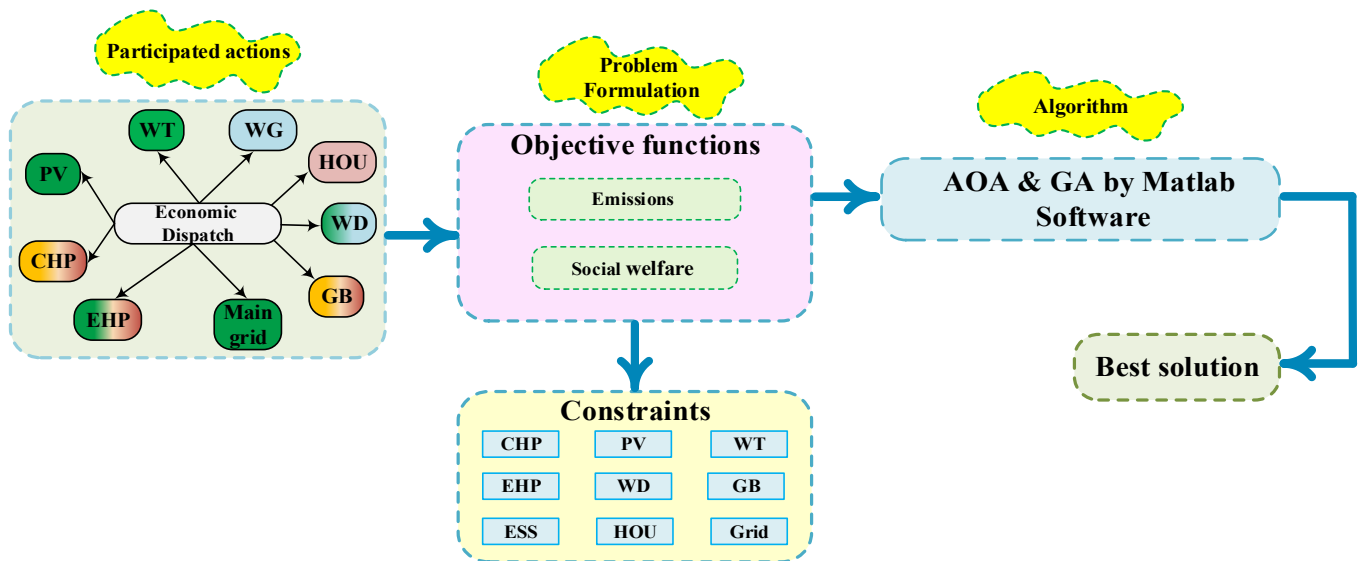
Figure 5. Proposed algorithm.

5.4. EH Methodology to Satisfy Electrical, Thermal, and Water Demand

In this study, electrical, thermal, and water demands are considered. The overall methodology for supplying all electrical, thermal, and water loads is discussed. In addition, priority should be given to the various components and networks of EH to supply aggregate demand. The methodology is illustrated in the following subsections.

5.4.1. A proposed Methodology to Satisfy Electrical Requirements

In the proposed EH, electrical loads are supplied by PV modules and WT. If the energy generated by RESs is more than the electrical demand, the surplus generated energy will be stored in the ES. Otherwise, if the energy produced by RESs is not sufficient to meet all the electrical loads, then the energy stored in the ES supplies the remaining part of the electrical loads. In all cases, if the energy produced from the RESs, and ES is not enough to supply demand requirements, the deficit energy is taken from CHP. If the energy produced from all EH units is not enough for demand, the required energy will be purchased from the electrical grid. On the other hand, whenever ES is fully charged and the energy produced from RESs and CHP is more than the electrical loads, the excess energy is sold to the electricity grid. Figure 6a illustrates the proposed methodology.

5.4.2. A Proposed Methodology to Satisfy Thermal Requirements

The GB, CHP, and EHP are considered heat generators in the proposed EH configuration. If the thermal energy generated by the CHP is greater than the heating requirements, the additional thermal energy is stored in HS. Otherwise, when the energy produced from CHP is not sufficient to supply the heating demand, the energy stored in the HS is used to feed the remainder of the load. In all cases, if the energy produced from the CHP, and HS, is not enough to supply demand requirements, the deficit energy is taken from EHP, GB, and HOU, respectively. Figure 6b shows the proposed heating demand-saving strategy.

5.4.3. A Proposed Methodology to Satisfy Water Requirements

In the proposed EH system, the WD unit is considered the main water source. If the water generated by the WD unit is greater than the water demand for the loads, the additional water is stored in WS. In cases where the energy produced from the WD unit and WS is not enough to supply demand requirements, the deficit water is taken from the public WG. On the other hand, when WS is charged and the water produced from the WD unit is more than the water demand, the excess water is sold to the WG. Figure 6c shows the proposed water demand-saving strategy.

(a)

(b)

(c)
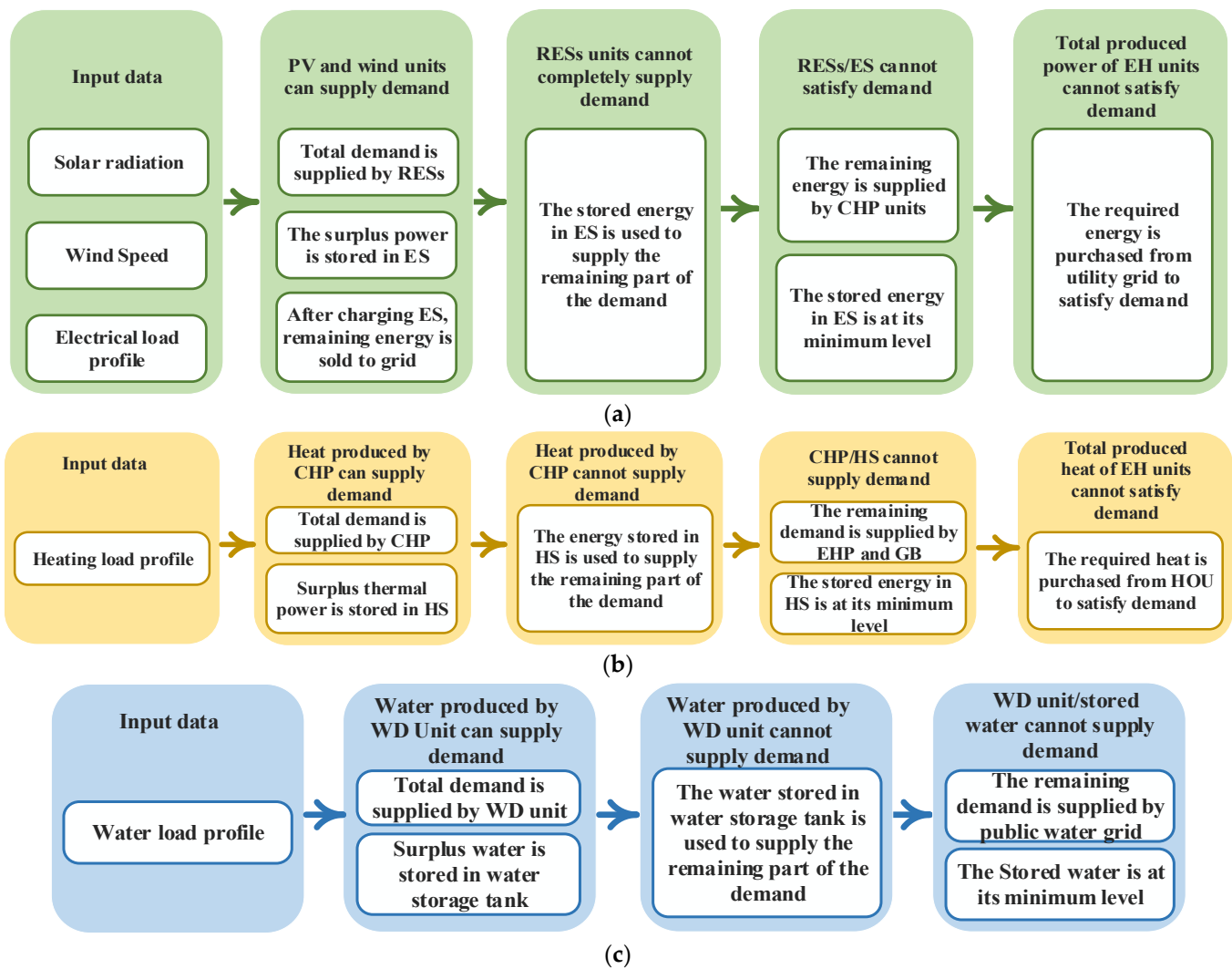
Figure 6. Proposed methodologies to satisfy load requirements (**a**) electrical (**b**) heat (**c**) water.

6. Simulation Results and Discussion

6.1. Simulation Setup

The methodology proposed is applied to an EH represented by a modified IEEE 5-bus electrical network over one day during a one-hour time interval. The modified IEEE 5-bus network, heat system, and water system are shown in Figure 7. Thermal, electrical, and water demands are assumed in the proposed EH as the curves shown in Figure 8 [19]. The electrical demand is divided into two parts, a fixed part (base load) and an elastic part (20% of the base demand). A percentage of the elastic part is fed only when the EH has a surplus of electrical power generation depending on the electricity price and amount of surplus power. Daily wind speed and solar radiation are shown in Figure 9 [32]. The data on the EH technologies are given in Appendix A. The optimization problem was solved for many case studies with various operating conditions and the results were analyzed. These simulations were carried out using MATLAB 2017a 64-bit version on a PC with an Intel (R) Core (TM) i5-8250U CPU 1.60 GHz, RAM 12 GB system, and 1 TB of storage.

Figure 7. The layout of the proposed EH system.

Figure 8. Energy carriers' demand for the day under study.
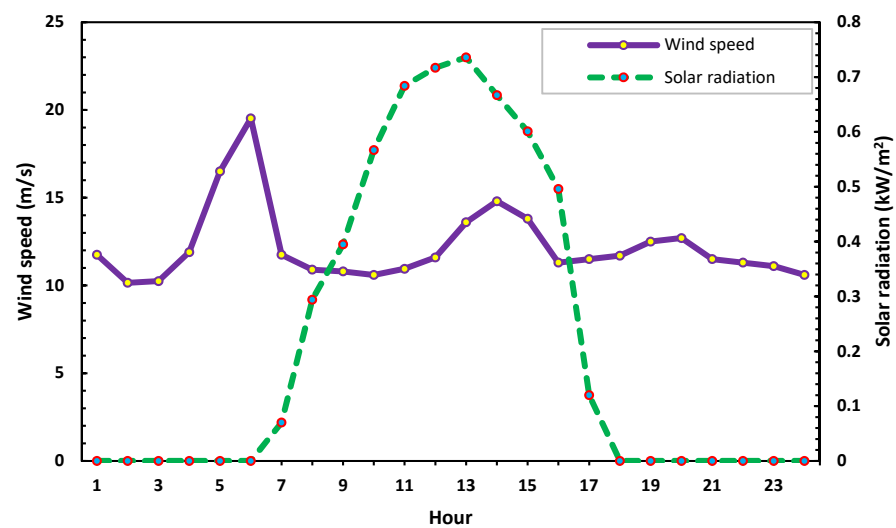
Figure 9. Wind speed and solar radiation.

6.2. Case Studies

Four cases are studied to explain the performance of CHP, WD, GB, and EHP, as shown in Table 2. In each case, many indicators are calculated, such as total SW, emissions, losses, and sold power/water to the electrical/water network are calculated (see Table 3).

Table 2. Case studies in this work.

Cases	Electricity/Heat/ Water Network	CHP	EHP	GB	RESs	WD	ESSs
Case 1 (base case)	✓	✗	✗	✗	✗	✗	✗
Case 2	✓	✓	✗	✗	✗	✗	✗
Case 3	✓	✓	✓	✓	✗	✓	✓
Case 4	✓	✓	✓	✓	✓	✓	✓

Table 3. Different EH configurations' daily operation results.

Case	SW ($)	Emissions (kg)	Energy Loss		Electrical Energy Requirement (MWh)	Power Sold to the Grid (MWh)	Water Sold to the Network (m³)
			Electrical (MWh)	Heat (MWhth)			
Case 1 (base case)	275,467.99	5638.27	3.05	108.27	2466.40	-	-
Case 2	292,150.20	5075.92	2.71	128.20	2484.00	23.20	-
Case 3	336,786.09	5848.00	2.72	131.40	3151.24	90.44	-
Case 4	379,648.00	4603.00	4.12	131.04	4269.82	512.26	149.4

By analyzing the data in the previous table, it can be observed that:

- In case 1 (base case), there is no EH and the loads are fed directly from electricity, HOU, and WG, respectively. This case was studied to explore the impact of EH on total SW, emissions, and losses. As reported in Table 3, total SW, emissions, and electrical and heat losses are 275,467.99 USD, 5638.27 kg, 3.05 MWh, and 108.27 MWhth, respectively. Additionally, there is no electrical power or water sold to the electricity grid and water network, respectively. The total electrical demand, in this case, is 2466.4 MWh (the base load curve).

- In case 2, CHP was integrated with the EH to show the effect of this unit on the performance parameters. The main source to supply heating demand requirements is the CHP unit during the day because of the low price of natural gas as shown in Figure 10a,b. With the integration of the CHP unit, SW increased by 5.71% and emissions decrease by 9.97%, respectively, compared with the base case. Additionally, the elastic part of the electrical demand supplied by the hub increased by 0.7% and the hub sold 23.2 MWh to the electricity grid.

■ In case 3, EHP, GB, WD units, and ESSs are added to the CHP in the previous case. This case results in an increase of 3151.24 MWh in the electrical demand because of adding the EHP and WD units. So, the total SW increased to 336,786.09 USD. On the other hand, total emissions increased a little compared to the base case. Figure 11 presents the results for this case.

■ In the last case (case 4), CHP, RESs, ESSs, EHP, WD, and GB are operating at the same time. This configuration enables the EH not only to meet demand requirements but also to sell electricity and water to the electrical and water networks during light load (11 AM to 5 PM in the electrical system and 1 AM to 10 AM in the water network) shown in Figure 12a–c. So, compared with the base case, all performance parameters are improved, and total SW and emissions are 379,648 USD and 4603 kg. In addition, the total electrical demand supplied by the hub increased to 4269.82 and the hub sold 512.26 MWh to the electricity grid and 149.4 m^3 to the water network.

Figure 13 shows the available power for both wind turbines and PV panels compared to the scheduled values. It has been found that this power changes throughout the day depending on the availability of wind and PV production for the plants and the electricity prices. With the increase in demand for electricity, electricity prices are relatively high. Thus, wind turbines and PV panels are at high risk when delivering a large amount of power generation at that time because they may contain high imbalanced charges in event of non-fulfillment of the scheduled power. Meanwhile, they can also provide high power generation when demand is low, hence the electricity prices are becoming lower.

(a)

(b)

(c)
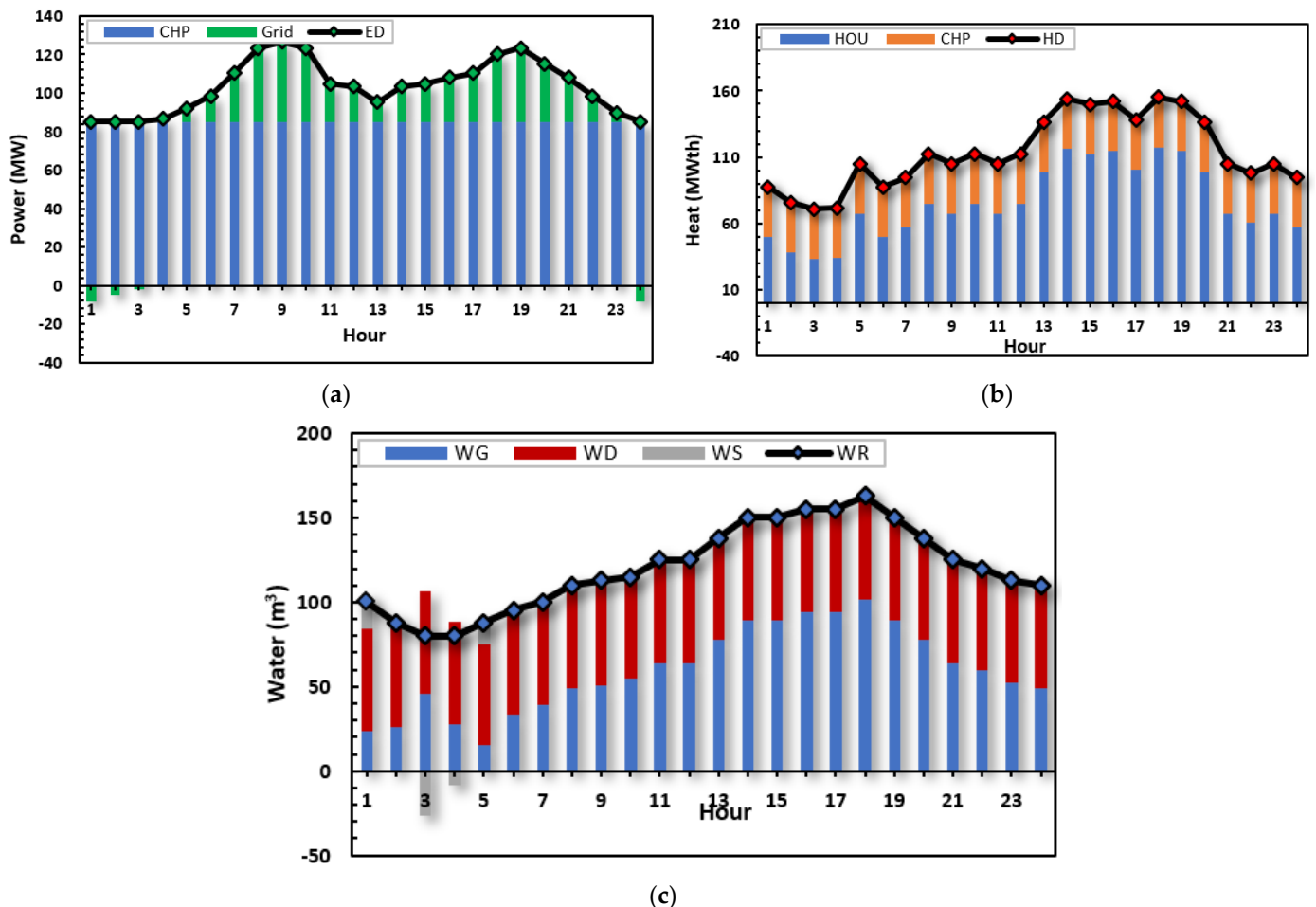
Figure 10. Generation outputs for case 2 (**a**) electricity (**b**) heat (**c**) water.
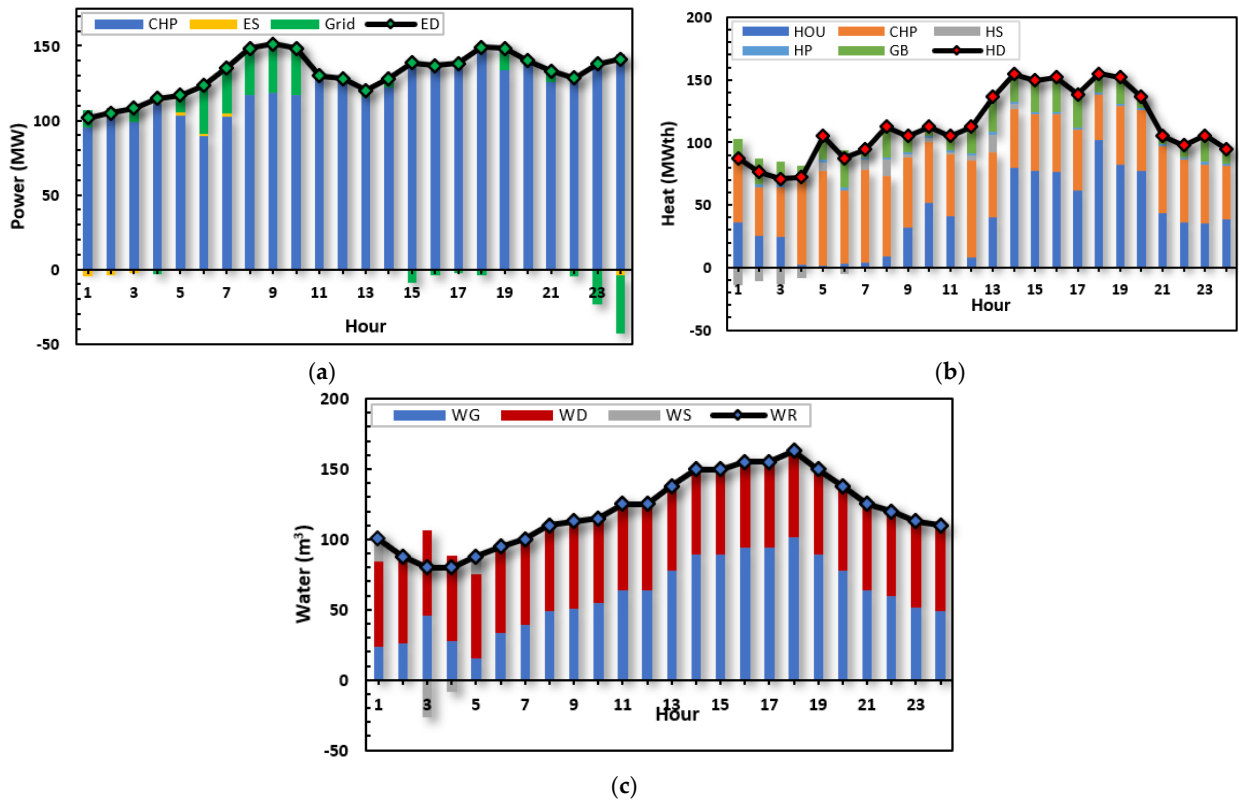
Figure 11. Generation outputs for case 3 (**a**) electricity (**b**) heat (**c**) water.
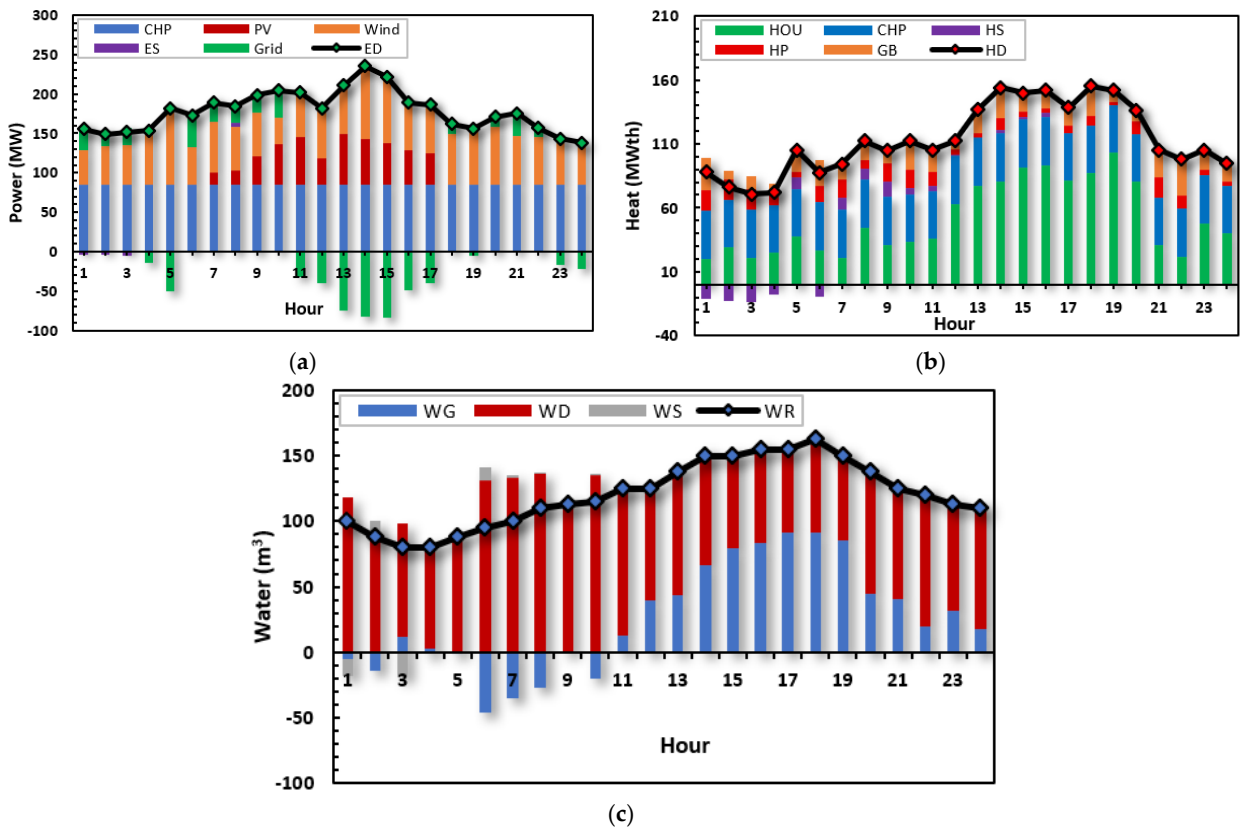
Figure 12. Generation outputs for case 4 (**a**) electricity (**b**) heat (**c**) water.
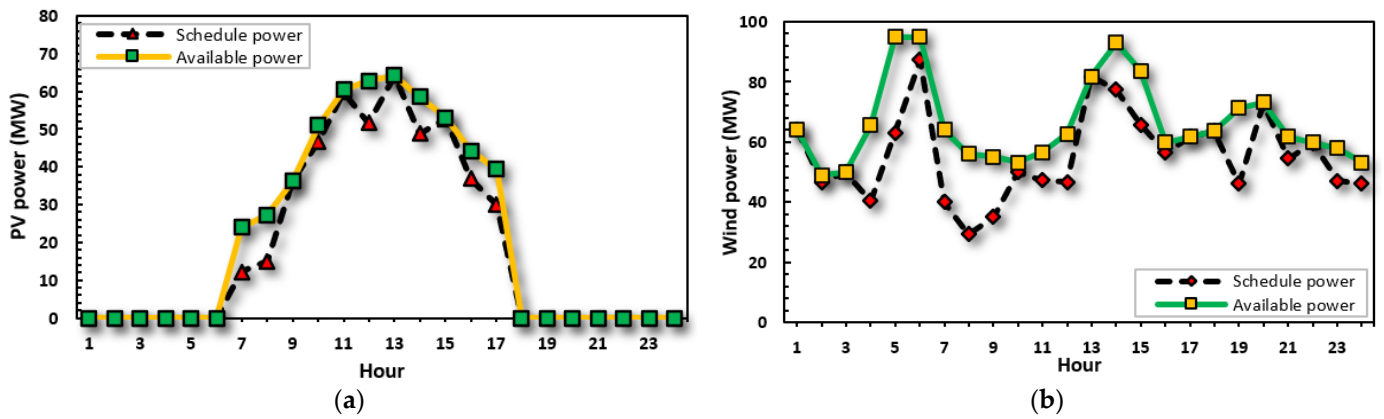
Figure 13. Comparison of available and scheduled power for: (**a**) PV power plant. (**b**) wind farm.

6.3. Proposed Algorithm Validation

To verify the efficiency of the AOA, the results of case 4 (the best case) solved by the AOA are compared with that obtained by GA. Table 4 shows the characteristics of each algorithm. Although GAs is often criticized for being too slow, the studied problem is a planning problem that only needs to be solved offline. That is why the simulation time is not of great importance as the capability to converge. It was noticed that the convergence curve of the AOA is quite smooth and with no oscillations, as shown in Figure 14. Additionally, the AOA needs less time than GA.

Table 4. AOA and GA characteristics.

AOA Characteristics	
Population Size	50
C_1	2
C_2	6
C_3	2
C_4	0.5
Number of iterations	100
GA Characteristics	
Population size	50
Number of iterations	100
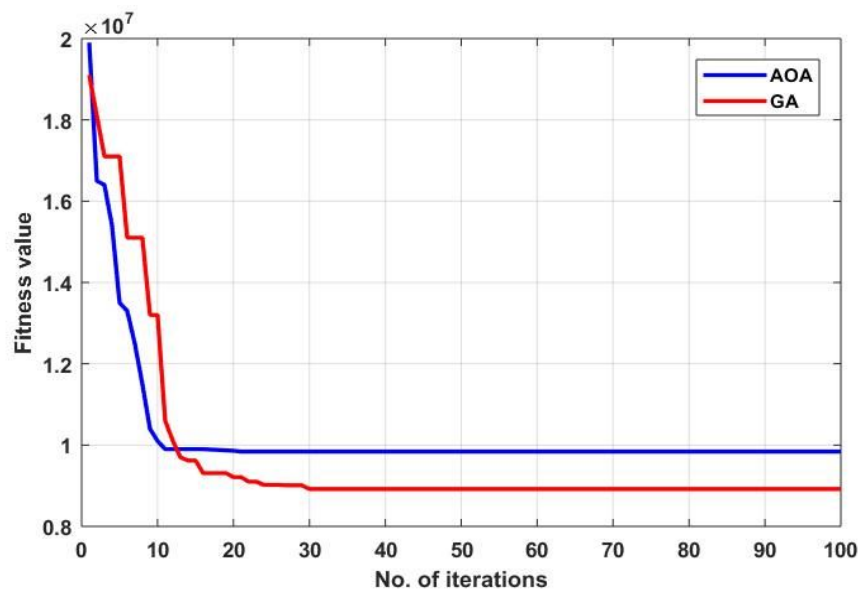
Figure 14. Fitness function convergence curves.

Tables 5 and 6 present the hourly optimal values of EH variables for case 4 by applying the AOA and GA, respectively. It is clear from these tables that the power/water taken from the electrical/water network in the case of the AOA is less than GA, which is reflected in the sold capacity of the network, as shown in Figure 15a,b. Additionally, the power taken from the CHP unit increases in the case of GA. On the other hand, the power taken from RESs increases in the case of the AOA which leads to a decrease in the total emissions, as shown in Figure 16 and Table 7, a decrease in the total losses, as shown in Figure 17a,b, and an increase in the total electrical demand, as shown in Figure 18.

Table 5. Hourly optimal values generated from the EH system of case 4 solved by AOA.

Hr.	Grid (MW)	PV (MW)	Wind (MW)	CHP-E (MW)	ES (MW)	HOU (MWth)	CHP-H (MWth)	EHP (MWth)	GB (MWth)	HS (MWth)	WG (m³)	WD (m³)	WS (m³)
1	8.69	0.00	43.84	85.10	−3.52	20.31	37.53	15.93	25.19	−11.23	−5.59	118.33	−12.23
2	−7.68	0.00	48.92	85.00	−3.95	29.00	37.51	15.93	6.37	−12.88	−13.83	88.25	12.58
3	−16.15	0.00	49.87	85.01	−5.81	21.03	37.51	15.99	10.37	−14.06	11.80	86.62	−18.92
4	−12.82	0.00	65.55	85.01	2.60	24.84	37.50	10.79	6.11	−7.48	2.96	76.90	−0.36
5	−45.59	0.00	95.00	85.00	1.98	37.48	37.50	4.54	16.62	8.93	−1.55	86.92	1.63
6	18.01	0.00	47.75	85.01	0.26	26.81	37.51	12.44	20.47	−9.55	−46.37	131.52	9.34
7	3.20	15.98	64.12	85.00	0.03	21.12	37.50	13.85	12.61	9.31	−34.85	133.29	2.06
8	14.17	17.57	56.05	85.00	4.39	44.70	37.50	6.62	14.92	8.55	−26.89	135.94	0.45
9	4.44	36.21	55.09	85.02	0.00	31.21	37.50	14.21	9.97	11.79	0.77	111.25	0.48
10	36.60	50.92	34.33	85.03	0.00	33.21	37.52	14.63	22.49	4.51	−20.37	135.18	0.69
11	−14.67	60.45	56.52	85.02	0.00	35.59	37.50	11.03	17.03	3.90	12.57	111.93	0.00
12	−52.25	33.73	62.70	85.07	0.00	63.19	37.51	3.86	6.50	1.26	39.22	85.18	0.10
13	−58.47	64.17	61.34	85.04	0.00	77.26	37.51	3.61	17.98	0.17	43.18	94.82	0.00
14	−38.49	57.30	93.09	85.01	0.00	80.59	37.50	8.73	24.20	3.16	66.21	83.79	0.00
15	−40.87	53.02	83.59	85.14	0.00	91.68	37.52	3.88	14.81	2.06	79.19	70.81	0.00
16	−16.40	44.29	59.84	85.03	0.00	93.49	37.51	3.56	14.43	3.03	83.61	70.89	0.00
17	10.10	39.38	61.74	85.00	0.00	80.94	37.53	5.97	14.04	0.00	91.29	63.21	0.00
18	12.12	0.00	63.65	85.01	0.00	87.14	37.50	7.55	23.10	0.00	91.55	70.45	0.00
19	31.11	0.00	71.25	85.02	0.00	102.84	37.52	2.77	8.85	0.00	85.64	64.36	0.00
20	28.41	0.00	73.13	85.01	0.00	80.31	37.50	9.79	8.62	0.00	44.10	93.90	0.00
21	17.68	0.00	61.75	85.00	0.00	30.60	37.51	15.99	21.01	0.00	40.87	83.63	0.00
22	38.54	0.00	59.85	85.00	0.00	21.92	37.52	10.06	28.60	0.00	19.50	100.50	0.00
23	2.86	0.00	57.95	85.00	0.00	48.03	37.54	3.86	15.82	0.00	31.93	80.57	0.00
24	−4.01	0.00	53.20	85.01	−0.24	39.86	37.51	3.41	14.03	0.00	17.42	92.08	0.00
Tot.	255.93	473.01	1480.11	2040.55	−4.26	1223.16	900.26	218.99	374.15	1.47	761.81	2270.3	−4.18

Table 6. Hourly optimal values generated from the EH system of case 4 solved by GA.

Hr.	Grid (MW)	PV (MW)	Wind (MW)	CHP-E (MW)	ES (MW)	HOU (MWth)	CHP-H (MWth)	EHP (MWth)	GB (MWth)	HS (MWth)	WG (m³)	WD (m³)	WS (m³)
1	−21.73	0.00	64.13	85.00	−6.00	40.98	37.50	2.00	16.24	−8.93	6.27	119.98	−25.75
2	−14.61	0.00	46.78	86.25	−1.21	8.75	38.95	3.03	27.15	−1.47	−20.18	89.84	17.34
3	−15.61	0.00	49.88	89.65	−0.24	16.37	37.50	4.51	24.93	−12.01	−8.90	88.40	0.00
4	−4.29	0.00	40.32	85.04	6.00	31.79	38.12	4.97	5.00	−8.00	18.71	85.55	−24.76
5	−22.34	0.00	63.14	85.26	0.00	36.89	41.01	2.07	23.69	1.81	−1.79	87.53	1.26
6	−28.69	0.00	87.75	85.74	0.00	44.12	38.45	5.71	5.00	−5.84	−1.25	95.75	0.00
7	24.79	12.23	39.95	85.00	0.00	36.21	37.50	4.76	5.00	10.92	−19.69	120.19	0.00
8	44.97	15.06	29.42	85.00	0.00	53.16	38.17	3.17	18.11	0.00	−34.33	131.25	12.58
9	36.84	36.23	35.04	85.36	0.00	31.62	37.50	9.37	17.71	8.80	−32.00	132.22	12.28
10	5.00	46.71	49.85	89.67	0.00	32.63	38.71	9.28	18.72	12.91	−20.35	135.85	0.00
11	−17.91	59.81	47.22	85.00	0.00	51.15	37.50	11.23	5.00	0.00	−0.44	124.94	0.00
12	−34.19	51.63	46.75	87.02	0.00	45.82	38.25	3.65	25.02	0.00	6.69	117.81	0.00
13	−89.16	64.18	81.70	88.01	0.00	81.19	43.49	6.65	5.00	0.00	38.28	99.72	0.00
14	−45.57	48.86	77.34	85.00	0.00	87.96	37.50	10.76	17.85	0.00	42.39	107.61	0.00
15	−47.54	52.72	65.86	85.28	0.00	88.09	37.89	3.62	20.52	0.00	21.35	128.65	0.00
16	−24.46	36.80	56.46	85.00	0.00	94.72	37.50	2.00	17.96	0.00	30.90	123.60	0.00
17	−9.85	29.96	61.75	85.00	0.00	61.80	37.50	10.00	29.41	0.00	59.18	95.32	0.00
18	15.42	0.00	63.63	85.23	0.00	75.21	49.37	4.40	26.68	0.00	61.12	100.88	0.00
19	51.59	0.00	46.20	85.00	0.00	71.96	50.41	9.50	20.46	0.00	41.40	108.60	0.00
20	4.35	0.00	72.89	88.23	0.00	87.47	37.95	2.77	8.17	0.00	6.69	131.31	0.00
21	17.57	0.00	54.48	94.34	0.00	44.30	41.41	9.46	9.92	0.00	19.27	105.23	0.00
22	−13.50	0.00	59.64	89.10	0.00	35.40	41.86	3.50	17.33	0.00	34.92	85.08	0.00
23	−1.23	0.00	47.02	85.15	0.00	51.81	39.13	6.42	7.71	0.00	35.89	76.61	0.00
24	−16.60	0.00	46.15	86.22	0.00	35.79	37.50	2.00	19.66	0.00	6.59	102.91	0.00
Tot.	200.53	454.18	1332.81	2075.53	−1.45	1245.20	950.67	134.85	392.25	−1.81	429.65	2594.82	−7.05

(**a**)

(**b**)
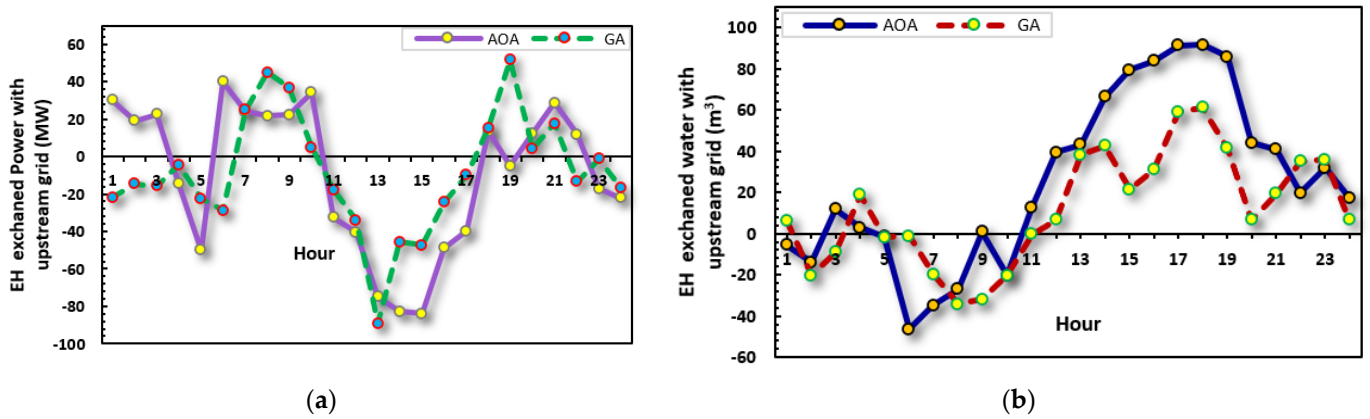
Figure 15. EH exchanged energy (**a**) EH exchanged power with the upstream grid (**b**) EH exchanged water with the water network.
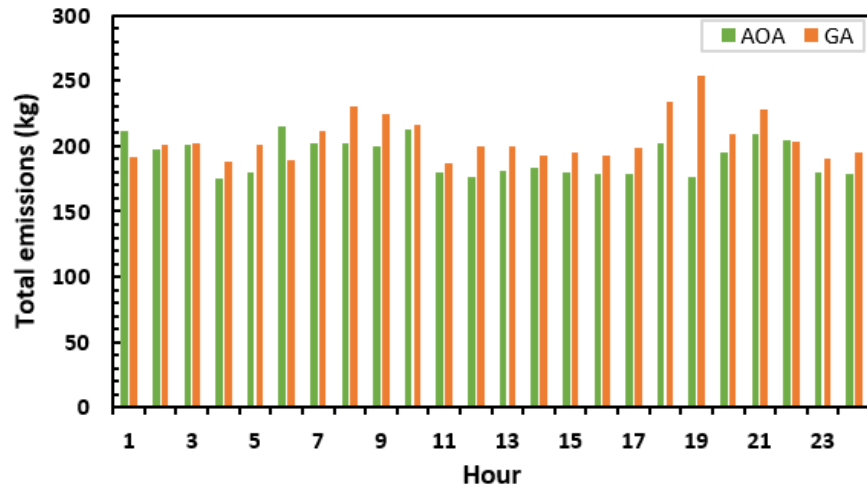
Figure 16. EH emissions.

Table 7. The results for daily operation in case 4.

Algorithm	SW (USD)	Emission (kg)	Energy Loss		Electrical Energy Demand (MWh)	Power Sold to the Grid (MWh)	Water Sold to the Network (m³)	Fitness Function
			Electrical (MWh)	Heat (MWhth)				
GA	364,203.14	4936.9	4.82	134.18	4061.62	407.28	138.89	8.9286×10^6
AOA	379,648.53	4603.0	4.12	131.04	4269.82	512.26	149.40	9.8439×10^6
Improvement (%)	4.06%	6.76%	14.52%	2.34%	4.87%	20.49%	7.03%	10.25%

(**a**)

(**b**)
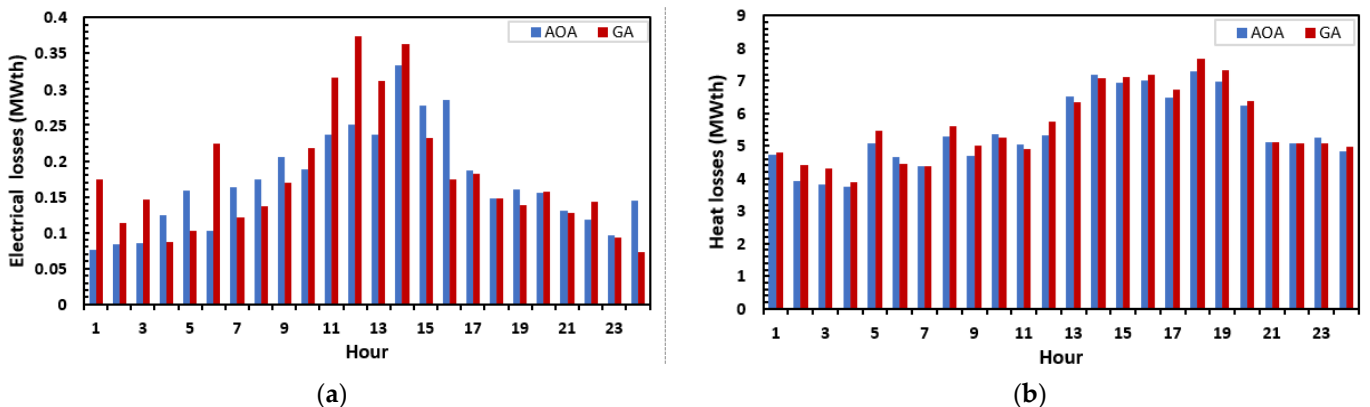
Figure 17. EH losses (**a**) electrical (**b**) heat.
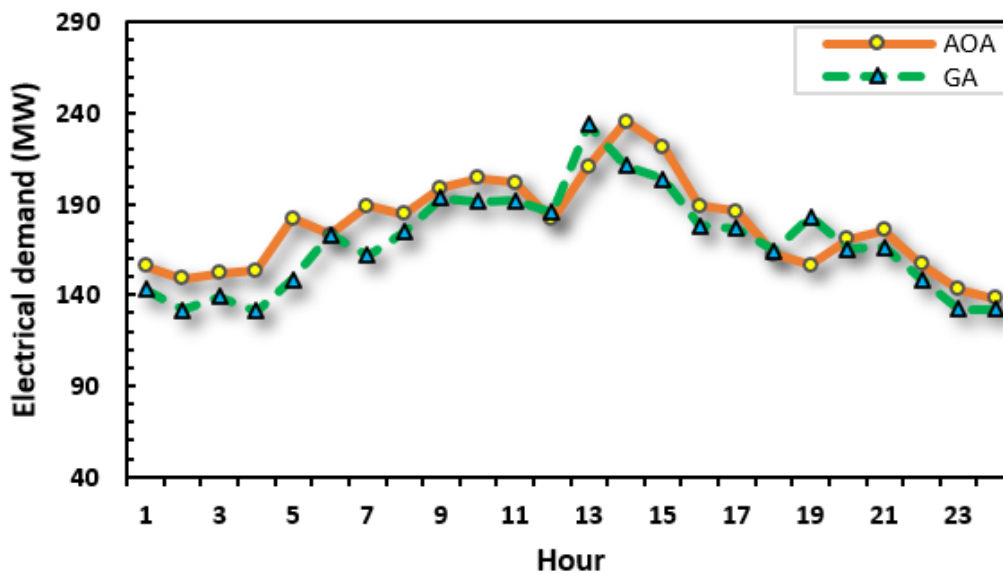
Figure 18. EH electrical demand.

Table 7 summarized the main results obtained from the two algorithms. It can be observed that all operating parameters of the EH system are improved when the AOA is used to solve the optimization problem. Total emissions and electrical/heat losses are reduced by 6.76%, 14.52%, and 2.34%, respectively, and total electrical demand, total SW, electrical power sold to the grid, and amount of water sold to the water network are increased by 4.06%, 20.49%, and 7.03%, respectively.

7. Conclusions

An optimum operation and configuration for an EH integrated with CHP was developed in this paper. The proposed configuration of the EH is composed of different types of energy sources, generation, and ESSs to feed different demands. The main objective was to maximize the total SW by reducing total operating costs and reducing total emissions value. The emissions of the EH were transformed into a penalty cost function via the emissions coefficient. Many case studies were proposed to satisfy the demands of the EH. The optimal operation problem was solved using the AOA algorithm to determine the energy generated from each source and satisfy objective functions and operational constraints. The optimization problem was implemented in the MATLAB environment. Four cases with different configurations were studied to analyze the performance of CHP with the EH. According to the results, the best performance in terms of configuration, operation, and emissions was obtained with the hub including a combination of CHP, PV, WT, EHP, GB, WD, and ESSs. The AOA was validated by solving the same problem of case 4 by GA. The results proved that the performance of the AOA is better than GA in terms of total operating cost and emissions. The numerical results illustrated the following points:

With the integration of the CHP unit, SW increased by 5.71% and emissions decreased by 9.97%, respectively, compared with the base case. Additionally, the total electrical demand supplied by the hub increased by 0.7% and the hub sold 23.2 MWh to the electricity grid.

- In case 4, all performance parameters were improved; the total SW and emissions are 379,648 USD and 4603 kg. Additionally, the total electrical demand supplied by the hub increased to 4269.82 MWh; the hub sold 512.26 MWh to the electricity grid and 149.4 m^3 to the water network.
- All operating parameters of the system (case 4) were improved by applying the AOA to solve the optimization problem. Total emissions and electrical/heat losses were reduced by 6.76%, 14.52%, and 2.34%, respectively, and total electrical demand, total SW, electrical power sold to the grid, and amount of water sold to the water network were increased by 4.06%, 20.49%, and 7.03%, respectively, compared to case 4 solved with GA.
- The number of emissions was converted to cost by using a penalty factor *h*. The aim was achieved and emissions were reduced, which in turn reduced all associated social and environmental aspects.

In future work, the problem must be represented as a long-term economic model with detailed modeling of the water distribution system, as well as taking into account the losses in the water system and all types of emissions.

Nomenclature

A. Abbreviations

AOA	Archimedes optimization algorithm
CHP	Combined heat and power
ED	Electric demand
EH	Energy hub
EHP	Electric heat pump
ES	Electric storage
ESS	Energy storage system
GA	Genetic algorithm
GAMS	General algebraic modeling language
GB	Gas boiler
HD	Heat demand
HOU	Heat only unit
HS	Heat storage
MILP	Mixed integer linear programming
MINLP	Mixed-integer nonlinear programming
NSGA-II	Non-dominated sorting genetic algorithm-II

C. Variables

PV	Photovoltaic
QPSO	Quantum Particle Swarm Optimization
RES	Renewable energy resource
SW	Social welfare
WD	Water desalination
WG	Water grid
WR	Water demand
WS	Water storage
WT	Wind turbine

B. Input values

$a_E, b_E, d_E, \gamma_E, \delta_E$	Emission coefficients of the thermal generators
a_G, b_G, c_G	Conventional generator cost coefficients
$a_{Co}, b_{Co}, c_{Co}, d_{Co}, e_{Co}, f_{Co}$	CHP generation cost coefficients
a_{EHP}	EHP unit cost coefficient (\$/MW)
a_{GB}	GB unit cost coefficient (\$/MW)
c	Form factor
$c_{p.W}, c_{p.PV}$	Over-estimation cost coefficient of WT and PV generators (\$/MW)
$c_{r.W}, c_{r.PV}$	Under-estimation cost coefficient of WT and PV generators (\$/MW)
C_{dsi}, C_{chi}	Discharging and charging cost of the ith ESSs (\$/MW)
COP	EHP coefficient of performance
d_W, h_{PV}	Operating cost of WT and PV generators (\$/MW)
DR_i, UR_i	Down-ramp rate and up-ramp rate limit of the ith unit
$E_{ESS_i}^{max}, E_{ESS_i}^{min}$	Maximum and minimum limit energy of ESSs (MWh)
$E_{ESS_i}^{ini}$	Initial energy of the ith ESSs (MWh)

$P_{CHP}^{max}, P_{CHP}^{min}$	Maximum and minimum power outputs of cogeneration generator (MW)
P_{EHP}^{max}	Maximum installed capacity of the EHP unit (MW)
P_{WD}^{max}	Maximum installed capacity of the WD unit (MW)
$Q_{CHP}^{max}, Q_{CHP}^{min}$	Maximum and minimum heat outputs of the CHP generator (MWth)
$Q_{HOU}^{max}, Q_{HOU}^{min}$	Maximum and minimum heat outputs of HOU (MWth)
Q_{EHP}^{max}	Maximum installed capacity of the EHP unit (MWth)
Q_{GB}^{max}	Maximum installed capacity of GB unit (MWth)
$S_{flow,i}^{max}$	Maximum apparent power flow limit in the ith line (MVA)
V_i^{max}, V_i^{min}	Maximum and minimum voltage limits of the ith bus (p.u)
$V_{HOU}, M_{HOU}, R_{HOU}$	Heat generation cost coefficients of HOU
v_i, v_o, v_r	Cut-in speed, cut-out speed, and rated speed (m/s)
γ_{GB}	GB coefficient of performance
η_{WD}	Performance coefficient of WD (m³/MW)
η_{PV}	PV cell efficiency
α, β	Beta *pdf* parameters
$\lambda_e, \lambda_h, \lambda_w$	Electrical, heat, and water consumed cost
$f_W(P_W), f_{PV}(P_{PV})$	Weibull *pdf* and beta *pdf* of WT and PV generator
$cost^{max}$	Highest predictable value of operating cost (\$)
C_{ESSi}	ESS power cost (\$)
C_{EHP}	Power absorbed by EHP cost (\$)
C_{GB}	Natural gas absorbed by GB cost (\$)
C_{HOU}	Produced heat by HOU cost (\$)
C_{WD}	Power absorbed by WD cost (\$)
C_{WG}	Total cost of water produced from WG (\$)
C_E	Corresponding cost of emissions (\$)
C_G	Total cost of power produced from grid (\$)
C_{CHP}	Total cost of energy produced from CHP (\$)
C_W, C_{PV}	Total cost of WT and PV generators (\$)
E_G	Total value of emissions (kg)
E_G^{max}	Highest estimated value for emissions (kg)
$G(t)$	Solar radiation at time t (kW/m²)
$P_{GB}(t)$	Quantity of natural gas absorbed by GB at time t (MW)
$P_{EHP}(t)$	EHP electrical energy produced (MW) at time t
$P_{WD}(t)$	Consumed electricity by WD (MW)
P_G	Power of the thermal generator (MW)
P_{CHP}, Q_{CHP}	Electrical and heating outputs of the CHP (MW/MWth)
P_W, P_{PV}	Scheduled output of WT and PV generator (MW)
P_{dsi}, P_{chi}	Discharging and charging power of the ith ESSs (MW)
P_{ES}	ES power (MW)
P_{loss}	Total power losses (MW)
$P_{i,t-1}$	Power of the ith unit at time $t-1$

$\hbar$	Penalty rate factor ($/kg)	$P_{i,t}$	Power of the ith unit at time t
k	Scale factor	Q_{HS}	Power of HS (MWth)
K_{WD}	WD unit cost coefficient ($/MW)	Q_{loss}	Heat loss (MWth)
K_{WG}	Cost coefficient of the WG ($/m^3)	$Q_{EHP}(t)$	EHP thermal energy produced at time t (MWth)
L, C, P	Output loads, coupling matrix, input energy carriers	$Q_{GB}(t)$	EHP thermal energy produced at time t (MWth)
P_{PVr}, P_{Wr}	PV and WT rated power (MW)	$S_{flow,i}$	Flow of apparent power in i^{th} line (MVA)
P_{PVav}, P_{Wav}	Available PV and WT power (MW)	$v(t)$	Actual wind speed at time t (m/s)
P_{ED}, Q_{HD}, W_{WR}	Electrical, heat, and water demand	W_{WG}	Volume of the water produced from the WG (m^3)
$P_{ESS_i}^{max}$, $P_{ESS_i}^{min}$	Maximum and minimum power limits of ESSs (MW)	$W_{WD}(t)$	Produced water by WD (m^3)
$P_{PV(K_{t\ max})}$	PV output power at maximum solar radiation (MW)	W_{WS}	Volume of water storage (m^3)

Appendix A

	Parameter	Unit	Value		Parameter	Unit	Value
CHP	a_{CO_i}	$	1250		a_G	$	550
	b_{CO_i}	$/MW	14.5	Grid	b_G	$/MW	8.1
	c_{CO_i}	$/MW^2	0.0345		c_G	$/MW^2	0.00028
	d_{CO_i}	$/MWth	4.2	HOU	R_{HOU}	$	100
	e_{CO_i}	$/MWth^2	0.03		M_{HOU}	$/MWth	0.1
	f_{CO_i}	$/MW.MWth	0.031		V_{HOU}	$/MWth^2	0.001
EHP	COP	-	2.5	WD	η_{WD}	m^3/MW	3.03
	P_{EHP}^{max}	MW	40		P_{WD}^{max}	MW	60
	a_{EHP}	$/MW	3.25		K_{WD}	$/MW	2.66
HS	η_{ch}	-	1	WG	K_{WG}	$/m^3	4
	η_{dis}	-	1	WS	η_{ch}	-	0.9
	E_{min}	MWhth	8		η_{dis}	-	0.9
	E_{max}	MWhth	60		Q_{min}	m^3/h	8
	E_{ini}	MWhth	12		Q_{max}	m^3/h	40
ES	η_{ch}	-	0.9		Q_{ini}	m^3/h	10
	η_{dis}	-	0.9				
	E_{min}	MWh	3.3				
	E_{max}	MWh	30				
	E_{ini}	MWh	3.3				

References

1. Mohamed, M.A.; Almalaq, A.; Mahrous Awwad, E.; El-Meligy, M.A.; Sharaf, M.; Ali, Z.M. An Effective Energy Management Approach within a Smart Island Considering Water-Energy Hub. *IEEE Trans. Ind. Appl.* **2020**, *9994*, 1–8. [CrossRef]
2. Jalili, M.; Sedighizadeh, M.; Sheikhi Fini, A. Optimal operation of the coastal energy hub considering seawater desalination and compressed air energy storage system. *Therm. Sci. Eng. Prog.* **2021**, *25*, 101020. [CrossRef]
3. Klemeš, J.J.; Van Fan, Y.; Jiang, P. COVID-19 pandemic facilitating energy transition opportunities. *Int. J. Energy Res.* **2021**, *45*, 3457–3463. [CrossRef] [PubMed]
4. Buheji, M.; da Costa Cunha, K.; Beka, G.; Mavrić, B.; Leandro do Carmo de Souza, Y.; Souza da Costa Silva, S.; Hanafi, M.; Chetia Yein, T. The Extent of COVID-19 Pandemic Socio-Economic Impact on Global Poverty. A Global Integrative Multidisciplinary Review. *Am. J. Econ.* **2020**, *10*, 213–224. [CrossRef]
5. Bilgen, S.; Keleş, S.; Sarikaya, I.; Kaygusuz, K. A perspective for potential and technology of bioenergy in Turkey: Present case and future view. *Renew. Sustain. Energy Rev.* **2015**, *48*, 228–239. [CrossRef]
6. Bhatia, S.C. *Advanced Renewable Energy Systems*; CRC Press: Boca Raton, FL, USA, 2014.
7. Sani, M.M.; Sani, H.M.; Fowler, M.; Elkamel, A.; Noorpoor, A.; Ghasemi, A. Optimal energy hub development to supply heating, cooling, electricity and freshwater for a coastal urban area taking into account economic and environmental factors. *Energy* **2022**, *238*, 121743. [CrossRef]
8. Mansouri, S.A.; Javadi, M.S.; Ahmarinejad, A.; Nematbakhsh, E.; Zare, A.; Catalao, J.P. A coordinated energy management framework for industrial, residential and commercial energy hubs considering demand response programs. *Sustain. Energy Technol. Assess.* **2021**, *47*, 101376. [CrossRef]
9. Xu, X.; Hu, W.; Liu, W.; Du, Y.; Huang, R.; Huang, Q.; Chen, Z. Look-ahead risk-constrained scheduling for an energy hub integrated with renewable energy. *Appl. Energy* **2021**, *297*, 117109. [CrossRef]
10. Karkhaneh, J.; Allahvirdizadeh, Y.; Shayanfar, H.; Galvani, S. Risk-constrained probabilistic optimal scheduling of FCPP-CHP based energy hub considering demand-side resources. *Int. J. Hydrogen Energy* **2020**, *45*, 16751–16772. [CrossRef]
11. Shahinzadeh, H.; Moradi, J.; Gharehpetian, G.B.; Abedi, M.; Hosseinian, S.H. Multi-Objective Scheduling of CHP-Based Microgrids with Cooperation of Thermal and Electrical Storage Units in Restructured Environment. In Proceedings of the 2018 Smart Grid Conference (SGC), Sanandaj, Iran, 28–29 November 2018; pp. 1–10. [CrossRef]

12. Moradi, S.; Ghaffarpour, R.; Ranjbar, A.M.; Mozaffari, B. Optimal integrated sizing and planning of hubs with midsize/large CHP units considering reliability of supply. *Energy Convers. Manag.* **2017**, *148*, 974–992. [CrossRef]

13. Zafarani, H.; Taher, S.A.; Shahidehpour, M. Robust operation of a multicarrier energy system considering EVs and CHP units. *Energy* **2020**, *192*, 116703. [CrossRef]

14. Rastegar, M.; Fotuhi-Firuzabad, M.; Lehtonen, M. Home load management in a residential energy hub. *Electr. Power Syst. Res.* **2015**, *119*, 322–328. [CrossRef]

15. Xie, S.; Wang, X.; Qu, C.; Wang, X.; Guo, J. Impacts of different wind speed simulation methods on conditional reliability indices. *Int. Trans. Electr. Energy Syst.* **2015**, *25*, 359–373. [CrossRef]

16. Davatgaran, V.; Saniei, S.; Mortazavi, S.S. Optimal bidding strategy for an energy hub in energy market. *Energy* **2018**, *148*, 482–493. [CrossRef]

17. Zhang, L.; Zhu, Y. Modeling of CHP-EHP coupled energy station considering load side flexibility. In Proceedings of the IEEE International Conference on Energy Internet, ICEI 2019, Nanjing, China, 21–31 May 2019; pp. 71–74. [CrossRef]

18. Mirhedayati, A.S.; Shahinzadeh, H.; Nafisi, H.; Gharehpetian, G.B.; Benbouzid, M.; Shaneh, M. CHPs and EHPs Effectiveness Evaluation in a Residential Multi-Carrier Energy Hub. In Proceedings of the 2021 25th Electrical Power Distribution Conference (EPDC), Karaj, Iran, 18–19 May 2021; pp. 42–47. [CrossRef]

19. Nosratabadi, S.M.; Jahandide, M.; Guerrero, J.M. Robust scenario-based concept for stochastic energy management of an energy hub contains intelligent parking lot considering convexity principle of CHP nonlinear model with triple operational zones. *Sustain. Cities Soc.* **2020**, *68*, 102795. [CrossRef]

20. Tay, Z.X.; Lim, J.S.; Alwi, S.R.W.; Manan, Z.A. Optimal Planning for the Cogeneration Energy System using Energy Hub Model. *Chem. Eng. Trans.* **2021**, *88*, 349–354. [CrossRef]

21. Shahrabi, E.; Hakimi, S.M.; Hasankhani, A.; Derakhshan, G.; Abdi, B. Developing optimal energy management of energy hub in the presence of stochastic renewable energy resources. *Sustain. Energy Grids Netw.* **2021**, *26*, 100428. [CrossRef]

22. Teng, Y.; Sun, P.; Leng, O.; Chen, Z.; Zhou, G. Optimal Operation Strategy for Combined Heat and Power System Based on Solid Electric Thermal Storage Boiler and Thermal Inertia. *IEEE Access* **2019**, *7*, 180761–180770. [CrossRef]

23. Zhou, Y.; Cao, S. Quantification of energy flexibility of residential net-zero-energy buildings involved with dynamic operations of hybrid energy storages and diversified energy conversion strategies. *Sustain. Energy Grids Netw.* **2020**, *21*, 100304. [CrossRef]

24. Zhang, H.; Cao, Q.; Gao, H.; Wang, P.; Zhang, W.; Yousefi, N. Optimum design of a multi-form energy hub by applying particle swarm optimization. *J. Clean. Prod.* **2020**, *260*, 121079. [CrossRef]

25. Wang, J.; Liu, Y.; Ren, F.; Lu, S. Multi-objective optimization and selection of hybrid combined cooling, heating and power systems considering operational flexibility. *Energy* **2020**, *197*, 117313. [CrossRef]

26. Ren, F.; Wang, J.; Zhu, S.; Chen, Y. Multi-objective optimization of combined cooling, heating and power system integrated with solar and geothermal energies. *Energy Convers. Manag.* **2019**, *197*, 111866. [CrossRef]

27. Shahzad, M.W.; Burhan, M.; Ng, K.C. Pushing desalination recovery to the maximum limit: Membrane and thermal processes integration. *Desalination* **2017**, *416*, 54–64. [CrossRef]

28. Nazari-Heris, M.; Mohammadi-Ivatloo, B.; Asadi, S. Optimal operation of multi-carrier energy networks with gas, power, heating, and water energy sources considering different energy storage technologies. *J. Energy Storage* **2020**, *31*, 101574. [CrossRef]

29. Ramos-Teodoro, J.; Gil, J.D.; Roca, L.; Rodríguez, F.; Berenguel, M. Optimal water management in agro-industrial districts: An energy hub's case study in the southeast of Spain. *Processes* **2021**, *9*, 333. [CrossRef]

30. Mokaramian, E.; Shayeghi, H.; Sedaghati, F.; Safari, A. Four-Objective Optimal Scheduling of Energy Hub Using a Novel Energy Storage, Considering Reliability and Risk Indices. *J. Energy Storage* **2021**, *40*, 102731. [CrossRef]

31. Mostafavi Sani, M.; Noorpoor, A.; Shafie-Pour Motlagh, M. Optimal model development of energy hub to supply water, heating and electrical demands of a cement factory. *Energy* **2019**, *177*, 574–592. [CrossRef]

32. Eladl, A.A.; El-Afifi, M.I.; Saeed, M.A.; El-Saadawi, M.M. Optimal operation of energy hubs integrated with renewable energy sources and storage devices considering CO_2 emissions. *Int. J. Electr. Power Energy Syst.* **2019**, *117*, 105719. [CrossRef]

33. Geidl, M. Integrated Modeling and Optimization of Multi-Carrier Energy Systems. Ph.D. Thesis, ETH Zurich, Zurich, Switzerland, 2007.

34. Hasankhani, A.; Hakimi, S.H. Stochastic energy management of smart microgrid with intermittent renewable energy resources in electricity market. *Energy* **2021**, *219*, 119668. [CrossRef]

35. Mokaramian, E.; Shayeghi, H.; Sedaghati, F.; Safari, A.; Alhelou, H.H. A CVaR-Robust-based multi-objective optimization model for energy hub considering uncertainty and E-fuel energy storage in energy and reserve markets. *IEEE Access* **2021**, *9*, 109447–109464. [CrossRef]

36. Eladl, A.A.; ElDesouky, A.A. Optimal economic dispatch for multi heat-electric energy source power system. *Int. J. Electr. Power Energy Syst.* **2018**, *110*, 21–35. [CrossRef]

37. Neves, D.; Silva, C.A. Modeling the impact of integrating solar thermal systems and heat pumps for domestic hot water in electric systems—The case study of Corvo Island. *Renew. Energy* **2014**, *72*, 113–124. [CrossRef]

38. Damodaran, S.K.; Kumar, T.K.S. Economic and emission generation scheduling of thermal power plant incorporating wind energy. In Proceedings of the IEEE Region 10 International Conference TENCON, Penang, Malaysia, 5–8 November 2017; pp. 1487–1492. [CrossRef]

39. Hetzer, J.; David, C.Y.; Bhattarai, K. An economic dispatch model incorporating wind power. *IEEE Trans. Energy Convers.* **2008**, *23*, 603–611. [CrossRef]

40. Wang, Z.; Zhong, J.; Chen, D.; Lu, Y.; Men, K. A multi-period optimal power flow model including battery energy storage. *IEEE Power Energy Soc. Gen. Meet.* 2013. [CrossRef]

41. Najafi, A.; Falaghi, H.; Contreras, J.; Ramezani, M. Medium-term energy hub management subject to electricity price and wind uncertainty. *Appl. Energy* **2016**, *168*, 418–433. [CrossRef]

42. Zhang, G.; Hu, W.; Cao, D.; Liu, W.; Huang, R.; Huang, Q.; Blaabjerg, F. Data-driven optimal energy management for a wind-solar-diesel-battery-reverse osmosis hybrid energy system using a deep reinforcement learning approach. *Energy Convers. Manag.* **2020**, *227*, 113608. [CrossRef]

43. Hashim, F.A.; Hussain, K.; Houssein, E.H.; Mabrouk, M.S.; Al-Atabany, W. Archimedes optimization algorithm: A new metaheuristic algorithm for solving optimization problems. *Appl. Intell.* **2021**, *51*, 1531–1551. [CrossRef]

44. Houssein, E.H.; Helmy, B.E.D.; Rezk, H.; Nassef, A.M. An enhanced Archimedes optimization algorithm based on Local escaping operator and Orthogonal learning for PEM fuel cell parameter identification. *Eng. Appl. Artif. Intell.* **2021**, *103*, 104309. [CrossRef]

Article

Experimental Investigation on Performance Enhancement of Parabolic Trough Concentrator with Helical Rotating Shaft Insert

Mohamed Allam [1,2], Mohamed Tawfik [2,*] , Maher Bekheit [2] and Emad El-Negiry [2]

[1] Misr International Technological University MITU, Cairo 11725, Egypt
[2] Mechanical Power Engineering Department, Faculty of Engineering, Mansoura University, Mansoura 35516, Egypt
* Correspondence: m_tawfik@mans.edu.eg

Abstract: The parabolic trough collector provides an extensive range of solar heating and electricity production applications in solar power plants. The receiver tube of the parabolic trough collector has a vital role in enhancing its performance by using different inserts inside it. In the present work, outdoor experimental tests were conducted to study the performance of a small-scale parabolic trough collector equipped with a centrally placed rotating helical shaft. Three cases were studied: a parabolic trough collector without helical shaft insert, a parabolic trough collector with stationary helical shaft insert, and a parabolic trough collector with a rotating helical shaft insert. The experiments are performed for different shaft rotational speeds (4, 11, and 21 RPM) and various flow rates (0.5, 1, 1.5, 2, and 2.5 LPM) of water as a heat transfer fluid. The fluid flow and heat transfer parameters (friction factor, Reynolds number, Nusselt number, and thermal enhancement factor) and performance parameters (thermal, overall, and exergetic efficiencies) are studied. The results indicated that the helical shaft insert had increased the required pumping power for the same flow rate. However, the parabolic trough collector thermal performance has enhanced with the shaft rotational speed. For all cases, the parabolic trough collector efficiency increases with the flow rate of the heat transfer fluid, but the percentage enhancement in efficiency decreases. Using a shaft rotational speed of 21 RPM and heat transfer fluid flow rates of 0.5 LPM leads to maximum thermal efficiency enhancement and a maximum friction factor ratio of 46.47% and 7.7 times, respectively, compared to plain tube. A comparison based on the same pumping power (thermal enhancement factor) shows that the maximum enhancement occurs at a flow rate of 1 LPM, and the efficiency enhancement is about 37% at a shaft rotational speed of 21 RPM. From an economic point of view, using a rotating helical shaft produces the lower annual cost of useful heat per kWh.

Keywords: solar concentrator; thermal; inserts; helical rotating shaft; active methods

1. Introduction

Fossil fuel consumption still significantly contributes to energy demand worldwide, so pollution and global warming have become critical problems [1]. At the same time, from 2003 to 2030, worldwide energy consumption is expected to grow by 71% [2]. Therefore, researchers try to address this issue using renewable energy sources, which may offer a solution. Solar thermal power is one of the valuable alternatives for reducing fossil fuel use, reducing greenhouse gases, and satisfying human needs. The concentrated solar power (CSP) technology is classified as line focus or point focus based on the receiving mechanism. The line focus systems include linear Fresnel reflectors and the parabolic trough, while the point focus systems include the parabolic dish, solar tower, and beam-down central receivers [3,4].

The most often applied technique in solar plants to produce electricity and in industrial and thermal processes is the parabolic trough collector (PTC) [5,6]. The concentrator and

the receiver tube are significant components of the solar field. The reflector surface of the concentrator reflects solar rays onto the receiving tube, which converts solar power into heat transmitted to the heat transfer fluid (HTF), such as air, water, or oil [7]. The receiver comprises a selective-coated metallic tube to enhance the absorption of solar irradiance. In addition, the entire tube is enveloped with a vacuumed glass tube with an anti-reflective coating to minimize heat loss by convection [8]. The most critical component of the PTC is the receiver tube, whose performance directly reflects the PTC thermal efficiency. The higher surface temperature of the receiver tube is the major problem that leads to uneven temperature distribution over the receiver. Thus, thermal stresses and losses of the receiver tube increase [9]. Therefore, the thermal efficiency decreases. Because of this, researchers have investigated ways to boost the heat transfer rate within the receiver to improve the PTC thermal performance.

Three techniques enhance heat transfer: passive, active, and compound [10]. The first technique is the passive method that does not consume energy, and the heat transfer rate can be augmented by inserting various inserts inside the receiver tube with a particular engineering design or modifying the entire receiver tube surface. The second technique is the active method, such as surface vibration and magnetic fields, which requires external energy to change the path of HTF to improve the heat transfer rate. Finally, the third technique is the compound method, which combines active and passive methods [11,12]. Low cost and simplicity are why different inserts inside the receiver tube make it the most common ordinary technique to improve heat transfer rate [13].

Using inserts inside the receiver tube augments the velocity fluctuation by forcing the flow beside the tube wall to mix within the flow at core regions [7], enhancing the heat transfer coefficient. Such enhancement reduces thermal losses of the receiver tube and temperature gradient, leading to enhanced thermal efficiency [11], while the significant penalty increases the cost of pumping power through the pressure drop increase [14]. Twisted tape, wire coils, porous inserts, fins, cylindrical/rods, rings, and other insert configurations represent the most common inserts [15]. Twisted tapes are the most often used insert to increase the swirling of the HTF flow to boost the thermal performance [16] and have been investigated in studies [17–24], as introduced in the following paragraphs.

Waghole and Shrivastva [17] assessed the influence of twisted tape within a PTC receiver with twisted ratios of 0.577, 1, and 1.732. Water and silver nanofluid were selected as HTFs under Re numbers (500–6000). Their results showed a rise in thermal efficiency, friction factor, and Nu number of 135–205%, 1–1.75 times, and 1.25–2.1 times, respectively, higher than expected by the conventional receiver. Furthermore, the water friction factor and heat transfer coefficient are lower than silver nanofluid of 0–0.1% volume concentration.

Nakhchi et al. [19] experimentally tested the thermal performance within a pipe with twisted tape inserts with double-cut. Water is chosen as the HTF under the Re numbers range (5000–15,000). The friction factors and Nusselt numbers were increased up to 489% and 177.4%, respectively, for pipes fitted with twisted tapes with a cut ratio of 0.90, compared to the typical tube.

Arunachala [20] experimentally analyzed the PTC performance when equipped with twisted tape and using SYLTHERM 800 as an HTF under Re numbers range of 544–1742 and the twisting ratio of 5.2, 4.1, and 2.7; then, they compared the results with an analytical model. Results showed that, at a minimum twisted ratio of 2.7, the maximum thermal efficiency of 40% is achieved, compared to 19.1% for a plain tube, while the thermo-hydraulic efficiency was decreased to 39.7% because of the increase in pressure drop.

Hosseinalipour et al. [21] numerically investigated decreasing temperature differences within a PTC receiver using a twisted tape insert. The investigation considered superheated steam as HTF with a Re number range (10^4–9.79×10^5) and used different twist ratios (2.5, 5, and 10) and various clearance ratios (0, 0.2, 0.3, 0.4, and 1). The results revealed friction factors and Nu number increases of 1.8–4.1 and 1.0–1.7, respectively. Moreover, the temperature differential over the circumference was reduced by 10–45%.

Elton and Arunachala [22] developed a correlation for the Nu number with twisted tape presence and absence. In addition, they used Soltrace to simulate non-uniform solar radiation. THERMINOL VP-1 was considered HTF and a range of Re numbers varying between (2300–2500). They found that the error in the developed correlations for standard and modified tubes lies within a range (±19% and ±20%), respectively.

Ghadirijafarbeigloo et al. [23] numerically investigated twisted louvered tapes and compared the findings with typically twisted tape inserts at various twisting ratios of 2.67, 4, and 5.33. BEHRAN thermal oil was applied as an HTF. In their study, the Re number range was (5000–25,000). They observed that twisted louvered tape had better thermal performance than standard twisted tape. A 210% and 150% increase in friction factor and Nu number was also found when the twisted louvered tape was used.

Song et al. [24] numerically studied using a helical insert and its impact on the PTC receiver thermal performance. First, they employed the Monte Carlo ray-tracing (MCRT) method to model the heat flux distribution over the receiver wall. Next, DOWTHERM-A was considered an HTF within a range of Re number (10,000–75,000) and inlet temperature (373–640 K). They found that at rates of mass flow of 0.11 and 0.6 kg/s, the heat losses were reduced by six and three times, fitting the helical insert. Moreover, a helical screw insert led to a pressure drop increase of 23 times.

Shashank and Sarviya [18] experimentally and numerically investigated the influence of double and single helical inserts with the various twisted ratios of 1.5, 2.5, and 3 inside tubes. They selected water as an HTF with different Re numbers (4000–16,000). They observed that the double-helical insert's Nu number and friction factor were higher than the single helical insert. Moreover, at a low twisted ratio, the maximum enhancement of Nu number was 112% for a double helical insert compared to an empty tube with an average friction factor of 9.1. Finally, the optimum value of entropy production number was achieved for double helical insert compared to single helical insert.

Another method to improve the thermal performance is rotating twisted tapes within the tube. This method was analyzed experimentally by Abdullah et al. [25]. The different twisted tape ratios and variable operating rotational speeds, under constant heat flux with air as HTF and three Re numbers 8000, 10,000, and 13,000. They observed a thermal enhancement for tubes with twisted rotational tape than tubes with fixed insert. Furthermore, the higher twisted tape rotational speed and lower twisted ratio demonstrated improved thermal performance with a higher friction factor.

Cong et al. [26] experimentally studied the flow characteristic and thermal performance of a tube with a stationary twisted tape and a rotating one at 4 RPM with TiO_2-water nanofluid as an HTF. In addition, different Re numbers from 600 to 7000 and different mass fractions of nanoparticles of 0.1%, 0.3%, and 0.5% were studied. They observed that using the applied nanofluid with rotating twisted tape improved the thermal performance by 53.1–101.6%. Furthermore, the exergy efficiency of the stationary twisted tape was increased compared to the plain tube case under similar pumping power. On the other hand, it can be reduced by using the combination of nanofluids and rotating twisted tape.

Pavan et al. [27] investigated experimentally using rotating twisted tape of twisted ratio 2.37 within a tube. Under constant heat flux affecting the tube, water-CuO nanofluid of 0.2% volume concentration was used as HTF for different twisted tape rotational speeds and flow rates. It was concluded that, at a higher rotational speed of 300 RPM, the highest increase in heat transfer coefficient was 347% while using rotating twisted tape and nanofluid together, compared with plain tube, but the friction factor was increased 3.3 times. Other researchers used different types of inserts or compared them to increase the heat transfer performance.

Promvonge [28] experimentally studied thermal performance enhancement in tubes supplied with twisted tapes and wire coils. The applied HTF was the air with Re numbers (3000–18,000) under constant heat flux. The experiment included wire coils with different pitch ratios and twisted tapes with various twist ratios. They observed a double rise in heat transfer when using twisted tapes with wire coils compared to twisted tape or wire

coils. They also observed that using wire coils and twisted tapes with a lower twist ratio and pitch could enhance thermal performance.

Varun et al. [29] compared the PTC performance with a wire matrix and twisted tape. The variable solar irradiance was simulated using the SOLTRACE software program. Two twisted tapes were presented with twisted ratios of 3.37 and 7.86, while three different configurations of wire matrices were presented. The selected HTF was SYNTHETIC oil under the Re number range of 1200–8200 and varying irradiation from 450 to 800 W/m^2. The experimental work showed that the augmentation in thermal efficiency for both twisted tape of 3.37 and medium dense wire matrix were 15.5% and 55.5%, respectively, with a comparable rise in pressure drop of 242% and 3602%, respectively. Regarding performance evaluation criterion analysis, the twisted tape of 3.37 is higher, whereas, in thermo-hydraulic analysis, the medium dense wire matrix is higher.

Other inserts were used to enhance heat transfer; Chakraborty et al. [30] utilized a helical coil within the receiver of a PTC. They simulated the cases using the ANSYS software for pure water mass flow rates (0.016–0.033 kg/s). The exergy and thermal efficiency were increased by 2.4–3.3% and 10–16%, respectively, when helical coils were inserted within the receiver, despite the increased pumping power. Zhao et al. [31] experimentally studied using pin fines within the PTC receiver tube, with air as an HTF for Re number range of 40,000–60,000. It can be concluded from the obtained results that PTC fitted with pin fines enhanced both exergy and energy efficiency by 2.55–4.29% and 10.4–14.5% in comparison with the plain receiver, while the pressure losses were increased about 10–20 times.

The use of metal foam within a PTC receiver was examined experimentally by Jamal-Abad et al. [32] using water as HTF at various Re numbers ranging from 750 to 2000. Results illustrated that using the receiver with metal foam resulted in Nu number and thermal efficiency increase by 1.01–1.80 and 1.03 to 1.08, respectively. Furthermore, the friction factor was intensified. The overall loss coefficient was reduced, which boosted the PTC thermal efficiency. The current study investigates the effect of rotating helical shaft within a PTC receiver using outdoor experimental work with water as HTF. The experimental work is performed for different shaft rotational speeds and flow rates. According to the literature, using a rotating helical shaft inside the PTC receiver as an enhanced insert has not been investigated before. Three cases are compared and studied: a PTC without insert, a PTC with the stationary helical shaft, and a PTC with the rotating helical shaft, to determine the optimum case with better heat transfer performance with a low penalty on pressure drop. The primary criteria for evaluating the examined cases depend on fluid flow, heat transfer, and performance parameters. Finally, an economic analysis is carried out to specify the benefits of the proposed systems from an economic point of view.

2. Materials and Methods

2.1. Experimental Test Rig

The experimental test rig was designed mainly to study the PTC performance with a helical shaft rotating centrally inside the receiver. An experimental test rig of PTC is shown in Figure 1, while its schematic diagram is illustrated in Figure 2. The main elements of the test rig comprise a PTC, a solar tracking mechanism, and measuring instruments.

(1)	Acrylic reflector sheet	(2)	Receiver tube	(3)	LDR sensor	(4)	Pressure gauge
(5)	Linear actuator	(6)	DC motor gearbox	(7)	Coupling	(8)	Storage water tank
(9)	Flowmeter	(10)	Drain tube	(11)	Bypass valve	(12)	Circulation pump
(13)	DC motor control circuit	(14)	ARDUINO circuit	(15)	Batteries	(16)	Data logger
(17)	Laptop						
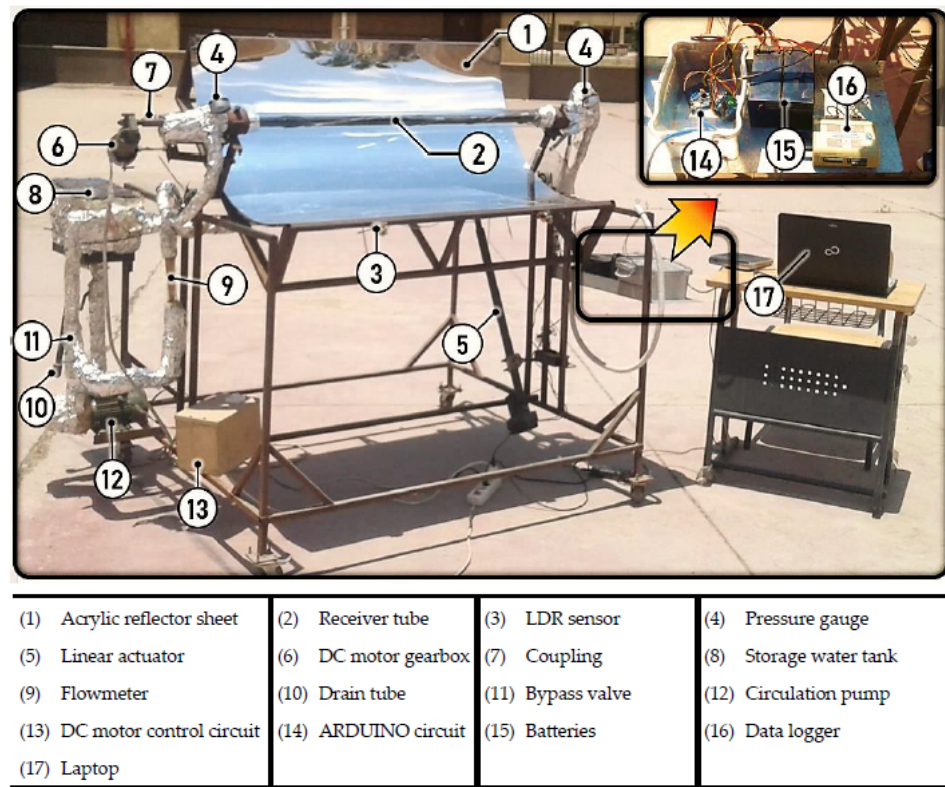
Figure 1. Experimental test rig of PTC.

(1)	Acrylic reflector sheet	(2)	Glass tube	(3)	LDR sensor	(4)	Pressure gauge
(5)	Copper tube	(6)	DC motor gearbox	(7)	Coupling	(8)	Storage water tank
(9)	Flowmeter	(10)	Bypass valve	(11)	Drain valve	(12)	Circulation pump
(13)	Flow control valve	(14)	ARDUINO circuit	(15)	Exit valve	(16)	Data logger
(17)	Laptop	(18)	Inlet temperature sensor	(19)	Outlet temperature sensor	(20)	Inside tank temperature sensor
(21)	Temperature sensors (T1–T16)	(22)	Ambient temperature sensor	(23)	Solar power meter	(24)	Helical shaft

Figure 2. The experimental test rig schematic diagram.

2.1.1. Parabolic Trough Solar Collector

The PTC comprises two main components, reflector and receiver.

The Reflector

A 2-mm-thick acrylic mirror sheet was used as a reflector, which can resist outdoor conditions, including heat, cold, and dampness, besides their lightweight and easy to fabricate. The solar-weighted spectral reflectance was tested using a JASCO V-570 Spectrophotometer. The results are plotted in Figure 3, which indicates an average solar weighted solar reflectance of 0.84. The reflector was designed in a parabola shape using two parameters of aperture width (*W*) and focal distance (*F*), as shown in Figure 4. The reflector sheet was fixed onto a 1.5-mm-thick steel sheet attached to three steel ribs to increase resistance against the wind load.
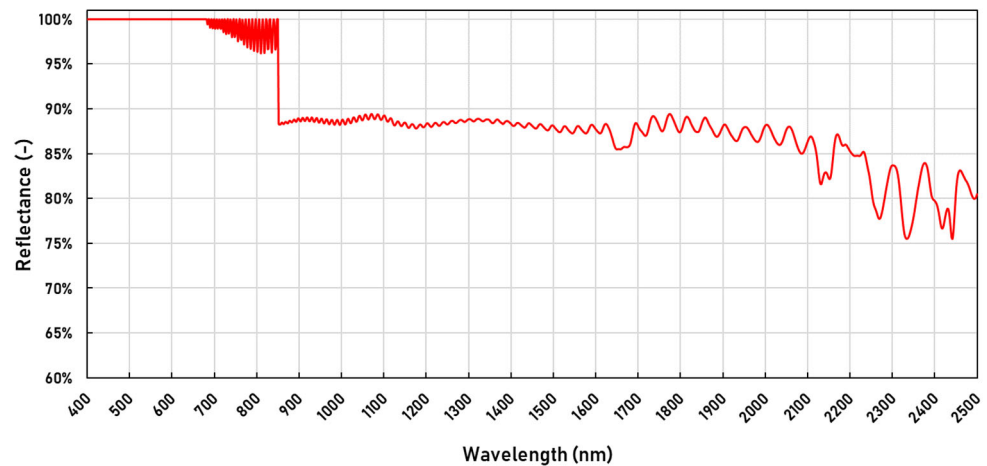
Figure 3. The spectral reflectance of the acrylic mirror sheet.
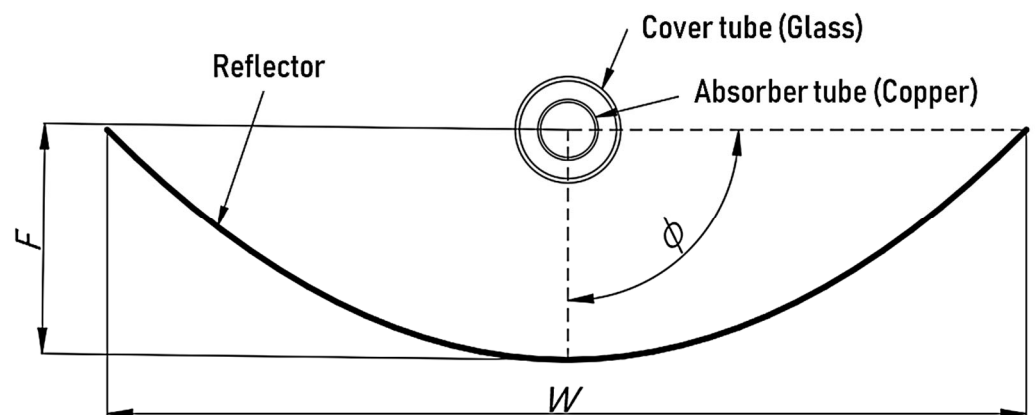
Figure 4. The characteristic dimensions of the tested PTC.

The width of the aperture, *W*, of the parabola and its focal length, *F*, are determined using the following Equations [33,34]:

$$W = \frac{2\,S\tan(0.5\phi)}{[sec(0.5\phi) + tan(0.5\phi) + ln(sec(0.5\phi) + tan(0.5\phi))]} \tag{1}$$

$$F = \frac{W}{4\,tan(0.5\phi)} \tag{2}$$

where ϕ is the rim angle, and *S* is the acrylic mirror width (arc length). The following equations were used to assess the correctness of the parabola drawing [35]:

$$y = \frac{x^2}{4F} \tag{3}$$

The concentration ratio, *C*, representing the concentrator aperture area to the receiver areas, is given by [36,37]:

$$C = \frac{W}{\pi D_o} \quad (4)$$

Specifications of the reflector are provided in Table 1

Table 1. Specification of the reflector.

Parameter	Value
Aperture width, W	0.871 m
The parabolic trough length, L	1.200 m
Aperture area, A_a	1.050 m^2
Rim angle, ϕ	90°
Focal line distance, F	0.218 m
wide of mirror acrylic sheet, S	1.000 m
Reflector sheet thickness, t	0.002 m
Reflectance of the mirror, ρ	0.840
The concentration ratio, C	11.70

The Receiver

The receiver is the most critical PTC component, directly affecting PTC performance. It was a black-painted red copper tube to enhance solar radiation absorbtance. It was enveloped by a borosilicate glass cylinder to prevent heat loss by convection, with a transmittance of 0.90 [38]. Specification of the receiver tube is given in Table 2. A representation of the receiver tube is demonstrated in Figure 5.

Table 2. Specification of the receiver tube.

Parameter	Value
Receiver absorptivity, α [39]	0.92
Copper tube length, L_c	1440 mm
Copper tube inside diameter, D_i	26.4 mm
Copper tube outside diameter, D_o	28.6 mm
Glass cover inside diameter, D_{gi}	54 mm
Glass cover outside diameter, D_{go}	60 mm
Glass tube length, L_g	1100 mm
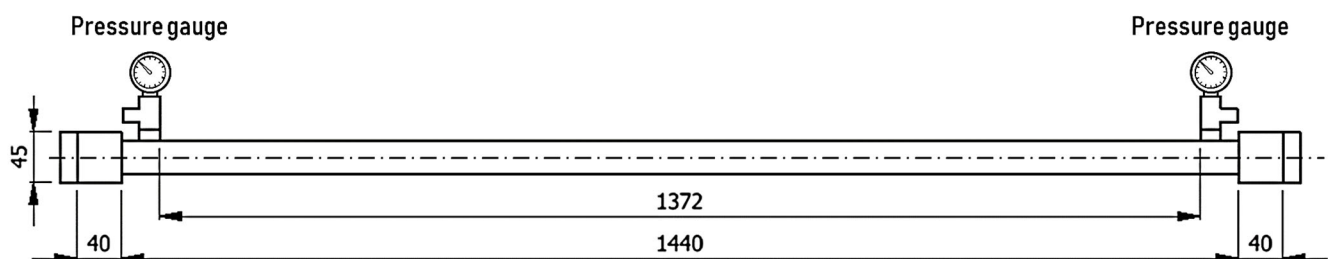
Figure 5. The receiver tube schematic diagram, dimensions in mm.

The Helical Shaft

Steel was selected as shaft material for its high strength, elasticity, and ability to withstand machining. Dimensions of the helical shaft are shown in Figure 6. The helical shaft was immersed in a nickel-chrome basin to prevent corrosion during experimental work. The two sides of the shaft were fixed onto an oil seal ring that bears a high temperature of 250 °C to prevent HTF leakage. Specification of the helical shaft is given in Table 3. DC motor gearbox of 24 V and 50 RPM was used to rotate the shaft at variable speeds of 4, 11, and 21 RPM, and it was connected to the shaft through a coupling and was fixed to the PTC structure.
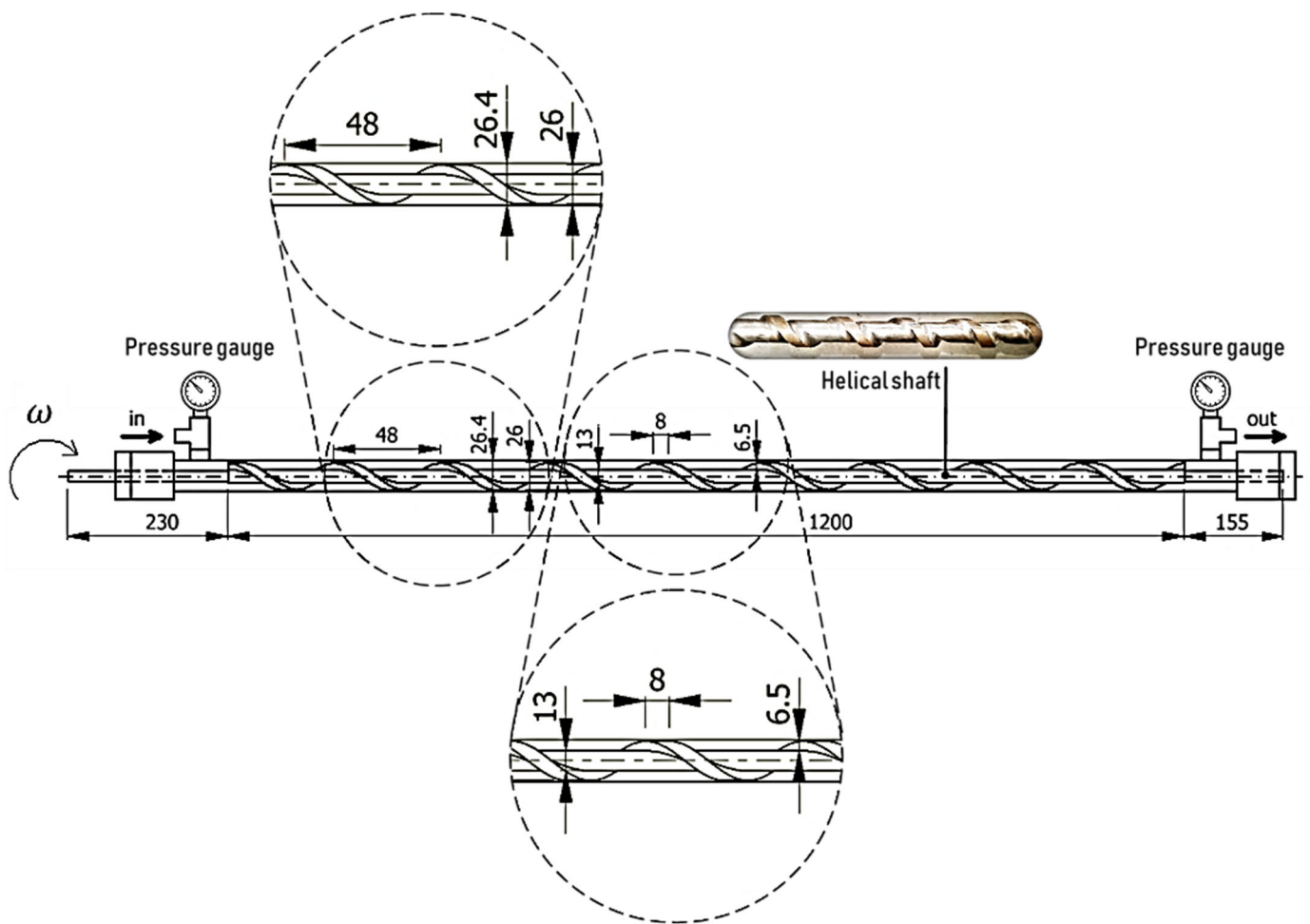
Figure 6. Longitudinal section of the helical shaft inside the receiver tube, dimensions in mm.

Table 3. Specification of the helical shaft.

Parameter	Value
The total length of the helical shaft, L_h	1585 mm
length of the helical section, l_h	1200 mm
Diameter of the helical shaft, D_h	26 mm
Pitch length of the helical shaft, p_h	48 mm
The thickness of the tooth, t_h	8 mm
Height of the tooth. H_h	6.5 mm

2.1.2. The Sun Tracking Mechanism

The PTC tracks the sun using a single-axis tracking approach where the tracking axis can be positioned in the East-West or the North-South directions. Since the North-South sun-tracking axis provides more solar energy yearly than the East-West sun-tracking axis [40], the collector was oriented to rotate about a horizontal North-South axis. The tracking mechanism consists of four light-dependent resistors (LDRs), detecting the solar irradiation and instructing the linear actuators through an Arduino circuit to track the sun.

2.1.3. The Measuring Instruments

The test rig was equipped with the following measuring instruments:

- Four K-type thermocouples with an accuracy of (± 0.1 °C) were calibrated and employed to detect the HTF and ambient temperatures. Two were located at the receiver tube entrance and exit, one in the HTF tank and one in the ambient atmosphere.

- The average receiver surface temperature was determined by placing sixteen calibrated thermocouples on the copper tube's outer surface in circular and longitudinal directions, as illustrated in Figure 7. The thermocouples were connected to a data logger recording the measured values with a range of (-129–$1372\ ^{\circ}$C).
- A digital portable solar power meter was used to measure the beam solar radiation at normal incidence through a scale of (1–1999 W/m^2) with an accuracy of (± 10 W/m^2).
- A rotameter was employed to measure the volume flow rate with a scale of (0.5–4 LPM) and accuracy ($\pm 4\%$ full scale) installed at the pump downstream.
- Since the HTF pressure is inversely proportional to the flow rate, three couples of pressure gauges were used to measure the pressure with an accuracy of ($\pm 1\%$ full scale). Two pressure gauges were located at the receiver tube inlet and outlet to evaluate the pressure drop across the receiver under technical data and operating conditions listed in Table 4. The third couple of pressure gauge monitored the HTF pressure over the outdoor tests to maintain the HTF temperature below its saturation point to maintain the HTF in the liquid state.
- A digital multimeter (40 mA–10 A) was used to measure the DC motor power consumption with an accuracy of ($\pm 0.8\% + 3$).
- A digital tachometer measured the helical shaft rotating speed with a scale of (2–20,000 RPM) and accuracy ($\pm 0.05\% + 1$ digits).

Table 4. Specification of pressure gauges used and operating conditions.

Gauge Number	Range (Pa)	Resolution (Pa)	Range of Flow Rates (LPM) *
1	2500	50	0.5–1.0 (indoor tests)
2	16,000	100	1.5–2.5 (indoor tests)
3	250,000	10,000	0.5–2.5 (outdoor tests)

* The range of flow rates where the gauge is used to determine the pressure drop over the receiver.
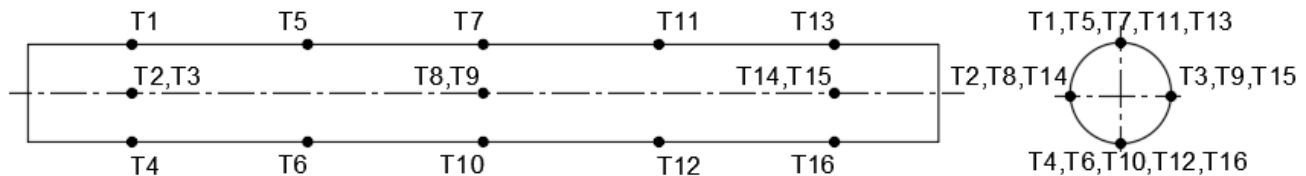
Figure 7. Thermocouple distribution over the copper tube surface.

2.1.4. System Operation

The outdoor experiments were conducted at Integrated Technical Education Institute, Cairo, Egypt. The latitude and the longitude of Cairo city are $30^{\circ}02'$ N and $31^{\circ}14'$ E, respectively. Using a linear actuator, the PTC axis was oriented to the North-South. The solar radiation HTF temperatures at the tank, ambient, test section inlet, and outlet were continuously detected and recorded. Over twenty-five clear days, within June, July, and August, the measured data were recorded every 15 min from 10:00 to 16:30. The irradiation over all experiments ranged from 600 to 1200 W/m^2. A 225 W pump circulated the HTF between the tank and the test section. After the HTF temperature increased in the receiver tube, the hot HTF was returned to the tank and then to the tube in a closed-loop cycle. The HTF flow rate was varied to obtain five variable flow rates of 0.5, 1, 1.5, 2, and 2.5 LPM using ball valves located at the inlet and exit of the HTF stream. DC motor rotational speeds (4, 11, and 21 RPM) were used.

2.2. Governing Equations

2.2.1. Friction Coefficient Evaluation

For Plain Receiver Tube

The average velocity (U_{av}) and Reynolds number (Re) are given as [6]:

$$U_{av} = \frac{\dot{V}}{\frac{\pi}{4}D_i^2} \tag{5}$$

$$\text{Re} = \frac{U_{av}\,D_i}{v} \tag{6}$$

For the Receiver with Helical Shaft Insert

U_{av} and Re are determined based on the measured flow rate according to the equivalent hydraulic diameter, D_{eq}. Where D_{eq} is evaluated experimentally by measuring the HTF volume, V, required to fill the entire length of the copper tube, L_c with the helical shaft insert as follows [41]:

$$V = \pi/4\,D_{eq^2}\ \times\ L_c \tag{7}$$

$$D_{eq} = (4V/\pi L_c)^{0.5} \tag{8}$$

The Re number of the flow within a tube is estimated as follows [42]:

$$\text{Re} = \frac{U_{av}\,D_{eq}}{v} \tag{9}$$

where v is the kinematic coefficient of viscosity of water and U_{av} is the average velocity in the receiver tube with helical shaft insert; determined from as:

$$U_{av} = \frac{\dot{V}}{\frac{\pi}{4}D_{eq}^2} + Np \tag{10}$$

where $\dot{V}$ is the volumetric flow rate of the HTF, N is the number of revolutions per minute, and p is the helical shaft pitch.

The Darcy–Weisbach friction factor is described as [18,30]:

$$f = \frac{\Delta P}{0.5\,\rho_f\,U_{av}^2\,\frac{l}{D_{eq}}} \tag{11}$$

where ΔP is pressure drop difference between pipe inlet and exit, that is determined experimentally, ρ_f is the density of HTF at the average bulk temperature $\left[T_{av} = 0.5(T_{fo} + T_{fi})\right]$ and l is the test section length (1.372 m).

2.2.2. Nusselt Number Evaluation

The average inner wall temperature of the receiver is [20,22]:

$$T_{wi}{}^\sim = T_{wo}{}^\sim - \frac{Q_u\,\ln\,(D_o/D_i)}{2\pi k_c l} \tag{12}$$

$$T_{wo}{}^\sim = \frac{\sum T_{wo}}{16} \tag{13}$$

where k_c, $T_{wo}{}^\sim$ are the thermal conductivity of the copper and average outer wall temperature of the receiver, respectively.

Log mean temperature difference:

$$LMTD = (\Delta T_1 - \Delta T_2)/ln\,(\Delta T_1/\Delta T_2) \tag{14}$$

where:

$$\Delta T_1 = T_{wi}{}^{\sim} - T_{fi} \tag{15}$$

$$\Delta T_2 = T_{wi}{}^{\sim} - T_{fo} \tag{16}$$

The average heat transfer coefficient for HTF was calculated by [43]:

$$h = \frac{Q_u}{A_i \; LMTD} \tag{17}$$

where Q_u is the heat absorbed by HTF. A_i is the inner surface area of the receiver, which can be expressed as:

$$A_i = \pi D_i l \tag{18}$$

The average Nusselt number is determined as follows [18]:

$$Nu = \frac{h D_{eq}}{k} \tag{19}$$

2.3. Performance Evaluation

2.3.1. Thermal Enhancement Factor

The thermal enhancement factor (TEF) is the ratio of the augmented surface heat transfer coefficient (inserted receiver tube), *h*, to that of a smooth surface (plain receiver tube), h_o, at the same pumping power. It is given as [11]:

$$TEF = \left[\frac{h}{h_o} \right]_{pp} = \left[\frac{Nu}{Nu_o} \right]_{pp} = \frac{(Nu/Nu_o)}{(f/f_o)^{(1/3)}} \tag{20}$$

where Nu and Nu_o are for the receiver with insert and the receiver without insert, respectively. The same is true for the friction factor (f and f_o).

2.3.2. Thermal Efficiency

The thermal efficiency is the heat absorbed by HTF (Q_u) to the total incident direct irradiance to the collector aperture. The instantaneous thermal efficiency can be determined as follows [36]:

$$\eta_{th,i} = \frac{Q_{u,i}}{H_{bn,i} \; A_a} \tag{21}$$

$$`Q_{u,i} = \dot{m}_f C_p \left(T_{fo} - T_{fi} \right)_i \tag{22}$$

The average daily thermal efficiency is:

$$\eta_{th} = \frac{Q_u}{Q_s} = \frac{\sum Q_{u,i}}{\sum H_{bn,i} A_a} \tag{23}$$

$$`Q_u = \sum Q_{u,i} \tag{24}$$

$$Q_s = \sum H_{bn,i} A_a \tag{25}$$

where $i = 1, 2, \ldots , n$ and n is the number of time intervals in the day.

T_{fi}, T_{fo}, H_{bn} and A_a are the inlet and outlet temperatures of the HTF, normal beam solar radiation at the collector plane, and aperture area, respectively.

2.3.3. Overall Efficiency

The average daily overall efficiency, η_{ov}, evaluates the net heat production, which can be represented as [44]:

$$\eta_{ov} = \frac{Q_u - \frac{P_P}{\eta_{el}} - P_{mo}}{Q_s} \tag{26}$$

where η_{el} and η_P are electrical and pump efficiency, 0.327 and 0.80, respectively [45–47]. While P_P and P_m are the pumping power and the power of the DC rotating motor, respectively. The pumping power is a critical parameter as using its value increases as a side effect of applying an insert turbulator within the thermal receiver. It can be calculated as follows [44]:

$$P_P = \frac{\Delta P \, V}{\eta_p} \tag{27}$$

2.3.4. Exergtic Efficiency

The exergtic efficiency of the PTC, η_{ex}, is a critical parameter that indicates the maximum work production extracted from the PTC, which is given below [48]:

$$\eta_{ex} = \frac{E_u}{E_s} \tag{28}$$

where, E_u and E_s are the useful output exergy of the HTF and the available solar exergy, respectively. E_u is obtained by [49]:

$$E_u = Q_u \left(1 - \frac{T_{am}}{T_m}\right) - \frac{T_{am}}{T_m} W_T \tag{29}$$

where, W_T is the total of power consumed by the pump and the DC motor. The power consumption of the DC motor is equal to 26.40, 13.68, and 7.44 at speeds of 4, 11, and 21 RPM, respectively. The available solar exergy is obtained from [50,51]:

$$E_s = Q_s \left(1 - \frac{4}{3}\cdot\frac{T_{am}}{T_{sun}} + \frac{1}{3}\cdot\left[\frac{T_{am}}{T_{sun}}\right]^4\right) \tag{30}$$

The mean temperature of fluid, T_m, can be written as [52]:

$$T_m = \frac{\left(T_{fo} - T_{fi}\right)}{ln\left(T_{fo}/T_{fi}\right)} \tag{31}$$

T_{am} is the ambient temperature and T_{sun} is the sun temperature, and it is equal to 5770 K.

The uncertainty analysis in experimental measuring parameters was presented by [53,54], which could be determined using a root–sum–square combination of each of the individual inputs. For example, the uncertainty of a function X can be determined as follows:

$$w_X = \sqrt{\left(\frac{\partial X}{\partial x_1}\, w_1\right)^2 + \left(\frac{\partial X}{\partial x_2}\, w_2\right)^2 + \cdots \left(\frac{\partial X}{\partial x_n}\, w_n\right)^2} \tag{32}$$

where w_X is the uncertainty of the value X, w is the uncertainty of the measured parameter, and X is a given function of the independent variables $x_1, x_2, x_3, \ldots, x_n$. Thus, $X = X(x_1, x_2, x_3, \ldots, x_n)$.

And then, the relative error λ_R is defined as:

$$\lambda_R = \frac{w_X}{X} \tag{33}$$

The relative error of friction factor, Nu number, thermal efficiency, and overall efficiency are 9.29%, 5.10%, 4.92%, and 5.12%, respectively.

3. Results and Discussion

The experimental runs were performed for three cases: (1) plain receiver tube (without insert), (2) receiver with stationary helical shaft (SHS) insert, and (3) receiver with helical shaft (RHS) insert rotating with different rotational speeds of 4 RPM (RHS1), 11 RPM

(RHS2), and 21 RPM (RHS3). All cases were tested at HTF flow rates of 0.5, 1.0, 1.5, 2.0, and 2.5 LPM. The data were continuously recorded every 15 min. A nomenclature summary of the tested cases is listed in Table 5.

Table 5. Nomenclature of tested cases; denotations and conditions.

Case	Denotation	Insert Rotating Speed (RPM)
WIR	Without-insert receiver (Plain tube)	—
SHS	Stationary helical shaft receiver	0
RHS1	Rotating helical shaft receiver—Case 1	4
RHS2	Rotating helical shaft receiver—Case 2	11
RHS3	Rotating helical shaft receiver—Case 3	21

All cases are tested at HTF flow rates of 0.5, 1.0, 1.5, 2.0, and 2.5 LPM.

The variation of Re with flow rate is presented in Figure 8. It can be noted that the Re rises with increasing the flow rate for all cases due to the axial velocity increase with the flow rate, while at the same flow rate, the axial velocity increased in the RHS cases more than in the SHS case as the axial velocity increased with the helical shaft rotation.
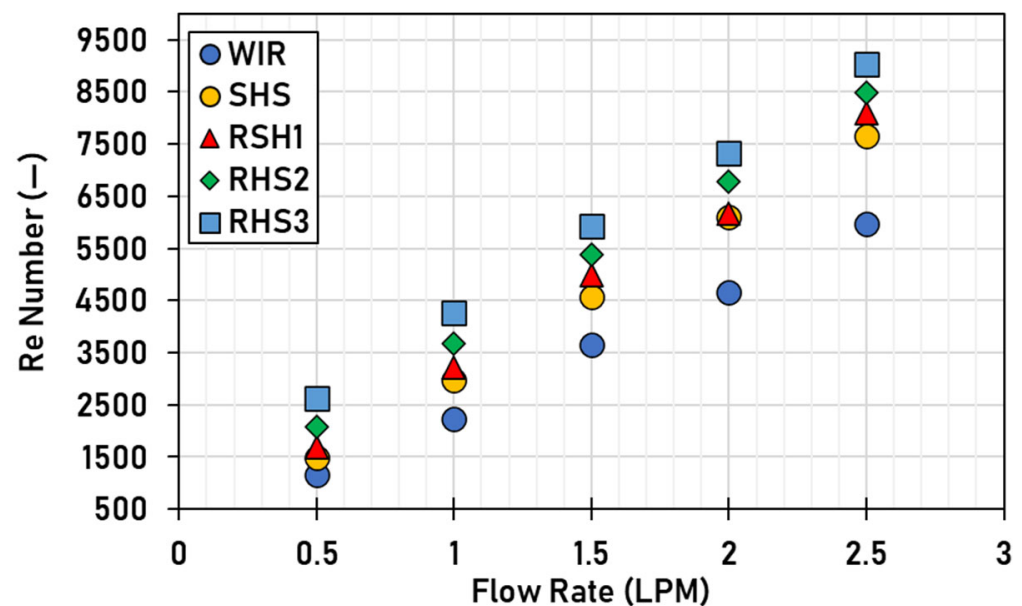
Figure 8. Reynolds number against flow rate in all tested cases.

Figure 9 shows the average heat transfer coefficient for all the examined cases of the PTC, which clearly shows that increasing the value of the average heat transfer coefficient with increasing the flow rate, which may be explained because more flow disturbance is created along the tube walls when the flow rate increases. Intense swirls enhance the fluid mixing between the core and near the wall regions and consequently enhance the average heat transfer coefficient by increasing the flow rate. In the cases of SHS and RHS and at a constant HTF flow rate, the helical shaft increases the intensity of swirl flow and resulting in higher contact surface area between the receiver and HTF, leading to an increase in the useful heat gain and consequently enhancing the average heat transfer coefficient with introducing SHS and RHS.
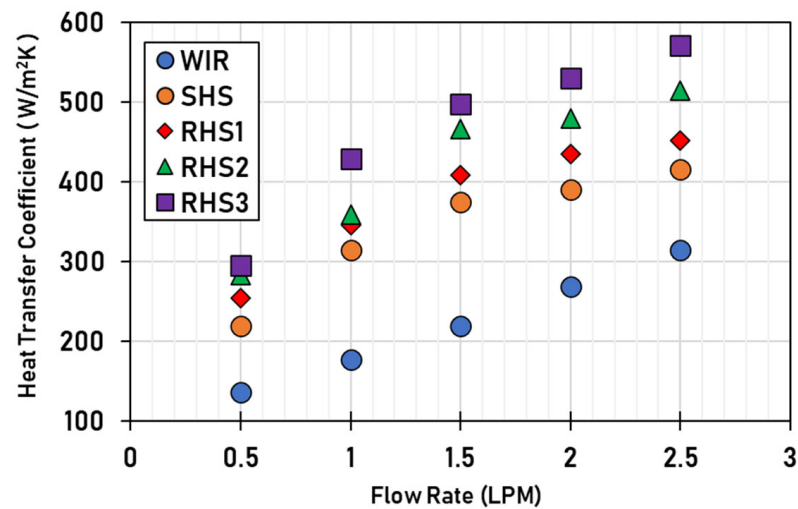
Figure 9. Average heat transfer coefficient against flow rate.

The variation of the Nu number corresponding to the average heat transfer coefficient in Figure 9 is shown in Figure 10a. The Nu number ratio with flow rate variation is illustrated in Figure 10b. The higher Nu number ratio is achieved at 1 LPM compared to the other flow rates, and it achieves a maximum of 2.42 for the case of RSHS3. Furthermore, the Nu number ratio decreases with the rise of flow rate from 1.5 LPM to 2.5 LPM for all cases, while at 0.5 LPM, the Nu number ratio reaches a higher value of 2.17 for the case of RSHS3 and reaches a lower value of 1.62 for the case of SHS.
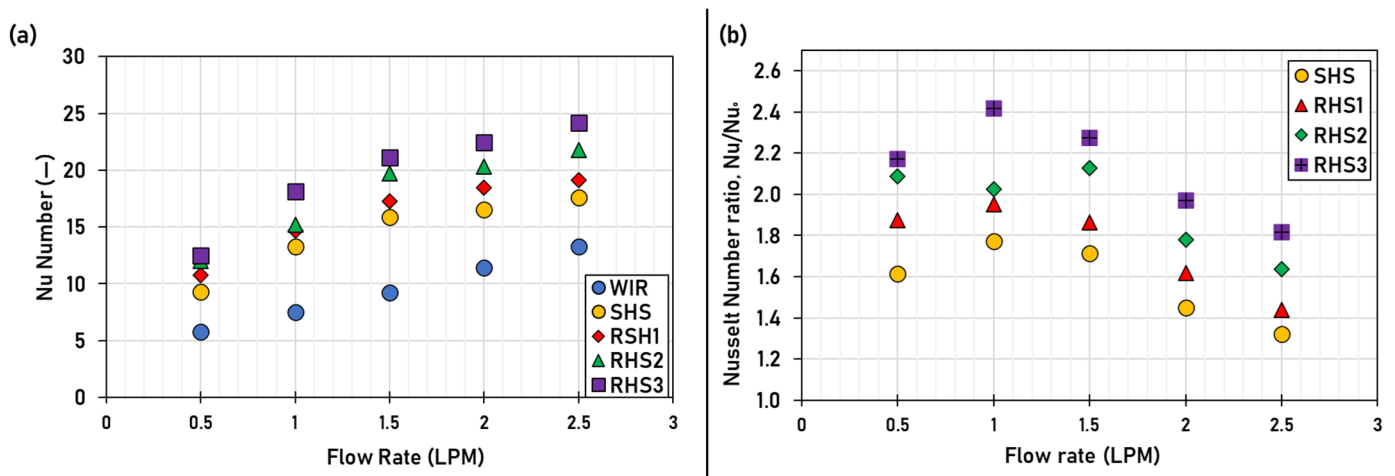
Figure 10. Nusselt number relations ratio against flow rate. (**a**) Nusselt number against flow rate. (**b**) Nusselt number ratio against flow rate.

The thermal efficiencies of all tested cases are shown in Figure 11. It can be noted that the instantaneous thermal efficiency varies with the experiment time over the day due to the rapid incident solar radiation variation. However, the thermal efficiency slightly varies when inserted the helical shaft inside the receiver tube since the helical shaft can compensate for the incident solar radiation variations over the daytime. Moreover, Figure 11a to Figure 11e indicate that increasing the helical shaft insert's rotation speed results in higher and more stabilized instantaneous thermal efficiency over the daytime. This result may be attributed to improved mixing, more intense secondary flow, and higher thermal boundary layer disruption due to shaft rotation. As a consequence, the convective heat transfer is improved.
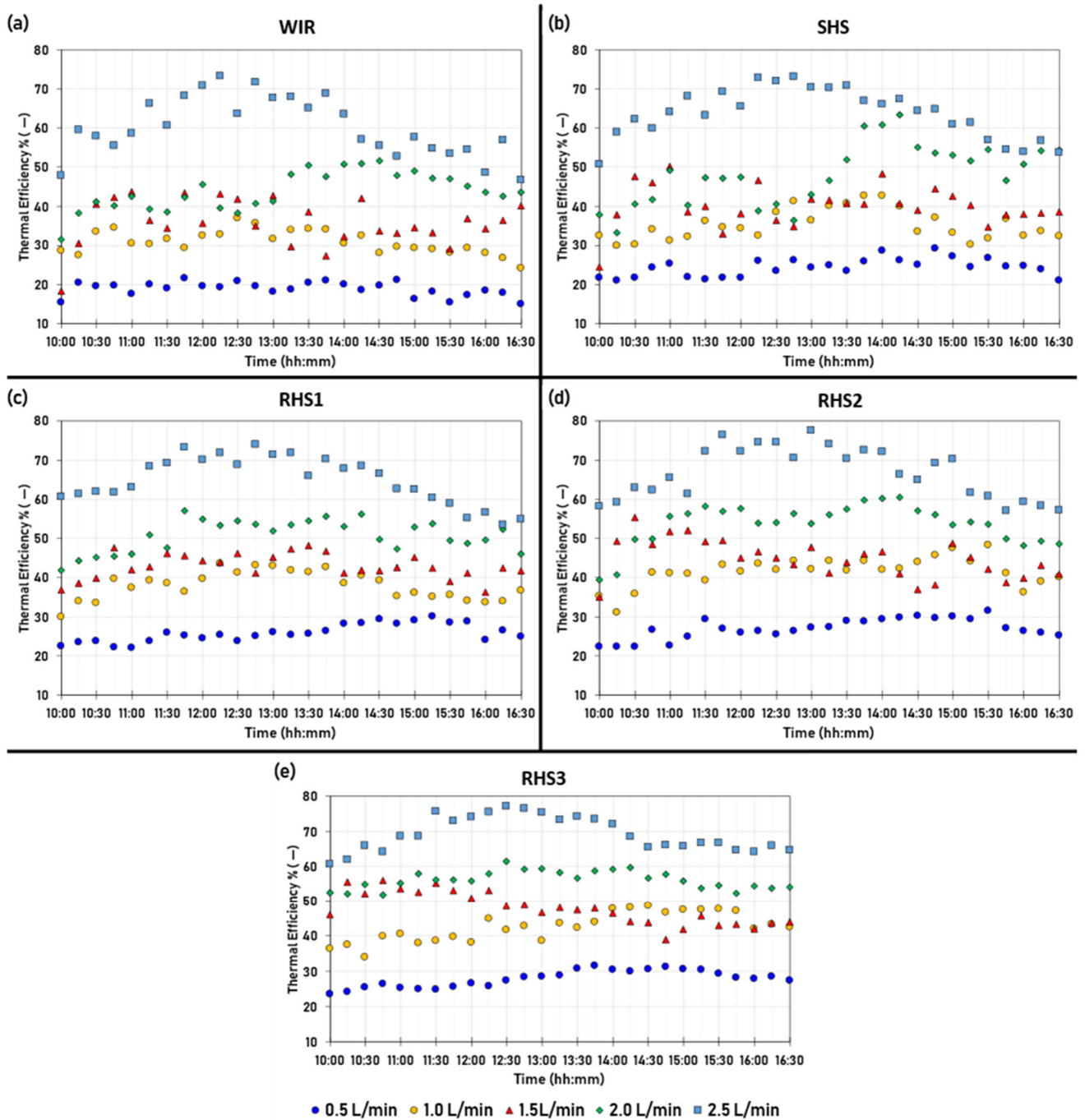
Figure 11. The instantaneous thermal efficiency against time in all tested cases.

Figure 12 shows temperature differences at a different flow rate for all cases. As the flow rate decreases from 2.5 to 0.5 LPM, the temperature difference increases, as stated in [55]. The reason is that, at the low flow rate, the HTF has a long time to increase its temperature along the receiver tube, so the temperature difference has a higher value. On the contrary, the HTF does not have enough time to increase its temperature at a high flow rate, so the temperature difference has a lower value.
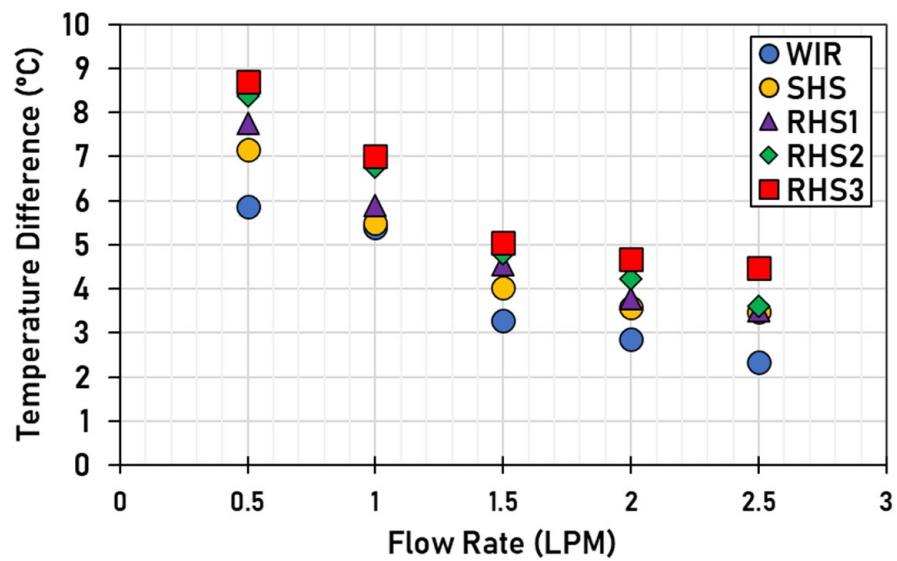
Figure 12. Temperature difference against flow rate.

Compared to a plain tube, the temperature differential is enhanced by using an insert within the receiver at a constant HTF flow rate. Furthermore, due to expanding the contact surface area for HTF with the shaft, the convective heat transfer rate is enhanced, and higher outlet temperature is observed, consequently increasing temperature difference. In addition, when the helical shaft rotates, it causes more intense secondary flow, more disturbance of the thermal boundary layer, and improved mixing. Consequently, the convective heat transfer rate and outlet temperature increase the temperature difference.

In addition, from Figure 13a, it can be observed that the increase in the HTF flow rate boosts the instantaneous thermal efficiency. These observed results are not limited to the instant thermal efficiency. However, they extend to average daily thermal efficiencies, as illustrated in Figure 13a. The thermal efficiency increase with increasing the flow rate is compatible with what was stated in [52,56] due to higher confrontation between the HTF particles and higher turbulence and, as a result, augmented thermal performance and efficiency. In the cases of RHS1, RHS2, and RHS3, the rotating helical shaft amplifies the intensity of swirl flow and enhances thermal efficiency compared to SHS. The efficiency of PTC for WIR, SHS, RHS1, RHS2, and RHS3 varies from 19% to 60.3%, 24.51% to 63.82%, 25.9% to 65.02%, 27.1% to 66.9%, and 27.9% to 69.25% with flow rate ranging from 0.5 to 2.5 LPM.
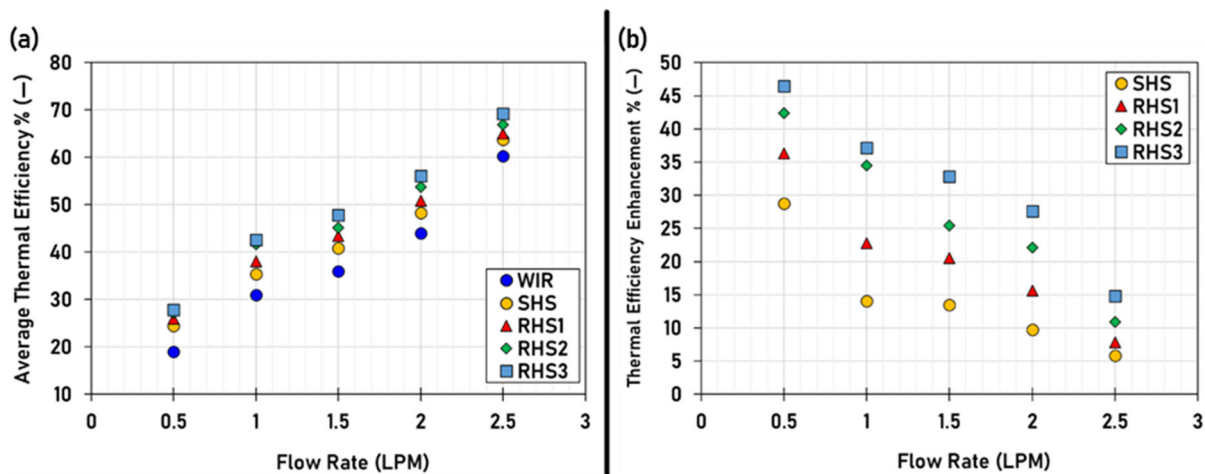
Figure 13. Thermal efficiency against flow rate. (**a**) Average daily efficiency vs. flow rate. (**b**) Efficiency enhancement % vs. flow rate.

However, the thermal efficiency enhancement, as plotted in Figure 13b, is observed to decrease with the rise of flow rate as the rate of growth of thermal efficiency for the plain tube with increasing flow rates is higher than the rate of growth in thermal efficiency for the receiver tube fitted with stationary or rotating helical shaft. As a result, the enhancement in thermal efficiency is reduced with increasing flow rates. Moreover, the enhancement is higher when the shaft rotates at a higher rotational speed than the stationary one. Using RHS3 leads to the maximum enhancement, ranging from 14.82 to 46.47% while using SHS leads to enhancement from 5.82% up to 28.78% compared to the plain tube.

The friction factor against flow rates for all tested cases is evaluated and plotted as illustrated in Figure 14a. As noted, the friction factor reduces as the flow rate increases, as indicated in [52]. Moreover, it increases in the cases of SHS, RHS1, RHS2, and RHS3 compared to the plain tube. This is because the shaft causes increases in swirl flow intensity, residence time, and contact surface area for SHS. In contrast, the long time inside the receiver tube increases the contact between the HTF particles and the receiver tube wall and, as a result, increases the friction factor and pressure drop. Moreover, for the cases of RHS1, RHS2, and RHS3, increasing the rotational speed magnifies the intensity of swirl flow and turbulence. As a result, it makes the HTF move over the longer paths, increasing the friction factor compared to RSHS. Consequently, the maximum friction factor is 1.3, and it is reached at a lower flow rate of 0.5 LPM and a higher rotational speed of 21RPM (RHS3), while the lower friction factor is 0.156 and reached at a higher flow rate of 2.5 LPM and stationary insert (SHS). Therefore, the friction factor ratio reduces with the growth in flow rate, while for the RHS3 and SHS cases, the friction factor ranges from 4.1 to 7.7 times and 1.9 to 4.1 times, respectively, compared to the WIR case, as seen in Figure 14b.
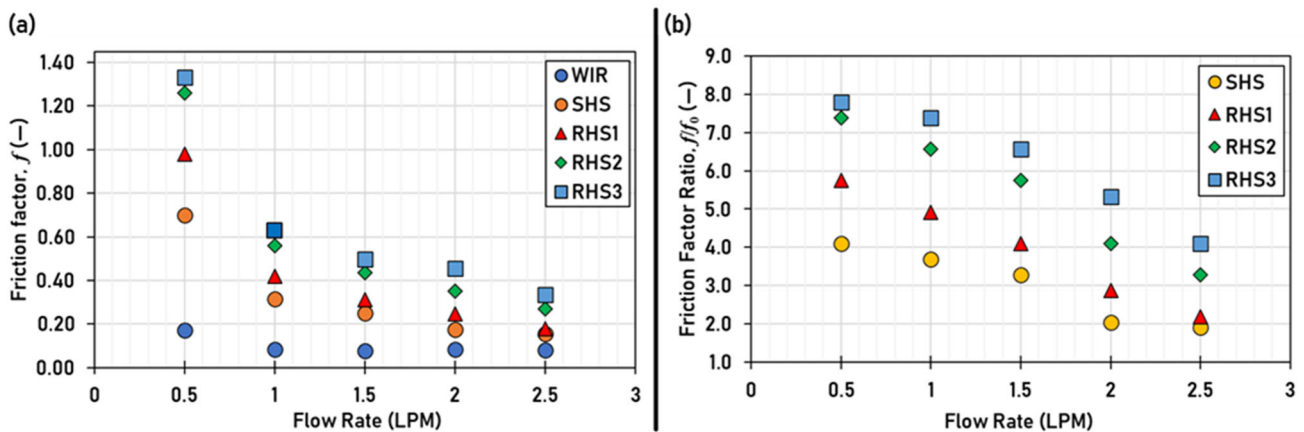
Figure 14. Friction factor against flow rate. (**a**) Friction factor vs. flow rate. (**b**) Friction factor ratio vs. flow rate.

The pumping power increases by increasing the flow and using the helical shaft insert, as illustrated in Figure 15a and stated in [18]. Moreover, using a shaft insert leads to higher pumping power in the cases of SHS, RHS1, RHS2, and RHS3 compared with the WIR. Raising the flow rate from 0.5 to 2.5 LPM increases the pressure drop from 250 to 1400 Pa, 350 to 1600 Pa, 450 to 2400 Pa, and 500 to 3000 Pa in the cases of SHS, RHS1, RHS2, and RHS3, respectively, and consequently increasing pumping power. However, the increase in pumping power, as plotted in Figure 15b, is observed to reduce with the flow rate rise as the pumping power is greater for the plain tube when increasing the flow rates compared to the rate of growth in pumping power for the receiver tube fitted with stationary or rotating helical shaft. As a result, the percentage rise in pumping power is decreased with rising flow rates. Moreover, the increase is higher when the shaft rotates at a higher rotational speed than the stationary one. Using RHS3 leads to the maximum increase, ranging from 404 to 850%, while using SHS increases 130 to 400% compared to the plain tube.
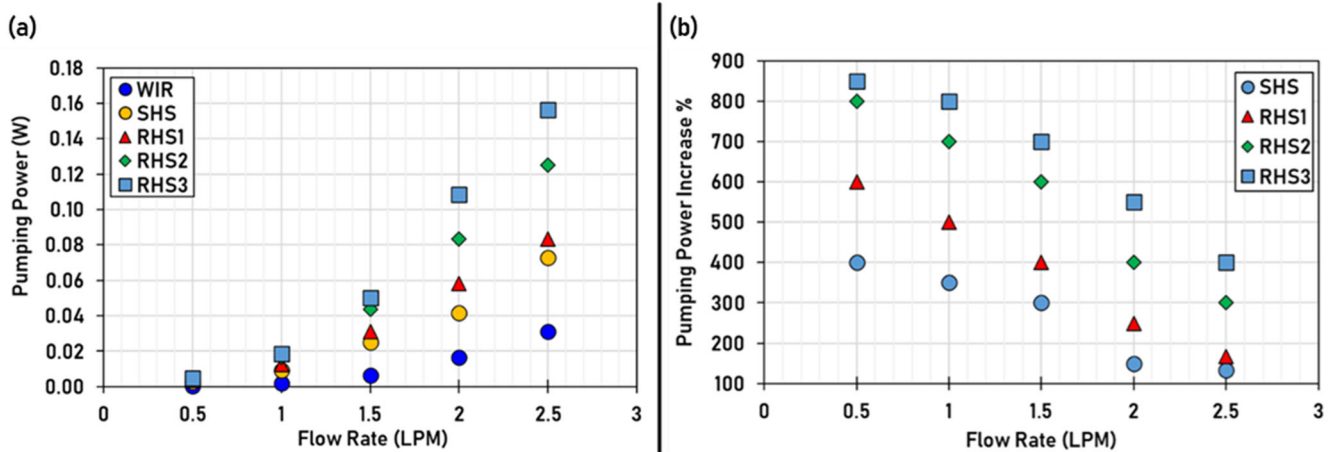
Figure 15. Pumping power relations ratio against flow rate. (**a**) Pumping power against flow rate (**b**) % increase in pumping power against flow rate.

Considering the effect of power consumed in the pump and the DC motor rotating the helical shaft, the overall efficiency can be used to evaluate the system; as shown in Figure 16a. It indicates an improvement of thermal efficiency for all cases with the flow rate increase due to the slight rise in the total power consumed compared to the higher growth in beneficial heat gain. So, the overall efficiency trend is the same for thermal, and the overall efficiencies enhancement is the same for the thermal efficiency enhancement, as shown in Figure 16b.
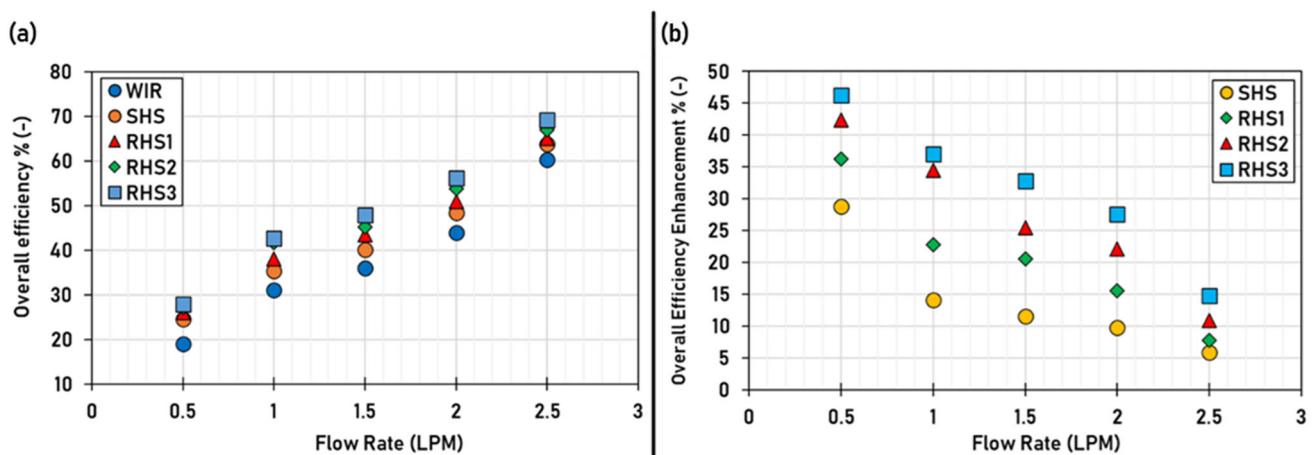
Figure 16. Efficiency relations against flow rate. (**a**) Overall efficiency against flow rate. (**b**) % enhancement of overall efficiency.

Figure 17 shows the variations of TEF against flow rate. TEF for all cases is higher than unity, while the heat transfer enhancement is higher than the pressure drop rise. The maximum TEF is 1.24, achieved at 1 LPM and in the case of RHS3.

The exergy efficiency with various flow rates in all tested cases is shown in Figure 18. Based on results plotted in Figure 18, raising the flow rate from 0.5 to 2.5 LPM increases the useful heat gain and results in exergy efficiency enhancement from 11.11% to 36.35% in the plain tube case stated in [50]. Inserting the helical shaft increases exergy efficiency from 14.16, 14.52, 15.14, and 15.23% to 37.81, 39.21, 38.98, and 40.41% for the cases of SHS, RHS1, RHS2, and RHS3, respectively, with raising the flow rate from 0.5 to 2.5 LPM. This result is attributed to the rising logarithmic mean temperature of the fluid, T_m. With boosting the flow rate that leads to both decreasing in the second term $(T_0/T_m W_T)$ and increasing the useful heat gain in the first term and consequently increasing the exergy

efficiency. Increasing the total power consumption at the same flow rate due to rotating the helical shaft in the cases of RHS1, RHS2, and RHS3 does not prevent enhancing the exergy efficiency because the rate of increasing the useful heat gain is higher than increasing the total power consumption that leads to enhancement in exergy efficiency.
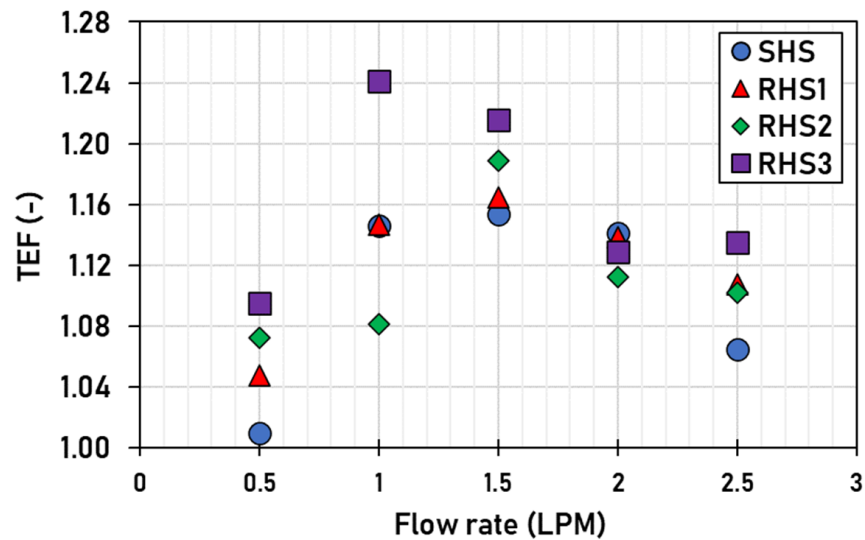
Figure 17. Variation of TEF against flow rate.
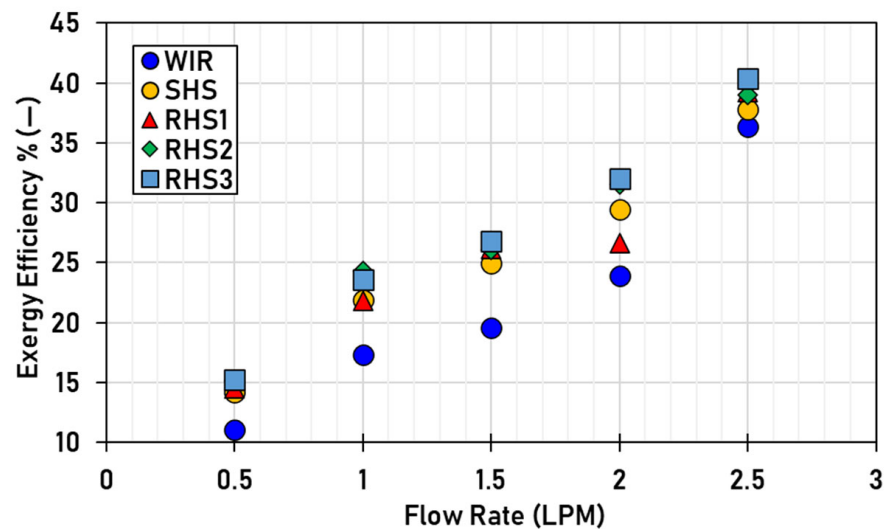
Figure 18. Exergetic efficiency against flow rate.

A comparison between the present work (static and rotating helical shaft) and different types of inserts in terms of thermal efficiency ratio, Nu number ratio, and friction ratio is provided in Table 6. The highest efficiency ratio is 2.33 for wire matrix and twisted tape [29]. On the other hand, they achieved a higher friction ratio of 36.02.

The filling porous [57] achieved a maximum Nu number ratio of 17.24 and a maximum friction factor ratio of 412.62. According to the reviewed literature, using twisted tape and fins can lead to higher thermal enhancement with a lower impact on the friction factor. The experimental study of the static helical shaft has a higher efficiency ratio of 1.28 and a lower friction ratio of 4.10 compared with a numerical study of twisted tape of 1.07 and a higher friction factor ratio of 6.15. While using the rotating helical shaft in the current study led to a maximum efficiency ratio of 1.46 and a maximum Nu number ratio of 2.41 compared to fins and twisted tape, but as a penalty of maximum friction factor ratio of 7.79.

Table 6. Comparison between present work and various inserts inside PTC.

Study Type	Type of Insert	η/η_o	Nu/Nu_o	f/f_o	Ref.
Exp.	Copper foam	1.03–1.08	1.01–1.80	95–250	[32]
Exp.	Wire matrix and twisted tape	1.35–2.33	1.67–2.60	36.02	[29]
Num.	Toroidal rings	1.00–1.037	1.00–2.33	1.00–14.62	[58]
Num.	Perforated plate	1.005–1.018	1.8–2.0	13.34–13.46	[59]
Num.	Filling porous	1.07	3.49–17.24	17.60–412.62	[57]
Num.	Twisted tape	1.005–1.015	1.70–1.77	4.17–6.15	[59]
Num.	Internal longitudinal fins	1.37–1.41	1.96–2.19	2.03–2.12	[60]
Exp.	Static helical shaft	1.05–1.28	1.32–1.77	1.91–4.10	Present work
Exp.	Rotating helical shaft	1.06–1.46	1.43–2.41	2.18–7.79	Present work

4. Economic Analysis

The utility of using the inserts inside PTC can be evaluated based on its economic viability. Fixed cost (FC) and annual variable cost (VC) are considered in order to estimate the total cost of PTC, while the initial cost is estimated by considering all components of building a system, and the operating cost is estimated by considering the effect of power consumed in the pump and DC motor. The cost data of components of PTC for three WIR, SHS, and RHS cases are listed in Table 7 according to the Egyptian market. The economic analysis is carried out at maximum TEF, achieved at 1 LPM and RHS3.

Table 7. The cost data of various components of PTC.

Sr.	Details of Component	Quantity (Units)	Unit Cost (USD/Unit)	Total Cost (USD)
1	Acrylic reflector sheet	1	66.7	66.7
2	Copper tube	1	16.7	16.7
3	Glass tube	1	11.1	11.1
4	Linear actuator	1	17.8	17.8
5	Pipes and accessories	1	31.4	31.4
6	valves	5	2.2	11.1
7	Storage water tank	1	38.9	38.9
8	Silicon	5	0.8	4.2
9	Insulation material	1	16.7	16.7
10	Circulation pump	1	19.4	19.4
11	ARDUINO circuit	1	33.3	33.3
12	Batteries	2	38.9	77.8
13	The metallic structure of PTC	1	61.1	61.1
14	Manufacture cost	1	55.6	55.6
A	**Total fixed cost**	**WIR**		**462**
15	Insert tape (steel)	1	27.8	27.8
16	Manufacture cost	1	61.1	61.1
B	**Total fixed cost**	**SHS**		**551**
17	Oil seal ring	2	2.2	4.4
18	DC motor gearbox and control circuit	1	25.0	25.0
19	Coupling	1	2.5	2.5
C	**Total fixed cost**	**RHS**		**583**

Bold rows (A, B, and C) represent the summation of total fixed costs of each case (WIR, SHS, and RHS), respectively.

Total Cost Estimation of PTC

The annual cost of useful heat per kWh (ACUH) can be calculated as follows [54]:

$$ACUH = TC/TUH \tag{34}$$

where, TC is the total cost and can be determined from Equation (35), while TUH is the total useful heat during the life span and is expressed by Equation (36).

$$TC = FC + VC \tag{35}$$

$$TUH = n \times \text{Yearly productivity} \tag{36}$$

where, n is the expected PTC lifetime, assumed to be 10 years. The yearly productivity can be calculated as follows:

$$\text{Yearly productivity} = (Q_u/\text{day}) \times \text{operating days} \tag{37}$$

where, the operating days were assumed to be 340 sunny days per year and (Q_u/day) is the useful heat per day for one cycle can be calculated as follows:

$$(Q_u/\text{day}) = Q_u \times \text{operating hours} \tag{38}$$

where, the operating hours were 7 h (from 9:30 to 16:30).

The economics of different cases of PTC based on estimated ACUH are presented in Table 8.

Table 8. The economic analysis for PTC with WIR, SHS, and RHS.

	WIR	**SHS**	**RHS**
Fixed cost (FC), USD	462	551	583
Annual variable cost (VC), USD	0.0004	0.0014	5.810
(Q_u/day), kWh	2.5	2.8	3.4
TUH, kWh	8414.3	9405.8	11,543.0
Total cost (TC), USD	462	551	588.4
ACUH, USD	0.055	0.059	0.051

The economic analysis in Table 8 shows that ACUH for PTC with WIR, SHS, and RHS are USD 0.055, USD 0.059, and USD 0.051, respectively. PTC with RHS has minimum ACUH, while SHS with PTC uses maximum ACUH. Therefore, using RHS is beneficial from an economic point of view compared to WIR and SHS, and using SHS without rotation has a poor impact on ACUH.

5. Conclusions

The influence of inserting a stationary and rotating helical shaft within the receiver on PTC performance was investigated in the present study. Three cases were investigated: A PTC without helical shaft insert, a PTC with stationary helical shaft insert, and a PTC with rotating helical shaft insert. The experiments were performed for different shaft rotational speeds of (4, 11, and 21 RPM) and various flow rates (0.5, 1, 1.5, 2, and 2.5 LPM) of water as an HTF. Moreover, the fluid flow and thermal parameters (friction factor, Re number, Nu number, and TEF) and performance parameters (thermal, overall, and exergetic efficiencies) were investigated. The following are the key findings of this investigation:

- The helical shaft insert has increased the required pumping power for the same flow rate.
- The pumping power rises with the shaft rotating speed, particularly at the high HTF flow rate.
- For the same flow rate, the helical shaft insert has enhanced the thermal performance (thermal, overall, and exergetic efficiencies) of the PTC.
- The thermal performance enhancement increases with growing the shaft rotating speed and the HTF flow rate.
- Compared to WIR, the friction factor ratios for RHS3 are higher than SHS, which are in the ranges of 4.1 to 7.79 times and 1.91 to 4.10 times, respectively. Furthermore,

Nu number ratios for RHS3 are higher than SHS in the ranges of 1.81 to 2.41 and 1.32 to 1.77.

- The maximum enhancement in thermal efficiency is 46.47%, achieved at a minimum flow rate of 0.5 LPM and RHS3.
- The maximum exergy efficiency is 40.41%, achieved at a higher flow rate of 2.5 LPM and RHS3.
- A comparison between the investigated three cases at the same pumping power using criteria of TEF shows that the maximum enhancement in thermal performance occurs at an HTF flow rate of 1 LPM, and the percentage enhancement in thermal efficiency is about 37% at shaft rotational speed of 21 RPM.
- The cost analysis shows that ACUH for RHS (USD 0.051) is lower than WIR and SHS (USD 0.059) at maximum TEF.

It can be concluded that using static and rotating helical shaft insert inside the receiver of PTC may be used for solar heating processes and power generation applications to enhance the performance of the PTC with a low penalty on pumping power compared to the other inserts. In the future, the use of nanofluids or hybrid nanofluids with rotating helical shafts is recommended, in order to investigate their effects on the thermal and hydraulic performance of PTC. Furthermore, a PV system coupled with PTC to supply the DC motor with power should be planned to reduce power consumption.

Author Contributions: Conceptualization, M.T., M.B. and E.E.-N.; methodology, M.A. and M.T.; data analysis, M.A. and M.T.; investigation, M.A., M.T., M.B. and E.E.-N.; writing—original draft preparation, M.A.; writing—review and editing, M.A. and M.T.; visualization, M.T.; supervision, M.T., M.B. and E.E.-N. All authors have read and agreed to the published version of the manuscript.

Informed Consent Statement: Not applicable.

Conflicts of Interest: The authors declare no conflict of interest.

Nomenclature

Symbols		*Subscripts*	
C	concentration ratio (-)	*a*	aperture
C_p	specific heat capacity (J/kg K)	*av*	average
D	diameter (m)	*am*	ambient
E	exergy rate (W)	*c*	copper tube
F	focal length (m)	*el*	electrical
f	friction factor (-)	*eq*	equivilant
H_{bn}	normal beam solar radiation (W/m²)	*ex*	exergetic
H	height (m)	*f*	fluid
h	heat transfer coefficient, W/m²K	*g*	glass tube
L	copper tube length (m)	*h*	helical shaft
l	test section length (m)	*i*	inner or inlet
$\dot{m}$	mass flow rate (kg/s)	*m*	logarithmic mean
N	revolutions per minute (RPM)	*mo*	motor
P	power (W)	*o*	outer or outlet
p	pitch (m)	*ov*	overall
Q	heat rate (W)	*p*	pump
S	reflector width (m)	*PP*	constant pumping power
T	temperature (°C)	*s*	solar
t	thickness (m)	*T*	total
U	velocity (m/s)	*u*	useful
V	volume (m³)	*w*	wall
$\dot{V}$	volumetric flow rate (m³/s)	*Abbreviations*	
W	aperture width (m)	HTF	heat transfer fluid

w	uncertainty (-)	LMTD	Log mean temperature difference
Greek Letters		LPM	liter per minute
α	absorptance (-)	PTC	parabolic trough collector
γ	intercept factor (-)	RHS	rotating helical shaft receiver
Δ	difference (-)	SHS	stationary helical shaft receiver
η	efficiency (-)	TEF	thermal enhancement factor
λ	relative error (-)	WIR	without-insert receiver
μ	dynamic viscosity (kg/m.s)	ACUH	annual cost of useful heat per kWh
v	kinematic coefficient of viscosity (m^2/s)	TC	total cost
ρ_f	density of HTF (kg/m^3)	TUH	total useful heat during the life span
ρ	reflectance (-)	FC	fixed cost
τ	transmittance (-)	VC	annual variable cost
ϕ	rim angle (°)	*Dimensionless Numbers*	
ω	angular velocity (rad/s)	Nu	Nusselt number
		Re	Reynolds number

References

1. Bilal, A.; Khan, M.N.; Zubair, M.; Bellos, E. Commercial Parabolic Trough CSP Plants: Research Trends and Technological Advancements. *Sol. Energy* **2020**, *211*, 1422–1458. [CrossRef]
2. Sarbu, I.; Sebarchievici, C. Introduction. In *Solar Heating and Cooling Systems*; Elsevier: Cambridge, MA, USA, 2017; pp. 1–11. ISBN 9780128116623.
3. Shouman, E.R.; Khattab, N.M. Future Economic of Concentrating Solar Power (CSP) for Electricity Generation in Egypt. *Renew. Sustain. Energy Rev.* **2015**, *41*, 1119–1127. [CrossRef]
4. Tawfik, M. A Review of Directly Irradiated Solid Particle Receivers: Technologies and Influencing Parameters. *Renew. Sustain. Energy Rev.* **2022**, *167*, 112682. [CrossRef]
5. Fernández-García, A.; Zarza, E.; Valenzuela, L.; Pérez, M. Parabolic-Trough Solar Collectors and Their Applications. *Renew. Sustain. Energy Rev.* **2010**, *14*, 1695–1721. [CrossRef]
6. Anabela, E.; Panduro, C.; Finotti, F.; Largiller, G.; Yngve, K. A Review of the Use of Nanofluids as Heat-Transfer Fluids in Parabolic-Trough Collectors. *Appl. Therm. Eng.* **2022**, *211*, 118346. [CrossRef]
7. Abed, N.; Afgan, I. An Extensive Review of Various Technologies for Enhancing the Thermal and Optical Performances of Parabolic Trough Collectors. *Int. J. Energy Res.* **2020**, *44*, 5117–5164. [CrossRef]
8. Kreith, F.; Goswami, D.Y. *Handbook of Energy Efficiency and Renewable Energy*; Taylor & Francis Group: New York, NY, USA, 2007.
9. Peng, H.; Li, M.; Liang, X. Thermal-Hydraulic and Thermodynamic Performance of Parabolic Trough Solar Receiver Partially Filled with Gradient Metal Foam. *Energy* **2020**, *211*, 119046. [CrossRef]
10. Parlamıs, H.; Ozden, E.; Sami, M. Experimental Performance Analysis of a Parabolic Trough Solar Air Collector with Helical-Screw Tape Insert: A Comparative Study. *Sustain. Energy Technol. Assess.* **2021**, *47*, 101562. [CrossRef]
11. Sharma, M.; Jilte, R. A Review on Passive Methods for Thermal Performance Enhancement in Parabolic Trough Solar Collectors. *Int. J. Energy Res.* **2021**, *45*, 4932–4966. [CrossRef]
12. Kumar, C.N.; Murugesan, P. Review on Twisted Tapes Heat Transfer Enhancement. *Int. J. Sci. Eng. Res.* **2012**, *3*, 1–9.
13. Mousa, M.H.; Miljkovic, N.; Nawaz, K. Review of Heat Transfer Enhancement Techniques for Single Phase Flows. *Renew. Sustain. Energy Rev.* **2021**, *137*, 110566. [CrossRef]
14. Hasanpour, A.; Farhadi, M.; Sedighi, K. A Review Study on Twisted Tape Inserts on Turbulent Flow Heat Exchangers: The Overall Enhancement Ratio Criteria. *Int. Commun. Heat Mass Transf.* **2014**, *55*, 53–56. [CrossRef]
15. Allam, M.; Tawfik, M.; Bekheit, M.; El-Negiry, E. Heat Transfer Enhancement in Parabolic Trough Receivers Using Inserts: A Review. *Sustain. Energy Technol. Assess.* **2021**, *48*, 101671. [CrossRef]
16. Garg, M.O.; Nautiyal, H.; Khurana, S.; Shukla, M.K. Heat Transfer Augmentation Using Twisted Tape Inserts: A Review. *Renew. Sustain. Energy Rev.* **2016**, *63*, 193–225. [CrossRef]
17. Waghole, D.R.; Warkhedkar, R.M.; Kulkarni, V.S.; Shrivastva, R.K. Experimental Investigations on Heat Transfer and Friction Factor of Silver Nanofluid in Absorber/Receiver of Parabolic Trough Collector with Twisted Tape Inserts. *Energy Procedia* **2014**, *45*, 558–567. [CrossRef]
18. Chaurasia, S.R.; Sarviya, R. Numerical and Experimental Thermal Performance with Entropy Generation Analysis on Tube with Helical Screw Tape Inserts at Number of Strips in Turbulent Flow. *Proc. Inst. Mech. Eng. Part C J. Mech. Eng. Sci.* **2021**, *235*, 1057–1070. [CrossRef]
19. Nakhchi, M.E.; Hatami, M.; Rahmati, M. Experimental Investigation of Heat Transfer Enhancement of a Heat Exchanger Tube Equipped with Double-Cut Twisted Tapes. *Appl. Therm. Eng.* **2020**, *180*, 115863. [CrossRef]
20. Arunachala, U.C. Experimental Study with Analytical Validation of Energy Parameters in Parabolic Trough Collector with Twisted Tape Insert. *J. Sol. Energy Eng.* **2020**, *142*, 1–12. [CrossRef]

21. Hosseinalipour, S.M.; Rostami, A.; Shahriari, G. Numerical Study of Circumferential Temperature Difference Reduction at the Absorber Tube of Parabolic Trough Direct Steam Generation Collector by Inserting a Twisted Tape in Superheated Region. *Case Stud. Therm. Eng.* **2020**, *21*, 100720. [CrossRef]

22. Elton, D.N.; Arunachala, U.C. Twisted Tape Based Heat Transfer Enhancement in Parabolic Trough Concentrator—An Experimental Study. *IOP Conf. Ser. Mater. Sci. Eng.* **2018**, *376*, 012034. [CrossRef]

23. Ghadirijafarbeigloo, S.; Zamzamian, A.H.; Yaghoubi, M. 3-D Numerical Simulation of Heat Transfer and Turbulent Flow in a Receiver Tube of Solar Parabolic Trough Concentrator with Louvered Twisted-Tape Inserts. *Energy Procedia* **2014**, *49*, 373–380. [CrossRef]

24. Song, X.; Dong, G.; Gao, F.; Diao, X.; Zheng, L.; Zhou, F. A Numerical Study of Parabolic Trough Receiver with Nonuniform Heat Flux and Helical Screw-Tape Inserts. *Energy* **2014**, *77*, 771–782. [CrossRef]

25. Mohammed, A.A.; Mohammed, A.A.; Falleh, M.A. Heat Transfer Augmentation in Tube Fitted with Rotating Twisted Tape Insert. *J. Mech. Eng. Res. Dev.* **2020**, *43*, 308–316.

26. Qi, C.; Wang, G.; Yan, Y.; Mei, S.; Luo, T. Effect of Rotating Twisted Tape on Thermo Hydraulic Performances of Nano Fluids in Heat Exchanger Systems. *Energy Convers. Manag.* **2018**, *166*, 744–757. [CrossRef]

27. Pavan, K.N.; Chethan, K.S.; Suresh, R.B. Investigation on Heat Transfer Augmentation in Tubes with Rotating Twisted Tape Insert Using Water and Copper Oxide Nanofluid as Heat Transfer Medium. *J. Crit. Rev.* **2020**, *7*, 1595–1600.

28. Promvonge, P. Thermal Augmentation in Circular Tube with Twisted Tape and Wire Coil Turbulators. *Energy Convers. Manag.* **2008**, *49*, 2949–2955. [CrossRef]

29. Varun, K.; Arunachala, U.C.; Elton, D.N. Trade-off between Wire Matrix and Twisted Tape: SOLTRACE® Based Indoor Study of Parabolic Trough Collector. *Renew. Energy* **2020**, *156*, 478–492. [CrossRef]

30. Chakraborty, O.; Das, B.; Gupta, R. Impact of Helical Coil Insert in the Absorber Tube of Parabolic Trough Collector. *Smart Innov. Syst. Technol.* **2021**, *206*, 177–187. [CrossRef]

31. Zhao, Z.; Bai, F.; Zhang, X.; Wang, Z. Experimental Study of Pin Finned Receiver Tubes for a Parabolic Trough Solar Air Collector. *Sol. Energy* **2020**, *207*, 91–102. [CrossRef]

32. Jamal-Abad, M.T.; Saedodin, S.; Aminy, M. Experimental Investigation on a Solar Parabolic Trough Collector for Absorber Tube Filled with Porous Media. *Renew. Energy* **2017**, *107*, 156–163. [CrossRef]

33. Anand, S.C.; Rai, D.A.K.; Sachan, V. Comparative Study of Parabolic Trough Concentrators. *Int. J. Mech. Eng. Technol.* **2014**, *5*, 65–73.

34. Subramaniyan, C.; Subramani, J.; Kalidasan, B.; Anbuselvan, N.; Yuvaraj, T.; Prabaharan, N.; Senjyu, T. Investigation on the Optical Design and Performance of a Single-Axis-Tracking Solar Parabolic Trough Collector with a Secondary Reflector. *Sustainability* **2021**, *13*, 9918. [CrossRef]

35. Arasu, A.V.; Sornakumar, T. Design, Manufacture and Testing of Fiberglass Reinforced Parabola Trough for Parabolic Trough Solar Collectors. *Sol. Energy* **2007**, *81*, 1273–1279. [CrossRef]

36. Kalogirou, S.A. *Solar Energy Engineering: Processes and Systems*, 2nd ed.; Elsevier Inc.: Amsterdam, The Netherlands, 2014.

37. Büker, M.S.; Parlamış, H.; Alwetaishi, M.; Benjeddou, O. Experimental Investigation on the Dehumidification Performance of a Parabolic Trough Solar Air Collector Assisted Rotary Desiccant System. *Case Stud. Therm. Eng.* **2022**, *34*, 102077. [CrossRef]

38. Goodfellow Ceramic & Glass Division. *Properties of Borosilicate Glass*; Goodfellow Ceramic & Glass Division: Pittsburgh, PA, USA, 2009.

39. Reddy, K.S.; Ravi Kumar, K.; Ajay, C.S. Experimental Investigation of Porous Disc Enhanced Receiver for Solar Parabolic Trough Collector. *Renew. Energy* **2015**, *77*, 308–319. [CrossRef]

40. Romero-Alvarez, M.; Zarza, E. Handbook of Energy Efficiency and Renewable Energy. *Choice Rev. Online* **2008**, *45*, 45-2629. [CrossRef]

41. Ibrahim, E.Z. Augmentation of Laminar Flow and Heat Transfer in Flat Tubes by Means of Helical Screw-Tape Inserts. *Energy Convers. Manag.* **2011**, *52*, 250–257. [CrossRef]

42. Mwesigye, A.; Bello-Ochende, T.; Meyer, J.P. Heat Transfer and Thermodynamic Performance of a Parabolic Trough Receiver with Centrally Placed Perforated Plate Inserts. *Appl. Energy* **2014**, *136*, 989–1003. [CrossRef]

43. Eiamsa-ard, S.; Thianpong, C.; Eiamsa-ard, P. Turbulent Heat Transfer Enhancement by Counter/Co-Swirling Flow in a Tube Fitted with Twin Twisted Tapes. *Exp. Therm. Fluid Sci.* **2010**, *34*, 53–62. [CrossRef]

44. Chakraborty, O.; Das, B.; Gupta, R.; Debbarma, S. Heat Transfer Enhancement Analysis of Parabolic Trough Collector with Straight and Helical Absorber Tube. *Therm. Sci. Eng. Prog.* **2020**, *20*, 100718. [CrossRef]

45. Xiao, H.; Liu, P.; Liu, Z.; Liu, W. Performance Analyses in Parabolic Trough Collectors by Inserting Novel Inclined Curved-Twisted Baffles. *Renew. Energy* **2021**, *165*, 14–27. [CrossRef]

46. Kumar, B.N.; Reddy, K.S. Numerical Investigations on Metal Foam Inserted Solar Parabolic Trough DSG Absorber Tube for Mitigating Thermal Gradients and Enhancing Heat Transfer. *Appl. Therm. Eng.* **2020**, *178*, 115511. [CrossRef]

47. Bellos, E.; Tzivanidis, C. Investigation of a Star Flow Insert in a Parabolic Trough Solar Collector. *Appl. Energy* **2018**, *224*, 86–102. [CrossRef]

48. Bellos, E.; Tzivanidis, C.; Antonopoulos, K.A.; Gkinis, G. Thermal Enhancement of Solar Parabolic Trough Collectors by Using Nano Fl Uids and Converging-Diverging Absorber Tube. *Renew. Energy* **2016**, *94*, 213–222. [CrossRef]

49. Bozorg, M.V.; Hossein Doranehgard, M.; Hong, K.; Xiong, Q. CFD Study of Heat Transfer and Fluid Flow in a Parabolic Trough Solar Receiver with Internal Annular Porous Structure and Synthetic Oil–Al$_2$O$_3$ Nanofluid. *Renew. Energy* **2020**, *145*, 2598–2614. [CrossRef]

50. Vahidinia, F.; Khorasanizadeh, H.; Aghaei, A. Comparative Energy, Exergy and CO$_2$ Emission Evaluations of a LS-2 Parabolic Trough Solar Collector Using Al$_2$O$_3$/SiO$_2$-Syltherm 800 Hybrid Nanofluid. *Energy Convers. Manag.* **2021**, *245*, 114596. [CrossRef]

51. Bellos, E.; Tzivanidis, C.; Daniil, I.; Antonopoulos, K.A. The Impact of Internal Longitudinal Fins in Parabolic Trough Collectors Operating with Gases. *Energy Convers. Manag.* **2017**, *135*, 35–54. [CrossRef]

52. Akbarzadeh, S.; Valipour, M.S. Energy and Exergy Analysis of a Parabolic Trough Collector Using Helically Corrugated Absorber Tube. *Renew. Energy* **2020**, *155*, 735–747. [CrossRef]

53. Holman, J.P. *Experimental Methods for Engineers*, 8th ed.; McGraw-Hill Series in Mechanical Engineering: New York, NY, USA, 2011; Volume s1-VIII.

54. Kabeel, A.E.; Sharshir, S.W.; Abdelaziz, G.B.; Halim, M.A.; Swidan, A. Improving Performance of Tubular Solar Still by Controlling the Water Depth and Cover Cooling. *J. Clean. Prod.* **2019**, *233*, 848–856. [CrossRef]

55. Kumar, D.; Kumar, S. Thermal Performance of the Solar Parabolic Trough Collector at Different Flow Rates: An Experimental Study. *Int. J. Ambient Energy* **2018**, *39*, 93–102. [CrossRef]

56. Bellos, E.; Tzivanidis, C. Enhancing the Performance of a Parabolic Trough Collector with Combined Thermal and Optical Techniques. *Appl. Therm. Eng.* **2020**, *164*, 114496. [CrossRef]

57. Zheng, Z.; Xu, Y.; He, Y. Thermal Analysis of a Solar Parabolic Trough Receiver Tube with Porous Insert Optimized by Coupling Genetic Algorithm and CFD. *Sci. China Technol. Sci.* **2016**, *59*, 1475–1485. [CrossRef]

58. Ahmed, K.A.; Natarajan, E. Thermal Performance Enhancement in a Parabolic Trough Receiver Tube with Internal Toroidal Rings: A Numerical Investigation. *Appl. Therm. Eng.* **2019**, *162*, 114224. [CrossRef]

59. Bellos, E.; Tzivanidis, C. Enhancing the Performance of Evacuated and Non-Evacuated Parabolic Trough Collectors Using Twisted Tape Inserts, Perforated Plate Inserts and Internally Finned Absorber. *Energies* **2018**, *11*, 1129. [CrossRef]

60. Laaraba, A.; Mebarki, G. Enhancing Thermal Performance of a Parabolic Trough Collector with Inserting Longitudinal Fins in the Down Half of the Receiver Tube. *J. Therm. Sci.* **2020**, *29*, 1309–1321. [CrossRef]

Article

Novel Biosynthesis of Graphene-Supported Zero-Valent Iron Nanohybrid for Efficient Decolorization of Acid and Basic Dyes

Mahmoud Samy [1], Marwa Elkady [2,3,*], Ayman Kamal [4,5], Noha Elessawy [6], Sahar Zaki [4] and Marwa Eltarahony [4,*]

1. Department of Public Works Engineering, Faculty of Engineering, Mansoura University, Mansoura 35516, Egypt
2. Chemical and Petrochemical Engineering Department, Egypt-Japan University of Science and Technology, New Borg El-Arab City, Alexandria 21934, Egypt
3. Fabrication Technology Department, Advanced Technology and New Materials Research Institute (ATNMRI), City of Scientific Research and Technological Applications, New Borg El-Arab City, Alexandria 21934, Egypt
4. Environmental Biotechnology Department, Genetic Engineering and Biotechnology Research Institute (GEBRI), City of Scientific Research and Technological Applications (SRTA-City), Alexandria 21934, Egypt
5. Faculty of Agriculture, Alexandria University, Alexandria 21544, Egypt
6. Computer Based Engineering Applications Department, Informatics Research Institute IRI, City of Scientific Research & Technological Applications (SRTA-City), Alexandria 21934, Egypt
* Correspondence: marwa.elkady@ejust.edu.eg (M.E.); m_eltarahony@yahoo.com (M.E.); Tel.: +20-100-978-2536 (Marwa Eltarahony)

Abstract: Herein, respiratory nitrate reductases (NAR) were utilized in the biosynthesis of zero-valent iron (ZVI) graphene nanocomposite as a simultaneous reducing and capping agent, for the first time, to efficiently adsorb methylene blue (MB) and direct red-81 (DR-81). Under anaerobic conditions, the greenly synthesized graphene was incubated with iron precursor in the presence of crude-NAR enzyme for 48 h to obtain the ZVI graphene composite followed by characterizing this composite using physiochemical analyses. Scanning and transmission electron microscopy, energy dispersive X-ray spectroscopy and X-ray diffraction techniques assured the chemical composition and the interaction between ZVI and graphene. The influences of operating conditions such as contact time, pH and adsorbent dose on the adsorption efficacy were explored in the case of ZVI graphene, graphene and ZVI. ZVI graphene nanocomposite displayed the highest removal efficiency of MB and DR-81 compared to graphene and ZVI-NPs. The removal percentages of DR-81 and MB by ZVI graphene nanocomposites were $88.3 \pm 2.66\%$ and $87.6 \pm 2.1\%$, respectively, at pH 7, adsorbent dose 20 mg/50 mL, initial MB or DR-81 concentration of 10 mg/L and shaking speed of 150 rpm. A pseudo first-order model could describe the adsorption kinetics, and the adsorption mechanism was discussed. The promising results of the current study support the potential of the recruitment of ZVI graphene nanocomposites in eliminating various pollutants from industrial effluents on a larger scale. Further, the prepared nanohybrid can be used in other applications such as photocatalysis, Fenton and persulfate activation processes.

Keywords: decolorization; direct red-81; graphene; methylene blue; nitrate reductases; operating parameters; zero-valent iron

1. Introduction

The expansion of industrial activities such as cosmetics, leather, ink, textiles and printing contributes to the release of heavily contaminated effluents containing dyes to water streams [1,2]. Azo dyes constitute almost 50% of the global production (700,000 ton/year) and during the dyeing process, about 20% of the dyes can be discharged to water sources [3]. The presence of dyes in water bodies inhibits light penetration and photosynthesis and reduces the dissolved oxygen ratios resulting in threats and risks to humans and animals [4].

Therefore, it is imperative to effectively treat effluents containing dyes before discharge to the environment. Many physical, chemical and biological treatment methods have been proposed for the removal of dyes [5–7]. The azo dyes are highly resistant to being degraded by microorganisms and they are toxic to bacteria which make the biological treatment ineffective [8]. Similarly, the removal of dyes by physical–chemical treatment processes such as adsorption, photocatalysis, ozonation and membrane filtration has been investigated [9–12]. However, these methods are associated with some drawbacks such as high costs and the production of toxic by-products [13].

The adsorption process is a promising, inexpensive, simple and efficient treatment process for the removal of industrial effluents (e.g., dyes) compared to previously mentioned techniques [14]. Activated carbon is a commonly employed adsorbent for the removal of bio-resistant pollutants (dyes) from aqueous solutions [15]. However, activated carbon challenges the high cost and requirement of frequent regeneration which obstruct the reusability and full-scale application [16]. Hence, there is an increasing need for the preparation of effective adsorbents with low costs. Zero-valent iron (ZVI) has recently pulled wide heed due to its low cost, high reactivity, green impact, high surface area as well as its capability to reduce oxidized contaminants [12,17]. ZVI is commonly prepared via the liquid-phase reduction in iron salts using strong reducing agents (e.g., sodium borohydride). In spite of the simplicity, short time and high reactivity of the liquid reduction method, this method suffers from shortcomings such as high costs, toxicity of the reducing agent and poor stability of prepared nanoparticles [18]. Moreover, the release of nanomaterials prepared from harmful chemicals after the treatment process has a negative impact on the aquatic and terrestrial environments [19]. Therefore, the efforts have been directed to prepare nanoparticles using ecofriendly materials (e.g., bacteria, plants, algae). In this study, we employed respiratory nitrate reductase (NAR) enzyme as a green reducing and stabilizing agent to replace toxic reducing agents needed in the preparation of ZVI nanoparticles. Due to the toxicity of metal ions to bacteria, bacteria start to protect themselves and then, metal ions can bioaccumulate or biomineralize into the cells after the reduction of metal ions to a lower state [20]. The biosynthesis of ZVI can reduce the cost, protect the environment from toxic chemicals and produce stable nanoparticles.

Another problem facing ZVI is the fast aggregation and formation of the iron oxide layer which reduces the reactivity and reducibility of ZVI [12,21]. To overcome this problem, pure ZVI can be supported with different materials such as silica, kaolinite, starch and graphene [22–24]. Several studies in recent years recorded the efficiency of graphene and its oxide, in particular as a nanosorbent, in different remediation applications of polluted environments by the dint of its high theoretical surface area ($\sim$2620 m^2/g), high electrical conductivity and stability [5]. In this work, a ZVI graphene nanocomposite was prepared by reducing iron salt in the presence of graphene, which was produced from plastic waste, by the catalysis of NAR enzyme. The use of graphene can reduce the agglomeration and the oxidation of ZVI, facilitate the electron transfer from ZVI surface to the pollutant and improve the dispersibility of the nanoparticles [25]. Moreover, the conversion of plastic waste (polyethylene terephthalic) to graphene participates in the management of environmental problems related to the release of plastic wastes to the environment and reduction in costs related to the disposal of plastic waste [26]. Liu et al. (2014) prepared ZVI supported by graphene for the removal of phosphorus from aqueous solutions [25]. They stated that the prepared composite attained a high removal of phosphorus.

In this study, the novel procedures for the biological synthesis of ZVI graphene nanocomposite were provided. The synthesized ZVI graphene nanocomposite was utilized for the removal of methylene blue (MB) and direct red-81 (DR-81). The effects of operating parameters such as contact time, pH and adsorbent dosage were investigated. The removal mechanism and adsorption kinetics of MB and DR-81 were explored.

2. Materials and Methods

2.1. Materials

Plastic bottle wastes were collected from the garbage of City of Scientific Research and Technological Applications in Borg Al Arab, Alexandria. Sodium citrate ($Na_3C_6H_5O_7$, 98%), hydrochloric acid (HCl, 97%), sodium chloride (NaCl, 97%), magnesium sulfate heptahydrate ($MgSO_4 \cdot 7H_2O$, 99%), ferrous chloride tetrahydrate ($FeCl_2 \cdot 4H_2O$, 95%), sodium molybdate ($Na_2MoO_4 \cdot 2H_2O$, 99%), copper sulfate ($CuSO_4 \cdot 5H_2O$, 95%), cobalt chloride hexahydrate ($CoCl_2 \cdot 6H_2O$, 98%), manganese chloride tetrahydrate ($MnCl_2 \cdot 4H_2O$, 97%), zinc sulfate ($ZnSO_4$, 93%), potassium phosphate (KH_2PO_4, 95%), dipotassium hydrogen phosphate ($K_2HPO_4 \cdot 7H_2O$, 97%) and potassium nitrate (KNO_3, 98%) were procured from Sigma-Aldrich and used without modifications.

2.2. Biosynthesis of ZVI Graphene Nanocomposite

Initially, graphene and ZVI-NPs were prepared following the procedures described in detail by El Essawy et al. (2017) and Zaki et al. (2019) [27,28]. For the preparation of ZVI graphene nanocomposite, respiratory membrane-bound nitrate reductase enzyme (NAR) was recruited as reducing and stabilizing agent simultaneously in an in situ synthesis process. NAR enzyme as well as electron shuttling molecules commence nitrate reduction and shuttle electrons to iron ions. Then, the oxidation states of metal ions can change via redox reaction until reaching zero-valent state and forming ZVI-NPs [28,29]. In the presence of graphene, the enzymatically generated ZVI-NPs bind to graphene particles, forming ZVI graphene nanocomposites. Firstly, about 10^8 CFU/mL (0.5 McFarland) of bionanofactory strain *P. mirabilis* 10B was precultured anaerobically in the optimized broth that enhances and induces the growth of NAR enzyme, of the following ingredients (g/L): sodium citrate 7.5, NaCl 0.5, $MgSO_4 \cdot 7H_2O$ 0.12, $FeCl_2 \cdot 4H_2O$ 0.24, $Na_2MoO_4 \cdot 2H_2O$ 0.015, $CuSO_4 \cdot 5H_2O$ 0.06, $CoCl_2 \cdot 6H_2O$ 0.04, $MnCl_2 \cdot 4H_2O$ 0.03, $ZnSO_4$ 0.31, KH_2PO_4 3.0, $K_2HPO_4 \cdot 7H_2O$ 1.0 and KNO_3 5.0 at pH 7.0. The inoculated broth was incubated anaerobically at 30 °C for 48 h in anaerobic jar. After incubation, a considerable bacterial biomass was harvested by centrifugation at 10,000 rpm for 20 min. The harvested cells were washed several times by sterile distilled water and the, suspended in 80 mM potassium phosphate buffer (pH 7.0) and exposed to mild osmotically shock disruption followed by centrifugation at 5000 rpm for 5 min to eliminate unbroken cells and cell debris. Thereafter, the obtained spheroplast was subjected to centrifugation at 10,000 rpm, 4 °C for 60 min. The precipitated pellets were resuspended in 80 mM potassium phosphate buffer (pH 7.0) and utilized as a complete membrane-bound $\alpha\beta\gamma$ complex of NAR. Finally, 0.2 gm of graphene was added to crude-NAR suspension that was supplemented by 1.5 mM of Fe $(NO_3)_3 \cdot 9H_2O$. The overall mixture was incubated under anaerobic conditions for 48 h at 30 °C. The obtained ZVI graphene nanocomposite was collected, washed and dried at 80 °C for 2 h for subsequent characterization and application.

2.3. Characterization of ZVI Graphene Nanocomposite

The crystallographic information of ZVI graphene nanocomposite was investigated by an X-ray diffraction (XRD, Shimadzu-7000, USA) using Cu Kα radiation (λ = 1.54056 Å), voltage of 40 KV, current of 30 mA and scan speed of 10 °/min. The incorporation of ZVI in carbon matrix of graphene was affirmed via the specification of elemental composition using energy dispersive X-ray spectroscopy (EDX) analyzer and elemental mapping combined with transmission electron microscope (TEM, JEOL JSM 6360LA, Japan). Additionally, TEM and scanning electron microscopy (SEM) (JEOL JEM-1230) with an accelerating voltage of 200 kV were employed to study the morphology of the synthesized composite. Raman spectra (Jaso, Japan) were recorded to specify the molecular structure of the synthesized nanoparticles. Raman spectra were set in the 4000–400 cm^{-1} region with a step size of 1 cm^{-1}. Fourier transform infrared spectroscopy (Shimadzu, FTIR-8400S) was performed to specify the functional groups using KBr pellets in the 4000–400 cm^{-1} region with a step size of 1 cm^{-1}. Surface area was estimated using Belsorp-max automated apparatus (BEL Japan)

and the sample was degassed at 200 °C for 3 h. The data of nitrogen (adsorption–desorption isotherms) were recorded at 77.53 K.

2.4. Experimental Procedures

A stock solution with a concentration of 1000 mg/L was prepared for direct red-81 (DR-81) and methylene blue (MB) by dissolving 1 g of the dye in 1 L of distilled water. The adsorption batch experiments were conducted in 100-mililter beaker with 50 mL of the dye solution and the solution was shaken at a speed of 150 rpm. The effects of different parameters such as contact time (15–120) min, adsorbent dose (20, 40, 60, 100 mg/50 mL), and pH (3, 7, 9, 11) were studied at an initial dye concentration of 10 mg/L. Samples were withdrawn and then centrifuged prior to the measurements by UV–Visible spectrophotometer (Labomed model, Inc., Los Angeles, CA, USA) at wavelengths of 500 and 664 nm for DR-81 and MB, respectively. The comparison between the performance of pure ZVI-NPs, graphene and ZVI graphene nanocomposite was performed at pH 7, initial dye concentration of 10 mg/L, adsorbent dose of 20 mg/50 mL and shaking speed of 150 rpm. The adsorption kinetics were investigated using pseudo first- and second-order models and intraparticle diffusion on a time range (0–90 min) at pH 7, adsorbent dose 20 mg/50 mL, initial MB or DR-81 concentration of 10 mg/L and shaking speed of 150 rpm. The equations and discussion of these models were provided in detail in our previous work [9]. In reusability study, the particles were compiled after each run and left at room temperature to dry, thence they can be used in next cycles.

3. Results and Discussion
3.1. Characterization of ZVI Graphene Nanocomposite

In the present study, the NAR enzyme was successfully utilized as a catalyzing and sta-bilizing agent to synthesize ZVI graphene nanohybrid. Generally, the biological approaches of nanomaterial synthesis are advantageous over other traditional physicochemical means. They are characterized by their cost-effectiveness, non-toxicity, biosafety and ecofriendli-ness. They reckon on the utilization of biological molecules in the reduction of bulk parent materials into their nanoform; neglecting by such way the usage of hazardous reductants, high-temperature or energy-intensive processing [28,29]. It is noteworthy to mention the characteristic role of nitrate reductases (NRs), which belong to oxidoreductases groups. They are mainly catalyzing organic material oxidation and play crucial function in pollution remediation and eventually participate in the nitrogen cycle. Recently, NRs were reported in various investigations addressing nanostructure synthesis in green biological meth-ods [29,30]. The ZVI graphene nanocomposite was analyzed by various characterization techniques. SEM and TEM images of pure graphene were provided in the Supplementary Materials (Figure S1) to show the changes in the morphology in the case of the composite. Figure 1a,b shows TEM and SEM images of ZVI graphene biocomposites with particle size ranged from 2.3 to 7 nm, indicating the incorporation of ZVI-NPs in the graphene matrix. However, the magnetic properties of ZVI-NPs resulted in the aggregation of ZVI-NPs in chain-like forms.

Additionally, the EDX pattern in Figure 1c confirmed the presence of both carbon and iron at their characteristic positions (0.277 and 6.4 keV, respectively) with atomic percentages of 50.8% and 36.5%, respectively. Other peaks at 0.39 and 2.3 keV were ascribed to nitrogen and sulfur with atomic ratios of 9.2 and 3.5%, respectively. Interestingly, the existence of nitrogen and sulfur might be owing to the bounded bacterial biomolecules during the synthesis process, such as amino groups ($-NH_3^+$) and sulfhydryl (SH) groups, which could eventually provide the nanocomposite with self-functionalizing and stabilizing properties. However, a Cu peak was also detected due to the copper grid that was used to hold the samples. The XRD pattern in Figure 1d demonstrates the XRD pattern of bare graphene showing only the diffraction planes of graphene. The XRD pattern in Figure 1e affirmed the interaction between the graphene and ZVI-NPs. The peak at 24.67° is attributed to the (002) diffraction plane of graphene [3]. The sharp peak at 44.4° is attributed to the

(110) diffraction plane of ZVI-NPs, whereas the peaks at 31.7°, 35.56°, 51.82° and 59.92° are attributed to the iron oxides formed on the ZVI surface due to the oxidation that might be occurred during washing, drying and processing of the nanocomposite [2,31].
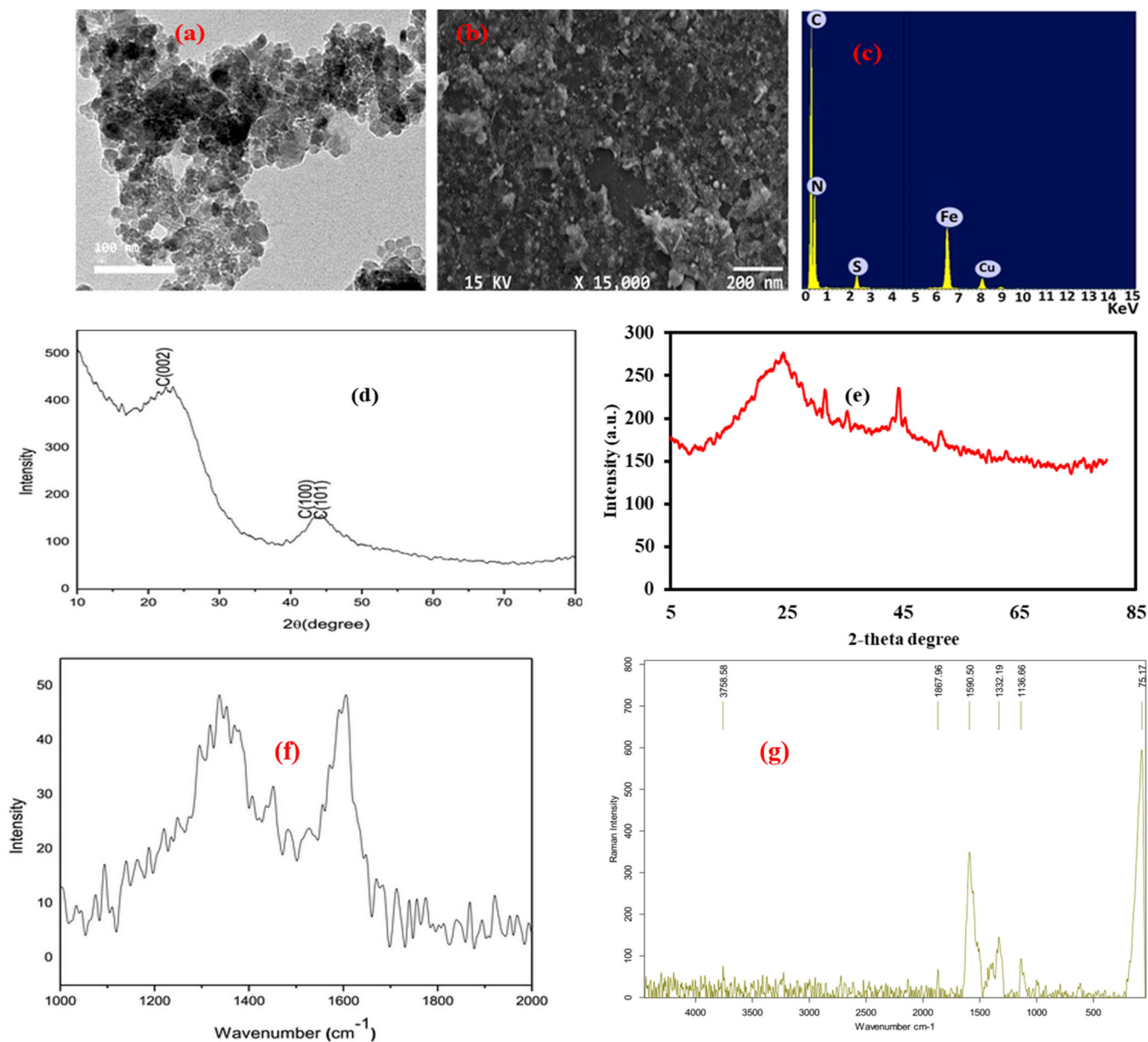
Figure 1. Physicochemical properties (**a**) TEM image, (**b**) SEM, (**c**) EDX pattern of ZVI graphene, (**d**) XRD pattern of graphene, (**e**) XRD of ZVI graphene, (**f**) Raman spectra of graphene and (**g**) Raman spectra of ZVI graphene [27].

Raman spectra of pristine graphene are given in Figure 1f, showing only the D and G bands of graphene. Figure 1g shows the Raman spectra of ZVI graphene. The peaks at 1332.19 cm^{-1} and 1590.5 cm^{-1} are ascribed to the D and G bands of graphene [25]. The peaks at wavenumbers lower than 1000 cm^{-1} (around 75 cm^{-1}, 550 cm^{-1} and 750 cm^{-1}) are attributed to the Fe-O bond, confirming the presence of iron oxides on the surface of ZVI-NPs [31]. Supplementary Materials Figure S2a,b shows the adsorption–desorption isotherms and FTIR spectra of graphene. The surface area was 721.7 m^2/g. The bands in FTIR spectra at 3447, 1636, 1219 and 1105 cm^{-1} are indexed to O-H, C=O, O-H, C-O-C and C-O bonds, respectively [27]. Additionally, the band at 1600 cm^{-1} is imputed to the

C==C bond [27]. Figure S2c,d demonstrates the FTIR spectra and adsorption–desorption isotherms of ZVI graphene. The presence of the hydroxyl group (O-H) was confirmed through the bands at 1610 and 3420 cm^{-1}. The band at 1350 cm^{-1} is assigned to the COO$^-$ group [32]. Moreover, the band at 1020 cm^{-1} is attributed to the C-O bond. The bands at 476 and 628 cm^{-1} are imputed to the Fe-O bond. The surface area of ZVI graphene was estimated (55 m^2/g). Figure S2e,f,g shows the elemental mapping of graphene and ZVI graphene [33]. In the case of graphene, only carbon was detected. Whereas carbon, iron and oxygen were detected in the elemental mapping of the composite.

3.2. Application of ZVI Graphene Nanocomposite in Cationic and Anionic Dye Removal

As observed in Figure 2a,b, the alterations in the UV–vis spectra (from 200 to 800 nm) of DR-81 and MB were monitored upon treatment with ZVI graphene nanocomposite, ZVI and graphene. The spectrum patterns of DR-81 and MB (controls) exhibited the main absorption peaks at 500 and 664 nm for DR-81 and MB, respectively, due to the azo bond, which almost disappeared in the supernatant of the treated samples especially in the case of ZVI graphene. Such vanishing of both peaks reflected the successful removal of both dyes. Our results are coincident with those investigated by Samy et al. (2020) [34]. However, the adsorption process was confirmed by SEM in Figure 2c,d. The pores in the case of ZVI graphene nanocomposite approximately disappeared due to the filling of pores by the dye molecules confirming the high adsorption performance of the dyes by the biosynthesized composite. These things considered, new peaks were formed due to the formation of chemical bonds between the iron oxide layer and dye molecules, as revealed by Raman spectroscopy (Figure 2e,f).
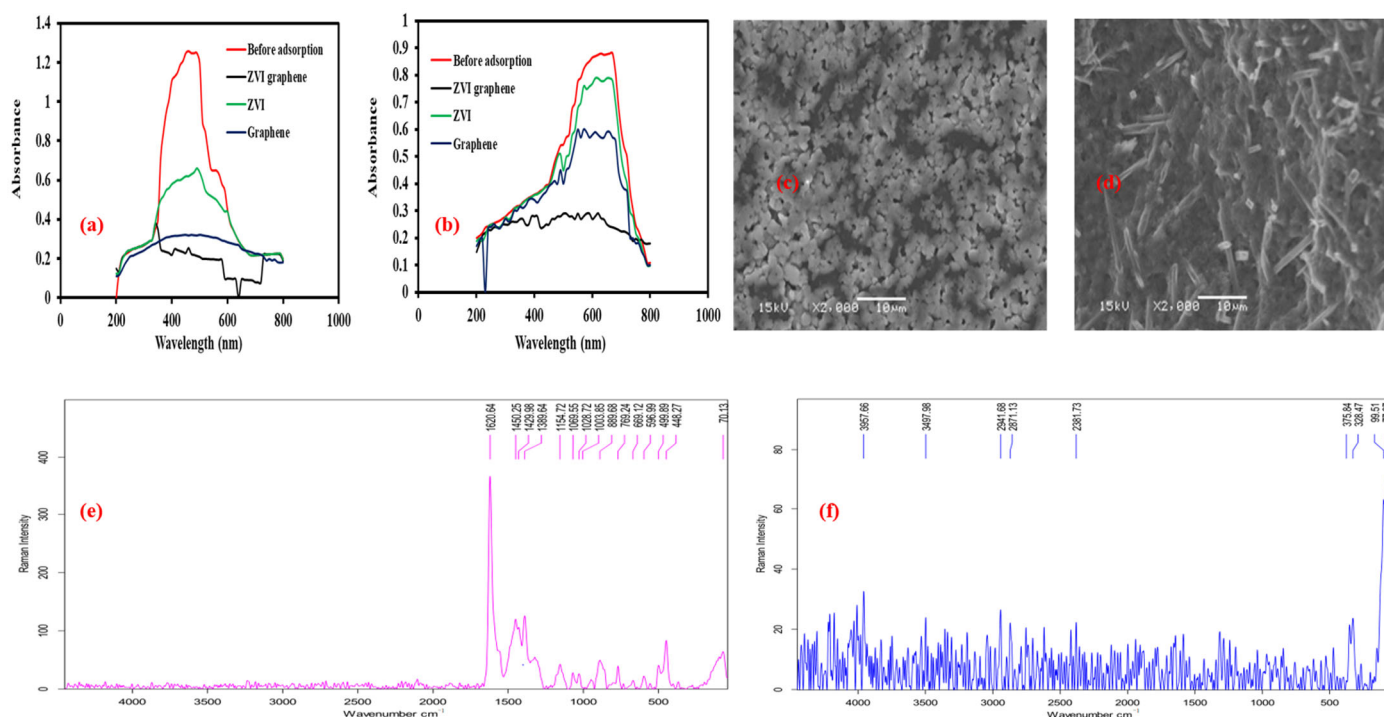
Figure 2. Absorption spectra of (**a**) DR-81 and (**b**) MB before and after adsorption over ZVI graphene, ZVI and graphene; SEM image of ZVI graphene after adsorption of (**c**) DR-81 and (**d**) MB; Raman spectra of ZVI graphene after adsorption of (**e**) DR-81 and (**f**) MB.

Additionally, XRD and FTIR of ZVI graphene after adsorption of DR-81 and MB are given in Supplementary Materials Figure S3a,b. The intensity and transmittance decreased after the adsorption of DR-81 and MB. The change in the intensity and transmittance might be due to the bonds formed between the adsorbent's surface and adsorbate. EDX of ZVI graphene after adsorption in Figure S3c,d showed the introduction of Cl and Na in

the case of MB and DR-81, reaffirming the bonding between the adsorbent's surface and the adsorbate.

3.3. Effect of Contact Time

A comparison between the adsorption performance of ZVI-NPs, graphene and ZVI graphene nanocomposite was conducted to specify the required time for achieving equilibrium and choose the best material, as shown in Figure 3a,b. The experiments were conducted at pH 7, adsorbent dose 20 mg/50 mL, initial MB or DR-81 concentration of 10 mg/L and shaking speed of 150 rpm. The results showed that 90 min was the equilibrium time in the cases of MB and DR-81. The prolonged equilibrium time indicated the porous structure and high surface area of the prepared composite. Gajera et al. (2022) reported an equilibrium time of 2 h [35]. Moreover, the ZVI graphene nanocomposite showed higher adsorption performance towards MB and DR-81 compared to ZVI-NPs and graphene. The removal efficiencies of DR-81 were $61.4 \pm 1.6\%$, $49.8 \pm 1.7\%$ and $88.3 \pm 2.66\%$ in the cases of graphene, ZVI-NPs and ZVI graphene nanocomposite, respectively, whereas the removal efficiencies of MB were $68.8 \pm 3.1\%$, $53.3 \pm 2.39\%$ and $87.6 \pm 2.1\%$ after 90 min with the same order. The extension of the reaction time did not greatly improve the removal percentage because the pores became saturated and the adsorbents' surfaces reached an equilibrium state [25]. The biogenic ZVI graphene nanocomposite attained a removal efficiency of 91.8% and 91.3% for DR-81 and MB, respectively, after 120 min. The synergistic effects of graphene and ZVI-NPs were the major reason for such high removal ratios. The graphene participated in the enhancement of ZVI-NPs dispersion and reduction in aggregation [36]. Graphene exhibited higher performance than ZVI-NPs due to its high surface area, while pure ZVI-NPs might agglomerate which decreased the surface area, thereby reducing the adsorption efficiency.
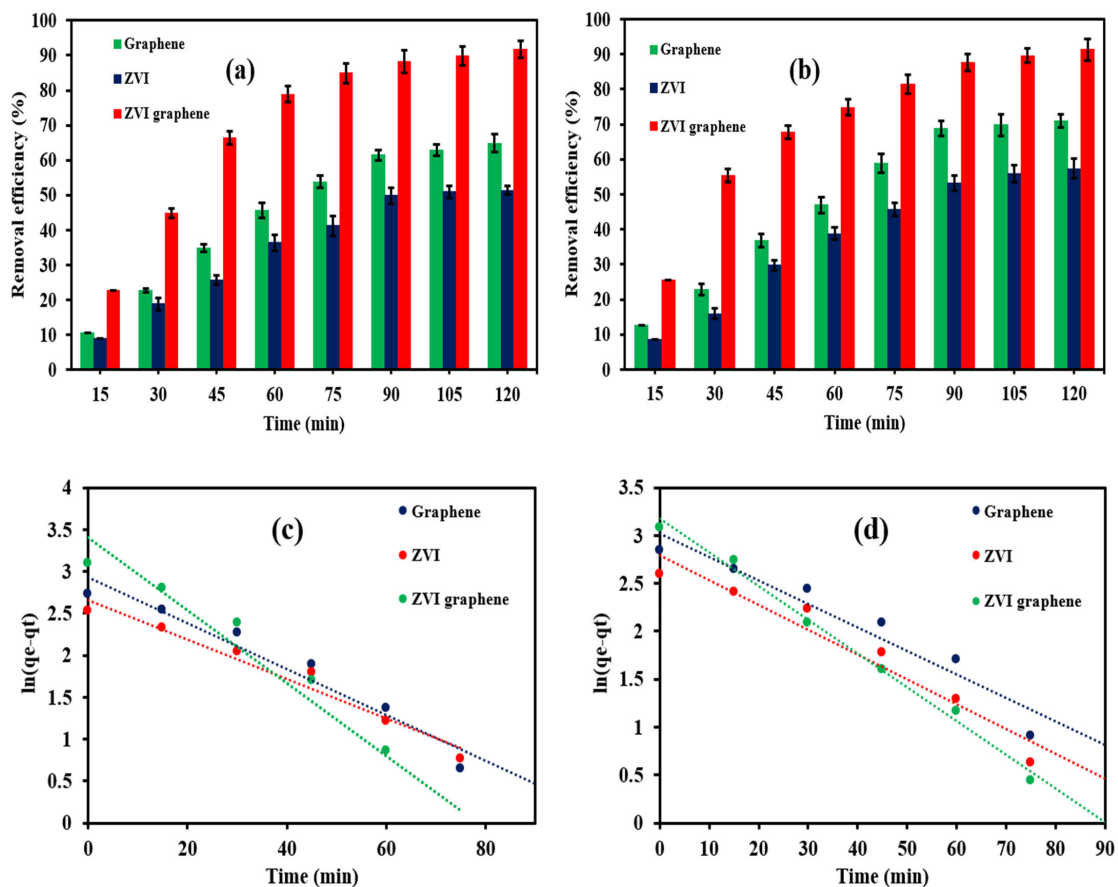
Figure 3. Effect of contact time on the adsorption efficiency of (**a**) DR-81 and (**b**) MB, and pseudo first-order kinetic model in the case of (**c**) DR-81 and (**d**) MB.

The rate constants of the pseudo first-order model were estimated in the case of graphene, ZVI and ZVI graphene via the linear plot of $\ln(q_e-q_t)$ versus time, as shown in Figure 3c,d. The high coefficient of determination values and the slight difference between experimental adsorption capacity and estimated adsorption capacity from the first-order model at equilibrium affirmed the suitability of the first-order model to describe adsorption kinetics. The rate constants were 0.0273, 0.0236 and 0.0434 min^{-1} for graphene, ZVI and ZVI graphene, respectively, in the case of DR-81, whereas the rate constants were 0.026, 0.0245 and 0.0352 min^{-1} for the synthesized materials with the same order in the case of MB. The high-rate constant in the case of the composite compared to graphene and ZVI was in agreement with the results obtained from the comparison between the three materials. Second-order and intraparticle diffusion models were also provided in the Supplementary Materials (Figure S4). Table S1 shows the constant rate (K_1 and K_2), coefficient of determination (R^2) and adsorption capacity at equilibrium (q_e) in the cases of first- and second-order models as well as the constants and R^2 of the intraparticle diffusion model. According to R^2 values in Table S1, the second-order model could not describe the adsorption process. Additionally, obtained q_e from the second-order model is far from the experimental value. The intraparticle diffusion model displayed the multilinearity of the adsorption process.

3.4. Effect of Adsorbent Dose

Figure 4a,b shows the effect of adsorbent dose on the removal efficiency of DR-81 and MB at pH 7, shaking speed at 150 rpm and initial dye concentration of 10 mg/L after a contact time of 90 min. The increase in the graphene dose from 20 mg/50 mL to 60 mg/50 mL resulted in the raising of the removal efficiency from 61.4 ± 1.6% to 88.9 ± 1.9% in the case of DR-81 and from 68.8 ± 3.1% to 89.8 ± 2.4% in the case of MB. However, the increase in graphene dose above 60 mg/50 mL did not show any amelioration in the removal efficiency in both dyes. Regarding ZVI, the increase in the ZVI dose above 60 mg/50 mL showed slight improvement in the adsorption efficiency. In the case of ZVI graphene, upon increasing the dose from 20 mg/50 mL to 40 mg/50 mL, the enhancement of the removal efficiency from 88.3 ± 2.66% to 96.88 ± 1.9% in the case of DR-81 and from 87.6 ± 2.1% to 98.66 ± 1.9% in the case of MB was noticed. The raising of ZVI graphene to 100 mg/50 mL just increased the removal efficiency to 99.77 ± 3.1% and 99.6 ± 2.6% in the cases of DR-81 and MB, respectively. In general, the raising of adsorbent dose increases the number of binding sites which contributes to the amelioration of adsorption performance. Howbeit, doses above the optimum value might decrease or cause a slight improvement of the removal efficiency because of the possible agglomeration of nanoparticles. The agglomeration of nanoparticles could decrease the surface area and, consequently, reduce the active adsorption sites [37]. Mensah et al. (2022) reported the same observation and showed that the increase in the adsorbent dose above 0.2 mg/mL did not boost the adsorption ratio [3].

The stability of the prepared composite was examined under five repetitive runs (450 min, 90 min for each run) for the adsorption of DR-81 and MB, as shown in Supplementary Materials Figure S5. The slight decrease in adsorption percentage in the sequential runs assured the stability of the composite. Howbeit, the decrease in the adsorption ratio might be due to the loss of adsorbent during sampling.
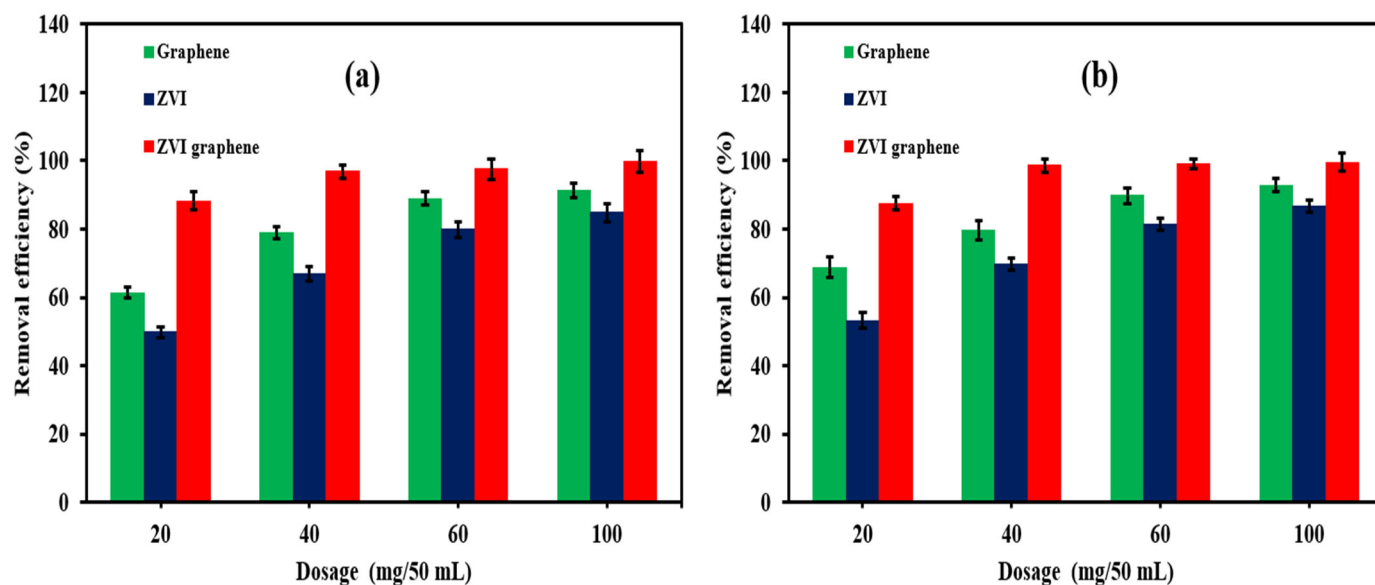
Figure 4. Effect of adsorbent dose on the removal efficiency of (**a**) DR-81 and (**b**) MB.

3.5. Effect of pH

The effect of pH was studied by varying pH from 3 to 11 (using 1 M of HCl or NaOH) at initial dye concentration of 10 mg/L, adsorbent dose of 40 mg/50 mL and shaking speed of 150 rpm, as shown in Figure 5. Point of zero charge (PZC) of ZVI is nearly eight, as reported by Sun et al. (2015) [38]. At pH < PZC, the adsorbent's surface charge becomes positive, and DR-81 is an ionic dye. Therefore, the removal efficiency was improved in acidic and neutral conditions due to the attractive forces between the adsorbent's surface and DR-81 molecules. The elimination efficiency increased from $96.88 \pm 1.67\%$ to $99.4 \pm 1.9\%$ by decreasing pH from 7 to 3 using the ZVI graphene nanocomposite. On the other hand, the removal efficacy went down in alkaline conditions due to the repulsive forces between negatively charged adsorbent's surface and anionic dye molecules. The removal efficiencies were $85.6 \pm 2.3\%$ and $78.9 \pm 2.67\%$ at pH 9 and 11, respectively, using the ZVI graphene nanocomposite. In the case of MB, the removal efficiencies decreased at pH 3 and it was $81.4 \pm 1.9\%$ due to the repulsive forces between positively charged sorbent's surface and cationic dye. However, at neutral pH, the removal efficiency was high. The increase in pH from 3 to 7 resulted in the raising of hydroxyl ions which could be adsorbed on the adsorbent's surface and, consequently, MB as a cationic dye could be adsorbed on the surface [39]. At high pH values, the removal efficiencies decreased to $88.7 \pm 1.4\%$ and $80.1 \pm 1.1\%$ at pH 9 and 11, respectively, in spite of the attractive forces between the adsorbent and adsorbate. At alkaline conditions, ZVI could be easily corroded and, consequently, iron hydroxides would be formed and precipitated [39]. The formed iron hydroxides could block the active sites and inhibit the electron transfer between ZVI and target pollutants which resulted in the decrease in removal efficiency [40]. Hamdy et al. (2018) reported the decrease in MB removal efficiency in alkaline condition due to the block of active sites of ZVI by the corrosion products [41]. In the case of the adsorption of MB and DR-81 over ZVI at pH > 7, the adsorption efficiency decreased due to the accelerated corrosion of ZVI, resulting in the formation of iron hydroxides that could block the binding sites and suppress the electron transfer [40]. At pH $\leq$ 7, the adsorption ratio went up in the case of DR-81 due to the attraction between DR-81 molecules and ZVI surface, whereas the adsorption percentage declined in the case of MB due to the repulsive forces [39]. The adsorption at pH 3 was lower than that of pH 7 due to the competition between MB molecules and Cl$^-$ on ZVI surface [42]. At pH $\leq$ 7, the graphene surface charge is positive, whereas it was negative at pH > 7, as reported by Yang et al. (2022) [43]. So, the adsorption efficiency improved in the case of DR-81 at pH < 7 due to the attraction forces, while the adsorption ratio of DR-81 went down at pH > 7 due to the repulsive forces. In the case of MB, the adsorption

proportion decreased at pH < 7 due to the repulsive forces and the adsorption went up at pH > 7 owing to the attractive forces. In the case of MB at pH 7, the adsorbed hydroxyl ions on the adsorbent's surface might increase the attractive forces, thus improving the degradation ratio.
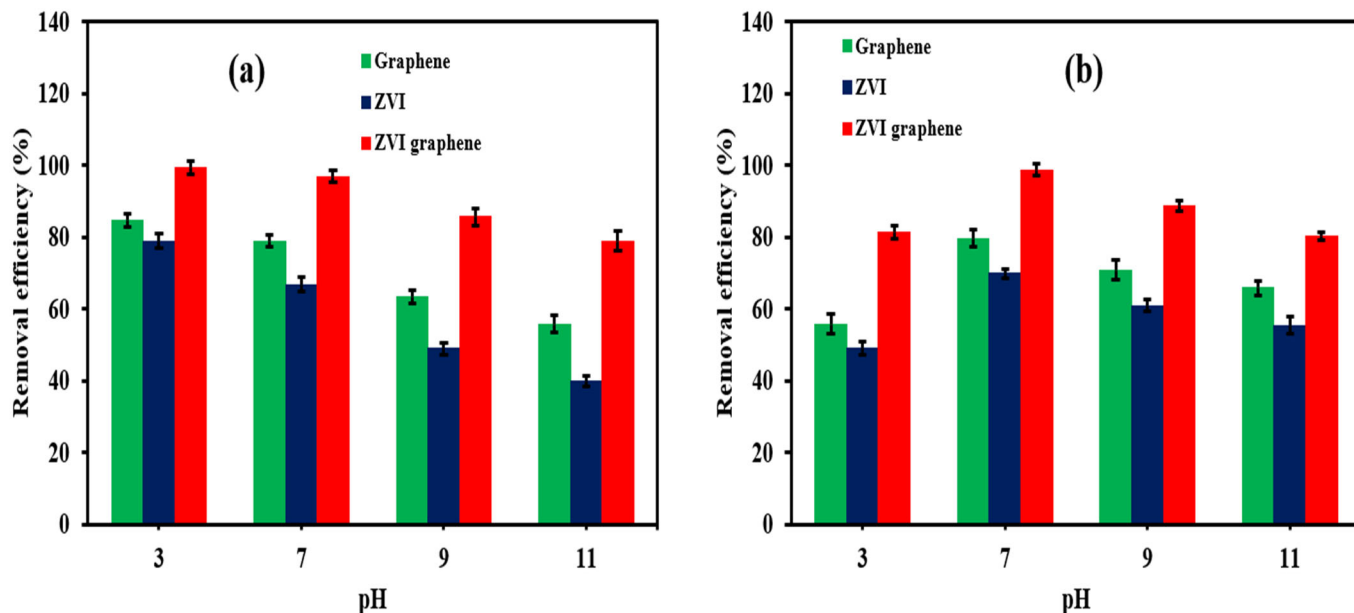
Figure 5. Effect of pH on the removal efficiency of (**a**) DR and (**b**) MB.

3.6. Adsorption Mechanism

Figure 6 demonstrates the adsorption mechanism of DR-81 and MB on ZVI graphene nanocomposite's surface. The adsorption of MB on the adsorbent's surface might be owing to the hydrogen bonding between OH and COOH groups of the adsorbent and NH group of MB [44]. In the case of DR-81, the adsorption took place via hydrogen bonding between SO_3^-, NH and N=N of DR-81 and the hydroxyl group in the adsorbent [45]. Additionally, the hydrogen bonding could happen between COOH of the adsorbent and the NH group of DR-81. The adsorption could take place due to the electrostatic interaction between the COO^- group (deprotonated form of COOH) of the adsorbent and NH^+ of MB. Moreover, the adsorption might occur due to the electrostatic interaction between Na^+ and the deprotonated form of COOH (COO^-) in the case of DR-81 [46]. Further, the adsorption of MB or DR-81 might take place due to the π-π stacking between aromatic groups of MB or DR-81 and oxygen of the hydroxyl group in the prepared adsorbent [45,47]. Additionally, the adsorption could take place due to the Yoshida hydrogen bonding between benzene ring of DR-81 or MB and H in the hydroxyl group [45,48]. The decolorization of DR-81 and MB might also take place due to the reduction by atomic hydrogen (H*) formed owing to the reaction between electrons and H^+ on the adsorbent's surface [49]. Furthermore, the formed iron hydroxides could adsorb DR-81 and MB. The adsorption of DR-81 or MB on ZVI graphene is governed by hydrogen bonding, electrostatic interaction (attractive and repulsive forces), Yoshida hydrogen bonding and π-π stacking. So, the increase or the decrease in the adsorption percentage can be affected by the attractive or repulsive forces between the adsorbent and adsorbate, as explained in Section 3.5. The adsorption in the case of graphene could take place via the same mechanisms (hydrogen bonding, electrostatic interaction (attractive and repulsive forces), Yoshida hydrogen bonding and π-π stacking based on its functional groups, as previously described in the literature) [3]. In the case of ZVI, adsorption could occur via hydrogen bonding, electrostatic interaction (attractive and repulsive forces), Yoshida hydrogen bonding and π-π stacking [49]. Additionally, the removal of dyes via ZVI might take place by reduction and precipitation [50].
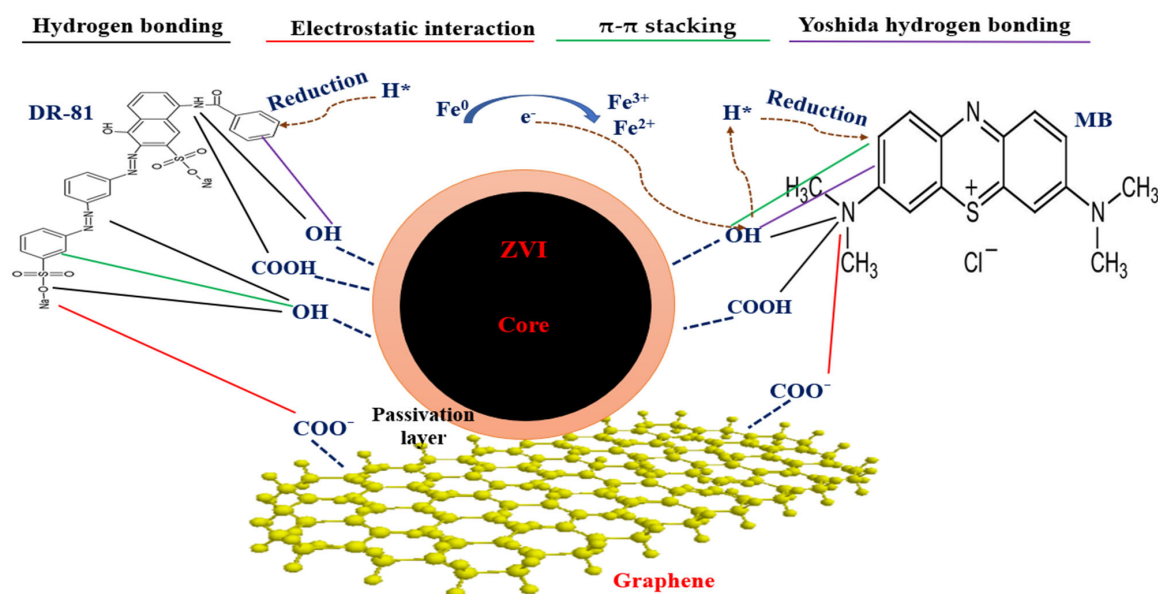
Figure 6. Adsorption mechanism of DR-81 and MB over ZVI graphene nanocomposite.

4. Conclusions

The excellent interaction between the graphene prepared from plastic waste and the biosynthesized ZVI under the catalysis of bacterial NAR enzyme was confirmed by different analytical techniques such as TEM, SEM, EDX, XRD and Raman spectra. The ZVI graphene nanocomposite achieved the highest removal efficiency compared to ZVI-NPs and graphene. The ZVI graphene nanocomposite attained a removal efficiency of $88.3 \pm 2.66\%$ and $87.6 \pm 2.1\%$ in the case of DR-81 and MB, respectively, after an equilibrium contact time of 90 min. The increase in adsorbent dose from 20 to 40 mg/50 mL resulted in the increase in the removal efficiency from $88.3 \pm 2.66\%$ to $96.88 \pm 1.9\%$ in the case of DR-81, compared to $87.6 \pm 2.1\%$ and $98.66 \pm 1.9\%$ in the case of MB. High removal efficiency of DR-81 was attained at acidic and neutral conditions, whereas the removal performance of MB was improved at neutral conditions using the ZVI graphene nanocomposite. The ZVI graphene had the highest adsorption rate in the case of MB and DR-81. The adsorption of MB or DR-81 on ZVI graphene surface could be due to hydrogen bonding, electrostatic interaction, Yoshida hydrogen bonding and π-π stacking. Such biogenic nanocomposite can contribute to lowering the toxicity and the costs of chemicals employed in the synthesis of ZVI-NPs and can overcome the hazards related to the plastic wastes. Additionally, the utilization of plastic wastes in the synthesis of graphene can contribute to the efficient management, reduction in greenhouse gases resulted from the burning or/and landfilling of plastic waste and scalable production of graphene. The high performance, biocompatibility and inexpensiveness of ZVI graphene nanocomposites can encourage decision makers to the full-scale treatment of industrial effluents by the biologically fabricated ZVI graphene nanocomposite. Further, we plan and advise other researchers to employ this efficient nanohybrid in other applications such as photocatalysis, Fenton reaction or persulfate activation system expecting high performance.

Author Contributions: Writing—original draft, M.S., M.E. (Marwa Elkady) and M.E. (Marwa Eltarahony); validation, M.S., S.Z. and A.K.; investigation, M.S., N.E. and M.E. (Marwa Eltarahony); formal analysis, M.S., N.E. and M.E. (Marwa Elkady); writing—review and editing, M.S., M.E. (Marwa Elkady) and M.E. (Marwa Eltarahony); methodology, M.E. (Marwa Eltarahony) and A.K.; supervision, M.E. (Marwa Eltarahony), S.Z. and M.E. (Marwa Elkady). All authors have read and agreed to the published version of the manuscript.

References

1. Samy, M.; Ibrahim, M.G.; Gar Alalm, M.; Fujii, M. Application of CNTs/LaVO 4 on Photocatalytic Degradation of Methylene Blue in Different Contact Modes. In Proceedings of the 2020 Advances in Science and Engineering Technology International Conferences (ASET), Dubai, United Arab Emirates, 4 February–9 April 2020.

2. Mensah, K.; Samy, M.; Ezz, H.; Elkady, M.; Shokry, H. Utilization of Iron Waste from Steel Industries in Persulfate Activation for Effective Degradation of Dye Solutions. *J. Environ. Manag.* **2022**, *314*, 115108. [CrossRef]

3. Mensah, K.; Mahmoud, H.; Fujii, M.; Shokry, H. Novel Nano-Ferromagnetic Activated Graphene Adsorbent Extracted from Waste for Dye Decolonization. *J. Water Process Eng.* **2022**, *45*, 102512. [CrossRef]

4. Wang, G.; Liao, Y.; Stejskal, J. Fabrication of Polyaniline/Poly(Vinyl Alcohol)/Montmorillonite Hybrid Aerogels toward Efficient Adsorption of Organic Dye Pollutants. *J. Hazard. Mater.* **2022**, *435*, 129004. [CrossRef]

5. Samy, M.; Ibrahim, M.G.; Gar Alalm, M.; Fujii, M.; Diab, K.E.; ElKady, M. Innovative Photocatalytic Reactor for the Degradation of Chlorpyrifos Using a Coated Composite of ZrV2O7 and Graphene Nano-Platelets. *Chem. Eng. J.* **2020**, *395*, 124974. [CrossRef]

6. Samy, M.; Ibrahim, M.G.; Fujii, M.; Diab, K.E.; Elkady, M.; Alalm, G. CNTs/MOF-808 Painted Plates for Extended Treatment of Pharmaceutical and Agrochemical Wastewaters in a Novel Photocatalytic Reactor. *Chem. Eng. J.* **2021**, *406*, 7. [CrossRef]

7. Samy, M.; Alalm, M.G.; Mossad, M. Utilization of Iron Sludge Resulted from Electro-Coagulation in Heterogeneous Photo-Fenton Process. *Water Pract. Technol.* **2020**, *15*, 1228–1237. [CrossRef]

8. Venkatesan, S.; Chen, Y.; Teng, H.; Lee, Y. Enhanced Adsorption on TiO2 Photoelectrodes of Dye-Sensitized Solar Cells by Electrochemical Methods Dye. *J. Alloys Compd.* **2022**, *903*, 163959. [CrossRef]

9. Mahanna, H.; Azab, M. Adsorption of Reactive Red 195 Dye from Industrial Wastewater by Dried Soybean Leaves Modified with Acetic Acid. *Desalin. Water Treat.* **2020**, *178*, 312–321. [CrossRef]

10. Samy, M.; Gar Alalm, M.; Fujii, M.; Ibrahim, M.G. Doping of Ni in MIL-125(Ti) for Enhanced Photocatalytic Degradation of Carbofuran: Reusability of Coated Plates and Effect of Different Water Matrices. *J. Water Process Eng.* **2021**, *44*, 102449. [CrossRef]

11. Elsayed, I.; Madduri, S.; El-giar, E.M.; Barbary, E. Effective Removal of Anionic Dyes from Aqueous Solutions by Novel Polyethylenimine-Ozone Oxidized Hydrochar (PEI-OzHC) Adsorbent. *Arab. J. Chem.* **2022**, *15*, 103757. [CrossRef]

12. Jankowska, K.; Su, Z.; Zdarta, J.; Jesionowski, T.; Pinelo, M. Synergistic Action of Laccase Treatment and Membrane Filtration during Removal of Azo Dyes in an Enzymatic Membrane Reactor Upgraded with Electrospun Fibers. *J. Hazard. Mater.* **2022**, *435*, 129071. [CrossRef]

13. Muthukumar, P.; Sowmiya, E.; Arunkumar, G.; Pannipara, M.; Al-sehemi, A.G.; Philip, S. Highly Enhanced Dye Adsorption of MoO3 Nanoplates Fabricated by Hydrothermal-Calcination Approach in Presence of Chitosan and Thiourea. *Chemosphere* **2022**, *291*, 132926. [CrossRef]

14. Chen, C.; Tseng, W.J. Preparation of TiN-WN Composite Particles for Selective Adsorption of Methylene Blue Dyes in Water. *Adv. Powder Technol.* **2022**, *33*, 103423. [CrossRef]

15. Zhang, R.; Zeng, L.; Wang, F.; Li, X.; Li, Z. Influence of Pore Volume and Surface Area on Benzene Adsorption Capacity of Activated Carbons in Indoor Environments. *Build. Environ.* **2022**, *216*, 109011. [CrossRef]

16. Chung, J.; Sharma, N.; Kim, M.; Yun, K. Activated Carbon Derived from Sucrose and Melamine as Low-Cost Adsorbent with Fast Adsorption Rate for Removal of Methylene Blue in Wastewaters. *J. Water Process Eng.* **2022**, *47*, 102763. [CrossRef]

17. Ren, J.; Zheng, L.; Su, Y.; Meng, P.; Zhou, Q.; Zeng, H. Competitive Adsorption of Cd(II), Pb(II) and Cu(II) Ions from Acid Mine Drainage with Zero-Valent Iron/Phosphoric Titanium Dioxide: XPS Qualitative Analyses and DFT Quantitative Calculations. *Chem. Eng. J.* **2022**, *445*, 136778. [CrossRef]

18. Puthukkara, A.R.P.; Jose, S.T.; Lal, D.S. Plant mediated synthesis of zero valent iron nanoparticles and its application in water treatment. *J. Environ. Chem. Eng.* **2021**, *9*, 104569. [CrossRef]

19. Bundschuh, M.; Filser, J.; Lüderwald, S.; Mckee, M.S.; Metreveli, G.; Schaumann, G.E.; Schulz, R.; Wagner, S. Nanoparticles in the Environment: Where Do We Come from, Where Do We Go To? *Environ. Sci. Eur.* **2018**, *30*, 6. [CrossRef]

20. Iravani, S. Bacteria in Nanoparticle Synthesis: Current Status. *Int. Sch. Res. Not.* **2014**, *2014*, 59316.

21. He, Y.; Fang, T.; Wang, J.; Liu, X.; Yan, Z.; Lin, H.; Li, F.; Guo, G. Insight into the Stabilization Mechanism and Long-Term Effect on As, Cd, and Pb in Soil Using Zeolite-Supported Nanoscale Zero-Valent Iron. *J. Clean. Prod.* **2022**, *355*, 131634. [CrossRef]

22. Ma, Q.; Teng, W.; Sun, Y.; Chen, Y.; Xue, Y.; Chen, X.; Zhang, C.; Zhang, H.; Fan, J.; Qiu, Y.; et al. Multi-Component Removal of Pb (II), Cd (II), and As (V) over Core-Shell Structured Nanoscale Zero-Valent Iron @ Mesoporous Hydrated Silica. *Sci. Total Environ.* **2022**, *827*, 154329. [CrossRef] [PubMed]

23. Kumari, B.; Dutta, S. Integrating Starch Encapsulated Nanoscale Zero-Valent Iron for Better Chromium Removal Performance. *J. Water Process Eng.* **2020**, *37*, 101370. [CrossRef]

24. Kakavandi, B.; Takdastan, A.; Pourfadakari, S. Heterogeneous Catalytic Degradation of Organic Compounds Using Nanoscale Zero-Valent Iron Supported on Kaolinite: Mechanism, Kinetic and Feasibility Studies. *J. Taiwan Inst. Chem. Eng.* **2019**, *96*, 329–340. [CrossRef]

25. Liu, F.; Yang, J.; Zuo, J.; Ma, D.; Gan, L.; Xie, B.; Wang, P.; Yang, B. Graphene-Supported Nanoscale Zero-Valent Iron: Removal of Phosphorus from Aqueous Solution and Mechanistic Study ScienceDirect Graphene-Supported Nanoscale Zero-Valent Iron: Removal of Phosphorus from Aqueous Solution and Mechanistic Study. *J. Environ. Sci.* **2014**, *26*, 1751–1762. [CrossRef] [PubMed]

26. Pet, P.; Waste, B. A Novel One Step Synthesis for Carbon Based Nanomaterials from a Novel One-Step Synthesis for Carbon-Based Nanomaterials from Polyethylene Terephthalate (PET) Bottles Waste. *J. Air Waste Manag. Assoc.* **2016**, *67*, 358–370. [CrossRef]

27. El, N.A.; Ali, S.M.; Farag, H.A.; Konsowa, A.H. Green Synthesis of Graphene from Recycled PET Bottle Wastes for Use in the Adsorption of Dyes in Aqueous Solution. *Ecotoxicol. Environ. Saf.* **2017**, *145*, 57–68. [CrossRef]

28. Zaki, S.A.; Eltarahony, M.M.; Abd-el-haleem, D.A. Disinfection of Water and Wastewater by Biosynthesized Magnetite and Zerovalent Iron Nanoparticles via NAP-NAR Enzymes of Proteus Mirabilis 10B. *Environ. Sci. Pollut. Res.* **2019**, *26*, 23661–23678. [CrossRef]

29. Eltarahony, M.; Zaki, S.; Elkady, M.; Abd-el-haleem, D. Biosynthesis, Characterization of Some Combined Nanoparticles, and Its Biocide Potency against a Broad Spectrum of Pathogens. *J. Nanomater.* **2018**, *2018*, 5263814. [CrossRef]

30. Golla, N.; Pradesh, A. Antibacterial and antiviral properties. *Int. J. Pharma Sci. Res.* **2019**, *10*, 1223–1228. [CrossRef]

31. Adel, A.; Alalm, M.G.; El-Etriby, H.K.; Boffito, D.C. Optimization and Mechanism Insights into the Sulfamethazine Degradation by Bimetallic ZVI/Cu Nanoparticles Coupled with H_2O_2. *J. Environ. Chem. Eng.* **2020**, *8*, 104341. [CrossRef]

32. Wu, M.; Ma, Y.; Wan, J.; Wang, Y.; Guan, Z.; Yan, Z. Investigation of Factors Affecting the Physicochemical Properties and Degradation Performance of NZVI@mesoSiO2 Nanocomposites. *J. Mater. Sci.* **2019**, *54*, 7483–7502. [CrossRef]

33. Ratanaphain, C.; Viboonratanasri, D.; Prompinit, P.; Krajangpan, S.; Khan, E.; Punyapalakul, P. Reactivity Characterization of SiO_2-Coated Nano Zero-Valent Iron for Iodoacetamide Degradation: The Effects of SiO_2 Thickness, and the Roles of Dehalogenation, Hydrolysis and Adsorption. *Chemosphere* **2022**, *286*, 131816. [CrossRef]

34. Samy, M.; Ibrahim, M.G.; Alalm, M.G.; Fujii, M. Modeling and Optimization of Photocatalytic Degradation of Methylene Blue Using Lanthanum Vanadate. *Mater. Sci. Forum* **2020**, *1008*, 97–103.

35. Gajera, R.; Patel, R.V.; Yadav, A.; Labhasetwar, P.K. Adsorption of Cationic and Anionic Dyes on Photocatalytic Flyash/TiO2 Modified Chitosan Biopolymer Composite. *J. Water Process Eng.* **2022**, *49*, 102993. [CrossRef]

36. Xing, R.; He, J.; Hao, P.; Zhou, W. Graphene oxide-supported nanoscale zero-valent iron composites for the removal of atrazine from aqueous solution. *Colloids Surfaces A Physicochem. Eng. Asp.* **2020**, *589*, 124466. [CrossRef]

37. Jing, Q.; Qiao, S.; Xiao, W.; Tong, L.; Ren, Z. Efficient Removal of 2,4-DCP by Nano Zero-Valent Iron-Reduced Graphene Oxide: Statistical Modeling and Process Optimization Using RSM-BBD Approach. *Adsorpt. Sci. Technol.* **2021**, *2021*, 7130581. [CrossRef]

38. Sun, X.; Kurokawa, T.; Suzuki, M.; Takagi, M.; Kawase, Y. Removal of Cationic Dye Methylene Blue by Zero-Valent Iron: Effects of PH and Dissolved Oxygen on Removal Mechanisms. *J. Environ. Sci. Health Part A* **2015**, *50*, 1057–1071. [CrossRef]

39. Elkady, M.F.; Hassan, H.S. Invention of Hollow Zirconium Tungsto-Vanadate at Nanotube Morphological Structure for Radionu-clides and Heavy Metal Pollutants Decontamination from Aqueous Solutions. *Nanoscale Res. Lett.* **2015**, *10*, 1–6. [CrossRef]

40. Khan, A.; Muthu, S.; Park, J.; Lee, W.; Chon, C.; Sung, J.; Lee, G. Azo Dye Decolorization by ZVI under Circum-Neutral PH Conditions and the Characterization of ZVI Corrosion Products. *J. Ind. Eng. Chem.* **2016**, *47*, 86–93. [CrossRef]

41. Hamdy, A.; Mostafa, M.K.; Nasr, M. Zero-Valent Iron Nanoparticles for Methylene Blue Removal from Aqueous Solutions and Textile Wastewater Treatment, with Cost Estimation from Aqueous Solutions and Textile Wastewater Treatment, with Cost Estimation. *Water Sci. Technol.* **2018**, *78*, 367–378. [CrossRef]

42. Samy, M.; Mossad, M.; El-Etriby, H.K. Synthesized Nano Titanium for Methylene Blue Removal under Various Operational Conditions. *Desalin. Water Treat.* **2019**, *165*, 374–381. [CrossRef]

43. Yang, J.; Shojaei, S.; Shojaei, S. Removal of Drug and Dye from Aqueous Solutions by Graphene Oxide: Adsorption Studies and Chemometrics Methods. *NPJ Clean Water* **2022**, *5*, 5. [CrossRef]

44. Thi, T.; Nguyet, P.; Trinh, X.; Minh, D.; Hoang, T. Preparing Three-Dimensional Graphene Aerogels by Chemical Reducing Method: Investigation of Synthesis Condition and Optimization of Adsorption Capacity of Organic Dye. *Surf. Interfaces* **2021**, *23*, 101023.

45. Shahinpour, A.; Tanhaei, B.; Ayati, A.; Beiki, H.; Sillanpää, M. Binary Dyes Adsorption onto Novel Designed Magnetic Clay-Biopolymer Hydrogel Involves Characterization and Adsorption Performance: Kinetic, Equilibrium, Thermodynamic, and Adsorption Mechanism. *J. Mol. Liq.* **2022**, *366*, 120303. [CrossRef]

46. Galdames, A.; Ruiz-rubio, L.; Orueta, M.; Miguel, S. Zero-Valent Iron Nanoparticles for Soil and Groundwater Remediation. *Int. J. Environ. Res. Public Health* **2020**, *17*, 5817. [CrossRef]

47. Pasinszki, T.; Krebsz, M. Synthesis and Application of Zero-Valent Iron Nanoparticles in Water Treatment, Environmental Remediation, Catalysis, and Their Biological Effects. *Nanomaterials* **2020**, *10*, 917. [CrossRef]

48. Figueiredo, T.; Mayara, P.; Roberto, V.; Nunes, B.; Siqueira, C.; Picone, F.; Prediger, P. Instantaneous Adsorption and Synergic Effect in Simultaneous Removal of Complex Dyes through Nanocellulose/Graphene Oxide Nanocomposites: Batch, Fixed-Bed Experiments and Mechanism. *Environ. Nanotechnol. Monit. Manag.* **2021**, *16*, 100584. [CrossRef]

49. Eltaweil, A.S.; El-tawil, A.M.; El-monaem, E.M.A.; El-subruiti, G.M. Zero Valent Iron Nanoparticle-Loaded Nanobentonite Intercalated Carboxymethyl Chitosan for Efficient Removal of Both Anionic and Cationic Dyes. *ACS Omega* **2021**, *6*, 6348–6360. [CrossRef]

50. Boparai, H.K.; Joseph, M.; O'Carroll, D.M. Kinetics and Thermodynamics of Cadmium Ion Removal by Adsorption onto Nano Zerovalent Iron Particles. *J. Hazard. Mater.* **2011**, *186*, 458–465. [CrossRef]

A Micro-Metal Inserts Based Microchannel Heat Sink for Thermal Management of Densely Packed Semiconductor Systems

Essam M. Abo-Zahhad [1,2] , Chaouki Ghenai [1,3] , Ali Radwan [3,4] , Osama Abdelrehim [4] ,
Mohamed S. Salem [4] , Mohamed R. Elmarghany [4] , Asmaa Khater [4] and Mahmoud A. Shouman [4,*]

1   Renewable Energy and Energy Efficiency Research Group, Sustainable Energy and Power Systems Research
     Centre, Research Institute for Sciences and Engineering (RISE), University of Sharjah,
     Sharjah P.O. Box 27272, United Arab Emirates
2   Mechanical Power Engineering Department, Faculty of Energy Engineering, Aswan University,
     Aswan 81528, Egypt
3   Department of Sustainable and Renewable Energy Engineering, College of Engineering, University of Sharjah,
     Sharjah P.O. Box 27272, United Arab Emirates
4   Mechanical Power Engineering Department, Faculty of Engineering, Mansoura University,
     Mansoura 35516, Egypt
*   Correspondence: m_shouman@mans.edu.eg

Abstract: The thermal management of high-heat-density devices is essential for reliable operation. In this work, a novel procedure is proposed and investigated for the efficient thermal management of such devices. The proposed procedure introduces different arrangements of metal inserts within a cooling channel heat sink. The objective of those inserts is to form boundary layers to prevent any hot spots from appearing within the flow and increase temperature uniformity. Five different arrangements are introduced and numerically investigated using the commercial software package ANSYS FLUENT 2021R1. The model was validated against previous findings and showed a good agreement with errors of less than 5.5%. The model was then used to study the heat transfer characteristics of the proposed cases compared to traditional straight channels under the same operating conditions. All the proposed arrangements displayed better heat transfer characteristics than the traditional configuration within the studied range. They also exhibited lower temperature nonuniformities, implying better temperature distribution. The temperature contours over the heat source top surface and the flow streamlines are also introduced. Among all the proposed arrangements cases, a microchannel with micro metal insert located at the top wall along with a second row of inserts covering two-thirds of the bottom wall is studied. This case achieved the best heat transfer characteristics and highest temperature uniformity, making it a viable candidate for high power density devices' thermal management.

Keywords: high-heat devices; electronics cooling; thermal management; CFD; heat transfer enhancement; microchannels; inserts

1. Introduction

Recently, there has been a considerable increase in compact, high-performance electronic devices in almost every aspect, including, but not limited to, manufacturing, education, communication, transportation, and entertainment. This has led to increasing demand for high-power micro-electronic chips [1,2]. To maintain the reliability and the high performance of said microchips, their operating temperatures should be kept below 85 °C. Therefore, controlling the microchips' temperatures has become one of the main challenges threatening the widespread electronics industry. This thermal management challenge arises due to two factors. The first one is the high-power density of these chips, which generates high heat flux rates exceeding 1000 W/cm^2 in some local spots [3,4]. The second factor is

the demand for a compact design of these chips, which reduces the available space for heat removal. These two factors eliminated the ability to use conventional thermal management techniques. Therefore, finding novel thermal management techniques that can fulfill the required heat dissipation rates has become an intriguing issue that has concerned many researchers. As part of these devoted efforts, researchers have employed nanofluids [5,6], phase change materials [7,8], and liquid metal [1] as cooling fluids.

Utilizing microchannel heat sinks is considered an efficient tool that can be used to cool down electronic components at a high heat rate. The first microchannel heat sink was presented by Tuckerman and Pease, who presented a simple design comprising several parallel channels [9] capable of dissipating up to 790 W/cm^2 from the surface of the chip with a relatively low pumping power. Since then, many researchers have tried to enhance the thermal performance of the microchannel heat sink with variable degrees of success.

The effect of using different channel configurations on heat transfer performance was previously investigated [10,11]. It was found that rectangular cross-section microchannels exhibit better heat transfer performance compared to trapezoidal and triangle cross-section microchannels. It was also concluded that the pressure loss is directly proportional to the channel aspect ratio. Hung et al. [12] numerically examined the effect of enlarging the outlet of the microchannel heat sink. The pressure drop was found to be reduced by the increase in the enlargement ratio. On the other hand, Nusselt number, temperature control, and heat transfer efficiency increased.

The impact of adding ribs to the side walls of straight microchannels on the heat transfer performance was also studied. Different cross sections of ribs were tested, including rectangular, semi-circular, and triangular, with different angles [13–15]. Using ribs improved the heat transfer performance at lower values of Re. On the other hand, a pressure drop increase was observed. Adding cavities to the straight channel reduced the pressure drop and the heat transfer performance. Thus, a combination between cavities and ribs could enhance heat transfer performance while maintaining an acceptable pressure drop value [16–18].

The use of wavy microchannels to reduce the temperature of the electronic components was also investigated [19–21]. It was noticed that a secondary flow was generated when the flow passed through the wavy channels, which resulted in an enhancement in the fluid mixing and an improved heat transfer performance [22]. A numerical investigation led by Mohammed et al. [23] estimated the optimal amplitude of the wavy channel to be between 0.063 and 0.22 μm. However, increasing the amplitude resulted in poor performance compared to conventional straight channels. The pressure drop and the friction factor were found to be increased with the increase of the amplitude. The effect of adding secondary branches to the wavy microchannels was numerically and experimentally studied by Chiam et al. [24]. The advantages of the secondary branches could be found at lower values of Re (<100), while increasing Re over that range resulted in a higher pressure drop compared to conventional wavy channels. This was not the case when secondary branches were added to wavy channels at relatively small amplitudes (<0.075 μm), with high transfer performance and lower pressure drop values.

Chuan et al. [25] and Gong et al. [26] utilized porous media within the walls of the microchannels. It was reported that porous walls reduced the viscous stresses and thus the pressure drop. The pressure drop was reduced by 48% when porous media was used compared to solid walls [25]. Also, the heat transfer performance was enhanced when porous walls were used.

The effect of adding a secondary channel to the flow path on the heat transfer performance of the microchannels was numerically studied [27,28]. Using secondary channels along with ribs reduced the pressure drop by up to 50%. The heat transfer was also enhanced by increasing the flow mixing between the channels [27]. Multi-objective algorithm optimization was used to find the best heat sink geometry with secondary flow channel design [28]. The optimization aimed to minimize the pressure drop and maximize the heat

transfer rate. The optimized microchannel reduced the pumping power and the thermal resistance by 23% and 29%, respectively.

As can be seen from the previous research, various efforts were applied to enhance heat transfer within microchannels. However, there is always room for more innovative ideas. The current work investigates the effect of inserting a structured micro-sized metal mesh into the streamline on the heat transfer performance. The proposed concept depends on inducing the formation of a boundary layer by attaching metal inserts with different placements to avoid any hot spots within the device. The design is based on constructal law adopted to modify an actual mini-size straight channels heat sink device. Different cases were studied by dividing the channel length into three zones with the same inlet and outlet conditions.

The main objectives of this work are listed in the following bullet points:

- To describe a promising approach to reduce the high-temperature gradient levels associated with the stream direction, which presents a main downside of the micro channel-based cooling systems;
- To introduce metal inserts to develop a secondary flow that improves the heat transfer and reduces the flow maldistribution;
- To remove any local hotspots which could harm the physical structure of the semiconductor devices, consequently, electronic components' life span and performance;
- To reduce thermal management systems' power consumption without compromising cooling performance and reliability.

2. Numerical Modeling and Simulation Analysis

A computational fluid dynamics (CFD) model is established using the commercial package ANSYS Fluent 2021R1 to simulate the thermal management system's fluid flow and heat transfer. The high-performance computing facility of Maha Cluster at the University of Sharjah was used for simulation. A detailed description of the modeling procedures and case setup is discussed in the following subsections.

2.1. Physical Model and Proposed Configurations

The physical description of the presented model is shown in Figure 1. The heat source is a microelectronic silicon chip with an area of 25 mm × 25 mm, directedly bonded to the main board from the bottom side. Meanwhile, the chip is directly attached to the bottom of a cooling channel. In the current work, the chip is simulated as a constant heat source that acts at the cooling channel bottom wall. The designs used in the current work are shown in Figure 2. The channel dimensions and geometries were designated considering the constraints of 3D metal printing and pumping requirements. The figure shows two schematic graphs to identify the characteristics of the channel geometry of a traditional straight channel and one of the newly introduced cases. An isometric view with a magnification of the internal channel structure sections A-A cross-sectional view of the channel in the middle of the coolant domain is presented. As illustrated in the figure, Case 0 refers to the baseline or the standard straight channel heat sink, whereas cases 1 to 5 present the modified channels. Micro metal inserts are placed in the flow stream at different configurations, as shown in the figure, to improve the heat transfer rate in the cooling channels. As seen from the figure, in Case 1, a single row of metal inserts is introduced in the upper half of the flow path. Case 2 introduces another shorter row of metal at the corner that occupies only about one-third of the area. Case 3 introduces the same second short row as in Case 2 but in the middle. Case 4 presents a longer second row that covers two-thirds of the flow area, whereas Case 5 introduces two complete rows that cover the whole area. The proposed idea is to develop boundary layers to break any hot spots within the device. A parametric study is performed to trade off heat dissipation rates and pumping requirements. As for the coolant, water is used as the working fluid during the numerical study with thermophysical properties carefully defined as polynomial equations

in temperature, as described in Table 1. The detailed heat sink and channel dimensions are listed in Table 2.
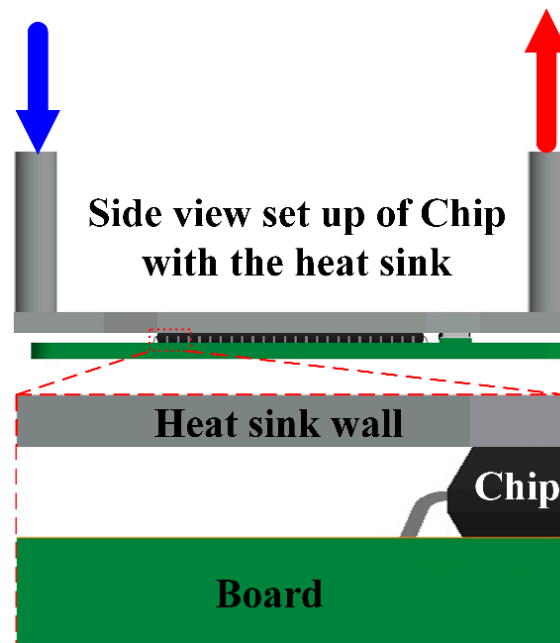
Figure 1. A schematic diagram of the proposed heat sink assembly with a chip in an integrated board.
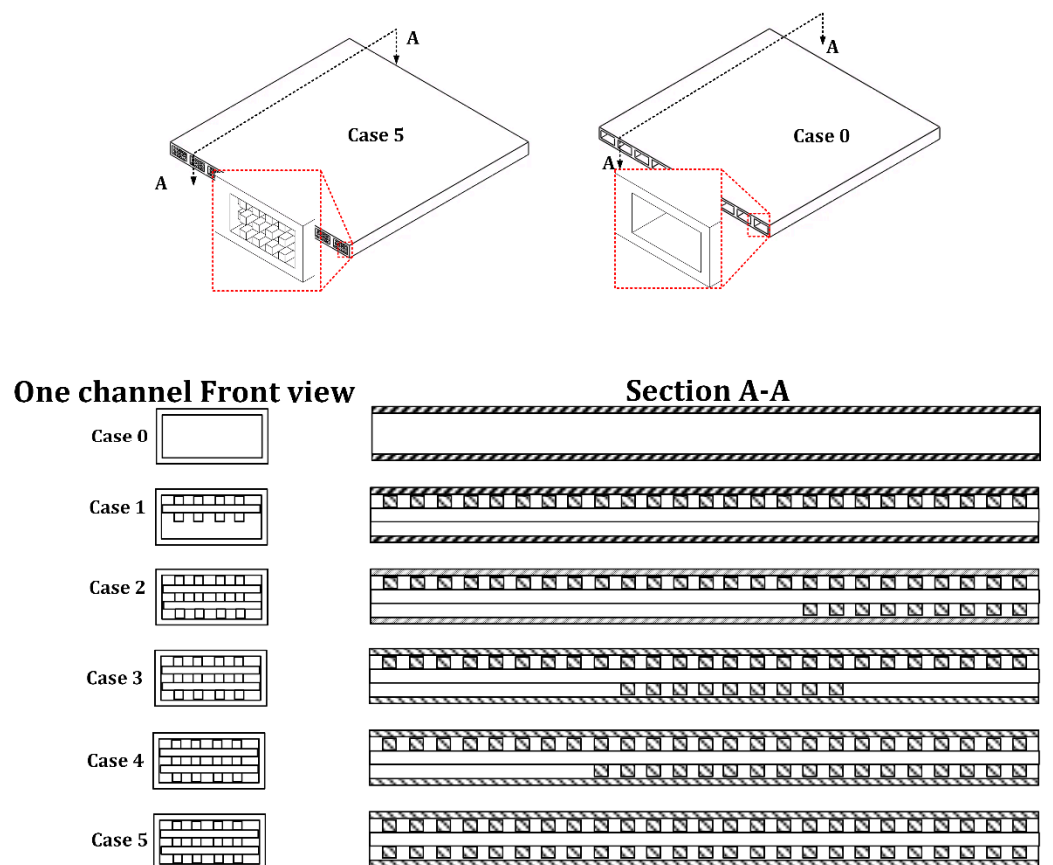
Figure 2. A schematic graph to identify the investigated channel geometry cases. A cross-sectional view of the channel in the middle of the coolant domain for Cases 0 through 5.

Table 1. Thermo-physical properties of cooling fluid as a function of the temperature [29,30].

Property = A + B × T + C × T² + D × T³ + E × T⁴, (T in Absolute)				
Coefficient	ρ (kg/m³)	C_p (J/kg·K)	K(W/m·K)	μ (Pa·s)
A	−1184.2713	5025.1	−0.785392198460943	0.41260813
B	24.66772581	−4.7536	0.00759075936901133	−0.004756694
C	−0.1032172737	0.0047	−0.00000993306796402867	0.000020683412
D	0.0001919823623	0.000006	-	−0.000000040117972
E	−0.0000001374629319		-	0.000000000029250643

Table 2. Detailed general dimensions of the cooling channel.

Term, Dimension	Value (mm)
Hest sink width	25
Hest sink Length	25
Channel height	2
Channel height	1
Walls thicknesses	0.5
Metal inserts width and height	0.2
Void width and height	0.2–0.3

2.2. Model Assumptions

In the current work, mass, momentum, and energy conservation are simultaneously solved to predict the flow characteristics. Some simplifications and assumptions are adopted to simulate the heat transfer and fluid flow characteristics of the current 3-dimensional (3D) model. Concerning the operating conditions:

- The simulations are contacted under 3D steady state steady flow conditions;
- Single-phase, incompressible, and laminar fluid flow prevails across the channel;
- The body forces and the effect of viscous heating are ignored;
- Very smooth walls (No-slip condition at walls). This assumption was based on Knudsen number (Kn) calculations. It is valid when the channel characteristic length is significantly bigger than the mean free path i.e., Kn < 0.001 [31]. In this case, as liquids are incompressible, the mean free path can be considered a constant. A good approach for water is to set the mean free path around 0.31 nm. Therefore, in microfluidic channels with characteristic length scales of more than 300 nm, we can safely assume no-slip boundary conditions;
- The gravity influence is neglected. This assumption is valid for small spaces and tight streams, as confirmed by Dang et al. [32]. As the height of the current cooling (H_{HS}) channel is only 1 mm, and the calculations are conducted under single-phase and incompressible flow circumstances, the consequence of gravity is ignored in the current simulation. Furthermore, forced convection is assumed to be dominant, with no local density differences.

2.3. Boundary Conditions

The boundary conditions used in the numerical model are depicted in Figure 3 and can be summarized as follows:

- Inlet working fluid velocity with Reynolds number (Re) spanning from 1000 to 2000;
- Inlet working fluid temperature of 293 K;
- Pressure outlet boundary;
- A heat flux of 100 W/cm² at the top wall;
- Symmetric left- and right-hand side walls;
- All other surfaces are considered adiabatic walls.
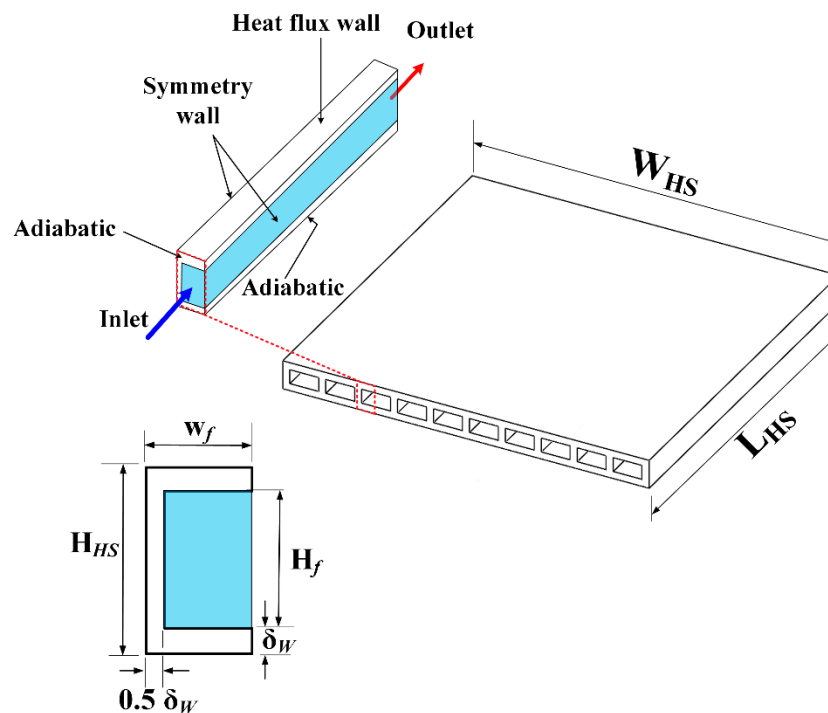
Figure 3. A schematic of the domains used in the CFD calculations and boundary conditions.

2.4. Grid Sensitivity Test

A structured mesh was generated using ANSYS Meshing. Figure 4a presents a sample of the structured mesh at different locations. A mesh-independence investigation was carried out before the model was used to study each design case. The grid sensitivity test was performed concerning the average interface temperature, temperature nonuniformity, and pressure drop. A Reynolds number of 2000, an ambient temperature of 293 K, and a heat flux of 100 W/cm^2 were selected as simulation conditions for the mesh sensitivity study. Different computational structured grid sizes were studied. All the studied grid sizes were physically controlled hexahedral configurations. The coarsest studied element size mesh was 250 μm, and the smallest mesh size was 20 μm. The coarse and extra fine mesh sizes element numbers were between 6000 and 8,000,000 elements, respectively. Figure 4b–d present the effect of changing mech size on the average wall temperature, the nonuniformity, and the pressure drop respectively. The percentage error between each consecutive mesh size was calculated to seek a < 1% error value. Therefore, a mesh of four million elements was chosen to reduce computation time while maintaining acceptable accuracy.
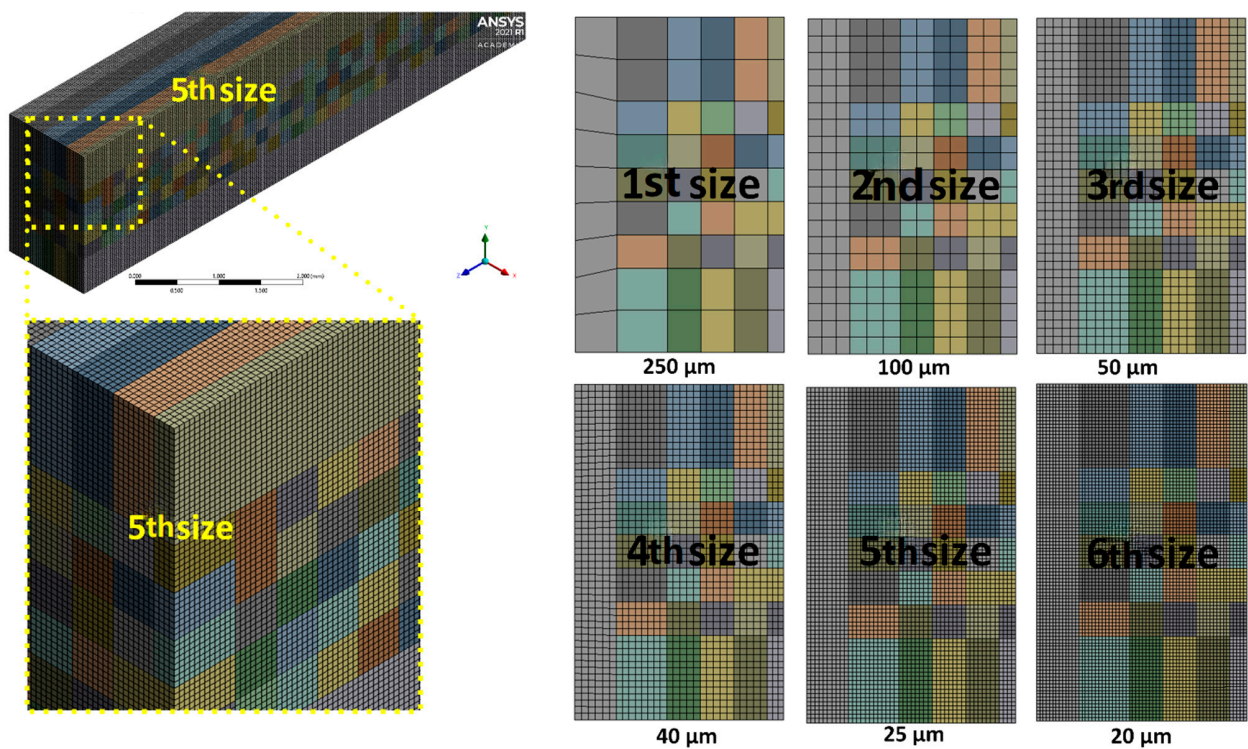
(**a**)
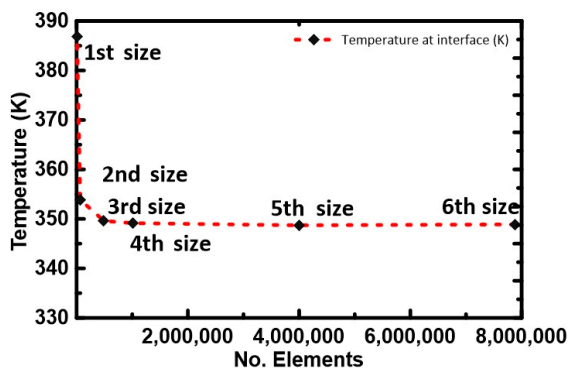
(**b**)
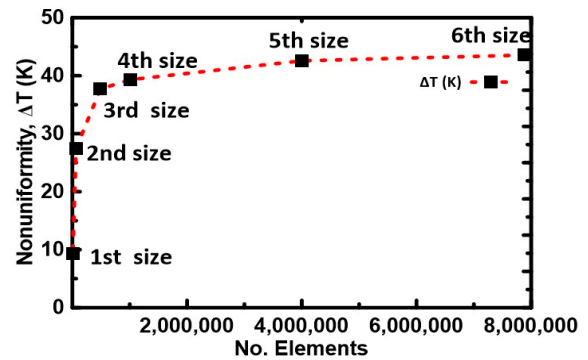
(**c**)
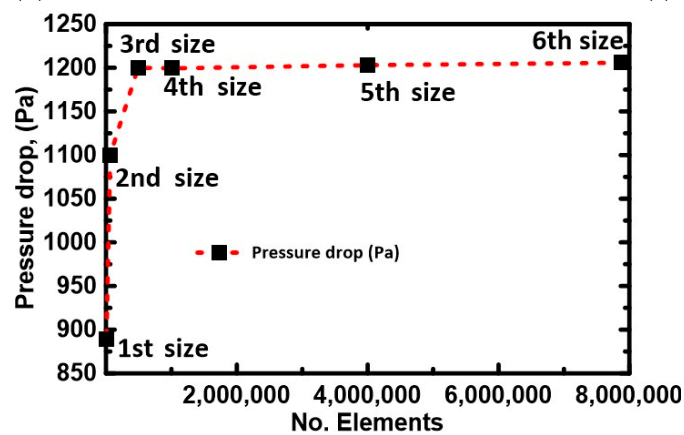
(**d**)

Figure 4. (**a**) Generated mesh at different locations and sensitivity test regarding; (**b**) average interface temperature; (**c**) temperature nonuniformity; and (**d**) pressure drop.

2.5. Model Validation

The CFD model is validated using previous literature investigations utilizing water as a single-phase coolant. The validation was conducted for multi-bifurcation cooling channel at different coolant flow rates, as shown in Figure 5. The numerical results are consistent with Xie et al. [33] data for the same conditions. Nusselt number and pressure drop values were compared. As can be seen from Figure 2a,b, the average variation between any two numerical values was found to be less than 5.5% for the Nusselt number and less than 2.8% for the pressure drop in all investigated cases. Also, the generated Nu values for case 0 were compared to the Sieder–Tate correlation [29] and were found to be in good agreement, as can be seen from Figure 2c. Hence, the mathematical model's dependability was confirmed and established.
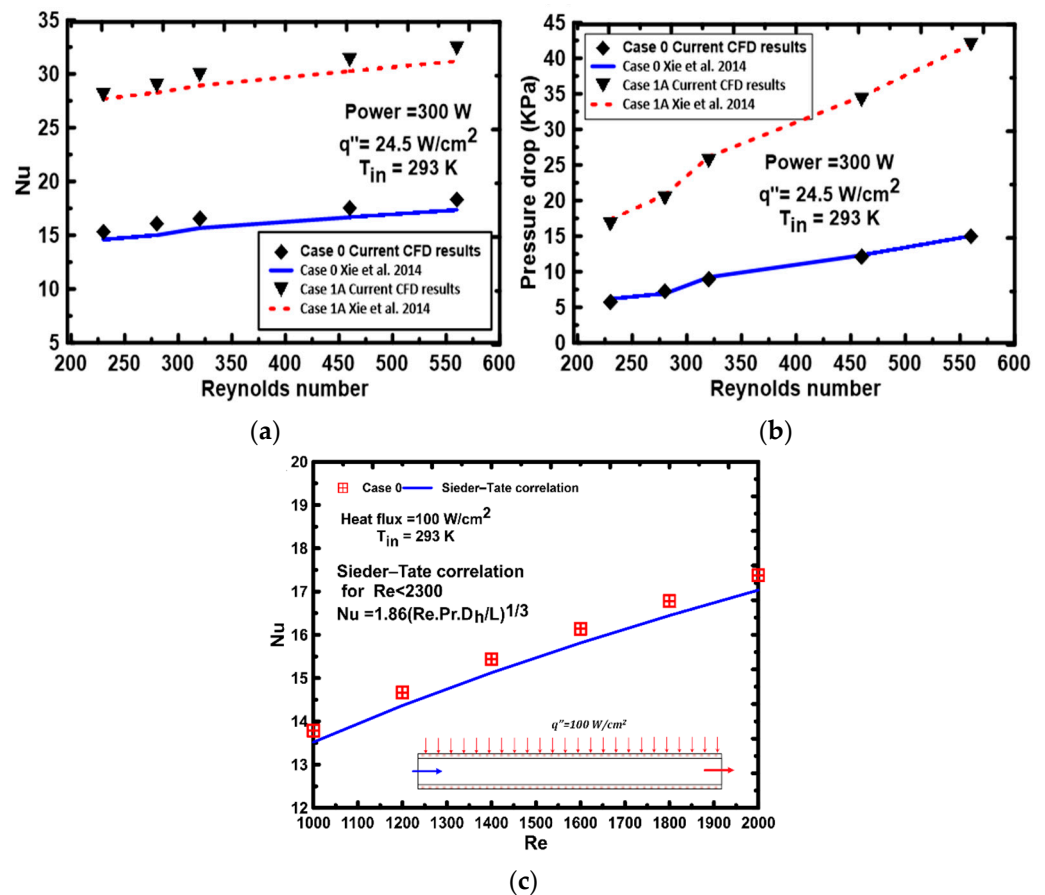
Figure 5. Comparing the current CFD data and Xie et al. [33] findings under identical conditions for (**a**) Nu and (**b**) pressure drop, respectively; and (**c**) Verifications Nu of Case 0 with Sieder–Tate correlation [29].

The error analysis was estimated using the root mean square percent deviation (RMSD) and the mean absolute percent error (MAE) [34] techniques as follows:

$$MAE(\%) = \frac{100}{n} \sum_{1}^{n} \left| \frac{X_{sim,i} - X_{exp,i}}{X_{exp,i}} \right| \qquad (1)$$

$$RMSD(\%) = 100 \times \sqrt{\frac{\sum_{1}^{n} \left(\frac{X_{sim,i} - X_{exp,i}}{X_{exp,i}} \right)^2}{n}} \qquad (2)$$

where $X_{sim,i}$, $X_{exp,i}$ are the predicted and experimental values. The range of errors using *MAE* and *RMSD* were 0.56% and 0.7% for Nusselt number. As for the pressure drop,

the error was very small (less than 0.1% for both techniques). The Nusselt number error analysis for case 0 had error of 1.85% and 1.89%, respectively.

The data obtained from the model was reduced using the equations mentioned in Appendix A.

3. Results and Discussion

Numerical studies of the heat transfer performance were carried out for all the considered cases with various metal mesh insert locations and lengths. The inlet Re was specified in the range of 1000 to 2000, and the corresponding ranges of the volumetric flow rate and inlet velocity were calculated. The convective heat transfer coefficient was evaluated in each case (Case 1 to Case 5) and compared with the reference case (Case 0). Figure 6 introduces the heat transfer coefficient and Nu change with the inlet Re for all investigated cases. Over the Re range, the heat transfer performance of Case 0 (a cooling channel without any metal insert) showed the lowest heat transfer performance.
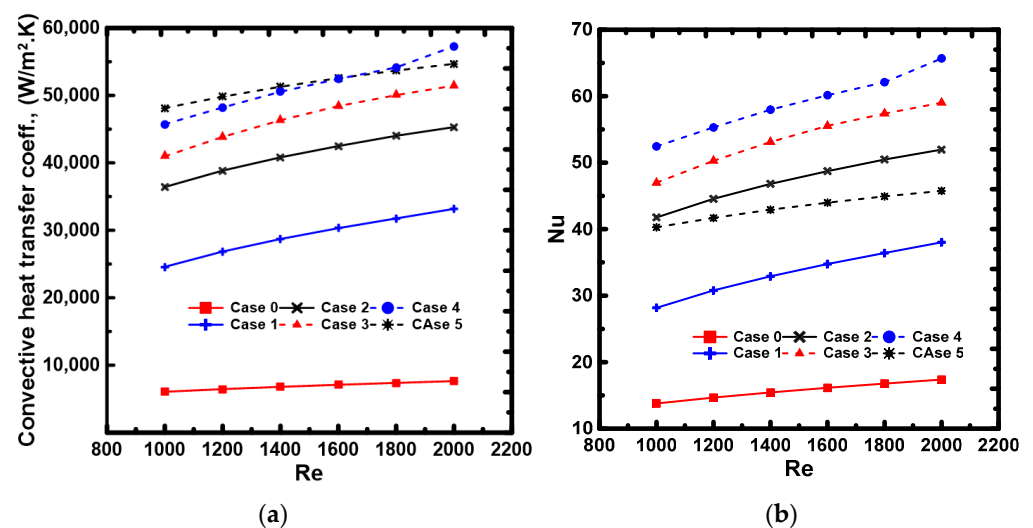
Figure 6. Comparison of (**a**) heat transfer coefficient; and (**b**) Nusselt number with the Re for all the studied cases.

As shown in Figure 6, the impact of the metal inserts on the heat transfer coefficient and Nu is significant compared to the reference case in all the proposed configurations. At the lowest inlet Re < 1000, cases 4 and 5 with a longer length of the second row of the metal insert attained a slightly higher heat transfer coefficient than that with a short length (Cases 2 and 3) and Case 1 with a single row. Although Case 5 exhibited comparable heat transfer coefficient values to those of Case 4, the Nu number values are relatively low due to the decrease in the hydraulic diameter. At the studied range, Case 4 had the highest values among all the cases. This means that Case 4 has the best thermal performance in heat transfer.

Figure 7 compares solid, fluid, and total thermal resistances between the conventional Case 0 and the enhanced Cases 1 to 5. All the thermal resistances' fluid thermal resistance decreased significantly with any increase in Re. As can be seen from the figure, the thermal resistance initially dramatically decreased with the increases of the Re, then the reduction rate diminishes for higher Re values.
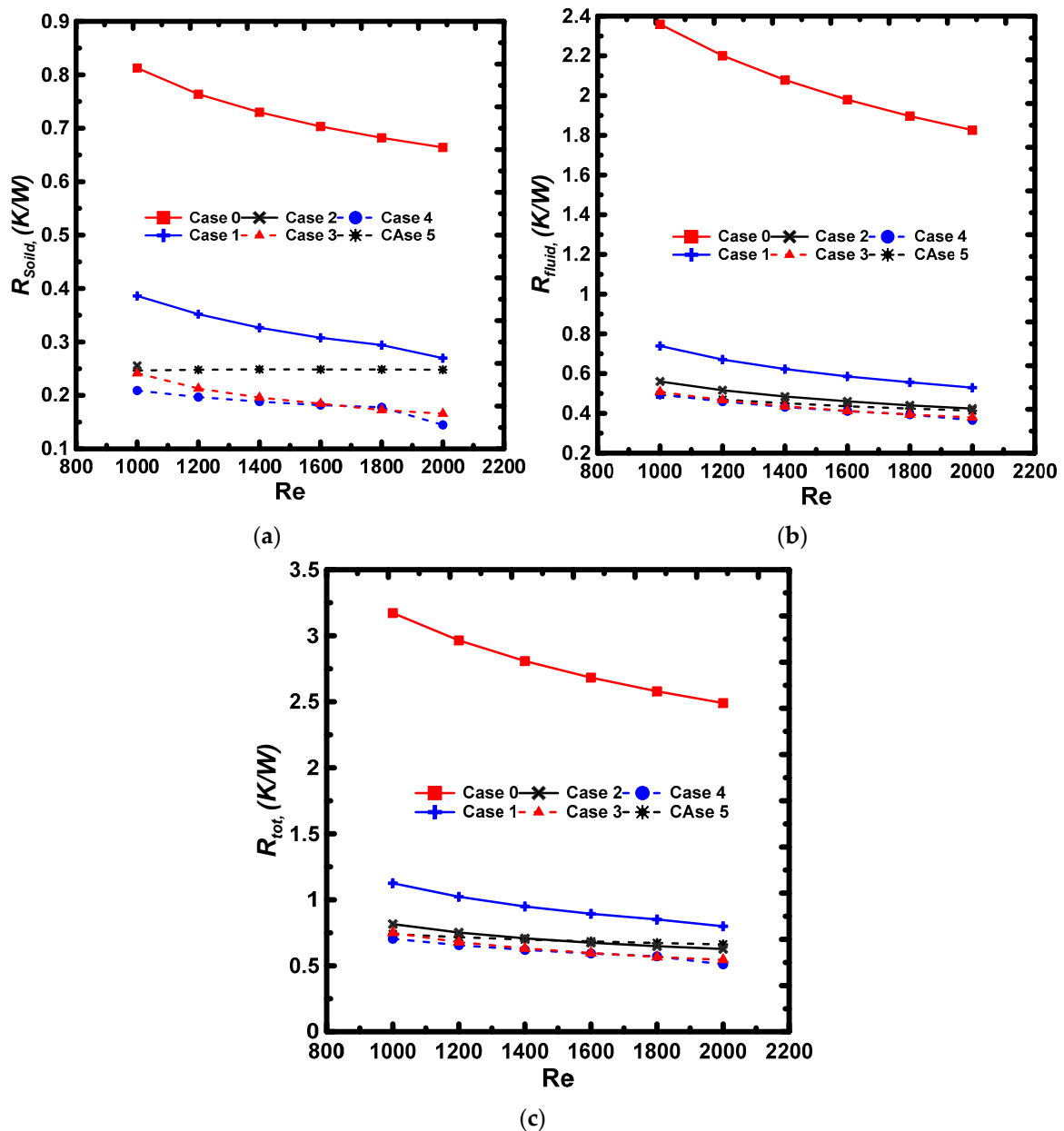
Figure 7. Comparison of thermal resistance (**a**) solid thermal resistance; (**b**) fluid thermal resistance; and (**c**) total thermal resistance.

Figure 8 shows the variations of the Nusselt number ratio (Nu/Nu_0) and the fanning friction factor ratio (f/f_0) with Re, where the denominators present the values for Case 0. From Figure 8a, increasing Re had no significant effect on the Nu/Nu_0, or the f/f_0 values within the studied range. Case 1 exhibited the lowest Nu/Nu_0 and f/f_0 values, whereas Case 4 attained the highest values of about $Nu/Nu_0 = 5$, and f/f_0 of about 15.
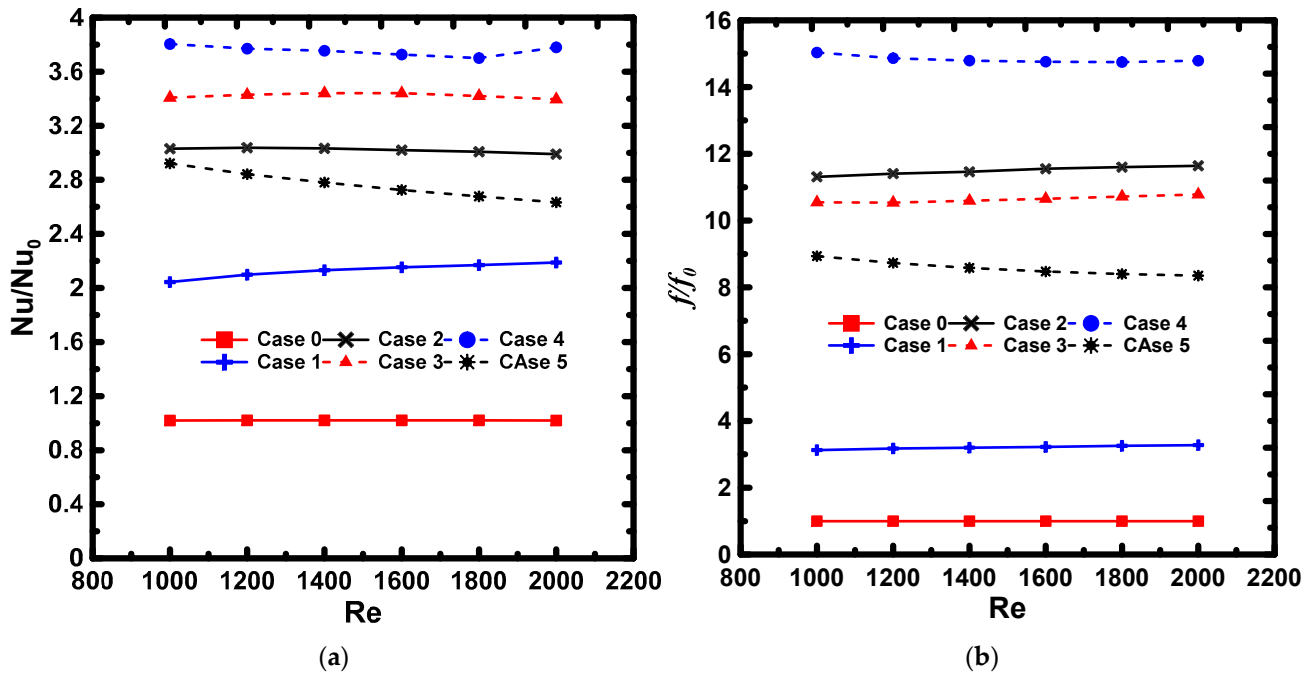
Figure 8. Variations of (**a**) Nu/Nu$_0$; and (**b**) f/f_0 with Re.

The efficiency evaluation criterion (EEC) is used to evaluate the enhanced performance at identical Re. From Figure 9, Re had a negligible effect on the thermal performance of all the investigated cases. Again, Case 4 exhibited the best performance within the studied range. The performance factor (PF), which measures the EEC to the power of 1/3, is used to gauge the overall effectiveness of the proposed design. The value of describes how successful the thermal system is in reducing pressure drop. If the value is more than 1, it means that thermal performance is better than pressure drop, and if it is less than 1, it means the opposite.
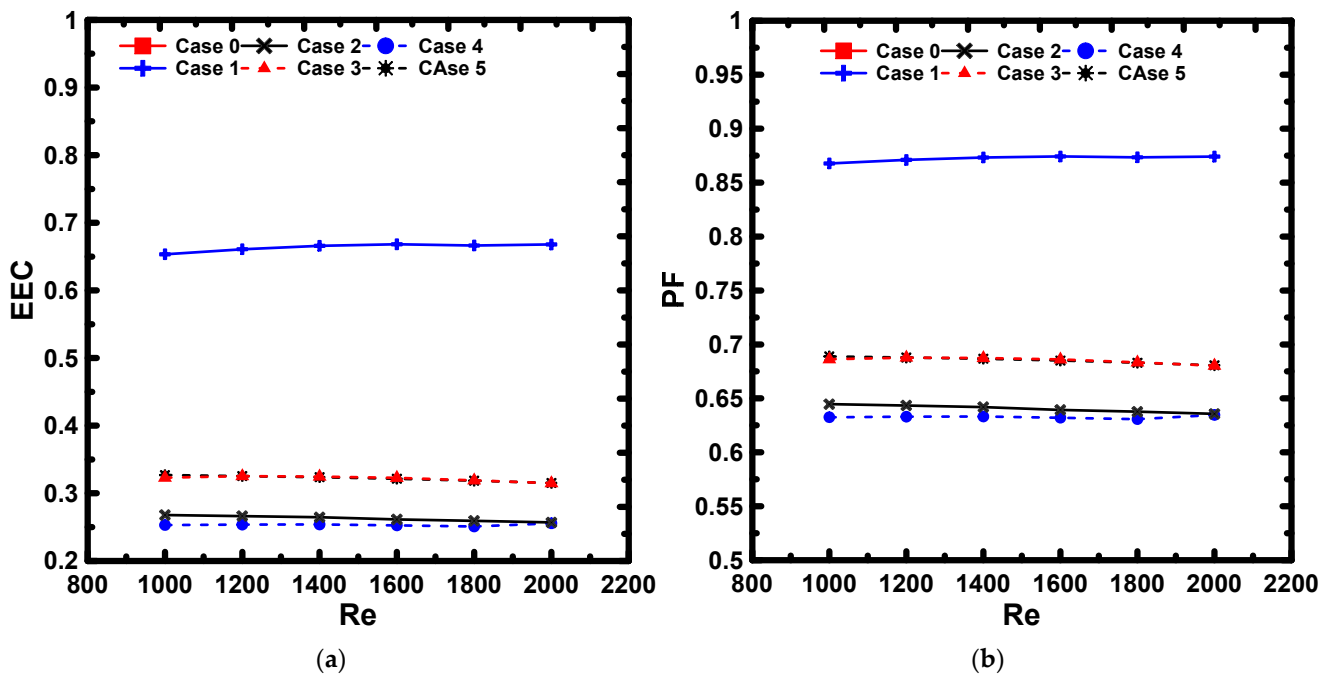
Figure 9. Variations of the efficiency: (**a**) evaluation criterion EEC; and (**b**) performance factor (PF) with Re.

The nonuniformity degree within the heat source for all the proposed configurations was compared with the base case to determine the impact of the metal inserts on the wall temperature uniformity at all Re ranges and the same operating conditions. It was observed that the temperature variation was decreased for all cases with the increase in Re, thereby enhancing the temperature distribution uniformity. It is also clear from the figure that the introduction of the metal inserts considerably enhanced the wall temperature uniformity and reduced the temperature gradient with the length of the device. Cases 3 and 4 showed the lowest nonuniformity levels over the Re range. For Cases 3 and 4, the average uniformity enhancement compared to Case 0 was about 85.4% and 86.6%, respectively. For instance, when Re = 2000, nonuniformity in Case 0 was 48 K, whereas it was 5.84 K and 4.7 K in Cases 3 and 4, respectively. For Cases 1, 2, and 5, the average enhancement of wall temperature uniformity was 67.1%, 82%, and 78.3%, respectively. The metal inserts improved the heat transfer generally and deduced flow and heat maldistribution, which can be interpreted as the metal inserts regenerating the boundary conditions, which kept the heat transfer capability of the working fluid along the flow stream (Figure 10).
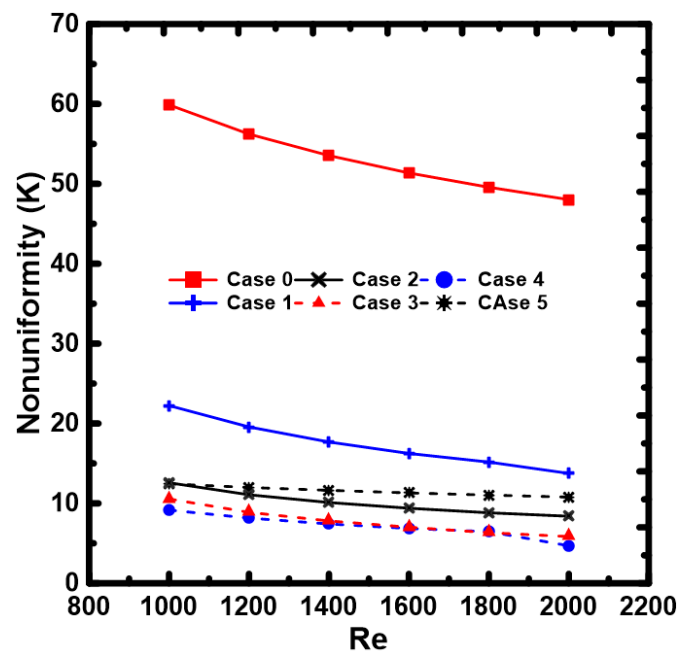
Figure 10. The effect of involving different metal inserts on temperature nonuniformity of the device when for all the considered cases.

Figure 11 shows the temperature contours of the heat source when the structured metal inserts are involved under the same heat flux of 100 W/cm^2 and Re = 2000. All the subfigures used different legends scales due to the significant difference in the obtained results. The figure shows the typical wall temperature distribution contours, which match the literature [33,35,36]. The contours show that the metal inserts considerably reduced the average wall temperature and nonuniformity. It is evident that the metal inserts' length and petition control the flow field and hotspot location. For more details, Cases 1 and 5 are comparable with Case 0 as the metal inserts were placed along the flow stream. However, in Case 5, the cooling channel is wholly packed with metal inserts, which is not the case in Case 1, where the metal inserts were placed in the top half of the channel. The difference between the two designs (Cases 1 and 5) is reflected in the pressure drop value, nonuniformity (even though the contours distribution is almost the same), and average wall temperature. For Case 2, the metal inserts had a negative effect where the hot spot occurred near the heat source center, a critical position in which any hotspots must be avoided. In the last two, Cases 3 and 4, the lowest nonuniformity levels were achieved, as depicted in the figure. However, Case 4 is preferable as the metal inserts were packed

after 1/3 of the channel length from the inlet. In the regions near the inlet, the cooling fluid temperature is typically low, so boundary regeneration is not as important.
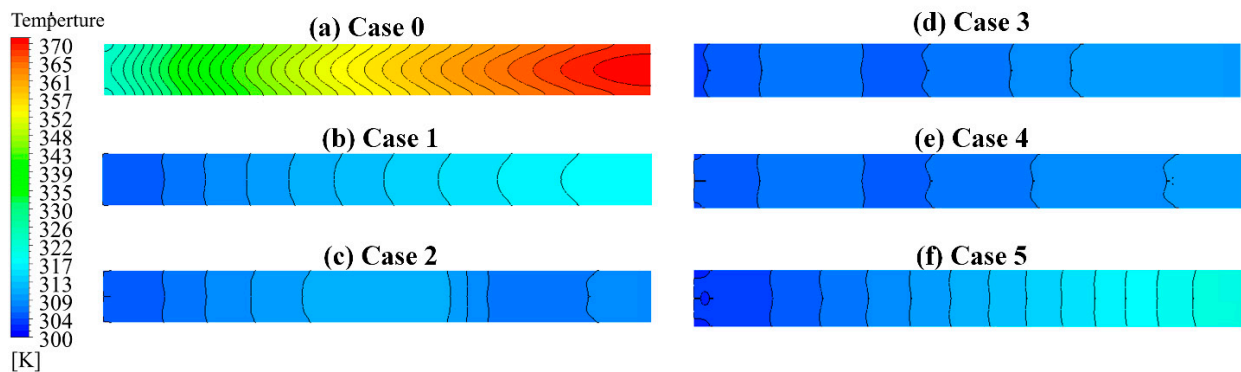
Figure 11. Temperature contour distributions over the heat source top surface for all cases, Re = 2000, heat flux = 100 W/cm² for the six investigated cases.

For more clarification, the streamlines of each case at Re = 2000 are shown in Figure 12. An automatically generated legend is used to show areas of high and low-velocity values. The enhancement in the average wall temperature, uniformity, and Nu mentioned earlier can be justified more with the flowing velocity streamlines. It can be noted that the flow inside the flow channel was distributed differently due to the packing of the metal inserts. Hence, higher interaction between the solid surface and the incoming flow. The effect of distributed flow channels generated by the metal inserts is reflected in the enhancement of heat transfer and heat dissipation. As shown in Figure 12a for Case 0, the large flow channels show low resistance to the incoming flow, simplifying its stream along the channel without any distributed manner.in contrast, in Cases 1 to 5, the complex micro inserts' inner structure forces the flow to change trajectory as it flows past the flow channel, inducing vortices that enhance turbulence and heat transfer.

Figure 12. *Cont.*

(d) Case 3

(e) Case 4

(f) Case 5
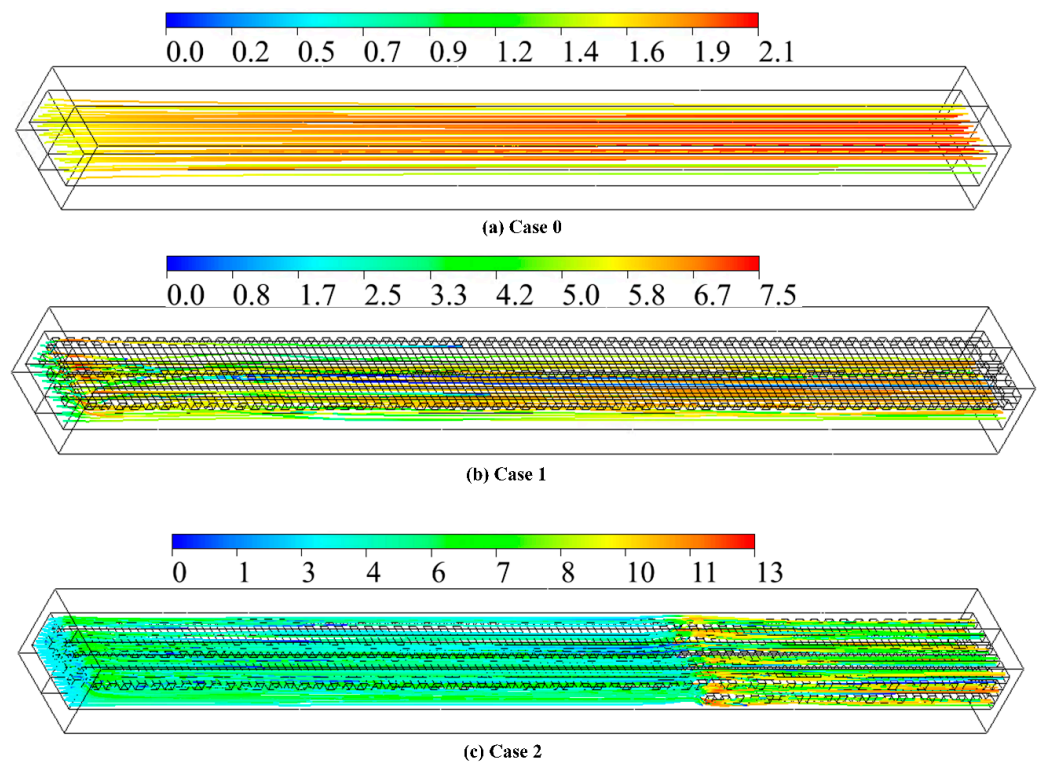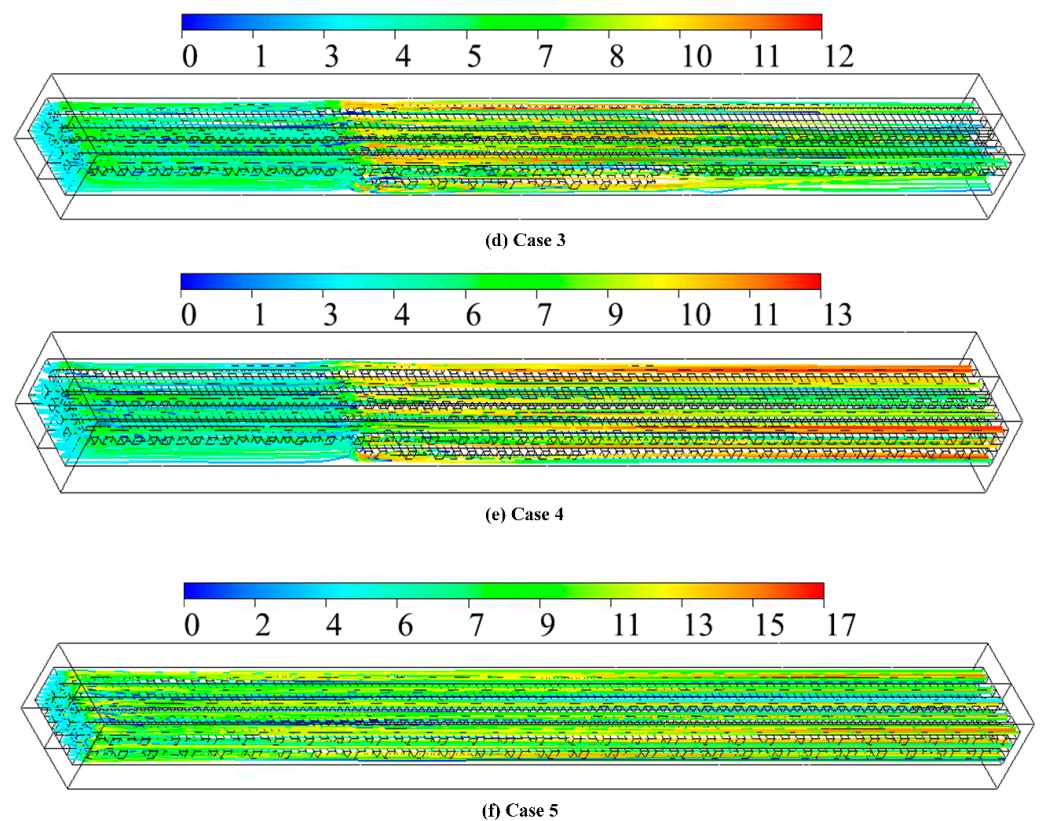
Figure 12. Velocity streamlines all the cases evaluated at Re = 2000 and heat flux = 100 W/cm^2 six investigated cases.

4. Conclusions

Thermal management of high heat flux surfaces is essential with the recent progress in the high computing devices. In this study, a new technique is proposed to improve the thermal management of high-power of these devices. The proposed technique introduces metal inserts within the flow path of a cooling channel. These inserts can be monolithically fabricated within the flow channel during the fabrication with the use of 3D metal printing technology. The intent of using the inserts is to break the flow and generate boundary layers that decrease the formation of hot spots within the flow. Five different configurations were introduced and numerically compared. The fluid flow and heat transfer characteristics of these configurations are compared. The results showed that using micro inserts in the microchannel enhances the heat transfer compared to the conventional channel without micro-metal inserts. For instance, using micro inserts on part of the bottom wall of the heated wall of the microchannel attained an average uniformity enhancement of 86.6% compared to the conventional smooth case. Further, at Re = 2000, the temperature non-uniformity decreased from 48 °C for the smooth case to 4.7 °C for the case with using metal inserts covering two-thirds of the bottom heated wall.

Conflicts of Interest: The authors declare no conflict of interests.

Nomenclature

Nomenclature

C	Specific heat, J/kg.K
D	Diameter, m
F	Friction factor
H	Height, m
K	Thermal conductivity, W/m.K
L	Length, m
Nu	Nusselt number
P	Pressure, Pa
PF	Performance factor
Pr	Prandtl number
Q	heat flux, W/m^2
R	Thermal resistance, K/W
Re	Reynolds number
T	Temperature, K
U	Axial velocity, m/s
$\vec{V}$	Velocity vector, m/s
W	Width, m

Greek symbols

μ	Dynamic viscosity, Pa.s
P	Density, kg/m^3

Subscripts

C	Channel wall
F	Fluid
H	Hydraulic
HS	Heat source
I	Inlet
Max	Maximum
S	Solid
S	Substrate
Tot	Total

Superscripts

T	Total

Abbreviations

CFD	Computational Fluid Dynamics
MAE	mean absolute error
RMSD	root mean square deviation

Appendix A. Data Reduction

To investigate the thermo-fluid performance of the presented heat exchanging technique, some dimensionless numbers should be defined, including Reynolds number, Nusselt number (Nu), and fanning friction factor (*f*). Those parameters are calculated using the following equations.

$$\text{Re} = \frac{\rho u_i D_h}{\mu} \tag{A1}$$

$$\text{Nu} = \frac{h D_h}{K} \tag{A2}$$

$$f = \frac{\Delta p}{(L/D_h)\rho u_i^2/2} \tag{A3}$$

where Δp presents the pressure drop calculated from inlet 1 [Pa], u_i is the average inlet velocity [m/s], D_h is the hydraulic diameter of the cross-sectional area [m], L is the heat source length [m], h is the convective heat transfer coefficient [W/m^2·K] which can be calculated using the equation:

$$h = \frac{qA_s}{A_c(T_w - \overline{T}_f)} \tag{A4}$$

where q represents the supplied heat flux to the substrate [W/m^2], A_s and A_c are the substrate bottom and the channel wall surface area [m^2], respectively, and T_w and $\overline{T}_f$ are the average channel wall temperature and the average fluid temperature across the channel [K], respectively.

On the other hand, the total thermal resistance (R_{tot}) [K/W], substrate thermal resistance (R_{solid}) [K/W], and fluid thermal resistance (R_f) [K/W] are defined as follows.

$$R_{tot} = \frac{T_{S,Max} - T_{in}}{qA_s} \tag{A5}$$

$$R_{Soild} = \frac{T_{S,Max} - T_w}{qA_s} \tag{A6}$$

$$R_{Fluid} = \frac{T_w - T_{in}}{qA_s} \tag{A7}$$

where $T_{s,max}$ and T_{in} is the maximum substrate temperature and the average fluid temperature at the channel inlet [K], respectively.

Finally, the efficiency evaluation criterion (*EEC*) is defined using the following equation to judge the thermal performance of the presented configurations.

$$EEC = \frac{Nu/Nu_0}{f/f_0} \tag{A8}$$

The performance factor (PF), which measures the EEC to the power of 1/3 is calculated as the following equation:

$$PF = \left(\frac{Nu/Nu_0}{f/f_0}\right)^{1/3} \tag{A9}$$

where Nu_0 is calculated for the Case 0 or the smooth channels [29]. On the other hand, f_o is calculated using the procedures described by Kandlikar et al. [37].

References

1. Yu, C.; Ji, Y.; Li, Y.; Liu, Z.; Chu, L.; Kuang, H.; Wang, Z. A Three-Dimensional Oscillating Heat Pipe Filled with Liquid Metal and Ammonia for High-Power and High-Heat-Flux Dissipation. *Int. J. Heat Mass Transf.* **2022**, *194*, 123096. [CrossRef]
2. Gholinia, M.; Ranjbar, A.A.; Javidan, M.; Hosseinpour, A.A. Employing a New Micro-Spray Model and (MWCNTs–SWCNTs)-H$_2$O Nanofluid on Si-IGBT Power Module for Energy Storage: A Numerical Simulation. *Energy Rep.* **2021**, *7*, 6844–6853. [CrossRef]
3. Jung, K.W.; Kharangate, C.R.; Lee, H.; Palko, J.; Zhou, F.; Asheghi, M.; Dede, E.M.; Goodson, K.E. Microchannel cooling strategies for high heat flux (1 kW/cm2) power electronic applications. In Proceedings of the 2017 16th IEEE Intersociety Conference on Thermal and Thermomechanical Phenomena in Electronic Systems (ITherm), Orlando, FL, USA, 30 May–2 June 2017; pp. 98–104. [CrossRef]
4. Asim, M.; Siddiqui, F.R. Hybrid Nanofluids—Next-Generation Fluids for Spray-Cooling-Based Thermal Management of High-Heat-Flux Devices. *Nanomaterials* **2022**, *12*, 507. [CrossRef] [PubMed]
5. Abdelrehim, O.; Khater, A.; Mohamad, A.A.; Radwan, A. Two-Phase Simulation of Nanofluid in a Confined Single Impinging Jet. *Case Stud. Therm. Eng.* **2019**, *14*, 100423. [CrossRef]
6. Mohammadi, M.; Taheri, A.; Passandideh-Fard, M.; Sardarabadi, M. Electronic Chipset Thermal Management Using a Nanofluid-Based Mini-Channel Heat Sink: An Experimental Study. *Int. Commun. Heat Mass Transf.* **2020**, *118*, 104836. [CrossRef]
7. Arshad, W.; Ali, H.M. Experimental Investigation of Heat Transfer and Pressure Drop in a Straight Minichannel Heat Sink Using TiO2 Nanofluid. *Int. J. Heat Mass Transf.* **2017**, *110*, 248–256. [CrossRef]
8. Righetti, G.; Zilio, C.; Doretti, L.; Longo, G.A.; Mancin, S. On the Design of Phase Change Materials Based Thermal Management Systems for Electronics Cooling. *Appl. Therm. Eng.* **2021**, *196*, 117276. [CrossRef]

9.   Tuckerman, D.B.; Pease, R.F.W. High-Performance Heat Sinking for VLSI. *IEEE Electron Device Lett.* **1981**, *EDL-2*, 126–129. [CrossRef]

10.   Gunnasegaran, P.; Mohammed, H.A.; Shuaib, N.H.; Saidur, R. The Effect of Geometrical Parameters on Heat Transfer Characteristics of Microchannels Heat Sink with Different Shapes. *Int. Commun. Heat Mass Transf.* **2010**, *37*, 1078–1086. [CrossRef]

11.   Wang, H.; Chen, Z.; Gao, J. Influence of Geometric Parameters on Flow and Heat Transfer Performance of Micro-Channel Heat Sinks. *Appl. Therm. Eng.* **2016**, *107*, 870–879. [CrossRef]

12.   Hung, T.C.; Huang, Y.X.; Yan, W.M. Thermal Performance of Porous Microchannel Heat Sink: Effects of Enlarging Channel Outlet. *Int. Commun. Heat Mass Transf.* **2013**, *48*, 86–92. [CrossRef]

13.   Chai, L.; Wang, L.; Bai, X. Thermohydraulic Performance of Microchannel Heat Sinks with Triangular Ribs on Sidewalls—Part 2: Average Fluid Flow and Heat Transfer Characteristics. *Int. J. Heat Mass Transf.* **2019**, *128*, 634–648. [CrossRef]

14.   Chai, L.; Xia, G.D.; Wang, H.S. Parametric Study on Thermal and Hydraulic Characteristics of Laminar Flow in Microchannel Heat Sink with Fan-Shaped Ribs on Sidewalls—Part 3: Performance Evaluation. *Int. J. Heat Mass Transf.* **2016**, *97*, 1091–1101. [CrossRef]

15.   Xia, G.; Ma, D.; Zhai, Y.; Li, Y.; Liu, R.; Du, M. Experimental and Numerical Study of Fluid Flow and Heat Transfer Characteristics in Microchannel Heat Sink with Complex Structure. *Energy Convers. Manag.* **2015**, *105*, 848–857. [CrossRef]

16.   Ghani, I.A.; Kamaruzaman, N.; Sidik, N.A.C. Heat Transfer Augmentation in a Microchannel Heat Sink with Sinusoidal Cavities and Rectangular Ribs. *Int. J. Heat Mass Transf.* **2017**, *108*, 1969–1981. [CrossRef]

17.   Chai, L.; Xia, G.; Zhou, M.; Li, J. Numerical Simulation of Fluid Flow and Heat Transfer in a Microchannel Heat Sink with Offset Fan-Shaped Reentrant Cavities in Sidewall. *Int. Commun. Heat Mass Transf.* **2011**, *38*, 577–584. [CrossRef]

18.   Li, Y.F.; Xia, G.D.; Ma, D.D.; Jia, Y.T.; Wang, J. Characteristics of Laminar Flow and Heat Transfer in Microchannel Heat Sink with Triangular Cavities and Rectangular Ribs. *Int. J. Heat Mass Transf.* **2016**, *98*, 17–28. [CrossRef]

19.   Sui, Y.; Teo, C.J.; Lee, P.S. Direct Numerical Simulation of Fluid Flow and Heat Transfer in Periodic Wavy Channels with Rectangular Cross-Sections. *Int. J. Heat Mass Transf.* **2012**, *55*, 73–88. [CrossRef]

20.   Ermagan, H.; Rafee, R. Numerical Investigation into the Thermo-Fluid Performance of Wavy Microchannels with Superhydrophobic Walls. *Int. J. Therm. Sci.* **2018**, *132*, 578–588. [CrossRef]

21.   Lin, L.; Zhao, J.; Lu, G.; Wang, X.D.; Yan, W.M. Heat Transfer Enhancement in Microchannel Heat Sink by Wavy Channel with Changing Wavelength/Amplitude. *Int. J. Therm. Sci.* **2017**, *118*, 423–434. [CrossRef]

22.   Sui, Y.; Teo, C.J.; Lee, P.S.; Chew, Y.T.; Shu, C. Fluid Flow and Heat Transfer in Wavy Microchannels. *Int. J. Heat Mass Transf.* **2010**, *53*, 2760–2772. [CrossRef]

23.   Mohammed, H.A.; Gunnasegaran, P.; Shuaib, N.H. Numerical Simulation of Heat Transfer Enhancement in Wavy Microchannel Heat Sink. *Int. Commun. Heat Mass Transf.* **2011**, *38*, 63–68. [CrossRef]

24.   Chiam, Z.L.; Lee, P.S.; Singh, P.K.; Mou, N. Investigation of Fluid Flow and Heat Transfer in Wavy Micro-Channels with Alternating Secondary Branches. *Int. J. Heat Mass Transf.* **2016**, *101*, 1316–1330. [CrossRef]

25.   Chuan, L.; Wang, X.D.; Wang, T.H.; Yan, W.M. Fluid Flow and Heat Transfer in Microchannel Heat Sink Based on Porous Fin Design Concept. *Int. Commun. Heat Mass Transf.* **2015**, *65*, 52–57. [CrossRef]

26.   Gong, L.; Li, Y.; Bai, Z.; Xu, M. Thermal Performance of Micro-Channel Heat Sink with Metallic Porous/Solid Compound Fin Design. *Appl. Therm. Eng.* **2018**, *137*, 288–295. [CrossRef]

27.   Ghani, I.A.; Sidik, N.A.C.; Mamat, R.; Najafi, G.; Ken, T.L.; Asako, Y.; Japar, W.M.A.A. Heat Transfer Enhancement in Microchannel Heat Sink Using Hybrid Technique of Ribs and Secondary Channels. *Int. J. Heat Mass Transf.* **2017**, *114*, 640–655. [CrossRef]

28.   Shi, X.; Li, S.; Mu, Y.; Yin, B. Geometry Parameters Optimization for a Microchannel Heat Sink with Secondary Flow Channel. *Int. Commun. Heat Mass Transf.* **2019**, *104*, 89–100. [CrossRef]

29.   Incropera, F.P.; DeWitt, D.P. *Fundamentals of Heat and Mass Transfer*; Wiley: New York, NY, USA, 1996; Volume 6, ISBN 0471304603.

30.   Dinçer, İ.; Zamfirescu, C. *Drying Phenomena: Theory and Applications*; John Wiley & Sons: Hoboken, NJ, USA, 2016.

31.   Rapp, B.E. Chapter 9—Fluids. In *Applied Mathematics and Mechanics*; Elsevier: Oxford, UK, 1989; Volume 1897, pp. 44–45. ISBN 9784431538592.

32.   Dang, T.; Teng, J.T.; Chu, J.C. A Study on the Simulation and Experiment of a Microchannel Counter-Flow Heat Exchanger. *Appl. Therm. Eng.* **2010**, *30*, 2163–2172. [CrossRef]

33.   Xie, G.; Zhang, F.; Sundén, B.; Zhang, W. Constructal Design and Thermal Analysis of Microchannel Heat Sinks with Multistage Bifurcations in Single-Phase Liquid Flow. *Appl. Therm. Eng.* **2014**, *62*, 791–802. [CrossRef]

34.   Kandil, A.A.; Awad, M.M.; Sultan, G.I.; Salem, M.S. Investigating the Performance Characteristics of Low Concentrated Photovoltaic Systems Utilizing a Beam Splitting Device under Variable Cutoff Wavelengths. *Renew. Energy* **2022**, *196*, 375–389. [CrossRef]

35.   Li, W.; Xie, Z.; Xi, K.; Xia, S.; Ge, Y. Constructal Optimization of Rectangular Microchannel Heat Sink with Porous Medium for Entropy Generation Minimization. *Entropy* **2021**, *23*, 1528. [CrossRef] [PubMed]

36.   Shen, H.; Wang, C.C.; Xie, G. A Parametric Study on Thermal Performance of Microchannel Heat Sinks with Internally Vertical Bifurcations in Laminar Liquid Flow. *Int. J. Heat Mass Transf.* **2018**, *117*, 487–497. [CrossRef]

37.   Kandlikar, S.G.; Garimella, S.; Li, D.; Colin, S.; King, M.R. *Heat Transfer and Fluid Flow in Minichannels and Microchannels*; Elsevier: Oxford, UK, 2006; ISBN 9780080445274.

Enhancement of Dye Separation Performance of Eco-Friendly Cellulose Acetate-Based Membranes

Omneya A. Koriem [1],*, Alaa Mostafa Kamel [1], Waleed Shaaban [2] and Marwa F. Elkady [1,3],*

[1] Chemical and Petrochemical Engineering Department, Egypt-Japan University of Science and Technology, New Borg El-Arab City, Alexandria 21934, Egypt

[2] Mechanical Engineering Department, Mansoura University, El-Mansoura 35516, Egypt

[3] Fabrication Technology Department, Advanced Technology and New Materials Research Institute (ATNMRI), City of Scientific Research and Technological Applications, New Borg El-Arab City, Alexandria 21934, Egypt

* Correspondence: omneya.koriem@ejust.edu.eg (O.A.K.); marwa.elkady@ejust.edu.eg (M.F.E.)

Abstract: Many reasons have caused a worldwide water stress problem. Thus, the recycling of wastewater streams has been extensively studied. In this work, eco-friendly mixed matrix membranes (MMMs) were fabricated, characterized, and tested for the removal of two separate dyes from simulated waste streams. The environmentally friendly nano activated carbon (NAC) was extracted from water hyacinth to be impregnated as a membrane nano-filler to enhance the neat membrane performance. The extracted NAC was further studied and characterized. Cellulose acetate (CA)-based membranes were obtained by phase inversion and electrospinning mechanisms. All four synthesized blank and MMMs were characterized via scanning electron microscope (SEM) and contact angle to study their structure and hydrophilic nature, respectively. However, the membrane with optimum performance was further characterized using Fourier transfer infrared (FTIR) and X-ray diffraction (XRD). The four prepared cast and electro-spun, blank, and mixed matrix CA-based membranes showed an acceptable performance in the removal and selectivity of methylene blue (MB) dye over Congo red (CR) dye with a removal percentage ranging from 31 to 70% depending on the membrane used. It was found that the CA/NAC hybrid nanofiber membrane possessed the highest removal efficiency for MB, where the dye concentration declined from 10 to 2.92 mg/L. In contrast, the cast blank CA membrane showed the least removal percentage among the synthesized membranes with only 30% removal. As a result, this paper suggests the use of the CA/NAC hybrid membrane as an alternative and cost-effective solution for MB dye removal.

Keywords: adsorption; membrane; adsorptive membrane; activated carbon; dye removal; hybrid membrane

1. Introduction

Due to globalization and the developed human lifestyle, dyes are widely used in various industrial fields. They are extensively used not only in the textile and paper industries, but also in food, pharmaceuticals, cosmetics, and many other vital industries [1]. In aqueous solutions, dyes are classified into two main categories: anionic and cationic [2]. It is estimated that around 10% of the textile industry's dyes are lost directly into water streams [3]. Even in low concentrations, most synthetic dyes have a harmful impact on flora and fauna, humans, and the environment. They are generally characterized by their toxicity, carcinogenic effects, and high color visibility [4–6]. Furthermore, they prevent the penetration of oxygen and sunlight into water systems. Consequently, they affect the photosynthetic ability of the flora, causing harm to aquatic life [7,8]. In addition, they are hardly removed from water bodies due to their high stability and water solubility [9–11]. As a result of the current water depletion situation, the available water sources need to be protected [12]. Accordingly, discharging industrial untreated waste streams containing dye contamination

is considered one of the main environmental problems that require immediate intervention. As a result, many researchers are eager to discover cost-effective and eco-friendly techniques to discard dyes and other pollutants from waterways [13–16]. Up to this point, numerous methods have been utilized in dye removal from waste streams. They can be categorized into physical, chemical, biological, or hybrid methods [17]. Those methods, including but not limited to, coagulation [18], adsorption [19], photolysis [20], electrochemical [21], biological treatment [22], membrane processes [23], and their hybrids [24–26] have all been investigated. Amongst them, adsorption is used for its efficiency, easy processing, and cheap cost [27], while membranes are used for their low required energy, low required space, reduced chemical consumption, and relatively low cost of operation [6]. However, they still have some limitations and drawbacks. Thus, the hybrid adsorptive membranes concept was investigated by incorporating adsorptive nanoparticles (NPs) into the synthesized membranes, resulting in a membrane that has the ability to possess the function of both systems [28–30].

For the process to be as effective as possible, the polymeric membrane material and the suitable incorporated adsorbent should be selected carefully. According to the literature, chitosan [31], alginate [32], and cellulose acetate [33] have been previously investigated for dye removal for their eco-friendly characteristics and removal efficiency. Amongst them, cellulose acetate (CA) has been extensively used because it is a biodegradable, low-cost, easily tailored, and available biopolymer [33,34]. Moreover, it is well known for its chemical and thermal stability [35]. Despite that, its inferior adsorption efficiency lessens its application for dye removal [36]. Therefore, impregnating adsorptive particles within CA may enhance the neat membrane adsorptive capacity [37]. The mechanism of adsorptive membranes depends on two steps: rejection and adsorption. In the rejection step, the particles with sizes larger than the pore size of the membrane are rejected by the membrane's surface, or what is called the membrane's active layer. In the next step, adsorption takes place, where small particles react or attach to the impregnated adsorbent, which in turn increases the overall removal efficiency of the membrane [38]. Previously, various adsorbents were tested for dye removal, namely zeolites, clay, limestone, lignite, and graphene oxide [39,40]. Among the most commonly used adsorbents, activated carbon (AC) is recognized as a perfect adsorbent for dye removal [41]. AC has an undoubtable dye removal performance, and it has previously proven to be a competitive adsorbent. AC is well known for its high adsorption capacity, large porous structure, high available active sites, and large surface area [42,43]. Additionally, nano activated carbon (NAC) is characterized by a much higher surface area and in return better adsorption capacity over AC [44]. Nevertheless, it has some limitations due to its high cost and non-renewable source. Thus, many studies have been conducted in order to provide an alternative low-cost adsorbent [34,45]. Agricultural wastes provide a competitive raw material for obtaining cheap, efficient, and renewable ACs [46]. Water hyacinth is an unwanted waste that can cause severe damage to aquatic life [47]. The control of water hyacinth is an effort, time, and money-consuming problem. Consequently, turning this irritating plant into an effective bio-sorbent could be more valuable [48,49].

To the best of the authors' knowledge, there is no other study that has investigated the impregnation of NAC fabricated from agricultural waste with blank cast and electro-spun CA-based membranes for dye decontamination from polluted water. Accordingly, in the current study, eco-friendly CA-based membranes were synthesized via phase inversion and electrospinning techniques. Additionally, nano activated carbon (NAC) was fabricated from Egyptian water hyacinths. The effect of impregnating the synthesized NAC bio-sorbent into the cast and the nanofibrous membranes was investigated. Methylene blue (MB) and Congo red (CR) were selected as cationic and anionic dyes, respectively. The selectivity of the fabricated, cast and electro-spun, neat CA and hybrid CA/NAC membranes towards MB and CR was studied.

2. Materials and Methods

2.1. Materials

All chemicals included in this study were used as purchased without any further modification. Cellulose acetate (CA) polymer with a molecular weight of 30,000 was supplied by Lobachemie, acetone (ACS > 99.5%) and dimethylformamide (DMF > 99.9%) were purchased from Fisher, sodium hydroxide (NaOH), methylene blue (MB) dye, and Congo red (CR) dye, and distilled water were bought from Sigma Aldrich. Additionally, activated carbon was prepared from Egyptian water hyacinth, which was collected from Itay El-Baroud Drainage, Al-Buhayrah governorate, Egypt.

2.2. Synthesis of Nano Activated Carbon (NAC)

Water hyacinth roots were used as the precursor for the preparation of dye removal bio-sorbent material [50]. To remove dust or any trapped particles, the collected raw precursor was rinsed extensively with distilled water. The washed water hyacinth was then dried in an electrical oven before being crushed into a fine powder. Then, for alkaline chemical treatment, 1 g of the obtained powder was further suspended in 100 mL of 2 M NaOH for 1 h under stirring at 60 °C. The chemically treated materials were then filtered and washed several times to get rid of any basic or acidic residuals. The treated washed materials were finally dried overnight at 70 °C, followed by a carbonization process in an Across muffle furnace for 1 h at 600 °C.

2.3. Synthesis of Neat and Composite CA-Based Dope Solutions

For the neat CA membrane, a suitable amount of CA polymeric powder was dissolved in a binary solvent mixture of acetone and DMF with a ratio of 2:1, respectively, to prepare a 15 wt% of neat CA dope solution. On the other hand, 5 wt% of the nano-filler (NAC) was sonicated firstly with the same binary solvent mixture for 1 h before the CA powder was added and stirred with it to obtain the composite CA/NAC dope solution. The previous solutions were then used to fabricate the neat and composite CA-based membranes via phase inversion and electrospinning techniques.

2.3.1. Synthesis of Cast Neat and Composite CA-Based Membranes

The membrane phase inversion method has been used for many years for the fabrication of flat sheet polymeric membranes [51–53]. The previously prepared blank CA and composite CA/NAC dope solutions were cast on a clean glass plate at room temperature. A doctor knife blade with a micrometer fixed at 0.25 mm was used to prepare the membranes with the required thickness. The cast films were left to evaporate in the air for 60 s before being immersed at (0–4 °C) in a distilled water bath. The obtained flat sheet membrane was then rinsed to get rid of any residual solvent. As a final treatment step, the membrane was then annealed at 80 °C for 10 min in another distilled water bath. The fabricated membranes were preserved in distilled water for at least 24 h for further use and characterization.

2.3.2. Synthesis of Electro-Spun Nanofibrous Neat and Composite CA-Based Membranes

Thanks to the electrospinning technique, the fabrication of nanofibrous membranes is possible. Due to the outstanding properties of higher surface area as well as higher membrane porosity [54,55], the technique was investigated. The pristine CA and hybrid CA/NAC polymeric solutions were spun with the help of (NanoNC) electro-spinning equipment under different conditions of feed pumping flow rate, applied voltage, and tip-to-collector distance. The optimum nanofibrous membrane was obtained at operating conditions of 0.7 mL/h, 19 kV, and 15 cm, respectively. The fabricated nanofiber membranes were then left to dry in a drying oven overnight for further use and characterization.

2.4. Characterization of the Extracted NAC and Fabricated CA-Based Membranes

Various techniques were involved in characterizing the synthesized electro-spun and cast CA-based membranes as well as the extracted NAC. Fourier transform infrared

spectroscopy (FTIR) (Bruker Vertex 70) was used to observe and confirm the presence of the functional groups of the used materials. A Shimadzu XRD-6100 X-ray diffraction (XRD) device was used to study the crystalline nature of the fabricated membranes. The spectra were recorded from 3500 to 500 cm^{-1}.

The morphology of the membranes and the extracted NAC was investigated using a scanning electron microscope (SEM) device (JOEL JSM-6010 LV). The hydrophilic/hydrophobic nature of the membranes was measured using a contact angle system (DSA 100, KRÜSS). For more accurate results, five random locations on each membrane surface were selected to measure the contact angle.

2.5. Performance Testing of the Synthesized Electro-Spun and Cast CA-Based Membranes

In this study, the performance of the fabricated neat and hybrid membranes in the removal of cationic (MB) and anionic (CR) dyes was investigated. All decolorization experiments were repeated 4 times and the average measurements were recorded for more accuracy. Accordingly, as shown in Figure 1, each membrane's efficiency was evaluated using an Amicon cell setup with an active filtration area of around 480 mm^2. Each membrane was divided into circular shapes similar to the active area of the cell. Two stock solutions of MB and CR, 10 ppm each, were prepared to simulate the industrial dye-containing waste streams. At room temperature, the cell was then filled with the dye solution and connected to a syringe pump to apply a small pressure that allowed the water to flow through the membrane. The filtrate was recirculated until equilibrium was reached. A sample of the filtrate of each cycle was taken and the dye concentration was measured using a spectrophotometer device.
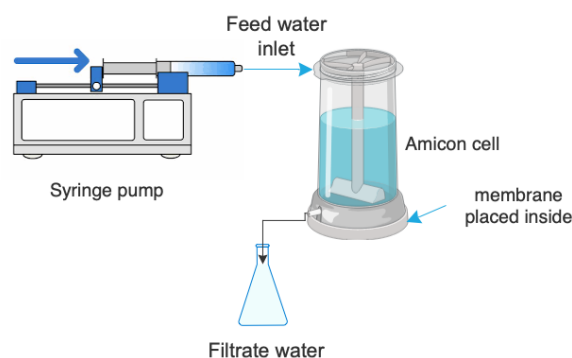
Figure 1. Amicon cell filtration setup.

The rejection factor (R) was calculated from Equation (1)

$$\%R = (1 - \frac{C_P}{C_R})$$

(1)

where C_P and C_R are the dye concentrations of the filtrate and the feed solution (mg/L), respectively.

3. Results and Discussion

3.1. Characterization of Nano Activated Carbon (NAC)

As the functional groups of the obtained NAC have an impact on the adsorption efficiency [56], FTIR was used to recognize those functional groups. As can be seen in Figure 2a, the peak at 3401 cm^{-1} refers to the O-H functional group, which gives an indication of the bonded hydroxide in the prepared NAC. The band found at 1635 cm^{-1} could be due to C=C or C=O stretching [57]. The broad band found at 1157 cm^{-1} suggests the surface group of C-O stretching [58]. The absorption band at 616 cm^{-1} might refer to the C-H stretching or C=O bonding [59].
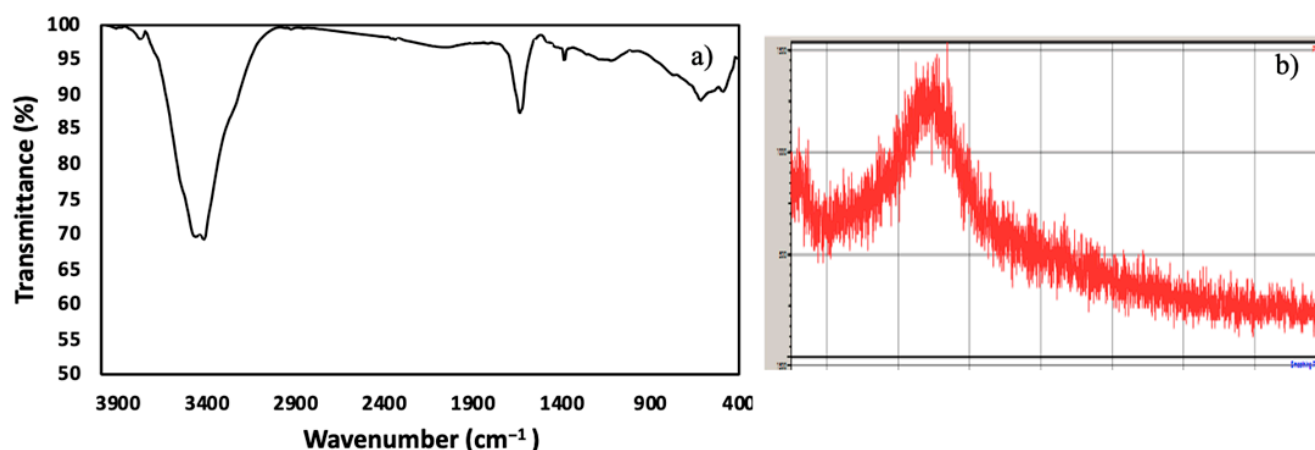
Figure 2. (**a**) FTIR spectrum (**b**) XRD pattern of the fabricated nano activated carbon NAC.

The XRD pattern was investigated in order to study the crystalline nature of the prepared NAC. As illustrated in Figure 2b, the obtained NAC has a semi-crystalline structure. In addition, the appearance of a broad peak in the range of 22° to 24° indicates the existence of carbon. On the other hand, the absence of other characteristic peaks gives an indication of the absence of any other contaminants [60].

The morphology of the prepared NAC was investigated by SEM images as presented in Figure 3a. SEM micrographs confirmed that a uniform nanosized material was obtained and the average diameter of the fabricated particles was estimated at 58 nm.
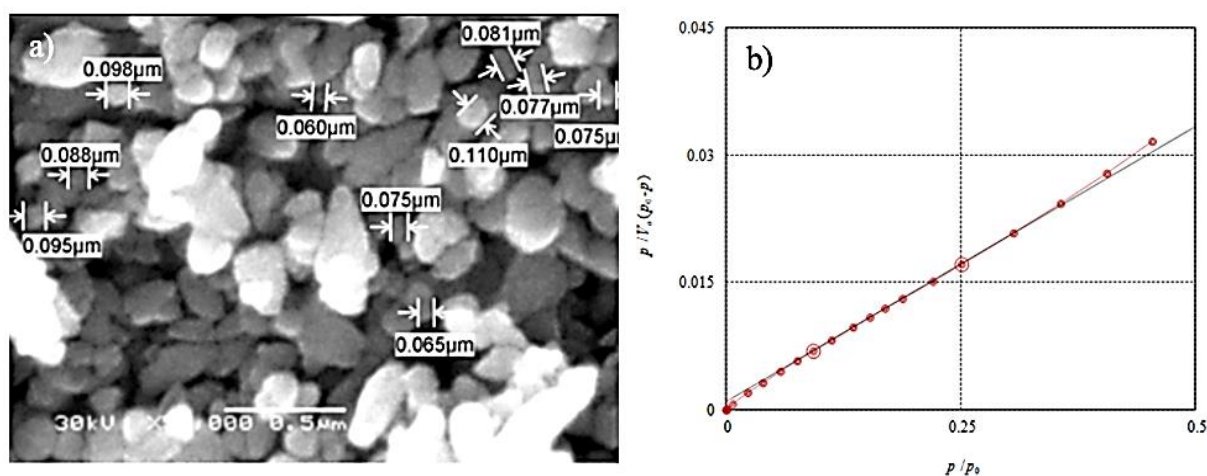
Figure 3. (**a**) SEM image (**b**) BET of the fabricated nano activated carbon (NAC).

The BET surface area of the fabricated NAC was measured to evaluate the material pore size, pore volume, and surface area. As shown in Figure 3b, N2 adsorption/desorption isotherm of the synthesized bio-sorbent was investigated. The NAC surface area was found to be 66.2 m^2/g. On the other hand, the total pore volume was measured as 0.25 cm^3/g, while its average pore size was recorded as 15.2 nm.

3.2. Characterization of Cast and Electro-Spun Neat and Composite CA-Based Membranes

As illustrated in Figure 4, the surface and cross-sectional structure of the cast neat CA and composite CA/NAC membranes was investigated via SEM images. Compared to the clear neat surface of CA, Figure 4a, the impregnated NAC clearly appears as white particles on the surface of the membrane in Figure 4b. This could give an indication of the successful dispersion of the NAC particles within the dope solution. In addition, from the cross-sectional images, it can be seen that the addition of NAC particles transformed

the structure of the blank CA membrane, Figure 4c, into a more porous structure. A few longitudinal pores of the composite CA/NAC membrane are demonstrated in Figure 4d.
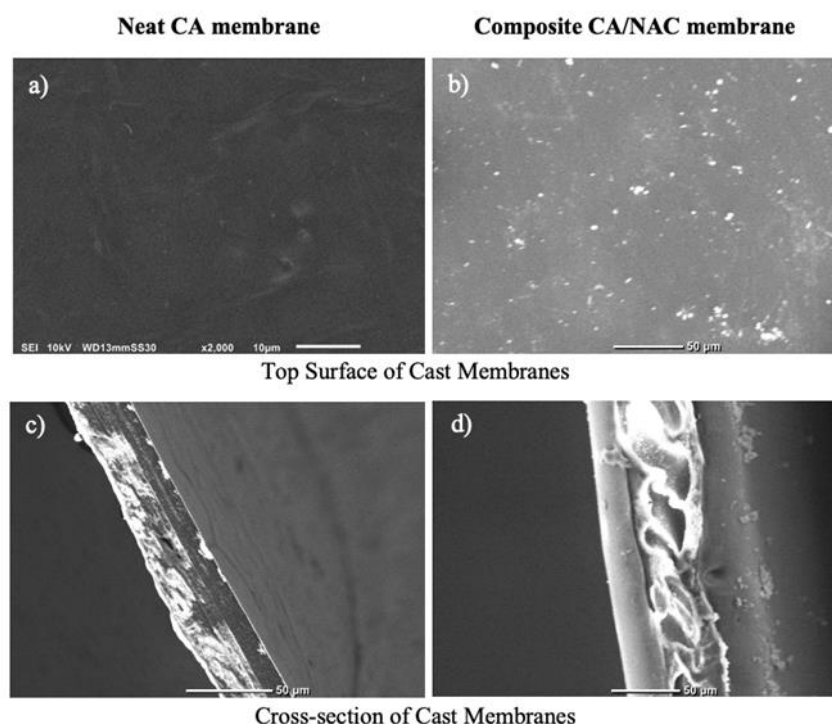
Figure 4. SEM images of cast membranes of "(**a,c**)" CA and "(**b,d**)" CA/NAC nanofiber membranes.

The optimum electro-spinning operating conditions were selected depending on the fiber shapes and diameters. The optimum conditions were used to fabricate a full matrix of CA and CA/NAC. The difference in the morphological structure between the synthesized blank and composite CA membranes can be seen in Figure 5. SEM images illustrate that both CA and CA/NAC membranes have uniform, straight, and bead-less fibers. In Figure 5a, the blank CA membrane nanofibers are shown as a uniform clear network. However, in Figure 5b, the loaded NAC can be seen as white dispersed particles and show good distribution with no agglomerations.
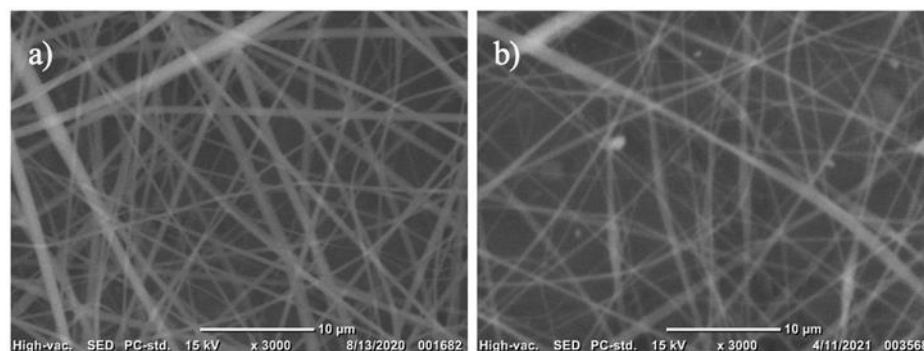
Figure 5. SEM images of "(**a**)" CA and "(**b**)"CA/NAC nanofiber membranes.

The surface wettability of the four fabricated cast and electro-spun membranes was investigated in order to study the effect of membrane surface morphology on the contact angle of each membrane. The hydrophilicity of the surface of the membrane affects the filtration flux [42]. The contact angle was expected to be less than 90° to be hydrophilic. Additionally, it was expected from the literature that the nanofibrous mat would be more hydrophilic than the cast one [61]. As displayed in Figure 6, all four membranes were found

to be hydrophilic to different degrees. The contact angle of the blank cast and nanofiber membranes decreased after the addition of NAC particles. The contact angle of the blank CA cast membrane decreased from 63.5° to 58.6°, while it lowered from 60.5° for the neat CA nanofibrous membrane to become 58° for the composite CA/NAC nanofibrous membrane. This means that the addition of NAC has enhanced the membrane's hydrophilicity, which is an important and crucial parameter in water filtration.
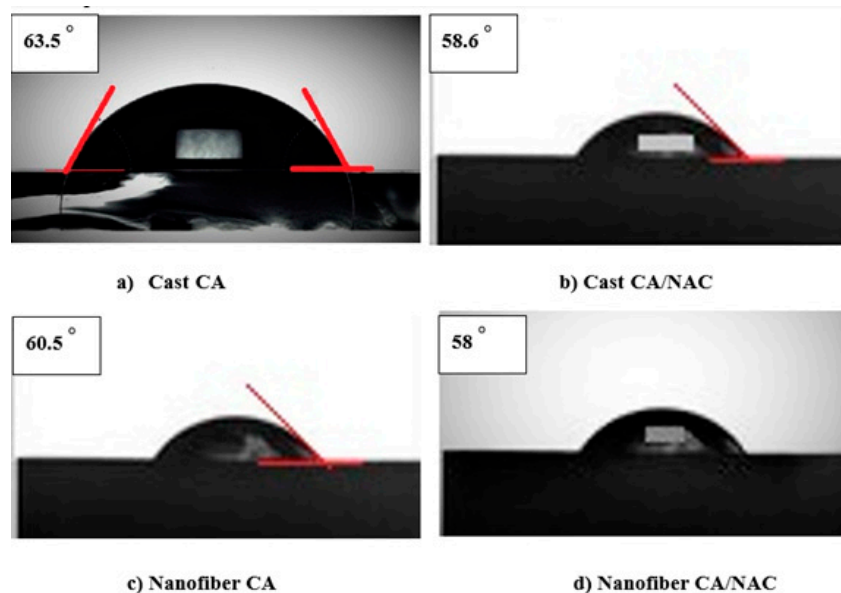
Figure 6. Contact angle of cast and electro-spun neat and composite CA-based membranes.

For nanofibrous blank CA and mixed matrix CA/NAC, FTIR spectra were further used to study the functional groups of both membranes. As demonstrated in Figure 6a, a wide band at 3395 cm^{-1} represents the presence of hydroxyl (–OH) stretching [62]. This band was shifted to 3474 cm^{-1} and its intensity decreased with the addition of NAC, as seen in Figure 7b. The carbonyl (C=O) group was observed at 1731 cm^{-1}. The adsorption peak at 1428 cm^{-1} refers to the (CH$_2$) deformation vibration. The characteristic (C-O-C) group can be seen at 1225 cm^{-1}. However, as represented in Figure 7b, this adsorption peak was shifted to become 1218 cm^{-1}. The stretching vibration of (C-OH) in the blank CA membrane was illustrated at 1029 cm^{-1} [63].
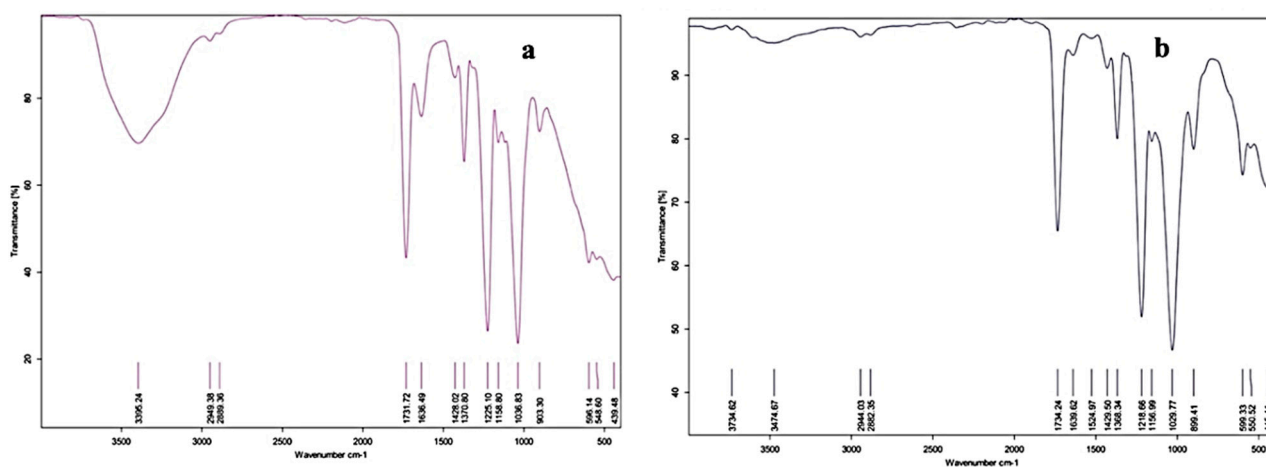
Figure 7. FTIR spectrum of "(**a**)" blank CA and "(**b**)" composite CA/NAC nanofibrous membranes.

As displayed in Figure 8, XRD was further used to give an indication of the successful impregnation of NAC. Figure 8a depicts the CA characteristic peaks at 10 and 20° [64]. Nonetheless, the intensity of the peak at 20° increased significantly.
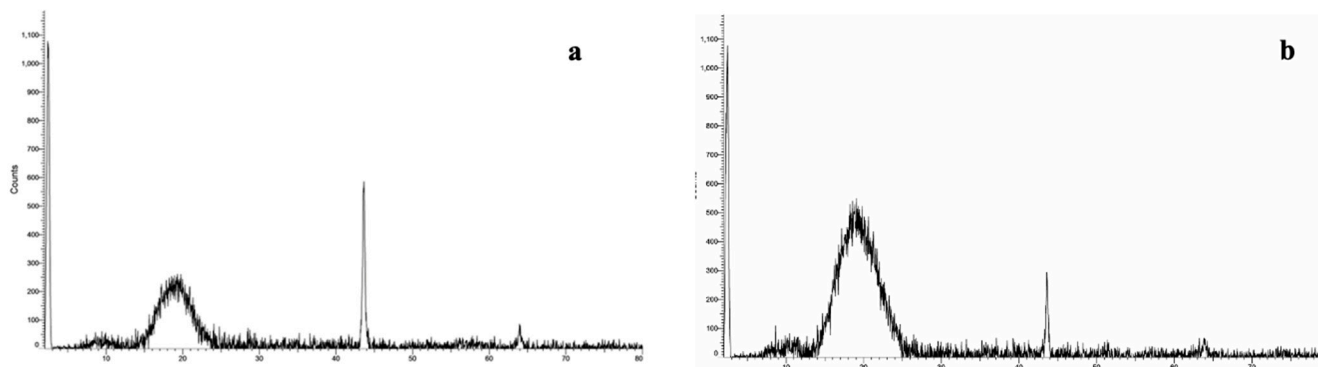
Figure 8. XRD pattern of (**a**) blank CA and (**b**) composite CA/NAC nanofibrous membranes.

This might be explained by the presence of carbon atoms and in return the impregnation of NAC particles.

3.3. Filtration Performance of Cast and Electro-Spun Neat and Composite CA-Based Membranes

The filtration performance of both blank and composite CA-based membranes for the removal of cationic MB and anionic CR was investigated using the previously mentioned Amicon cell setup. Generally, the four membranes showed a better affinity towards MB removal than CR. As illustrated in Figures 9 and 10, all the membranes had a noticeable effect on MB final concentration, while they had a negligible effect on CR final concentration.
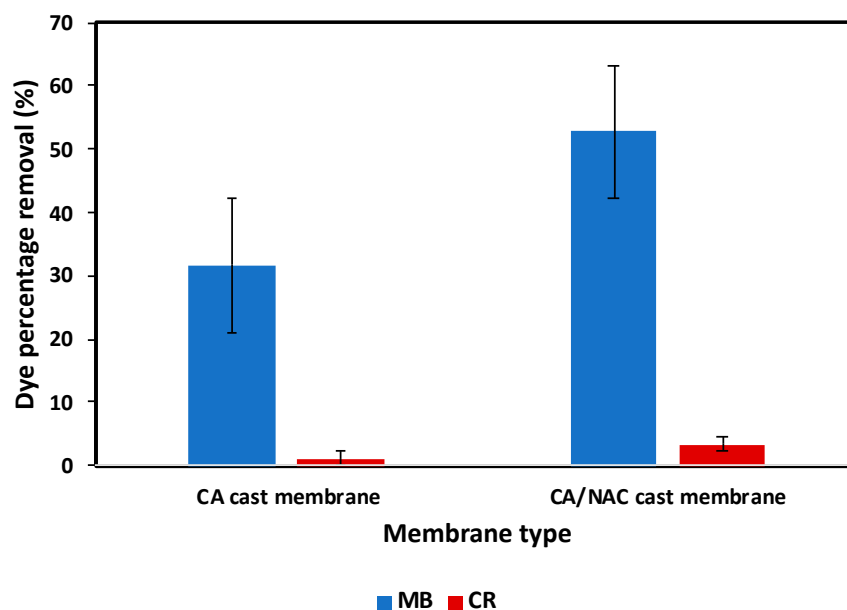
Figure 9. Performance of blank and composite cast membranes on the removal of MB and CR.
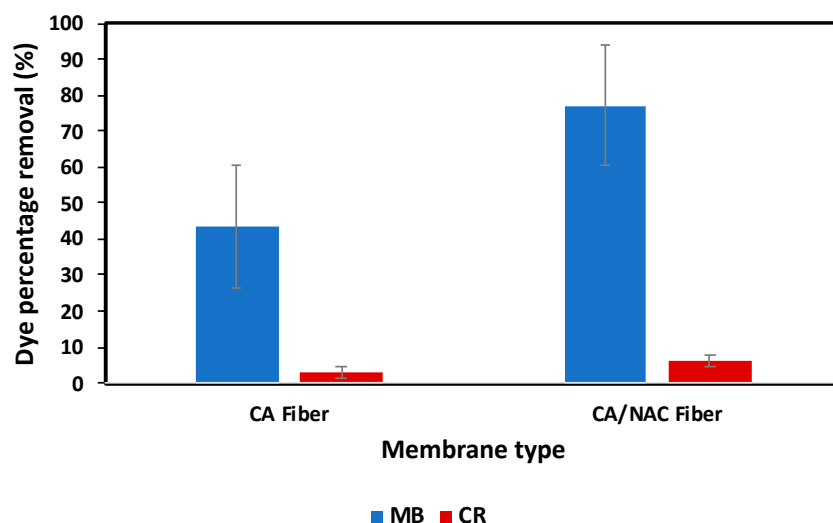
Figure 10. Performance of blank and composite nanofibrous membranes on the removal of MB and CR.

As clarified in Figure 9, the equilibrium concentration of the MB on the blank CA cast membrane was reached at 6.84 ppm with a removal percentage of 31.6%. However, the equilibrium concentration of CR on the same membrane was reached at 9.89 ppm with only 1.1% removal.

From Figure 9, it was noticed that the addition of NAC had a positive effect on the performance of the blank membrane. As illustrated, the equilibrium concentration of MB was reduced to be reached at 4.73 ppm, with around 53% removal for the cast CA/NAC composite membrane. However, this removal percentage is considered higher than that of the early reported cast CA/MWCNTs membrane. It was found that for 5 mg/L MB concentration, the recorded removal was less than 30% [65]. Unfortunately, regarding CR, the equilibrium concentration was affected slightly by the addition of NAC and was reached at 9.67 ppm to achieve a low removal percentage of only 3.3%.

On the other hand, the performances of the blank and impregnated CA-based nanofiber membranes are demonstrated in Figure 10. The fibrous membranes were also selective for MB over CR. The equilibrium concentration of MB over the blank CA fibrous membrane was found to be 5.67 ppm and after the addition of NAC, it became even lower until it reached almost 2.92 ppm. In other words, MB was removed using blank and impregnated fiber membranes by 43% and 70%, respectively.

On the contrary, CR reached the equilibrium concentration at 9.73 ppm using the blank CA fiber membrane and 9.41 ppm using the impregnated CA/NAC fiber membrane. The removal of CR using blank CA and impregnated CA/NAC fiber membranes was recorded at very small amounts of 2.7% and 5.9%, sequentially.

The presence of both the acetyl (CH_3CO^-) and the hydroxyl (OH^-) groups led to the negatively charged surface of the CA-based membranes. Thus, the selective behavior and better performance of CA-based membranes towards MB over CR could be due to the electrostatic interaction that takes place between MB molecules (positively charged) and the membrane surface (negatively charged) [30].

Regarding MB removal, Figure 11 compares the performance of the four membranes. Overall, the performance of fibers was better than that of cast membranes. At equilibrium, CA fiber removed 43.3% of methylene blue, while the blank cast membrane removed only 31%. The CA/NAC fiber presented the best behavior in removing the MB dye as it removed more than 70% of the dye. The removal of MB dye on the CA/NAC fiber at a neutral pH value was higher than that of the previously investigated CA/GO/TiO$_2$-NH$_2$ composite membrane. The literature reported that MB removal efficiency was about 60% at pH = 7 [66]. To conclude, the addition of NAC improved the performance of the blank CA membranes. This might be due to the existence of NAC resulting in an increase in the available active adsorbent sites in the fabricated adsorptive membranes. Those active sites

may have captured more MB molecules within its porous structure, and this led to the enhancement of the blank CA membrane's performance [30].
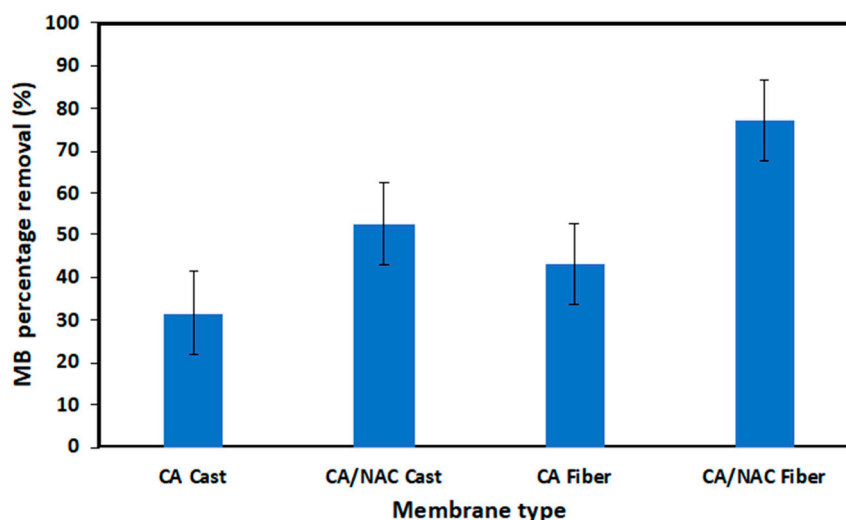
Figure 11. Comparison between the performance of the fabricated cast and nanofibrous CA-based membranes on the removal of MB dye.

4. Conclusions

The current study used water hyacinth biomass as a raw material for the extraction of nano activated carbon to be used as a filler to enhance the performance of the blank CA membrane for water treatment. Through this study, the problem of water hyacinth spreading as a biomass waste could be solved. In addition, a more useful and cheaper bio-sorbent filler can be synthesized from this waste by a simple and facile technique. In return, this will help in solving an irritating water pollution problem. The characteristics of the synthesized NAC and the four fabricated membranes were studied by SEM, FTIR, and XRD. All the used techniques have allowed the successful impregnation of NAC into CA membranes. SEM images displayed the surface characteristics of NAC as well as all the fabricated membranes. FTIR and XRD were used to investigate and confirm the differences between the neat and composite CA-based membranes. In addition, the contact angle was used to explore the membrane hydrophilicity. The results showed the hydrophilic nature of all the fabricated membranes. Moreover, it proved that the nanofibrous mat had a better hydrophilic nature than the cast one. The performance of the four membranes was evaluated using an Amicon cell setup. It was found that all the membranes had a better removal selectivity towards MB dye than CR. Furthermore, the addition of NAC enhanced the blank CA membrane dye removal efficiency. Among the four tested membranes, the composite cast and electro-spun CA/NAC recorded the best performances of 52.7 and 70%, respectively. However, the performance of the neat cast and electro-spun CA membrane achieved only 30 and 43.3%. In conclusion, the nanofibrous membrane showed a better performance than the cast membranes. Moreover, the impregnation of NAC had a positive effect on the membrane dye removal efficiency.

Data Availability Statement: All data are provided.

Conflicts of Interest: The authors declare no conflict of interest.

References

1. Li, Z.; Hanafy, H.; Zhang, L.; Sellaoui, L.; Netto, M.S.; Oliveira, M.L.S.; Seliem, M.K.; Dotto, G.L.; Bonilla-Petriciolet, A.; Li, Q. Adsorption of congo red and methylene blue dyes on an ashitaba waste and a walnut shell-based activated carbon from aqueous solutions: Experiments, characterization and physical interpretations. *Chem. Eng. J.* **2020**, *388*, 124263. [CrossRef]

2. Xiao, J.; Lv, W.; Xie, Z.; Tan, Y.; Song, Y.; Zheng, Q. Environmentally friendly reduced graphene oxide as a broad-spectrum adsorbent for anionic and cationic dyes: Via π-π Interactions. *J. Mater. Chem. A* **2016**, *4*, 12126–12135. [CrossRef]

3. Adesina, A.O.; Elvis, O.A.; Mohallem, N.D.S.; Olusegun, S.J. Adsorption of Methylene blue and Congo red from aqueous solution using synthesized alumina–zirconia composite. *Environ. Technol.* **2021**, *42*, 1061–1070. [CrossRef]

4. Ardila-Leal, L.D.; Poutou-Piñales, R.A.; Pedroza-Rodríguez, A.M.; Quevedo-Hidalgo, B.E. A brief history of colour, the environmental impact of synthetic dyes and removal by using laccases. *Molecules* **2021**, *26*, 3813. [CrossRef]

5. Ganapuram, B.R.; Alle, M.; Dadigala, R.; Dasari, A.; Maragoni, V.; Guttena, V. Catalytic reduction of methylene blue and Congo red dyes using green synthesized gold nanoparticles capped by *Salmalia malabarica* gum. *Int. Nano Lett.* **2015**, *5*, 215–222. [CrossRef]

6. Moradihamedani, P. Recent advances in dye removal from wastewater by membrane technology: A review. *Polym. Bull.* **2022**, *79*, 2603–2631. [CrossRef]

7. Sharma, J.; Sharma, S.; Soni, V. Classification and impact of synthetic textile dyes on Aquatic Flora: A review. *Reg. Stud. Mar. Sci.* **2021**, *45*, 101802. [CrossRef]

8. Chowdhury, S.; Pan, S.; Balasubramanian, R.; Das, P. Date Palm Based Activated Carbon for the Efficient Removal of Organic Dyes from Aqueous Environment. In *Sustainable Agriculture Reviews 34: Date Palm for Food, Medicine and the Environment*; Naushad, M., Lichtfouse, E., Eds.; Springer International Publishing: Cham, Switzerland, 2019; pp. 247–263. [CrossRef]

9. Lellis, B.; Fávaro-Polonio, C.Z.; Pamphile, J.A.; Polonio, J.C. Effects of textile dyes on health and the environment and bioremediation potential of living organisms. *Biotechnol. Res. Innov.* **2019**, *3*, 275–290. [CrossRef]

10. Raza, A.; Rehman, R.; Batool, M. Recent Review of Titania-Clay-Based Composites Emerging as Advanced Adsorbents and Photocatalysts for Degradation of Dyes over the Last Decade. *Adsorpt. Sci. Technol.* **2022**, *2022*, 3823008. [CrossRef]

11. Elessawy, N.A.; El-Sayed, E.M.; Ali, S.; Elkady, M.F.; Elnouby, M.; Hamad, H.A. One-pot green synthesis of magnetic fullerene nanocomposite for adsorption characteristics. *J. Water Process Eng.* **2020**, *34*, 101047. [CrossRef]

12. Praveen, S.; Jegan, J.; Pushpa, T.B.; Gokulan, R.; Bulgariu, L. Biochar for removal of dyes in contaminated water: An overview. *Biochar* **2022**, *4*, 10. [CrossRef]

13. Labena, A.; Abdelhamid, A.E.; Amin, A.S.; Husien, S.; Hamid, L.; Safwat, G.; Diab, A.; Gobouri, A.A.; Azab, E. Removal of Methylene Blue and Congo Red Using Adsorptive Membrane Impregnated with Dried *Ulva fasciata* and *Sargassum dentifolium*. *Plants* **2021**, *10*, 384. [CrossRef] [PubMed]

14. Yang, G.; Wu, L.; Xian, Q.; Shen, F.; Wu, J.; Zhang, Y. Removal of Congo red and methylene blue from aqueous solutions by vermicompost-derived biochars. *PLoS ONE* **2016**, *11*, e0154562. [CrossRef] [PubMed]

15. Pai, S.; Kini, M.S.; Selvaraj, R. A review on adsorptive removal of dyes from wastewater by hydroxyapatite nanocomposites. *Environ. Sci. Pollut. Res.* **2021**, *28*, 11835–11849. [CrossRef] [PubMed]

16. Elkady, M.F.; Hassan, H.S. Invention of Hollow Zirconium Tungesto-Vanadate at Nanotube Morphological Structure for Radionuclides and Heavy Metal Pollutants Decontamination from Aqueous Solutions. *Nanoscale Res. Lett.* **2015**, *10*, 474. [CrossRef]

17. Gürses, A.; Güneş, K.; Şahin, E. Chapter 5-Removal of dyes and pigments from industrial effluents. In *Advances in Green and Sustainable Chemistry*; Sharma, S.K., Ed.; Elsevier: Amsterdam, The Netherlands, 2021; pp. 135–187. [CrossRef]

18. Mcyotto, F.; Wei, Q.; Macharia, D.K.; Huang, M.; Shen, C.; Chow, C.W.K. Effect of dye structure on color removal efficiency by coagulation. *Chem. Eng. J.* **2021**, *405*, 126674. [CrossRef]

19. Khodaie, M.; Ghasemi, N.; Moradi, B.; Rahimi, M. Removal of methylene blue from wastewater by adsorption onto znclactivated corn husk carbon equilibrium studies. *J. Chem.* **2013**, *2013*, 383985. [CrossRef]

20. Mohammed, H.A.; Khaleefa, S.A.; Basheer, M.I. Photolysis of Methylene Blue Dye Using an Advanced Oxidation Process (Ultraviolet Light and Hydrogen Peroxide). *J. Eng. Sustain. Dev.* **2022**, *25*, 59–67. [CrossRef]

21. Beddai, A.A.; Badday, B.A.; Al-Yaqoobi, A.M.; Mejbel, M.K.; Hachim, Z.S.A.; Mohammed, M.K.A. Color Removal of Textile Wastewater Using Electrochemical Batch Recirculation Tubular Upflow Cell. *Int. J. Chem. Eng.* **2022**, *2022*, 4713399. [CrossRef]

22. Bhatia, D.; Sharma, N.R.; Singh, J.; Kanwar, R.S. Biological methods for textile dye removal from wastewater: A review. *Crit. Rev. Environ. Sci. Technol.* **2017**, *47*, 1836–1876. [CrossRef]

23. Kadhim, R.J.; Al-Ani, F.H.; Al-Shaeli, M.; Alsalhy, Q.F.; Figoli, A. Removal of dyes using graphene oxide (Go) mixed matrix membranes. *Membranes* **2020**, *10*, 366. [CrossRef] [PubMed]

24. Alardhi, S.M.; Albayati, T.M.; Alrubaye, J.M. A hybrid adsorption membrane process for removal of dye from synthetic and actual wastewater. *Chem. Eng. Process. Process Intensif.* **2020**, *157*, 108113. [CrossRef]

25. Hai, F.I.; Yamamoto, K.; Fukushi, K. Hybrid treatment systems for dye wastewater. *Crit. Rev. Environ. Sci. Technol.* **2007**, *37*, 315–377. [CrossRef]

26. Ledakowicz, S.; Pázdzior, K. Recent achievements in dyes removal focused on advanced oxidation processes integrated with biological methods. *Molecules* **2021**, *26*, 870. [CrossRef] [PubMed]

27. Wong, S.; Ghafar, N.A.; Ngadi, N.; Razmi, F.A.; Inuwa, I.M.; Mat, R.; Amin, N.A.S. Effective removal of anionic textile dyes using adsorbent synthesized from coffee waste. *Sci. Rep.* **2020**, *10*, 2928. [CrossRef]

28. Qalyoubi, L.; Al-Othman, A.; Al-Asheh, S. Recent progress and challenges of adsorptive membranes for the removal of pollutants from wastewater. Part II: Environmental applications. *Case Stud. Chem. Environ. Eng.* **2021**, *3*, 100102. [CrossRef]

29. Chen, Y.S.; Ooi, C.W.; Show, P.L.; Hoe, B.C.; Chai, W.S.; Chiu, C.-Y.; Wang, S.S.-S.; Chang, Y.-K. Removal of Ionic Dyes by Nanofiber Membrane Functionalized with Chitosan and Egg White Proteins: Membrane Preparation and Adsorption Efficiency. *Membranes* **2022**, *12*, 63. [CrossRef]

30. Tahazadeh, S.; Mohammadi, T.; Tofighy, M.A.; Khanlari, S.; Karimi, H.; Emrooz, H.B.M. Development of cellulose acetate/metal-organic framework derived porous carbon adsorptive membrane for dye removal applications. *J. Memb. Sci.* **2021**, *638*, 119692. [CrossRef]

31. Li, C.; Lou, T.; Yan, X.; Long, Y.Z.; Cui, G.; Wang, X. Fabrication of pure chitosan nanofibrous membranes as effective absorbent for dye removal. *Int. J. Biol. Macromol.* **2018**, *106*, 768–774. [CrossRef]

32. Ma, Y.; Qi, P.; Ju, J.; Wang, Q.; Hao, L.; Wang, R.; Sui, K.; Tan, Y. Gelatin/alginate composite nanofiber membranes for effective and even adsorption of cationic dyes. *Compos. B Eng.* **2019**, *162*, 671–677. [CrossRef]

33. Cheng, J.; Zhan, C.; Wu, J.; Cui, Z.; Si, J.; Wang, Q.; Peng, X.; Turng, L.-S. Highly Efficient Removal of Methylene Blue Dye from an Aqueous Solution Using Cellulose Acetate Nanofibrous Membranes Modified by Polydopamine. *ACS Omega* **2020**, *5*, 5389–5400. [CrossRef] [PubMed]

34. Rana, J.; Goindi, G.; Kaur, N. Potential of cellulose acetate for the removal of methylene blue dye from aqueous streams. *Int. J. Innov. Technol. Explor. Eng.* **2019**, *8*, 1379–1382. [CrossRef]

35. Rambabu, K.; Velu, S. Modified cellulose acetate ultrafiltration composite membranes for enhanced dye removal. *Int. J. Chem. Sci.* **2016**, *14*, 195–205.

36. Chen, W.; Ma, H.; Xing, B. Electrospinning of multifunctional cellulose acetate membrane and its adsorption properties for ionic dyes. In *International Journal of Biological Macromolecules*; Elsevier: Amsterdam, The Netherlands, 2020; Volume 158, pp. 1342–1351. [CrossRef]

37. Abu-Dalo, M.A.; Al-Rosan, S.A.; Albiss, B.A. Photocatalytic degradation of methylene blue using polymeric membranes based on cellulose acetate impregnated with zno nanostructures. *Polymers* **2021**, *13*, 3451. [CrossRef] [PubMed]

38. Qalyoubi, L.; Al-Othman, A.; Al-Asheh, S. Recent progress and challenges on adsorptive membranes for the removal of pollutants from wastewater. Part I: Fundamentals and classification of membranes. *Case Stud. Chem. Environ. Eng.* **2021**, *3*, 100086. [CrossRef]

39. Osagie, C.; Othmani, A.; Ghosh, S.; Malloum, A.; Esfahani, Z.K.; Ahmadi, S. Dyes adsorption from aqueous media through the nanotechnology: A review. *J. Mater. Res. Technol.* **2021**, *14*, 2195–2218. [CrossRef]

40. Homaeigohar, S.; Zillohu, A.U.; Abdelaziz, R.; Hedayati, M.K.; Elbahri, M. A novel nanohybrid nanofibrous adsorbent for water purification from dye pollutants. *Materials* **2016**, *9*, 848. [CrossRef]

41. Bhatnagar, A.; Hogland, W.; Marques, M.; Sillanpää, M. An overview of the modification methods of activated carbon for its water treatment applications. *Chem. Eng. J.* **2013**, *219*, 499–511. [CrossRef]

42. Zhao, X.; Huang, C.; Zhang, S.; Wang, C. Cellulose Acetate/Activated Carbon Composite Membrane with Effective Dye Adsorption Performance. *J. Macromol. Sci. Part B Phys.* **2019**, *58*, 909–920. [CrossRef]

43. Moosavi, S.; Lai, C.W.; Gan, S.; Zamiri, G.; Pivehzhani, O.A.; Johan, M.R. Application of efficient magnetic particles and activated carbon for dye removal from wastewater. *ACS Omega* **2020**, *5*, 20684–20697. [CrossRef]

44. Shokry, H.; Elkady, M.; Hamad, H. Nano activated carbon from industrial mine coal as adsorbents for removal of dye from simulated textile wastewater: Operational parameters and mechanism study. *J. Mater. Res. Technol.* **2019**, *8*, 4477–4488. [CrossRef]

45. Kanawade, S.M.; Gaikwad, R.W. Removal of Methylene Blue from Effluent by Using Activated Carbon and Water Hyacinth as Adsorbent. *Int. J. Chem. Eng. Appl.* **2011**, *2*, 317–319. [CrossRef]

46. Köseoğlu, E.; Akmil-Başar, C. Preparation, structural evaluation and adsorptive properties of activated carbon from agricultural waste biomass. *Adv. Powder Technol.* **2015**, *26*, 811–818. [CrossRef]

47. Malik, A. Environmental challenge vis a vis opportunity: The case of water hyacinth. *Environ. Int.* **2007**, *33*, 122–138. [CrossRef] [PubMed]

48. Mahamadi, C. Water hyacinth as a biosorbent: A review. *Afr. J. Environ. Sci. Tech.* **2012**, *5*, 1137–1145. [CrossRef]

49. Li, F.; He, X.; Srishti, A.; Song, S.; Tan, H.T.W.; Sweeney, D.J.; Ghosh, S.; Wang, C.-H. Water hyacinth for energy and environmental applications: A review. *Bioresour. Technol.* **2021**, *327*, 124809. [CrossRef] [PubMed]

50. Shokry, H.; Elkady, M.; Salama, E. Eco-friendly magnetic activated carbon nano-hybrid for facile oil spills separation. *Sci. Rep.* **2020**, *10*, 10265. [CrossRef] [PubMed]

51. Strathmann, H.; Scheible, P.; Baker, R.W. A rationale for the preparation of Loeb-Sourirajan-type cellulose acetate membranes. *J. Appl. Polym. Sci.* **1971**, *15*, 811–828. [CrossRef]

52. Sahraei, R.; Shahalizade, T.; Ghaemy, M.; Mahdavi, H. Fabrication of cellulose acetate/Fe$_3$O$_4$@GO-APTS-poly(AMPS-co-MA) mixed matrix membrane and its evaluation on anionic dyes removal. *Cellulose* **2018**, *25*, 3519–3532. [CrossRef]

53. Ghaseminezhad, S.M.; Barikani, M.; Salehirad, M. Development of graphene oxide-cellulose acetate nanocomposite reverse osmosis membrane for seawater desalination. *Compos. B Eng.* **2019**, *161*, 320–327. [CrossRef]
54. Thamer, B.M.; Aldalbahi, A.; Moydeen, M.A.; Rahaman, M.; El-Newehy, M.H. Modified electrospun polymeric nanofibers and their nanocomposites as nanoadsorbents for toxic dye removal from contaminated waters: A review. *Polymers* **2021**, *23*, 20. [CrossRef] [PubMed]
55. Subrahmanya, T.M.; Arshad, A.B.; Lin, P.T.; Widakdo, J.; Makari, H.K.; Austria, H.F.; Hu, C.C.; Lai, J.Y.; Hung, W.S. A review of recent progress in polymeric electrospun nanofiber membranes in addressing safe water global issues. *RSC Adv.* **2021**, *11*, 9638–9663. [CrossRef]
56. Elkady, M.; Shokry, H.; Hamad, H. New activated carbon from mine coal for adsorption of dye in simulated water or multiple heavy metals in real wastewater. *Materials* **2020**, *13*, 2498. [CrossRef] [PubMed]
57. Liu, Y.; Liu, X.; Dong, W.; Zhang, L.; Kong, Q.; Wang, W. Efficient Adsorption of Sulfamethazine onto Modified Activated Carbon: A Plausible Adsorption Mechanism. *Sci. Rep.* **2017**, *7*, 12437. [CrossRef] [PubMed]
58. Yu, X.; Han, Z.; Fang, S.; Chang, C.; Han, X. Optimized Preparation of High Value-Added Activated Carbon and Its Adsorption Properties for Methylene Blue. *Int. J. Chem. React. Eng.* **2019**, *17*, 20180267. [CrossRef]
59. Kebir, M.; Trari, M.; Maachi, R.; Nasrallah, N.; Amrane, A. Valorization of Inula viscosa waste extraction, modeling of isotherm, and kinetic for the tartrazine dye adsorption. *Desalination Water Treat* **2015**, *54*, 2806–2816. [CrossRef]
60. Kalyani, P.; Anitha, A. Refuse derived energy-tea derived boric acid activated carbon as an electrode material for electrochemical capacitors. *Port. Electrochim. Acta* **2013**, *31*, 165–174. [CrossRef]
61. Ding, B.; Li, C.; Hotta, Y.; Kim, J.; Kuwaki, O.; Shiratori, S. Conversion of an electrospun nanofibrous cellulose acetate mat from a super-hydrophilic to super-hydrophobic surface. *Nanotechnology* **2006**, *17*, 4332–4339. [CrossRef]
62. Namjoufar, M.; Farzi, A.; Karimi, A. Removal of Acid Brown 354 from wastewater by aminized cellulose acetate nanofibers: Experimental and theoretical study of the effect of different parameters on adsorption efficiency. *Water Sci. Technol.* **2021**, *83*, 1649–1661. [CrossRef]
63. Sudiarti, T.; Wahyuningrum, D.; Bundjali, B.; Arcana, I.M. Mechanical strength and ionic conductivity of polymer electrolyte membranes prepared from cellulose acetate-lithium perchlorate. *IOP Conf. Ser. Mater. Sci. Eng.* **2017**, *223*, 012052. [CrossRef]
64. Baniasadi, J.; Shabani, Z.; Mohammadi, T.; Sahebi, S. Enhanced performance and fouling resistance of cellulose acetate forward osmosis membrane with the spatial distribution of TiO_2 and Al_2O_3 nanoparticles. *J. Chem. Technol. Biotechnol.* **2021**, *96*, 147–162. [CrossRef]
65. Silva, M.A.; Hilliou, L.; de Amorim, M.T.P. Fabrication of pristine-multiwalled carbon nanotubes/cellulose acetate composites for removal of methylene blue. *Polym. Bull.* **2020**, *77*, 623–653. [CrossRef]
66. Aboamera, N.M.; Mohamed, A.; Salama, A.; Osman, T.A.; Khattab, A. An effective removal of organic dyes using surface functionalized cellulose acetate/graphene oxide composite nanofibers. *Cellulose* **2018**, *25*, 4155–4166. [CrossRef]

Article

Effect of Mushy Zone Parameter on Phase Change Behavior of Different Configurations Storage Unit: Numerical Simulation and Experimental Validation

Ahmed Saad Soliman [1], Ahmed A. Sultan [1,*] and Mohamed A. Sultan [2]

1 Mechanical Power Engineering Department, Mansoura University, El-Mansoura 35516, Egypt
2 Mechanical Engineering Department, Higher Future Institute of Engineering and Technology, El-Mansoura 35516, Egypt
* Correspondence: aasultan@mans.edu.eg

Abstract: The melting process of paraffin wax placed in storage capsules of different shapes was experimentally and numerically studied. The phase change material (PCM) was initially at 27 °C. The effect of the mushy zone parameter (A_{mush}) value on the melting process of the PCM was studied with storage capsules of different shapes (circular, vertical oval, and horizontal oval). The results of the numerical model were validated with the experimental results to obtain the optimum A_{mush} value for each shape of the latent heat storage unit. The results showed that the value of the A_{mush} has a great impact on the numerical results of the PCM melting process and changes with the shape of the storage capsule. The rate of heat transfer, convection, and fluid velocity all decrease as the A_{mush} value rises. The experimental results of the circular, vertical oval, and horizontal oval capsules match very well with the numerical model with A_{mush} values equal to 2×10^6, 1×10^5, and 1×10^6, respectively.

Keywords: natural convection; CFD; melting PCM; enthalpy-porosity method; mushy zone parameter

1. Introduction

Energy can be stored in several forms, such as sensible, latent, and thermochemical heat storage. Phase change materials (PCMs) are used in latent heat energy storage (LHES) systems, which have more desirable characteristics than conventional heat storage systems. PCMs offer a number of beneficial characteristics, including the ability to be used as a heat source at a constant temperature, with only slight temperature fluctuations through heat recovery. They possess a low vapour pressure at operating temperature, chemical stability, non-corrosion, and a high energy density with small storage space requirements [1]. Thus, PCMs demonstrate one of the best techniques used in thermal energy storage applications [2,3]. They are used in several engineering applications, for example, the technology of electronic cooling, waste heat recovery systems [4,5], solar cell systems [6], absorption systems [7], ventilation, and air conditioning (HVAC) systems [8].

1.1. Numerical Techniques Limitations

The numerical modeling of thermal energy storage (TES) systems has recently received a great deal of interest. Although the most appropriate numerical techniques can vary greatly depending on the system, cost and time restrictions are virtually always the driving forces behind their employment. Numerical models are now increasingly necessary to accurately explain the behaviour of TES systems, enabling computational tools to assist in the solution of governing equations. As a result, a significant portion of the research on this topic shows the development of adequate numerical analysis [9]. The heat transfer mechanism through the melting process is initially controlled by conduction; then, natural

convection begins, and this process of natural convection has a great impact and cannot be ignored [10,11].

Different modeling approaches for the solid–liquid phase change have been developed in recent decades. The most widely used methodology for numerically simulating the phase change phenomenon in several types of research is the enthalpy-porosity technique [12,13]. The other approaches to doing the same thing depend on varying the PCM's specific heat during the phase transition temperature [14]. The enthalpy-porosity approach can be used in all forms of the melting process, whereas the other methods are more suited to phase changes that are dominated by conduction [15]. The coupled convection–diffusion phase transition was numerically studied using the enthalpy-porosity technique [16]. This approach avoids directly following the solid–liquid contact. With appropriate momentum sink factors added to momentum equations, the solid–liquid mushy zone is viewed as a porous zone with a quantity denoted as a liquid fraction as its "porosity," which is the reason for the pressure reduction as the resulting solid material comes into existence.

1.2. Mushy Zone Effect

The thin mushy zone that divides the areas occupied by the solid and liquid PCMs contains a parameter known as the mushy zone constant that measures the resistance to the flow of liquid PCMs in this region. The literature demonstrates that the value of this constant affects simulation outcomes [17–19], and that the best value for agreement with experiments varies depending on the situation [18,20]. The cell porosity, which is calculated using the cell enthalpy, is a non-linear function of this parameter. Thus, the parameter was designed in such a way that it would be zero for entirely liquid cells and have no effect, while it would be in the same order as the other transport terms for cells going through a phase transition. The parameter's value would be high enough for totally solid cells to essentially push any velocity prediction to zero. The parameter also contains a constant known as the mushy zone parameter, A_{mush}, which captures the impact of the shape of the mushy zone [15].

The mushy zone is considered to be a semi-solid that exists at the boundary between the melted and un-melted portion of a PCM through the melting or freezing process. The amplitude of the damping is measured by the mushy zone parameter A_{mush}; the higher this value, the steeper the transition of the velocity of the material to zero as it solidifies. The predicted solution might oscillate at very high values of A_{mush} [21]. The overall phase transition process and the degree of phase interaction are both greatly influenced by the value of A_{mush}. However, the A_{mush} value may vary depending on the substance. For Rubitherm RT82, the value of A_{mush} ranges from 1×10^5 [22] to 1.6×10^6 [23] whereas for gallium it ranges from 1×10^5 to 1×10^{15} [24,25]. Several studies have found a correlation between the value of A_{mush} and the solid particle diameters within the mushy zone constant [26,27]. Thus, the choice of mushy zone constant becomes very important as the behaviour predicted using the enthalpy-porosity technique for the same material can differ significantly at different values of A_{mush}.

In previous studies, the A_{mush} value was studied for different types of phase change materials and it was observed that this value has a great impact on the melting process results of the numerical model. In the present work, the effect of the A_{mush} value on the PCM melting process was studied with different shapes of storage capsules (circular, horizontal oval, and vertical oval), which are filled with paraffin wax, which has not been previously studied. The melting process of the PCM was experimentally and numerically investigated in a circular, horizontal, and vertical oval storage units. The results that were obtained from the numerical model were validated with the experimental results to obtain the optimum value of A_{mush} for each shape of the latent heat storage unit.

The effects of A_{mush} through the storage units of circular, vertical oval, and horizontal oval capsules have not been previously studied. However, it can be used in energy-saving building applications.

2. Experimental Setup and Procedures

An image of the test rig is shown in Figure 1, while the layout is shown in Figure 2. The test rig consists of the water tank (10), which is made of galvanized sheet with a diameter of 40 cm and a height of 40 cm. The tank is used to supply the test section with hot water (11) at a constant temperature value. The tank is insulated with glass wool insulation to decrease the heat lost from hot water in the tank. The tank is equipped with a 1 kW electric heater (12) connected to the electrical main supply with a TROIDC type electric transformer (13). The electric transformer provides a voltage variation from 0 to 220 V to adjust the water temperature in the tank at a predefined temperature. The tank is equipped with a small 100-Watt water pump (8) connected to the tank bottom via an inlet connection (4) to supply the test section with the required hot water. The hot water is used to heat the capsule at different velocities using a supply valve (5) which regulates the water discharge rate to the test section (1). The valve (7) is used to bypass the excess water from the pump to the tank via a bypass connection (6), to prevent the pump from overheating.
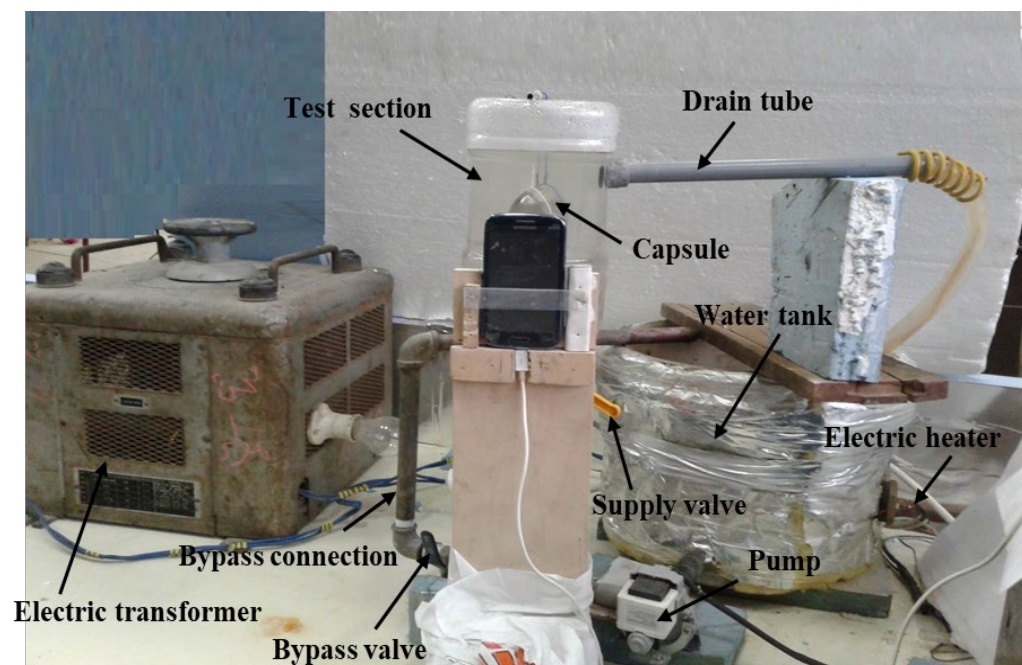
Figure 1. Photography of the experimental setup.

The test section (1) is a rectangular cross-section channel of 8 cm by 10 cm, and 15 cm in height. Hot water is brought to it via a $\frac{1}{2}$-inch diameter pipe (4) connected to the bottom of the channel through the pump (8). To drain the water into the hot water tank, a hole of 1/2 inch diameter is used and a tube (9) of the same diameter is connected to one side near the top of the channel to return the water to the hot water tank. The inlet water temperature is measured using the thermometer (3). The capsule (2) filled with PCM is placed in a horizontal position using a 1 mm diameter wire carrier.

Two Pyrex glass capsules are used, as seen in Figure 3; one has a circular cross-section with a 4 cm diameter and 6 cm length. The second capsule has an elliptical cross-section, the axes of which have dimensions of 6.2 and 2.6 cm. The two capsules are filled with the molten paraffin, then left to cool and closed with the resulting solid paraffin. The PCM thermophysical properties are represented in Table 1.
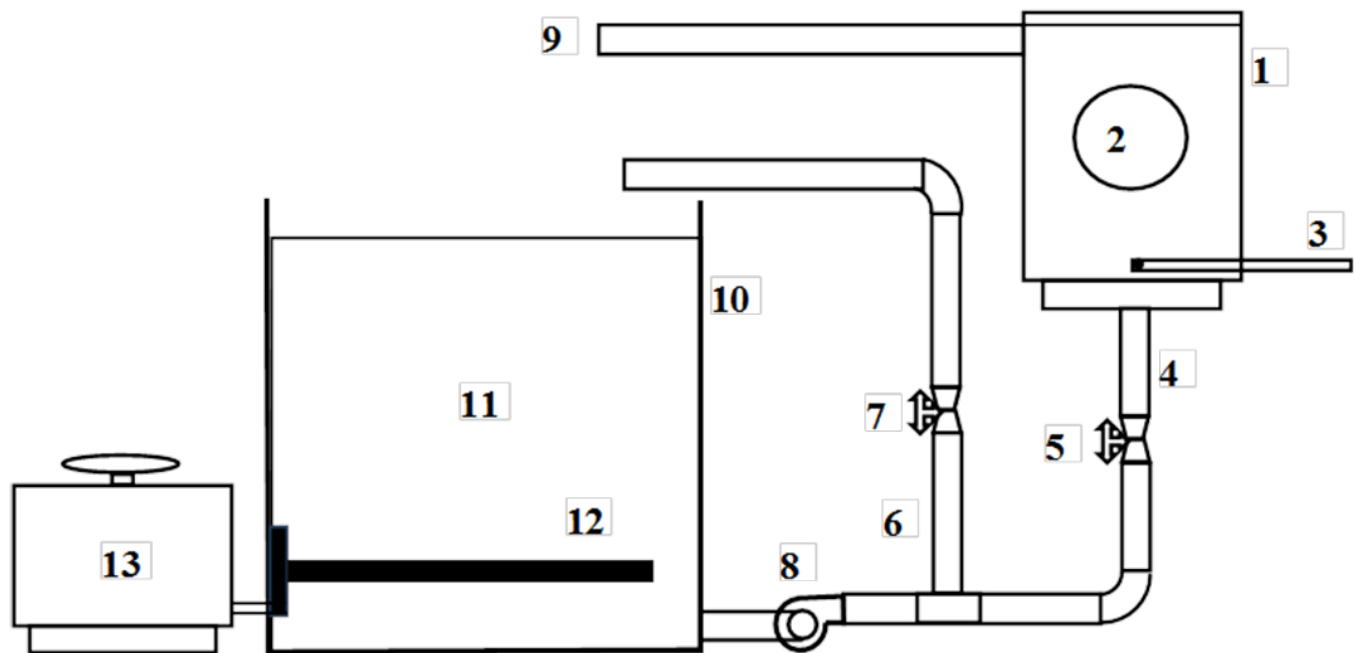
1-Test section   **2-PCM capsule**   **3-Thermometer**   **4-Inlet connection**

5-Supply valve   **6-Bypass connection**   **7-Bypass valve**   **8-Water pump**

9-Outlet connection   **10-Water tank**   **11-Hot water**   **12-Electric heater**

13-Electric transformer

Figure 2. Schematic representation of the experimental setup.

Table 1. PCM thermophysical properties.

Thermophysical Properties	Paraffin Wax [11]	Thermophysical Properties	Paraffin Wax [11]
K_s (W/m.K)	0.15	CP_l (kJ/kg.K)	2.44
K_l (W/m.K)	0.15	Kinematic viscosity (m^2/s)	8.31×10^{-5}
ρ_s (kg/m^3)	890	Melting point (°C)	54.22/56.22
ρ_l (kg/m^3)	712	Heat of fusion (kJ/kg)	278.8
CP_s (kJ/kg. K)	2.384	Thermal exp. Coeff (l/k)	0.000714

To facilitate the viewing and imaging of the capsule, the test section was made from Pyrex glass. In order to measure the average temperature of the water before interring the channel, a thermometer (3) was fixed inside the channel (1). The rate of hot water passing through the test section was measured by the amount of water collected at a given time during the experiment.

Khot et al., [28] observed that the use of thermocouples inside the PCM capsule restricted the solid PCM from sinking to the bottom of the spherical capsule. Therefore, the unconstrained PCM melted faster than the constrained one. Based on the previous study, the experimental investigation was made to validate the results obtained by the Ansys Fluent software wherein there is no thermocouple embedded inside the capsules to measure the temperature distribution inside it. The image processing technique for the experimental liquid fraction photos was used to detect the value of the PCM liquid fraction.
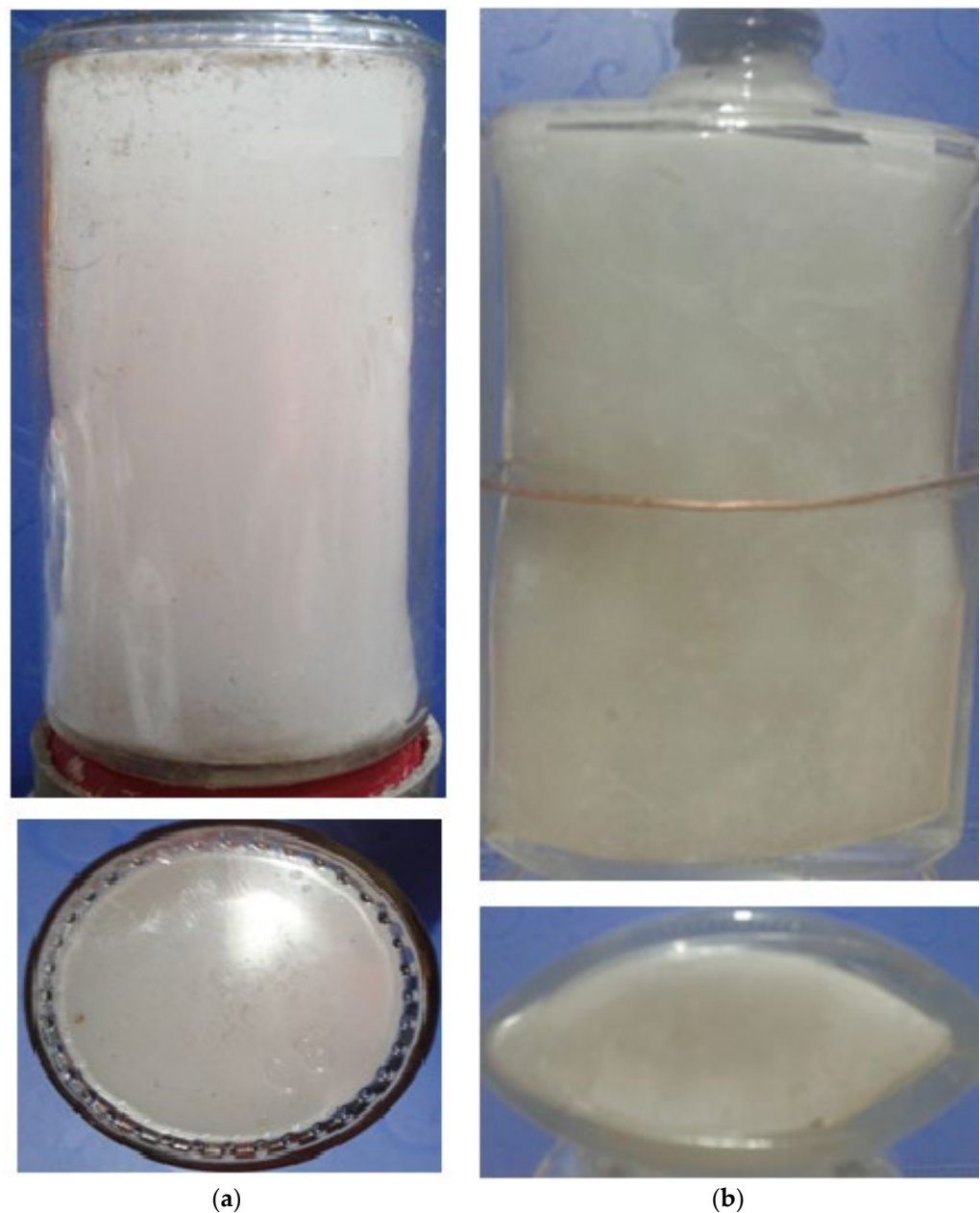
Figure 3. Photos of experimental capsules for (**a**) circular and (**b**) elliptical cross-section.

3. Experimental Measurements

First of all, we checked the system against leakage by turning on the pump and monitoring the system connections. Then, we measured the flow rate of water and adjusted the two valves (5 and 7) to reach the predetermined mean velocity of the water. After that, we regulated the electric transformer to vary the voltage supplied to the electric heater and let the system work, monitoring the reading of the thermometer until reaching the wanted temperature of hot water interring the test section. After reaching the suggested temperature, we turned the circular cross-section PCM capsule in place inside the channel, into a horizontal position. We took photos of the capsule cross-section every five minutes until the total melting of the PCM. Finally, we repeated the previous steps for the capsule of the elliptical cross-section on its largest axes, vertical and horizontal, one at a time to investigate the two radii ratios.

The cross-section area of the elliptical cross-section can be calculated as:

$$Ac = \pi\, a\, b \tag{1}$$

where a is half the smallest axis and b is half of the largest axis of the ellipse as shown in Figure 4.
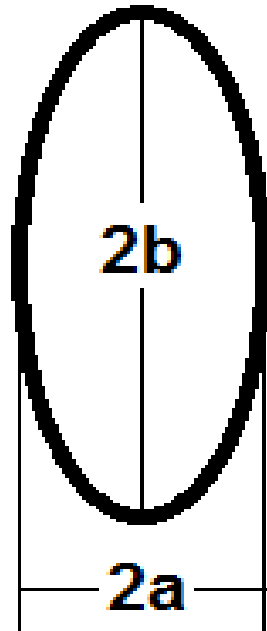
Figure 4. The main axes of the elliptical cross-section.

The surface area of the elliptical cross-section capsule can be calculated as:

$$As = C\, l \tag{2}$$

where l is the cylinder length and C is its perimeter.

The more accurate perimeter of the elliptical cross-section as a function of its axes using the Ramanujan second approximation [29] can be calculated as shown in the following equation:

$$C \approx \pi(a+b)\left(1 + \frac{3\left(\frac{a-b}{a+b}\right)^2}{10 + \sqrt{4 - 3\left(\frac{a-b}{a+b}\right)^2}}\right) \tag{3}$$

Two positions of the elliptical cross-section are discussed. The first position is a vertical oval with an axes ratio of Ar = 0.383, and the second position is a horizontal oval with an axes ratio of Ar = 2.6.

4. Uncertainty Analysis

Calculation and measurement errors resulting from human and instrumental errors are presented. Repeating measurements several times can help eliminate or reduce individual errors. As demonstrated in Table 2, the instrumental errors are due to the accuracy of the measuring devices. Based on the uncertainty of the primary measurements, the uncertainty of the computation results was calculated.

Table 2. Measurement device errors.

Measured Value	Measured Value Error
Temperature	+0.1 °C
Diameter	+0.5 mm
Voltage	+0.1 Volt
Resistance	+0.1 Ohm

Error propagation is estimated by using the root sum square method. Given the specific result Z, as follows:

$$Z = z(x1, x2, \ldots, xn) \tag{4}$$

where x_i is independently measured quantity, the uncertainty ω_i is the uncertainty of independent variables, and the uncertainty ω_z in the result, Z is assumed as follows:

$$\omega_z = \left[\left(\frac{\partial Z}{\partial x_1} . \omega_1 \right)^2 + \left(\frac{\partial Z}{\partial x_2} . \omega_2 \right)^2 + \ldots + \left(\frac{\partial Z}{\partial x_{n-1}} . \omega_{n-1} \right)^2 + \left(\frac{\partial Z}{\partial x_n} . \omega_n \right)^2 \right]^{0.5} \tag{5}$$

5. Numerical Modeling

The Boussinesq approximation, which incorporates thermal buoyancy, represents the liquid PCM density difference in the buoyancy term. As a result, the 2D transient laminar flow containing buoyancy-driven conventional governing equations can be expressed by the following equations [11]:

Continuity equation:

$$\frac{\partial \rho}{\partial t} + \frac{1}{r} \frac{\partial (r \rho V_r)}{\partial r} + \frac{1}{r} \frac{\partial (\rho V_\theta)}{\partial \theta} = 0 \tag{6}$$

Momentum equations:
Momentum *r*:

$$\begin{aligned}
&\rho \left(\frac{\partial (V_r)}{\partial t} + V_r \frac{\partial (V_r)}{\partial r} + \frac{V_\theta}{r} \frac{\partial (V_r)}{\partial \theta} - \frac{V_\theta^2}{r} \right) \\
&= -\frac{\partial P}{\partial r} + \mu \left[\frac{1}{r} \frac{\partial}{\partial r} \left(r \frac{\partial (V_r)}{\partial r} \right) - \frac{V_r}{r^2} + \frac{1}{r^2} \frac{\partial^2 (V_r)}{\partial \theta^2} - \frac{2}{r^2} \frac{\partial (V_\theta)}{\partial \theta} \right] + \rho g \beta (T - T_m) + S
\end{aligned} \tag{7}$$

Momentum *θ*:

$$\begin{aligned}
&\rho \left(\frac{\partial (V_\theta)}{\partial t} + V_r \frac{\partial (V_\theta)}{\partial r} + \frac{V_\theta}{r} \frac{\partial (V_\theta)}{\partial \theta} + \frac{V_r V_\theta}{r} \right) \\
&= -\frac{1}{r} \frac{\partial P}{\partial \theta} + \mu \left[\frac{1}{r} \frac{\partial}{\partial r} \left(r \frac{\partial (V_\theta)}{\partial r} \right) - \frac{V_\theta}{r^2} + \frac{1}{r^2} \frac{\partial^2 (V_\theta)}{\partial \theta^2} - \frac{2}{r^2} \frac{\partial (V_r)}{\partial \theta} \right] + S
\end{aligned} \tag{8}$$

The parameters s are Darcy's law damping terms added to the momentum equation as a convective phase change effect. These terms depend on both the existing constant A_{mush} and a liquid fraction (λ), which can be expressed as follows:

$$\vec{S} = \frac{(1 - \lambda)^2}{(\lambda^3 + \gamma)} A_{mush.} \vec{V}$$

The minor number γ is used to avoid division by zero, and it is naturally about 10^{-3}. The mushy zone constant A_{mush} explains how steeply its velocity is condensed to zero when the material solidifies. Its value depends on the morphology of the medium. This value is frequently high and typically runs from 10^4 to 10^8. The same occurred when the local liquid fraction becomes high, and the velocity is reduced to zero. Numerous academics advise taking into account the A_{mush} value of 10^6 as the best value. This value offers a good agreement between their experimental and numerical results [30]. In this

study, A_{mush} varies throughout the whole simulation, where it attains the best conformity between the experimental and numerical results.

Energy equation:

$$\frac{\partial h}{\partial t} + \frac{\partial H}{\partial t} + \nabla \cdot \left(\overrightarrow{V} h \right) = \nabla \cdot \left(\frac{k}{\rho c_p} \nabla h \right) \tag{9}$$

where H is the enthalpy of the PCM and is estimated as the summation of the sensible enthalpy, h_1, and the latent heat ΔH:

$$H = h_1 + \Delta H \tag{10}$$

$$h_1 = h_{ref} + \int_{T_{ref}}^{T} C_p \, dT \tag{11}$$

where h_{ref} is the enthalpy reference at temperature reference T_{ref} and latent heat term can be expressed in the form of the latent heat of the PCMs (L) as follows:

$$\Delta H = \lambda \, L \tag{12}$$

where ΔH can vary from zero (solid) to L (liquid). Therefore, the liquid fraction λ can be articulated as follows:

$$\lambda = \begin{cases} \frac{\Delta H}{L} = 0 \; T < T_m \\ \frac{\Delta H}{L} = \frac{T - T_{solidus}}{T_{liqudus} - T_{solidus}} \; T_m < T < T_m + \Delta T_m \\ \frac{\Delta H}{L} = 1 \; T > T_m + \Delta T_m \end{cases} \tag{13}$$

where T_m is the PCM melting temperature, and ΔT_m is the range between liquid and solid phase, which is expressed as the difference between liquidus temperature and solidus temperature, as demonstrated in Equation (14):

$$\Delta T_m = T_{liquidus} - T_{solidus} \tag{14}$$

The PCM density and thermal conductivity depend on the phase change process as follows:

$$\rho_{\text{PCM}} = \begin{cases} \rho_s \; T < T_m \\ \frac{\rho_s + \rho_l}{2} \; T_m < T < T_m + \Delta T_m \\ \rho_l \; T > T_m + \Delta T_m \end{cases} \tag{15}$$

$$k_{\text{PCM}} = \begin{cases} k_s \; T < T_m \\ \frac{k_s + k_l}{2} \; T_m < T < T_m + \Delta T_m \\ k_l \; T > T_m + \Delta T_m \end{cases} \tag{16}$$

5.1. Initial and Boundary Conditions

The previous governing equations were solved together with the following initial and boundary conditions. Initially, the system was at the ambient temperature of 27 °C, and the storage capsules were filled with solid paraffin wax, which was at a temperature lower than the melting point. The outer side of the tank was insulated; in addition, the inlet of the hot water was defined as the velocity inlet and the outlet of the hot water was defined as the pressure outlet, as shown in Figure 5.
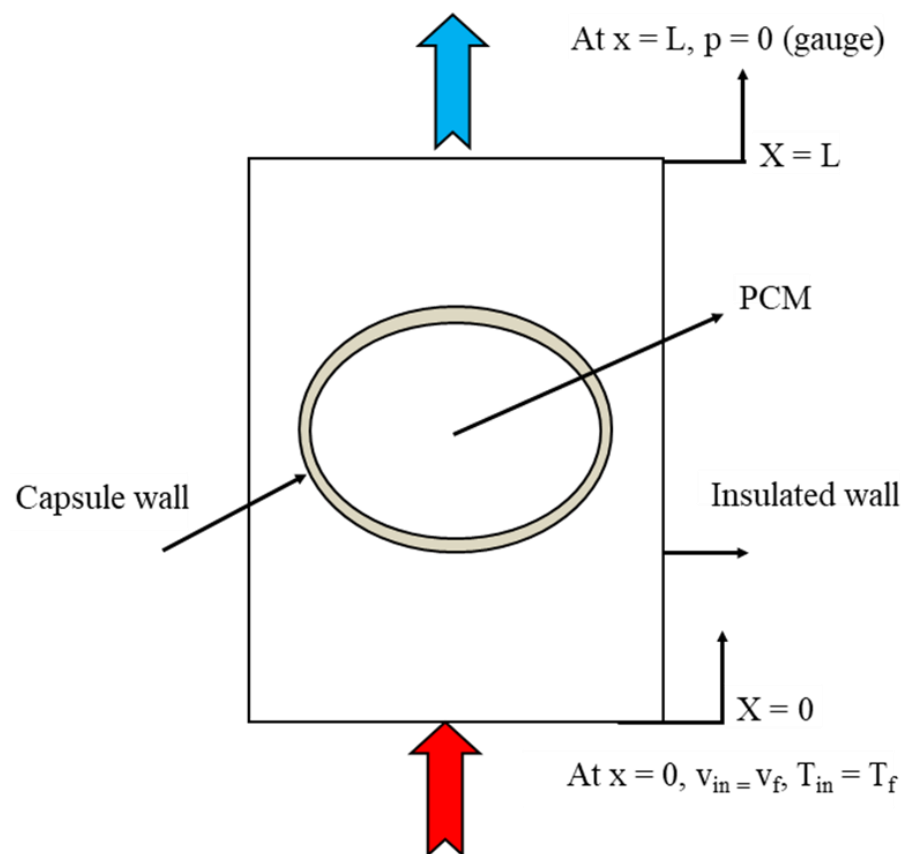
Figure 5. Test section with boundary conditions.

5.2. Numerical Procedure and Validation

The numerical simulation was established using the ANSYS 2022 R2 program. The Semi-Implicit Method for the Pressure-Linked Equations (SIMPLE) scheme was used to calculate the pressure–velocity coupling equations in the PCM. A control volume approach was used to explain the governing equations in conjunction with the boundary and initial conditions. The diffusion and convection terms are described using the central difference and QUICK techniques, respectively. The pressure–velocity coupling was handled using the SIMPLER algorithm. By solving the governing equations at each time step, the liquid fraction could be changed using Equation (13). After carefully evaluating the independence of the results for high accuracy, the size of the grid and the time steps were selected. The calculation process continued until a relative convergence criterion of 10^{-6} was satisfied by all the present case variables.

To validate the numerical model of melting in the present finite volume computational fluid dynamic (CFD) code, an initial run was established and compared to the experimental results of Soliman et al. [10,11] for a vertical cylinder that was heated by a constant heat flux, and Kamkari and Amlashi [31] for a vertical enclosure that was heated by a constant wall temperature. The computational model and the experimental study were established under the same operating conditions. Figure 6 displays the PCM temperature and liquid fractions, with the melting time for the experimental results of [11,31], respectively, with the present numerical results. As can be noted from the figure, the numerical results are in good agreement with the experimental results.
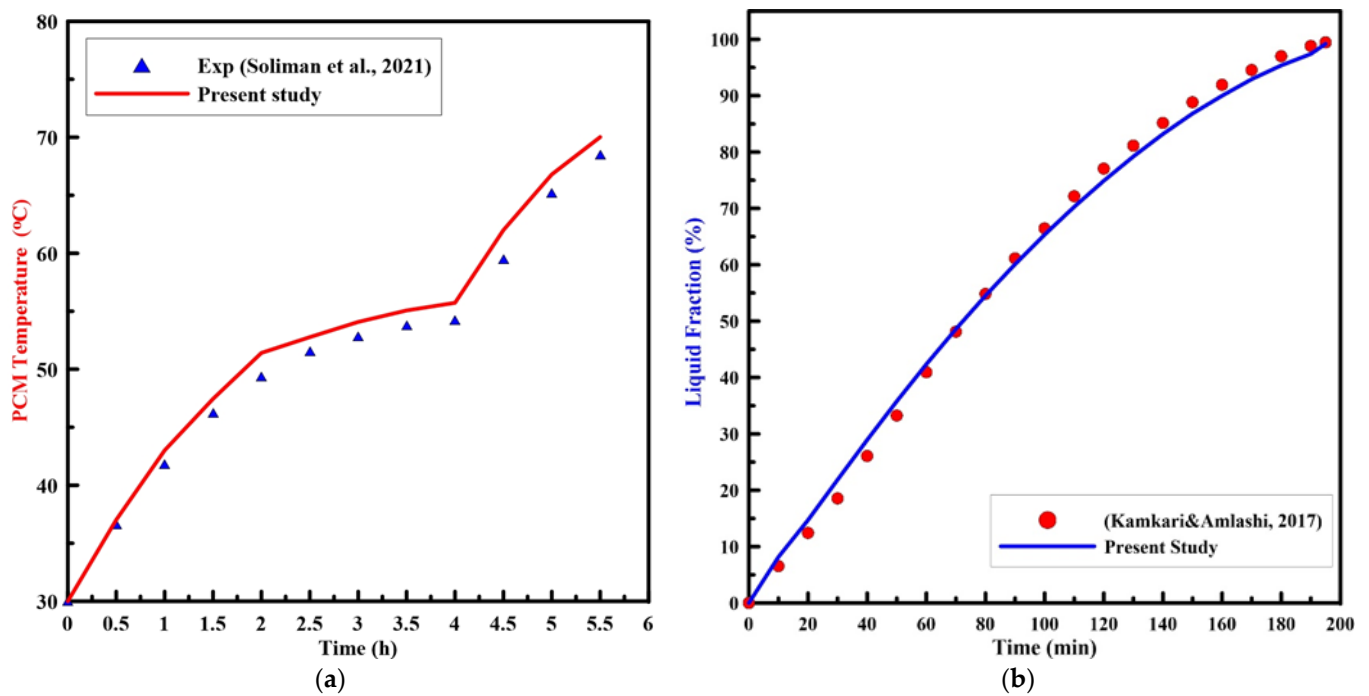
Figure 6. Experimental results of PCM (**a**) temperature [11], and (**b**) liquid fraction [31] vs. time with the present numerical study.

5.3. Mesh Dependency Study

Free triangular mesh has been adapted in the numerical model. In order to test the dependency of numerical results on the mesh element size, a simulation was run with a circular capsule of 4 cm in diameter and 6 cm in length. The capsule was initially at 300 K. At any time, t > 0, the boundary of the capsule was at 340 K. The average temperature and liquid fraction of the PCM for the circular capsule were compared for different numbers of elements size (20,062, 32,634, 45,409, 68,312, and 87,472) as shown in Figure 7a,b. It is observed from the figure that there is a slight difference between the number of elements 68,312 and 87,472. Therefore, the number of elements equal to 68,312 is selected for the present study to save time. Similarly, a grid independency test has also been carried out for other configurations. The time steps used in the analysis is 0.3 sec throughout all models.
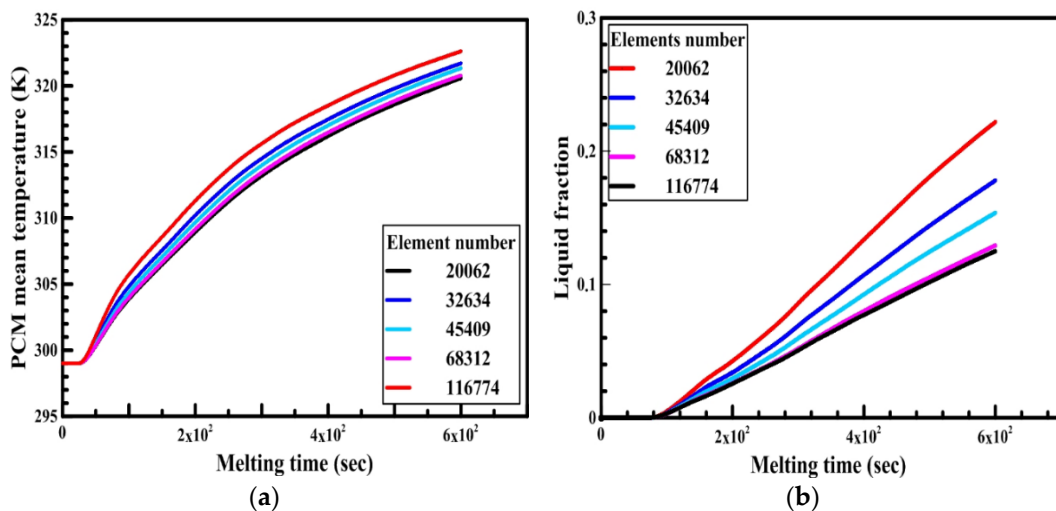
Figure 7. Effect of elements size number on the PCM (**a**) temperature and (**b**) liquid fraction.

6. Results and Discussion

In this section, firstly, a comparison between the experimental results of different shapes of storage capsules (circular, horizontal oval, and vertical oval) is established with the theoretical results of the same shape and dimensions from the numerical model. Tables 3–5 illustrate the variation of the liquid fraction contours of the PCM melting process with the photos captured during the experiments.

Table 3. Comparison between liquid fraction contours and camera photos for circular cross-section capsule.
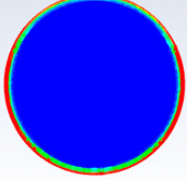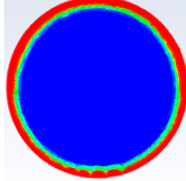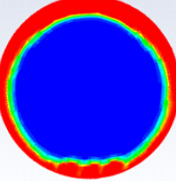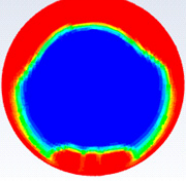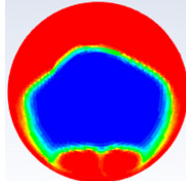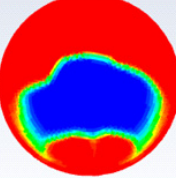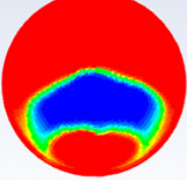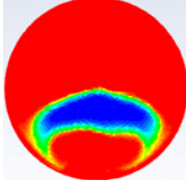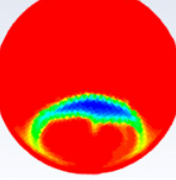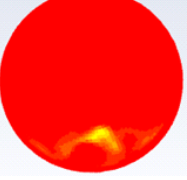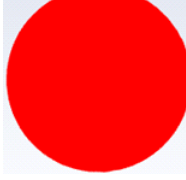
Theoretical	Exp.	Theoretical	Exp.	Theoretical	Exp.
Time = 0 min		Time = 10 min		Time = 20 min	
Time = 30 min		Time = 40 min		Time = 50 min	
Time = 60 min		Time = 70 min		Time = 80 min	
Time = 90 min		Time = 100 min		106 min	104 min

Table 4. Comparison between liquid fraction contours and camera photos for circular cross-section capsule of Ar = 0.383.

Theoretical	Exp.	Theoretical	Exp.	Theoretical	Exp.
Time = 0 min		Time = 8 min		Time = 18 min	
Time = 28 min		Time = 38 min		Time = 48 min	
Time = 58 min		Time = 63 min		67 min	66 min
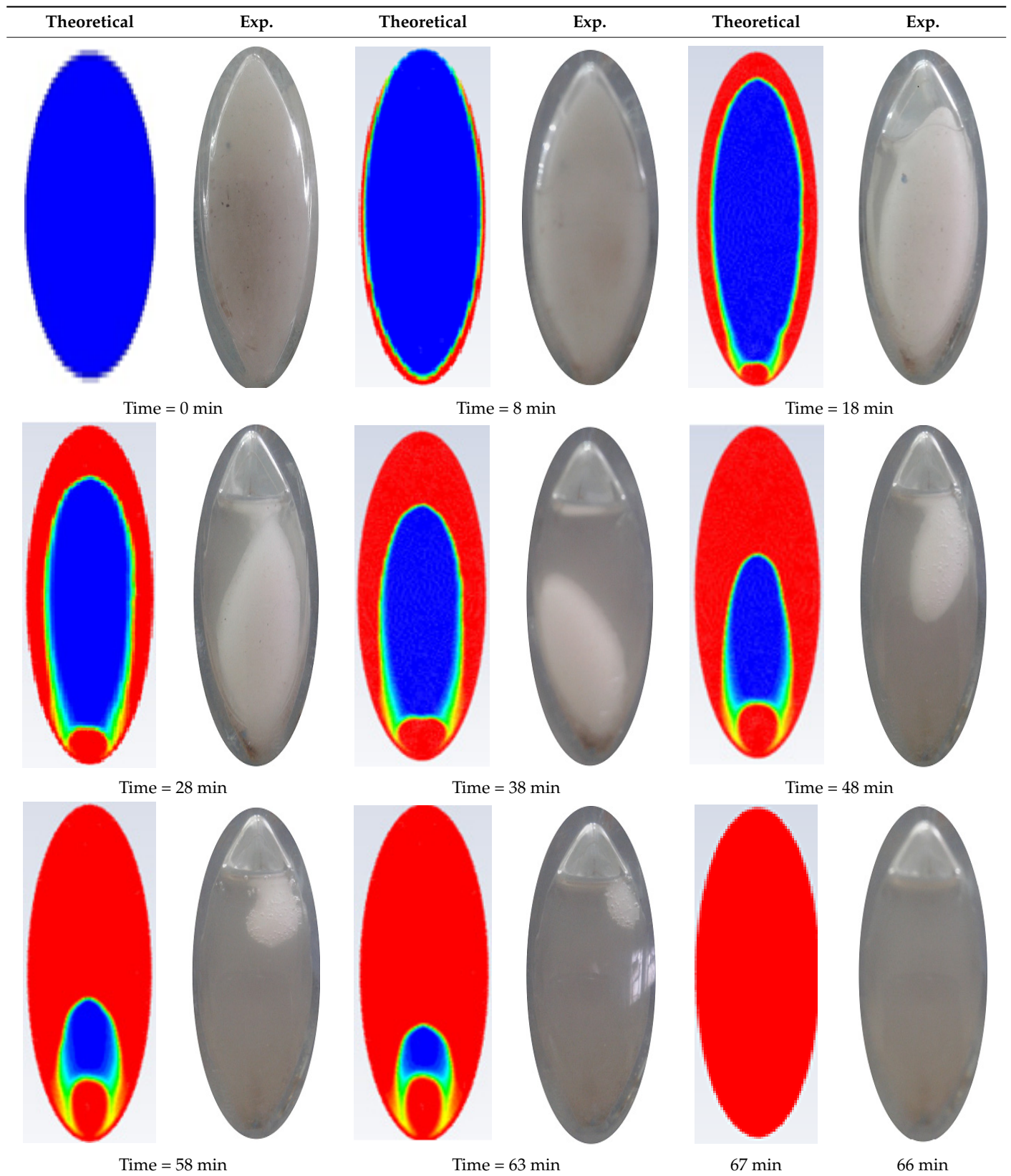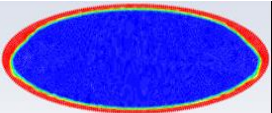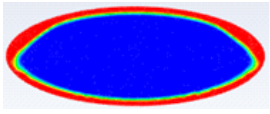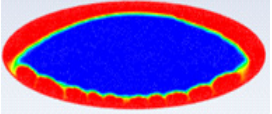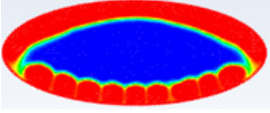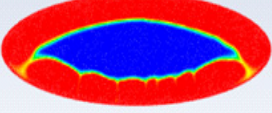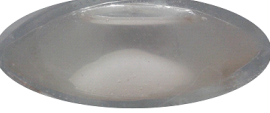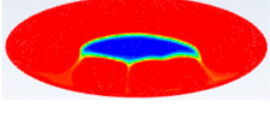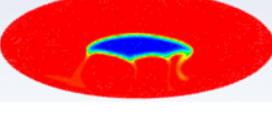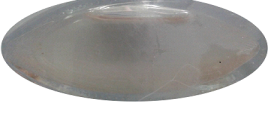
Table 5. Comparison between liquid fraction contours and camera photos for circular cross-section capsule of Ar = 2.6.

Theoretical	Exp.	Theoretical	Exp.
Time = 0 min		Time= 7 min	
Time = 15 min		Time = 27 min	
Time = 37 min		Time = 47 min	
Time = 57 min		Time = 59 min	
66 min	64 min		

Secondly, the effect of the mushy zone parameter on the PCM melting process is studied and validated with the experimental results to obtain the optimum value of A_{mush} for each shape. Figures 8–10 illustrate the PCM liquid fraction with the melting time of the experimental result and the numerical results with different values of the mushy zone parameter.

Table 3 represents the comparison between the liquid fraction contours of a circular capsule with the experimental photos. The circular cross-section capsule is 4 cm in diameter (axes ratio of 1) and 6 cm in length for heat transfer fluid (HTF) initial temperature of 340 K and a velocity of 0.003 m/s. Within the experimental photos, the white part is a solid PCM and the transparent part is a liquid PCM. Within the numerical contours, the blue color signifies the solid PCM and the red color denotes the liquid PCM. The solid PCM sinks to the bottom of the capsule due to the force of gravity for both the numerical and experimental results. The experimental total melting time is less than that of the theoretical one by 2 min.

Table 4 represents the comparison between the liquid fraction contours of the elliptical cross-section capsule with the experimental photos. The elliptical cross-section capsule is in a vertical position with an axes ratio of 0.383 for the HTF initial temperature of 340 K and a velocity of 0.003 m/s. The experimental total melting time is less than that of the theoretical one by 1 min.

Table 5 represents the comparison between the liquid fraction contours of the elliptical cross-section capsule with the experimental photos. The elliptical cross-section capsule is in a horizontal position with an axes ratio of 2.6 for the HTF initial temperature of 340 K and a velocity of 0.003 m/s. The experimental total melting time is less than that of the theoretical one by 2 min.

It is demonstrated in the figures that there is a fair agreement between the experimental and theoretical results and the shape of molten and solid paraffin. The fair agreement between experimental and theoretical results ensures the validity of the theoretical model and the accuracy of the different thermal properties of the paraffin wax.
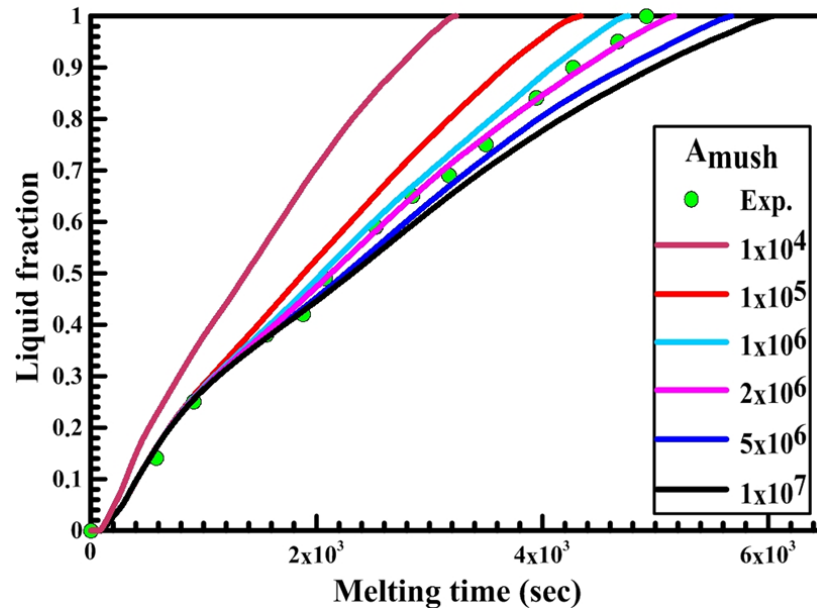
Figure 8. Experimental and numerical liquid fraction vs. time for a circular capsule.
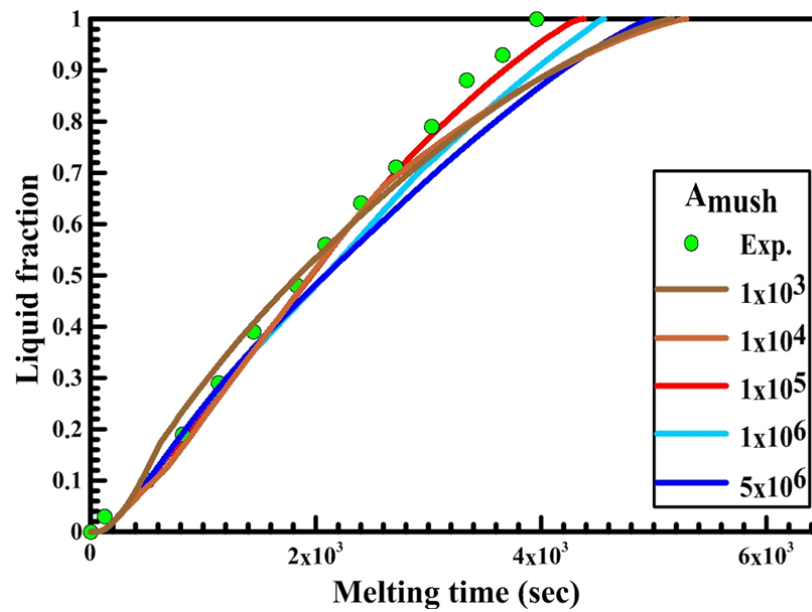
Figure 9. Experimental and numerical liquid fraction vs. time for a vertical oval capsule.
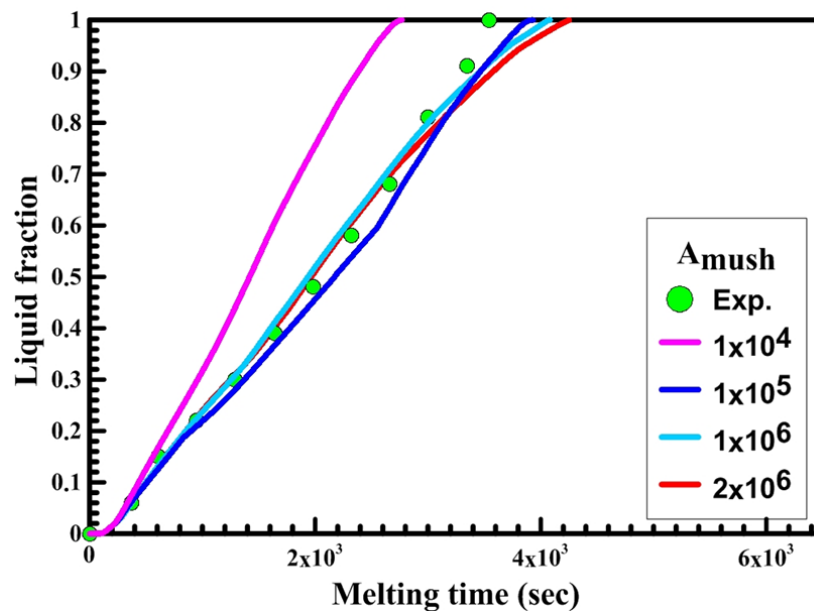
Figure 10. Experimental and numerical liquid fraction vs. time for a horizontal oval capsule.

The experimental investigation was made to validate the results obtained by the Ansys Fluent software. Khot et al. [28] observed that using the thermocouples inside the PCM throughout the melting process restricted the solid PCM from moving, which affected the melting process. Therefore, there is no thermocouple embedded inside the circular and oval capsules to measure the temperature distribution inside it. The experimental results of the liquid fraction are calculated using the image processing method, which enables the determination of the percentage of the solid "white color" and the liquid "gray color".

Figure 8 shows the relation between liquid fraction and time for both experimental and numerical results for a circular capsule at the HTF inlet temperature of 340 K and a velocity of 0.003 m/s. The numerical results are obtained with different values of A_{mush} (1×10^4, 1×10^5, 2×10^6, 5×10^6, 1×10^7). It is observed from the figure that the melting rate of the numerical results is slow at $A_{mush} = 1 \times 10^7$, while at $A_{mush} = 1 \times 10^4$ the melting rate of the numerical results increases, and its value is greater than the experimental results.

The previous phenomena are due to the great effect of A_{mush} on the convection effect. Increasing the A_{mush} value leads to a reduction in the convection effect and the melting rate. For the circular capsule, the experimental results have a good agreement with the numerical results at the value of A_{mush} equal to 2×10^6.

Figure 9 displays the relation between liquid fraction and time for both experimental and numerical results for a vertical oval capsule at the HTF inlet temperature of 340 K and a velocity of 0.003 m/s. The numerical results are obtained with different numbers of A_{mush} (1×10^4, 1×10^5, 1×10^6, 5×10^6). It can be observed from the figure that the melting rate of the numerical results is slow at $A_{mush} = 5 \times 10^6$, while at $A_{mush} = 1 \times 10^6$, and 5×10^6 the melting rate of the numerical results is close to the experimental results. For the vertical oval capsule, the experimental results have a good agreement with the numerical results at the value of A_{mush} equal to 1×105.

Figure 10 illustrates the relation between liquid fraction and time for both experimental and numerical results for a horizontal oval capsule at HTF inlet temperature of 340 K and a velocity of 0.003 m/s. The numerical results are obtained with different numbers of A_{mush} (1×10^4, 1×10^5, 1×10^6, 2×10^6).

It can be observed from Figure 10 that the melting rate of the numerical results increases and its value is greater than the experimental results at $A_{mush} = 1 \times 10^4$, while at $A_{mush} = 1 \times 10^6$ and 2×10^6, the melting rate of the numerical results is close to the experimental results. For the horizontal oval capsule, the experimental results have a good agreement with the numerical results at the value of A_{mush} equal to 1×10^6.

From the present study, it can be observed that the mushy zone parameter (A_{mush}) has a great impact on the numerical model results of the PCM melting process and changes with the shape of the storage unit. The present study provides a range of the mushy zone parameter for the numerical modeling of the melting process in the circular, horizontal oval, and vertical oval capsules in future work to obtain more accurate results. Table 6 represents the optimum number of the mushy zone parameter for circular, vertical oval, and horizontal oval capsules.

Table 6. Optimum number of the mushy zone parameter for circular, vertical oval, and horizontal oval capsules.

Cases	Shape	Dimensions	A_{mush} Range	Outcomes
Circular capsule		Ar = 1	1×10^4 1×10^5 2×10^6 5×10^6 1×10^7	Good agreement with the experimental results at A_{mush} equal to 2×10^6.
Vertical oval capsule		Ar = 0.383	1×10^4 1×10^5 1×10^6 5×10^6	Good agreement with the numerical results at A_{mush} equal to 1×10^5.
Horizontal oval capsule		Ar = 2.6	1×10^4 1×10^5 1×10^6 2×10^6	Good agreement with the numerical results at A_{mush} equal to 1×10^6.

7. Conclusions

The melting process of a phase change material (PCM) was experimentally and numerically investigated in storage capsules of different shapes (circular, vertical oval, and horizontal oval). The numerical model was established to study the effect of the A_{mush} (mushy zone parameter) on the thermal performance of the PCM melting process. The model was validated with previous related work, and the results exhibited good agreement. The results of the numerical model were validated with the experimental results to obtain the optimum value of A_{mush} for each shape of the latent heat storage unit. According to the present experimental/numerical results of the PCM melting process inside different capsules, the following conclusions can be drawn:

1. The value of A_{mush} has a great impact on the numerical model results of the PCM melting process and changes with the shape of the storage unit;
2. The rate of heat transfer, convection, and fluid velocity all decrease as the value of A_{mush} rises;
3. The experimental results of the circular, vertical oval, and horizontal oval capsules match well with the numerical model at the value of A_{mush} equal to 2×10^6, 1×10^5, and 1×10^6, respectively.

The effect of nanoparticles on the mushy zone parameter should be taken into account in future research due to their great effect upon the enhancement of the pelting process.

References

1. Hosseini, M.J.; Ranjbar, A.A.; Sedighi, K.; Rahimi, M. A Combined Experimental and Computational Study on the Melting Behavior of a Medium Temperature Phase Change Storage Material inside Shell and Tube Heat Exchanger. *Int. Commun. Heat Mass Transf.* **2012**, *39*, 1416–1424. [CrossRef]
2. Guerraiche, D.; Bougriou, C.; Guerraiche, K.; Valenzuela, L.; Driss, Z. Experimental and Numerical Study of a Solar Collector Using Phase Change Material as Heat Storage. *J. Energy Storage* **2020**, *27*, 101133. [CrossRef]
3. Haghighi, A.; Babapoor, A.; Azizi, M.; Javanshir, Z.; Ghasemzade, H. Optimization of the Thermal Performance of PCM Nanocomposites. *J. Energy Manag. Technol.* **2019**, *4*, 14–19.
4. Soliman, A.S.; Zhu, S.; Xu, L.; Dong, J.; Cheng, P. Efficient Waste Heat Recovery System for Diesel Engines Using Nano-Enhanced Phase Change Materials. *Case Stud. Therm. Eng.* **2021**, *28*, 101309. [CrossRef]
5. Soliman, A.S.; Radwan, A.; Xu, L.; Dong, J.; Cheng, P. Energy Harvesting in Diesel Engines to Avoid Cold Start-up Using Phase Change Materials. *Case Stud. Therm. Eng.* **2022**, *31*, 101807. [CrossRef]
6. Soliman, A.S.; Xu, L.; Dong, J.; Cheng, P. A Novel Heat Sink for Cooling Photovoltaic Systems Using Convex/Concave Dimples and Multiple PCMs. *Appl. Therm. Eng.* **2022**, *215*, 119001. [CrossRef]
7. Soliman, A.S.; Zhu, S.; Xu, L.; Dong, J.; Cheng, P. Design of an H2O-LiBr Absorption System Using PCMs and Powered by Automotive Exhaust Gas. *Appl. Therm. Eng.* **2021**, *191*, 116881. [CrossRef]
8. Dhaidan, N.S.; Khodadadi, J.M. Melting and Convection of Phase Change Materials in Different Shape Containers: A Review. *Renew. Sustain. Energy Rev.* **2015**, *43*, 449–477. [CrossRef]
9. Fadl, M.; Eames, P.C. Numerical Investigation of the Influence of Mushy Zone Parameter Amush on Heat Transfer Characteristics in Vertically and Horizontally Oriented Thermal Energy Storage Systems. *Appl. Therm. Eng.* **2019**, *151*, 90–99. [CrossRef]
10. Soliman, A.S.; Zhu, S.; Xu, L.; Dong, J.; Cheng, P. Melting Enhancement of Nano-Phase Change Material in Cylindrical Enclosure Using Convex/Concave Dimples: Numerical Simulation with Experimental Validation. *J. Energy Storage* **2021**, *44*, 103470. [CrossRef]
11. Soliman, A.S.; Zhu, S.; Xu, L.; Dong, J.; Cheng, P. Numerical Simulation and Experimental Verification of Constrained Melting of Phase Change Material in Cylindrical Enclosure Subjected to a Constant Heat Flux. *J. Energy Storage* **2021**, *35*, 102312. [CrossRef]
12. Voller, V.R.; Cross, M.; Markatos, N.C. An Enthalpy Method for Convection/Diffusion Phase Change. *Int. J. Numer. Methods Eng.* **1987**, *24*, 271–284. [CrossRef]
13. Voller, V.R.; Prakash, C. A Fixed Grid Numerical Modeling Methodology for Convection-Diffusion Mushy Region Phase-Change Problems. *Int. J. Heat Mass Transf.* **1987**, *30*, 1709–1719. [CrossRef]
14. Ehms, J.H.N.; de Césaro Oliveski, R.; Rocha, L.A.O.; Biserni, C.; Garai, M. Fixed Grid Numerical Models for Solidification and Melting of Phase Change Materials (PCMs). *Appl. Sci.* **2019**, *9*, 4334.
15. Singh, V.K.; Patel, A. Effect of Mushy Zone Constant on the Melting of a Solid-Liquid PCM under Hyper-Gravity Conditions. *Int. Commun. Heat Mass Transf.* **2022**, *134*, 105993. [CrossRef]
16. Brent, A.D.; Voller, V.R.; Reid, K.J. Enthalpy-Porosity Technique for Modeling Convection-Diffusion Phase Change: Application to the Melting of a Pure Metal. *Numer. Heat Transf.* **1988**, *5720*, 297–318.
17. Kumar, M.; Krishna, D.J. Influence of Mushy Zone Constant on Thermohydraulics of a PCM. *Energy Procedia* **2017**, *109*, 314–321. [CrossRef]
18. Shmueli, H.; Ziskind, G.; Letan, R. Melting in a Vertical Cylindrical Tube: Numerical Investigation and Comparison with Experiments. *Int. J. Heat Mass Transf.* **2010**, *53*, 4082–4091. [CrossRef]
19. Arena, S.; Casti, E.; Gasia, J.; Cabeza, L.F.; Cau, G. Numerical Simulation of a Finned-Tube LHTES System: Influence of the Mushy Zone Constant on the Phase Change Behaviour. *Energy Procedia* **2017**, *126*, 517–524. [CrossRef]
20. Hosseinizadeh, S.F.; Rabienataj Darzi, A.A.; Tan, F.L.; Khodadadi, J.M. Unconstrained Melting inside a Sphere. *Int. J. Therm. Sci.* **2013**, *63*, 55–64. [CrossRef]
21. Ansys. *"Ansys Fluent 12.0 User's Guide." Fluent Documentation*; Ansys: Canonsburg, PA, USA, 2009.

22. Abdulateef, A.M.; Abdulateef, J.; Mat, S.; Sopian, K.; Elhub, B.; Mussa, M.A. Experimental and Numerical Study of Solidifying Phase-Change Material in a Triplex-Tube Heat Exchanger with Longitudinal/Triangular Fins. *Int. Commun. Heat Mass Transf.* **2018**, *90*, 73–84. [CrossRef]

23. Nithyanandam, K.; Pitchumani, R. Computational Modeling of Dynamic Response of a Latent Thermal Energy Storage System with Embedded Heat Pipes. *J. Sol. Energy Eng. Trans. ASME* **2014**, *136*, 011010. [CrossRef]

24. Yang, X.H.; Tan, S.C.; Liu, J. Numerical Investigation of the Phase Change Process of Low Melting Point Metal. *Int. J. Heat Mass Transf.* **2016**, *100*, 899–907. [CrossRef]

25. Kousksou, T.; Mahdaoui, M.; Ahmed, A.; Msaad, A.A. Melting over a Wavy Surface in a Rectangular Cavity Heated from Below. *Energy* **2014**, *64*, 212–219. [CrossRef]

26. Tabassum, T.; Hasan, M.; Begum, L. 2-D Numerical Investigation of Melting of an Impure PCM in the Arbitrary-Shaped Annuli. *Int. J. Therm. Sci.* **2017**, *114*, 296–319. [CrossRef]

27. Libeer, W.; Ramos, F.; Newton, C.; Alipanahrostami, M.; Depcik, C.; Li, X. Two-Phase Heat and Mass Transfer of Phase Change Materials in Thermal Management Systems. *Int. J. Heat Mass Transf.* **2016**, *100*, 215–223. [CrossRef]

28. Khot, S.A.; Sane, N.K.; Gawali, B.S. Experimental Investigation of Phase Change Phenomena of Paraffin Wax inside a Capsule. *Int. J. Eng. Trends Technol.* **2011**, *2*, 67–71.

29. Villarino, M.B. Ramanujan's Perimeter of an Ellipse. *arXiv* **2005**, arXiv:0506384.

30. Emam, M.; Ahmed, M. Cooling Concentrator Photovoltaic Systems Using Various Configurations of Phase-Change Material Heat Sinks. *Energy Convers. Manag.* **2018**, *158*, 298–314. [CrossRef]

31. Kamkari, B.; Amlashi, H.J. Numerical Simulation and Experimental Verification of Constrained Melting of Phase Change Material in Inclined Rectangular Enclosures. *Int. Commun. Heat Mass Transf.* **2017**, *88*, 211–219. [CrossRef]

Article

Simulation Assessment of Inlet Parameters and Membrane-Surface-Structure Effects on CO₂ Absorption Flux in Membrane Contactors

Amin Mojarad Garehbagh [1], Saeid Rajabzadeh [2,3,*], Mahmoud A. Shouman [4], Mohamed R. Elmarghany [4], Mohamed S. Salem [4], Nasrul Arahman [5], Toraj Mohammadi [1] and Hideto Matsuyama [3]

1 Centre of Excellence for Membrane Science and Technology, Department of Chemical, Petroleum and Gas Engineering, Iran University of Science and Technology (IUST), Narmak, Tehran 16846-13114, Iran
2 School of Civil and Environmental Engineering, University of Technology Sydney (UTS), City Campus, Broadway, NSW 2007, Australia
3 Research Center for Membrane and Film Technology, Department of Chemical Science and Engineering, Kobe University, Rokkodaicho 1-1, Nada, Kobe 657-8501, Japan
4 Mechanical Power Engineering Department, Faculty of Engineering, Mansoura University, Mansoura 35516, Egypt
5 Department of Chemical Engineering, Universitas Syiah Kuala, Banda Aceh 23111, Indonesia
* Correspondence: rajabzadehk@people.kobe-u.ac.jp

Abstract: The management of global carbon dioxide (CO₂) emissions is considered one of the main environmental problems facing the modern world. One of the potential techniques for CO₂ capture is absorption, using membrane contactor modules. Most of the previous research that dealt with membrane contactor simulations considered the whole membrane surface as the active reaction surface. However, in this paper, a more realistic model of the membrane-contactor module is presented, taking into account the effects of the pore size and surface porosity. CO₂ absorption into the monoethanolamine (MEA) solution in hollow fiber membrane-contactor modules was numerically investigated. A computational fluid dynamics simulation was established using essential basic fluid dynamics and mass transfer equations in reactive mode. An algorithmic function was used to present the relations between the CO₂ absorption flux and the hollow fiber length, membrane surface pore size, and porosity. The simulation results were compared to previously obtained experimental results without using any fitting parameters, and a good agreement was found with an average error of 8.5%. The validated simulation was then used to predict the effects of the MEA inlet velocity and concentration, the membrane surface pore size, and porosity on the total CO₂ absorption flux. A maximum absorption flux of about 1.8 mol/m²·s was achieved at an MEA concentration of 4 M with a pore size of 0.2 microns, a surface porosity of 1%, and an inlet velocity of 0.25 m/s. The extrapolation technique was then used to predict the values of the absorption flux at longer fiber lengths. The concentration profiles around the pores at the gas–liquid contact surface of the membrane were obtained and presented. The proposed model exhibited excellent potential to evaluate the effective reaction surface in hollow fiber membrane contactors. This model could be considered the first step to obtaining accurate predictions of the membrane contactor gas absorption performance based on its surface structure.

Keywords: CO₂ absorption; MEA; membrane contactor; CFD; porosity; pore size

1. Introduction

In recent decades, the development of industrial activities has increased greenhouse gas concentration in the atmosphere, including carbon dioxide (CO₂). Increased CO₂ emissions are significant contributors to catastrophic environmental changes. Carbon dioxide gas contributes to around 55% of the observed global warming [1]. This vital issue sparked interest in CO₂ capture [2]. Hollow fiber membrane contactor (HFMC)

technology is a potential candidate for greenhouse gases (especially CO_2) abatement. It has considerable advantages over conventional CO_2 recovery techniques [1,3,4]. In HFMC modules, the membrane lumen, bulk, and module shell enable direct contact between gas and liquid phases without the dispersion of one phase into the other. While acid gases flow on one side of the membrane, filling the membrane bulk structure to reach the other side, absorbent liquid flows on the other surface of the membrane. Tiny liquid–gas interfaces are formed in the openings of the pores adjacent to the absorbent liquid. It is a crucial point in the gas–liquid contacting process to avoid entering absorbent liquid into the membrane pores. This phenomenon is known as wetting in HFMC, and it sharply and strongly decreases the module performance [5].

Yan et al. [6] compared the performance of several chemical and physical absorbents and concluded that chemical absorbents have better performance because of their higher absorption rate due to their fast reaction with CO_2. Several kinds of chemicals were used to absorb CO_2 in the liquid phase, including organic and inorganic bases [7–12]. Among the reported chemical absorbents, different types were used. The amine solutions exhibited fast reaction rates, resulting in a higher CO_2 absorption flux, minor damage to the membrane structure, and less toxicity and safety issues [7,11]. Monoethanolamine (MEA) solution was widely used in HFMC processes with considerable reported advantages. According to previous investigations, MEA exhibited higher CO_2 removal performance, compared to other absorbents, such as sodium hydroxide (NaOH), triethanolamine (TEA), diethanolamine (DEA), and 2-amino-2-methyl-1-propanol (AMP) [8,10].

CO_2 capture techniques were previously investigated, taking into account various parameters, such as solvent absorption, pressure, and temperature-swing adsorption in the presence of a variety of solid sorbents, membranes, and cryogenic distillation [13]. Using MEA as a liquid absorbent showed high potential as a technique for carbon capture. On the other hand, with the development in the production of ceramic and metallic membranes, effective membranes could be fabricated with significantly effective separation, compared to the liquid absorption technique. A study was held to investigate the feasibility of using membrane-based carbon capture technology compared to the amine-based absorption technique [14]. The study compared the use of three plants: two of them use amine liquid absorption, and the third is a membrane-based plant. The latter showed high potential compared to the other two. A CO_2 avoided cost, which is an economic indicator to estimate the additional cost of processing the carbon capture facility, of 46 USD/tons was established using a membrane-based plant compared to 58 and 71 USD/tons exhibited by the other two plants. The merits of membrane-based plants may include compactness, as membranes may provide 1000 times more interfacial area per unit volume compared to absorption–adsorption processes [2]. Other advantages are modularity, ease of installation, flexibility, lower cost with lesser energy consumption, and fewer chemical requirements [15,16].

Kreulen et al. [17,18] established that a very thin layer covers the membrane contactor surface, and a gas–liquid reaction occurs at this thin film layer at the mouth of the pores. The thin film gas-absorbed layer theory is dominated by physical absorption, even for very low porosity membranes. Even in the cases of membranes with very low surface porosity (<3%) and pore size of 5 nm, when water was used as the absorbent liquid (physical absorption), the membrane surface pore size and porosity had little to no effect on the gas absorption flux. Therefore, this assumption was used in most gas–liquid membrane contacting simulations. Although the membrane surface pore size and porosity effects were very well evaluated for physical gas absorption by Kreulen et al. [18], no such evaluation was performed for chemical absorption processes. While the effects of membrane surface pore size and porosity on the performance of the membranes used in liquid filtration are very well studied in many studies [19,20], this effect is still not clear for gas absorption processes, and more evaluation is still needed. In our previous studies [21,22], we considered that all membrane surfaces were active for the reaction based on the aforementioned studies [17,18]. According to our previous studies, at high MEA concentrations (higher than 2 mol/L and especially for 4 mol/L) and low porosity membranes, the assumption of a thin film of a

saturated MEA layer at the reaction interface was found to be lacking. Simulation results considerably deviated from the experimental results. Comite et al. [23] observed a very similar trend when they used a membrane with a high porosity of 60%. Although they considered the effect of amine reaction products on the CO_2 absorption flux, the effects of the membrane surface porosity and pore size were also neglected.

In this study, we systematically considered the membrane surface porosity and pore size effects on the CO_2 gas absorption flux. In previously reported papers, all the membrane surfaces were considered active areas for reaction. In the current study, we tried to fulfill the gas–liquid membrane contacting simulation without considering the assumption of covering thin film over the pores. Our simulation results, without using any fitting parameters, show that at high MEA concentration, membrane surface pore size and porosity play key roles in determining the absorption flux. Simulation results were compared with experimental results obtained in our previous study [21,22]. The agreement between the simulation and experimental results was satisfactory.

2. Computational Fluid Dynamics (CFD) Simulation in Reactive Mode

In this study, a 3D model was established using the commercial software package COMSOL Multiphysics 5.4 to assess the effects of the membrane surface pore size and porosity on the CO_2 absorption into MEA solution. Since many experimental and simulation studies [23–25] were performed on CO_2 absorption into the MEA solution, this system was selected for more reliable access to the established physical properties and previous experimental results published, including the authors' [22]. This led to more dependable simulation results with less deviation from the experimental data. Generally, an HFMC configuration usually comprises several hollow fibers, each performing independently. Therefore, investigating a single fiber performance can be sufficient to predict the performance of the whole HFMC module [23,24,26,27]. The proposed model is based on the assumption of non-wetted mode, where the CO_2 gas completely fills the membrane pores. In this model, the CO_2 was fed into the shell side of the HFMC, while the MEA solution went through the lumen. Due to the non-wetted assumption, the contact between the two fluids only occurred over the membrane pores surface within the lumen side, as shown in Figures 1 and 2. In the simulation, the CO_2 was transported from the shell to the lumen side through tiny cylinders representing the membrane pores. The effects of the membrane surface pore size and porosity on the CO_2 absorption flux at the interface of the MEA and CO_2 were numerically evaluated.
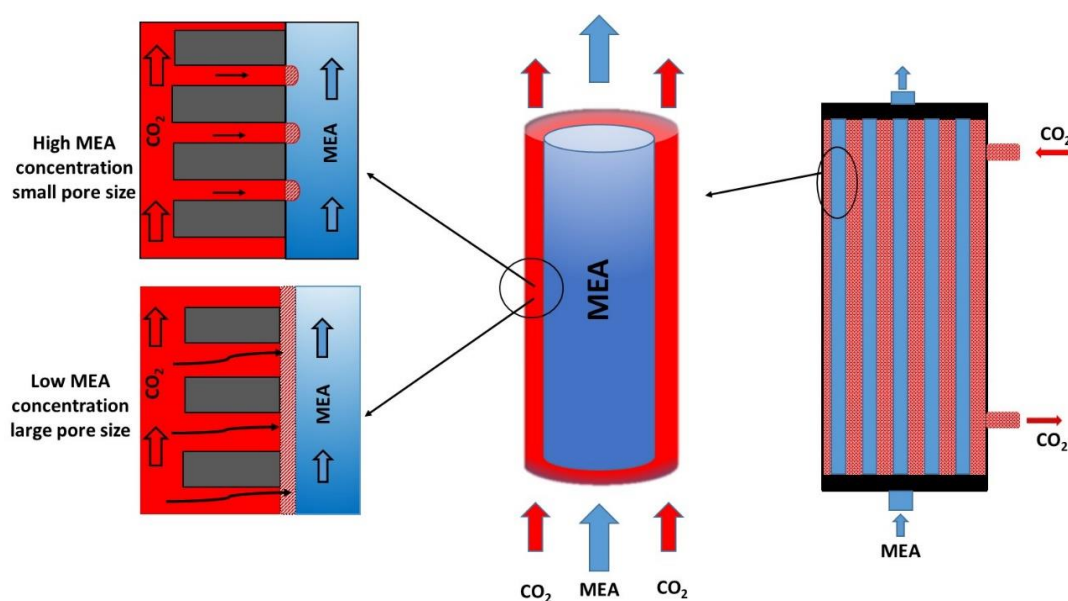
Figure 1. A schematic diagram of a membrane contactor module.
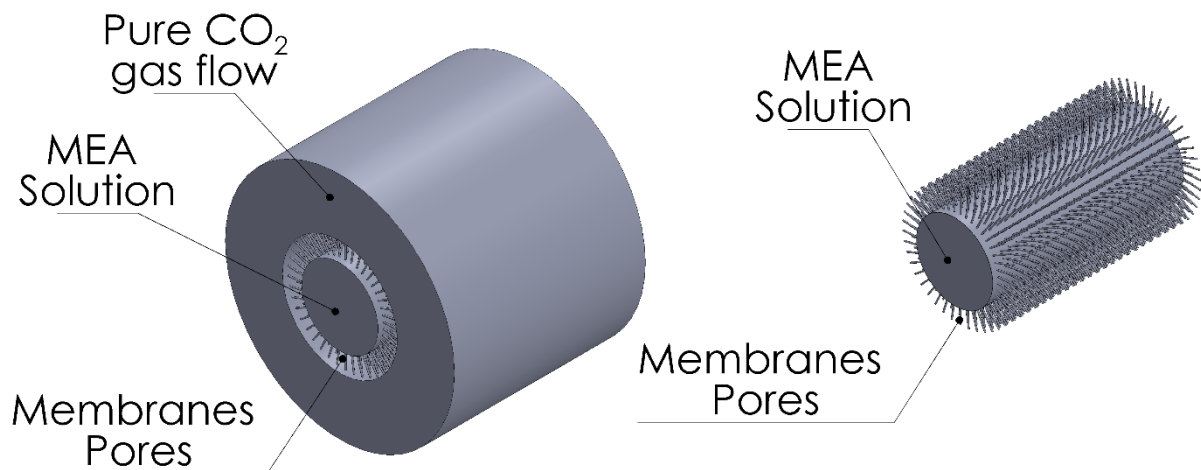
Figure 2. A schematic diagram of the feed flow in a hollow fiber membrane; The cylinders represent the membrane pores in the model extended in the membrane thickness.

2.1. Simulation Assumptions

The main simulation assumptions are summarized as follows:

- Feed gas on the shell side is pure CO_2 to simplify the mass transfer resistance on the gas side. Otherwise, gas phase resistance becomes important, and the whole membrane with tortuosity and pore size should be considered, which is practically impossible to run, even with a supercomputer.
- Laminar and a steady-state hydrodynamically fully developed MEA solution is considered for feed flow. Although this assumption might not be ideal for the entrance length, it is the most suitable assumption. Otherwise, it would take too much processing time and power without much change in results.
- Isothermal feed flow all over the module.
- A very smooth wall (no-slip condition at the wall).
- Gravity effects are neglected in this simulation as evident in previous studies [28–30].
- Henry's law was applied to calculate the CO_2 concentration at the interface of the gas–liquid contact at the mouth of the pores (i.e., thermodynamic equilibrium state).
- The non-wetted mode was assumed, indicating that the pores are filled with CO_2 with no absorbent entry into the pores.
- The reaction between CO_2 and the MEA is very fast (instantaneous), as the reaction parameters satisfied the instantaneous reaction regime conditions, as can be seen in [22].
- Axis symmetry condition is assumed at the hollow fiber axis.

2.2. Governing Equations

Based on the previous assumptions, the steady-state material balance equations can be expressed as follows [18]:

$$D_{CO_2}\left(\frac{\partial^2 C_{CO_2}}{\partial r^2} + \frac{1}{r}\frac{\partial C_{CO_2}}{\partial r}\right) - u_z\frac{\partial C_{CO_2}}{\partial z} - k\,C_{CO_2}C_{MEA} = 0 \tag{1}$$

$$D_{MEA}\left(\frac{\partial^2 C_{MEA}}{\partial r^2} + \frac{1}{r}\frac{\partial C_{MEA}}{\partial r}\right) - u_z\frac{\partial C_{MEA}}{\partial z} - 2\,k\,C_{CO_2}C_{MEA} = 0 \tag{2}$$

where D presents the species diffusivity (m^2/s), C is the species concentration (mole/m^3), and k is the reaction rate coefficient [m^3/mol·s]. The CO_2 concentration (mol/m^3) inside the absorbent at the pores surfaces mouths is calculated by Equation (3):

$$C_{CO_2} = P_{CO_2} \cdot H_{CO_2} \tag{3}$$

where P represents the CO_2 pressure (atm), and H is Henry's constant (mol/m^3·atm).

The velocity distribution for the MEA, $u(r)$, can be estimated as a flow in a circular pipe using Equation (4) [31].

$$u(r) = u_{max}\left(1 - \left(\frac{r}{R}\right)^2\right) \tag{4}$$

where r is the radius (m), R is the fiber inner radius (m), and u_{max} (m/s) is the maximum liquid velocity in the membrane lumen, which can be obtained by dividing the liquid flow rate by the area of the lumen of the HFMC.

The reaction between the gas and the MEA, which is assumed to occur at the lumen side and be instantaneous, can be expressed using Equation (5). The reaction rate constant of the reaction reported by Hikita et al. [32] was used in the simulation (5.92 m^3/mol. s at 25 °C):

$$CO_2 + 2RNH_2 \leftrightarrow RNHCOO^- + RNH^+_3 \tag{5}$$
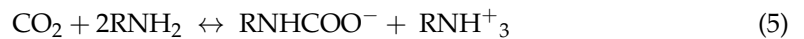
$$rate = \frac{-dC_{CO_2}}{dt} = -\left(\frac{1}{2}\right)\left(\frac{-dC_{MEA}}{dt}\right) = k\, C_{CO_2} C_{MEA} \tag{6}$$

Table 1 summarizes the different physical properties that are used in this simulation, considering the effect of amine products on the physical properties of the MEA solution [22].

Table 1. Physical properties at different MEA concentrations.

MEA Concentration (M)	1	2	3	4
D_{CO_2} (m^2/s)	1.66×10^{-9}	1.397×10^{-9}	1.17×10^{-9}	9.49×10^{-10}
D_{MEA} (m^2/s)	9.45×10^{-10}	7.96×10^{-10}	6.68×10^{-10}	5.41×10^{-10}
H_{CO_2} (mol/m^3·kPa)	0.217	0.135	0.1385	0.142
k (m^3/mol·s)		5.92		

The CO_2 absorption flux (J) (mol/m^2. s) can be estimated using Equation (7) [25], assuming instantaneous reaction, thus no CO_2 in the MEA outflow.

$$J_{CO_2} = \frac{1}{2\pi RL}\left(\frac{1}{2}\left[\int_0^R 2\pi r u(r)(C_{MEA-inlet} - (C_{MEA-interface}(r))_{z=L})dr \right.\right.$$
$$\left.\left. +2\int_0^R 2\pi r u(r)(C_{co_2-interface}(r))_{z=L}dr\right]\right) \tag{7}$$

For the simulation, the following boundary conditions were used:

- Zero CO_2 concentration is assumed at the hollow fiber inlet with the MEA concentration equal to the feed concentration.
- CO_2 concentration is calculated using Equation (3) with no MEA flux at the pore mouths.
- Outflow condition is also considered at the fiber outlet.
- The rest of the membrane surfaces are considered walls with no-slip conditions.

2.3. Simulation Time Reduction

Firstly, to reduce the simulation time while maintaining an acceptable level of accuracy, several cuts of hollow fiber were created with different angles, as shown in Figure 3. The chosen angles were 90°, 45°, 27°, 9°, and 2.5°. Additionally, several fiber lengths ranging from 100 microns up to 7200 microns were investigated. As described in Table 2, HFMC absorption flux with a very short length was calculated to evaluate the effect of cutting angle. Later on, calculations for longer lengths of the HFMC were performed, and the results were extrapolated for the full length of the fiber. The extrapolated results were then compared to the experimental results as will be shown in the following section of the manuscript. The main used input parameters are summarized in Table 3. The absorption flux was estimated for each case and is shown in Table 3.
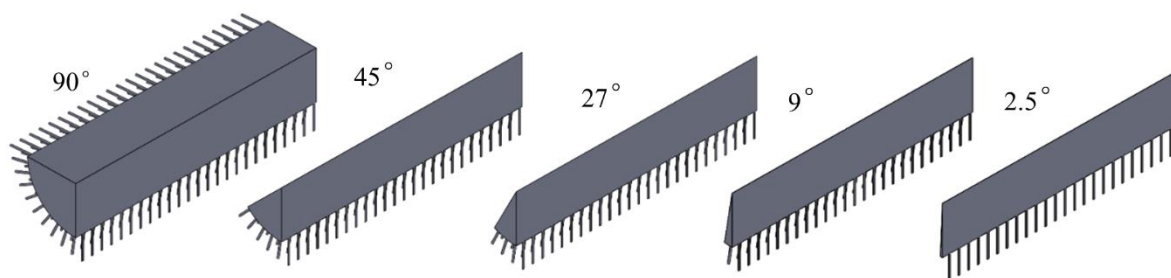
Figure 3. Different angle cuts of the hollow fibers.

Table 2. Absorption flux simulation values at different angle cuts and lengths.

Cutting Angle (°)	90	45	27	9	2.5
Fiber Length (μm)	Absorption Flux (mol/m^2·s)				
100	0.932	0.931	0.931	0.930	0.930
300	0.392	0.392	0.390	0.390	0.389
600	-	0.260	0.259	0.258	0.258
900	-	-	0.24	0.24	0.24
1800	-	-	-	0.199	0.198
3600	-	-	-	0.174	0.174
7200	-	-	-	-	0.161

Table 3. Main input parameters for the mesh dependency test.

MEA Concentration (mol/L)	Absorbent Velocity (m/s)	Pore Size (μm)	Surface Porosity
2	0.25	0.1	1%

As shown in Table 3, the hollow fiber cutting angle seems to have a negligible effect on the CO_2 absorption flux simulated values at different lengths, with a maximum error of about 0.8%. Therefore, a 2.5° angle was used to expedite the simulation process. The results were extended over the whole fiber to decrease the simulation time. As it is clear from Table 3, the CO_2 absorption flux is extraordinarily high at the entrance of the membrane, and it sharply decreases by increasing the membrane length. This is because, at the entrance, no layer was yet formed across the membrane surface to decrease the diffusion rate, hence decreasing the flux.

2.4. Mesh Dependency Test

A mesh dependency test was performed to determine the proper mesh size for the required simulation. Four fibers with a length of 1 mm and 2.5° cut and different mesh sizes from 430,327 elements to 2,958,891 elements were investigated. The absorption flux and MEA concentration profile at the fiber outlet were estimated for each case. The mesh dependency test results are shown in Figure 4. Considering the absorption flux (Figure 4a), the error between the mesh with 1,427,212 elements and the finer mesh with 2,958,891 elements is about 4.5%. Therefore, this mesh size (1,427,212 elements) was chosen for completing the results, thus allowing for faster calculations while maintaining reasonable accuracy. The difference in the MEA profile for different mesh sizes was completely negligible for all mesh sizes as shown in Figure 4b. Although not shown here, the MEA concentration profile in this study is very similar to our previous MEA concentration profile [22].
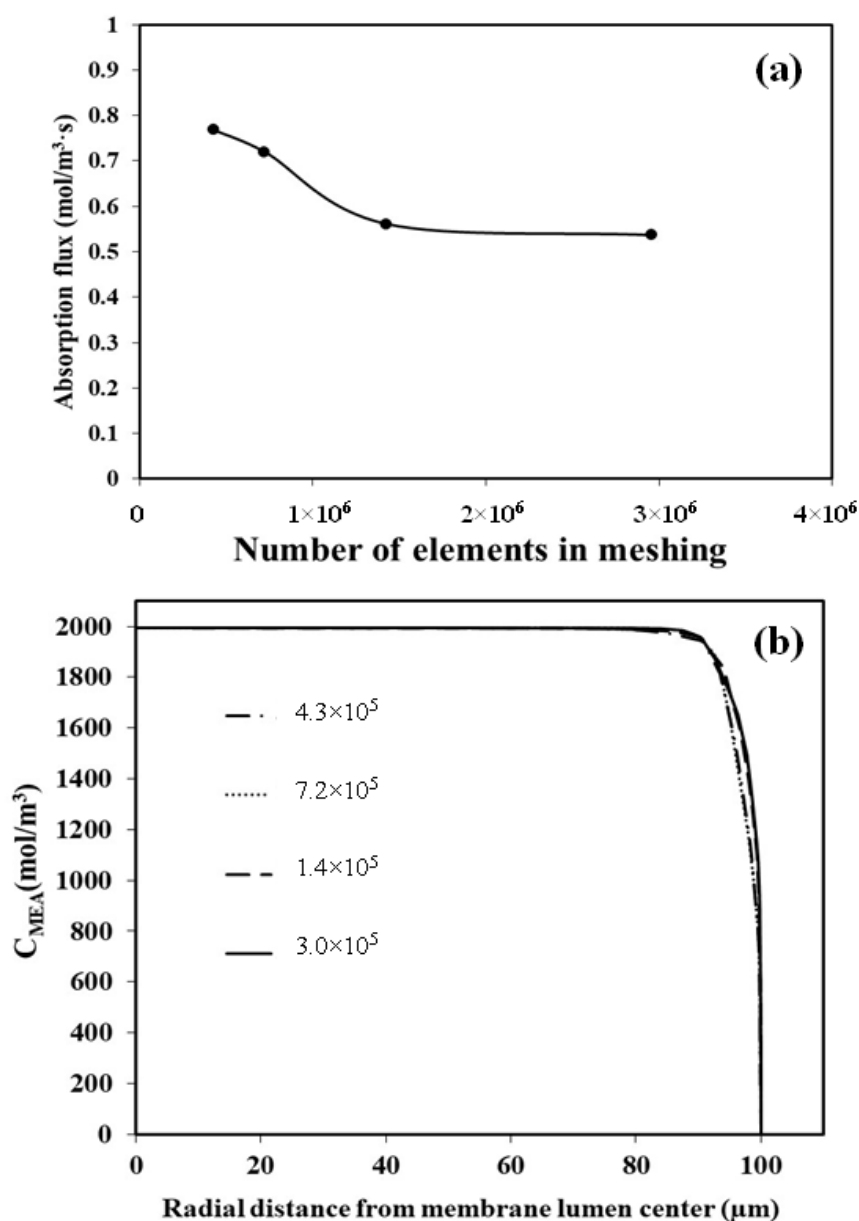
Figure 4. Effect of mesh size on (**a**) absorption flux and (**b**) MEA concentration profile.

3. Results and Discussion

3.1. Simulation Validation

Instead of actually simulating the absorption flux in the full length of the hollow fiber, which would have needed too many calculations, memory, computing power, and time, another approach was chosen to estimate the CO_2 absorption flux. The absorption flux of several hollow fibers with different short lengths was calculated. Then, the calculated CO_2 absorption flux was used to calculate the coefficients of a mathematical function that could be used to present the relation between the actual hollow fiber length in the experimental condition and the calculated absorption flux. This function was then used to extrapolate the absorption flux of the actual length, and the estimated results were then compared to experimental results in our previous studies. The simulation results of the absorption flux at different fiber lengths for different MEA concentrations are shown in Figure 5. By increasing the fiber length, the CO_2 absorption flux was noticed to sharply decrease at first, and then its change became almost flat. We think the initial extraordinarily high CO_2 absorption flux is due to the non-fully developed MEA concentration boundary layer at

the membrane entrance. By increasing the length, the flow regime became fully developed, and the concentration boundary layer formed, thus decreasing the CO_2 contact with a fresh, non-saturated MEA solution. Subsequently, the CO_2 absorption flux sharply decreased. Based on the results in Figure 5, for more than 1000 μm of the hollow fiber length, the trend of the CO_2 absorption flux becomes almost linear in the logarithmic figure. The trendline for the relationship between the fiber length and the absorption fluxes was noticed to be similar to an algorithmic relation ($y = A + B * \ln(x)$). Thus, the curve-fitting technique was used to estimate the function coefficients A and B values at different MEA concentrations. These values were calculated and are tabulated in Table 4.
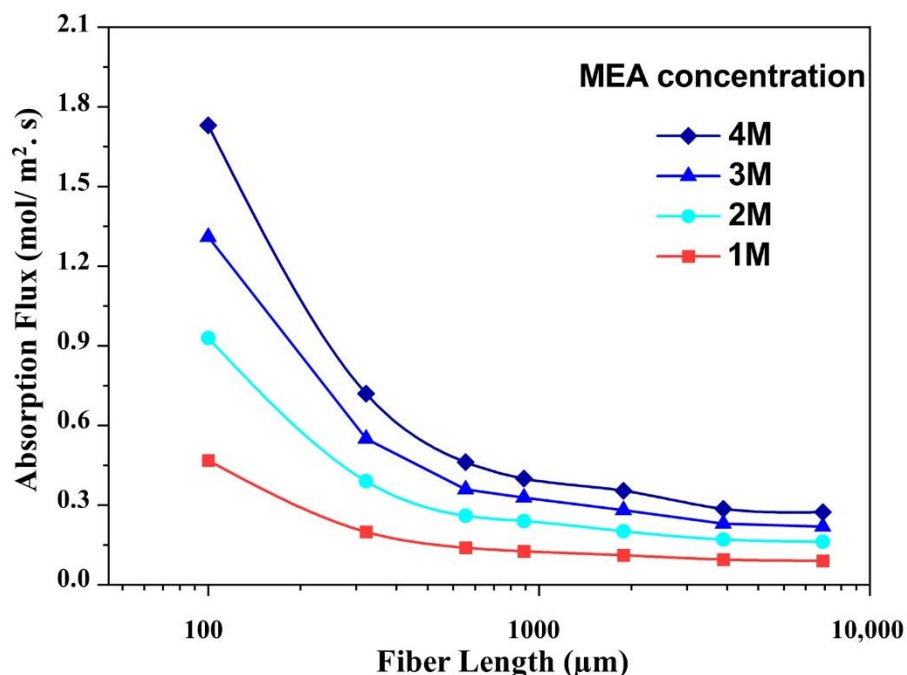
Figure 5. The estimated absorption flux at different fiber lengths for four different MEA concentrations; The main parameters for this calculation are membrane surface porosity of 1%, a pore diameter of 0.2 μm, and an MEA average velocity of 0.25 m/s.

Table 4. Algorithmic function coefficients for different MEA concentrations.

MEA Concentration (mol/L)	1	2	3	4
A	0.2634	0.5194	0.7055	0.8807
B	−0.04652	−0.09283	−0.1269	−0.1592

Kumar et al. [26] found that when a physical absorption was applied for HFMC, by increasing the absorbent inlet velocity from 0.1 to 0.5 m/s, the effect of the membrane length on the local CO_2 absorption flux decreased sharply. At an inlet velocity of 0.5 m/s, no considerable change was noticed in the local CO_2 absorption flux over the length of the HFMC. It was reported by Shirazian et al. [12] that when a fast reaction occurs between CO_2 and the chemical absorbent, the CO_2 removal efficiency does not change with the membrane length very much. By decreasing the reaction rate, the membrane length effect becomes considerable. Since MEA was used for CO_2 absorption in our study, and the reaction rate for CO_2 in MEA is instantaneous, extrapolating the CO_2 absorption flux over the hollow fiber membrane length looks reasonable. Although not shown here, as it is still under current investigation, the calculation time and memory were considerably decreased when a different software was used to make the HFMC simulation, and the results were then exported to Comsol. Then, we were able to extend our calculation to nearly 15 cm length of the fiber (15 times longer than the current calculation). The new simulation and

calculation results showed similar results to the current calculation and extrapolation that was performed here with less than 8% error.

Using the estimated relation, the absorption flux was estimated under the same conditions as the previous experimental results, and the simulation results were compared to the actual experimental results of Rajabzadeh et al. [22]. The comparison results are shown in Figure 6. The simulation results show an acceptable agreement with the experimental results in all ranges of the studied MEA concentration, with a maximum error of less than 20%, which validates the proposed simulation. This agreement becomes clearer at high MEA concentration (4 mol/L). Comparing our current calculation with that of the calculation we performed in our previous work with all surfaces as active layers available for reaction shows that the current calculation considering the pore size and porosity shows much better agreement with experimental results. Thus, it can be concluded that the simulation and the curve fitting techniques used could estimate the CO_2 absorption flux of the membrane contactor with an acceptable degree of accuracy. It is worth mentioning that the effect of the amine reaction products is already included in our previous simulation. Therefore, we firmly believe that changing the CO_2 absorption flux, especially at a high MEA concentration (4 mol/L), is related to the effect of membrane surface porosity.
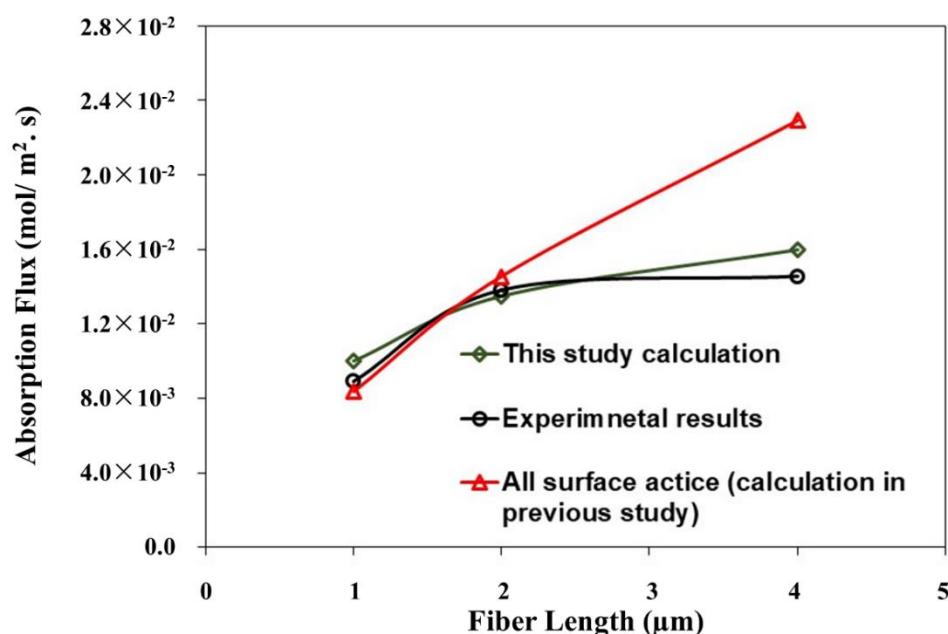
Figure 6. Comparing the simulation results in the current study with that of the experimental results and simulation without considering the effect of the membrane surface porosity [22]; fiber length of 27 cm, a pore diameter of 0.2 μm, and an MEA average velocity of 0.25 m/s.

Figure 7 shows the CO_2 concentration distribution contours over the membrane pores at two different MEA concentrations of 1 and 4 mol/L. It is noteworthy that by increasing the absorbent concentration, the CO_2 concentration around the pores decreases. It approaches the saturation concentration just at the mouth of the pores, and the chance for CO_2 to diffuse around the pores sharply decreases. This is because the reaction rate of the MEA with CO_2 considerably increases. On the other hand, at low MEA concentrations, the CO_2 finds the chance to diffuse around the pores. Therefore, there is a chance to make a saturated CO_2-absorbed layer over the pores which covers the membrane surface, thus making the membrane structure effect negligible.
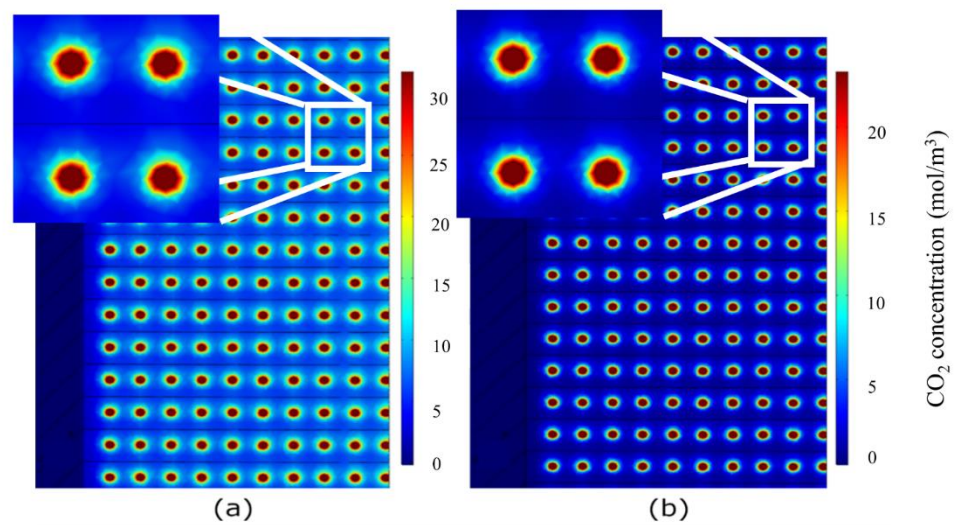
Figure 7. CO_2 concentration distribution over the membrane surface (absorbent concentration: (**a**) 1 mol/L and (**b**) 4 mol/L with pores diameter of 0.2 μm. circles in the figure show a hollow fiber pore mouth.

3.2. Effect of Average Absorbent Velocity

In order to further verify our developed simulation, we tried to compare our simulation results with that of the experimental results [22] when the average absorbent velocity is changed. The results are shown in Figure 8. As can be clearly seen, the simulation results are in good agreement with the experimental results. Hence, this confirms the ability of the simulation and extrapolating techniques to estimate the CO_2 absorption flux of the membrane contactor with an acceptable degree of accuracy.
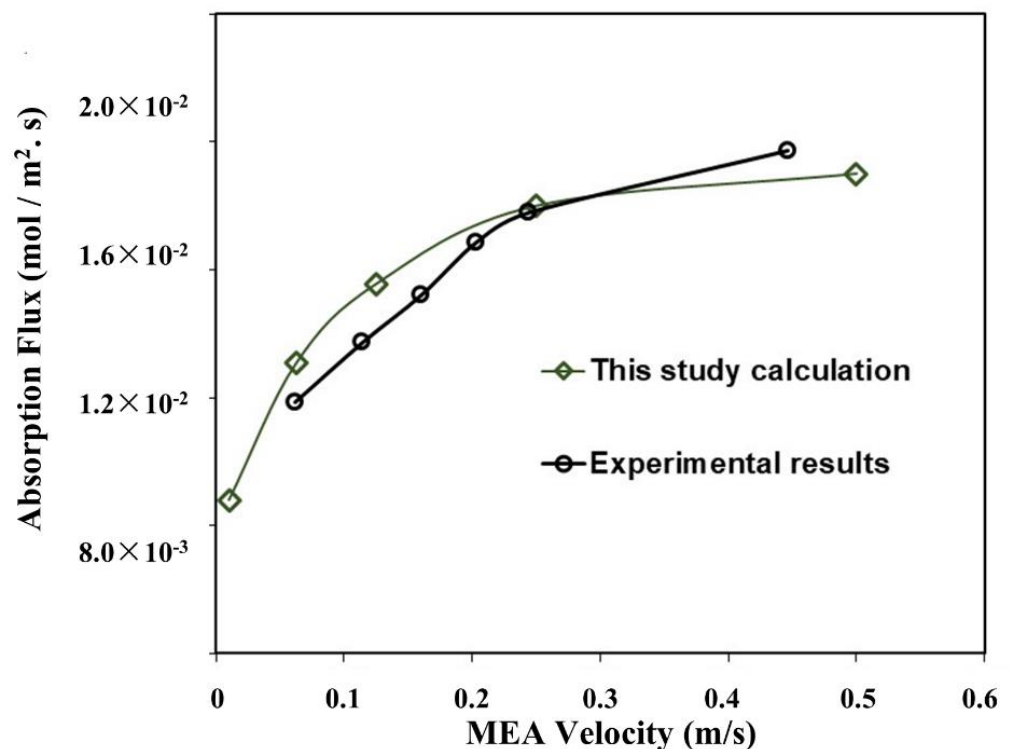
Figure 8. Simulation results versus experimental results at different absorbent average velocities; Main parameters for simulations: Fiber length of 27 cm, a membrane surface porosity of 1%, a pore diameter of 0.2 μm, and an absorbent concentration of 2 mol/L.

Figure 9 presents the CO_2 concentration distribution contours over the membrane pores at two different inlet absorbent velocities. As can be seen, by increasing the absorbent flow rate, the CO_2 concentration around the pores decreases. The CO_2 concentration approaches the saturation concentration just at the mouth of the pores, and the chance for CO_2 to diffuse around the pores decreases sharply. By increasing the absorbent velocity, the thickness of the concentration boundary layer of MEA at the membrane surface decreases, and the CO_2 reaction rate increases since the chance of contacting CO_2 with fresh MEA increases. Contrary to the high absorbent average velocity, CO_2 finds the chance to diffuse slightly more around the pores at a low absorbent velocity. This condition increases the chance of making a saturated CO_2-absorbed layer on the pores covering the membrane surface, decreasing the effect of the membrane structure. However, this effect is not as clear as changing the absorbent concentration.
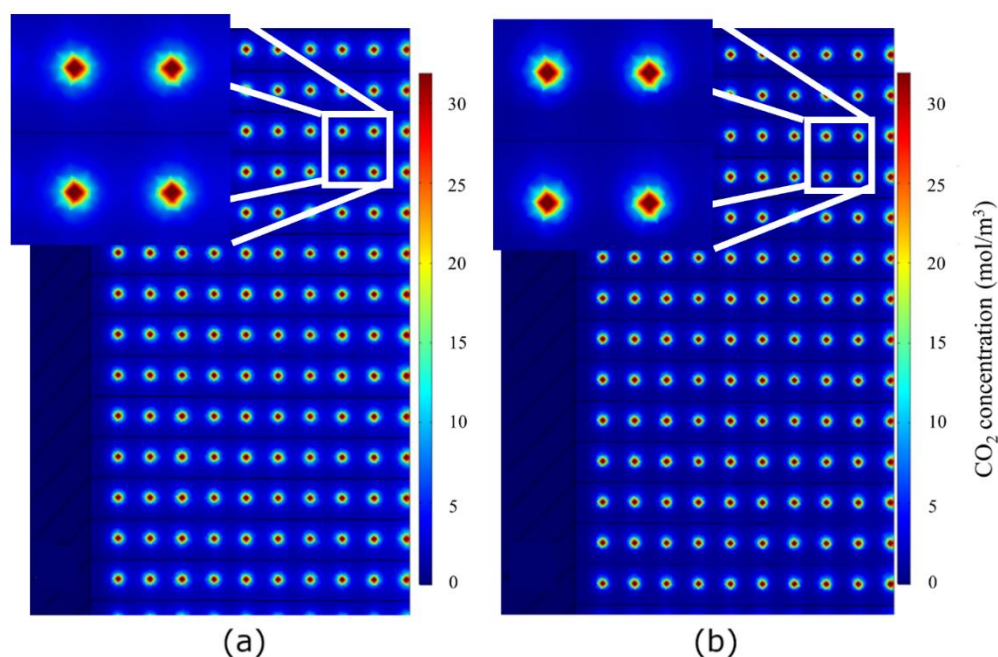
Figure 9. CO_2 concentration distribution over the membrane surface; absorbent average velocity: (**a**) 0.062 m/s and (**b**) 0.5 m/s, pore diameter of 0.1 μm, and an absorbent concentration of 2 mol/L.

3.3. The Effect of Changing the Porosity and Pore Size

The model was then used to study the effect of the membrane porosity and pore size on the CO_2 absorption flux at four different MEA solution concentrations. The pore size increased from 0.05 μm to 0.2 μm while keeping the number of pores the same, thus, increasing the surface porosity with the increase in pore size. The simulation results are shown in Figure 10. Increasing the surface porosity by increasing the membrane surface pore size was found to significantly enhance the CO_2 absorption flux, as shown in Figure 10. Increasing CO_2 absorption flux by increasing the surface porosity is entirely plausible since it provides a higher chance of contact between CO_2 and MEA and results in higher CO_2 absorption flux. When the chemical reaction is used for HFMC gas absorption at low surface porosity at the interface, it is the absorption-controlling step.
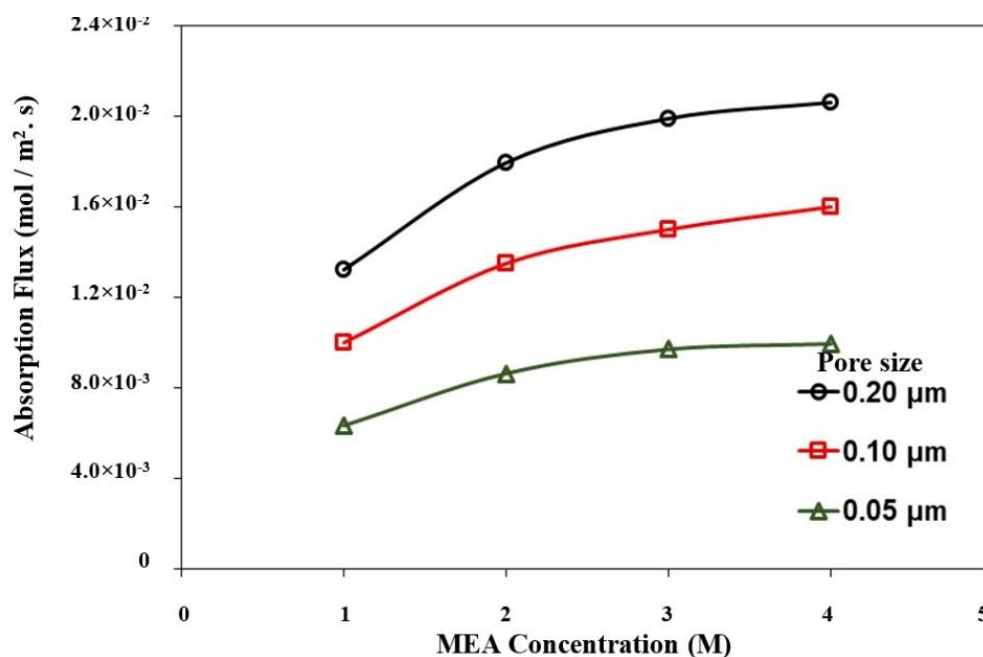
Figure 10. The effect of the membrane surface porosity on the CO_2 absorption flux. The number of pores was kept constant, and the pore size varied from 0.05 μm to 0.2 μm.

The effect of the membrane pore size on the CO_2 absorption flux at a fixed surface porosity of 1% was evaluated by changing the pore size diameter with changing the number of pores to keep the porosity fixed at 1%. Figure 11 shows the effect of the membrane surface pore size on the CO_2 absorption flux at fixed surface porosity for two different pore sizes of 0.1 μm and 0.2 μm. Additionally, Figure 12 presents the flux contours around the pores for two different pore sizes, namely 0.1 and 0.2 microns. It should be mentioned here that the number of pores in the simulation increases exponentially by decreasing the pore diameter. In this study, when the pore size is decreased to 0.05 μm, the calculation time and needed memory are increased exponentially. Thus, we could not perform the calculation for 0.05 μm pore size, as it was far beyond our workstation capabilities. Surprisingly, we can see that membranes with a smaller pore size showed a higher gas absorption flux. This trend sounds interesting because it is strongly in line with our raised hypothesis that when the pore size is large, the possibility of forming the thin film layer of MEA with dissolved CO_2 near the pore mouth increases. When this layer forms, the CO_2 cannot contact fresh MEA, and the reaction rate and CO_2 absorption flux decrease. On the other hand, when the pore size is small, the chance for CO_2 to diffuse around the pore mouth and make a thin layer decreases as soon as CO_2 exits from the pore and contacts the fresh MEA. Therefore, the reaction rate and CO_2 absorption flux increase. This phenomenon is schematically shown in Figure 1. It can be concluded that using a membrane with a small pore size at a fixed surface porosity is much more beneficial for the CO_2 absorption flux. However, fabrication costs would probably increase. A future economic study is required to estimate the optimal pore size which can achieve high performance at a reasonable cost.
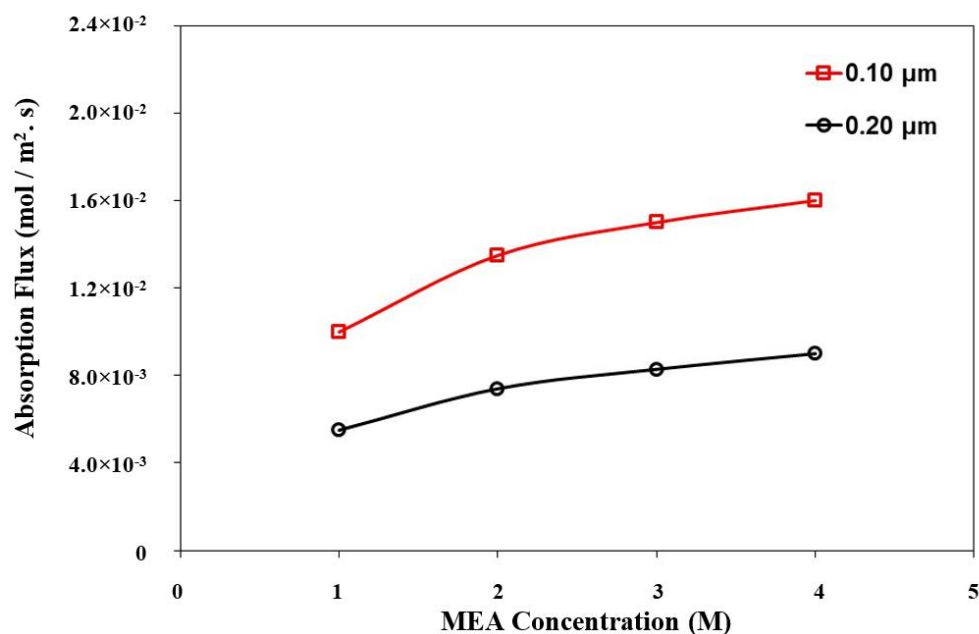
Figure 11. The effect of the membrane pore size on the CO_2 absorption flux. The surface porosity was fixed at 1%, and the pore size varied from 0.1 μm to 0.2 μm.
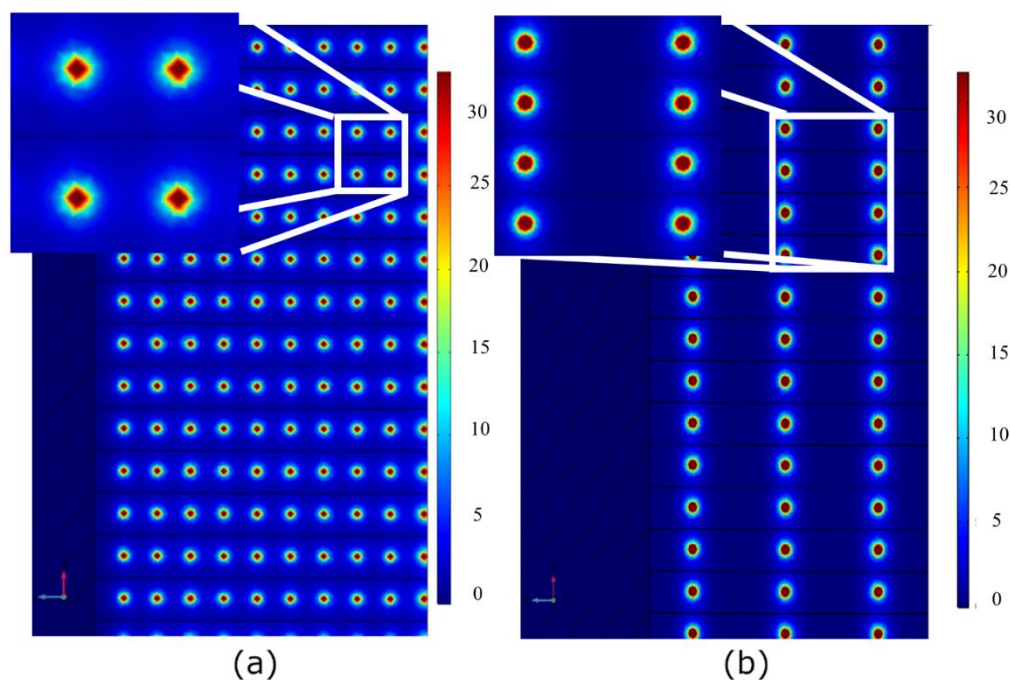
Figure 12. CO_2 concentration distribution over the membrane surface: pore diameter: (**a**) 0.1 μm and (**b**) 0.2 μm, an absorbent average velocity of 0.062 m/s, and an absorbent concentration of 2 mol/L.

4. Conclusions and Future Work

A numerical simulation was established to simulate the absorption of CO_2 into MEA within hollow fiber membrane contactor modules. The simulation was used to establish a relationship between the absorption flux and the fiber length, which was used to estimate the CO_2 absorption flux at long hollow fibers. The simulation results were validated using experimental data from our previously published paper. The simulation results were in good agreement with the experimental results with a maximum error of less than 20%. The

validated simulation was then used to investigate the effects of the absorbent inlet velocity and concentration and membrane surface pore size and porosity at the liquid–gas interface on the CO_2 absorption flux and the CO_2 concentration profiles. Using high absorbent velocity, MEA concentration, porosity, and small pore size at a fixed-surface porosity was beneficial for obtaining high CO_2 absorption flux. The CO_2 concentration contours showed that by using high absorbent velocity, MEA concentration, low porosity, and small pore size at a fixed surface porosity, the CO_2 concentration is limited just to the mouth of the pores of the membrane. In this situation, the possibility of CO_2 diffusion around the mouth of the pore decreases, and the CO_2 absorption flux increases. Although it needs more detailed investigations, the established simulation showed the potential to be efficiently utilized to study the absorption phenomenon within the membrane contactors.

Future investigations regarding the model may include a full parametric investigation to study the limits of the proposed model and the effects of changing the pore size and porosity of the membrane on the model results compared to the experimental results. Using the same model for other absorption pairs is also an important study. Applying the fitting over long hollow fiber lengths is also in the works. The effect of impurities in the CO_2 stream should also be investigated, as it may block the membrane pores which may decrease the absorption flux and affect the module performance. Additionally, the effects of long-term operation on the module performance are a very vital parameter for practical applications.

Author Contributions: Conceptualization, S.R. and T.M.; methodology, M.A.S. and M.S.S.; software, A.M.G.; validation, M.R.E. and N.A.; formal analysis, S.R.; writing—original draft preparation, A.M.G.; writing—review and editing, S.R. and M.S.S.; supervision, T.M. and H.M. All authors have read and agreed to the published version of the manuscript.

Institutional Review Board Statement: Not applicable.

Informed Consent Statement: Not applicable.

Data Availability Statement: The data supporting reported results are available upon request.

Conflicts of Interest: The authors declare no conflict of interest.

References

1. Gabelman, A.; Hwang, S.T. Hollow Fiber Membrane Contactors. *J. Membr. Sci.* **1999**, *159*, 61–106. [CrossRef]
2. Sreenivasulu, B.; Gayatri, D.V.; Sreedhar, I.; Raghavan, K.V. A Journey into the Process and Engineering Aspects of Carbon Capture Technologies. *Renew. Sustain. Energy Rev.* **2015**, *41*, 1324–1350. [CrossRef]
3. Li, J.L.; Chen, B.H. Review of CO_2 absorption Using Chemical Solvents in Hollow Fiber Membrane Contactors. *Sep. Purif. Technol.* **2005**, *41*, 109–122. [CrossRef]
4. Mansourizadeh, A.; Ismail, A.F. Hollow Fiber Gas-Liquid Membrane Contactors for Acid Gas Capture: A Review. *J. Hazard. Mater.* **2009**, *171*, 38–53. [CrossRef] [PubMed]
5. Mosadegh-Sedghi, S.; Rodrigue, D.; Brisson, J.; Iliuta, M.C. Wetting Phenomenon in Membrane Contactors—Causes and Prevention. *J. Membr. Sci.* **2014**, *452*, 332–353. [CrossRef]
6. Yan, Y.; Zhang, Z.; Zhang, L.; Chen, Y.; Tang, Q. Dynamic Modeling of Biogas Upgrading in Hollow Fiber Membrane Contactors. *Energy Fuels* **2014**, *28*, 5745–5755. [CrossRef]
7. Wang, R.; Li, D.F.; Liang, D.T. Modeling of CO_2 Capture by Three Typical Amine Solutions in Hollow Fiber Membrane Contactors. *Chem. Eng. Process. Process Intensif.* **2004**, *43*, 849–856. [CrossRef]
8. Nakhjiri, A.T.; Heydarinasab, A.; Bakhtiari, O.; Mohammadi, T. The Effect of Membrane Pores Wettability on CO_2 Removal from CO_2/CH_4 Gaseous Mixture Using NaOH, MEA and TEA Liquid Absorbents in Hollow Fiber Membrane Contactor. *Chin. J. Chem. Eng.* **2018**, *26*, 1845–1861. [CrossRef]
9. Rosli, A.; Shoparwe, N.F.; Ahmad, A.L.; Low, S.C.; Lim, J.K. Dynamic Modelling and Experimental Validation of CO_2 Removal Using Hydrophobic Membrane Contactor with Different Types of Absorbent. *Sep. Purif. Technol.* **2019**, *219*, 230–240. [CrossRef]

10. Rongwong, W.; Jiraratananon, R.; Atchariyawut, S. Experimental Study on Membrane Wetting in Gas-Liquid Membrane Contacting Process for CO_2 Absorption by Single and Mixed Absorbents. *Sep. Purif. Technol.* **2009**, *69*, 118–125. [CrossRef]

11. Shoukat, U.; Pinto, D.D.D.; Knuutila, H.K. Study of Various Aqueous and Non-Aqueous Amine Blends for Hydrogen Sulfide Removal from Natural Gas. *Processes* **2019**, *7*, 160. [CrossRef]

12. Shirazian, S.; Nakhjiri, A.T.; Heydarinasab, A.; Ghadiri, M. Theoretical Investigations on the Effect of Absorbent Type on Carbon Dioxide Capture in Hollow-Fiber Membrane Contactors. *PLoS ONE* **2020**, *15*, e0236367. [CrossRef] [PubMed]

13. Aaron, D.; Tsouris, C. Separation of CO_2 from Flue Gas: A Review. *Sep. Sci. Technol.* **2005**, *40*, 321–348. [CrossRef]

14. Ji, G.; Zhao, M. Membrane Separation Technology in Carbon Capture. In *Recent Advances in Carbon Capture and Storage*; Yun, Y., Ed.; InTech: Rijeka, Croatia, 2017; Chapter 3. ISBN 978-953-51-3006-2.

15. Seader, J.D.; Henley, E.J.; Roper, D.K. Separation Process Principles. *Choice Rev. Online* **1999**, *36*, 36–5112. [CrossRef]

16. He, X.; Hägg, M.B. Membranes for Environmentally Friendly Energy Processes. *Membranes* **2012**, *2*, 706–726. [CrossRef] [PubMed]

17. Kreulen, H.; Smolders, C.A.; Versteeg, G.F.; van Swaaij, W.P.M. Microporous Hollow Fibre Membrane Modules as Gas-Liquid Contactors. Part 1. Physical Mass Transfer Processes. A Specific Application: Mass Transfer in Highly Viscous Liquids. *J. Membr. Sci.* **1993**, *78*, 197–216. [CrossRef]

18. Kreulen, H.; Smolders, C.A.; Versteeg, G.F.; van Swaaij, W.P.M. Microporous Hollow Fibre Membrane Modules as Gas-Liquid Contactors Part 2. Mass Transfer with Chemical Reaction. *J. Membr. Sci.* **1993**, *78*, 217–238. [CrossRef]

19. Yuliwati, E.; Ismail, A.F. Effect of Additives Concentration on the Surface Properties and Performance of PVDF Ultrafiltration Membranes for Refinery Produced Wastewater Treatment. *Desalination* **2011**, *273*, 226–234. [CrossRef]

20. Yuliwati, E.; Ismail, A.F.; Matsuura, T.; Kassim, M.A.; Abdullah, M.S. Effect of Modified Pvdf Hollow Fiber Submerged Ultrafiltration Membrane for Refinery Wastewater Treatment. *Desalination* **2011**, *283*, 214–220. [CrossRef]

21. Rajabzadeh, S.; Yoshimoto, S.; Teramoto, M.; Al-Marzouqi, M.; Ohmukai, Y.; Maruyama, T.; Matsuyama, H. Effect of Membrane Structure on Gas Absorption Performance and Long-Term Stability of Membrane Contactors. *Sep. Purif. Technol.* **2013**, *108*, 65–73. [CrossRef]

22. Rajabzadeh, S.; Yoshimoto, S.; Teramoto, M.; Al-Marzouqi, M.; Matsuyama, H. CO_2 absorption by Using PVDF Hollow Fiber Membrane Contactors with Various Membrane Structures. *Sep. Purif. Technol.* **2009**, *69*, 210–220. [CrossRef]

23. Albarracin Zaidiza, D.; Wilson, S.G.; Belaissaoui, B.; Rode, S.; Castel, C.; Roizard, D.; Favre, E. Rigorous Modelling of Adiabatic Multicomponent CO_2 Post-Combustion Capture Using Hollow Fibre Membrane Contactors. *Chem. Eng. Sci.* **2016**, *145*, 45–58. [CrossRef]

24. Kumar, P.S.; Hogendoorn, J.A.; Feron, P.H.M.; Versteeg, G.F. Approximate Solution to Predict the Enhancement Factor for the Reactive Absorption of a Gas in a Liquid Flowing through a Microporous Membrane Hollow Fiber. *J. Membr. Sci.* **2003**, *213*, 231–245. [CrossRef]

25. Albarracin Zaidiza, D.; Billaud, J.; Belaissaoui, B.; Rode, S.; Roizard, D.; Favre, E. Modeling of CO_2 Post-Combustion Capture Using Membrane Contactors, Comparison between One- and Two-Dimensional Approaches. *J. Membr. Sci.* **2014**, *455*, 64–74. [CrossRef]

26. Kumar, P.S.; Hogendoorn, J.A.; Feron, P.H.M.; Versteeg, G.F. New Absorption Liquids for the Removal of CO_2 from Dilute Gas Streams Using Membrane Contactors. *Chem. Eng. Sci.* **2002**, *57*, 1639–1651. [CrossRef]

27. Rezakazemi, M.; Niazi, Z.; Mirfendereski, M.; Shirazian, S.; Mohammadi, T.; Pak, A. CFD Simulation of Natural Gas Sweetening in a Gas–Liquid Hollow-Fiber Membrane Contactor. *Chem. Eng. J.* **2011**, *168*, 1217–1226. [CrossRef]

28. Yuan, C.; Li, L.; Li, Y.; Pan, Z.; Zhang, N.; Borhani, T.N.; Zhang, Z. Modeling of CO_2 Absorption into 4-Diethylamino-2-Butanol Solution in a Membrane Contactor under Wetting or Non-Wetting Conditions. *Carbon Capture Sci. Technol.* **2022**, 100069. [CrossRef]

29. Ismail, M.S.; Mohamed, A.M.; Poggio, D.; Walker, M.; Pourkashanian, M. Modelling Mass Transport within the Membrane of Direct Contact Membrane Distillation Modules Used for Desalination and Wastewater Treatment: Scrutinising Assumptions. *J. Water Process Eng.* **2022**, *45*, 102460. [CrossRef]

30. Zhang, X.; Koirala, R.; Date, A.; Jegatheesan, V. Modelling and Simulation of Flux Prediction and Salinity Variation in Direct Contact Membrane Distillation for Seawater Desalination and Brine Treatment. *Desalination* **2022**, *540*, 116021. [CrossRef]

31. Bird, R.B.; Stewart, W.E.; Lightfoot, E.N. *Transport Phenomena, Revised Se*; John Wiley & Sons: New York, NY, USA, 2006.

32. Hikita, H.; Asai, S.; Ishikawa, H.; Honda, M. The Kinetics of Reactions of Carbon Dioxide with Monoethanolamine, Diethanolamine and Triethanolamine by a Rapid Mixing Method. *Chem. Eng. J.* **1977**, *13*, 7–12. [CrossRef]

Article

Synthesis of Urchin-Shaped Gold Nanoparticles Utilizing Green Reducing and Capping Agents at Different Preparation Conditions: An In Vitro Study

Mohamed S. Salem [1] , Mohamed R. Elmarghany [1,*] , Noha Salem [2] and Norhan Nady [2,*]

[1]   Mechanical Power Engineering Department, Faculty of Engineering, Mansoura University, Mansoura 35516, Egypt
[2]   Polymeric Materials Research Department, City of Scientific Research and Technological Applications (SRTA-City), Borg El-Arab City, Alexandria 21934, Egypt
*   Correspondence: mohamed_ragab@mans.edu.eg (M.R.E.); norhan.nady77@yahoo.com (N.N.); Tel.: +20-01007121799 (M.R.E.); +20-1090918521 (N.N.)

Abstract: Employing environmentally friendly reducing and capping materials to synthesize gold nanoparticles is an exciting research point. However, the used materials usually need a long reduction time that can take days. In this work, the instantaneous production of small-sized (less than 20 nm) gold nanoparticles is investigated using ascorbic acid, gelatin, and a mixture of the two agents at different preparation conditions (at room temperature; 20 ± 3 °C and near boiling temperature; 95 ± 3 °C). Particle size analysis, as well as transmission electron microscopy, were used to assess the produced particles' physical characteristics. The structural changes and optical characteristics of the nanoparticles were monitored using UV–visible spectroscopy. Fourier Transform Infrared spectroscopy (FTIR) was used to establish the presence of a gelatin coating over the gold nanoparticles. The morphology of the produced nanoparticles at 95 ± 3 °C was spherical with a size ranging from 8–18 nm, whereas urchin-shaped nanoparticles ranging from 24–100 nm were formed at 20 ± 3 °C reaction temperature. The presence of hydroxyl and amine groups associated with the gelatin was confirmed using FTIR. This could be a step for wider usage of green synthesized nanogold particles in several applications.

Keywords: gold nanoparticles; instant nanosynthesis; urchin-shaped nanogold; green capping agent; biocompatible nanogold

1. Introduction

Nanotechnology research has recently emerged as a vital key to obtaining novel, desirable properties from well-known conventional materials [1]. Nanomaterials have at least one dimension within the nanometer range [2]. Although almost any material in existence could exist within the nanoscale, noble metals-based nanoparticles hold a special value. They generally have some exceptional characteristics that can be tailored for many useful applications.

Gold is considered one of the most famed noble metals to be prepared in nanoscale forms [3]. Gold nanoparticles drew increasing interest due to their excellent optical, electronic, and magnetic properties [4], as well as their biocompatibility [5] and non-toxicity [6]. Gold-based nanomaterials have been previously prepared in different nanostructures like nanoparticles [7,8], nanorods [9,10], nanowires [11,12], nanostars [13,14], nanospheres [15,16], and nanotriangles [17,18]. Nanogold-based materials were utilized for different purposes, such as catalysis [19], energy storage and conversion [20], biomedical therapeutics [20–22], drug delivery [23], photonics [24], and biosensing [25,26].

Composite nanostructures that combine gold with other materials, such as iron [27], silver [28], and graphene [28], were also investigated and prepared. Moreover, researchers managed to prepare fairly complicated composite morphologies. For example, Nghiem et al. [29] managed to prepare a composite comprising a core–shell nanostructure, combining a silica core with a gold shell.

Nanostructure attributes are greatly influenced by their physicochemical characteristics, which include particle volume, form, and composition. Furthermore, for composite nanostructures, the properties are also affected by the molecular distribution within the particle [30]. Tuning and manipulating these characteristics allows control or maximization of the desired attribute to be suitable for a specific application. In the case of catalysis, for example, catalytic activity and selectivity are strongly influenced by the surface area, composition, and shape of the nanostructure [31]. On the other hand, when the object is to enhance the optical attributes of a nanostructure for imaging functions, controlling those characteristics would impact absorption and scattering efficiency [32].

It is evident that the manipulation of these nanostructures during the synthesis process is essential to produce predictable and distinct physical and chemical properties. This is critical not only for optimizing their performances but also for understanding the structure-performance relations. This can be partly achieved through the nanostructure controllable preparation method.

Microemulsion [33], reversed micelles [34], seeding growth [35], sonochemistry [36], photochemistry [37], radiolysis [38], and chemical reduction [39] techniques have all been used for gold nanostructure preparation. Several chemical reductants have been used to reduce the gold precursor (chloroauric acid, $HAuCl_4$), such as 1-amino-2-naphthol-4-sulphonic acid [40], monosodium glutamate [41], sodium borohydride [42], amine [43], etc. Recently, natural materials have been used as green reductants, such as ascorbic acid [44], piper beetle leaf broth [45], a polyphenol extracted from leaf buds of camellia Sinensis tea [46], aspartame [47], Rhizopus oryzae fungal strain [48], and gelatin [3].

One of the earliest and simplest methods for preparing gold nanoparticles is the Turkevich technique [49], which uses sodium citrate to both reduce the gold precursor ($HAuCl_4$) and prevent further particle development and retain the formed gold in the nano range as well as prevent the nanogold from aggregation. The second role of the used sodium citrate is a capping agent that can offset the Van der Waals tractive forces through steric and electrostatic repulsions, hence reducing the aggregation phenomenon. However, the stability and dispersity of the produced gold nanoparticles are often poor [50]. In recent years, another technique was developed to adjust the reaction pH utilizing a buffer rather than a solution to present nanoparticles with high monodispersity [51]. Also, ethylenediaminetetraacetic acid (EDTA) was used to improve the uniformity of the produced nanogold with better size control [52].

Gold nanoparticles have excellent potential for the immobilization of biomolecules because they are biocompatible and bind readily to a range of biomolecules, such as amino acids, proteins, DNA, and enzymes. Nanogold membranes can be used as templates for the immobilization of enzymes [53]. Consequently, the bioconjugate material could be easily separated after reaction by mild centrifugation and easily reused. This membrane can also be used in nanoplasmonic sensors [54].

As can be seen, the search continues for producing proficient gold nanostructures using green reducing and capping agents that combine sustainability and efficiency [55]. In the literature, some authors used surfactants to obtain such small sizes that resulted in chemical contamination. Others claimed to produce nanoparticles instantaneously without quantifying the exact reaction time. On the other hand, most of the published research did not obtain uniform shapes but mostly a mixture of different shapes [56]. In this work, the instantaneous fabrication of gold nanoparticles with two different morphologies using a green, reducing agent (ascorbic acid) and a green capping agent (gelatin) along with distilled water as solvent was investigated and presented. Ascorbic acid (B_1), gelatin (B_2), as well as a mixture of both (M) were tested as reducing agents of the gold precursor. Two different morphologies were obtained under the sole influence of changing the reaction temperature. Particle size analysis, as well as transmission electron microscopy, were used to assess the produced particles' physical characteristics. The structural changes and optical characteristics of the nanoparticles were monitored using UV–visible spectroscopy. Moreover, the crystal nature of the prepared gold nanoparticles was determined by X-ray

Diffraction (XRD), and Fourier transform infrared spectroscopy (FTIR) was used to establish the presence of a gelatin coating over the gold nanoparticles. Small-sized spherical and urchin-shaped nanoparticles were successfully obtained. Urchin-shaped nanoparticles were formed. This unique shape has special plasmon properties due to the unsmooth surface that causes a greater enhancement of the electromagnetic field at the ends of the urchin-shaped nanoparticle spikes supplemented by a red shift in the peak [57]. For that, disease diagnostics and therapy are strongly suggested as some of the potential applications of the prepared unique urchin-shaped nanogold.

2. Materials and Methods

2.1. Materials

Ascorbic acid (B_1) was purchased from HiMedia chemicals. Hydrogen tetrachlorourate (III) ($HAuCl_4$, 30%wt in HCl) and gelatin (B_2) from the skin were purchased from Sigma-Aldrich. Ferulic acid ($\geq$99.5%) was obtained from Fluka (Schwerte, Germany). Glycerin (>98%) was purchased from Oxford Laboratory Reagent (Mumbai, India) Ethanol (purity $\geq$ 98%) was acquired from Sigma-Aldrich. Formic acid (85%) was obtained from Laboratory Chemicals (Cairo, Egypt). For the preparation of the mixture solution, distilled water was used. Figure 1 presents the chemical composition of ascorbic acid and gelatin.

| (a) | (b) |
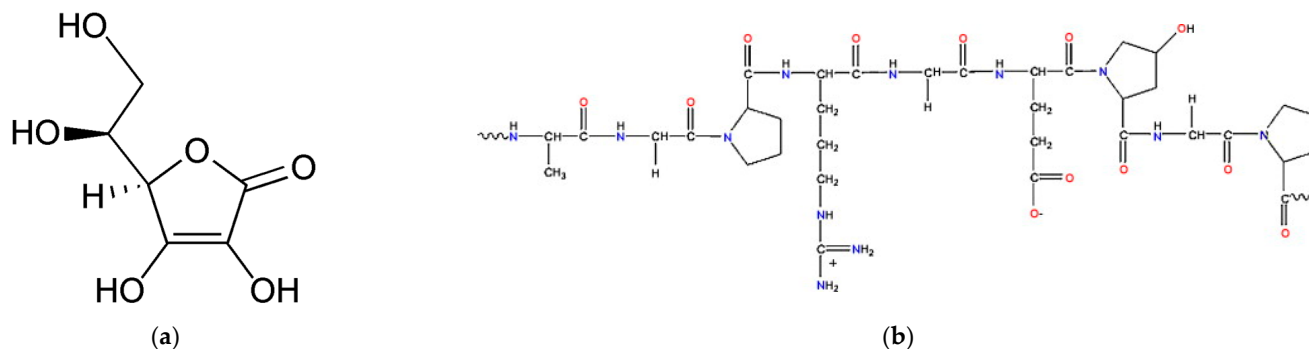
Figure 1. Structure of ascorbic acid (**a**) and gelatin (**b**).

2.2. Methods

Gold Nanoparticles Preparation

Six different sets of experiments were performed to synthesize gold nanoparticles. The nanoparticles were synthesized using only ascorbic acid (B_1), only gelatin (B_2), and a mixture of them (M) at two different temperatures: near boiling temperature(BT) (95 $\pm$ 3 °C) and at room temperature (RT) (20 $\pm$ 3 °C). In a beaker, a quantity of 10 mL was taken from tetrachloroauric acid (with 30% Au) solution and diluted with 40 mL of distilled water. It was then heated to near boiling temperature with a continuous stirring at 200 rpm. It formed a clear pale yellowish solution (pH 2 $\pm$ 0.07). In another beaker, a gelatin solution (1% by volume; pH 4.3 $\pm$ 0.02), an ascorbic acid (1% by volume; pH 3.9 $\pm$ 0.04), and a mixture of both (1% by volume; pH 4) were prepared at the same temperature (95 $\pm$ 3 °C) along with stirring for 15 min. The boiled solution of the components was immediately poured into the gold precursor solution with continuous mixing (pH 3.3 $\pm$ 0.02). The same process was repeated at RT (20 $\pm$ 3 °C) without heating. Only a little heating (10 min at 40 °C) was used to dissolve the gelatin, then it was kept until it cooled down to RT before use.

2.3. Characterization

2.3.1. UV–Visible Spectrophotometer Measuring

UV–visible spectra of the instantly-formed gold nanoparticle solutions were recorded over a 200–900 nm wavelength by a Libra S32 Spectrophotometer (Biochrom, UK). The mixing was done immediately inside the used cuvette before measuring.

2.3.2. Transmission Electron Microscopy (TEM) imaging

TEM images were performed by JEM-2100F Transmission Electron Microscope (JEOL, Tokyo, Japan). A drop of gold solution was poured into a water sample over a copper mesh, then dried at room temperature for one day to prepare the sample. The histograms of the particle size distribution were estimated using ImageJ software.

2.3.3. Particle Size Analysis

The samples were recorded by a Tensor 27 Bruker spectrophotometer with 32 scans, 2 cm^{-1} resolution. The used gold solution was freshly prepared before measuring.

2.3.4. X-ray Diffraction (XRD) Analysis

The morphology of the prepared gold nanoparticles was carried out using a Bruker AXS XRD with CuKα as an X-ray source at 50 kV and 100 mA. The formed nanoparticle was drop-coated onto a glass substrate and dried in a desiccator for 24 h before measuring.

2.3.5. Fourier Transform-Spectroscopy (FT-IR) Analysis

An FT-IR spectrometer (Bruker, Japan) was used to study the chemical structure of the produced gold nanoparticles. FT-IR spectra in the range of 4000 to 400 cm^{-1} with a resolution of 4 cm^{-1} were used. The gold nanoparticles were precipitated and washed with ethanol and then dried in the desiccators at RT for a day before measuring.

3. Results and Discussion

Figure 2 presents the different stages of the gold nanoparticle preparation process. It was noticed that in the case of using the mixture and preparing at near boiling temperature, the solution color changed from pale yellowish to red almost immediately with the addition of the first drop of the gold precursor into the reducing and capping agents (Figure 2b). The red color indicates gold nanoparticle formation, which increases with adding more from the mixture, as shown in Figure 2c. On the other hand, in the case of using the mixture and preparation at room temperature, the color change was not noticed by the naked eye for almost 15 min. As for the blank experiments, i.e., ascorbic acid and gelatin at room temperature ($B_{1,RT}$, $B_{2,RT}$) and near-boiling temperature ($B_{1,BT}$, $B_{2,BT}$), it took up to 30 min before a change in color could be noticed. After adding absolute ethanol, precipitation of the gold nanoparticles could be observed, as seen in Figure 2d.

The morphology of the green synthesized gold nanoparticles was observed by TEM. Figure 3 shows samples of TEM images of the gold nanoparticles formed using only ascorbic acid at RT and BT, only gelatin at RT and BT, and a mixture of ascorbic acid and gelatin together at the different preparation temperatures. Figure 4 presents histograms of the particle size distribution estimated using ImageJ software. As can be seen from the figures, most gold nanoparticles formed near boiling temperature had a spherical shape. The average diameter was in the range of 5–20 nm in the case of using the ascorbic acid ($B_{1,BT}$), and in the range of 3–14 nm in the case of using the gelatin ($B_{2,BT}$). However, the average diameter of the instantly formed gold particles when using the mixture at (M_{BT}) was in the range of 5–22 nm. On the other hand, the gold nanoparticles formed at room temperature had different shapes. Irregular shapes with an average diameter in the range of 9–34 nm were formed when using ascorbic acid alone $B_{1,RT}$. A mixture of spherical and urchin-shaped gold nanoparticles with an average diameter range of 2–8 nm was obtained using gelatin ($B_{2,RT}$). Surprisingly, using both ascorbic acid and gelatin together at room temperature (M_{RT}) resulted in the formation of urchin-shaped nanoparticles with particle sizes ranging from 20–120 nm. A larger size of particle than the spherical-shaped particles was obtained at M_{BT}. In general, the reaction temperature affected not only the shape but also the size range of the formed gold nanoparticles. Table 1 summarizes the mean diameter and standard deviation of each case.
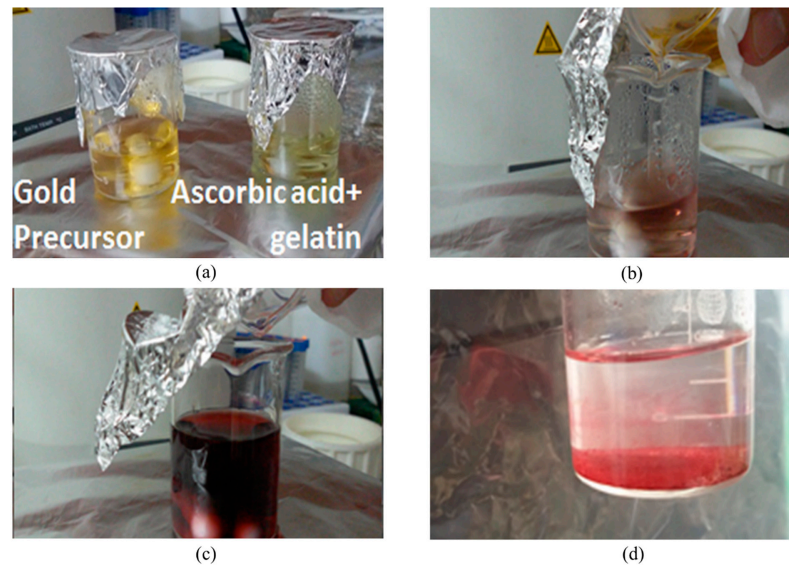
Figure 2. Preparing gold nanoparticles using a mixture of ascorbic acid and gelatin at 95 ± 3 °C (**a**) before mixing, (**b**) one second after mixing starts, (**c**) after mixing for one minute, and (**d**) gold nanoparticles precipitation after adding ethanol.
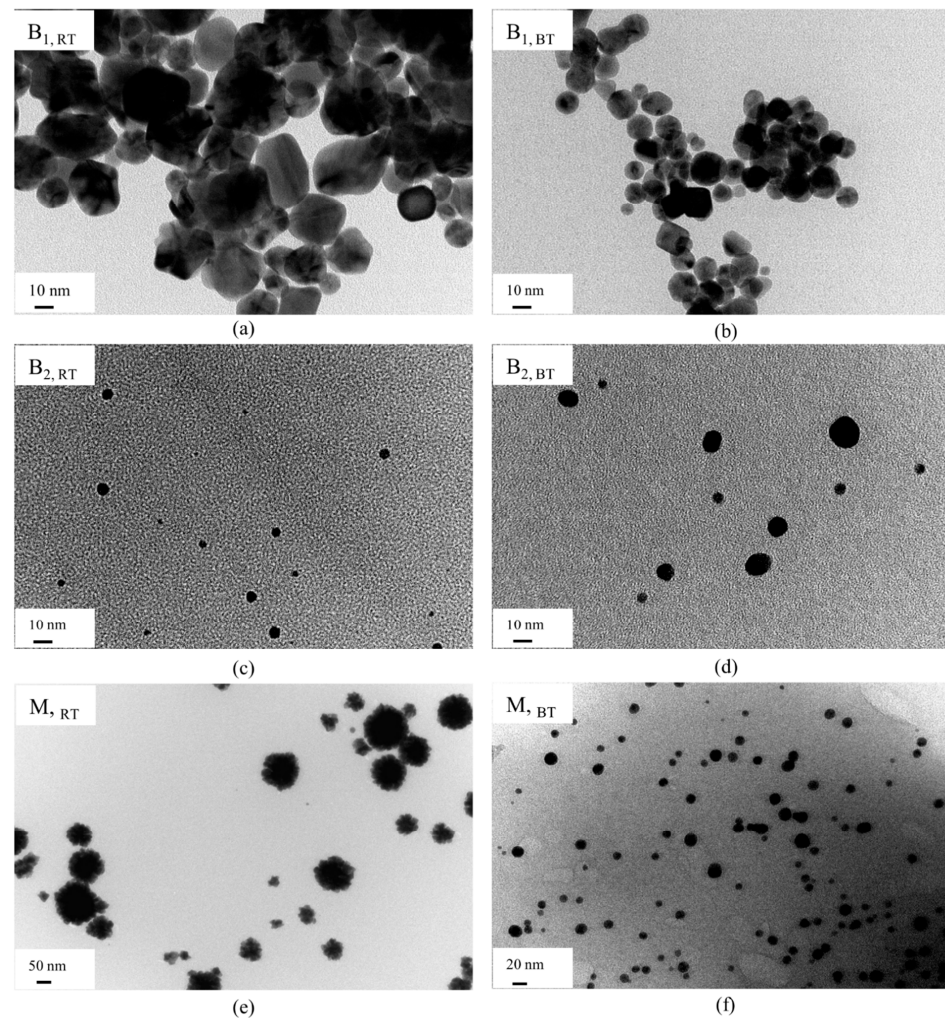

Figure 3. TEM images of the formed gold nanoparticles using only ascorbic acid at; (**a**) 20 ± 3 °C (B$_{1,RT}$), (**b**) 95 ± 3 °C (B$_{1,BT}$), only gelatin at (**c**) 20 ± 3 °C (B$_{2,RT}$), (**d**) 95 ± 3 °C (B$_{2,BT}$), and a mixture at (**e**) 20 ± 3 °C (M$_{,RT}$), and (**f**) 95 ± 3 °C (M$_{,BT}$).
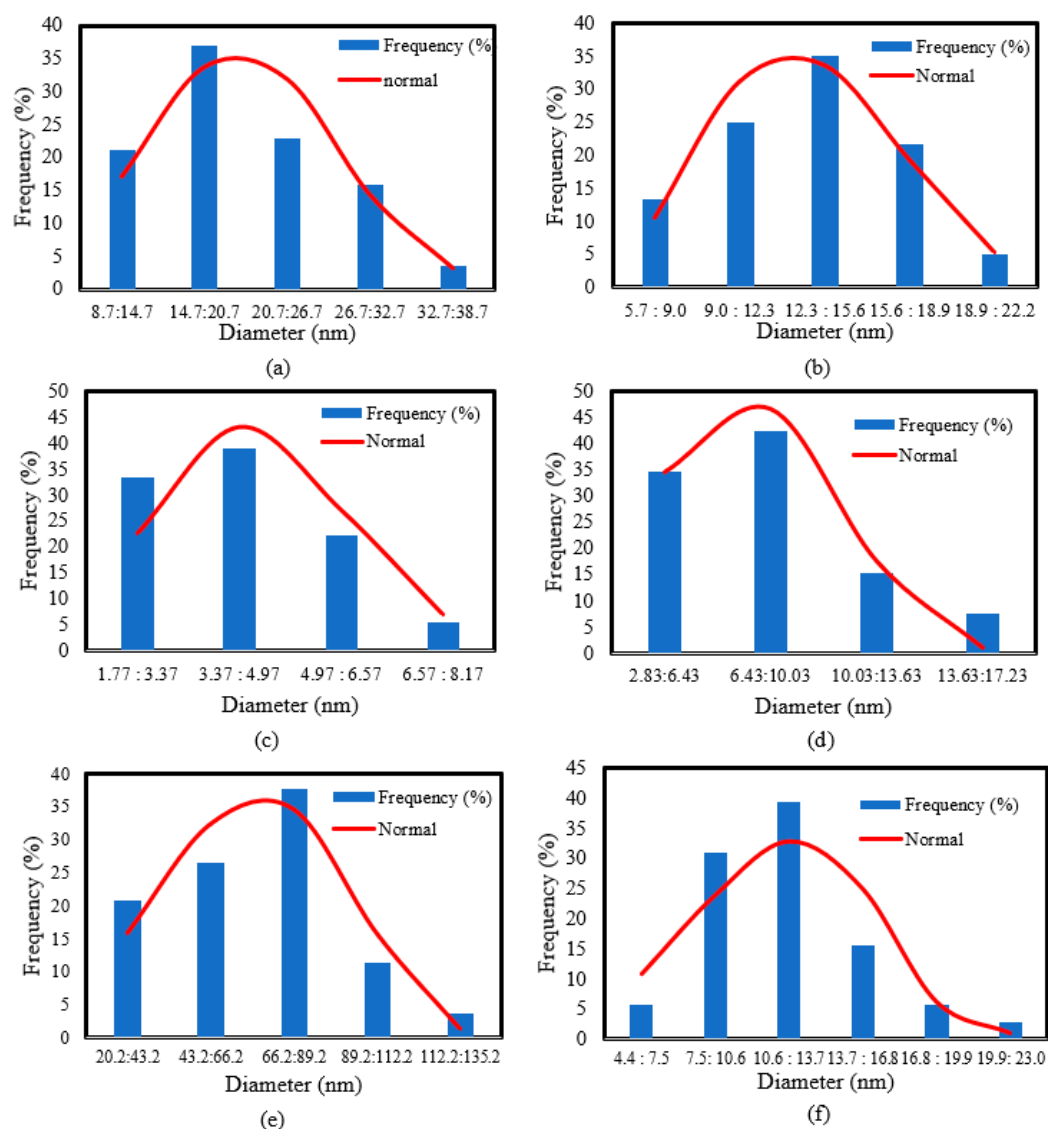
Figure 4. Histograms of the particle size distribution via TEM images of the formed gold nanoparticles using only ascorbic acid at (**a**) $20 \pm 3\,°C$ ($B_{1,RT}$), (**b**) $95 \pm 3\,°C$ ($B_{1,BT}$); only gelatin at (**c**) $20 \pm 3\,°C$ ($B_{2,RT}$), (**d**) $95 \pm 3\,°C$ ($B_{2,BT}$), and a mixture at (**e**) $20 \pm 3\,°C$ ($M_{,RT}$), and (**f**) $95 \pm 3\,°C$ ($M_{,BT}$).

Table 1. Summary of the mean value and standard deviation of the obtained gold nanoparticles at two different reaction temperatures.

Sample	Mean Value (nm)	Standard Deviation (nm)
$B_{1,RT}$	20.3	6.6
$B_{1,BT}$	14.0	3.6
$B_{2,RT}$	4.3	1.5
$B_{2,BT}$	7.2	3.2
$M_{,RT}$	65.6	25.1
$M_{,BT}$	11.8	3.6

The obtained results show that the higher temperature of the reaction resulted in the almost instantaneous creation of gold nanoparticles in a uniform shape. This is in full agreement with previous research [57–59], in which the reaction temperature decisively controlled the formation of small gold nanoparticles. Generally, the temperature accelerates the nucleation process and with the aid of the used capping agent, the gold nanoparticles are able to maintain their small size. However, the lower reaction temperature causes a limited nucleation process

and provides a chance for particle growth to yield a larger particle size, which the naked eye can notice after longer reaction times (15–30 min). On the other hand, at a relatively low pH medium (pH 3.3 ± 002), the formation of gold nanoparticles is carried out through an intermediate $[AuCl_3(OH)]^-$ which undergoes a LaMer burst nucleation within about 10 s [60,61]. However, at higher pH mediums, a much longer nucleation time (around 60 s) is required, and the particles undergo reduction through $[AuCl_2(OH)]_2^-$ and $[AuCl(OH)]_3^-$ followed by a much slower growth process. When coupling both effects of high temperature and pH, a uniform low-size range of gold nanoparticles could be produced [58,61].

UV–visible spectroscopy can check for morphological changes and optical properties as nanoparticles display surface plasmon resonance (SPR) varying with its form and size at different frequencies [57,61]. The reaction was executed inside the device cuvette for 30 s and the measurement of the mixed solution was done immediately for higher accuracy. Figure 5a shows a UV–visible spectrum of an aqueous solution of gold precursor in water at room temperature (20 ± 3 °C), mixed with only ascorbic acid ($B_{1,RT}$), and mixed with only gelatin ($B_{2,RT}$). The figure also presents the spectra of the gold prosecutor mixed with both agents at room temperature (M_{RT}) as well as near boiling temperature (M_{BT}). All the measurements took place within 2 min from the reaction beginning (i.e., 30 s for mixing and around 60 s for measuring). As noted, there are no peaks for the used gold precursor solution in water or the solution of gold precursor with the ascorbic acid. However, the presence of gelatin with the gold precursor shows a surface plasmon resonance broad band at around 570–600 nm. In the case of the gold prosecutor with the mixture, a strong absorption band around 500–600 nm is observed that corresponds to the excitation of surface plasmon vibrations in the gold nanoparticles. The presence of both ascorbic acid and gelatin shows a broader SPR beak at around 507–667 nm. It can be seen that the peak was broadened with urchin-shaped gold nanoparticles, as illustrated in TEM images in the previous section, which was prepared at RT (20 ± 3 °C). This broad peak can be attributed to the existence of transversal and longitudinal SPR [62]. The sharp increase in the UV band at a wavelength of about 500 nm may be due to the instantaneous formation of the nanogold particles during the measurement, as the reaction was processed within the measuring cuvette for maximum accuracy. The unsmooth surface causes a greater enhancement of the electromagnetic field at the ends of the urchin-shaped nanoparticle spikes supplemented by a red shift in the peak [57].

Additionally, the uneven distribution of the surface electron layers in the urchin-shaped gold nanoparticles is what causes the difference in absorption qualities between them and the spherical ones [45,63]. On the other hand, the much less broad SPR absorption band of gold nanoparticle that was prepared near boiling temperature (95 ± 3 °C) appeared at 540 nm. Figure 5b shows there was not a noticeable difference in the SPR after 12 min of mixing the gold precursor and both ascorbic acid and gelatin together at room temperature (the measuring was executed with 2-min intervals).

Furthermore, Figure 5c shows the same determined SPR band after 12 min mixing between the gold precursor mixed with both ascorbic acid and gelatin at near boiling temperature (95 ± 3 °C). Regarding using only ascorbic acid with the gold precursor near BT ($B_{1,BT}$), a small SPR band was formed compared to ($B_{1,RT}$) in Figure 5a, which can be ascribed to the fast growth of gold nanoparticles with the ascorbic acid with heating.

It is considered common knowledge that gold nanoparticles smaller than 2 nm do not demonstrate SPR [57,64]. Such small gold nanoparticles can be determined by using a particle size analyzer as shown in Figure 6. The use of either ascorbic acid or gelatin at near boiling temperature (95 ± 3 °C) can produce gold nanoparticles. To stop the growth of gold particles and/or to reduce the nanoparticle aggregation, the addition of pure ethanol with a ratio of 3:1 ethanol/reaction solution was done after 2 min of mixing at BT and after 15 min mixing at RT. The effect of ethanol is strongly illustrated by a reduction in the particle size of the formed gold nanoparticles produced using only the reducing agent (ascorbic acid) at 95 ± 3 °C from 257–421 nm to a much narrower 6–13 nm size, whereas the addition of ethanol to the solution of gold precursor and gelatin at BT resulted in shifting the particle size range from 45–74 nm to 95–200 nm.
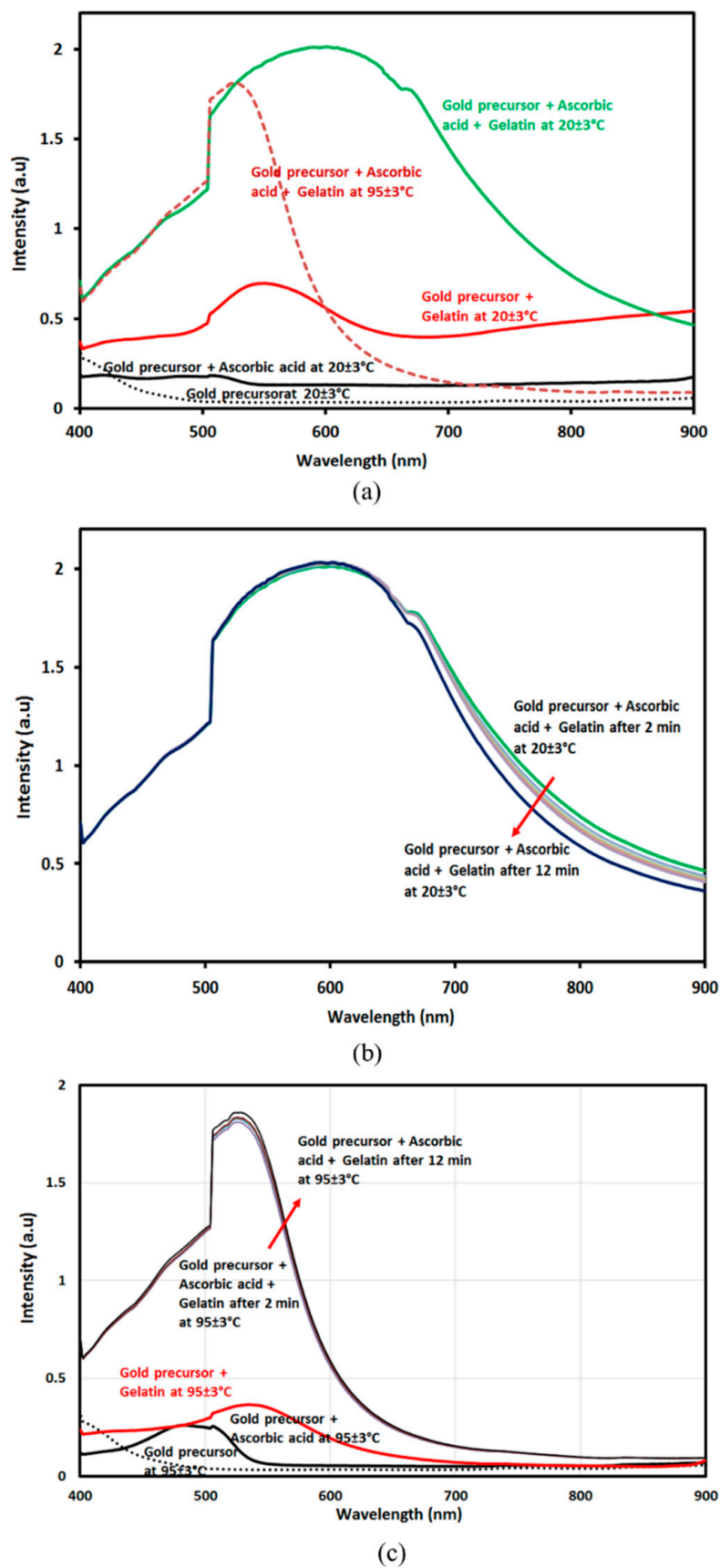
Figure 5. UV–visible spectra of the formed gold nanoparticles at two different temperatures (RT; 20 ± 3 °C and near BT; 95 ± 3 °C) after 2 min reaction time (**a**) and after 12 min reaction time ((**b**); 20 ± 3 °C and (**c**); 95 ± 3 °C).
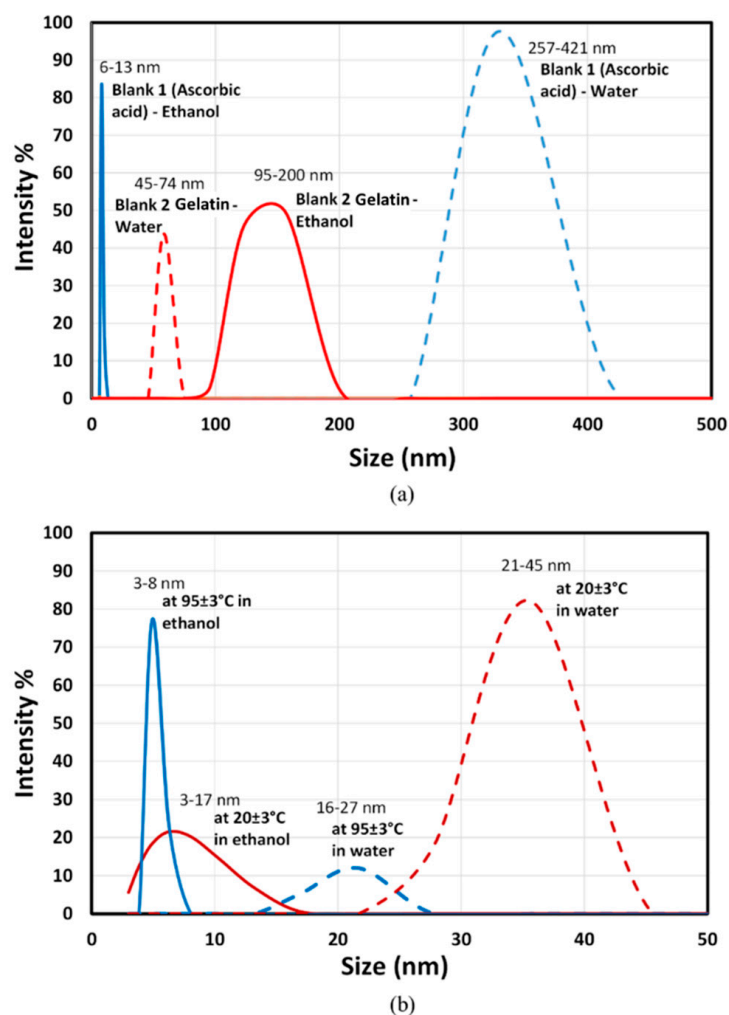
Figure 6. Particle size analyzer of the formed gold nanoparticles suspended in the reaction solution, and after adding ethanol. The nanoparticles were synthesized using (**a**) only ascorbic acid ($B_{1,BT}$) and only gelatin ($B_{2,BT}$). (**b**) Using both ascorbic acid and gelatin at both room temperature (M_{RT}), and near the boiling point ($M_{,BT}$).

It seems the role of ethanol is different in the two cases; in the case of using ascorbic acid, the used ethanol may reduce the particle size growth, but in the case of using gelatin, the used ethanol reduced the role of gelatin as a capping agent and enhanced the particle aggregation. The degradation effect of the ethanolic solution on the ascorbic acid was previously proven [64] in which the higher ethanol concentration (>50%) promotes lowering the water activity environment that supports the degradation of ascorbic acid into a transitional compound; L-xylosone, and then to other carbon compounds [65]. Therefore, adding the ethanol solution will lead to stopping the reducing reaction and result in a reduction in the particle size of the produced nanogold. Meanwhile, ethanol with a high concentration (>50%) works on the precipitation of gelatin into particles [66]. Therefore, the effectiveness of the gelatin as a capping agent is weakened, and a larger gold particle size is formed. The results of $B_{1,RT}$, and $B_{2,RT}$ were not within the measuring limit, which may be attributed to the formation of an extremely small particle size (out of the measuring limits of the particle size analyzer; <3 nm). In the case of using both ascorbic acid and gelatin near BT as shown in Figure 6B, the size of produced nanoparticle shifted from 16–27 nm to 3–8 nm. In the case of using both ascorbic acid and gelatin at RT, the size of produced urchin-shaped gold nanoparticles shifted from 21–45 nm to 3–17 nm. From the obtained results, we can assume that the addition of ethanol may be a tool to control the size of the gold nanoparticles according to the targeted final gold particle size.

The existence of gold nanoparticles was verified using XRD. Figure 7 shows diffraction peaks for the used gold precursor in distilled water at 95 ± 3 °C reaction temperature and the green synthesized nanoparticles using a mixture of ascorbic acid and gelatin as a reducing agent and a capping agent, respectively at 95 ± 3 °C reaction temperature. The determined four strong Bragg diffraction peaks at 38.18°, 44.02°, 65.75°, and 78.02° can be assigned to the (111), (200), (220), and (311) planes [67,68]. It is possible to interpret these diffraction peaks as a face-centered cubic of gold and a natural crystal structure [58,59].
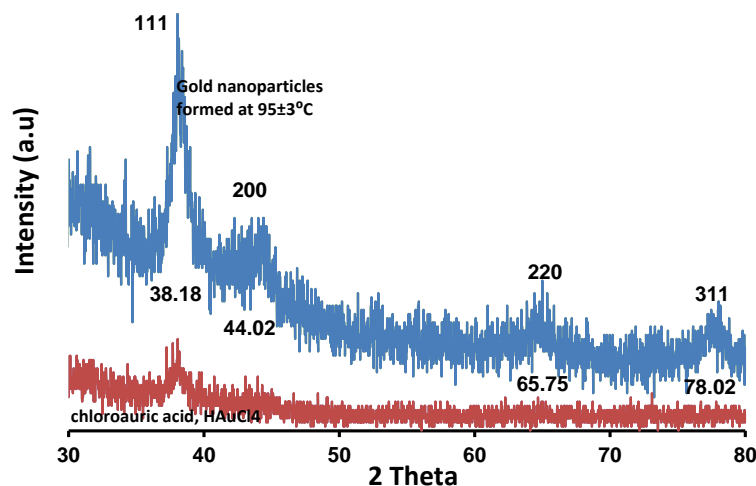
Figure 7. XRD diffraction patterns of gold precursor (hydrogen tetrachlorourate) and the formed gold nanoparticles at 95 ± 3 °C after adding ethanol, decantation, and drying in a desiccator.

The FT-IR spectrum shown in Figure 8 illustrates the existence of the following groups: the strong, broad band observed at 3414 cm^{-1} suggests the existence of the O-H group and primary amine O-H band. The band at 2953 cm^{-1} may correspond to C-H stretching vibrations of the alkanes group, and the band at 1641 cm^{-1} indicates the existence of amide I. The narrow peak at 1541 cm^{-1} can be assigned for the presence of amide II. The peak at 1437 cm^{-1} may be attributed to –N-H. The peak at 1257 cm^{-1} can be assigned to –C-O. The narrow peak at 1084 cm^{-1} can be attributed to the presence of C-N stretching vibrations of aliphatic amines. This FT-IR spectrum indicates the presence of gelatin as a capping agent for gold nanoparticles even after the addition of ethanol to the formed gold nanoparticles. FT-IR proposed that both carboxylic acid groups and amine groups share the conjugation with gold surfaces as well as the possibility of further conjugation with other molecules.
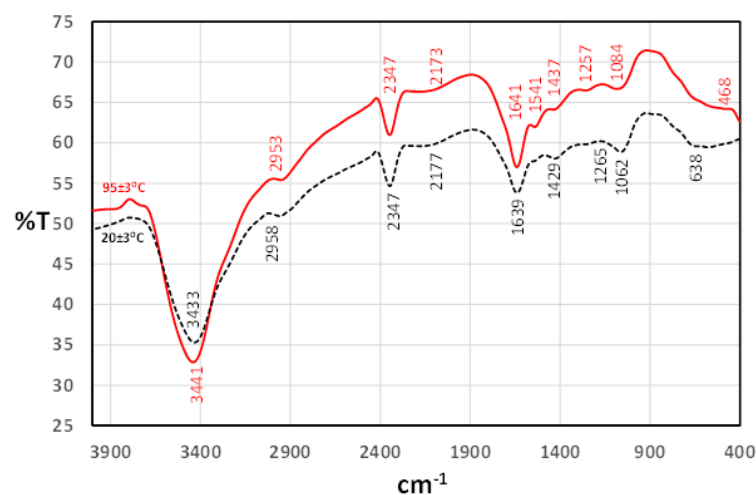
Figure 8. FT-IR spectra of gold nanoparticles formed near BT (red solid line) and at RT (black dashed line).

4. Conclusions

Spherical gold nanoparticles and urchin-shaped gold nanoparticles were successfully and instantly produced using a green-natured reducing agent (ascorbic acid), and a green-natured capping agent (gelatin). Gelatin could be used as both a reducing and capping agent as reported in previous research [67], but the formed gold nanoparticles are not urchin-shaped. In in vivo applications, urchin-shaped particles are preferred to spherical ones because they have a lower background and more effectively transmit near-infrared light through biological tissues [58]. For that, the authors strongly propose utilizing the prepared unique urchin-shaped nanogold in disease diagnostics and therapeutical applications.

Table 2 shows that using both ascorbic acid and gelatin together resulted in an instant production of two different morphologies of gold nanoparticles as the effect of the reaction temperature: at RT (20 ± 3 °C) and near BT (95 ± 3 °C). The role of gelatin is mainly as a capping agent, although it can be considered as a second reducing agent. The mixing time in a mixture of ascorbic acid and gelatin was shorter than those of either only ascorbic acid or only gelatin, especially at a room temperature reaction, due to the higher reaction rates indicated by the change in the solution reaction. Using both gelatin and ascorbic acid together resulted in a spontaneous reaction that can be used to shift the formed gold particles to extremely small sizes. The use of ethanol effectively reduced the aggregation of the particles. However, it had the opposite effect in the case of using gelatin alone. Regarding the used analysis techniques, the particle size analyzer was proved unsuitable for irregular (urchin-shaped) nanoparticles. However, it could be used as an indication of the formed, small, and smooth morphology.

From this study, it is clear that the synthesis of biocompatible gold nanoparticles using both ascorbic acid and gelatin together as reducing and capping agents, respectively, is an instant, flexible, and green method. They produced spherical and urchin-shaped gold nanoparticles, which are candidates for use in medical, pharmaceutical, food, and cosmetics applications.

Table 2. Summary of the size range and morphology of the obtained gold nanoparticles at two different reaction temperatures.

Preparation Temperature	Property	Ascorbic Acid (B$_1$) pH 3.6 ± 0.02			Gelatin (B$_2$) pH 3.1 ± 0.01			Ascorbic Acid and Gelatin (M) pH 3.3 ± 0.02		
		TEM (water)	Particle size		TEM (water)	Particle size		TEM (water)	Particle size	
			Water	Eth.		water	Eth.		water	Eth.
RT (20 ± 3 °C)	Determined Size (nm)	9–34	-	-	2–8	-	-	20–120	21–45	3–17
	Morphology	Irregular			Spherical/Urchin mix			Urchin		
	Mixing time	30 min			30 min			15 min		
BT (95 ± 3 °C)	Determined Size (nm)	TEM (water)	Particle size		TEM (water)	Particle size		TEM (water)	Particle size	
			Water	Eth.		water	Eth.		water	Eth.
		5–20	257–421	6–13	3–14	45–74	95–200	5–22	16–27	3–8
	Morphology	Spherical								
	Mixing time	10 min			20 min			2 min		

Informed Consent Statement: Not applicable.

Data Availability Statement: All data generated or analyzed during this study are included in this published article.

Conflicts of Interest: The authors declare no conflict of interest.

References

1. Boisselier, E.; Astruc, D. Gold Nanoparticles in Nanomedicine: Preparations, Imaging, Diagnostics, Therapies and Toxicity. *Chem. Soc. Rev.* **2009**, *38*, 1759–1782. [CrossRef]
2. Jain, P.K.; Huang, X.; El-Sayed, I.H.; El-Sayed, M.A. Noble Metals on the Nanoscale: Optical and Photothermal Properties and Some Applications in Imaging, Sensing, Biology, and Medicine. *Acc. Chem. Res.* **2008**, *41*, 1578–1586. [CrossRef]
3. Zhou, J.; Ralston, J.; Sedev, R.; Beattie, D.A. Functionalized Gold Nanoparticles: Synthesis, Structure and Colloid Stability. *J. Colloid Interface Sci.* **2009**, *331*, 251–262. [CrossRef] [PubMed]
4. Sardar, R.; Funston, A.M.; Mulvaney, P.; Murray, R.W. Gold Nanoparticles: Past, Present, and Future. *Langmuir* **2009**, *25*, 13840–13851. [CrossRef] [PubMed]
5. Shukla, R.; Bansal, V.; Chaudhary, M.; Basu, A.; Bhonde, R.R.; Sastry, M. Biocompatibility of Gold Nanoparticles and Their Endocytotic Fate inside the Cellular Compartment: A Microscopic Overview. *Langmuir* **2005**, *21*, 10644–10654. [CrossRef] [PubMed]
6. Alkilany, A.M.; Murphy, C.J. Toxicity and Cellular Uptake of Gold Nanoparticles: What We Have Learned so Far? *J. Nanoparticle Res.* **2010**, *12*, 2313–2333. [CrossRef] [PubMed]
7. Rodríguez-Fernández, J.; Pérez-Juste, J.; García De Abajo, F.J.; Liz-Marzán, L.M. Seeded Growth of Submicron Au Colloids with Quadrupole Plasmon Resonance Modes. *Langmuir* **2006**, *22*, 7007–7010. [CrossRef]
8. Hammami, I.; Alabdallah, N.M. Gold Nanoparticles: Synthesis Properties and Applications. *J. King Saud Univ.* **2021**, *33*, 101560. [CrossRef]
9. Vigderman, L.; Khanal, B.P.; Zubarev, E.R. Functional Gold Nanorods: Synthesis, Self-Assembly, and Sensing Applications. *Adv. Mater.* **2012**, *24*, 4811–4841. [CrossRef]
10. Pellas, V.; Hu, D.; Mazouzi, Y.; Mimoun, Y.; Blanchard, J.; Guibert, C.; Salmain, M.; Boujday, S. Gold Nanorods for LSPR Biosensing: Synthesis, Coating by Silica, and Bioanalytical Applications. *Biosensors* **2020**, *10*, 146. [CrossRef]
11. Kim, F.; Sohn, K.; Wu, J.; Huang, J. Chemical Synthesis of Gold Nanowires in Acidic Solutions. *J. Am. Chem. Soc.* **2008**, *130*, 14442–14443. [CrossRef] [PubMed]
12. Jiang, X.; Qiu, X.; Fu, G.; Sun, J.; Huang, Z.; Sun, D.; Xu, L.; Zhou, J.; Tang, Y. Highly Simple and Rapid Synthesis of Ultrathin Gold Nanowires with (111)-Dominant Facets and Enhanced Electrocatalytic Properties. *J. Mater. Chem. A* **2018**, *6*, 17682–17687. [CrossRef]
13. Senthil Kumar, P.; Pastoriza-Santos, I.; Rodríguez-González, B.; Javier García De Abajo, F.; Liz-Marzán, L.M. High-Yield Synthesis and Optical Response of Gold Nanostars. *Nanotechnology* **2008**, *19*, 15606. [CrossRef]
14. Andreiuk, B.; Nicolson, F.; Clark, L.M.; Panikkanvalappil, S.R.; Kenry; Rashidian, M.; Harmsen, S.; Kircher, M.F. Design and Synthesis of Gold Nanostars-Based SERS Nanotags for Bioimaging Applications. *Nanotheranostics* **2022**, *6*, 10–30. [CrossRef] [PubMed]
15. Yoon, J.H.; Selbach, F.; Langolf, L.; Schlücker, S. Ideal Dimers of Gold Nanospheres for Precision Plasmonics: Synthesis and Characterization at the Single-Particle Level for Identification of Higher Order Modes. *Small* **2018**, *14*, 1702754. [CrossRef] [PubMed]
16. Xuan, Y.; Zhang, R.Y.; Zhao, D.H.; Zhang, X.S.; An, J.; Cheng, K.; Hou, X.L.; Song, X.L.; Zhao, Y.D.; Yang, X.Q. Ultrafast Synthesis of Gold Nanosphere Cluster Coated by Graphene Quantum Dot for Active Targeting PA/CT Imaging and near-Infrared Laser/PH-Triggered Chemo-Photothermal Synergistic Tumor Therapy. *Chem. Eng. J.* **2019**, *369*, 87–99. [CrossRef]
17. Scarabelli, L.; Coronado-Puchau, M.; Giner-Casares, J.J.; Langer, J.; Liz-Marzán, L.M. Monodisperse Gold Nanotriangles: Size Control, Large-Scale Self-Assembly, and Performance in Surface-Enhanced Raman Scattering. *ACS Nano* **2014**, *8*, 5833–5842. [CrossRef]
18. Koetz, J. The Effect of Surface Modification of Gold Nanotriangles for Surface-Enhanced Raman Scattering Performance. *Nanomaterials* **2020**, *10*, 2187. [CrossRef]
19. Carabineiro, S.A.C. Supported Gold Nanoparticles as Catalysts for the Oxidation of Alcohols and Alkanes. *Front. Chem.* **2019**, *7*, 702. [CrossRef]
20. Anjana, P.M.; Bindhu, M.R.; Rakhi, R.B. Green Synthesized Gold Nanoparticle Dispersed Porous Carbon Composites for Electrochemical Energy Storage. *Mater. Sci. Energy Technol.* **2019**, *2*, 389–395. [CrossRef]
21. Vasam, M.; Punagoti, R.A.; Mourya, R. Biomedical Applications of Gold Nanoparticles. *Nanotechnol. Life Sci.* **2021**, *15*, 41–59. [CrossRef]

22. Nawaz, A.; Ali, S.M.; Rana, N.F.; Tanweer, T.; Batool, A.; Webster, T.J.; Menaa, F.; Riaz, S.; Rehman, Z.; Batool, F.; et al. Ciprofloxacin-Loaded Gold Nanoparticles against Antimicrobial Resistance: An In Vivo Assessment. *Nanomaterials* **2021**, *11*, 3152. [CrossRef] [PubMed]

23. Riaz, S.; Fatima Rana, N.; Hussain, I.; Tanweer, T.; Nawaz, A.; Menaa, F.; Janjua, H.A.; Alam, T.; Batool, A.; Naeem, A.; et al. Effect of Flavonoid-Coated Gold Nanoparticles on Bacterial Colonization in Mice Organs. *Nanomaterials* **2020**, *10*, 1769. [CrossRef] [PubMed]

24. Budaszewski, D.; Chychłowski, M.; Budaszewska, A.; Bartosewicz, B.; Jankiewicz, B.; Woliński, T.R. Enhanced Efficiency of Electric Field Tunability in Photonic Liquid Crystal Fibers Doped with Gold Nanoparticles. *Opt. Express* **2019**, *27*, 14260–14269. [CrossRef] [PubMed]

25. Li, Y.; Schluesener, H.J.; Xu, S. Gold Nanoparticle-Based Biosensors. *Gold Bull.* **2010**, *43*, 29–41. [CrossRef]

26. Soares, A.L.; Hryniewicz, B.M.; Deller, A.E.; Volpe, J.; Marchesi, L.F.; Souto, D.E.P.; Vidotti, M. Electrodes Based on PEDOT Nanotubes Decorated with Gold Nanoparticles for Biosensing and Energy Storage. *ACS Appl. Nano Mater.* **2021**, *4*, 9945–9956. [CrossRef]

27. Teng, Y.; Shi, J.; Pong, P.W.T. Sensitive and Specific Colorimetric Detection of Cancer Cells Based on Folate-Conjugated Gold-Iron-Oxide Composite Nanoparticles. *ACS Appl. Nano Mater.* **2019**, *2*, 7421–7431. [CrossRef]

28. Homik, Z.; Kopniczky, J.; Smausz, T.; Berkesi, D.; Hopp, B. Formation of Gold/Silver Composite Nanoparticles by Pulsed Laser Ablation of Gold–Silver Layered Films in Liquid. *Appl. Phys. A Mater. Sci. Process.* **2022**, *128*, 797. [CrossRef]

29. Nghiem, T.H.L.; Le, T.N.; Do, T.H.; Vu, T.T.D.; Do, Q.H.; Tran, H.N. Preparation and Characterization of Silica-Gold Core-Shell Nanoparticles. *J. Nanoparticle Res.* **2013**, *15*, 2091. [CrossRef]

30. Xia, Y.; Xiong, Y.; Lim, B.; Skrabalak, S.E. Shape-Controlled Synthesis of Metal Nanocrystals: Simple Chemistry Meets Complex Physics? *Angew. Chem. Int. Ed.* **2009**, *48*, 60–103. [CrossRef]

31. Zecchina, A.; Groppo, E.; Bordiga, S. Selective Catalysis and Nanoscience: An Inseparable Pair. *Chem.-A Eur. J.* **2007**, *13*, 2440–2460. [CrossRef] [PubMed]

32. Nehl, C.L.; Hafner, J.H. Shape-Dependent Plasmon Resonances of Gold Nanoparticles. *J. Mater. Chem.* **2008**, *18*, 2415–2419. [CrossRef]

33. Rajapantulu, A.; Bandyopadhyaya, R. Formation of Gold Nanoparticles in Water-in-Oil Microemulsions: Experiment, Mechanism, and Simulation. *Langmuir* **2021**, *37*, 6623–6631. [CrossRef] [PubMed]

34. Revina, A.A.; Chernyshova, K.F.; Tabachkova, N.Y.; Parkhomenko, Y.N. Gold Nanoparticles in Reverse Micellar Solutions: Preparation, Optical Properties, and Dimensional Characteristics. *Russ. Chem. Bull.* **2019**, *68*, 1164–1170. [CrossRef]

35. Yahaya, M.L.; Zakaria, N.D.; Noordin, R.; Abdul Razak, K. Synthesis of Large and Stable Colloidal Gold Nanoparticles (AuNPs) by Seeding-Growth Method. *Mater. Today Proc.* **2022**, *66*, 2943–2947. [CrossRef]

36. Dheyab, M.A.; Aziz, A.A.; Jameel, M.S. Recent Advances in Inorganic Nanomaterials Synthesis Using Sonochemistry: A Comprehensive Review on Iron Oxide, Gold and Iron Oxide Coated Gold Nanoparticles. *Molecules* **2021**, *26*, 2453. [CrossRef]

37. Bianchi, P.; Petit, G.; Monbaliu, J.C.M. Scalable and Robust Photochemical Flow Process towards Small Spherical Gold Nanoparticles. *React. Chem. Eng.* **2020**, *5*, 1224–1236. [CrossRef]

38. Bondaz, L.; Fontaine, P.; Muller, F.; Pantoustier, N.; Perrin, P.; Morfin, I.; Goldmann, M.; Cousin, F. Controlled Synthesis of Gold Nanoparticles in Copolymers Nanomolds by X-ray Radiolysis. *Langmuir* **2020**, *36*, 6132–6144. [CrossRef]

39. Daruich De Souza, C.; Ribeiro Nogueira, B.; Rostelato, M.E.C.M. Review of the Methodologies Used in the Synthesis Gold Nanoparticles by Chemical Reduction. *J. Alloy. Compd.* **2019**, *798*, 714–740. [CrossRef]

40. Rawat, P.; Rajput, Y.S.; Bharti, M.K.; Sharma, R. A Method for Synthesis of Gold Nanoparticles Using 1-Amino-2-Naphthol-4-Sulphonic Acid as Reducing Agent. *Curr. Sci.* **2016**, *110*, 2297–2300. [CrossRef]

41. Johan, M.R.; Chong, L.C.; Hamizi, N.A. Preparation and Stabilization of Monodisperse Colloidal Gold by Reduction with Monosodium Glutamate and Poly (Methyl Methacrylate). *Int. J. Electrochem. Sci.* **2012**, *7*, 4567–4573.

42. Yang, S.K.; Kim, Y. Nanogold Particles Produced by $NaBH_4$ Reduction of Gold Salt in the Presence of Laponite Sol. *Bull. Korean Chem. Soc.* **2013**, *34*, 363–364. [CrossRef]

43. Newman, J.D.S.; Blanchard, G.J. Formation of Gold Nanoparticles Using Amine Reducing Agents. *Langmuir* **2006**, *22*, 5882–5887. [CrossRef] [PubMed]

44. Khan, Z.; Singh, T.; Hussain, J.I.; Hashmi, A.A. Au(III)-CTAB Reduction by Ascorbic Acid: Preparation and Characterization of Gold Nanoparticles. *Colloids Surf. B Biointerfaces* **2013**, *104*, 11–17. [CrossRef]

45. Mallikarjuna, K.; Sushma, N.J.; Deva Prasad Raju, B. Novel, Fast, Bio-Derivatized Sonochemical Synthesis of Gold Nanoparticles by Using Piper Betle Leaf Broth as a Reducing and Capping Agent. In *Springer Proceedings in Physics*; Springer: Berlin/Heidelberg, Germany, 2013; Volume 143, pp. 41–49. ISBN 9783642342158.

46. Boruah, S.K.; Boruah, P.K.; Sarma, P.; Medhi, C.; Medhi, O.K. A Study on the Electrospinning Behaviour and Nanofibre Morphology of Anionically Charged Lignin. *Adv. Mater. Lett.* **2012**, *3*, 481–486. [CrossRef]

47. Wu, S.; Yan, S.; Qi, W.; Huang, R.; Cui, J.; Su, R.; He, Z. Green Synthesis of Gold Nanoparticles Using Aspartame and Their Catalytic Activity for P-Nitrophenol Reduction. *Nanoscale Res. Lett.* **2015**, *10*, 213. [CrossRef] [PubMed]

48. Das, S.K.; Das, A.R.; Guha, A.K. Gold Nanoparticles: Microbial Synthesis and Application in Water Hygiene Management. *Langmuir* **2009**, *25*, 8192–8199. [CrossRef]

49. Turkevich, J.; Stevenson, P.C.; Hillier, J. A Study of the Nucleation and Growth Processes in the Synthesis of Colloidal Gold. *Discuss. Faraday Soc.* **1951**, *11*, 55–75. [CrossRef]

50. Verma, H.N.; Singh, P.; Chavan, R.M. Gold Nanoparticle: Synthesis and Characterization. *Vet. World* **2014**, *7*, 72–77. [CrossRef]

51. Schulz, F.; Homolka, T.; Bastús, N.G.; Puntes, V.; Weller, H.; Vossmeyer, T. Little Adjustments Significantly Improve the Turkevich Synthesis of Gold Nanoparticles. *Langmuir* **2014**, *30*, 10779–10784. [CrossRef]

52. Dozol, H.; Mériguet, G.; Ancian, B.; Cabuil, V.; Xu, H.; Wang, D.; Abou-Hassan, A. On the Synthesis of Au Nanoparticles Using EDTA as a Reducing Agent. *J. Phys. Chem. C* **2013**, *117*, 20958–20966. [CrossRef]

53. Chae, S.Y.; Son, S.; Lee, M.; Jang, M.K.; Nah, J.W. Deoxycholic Acid-Conjugated Chitosan Oligosaccharide Nanoparticles for Efficient Gene Carrier. *J. Control. Release* **2005**, *109*, 330–344. [CrossRef] [PubMed]

54. Rodrigues, M.S.; Borges, J.; Lopes, C.; Pereira, R.M.S.; Vasilevskiy, M.I.; Vaz, F. Gas Sensors Based on Localized Surface Plasmon Resonances: Synthesis of Oxide Films with Embedded Metal Nanoparticles, Theory and Simulation, and Sensitivity Enhancement Strategies. *Appl. Sci.* **2021**, *11*, 5388. [CrossRef]

55. Uzair, B.; Liaqat, A.; Iqbal, H.; Menaa, B.; Razzaq, A.; Thiripuranathar, G.; Fatima Rana, N.; Menaa, F. Green and Cost-Effective Synthesis of Metallic Nanoparticles by Algae: Safe Methods for Translational Medicine. *Bioengineering* **2020**, *7*, 129. [CrossRef]

56. Britto Hurtado, R.; Cortez-Valadez, M.; Ramírez-Rodríguez, L.P.; Larios-Rodriguez, E.; Alvarez, R.A.B.; Rocha-Rocha, O.; Delgado-Beleño, Y.; Martinez-Nuñez, C.E.; Arizpe-Chávez, H.; Hernández-Martínez, A.R.; et al. Instant Synthesis of Gold Nanoparticles at Room Temperature and SERS Applications. *Phys. Lett. A* **2016**, *380*, 2658–2663. [CrossRef]

57. Nguyen, D.T.; Kim, D.J.; So, M.G.; Kim, K.S. Experimental Measurements of Gold Nanoparticle Nucleation and Growth by Citrate Reduction of HAuCl$_4$. *Adv. Powder Technol.* **2010**, *21*, 111–118. [CrossRef]

58. Neupane, M.P.; Lee, S.J.; Park, I.S.; Lee, M.H.; Bae, T.S.; Kuboki, Y.; Uo, M.; Watari, F. Synthesis of Gelatin-Capped Gold Nanoparticles with Variable Gelatin Concentration. *J. Nanoparticle Res.* **2011**, *13*, 491–498. [CrossRef]

59. Nellore, J.; Pauline, P.C.; Amarnath, K. Biogenic Synthesis by Sphearanthus Amaranthoids; towards the Efficient Production of the Biocompatible Gold Nanoparticles. *Dig. J. Nanomater. Biostructures* **2012**, *7*, 123–133.

60. Robb, D.T.; Privman, V. Model of Nanocrystal Formation in Solution by Burst Nucleation and Diffusional Growth. *Langmuir* **2008**, *24*, 26–35. [CrossRef]

61. Thanh, N.T.K.; Maclean, N.; Mahiddine, S. Mechanisms of Nucleation and Growth of Nanoparticles in Solution. *Chem. Rev.* **2014**, *114*, 7610–7630. [CrossRef]

62. Mountrichas, G.; Pispas, S.; Kamitsos, E.I. Effect of Temperature on the Direct Synthesis of Gold Nanoparticles Mediated by Poly(Dimethylaminoethyl Methacrylate) Homopolymer. *J. Phys. Chem. C* **2014**, *118*, 22754–22759. [CrossRef]

63. Lim, S.; Gunasekaran, S.; Imm, J.Y. Gelatin-Templated Gold Nanoparticles as Novel Time-Temperature Indicator. *J. Food Sci.* **2012**, *77*, N45–N49. [CrossRef] [PubMed]

64. Mock, A.J.; Kang, J. Comment on Degradation of Ascorbic Acid in Ethanolic Solutions. *J. Agric. Food Chem.* **2013**, *61*, 2580–2582. [CrossRef] [PubMed]

65. Yuan, J.P.; Chen, F. Degradation of Ascorbic Acid in Aqueous Solution. *J. Agric. Food Chem.* **1998**, *46*, 5078–5082. [CrossRef]

66. Mohanty, B.; Bohidar, H.B. Systematic of Alcohol-Induced Simple Coacervation in Aqueous Gelatin Solutions. *Biomacromolecules* **2003**, *4*, 1080–1086. [CrossRef]

67. Suarasan, S.; Focsan, M.; Soritau, O.; Maniu, D.; Astilean, S. One-Pot, Green Synthesis of Gold Nanoparticles by Gelatin and Investigation of Their Biological Effects on Osteoblast Cells. *Colloids Surf. B Biointerfaces* **2015**, *132*, 122–131. [CrossRef]

68. Allouche, J.; Soulé, S.; Dupin, J.C.; Masse, S.; Coradin, T.; Martinez, H. Design of Gold Nanoshells via a Gelatin-Mediated Self-Assembly of Gold Nanoparticles on Silica Cores. *RSC Adv.* **2014**, *4*, 63234–63237. [CrossRef]

Article

Numerical Investigation of the Ribs' Shape, Spacing, and Height on Heat Transfer Performance of Turbulent Flow in a Flat Plate Heat Exchanger

Ahmed Saad Soliman [1,*] , Li Xu [2], Junguo Dong [2] and Ping Cheng [2]

1 Mechanical Power Engineering Department, Mansoura University, El-Mansoura 35516, Egypt
2 School of Environmental and Chemical Engineering, Shanghai University, Shanghai 200444, China
* Correspondence: asaad200@mans.edu.eg

Abstract: This paper presents a numerical study of detailed heat transfer and flow field characteristics in a flat plate heat exchanger with different types of ribs (rectangular and triangular) with different heights (H: 2.5, 5, 7.5, and 10 mm) and spacings (S: 75, 95, 128, and 195 mm). A comprehensive numerical model was established and validated with experimental data in the literature, resulting in good agreement. The effects of the height, spacing, and shape of the ribs in addition to thermal-hydraulic parameters were investigated over two values of the Reynolds number (9880–3210). The results concluded that the highest values of the thermal-hydraulic parameters are 1.62 and 1.84 for the hot and cold air sides, in the rectangular ribs, with a thickness, height, and spacing of 75 mm, and 95 mm, respectively. It is worth mentioning that the rectangular ribs have the maximum value of thermal performance at the high and low values of the Reynolds number of turbulent flows. The present design can be used in waste heat recovery systems.

Keywords: numerical simulation; heat transfer enhancement; turbulent flow; plate heat exchanger

1. Introduction

Heat transfer augmentation techniques are essential in many industrial applications because they allow for compact heat exchangers with high thermal performance [1].

Several studies have shown interest in improving heat transfer in engineering applications. There are typically three methods for improving heat transfer: Active, passive, and compound techniques. In the active technique, an external source of energy is required to enhance the heat transfer such as surface vibration, magnetic field, jet impingement, etc. In the passive technique, the configuration of the system has some modifications to improve the heat transfer such as ribs and dimples, rough surfaces, nanoparticles, etc. In the compound technique, the combination of active and passive methods occurs [2].

The passive technique can be divided into three groups (using nanoparticles, geometry modifications, and a combination between nanoparticles and geometry modifications) as follows:

Firstly, nanoparticles are added to the fluid to create nanofluids. Nanofluids have recently been seen as a promising choice for thermal fluids and can be effectively used for heat transfer. The nanofluids significantly enhance the heat exchanger's thermal performance in various applications, such as CPU (central processing unit) coolers [3] and annulus and plate heat exchangers [4]. On the other hand, the nanoparticles were also added to phase-change materials (PCMs) to enhance their thermal conductivity in different applications [5,6].

Secondly, geometry modifications are made by using dimples [7] or roughening the heat transfer surfaces using grooves, ribs or wires, or helically corrugated tubes [8–10]. Artificial roughness is used in several applications such as evaporators, steam condensers, blades of gas turbines, cooling channels, heat exchangers, and solar air heaters [11,12].

Due to the secondary flow areas that form near the wall and decrease the thickness of the thermal boundary layer in a way that increases the rate of heat transfer, these modified geometries produce good mixing in the fluid flow.

Unfortunately, adopting these methods to speed up the heat transfer rate sometimes results in an increase in the pressure drop as a side effect [8,9]. The impact of the channel rib and flow features on heat transfer and friction factor characteristics has been demonstrated by several experimental and numerical studies [13,14].

Moon et al. [15] numerically investigated the configuration of 16 ribs with various cross-sectional shapes and found that boot-shaped rib turbulators have the maximum heat transfer performance with a similar pressure penalty to that of the square rib. In addition, the size of the recirculating zone is directly impacted by the slope of the front surface of the rib, making it a crucial component in determining the performance of heat transfer.

Pingan et al. [11] numerically studied the heat transfer of the airflow in a channel with various rib shapes (triangular, semi-circular, and rectangular) using a standard k-ε turbulent model with enhanced wall treatment. It was found that the maximum and minimum values of the average Nusselt number of the channel occurred with the triangular and rectangular ribs, respectively.

Finally, several researchers concentrated on utilizing both previous methods of enhancing heat transfer (using ribs and nanoparticles). For instance, Wongcharee and Eiamsa-ard [16] conducted an experimental study on the flow of a turbulent CuO-water nanofluid inside a corrugated tube. It was observed that the heat transfer for this geometry increases by 1.57 times compared to the pure fluid inside the simple tube when a 0.7% volume fraction of CuO is used.

Manca et al. [17] numerically investigated the turbulent forced convection of an Al_2O_3-water nanofluid in a ribbed channel with different rib shapes (square and rectangular). It was observed that although there is a greater pressure drop penalty, the enhancement of heat transfer grows with the volume fraction of the particles and Reynolds number. The pressure drop and heat transfer rate are improved by using the ribbed surfaces and adding nanoparticles to the base fluid.

Overall, the spanwise vortices created by the ribs break up the boundary layer and cause flow separation and reattachment in the inter-rib area, which causes turbulence. A higher rate of convective heat transfer results from the high magnitude of turbulent transport because it improves heat exchange through good mixing. However, the rib turbulators also increase the pressure drop and the consumption of energy, which has an impact on the thermal system's total thermo-hydraulic performance [18]. Therefore, finding the optimum rib design is crucial in order to maximize heat transfer while minimizing pressure drop.

As previously mentioned, the flow behavior in ribbed channels was studied to produce a significant enhancement in heat transfer rates. The flow recirculation patterns around a single rib are described by Cho et al. [19]. A large recirculation zone is created at the lee-side regions downstream of the rib, accompanied by a small vortex in the vicinity of the bottom corner of the rib. These recirculation zones encompass a sizable portion of the rib and bottom wall, which is frequently regarded as having poor heat transfer and locally low surface Nusselt numbers [20].

Consequently, the optimum design is the case that increases the performance of heat transfer with a small value of pressure drop. Therefore, to obtain the best design conditions, a trade-off between the increase in heat transfer and the decrease in the pressure drop should be performed.

It can be observed from the previous literature review that most of the studies focused separately on the effect of the rib shape, spacing, and height in a duct or a tube with one fluid. The optimum rib shape in a counter flat plate heat exchanger (hot and cold flow) for a complete heat transfer process between two turbulent fluids has not been studied before.

This research gap is the aim of this paper, and the present design can be used in waste heat recovery systems. In the present paper, the influence of the different rib shapes

(rectangular and triangular) with different heights (H: 2.5, 5, 7.5, and 10 mm) and spacing (S: 75, 95, 128, and 195 mm) is investigated on the performance of the heat transfer and pressure drop. The thermal-hydraulic parameter, which combines an enhancement of the rate of heat transfer and the pressure drop due to friction, is also studied on hot and cold sides to obtain the best design of the flat plate heat exchanger.

2. Theoretical Modeling

The current work studied the different types of rib shapes, heights, and spaces to optimize the design that can improve the thermal performance of the heat exchanger. The flat plate heat exchanger consisted of five channels: Three channels for the hot air flow (at Re = 3210 and T = 260 °C) and two channels for the cold air flow (at Re = 9880 and T = 27 °C). The previous conditions were selected to match the velocity of the hot fluid (exhaust gases) and cold fluid (intake air) in waste heat recovery systems, especially for a cold start-up in diesel engines as in Ref [6,21]. The length and width of the heat exchanger were 400 mm and 180 mm, respectively, with a 30 mm height for the hot and cold channels. A counterflow was created between the hot and cold air, which can increase the heat transfer between them. The cold air passes through two channels (L × W × H: 400 × 180 × 30 mm) and the hot air passes through three channels of the same dimensions. The separation wall between the hot and cold channels was made of aluminum with a 4 mm thickness. Two types of ribs (rectangular and triangular shapes) were studied to compare the results and obtain the optimum design.

Different numbers of ribs with increasing spacings (S: 75, 95, 128, and 195 mm) and heights (H: 2.5, 5, 7.5, and 10 mm) in two shapes (rectangular and triangular) were simulated in cases A, B, C, and D. The rectangular ribs were represented in case A, and the triangular ribs with sloping in the direction of the cold airflow and the hot airflow were represented in cases B and C, respectively. The previously mentioned cases with case D (no ribs) are displayed in Figure 1, and the geometry of the triangular and rectangular ribbed flat plate heat exchangers is presented in Figure 2.
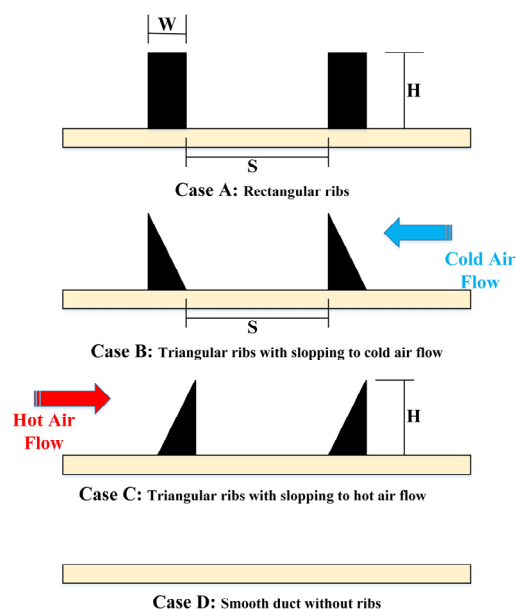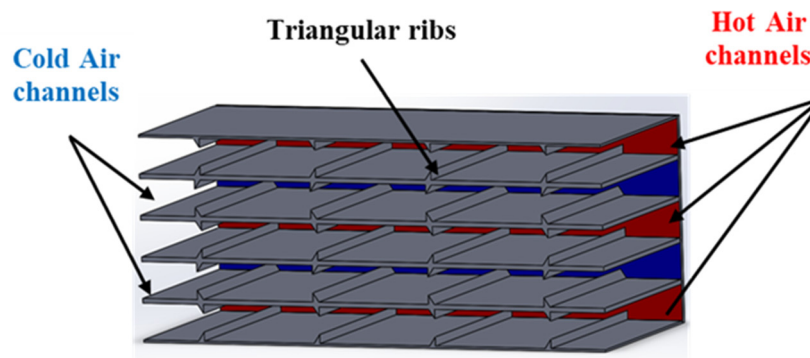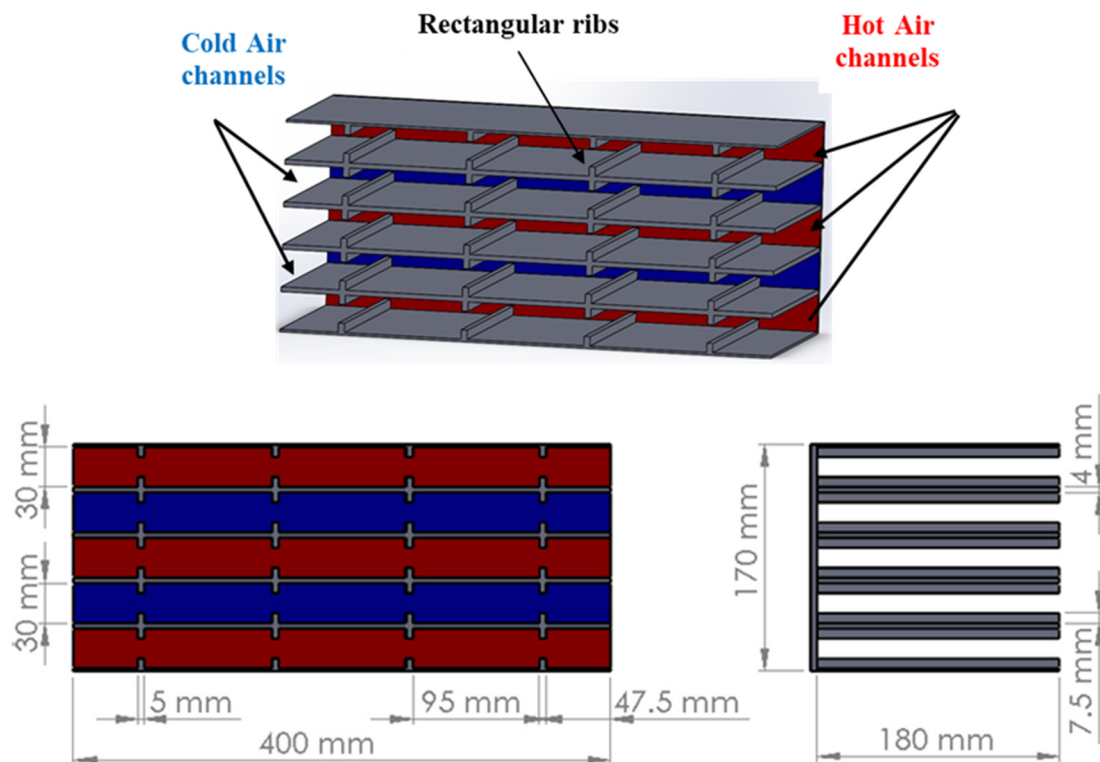

Figure 1. Rib configurations.

Figure 2. Heat exchanger with (**a**) triangular and (**b**) rectangular ribs.

The turbulent renormalization group model (RNG k-ε model) displays the flow regime of the turbulent flow of the cold and hot air. The governing equations that rule the heat transfer and the motion of a fluid are the continuity, momentum, and energy equations, which can be described as follows [6,21]:

Continuity:

$$\frac{\partial \rho}{\partial t} + \frac{\partial}{\partial x_i}(\rho u_i) = 0 \tag{1}$$

Momentum:

$$\frac{\partial}{\partial t}(u_i) + \frac{\partial}{\partial x_j}(u_i u_j) = -\frac{1}{\rho}\frac{\partial P}{\partial x_i} + \frac{\partial}{\partial x_j}\left(\nu S_{ij} - \overline{u'_i u'_j}\right) \tag{2}$$

where S_{ij} is the main strain rate and is estimated by the following equation:

$$S_{ij} = \frac{1}{2}\left(\frac{\partial u_i}{\partial x_j} + \frac{\partial u_j}{\partial x_i}\right) \tag{3}$$

$\overline{u'_i u'_j}$ represents the unknown turbulent or Reynolds-stress tensor and u'_i signifies the velocity fluctuation in the i-direction.

Energy:

$$\frac{\partial}{\partial t}(\rho E) + \frac{\partial}{\partial x_i}[u_i(\rho E + p)] = \frac{\partial}{\partial x_j}\left[\left(k + \frac{c_p \mu_t}{Pr_t}\right)\frac{\partial T}{\partial x_j} + u_i(\tau_{ij})_{\text{eff}}\right] \tag{4}$$

where E indicates the total energy, (τ_{ij}) eff denotes the stress tensor, k represents the thermal conductivity (W/m °C), and Pr_t is a turbulent Prandtl number.

$$(\tau_{ij})_{eff} = \mu_{eff}\left[\frac{\partial u_j}{\partial x_j} + \frac{\partial u_i}{\partial x_j}\right] - \frac{2}{3}\mu_{eff}\frac{\partial u_i}{\partial x_i}\delta_{ij} \tag{5}$$

The description of turbulence using two transport partial differential equations is given by the k-ε model (PDEs). It can be divided into three types, standard, renormalization group (RNG), and realizable k-ε models. The theory of the renormalization group is a statistical technique that is used to develop the RNG model. The transport equation of k (turbulence kinetic energy) and ε (turbulence dissipation rate) for steady flow can be defined as follows [22]:

$$\frac{\partial}{\partial t}(\rho k) + \frac{\partial}{\partial x_i}(\rho k u_i) = \frac{\partial}{\partial x_j}\left[\alpha_k \mu_{eff}\frac{\partial k}{\partial x_j}\right] + G_k + G_b - \rho_\varepsilon - Y_M + S_k \tag{6}$$

and

$$\frac{\partial}{\partial t}(\rho\varepsilon) + \frac{\partial}{\partial x_i}(\rho\varepsilon u_i) = \frac{\partial}{\partial x_j}\left[\alpha_\varepsilon \mu_{eff}\frac{\partial \varepsilon}{\partial x_j}\right] + C_{1\varepsilon}\frac{\varepsilon}{k}(G_k + C_{3\varepsilon}G_b) - C_{2\varepsilon}\rho\frac{\varepsilon^2}{k} + S_\varepsilon \tag{7}$$

where:

μ_{eff} denotes the effective viscosity at the high values of Reynolds numbers.

α_k and α_ε indicate the inverse effective Prandtl numbers ($\alpha_k = \alpha_\varepsilon = 1.393$).

G_k is the generation of turbulence kinetic energy due to the mean velocity gradients.

G_b is the generation of turbulence kinetic energy due to buoyancy.

Y_M is the effect of the fluctuating dilatation incompressible turbulence on the overall dissipation rate.

S_k and S_ε are user-defined source terms.

$$\mu_{eff} = \rho C_\mu \frac{k^2}{\varepsilon} \tag{8}$$

The present model is established by the following model constants: $C_\mu = 0.0845$, $C_{1\varepsilon} = 1.44$, and $C_{2\varepsilon} = 1.92$.

The enhancement of the heat transfer rate can be calculated in terms of the thermal-hydraulic parameter (η), which is described by the following equation [23]:

$$\eta = \frac{\frac{Nu}{Nu_s}}{\left(\frac{f}{f_s}\right)^{\left(\frac{1}{3}\right)}} \tag{9}$$

where f and f_s represent the friction coefficients for the ribbed channel and the smooth channel, respectively. In addition, Nu and Nu_s are the Nusselt numbers for the ribbed channel and the smooth channel, respectively.

The thermal-hydraulic parameter combines the enhancement of the rate of heat transfer and the pressure drop due to friction to obtain the best design of the flat plate heat exchanger.

3. Numerical Simulation

Numerical simulations were carried out to analyze the process of heat transfer using commercial code ANSYS 2022 R2, thereby employing a finite volume approach to discretize the governing equations.

3.1. Boundary and Initial Conditions

The entire device was initially at an ambient temperature of 27 °C. For the inlet of both the hot and cold airflow, a uniform velocity distribution with uniform temperature was created. The boundary conditions for the inlets of the duct were estimated to be a velocity inlet. At the same time, the pressure outlets were selected for the duct's exits and the outer walls of the heat exchangers were insulated.

3.2. Solution Procedures

The turbulence model for hot and cold airflows was considered along with initial and boundary conditions. The numerical simulation of the model was developed using ANSYS 2022 R2 software. The pressure–velocity coupling equations were determined using the semi-implicit method for the pressure-linked equations (SIMPLE) scheme. The governing equations in conjunction with the boundary and initial conditions were described using a control volume approach. The central difference and QUICK schemes were used to describe the diffusion and convection terms, respectively. For velocity–pressure coupling, the SIMPLER algorithm was applied. Iterative calculations were nonstop until all problem variables satisfied a relative convergence criterion of 10^{-6}.

3.3. Model Validation

The present model was numerically solved, and the predicted results were compared with the experimentally published results of the turbulence model. Under the same operating conditions, the numerical results were validated.

The turbulent flow through the hot and cold air channels was fabricated, and the numerical model recognized in this work was validated against the numerical study by Menge et al. [24]. Figure 3 illustrates the boundary conditions of the published model [24] as follows: The inlet boundary is defined as a velocity inlet with a uniform velocity of 1 m/s. In addition, at the inlet, the relative turbulent intensity is equal to 5%. The outlet boundary is defined as a pressure outlet with an average static reference pressure of 0 Pa. The Solver was double precision, pressure based, and implicit. The pressure–velocity coupling was SIMPLE, and the turbulent kinetic energy and the turbulent dissipation rate were second-ordered upwind with a convergence criterion of 1×10^{-6}.
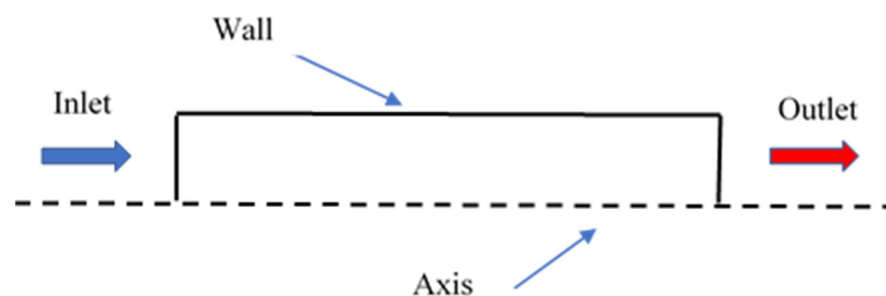

Figure 3. Boundary conditions of the published model [24].

Figure 4 indicates the relationship between the axial velocity and the pipe inlet position to the point at which the entire pipe reaches a constant value using the present numerical model and the published model. As seen in the figure, they match each other well.
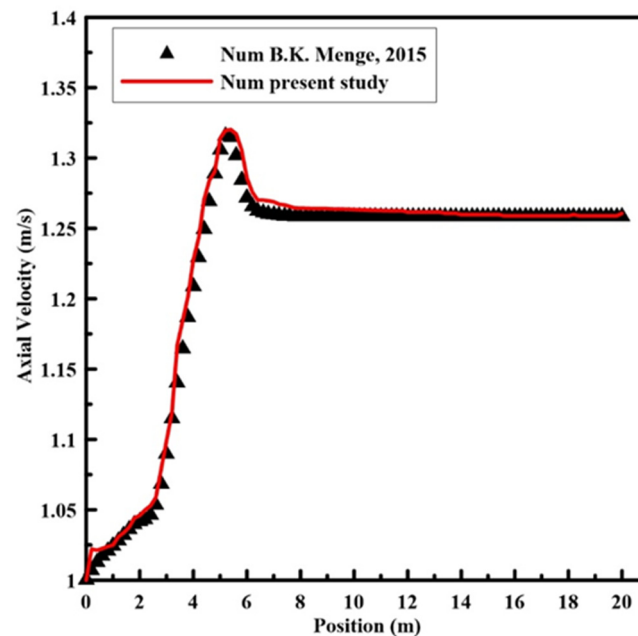

Figure 4. Numerical axial velocity of [24] and the present model versus the distance from the pipe inlet.

3.4. Mesh Generation and Mesh Independence Test

ANSYS-Design Modeler 2022 R2 software was used to create the fluid domain for a fully developed channel with a certain height (*h*). The dimensions were chosen to confirm a fully developed flow and to facilitate a comparison with Blasius. The fluid region was discretized by using the finite element method through the ANSYS-Mesh 2022 R2. Two different techniques are used to distribute the cell through the cold and hot channels. Firstly, through the channel length in the x-direction, the cells were uniformly distributed. Secondly, through the channel height in the y-direction, the cells were non-uniformly distributed. The grid was recognized so that it could capture the velocity distribution in all near-wall regions of the flow. ANSYS-Mesh 2022 R2 software was used to generate the mesh independence test with a non-uniform range of cells. The cell number started with 20 to 50 cells, which were distributed through the height of the channel with a growth rate (GR) equal to 1.1. The RNG k-ε model was employed with enhanced wall treatment, which can be simulated in the near-wall region. Using this option, the height of the first cell near the wall, which is called y^+, is acceptable when $y^+ < 4$ [22]. A numerical study was established to study the two-dimensional (2-D) flow and heat transfer in the ribbed duct at two values of Reynolds numbers when using rectangular and triangular ribs.

In FLUENT, the finite volume technique was used to solve the continuity, momentum, and energy equations that define heat transfer and fluid flow under given boundary conditions. The continuity and momentum equation residuals have been estimated to be 10^{-4} and 10^{-6} for the energy equation.

Figure 5 compares the skin coefficient values (C_f) at different cell numbers per height for both hot and cold channels, and the skin coefficient drops with the increase in the cell number. The relationship between the skin coefficients of both hot and cold channels at different values of the first cell height y^+ ($y^+ = u_\tau y / \nu$) is shown in Figure 6, and the skin coefficient declines when reducing the first cell height.
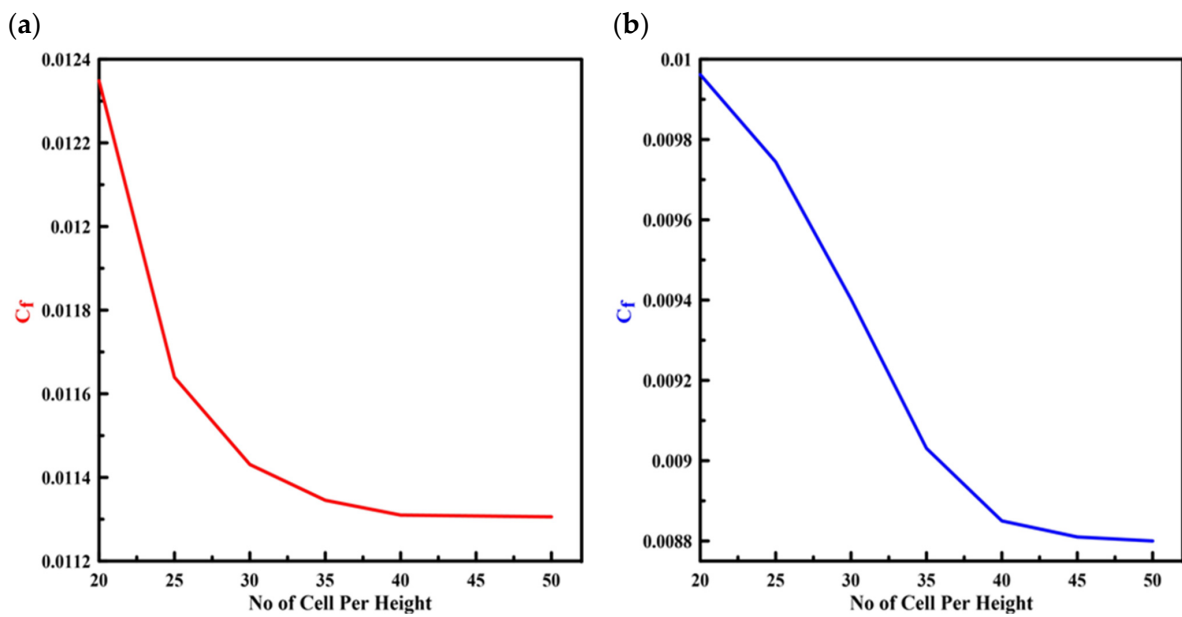
(a)

(b)

Figure 5. Skin coefficient with the number of cells per height for (**a**) hot air and (**b**) cold air.
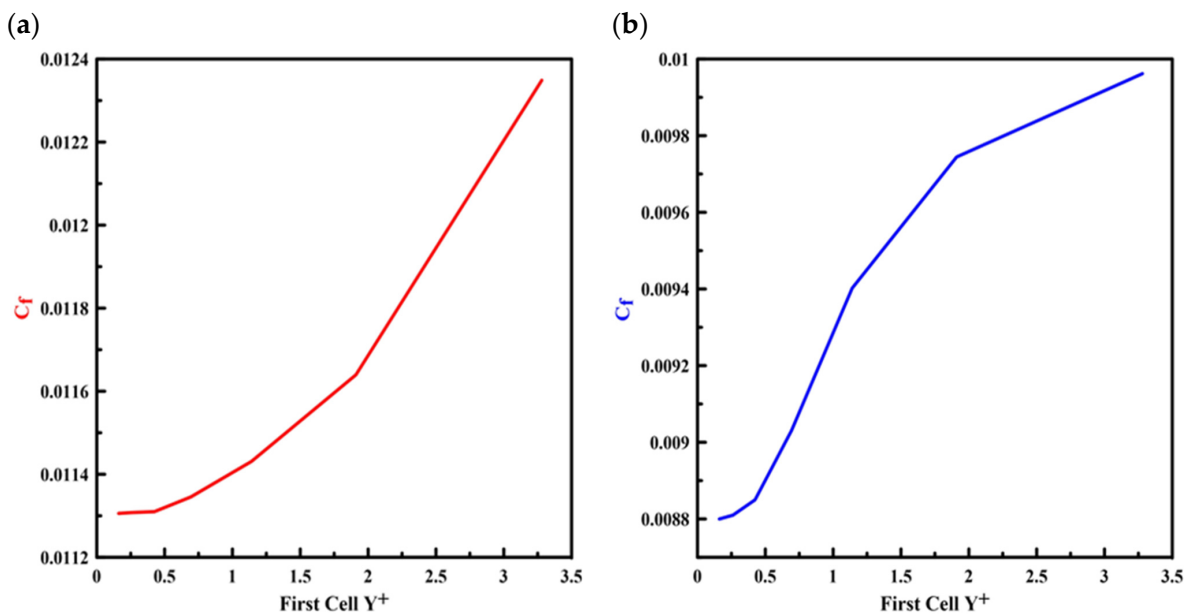
(a)

(b)

Figure 6. Skin coefficient versus the height of the first cell (y^+) for (**a**) hot air and (**b**) cold air.

It is observed from the figures that, for both hot and cold air flows, the skin coefficient value shows a slight change when the number of cells per height increases above 45 cells. Thus, the optimal cell number per channel height with a small error in the results is 45 cells at a growth rate of 1.1 and y^+ of 0.26.

4. Results and Discussion

The obtained results elucidate the effect of rectangular and triangular ribs on the thermal performance of the flat plate heat exchanger and compare them to obtain the optimum design.

4.1. Flow Structure in Ribbed Duct

The main concept of designing ribbed ducts is to achieve higher flow turbulence and hence greater heat transfer. The predicted velocity contours for the rectangular and

triangular ribs are shown in Table 1. It can be observed that both hot and cold airflow accelerates and decelerates through the passage due to the contraction and expansion caused by the ribs.

Table 1. Velocity contours for the rectangular and triangular ribs.

Rectangular Ribs	Triangular Ribs

195 mm spacing

128 mm spacing

95 mm spacing

75 mm spacing
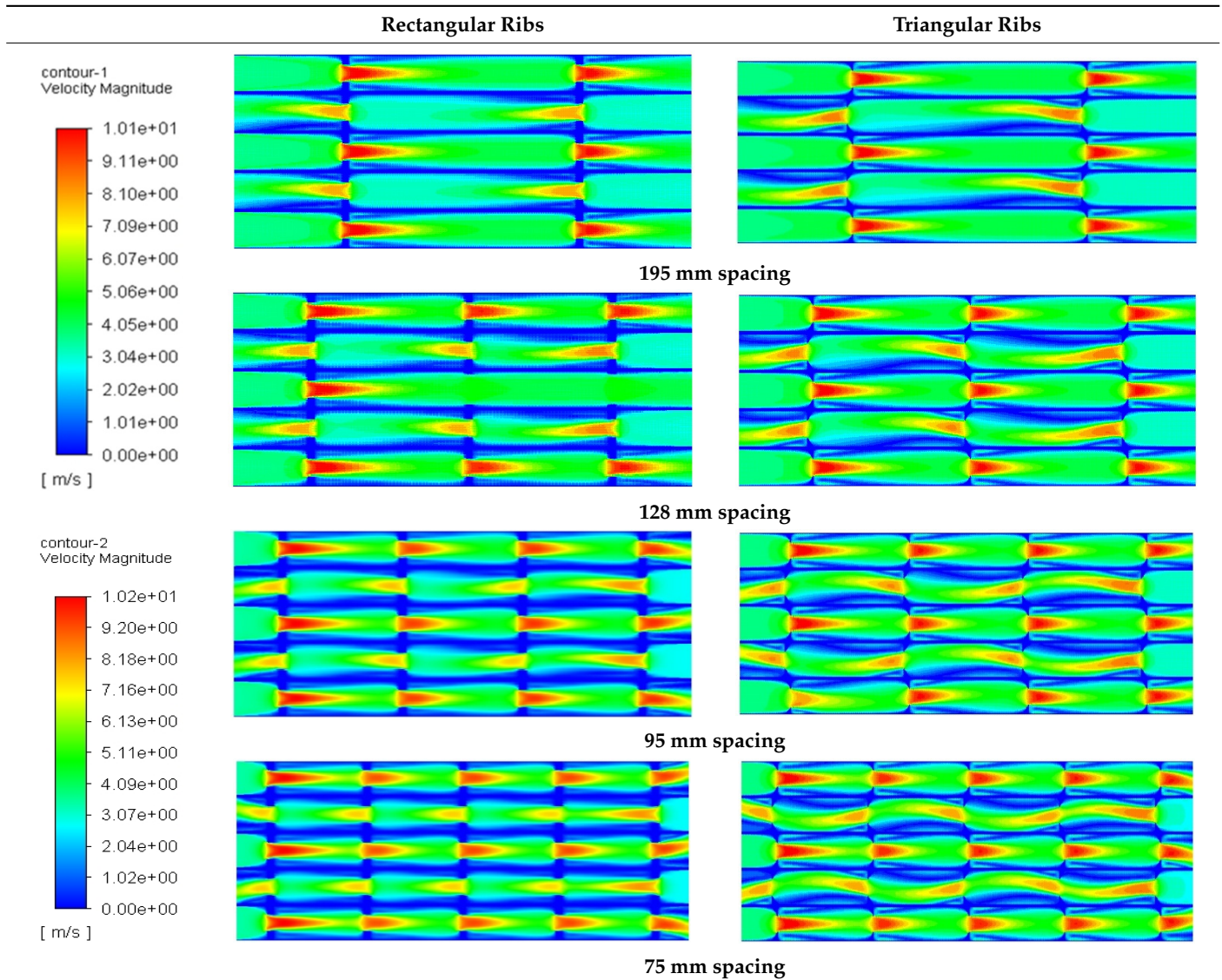
In the triangular ribs, the fluid motion of a highly turbulent Reynolds number in the cold airflow has a wavy style due to the slope of the ribs. In addition, the recirculation regions developed by the ribs are increased with the increase in the Reynolds number as mentioned in Ref [25]. However, through the rectangular ribs, the fluid motion through the high- and low-turbulence Reynolds numbers is stable. The flow separates and then reattaches as mentioned in Refs [26,27]; therefore, there is non-complete contact with the wall at some points on the cold air side (high Reynolds number), but on the hot air side (low Reynolds number), it is uniform in the triangular ribs.

In the rectangular ribs, when the flow is on the upper side, a large recirculation zone is created at the lee-side regions on the lower side of the rib. Moreover, when the flow is on the lower side, a large recirculation zone is created at the lee-side regions on the upper side of the rib. For both of the previous positions, there is a small vortex in the vicinity of the bottom corner of the rib. This description of the flow is in agreement with that mentioned in Ref [19]. These recirculation zones encompass a sizable portion of the rib and bottom

wall, which is frequently regarded as having poor heat transfer and locally low surface Nusselt numbers [20]. On the other hand, the low Reynolds number in the hot airflow has no wavy motion through the velocity contours.

Table 2 shows the contours of the turbulence intensity for all cases of the RNG turbulence model. It can be realized from these contours that the turbulence intensity is higher downstream of the upper edge of the ribs where the major shear layer region is located due to the non-uniform velocity and motion of the fluid through the triangular ribs as mentioned before due to the separation and reattaching of the fluids. This motion makes non-complete contact with the wall at some points on the cold air side (high Reynolds number) but the hot air side (low Reynolds number) is uniform. The turbulence intensity is also non-uniform, especially in the highly turbulent Reynolds number as in the cold airflow.

Table 2. Turbulence intensity contours for the rectangular and triangular ribs.
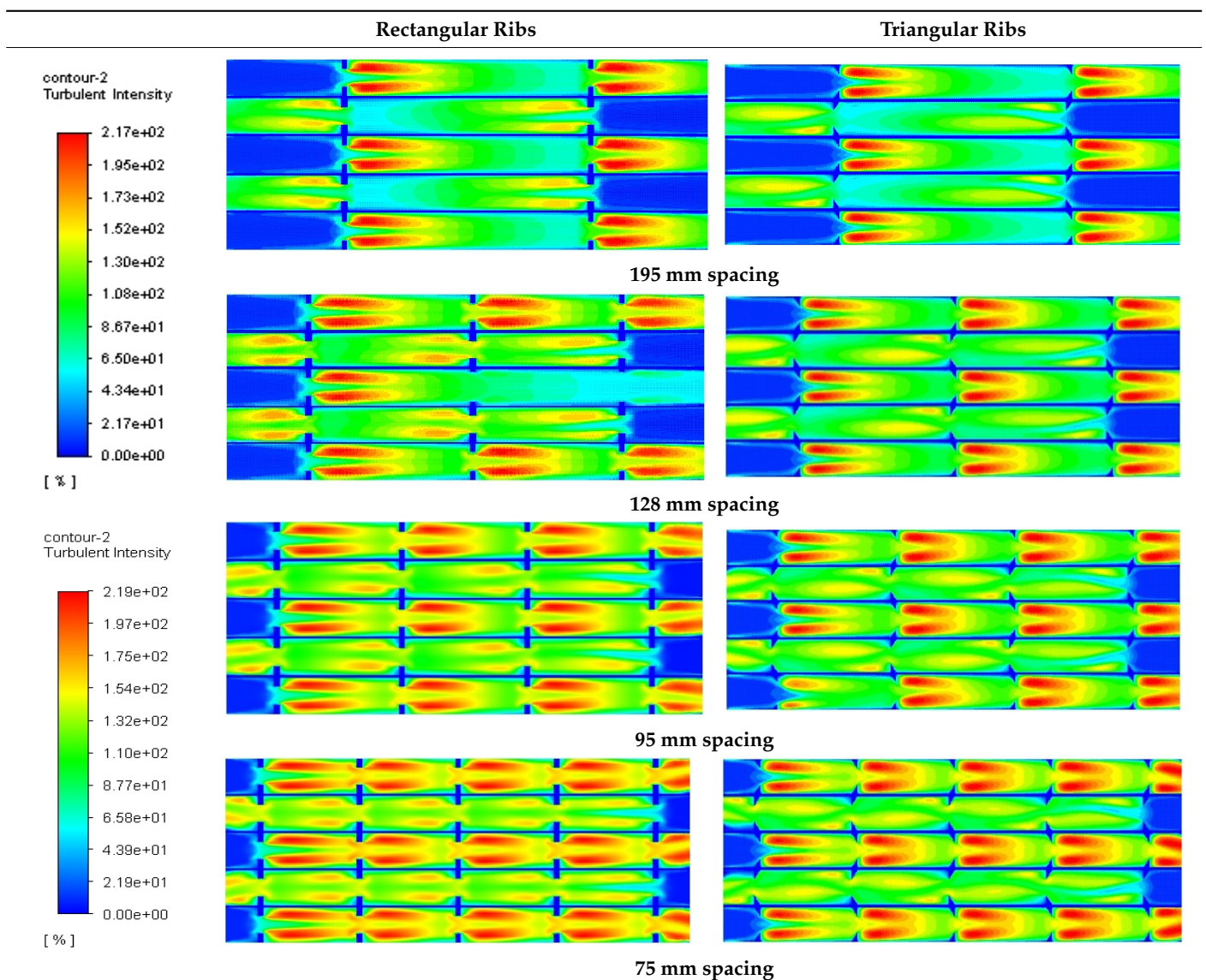
As shown in the contours, the weak and robust intensity is established according to the cold air position after the ribs. The cold-air-side turbulence intensity in rectangular ribs is higher than in triangular ribs due to the aforementioned intensity fluctuations. However, on the hot air side, the slope of the triangular ribs causes the intensity after the ribs to be more concentrated than the rectangular ones.

The predicted contours of the temperature distribution for the ribbed cross-sectional passages are shown in Table 3. It was found that the temperature of both fluids near the wall was most affected by the ribs. Due to the effect on the circulation generated by the ribs, the heat transfer between the cold and hot fluid flows is increased.

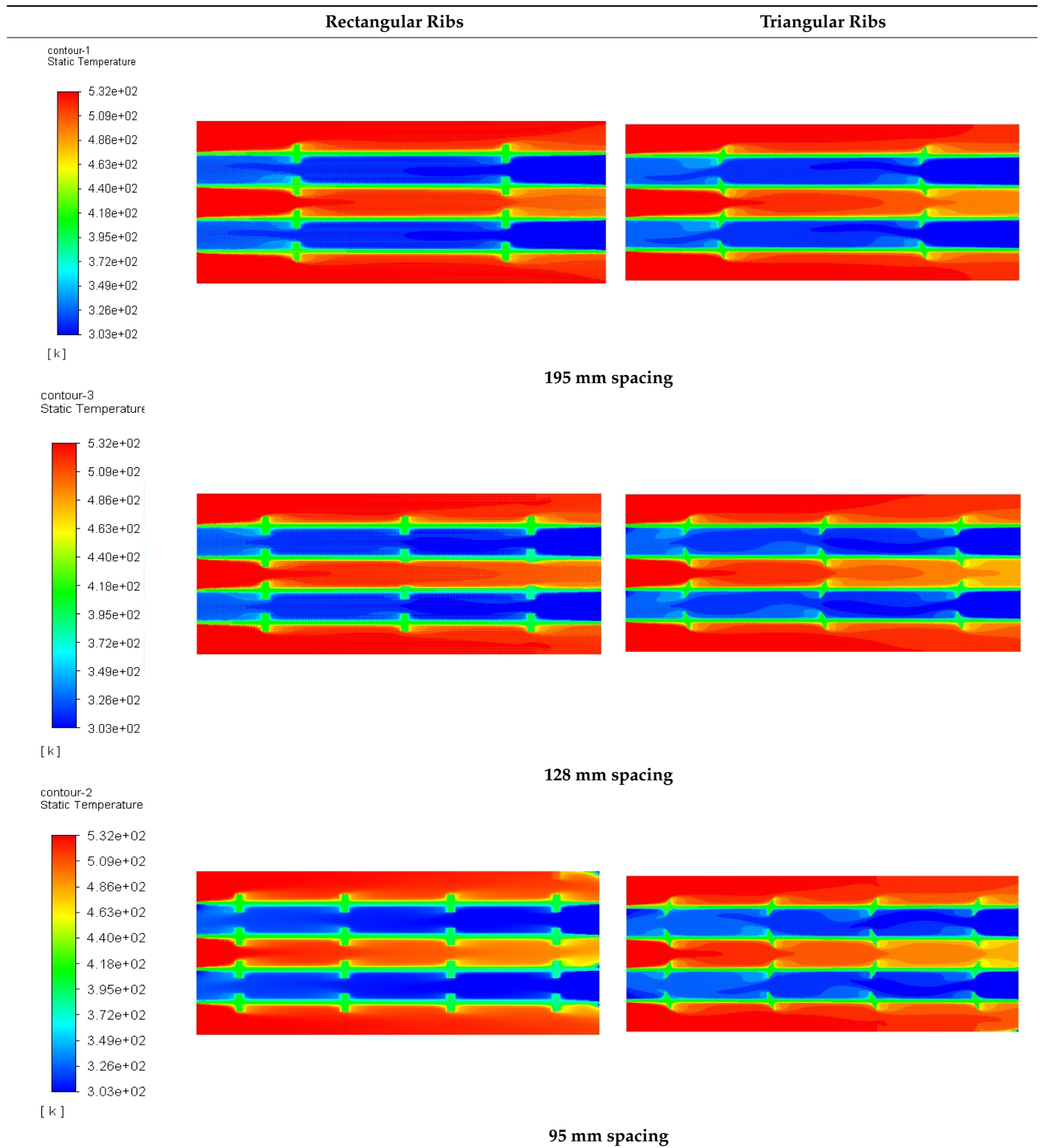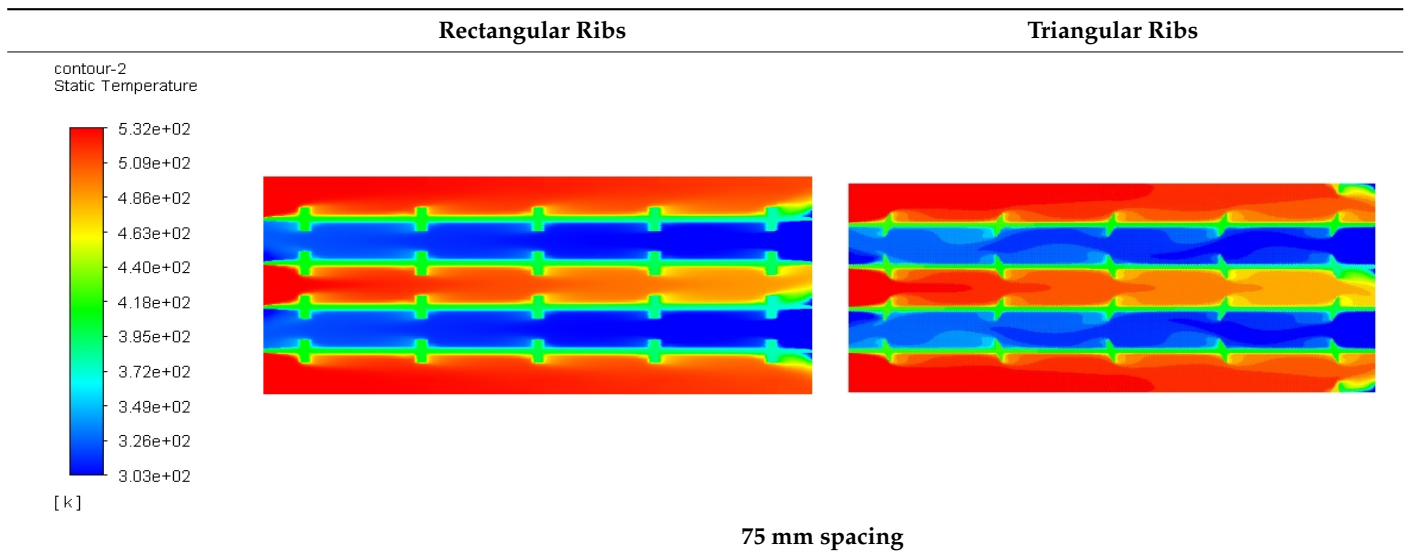**Table 3.** Temperature contours for the rectangular and triangular ribs.

Rectangular Ribs	Triangular Ribs

195 mm spacing

128 mm spacing

95 mm spacing

Table 3. *Cont.*

Rectangular Ribs	Triangular Ribs

75 mm spacing

4.2. The Ribs' Height Effect

Figure 7 illustrates the variation of the convection heat transfer coefficient for the hot and cold channels with different heights, spacings, and shapes of ribs. The figure also demonstrates that the convection heat transfer coefficient increases with the increase in the rib height, and the maximum value occurs at a spacing of 75 mm for the rectangular and triangular ribs. The convection heat transfer coefficient in the triangular ribs is higher than in the rectangular ones, especially for the hot air side.
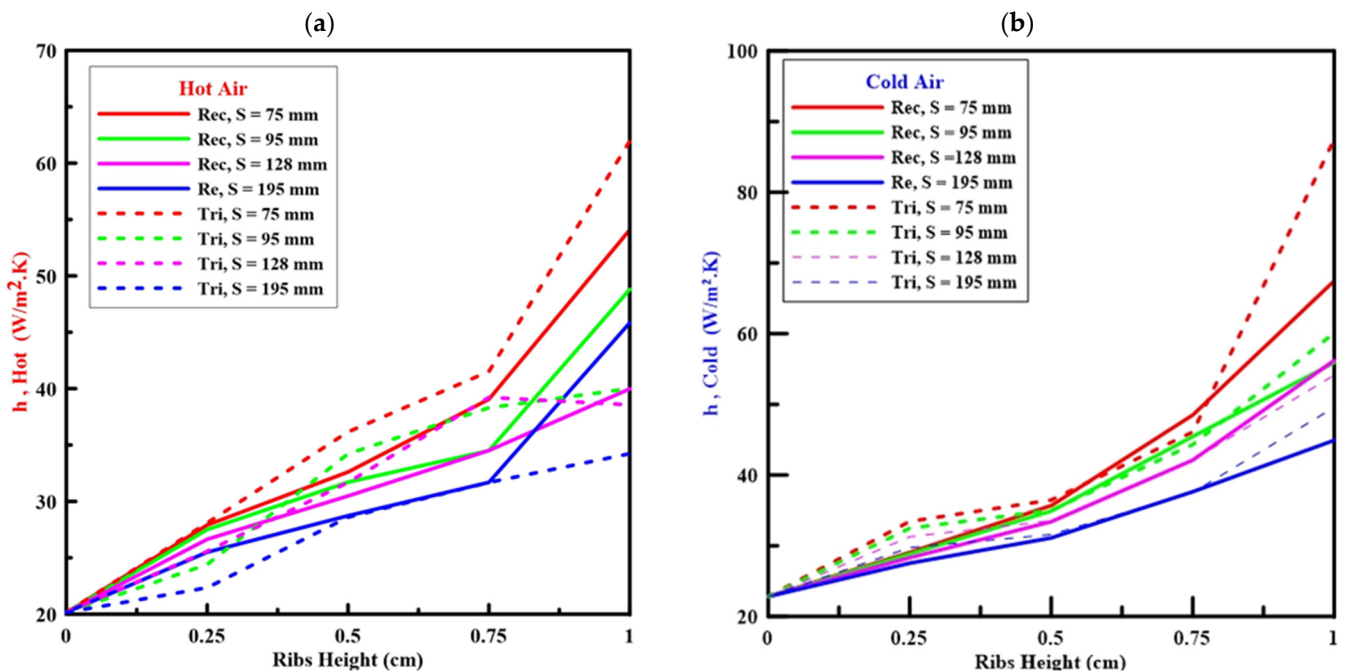
Figure 7. Convection heat transfers versus cell height for all cases of (**a**) hot and (**b**) cold air sides.

For both rectangular and triangular ribs, the convection heat transfer coefficient gradually increases until the rib height reaches 7.5 mm. At this rib height, there is a significant increase in the convection coefficient due to the higher flow turbulence as mentioned in Tables 1–3.

Figure 8 shows the pumping power variations through the channel of the hot and cold air sides with the rib height for different shapes of ribs. It can also be seen that the pumping power increases with the increase in rib height, and the maximum value occurs at 75 mm of rib spacing for the rectangular and triangular ribs.
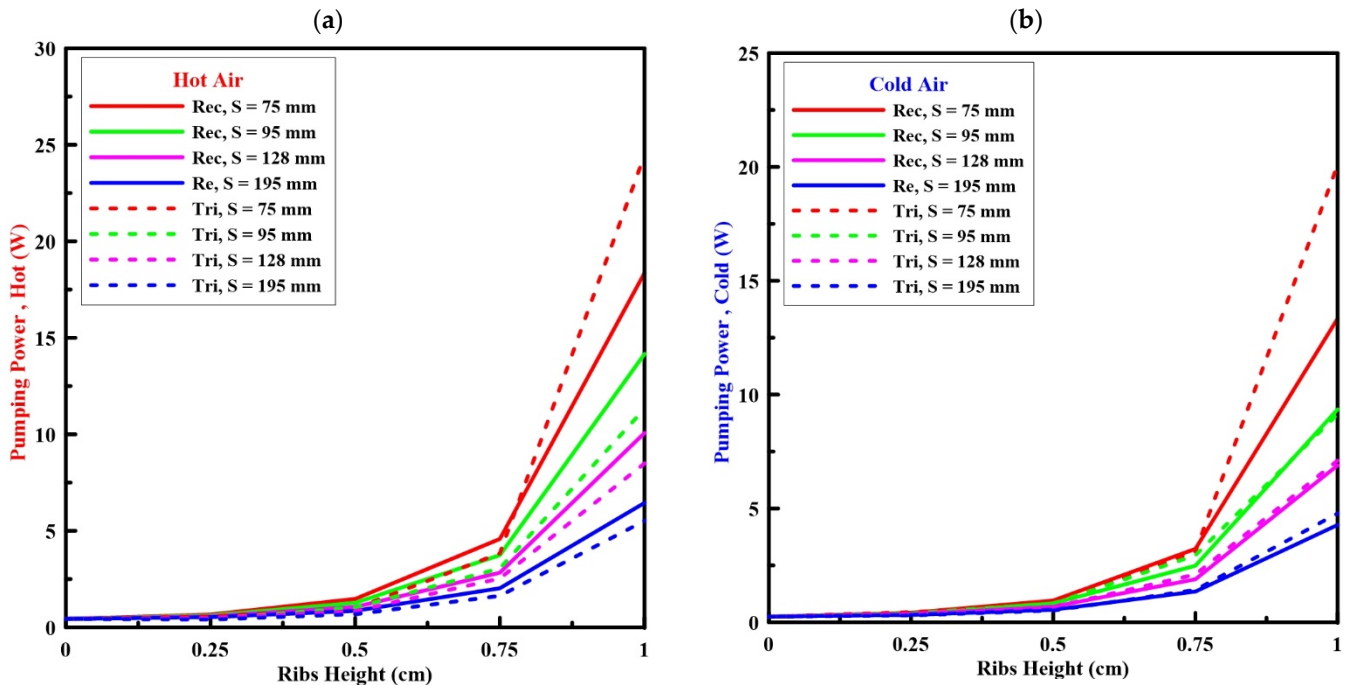

Figure 8. Pumping power required with cell height for the (**a**) hot and (**b**) cold air sides.

For the hot and cold air sides, the pumping power for rectangular and triangular ribs almost has the same value and gradually increases with the rib height until it reaches 7.5 mm. At this rib height, there is a significant increase in the pumping power due to the big increase in the friction value.

It can be observed that increasing the rib's height and number increases the turbulence intensity and velocity, which can improve the thermal performance of the flat plate heat exchanger. However, the enhancement of heat transfer by using ribs occurs with an increase in the friction value. Therefore, it is essential to calculate the thermal-hydraulic parameter, which combines the enhancement in the heat transfer and pressure drop due to friction through the channel, to obtain the best number and height of the cell.

Figure 9 shows the disparity of the overall heat transfer coefficient at different heights of ribs, as the overall heat transfer coefficient increases when increasing the height of ribs. The overall heat transfer has a rapid increase after the rib height of 7.5 mm in both shapes due to the increase in the turbulence intensity in the fluid flow because of increasing the rib height. The overall heat transfer coefficient has a small increase with the rib height at the spacing of 195 mm in the two shapes of ribs. The other ribs' spacings have slight differences between the triangular and rectangular ribs until reaching the 7.5 mm rib height. The overall heat transfer coefficient in the rectangular ribs is greater than the triangular ribs in the spacing cases of 95 and 128 mm due to the separation of the fluid in the triangular rib after this height. The spacing of 75 mm (5 ribs) creates a small distance between ribs, therefore the effect of fluid separation in triangular ribs decreases and has a higher overall heat transfer value than in rectangular ribs.
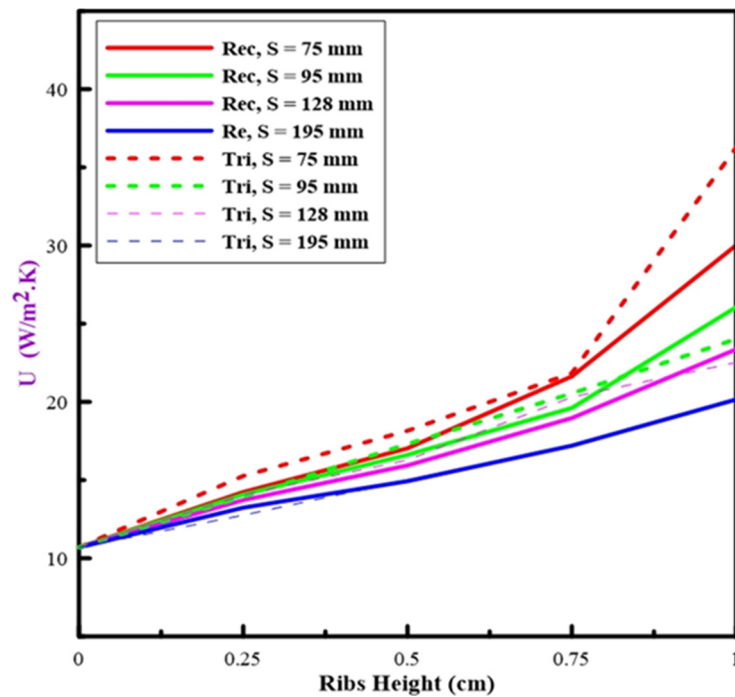
Figure 9. Overall heat transfer coefficient versus cell height for all cases.

Figure 10 presents the thermal-hydraulic parameter with the rib's height. With an increasing rib height, the thermal-hydraulic parameter increases until it reaches the highest value and then begins to decrease for both hot and cold airflow due to the increase in the value of the friction. At this point, the fiction value is higher than the improvement in the heat transfer rate.
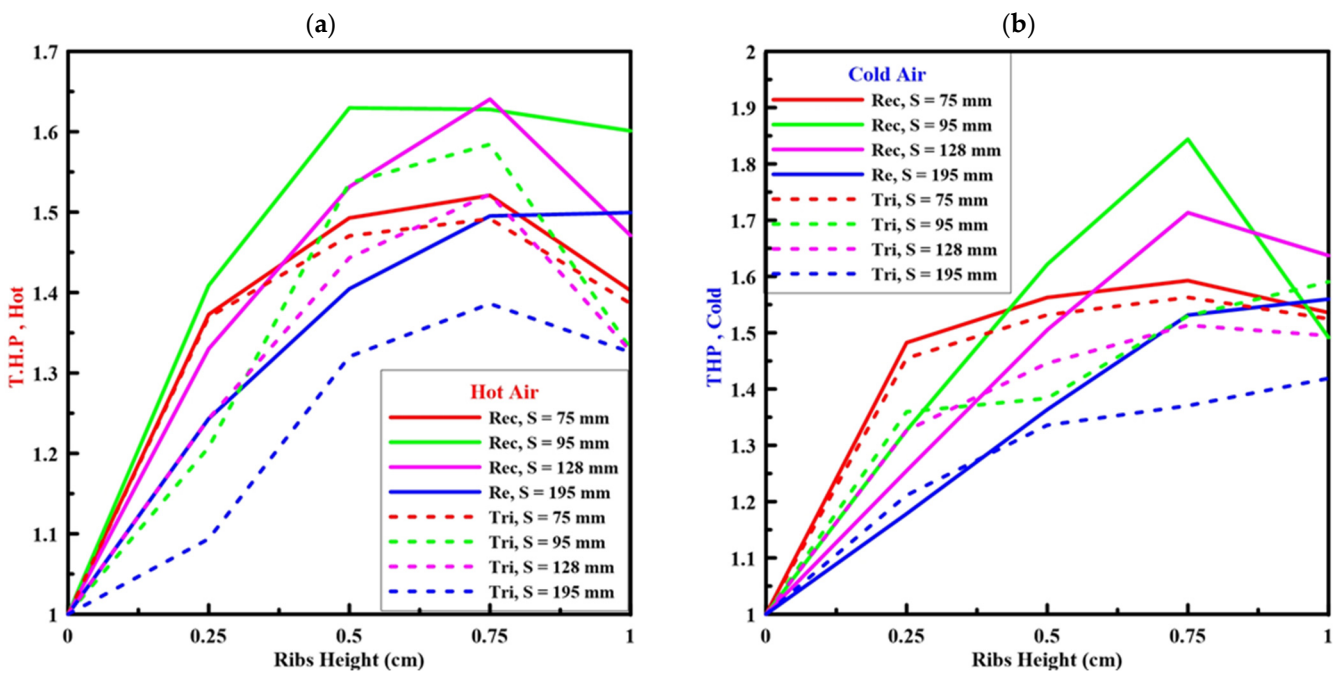

Figure 10. Thermal hydraulic parameter with the cell height for (**a**) hot and (**b**) cold air sides.

The thermal-hydraulic parameter value with rectangular ribs is higher than the value of triangular shapes. The maximum thermal-hydraulic parameters are 1.62 and 1.84 for the hot and cold airflow at a height of 75 mm and a spacing of 95 mm, respectively. According

to the previous results, ribs with a height and spacing of 75 mm and 95 mm, respectively, were selected as the optimal design for the flat plate heat exchanger.

5. Conclusions

A numerical simulation for the heat transfer and fluid flow in the ribbed flat plate heat exchanger (rectangular and triangular ribs) is developed for various spacing distances and heights, and the following results are drawn from this work:

1. The ribs' shape and the value of the Reynolds number have a great effect on the fluid motion. Therefore, the motion of a high-Reynolds-number fluid as in the cold airflow has a wavy style when passing through the triangular ribs. Due to that, there is non-complete contact with the wall at some points on the cold air side.
2. The highest values of the thermal-hydraulic parameters are 1.62 and 1.84 for the hot air and cold air sides, in the rectangular ribs, with a thickness, height, and spacing of 5mm, 75 mm, and 95 mm, respectively.

It is worth mentioning that the rectangular ribs have the maximum value of thermal performance at high and low values of the Reynolds number of turbulent flows compared to the triangular ribs. The present design of a flat plate heat exchanger can be used in waste heat recovery systems.

References

1. Promvonge, P.; Skullong, S. Augmented Heat Transfer in Tubular Heat Exchanger Fitted with V-Baffled Tapes. *Int. J. Therm. Sci.* **2020**, *155*, 106429. [CrossRef]
2. Ajarostaghi, S.S.M.; Zaboli, M.; Javadi, H.; Badenes, B.; Urchueguia, J.F. A Review of Recent Passive Heat Transfer Enhancement Methods. *Energies* **2022**, *15*, 986. [CrossRef]
3. Sarafraz, M.M.; Hormozi, F. Comparatively Experimental Study on the Boiling Thermal Performance of Metal Oxide and Multi-Walled Carbon Nanotube Nanofluids. *Powder Technol.* **2016**, *287*, 412–430. [CrossRef]
4. Sarafraz, M.M.; Nikkhah, V.; Madani, S.A.; Jafarian, M.; Hormozi, F. Low-Frequency Vibration for Fouling Mitigation and Intensification of Thermal Performance of a Plate Heat Exchanger Working with CuO/Water Nanofluid. *Appl. Therm. Eng.* **2017**, *121*, 388–399. [CrossRef]
5. Soliman, A.S.; Zhu, S.; Xu, L.; Dong, J.; Cheng, P. Melting Enhancement of Nano-Phase Change Material in Cylindrical Enclosure Using Convex/Concave Dimples: Numerical Simulation with Experimental Validation. *J. Energy Storage* **2021**, *44*, 103470. [CrossRef]
6. Soliman, A.S.; Zhu, S.; Xu, L.; Dong, J.; Cheng, P. Efficient Waste Heat Recovery System for Diesel Engines Using Nano-Enhanced Phase Change Materials. *Case Stud. Therm. Eng.* **2021**, *28*, 101390. [CrossRef]
7. Soliman, A.S.; Xu, L.; Dong, J.; Cheng, P. A Novel Heat Sink for Cooling Photovoltaic Systems Using Convex/Concave Dimples and Multiple PCMs. *Appl. Therm. Eng.* **2022**, *215*, 119001. [CrossRef]
8. Rafee, R. Entropy Generation Calculation for Laminar Fully Developed Forced Flow and heat Transfer of Nanofluids inside Annuli. *J. Heat Mass Transf. Res.* **2014**, *1*, 25–33.
9. Duangthongsuk, W.; Wongwises, S. An Experimental Study on the Heat Transfer Performance and Pressure Drop of TiO_2-Water Nanofluids Flowing under a Turbulent Flow Regime. *Int. J. Heat Mass Transf.* **2010**, *53*, 334–344. [CrossRef]
10. Soliman, A.S.; Zhu, S.; Xu, L.; Dong, J.; Cheng, P. Design of an H_2O-LiBr Absorption System Using PCMs and Powered by Automotive Exhaust Gas. *Appl. Therm. Eng.* **2021**, *191*, 116881. [CrossRef]

11. Li, Z.; Lu, J.; Tang, G.; Liu, Q.; Wu, Y. Effects of Rib Geometries and Property Variations on Heat Transfer to Supercritical Water in Internally Ribbed Tubes. *Appl. Therm. Eng.* **2015**, *78*, 303–314. [CrossRef]

12. Durga Prasad, P.V.; Gupta, A.V.S.S.K.S.; Sreeramulu, M.; Sundar, L.S.; Singh, M.K.; Sousa, A.C.M. Experimental Study of Heat Transfer and Friction Factor of Al$_2$O$_3$ Nanofluid in U-Tube Heat Exchanger with Helical Tape Inserts. *Exp. Therm. Fluid Sci.* **2015**, *62*, 141–150. [CrossRef]

13. Furlani, L.; Armellini, A.; Casarsa, L. Rotational Effects on the Flow Field inside a Leading Edge Impingement Cooling Passage. *Exp. Therm. Fluid Sci.* **2016**, *76*, 57–66. [CrossRef]

14. Ma, C.; Chen, X.; Wang, J.; Zang, S.; Ji, Y. An Experimental Investigation of Heat Transfer Characteristics for Steam Cooling and Air Cooling in a Rectangular Channel Roughened with Parallel Ribs. *Exp. Therm. Fluid Sci.* **2015**, *64*, 142–151. [CrossRef]

15. Moon, M.A.; Park, M.J.; Kim, K.Y. Evaluation of Heat Transfer Performances of Various Rib Shapes. *Int. J. Heat Mass Transf.* **2014**, *71*, 275–284. [CrossRef]

16. Wongcharee, K.; Eiamsa-ard, S. Heat Transfer Enhancement by Using CuO/Water Nanofluid in Corrugated Tube Equipped with Twisted Tape. *Int. Commun. Heat Mass Transf.* **2012**, *39*, 251–257. [CrossRef]

17. Manca, O.; Nardini, S.; Ricci, D. A Numerical Study of Nanofluid Forced Convection in Ribbed Channels. *Appl. Therm. Eng.* **2012**, *37*, 280–292. [CrossRef]

18. Casarsa, L.; Arts, T. Experimental Investigation of the Aerothermal Performance of a High Blockage Rib-Roughened Cooling Channel. *J. Turbomach.* **2005**, *127*, 580–588. [CrossRef]

19. Cho, H.H.; Lee, S.Y.; Wu, S.J. The Combined Effects of Rib Arrangements and Discrete Ribs on Local Heat/Mass Transfer in a Square Duct. In *Turbo Expo: Power for Land, Sea, and Air*; American Society of Mechanical Engineers: New York, NY, USA, 2001.

20. Ligrani, P.M.; Mahmood, G.I. Spatially Resolved Heat Transfer and Friction Factors in a Rectangular Channel with 45-Deg Angled Crossed-Rib Turbulators. *J. Turbomach.* **2003**, *125*, 575–584. [CrossRef]

21. Soliman, A.S.; Radwan, A.; Xu, L.; Dong, J.; Cheng, P. Energy Harvesting in Diesel Engines to Avoid Cold Start-up Using Phase Change Materials. *Case Stud. Therm. Eng.* **2022**, *31*, 101807. [CrossRef]

22. ANSYS. *Ansys Fluent 12.0 User's Guide*; Fluent Documentatation; Ansys: Canonsburg, PA, USA, 2009.

23. Nanan, K.; Piriyarungrod, N.; Thianpong, C.; Wongcharee, K.; Eiamsa-ard, S. Numerical and Experimental Investigations of Heat Transfer Enhancement in Circular Tubes with Transverse Twisted-Baffles. *Heat Mass Transf.* **2016**, *52*, 2177–2192. [CrossRef]

24. Menge, B.K. Analysis of Turbulent Flow in a Pipe at Constant Reynolds Number Using Computational Fluid Dynamics. Ph.D. Thesis, Jomo Kenyatta University of Agriculture and Technology, Juja, Kenya, 2014.

25. Abdurazzaq, T.; Togun, H.; Kazi, S.; Mariah Adam, N. Numerical Simulation on Heat Transfer Enhancement in Channel by Triangular Ribs. *Int. J. Mech. Ind. Sci. Eng.* **2013**, *7*, 434–438.

26. Wang, H.T.; Lee, W.B.; Chan, J.; To, S. Numerical and Experimental Analysis of Heat Transfer in Turbulent Flow Channels with Two-Dimensional Ribs. *Appl. Therm. Eng.* **2015**, *75*, 623–634. [CrossRef]

27. Manca, O.; Nardini, S.; Ricci, D. Numerical Analysis of Water Forced Convection in Channels with Differently Shaped Transverse Ribs. *J. Appl. Math.* **2011**, *2011*, 323485. [CrossRef]